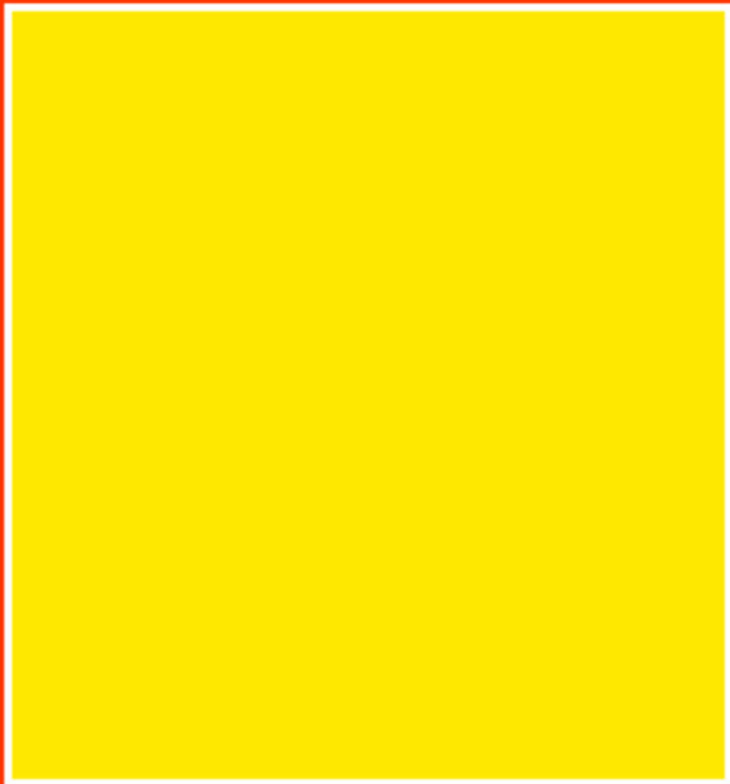




Edited by
F.R.N. Nabarro and J.P. Hirth

Dislocations in Solids

Volume 12



Dislocations in Solids

Volume 12

This page intentionally left blank

Dislocations in Solids

Volume 12

Edited by
F. R. N. NABARRO

*School of Physics
University of the Witwatersrand
Johannesburg, South Africa*

and

J. P. HIRTH
Hereford, AZ, USA

2004



Amsterdam • Boston • Heidelberg • London • New York • Oxford
Paris • San Diego • San Francisco • Singapore • Sidney • Tokyo

ELSEVIER B.V. ELSEVIER Inc. ELSEVIER Ltd ELSEVIER Ltd
Sara Burgerhartstraat 25 525 B Street, Suite 1900 The Boulevard, Langford Lane 84 Theobalds Road
P.O. Box 211, San Diego, CA 92101-4495 Kidlington, Oxford OX5 1GB London WC1X 8RR
1000 AE Amsterdam USA UK UK
The Netherlands

© 2004 Elsevier B.V. All rights reserved.

This work is protected under copyright by Elsevier B.V., and the following terms and conditions apply to its use:

Photocopying

Single photocopies of single chapters may be made for personal use as allowed by national copyright laws. Permission of the Publisher and payment of a fee is required for all other photocopying, including multiple or systematic copying, copying for advertising or promotional purposes, resale, and all forms of document delivery. Special rates are available for educational institutions that wish to make photocopies for non-profit educational classroom use.

Permissions may be sought directly from Elsevier's Rights Department in Oxford, UK: phone (+44) 1865 843830, fax (+44) 1865 853333, e-mail: permissions@elsevier.com. Requests may also be completed on-line via the Elsevier homepage (<http://www.elsevier.com/locate/permissions>).

In the USA, users may clear permissions and make payments through the Copyright Clearance Center, Inc., 222 Rosewood Drive, Danvers, MA 01923, USA; phone: (+1) (978) 7508400, fax: (+1) (978) 7504744, and in the UK through the Copyright Licensing Agency Rapid Clearance Service (CLARCS), 90 Tottenham Court Road, London W1P 0LP, UK; phone: (+44) 20 7631 5555; fax: (+44) 20 7631 5500. Other countries may have a local reprographic rights agency for payments.

Derivative Works

Tables of contents may be reproduced for internal circulation, but permission of the Publisher is required for external resale or distribution of such material. Permission of the Publisher is required for all other derivative works, including compilations and translations.

Electronic Storage or Usage

Permission of the Publisher is required to store or use electronically any material contained in this work, including any chapter or part of a chapter.

Except as outlined above, no part of this work may be reproduced, stored in a retrieval system or transmitted in any form or by any means, electronic, mechanical, photocopying, recording or otherwise, without prior written permission of the Publisher.

Address permissions requests to: Elsevier's Rights Department, at the fax and e-mail addresses noted above.

Notice

No responsibility is assumed by the Publisher for any injury and/or damage to persons or property as a matter of products liability, negligence or otherwise, or from any use or operation of any methods, products, instructions or ideas contained in the material herein. Because of rapid advances in the medical sciences, in particular, independent verification of diagnoses and drug dosages should be made.

First edition 2004

Library of Congress Cataloging in Publication Data

A catalog record is available from the Library of Congress.

British Library Cataloguing in Publication Data

Dislocations in solids

Vol. 12

1. Dislocations in crystals

I. Nabarro, F. R. N. (Frank Reginald Nunes), 1916- II. Hirth, John Price, 1930-

548.8'42

ISBN: 0-444-51483-X (volume)

ISBN: 0-444-85269-7 (set)

ISSN: 1572-4859

⊗ The paper used in this publication meets the requirements of ANSI/NISO Z39.48-1992 (Permanence of Paper).

Printed in The Netherlands.

Preface

This is the first volume to appear under our joint editorship. While Volume 11 concentrated on the single topic of dislocations and work hardening, the present volume spreads over the whole range of the study of dislocations from the application by Kléman and his colleagues of homotopy theory to classifying the line and point defects of mesomorphic phases to Chaudhri's account of the experimental observations of dislocations formed around indentations.

Chapter 64, by Cai, Bulatov, Chang and Yip, discusses the influence of the structure of the core of a dislocation on its mobility. The power of modern computation allows this topic to be treated from the first principles of electron theory, and with empirical potentials for more complicated problems. Advances in electron microscopy allow these theoretical predictions to be tested.

In Chapter 65, Xu analyzes the emission of dislocations from the tip of a crack and its influence on the brittle to ductile transition. Again, the treatment is predominantly theoretical, but it is consistently related to the very practical example of alpha iron.

In a dazzling interplay of experiment and abstract mathematics, Kléman, Lavrentovich and Nastishin analyze the line and point structural defects of the many mesomorphic phases which have become known in recent years.

Chapter 67, by Coupeau, Girard and Rabier, is essentially experimental. It shows how the various modern techniques of scanning probe microscopy can be used to study dislocations and their interaction with the free surface.

Chapter 68, by Mitchell and Heuer, considers the complex dislocations that can form in ceramic crystals on the basis of observations by transmission electron microscopy and presents mechanistic models for the motion of the dislocations in various temperature regimes.

While the underlying aim of the study of dislocations in energetic crystals by Armstrong and Elban in Chapter 69 is to understand the role of dislocations in the process of detonation, it has the wider interest of studying dislocations in molecular crystals which are "elastically soft, plastically hard, and brittle".

Chaudhri in Chapter 70 discusses the role of dislocations in indentation processes, largely on the basis of the elastic analysis by E.H. Yoffe. The special case of nanoindentations is treated only briefly.

F.R.N. Nabarro
J.P. Hirth

This page intentionally left blank

Contents

Volume 12

Preface v

Contents vii

List of contents of Volumes 1–11 ix

64. W. Cai, V.V. Bulatov, J. Chang, J. Li and S. Yip
Dislocation Core Effects on Mobility 1
65. G. Xu
Dislocation Nucleation from Crack Tips and Brittle to Ductile Transitions in Cleavage Fracture 81
66. M. Kleman, O.D. Lavrentovich and Yu.A. Nastishin
Dislocations and Disclinations in Mesomorphic Phases 147
67. C. Coupeau, J.-C. Girard and J. Rabier
Scanning Probe Microscopy and Dislocations 273
68. T.E. Mitchell and A.H. Heuer
Dislocations and Mechanical Properties of Ceramics 339
69. R.W. Armstrong and W.L. Elban
Dislocations in Energetic Crystals 403
70. M.M. Chaudhri
Dislocations and Indentations 447

Author Index 551

Subject index 569

This page intentionally left blank

CONTENTS OF VOLUMES 1–11

VOLUME 1. The Elastic Theory

1979, 1st repr. 1980; ISBN 0-7204-0756-7

- J. Friedel, *Dislocations – an introduction* 1
- 1. A.M. Kosevich, *Crystal dislocations and the theory of elasticity* 33
- 2. J.W. Steeds and J.R. Willis, *Dislocations in anisotropic media* 143
- 3. J.D. Eshelby, *Boundary problems* 167
- 4. B.K.D. Gairola, *Nonlinear elastic problems* 223

VOLUME 2. Dislocations in Crystals

1979, 1st repr. 1982; ISBN 0-444-85004-x

- 5. R. Bullough and V.K. Tewary, *Lattice theories of dislocations* 1
- 6. S. Amelinckx, *Dislocations in particular structures* 67
- 7. J.W. Matthews, *Misfit dislocations* 461

VOLUME 3. Moving Dislocations

1980; 2nd printing 1983; ISBN 0-444-85015-5

- 8. J. Weertman and J.R. Weertman, *Moving dislocations* 1
- 9. *Resistance to the motion of dislocations* (to be included in a supplementary volume),
- 10. G. Schöck, *Thermodynamics and thermal activation of dislocations* 63
- 11. J.W. Christian and A.G. Crocker, *Dislocations and lattice transformations* 165
- 12. J.C. Savage, *Dislocations in seismology* 251

VOLUME 4. Dislocations in Metallurgy

1979; 2nd printing 1983; ISBN 0-444-85025-2

- 13. R.W. Balluffi and A.V. Granato, *Dislocations, vacancies and interstitials* 1
- 14. F.C. Larché, *Nucleation and precipitation on dislocations* 135
- 15. P. Haasen, *Solution hardening in f.c.c. metals* 155
 - H. Suzuki, *Solid solution hardening in body-centred cubic alloys* 191
 - V. Gerold, *Precipitation hardening* 219
- 16. S.J. Basinski and Z.S. Basinski, *Plastic deformation and work hardening* 261
- 17. E. Smith, *Dislocations and cracks* 363

VOLUME 5. Other Effects of Dislocations: Disclinations

1980; 2nd printing 1983; ISBN 0-444-85050-3

- 18. C.J. Humphreys, *Imaging of dislocations* 1
- 19. B. Mutaftschiev, *Crystal growth and dislocations* 57
- 20. R. Labusch and W. Schröter, *Electrical properties of dislocations in semiconductors* 127
- 21. F.R.N. Nabarro and A.T. Quintanilha, *Dislocations in superconductors* 193
- 22. M. Kléman, *The general theory of disclinations* 243

23. Y. Bouligand, *Defects and textures in liquid crystals* 299
 24. M. Kléman, *Dislocations, disclinations and magnetism* 349

VOLUME 6. Applications and Recent Advances

1983; ISBN 0-444-86490-3

25. J.P. Hirth and D.A. Rigney, *The application of dislocation concepts in friction and wear* 1
 26. C. Laird, *The application of dislocation concepts in fatigue* 55
 27. C.A.B. Ball and J.H. van der Merwe, *The growth of dislocation-free layers* 121
 28. V.I. Startsev, *Dislocations and strength of metals at very low temperatures* 143
 29. A.C. Anderson, *The scattering of phonons by dislocations* 235
 30. J.G. Byrne, *Dislocation studies with positrons* 263
 31. H. Neuhäuser, *Slip-line formation and collective dislocation motion* 319
 32. J.Th.M. De Hosson, O. Kanert and A.W. Sleeswyk, *Dislocations in solids investigated by means of nuclear magnetic resonance* 441

VOLUME 7

1986; ISBN 0-444-87011-3

33. G. Bertotti, A. Ferro, F. Fiorillo and P. Mazzetti, *Electrical noise associated with dislocations and plastic flow in metals* 1
 34. V.I. Alshits and V.L. Indenbom, *Mechanisms of dislocation drag* 43
 35. H. Alexander, *Dislocations in covalent crystals* 113
 36. B.O. Hall, *Formation and evolution of dislocation structures during irradiation* 235
 37. G.B. Olson and M. Cohen, *Dislocation theory of martensitic transformations* 295

VOLUME 8. Basic Problems and Applications

1989; ISBN 0-444-70515-5

38. R.C. Pond, *Line defects in interfaces* 1
 39. M.S. Duesbery, *The dislocation core and plasticity* 67
 40. B.R. Watts, *Conduction electron scattering in dislocated metals* 175
 41. W.A. Jesser and J.H. van der Merwe, *The prediction of critical misfit and thickness in epitaxy* 421
 42. P.J. Jackson, *Microstresses and the mechanical properties of crystals* 461
 43. H. Conrad and A.F. Sprecher, *The electroplastic effect in metals* 497

VOLUME 9. Dislocations and Disclinations

1992; ISBN 0-444-89560-4

44. G.R. Anstis and J.L. Hutchison, *High-resolution imaging of dislocations* 1
 45. I.G. Ritchie and G. Fantozzi, *Internal friction due to the intrinsic properties of dislocations in metals: Kink relaxations* 57
 46. N. Narita and J.-I. Takamura, *Deformation twinning in f.c.c. and b.c.c. metals* 135
 47. A.E. Romanov and V.I. Vladimirov, *Disclinations in crystalline solids* 191

VOLUME 10. Dislocations in Solids

1996; ISBN 0-444-82370-0

48. J.H. Westbrook, *Superalloys (Ni-base) and dislocations* 1
49. Y.Q. Sun and P.M. Hazzledine, *Geometry of dislocation glide in L1₂ γ'-phase* 27
50. D. Caillard and A. Courret, *Dislocation cores and yield stress anomalies* 69
51. V. Vitek, D.P. Pope and J.L. Bassani, *Anomalous yield behaviour of compounds with L1₂ structure* 135
52. D.C. Chrzan and M.J. Mills, *Dynamics of dislocation motion in L1₂ compounds* 187
53. P. Veyssiére and G. Saada, *Microscopy and plasticity of the L1₂ γ' phase* 253
54. K. Maeda and S. Takeuchi, *Enhancement of dislocation mobility in semiconducting crystals* 443
55. B. Joós, *The role of dislocations in melting* 505

VOLUME 11. Dislocations in Solids

2002; ISBN 0-444-50966-6

56. M. Zaiser and A. Seeger, *Long-range internal stress, dislocation patterning and work-hardening in crystal plasticity* 1
57. L.P. Kubin, C. Fressengeas and G. Ananthakrishna, *Collective behaviour of dislocations in plasticity* 101
58. L.M. Brown, *Linear work-hardening and secondary slip in crystals* 193
59. D. Kuhlmann-Wilsdorf, *The LES theory of solid plasticity* 211
60. H. Mughrabi and T. Ungár, *Long-range internal stresses in deformed single-phase materials: The composite model and its consequences* 343
61. G. Saada and P. Veyssiére, *Work hardening of face centred cubic crystals. Dislocations intersection and cross-slip* 413
62. B. Viguier, J.L. Martin and J. Bonneville, *Work hardening in some ordered intermetallic compounds* 459
63. T.M. Pollock and R.D. Field, *Dislocations and high-temperature plastic deformation of superalloy single crystals* 547

This page intentionally left blank

Dislocation Core Effects on Mobility

WEI CAI* AND VASILY V. BULATOV†

Lawrence Livermore National Laboratory, University of California, Livermore, CA 94551, USA

and

JINPENG CHANG, JU LI‡ AND SIDNEY YIP§

Department of Nuclear Engineering, Massachusetts Institute of Technology, Cambridge, MA 02139, USA

*Present address: Department of Mechanical Engineering, Stanford University, Stanford, CA 94305.

†Phone: (925)423-0124. E-mail: bulatov1@lbl.gov

‡Present address: Department of Materials Science and Engineering, Ohio State University, Columbus, OH 43210.

§To whom correspondence should be addressed. Mailing address: M.I.T. Room 24-208, 77 Mass Ave, Cambridge, MA 02139. Phone: (617)253-3809. Fax: (617)258-8863. E-mail: syip@mit.edu

Contents

1. Introduction 3
 - 1.1. Basic concepts 4
2. FCC metals 6
 - 2.1. Core structure 6
 - 2.2. Mobility 9
 - 2.3. Junctions 12
 - 2.4. Cross-slip 15
 - 2.5. Interaction with point defects 17
 - 2.6. Outstanding issues 21
3. Diamond-cubic semiconductors 21
 - 3.1. Introduction 21
 - 3.2. Core structure and lattice resistance 25
 - 3.3. Secondary core defects 31
 - 3.4. Dislocation mobility 41
 - 3.5. Outstanding issues 52
4. BCC metals 53
 - 4.1. Introduction 53
 - 4.2. Core structure and lattice resistance 55
 - 4.3. Secondary core defects 61
 - 4.4. Dislocation mobility 67
 - 4.5. Outstanding issues 74
5. Concluding remarks 75
- Acknowledgements 76
- References 76

1. Introduction

The purpose of this chapter is to discuss the atomic structure and interactions in the dislocation core and their effects on dislocation mobility from the standpoint of theoretical concepts, physical models and simulation studies, with due consideration of relevant experimental results. Several previous chapters in this series provide the necessary background and more extensive exposition into several topics to be discussed here: Bullough and Tewary, “Lattice Theories of Dislocations” (vol. 2, 1979), Weertman and Weertman, “Moving Dislocations” (vol. 3, 1980), Schoeck, “Thermodynamics and Thermal Activation of Dislocations” (vol. 3, 1980), and M. Duesbery, “The Dislocation Core and Plasticity” (vol. 8, 1989). Rather than being comprehensive, our intent in this new chapter is to highlight some of the recent developments in understanding dislocation core structure and mobility. These include the driving forces and activation barriers for dislocation motion, the models which relate mobility to core properties, and the results of atomistic simulations at the levels of first-principles calculations and empirical and semi-empirical interatomic potentials. In our discussions, the major emphasis is placed on physical ideas and observations. In fact, technical details of modelling and experiments are only briefly mentioned and only where required for clarification of physics issues or for interpretation of results.

In this introductory section we provide general background and introduce several basic concepts in order to frame the discussion given in three subsequent sections dealing with particular crystal structures and material types: FCC metals, diamond-cubic semiconductors, and BCC metals. The reason for treating FCC materials first is that historically the understanding of core effects on dislocation mobility developed mostly in conjunction with this crystallography class. FCC systems give us a good chance to discuss some of the better established views and approaches and set the stage for contrasting these with more recent observations of core effects in other materials. Dislocation cores in FCC materials tend to be planar and spread out in extent; they dissociate into partials that interact with each other and move by gliding on a slip plane. Dislocation response to stress in these systems generally obeys the Schmid law established for macroscopic crystal plasticity. A well-known model, due to Peierls and Nabarro, provides a simple framework that captures dislocation core and mobility behaviour in FCC metals reasonably well. In contrast, dislocation cores and dislocation mobility in semiconductors are affected by strong directional bonding that is responsible for the appearance of a rich family of secondary core defects. The existence of glide and shuffle sets of dislocation positions in diamond cubic semiconductors introduces still more complexity with regard to the role of core mechanisms in dislocation motion. Plasticity behaviour of BCC metals is controlled, to a large extent, by the motion of screw dislocations. The core of screw dislocations is relatively compact but in some BCC metals exhibits a tendency to three-way non-planar dissociation or polarization. Dislocation mobility exhibits large deviation from the canonical Schmid behaviour as a function of stress. The connection between details of core structure and mobility of screw

dislocations in BCC metals has been a topic of intense research but remains somewhat controversial. Of all known material systems, the most pronounced and intricate core effects arguably are observed in ordered inter-metallic alloys, such as nickel-based superalloys or TiAl composites. These however are discussed in great detail in a recent volume (vol. 10) of this series and will not be considered here.

Since the most recent chapter by M.S. Duesbery (vol. 8) that was dedicated to dislocation core and crystal plasticity, several important developments have appeared that brought about significant progress towards quantitative analysis of the dislocation core structure and its effects on mobility. A major factor in these recent developments is the emergence of new capabilities for accurate first-principles electronic structure calculations of dislocation core structure, energy and mobility. Over the same period, the models based on the empirical potentials have been used to explore realistic complexity of fully three-dimensional dynamics of individual dislocations and dislocation groups. These recent simulations revealed a rich sub-structure of secondary core defects and multiple mechanisms of dislocation motion in 3D. Yet another principal development of the past decade is the emergence of the fully three-dimensional mesoscale simulation methodology of Dislocation Dynamics (DD) that can be used, in principle, for computational prediction of overall crystal plasticity behaviour from the underlying physics of dislocation motion. For this impressive development to deliver on its ultimate promise, understanding of the core mechanisms of dislocation mobility is crucial. Fidelity of DD simulations places high demands on the accuracy of dislocation mobility functions that can be derived and parameterised from direct atomistic simulations, dislocation theory and experimental observations. On the experimental side, new capabilities for HREM allow for direct observations of the secondary structure of dislocations and approach the limits of resolution required to resolve the relevant details of the dislocation core structure [1].

However, reading through this chapter one is likely to observe that the progress towards understanding dislocation core effects has not been always steady. A few seemingly well established ideas and concepts now appear to be in conflict with the more recent data, while other previous inconsistencies no longer exist in light of the new results. Even if it is disturbing that a number of key issues in dislocation mobility remain controversial, we consider this as an indication to critically revisit, given the new capabilities, some of the existing concepts in dislocation physics. We believe the situation presents an opportunity to develop new knowledge of dislocation mobility that is more coherent and quantitative than previously existed.

1.1. Basic concepts

Plastic strain produced in response to shear stress is a cumulative result of multiple displacements along the crystallographic slip planes in quanta of the Burgers vector. Conservative dislocation motion or glide involves local atomic displacements that proceed through switching one or few interatomic bonds at a time. In comparison, homogeneous shear along the crystallographic slip plane requires switching all interatomic bonds across the plane at once and, as such, must be prohibitively expensive energetically unless the stress reaches rather high values near the theoretical shear strength (typically of the order of $\mu/10$, with

μ the shear modulus of the material). Experimentally observed values of the yield stress are typically much lower than this ideal shear resistance, with notable exceptions of deformation response of whiskers [2] and single crystals under nano-indentation [3,4].

Exactly how a dislocation moves is defined by the energetics of bond-switching rearrangements required for its translation by a unit atomic distance in the glide plane. Some what loosely, one can define the core as a region of crystal lattice around the dislocation line in which the relative displacements of the neighbouring atoms exceed the elastic limit (say 2% in terms of the local shear strain). Given the highly non-linear character of interatomic interactions in the core, it is clearly the relative motion of the core atoms that contributes most to the energetics of dislocation translation. Conversely, the relative displacements of the atoms outside the core will not contribute as much to the energy of dislocation translation. The latter is a sensitive function of the core structure, including the details of the atomic arrangement in the core, and of the atomic pathways by which this structure changes when the dislocation moves. Core structure under zero stress has received much attention over the years given its real or presumed connection to the mechanisms of dislocation motion. In the subsequent sections we will discuss various approaches to modelling and observing dislocation core structure developed for various materials. We will also give examples of insights one can obtain by considering the core structure of dislocation both under zero and non-zero stress.

The core could exist in several metastable structures that differ from each other by virtue of some in-core rearrangements. Here, the nonlinear interatomic forces between the individual atoms including the local bonding topology come into play. The difference between one core structure and another manifests itself in a difference in the core free energy. Experiments are unable to provide precise information on the core energies: such data can be obtained only from atomistic calculations. Although the total (elastic + core) energy of the dislocation is a physical quantity, its partitioning into core and elastic energies is, to a large extent, arbitrary and depends on the choice of the core cutoff parameter—core reference radius. The latter should not be identified with a physical extent of the non-linear region of the core, although these two parameters are often confused. The core free energy is the factor that determines the stability of a particular atomistic structure. In comparing core energies of various metastable core structures, one must use the same core cutoff parameter which, otherwise, can be arbitrary. For the same reason, one must report a particular value of the core cutoff radius selected for partitioning the dislocation energy.

Another fundamental property is the minimum stress required for the dislocation to move, i.e. the Peierls stress. Given the defining role dislocations play in crystal plasticity, the Peierls stress is related, although not necessarily directly, to the macroscopic yield stress above which the crystal deforms plastically. In reality, dislocation motion can be assisted by thermal fluctuations. Thus the minimal stress to move a dislocation is a function of temperature and the time over which dislocation motion is observed, both in simulations or and in laboratory experiments. In contrast, Peierls stress is an idealized concept, defined as the minimal stress to move a dislocation at zero temperature. Experimentally, this is related to the yield stress measured at vanishingly low temperatures. In computational models, the zero temperature condition corresponds to quasi-static relaxations, where the system stays close to its ground state. In such cases, quantum effects of the nuclei, such as zero-point vibrations, are usually ignored, even though the interaction forces

between atoms can be solved by quantum mechanical treatment of the electrons. When the conditions are met where both thermal fluctuation and quantum tunnelling effects can be ignored, Peierls stress becomes a well defined measure of intrinsic lattice resistance to dislocation motion, and serves as a connection between experiments and simulations. We will encounter it frequently in the discussions throughout the chapter.

Closely related to the Peierls stress is another measure of the lattice resistance to dislocation motion—the Peierls barrier. It is defined as the energy barrier that a straight dislocation must surmount in order to move to a neighbouring lattice position—Peierls valley. The Peierls barrier is of course defined per unit length of the dislocation line. At a low but non-zero temperature this barrier can be overcome locally, by spontaneous formation of a kink pair which throws a small part of the dislocation into the neighbouring Peierls valley. The kinks can then propagate along the line and either recombine or run away from each other, completing translation of the whole line. Under zero stress the barriers for forward and backward motion are exactly equal. However, under non-zero stress one of these barriers is reduced while the other one becomes higher so that directional dislocation motion (glide) begins. If the stress rises still further, at some point the smaller of the two barriers vanishes altogether—this condition corresponds to reaching the Peierls stress. Also, at high enough temperatures the Peierls barrier can become totally washed out: in such conditions kink mechanisms play no or little role while the overall mobility of an unpinned dislocation is controlled by viscous friction due to the interaction between moving dislocations and phonons and electrons. All these and other, less apparent, regimes of dislocation motion are discussed in the following three sections in conjunction with FCC, diamond cubic and BCC material systems.

2. FCC metals

At room temperature, noble metals (Cu, Ag, Au), platinum group metals (Rh, Pd, Pt, Ir), some alkaline metals (Ca, Sr) and Al, Ni and Pb assume the face-centred cubic (FCC) close packed structure. FCC metals and alloys are technologically important both as structural materials (especially Al alloys and stainless steel) and as special application materials, e.g. interconnects in the electronic circuitry. Most FCC materials can combine stiffness with formability and remain ductile down to low temperatures. Because their mechanical properties can be significantly affected and improved by alloying, FCC metals are ideal base materials for alloy design. Many of the useful properties of these materials are direct results of the underlying dislocation behaviour. As such, dislocations in FCC and other close-packed metals have been the focus of much attention in the past, making these materials the most widely studied group from this point of view.

2.1. Core structure

Much of the dislocation behaviour observed in FCC metals and alloys results from the Shockley dissociation, by which perfect $\frac{1}{2}\langle 110 \rangle$ dislocations split into two partial dislo-

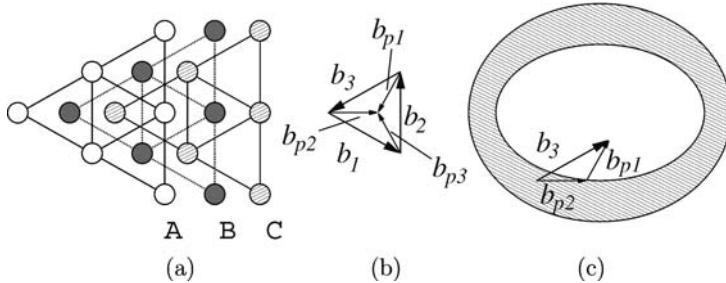


Fig. 1. (a) Plane-on view of the {111} plane of FCC lattice. (b) Perfect Burgers vectors $\vec{b}_{1,2,3}$ and partial Burgers vectors $\vec{b}_{p1,p2,p3}$ on the {111} plane. (c) A perfect dislocation loop with Burgers vector \vec{b}_3 , formed by first shifting the lattice by \vec{b}_{p2} in the outer loop, and then shifting the lattice by \vec{b}_{p1} in the inner loop, eliminating the stacking fault.

tions, bounding an area of stacking fault (SF). Expressed in Miller index notation such a reaction reads

$$\frac{1}{2}[110] = \frac{1}{6}[21\bar{1}] + \text{SF} + \frac{1}{6}[121]. \quad (1)$$

While the reduction of elastic energy achieved by this dissociation is considerable, this reaction can occur only if a stable low-energy stacking fault exists. In FCC materials stable stacking faults are found only in the {111} planes. The dissociated dislocations glide in the planes containing the stacking faults which simply move along with the partial dislocations. We emphasize that it is the availability of stable stacking faults in the {111} planes that defines the well-known predisposition for dislocations to glide on these planes, rather than the fact that these planes are the most widely spaced. In other material systems where stable stacking faults do not exist, the preference to gliding on any particular system of slip planes is less distinct (see for example the BCC section). Even in FCC aluminium which has a relatively high SF energy on the {111} plane, slip activity on {001} planes is sometimes observed [5] (p. 272).

The existence of low-energy SF on the {111} planes is a consequence of the particular packing sequence of {111} atomic layers, a universal characteristic of all FCC metals. This packing is illustrated in a plane-on view through {111} planes (see Fig. 1(a)) in which three types of atomic layers with different in-plane positions are marked as A, B and C. Notice that the three layers are shifted by $1/3(111)$ along the plane normal, forming a repeat pattern with periodicity (111) . Each layer presents a regular triangular arrangement of atoms, the layers being stacked in such a way that atoms in layer B are lined up over the centres of the triangles formed by the atoms in layer A. Likewise, atoms in C are at the corresponding centres of the triangles in B or, equivalently, in the centres of the alternate triangles in A. Atoms in the next layer A are exactly aligned with the atoms in the layer A at the bottom, thus completing the stacking period.

An intrinsic stacking fault (ISF) is formed when atoms of one layer, say C, are shifted into the “wrong” triangles of the underlying B layer, and all the layers above C are shifted by the same amount leaving the relative stacking of all other layers unchanged. At this

point, atoms in the shifted layer C are aligned with the atoms in the bottom layer A. Therefore the stacking sequence changes from $\cdots ABCAB \cdots$ to $\cdots AB|ABC \cdots$, where | indicates the location of the stacking fault. By shifting every second {111} layer, the FCC stacking can be entirely transformed into a HCP structure, $\cdots ABABAB \cdots$. Given that this shift does not affect the relative positions of first and second nearest neighbours (18 atoms altogether), the energy difference between the two structures is expectedly small. With few notable exceptions, the energy of an isolated ISF is indeed quite low for most FCC metals, typically in the range from 10 to 200 mJ/m² [5] (p. 839). Shifting successively two layers in the same sense creates the so-called extrinsic stacking fault ($\cdots AB|A|CABC \cdots$). Finally, shifting every layer above a pre-selected {111} plane in the same sense creates a perfect twin ($\cdots CBABCA \cdots$).

A partial dislocation loop can be viewed as the boundary separating an area of ISF from the rest of the plane. This partial shift can occur in any of the three equivalent directions $\vec{b}_{p1}, \vec{b}_{p2}, \vec{b}_{p3}$, shown by the arrows in Fig. 1(b). To make a complete (perfect) dislocation, two atomic layers bounding the ISF inside the first partial loop have to be shifted again along another partial shift direction. However, to avoid the atoms moving on top of each other, the second shift should be chosen from a different set of three partial shift directions, Fig. 1(c). Clearly, for every perfect dislocation with Burgers vector \vec{b} , only one combination of partial shifts \vec{b}_{p1} and \vec{b}_{p2} exists that avoids atomic run-ons and then only if introduced in a certain order. This simple observation lies behind the well-known leading-trailing partial rule usually formulated using the Thompson tetrahedron notation, see Fig. 3 (axiom 10-1 in [5]).

The separation distance between two partials is defined mainly by the balance of two forces, the elastic repulsion between the partials and the attractive “glue” force due to the ISF. For the dissociation reaction of eq. (1), continuum elasticity predicts that the equilibrium spacing X_0 between two straight parallel partial dislocations under zero stress is

$$X_0 = \frac{K'b^2}{\gamma_{\text{ISF}}}, \quad (2)$$

where K' is a certain combination of elastic constants that depends on the dislocation character angle, and γ_{ISF} is the stacking fault energy. In obtaining this formula, one considers the two partials as separate dislocations connected by an ISF. Alternatively, the whole assembly of two partials and the ISF can be viewed as an extended core of the perfect dislocation. This particular core structure of $\frac{1}{2}(110)$ dislocations determines their mobility and, through that, the overall plasticity behaviour of FCC metals and alloys.

Similar, albeit more complicated, dissociation reactions occur in $L1_2$ and $L1_0$ alloys. However, in contrast to FCC metals, dislocations in these ordered alloys can dissociate in rather complex ways due to the availability of stable stacking faults and anti-phase boundaries in various crystallographic planes. As a consequence, the ordered inter-metallic alloys exhibit perhaps the most interesting core effects in dislocation mobility. These have been reviewed extensively in volume 10 of this series.

2.2. Mobility

The common characteristic of highly mobile dislocations in FCC metals and alloys is a clear reflection of the common core structure of these dislocations. Atomistic calculations show that in FCC metals the Peierls stress is of the order of 100 MPa or lower for dislocations of all characters [6]. Correspondingly the value of the Peierls barrier is of the order of $\sim 0.005 \text{ eV}/b$. Therefore, even modest thermal agitation at low temperatures should be sufficient to surmount such a small barrier. For this reason the kink mechanisms that are so important in materials with high lattice resistance to dislocation motion (see the following sections) are not expected to play a major role in FCC metals. Molecular Dynamics (MD) simulations also reveal that at room temperature dislocations do not move in a fashion consistent with kink mechanisms; they continuously undergo small oscillations in response to thermal fluctuations. The resulting mobility is so high that in laboratory measurements it would be difficult to extract the intrinsic lattice resistance to dislocation motion where various extrinsic effects, such as dislocation–impurity interactions, are generally present. Indeed, experiments on very pure single crystals of Cu show that the yield stress essentially vanishes with increasing sample purity [7].

The reason for the low intrinsic resistance is generally the extended and planar nature of the dislocation core combined with the reduced Burgers vector of the partial dislocations. In addition to extension by dissociation, the core of partial dislocations is also planar and rather wide. It is exactly for this situation that the well-known model of Peierls and Nabarro (PN) was initially developed. This model relates resistance to dislocation motion to variations of dislocation energy as a function of the dislocation character reflecting periodicity of the host lattice. The energy is assumed to consist of two parts, an elastic strain energy stored in the two half-crystals, and a non-linear misfit energy γ due to bond distortions across the plane in which the core spreads. Suppose we consider the dislocation to be spread out in the $x-z$ plane with the dislocation line running along the z -axis, and the displacement \mathbf{u} oriented parallel to the Burgers vector \mathbf{b} . The dislocation is represented by a continuous distribution of inter-planar misfit across the special plane given by the density of a continuous dislocation distribution $\rho(x) = du/dx$, normalized to the magnitude of the Burgers vector,

$$\int_{-\infty}^{\infty} \rho(x) dx = b. \quad (3)$$

The solution appears from a balance between the stress induced by $\rho(x)$ and the restoring force $f(u) = -d\gamma/du$,

$$A \int_{-\infty}^{\infty} \frac{\rho(x')}{x - x'} dx' = -d\gamma/du = f(u), \quad (4)$$

where A is an appropriate constant and γ is assumed to be a periodic function of u . The function $\gamma(u)$ is usually referred to as the generalized stacking fault energy, or γ -surface. Mathematically the model can be viewed as a Hilbert transform between $\rho(x)$ and $f(u)$;

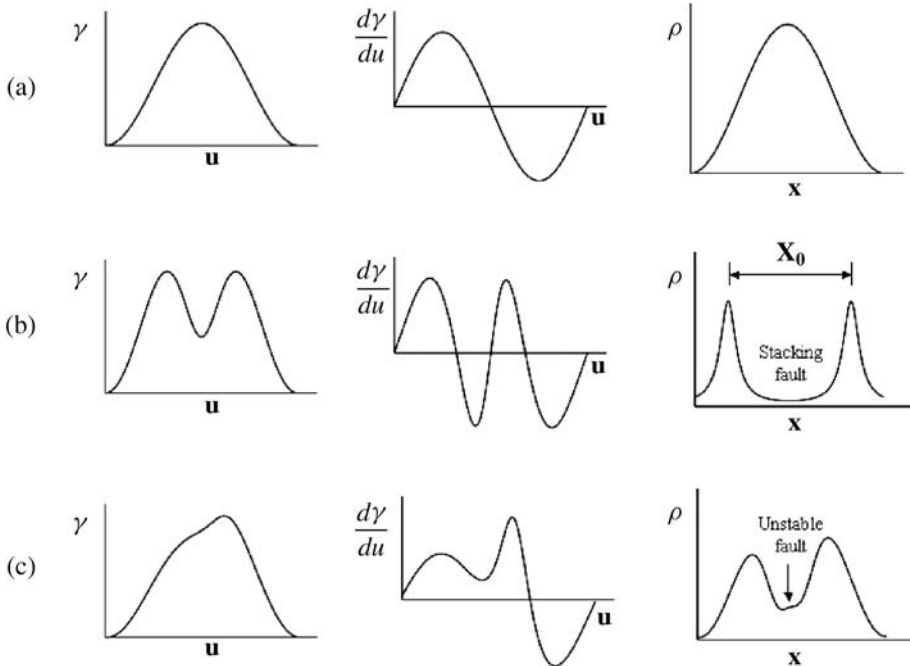


Fig. 2. The generalized stacking fault energy $\gamma(u)$, its derivative $f(u) = d\gamma(u)/du$ and the distribution of Burgers vectors $\rho(x)$, whose relationship is given in eq. (3). (a) A single peak in $\gamma(u)$ corresponds to a perfect (non-dissociated) dislocation. (b) A local minimum in $\gamma(u)$ corresponds to the stacking fault region of a dissociated dislocation. (c) Fractional dislocations bounding an unstable stacking fault.

given $\gamma(u)$ one can find $\rho(x)$ and vice versa. Fig. 2 shows three possibilities¹, a perfect dislocation (a) expressed by a single peak in $\gamma(u)$, a dislocation split into two partials with a stacking fault in between (b) showing a local minimum in $\gamma(u)$, and a dissociated dislocation with an unstable stacking fault (c) with some structure in $\gamma(u)$ but no local minimum. In case (c), one has two fractional dislocations with no well-defined stacking fault in between.

Based on the Peierls–Nabarro (PN) model, estimates of the Peierls stress τ_{PN} have been given for various materials [8–13]. According to this model [9,10], a wide core combined with a reduced Burgers vector should result in a reduced Peierls barrier. A similar relationship seems to hold for dislocation kinks: one extreme illustration was given in [13] where kinks on dissociated dislocations in Cu were examined. The kinks were found to have widths of the order of $50b$. Fittingly, the barrier for kink migration was so small that a value could not be determined. The reported upper bound estimate of the migration barrier was only 10^{-6} eV showing that the description of dislocation mobility in terms of kink mechanisms is hardly appropriate in FCC metals.

¹Based on a lecture by V. Vitek at the Tri-Lab Short Course, “Dislocations in Materials”, June 8–10, 1998, Lawrence Livermore National Laboratory, Livermore, CA.

It was noticed earlier that the interaction between partials can lead to further reduction of the lattice resistance to dislocation motion. Benoit et al. [14] observed that, depending on the balance between inter-partial repulsion and SF attraction, the distance between the partials may become incommensurate with the periodicity of the Peierls potential. Under such conditions, dislocation mobility can be further reduced by the partials overcoming the Peierls barrier in an anti-phase manner. That is, while the leading partial is scaling up the barrier the trailing partial is already on the descending slope and vice versa. On the other hand, when the equilibrium distance is commensurate with the Peierls potential, the partials have to climb up the barrier simultaneously. This idea was further explored and quantified by Schoek [15] and Nabarro [12]. Specifically, when the separation between the partials is incommensurate with the Peierls potential, the effective Peierls stress becomes much smaller than that in the commensurate case, and acquires an exponential dependence similar to the original P-N formula. Nabarro [12] thus explains the above mentioned controversy by arguing that it is the dislocations with partial separations at a half-integral multiple of the Peierls valley spacing that controls the flow stress and Harper–Dorn creep experiments. This is due to the fluctuation of the internal stresses which cause the fluctuation of the partial separation, and the fact that the least strongly pinned dislocations control the experiment. On the other hand, the Bordoni peak experiments probe all the segments of the dislocation network, and the signal is not affected much by the internal stresses. Thus, the measurements agree better with Huntington’s expression.

We note in passing that, in most FCC metals, such a coupling between the partials is expected to have a minor effect on dislocation mobility given that the lattice resistance to dislocation motion is very small in the first place. Such dynamic couplings are more likely to play a role in materials with high Peierls stress, such as silicon, as will be discussed in Section 3.

At temperatures that are not too low, dislocation mobility is controlled by various modes of dislocation–phonon interaction commonly referred to as phonon drag [16,17]. MD simulations of dislocation motion in FCC metals are relatively straightforward and allow direct calculations of the drag coefficient [18,19], which is the ratio between applied stress and dislocation velocity. In addition to high mobility, dislocation motion was observed to involve “breathing modes” in which the separation between two partials varies in time in a quasi-periodic fashion [20]. No noticeable anisotropy of dislocation mobility between edge and screw dislocations has been observed. At temperatures about 30 K and below, interaction with electrons becomes important; this aspect of the problem is beyond the reach of MD simulations.

Because the intrinsic lattice resistance to the primary $\frac{1}{2}\langle 110 \rangle\{111\}$ slip is low in FCC metals, it is mainly the interaction between dislocations with other defects that gives rise to mechanical strength of the material. For example, the formation of LC junctions by two dislocations zipping together gives rise to work hardening. At the same time, interaction between dislocations and point defects, especially impurities, is an issue of considerable practical importance, given that solution hardening is a major means for altering mechanical properties of alloys. Below we discuss the effects of dislocation interactions with other defects on its mobility in FCC metals and alloys.

2.3. Junctions

Interactions between dislocations result in the formation of junctions. The constraining effect of dislocation junctions on dislocation motion becomes increasingly more important with increasing strain. In FCC systems, junctions are formed in the collisions of two dislocations gliding on different {111} planes. For the description of dislocation reactions in FCC metals, the Thompson tetrahedron, shown in Fig. 3 [5], is helpful. Pairs of Roman letters represent perfect Burgers vectors, such as $AB = \frac{1}{2}[\bar{1}10]$, and Greek–Roman pairs represent partial Burgers vectors, such as $A\delta = \frac{1}{6}[\bar{1}2\bar{1}]$.

A Lomer–Cottrell (LC) junction is formed when two glissile dislocations BC on plane $d = (111)$ and CD on plane $b = (1\bar{1}\bar{1})$ collide and zip along direction AC . The reaction, expressed in Burgers vectors, is

$$BC(d) + CD(b) \rightarrow BD, \quad (5)$$

$$\frac{1}{2}[10\bar{1}] + \frac{1}{2}[\bar{1}\bar{1}0] \rightarrow \frac{1}{2}[0\bar{1}\bar{1}]. \quad (6)$$

The resulting dislocation has the same type of Burgers vector ($BD = \frac{1}{2}[0\bar{1}\bar{1}]$) as the incoming dislocations. But, because it is aligned along direction $AC = [01\bar{1}]$, its glide plane is (100). To appreciate the core structure of the LC junction dislocation, we note that both incoming dislocations are dissociated,

$$BC = B\delta + \delta C, \quad (7)$$

$$CD = C\beta + \beta D. \quad (8)$$

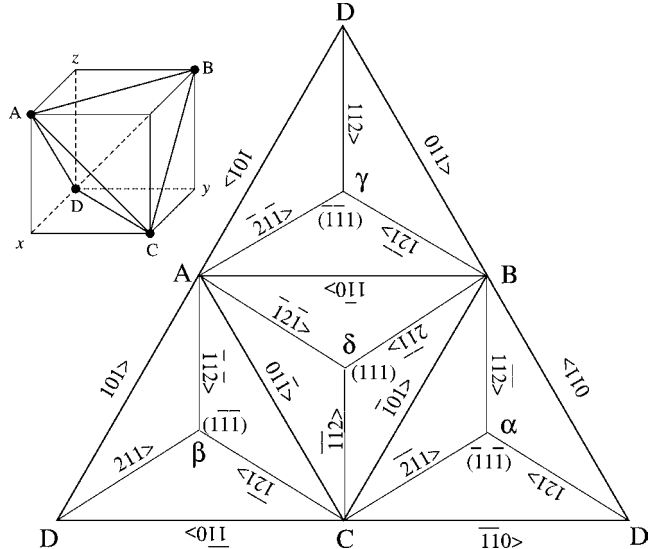


Fig. 3. Thompson tetrahedron notation for FCC slip systems.

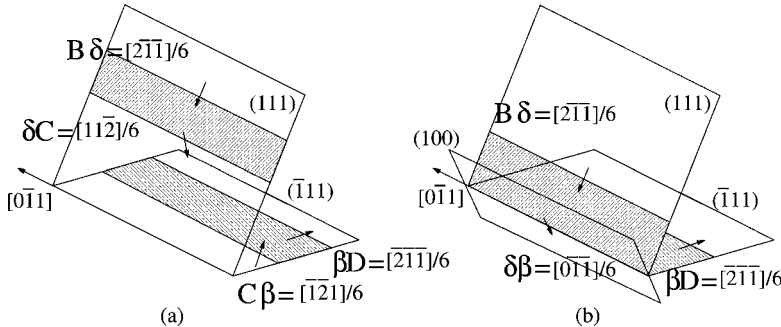


Fig. 4. Formation of Lomer–Cottrell lock junction dislocation by reaction of two glissile dissociated dislocations.

As shown in Fig. 4, the leading partials of the incoming dislocations react, thus forming a stair-rod dislocation through the reaction,

$$\delta C + C\beta \rightarrow \delta\beta, \quad (9)$$

$$\frac{1}{6}[11\bar{2}] + \frac{1}{6}[\bar{1}21] \rightarrow \frac{1}{6}[0\bar{1}\bar{1}]. \quad (10)$$

The resulting stair-rod dislocation has a Burgers vector exactly $1/3$ of that of the LC junction dislocation and lies on the same (100) glide plane. From Fig. 4(b) it is easy to see that the LC dislocation is difficult to move because it is dissociated into two {111} planes that are inclined with respect to its own glide plane (100). This is supported by direct atomistic calculations that predict that the Peierls stress of extended junction locks in Ni is of the order of 10 GPa [21,22]. The core structure of the LC junction is shown in Fig. 5.

Recently, several large-scale atomistic simulations on dislocation junction in FCC metals [21,23,24] have shown that the junction energetics computed from atomistic simulations [23] can also be accurately reproduced using a continuum model of dislocations, such as in dislocation dynamics (DD) [24]. Remarkably, two separate simulations [23,24] agreed not only in the general appearance and strength of the Lomer–Cottrel (LC) junctions in Al but also in the fine details of junction configurations. The conclusion reached in this study was that the core does not contribute appreciably to the energetics of junction formation and destruction as long as these processes proceed through the zipping-unzipping mechanisms. The same conclusion was earlier made by Friedel [25] and confirmed in [21]. However, here we note that the sessile nature of the LC junction is another very strong effect of the core structure on dislocation mobility. In the above studies, the junction dislocation never moves in its nominal (100) glide plane; the only motion that is taking place is the translation of the triple nodes along the intersection line (Fig. 6). The junction strength against unzipping is defined as the stress at which the length of the junction dislocation reduces to zero, i.e. when the junction fully unzips. Assuming that the LC junction is completely sessile in the first place (a strong core effect), the critical stress to unzip the junction can be described quite accurately by continuum models (i.e. without any core contribution). If, on the other hand, the LC junction could move in its glide plane in response to, possibly

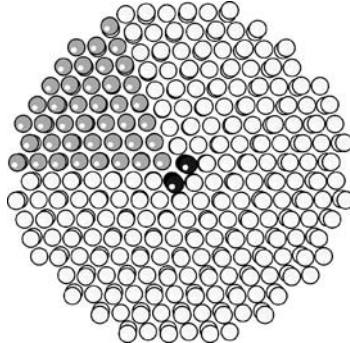


Fig. 5. Core structure of LC junction dislocation [21] viewed along $[10\bar{1}]$ junction line. The junction (black atoms) appears at the intersection of two stacking faults resulting from two intersecting partial dislocations, each of a mixed, 30° character with respect to the junction line direction. In terms of atomic displacement, the combination of the two partials is equivalent to carving out a triangular wedge (grey atoms) and displacing the wedge matter away from the junction by $1/6[1\bar{0}\bar{1}]$ and along the junction line by $1/4[10\bar{1}]$.

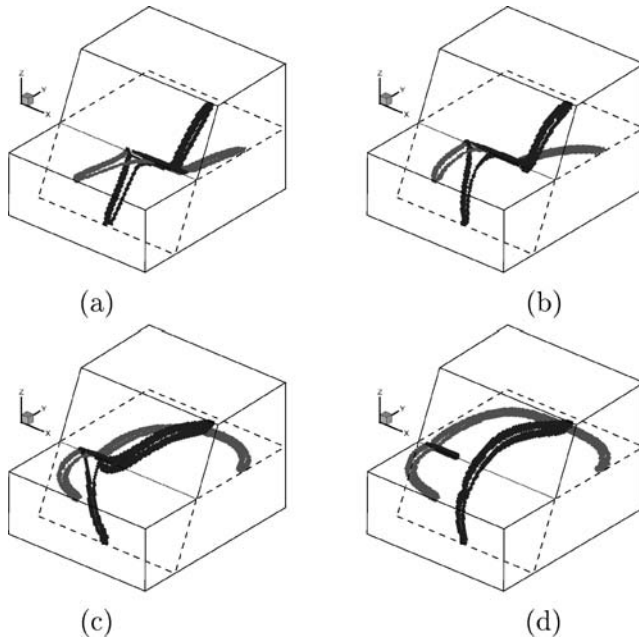


Fig. 6. Unzipping of LC lock under increasing stress [23]. Stress is (a) 0.0μ , (b) 0.011μ , (c) 0.018μ , just before the junction breaks, and (d) 0.018μ at the end of the simulation.

large, stress, the dislocation core would have a large effect on the lattice resistance to the junction motion. This possibility will be discussed shortly.

An interesting consequence of junction zipping and unzipping was uncovered in [21]. This is the mechanism of “junction replacement” involving three dislocations. Initially, a

pair of dislocations was observed to form a LC junction that unzips at a later stage in favour of a new, stronger junction, formed in a collision of one of the first two dislocations with a third dislocation. This observation suggested an interesting unit mechanism of “survival of the fittest” by which the distribution of junction strength is gradually shifted, in the course of strain hardening, towards stronger and stronger junctions. This is also a mechanism by which dislocation fluxes can effectively propagate through various elements of the hardening microstructure, e.g. dislocation bundles or cell walls, so that dislocations incorporated in a bundle or wall are released by incoming dislocations with the same Burgers vectors.

Let us now examine in more detail the core structure and its possible effect on the mobility of LC junctions. Consider the core shown in Fig. 4(b). It has been predicted that the equilibrium configuration of this complex core should be asymmetric, with one of the two stacking faults more extended than the other [26]. Indeed, such an asymmetric configuration was observed in silicon by HREM [27]. Because the symmetry can break in two ways, the ground state core structure becomes doubly degenerate. This, as always, brings about a possibility of special point defects that can form at the boundary between two alternative core variants. In the following we will often refer to such zero-dimensional objects as reconstruction defects (RD). This fine structure of the core can affect the lock strength in the sense that lock dislocations may be able to move under stress, contrary to the commonly accepted notion of their sessile nature. This is because the extent of non-planar dissociation at the RD is significantly reduced compared to the rest of the LC dislocation: this local constriction creates a soft spot for possible mobility initiation on the {100} plane. Another possible way for “sessile” locks to move is nodal mechanisms. We note that one of the triple nodes on the LC junction can become fully or partially constricted. If so, the lock dislocations can respond to stress by moving this triple node in the plane containing the lock’s Burgers vector. That the locks can be removed was actually reported based on a series of TEM observations [28]. This three-dimensional nature of dislocation junctions and locks is an interesting venue for further study.

2.4. Cross-slip

Cross-slip and climb are two mechanisms enabling dislocations to leave their glide planes. However, at low and moderate temperatures where climb is not operational, cross-slip of screw dislocations is the only means by which dislocation motion can spread to adjacent glide planes. In FCC systems, because of the planar dissociation into the Shockley partials, dislocations are confined to {111} planes in which they dissociate. Even if a dislocation is locally in a screw orientation, the planar dissociation confines it to move in the dissociation plane. Only rarely does some special event (cross-slip) takes place so that a dissociated screw dislocation changes its dissociation plane from the original glide plane to the cross-slip plane. In fact, in pure Al, where the SF energy is high and dissociation is largely suppressed, the confining effect of the {111} planes is greatly diminished and slip in planes other than {111} is observed [5] (p. 272). Consequently, cross slip in Al is expected to occur much more frequently than in other FCC metals with lower SF energy, such as Cu or Ag.

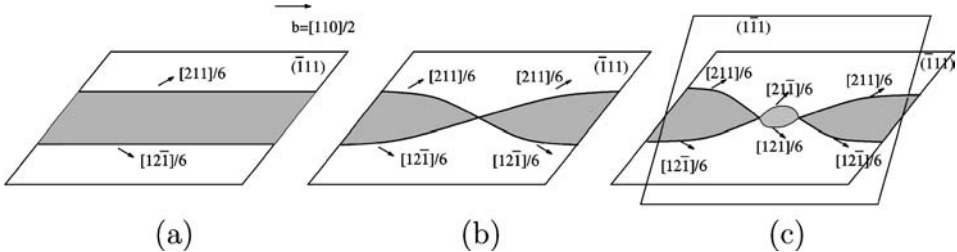


Fig. 7. Friedel–Escaig mechanism of dislocation cross-slip in FCC metals.

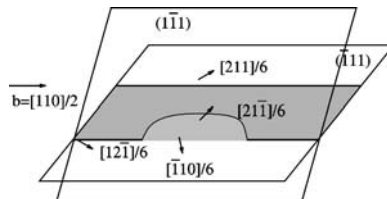


Fig. 8. Fleischer mechanism of dislocation cross-slip in FCC metals.

Two mechanisms, namely Friedel–Escaig (FE) and Fleischer (FL), have been proposed so far for dislocation cross slip in FCC metals, and are illustrated in Figs 7 and 8, respectively. The FE mechanism, which has received wide attention, involves constriction of two partials in the initial glide plane followed by re-dissociation into the cross-slip plane. In Fig. 7(a), a screw dislocation with total Burgers vector $\frac{1}{2}[110]$ is initially dissociated in $(\bar{1}11)$ plane, with the Burgers vectors for leading and trailing partials being $\frac{1}{6}[211]$ and $\frac{1}{6}[12\bar{1}]$, respectively. In Fig. 7(b), the two partials are shown to constrict to a point, assisted by thermal fluctuation and, possibly, local stress. Finally, in Fig. 7(c) the dislocation re-dissociates in $(\bar{1}11)$ plane at the constriction point into two different partials, $\frac{1}{6}[21\bar{1}]$ and $\frac{1}{6}[121]$ respectively.

Although the FE mechanism has become widely accepted, until recently there has been no conclusive data to support its validity, except some indirect experimental evidence [29]. Recently, the mechanism of cross-slip in FCC Cu was examined in full atomistic details [30–32]. The FE cross-slip mechanism was shown to have a reasonably low activation barrier, especially if cross-slip is initiated at a pre-existing jog. Although the activation energy for the FE mechanism is seemingly in agreement with experimental estimates, some uncertainty still exists since the Fleischer (FL) mechanism of cross-slip may be a viable alternative to FE.

In the FL mechanism, dislocation constriction is not required. As shown in Fig. 8, a small segment on the trailing partial emits a small area of stacking fault in the cross-slip plane. In the cross-slip plane, this stacking fault is bounded by the leading $\frac{1}{6}[21\bar{1}]$ partial on one side and a $\frac{1}{6}[\bar{1}10]$ stair rod on the other. As the stacking fault in the cross-slip plane expands, the stacking fault on the original plane contracts around the stair rod dislocation. The leading $\frac{1}{6}[211]$ partial in the original plane eventually combines with the stair rod

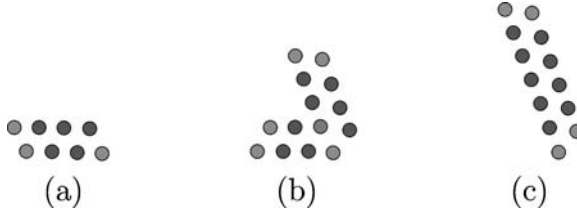


Fig. 9. Fleisher mechanism of dislocation cross slip in FCC Al observed in atomistic simulations. Atoms are shaded according to the so called centro-symmetry deviation (CSD) parameter. Only atoms with CSD significantly different from zero, i.e. local packing different from perfect FCC are shown.

dislocation and forms the trailing $\frac{1}{6}[121]$ partial which is now ready to glide on the cross-slip plane. The end result is exactly the same as that shown in Fig. 7(c) but the atomic pathway is very different from the FE mechanism.

The FL mechanism was observed [198] in atomistic simulations of stress driven cross-slip in FCC Al, using the Ercolessi–Adams potential [34]. Fig. 9 shows the dislocation core structure before, during and after the cross-slip event. Only atoms with local packing significantly different from that of FCC are shown, indicating the position of stacking faults and partials. The simulation is quasi 2-dimensional in that the simulation cell is periodic along the dislocation line. In this case, the entire dislocation line undergoes cross-slip simultaneously, which is not exactly the same as the FL mechanism as shown in Fig. 8. Nonetheless, the cross-slip pathway clearly does not involve constriction and the non-planar core structure observed during the transition is in agreement with the FL mechanism. The core structure of the dislocation undergoing cross-slip via the FL mechanism resembles that of the Lomer–Cottrell dislocation junction, where the dislocation core dissociates into two {111} planes, bounding a stair-rod dislocation.

The above simulation was performed at zero temperature under shear stress τ applied in the plane perpendicular to the original glide plane. Cross-slip occurs when τ reaches 1.4 GPa. This is suggestive that the FL mechanism may become more favourable under high stress. On the other hand, the FE mechanism is usually considered to operate under low stress conditions. Further atomistic simulations in three dimensions can help establish the relative role of FE and FL mechanisms, but care should be taken to allow dislocations to explore a variety of cross-slip paths. In that regard, it should be noted that the simulations [32] that revealed the FE mechanism relied on the so called Nudged Elastic Band (NEB) method for finding a low energy pathway. Principally, the latter method is unable to sample transition paths that deviate significantly from the initial trial (or guess) path, which is usually taken as a straight line (in multi-dimensions) connecting the initial and final states. In [30–32] the initial and final states chosen for the NEB method favour the FE mechanism by symmetry.

2.5. Interaction with point defects

In this subsection we discuss a few recent results revealing the mechanisms of dislocation interaction with point defects and clusters in FCC metals. The classical theory predicts

dislocation mobility to be highly sensitive to the nature of impurities, their concentration and mobilities. A variety of interaction mechanisms have been discussed in the context of Cottrell, Suzuki and Snoek atmospheres [5] (p. 639). Although generic aspects of interaction between substitutional impurities and dislocations are well understood, computational capabilities for predictive modelling are still lacking.

The problem of dislocation–point defect interaction is complex. The simplest case is probably the interaction with a substitutional atom at a large distance away from the dislocation. In this case, electronic structure calculations can be used to compute the size and stiffness misfit associated with the alloying impurity atoms [35]. This information can then be used in an elastic model to obtain the hardening effect of the impurity due to its long range interactions with dislocations.

When point defects are mobile, or they happen to lie on the path of a moving dislocation, it becomes important to account for their short-range (core) interactions. In this case, it is necessary to study systems with a large number of atoms, which are beyond the reach of accurate electronic structure methods. Direct MD simulations of the type presented in [36] in the context of pipe diffusion can be employed for the purpose. As we are forced to use molecular dynamics methods with empirical potentials, the major difficulty is of course the notorious inaccuracy or, often, complete lack of interatomic potentials for atom–atom interactions in metals and alloys.

Considerable progress has been achieved recently in direct Molecular Dynamics modelling of dislocation interaction with interstitial and vacancy clusters in FCC metals Ni and Cu, for which reasonable interatomic potentials do exist [18,37,38]. Both vacancy and interstitial type defects were found to serve as pinning obstacles to dislocation motion and, in the short-range collisions, to be partially or completely absorbed or transformed. These mechanisms are especially important for understanding the mechanical behaviour of irradiated materials where collision cascades produce a large number of displaced atoms whose subsequent motion results in gradual evolution of radiation-induced defect microstructure, from Frenkel pairs to a distribution of defect clusters. These defects offer considerable resistance to dislocation motion and are thought to harden or even shut down dislocation multiplication leading to a characteristic upper yield behaviour followed by a sharp stress decrease at the lower yield point. At this point considerable shear localization is observed in the form of clear channels [39]. Shear localization results in high stress concentrations at the grain boundaries and can eventually lead to crack initiation.

The interaction between a moving edge dislocation and a small self-interstitial (SI) loop is considered in [18]. A four-interstitial cluster is introduced away from the glide plane of the dislocation. The interstitial cluster then relaxes into a prismatic dislocation loop that is highly mobile in the direction along its Burgers vector. The loop is observed to move to the glide plane of the dislocation and react with the leading partial. After the reaction, the loop flips its Burgers vector to direction *AD*, which is in the dislocation glide plane, but at 60° degrees to the dislocation Burgers vector, as shown in Fig. 10(a). This interstitial loop acts as a dragging point impeding dislocation motion. Fig. 10(d) shows the dislocation velocity as a function of stress with and without the attached interstitial loop. When the dislocation is free from the loop, its velocity is linear in stress at small stresses, with a friction coefficient $v_0 = \sigma b/v = 5 \times 10^{-6}$ Pa s ($T = 100$ K). At higher stress the velocity function bends and reaches a plateau at about 72% of the transverse sound wave velocity

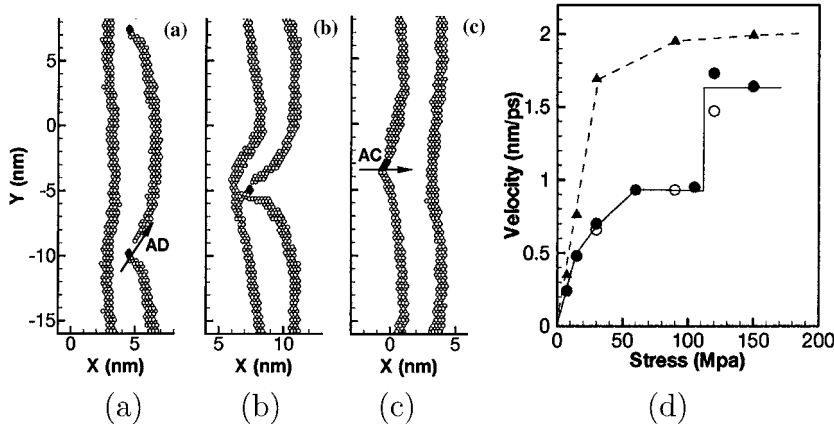


Fig. 10. (a–c) MD snapshots of edge dislocation interaction with an interstitial loop in Ni. (d) Dislocation velocity as a function of stress. The dashed curve corresponds to free dislocation at $T = 100$ K. Solid curve is for dislocation with an attached interstitial loop, with empty symbols for $T = 10$ K, full symbols for $T = 100$ K [18].

(2.9 nm/ps). This behaviour is similar to that of the edge dislocation in BCC metal Mo [40] (see Section 4).

When the loop is attached to the dislocation, as in Fig. 10(a), it increases the friction coefficient to $\nu = 8 \times 10^{-6}$ Pa s at low stresses. The dislocation velocity also saturates at a lower velocity of 0.9 nm/ps. This appears to be in line with the fact that motion direction of the loop is at 60° degrees to that of the dislocation line, so that the terminal velocity of the dislocation with the loop attached is limited to half of that of a freely gliding dislocation. Upon further increase of stress, the trailing partial catches up with the leading one, as shown in Fig. 10(b). More core reactions take place resulting in the loop attachment to the trailing partial, with its Burgers vector rotated again in the direction AC , parallel to the direction of motion of the dislocation [Fig. 10(c)]. This allows the dislocation to resume motion at a higher speed, as shown in Fig. 10(d).

The vacancy clusters in irradiated FCC metals are found to form stacking fault tetrahedra (SFT) (see [41] and references therein). The interaction between an edge dislocation and a SFT is examined in [38]. Fig. 11 shows a series of MD simulation snapshots (in a near $\bar{1}\bar{1}1$ projection) of the interaction between a moving, dissociated edge dislocation and a perfect SFT that lies on its path. The simulation was performed at an initial temperature of 100 K and under applied shear stress of 300 MPa. Fig. 11(a) is a snapshot showing the edge dislocation dissociated into two Shockley partials and the SFT at 10 ps after applying the stress. The next snapshot taken at 19.5 ps shows the leading partial that has just bypassed the SFT shearing its top by $a/6(112)$ in the process. The SFT is seen to act as a strong but shearable obstacle whose strength is expressed by the cutting angle of $\sim 80^\circ$. At 23.3 ps the trailing partial passes through the SFT that offers now significantly less resistance (Fig. 11(c)). Taking advantage of the periodic boundary conditions, the simulation was continued long enough to allow the dislocation to cut through the SFT five more times. Notably, the SFT was neither destroyed nor absorbed. Although considerably sheared, it remains largely intact (Fig. 11(d)). Qualitatively similar behaviour was observed in other

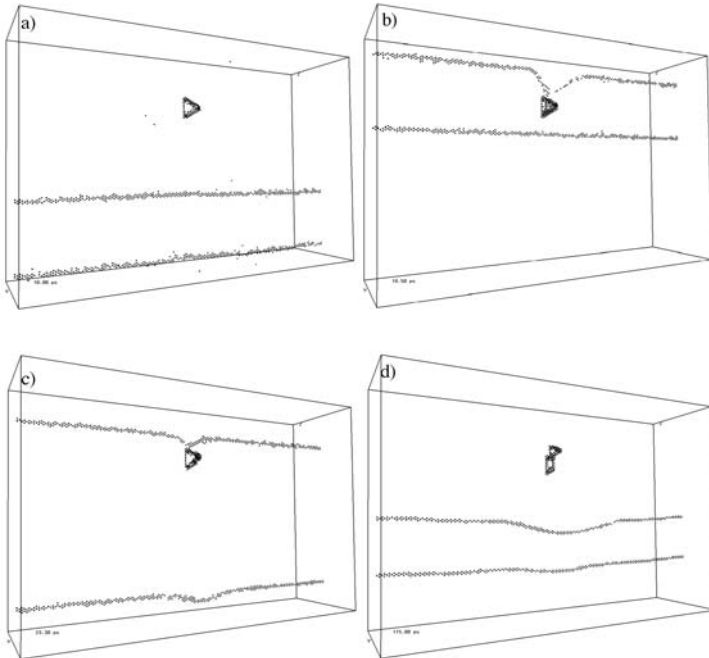


Fig. 11. MD snapshots of edge dislocation interaction with a perfect SFT in Cu at (a) 10 ps, (b) 19.5 ps, (c) 23.3 ps and (d) 115.0 ps.

simulations performed in a range of applied stress from 50 to 300 MPa for varying SFT positions with respect to the glide plane. In all cases, the initially perfect SFT acts as a strong barrier that, although considerably sheared, remains intact following the dislocation passage.

However, a totally different behaviour was observed in the case where the SFT is not initially perfect but consists of two overlapping, truncated SFTs [38]. The latter configuration has been predicted in the earlier MD and kMC simulations [42] and is more consistent with HREM images. It was found that upon contact the leading partial absorbs vacancies making up a part of the truncated SFT and climbs, forming a pair of superjogs that effectively pin this dislocation. The trailing partial eventually catches up with the leading partial, climbs and absorbs the remaining vacancies, and constricts with the leading partial at the superjogs. After that the constricted and jogged partials move together albeit with a decreased velocity. Eventually the climbed dislocation segment is seen to dissociate into separate partials again, apparently after spewing out a vacancy cluster from one of the superjogs. Although the detailed mechanism of SFT absorption has not been fully analysed, it is clear that both perfect and truncated SFT offer considerable resistance to dislocation motion.

Similar dislocation climb behaviour resulting from defect absorption was observed in [37] in molecular static simulations of the interaction between edge dislocations and self-interstitial clusters in Ni. In that case of course the dislocation climbs in the opposite

direction. One of the superjogs produced after collision is initially constricted, presumably in the form of a Lomer segment. This superjog is sessile but can transform to a glissile configuration through the incorporation of three self-interstitials, as discussed in [37]. This mechanism could explain the vacancy cluster left by the superjog in the above simulation of dislocation–SFT interaction [38].

Recent TEM observations suggest that screw dislocations in irradiated FCC metals move faster than edges, and that the screws seem more effective in both absorbing and producing the point defects [43]. In light of these observations it appears important to undertake a study similar to the one described above but for screw dislocations.

2.6. Outstanding issues

A number of outstanding issues concerning core effects on dislocation mobility in FCC metals and alloys could be mentioned. Mobility of dislocations containing extended jogs is one example. Unpinning from such obstacles involves, in some cases, non-conservative mechanisms that produce or absorb point defects or clusters. This may be true not only for screw dislocations but also for non-screws that are sometimes observed to engage in non-conservative processes [37]. Mechanisms of screw dislocation motion under high stress are poorly understood. In view of experimental indications that fast moving dislocations produce a large amount of debris [43], it appears possible that cross-slip mechanisms at high stress are very different from those at low stresses. The latter too may be a more complicated phenomenon than is currently recognized; continuum elasticity estimates and atomistic simulations both suggest that multiple mechanisms of cross-slip are likely to operate even under low stress conditions. The effect of junction nodes on the mobility of dislocations entering the node is interesting, due to the possibility of allowing glide of otherwise sessile dislocation junctions, such as extended LC locks. Finally, a major challenge for dislocation modelling is an accurate and realistic description of interactions between moving dislocations and impurity atoms and clusters. Such a description can provide the basis for understanding the thermodynamics and kinetics of co-evolution of dislocation and alloy microstructures.

3. Diamond-cubic semiconductors

3.1. Introduction

For over 40 years dislocations in semiconductors, especially in silicon, have been an active field of research driven by the need for a better understanding of defect behaviour in electronic components. At the same time, the relative ease of growing high purity single crystals with zero dislocation content makes silicon an ideal test-bed material for experiment, theory and modelling. The nucleation and migration of dislocations are of fundamental concern because their electrical activity can seriously degrade device functionality.

To a considerable extent, dislocation behaviour is determined by the structure of the host crystal lattice. Here we focus on the group with diamond cubic structure among which are

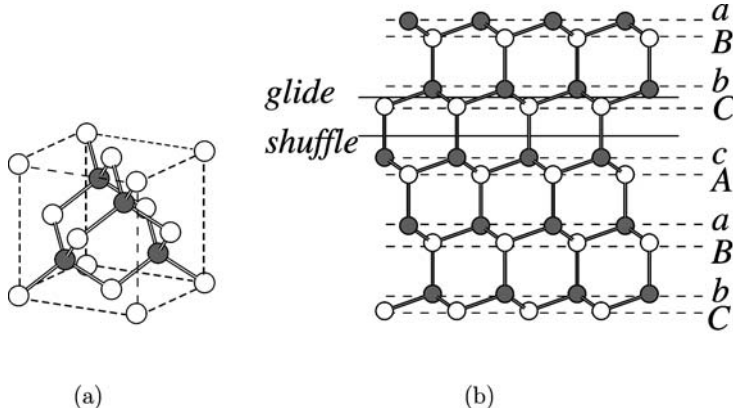


Fig. 12. Diamond cubic structure of Si lattice. The two inter-penetrating FCC lattices are shown as white and black atoms, respectively. (a) A primitive cell of the diamond cubic lattice. (b) Glide and shuffle sets of (111) planes.

elemental Si and Ge and zinc-blende III-V (GaAs) and II-VI (InP) compounds. The structure of diamond cubic lattice, consisting of two inter-penetrating face-centred-cubic (FCC) lattices offset by $\frac{1}{4}[111]$ is shown in (Fig. 12(a)). A zinc-blende structure is obtained when the two sub-lattices are occupied by different atoms, such as Ga and As. The slip systems in diamond-cubic crystals are the same as in FCC metals (see the preceding section), i.e. $\frac{1}{2}[110](111)$. However, due to the coexistence of two FCC sub-lattices, there are two different sets of (111) planes (Fig. 12(b)). The closely spaced set, e.g. between atom layers *b* and *C*, is called the *glide* set. The widely spaced set, e.g. between atom layers *C* and *c*, is called the *shuffle* set. The set of (111) planes on which dislocations reside and move has been a topic of controversy for over forty years.

Stable stacking faults can exist only in the glide set. TEM observations have produced ample evidence that dislocations in DC crystals are dissociated both in motion and at rest, at least in the usual range of experimental conditions (e.g. $T = 800\text{--}1000\text{ K}$, $\tau = 1\text{--}1000\text{ MPa}$). A typical weak-beam micrograph is shown in Fig. 13. This and other similar observations have been used to argue for the preference for dislocations to reside on the glide rather than the shuffle set, on the grounds that by dissociating into partials, a dislocation reduces its elastic energy. However, a more detailed analysis shows that core reconstruction of the partial dislocations also has to be taken into account. At moderate temperature and strain the dislocations are observed to form hexagonal loops, as in Fig. 13. In these loops the dislocations line up along the [110] directions which suggests a high Peierls barrier for the motion of 0° (screw) and 60° (mixed) dislocations.

Recently non-dissociated dislocations have been observed after deformation at low temperature and under high confining pressure. The TEM micrograph in Fig. 14 shows perfect dislocations aligned along the [110], [112] and [123] directions. The latter two directions have not been seen previously in the conventional experiments, suggesting a different core structure under large pressure. The observation of wavy slip traces is still another indication that the observed dislocations cross-slip frequently and therefore are likely to be non-

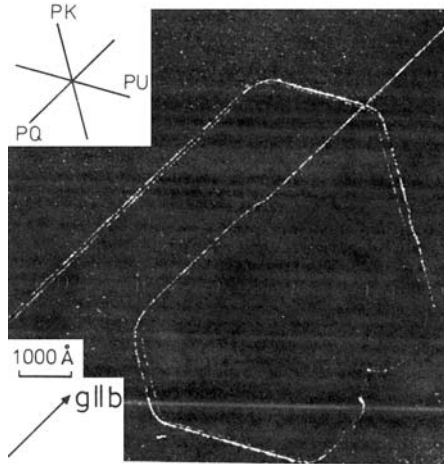


Fig. 13. Weak beam micrograph of a dissociated loop in silicon [44] deformed for 45 min at $T = 420^\circ\text{C}$ and $\tau = 256 \text{ MPa}$.

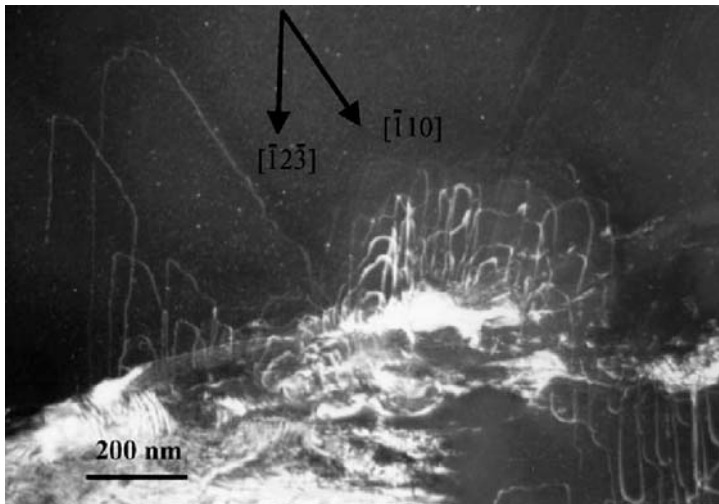


Fig. 14. Dislocation microstructure at room temperature and under confining pressure of 5 GPa. The dislocations are mostly aligned along [110] and [12̄3] directions [45].

dissociated. All this evidence points to a transition from glide to shuffle core occurring under low-temperature, high-stress deformation conditions. This topic will be discussed in light of the atomistic simulation results presented below.

Fig. 15 shows a typical set of stress-strain responses of silicon single crystals at several test temperatures. A common feature is a pre-yield peak followed by a post-yield drop. This transient behaviour reflects the delayed kinetics of dislocation multiplication and is a function of initial dislocation density. Eventually, the rate of dislocation multiplication

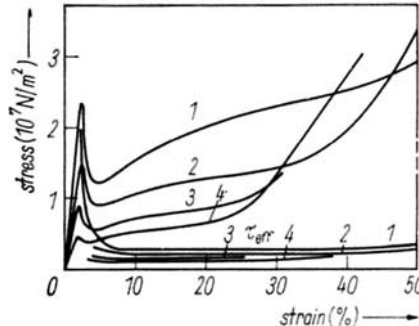


Fig. 15. Stress–strain curve of Si for strain rate $\dot{\epsilon} = 1.2 \times 10^{-4}$ and initial dislocation density $N_0 = 2 \times 10^4 \text{ cm}^{-2}$. (1) $T = 800$, (2) 850 , (3) 900 , (4) 950°C . The effective stress τ_{eff} is also plotted, which is the external stress minus the (estimated) internal stress due to mutual interactions between dislocations [46].

settles to a steady-state flow value beyond the yield point. This stress value, called the lower yield stress τ_{ly} , is often used to characterize the plastic response of the material. It is found that over a wide range of temperatures ($T = 700\text{--}2000 \text{ K}$), τ_{ly} can be represented by an exponential function

$$\tau_{\text{ly}} = C_{\text{ly}} \dot{\epsilon}^n \exp\left(\frac{Q}{nk_{\text{B}}T}\right), \quad (11)$$

where C_{ly} and n are constants independent of T and strain rate $\dot{\epsilon}$, and Q is the activation energy ($Q \sim 2 \text{ eV}$) [47]. This observation suggests that dislocation motion and, hence, plastic deformation in silicon are thermally activated.

Deviations from eq. (11) beyond the usual mid-temperature range have been reported recently. In particular, the effective activation energy was found to increase at temperatures above 1200 K . This transition is also seen in dislocation mobility measurements although its origin remains controversial. It has been suggested that a change of self diffusion mechanism in silicon at elevated temperatures is the cause [48,50]. Alternatively, the effect of dislocation–dislocation interactions has been proposed as an explanation [51]. At the low temperature end, the yield deviates from the mid-temperature behaviour but in a different sense; both the activation energy Q and the yield stress become lower than what eq. (11) would predict. This low temperature behaviour is observed in almost all diamond-cubic semiconductors, as shown in Fig. 16(b). The aforementioned change of the dislocation core structure from dissociated glide to perfect shuffle core is likely to be related to this macroscopic transition.

In the following we discuss the current understanding of dislocation core structure and the mechanisms of its motion. We will focus on those aspects of atomistic and mesoscopic theory and simulations that help in interpreting the experimental findings as well as give predictions.

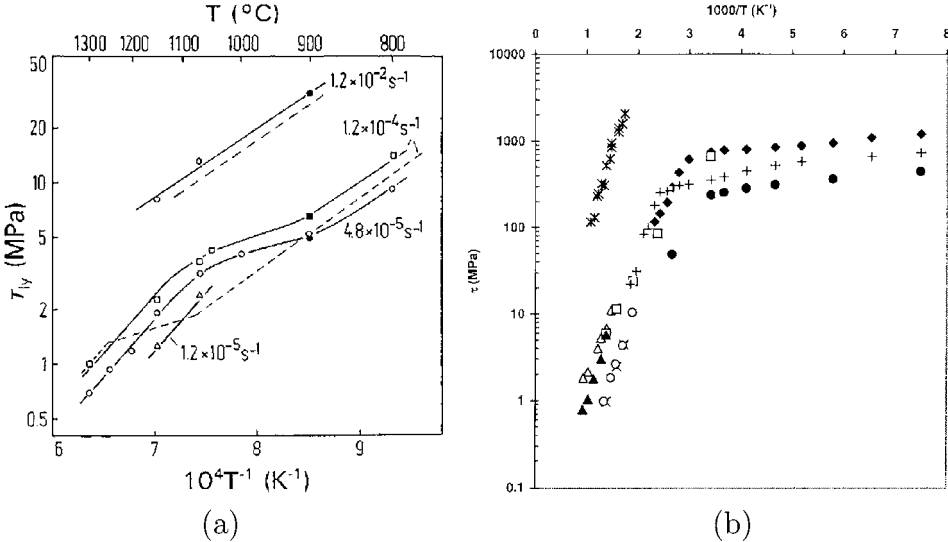


Fig. 16. (a) Lower yield stress as a function of temperature for dislocation free Si samples [48]. (b) Yield stress of Si (*), GaAs (□, ◆, △), InP (+, ▲, ×) and InSb (○, ●) as a function of temperature [49].

3.2. Core structure and lattice resistance

3.2.1. Glide-set partial dislocations

Under moderate stress and temperature conditions the dislocations in silicon and other semiconductors are generally seen to stretch along the $\langle 110 \rangle$ directions forming hexagon-shaped loops on the (111) glide plane. The dislocations are dissociated into Shockley partials connected by an intrinsic stacking fault (SF), as in

$$\frac{1}{2}[1\bar{1}0] = \frac{1}{6}[1\bar{2}1] + \frac{1}{6}[2\bar{1}1]. \quad (12)$$

Given the predominant screw or 60° character of the full dislocations, the partials are either 30° or 90° , as shown in Fig. 17. The SF energy can be estimated by comparing the separation between two partials observed in experiment [1] to that predicted by linear elasticity theory [5]. For silicon the resulting estimates range from 50 to 70 mJ/m².

A low SF energy is usually taken to be a sufficient condition for the dislocations on the glide set to dissociate, given that dissociation lowers the elastic energy of the dislocation. However, recent atomistic calculations suggest that core reconstruction can significantly alter the energy balance of the dissociation reactions in silicon [52]. Using the Stillinger-Weber (SW) interatomic model, it has been shown that only after bond reconstruction in the cores of the two partials has taken place, does dislocation dissociation become more energetically favourable than the undissociated (perfect) state.

That dislocations form hexagon-shaped loops by stretching under stress along the $\langle 110 \rangle$ directions is clearly a core effect. Since the elastic energy of dislocations is a smooth featureless function of the character angle and does not favour any particular character, except

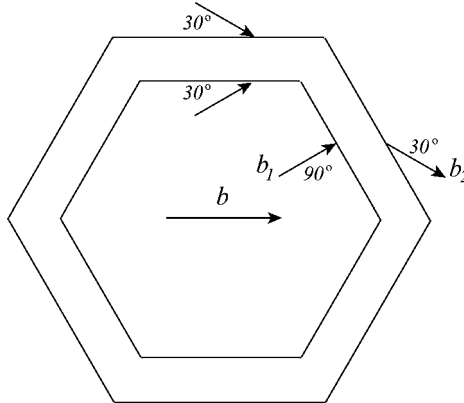


Fig. 17. Preferred dislocation line directions in silicon.

possibly screw, it must be the core energy or, even more likely, the anisotropy of dislocation mobility that is responsible for this behaviour.

Fig. 18(a) shows two atomic layers in a perfect diamond-cubic lattice; atoms above and below the (111) glide plane are denoted by white and black circles respectively. For compound semiconductors with zinc-blende structure, the open and closed circles sites would be occupied by atoms of different species. In this projection, each atom layer forms a triangular lattice so that black atoms are situated at the centres of the white triangles. Similar to FCC metals, an intrinsic stacking fault can be formed by shifting the black atoms into unoccupied white triangles. There are three ways of doing this, as indicated in Fig. 18(a). When the boundary line between the stacking fault and the perfect lattice region is drawn along a $\langle 110 \rangle$ direction, the interface (line) becomes either a 30° or a 90° partial dislocation, depending on the angle between the line and the shift direction. Fig. 18(b) shows a 30° partial. This dislocation is produced by shifting every black atom above the line along the \vec{b}_{30} direction. Fig. 18(c) shows a 90° partial obtained by shifting all black atoms above the line along the \vec{b}_{90} direction. In both cases, the dislocation line separates the SF (top) from the perfect crystal (bottom).

It was shown that [52] a screw dislocation dissociated into two 30° partials having the core structures given in Fig. 18(b) actually may have a higher total energy than its perfect non-dissociated counterpart. Nevertheless dissociation is still favoured because the cores of the partial dislocation can reconstruct to significantly reduce the final total energy. The final configuration requires some additional lattice distortions to bring the core atoms together, but this is more than off-set by a significant energy reduction associated with the pairing of the dangling bonds present in the unreconstructed cores (see Fig. 18). Removal of the dangling bonds by reconstruction is consistent with the experiments suggesting that less than 3% of the atomic sites in partial dislocation cores have unpaired orbitals [53].

In the reconstruction of the 30° partial dislocation, pairs of core atoms move towards each other to form bonded dimers, as in Fig. 19(a). As a result, the repeat distance along the dislocation core increases two-fold, from $b = \frac{1}{2}[110]$ to $2b$. *Ab initio* calculations confirm that this double-period (DP) reconstruction reduces the core energy very significantly, by

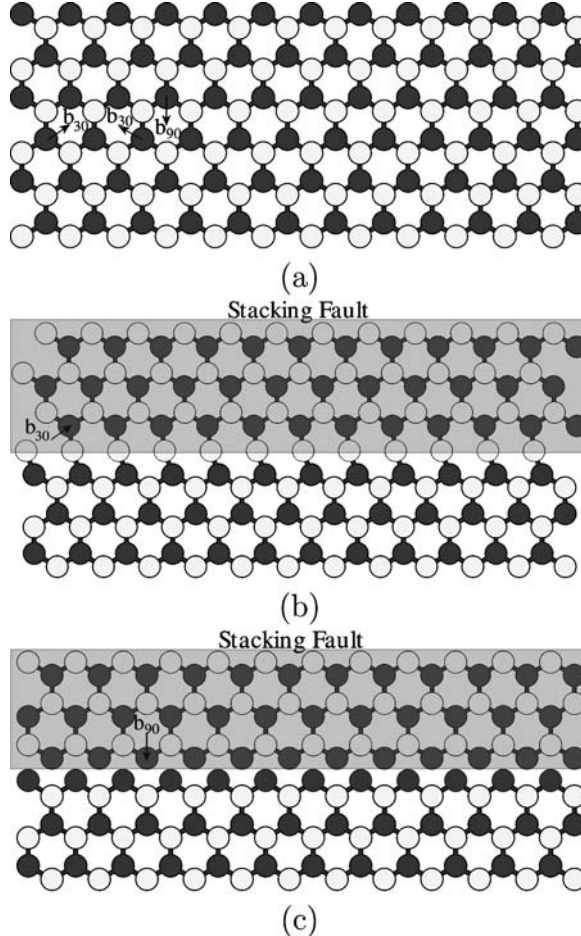


Fig. 18. (a) Perfect diamond cubic lattice. Two layers of atoms, immediately above (white) and immediately below (dark) the glide-set (111) plane are shown. Each atom has four bonds, but the fourth bonds are out of the plane and are not shown. Stacking fault can be formed by dark atoms slipping into adjacent centres of the white triangular lattice in three ways. (b) The core of a 30° partial (unreconstructed), as an interface between the stacking fault and the perfect lattice. (c) The core of a 90° partial (unreconstructed).

1.02 eV per dimer according to [54]. Core reconstruction energies in units of eV/ b from different calculations are listed in Table 1.

The 90° partial core can reconstruct in more than one way. In Fig. 19(b), two rows of atoms with dangling bonds form bonded dimers by bridging across the core. This entails some lattice distortion which, however, is more than compensated by the energy gain from the pairing of dangling bonds. The repeat distance along the dislocation line remains at b , but the mirror symmetry with respect to the plane perpendicular to the dislocation line is now broken. *Ab initio* calculations predict a energy gain for this single-period (SP) core reconstruction, at 0.42 eV/ b according to [54]. Alternatively, the dangling bonds in the 90°

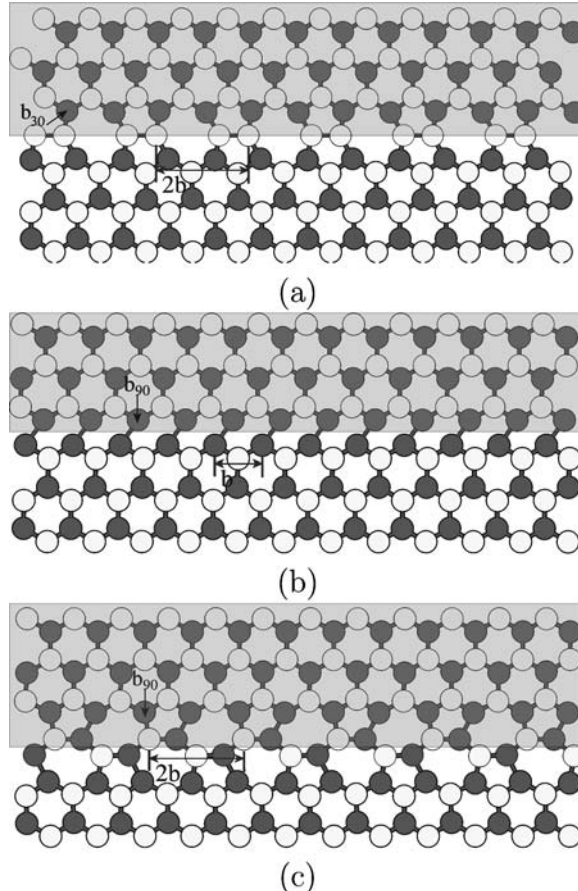


Fig. 19. Reconstructed core structures of partial dislocations in silicon. (a) Double-period core of 30° partial.
 (b) Single-period core of 90° partial. (c) Double-period core of 90° partial.

partial can be removed by a double-period (DP) reconstruction, such as shown in Fig. 19(c). This atomic rearrangement simultaneously breaks both mirror and translational symmetries of the unreconstructed core. Recent *ab initio* calculations [54–57] show that the DP core has a slightly lower energy (by ~ 0.03 eV/b) than the SP core. With the energy difference being so small, both core variants can co-exist at room temperature.

Core reconstruction is expected to have a strong influence on dislocation mobility [58], since it lowers the ground state dislocation energy and thus anchors the dislocation more strongly to the lattice. A simple measure of dislocation-lattice coupling is the Peierls stress, a minimal stress needed to move a straight dislocation at zero temperature. Atomistic simulations using SW potential have given [59] Peierls stress values for 30° and 90° partials at 21 GPa and 17 GPa, respectively; however, these results have to be taken with caution. First, the SW potential is known to have difficulty in properly describing the core reconstructions [60]. Second, the type of boundary conditions used in this study [59] has been

Table 1

Core reconstruction energy (in eV/ b , $b = 3.84 \text{ \AA}$) of 30° and 90° partials in silicon from different calculations. The energy of double-period (DP) core of 90° partial is given relative to that of the single-period (SP) core.

		30°	90° SP	90° DP
SW	[65]	0.81		
Tersoff	[66]	0.54	0.46	
EDIP	[58]	0.45	0.80	
TB	[67]	1.38	0.69	
DFT	[68]	0.53 [†]		
DFT	[54]	0.52		
DFT	[54]	0.44		
TB	[69]		0.69	
DFT	[70]		0.88	
DFT	[54]		0.42	
TB	[56]			$E_{\text{SP}} - 0.21$
DFT	[56]			$E_{\text{SP}} - 0.26$
DFT	[57]			$E_{\text{SP}} - 0.042$
DFT	[54]			$E_{\text{SP}} - 0.19$

[†]Free energy at 930 K.

found to have a large effect on the calculations of Peierls stress [52]. Nonetheless, it is generally accepted that the Peierls stress of the glide-set partials is quite high, of the order of 10 GPa, which is consistent with the observed low mobility of dislocations in silicon and its brittle behaviour at temperatures below 0.6 of the melting temperature [61]. A possible way to interpret this brittleness is to say that dislocation nucleation and propagation are insufficient to relieve the stress concentration at the crack tip [62].

Conceivably the levels of stress approaching the Peierls value for glide partials may never be achieved in a deformation experiment. This is because recent data suggest that low-temperature, high-stress plasticity is controlled by the shuffle dislocations. The highest stress of 2 GPa so far achieved in the experiment [49] is in the range of the Peierls stress for shuffle partials, but is still considerably below the estimated 10 GPa for the glide partials. On the other hand, the situation may change for compound semiconductors, given the strong influence of core reconstruction on dislocation mobility. As shown in Fig. 19, core reconstruction in the partials requires bonding of atoms of the same type. With the increasing polarity of compound semiconductors on going from IV-IV alloys, to III-V and II-VI compounds, the energy reduction by reconstruction is expected to decrease, and may eventually make core reconstruction unfavourable [63]. Consequently, the Peierls stress for partial dislocations may become much lower. Recent *ab initio* calculations suggest a strong relationship between the strength of partial reconstruction and the experimentally measured activation energy Q of dislocation mobility. As is shown in Fig. 20, Q decreases with increasing polarity, hand in hand with the decreasing reconstruction strength [64]. Additional complications arise in the compound semiconductors where two types of dislocation exist with two different types of atoms (e.g. Ga or As) residing in the core. The partials then may become charged, giving rise to strong electro-mechanical coupling.

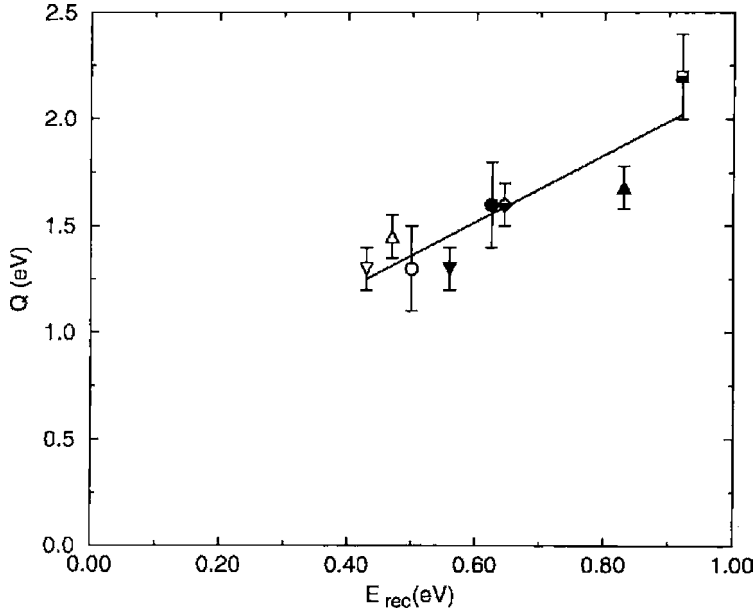


Fig. 20. Calculated core reconstruction energies for 30° partials versus experimental activation energies of 60° dislocations in type IV, Si (\square) and Ge (\diamond), and type III-V, GaP (\triangle), GaAs (∇) and GaSb (\circ), semiconductors. Open and closed symbols represent α and β dislocations, respectively. Half-filled symbols are for type IV materials [64].

3.2.2. Shuffle-set perfect dislocations

Recent experiments indicate a change of deformation mechanism in semiconductors with decreasing temperature. The signatures of this transition include a bend in the yield stress–temperature curves, such as in Fig. 16(b), as well as a change in the dislocation microstructure, as in Fig. 14. Wavy slip lines can be interpreted as indications of frequent cross slip events; they also suggest that the shuffle-set perfect screw dislocations play an important role in low temperature deformation.

Two different core structures can be considered for the perfect screw dislocations in silicon on the shuffle-set plane, as shown in Fig. 21(a) and (b). Core A [71] is centred in the 6-member ring of atoms, while core B [52] is centred on the bond between two atoms. These two different core structures allow the following interpretation. Of the two $\{111\}$ planes on which the screw dislocation can potentially move, core A is centred at the intersection of two shuffle-set planes, while core B is at the intersection of a glide-set with a shuffle-set of planes. Core A, while on shuffle-set planes, is likely to be involved in cross-slip often observed in the low temperature–high stress experiments. Core B, being in the glide set, can dissociate into glide partials and may be involved in transitions between the glide-set and shuffle-set dislocations. To understand the various possible behaviours associated with the perfect screw dislocations, an examination of the energetics of the various core configurations is in order.

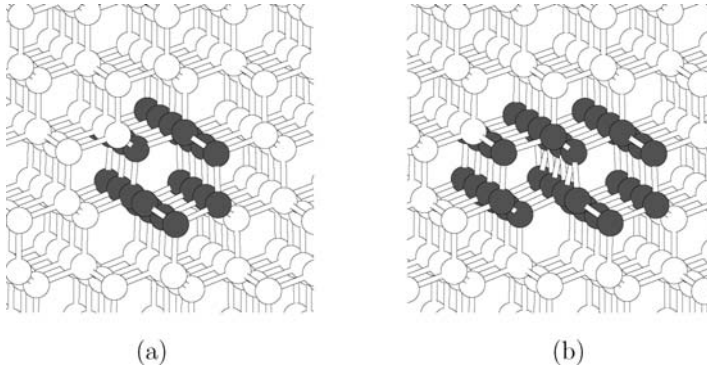


Fig. 21. Core structures of shuffle-set screw dislocation in Si. The high energy core atoms are shown in dark color. (a) Core A resides in a hexagonal ring. (b) Core B resides at the boundary between two hexagonal rings.

Recent atomistic simulations based on the SW potential [72] predicted that core B has lower energy than core A by $0.14 \text{ eV}/b$ [52]. However, still more recent *ab initio* calculations show that core A is the ground state of a perfect screw dislocation in Si, while core B is metastable, with an energy $0.38 \text{ eV}/b$ higher than that of core A [73]. This is consistent with another independent study giving $E(B) - E(A) = 0.32 \text{ eV}/b$ [74]. In addition to being metastable with respect to core A, core B is likely to be unstable at finite temperatures with respect to dissociation into glide partials. Core A, on the other hand, may be reasonably stable at lower temperatures and can contribute to plastic response.

Several attempts have been made to determine the Peierls stress of a perfect shuffle-set screw dislocation using the SW potential. The value of 5 GPa [59] first reported appears to be inaccurate, possibly due to inadequate boundary conditions. A second calculation produced a lower value of 2 GPa, which was then confirmed by still another study, this time using periodic boundary conditions [75]. Recent *ab initio* calculations predict the Peierls stress to be $3.3 \pm 0.2 \text{ GPa}$ [73] (at zero pressure). This is reasonably consistent with the low temperature yield stress measurements, which approach 1 GPa at 300 K [49]. Furthermore, compilation of low temperature data on the shear stress in semiconductors produced an estimate of 0.05μ [76], where μ the shear modulus. For silicon, this would correspond to 3.4 GPa ($\mu = 98 \text{ GPa}$), in agreement with the *ab initio* results. Given that the experiments are performed at high pressure $\sim 10 \text{ GPa}$, it is of considerable interest to compute the pressure dependence of Peierls stress *ab initio*.

3.3. Secondary core defects

The dislocation cores we have considered thus far are “perfect” one-dimensional defects. In reality, secondary point-like defects should naturally exist in the dislocation cores. Reconstruction defects (RD) are expected at the boundaries separating two core segments which have undergone atomic rearrangements in the opposite sense. They are also known as anti-phase defects, or topological solitons. Another type of point defect is a vacancy or an interstitial bound to the core, which is the unit of dislocation climb between shuffle-set

and glide-set planes. Perhaps the most important core defects are dislocation kinks, the nucleation and migration of which control the mobility of dislocations at finite temperatures. In this subsection, we discuss these three types of core defects and their possible combinations, as well as the role they play in facilitating dislocation motion.

Our discussion focuses exclusively on core defects in the glide-set partial dislocations because very little is known about the shuffle-set dislocations. We should emphasize, however, that given the importance of the shuffle-set perfect dislocations in low-temperature deformation that has been recently established, the investigation of their core defects warrants attention. We may speculate that because the core structure of the shuffle-set dislocations is simpler than that of the glide-set partials, these defects are likely to be less complex thus presenting an opportunity for a definitive study.

Much of the current understanding of the structure and energetics of core defects has come from computer simulations that rely on the use of empirical interatomic potentials and, more recently, on *ab initio* methods. Experimental evidence, while useful, has been scarce and subject to the limits of HREM. Atomistic simulation results have provided information on the various types of core defects in the glide-set partials and their topological characteristics. On the other hand, the energies of these defects are still uncertain. For various reasons, there is considerable discrepancy among the calculations reported by different groups, sometimes using the same computational models. These differences remain the major obstacles to a quantitative and predictive modelling of dislocation mobility (see next subsection) based on atomistic mechanisms. With increasing computing capabilities allowing the use of more accurate methods and larger simulation cells, many of the calculations should be repeated to obtain converged results on the core defect properties.

3.3.1. Reconstruction defects

When a symmetry-breaking reconstruction takes place, symmetry is traded for degeneracy, but it is not completely “lost” in the sense that different degenerate variants of the reconstructed core are related to each other by this symmetry operation. As an example, consider the reconstruction of the 30° partial, from Fig. 18(b) to Fig. 19(a) where the translational symmetry along the core with repeat period b is broken. As a result of reconstruction the repeat distance along the core is doubled to $2b$. At the same time, each core atom in Fig. 18(b) can choose to bond with either of its two neighbours. This leads to two variants of core reconstruction that are energetically degenerate and related to each other precisely by the broken-symmetry operation, namely translation by b . The boundary between these two reconstruction domains, a reconstruction defect (RD), is an atom that has no partner with which to bond, as shown in Fig. 22(a).

The reconstruction defects in the 90° partial appear in more varieties and are more complex. In the single-period (SP) core, the broken symmetry is the mirror symmetry with respect to the plane perpendicular to the dislocation line. Hence there are two degenerate variants of the SP core that are mirror reflections of each other. As can be seen in Fig. 22(b), there are two RD’s at the boundaries between the two variants. In the alternative double-period (DP) reconstruction of the 90° partial both the translational symmetry and the mirror symmetry are broken. To observe the breaking of the mirror symmetry, notice that the bonds parallel to the core centre (dashed line) connect either white to black atoms or black

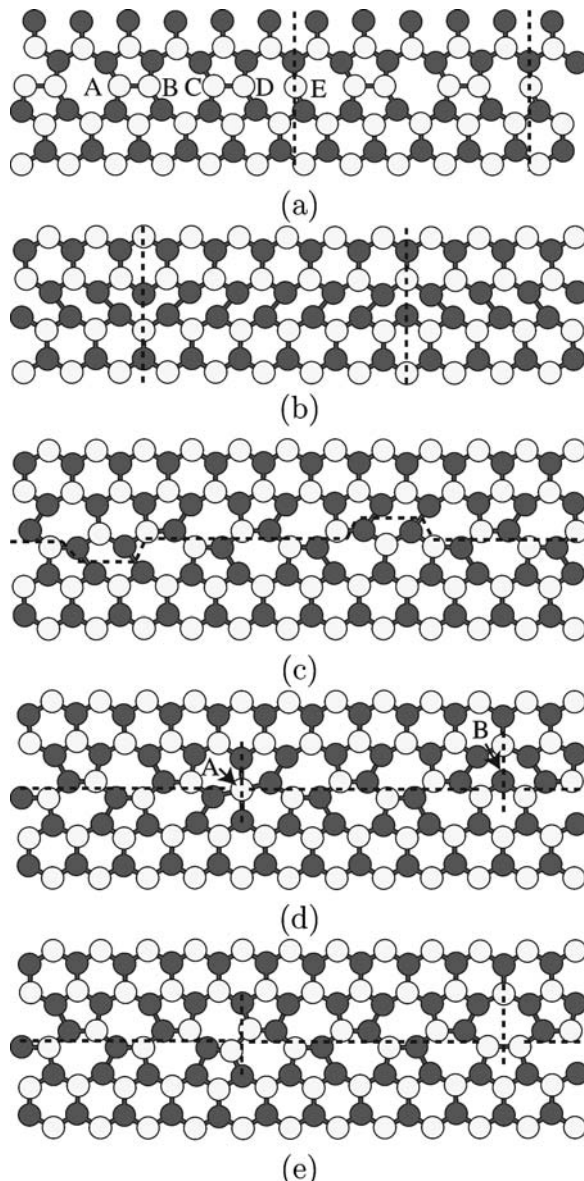


Fig. 22. Reconstruction defects (RD) in the partial dislocation cores in silicon, indicated by vertical dashed lines. (a) RD's on 30° partial. (b) RD's on single-period 90° partial. (c) RD's connecting double-period 90° partial cores that are related by translation symmetry. (d) RD's connecting double-period 90° partial cores that are related by mirror symmetry. (e) Combination of RD's in (d) with interstitial and vacancy.

to white, on going from left to right. Given that each of the two broken symmetries is a two-fold operation, the ground state of the DP core is four-fold degenerate.

Fig. 22(c) shows two DP cores that are related by translation symmetry separated by RD's. These types of RD's can be considered as short segments of the SP core, the energy of which has been calculated to be around 0.4 eV [55]. Two more reconstruction defects are shown in Fig. 22(d) separating two DP cores related to each other by the mirror symmetry. Notice that defect *A* has an over-coordinated atom while defect *B* has an under-coordinated atom (with a dangling bond). To restore four-fold coordination, one can remove the atom at *B* and insert it into *A*. The resulting configuration can be considered as composed of complexes of two RD's with a vacancy and an interstitial, respectively (Fig. 22(e)). The energies of these two complexes, computed using tight-binding methods, are 0.65 eV [55]. Complexes like these are likely to be less mobile than those in Fig. 22(d) since their motion requires that an interstitial and or a vacancy has to diffuse along with the RD's.

3.3.2. Core vacancies and interstitials

Experiments have shown that plastic deformation in semiconductors produces an elevated density of point defects [77–80]. The latter can be detected by the electron paramagnetic resonance (EPR) technique, also known as electron spin resonance—ESR. The *g* tensor of the line centres was found to be of dangling bond type, because it is almost axially symmetric. Several line centres in the spectrum, such as Si-K3 and Si-K7, were attributed to bulk vacancies and vacancy clusters, due to their comparable intensity in all crystallographically equivalent orientations. It was also observed that the production of such point defects does not seem to involve dislocation interactions, because the signal was insensitive to single slip or multi slip orientation [77].

On the other hand, line centres such as Si-K1, Si-K2 and Si-Y were attributed to vacancies inside the dislocation core, because they are not observed for all crystallographically equivalent orientations. By means of an analysis of the orientation symmetry of the signal and energy spectrum, these three line centres were identified with different vacancy configurations along the 30° partial [79,80]. Annealing the sample at $T > 800^\circ\text{C}$ was found to lead to the disappearance of K1, K2 and Y lines. Electric dipole spin resonance (EDSR) signals are also detected under such conditions, suggesting complete elimination of dangling bonds in the core [80].

Consider an imperfectly reconstructed 30° partial dislocation core as shown in Fig. 22(a). Atom *E* in the RD is bonded with three atoms (the vertical bond with an atom immediately above is not shown). Removal of atom *E* creates a vacancy with three neighbouring atoms, or V_{3c} . The symmetry of this defect, which is the combination of an RD and a vacancy, is found to be consistent with the Si-Y line of EPR. If, on the other hand, a reconstructed atom such as *A* is removed, the resulting vacancy has four neighbouring atoms, i.e. V_{4c} . This defect is consistent with the Si-K1 line of EPR. If we remove a string of core atoms, such as *A*, *B*, *C*, *D*, etc., the result is a linear chain of V_{3c} defects. This corresponds to the Si-K2 line, which was identified as a linear chain of spin centres [79].

Ab initio calculations have been carried out to study the energetics of V_{3c} , V_{4c} and V_{3c} clusters in the 30° partial dislocation core [81], corresponding to the Si-Y, K1 and K2 lines of EPR. The formation energies of such defects are 0.9 eV, 2.4 eV and 1.9 eV per vacancy, and their formation entropy is around $2k_B$. In comparison, the formation energy of a bulk

vacancy is 3.6 eV. Therefore, it is energetically favourable for bulk vacancies to agglomerate into 30° partial dislocation cores. Furthermore, they are likely to bind either with the RD or among themselves to form short segments of “hollow” dislocations. Because of its considerable formation energy, vacancy concentration in the 30° core still should be negligible at thermal equilibrium. However, this no longer needs to be the case when dislocations are driven to move by external stress, which is a highly non-equilibrium process. Complicated dislocation–point defect interactions can be expected under such conditions, where a moving dislocation core can collect vacancies from the bulk, or inject point defects into the bulk. The point defects can also facilitate or obstruct the motion of dislocations, as discussed in the next subsection.

High resolution electron microscopy (HREM) observations of dislocation cores provide valuable information [63], although the resolution is not high enough to draw definitive conclusions. Images of 90° partials are found to agree with computer models of perfectly reconstructed core atoms, indicating a low concentrations of vacancies and interstitials in the 90° partial. On the other hand, the HREM contrast in the 30° partial core is rather weak, suggesting a density of core atoms to be between 0.5 to 1.5 per core site. This suggests that the 30° partial could have a complex core structure with alternating vacancy and interstitial segments.

The conglomeration of vacancies or interstitials in the glide-set partial dislocations may give rise to structures that are equivalent to partial dislocations on the shuffle-set [63]. Such partials, produced by the climb of glide-set partials through the absorption or emission of vacancies or interstitials, round out the possible types of dislocations in diamond cubic semiconductors.

3.3.3. Kinks

The most extensively studied defects in the dislocation core are kinks. Their importance derives from the widely accepted belief that their nucleation and migration along the dislocation line are the primary mechanisms of dislocation motion at finite temperatures [5]. Atomic-sized kinks connect dislocation segments lying in the adjacent Peierls valleys separated by the smallest translation period. A kink-pair on a 30° partial [65] is shown in Fig. 23(a). The width of this kink-pair is $3b$. This defect is formed by shifting three black atoms (under the hump delineated by the dashed line) from their perfect lattice positions. Notice that the atomic configurations of the left (LK) and right (RK) kinks are topologically different from each other.

The kink-pair shown in Fig. 23(a) is not the smallest possible. The most narrow kink-pair is obtained by shifting just one black atom to form a configuration where LK and RK are immediately adjacent to each other. Subsequent migration of LK to the left and RK to the right, such as under the influence of external stress, increases their separation in discrete steps, eventually resulting in the translation of the entire partial upward by one repeat step from its original position. Fig. 23(b) shows the double-kink obtained by moving LK to the left and RK to the right, both by one b , from their positions in Fig. 23(a). Notice that the bonding configuration of the resulting left kink (LK') and right kink (RK') are different from their respective counterparts in Fig. 23(a). This is a consequence of the doubled periodicity in a reconstructed 30° partial core. Only after the left kink (or right kink) moves by $2b$ along the dislocation line is its original bonding configuration restored.

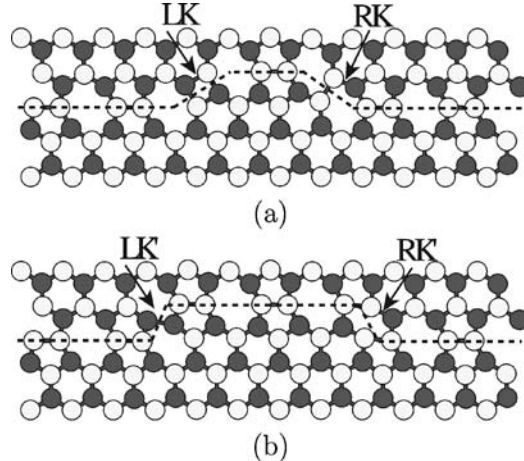


Fig. 23. Kink pairs on 30° partial, (a) LK and RK, (b) LK' and RK'.

A detailed discussion of the relationship between kink multiplicity and symmetry breaking was given in [87].

Additional species of kinks can be formed by combining those we have just identified, LK, RK, LK' and RK', with the reconstruction defect RD, thus leading to kink-RD complexes. When the core of a kink overlaps with an RD the resulting configuration can have significantly lower energy. This means that these two defect species will tend to bind and form a new type of core defect. The following two reactions have been found to be energetically favourable, resulting in the formation of a left kink complex (LC) and a right kink complex (RC),



The energy gains of the LC and RC reactions are 0.51 eV and 0.84 eV respectively [65] computed using the SW potential, and 0.80 eV and 0.42 eV using a TB model [67]. Although two sets of calculated results are rather different, both suggest a strong binding between kinks and RD. The complexes formed by combining LK' and RK' with RD are not energetically stable [67]. The two important kink energy parameters that affect dislocation mobility are their formation energies E_k and migration energy barriers W_m . Their values calculated for different kink species and complexes are given in Table 2. By binding with kinks, RD's are seen to either lower or raise the kink migration barrier. It was found that RD can facilitate kink-pair nucleation and pre-existing kinks can also serve as preferential sites for RD-pair nucleation [65]. Thus, the complex interaction between kinks and RD's is expected to play a role in dislocation mobility.

The family of kink species is even more extended in the 90° partials, given that it has two competing core reconstructions (SP and DP), each with several species of RD's that can combine with kinks. The unreconstructed 90° partial is symmetric under mirror inversion

Table 2

Kink and APD formation energy E_k and migration barrier W_m (in eV) in 30° partials in silicon. Experimental estimates of kink energies are also listed. Note that experiments do not differentiate the various kink species. Instead effective kink energies are estimated.

		E_k					W_m				
		LK	RK	LC	RC	APD	LK	RK	LC	RC	APD
SW	[60]	1.2				0.84					
SW	[65]	0.82	0.82	1.12	0.79	0.81	0.82	0.74	0.22	1.04	0.17
SW	[54]	0.98	0.65	1.29	0.63						
EDIP	[58]	0.65	0.39	0.90	0.83	0.49	1.46	0.89			
TB	[67]	0.35	1.24	0.88	2.15	1.33	1.53	2.10			0.3
DFT	[82]					0.65					
DFT	[83]							2.1			
TEM	[84]						1–1.2				
HREM	[1]	0.8					1.55				
TEM	[85]	0.9					1.3				
IL [†]	[86]	0.62					1.58				

[†]Intermittent loading of 60° dislocations.

with respect to the plane normal to the dislocation line. Therefore, in the unreconstructed 90° partial, left and right kinks are exact mirror images of each other. However, since both (SP) and (DP) reconstructions break the mirror symmetry, multiple kink species are formed. At the same time, every left kink finds an exact mirror image in one of the right kinks.

By convention, different types of kinks in the SP core are labelled according to the geometric characteristics of their right kinks representatives [67]. All the left kinks then can be obtained by a mirror reflection. The kinks are named by the sense of core reconstruction on both sides of the kink. Consider the right kink in Fig. 24(a) as an example. Going from left to right side of the kink, the reconstruction bonds first tilt to the right and then to the left. This kink was therefore denoted as a right-left kink (RL). To label the left kink in Fig. 24(a) according to the nomenclature first proposed in [67], one should first mirror-invert this kink. The resulting right kink will have a left-right sequence of tilts and is called left-right (LR) kink. Similarly, the two kinks in Fig. 24(b) are called right-right (RR) and left-left (LL). Tight-binding (TB) calculations [67] predicted the formation energies for LR and RL kinks to be about 0.12 eV. The LL and RR kinks can be considered as complexes of LR and RL kinks with RD's but were found to be unstable in finite temperature simulations: the LL and RR kinks spontaneously dissociated into LR and RL kinks while emitting RD's.

In the DP core of the 90° partial, there must be five different species of RD's and eight topologically distinct species of kinks [54]. These have not been examined and we will not attempt to enumerate all of them here. Instead, we want to point out an interesting possibility in which a conventional (full) kink dissociates into two partial kinks enclosing a segment of the SP core. This is analogous to the dissociation of a perfect dislocation into two partials, bounding an area of the stacking fault, except that kink dissociation involves two 0D defects (partial kinks) and a 1D stacking fault (the SP segment). An example of

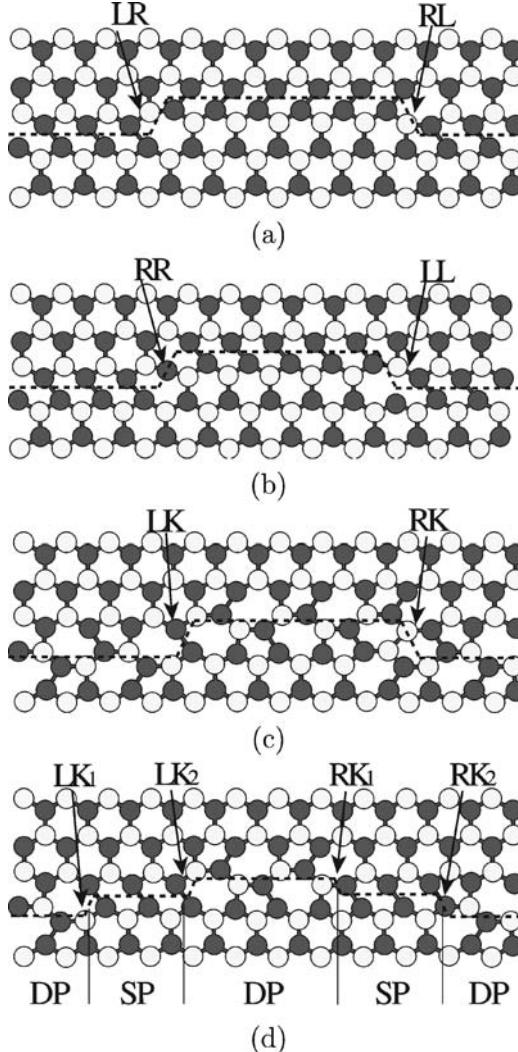


Fig. 24. Kinks in 90° partial. (a) Kink pair LR and RL in a single-period (SP) 90° partial. (b) Kink pair RR and LL on (SP) 90° partial. (c) A kink pair on double-period (DP) 90° partial. (d) Dissociation of kinks shown in (c) into partial kinks bounding short segments of SP core.

such dissociated kinks in the DP core is shown in Fig. 24(c). Here we arbitrarily call the left and right kinks LK and RK, respectively. Let us first observe that the minimal spacing between two SP and DP cores in a 90° partial is only half of the full translation period. Therefore, both the left and right kinks on a DP core can split into partial kinks bounding a segment of the SP core, shown in Fig. 24(d), through the following reactions,

$$LK \rightarrow LK_1 + SP + LK_2, \quad (15)$$



Here the partial kinks are arbitrarily marked LK_1 , LK_2 and RK_1 , RK_2 to acknowledge that many species of full and partial kinks can exist in the 90° partial.

Provided that an SP core has slightly higher energy than a DP core [55], an SP segment acts here as a “one-dimensional stacking fault”, exerting a force on the partial kinks LK_1 and LK_2 (also between RK_1 and RK_2), which, by themselves, repel each other through elastic interactions. The width of a dissociated kink is dictated by the balance between elastic repulsion and the stacking-fault attraction forces. For the Tersoff [88] potential, the equilibrium partial kink separation between LK_1 and LK_2 was found to be $2b$, with a total energy reduction of 0.04 eV due to dissociation [54]. While no systematic study of the partial kink energies in 90° partial has been undertaken, it is reasonable to expect that dissociation can reduce the kink energy, suggesting that more kinks can be available on the 90° partial for dislocation motion. The existence of two types of Peierls valleys can be yet another possible reason why the 90° partials have higher mobility than the 30° partials.

Unfortunately, there is still a sizeable gap between the resolution of computer models and that of HREM observations. Direct observation of kinks has been reported only recently using a new technique [1] that allows a “plane-on” view of stacking faults using forbidden reflections. Shown in Fig. 25 are two partial dislocations bounding a dark stacking fault. In this case, dissociated 60° dislocations were examined to enable simultaneous observation of 30° and 90° partials.

Due to limited resolution, it was not possible to determine the exact positions of the kinks, let alone the detailed atomic arrangements in the core of kinks and partial dislocations. Nonetheless, this experiment is the most direct observation of kinks to date. It provided useful information about kinks spacing that can be compared with theoretical models. The sample was initially deformed under high stress and temperature and subsequently quenched so that the partials were trapped at non-equilibrium separations. The sample was then heated in an electron microscope. Only the 90° partials moved in the measurements and their kink density was consistently about 3 times higher than in the 30° partials. Measurements of kink velocities *in situ* indicated that the kink migration barrier on 90° partial was $W_m = 1.24 \pm 0.07$ eV. However, kink pinning at invisible obstacles was also observed. These obstacles have been postulated to be oxygen atoms. The energy barrier for overcoming the obstacles was estimated to be 2.4 eV. An analysis of the width distribution of kink pairs led to an estimate of kink formation energies of $E_k \approx 0.81$ eV for 30° partials and $E_k \approx 0.74$ eV for 90° partials (free energies were estimated to be 0.797 eV and 0.727 eV, respectively). However, the estimates of E_k could have large error bars due to the scarcity of data points (only 7 kink pairs were counted for the 90° partial). Also, given that the kinks might have been pinned at invisible obstacles, the observed kink-pair width distribution could be a reflection of the obstacle spacing rather than a function of the kink formation energy.

Tables 2 and 3 show various calculated and measured values of the formation energies E_k and migration energy barriers W_m for different kink species and RD’s on 30° and 90° partials in silicon. A conclusion that can be drawn from these data is that, despite decades of effort, there is not a single converged data point in these two tables. Computations based on empirical interatomic potentials, tight-binding methods, and *ab initio* methods, produced

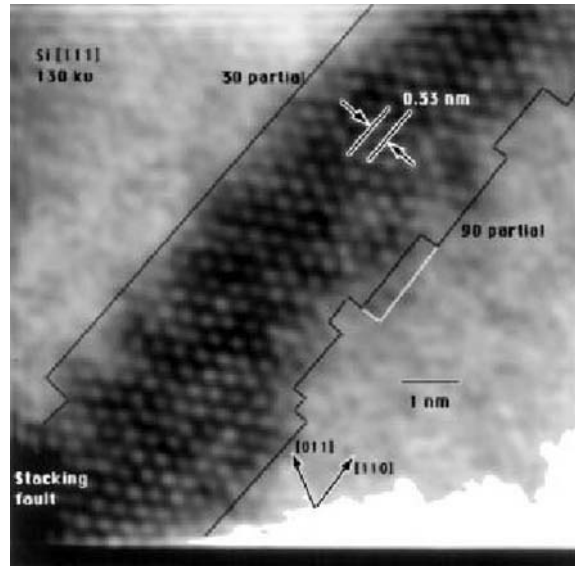


Fig. 25. Kinks on 30° and 90° partials of a 60° dislocation observed in HREM [1].

very different results. In a few cases, different groups using the same potential models have reported significantly different values for the same parameter [52,59]. This makes us think that, for the calculations of dislocation properties to be accurate, one should use not only an accurate description of interatomic interactions, but also a proper treatment of boundary conditions. The boundary condition issue is much more serious for DFT and TB simulations that employ relatively small computational cells. Possibly, some of the *ab initio* calculations reported so far [94] have produced results that are less accurate than the interatomic potential simulations.

Despite the limited accuracy, some qualitative trends can be seen in Tables 2 and 3. In cases when data for the same defect are available from several models, we tend to trust *ab initio* results more than that of tight-binding methods, and more than the data obtained using empirical potential models.² For the most accurate results to date, the kink formation energies on 90° partials are generally smaller than those on 30° partials. In this regard, tight binding results seem to agree with *ab initio* data in giving very low kink energy (about 0.1 eV) for the kinks on the 90° partials. Unfortunately, no *ab initio* data are available for kinks on 30° partials. The smallest kink energy on 30° partial from tight-binding calculations is 0.35 eV.

All the kink results given in Table 3 refer to the SP core of the 90° partial. It is now generally accepted that this partial can also undergo the DP core reconstruction that results in a slightly lower core energy than the SP core. At present, there is little information on the kinks on DP core and the partial kinks linking a DP core and an SP core. What is available are only results from atomistic simulations using empirical potentials. Nonetheless, if one

²This is on the condition that in all calculations the boundary effects have been properly taken care of, and the convergence with respect to the simulation cell size has been reached.

Table 3

Kink and APD formation energy E_k and migration barrier W_m (in eV) on 90° partials with SP core reconstruction in silicon. Experimental estimates of kink energies are also listed. Note that experiments do not differentiate different kink species. Instead effective kink energies are estimated.

	E_k	W_m							
		LR/RL	LL	RR	APD	LR/RL	LL	RR	APD
EDIP	[58]	0.70	0.84	1.24	0.65	0.62			
Tersoff	[66]	0.12							
Tersoff	[60]	0.90			0.37				
TB	[89]	0.50 [†]	1.74*	2.04*	1.31	1.87			0.04
TB	[67]	0.12	*	*	1.45	1.62			0.04
DFT	[90]				1.2				
DFT	[91]	0.1				1.8			
DFT	[92]	0.04				1.09			
TEM	[93]	≥ 0.4				≤ 1.2			
TEM	[84]					1–1.2			
HREM	[1]	0.74				1.55			

* Approximate energy, defect unstable.

† Not fully converged [67].

accepts the fact that dissociation of full kinks into partial kinks further reduces kink formation energies, then the arguments in favour of higher mobility of the 90° partials become even more compelling.

It is not surprising that more data for different kinks species are available from empirical potential calculations than from *ab initio* calculations. The technical difficulties and computational expense of the latter are the reasons why very few types of kinks have been studied. On the other hand, experimental estimates for kink energies cannot differentiate kink species at all. Instead, an effective value describing the average effect of all kinks is estimated. Therefore, it would be misleading to directly compare *ab initio* results for a given kink species with experimental estimates.

So far we have discussed kink mechanisms of dislocation motion that are purely conservative, i.e. do not involve mass transport by diffusion. Diffusional mechanisms could play an important role at high temperatures. It has been suggested that [63] vacancy pipe diffusion along dislocation core can facilitate kink-pair nucleation and kink migration. This is because these kink mechanisms entail either bond switching or exchange. If one of the sites involved in the atomic rearrangement is occupied by a vacancy, then switching of the bond can also be accomplished simply by a vacancy jump. At high temperatures, such non-conservative kink mechanisms may well be competitive with the conservative mechanisms discussed earlier.

3.4. Dislocation mobility

The main purpose of studying dislocation core and secondary core defects is to understand how dislocations move. In principle atomistic simulations, such as those discussed above, are capable of giving results that not only enable the understanding of existing data on

dislocation mobility, but also lead to further predictions outside the range of experimental conditions. At present, quantitative predictions of dislocation motion from first principles are not feasible. At the same time, different measurements of dislocation velocity show considerable scatter to such an extent that there is little consensus on what is the controlling mechanism for dislocation motion in semiconductors. Despite these problems, there are certain trends that may be considered established and theoretical models that have found support from the experiments.

3.4.1. General behaviour

A set of experimental data on dislocation mobility in silicon is shown in Fig. 26. The dislocations were imaged using X-ray topography and the velocities v of screw and 60° dislocations were measured over a range of resolved shear stress τ and temperature T conditions. Following [96] we refer to the temperature and stress range of these experiments as the “central” range, i.e. $0.45T_m < T < 0.65T_m$, $5 \times 10^{-5} \mu < \tau < 10^{-3} \mu$, where $T_m = 1693$ K is the melting temperature and $\mu = 68$ GPa is the shear modulus of silicon. A number of measurements in this parameter range using various techniques have been reported [84, 86, 93, 95, 97–107]. While their general trends, particularly with regard to temperature dependence, are consistent, the absolute values of the velocities can differ by about a factor of two [96].

Dislocation mobility in this “central” range is often described using the following empirical relationship

$$v(\tau, T) = C(\tau) \exp\left(-\frac{Q(\tau)}{k_B T}\right). \quad (17)$$

The Arrhenius plots of dislocation velocity versus the inverse temperature, such as in Fig. 26(a), show straight lines whose slopes are the activation energies Q . In this series of measurements [95], a Q_s value (for screw dislocations) around 2.2 eV was obtained over the entire stress range, while Q_{60° (for 60° dislocations) increases from 2.16 eV to 2.43 eV as the stress decreases from $\tau = 30$ MPa to 4 MPa. A later experiment [104] using *in situ* X-ray topography together with presumably purer silicon samples gave $Q_s = 2.35$ eV and $Q_{60^\circ} = 2.2$ eV for stresses ranging from 2 to 20 MPa. The effective activation energy Q having a value 2.2 to 2.3 eV has been verified by several groups and is now widely accepted. All the experiments indicate that 60° dislocations (comprised of a 90° and a 30° partials) are generally more mobile than screws (comprised of two 30° partials). This is also in agreement with TEM observations showing that 90° partials are more mobile than 30° partials [53].

The stress dependence of dislocation velocity is by comparison more controversial. For a given temperature the variation of dislocation velocity with stress is empirically described as $v \sim \tau^m$. The standard kink diffusion model [5], to be discussed later, predicts a linear relationship between stress and velocity, i.e. $m = 1$. From Fig. 26(b) it is clear that this behaviour is not seen at low stress. Also, m is found to depend on temperature [95] suggesting that the intrinsic mechanism of kink diffusion cannot account for the details of the experimental findings. In order to explain this discrepancy a concept of weak obstacles was invoked. On the other hand, later *in situ* X-ray topography experiments [104] reported that the relationship between stress and velocity remains linear from 2 MPa to 20 MPa.

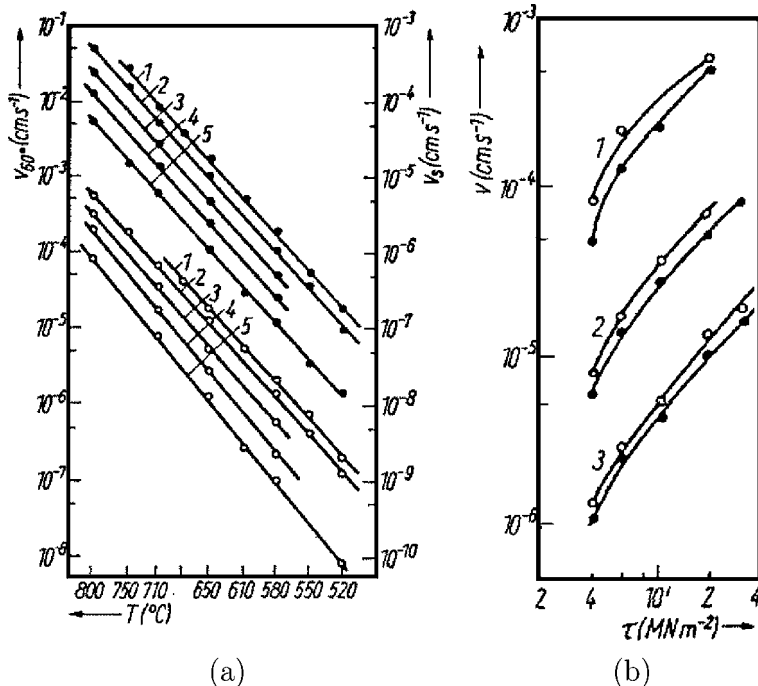


Fig. 26. (a) Temperature dependence of velocity of screw (●) and 60° (○) dislocations in intrinsic Si at stresses (1) $\tau = 30$, (2) 19, (3) 10, (4) 6, (5) 4 MPa. (b) Stress dependence of velocity of screw (●) and 60° (○) dislocations in intrinsic Si at temperatures (1) $T = 800$, (2) 710, (3) 650°C [95].

In the range of resolved shear stress τ between 30 MPa to 300 MPa, it has been found that dislocation velocity can be expressed as $v = v_0(\tau/\tau_0)^m$, with $1.2 \leq m \leq 2.2$ [102]. However, the actual value of m appears to depend not only on the type of dislocations, but also on the orientation of Burgers vector with respect to the compression axis. This observation suggests a breakdown of the Schmid's law in silicon at high stresses. We would argue that Schmid's law is also violated at low stresses, as shown by the large scatter in the velocity data measured at the same resolved shear (Schmid) stress. Mitchell et al. [108] have shown that velocity dependence of the type observed in [104] can be fitted by the kink diffusion model [5] if one includes the stress dependence in the free-energy of kink-pair formation.

At temperatures higher than $0.7T_m$ the dislocation mobility exhibits another transition [102]. Fig. 27 shows that, as the temperature increases above $0.7T_m$, the behaviour of dislocation mobility undergoes a change. The effective activation energy increases to $Q \approx 4.0 \pm 0.1$ eV, accompanied by a corresponding increase in the pre-exponential factor. This behaviour shows up in the velocity plots as a characteristic bend. Mechanistic understanding of this transition is still lacking even though it has been proposed that, at such high temperatures, vacancies can facilitate kink-pair nucleation and migration [63].

In analysing the experimental data one can observe considerable scatter among the different measurements that cannot be explained within a single theoretical model. To es-

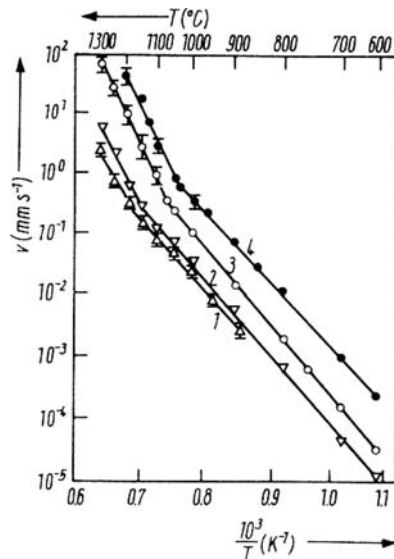


Fig. 27. Temperature dependence of 60° dislocation velocity in Si [103] for different stresses (1) 2 MPa, (2) 5 MPa, (3) 10 MPa, (4) 45 MPa.

tablish a consistent picture of dislocation motion, it is important to recognize the limitations and possible artefacts of the different techniques used to measure dislocation velocity. Three approaches are widely used to observe dislocations, selective etching [103,109], X-ray topography [95,104], and transmission electron microscopy (TEM) [84,93,101].

In the case of etching the intersection between a dislocation line and the free surface, an etch pit, is exposed. To measure the dislocation displacement from the etch pit position, one has to assume the dislocation remains straight beneath the surface. Although this can be verified by observing the shape of the etch pit and by repeated etching, the confirmation is indirect. Chemical solutions used in etching could introduce impurity atoms to the surface which then can pin the dislocation. This can be the reason why a starting stress effect (existence of a critical stress below which dislocations cease to move) has been observed in etching experiments [109] but not in X-ray experiments.

The resolution of X-ray topography is about $2.5 \mu\text{m}$, comparable to that of selective etching. Hence, only large scale behaviour of dislocation motion can be observed. Smaller scale details, such as impurity clusters, jogs, etc, are not observed, as these effects are smeared out in the overall dislocation velocity that is measured. The exposure time in the X-ray topography is long so that it is difficult to image dislocations *in situ*, unless a strong X-ray source is used. If the measurements are not performed *in situ*, dislocation and point defect microstructures can change during heating and cooling cycles between loading, which may affect the measured dislocation velocity [104].

Because a small concentration of impurity atoms (such as oxygen) can have a large effect on dislocation mobility, careful characterization of all impurity species in the specimens is a requirement for all experiments. For example, it was found [104] that boron has essentially no effect on dislocation mobility up to a concentration of $1.4 \times 10^{19} \text{ atoms cm}^{-3}$,

while earlier measurements seemed to show a pinning effect associated with boron. It was argued [104] that the discrepancy could be a result of an unnoticed oxygen impurity concentration in other experiments.

Non-Schmid behaviour also has been observed in silicon. The dislocation velocity was found to have a dependence on stress components other than the Schmid (or glide) stress τ_s . In particular, the velocity of the 60° dislocation is dependent on the climb stress (τ_c). Which of the two partials, 30° or 90° , is leading also seems to make a difference. As we will explain in the next subsection, it can be expected that the Escaig stress component (τ_e), which exerts opposite glide forces on the two partials, can play an important role in dislocation mobility. These observations suggest that it is necessary to take the other stress components (besides the glide stress) into account when comparing two experimental reports. This may resolve some of the discrepancies among the different experiments. Parenthetically, the discrepancy between the two mentioned X-ray topography measurements [95] and [104] may be attributed, at least partly, to differences in loading conditions. In [95] a tensile load was applied along $[1\bar{2}3]$ direction while in [104] the tensile axis was $[11\bar{2}]$.

In situ TEM measurements offer a unique opportunity to observe dislocation motion in detail but the method has its own disadvantages. The application and measurement of stress are difficult. Stress is usually estimated from the local curvature of dislocations, or from the width of the stacking fault between the partials. This makes any reported stress value only approximate. Because very thin films are used in TEM, surface effects are more serious than in other techniques. Examples of surface effects include the image stress on dislocations and enhanced kink nucleation at the free surfaces which can significantly increase the dislocation velocity [101]. Dislocations under TEM are often seen to be pinned by invisible strong obstacles [1,93], possibly impurity atoms (clusters) diffused from the surface of the thin film, or produced as a radiation damage by-product of the electron beam itself. At the same time, the electron beam increases the dislocation mobility by producing excitations, e.g. electron-hole pairs, that enhance the rate of kink-pair nucleation and kink migration. All in all, the dislocations may behave differently in the bulk than under the electron microscope.

3.4.2. Stochastic discrete kink model of dislocation mobility

In this subsection we discuss a mesoscale model that overcomes the computational limitations of direct atomistic simulations to reach the length and time scales of dislocation motion in the laboratory experiment. To provide a reference point for the model development, we briefly recall a few relevant features of a well known kink diffusion model due to Hirth and Lothe [5], referred to here as the HL model.

The basic assumption of the HL model is that a dislocation moves in a stochastic sequence of thermally activated, random kink-pair nucleation and migration events. The rate of kink-pair nucleation is defined by the nucleation barrier that depends on the kink-pair formation energy, kink migration barrier, elastic attraction between two kinks of the same pair and the applied stress. Once nucleated, kinks diffuse along the dislocation line and either recombine with other kinks or pile up at the ends of the line. By considering the bal-

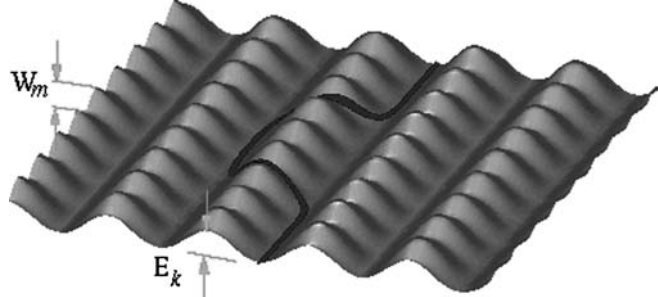


Fig. 28. Schematic of the Peierls barrier and kink mechanism for dislocation motion. Dislocation is represented as a continuous line, which resides mostly at the bottom of the Peierls energy surface except at kinks.

ance of kink-pair nucleation and migration rates under stress, one can relatively straightforwardly to obtain (in the limit of long dislocations)

$$v = v_D \frac{\tau abh^2}{k_B T} \exp\left(-\frac{E_k + W_m}{k_B T}\right), \quad (18)$$

where v is the dislocation velocity, v_D is the Debye frequency, τ is the resolved shear stress on the dislocation, a , b and h are the dislocation period, Burgers vector and kink height, respectively, E_k is the kink nucleation energy and W_m is the kink migration barrier. Experimental data on the temperature and stress dependence of dislocation mobility in the “central” range is generally consistent with eq. (18). Furthermore, the estimates for kink formation and migration energies based on this equation are in reasonable agreement with the atomistic simulation results.

Overall, despite reports of its shortcomings and given its analytical simplicity, the HL model is remarkably successful in describing dislocation mobility in silicon. As an example, let us consider the claim that experimental data presented in [104] can not be explained by the HL model. By comparing eq. (18) with the empirical relationship found in [104],

$$v = v_0 \tau \exp\left(-\frac{Q}{k_B T}\right), \quad (19)$$

one can readily see that

$$v_0 = v_D \frac{abh^2}{k_B T}, \quad (20)$$

$$Q = E_k + W_m. \quad (21)$$

Using their own experimental data Imai and Sumino obtained $v_0 \approx 10^4 \text{ m s}^{-1} \text{ MPa}^{-1}$ whereas by plugging into the right hand side of eq. (20) the values appropriate for silicon, one obtains $v_0 \approx 10 \text{ m s}^{-1} \text{ MPa}^{-1}$ which is lower by three orders of magnitude than the measured value.

However, this discrepancy is only apparent, because the entropy factors in double kink nucleation and kink migration processes have been ignored in [104]. In eq. (18) E_k and W_m should be replaced by free energies, $E_k - TS_k$ and $W_m - TS_m$, where S_k and S_m are entropies for the nucleation and migration processes. Therefore, eq. (20) should be replaced by

$$v_0 = v_D \frac{abh^2}{k_B T} \exp\left(\frac{S_k + S_m}{k_B}\right). \quad (22)$$

To account for the difference in three orders of magnitude, $S_k + S_m \approx 7k_B$ would be needed. This is actually not unreasonable considering the estimate of $3k_B$ for both S_k and S_m obtained in the earlier atomistic calculations [110]. Therefore, the experimental data of [104] should not be viewed as evidence of the failure of the HL model, but instead as confirmation of the importance of the entropy factors.

The HL model is nevertheless a simplification that ignores, for example, the fact that dislocations in silicon, at least in the “central” parameter range, are dissociated. Although the values for E_k and W_m used in the HL model refer to partial dislocations, the process where two partials interact strongly with each other and move together is usually not considered. When the applied stress is much larger than the interaction stress between the partials, the partials are likely to be relatively independent of each other, in which case this simplification is justified. The simplification is also valid for materials with a small stacking fault energy γ_{ISF} , in which case the separation between partials X_0 is large and their coupling becomes weak. If, on the other hand, the applied stress is small, then the coupling between partials can have a significant effect on dislocation mobility in silicon. In other words, the mobility of two interacting partials forming a bound state may not be well described by the generic HL model. There have been a number of reports of anomalous behaviour of dislocation velocity at low stress [95]. It appears possible to attribute such low-stress anomalies to the coupling between partial dislocations.

The effect of coupling between the partials on their mobility has been examined by Möller [111]. It was assumed that nucleation of kink-pairs on two partials becomes correlated when stress is lower than a critical value τ_c , while it is not correlated at higher stress. Below the threshold stress kink-pairs have to nucleate simultaneously on both partials in close vicinity, which makes kink-pair nucleation considerably less frequent than what the HL model would predict. Using this model Möller attempted to explain the experimental mobility data at low stress without the need for the *ad hoc* postulate of weak obstacles which had been previously introduced for this purpose. Unfortunately, the model was not successful in accounting for the experimental data, making it necessary to re-introduce some obstacles back into the description. Besides this inconsistency, the model was unable to resolve another controversy. While some experiments found a non-linear stress–velocity behaviour [95], other experiments found a linear relation down to very low stress [104].

To make his model analytically tractable, it was necessary for Möller [111] to introduce simplifying approximations. Recently a different approach, one based on kinetic Monte Carlo (kMC) simulation, has given new insights into the effects of partial dislocations interacting with each other on their mobility [112]. In the kMC description, two partial dislocations move together via kink-pair nucleation and kink migration while interacting

through the Peach–Koehler forces. The simulations reveal a rather subtle coupling effect between the partials.

To understand the effect, assume for a moment that there is no Peierls barrier and consider the equilibrium separation X_0 between the partial dislocations. This distance is determined by a force balance between two competing terms. One is the repulsion between the partials, an elastic interaction with a force inversely proportional to their separation. Another arises from the stacking fault which exerts a constant attractive force between them. X_0 is the separation at which these two forces balance each other, i.e.

$$X_0 = \mu b^2 \alpha / (\gamma_{\text{ISF}} - \tau_e b \beta), \quad (23)$$

where $\alpha = [1/4 - 1/12(1 - \nu)]/(2\pi)$, $\beta = \sqrt{3}/6$ for screw dislocations dissociated into two 30° partials, μ is the shear modulus, τ_e is the so called Escaig stress, i.e. the resolved shear stress along the edge components of the partial Burgers vectors, which exerts equal but opposite forces on the two partials. Therefore, X_0 is a continuous function of the stacking fault energy and the Escaig stress τ_e . However, because of a very high Peierls barrier in silicon, the actual separation X between the partials can only be an integer multiple of $h = b\sqrt{3}/2$. If X_0/h happens to be an integer, then the ideal spacing is commensurate with the lattice period. Any perturbation of this ideal spacing, such as kink-pair nucleation, will incur additional energy cost. However, this cost is significantly reduced if kink-pair nucleation takes place on both partials simultaneously so that the ground state spacing X_0 is preserved between the two kink-pairs. Such correlations are suppressed when the stress driving kink-pair formation and motion becomes high enough to overcome the interaction between kinks on the two partials.

The situation is different when X_0/h is a half-integer, in which case the ground state of the two partials becomes doubly degenerate, i.e. $X = X_\pm = X_0 \pm 1/2$. When the partials are separated by X_- , forward kink-pair nucleation and propagation on the leading partial extends the stacking fault width to X_+ , which is another ground state. Likewise, in the state X_+ , forward kink-pair nucleation on the trailing partial does not require any kink activity on the leading partial. In this case, there is no commensurability barrier and mobility of the whole assembly should be relatively high because the two partials can now move sequentially through alternate contraction and expansion of the stacking fault.

Fig. 29 shows the simulated velocity of a dissociated screw dislocations as a function of Schmid stress. Two sets of data are shown with X_0 equal to $10.0h$ and $10.5h$, respectively. The change of X_0 can be realized by either changing the stacking fault energy (by 5%) or by applying an Escaig stress of 25 MPa. When X_0/h is a half-integer, the function remains linear down to very low stresses. On the other hand, when X_0/h is an integer, the mobility drops super-linearly below 20 MPa. Also plotted in Fig. 29 are two sets of conflicting experimental data [100,104] resembling the two simulated curves. While a linear velocity-stress relationship was reported in [104], a non-linear velocity reduction was observed in [100], albeit at a smaller critical stress. The magnitude of this mobility reduction is also smaller than in the simulated case of $X_0/h = 10$.

It was argued in [104] that the discrepancy between the two experiments was due to a higher purity of samples used in [104]. However, given that a small change of X_0 can have a large effect on the low-stress mobility, another explanation could be the different averaged

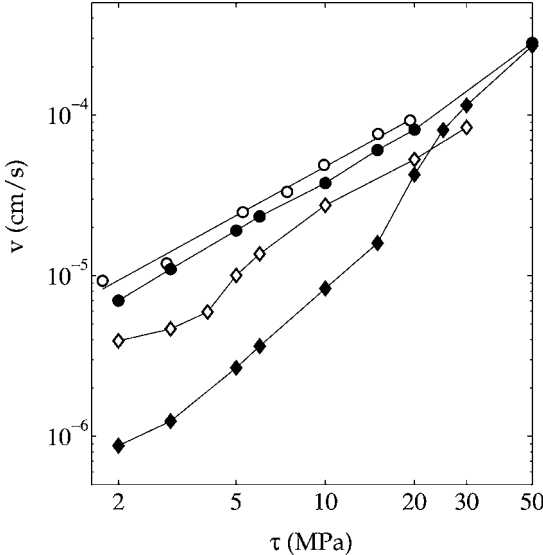


Fig. 29. Velocity of a screw dislocation in Si as a function of stress. kMC prediction at temperature $T = 1000$ K for a commensurate case ($X_0 = 10.0h$) is shown as \blacklozenge , with a “starting stress” at about 20 MPa. Experimental data from [100] at temperature $T = 983$ K shows similar velocity variation, plotted as \lozenge . kMC results for a non-commensurate case ($X_0 = 10.5h$) are plotted as \bullet , demonstrating linear stress–velocity relationship, in agreement with other experiments, at temperature $T = 1005$ K plotted as \circ [104].

values of the parameter X_0 in the two experiments. Assuming that both measurements used similar materials with the same stacking fault energy (albeit unknown to within an accuracy of 5%), then the difference in X_0 could potentially come from the different values of the Escaig stress. Indeed, the experiment [100] was conducted with a tensile axis $\overline{[123]}$. The corresponding primary slip system was $(\overline{111})[\overline{101}]$, with a Schmid factor of $s = 0.4667$. By analogy to the Schmid factor, let us define an Escaig factor as the ratio of Escaig stress to the tensile stress. The Escaig factor was $e = 0.1347$ in [100] while the ratio of Escaig and Schmid factors in this experiment was $\tau_e/\tau_s = 0.2887$.

The tensile axis in [104] was $[11\overline{2}]$, with the primary slip system $(\overline{111})[01\overline{1}]$. The corresponding Schmid and Escaig factors were $s = 0.4082$, $e = 0.0786$, respectively, and their ratio was $\tau_e/\tau_s = 0.1925$. We notice that the velocity data points reported were plotted against Schmid stress only, although Escaig stresses in these two experiments were markedly different. For example, for a Schmid stress of 4 MPa, X_0 for these two loading conditions can be different by $0.008h$. This is not large, compared with the two extreme cases studied in the kMC simulation in which X_0 changes by $0.5h$. However, it is reasonable to expect that such a change of X_0 could lead to a noticeable change of dislocation mobility, comparable to the discrepancy that exists between these two experiments.

It appears possible to directly observe the effect of Escaig stress on dislocation mobility through the modulation of stacking fault width by experiments. Evidently this effect should be more pronounced when the Escaig stress is large. For example, when the loading condition is such that the ratio of Escaig and Schmid stresses is $\tau_e/\tau_s = -6.25$, kinetic

Monte Carlo simulations [112] predict that the variation of dislocation velocity plotted with Schmid stress should exhibit oscillatory behaviour with a period of about 8 MPa. This is consistent with the fact that it takes 25 MPa of Escaig stress to change X_0 by $0.5h$. A possible set up for the experiments to verify this effect has been proposed [113].

3.4.3. Kink diffusion versus obstacles

While the HL kink diffusion model and its extensions have been quite widely adopted, alternative views on the mechanisms controlling dislocation mobility in semiconductors also have been put forth. The basic assumption of the HL model has been called into question (see for example [114]) and point defects, instead of dislocation kinks, were suggested as being responsible for the lattice resistance to dislocation motion [115,116]. As was already discussed, the generic HL model can not explain the low stress dislocation mobility behaviour, which shows significant non-linearity. To remedy this situation the idea of “weak obstacles” was proposed as an extension of the HL model in order to explain such behaviour [47,117]. These obstacles are assumed to impede kink migration along the dislocation line; they must be weak so that at high stress they are no longer effective and the dislocation velocity-stress relationship becomes linear. The weak-obstacles theory, on the other hand, has its difficulties; to fit the experimental data a very high density of obstacles is required. In pure silicon, it is hard to imagine what kind of extrinsic defects can fit the description [114]. As mentioned above, the HL kink diffusion model, when extended to account for the coupling between the partials, can explain the low stress mobility behaviour without the need for any additional entities, such as weak-obstacles.

One way to make use of the HL kink diffusion theory is to extract values of kink formation and migration energies from velocity measurements which are normally inverted to give the sum of the two energies. The results can be tested against TEM data which can give the two energies separately. For example, it is found that dislocation velocity is proportional to dislocation length for lengths smaller than $0.2\text{--}0.4 \mu\text{m}$ [93], a behaviour which is given by the HL model. From this value one can estimate the kink migration energy (see previous subsections). In other experiments, the samples were first deformed at high stress and temperature and then quickly cooled down, so that dislocations were trapped at non-equilibrium configurations with large stacking fault widths and high density of kinks. Subsequent annealing under the electron microscope allows direct observation of dislocation motion via migration of pre-existing kinks [84], from which kink migration energy was estimated ($W_m = 1\text{--}1.2 \text{ eV}$). These findings are in general agreement with the HL model and atomistic calculations of kink energies.

Kink nucleation and migration contributions can be also isolated in the intermittent loading experiments [86,107]³, where a stress pulses of length t_i are separated by pause periods of length t_p . Kinks of the kink-pairs nucleated during the pulse period may become unstable during the pause period and may recombine with each other. In such conditions, the dependence of dislocation velocity on t_i and t_p can be used to estimate kink formation and migration energies. The data reported in [86] leads to $W_m = 1.58 \text{ eV}$ for the kink migration energy and to $E_k = 0.62 \text{ eV}$ for the kink formation energy, consistent with the atomistic

³Internal friction [114,118] measurements were also performed earlier that could achieve the same effect, but they became less popular because of the difficulty of relating the data on absorption peak to kink energies [101].

models. Alternatively, if one adopts the obstacle theory, the same data can be used to estimate the strength and the length distribution of obstacles.

The authors [86] present their data as evidence against the HL model on the basis of the following argument. From the estimated value of E_k , one can also estimate the dislocation Peierls stress according to [86],

$$\tau_{PN} = \frac{\pi^3 E_k^2}{2a^2 b^4 \mu} \approx 760 \text{ MPa}, \quad (24)$$

where a is the kink height, b is the Burgers vector, and μ is the shear modulus. This value is indeed too low compared with other experiments that clearly show that $\tau_{PN} > 1 \text{ GPa}$. On the other hand, recent atomistic calculations show that kink energy of $E_k \approx 0.6 \text{ eV}$ is fully consistent with very high values of the Peierls stress for partial dislocations, at $\tau_{PN} > 5 \text{ GPa}$. This suggests that eq. (24) is inaccurate and should not be used for quantitative comparison.

While we argue that much of the observed phenomenology of dislocation motion in semiconductors can be explained quite well within the HL kink diffusion model, there is no doubt that point defects, such as vacancies, interstitials, and impurity atoms, interact with dislocations and can affect dislocation mobility under certain conditions. Intrinsic point defects can also be produced by dislocations during deformation, making for rather complex interactions between point defects and dislocations.

In situ high resolution TEM experiments [1] provide possibly the most direct observation of obstacles for dislocation motion in showing that kinks can be trapped by invisible strong pinning centres. Yet, such obstacles may well be experimental artefacts, produced, for example, by impurity atoms diffusing in from the surface, or by the high energy electron beam itself. Thus they may be irrelevant for bulk semiconductors.

Certain types of impurity atoms are found to have a strong effect on dislocation mobility while others do not. *In situ* X-ray topography [104] data suggests that impurity atoms, such as nitrogen, oxygen, phosphorus and boron, tend to make dislocations immobile at stress below certain critical value, 3–5 MPa, depending on impurity type and concentration. Above the critical stress, these impurities are reported to have different effects. Nitrogen is seen to have no effect after reaching the threshold stress, while oxygen causes dislocation velocity–stress relationship to become non-linear in the low stress regime. Likewise, boron (in p-type Si) does not seem to have much effect once dislocations begin to move, but phosphorous (in n-type Si) is known to enhance dislocation mobility. Because it is difficult to ensure that there is only one type of impurity in the sample, the above conclusions must be taken with caution. The effect of electrically active impurities (B and P) on dislocation mobility was explained by the electron hole transfer between bulk crystal and dislocation levels [119].

Selective etching experiments also showed that phosphorous doped silicon sample has a starting stress of about 2 MPa for dislocation motion [107]. This was explained by kink expansion through randomly distributed obstacles. This result too may be subject to experimental artefacts due to surface effects. Starting stress behaviour was also observed in SiGe crystals with different Ge concentrations [120]. It was proposed, that at small Ge

concentration, dislocations drag a Cottrell atmosphere, while at large Ge concentrations kinks drifting along a dislocation would interact with random obstacles.

While the dragging effect of impurity atoms is expected, the effect of intrinsic point defects on dislocation mobility in pure silicon remains unclear. It was found that 60° dislocations, when subject to climb forces, may become unstable during motion, i.e. some segments move faster than others so that the dislocation line becomes ragged [97]. It was postulated that this is due to vacancy absorption or emission by a dislocation, which in turn modifies the dislocation core. However, a detailed atomistic mechanism is lacking. Double cross slip of screw dislocations also has been proposed as a mechanism for dislocation point defect interaction [116]. The motion of screw dislocations after double cross slip requires jog dragging which depends on the rate of emission or absorption of point defects. Interaction with intrinsic point defect and climb also seem to be necessary to explain the forward-backward asymmetry of dislocation mobility observed in [105].

3.5. Outstanding issues

Although silicon has been a favourite material for theoretical and experimental investigations on dislocation mobility, many issues still remain unresolved. It appears that dissociated glide-set dislocations and perfect shuffle-set dislocations control the plastic deformation of semiconductors at high and low temperature regimes, respectively. However, a satisfactory explanation of the origin of this transition is lacking. Specifically, the atomistic pathways for a shuffle-set dislocation to transform into the glide-set are poorly understood. Atomistic modelling coupled with experimental observations should be able to resolve this issue.

The disagreement among theoretical values for the formation and migration energies of kinks on the glide-set partial dislocations reported by different groups is a serious concern. While some of the disagreement can be attributed to the multiplicity of kink species, the fidelity of the atomistic models themselves is an issue. *Ab initio* DFT calculations are the most accurate among the approaches currently in use, but they suffer from the artefacts of boundary conditions in small computational volumes. The situation is expected to improve with the increasing availability of more powerful computers and algorithmic improvements. One particular aspect ripe for theoretical exploration is kink mechanisms in the perfect shuffle-set dislocations. Recent experimental data provide ample evidence for their importance. In fact, given the relative simplicity of the shuffle dislocations compared to the glide partials, it may be possible to establish a consistent picture of kink dynamics in the shuffle-set perfect dislocations first.

Better mechanistic understanding of interactions between intrinsic point defects and the dislocation core is needed. These include climb and cross slip, as well as point defect generation as a result of dislocation motion, such as by jog dragging. There are still debates on whether kinks or point defects are the controlling factor for dislocation motion. The effect of electrically active dopants on dislocation core, i.e. the electro-mechanical coupling, is a promising area where *ab initio* calculations and experiments can be combined to address technologically important questions. Atomistic mechanisms of dislocation nucleation in

misfit layers and surface effects on dislocation mobility and multiplication are two more issues of significant technological importance and theoretical interest.

Evidently, the complexity of atomistic mechanisms in the dislocation core is nearly “bottomless”. A “bottom-up” approach, in which one attempts to predict the complete behaviour of dislocations after mastering “all” the atomistic mechanisms, seems to be impractical. Instead, a “top-down” approach could be more promising where a larger scale dislocation model is used to provide guidance on which of the atomistic mechanisms are important and under what conditions. Once this is established, high-accuracy calculations can be performed to determine a selected set of important parameters.

4. BCC metals

4.1. Introduction

BCC metals and alloys have been heavily used by humankind since the Iron Age. Their most useful property is high strength over a wide range of temperature and straining conditions. Combined with the abundance of the iron ores, the relatively straightforward technologies for metal extraction and the high formability at reasonable temperatures, iron alloys naturally became and continue to be the kings of structural materials. BCC metals, e.g., the refractory metals Mo, W, Nb, Ta and others, also served as important elements for more specialized applications; when used in combinations with Fe, they can greatly improve the quality of structural materials.

Although there are considerable variations in the plasticity behaviour of BCC materials, it is well recognized that certain generic behaviour can be attributed to their common lattice crystallography. Among these characteristics are the prominent temperature and strain-rate dependence of the yield stress, features of slip crystallography, and the existence of a ductile-to-brittle transition at low temperatures. This last property is a manifestation of the inability of dislocations to multiply and/or move fast enough, at low temperatures, to relieve the stress concentrations that are the causes of cracking.

As shown in Fig. 30(a) [121], TEM micrographs of deformed specimens show characteristic features of long screw dislocations often stretching along many micrometers, with no or very little deviation from the perfect screw orientation. This anisotropy of dislocation microstructure directly reflects the anisotropy of dislocation mobility. *In situ* TEM observations [122] show very clearly that at low and moderate temperatures screw dislocations move much slower than edge and mixed dislocations. For example, in pure molybdenum at room temperature the velocity of screw dislocation has been estimated to be 40 times lower than that of edge dislocations [123]. The pre-strained microstructure dominated by long screw segments is produced by rapidly moving edge dislocations under stress. Some early dislocation velocity measurements have suggested that screws actually move faster than edges [124–126]; however, such behaviour could be due to surface related enhancement of screw mobility or even the artefacts of chemical etching used to monitor dislocation motion, and in any event it is unlikely that such data are representative of dislocation behaviour in the crystal bulk.

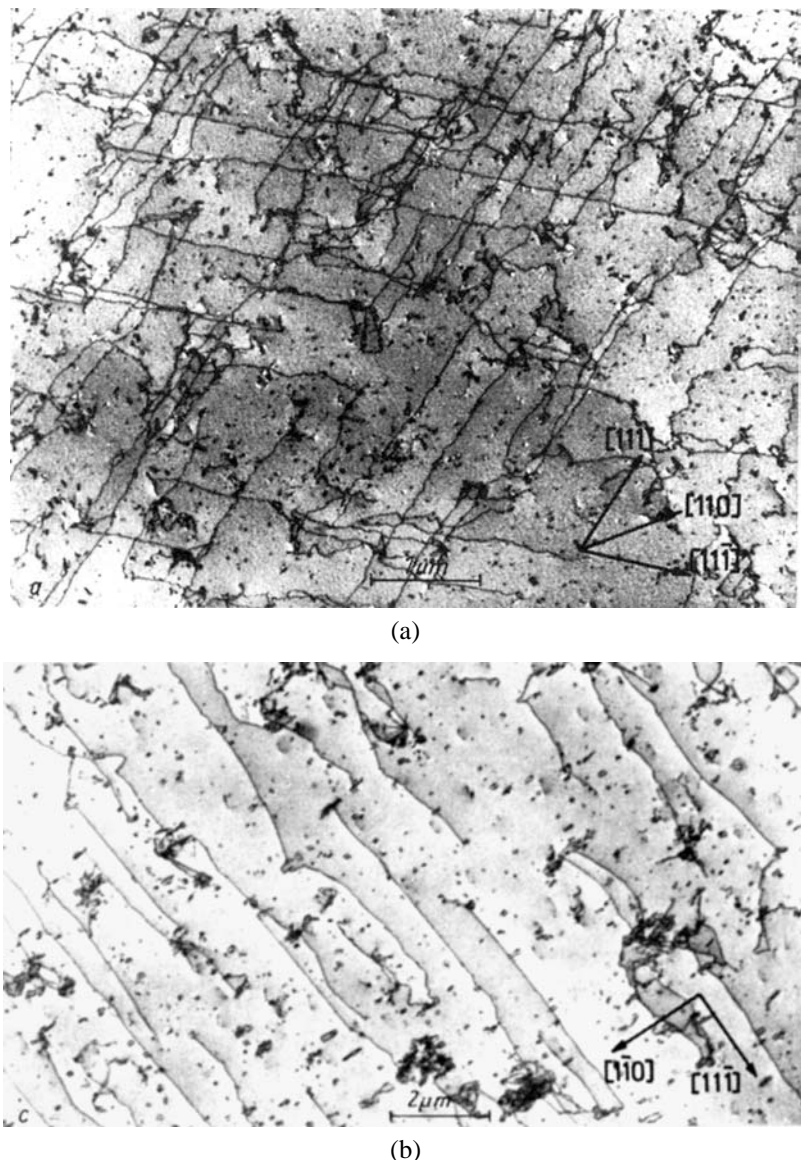


Fig. 30. (a) Dislocation microstructure in Mo under 2% tensile strain along $[110]$ at 77 K. (b) Dislocation microstructure in Mo under 5.8% tensile strain at 293 K [121].

Another common element of the microstructure in BCC metals is a high concentration of debris in the form of vacancy and interstitial loops, which are often observed after deformation, as shown in Fig. 30(b) [121]. The debris concentration typically increases with increasing straining rate. While mechanisms of such debris production are not entirely

clear at present, a possible explanation for this behaviour will be discussed later in this section.

The dominant dislocation type has Burgers vector $\frac{1}{2}\langle 111 \rangle$, which is the smallest repeat vector of the BCC lattice. $\langle 100 \rangle$ dislocations are also observed. The latter are thought to be products of reactions between $\frac{1}{2}\langle 111 \rangle$ dislocations. Slip trace analysis reveals slip in $\{110\}$, $\{112\}$ and even $\{123\}$ planes of the $\langle 111 \rangle$ zone [5,127]. At higher temperatures, the so-called pencil or non-crystallographic slip is observed such that the slip plane, on average, follows the maximum resolved shear stress (MRSS) plane, with the slip traces having a wavy appearance [128–130]. The zonal character of dislocation slip and the mentioned TEM observations underscore the prominent role of screw dislocations in the plasticity of BCC metals. In the kinematical sense, at low and moderate temperatures (below ~ 400 K) the non-screw dislocations behave as “slaves” to the dominant screws.

Both calculations and experimental observations suggest that there are no stable stacking faults in BCC metals, at least in ambient conditions. If so, then the dislocations in these solids should not dissociate in a planar, FCC-like fashion. Combining this with the fact that the BCC dislocation cores are observed to be rather compact and the pre-dominance of screw dislocations already mentioned, one sees that plasticity in BCC metals should be strongly influenced by cross-slip processes. The very term “cross-slip” coined to describe rather infrequent events where the dislocation changes glide plane in FCC metals, could be somewhat misleading when used to describe the motion of screw dislocations in BCC metals. Given its compact core, a screw dislocation does not have to first constrict in order to change its glide plane; there would be always more than one glide plane that is available. The selection of glide plane and resulting slip crystallography are likely to be governed by rather more subtle effects in the core of the screw dislocation than the planar dissociation invariably observed in FCC metals. As recently emphasized by Duesbery and Vitek [131], existing perceptions about dislocation behaviour in BCC metals are heavily influenced by the views developed earlier for FCC and HCP metals. Since the extrapolation of these views beyond these crystallographic classes has not been well justified, the “FCC ideology” should not be applied to BCC metals without a sound basis.

4.2. Core structure and lattice resistance

4.2.1. Screw dislocations

The early ideas about the structure of screw dislocation core are centred around the hypothesis of FCC-like planar splitting for explaining the observed slip phenomenology [132–134]. In a drastic departure, Hirsch suggested that screws can dissociate in more than one plane and that such a non-planar dissociation can explain the observed high Peierls barrier and the strong temperature dependence of the yield stress [135]. Initially, various variants of screw dislocation splitting were considered (for a review see [136]). Eventually, with the help of computer simulations, the thinking converged to the well-known three-way dissociation into three equivalent $\{110\}$ planes. Vitek et al. [136,137] and Duesbery et al. [131, 138] have clearly shown that such a dissociation can occur even when no plane of the $\{111\}$ zone contains a stable stacking fault. Still, the use of the term “dissociation” implies that the perfect screw dislocation somehow splits into several partials or, fractional dislocations.

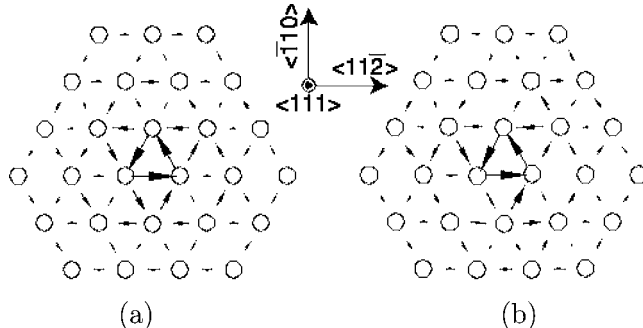


Fig. 31. Differential displacement map of screw dislocation core in BCC metals, (a) symmetric core, (b) asymmetric core [139].

We think that such a picture is not necessarily appropriate for describing the screw dislocation core in BCC metals as it could lead to complications and even misunderstanding. In the following, we will refer to dislocation core spreading as “polarization”, resulting from a symmetry-breaking core reconstruction.

Fig. 31 shows differential displacement maps (DDM) [140] of screw dislocations. Each circle represents a column of atoms. The dislocation line and Burgers vector are parallel to the atom columns, i.e. along z direction (out of the plane). The DDM map is constructed by first computing the atom displacement (along z direction) with respect to perfect lattice for each column. The arrows then indicate the difference between displacements of neighbouring columns. The length of the arrow is proportional to the magnitude of displacement difference and the direction of the arrow indicate the sign of the displacement difference, i.e. the column that the arrow points to has a larger displacement than the column on the other end of the arrow. Because the lattice is periodic in z direction by Burgers vector b , the displacement difference, i.e. the differential displacement, between any two columns can be only defined *modulo b*. By convention, the differential displacement is always mapped into the domain of $(-b/2, b/2]$ by adding or subtracting multiples of b . Among the three atoms in Fig. 31(a) that surround the centre of dislocation, the DDM arrows form a closed circuit. The differential displacement between any two atoms out of these three, going counterclockwise, is $b/3$. By going around any circle containing the dislocation centre, one accumulates a total displacement b . We should emphasize that while the arrows in the DDM are all in the plane for convenience of visualization, the displacement component they represent is strictly out of the plane.

It should be noted that, regardless of the details of misfit distribution, the core is rather compact. That the core spreads is a consequence of elastic-energy reduction; any such spreading can be interpreted as fractional splitting of the perfect screw dislocation core into the planes of the $\{111\}$ zone. Less obvious is which directions and planes the spreading entails. The fine structure of the core would depend on subtle details of atomic interactions in the core. Some atomistic models predict nearly equal core extensions in all directions while others show a characteristic splitting into three directions on three $\{110\}$ planes of the zone. The latter can be interpreted as a core reconstruction that also spontaneously

breaks the symmetry of the host lattice.⁴ The atomistic meaning of this core reconstruction is very simple: three rows of atoms immediately bounding the geometric centre of the screw dislocation shift in the same direction along the Burgers vector [141]. This shift can take place in either of the two directions along the dislocation line, giving rise to two energetically equivalent but geometrically distinguishable core variants. We will discuss the possible consequences of such core reconstruction, aka polarization, later on in this section.

The detailed structure of screw dislocation core in BCC metals has been examined through atomistic simulations [139,142–147], particularly with regard to the effects of in-core relaxation. Most of the earlier calculations predicted a polarized core structure that was seemingly observed in HREM experiments [148]. Polarization was a significant issue since the details of the atomic rearrangement in the core were thought to have an effect on the lattice resistance to dislocation motion. Specifically it has been an almost universal belief that the high Peierls stress of the screw dislocation is a direct consequence of its non-planar core structure. According to this view, the mobility of the screw dislocation must be limited because, by spreading into several planes of the zone, the dislocation effectively anchors itself to the lattice, such that in order to translate through the lattice it has to retract some of its extension, a process that requires considerable energy. The anchoring effect of non-planar dissociation is thought to be more pronounced when the core is polarized, since then the core extension would be maximum [149]. Recently this belief has been called into question by *ab initio* calculations [139] which presented evidence that even non-polarized screw dislocations in Mo and Ta have high Peierls stress, of the order of 1 GPa. On the other hand, it has also been observed that the Peierls stress is a sensitive function of core polarization [150]. In view of these contradictory results, it seems prudent to conclude that high Peierls stress is not necessarily caused by non-planar core dissociation or polarization, and yet, with all things being equal, core polarization may have an effect on the Peierls stress. That core polarization may not be the dominant factor for the magnitude of Peierls stress is consistent with the observation that, under shear stress approaching the maximum (Peierls) sustainable level, the dislocation core undergoes profound changes that effectively wipe out the features of core structure observed at zero stress [151,152].

That the compactness of the core gives rise to a large Peierls stress is also an effect described by the Peierls model of dislocation core. It is evident that, for a dislocation to translate from one lattice position to the one adjacent, the more extended the core the less each atom in the core has to move relative to its neighbours. While clearly more atoms take part in the translation of a wider core, the Peierls barrier for the wider core is lower because of the highly non-linear character of interatomic interactions in the core. This effect is also seen from a well known correlation between the core width and Peierls stress in FCC metals [6]. The opposite effect can also occur—a dislocation with narrow core, notably in Si, can have very high Peierls stress, approaching the ideal shear resistance of the crystal [59] (see the preceding section).

⁴The symmetric core configuration is sometimes unfortunately referred to as six-fold symmetric, whereas the symmetry-broken structure is described as three-fold symmetric. This description is incorrect and misleading. The symmetry around the {111} zonal axis remains three-fold, regardless of the core reconstruction. The symmetry that is broken is that with respect to 180°-rotation around any of three {110} axes of the zone [5] (p. 370).

In atomistic simulation when the applied stress reaches the Peierls value, a screw dislocation responds by moving along one of the crystallographic planes of the $\frac{1}{2}\langle 111 \rangle$ Burgers vector zone, most often a $\{110\}$ plane closest to the MRSS plane. Depending on the interatomic potential, the translation plane can be $\{112\}$ [152] as well. For example, the FS model potential predicts that screw dislocations in Mo move along $\{110\}$, but in Ta they move along $\{112\}$ [131]. Also, screw dislocations simulated by using Finnis–Sinclair’s model of bcc-Fe are observed to move on either a $\{112\}$ or a $\{110\}$ plane depending on the orientation of the MRSS plane [33]. The slip-plane selection and critical stress condition for screw dislocations are clearly in violation of the Schmid law [153]. For example, in cases where the screw dislocations show a definite preference to glide, say, on $\{110\}$ plane the Schmid law specifies which of the three $\{110\}$ planes of the zone will be selected, as well as the level of applied stress σ_{ij} at which the dislocation should begin to move, the latter being given by

$$\sigma_{ij} s_{ij} = \tau_{PN}, \quad (25)$$

where τ_{PN} is the Peierls stress and s_{ij} is the Schmid tensor of the given plane. For a pure shear stress σ applied along the Burgers vector, the relation reduces to

$$\sigma = \tau_{PN} / \cos(\chi), \quad (26)$$

where χ is the angle between the MRSS plane and the nearest $\{110\}$ plane. Relative to the Peierls stress for $\chi = 0$, the Peierls stress variation specified by the Schmid law is shown in Fig. 32. The variation simulated using an atomistic model of Mo, also shown, is clearly in considerable disagreement with the Schmid law [153,154]. This and almost all other atomistic calculations reported so far showed that the motion of screw dislocation in BCC metals at low temperature does not follow the prescriptions of Schmid law [153]. The origin of the non-Schmid behaviour is largely due to the twining-antitwining asymmetry of the BCC lattice, which makes $\chi = 30^\circ$ and $\chi = -30^\circ$ drastically different from each other. In addition to the non-Schmid χ -dependence, other stress components have been found to affect the critical stress, most notably the components perpendicular to the Burgers vector [155,156]. Duesbery and Vitek [131] traced such non-Schmid effects to a coupling between the applied stress and small but resolvable edge components of displacement observed in the core of the screw dislocations. An extensive and thorough analysis of various non-Schmid couplings affecting the motion of screw dislocations in BCC metals was presented by Duesbery in volume 8 of this series. An alternative to coupling with edge components is that the activation energy for motion couples to other stress components via the activation strain. A specific case would be coupling of isostatic stress to a variation in the nonlinear dilatometric field of the dislocation, which could vary during kink formation.

Given that the Peierls stress of a screw dislocation is considerably higher than that of non-screw components, it is usually assumed that the macroscopic yield stress at low temperatures is closely related to this stress, a reasoning that finds support in the results of Dislocation Dynamics simulations [157]. As we have just discussed, the well-documented violations of the Schmid law in the yield behaviour of BCC metals are in general agreement with atomistic simulations [139,143,145,147]. In this context, the current discrepancy between the computed and experimental estimates of the Peierls stress is puzzling.

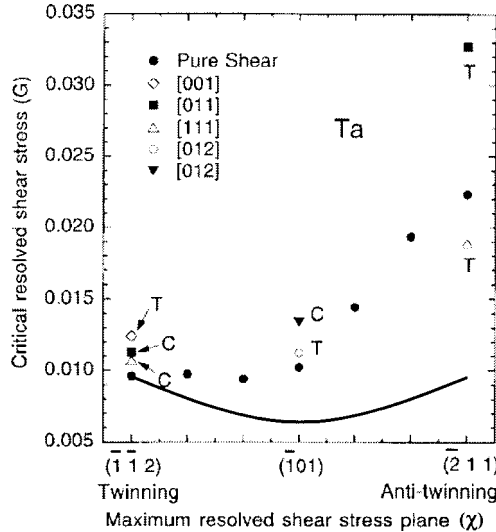


Fig. 32. Screw dislocation Peierls stress for different loading stress directions in the {111} zone. The solid line shows the prediction of Schmid law and the symbols show typical atomistic simulation results [145].

The atomistic calculations consistently overestimate the yield stress (see e.g. [121,158]) by a factor of 2–4. For example, the zero-temperature limit of yield stress for Mo is 750 MPa [121] while the Peierls stress for screw dislocation from atomistic calculations is around 2–3 GPa [146,147]. Attributing the discrepancy to the inadequacy of interatomic potentials, while seemingly reasonable, is not supported by recent DFT calculations [139] which also gave Peierls stress values for Mo and Ta several multiples of the experimental estimates. Another hypothesis suggests that the lower experimental values reflects the collective motion of dislocations in groups and amplification of the applied stress through the mutual interaction of dislocations in each group [159]. This explanation appears tenuous and does not provide a mechanistic interpretation. At present the consistently lower values of the experimental yield stress point to a fundamental aspect of dislocation behaviour in BCC metals that remains to be explained. In the next subsection concerning secondary core defects, we will discuss simulation findings that relate the yield-stress discrepancy to particular features of interaction between screw dislocations.

4.2.2. Non-screw dislocations

The core structure of edge (Fig. 33) and other non-screw dislocations, is relatively unremarkable when compared to the screws. The core shows moderate spreading in the glide plane although no clear planar dissociation can be detected. The Peierls stress of non-screw dislocations in BCC metals is commonly assumed to be low. Duesbery and Xu [160] have challenged this belief by presenting atomistic simulations that gave a high Peierls stress for pure edge dislocations in Mo (FS potential), of the order of 0.5 GPa. The authors assumed that mobility of edge dislocations at non-zero temperatures should be controlled by kink mechanisms, similar to the ones operating in screw dislocations. This interpretation was in turn called into question by another simulation study giving more attention to the effects of

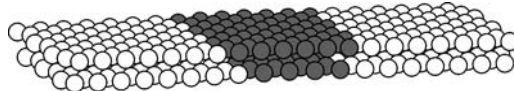


Fig. 33. Core structure of an edge dislocation. Two layers of atoms immediately above and below the glide plane are shown. Atoms with local energy 0.1 eV higher than the bulk are plotted in black to show the dislocation core.

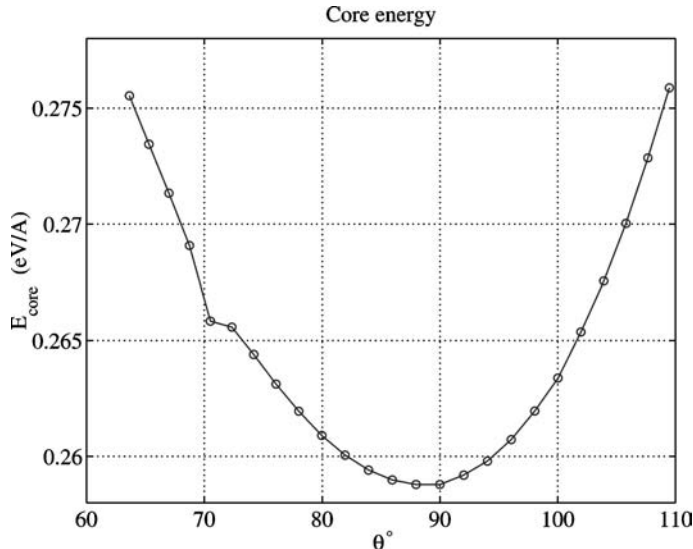


Fig. 34. Core energy of non-screw dislocations in BCC Mo as a function of character angle, with core radius $r_c = 1b$.

boundary conditions as a source of error in determining the Peierls stress [40]. The present status is that a converged Peierls stress value for pure edge dislocations, obtained using the FS model of Mo, is just 25 MPa, more than an order of magnitude lower than that reported in [160]. Although different boundary conditions, fixed and periodic, respectively, were used in the two studies, it is evident that finite-size simulation cell effects, if not properly treated, can lead to serious errors.

An implication of the above noted discrepancy is that the relation between Peierls stress and the dislocation character remains to be clarified. There is an indication from atomistic calculations that some non-screw dislocations have much higher Peierls stress than the others [161]. In contrast to the earlier work [160], it is not the pure edge dislocations that have exceptionally high Peierls stress but the 71° -mixed dislocations denoted M111 in [161, 162]. For the latter the fully converged Peierls stress value for the same FS model potential is 320 MPa, whereas for the other non-screw dislocations on $\{110\}$ planes the stress is generally 20–30 MPa. These values are in contrast to the value of 2.4 GPa obtained for screw dislocations using the same potential model. That the M111 dislocations are special is indicated by the observation of a cusp-like dependence of the dislocation core energy on the character angle, with the cusp centred precisely on the M111 character angle (Fig. 34).

This cusp resembles the well-known behaviour of the grain boundary energy as a function of the misorientation angle, near a special low- Σ boundary [163]. The essential difference here is that dislocations, unlike grain boundaries, produce long-range elastic fields; their energy is dominated, in most cases of interest, by the elastic energy. Since the dominant elastic component of the dislocation energy is generally a smoothly varying function of the character angle, the cusp-like feature shown in Fig. 34 is not as distinct as that seen in the grain-boundary energy. It takes a special effort and the use of very accurate methods [164] to observe cusp-like features in atomistic calculations of dislocation energies.

The observation of dislocation energy cusps implies that the two orientations (screw and M111) correspond to particularly favourable packing of atoms in the dislocation core. Analogous to special grain boundaries, at both orientations the dislocation displays special properties, notably a high Peierls stress. It would be useful to examine whether kink mechanisms operate in the M111 dislocations at non-zero temperatures and if the cusp-like behaviour can result in experimentally detectable features of dislocation microstructure.

4.3. Secondary core defects

4.3.1. Reconstruction defect

It has been already noted that polarization of the screw dislocation core in BCC metals is a special case of symmetry-breaking core reconstruction. Symmetry arguments in fact provide a unique perspective from which to analyse the core structure. This particular core reconstruction breaks a dyadic symmetry with respect to 180°-rotation around a $\langle 110 \rangle$ axis, resulting in a two-fold degenerate core, i.e. there exist two geometrically distinguishable but energetically equivalent variants of the reconstructed (polarized) ground-state core structure. This suggests that reconstruction defects (RD), or anti-phase defects should appear where the dislocation core divides into two segments, each with a different reconstructed core. As noted in [141,165] there are two types of RD in a reconstructed $\frac{1}{2}\langle 111 \rangle$ screw dislocation in BCC lattice, denoted as AxB and BxA flips. The meaning of these terms is easy to understand by observing that the core reconstruction involves moving three central rows of atoms together in the same direction with respect to their immediate neighbour rows. One variant of the core reconstruction produces a shift in, say, positive Z direction (along the Burgers vector), while the other variant results in an identical shift in the opposite direction. When two adjacent core segments shift in opposite directions, they will either shift towards each other or move apart, to produce respectively a compressed region (BxA -flip, positive pressure), as shown in Fig. 35, or an extended region (AxB -flip, negative pressure). If the displacement of three central rows is equal to $b/6$, the maximum possible value, then a BxA -flip is an interstitial-like defect while the AxB -flip defect is vacancy-like. In atomistic calculations smaller displacements leading to partial interstitial or vacancy-type defects have been observed [166].

Given that core degeneracy can affect screw dislocation motion, it is appropriate to examine if and how this degeneracy can be removed by stress. Using the Finnis–Sinclair potential model, we find [73] that energy degeneracy of the two variants of a polarized screw dislocation core in Mo is indeed removed by either one of the two glide stress components, shear stresses applied along the Burgers vector on any plane of the zone. Furthermore, the

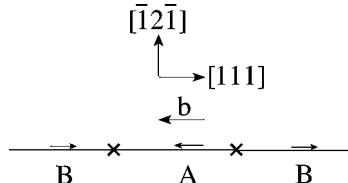


Fig. 35. Schematics of reconstruction defects (RD) on screw dislocation core in BCC lattice. The arrows indicate the direction of reconstruction displacements of the three atom columns in the core. They are opposite in *A* and *B* type cores, forming two types of RD's, *AxB* and *BxA* [141].

non-glide stress component, called “edge” stress, also removes the degeneracy. This means that under the action of an appropriate stress component, one of the polarization variants of a screw dislocation core becomes energetically favoured relative to the other, and occupies a larger fraction of the core length. Furthermore, if the “wrong” core variant were somehow created, it would have a tendency to convert to the low energy variant, most probably by the stress-induced drifting of RD's. In other words, the motion of RD's along the screw dislocation core could be coupled to the external stress. Activation of one or the other core variant and the conversion rate will depend on the magnitude of the degeneracy splitting and the kinetics of flip nucleation and motion. This effect contributes further to the already complex picture of how the glide and non-glide stress components can affect the choice of slip planes of screw dislocation.

4.3.2. Kinks

A Peierls stress of the order of 1 GPa signifies a correspondingly high energy (Peierls) barrier and motion of screw dislocation at non-zero temperature, via thermally and stress-activated kink-pair mechanisms (see the preceding section). Early calculations by Duesbery showed that nucleated kinks experience very low resistance to their motion along the screw line [141], consistent with the observation of very long and geometrically straight screw dislocations [122]. Therefore, the overall rate of dislocation motion seems to be controlled by kink-pair nucleation events. Later calculations confirmed that the kink migration barrier [40] is indeed low relative to the kink-pair nucleation barrier and the energy of a stand-alone kink [143]. For example, the FS model potential for Mo predicts that kink-pair nucleation energy is 1.2 eV while the Peierls stress for kink motion along the line is 20 MPa, quite similar to the Peierls stress of pure edge dislocations [40].

Historically, various continuum models have been used to model kinks in screw dislocations in BCC metals. Dorn and Rajnak [167] have applied a line tension model to examine analytically the transition state for kink-pair nucleation. This model provides a useful relationship between the Peierls stress, Peierls barrier, and kink-pair formation energy, which is given earlier in eq. (24). Early in the 70's several other continuum models were proposed based on the understanding at the time of the structure of screw dislocation core [168]. Recently, Ngan proposed a Peierls–Nabarro model that treats the three-fold non-planar extension of the screw core [169,170]. In principle, a model like this should allow numerical evaluation of kink energies using the gamma-surface data as an input, however care should be taken in partitioning the misfit among three planes in a consistent manner. In comparison, direct atomistic calculations of kinks to be discussed below, are

still too expensive and/or inaccurate and have so far produced relatively few data points for kink energetics. The continuum models, although approximate, provide an inexpensive alternative to atomistic calculations for a general study of variation of kink-pair energy with stress. By matching the continuum models to suitable atomistic counterparts at selected data points, one can hope to achieve results valid over a wide range of temperature and stress conditions.

An interesting continuum model of kink-pairs in screw dislocations in BCC metals was suggested by Edagawa et al. [171] which departs completely from the FCC-inspired notion of the γ -surface as the core misfit potential. Instead it is assumed that the dislocation-lattice coupling (Peierls potential for the screw dislocation) can be specified as a 2D surface in the XY plane perpendicular to the direction of the Burgers vector:

$$E[x(z), y(z)] = \int_{-\infty}^{\infty} \left\{ \frac{\Gamma}{2} \left[\left(\frac{dx}{dz} \right)^2 + \left(\frac{dy}{dz} \right)^2 \right] + V_p(x, y) - \tau b(x \cos \chi + y \sin \chi) \right\} dz, \quad (27)$$

where E is the total-energy of the dislocation having the configuration $\mathbf{r}(z) = [x(z), y(z)]$ with respect to the initial equilibrium configuration at $\mathbf{r}_0 = (x_0, y_0)$, Γ denotes the line-tension of the dislocation and $V_p(x, y)$ is the effective Peierls potential and the third term is the work done by stress. This model appears to be most appropriate for describing screw dislocations in BCC metals, accounting correctly for their non-planar core structure and motion. The model also provides a reasonable description of the kink-pair nucleation barrier and its dependence on stress, and even the χ -dependence of Peierls stress discussed above is correctly reproduced [171]. Consequently, such a formulation may be suitable for parameterisation against atomistic calculations, in which case just two parameters are sufficient to fully define the non-planar misfit potential (equation above). One may use, for example, an atomistic value of the kink-pair energy at zero stress and, in the opposite limit, a value of the Peierls stress, say, for $\chi = 0$. The misfit potential thus produced can be used to compute and tabulate the kink-pair nucleation barrier in the entire range of applied stress. Used in this manner, the model serves as an interpolation function for kink-pair nucleation barrier between two limits, a state of zero stress and that of Peierls stress.

However useful, the continuum models nevertheless cannot account for salient atomistic features of the dislocation core structure and dislocation motion. Only calculations taking into account explicitly the atomic degrees of freedom can properly describe the subtleties of dislocation behaviour in BCC metals in their full complexity. These are discussed below.

Fig. 36 shows the schematics of core atoms in screw dislocations with kinks on the {110} plane. Because the BCC lattice is not symmetric with respect to 180° rotation along {111} directions, the left and right kinks on the screw dislocation are not degenerate, even when the core is not polarized [87]. For the polarized core, there are six different kink types in various combinations of two RD's and two original kinks [87]. Duesbery has referred to the kinks with the same sense of polarization on each side and the kinks separating two segments of opposite polarization as homokinks and heterokinks respectively [141]. In view of the possible kink pairs on {110} planes, there are several distinct combinations of homo-

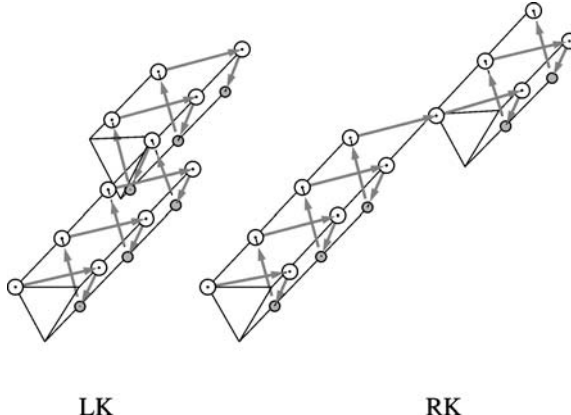


Fig. 36. Core atoms of a screw dislocation in BCC lattice with left kink (LK) and right kink (RK). LK and RK are different because of the lack of 180° rotation symmetry along $\langle 111 \rangle$ direction of the BCC lattice.

and heterokinks that may contribute to dislocation motion [159]. Atomistic calculations performed so far indicate that one particular kink-pair, namely the pair called *BnApB* in [159], has the lowest nucleation barrier. When the dislocations move by nucleating and expanding this kink pair, its core polarity will be reversed each time it moves by a unit step on the $\{110\}$ planes. As shown in [159], this kink pair provides a 3D atomistic path for dislocation translation that is consistent with the zig-zagging motion of straight screw dislocations observed in the earlier 2D simulations [152]. Thus, a case can be made for this particular kink pair as the dominant translation mechanism below the Peierls stress. As a cautionary note, we observe that, just like in the case of kinks in glide partials in Si (see the preceding section), the flips that can be present in the core may facilitate the nucleation of other kink-pairs that can compete with this pair. If this is the case, dislocation motion under stress can proceed through a complex sequence in which several types of kink-pairs contribute simultaneously. Later on, we will discuss yet another possible contribution of flips to the “rough” motion of screw dislocations under high stress.

Atomistic simulations have found that the centre of the dislocation has to reside in one type of the triangles (either Δ or ∇ , depending on the Burgers vector) in the triangular lattice of atom rows when looking along the Burgers vector direction (Fig. 31). Centring the dislocation in the “wrong” triangle will result in three core atoms sitting on top of each other, resulting in the high energy “hard core” configuration, instead of the low energy “easy core” configuration [143]. For this reason, translation of the dislocation core on the $\{110\}$ plane, or equivalently along the $\langle 112 \rangle$ direction requires a minimum core displacement from one “easy” position to another. Translation on the $\{112\}$ plane, or equivalently along the $\langle 110 \rangle$ direction requires a displacement that is $\sqrt{3}$ times larger. Therefore, most atomistic simulations have focused on kinks on the $\{110\}$ plane. Duesbery has shown that at zero stress the $\{112\}$ kink pairs, being unstable, dissociate into shorter $\{110\}$ kinks. In this as yet unpublished work, Duesbery used the NEB technique [172,173] to explore the atomistic paths for kink-pair nucleation in which the final (destination) state of the dislocations contains a $\{112\}$ kink pair. The search showed that the dislocation, although forced

to make a large $\{112\}$ step, preferred to do it in two smaller $\{110\}$ steps. On the other hand, Seeger considered kink-pairs in the $\{112\}$ plane and developed a theory that agrees well with experimental data on internal friction. Therefore, which kink matters in what conditions is still an open issue.

According to the elasticity theory kinks on $\{110\}$ plane should have $1/3$ the energy of those on $\{112\}$ plane simply because kink energy is proportional to the square of its height. Atomistic simulations of straight screw dislocations at zero temperature show that, depending on the interatomic potential, dislocations can move on $\{112\}$ planes under stresses equal to or exceeding the Peierls value [131]. Such motion can be viewed as a limiting case in which the stress is sufficiently high to overcome any effect of the kink-pair nucleation barrier. That dislocations move along the $\{112\}$ planes at stress equal to the Peierls stress implies that as the stress levels approaches this critical value from below, the effective barrier for $\{112\}$ kink-pair nucleation must have been greatly reduced to allow this mechanism to operate. At low stress the $\{110\}$ kink-pairs should be still favoured given their lower nucleation energies at zero stress. The overall stress dependence of kink-pair nucleation barrier can be one which connects smoothly the high-stress limit favouring the $\{112\}$ kink-pairs with the low-stress limit where the $\{110\}$ kink-pairs dominate, as depicted schematically in Fig. 37. A crossover between the two regimes offers a possible resolution of the current controversy.

Recently Wen and Ngan presented an exploration of atomistic mechanisms of kink-pair nucleation in α -Fe [174]. Their results show that the $BnApB$ kink-pair has the lowest activation barrier among all possible candidates. Seen in Fig. 7 in their paper [174] are signs of a degeneracy-removing coupling between the glide stress and the core polarization. This work is a definitive description of atomistic mechanisms of kink-pair nucleation in the relevant range of applied stress, from zero to Peierls, which should pave the way for similar future studies. The main conclusion that core polarization favours pencil glide, however, appears to be questionable. The mixing of two different translation directions, as required for pencil glide, is more likely when the core is not polarized so that the screws can translate by any of the six $\{110\}$ kink-pairs. In this case, the ratio of glide stress resolved on two neighbouring $\{110\}$ planes can be anywhere between 0.5 and 1.0. In the case of a strong core polarization considered by the authors, i.e. when translations can take place only by three kink pairs of the $BnApB$ type, the resolved stress ratio spans a significantly wider range from -0.5 to 1.0. Most of this range is far from the ratio of 1.0 ideal for the pencil glide mixing.

4.3.3. Junction nodes

The junction node where three dislocation segments meet is a special (point-like) entity which can play a significant role with regard to the above mentioned discrepancy between the Peierls stress determined atomistically and the observed low temperature limit of the yield stress. Matsui et al. [175] have suggested that the junction nodes at the ends of a dislocation junction can act as sources of dislocation kinks, thereby explaining the anomalous slip behaviour observed in some high-purity BCC metals at low temperatures [176]. According to the proposed Co-planar Double Slip (CDS) mechanism, the enhanced kink nucleation at the nodes can more than compensate for a low resolved stress on the anomalous slip system which then becomes more active than other more highly stressed systems. Sub-

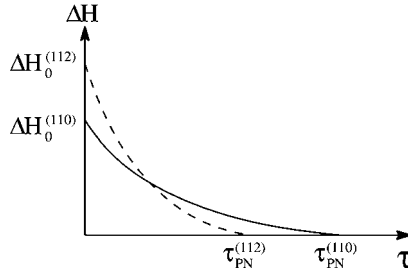


Fig. 37. Double kink nucleation barrier as a function of stress. Solid and dashed curves represent kinks on (110) and (112) planes respectively.

sequently, Saka et al. [177] observed motion of co-planar junction networks using *in situ* TEM. However, this observation was challenged by Garratt-Reed and Taylor [178], who noted that dislocations had to move against the applied stress in some stage of the CDS glide and therefore such a mechanism was unlikely to operate. Garratt-Reed and Taylor suggested an alternative mechanism for facilitating screw dislocation motion in the glide plane [178]. In their mechanism the dislocations approaching each other do not need to form a junction to move faster; they can exert torques on each other causing them to bend in the anomalous {110} plane. While such local bends may prevent the dislocation from getting any closer, they can also be an efficient source of kink nucleation. The two hypotheses, although differing in details, both emphasize that dislocation interactions, whether local as in CDS or remote as in Taylor's mechanism, can enhance dislocation mobility rather significantly.

Recently, direct atomistic simulations of the motion of a screw dislocation network have been performed to verify the feasibility of the CDS mechanism in BCC metals [179]. As two sets of $\frac{1}{2}\langle 111 \rangle$ screw dislocations zipped together to form {001} junctions, a dislocation network is generated on the {110} plane. It was found that the network can move conservatively in any direction in the {110} plane, provided the stress direction and magnitude are chosen appropriately. It was also found that the network begins to move at stress levels well below the Peierls values for its constituent dislocations, for all directions of stress in the {110} plane. The results of these calculations are shown in Fig. 38, in terms of the critical stress required to move the junction network as a function of stress direction, expressed in polar coordinates with stress magnitude and direction angle as variables. The nodal effect on dislocation mobility is seen here in the clustering of the data points from atomistic calculations inside the envelope formed by the Peierls stress values computed for each of the three constituent dislocations in isolation.

While kink nucleation at the nodes appears to be the mechanism for enhanced mobility, contrary to the original hypothesis of Matsui and Kimura the kinks were observed to nucleate at the trailing node of the moving junctions and then to converge on their leading nodes. Otherwise, the CDS mechanism seems to be supported by the atomistic calculations. It was also confirmed that such a nodal enhancement of dislocation mobility requires two conditions to be satisfied simultaneously, a high barrier for kink-pair nucleation on a straight screw dislocation, and a low kink migration barrier. In these calculations using the Finnis–Sinclair model of Mo, the Peierls stress value of 2.4 GPa obtained indeed indicates

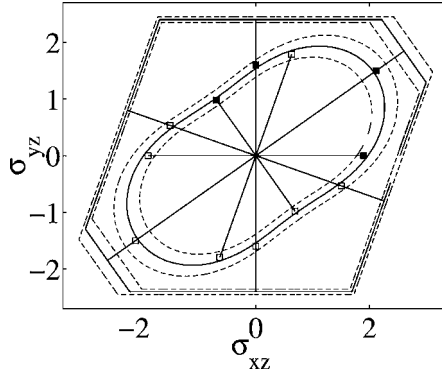


Fig. 38. Peierls stress of the dislocation network as a function of stress orientation. Filled symbols show the values of critical stress for the four directions actually tested. Open symbols are obtained by symmetry. Dashed lines indicate the range of error in the computed Peierls stress [179]. The hexagonal envelop corresponds to conditions when at least one of the three dislocations see a resolved stress exactly equals to its Peierls stress.

a high nucleation barrier. At the same time, the Peierls stress for kink migration is 20 MPa, two orders of magnitude lower. We expect that when these energetic conditions are met, the nodal effect on dislocation mobility will be even more dramatic at finite temperature. Even though the atomistic study confirms the CDS mechanism, it is possible that the mechanism suggested in [178] also can be important. Similar simulations examining the effect of torques on dislocation mobility would be instructive.

4.4. Dislocation mobility

4.4.1. Experiments

Experimental measurements of dislocation mobility in BCC metals are more difficult compared to the case of Si (see the preceding section), mainly due to the problem of obtaining samples with low dislocation density. Early experimental results on screw and edge dislocation mobility may be contaminated by the interaction of moving dislocations with grown-in dislocations and the free surfaces. For example, it was reported that edge dislocations [124] have a lower mobility than screw dislocations [125, 180–182]. This has led to the conclusion [126] that kink mechanisms do not play a role in screw dislocations, which is in contradiction with the current understanding.

More recent *in situ* TEM observations have established that edge dislocations move much faster than screw dislocations [122], consistent with TEM observation of dislocation microstructures dominated by screw dislocations. Unfortunately, it is difficult to estimate the actual stress exerted on dislocations in *in situ* TEM experiments. This can be seen from the large difference between the applied stress and the estimated local stress on dislocations in Fig. 39 [122].

In addition to the large mobility difference between edge and screw segments, TEM observations have provided ample evidence that dislocation motion by itself can produce

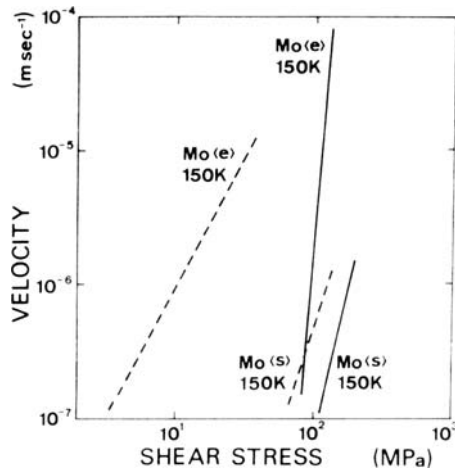


Fig. 39. Velocity of edge (e) and screw (s) dislocations in Mo as a function of stress by *in situ* high voltage electron microscopy [122]. Solid lines represent external stress, and dashed line represent estimated local stress on dislocations taking into account mutual dislocation interactions.

high density of point defects and point defect clusters, in the form of prismatic dislocation loops. This behaviour is similar to FCC metals, where a large density of Stacking Fault Tetrahedra (SFT) is observed in pure material deformed at high strain rate [183]. Generally, the higher the strain-rate the larger the observed concentration of defect debris [184]. The resolution of TEM observations of defect size distribution is limited to about 2 nm; defects at smaller sizes are not visible. The defect spectrum appears to be similar to the microstructures found in the same materials after irradiation. These observations also reveal characteristic shapes of screw dislocations with extended cusp-like features, as shown in Fig. 30(b). Although some of these features are likely to be due to dislocation interaction with extrinsic defects (impurities, precipitates), a large density of debris is also observed in very pure metals. The implication is that such behaviour is intrinsic to high strain-rate deformation of metals. Recent simulation results revealing the underlying mechanisms of debris production will be discussed later in this subsection.

Atomistic simulations have been carried out to make direct contact with measurements of dislocation mobility. While it is still too early to expect quantitative comparisons with experiments (which show large error bars as well), the simulations have been helpful in elucidating the qualitative behaviour and mechanisms of dislocation motion. In the following we will discuss a number of recent results of direct Molecular Dynamics simulations of screw and edge dislocations in BCC metals.

4.4.2. Screw dislocations

Fig. 40 shows two snapshots from a series of MD simulations of screw dislocation motion in BCC Mo (Finnis–Sinclair model [185]) at 10 K [186]. The simulations are quasi 2-dimensional in that the simulation cell is periodic along the dislocation line of length equal to five Burgers vectors. A constant strain rate is imposed to move the dislocation at the average velocity 200 m/s on the (110) plane. The internal stress fluctuates with considerable

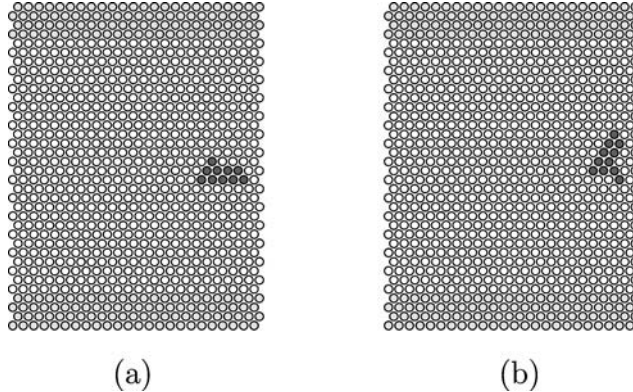


Fig. 40. Snapshots of quasi-2D MD simulation of screw dislocation motion in BCC Mo at 10 K. Atoms with local energy 0.1 eV higher than that of the perfect lattice atoms are plotted in dark color to show the dislocation core. The simulation cell is periodic along the horizontal direction (along which dislocation moves) as well as along the dislocation line (out of plane). The grey atoms in the upper and lower layers of the cell are forced to displace at a constant velocity corresponding to a fixed strain rate.

amplitude about the Peierls value as the dislocation moves intermittently, with bursts over several atomic spacings. This behaviour, reminiscent of the Portevin–LeChatelier (PLC) effect in crystal plasticity [187], is likely due to the small size of the simulation cell and the constant strain rate boundary-conditions. Nonetheless, certain qualitative features observed from these simulations may be relatively free from simulation artefacts. First, the dislocation core under stress, at rest and in motion, looks very different from the core under zero stress. The three-way splitting is not observed, instead, the core structure seems rather planar, as shown in Fig. 40, similar to earlier calculations of static relaxation under high stress [151]. Second, several cross-slip events were detected, prior to each the core was seen to fork or bifurcate onto the two candidate cross-slip {110} planes at 60° to the horizontal plane, as shown in Fig. 40(b). In all cases, cross-slip occurs in the upward direction even though the resolved stress on both potential cross-slip planes is the same. On reversing the straining direction, the cross-slip direction remains upward, which can be understood as a manifestation of the twinning-antitwining asymmetry on the atomistic level.

While capturing certain mechanistic aspects of screw dislocation motion, the foregoing simulations are not expected to be able to adequately account for the three-dimensional motion of a screw dislocation. An obvious constraint is the short dislocation length of 5 Burgers vectors which cannot accommodate even a single kink. According to previous simulations, a minimal kink would have to be at least $5b$ to $10b$ in width. Extending the simulations to much longer screw dislocations, one finds a greater complexity of kink mechanisms during dislocation motion.

A series of MD simulations of a $100b$ long screw dislocation moving in α -Fe (Finnis–Sinclair model [188]) has been performed [33]. The boundary condition is similar to that in Fig. 40 except that surface traction forces are applied to top and bottom layers of atoms to impose a constant-stress condition. As a point of reference, the Peierls stress for this

dislocation is 900 MPa. At 300 K and under applied stress of 400 MPa, dislocation motion via a sequence of kink-pair nucleation and kink migration events was observed. Almost equal number of kinks were nucleated on the horizontal {110} plane as on the “cross-slip” {110} plane inclined at 60°. This possibly reflects the twinning-antitwinning asymmetry in BCC lattice, just as in the 2D simulation above. During the simulation the dislocation was resting most of the time, whereas the kinks moved rapidly along the dislocation line once nucleated. On average, the dislocation moved at a velocity 88 m/s at 25° to the horizontal (MRSS) plane.

A high mobility of the nucleated kinks is to be expected given that the applied stress (400 MPa) far exceeds the Peierls stress for kinks (20 MPa), so that kink motion is limited only by the phonon drag mechanisms. The interplay between the rate of kink-pair nucleation J and the kink migration velocity v_k gives rise to a particular length scale λ such that, when a dislocation is shorter than λ , kink-nucleation would be rare and existing kinks will tend to glide along the dislocation line through the periodic boundary and recombine, before the next kink-nucleation event occurs. Under this condition, the dislocation velocity should be proportional to its length, since the number of double-kink nucleation sites is proportional to its length. This behaviour has been reproduced in mesoscale kinetic Monte Carlo simulations [189]. For the simulation conditions described above, taking $v_k \sim 2000$ m/s, $J \sim 3 \times 10^{17}$ m⁻¹ s⁻¹, one can estimate that $\lambda = \sqrt{v_k/J} \sim 300b$, which is consistent with the actual observation of at most only one kink pair on the dislocation line.

On dislocations with length longer than λ , another kink-pair can form while the previously nucleated kinks are still gliding along the line. Kinks from the same pair will not be able to recombine with each other while encountering kinks from the subsequent nucleation events. It is then generally expected that the dislocation velocity will reach a plateau value and become length-independent [5]. However, results of both atomistic and mesoscale simulations reveal the possibility of a much more complex behaviour for screw dislocations in BCC metals due to their ability to cross-slip easily.

The characteristic length λ can be readily varied by setting the temperature and/or applied stress. This is because stress and temperature have very different effects on the thermally activated kink-pair nucleation and phonon-drag controlled kink migration. In particular, kink migration velocity should be proportional to stress and must decrease with increasing temperature. At the same time, the kink-pair nucleation rate should rise very quickly with increasing stress or temperature. Thus λ must be a sensitive function of σ and T . For example, the condition of $\lambda < 100b$ is reached in a similar simulation at the temperature of 100 K and a stress of 750 MPa. A snapshot of such a simulation is shown in Fig. 41. The dislocation is seen to leave a significant amount of debris in its wake. This observation of debris formation confirms our earlier hypothesis [189] that, given the ease of cross-slip, a moving screw dislocation can contain both “glide” kink-pairs and “cross-slip” kink pairs, provided $l > \lambda$. A collision of glide and cross-slip kinks produces non-planar defects which have been called “cross-kinks” in the context of TiAl [191], as shown in Fig. 42(a). Such collisions create topological conflicts that, according to [191], can be resolved by one of two ways, sweeping the cross-kinks along the line akin to the pinning-unpinning mechanisms suggested in [191], or non-conservative jog-dragging previously suggested in [192]. Our MD simulations show that the way the conflict is resolved is completely different. Similar to a previously suggested mechanism [189], the dislocation

extracts itself from the conflict by moving by purely conservative double-kink nucleation, leaving behind prismatic loops, as shown in Fig. 42(b) and (c). No diffusional transport of vacancies or interstitials is involved in this process. That diffusion-less jog-dragging is possible was also suggested in [5] (p. 596).

The results just discussed show how important it is to let dislocations evolve freely in 3D and to probe the mechanisms of dislocation motion by large-scale MD simulations. In the 2D simulations shown in Fig. 40, such observation would not have been possible. In fact, the very same simulation depicted in Fig. 41 but repeated for a dislocation that is just $50b$ long, shows no roughening behavior: the dislocation glides smoothly through nucleation and propagation of kink-pairs. These observations suggest that one must exercise caution in interpreting the data of 2D simulations that, thus far, have greatly outnumbered 3D simulations.

4.4.3. Edge dislocations

The mobility of the non-screw dislocations has been observed to be much higher than that of the screws. It is then generally expected that the velocity of non-screw dislocations is limited only by the viscous drag due to their interactions with the lattice vibrations. While this belief was challenged by Duesbery and Xu [160], who found a rather high Peierls stress for edge dislocations in Mo (~ 0.5 GPa) and were then compelled to postulate the kink mechanisms to account for the known high mobility, more recent Peierls stress calculations found that their result is probably inaccurate. The value of the Peierls stress for an edge dislocation obtained using the same potential [40] is predicted to be only 25 MPa. Subsequent direct MD simulations [40] confirm that the mobility of edge dislocations is indeed controlled by phonon drag, and that kinks do not play a significant role.

The simulations made use of a simulation cell with a periodic boundary condition containing an edge dislocation dipole [40]. A constant stress is applied by the Parrinello–Rahman method [193]. The shape of the cell is chosen such that the interaction between the two dislocations and their periodic images is negligible. Fig. 43 shows the stress variation of dislocation velocity at 300 K. The two edge dislocations moved readily and smoothly at 100 MPa stress, consistent with their low Peierls stress. The velocity–stress relationship remains linear at velocities up to 1000 m/s. From the ratio between stress and velocity in this linear regime one can extract the phonon drag coefficient $B = \sigma/v = 0.7$ MPa s/m. The drag coefficient is found to increase with increasing temperature. All of these features indicate that edge dislocation mobility is controlled by the phonon drag mechanism. Similar simulations were repeated for edge dislocations with a pre-existing kink, which gave essentially the same results, thus providing direct evidence that kinks play no significant role in edge dislocation motion.

At stresses above 500 MPa, the dislocation velocity starts to level off, possibly due to relativistic effects, as shown in Fig. 43. In simulations using sufficiently large cells, the velocity value was found to be always lower than the transverse sound speed (3000 m/s). Recent MD simulations of edge dislocation motion have been focused mostly on very fast motion in which dislocation velocity can approach the sound speed [194]. Whether dislocations can move with velocities exceeding the sound velocity is still an open question. On the one hand, it has been argued that supersonic motion is impossible [195]. On the other hand, several direct MD simulations show that dislocations can move trans-sonically (be-

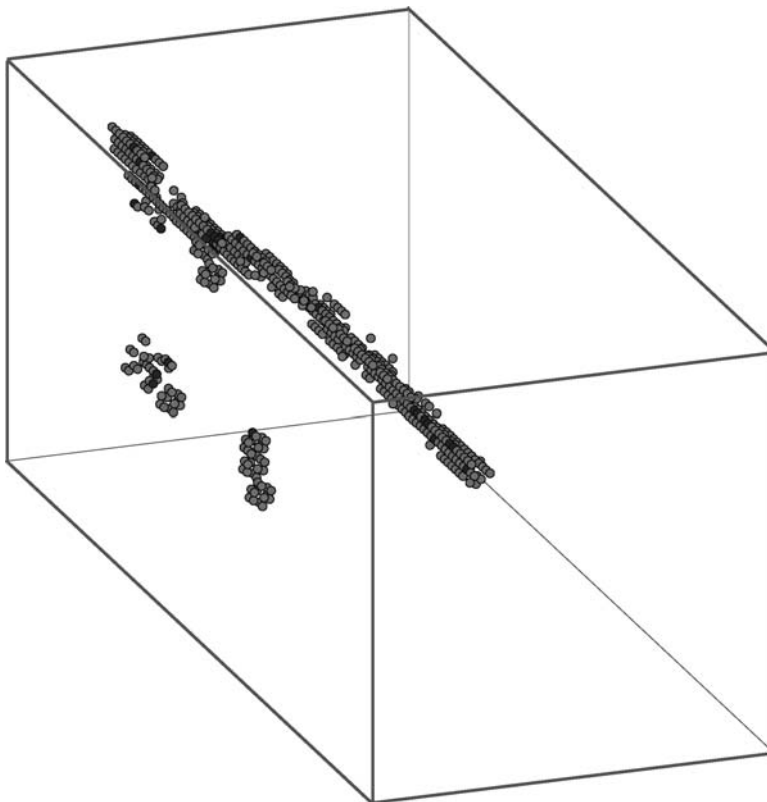


Fig. 41. Snapshot of MD simulation of screw dislocation motion in BCC Fe at temperature 100 K and 750 MPa shear stress. Only atoms with central symmetry parameters [190] significantly deviate from that of perfect BCC lattice are shown. Debris in the form of vacancy and interstitial loops are left in the wake of the moving dislocation [33].

tween transverse and longitudinal sound velocities) and even supersonically, provided that they are nucleated directly into such a fast moving state [194]. In the above set of simulations, trans- and super-sonic dislocation motion were observed, when a small simulation cell was subjected to a high shear rate. However, such high speed dislocation motion was not observed in larger cells, in which the dislocation could not keep up with the shear rate and the crystal undergoes a shear collapse. Given that the effective dislocation density in the smaller cells is unrealistically high, in the range of 10^{16} – 10^{17} m^{-2} , the behaviour observed in the larger cells is more convincing, in which the dislocation density approaches more realistic values, around 10^{15} m^{-2} .

It is generally believed that there should be a transition from kink mechanism to phonon drag for dislocation motion as the applied stress increases. Interestingly, this transition has not yet been observed by direct MD simulations for either screw or edge dislocations. For screw dislocations, their ease of cross-slip introduces a new mechanism at high stresses, i.e. the formation of “cross-kink” and debris loops, which significantly limits the dislocation

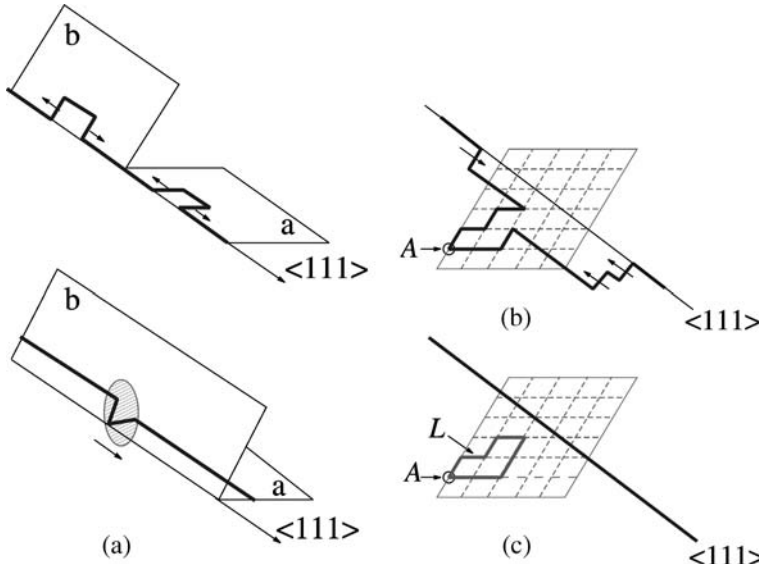


Fig. 42. Schematic representation of the formation of (a) two kinks forming a cross-kink, (b) more kinks joining the cross-kink at point A , and (c) debris loop L formation with the primary dislocation breaking away from the self-pinning point A .

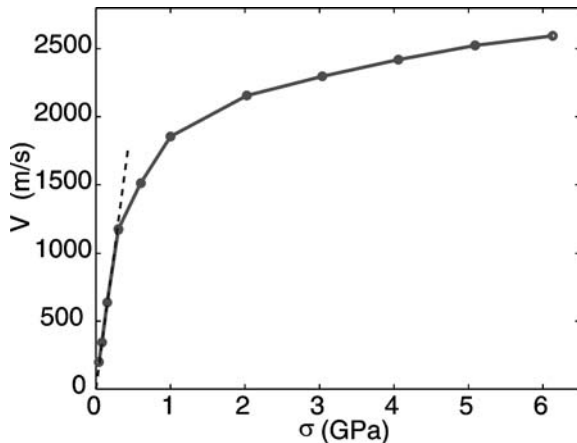


Fig. 43. Edge dislocation velocity (\bullet) as a function of stress in MD simulations of BCC Mo at 300 K [40]. Linear relationship is observed at low stress–low velocity regime, indicated by the dashed line.

velocity even above the Peierls stress. For edge dislocations, their exceedingly small Peierls stress makes the kink mechanism unlikely under most temperature and stress conditions. In the search for a direct realization of such a transition, we note that the mixed 71° (M111) has a much higher Peierls stress (320 MPa), and being non-screw, is not able to cross-slip. Therefore, the 71° dislocation is a promising candidate to reveal the transition from kink

mechanisms to phonon drag in dislocation motion. One interesting question that can be raised in this regard is, does the Peierls stress indeed define the transition?

4.5. Outstanding issues

The above discussions centred on the core effects on dislocation mobility in BCC metals. One of the key uncertainties yet to be settled is whether, in what sense and how much core polarization affects the motion of screw dislocations. The idea that polarization is the reason for the high Peierls barrier is well ingrained into the thinking about plasticity of BCC structures. Recent results [139,144] obtained with DFT methods suggest that both in Ta and Mo the ground state of the core is not polarized, while previously most empirical potentials models predicted substantial core polarization in Mo [143,145] and, with some exceptions, also in Ta [196]. At the same time, some of the same recent calculations show that, despite the observed absence of polarization, the Peierls stress is high, of the order of 1–2 GPa. Although these latest calculations may contain some errors from the necessary use of small supercells, the notion that a high Peierls stress can be sustained in the absence of polarization seems to be well grounded. It is tempting to conclude that high lattice resistance to screw motion is a generic property of all BCC materials. Supporting this assertion is the observation that, under high stresses approaching the Peierls value, the structure of the dislocation core looks unpolarized. Thus, it is not clear how the zero-stress structure, even when it shows a strong polarization, can affect the magnitude of the Peierls stress.

Recent MD simulations indicate that the mechanisms of dislocation motion in the vicinity of the Peierls stress may be more complex than previously assumed. A common expectation is that below the Peierls stress level dislocations move via kink-pair nucleation and migration, while above the Peierls stress the motions are controlled by phonon-drag. This view now has been called into question by simulations which show that the screw dislocation motion becomes rough below Peierls stress and continues to be rough at and above the Peierls stress, with no visible signs of a transition to phonon drag. Furthermore, the screw motions produced large quantities of debris, both isolated defects and clusters. There is little or no mass transport associated with this defect production. Instead, the debris seemed to be formed entirely via conservative mechanisms. Given the singular character of the screws, it will be important to investigate if and how the transition takes place for non-screw dislocations.

The discrepancy between calculated and experimental estimates of the Peierls stress is a lingering issue despite attempts to reconcile the two values. Recently, Moriarty *et al.* [197] presented calculations for Ta using a newly developed potential based on the Generalized Pseudopotential Theory. The Peierls stress computed using the new MGPT potential is 500 MPa, considerably closer to the experimental estimates of 260 MPa, whereas all the previous calculated results were around 1.5 GPa. This “convergence” could be taken to mean that it was the inaccuracy of the previous potential models that is responsible for the discrepancy. On the other hand, recent calculations based on the DFT method, which are presumably more accurate, produced Peierls stress values which are still around 0.7 GPa [139]. In light of these results, the discrepancy is still a fundamental issue that

reflects an incomplete understanding of the mechanisms of dislocation motion in BCC metals.

The cross-slip of screw dislocation, with its compact core, must be sufficiently frequent to make the dislocation motion fully three-dimensional, especially in the so-called pencil glide regime. When this is the case, both screw and non-screw dislocations may find themselves in almost any plane of the $\langle 111 \rangle$ zone. Hence, it is important to examine dislocation mobility as a function of its generalized character, by which we mean a combination of two angles defining the orientation of the dislocation line with respect to the Burgers vector. One of these angles is the usual character angle, while the other one defines the angle between the glide plane and some reference plane of the zone. For BCC materials, it would be appropriate to re-examine the mechanisms and resistance to dislocation motion for different combinations of the two character angles. So far, attention has focused mostly on the $\{110\}$ plane with occasional emphasis on the $\{112\}$ plane. However, even within one plane, say $\{110\}$, the mechanisms and magnitude of resistance to dislocation motion can vary significantly. Our recent results for the M111 dislocation is just one example. All these considerations indicate that dislocation mobility in BCC metals is a more complex phenomenon than it appeared some 10 years ago.

5. Concluding remarks

The discussions presented in this chapter focused on the intimate connection between the structure and energetics of dislocation core and dislocation mobility mechanisms. From the theory standpoint, the ultimate objective is to be able to compute dislocation mobility from the underlying atomistic processes, preferably with no adjustable parameters. The feasibility of this program depends on a successful resolution of several issues, each posing a challenge in and of itself. A foremost concern is our ability to compute accurately. The increasing use of more reliable descriptions of interatomic interactions is expected to continue in the future, gradually making it possible to study dislocation behaviour in increasingly more realistic physical environments. A second challenge is to connect predictive theory and simulation with experiments. A gap still exists between the time and length scales accessible to simulation and those pertinent to experiments. Recent and continuing advances in various experimental techniques for microscopic analysis, including *in situ* and subatomic scale resolution methods, create much excitement in the materials theory and modelling community. In response, new and more powerful computational methods spanning multiple time and length scales are being developed to deal with microstructural effects which need to be incorporated into our understanding. The core effects on dislocation mobility and crystal plasticity considered here are a microcosm of these more general developments in the physics of materials.

Multiscale modelling has come to symbolize the emerging notion of linking simulation models and techniques across the micro-to-macro length and time scales. The expectation is that by combining the different methods of calculation, one can attack a fundamental problem in a more comprehensive manner than where the methods are used individually. As we unravel the structural complexities of the dislocation core and begin to understand how it responds to stress and temperature effects at the local (atomistic) level, it would

be important to transfer the “unit process” description of nucleation and migration to the microstructural (mesoscale) level where the collective behaviour of dislocation interactions dominate. Work is on-going to feed the results of atomistic calculations into dislocation dynamics simulations of the evolution of a large collection of dislocation lines, and into finite-element and continuum models capable of dealing with system behaviour on length and time scales appropriate for measurements. This is a vision that has considerable appeal to the community as can be seen from recent conferences [for example, the Workshop on Multiscale Modelling of Materials Strength and Failure, Bodega Bay, CA, Oct. 7–10, 2001, and International Conference on Multiscale Materials Modelling, Queen Mary, Univ. London, June 17–20, 2002], special issues of journals, and funding initiatives. In view of the current interest and activities, one can look forward to significant advances in the microscopic understanding of the dislocation core and its effects on dislocation mobility.

Acknowledgements

We thank J.P. Hirth for suggesting the topic and J.P. Hirth and F.R.N. Nabarro for critical reading and invaluable comments on the manuscript. This work was performed under the auspices of the U.S. Department of Energy by Lawrence Livermore National Laboratory under Contract W-7405-Eng-48. Work of W.C., J.C. and S.Y. was partially supported by LLNL under an ASCI Level II grant. V.V.B. also acknowledges support from the Office of Basic Energy Sciences, U.S. Department of Energy. In addition, J.C., J.L., and S.Y. would like to acknowledge support by the AFOSR, Honda R&D, Ltd., and NSF-KDI and ITR initiatives.

References

- [1] H.R. Kolar, J.C.H. Spence and H. Alexander, Phys. Rev. Lett. 77 (1996) 4031.
- [2] S.S. Brenner, in: Growth and Perfection of Crystals, eds R.H. Doremus, B.W. Roberts and D. Turnbull (Wiley, New York, 1958) p. 3.
- [3] S. Suresh, T.-G. Nieh and B.W. Choi, Script. Mater. 41 (1999) 951.
- [4] A. Gouldstone, H.-J. Koh, K.-Y. Zeng, A.E. Giannakopoulos and S. Suresh, Acta Mater. 48 (2000) 2277.
- [5] J.P. Hirth and J. Lothe, Theory of Dislocations, 2nd edn (Wiley, New York, 1982).
- [6] V.V. Bulatov, D. Richmond and M.V. Glazov, Acta Mater. 47 (1999) 3507.
- [7] A.S. Argon, private communication.
- [8] H.B. Huntington, Proc. Phys. Soc. B 68 (1955) 1043.
- [9] R.E. Peierls, Proc. Phys. Soc. 52 (1940) 23.
- [10] F.R.N. Nabarro, Proc. Phys. Soc. 59 (1947) 526.
- [11] A.H. Cottrell, Dislocations and Plastic Flow in Crystals (Clarendon Press, Oxford, 1953).
- [12] F.R.N. Nabarro, Philos. Mag. A 75 (1997) 703.
- [13] T. Vegge, J.P. Sethna, S.A. Cheong, K.W. Jacobsen, C.R. Myers and D.C. Ralph, Phys. Rev. Lett. 86 (2001) 1546.
- [14] W. Benoit, M. Bujard and G. Gremaud, Phys. Stat. Solidi A 104 (1987) 427.
- [15] G. Schoeck, Script. Metall. Mater. 30 (1994) 611.
- [16] V.I. Alshits and V.L. Indenbom, Sov. Phys. Usp. 18 (1975) 1.
- [17] V.I. Alshits and V.L. Indenbom, in: Dislocation in Solids, Vol. 7, ed. F.R.N. Nabarro (North-Holland, Amsterdam, 1986) p. 43.

- [18] D. Rodney and G. Martin, Phys. Rev. Lett. 82 (1999) 3272.
- [19] J. Chang, W. Cai, V.V. Bulatov and S. Yip, Comput. Mater. Sci. 23 (2002) 111.
- [20] Y. Ashkenazy, I. Kelson, G. Makov and D. Mordehai, Abstracts, APS Annual Meeting, Seattle, Washington.
- [21] V.V. Bulatov, F.F. Abraham, L. Kubin, B. Devincre and S. Yip, Nature 391 (1998) 669.
- [22] M.I. Baskes, R.G. Hoagland and T. Tsuji, Modelling Simul. Mater. Sci. Eng. 6 (1998) 9.
- [23] D. Rodney and R. Phillips, Phys. Rev. Lett. 82 (1999) 1704.
- [24] V.B. Shenoy, R.V. Lukta and R. Phillips, Phys. Rev. Lett. 84 (2000) 1491.
- [25] J. Friedel, Dislocations (Pergamon, Oxford, 1964).
- [26] A. Korner, H. Schmid and F. Prinz, Phys. Stat. Solidi A 51 (1979) 613.
- [27] M. Elkajbaji, H.O. Kirchner and J. Thibault-Desseaux, Phil. Mag. A 57 (1988) 631.
- [28] A. Korner and H.P. Karrhaller, Phil. Mag. A 44 (1981) 275.
- [29] J. Bonneville and B. Escaig, Acta Metall. 27 (1979) 1477.
- [30] T. Rasmussen, K.W. Jacobsen, T. Leffers, O.B. Pedersen, S.G. Srinivasan and H. Jónsson, Phys. Rev. Lett. 79 (1997) 3676.
- [31] T. Rasmussen, K.W. Jacobsen, T. Leffers and O.B. Pedersen, Phys. Rev. B 56 (1997) 2977.
- [32] T. Vegge, T. Rasmussen, T. Leffers, O.B. Pedersen and K.W. Jacobsen, Phys. Rev. Lett. 85 (2000) 3866.
- [33] J. Marian, W. Cai and V.V. Bulatov, Nature Mater. 3 (2004) 158.
- [34] F. Ercoli and J.B. Adams, Europhys. Lett. 26 (1994) 583.
- [35] C. Woodward, S.I. Rao and D.M. Dimiduk, JOM – J. Min. Met. Mat. S. 50 (1998) 37.
- [36] J. Huang, M. Meyer and V. Pontikis, Phil. Mag. A 63 (1991) 1149.
- [37] D. Rodney and G. Martin, Phys. Rev. B 61 (2000) 8714.
- [38] B.D. Wirth, V.V. Bulatov and T.D. de la Rubia, J. Eng. Mater. Tech. 124 (2002) 329.
- [39] M. Victoria, N. Baluc, C. Bailat, Y. Dai, M.T. Luppo, R. Schaublin and B.N. Singh, J. Nucl. Mater. 276 (2000) 114.
- [40] J. Chang, W. Cai, V.V. Bulatov and S. Yip, unpublished.
- [41] B.D. Wirth, V.V. Bulatov and T.D. de la Rubia, J. Nucl. Mater. 283–287 (2000) 773.
- [42] K. Norlund and F. Gao, Appl. Phys. Lett. 74 (1999) 2720.
- [43] Y. Dai and M. Victoria, Acta Mater. 45 (1997) 3495.
- [44] K. Wessel and H. Alexander, Phil. Mag. 35 (1977) 1523.
- [45] J. Rabier, P. Cordier, T. Tondellier, J.L. Demenet and H. Garem, J. Phys. Condens. Matter 12 (2000) 10059.
- [46] I. Yonenaga and K. Sumino, Phys. Stat. Solidi A 50 (1978) 685.
- [47] H. Alexander, in: Dislocation in Solids, Vol. 7, ed. F.R.N. Nabarro (North-Holland, Amsterdam, 1986) p. 113.
- [48] H. Siethoff, H.G. Brion and W. Schroter, Appl. Phys. Lett. 43 (1999) 1505.
- [49] J. Rabier and J.L. Demenet, Phys. Stat. Solidi B 222 (2000) 63.
- [50] M. Tang, L. Colombo, J. Zhu and T.D. de la Rubia, Phys. Rev. B 55 (1999) 14279.
- [51] J. Rabier and A. George, Revue Phys. Appl. 22 (1987) 1327.
- [52] H. Koizumi, Y. Kamimura and T. Suzuki, Phil. Mag. A 80 (2000) 609.
- [53] H. Alexander and H. Teichler, in: Materials Science and Technology, Vol. 4, eds P. Haasen and E.J. Kramer (VCH Weinheim, 1991) p. 249.
- [54] V.V. Bulatov, J.F. Justo, W. Cai, S. Yip, A.S. Argon, T. Lenosky, M. de Koning and T.D. de la Rubia, Phil. Mag. A 81 (2001) 1257.
- [55] J. Bennetto, R.W. Nunes and D. Vanderbilt, Phys. Rev. Lett. 79 (1997) 245.
- [56] R.W. Nunes, J. Bennetto and D. Vanderbilt, Phys. Rev. B 58 (1998) 12563.
- [57] N. Lehto and S. Öberg, Phys. Rev. Lett. 80 (1998) 5568.
- [58] J.F. Justo, V.V. Bulatov and S. Yip, J. Appl. Phys. 86 (1999) 4249.
- [59] Q. Ren, B. Joos and M.S. Duesbery, Phys. Rev. B 52 (1995) 13223.
- [60] M.S. Duesbery, B. Joos and D.J. Michel, Phys. Rev. B 43 (1991) 5143.
- [61] R. Hull (ed.), Properties of Crystalline Silicon (INSPEC, London, 1999).
- [62] B.J. Gally and A.S. Argon, Phil. Mag. A 81 (2001) 699.
- [63] F. Louchet and J. Thibault-Desseaux, Revue Phys. Appl. 22 (1987) 207.
- [64] J.F. Justo, A. Antonelli and A. Fazzio, Solid State Communications 118 (2001) 651.
- [65] V.V. Bulatov, S. Yip and A.S. Argon, Phil. Mag. A 72 (1995) 453.

- [66] M.I. Heggie and R. Jones, Inst. Phys. Conf. Ser. 87 (1987) 367.
- [67] R.W. Nunes, J. Bennetto and D. Vanderbilt, Phys. Rev. B 57 (1998) 10388.
- [68] T.D. Engeness and T.A. Arias, Phys. Rev. Lett. 79 (1997) 3006.
- [69] L.B. Hansen, K. Stokbro, B.I. Lundqvist, K.W. Jacobsen and D.M. Deaven, Phys. Rev. Lett. 75 (1995) 4444.
- [70] J.R.K. Bigger, D.A. McInnes, A.P. Sutton, M.C. Payne, I. Stich, R.D. King-Smith, D.M. Bird and L.J. Clarke, Phys. Rev. Lett. 69 (1992) 2224.
- [71] T.A. Arias and J.D. Joannopoulos, Phys. Rev. Lett. 73 (1994) 680.
- [72] F.H. Stillinger and T.A. Weber, Phys. Rev. B 31 (1985) 5262.
- [73] W. Cai, unpublished.
- [74] L. Pizzagalli, P. Beauchamp and J. Rabier, Phil. Mag. A (2002) submitted.
- [75] W. Cai, V.V. Bulatov, J. Chang, J. Li and S. Yip, Phil. Mag. 83 (2003) 539.
- [76] T. Suzuki, T. Yasutomi and T. Tokuoka, Phil. Mag. A 79(11) (1999) 2637.
- [77] E. Weber and H. Alexander, Inst. Phys. Conf. Ser. 31 (1977) 266.
- [78] L.C. Kimerling and J.R. Patel, Appl. Phys. Lett. 34 (1979) 73.
- [79] C. Kisielowski-Kemmerich, Phys. Stat. Solidi B 161 (1990) 11.
- [80] J. Weber, Solid State Phenomena 37–38 (1994) 13.
- [81] J.F. Justo, M. de Koning, W. Cai and V.V. Bulatov, Phys. Rev. Lett. 84 (2000) 2172.
- [82] G. Csányi, S. Ismail-Beigi and T.A. Arias, Phys. Rev. Lett. 80 (1998) 3984.
- [83] Y.M. Huang, J.C.H. Spence and O.F. Sankey, Phys. Rev. Lett. 74 (1995) 3392.
- [84] H. Gottschalk, H. Alexander and V. Dietz, Inst. Phys. Conf. Ser. 87 (1987) 339.
- [85] G. Vanderschaeve, C. Levade and D. Caillard, J. Phys. Condens. Matter 12 (2000) 10093.
- [86] B.Y. Farber, Y.L. Iunin and V.I. Nikitenko, Phys. Stat. Solidi A 97 (1986) 469.
- [87] V.V. Bulatov, J.F. Justo, W. Cai and S. Yip, Phys. Rev. Lett. 79 (1997) 5042.
- [88] J. Tersoff, Phys. Rev. Lett. 56 (1986) 632.
- [89] R.W. Nunes, J. Bennetto and D. Vanderbilt, Phys. Rev. Lett. 77 (1996) 1516.
- [90] M.I. Heggie, R. Jones and A. Umerski, Phys. Stat. Solidi A 138 (1993) 383.
- [91] S. Oberg, P.K. Sitch, R. Jones and M.I. Heggie, Phys. Rev. B 51 (1995) 13138.
- [92] A. Valladares, J.A. White and A.P. Sutton, Phys. Rev. Lett. 81 (1998) 4903.
- [93] P.B. Hirsch, A. Ourmazd and P. Pirouz, Inst. Phys. Conf. Ser. 60 (1981) 29.
- [94] M. Miyata and T. Fujiwara, Phys. Rev. B 63 (2001) 45206.
- [95] A. George and G. Champier, Phys. Stat. Solidi A 53 (1979) 529.
- [96] A. George and J. Rabier, Revue Phys. Appl. 22 (1987) 941.
- [97] A. George, C. Escaravage, G. Champier and W. Schröter, Phys. Stat. Solidi B 53 (1972) 483.
- [98] A. George, C. Escaravage, W. Schröter and G. Champier, Cryst. Latt. Def. 4 (1973) 29.
- [99] P. Tu and H. Yizhen, Phys. Stat. Solidi A 59 (1980) 195.
- [100] A. George, J. Phys. (Paris) 40 C-6 (1979) 133.
- [101] F. Louchet, Phil. Mag. A 43 (1981) 1289.
- [102] F. Louchet and A. George, J. Phys. (Paris) C4 (1983) 44.
- [103] B.Y. Farber and V.I. Nikitenko, Phys. Stat. Solidi A 73 (1982) K141.
- [104] M. Imai and K. Sumino, Phil. Mag. A 47 (1983) 599.
- [105] V.I. Nikitenko, B.Y. Farber and E.B. Yakimov, Cryst. Res. & Technol. 19 (1984) 295.
- [106] V.I. Nikitenko, B.Y. Farber and H.G. Minasyan, in: Defect Control in Semiconductors, ed. K. Sumino (Elsevier Science Publishers, B.V., North-Holland, 1990).
- [107] V.I. Nikitenko, B.Y. Farber, Y.L. Iunin and V.I. Orlov, in: Springer Proceedings in Physics, Vol. 54, eds J.H. Werner and H.P. Strunk (Springer-Verlag, Berlin, Heidelberg, 1991).
- [108] T.E. Mitchell, J.P. Hirth and A. Misra, Acta Mater. 50 (2002) 1087.
- [109] V.N. Erofeev, V.I. Nikitenko and V.B. Osvenskii, Phys. Stat. Solidi 35 (1969) 79.
- [110] S. Marklund, Solid State Communications 54 (1985) 555.
- [111] H.J. Möller, Acta Metall. 26 (1978) 963.
- [112] W. Cai, V.V. Bulatov, J.F. Justo, S. Yip and A.S. Argon, Phys. Rev. Lett. 84 (2000) 3346.
- [113] A. Jacques and A. George, Script. Metall. 45 (2001) 1279.
- [114] R. Jones, J. Phys. (Paris) 44 (1983) C4–61.

- [115] K. Maeda and Y. Yamashita, *IPCS* 104 (1989) 269.
- [116] S.A. Erofeeva, *Phil. Mag. A* 70 (1994) 943.
- [117] V. Celli, M. Kabler, T. Ninomiya and R. Thomson, *Phys. Rev.* 131 (1963) 58.
- [118] H.-J. Möller and J. Buchholz, *Phys. Stat. Solidi A* 20 (1973) 545.
- [119] P.B. Hirsch, *J. Phys. (Paris)* 40 (1979) C6–117.
- [120] N.V. Abrosimov, V. Alex, D.V. Dyachenko-Dekov, Y.L. Iunin, V.I. Nikitenko, V.I. Orlov, S.N. Rossolenko and W. Schroeder, *Mater. Sci. Eng. A* 234 (1997) 735.
- [121] H.-J. Kaufmann, A. Luft and D. Schulze, *Cryst. Res. Technol.* 19 (1984) 357.
- [122] T. Imura, K. Noda, H. Matsui, H. Saka and H. Kimura, in: *Dislocations in Solids* (University of Tokyo Press, 1985) p. 287.
- [123] A. Lawley and H.L. Gaigher, *Phil. Mag.* 10.
- [124] H.L. Prekel, A. Lawley and H. Conrad, *Acta Metall.* 16 (1968) 337.
- [125] E.B. Leiko and E.M. Nadgornyi, *Kristallografiya* 19 (1974) 584.
- [126] E. Nadgornyi, *Prog. Mater. Sci.* 31 (1988) 1.
- [127] C.S. Barrett, G. Ansel and R.F. Mehl, *Trans. ASM* 25 (1937) 702.
- [128] G.I. Taylor and C.F. Elam, *Proc. R. Soc. London A* 112 (1926) 337.
- [129] J.F.L. Vogel and R.M. Brick, *Trans. AIME* 197 (1953) 700.
- [130] B. Sestak and S. Libovicky, *Acta Metall.* 11 (1963) 1190.
- [131] M.S. Duesbery and V. Vitek, *Acta Mater.* 46 (1998) 1481.
- [132] A.H. Cottrell and B.A. Bilby, *Phil. Mag.* 42 (1951) 573.
- [133] J.B. Cohen, R. Hinton, K. Lay and S. Sass, *Acta Metall.* 10 (1962) 894.
- [134] F.C. Frank and J.F. Nicholas, *Phil. Mag.* 44 (1953) 1213.
- [135] P.B. Hirsch, in: *5th International Conference on Crystallography* (Cambridge University, 1960) p. 139.
- [136] V. Vitek, *Cryst. Latt. Def.* 5 (1974) 1.
- [137] V. Vitek and F. Kroupa, *Phil. Mag.* 19 (1969) 265.
- [138] M.S. Duesbery and G.Y. Richardson, *Critical Reviews in Solid State and Materials Sciences* 17(1) (1991) 1.
- [139] C. Woodward and S.I. Rao, *Phys. Rev. Lett.* 88 (2002) 216402.
- [140] V. Vitek, R.C. Perrin and D.K. Bowen, *Phil. Mag.* 21 (1970) 1049.
- [141] M.S. Duesbery, *Acta Metall.* 31 (1983) 1747.
- [142] W. Xu and J. Moriarty, *Phys. Rev. B* 54 (1996) 6941.
- [143] W. Xu and J. Moriarty, *Comput. Mater. Sci.* 9 (1998) 348.
- [144] S. Ismail-Beigi and T.A. Arias, *Phys. Rev. Lett.* 84 (2000) 1499.
- [145] L.H. Yang, P. Soderlind and J.A. Moriarty, *Phil. Mag. A* 81 (2001) 1355.
- [146] L.H. Yang, P. Soderlind and J.A. Moriarty, *Mater. Sci. Eng. A* 309 (2001) 102.
- [147] C. Woodward and S.I. Rao, *Phil. Mag. A* 81 (2001) 1305.
- [148] W. Sigle, *Phil. Mag. A* 79 (1999) 1009.
- [149] A. Seeger and C. Wuthrich, *Nuovo Cimento* 33B (1976) 38.
- [150] G. Wang, unpublished.
- [151] M.S. Duesbery, V.V. Vitek and D.K. Bowen, *Proc. R. Soc. Lond. A* 332 (1973) 85.
- [152] V. Vitek, *Proc. R. Soc. Lond. A* 352 (1976) 109.
- [153] E. Schmid and W. Boas, *Plasticity of Crystals*, with Special Reference to Metals (F.A. Hughes, London, 1950).
- [154] E. Schmid, *PICAM* (1924) 342.
- [155] M.S. Duesbery, *Proc. R. Soc. Lond. A* 392 (1984) 145.
- [156] M.S. Duesbery, *Proc. R. Soc. Lond. A* 392 (1984) 175.
- [157] M. Tang, L.P. Kubin and G.R. Canova, *Acta Mater.* 46 (1998) 3221.
- [158] S. Takeuchi and K. Maeda, *Acta Metall.* 25 (1977) 1485.
- [159] A.H.A. Ngan and M. Wen, *Phys. Rev. Lett.* 8707 (2001) 075505.
- [160] M.S. Duesbery and W. Xu, *Script. Metall.* 39 (1998) 283.
- [161] V. Vitek and M. Yamaguchi, *J. Phys. F Metal Phys.* 3 (1973) 537.
- [162] M. Yamaguchi and V. Vitek, *J. Phys. F Metal Phys.* 3 (1973) 523.
- [163] A.P. Sutton and R.W. Balluffi, *Interfaces in Crystalline Materials* (Oxford University Press, New York, 1996).

- [164] W. Cai, V.V. Bulatov, J. Chang, J. Li and S. Yip, Phys. Rev. Lett. 86 (2001) 5727.
- [165] C. Wuthrich, Phil. Mag. 35 (1977) 325.
- [166] C. Wuthrich, Phil. Mag. 35 (1977) 337.
- [167] J.E. Dorn and S. Rajnak, Trans. Met. Soc. AIME 45 (1967) 983.
- [168] M.S. Duesbery, in: Dislocations in Solids, Vol. 8, ed. F.R.N. Nabarro (Elsevier, Amsterdam, 1989).
- [169] A.H.W. Ngan, in: Mater. Res. Soc. Symp. Proc., Vol. 538, eds V.V. Bulatov, T.D. de la Rubia, R. Phillips, E. Kaxiras and N. Ghoniem (1999) p. 113.
- [170] A.H.W. Ngan, Phil. Mag. A 79 (1999) 1697.
- [171] K. Edagawa, T. Suzuki and S. Takeuchi, Phys. Rev. B 55 (1997) 6180.
- [172] G. Henkelman, B.P. Uberuaga and H. Jónsson, J. Chem. Phys. 113 (2000) 9901.
- [173] G. Henkelman and H. Jónsson, J. Chem. Phys. 113 (2000) 9978.
- [174] M. Wen and A.H.W. Ngan, Acta Mater. 48 (2000) 4255.
- [175] H. Matsui and H. Kimura, Script. Metall. 9(9) (1975) 971.
- [176] W. Wasserbäch, Phil. Mag. 51 (1985) 619.
- [177] H. Saka, K. Noda, T. Imura, H. Matsui and H. Kimura, Phil. Mag. 34(1) (1976) 33.
- [178] A.J. Garratt-Reed and G. Taylor, Phil. Mag. A 39 (1979) 597.
- [179] V.V. Bulatov and W. Cai, Phys. Rev. Lett. 89 (2002) 115501.
- [180] E.B. Leiko, D.V. Lotsko, E.M. Nadgorny and V. I. Trefilov, Sov. Phys. Solid State 17 (1975) 1814.
- [181] E.B. Leiko, A. Luft and E.M. Nadgorny, Phys. Stat. Solidi A 44 (1977) 285.
- [182] E.B. Leiko and A. Luft, Phys. Stat. Solidi A 67 (1981) 435.
- [183] M. Kiritani, K. Yasunaga, Y. Matsukawa and M. Komatsu, Rad. Eff. Defect. Solids 157 (2002) 3.
- [184] A. Luft, Phys. Stat. Solidi 42 (1970) 429.
- [185] G.J. Ackland and R. Thetford, Phil. Mag. A 56 (1987) 15.
- [186] W. Cai, Atomistic and mesoscale modeling of dislocation mobility, Ph.D. thesis, Massachusetts Institute of Technology (June 2001).
- [187] A. Portevin and F. Lechatelier, C. R. Acad. Sci. 176 (1923) 507.
- [188] G.J. Ackland, D.J. Bacon, A.F. Calder and T. Harry, Phil. Mag. A 75 (1997) 713.
- [189] W. Cai, V.V. Bulatov, S. Yip and A.S. Argon, Mater. Sci. Eng. A 309 (2001) 270.
- [190] C.L. Kelchner, S.J. Plimpton and J.C. Hamilton, Phys. Rev. B 58 (1998) 11085.
- [191] F. Louchet and B. Viguier, Phil. Mag. A 80 (2000) 765.
- [192] S. Sriram, D.M. Dimiduk, P.M. Hazzeldine and V.K. Vasudevan, Phil. Mag. A 76 (1997) 965.
- [193] M. Parrinello and A. Rahman, J. Appl. Phys. 52 (1981) 7182.
- [194] P. Gumbsch and H. Gao, Science 283 (1999) 968.
- [195] J.J. Gilman, Metall. Mater. Trans. A 31 (2000) 811.
- [196] G. Chang, A. Stracha, T. Cagin and W.A. Goddard, J. Computer-Aided Materials Design 8 (2002) 117.
- [197] J.A. Moriarty, J.F. Belak, R.E. Rudd, P. Soderlind, F.H. Streitz and L.H. Yang, J. Phys. Condens. Matter 14 (2002) 2825.
- [198] J. Marian, unpublished.

Dislocation Nucleation from Crack Tips And Brittle to Ductile Transitions in Cleavage Fracture

GUANSHUI XU*

Department of Mechanical Engineering, University of California at Riverside, Riverside, CA 92521, USA

*E-mail: gxu@engr.ucr.edu

Contents

1. Introduction 83
 2. Fundamental concepts of dislocation nucleation from crack tips 85
 3. Coupled tension and shear interlayer potentials 92
 4. Modeling of dislocation nucleation from crack tips 105
 5. Dislocation nucleation modes 109
 6. Analysis of dislocation nucleation from crack tips 111
 - 6.1. Two-dimensional dislocation nucleation under mode II loading 112
 - 6.2. Three-dimensional dislocation nucleation under mode II loading 114
 - 6.3. Dislocation nucleation under mixed mode loading 118
 - 6.4. Dislocation nucleation on inclined slip planes 121
 - 6.5. Dislocation nucleation on the oblique plane 126
 - 6.6. Dislocation nucleation on the cleavage ledge 133
 7. Estimates of the brittle to ductile transition temperature 138
 8. Summary and discussions 142
- Acknowledgements 144
References 144

1. Introduction

The fundamental mechanism of brittle versus ductile behavior of crystalline materials has been of major scientific and technological interest in materials science. It has been generally recognized that the intrinsic brittle versus ductile behavior of a single crystal is governed by the competition between cleavage fracture by atomic decohesion and plastic deformation initiated by dislocation nucleation and motion at the crack tip. The observed abrupt brittle to ductile transition in certain intrinsic brittle crystals, depending on the temperature and the strain rate, results from the eventual dislocation initiated plastic shielding of the propagating cleavage crack. The energetics of dislocation nucleation, motion, and multiplication in the highly stressed crack tip region therefore plays the major role in understanding the brittle versus ductile behavior of crystalline materials.

The theory described above may date back to the early work by Armstrong [1] and Kelly et al. [2]. They modeled brittle versus ductile response of materials as the competition between cleavage fracture and plastic shear at the crack tip and characterized materials as either ductile or brittle based on the ratios of their theoretical shear strength to theoretical tensile strength. Recognizing this characterization to be too simplistic because of unrealistic uniform deformation assumed at the crack tip during the fracture process, Rice and Thomson [3] improved this model by including the process of dislocation nucleation to account for the non-uniform deformation at the crack tip. They considered an atomically sharp crack in a crystal in the absence of any other form of plastic response of the background. The fracture behavior of the crystals is assumed to be governed by either nucleation of dislocations from the crack tip or by cleavage fracture propagation with the presence of an energy barrier to the emission of such dislocations. In the first instance the material is designated as intrinsically ductile and incapable of exhibiting a fracture transition, while in the second instance it is designated as intrinsically brittle and capable of exhibiting a fracture transition from brittle cleavage to ductile forms at a characteristic transition temperature. Experimental studies have demonstrated that mere dislocation nucleation from the crack tip does not necessarily assure ductile behavior [4,5]. The Rice and Thomson model, nevertheless, comes close to the threshold process that triggers ductile behavior in a class of intrinsically brittle materials with relatively high dislocation mobility, such as bcc transition metals and most alkali halides. Fully satisfactory experimental confirmation of this limiting response is rare, outside an experiment by Gilman et al. [6] of crack arrest in LiF.

The fundamental supposition of the Rice–Thomson model is that while the background plastic relaxation can suppress the transition temperature, the transition is ultimately arbitrated by dislocation nucleation from crack tips. Emission of the nucleated dislocations triggers widespread plastic deformation that shields the entire crack front to prevent crack cleavage propagation. The model, however, seriously overestimates the energy barrier for dislocation nucleation even with incorporating refinements such as crack tip

non-linearity [7] and tension softening across the slip plane [8]. It was pointed out that the use of continuum dislocation theory with a core cut-off parameter may not be appropriate since the activation process involves the formation of an imperfect dislocation which requires the incorporation of at least a minimum of atomic information in the analysis [7].

In distinction to the nucleation controlled response described above is the well established response of Si and, presumably, many other covalent materials and compounds with sluggish dislocation mobility. The brittle to ductile transitions in those materials are believed to be governed by dislocation mobilities in the crack tip region [9–12]. In either the nucleation or the mobility controlled transition scenario dislocation nucleation from the crack tip occurs preferentially from specific crack tip sites. Assurance of full ductile behavior requires that all parts of the crack front be shielded to prevent continued brittle behavior by local break-out of the cleavage crack from unshielded portions of the crack front [11,12].

A comprehensive understanding of brittle to ductile transition therefore requires accurate analysis of the energetics of dislocation nucleation from the crack. Theoretically, this can only be achieved by the direct atomistic simulation since the phenomenon is the atomic scale process. The available *ab initio* calculations are impractical since the system size is too large even for the foreseeable future. Atomic simulation based on empirical potentials can handle relatively large systems that may encompass certain simple dislocation configurations. Its applicability to this problem is, however, seriously limited by the lack of effective ways to determine unstable saddle point configurations of embryonic dislocations and their associated thermal activation energies. Furthermore, the uncertainty in the selected atomic potential for the largely distorted atomic bonds existing in dislocations vitiates the more definitive solutions, although the method itself provides an effective alternative approach to probe dislocation nucleation mechanisms.

At present, it appears that only a model that embodies both atomistic information and continuum features can be used to quantitatively study the energetics of dislocation nucleation. Much progress has been made by recourse to a combined atomistic and continuum approach recently advanced based on the Peierls–Nabarro dislocation model [13,14]. In this approach, the process of dislocation nucleation at a stressed crack tip is modeled as the continuous evolution of a slip event leading to a fully formed dislocation, therefore, eliminating the poorly defined core cut-off parameter existing in the previous analysis of this problem. By incorporating coupled tension and shear interlayer potentials into a variation boundary integral method, Xu et al. [15,16] further advanced this approach with the required flexibility to deal with realistic dislocation nucleation in the expected three-dimensional configurations. They solved the saddle point configurations of embryonic dislocations and calculated their associated activation energies for thermally assisted dislocation nucleation. By comparison of the estimated transition temperatures based on the energetics of various nucleation modes, typically in the transition metal α -Fe, they found that only dislocation nucleation on the cleavage ledge along the crack front furnishes realistic estimation of the transition temperature. This study provides further support for the view that dislocation nucleation from the crack tip is a rare event which occurs preferentially at geometrical heterogeneities along the crack front [11,12,17,18].

In this paper we present the recent development of modeling dislocation nucleation from crack tips and discuss its relevance to understanding the fundamental governing processes

of brittle to ductile transitions in cleavage fracture. We first review the fundamental concepts of modeling dislocation nucleation from the crack tip based on the Peierls–Nabarro dislocation model in Section 2. The development of coupled tension and shear interlayer potentials at the crack tip, including the surface production effect, is then presented in Section 3. In Section 4 we describe the three-dimensional modeling of dislocation nucleation from the crack tip by incorporating the interlayer potential into the variational boundary integral method. Several possible modes of dislocation nucleation are described in Section 5. The numerical analyses of these nucleation modes, particularly in α -Fe, are presented subsequently in Section 6, in which the saddle point configurations of embryonic dislocations and their associated activation energies are calculated. Related issues such as the effects of tension softening and surface production are also addressed in this section. These results are subsequently used to estimate the brittle to ductile transition temperature in α -Fe in Section 7. The preferred nucleation mode is identified as the one that gives the lowest and realistic value of the brittle to ductile transition temperature. Finally, some issues related to the subject are discussed in Section 8.

2. Fundamental concepts of dislocation nucleation from crack tips

Recent modeling of dislocation nucleation based on the Peierls–Nabarro dislocation model provides a powerful approach to incorporate atomic information into the continuum approach to study the evolution of embryonic dislocation formation that occurs at the scale neither continuum mechanics nor atomistic simulation is effective. In the classic Peierls–Nabarro dislocation model of a straight edge dislocation [19,20], the profile of the dislocation along the slip plane, corresponding to the relative displacement between two atomic layers, is modeled as continuous distribution of infinitesimal dislocations [21]. The simple sinusoidal shear resistance relation is assumed along the slip plane, while the crystal blocks above and below the slip plane are treated as linear elastic media. The balance of the lattice restoring stress and the elastic stress due to all infinitesimal dislocations across the slip plane results in an integrodifferential equation that leads to an analytical solution of the dislocation profile. Since this solution removes the singularity of the classical Volterra dislocation, the Peierls–Nabarro dislocation model has been widely used to determine the size of the dislocation core and the energy barrier associated with it, albeit with its unrealistic use of the linear elasticity in the highly non-linear and discrete core region, e.g. [22].

It should be pointed out that the classical formulation of the Peierls–Nabarro dislocation model is somewhat ambiguous in the sense of continuum mechanics because continuous distribution of infinitesimal dislocations can only model the displacement discontinuity defined on a thickless surface but rather than the relative displacement between the two atomic layers of a finite distance. Rice [14] introduced a more rigorous formulation by distinguishing the total displacement Δ and the inelastic displacement δ between two adjacent atomic layers. The total displacement Δ is viewed as the inelastic displacement δ defined on the mathematical cut half way between the two adjacent atomic layers plus an additional elastic shear displacement by the amount of τ/μ over a distance h perpendicular to the cut. Here τ is the shear stress between the atomic layers, μ is the shear modulus,

and h is the atomic spacing of atomic layers. The dislocation profile is then precisely related to the inelastic displacement only. We remark that the Rice modification localizes the nonlinear deformation more strongly on the thickless slip plane. Therefore, it is difficult to conjecture whether this modification shall provide more accurate results than the classical formulation. For various reasons, the classical formulation of the Peierls–Nabarro dislocation model is still widely used in the literature. The analysis of homogeneous nucleation of a dislocation loop indicates that the Rice model gives a moderately larger activation energy than the classic Peierls–Nabarro dislocation model [23]. The Peierls stress calculated based on the Rice–Thomson model, however, is about several orders lower than that obtained based on the classic Peierls–Nabarro dislocation model [24].

To understand the shear stress and displacement relation between atomic layers, we follow the Rice description and consider the states of shear of an initially rectangular lattice illustrated in Fig. 1. The relative shear stress and displacement of the central pair of planes is denoted τ and Δ , respectively. The planes are separated by a distance h and will ultimately be displaced by a lattice distance b , equivalent to the magnitude of the Burgers vector. Lattice configurations (a)–(d), starting at the lower left and going clockwise, correspond to point (a)–(d) on the τ versus Δ curve. All the configurations shown are homogeneous in the direction of the shear displacement, but not perpendicular to it. When sufficiently sheared, as in (c) and (d), there exist configurations in which the lattice is not homogeneously strained, as it is in (b). At these stages, the central pair of planes corresponds to a Δ along the descending part of the τ versus Δ relation, while the crystal outside is stressed at the same level at an amount of shear corresponding to the rising part of the curve. Position (d) corresponds to the unstressed but unstable equilibrium state for which the central pair of lattice planes is displaced by $b/2$ while the crystal outside is unstrained. This is an unstable stacking configuration and the work to create it (area under τ versus Δ between $\Delta = 0$ and $b/2$) has been labeled by Rice [14] as the unstable stacking energy γ_{us} , which scales the energy required for nucleation of a dislocation.

If $\tau = F(\Delta)$, of period b , describes the τ versus Δ relation of Fig. 1, where $F(0) = 0$ and $F'(0) = \mu/h$, then the τ versus δ relation, $\tau = f(\delta)$ is given parametrically by $\tau = F(\Delta)$ and $\delta = \Delta - h\tau/\mu = \Delta - F(\Delta)/F'(0)$. The function $f(\delta)$ is also of period b and $f'(\delta)$ is unbounded at $\delta = 0$, as illustrated in Fig. 2(b). The transformation from Δ to δ as displacement variable preserves the area, namely, γ_{us} , under the stress versus displacement curve between the origin and the next zero of the stress. Defining energy $\Psi(\Delta)$ through $d\Psi = \tau d\Delta$, and $\Phi(\delta)$ through $d\Phi = \tau d\delta$, it can be shown that $\Phi(\delta) = \Psi(\Delta) - h\tau^2(\Delta)/2\mu$. The maximum value of Ψ or Φ along the slip path is equal to the unstable stacking energy γ_{us} , representing the energy barrier to be overcome in block-like shear. This definition is consistent with the previous more general definition of the so called γ -surface, also termed the generalized stacking fault energy, representing the energy changes as two blocks of crystals slide uniformly across the slip plane in an arbitrary direction. A number of atomic models can be used to calculate unstable stacking energy or the γ -surface [25–29], as discussed by Rice et al. [30]. Schoeck [31] also proposed an approach to model the interlayer potential directly from the γ -surface.

For the case of the $\tau = F(\Delta)$ relation represented by the sinusoidal function,

$$\tau = \frac{\mu b}{2\pi h} \sin\left(\frac{2\pi\Delta}{b}\right), \quad (1)$$

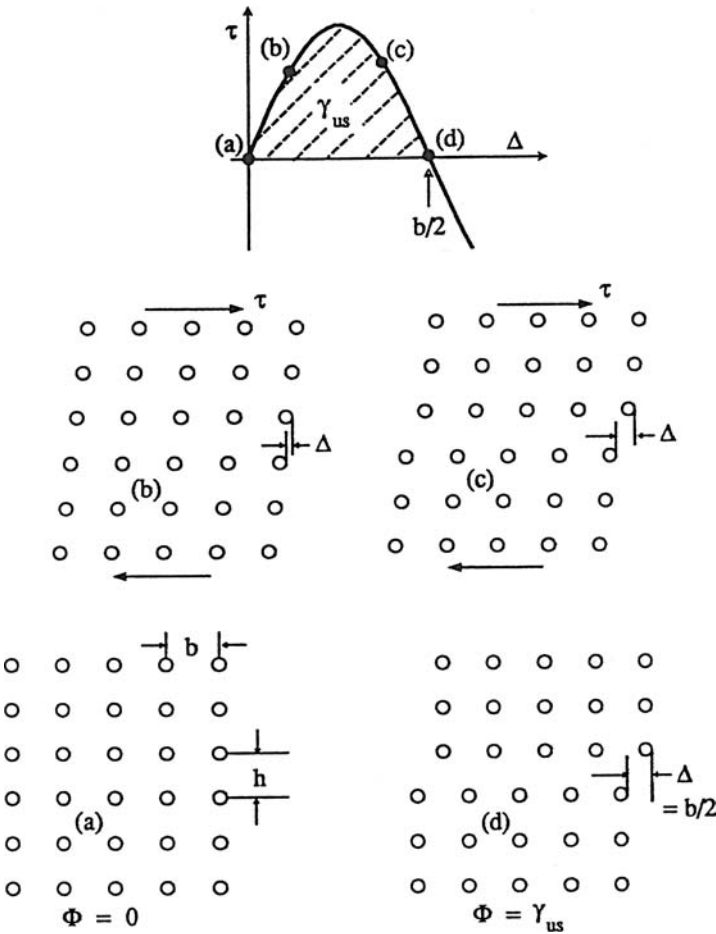


Fig. 1. Various states of shear for a simple cubic lattice; state (d) shows the unstable stacking configuration, with energy γ_{us} per unit area of slip plane. (Reprinted from [14] by permission.)

$$\delta = \Delta - \frac{b}{2\pi} \sin\left(\frac{2\pi\Delta}{b}\right), \quad (2)$$

and the energies Ψ and Φ are

$$\Psi = \frac{\mu b^2}{2\pi^2 h} \sin^2\left(\frac{\pi\Delta}{b}\right), \quad (3a)$$

$$\Phi = \frac{\mu b^2}{2\pi^2 h} \sin^4\left(\frac{\pi\Delta}{b}\right). \quad (3b)$$

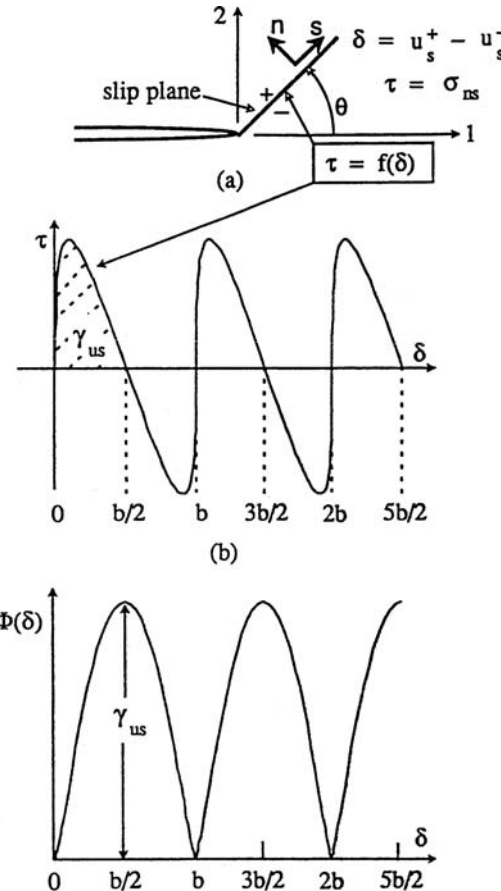


Fig. 2. (a) Crystal slip plane emanating from a crack tip. (b) Periodic relation between stress and shear displacement discontinuity. (c) Energy associated with slip discontinuity. (Reprinted from [14] by permission.)

Now we consider a semi-infinite cleavage crack and a slip plane intersecting the atomically sharp crack front, as depicted in Fig. 2(a). The described shear resistance τ and the slip displacement δ are adopted along the slip plane. The crack is assumed to be loaded remotely under a K -field. The crystallographic slip plane is selected to be the most advantageous one for slip. As the driving force increases, an embryonic dislocation forms progressively until it reaches an unstable equilibrium configuration. The question of interest is the critical loading condition for nucleation of a dislocation from the crack tip, assuming that cleavage decohesion does not occur first. Here, if \mathbf{s} and \mathbf{n} are unit vectors in slip direction and normal to the slip plane, then $\delta = u_s^+ - u_s^-$, where $u_s = \mathbf{s} \cdot \mathbf{u}$; \mathbf{u} is the displacement vector, and + and - refer to the two sides of the slip plane with \mathbf{n} pointing from - to +. The shear resistance along the slip plane $\tau = n_\alpha \sigma_{\alpha\beta} n_\beta = \sigma_{ns}$, where $\sigma_{\alpha\beta}$ is the stress tensor.

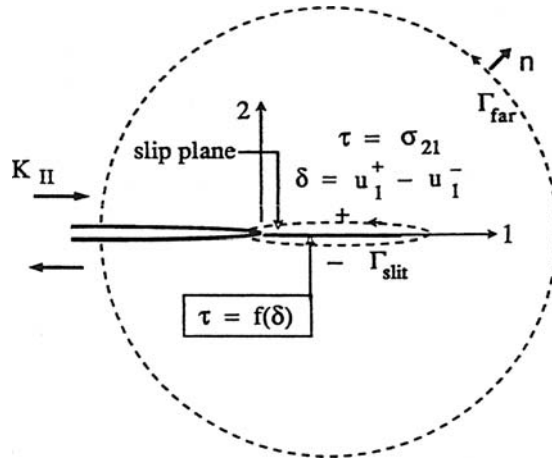


Fig. 3. Coincident crack and slip plane under mode II loading. (Reprinted from [14] by permission.)

To demonstrate the basic feature of dislocation nucleation at the crack tip, we summarize the Rice analysis for a simplified geometry, in which the extension of the crack is the slip plane and the slip direction is perpendicular the crack front. The crack is assumed to be sufficiently long that any region near its tip where significant slip develops is assumed to be of negligible length compared to the crack length and overall dimension of the cracked solid, such as distance to boundaries and to points of external force application. In that case it suffices to consider the crack as a semi-infinite slit in an unbounded solid, with all loading applied at infinitely remote distance so that all that needs to be considered is the singular crack tip stress field, characterized by stress intensity factors, K_I , K_{II} , K_{III} . When only K_{II} is assumed to be non-zero, the emerging dislocation is of edge character. Along the prolongation of the crack into the slip plane in Fig. 3, $\delta = u_1^+ - u_1^-$, $\tau = \sigma_{12} = K_{II}/\sqrt{2\pi r}$, and u_2 and u_3 are continuous. The crack faces are assumed to be traction free, where τ versus δ relation is not applied. For an isotropic solid, the Irwin energy release rate G_{II} , also referred as the crack driving force in this paper, is given by

$$G_{II} = \frac{1-\nu}{2\mu} K_{II}^2, \quad (4)$$

where ν is Poisson's ratio.

As the applied K_{II} and hence G_{II} increases from zero, the displacement δ along the slip plane, with the maximum value δ_{tip} at the tip, represents an embryonic dislocation. The relation between the external loading K_{II} and the formation of the dislocation is obtained by Rice [14] as

$$G_{II} = \frac{1-\nu}{2\mu} K_{II}^2 = \int_0^{\delta_{tip}} \tau d\delta = \Phi(\delta_{tip}) \quad (5)$$

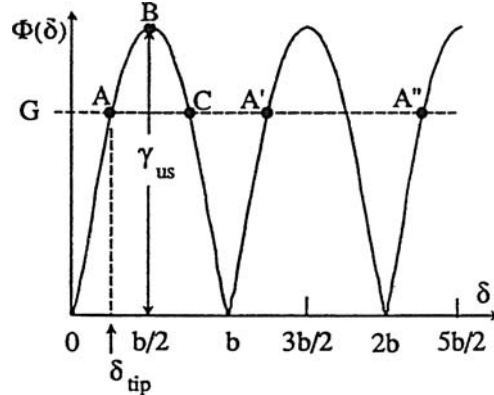


Fig. 4. Solution for the slip displacement at the crack tip, for stable solution A (and A' , A'' , ..., corresponding to one, two, or more previously emitted dislocations), and for 2D saddle point configuration C . (Reprinted from [32] by permission.)

based on the application of the path-independent J -integral on two contours Γ_{far} and Γ_{slit} , where Γ_{far} lies far from the crack tip and the nonlinear perturbation of the linear elastic field due to the incipient slip process near the tip, and Γ_{slit} coincides with the upper and lower surfaces of the slit lying ahead of the crack tip on which the displacement u_1 is discontinuous by an amount δ , as shown in Fig. 3. For the sinusoidal shear resistance relation it is evident that the embryonic dislocation loses stability when the displacement δ_{tip} reaches $b/2$ at which point G_{II} is equal to γ_{us} , the maximum value of Φ . Hence

$$G_{\text{II,cd}} = \gamma_{\text{us}} \quad (6)$$

represents the athermal critical driving force for nucleation of a fully formed edge dislocation at the mode II crack tip.

For $G_{\text{II}} < \gamma_{\text{us}}$ the equation $G_{\text{II}} = \Phi(\delta_{\text{tip}})$ has multiple solutions, illustrated by solution point A , C , A' , A'' , etc. in Fig. 4. Points A' , A'' , etc. correspond to stable embryonic dislocation configurations after one, two, etc. full dislocations have already been formed from the crack tip. The point C represents a saddle-point configuration, in which the slip distribution corresponding to C is unstable as is clear from the fact that the equilibrating load decreases as the distribution expands outward. For a given applied energy release rate $G_{\text{II}} < G_{\text{II,cd}}$, the activation energy, which is the energy required for thermally assisted dislocation nucleation, is given by

$$\Delta U_{\text{act}} = U[\delta_{\text{sad}}(x)] - U[\delta_{\text{sta}}(x)], \quad (7)$$

where $\delta_{\text{sad}}(x)$ denotes the solution for $\delta(x)$ having $\delta(0) = \delta_{\text{tip}}$ on branch C , $\delta_{\text{sta}}(x)$ is the solution on branch A , and U represents the total energy of the crack and dislocation system. The solutions of such saddle point configurations and their associated energies in the plane strain condition are obtained by Rice and Beltz [32] as illustrated in Fig. 5. The solid lines represent the stable embryonic dislocation profiles ahead of the crack tip at various loading

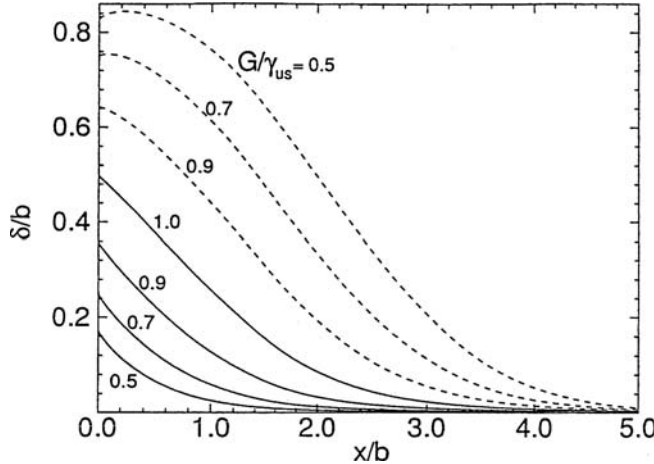


Fig. 5. Displacement profiles for various loads; the solid lines are the minimum energy solutions and the dashed lines are the corresponding saddle point solutions. (Reprinted from [32] by permission.)

levels up to instability. The dashed lines represent the corresponding unstable embryonic dislocation profiles at the same loading levels. The activation energy per unit length scaled by the unstable stacking energy is represented by a dashed line in Fig. 21. It is almost coincident with the solid line labeled with $\beta = 1$, where β is a parameter scaling the more realistic skewed shear resistant profile which we will discuss later.

Rice [14] also analyzed the critical condition for nucleation of a fully formed dislocation in a more general geometry, in which the slip plane makes a non-zero angle θ relative to the crack plane, and the Burgers vector direction along that plane makes an angle ϕ with a line drawn perpendicular to the crack front, as depicted in Fig. 6. The crack under mode I loading is of primary interest, for which dislocation nucleation versus cleavage fracture can be studied by comparing the values of energy release rate for both cases. Crack tip blunting by dislocation nucleation should occur before the condition for decohesion by cleavage is met if the latter energy release rate exceeds the former. Adopting the concept of effective stress intensity factors [33], Rice [30] estimated the critical energy release rate for dislocation nucleation in an isotropic solid to be

$$G_{cd} = 8 \frac{1 + (1 - \nu) \tan^2 \phi}{(1 + \cos \theta) \sin^2 \theta} \gamma_{us}. \quad (8)$$

The condition for the propagation of a cleavage crack, on the other hand, is

$$G_{IC} = 2\gamma_s. \quad (9)$$

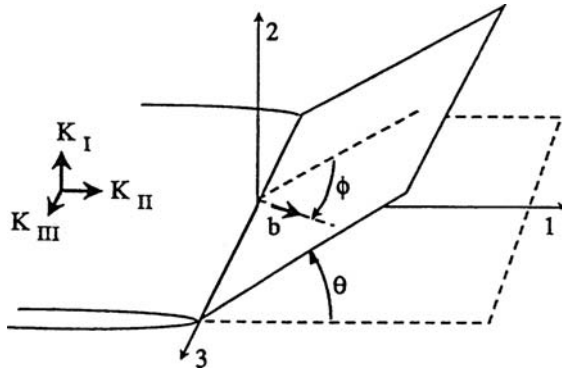


Fig. 6. Slip plane inclined at angle θ with the prolongation of the crack plane; slip direction inclined at angle ϕ with the normal to the crack tip. (Reprinted from [14] by permission.)

The condition for crack tip blunting by dislocation emission to precede cleavage fracture is then $G_{cd} < G_{IC}$, which gives

$$\frac{\gamma_s}{\gamma_{us}} > 4 \frac{1 + (1 - v) \tan^2 \phi}{(1 + \cos \theta) \sin^2 \theta}. \quad (10)$$

Noting that the softening effect of temperature on shear is more significant than tension, and that γ_{us} and γ_s are scaled by shear and Young's modulus respectively, we may assume that γ_{us} decreases with temperature more rapidly than γ_s . Therefore, a condition such as (10) appears to have the potential for explaining the brittle to ductile transition in intrinsically brittle materials all by itself. However, this cannot be the case since the temperature required for the sufficient decrease of γ_{us} to result in a transition is most probably much higher than the transition temperatures observed experimentally.

3. Coupled tension and shear interlayer potentials

The slip plane at the crack tip is generally subject to complex loading. The high tensile stress across the slip plane may facilitate dislocation nucleation. Therefore, it is necessary to consider the coupled tension and shear potential across the slip plane instead of the pure shear potential adopted in the previous section. Such a coupled tension and shear interlayer potential, which combines the sinusoidal shear relation and the Rose–Ferrante–Smith universal binding relation [34], was developed by Beltz and Rice [35,30]. Xu et al. [15] further modified this type of potential to include the skewed shear resistance profile and the surface production resistance at the crack tip.

To summarize these developments, we first envision two rigid half-crystals sliding uniformly across a slip plane of thickness h , as shown in Fig. 7. Let Δ_r and Δ_θ denote the relative shear and opening displacements across the slip plane, τ and σ the shear and normal stress acting between the blocks. The relative inelastic displacements δ_r and δ_θ are

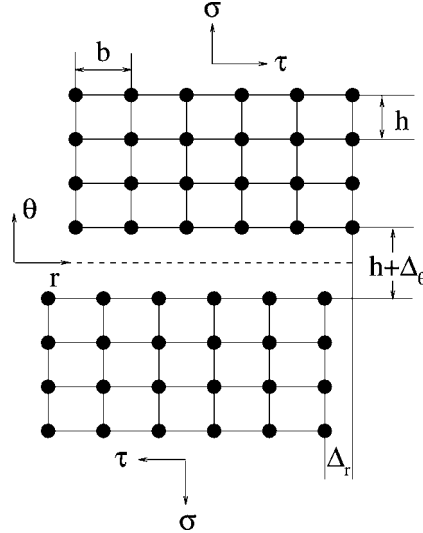


Fig. 7. Block-like lattice sliding and opening displacement of atomic layers bounding a slip plane.

then defined as

$$\delta_r = \Delta_r - h\tau(\Delta_r, \Delta_\theta)/\mu, \quad (11a)$$

$$\delta_\theta = \Delta_\theta - h\sigma(\Delta_r, \Delta_\theta)/c, \quad (11b)$$

where $c = \lambda + 2\mu$ is the uniaxial strain elastic modulus, and λ is the Lame constant.

Beltz and Rice [35] assumed that the interlayer traction–displacement relation can be expressed in the general form

$$\tau(\Delta_r, \Delta_\theta) = A(\Delta_\theta) \sin\left(\frac{2\pi\Delta_r}{b}\right), \quad (12a)$$

$$\sigma(\Delta_r, \Delta_\theta) = \left[B(\Delta_r) \left(\frac{\Delta_\theta}{L} \right) - C(\Delta_r) \right] \exp\left(-\frac{\Delta_\theta}{L}\right), \quad (12b)$$

where $A(\Delta_\theta)$, $B(\Delta_r)$ and $C(\Delta_\theta)$ are functions to be determined, and L is the characteristic length of the decohesion process which scales with the Thomas–Fermi screening distance in elemental metals [34]. In simple tension, σ reaches its maximum at $\Delta_\theta = L$.

The functions $A(\Delta_\theta)$, $B(\Delta_r)$ and $C(\Delta_\theta)$ are determined by enforcing selected subsidiary constraints. Firstly, the traction–displacement relations are required to reduce to the sinusoidal form in simple shear and the Rose–Ferrante–Smith universal binding relation in simple tension. This gives

$$\tau(\Delta_r, 0) = \frac{\pi \gamma_{us}^{(u)}}{b} \sin\left(\frac{2\pi\Delta_r}{b}\right), \quad (13a)$$

$$\sigma(0, \Delta_\theta) = \frac{2\gamma_s}{L} \frac{\Delta_\theta}{L} \exp\left(-\frac{\Delta_\theta}{L}\right), \quad (13b)$$

where γ_s is the surface energy, and $\gamma_{us}^{(u)}$ is the unrelaxed unstable stacking energy parameter defined as the energy attained at the unstable equilibrium configuration in simple shear in the absence of an opening displacement. If $\Delta_r = b^*$ in this configuration, then

$$\gamma_{us}^{(u)} = \int_0^{b^*} \tau(\Delta_r, 0) d\Delta_r. \quad (14)$$

For slip along a translation vector of the lattice, such as what corresponds to a perfect dislocation, the symmetry of the lattice necessitates $b^* = b/2$. By contrast, the precise value of b^* for slip associated with a partial dislocation does not follow from symmetry considerations alone and requires an atomic calculation for its determination. Secondly, the assumption of the existence of a joint conservative potential $\Psi(\Delta_r, \Delta_\theta)$ for the traction-displacement relations (12a) and (12b) requires that the Maxwell reciprocal relation

$$\frac{\partial \tau}{\partial \Delta_\theta} = \frac{\partial \sigma}{\partial \Delta_r} \quad (15)$$

be satisfied. Moreover, the shear resistance must approach zero as the normal displacement increases to infinity, i.e. $\tau \rightarrow 0$, as $\Delta_\theta \rightarrow \infty$. The functions $A(\Delta_\theta)$, $B(\Delta_r)$ and $C(\Delta_r)$ which satisfy these constraints are given by

$$A(\Delta_\theta) = \frac{\pi \gamma_{us}^{(u)}}{b} \left[1 + \frac{1}{q} \frac{q-p}{1-p} \frac{\Delta_\theta}{L} \right] \exp\left(-\frac{\Delta_\theta}{L}\right), \quad (16a)$$

$$B(\Delta_r) = \frac{2\gamma_s}{L} \left[1 - \frac{q-p}{1-p} \sin^2\left(\frac{\pi \Delta_r}{b}\right) \right], \quad (16b)$$

$$C(\Delta_r) = \frac{2\gamma_s}{L} \frac{p(1-q)}{1-p} \sin^2\left(\frac{\pi \Delta_r}{b}\right), \quad (16c)$$

where

$$q = \frac{\gamma_{us}^{(u)}}{2\gamma_s}, \quad (17a)$$

$$p = \frac{\Delta_\theta^*}{L}. \quad (17b)$$

In these relations, Δ_θ^* is the relaxed opening displacement corresponding to a vanishing normal traction, $\sigma = 0$, at the unstable equilibrium configuration in shear. The parameter p is sometimes referred to as the dilation parameter. The parameters p and q jointly characterize the tension and shear coupling in the traction-displacement relations. If the relaxed unstable stacking energy $\gamma_{us}^{(r)}$ is defined as the energy in the relaxed unstable equilibrium

configuration in shear, the parameter p can then be related to unstable stacking energies through the following relation

$$\frac{\gamma_{us}^{(r)} - \gamma_{us}^{(u)}}{\gamma_{us}^{(u)}} = \frac{1-q}{q} \left[1 - \frac{1}{1-p} \exp(-p) \right]. \quad (18)$$

We note that $p = 0$ when $\gamma_{us}^{(r)} = \gamma_{us}^{(u)}$. Finally, the associated coupled tension and shear potential can be expressed as

$$\begin{aligned} \Psi(\Delta_r, \Delta_\theta) = 2\gamma_s & \left\{ 1 - \left[1 + \left(\frac{\Delta_\theta}{L} \right) \right] \exp\left(-\frac{\Delta_\theta}{L}\right) \right. \\ & \left. + \sin^2\left(\frac{\pi\Delta_r}{b}\right) \left[q + \left(\frac{q-p}{1-p} \right) \left(\frac{\Delta_\theta}{L} \right) \right] \exp\left(-\frac{\Delta_\theta}{L}\right) \right\} \end{aligned} \quad (19)$$

and

$$\Phi(\delta_r, \delta_\theta) = \Psi(\Delta_r, \Delta_\theta) - \frac{h}{2\mu} \tau^2(\Delta_r, \Delta_\theta) - \frac{h}{2c} \sigma^2(\Delta_r, \Delta_\theta). \quad (20)$$

In the sinusoidal shear resistance model, the unrelaxed unstable stacking energy $\gamma_{us}^{(u)}$ is given by

$$\gamma_{us}^{(u)} = \frac{\mu b^2}{2\pi^2 h}. \quad (21)$$

However, atomistic calculations using the embedded atom method [27] and the density functional theory with local density approximation [28] show that relation (21) often overestimates $\gamma_{us}^{(u)}$. The values of unstable stacking energy for Si, Ni₃Al, Fe, Ni, Al calculated from equation (21) are tabulated in the Table 1, where the elastic constants at different temperatures are also collected [36,37]. The corresponding values of the unrelaxed and relaxed unstable stacking energy $\gamma_{us}^{(u)}$ and $\gamma_{us}^{(r)}$ as calculated by Sun et al. [27] and by Kaxiras and Duesbery [28] are both included in the Table for comparison. The discrepancies between relation (21) and the atomistic calculations suggest that the shear resistance between two adjacent atomic layers in general does not follow the simple sinusoidal relation.

This was also recognized by Foreman et al. [38], who noted that the stress required to move a dislocation particularly in metals is usually far less than what is predicted by the Peierls–Nabarro dislocation model based on the sinusoidal shear resistance relation. By using the skewed shear resistance profiles in the Peierls–Nabarro dislocation model, Foreman et al. demonstrated that wider dislocation cores can be obtained, resulting in dislocation motion at substantially reduced levels of stress. In the present context, such a modification on the shear resistance seems to be necessary since it may have a strong effect on the energetics of dislocation nucleation. We note, parenthetically, that in the well-known Bragg bubble model [39], which has provided a useful analog for exploring crystal

defects and structure in amorphous materials, the inter-bubble potential is very markedly skewed [40,41].

In order to more realistically reflect the shear resistance profiles of atomic layers in the spirit of Foreman et al. [38], and to decouple the unstable stacking energy from the shear modulus, we represent the shear resistance relation by the general Fourier expansion

$$\tau(\Delta_r) = \sum_{n=1}^{\infty} \lambda_n \sin\left(\frac{2n\pi\Delta_r}{b}\right). \quad (22)$$

Evidently, the simple sinusoidal relation (13a) is recovered by retaining only the first component in the expansion. The identification of the Fourier coefficients λ_n of all orders would require a wealth of experimental data or a full atomistic calculation. In all subsequent developments, we shall truncate (22) beyond the second term, i.e. we shall presume $\lambda_n \approx 0$ for $n > 2$. The second term in the expansion furnishes the lowest order correction to the sinusoidal relation, and thus provides a basis for a systematic investigation of the effect of deviations from the simple sinusoidal model.

The parameters λ_1 and λ_2 in (22) are readily determined by requiring that the initial slope match the shear modulus, i.e.

$$h \frac{d\tau}{d\Delta_r} \Big|_{\Delta_r=0} = \mu, \quad (23)$$

and that the unstable stacking energy by (14) take a prescribed value. These requirements yield

$$\lambda_1 = \frac{\pi \gamma_{us}^{(u)}}{b}, \quad (24a)$$

$$\lambda_2 = \frac{\pi \gamma_{us}^{(u)}}{b} \frac{1}{2}(\beta - 1), \quad (24b)$$

where the parameter β , defined as

$$\beta = \frac{\gamma_{us}^{(sin)}}{\gamma_{us}^{(u)}} = \frac{\mu b^2}{2\pi^2 h \gamma_{us}^{(u)}}, \quad (1 \leq \beta \leq 2), \quad (25)$$

measures the skewness of the function $\tau(\Delta_r)$ and effectively decouples the shear modulus from the unstable stacking energy. Substitution of (24a), (24b) into (22) and (11a) gives the simple shear resistance relation as

$$\tau = \frac{\pi \gamma_{us}^{(u)}}{b} \left[\sin\left(\frac{2\pi\Delta_r}{b}\right) + \frac{\beta - 1}{2} \sin\left(\frac{4\pi\Delta_r}{b}\right) \right], \quad (26a)$$

$$\delta_r = \Delta_r - \frac{b}{\pi} \frac{1}{\beta} \left[\sin\left(\frac{2\pi\Delta_r}{b}\right) + \frac{\beta - 1}{2} \sin\left(\frac{4\pi\Delta_r}{b}\right) \right]. \quad (26b)$$

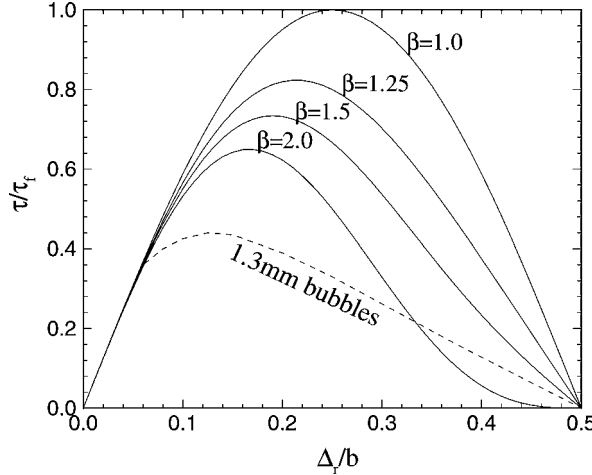


Fig. 8. Shear stress versus shear displacement for various β . The dashed line represents the Bragg bubble model.

The influence of β on the shear resistance profile is illustrated in Fig. 8; the dashed line represents the bubble model. Evidently, the sinusoidal shear model is recovered upon setting $\beta = 1$.

Complete traction–displacement relations can be derived following the approach as outlined above. They are

$$\tau(\Delta_r, \Delta_\theta) = A(\Delta_\theta) \left[\sin\left(\frac{2\pi\Delta_r}{b}\right) + \frac{\beta-1}{2} \sin\left(\frac{4\pi\Delta_r}{b}\right) \right], \quad (27a)$$

$$\sigma(\Delta_r, \Delta_\theta) = \left[B(\Delta_r) \left(\frac{\Delta_\theta}{L} \right) - C(\Delta_r) \right] \exp\left(-\frac{\Delta_\theta}{L}\right), \quad (27b)$$

where

$$A(\Delta_\theta) = \frac{\pi \gamma_{us}^{(u)}}{b} \left[1 + \frac{1}{q} \frac{q-p}{1-p} \frac{\Delta_\theta}{L} \right] \exp\left(-\frac{\Delta_\theta}{L}\right), \quad (28a)$$

$$B(\Delta_r) = \frac{2\gamma_s}{L} \left\{ 1 - \frac{q-p}{1-p} \left[\sin^2\left(\frac{\pi\Delta_r}{b}\right) + \frac{\beta-1}{4} \sin^2\left(\frac{2\pi\Delta_r}{b}\right) \right] \right\}, \quad (28b)$$

$$C(\Delta_r) = \frac{2\gamma_s}{L} \frac{p(1-q)}{1-p} \left[\sin^2\left(\frac{\pi\Delta_r}{b}\right) + \frac{\beta-1}{4} \sin^2\left(\frac{2\pi\Delta_r}{b}\right) \right]. \quad (28c)$$

Table 1
Material properties.

Material and slip system	T (K)	c_{11} (10^5 MN m $^{-2}$)	c_{12} (10^5 MN m $^{-2}$)	c_{44} (10^5 MN m $^{-2}$)	μ (10^5 MN m $^{-2}$)	c (10^5 MN m $^{-2}$)	a_0 Å
Si($\frac{1}{6}(\bar{2}11)$)(111) (m1)	77.2	1.677	0.650	0.804	0.610	2.064	5.41
Si($\frac{1}{2}(0\bar{1}1)$)(111) (m2)	77.2	1.677	0.650	0.804	0.610	2.064	5.41
Ni ₃ Al($\frac{1}{6}(\bar{2}11)$)(111) (m3)	–	2.160	1.390	1.240	0.670	3.300	3.57
Fe($\frac{1}{2}[111]$)(1 $\bar{1}0$) (m4)	4.2	2.431	1.381	1.219	0.756	3.125	2.87
Fe($\frac{1}{2}[\bar{1}\bar{1}1]$)(112) (m5)	4.2	2.431	1.381	1.219	0.756	3.125	2.87
Ni($\frac{1}{6}(\bar{2}11)$)(111) (m6)	0	2.612	1.508	1.317	0.807	3.632	3.51
Ni($\frac{1}{2}(0\bar{1}1)$)(111) (m7)	0	2.612	1.508	1.317	0.807	3.632	3.51
Al($\frac{1}{6}(\bar{2}11)$)(111) (m8)	0	1.143	0.619	0.316	0.280	1.215	4.05
Al($\frac{1}{2}(0\bar{1}1)$)(111) (m9)	0	1.143	0.619	0.316	0.280	1.215	4.05

Table 1
(Continued).

Material and slip system	γ_{us}^{\sin} (J m ⁻²)	$\gamma_{us}^{(r)}$ (J m ⁻²)	$\gamma_{us}^{(u)}$ (J m ⁻²)	$2\gamma_s$ (J m ⁻²)	β	p	q	L/b
Si($\frac{1}{6}$)[211](111) (m1)	1.932	1.91	2.02	3.12	0.96	0.376	0.647	0.156
Si($\frac{1}{2}$)[011](111) (m2)	1.932	1.67	1.81	2.68	1.07	0.452	0.675	0.144
Ni ₃ Al($\frac{1}{6}$)[$\bar{2}$ 11](111) (m3)	0.350	0.316	0.348	3.30	1.01	0.140	0.105	0.312
Fe($\frac{1}{2}$)[111](1 $\bar{1}$ 0) (m4)	1.166	0.438	0.517	3.33	2.25	0.217	0.155	0.187
Fe($\frac{1}{2}$)[1 $\bar{1}$ 1](112) (m5)	1.010	0.497	0.581	3.80	1.74	0.210	0.153	0.215
Ni($\frac{1}{6}$)[$\bar{2}$ 11](111) (m6)	0.414	0.226	0.260	2.87	1.59	0.152	0.091	0.279
Ni($\frac{1}{2}$)[011](111) (m7)	1.243	—	1.176	2.87	1.06	0.323	0.410	0.161
Al($\frac{1}{6}$)[$\bar{2}$ 11](111) (m8)	0.166	0.080	0.092	1.13	1.80	0.147	0.081	0.282
Al($\frac{1}{2}$)[011](111) (m9)	0.498	—	0.418	1.13	1.19	0.301	0.370	0.163

The corresponding potentials are

$$\begin{aligned} \Psi(\Delta_r, \Delta_\theta) = 2\gamma_s & \left\{ 1 - \left[1 + \left(\frac{\Delta_\theta}{L} \right) \right] \exp\left(-\frac{\Delta_\theta}{L}\right) \right. \\ & + \left[\sin^2\left(\frac{\pi \Delta_r}{b}\right) + \frac{\beta - 1}{4} \sin^2\left(\frac{2\pi \Delta_r}{b}\right) \right] \\ & \times \left. \left[q + \left(\frac{q-p}{1-p} \right) \left(\frac{\Delta_\theta}{L} \right) \right] \exp\left(-\frac{\Delta_\theta}{L}\right) \right\}. \end{aligned} \quad (29)$$

The relation between $\gamma_{us}^{(r)}$ and $\gamma_{us}^{(u)}$ is still given by (18) independently of β . The values of p in the Table 1 are determined from (18). For Ni(1/2)[0̄1̄1](111) and Al(1/2)[0̄1̄1](111), the value of $\gamma_{us}^{(r)}$ is not available and p is determined by taking $\gamma_{us}^{(r)} / \gamma_{us}^{(u)} = 0.9$, which is roughly in keeping with ratios computed for other materials [27]. For Fe(1/2)[111](1̄1̄0) we obtain the limiting value $\beta = 2$, which signals the largest possible departure from the sinusoidal relation. By contrast, we obtain $\beta = 1$ for Si in the glide system (1/6)[2̄1̄1](111), in accordance with the sinusoidal model. To complete the Table 1, L is determined by matching the uniaxial strain modulus c , which yields the relation

$$L = \sqrt{\frac{2\gamma_s h}{c}}. \quad (30)$$

Figs 9 and 10 show τ as a function of Δ_r of the materials in the Table 1 for the cases $\Delta_\theta = 0$ and $\Delta_\theta = L$, respectively. The tension softening effect is clearly apparent in Fig. 10. It is readily verified that the tension softening effect is inversely proportional to

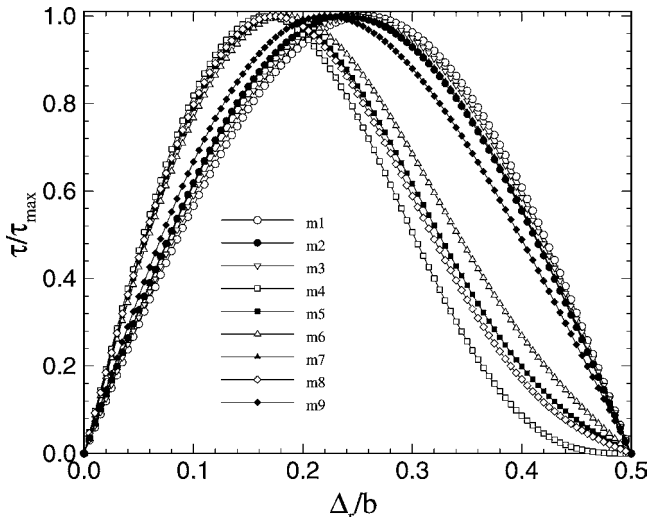


Fig. 9. Shear resistance τ versus shear displacement Δ_r for tensile opening displacement $\Delta_\theta = 0$. The nomenclature refers to the Table 1.

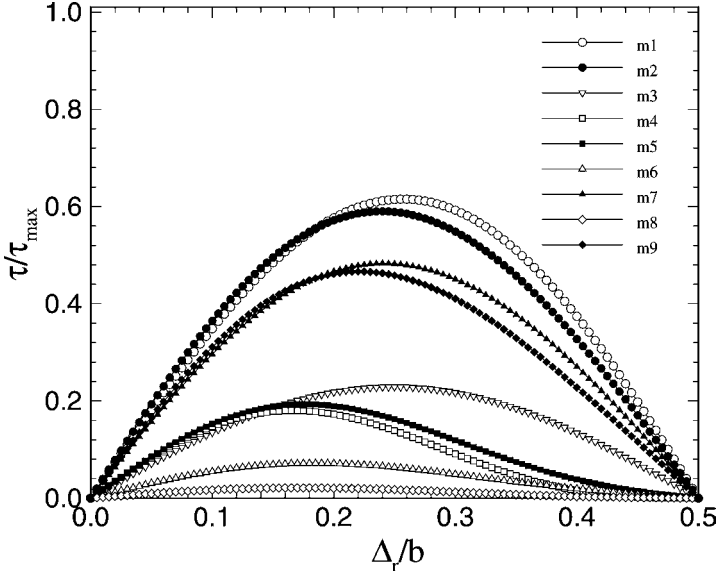


Fig. 10. Shear resistance τ versus shear displacement Δ_r for tensile opening displacement $\Delta_\theta = L$. The nomenclature refers to the Table 1.

the value of q , the ratio of the unstable stacking energy to the surface energy. Similarly, Figs 11 and 12 show σ as a function of Δ_θ for the cases $\Delta_r = 0$ and $\Delta_r = b/2$, respectively. Interestingly, the cohesive strength is also reduced by the shear displacement Δ_r . However, this effect is less pronounced than the reduction of τ by Δ_θ . The strong reciprocal softening effects between shear and tension can ultimately be traced to the existence of the coupled interlayer potential. While the softening of the shear resistance in tension is consistent with intuition, the converse softening of the tensile resistance in shear is less intuitive. Nevertheless, we shall accept the consequences of the interlayer potential and will not pursue other possible coupling relations. We remark that Rice and Beltz [32] suggested taking the interlayer spacing h in (20) as an adjustable parameter in order to relax the relation between the unstable stacking energy and the shear modulus. Rice [42] has also devised a two-parameter tension and shear interlayer potential which serves purposes similar to our present modeling.

When an edge dislocation is nucleated on an inclined slip plane containing the crack front, the production of the new surface at the crack tip requires additional energy (see Zhou et al. [43] based on a lattice Green function method, and Juan and Kaxiras [44] based on a first principles approach). This effect may be accounted in a continuum model by considering a quarter-space block sliding rigidly over a half plane block, as shown in Fig. 13. Initially, the blocks are configured so that the free boundary is smooth. As the blocks slide, bonds are severed at the intersection between the slip plane and the free boundary at some expense in energy. We define the surface production resistance, τ_s , as the shear resistance in excess of the shear resistance τ_r against slip alone in an infinite crystal. Intuitively, the surface production resistance should decrease rapidly from the corner and

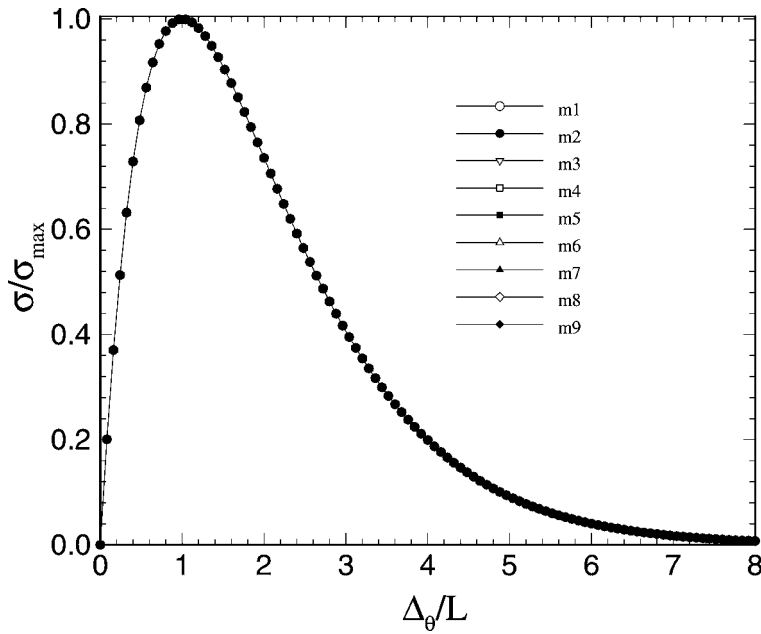


Fig. 11. Tensile separation resistance σ versus tensile displacement Δ_θ for a shear displacement $\Delta_r = 0$. The nomenclature refers to the Table 1.

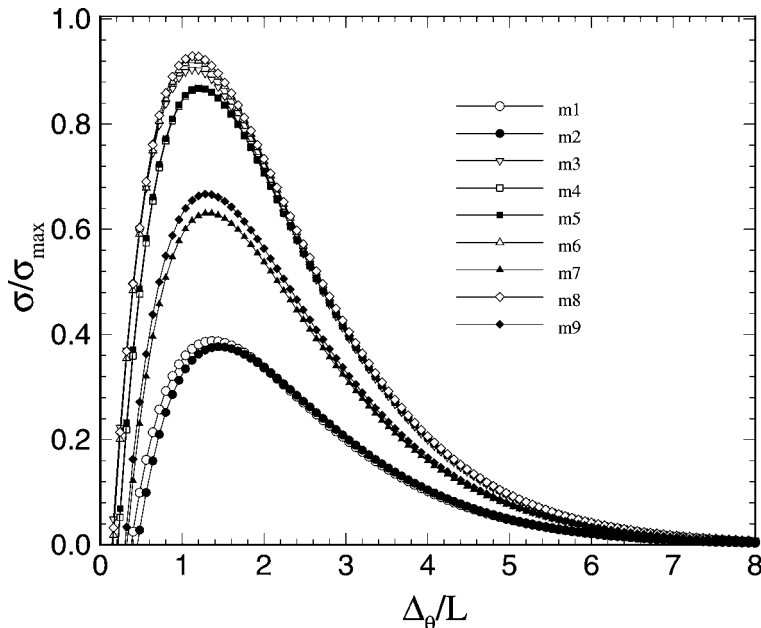


Fig. 12. Tensile separation resistance σ versus tensile displacement Δ_θ for a shear displacement $\Delta_r = b/2$. The nomenclature refers to the Table 1.

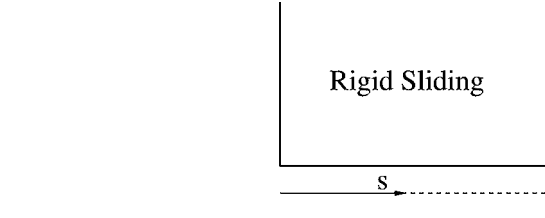


Fig. 13. Model of surface production at a corner.

become vanishingly small several atomic spacings away from the corner. The work done against this resistance as the two blocks slide by one Burgers vector must equal $\gamma_s b$, as required by energy conservation. This gives the condition

$$\int_0^\infty \int_0^b \tau_s d\Delta_r ds = \gamma_s b, \quad (31)$$

where s is the distance from the corner. Because of the periodicity of the lattice, τ_s may be reasonably expected to be periodic itself in Δ_r for fixed s . In addition, surface fields are often found to decay exponentially with depth (e.g. [45]). Here again, the precise characterization of τ_s requires atomistic modeling. In lieu of such information, we postulate the following form

$$\tau_s = \frac{\lambda \gamma_s}{b} \exp\left(-\frac{\lambda s}{b}\right) \left[1 - \cos\left(\frac{2\pi \Delta_r}{b}\right) \right] \quad (32)$$

which satisfies all the aforementioned constraints. In (32), the parameter λ represents the depth of decay of τ_s . In the limit of $\lambda \rightarrow \infty$, (32) reduces to two concentrated loads at $s = 0$, in accordance with the conventional description of surface tension. In the opposite limit of $\lambda \rightarrow 0$, the surface production resistance reduces to zero uniformly. The value of λ is expected to be in the range of 1 to 2, and to be larger for covalent materials than for metallic materials. In addition, λ is an as yet unknown function of the inclination θ of the slip plane. In view of these uncertainties, we shall treat λ as a parameter and investigate its effect by varying it within its expected range.

We proceed to incorporate the surface production resistance into the conservative interlayer potential. The total shear resistance τ near the surface may be written as

$$\tau = \tau_r + \tau_s, \quad (33)$$

where τ_r is the shear resistance against slip in an infinite crystal, which we take to be of the form (25a), and τ_s is the excess shear resistance near the free surface, which we take to be of the form (32). Proceeding as in the treatment of coupled tension and shear, we find

$$\tau(\Delta_r, \Delta_\theta; s) = A'(\Delta_\theta; s) \left[\sin\left(\frac{2\pi \Delta_r}{b}\right) + \frac{\beta - 1}{2} \sin\left(\frac{4\pi \Delta_r}{b}\right) \right]$$

$$+ \frac{\rho(s)}{2\pi q} - \frac{\rho(s)}{2\pi q} \cos\left(\frac{2\pi \Delta_r}{b}\right)\Big], \quad (34a)$$

$$\sigma(\Delta_r, \Delta_\theta; s) = \left[B'(\Delta_r; s) \left(\frac{\Delta_\theta}{L} \right) - C'(\Delta_r; s) \right] \exp\left(-\frac{\Delta_\theta}{L}\right), \quad (34b)$$

and

$$A'(\Delta_\theta; s) = \frac{\pi \gamma_{us}^{(u)}}{b} \left[1 + \frac{1}{q} \frac{q - p(s)\alpha(s)}{1 - p(s)} \frac{\Delta_\theta}{L} \right] \exp\left(-\frac{\Delta_\theta}{L}\right), \quad (35a)$$

$$\begin{aligned} B'(\Delta_r; s) = & \frac{2\gamma_s}{L} \left\{ 1 - \frac{q - p(s)\alpha(s)}{1 - p(s)} \left[\sin^2\left(\frac{\pi \Delta_r}{b}\right) + \frac{\beta - 1}{4} \sin^2\left(\frac{2\pi \Delta_r}{b}\right) \right. \right. \\ & \left. \left. + \frac{\rho(s)}{2q} \left(\frac{\Delta_r}{b} \right) - \frac{\rho(s)}{4\pi q} \sin\left(\frac{2\pi \Delta_r}{b}\right) \right] \right\}, \end{aligned} \quad (35b)$$

$$\begin{aligned} C'(\Delta_r; s) = & \frac{2\gamma_s}{L} \frac{p(s)(\alpha(s) - q)}{1 - p(s)} \left[\sin^2\left(\frac{\pi \Delta_r}{b}\right) + \frac{\beta - 1}{4} \sin^2\left(\frac{2\pi \Delta_r}{b}\right) \right. \\ & \left. + \frac{\rho(s)}{2q} \left(\frac{\Delta_r}{b} \right) - \frac{\rho(s)}{4\pi q} \sin\left(\frac{2\pi \Delta_r}{b}\right) \right], \end{aligned} \quad (35c)$$

where

$$q = \frac{\gamma_{us}^{(u)}}{2\gamma_s}, \quad (36a)$$

$$p(s) = \frac{\Delta_\theta^*(s)}{L}, \quad (36b)$$

$$\rho(s) = \lambda \exp\left(-\frac{\lambda s}{b}\right), \quad (36c)$$

$$\alpha(s) = \frac{4q}{4q + \rho(s)}. \quad (36d)$$

The corresponding tension and shear potential becomes

$$\begin{aligned} \Psi(\Delta_r, \Delta_\theta; s) = & \gamma_s \left\{ 1 - \left[1 + \left(\frac{\Delta_\theta}{L} \right) \right] \exp\left(-\frac{\Delta_\theta}{L}\right) \right. \\ & + \left[\sin^2\left(\frac{\pi \Delta_r}{b}\right) + \frac{\beta - 1}{4} \sin^2\left(\frac{2\pi \Delta_r}{b}\right) + \frac{\rho(s)}{2q} \left(\frac{\Delta_r}{b} \right) - \frac{\rho(s)}{4\pi q} \sin\left(\frac{2\pi \Delta_r}{b}\right) \right] \\ & \times \left. \left[q + \left(\frac{q - p\alpha(s)}{1 - p} \right) \left(\frac{\Delta_\theta}{L} \right) \right] \exp\left(-\frac{\Delta_\theta}{L}\right) \right\}. \end{aligned} \quad (37)$$

Some limitations of the above model should be carefully noted. For instance, our approach does not explicitly account for the effects of local stress concentrations and reconstruction on the interlayer potential. It might also be more appropriate to replace Δ_r in (32)

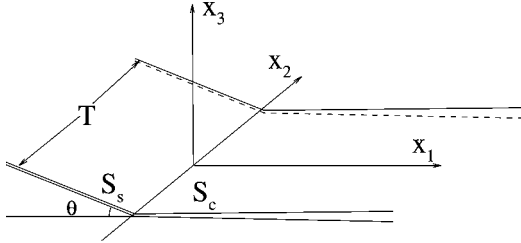


Fig. 14. A semi-infinite crack with an inclined slip plane containing the crack front. S_c and S_s represent the crack surface and the slip plane respectively.

by the inelastic displacement δ_r . This, however, complicates the model by, for instance, rendering p coordinate dependent. Since p measures the relaxation of shear resistance as atoms move relative to each other, its effect on dislocation nucleation should decrease as the tensile stress increases. In the simple shear case, the critical energy release rate for dislocation nucleation is lowered by about 10% if relaxation is allowed for [27]. However, this effect may be expected to be lessened in the presence of substantial tension softening, which is always present in situations where dislocation nucleation and cleavage fracture are in competition. For simplicity, when such a scenario is involved in calculations we set $p = 0$, corresponding to no relaxation.

4. Modeling of dislocation nucleation from crack tips

Dislocation nucleation from crack tips in general three-dimensional configurations can be analyzed using the variational boundary integral method developed by Xu and Ortiz [46]. Without loss of generality, we consider a semi-infinite crack and an inclined slip plane containing the crack front. The crack is subject to remote loading, which is characterized by stress intensity factors (K_I , K_{II} , K_{III}) and induces a standard elastic K -field in the absence of dislocation nucleation. The coupled tension and shear interlayer potential described in Section 3 is assumed to hold on the slip plane. As the load increases to a critical value, an embryonic dislocation can form progressively to a full dislocation and emit into the slip plane.

The solution of the crack opening displacement and the interlayer displacement follows minimization of the potential energy

$$\Pi[\mathbf{u}] = W[\mathbf{u}] + V[\mathbf{u}] - P[\mathbf{u}], \quad (38)$$

where W is the elastic strain energy, V the interlayer energy, and P the work of the external force. By representing the crack opening displacement and the interlayer displacement as continuous distribution of dislocation loops, and using the expression for the interaction energy between dislocation loops [22], Xu and Ortiz [46] obtained the strain energy of the system as

$$\begin{aligned}
W[\mathbf{u}] = & \frac{\mu}{4\pi} \int_{S_c+S_s} \int_{S_c+S_s} \frac{[\mathbf{e}_i \cdot (\mathbf{n} \times \nabla u_j)_2][\mathbf{e}_j \cdot (\mathbf{n} \times \nabla u_i)_1]}{R} dS_1 dS_2 \\
& - \frac{\mu}{8\pi} \int_{S_c+S_s} \int_{S_c+S_s} \frac{[\mathbf{e}_i \cdot (\mathbf{n} \times \nabla u_i)_1][\mathbf{e}_j \cdot (\mathbf{n} \times \nabla u_j)_2]}{R} dS_1 dS_2 \\
& + \frac{\mu}{8\pi(1-\nu)} \int_{S_c+S_s} \int_{S_c+S_s} [(\mathbf{e}_i \times (\mathbf{n} \times \nabla u_i)_1) \cdot \mathbf{T} \cdot ((\mathbf{e}_j \times (\mathbf{n} \times \nabla u_j)_2)] dS_1 dS_2,
\end{aligned} \tag{39}$$

where S_c and S_s represent the crack surface and the slip plane, respectively; $(.)_1$ and $(.)_2$ denote two different points on the surfaces S_c and S_s ; R is the distance between these two points; \mathbf{e}_i , $i = 1, 2, 3$, are Cartesian basis vectors; \mathbf{n} is the normal vector to the crack surface or the slip plane; and \mathbf{T} is a tensor with components

$$T_{ij} = \frac{\partial^2 R}{\partial x_i \partial x_j}. \tag{40}$$

The interlayer energy is

$$V[\mathbf{u}] = \int_{S_s} \Phi[\mathbf{u}] dS, \tag{41}$$

where $\Phi[\mathbf{u}]$, the interlayer potential defined per unit area of the slip plane, is given in Section 3. Finally the work of tractions \mathbf{t} applied on the crack surfaces is

$$P[\mathbf{u}] = \int_{S_c} \mathbf{t} \cdot \mathbf{u} dS. \tag{42}$$

In subsequent analyses, the crack surfaces are assumed to be traction free, and, consequently, $\mathbf{t} = \mathbf{0}$.

To solve for the displacements \mathbf{u} numerically, the analysis has to be reduced to a bounded domain. Following the treatment of semi-infinite periodic cracks given by Xu and Ortiz [46], this reduction can be achieved by writing

$$\mathbf{u} = \bar{\mathbf{u}} + \delta, \tag{43}$$

where $\bar{\mathbf{u}}$ is the displacement of a standard K -field for a reference semi-infinite crack. Choose Cartesian axes such that the crack occupies the domain $x_3 = 0$, $x_1 > 0$. Then, $\bar{\mathbf{u}} = \mathbf{0}$ for $x_1 < 0$ and

$$\bar{u}_1 = \frac{K_I}{\mu} \frac{4(1-\nu)}{\sqrt{2\pi}} \sqrt{x_1}, \tag{44a}$$

$$\bar{u}_2 = \frac{K_{II}}{\mu} \frac{4(1-\nu)}{\sqrt{2\pi}} \sqrt{x_1}, \tag{44b}$$

$$\bar{u}_3 = \frac{K_{\text{III}}}{\mu} \frac{4}{\sqrt{2\pi}} \sqrt{x_1} \quad (44c)$$

for $x_1 \geq 0$.

The term $\bar{\mathbf{u}}$ matches the behavior of the opening displacements for large x_1 , i.e. far from the crack front. Consequently, the remaining term δ , which is the primary unknown in the calculations, decays rapidly to zero with x_1 . This situation is exploited by setting $\delta = \mathbf{0}$ for $x_1 \geq x_1^c$, i.e. beyond some distance x_1^c from the crack front. Far from the crack front on the slip plane δ is also expected to become negligibly small. In this manner, δ can be restricted to a finite domain $\hat{S}_c \cup \hat{S}_s$, where \hat{S}_c lies on the crack surface and \hat{S}_s on the slip plane. Noting that $P[\bar{\mathbf{u}}] = 0$ and the interlayer potential only applies on the slip plane, the potential energy of the crack and slip plane system can then be written as

$$\Pi[\bar{\mathbf{u}} + \delta] = W[\bar{\mathbf{u}} + \delta] + V[\delta] = W_1[\bar{\mathbf{u}}] + W_1[\delta] + W_2[\bar{\mathbf{u}}, \delta] + V[\delta], \quad (45)$$

where we identify $W_1[\bar{\mathbf{u}}]$ as the self energy of the system, free of inelastic modifications; $W_1[\delta] + V[\delta]$ as the self energy of the system of inelastic modifications consisting of the distributed dislocations and the interlayer interaction energy on the slip plane; and $W_2[\bar{\mathbf{u}}, \delta]$ is the interaction energy of the initial unmodified system with the second system of modifications. Hence,

$$\begin{aligned} W_1[\delta] &= \frac{\mu}{4\pi} \int_{\hat{S}_c + \hat{S}_s} \int_{\hat{S}_c + \hat{S}_s} \frac{[\mathbf{e}_i \cdot (\mathbf{n} \times \nabla \delta_j)_2][\mathbf{e}_j \cdot (\mathbf{n} \times \nabla \delta_i)_1]}{R} dS_1 dS_2 \\ &\quad - \frac{\mu}{8\pi} \int_{\hat{S}_c + \hat{S}_s} \int_{\hat{S}_c + \hat{S}_s} \frac{[\mathbf{e}_i \cdot (\mathbf{n} \times \nabla \delta_i)_1][\mathbf{e}_j \cdot (\mathbf{n} \times \nabla \delta_j)_2]}{R} dS_1 dS_2 \\ &\quad + \frac{\mu}{8\pi(1-\nu)} \int_{\hat{S}_c + \hat{S}_s} \int_{\hat{S}_c + \hat{S}_s} [(\mathbf{e}_i \times (\mathbf{n} \times \nabla \delta_i)_1) \cdot \mathbf{T} \cdot (\mathbf{e}_j \times (\mathbf{n} \times \nabla \delta_j)_2)] dS_1 dS_2, \end{aligned} \quad (46)$$

and

$$V[\delta] = \int_{\hat{S}_s} \Phi[\delta] dS. \quad (47)$$

Following the treatment of semi-infinite periodic cracks given by Xu and Ortiz [46], the interaction energy W_2 of the displacement $\bar{\mathbf{u}}$ of the standard K -field and the inelastic displacement correction δ can be written as

$$W_2[\bar{\mathbf{u}}, \delta] = K_I Q_I[\delta] + K_{II} Q_{II}[\delta] + K_{III} Q_{III}[\delta], \quad (48)$$

where

$$Q_I[\delta] = \int_{\hat{S}_c + \hat{S}_s} \mathbf{n} \cdot \boldsymbol{\sigma}_I \cdot \delta dS, \quad (49a)$$

$$Q_{\text{II}}[\delta] = \int_{\hat{S}_c + \hat{S}_s} \mathbf{n} \cdot \boldsymbol{\sigma}_{\text{II}} \cdot \boldsymbol{\delta} \, dS, \quad (49\text{b})$$

$$Q_{\text{III}}[\delta] = \int_{\hat{S}_c + \hat{S}_s} \mathbf{n} \cdot \boldsymbol{\sigma}_{\text{III}} \cdot \boldsymbol{\delta} \, dS \quad (49\text{c})$$

and $\boldsymbol{\sigma}_{\text{I}}$, $\boldsymbol{\sigma}_{\text{II}}$ and $\boldsymbol{\sigma}_{\text{III}}$ are stresses of K -fields of modes I, II and III, respectively, for unit stress intensity factors. The integration is partly extended over the real crack surface since the crack front of the reference semi-infinite crack is actually located some distance from the physical crack front. This treatment allows us to use the general solution of a non-singular Dugdale–Barenblatt crack as the reference solution [47], so that the quality of the computational results can be significantly improved.

The unknown displacements $\boldsymbol{\delta}$ can then be solved by rendering the potential energy $\Pi[\bar{\mathbf{u}} + \boldsymbol{\delta}]$ stationary. Noting that the first term on the right-hand side of (45) is independent of $\boldsymbol{\delta}$ and can, therefore, be disregarded, the variation leads to the Euler equation

$$\frac{\partial W_1[\boldsymbol{\delta}]}{\partial \boldsymbol{\delta}} + \frac{\partial V[\boldsymbol{\delta}]}{\partial \boldsymbol{\delta}} - K_{\text{I}} \frac{\partial Q_{\text{I}}[\boldsymbol{\delta}]}{\partial \boldsymbol{\delta}} - K_{\text{II}} \frac{\partial Q_{\text{II}}[\boldsymbol{\delta}]}{\partial \boldsymbol{\delta}} - K_{\text{III}} \frac{\partial Q_{\text{III}}[\boldsymbol{\delta}]}{\partial \boldsymbol{\delta}} = 0. \quad (50)$$

A finite element methodology is employed to solve the above integral equation. The six-node triangular elements are used to discretize the crack surface and the slip plane. The $1/R$ singularity in the kernel of the double integration is handled by an effective and accurate numerical scheme. The resulting discretized nonlinear equations are solved by the Newton–Raphson iteration. The saddle-point configurations of dislocations are solved by recourse to displacement control, which is, in essence, the characteristic of a system with equality constraints enforced by Lagrange multipliers. For purposes of illustration, consider the pure mode II case corresponding to $K_{\text{I}} = K_{\text{III}} = 0$. The resulting system of equations is of the form

$$\mathbf{F}(\boldsymbol{\delta}) = K_{\text{II}} \mathbf{f}, \quad (51)$$

where $\boldsymbol{\delta}$ now denotes the array of nodal values of the field $\boldsymbol{\delta}(\mathbf{x})$, \mathbf{F} is the internal force array, and \mathbf{f} is the external force array normalized to $K_{\text{II}} = 1$. Instead of enforcing the value of K_{II} , which is not possible beyond the critical point, we augment the system (51) by the addition of the kinematic constraint

$$\mathbf{f} \cdot \boldsymbol{\delta} - \bar{\delta} = 0. \quad (52)$$

Here, $\mathbf{f} \cdot \boldsymbol{\delta}$ is the displacement parameter conjugate to K_{II} and $\bar{\delta}$ its prescribed value. The unknowns of the combined system of equations (51) and (52) are $\boldsymbol{\delta}$ and K_{II} . Thus, K_{II} is not prescribed but computed as a function of the effective displacement $\bar{\delta}$, which can be increased monotonically from zero. Linearization of (51) and (52) yields an incremental system of the form

$$\begin{pmatrix} \mathbf{K} & -\mathbf{f} \\ -\mathbf{f}^T & 0 \end{pmatrix} \begin{pmatrix} \Delta \boldsymbol{\delta} \\ \Delta K_{\text{II}} \end{pmatrix} = \begin{pmatrix} 0 \\ -\Delta \bar{\delta} \end{pmatrix}, \quad (53)$$

where \mathbf{K} is a symmetric tangent stiffness matrix.

5. Dislocation nucleation modes

Several alternative modes of dislocation nucleation from crack tips are identified. These modes differ mainly in the relative geometry of the slip plane, the crack surface, and the crack front. The configurations considered include dislocation nucleation on the extension of the crack surface (Fig. 15(a)), the inclined plane containing the crack front (Fig. 15(b)), the oblique plane intersecting the crack front (Fig. 15(c)), and the cleavage ledge along the crack front (Fig. 15(d)).

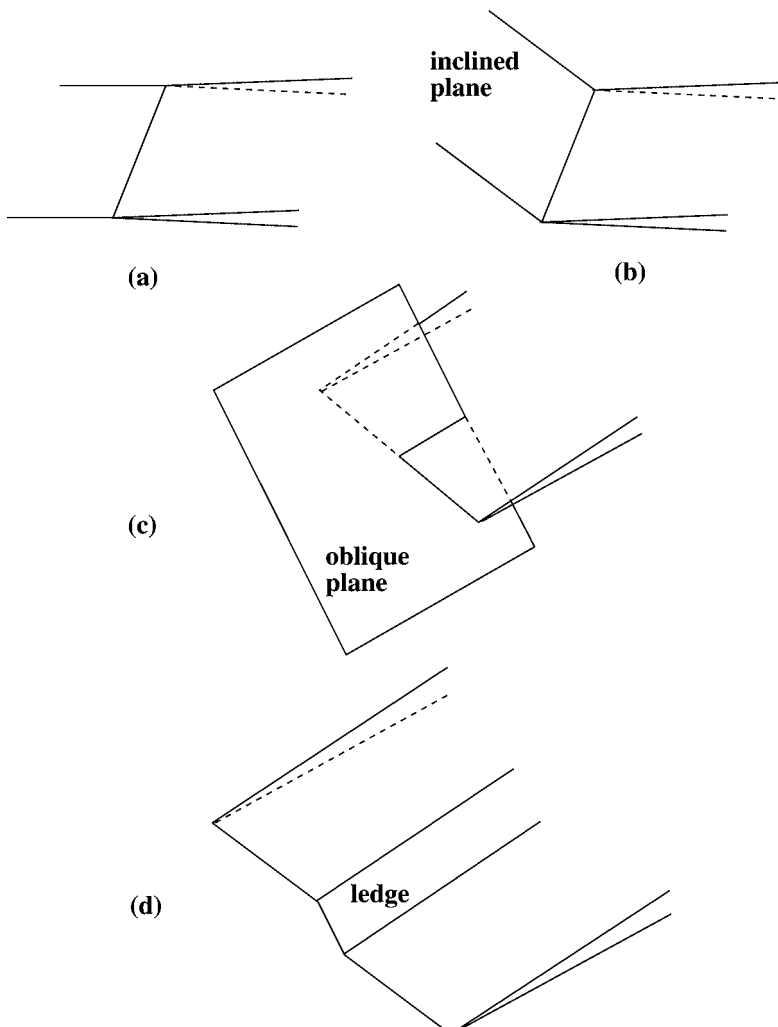


Fig. 15. Alternative modes of dislocation nucleation from crack tips.

Dislocation nucleation on the extension of the crack surface under shear loading configures the simplest geometry and has been studied extensively [13–15,30,32]. In addition to the presented analysis of idealistic nucleation of a straight dislocation from the crack tip in the plane strain condition, the more realistic scenario involves localized outward protrusion of slip from the stable embryonic configuration of the straight dislocation. Schoeck and Pueschl [13] first studied this problem based on the Peierls–Nabarro dislocation model by presuming the saddle point dislocation configuration to have a rectangular shape. Rice and Beltz [32] studied this problem using a first order perturbation approach. The more accurate general solution of this problem is obtained by Xu et al. [15] based on the method described in the previous section. The comparison of the results of these analyses is presented in Section 6.2.

Xu et al. [15] also studied dislocation nucleation on the inclined slip planes using the coupled tension and shear potential (37) so as to account for the surface production resistance at the crack tip. Their studies reveal that, while tension softening facilities dislocation nucleation on the inclined slip planes, the surface production resistance impedes it. The quantitative calculations suggest that homogeneous nucleation of dislocations on the inclined planes appears to be unlikely for all materials but a few intrinsic ductile materials, which have the lowest of unstable stacking energy to surface energy ratios.

Experimental observations [4,5] and consideration of the peak stress level at the crack tip [7] point to possible dislocation nucleation on the oblique slip plane, such as the one shown in Fig. 15(c), as a likely dislocation nucleation mechanism. This non-blunting dislocation nucleation mechanism has apparent additional advantage of involving nearly no free surface production. Moreover, as observed by Burns and Webb [4,5] and pointed out by Argon [7], the nucleated dislocation on the oblique plane can extend self-similarly as a loop attached to the crack tip, resulting in steady state shielding. Notwithstanding these favorable features, however, approximate analysis carried out by Argon [7] suggests that this mode of nucleation fail to furnish the realistic value for the transition temperature. This conclusion is reinforced by more accurate analysis in Section 6.5.

The described nucleation modes are examples of homogeneous nucleation, inasmuch as all points along the crack front are accorded an equal probability of being a nucleation site. However, many experiments [18,48–51] have shown that actual nucleation events occur only at special sites along the crack front, namely at geometrical heterogeneities. Extensive documentation of these special sites by George and Michot [18] has shown that these sites are most likely associated with cleavage ledges. These ledges form frequently in response to local deviations of the crack driving force away from the crack plane. In the case that the local stress intensity on the cleavage ledge has a substantial K_{III} component, a dislocation of screw type can be nucleated without surface production. Moreover, the substantial K_I component acting across the plane of ledge further promotes this mode of nucleation. The analysis in Section 6.6 reveals that, of all the modes considered, dislocation nucleation on the ledge is most energetically favorable and leads to the most realistic prediction of the brittle to ductile transition temperature.

To compare the activation energies for dislocation nucleation in various modes for definiteness in the following analysis, we restrict our attention to α -Fe for the reason that the brittle to ductile transition in α -Fe is likely controlled by the process of dislocation nucleation. The possible critical configurations for dislocation nucleation in α -Fe are illustrated

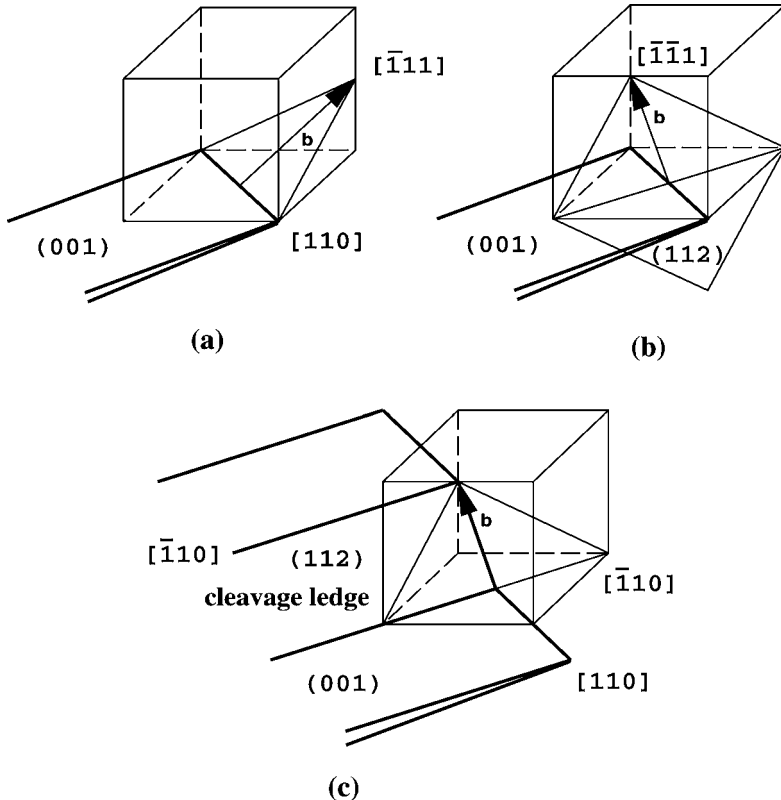


Fig. 16. Alternative modes of dislocation nucleation from crack tips in α -Fe: (a) $(1/2)[\bar{1}11]$ dislocation nucleation on an inclined $(1\bar{1}2)$ plane; (b) $(1/2)[\bar{1}\bar{1}1]$ dislocation nucleation on an oblique (112) plane; (c) $(1/2)[\bar{1}11]$ dislocation nucleation on a cleavage ledge on the (112) plane.

in Fig. 16. The preferred growth direction of a $\{100\}$ cleavage crack can be ascertained by computing the dependence of the energy release rate on the crack front direction based on the theory of fracture mechanics in anisotropic linear elasticity. For pure mode I loading, the analysis [16] reveals that the energy release rate is minimum for the crack front in the $\langle 110 \rangle$ direction, which is therefore taken to be the most likely crack front direction. Fig. 16 depicts the crystallography of the nucleation configurations: $(1/2)[\bar{1}11]$ dislocation nucleation on an inclined $(1\bar{1}2)$ plane in Fig. 16(a), $(1/2)[\bar{1}\bar{1}1]$ dislocation nucleation on an oblique (112) plane in Fig. 16(b), and $(1/2)[\bar{1}11]$ dislocation nucleation on a cleavage ledge on the (112) plane in Fig. 16(c). These configurations are selected so that each of them represents the most preferable configuration for each mode of nucleation.

6. Analysis of dislocation nucleation from crack tips

In following sections we present the analyses of dislocation nucleation in various modes based on the method described in the previous sections. The primary objective of these

analyses is to determine the saddle point configurations of the embryonic dislocations and the dependence of their associated activation energies on the crack driving force. The results for dislocation nucleation in various modes in α -Fe are subsequently used in Section 7 to estimate the brittle to ductile transition temperatures. The preferred nucleation mode is identified as the one that gives the lowest and realistic value of the brittle to ductile transition temperature.

6.1. Two-dimensional dislocation nucleation under mode II loading

We begin by considering dislocation nucleation in a two dimensional configuration, in which a straight edge dislocation is assumed to be nucleated on the extension of a crack. The crack is subjected to mode II loading, characterized by either the stress intensity factor K_{II} or the energy release rate G_{II} . The Burgers vector of the dislocation is perpendicular to the crack front. The periodic shear resistance relation (26a), (26b) is assumed to hold along the slip direction on the slip plane.

In the analysis, the Burgers vector b is taken as the normalizing length parameter and the Poisson's ratio ν is set to 0.3. Fig. 17 plots the variation of the displacement at the crack tip δ_{tip} with the stress intensity factor K_{II} . The corresponding profile of the dislocation being emitted is shown in Fig. 18, for $\beta = 1$; Fig. 19, for $\beta = 1.5$; and Fig. 20, for $\beta = 2$. The solid lines in these figures represent the displacement profiles in the stable equilibrium configurations as G_{II} is increased from zero to G_{cd} , where G_{cd} is the critical driving force for

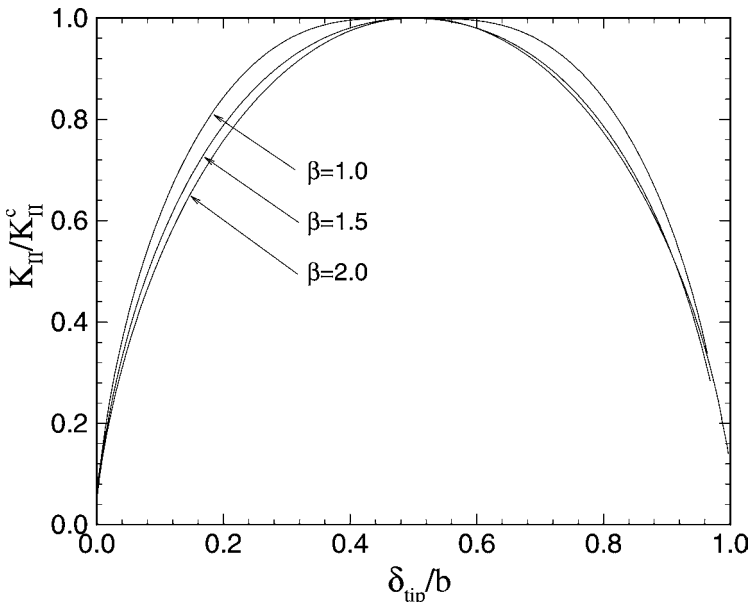


Fig. 17. The variation in the inelastic shear displacement δ_{tip} at the crack tip with the applied stress intensity factor K_{II} .

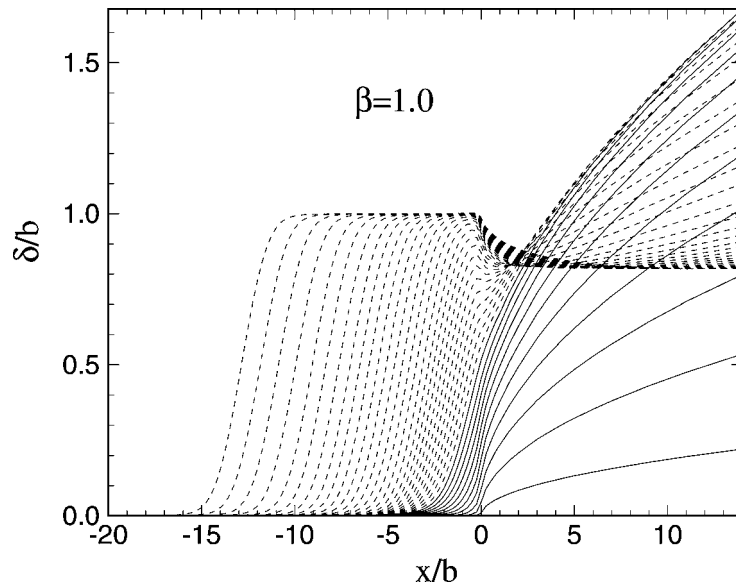


Fig. 18. Successive profiles of the emitted dislocation in pure mode II, $\beta = 1.0$.

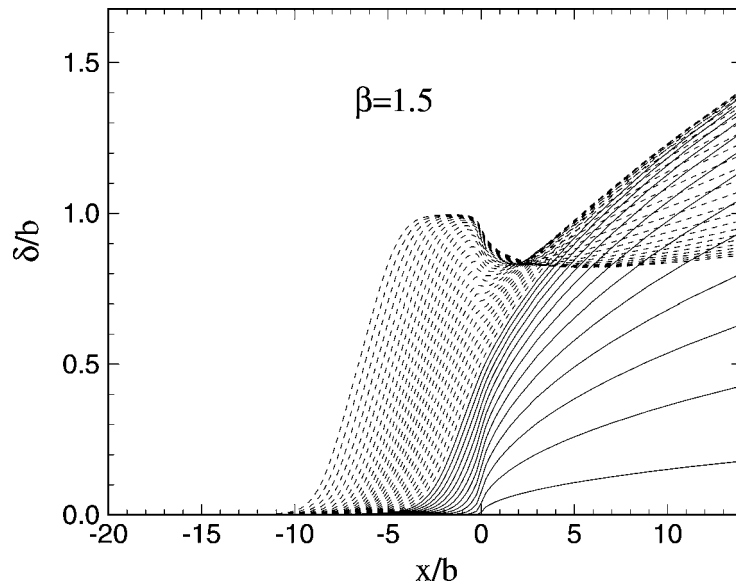


Fig. 19. Successive profiles of the emitted dislocation in pure mode II, $\beta = 1.5$.

nucleation of a fully formed dislocation. The dashed lines correspond to the displacement profiles in the unstable configurations as G_{II} decreases from G_{cd} . The various levels of the

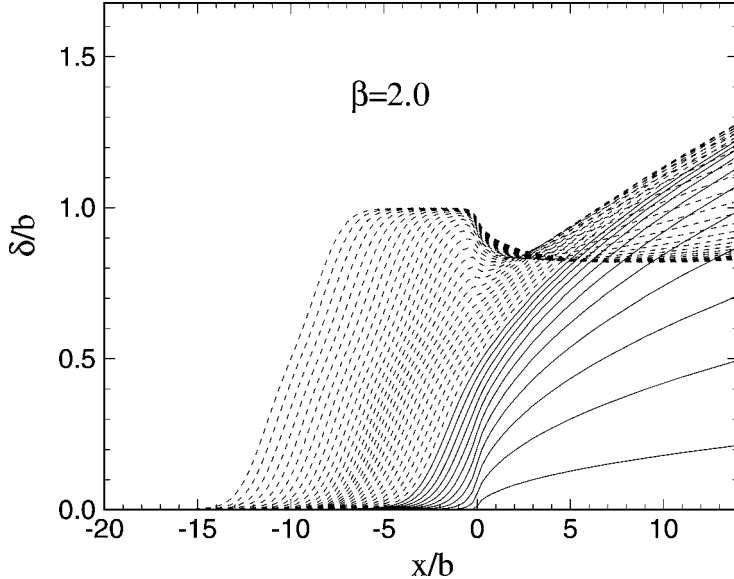


Fig. 20. Successive profiles of the emitted dislocation in pure mode II, $\beta = 2$.

opening front can be identified with reference to Fig. 17. The unrelaxed unstable stacking energy $\gamma_{us}^{(u)}$ is kept constant in all three cases, which requires μ to be adjusted according to (24). As a remark, the core width of the emitted dislocation depends sensitively on β . For large value of β the displacement distribution at the center of the dislocation is flatter, which is in agreement with the results of Foreman et al. [38].

The dependence of the activation energy ΔU_{act}^{2D} per unit length on G_{II}/G_{cd} is shown in Figs 21 and 22. It is shown in Fig. 21 that, for equal unstable stacking energy $\gamma_{us}^{(u)}$, the activation energy for dislocation emission increases with β . This implies that the activation energy for dislocation emission does not strictly scale with $\gamma_{us}^{(u)}$ but also depends on the skewness of the shear resistance curve. By contrast, when scaled with the line energy, the activation energy depends less strongly on β as shown in Fig. 21. By way of comparison, the figures also include the analytical results of Rice and Beltz [32], which corresponds to the case $\beta = 1$. The close agreement with our calculations attests to the accuracy of the numerical procedure.

6.2. Three-dimensional dislocation nucleation under mode II loading

The preceding two-dimensional analysis artificially restricts the emitted dislocation to be straight. The actual saddle-point configuration involves a localized outward protrusion of the slip from the stable two-dimensional embryonic dislocation. Schoeck and Pueschl [13] analyzed this problem by assuming the protrusion is in rectangular shape. Rice and Beltz [32] performed a first order perturbation analysis. In contrast to these approximate analyses, we present a more general accurate three-dimensional analysis, which

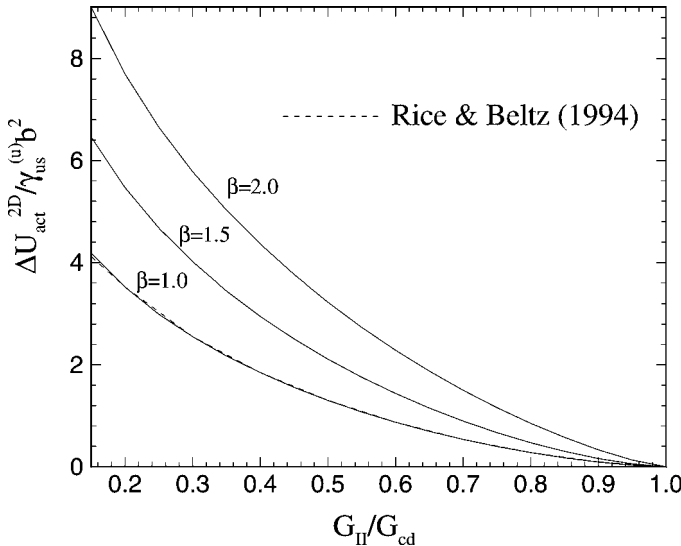


Fig. 21. The activation energy per unit length for two-dimensional dislocation emission in pure mode II scaled by unstable stacking energy.

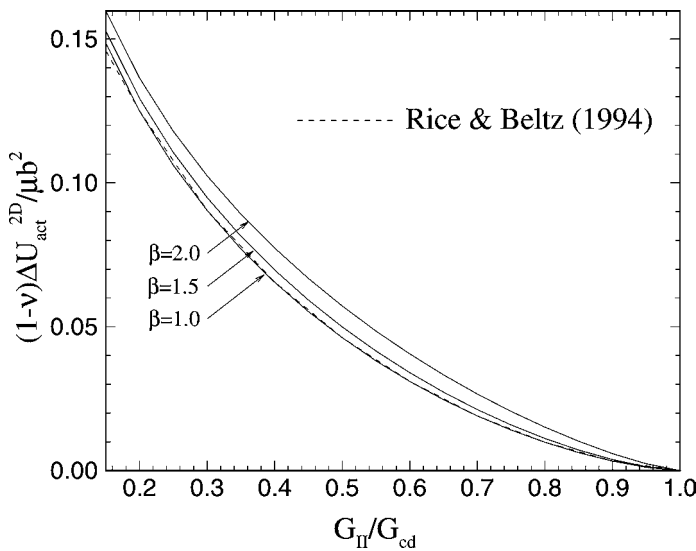


Fig. 22. The activation energy per unit length for two-dimensional dislocation emission in pure mode II scaled by line tension.

allows for arbitrary dislocation shapes. The periodic dislocation configurations in the direction of the crack front are implemented so that the analysis can be conducted on the finite domain. The activation energy is understood to be the activation energy per period. While

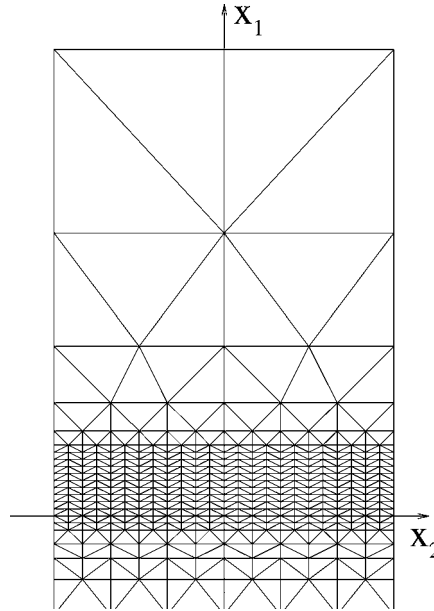


Fig. 23. Mesh used in the analysis of three-dimensional dislocation nucleation under mode II loading. The crack front is along the x_2 direction. The slip plane takes up the domain with $x_1 > 0$. The period of the mesh in the x_2 direction is $T = 24b$.

the assumption of periodicity is a geometrical restriction, its influence can be minimized by adopting a period T much larger than the lateral dimension of the protruding dislocation loops, considering the interaction energy between the loops dies off rapidly with their separation. Nevertheless, the dependence of the activation energy on the period T is included in the following analysis.

Fig. 23 shows the mesh used in the analysis. The crack front is along the x_2 direction. The slip plane takes up the domain with $x_1 > 0$. The period of the mesh in the x_2 direction is $T = 24b$. In order to trigger non-straight unstable solutions, a small perturbation of the form

$$\Delta\delta(x_1, x_2) = \epsilon \cos\left(\frac{2\pi x_2}{T}\right) \exp\left(-\frac{x_1^2}{b^2}\right) \quad (54)$$

is introduced, with $\epsilon = 0.005b$, as the loading parameter G_{II} begins to decrease from the critical value G_{cd} . This type of approach is commonly adopted in post-buckling or post-bifurcation analyses of mechanical systems [52,53]. In this context, the most effective imperfection is found to coincide with the most critical buckling mode. In a similar vein, the x_2 -dependence of $\Delta\delta$ adopted here is suggested by Bower and Ortiz's [54] analysis of unstable crack growth into a region of diminishing toughness, which shows that the long wavelength distortions of the crack front are the most critical. The first-order perturbation analysis of Rice and Beltz [32] also reveals the similar trend. The allowed longest wavelength in the present model coincides with the period T of the mesh, which accounts for

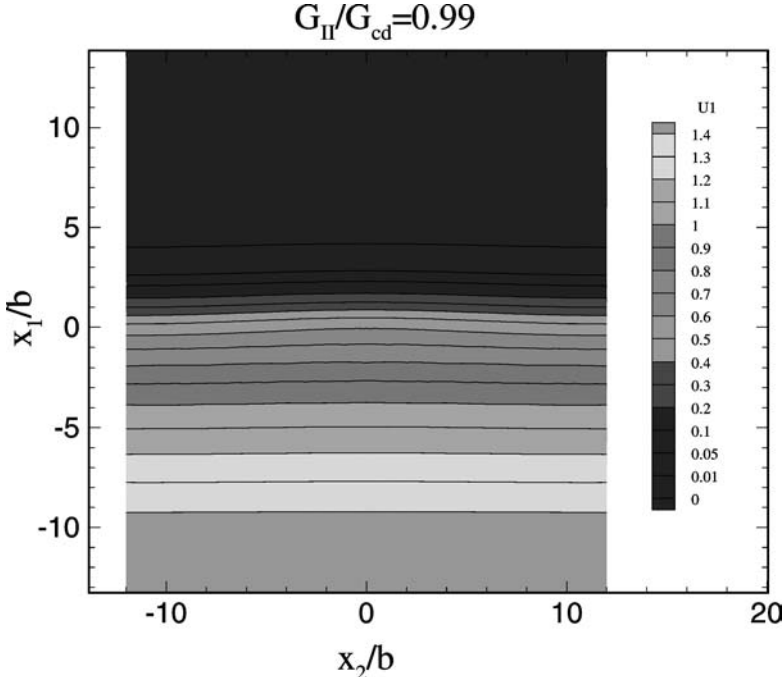


Fig. 24. The saddle point configuration at $G_{\text{II}}/G_{\text{cd}} = 0.99$ under mode II loading, $\beta = 1$. The contour variable U_1 represents the inelastic shear displacement in x_1 -axis.

the term $\cos(2\pi x_2/T)$ in (54). A more systematic method for determining the dominant unstable mode is provided by Vineyard's theory of rate processes [55]. However, Vineyard's theory requires the solution of a full eigenvalue problem obtained by linearization at the critical point, which is computationally demanding even if the subspace iteration procedure is considered in the manner of Clough and Pluzilu [56]. The simple approach adopted here appears to be effective and, therefore, more rigorous alternatives will not be pursued.

The saddle-point configurations of the emitted dislocations are shown in Figs 24–27 for decreasing values of $G_{\text{II}}/G_{\text{cd}}$. The skewness parameter β is set to 1, which is representative of Si. Figs 28–31 concern the case $\beta = 2$, which is representative of Fe. The curves represent level contours of the inelastic shear displacement in the x_1 -direction. Remarkably, dislocation emission is seen to take place by the bulging out of a dislocation packet in the form of a “double kink”, which subsequently spreads out along the crack front at decreasing driving force $G_{\text{II}}/G_{\text{cd}}$. The kinks spread out more rapidly with increasing β . This effect may be attributable to the larger shear resistance in the direction of emission relative to the case of $\beta = 1$, where the drop of resistance is steeper in the forward direction.

The dependence of the activation energy on $G_{\text{II}}/G_{\text{cd}}$ is plotted in Figs 32 and 33, normalized by the unstable stacking energy and the dislocation line energy, respectively. Rice and Beltz [32] solution comes in tangent to the curve $\beta = 1$ at $G_{\text{II}}/G_{\text{cd}} = 1$ but diverges from it away from the critical point, as expected from the character of the perturbation

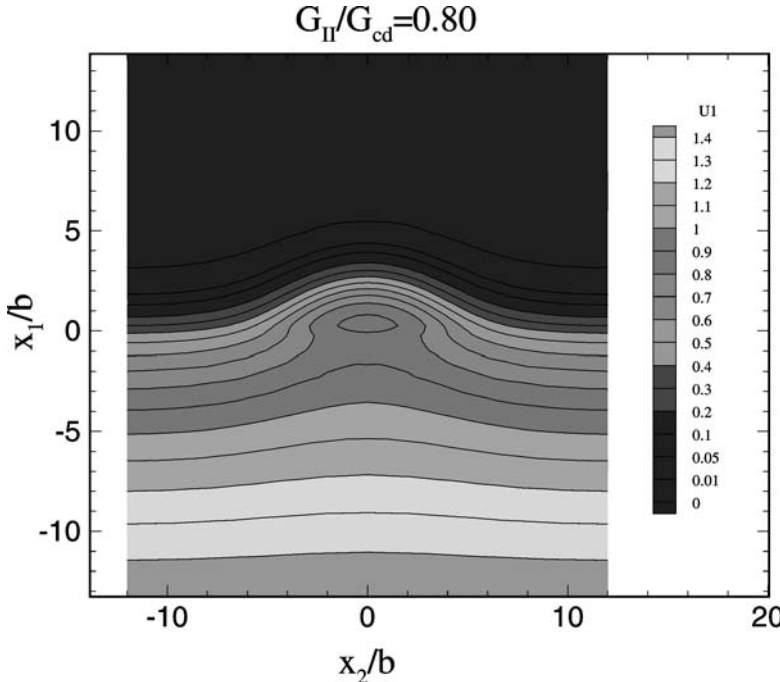


Fig. 25. The saddle point configuration at $G_{II}/G_{cd} = 0.80$ under mode II loading, $\beta = 1$. The contour variable U_1 represents the inelastic shear displacement in x_1 -axis.

analysis. By contrast, the Schoeck and Pueschl [13] solution is less accurate in the vicinity of the critical point but closer to the curve elsewhere.

It should be noted that the presented solution underestimates the activation energy owing to the periodicity of the model and the resulting attraction between neighboring kinks. This effect can be minimized by increasing the period T of the mesh. Fig. 36 shows the dependence of the calculated activation energies on T . The results are insensitive to T for $G_{II}/G_{cd} > 0.5$. The activation energy for nucleation of an isolated dislocation loop can be estimated by extrapolating the results from several periods to the limit $T \rightarrow \infty$. The result of this extrapolation is shown as the dashed line in Fig. 34. From this estimate it may be concluded that a period of $T = 32b$ suffices to closely approximate the activation energy of an isolated dislocation loop over a broad range of G_{II}/G_{cd} .

6.3. Dislocation nucleation under mixed mode loading

In this section we investigate a case which illustrates the tension-softening effect on dislocation nucleation. We envision a semi-infinite crack probing on the (112) slip plane of a bcc crystal as shown in Fig. 35. The crack front is parallel to the [110] direction and the Burgers vector is $1/2[\bar{1}\bar{1}1]$, which is perpendicular to the crack front. The crack is subject to mixed mode I and II loading. The coupled tension and shear coupling interlayer

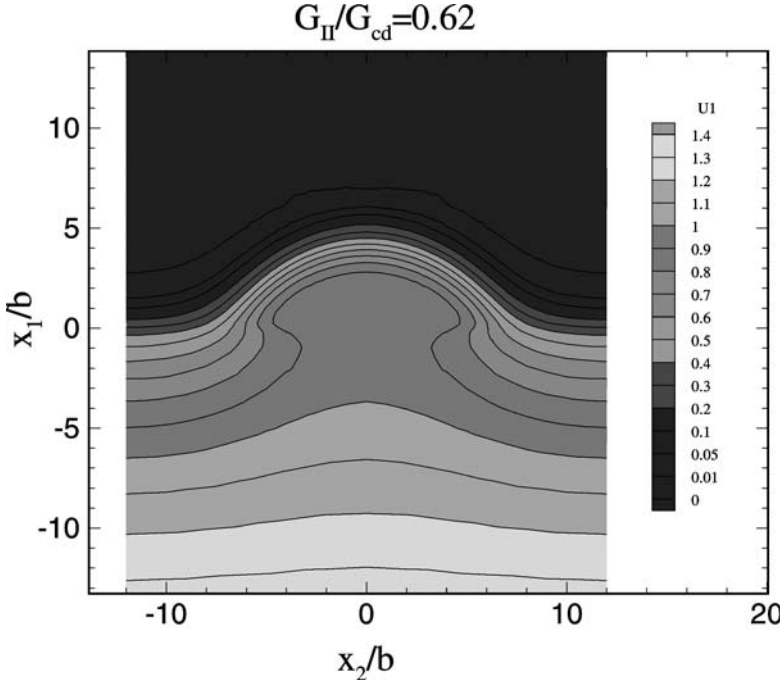


Fig. 26. The saddle point configuration at $G_{II}/G_{cd} = 0.62$ under mode II loading, $\beta = 1$. The contour variable U_1 represents the inelastic shear displacement in x_1 -axis.

relations (27a), (27b) are assumed to hold in the slip direction on the slip plane. We set $\beta = 1.74$, which is representative of the system (1/2)[1̄1̄](112) of α -Fe. The remaining parameters are selected from the Table 1.

Fig. 36 shows the result of two-dimensional calculations giving the dependence of the critical mode II stress intensity factor K_{IId} for nucleation of a straight dislocation on the applied mode I stress intensity factor K_I . Evidently, the application of mode I loading facilitates dislocation nucleation. However, this effect is small up to values of K_I of the order of 95% of the Griffith cleavage toughness K_{IC} . The underlying reason for the weak mode I and mode II coupling is apparent in Fig. 37, which depicts the sequence of opening and shear displacements for a loading program consisting of an initial increase of K_I from 0 to $0.9K_{IC}$ followed by displacement control in mode II at constant K_I . It is observed in this figure that the opening displacement δ_θ decays rapidly away from the crack front, and does not significantly overlap with the dislocation core. This effectively precludes a strong tension-shear coupling except for values of K_I close to K_{IC} . The dashed lines in Fig. 37 represent the two-dimensional unstable equilibrium configurations. The inset gives the variation of K_{II} with the crack tip inelastic shear displacement at $K_I = 0.9K_{IC}$. The shear instability occurs at the peak of the curve, which determines the critical value K_{IId} .

It is interesting to note that K_{IId} exhibits a sharp downturn as K_I approaches K_{IC} . The numerical simulations show that at about $K_I \simeq 0.95K_{IC}$ cleavage and dislocation nucleation occur simultaneously and the crack extends in a steady state.

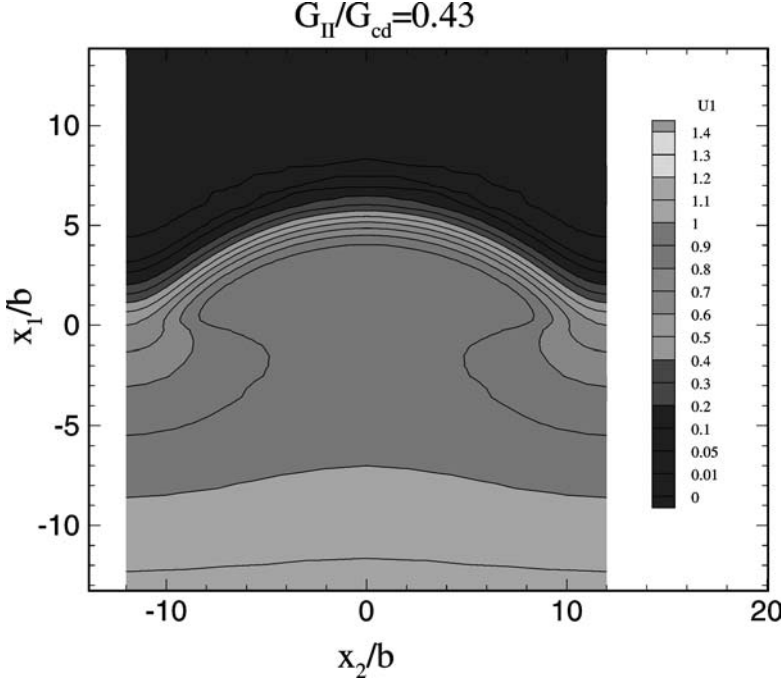


Fig. 27. The saddle point configuration at $G_{II}/G_{cd} = 0.43$ under mode II loading, $\beta = 1$. The contour variable U_1 represents the inelastic shear displacement in x_1 -axis.

The dependence of the critical energy release rate

$$G_{cd} = \frac{1-\nu}{2\mu} [K_I^2 + K_{IId}^2(K_I)] \quad (55)$$

for dislocation emission on the phase angle

$$\psi = \arctan\left(\frac{K_{IId}(K_I)}{K_I}\right) \quad (56)$$

is plotted by the solid line in Fig. 38. For pure mode II loading, $\psi = 90^\circ$, it follows that $G_{cd} = \gamma_{us}^{(r)}$, while for pure mode I loading, $\psi = 0^\circ$, one has $G_{cd} = 2\gamma_s$. Based on a shear-only model, Sun et al. [27] obtained an elegant analytical relation

$$G_{cd} = \frac{1}{\sin^2 \psi} [\gamma_{us}^{(r)} - \alpha(\gamma_{us}^{(u)} - \gamma_{us}^{(r)}) (\pi/2 - \psi)], \quad (57)$$

where α is a reduction coefficient which is determined by fitting the coupled tension–shear results. Equation (57) with $\alpha = 0.856$ is plotted as the dashed line in Fig. 38. The agreement with the numerical results is remarkably good in the range $\psi \geq 20^\circ$.

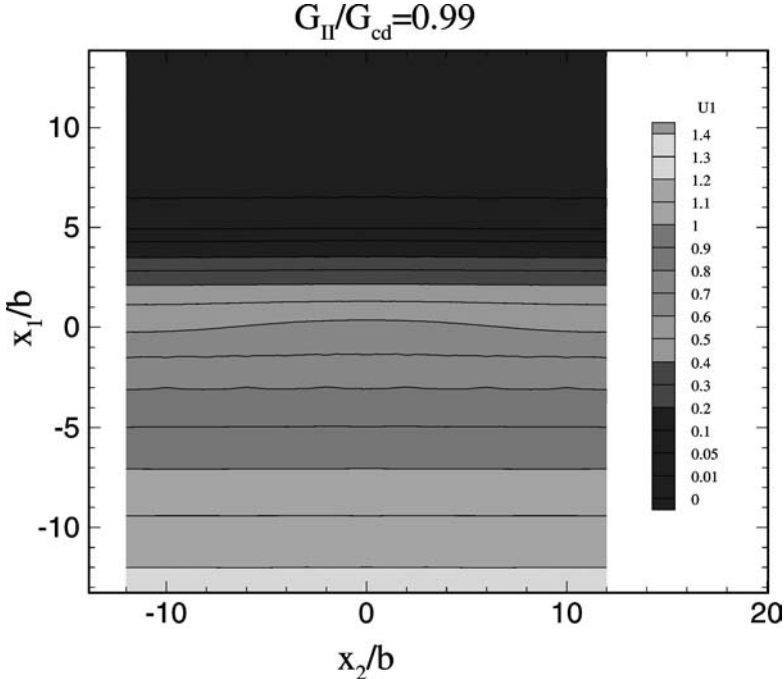


Fig. 28. The saddle point configuration at $G_{\text{II}}/G_{\text{cd}} = 0.99$ under mode II loading, $\beta = 2$. The contour variable U_1 represents the inelastic shear displacement in x_1 -axis.

6.4. Dislocation nucleation on inclined slip planes

Consider an idealized configuration in which the Burgers vector is perpendicular to the crack front, i.e. $\phi = 0^\circ$ in Fig. 6. The slip plane is selected so that $\theta = 45^\circ$ or $\theta = 90^\circ$. Along the slip plane is assumed the coupled tension and shear interlayer potential (37). We set the ratio of Burgers vector to interlayer spacing $b/h = 1$, Poisson's ratio $\nu = 0.3$, and skewness parameter $\beta = 1$. The crack is subject to mode I loading characterized by crack driving force

$$G_{\text{I}} = \frac{1 - \nu}{2\mu} K_{\text{I}}^2. \quad (58)$$

Fig. 39 plots the dependence of the critical driving force $G_{\text{cd}}/G_{\text{IC}}$ on the parameter q for nucleation of a straight dislocation on 45° slip plane. We note that a high ratio $G_{\text{cd}}/G_{\text{IC}}$ is indicative of a tendency towards brittle behavior, while a low value of $G_{\text{cd}}/G_{\text{IC}}$ denotes a propensity for ductile behavior. In addition, a small value of q is expected to favor ductile behavior, while a large value of q should promote brittle behavior, as revealed by (8). The expectation is that $G_{\text{cd}}/G_{\text{IC}}$ be an increasing function of q . Our results indeed exhibit this trend as shown in Fig. 39. We note, however, that the dependence of $G_{\text{cd}}/G_{\text{IC}}$ on q is not linear as predicted by (8). This can be attributed to the tension-softening effect which is

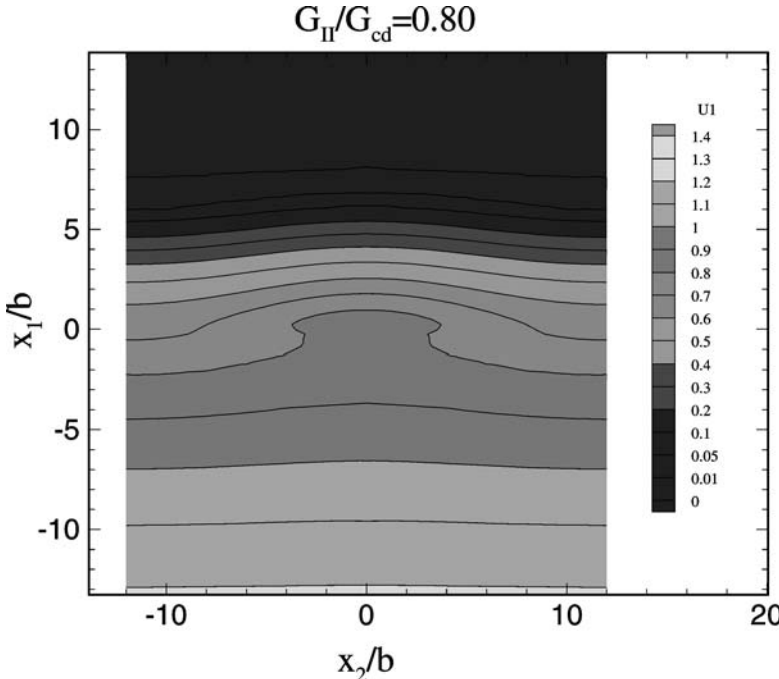


Fig. 29. The saddle point configuration at $G_{II}/G_{cd} = 0.80$ under mode II loading, $\beta = 2$. The contour variable U_1 represents the inelastic shear displacement in x_1 -axis.

neglected in deriving (8). The departure from proportionality is more severe for large q , where G_{cd}/G_{IC} reaches asymptotically a constant value. This constant is of the order of the energy release rate G_I/G_{IC} required to cleave the slip plane, which is shown as a dashed line in Fig. 39. The Rice relation closely matches the computed behavior for $\lambda = 0$ in the range $q < 0.15$. In all other cases, it overestimates the critical driving force relative to the computed values.

The effect of the surface production shear resistance is taken into account for $\lambda = 1$, and is neglected for $\lambda = 0$. Interestingly, the surface production shear resistance results in significantly higher values of G_{cd}/G_{IC} for $q < 0.2$, and therefore causes a substantial embrittlement of the material. This result suggests that, even in nominally ductile materials, i.e. materials with small q , dislocation nucleation on inclined slip planes may not be energetically favored at low temperatures. This, in turn, highlights the importance of other dislocation nucleation modes such as nucleation on oblique slip planes and/or inhomogeneous nucleation at the crack front, which have been amply observed experimentally [18, 48–51].

Fig. 40 plots the dependence of G_{cd}/G_{IC} on q for nucleation of a straight dislocation on 90° slip plane. While trends similar to the 45° case are evident from the figure, the rate at which the horizontal asymptote is approached is much slower in the 90° case. The results attest to the considerable difficulty in nucleating a dislocation on 90° slip plane against the surface production resistance.

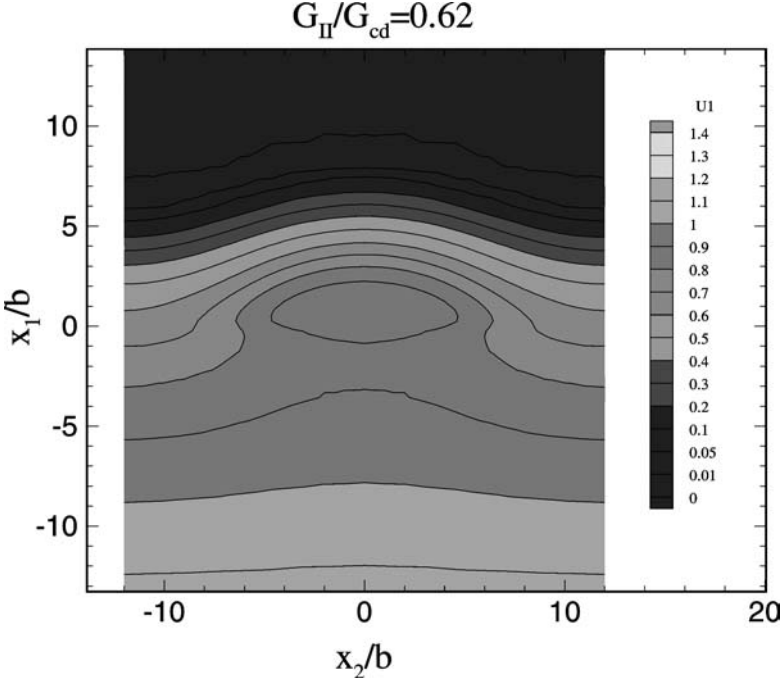


Fig. 30. The saddle point configuration at $G_{\text{II}}/G_{\text{cd}} = 0.62$ under mode II loading, $\beta = 2$. The contour variable U_1 represents the inelastic shear displacement in x_1 -axis.

The effect of the parameter λ on $G_{\text{cd}}/G_{\text{IC}}$ is shown in Fig. 41 for the typical case of $q = 0.125$. As pointed out earlier, the limit of $\lambda \rightarrow \infty$ corresponds to the conventional treatment of surface production through surface tension. This limiting behavior is ostensibly attained for $\lambda > 0.5$, in the case of 45° and $\lambda > 2$, in the case 90° . Beyond these values, $G_{\text{cd}}/G_{\text{IC}}$ is essentially independent of λ .

Finally, for comparison with the other modes of nucleation, we examine nucleation of a dislocation on the inclined plane of the $\{112\}$ type in α -Fe as depicted in Fig. 16(a). We begin by solving the saddle point configurations of the $(1/2)[\bar{1}11]$ dislocation under a pure mode II loading. Two representative saddle point configurations of the dislocation embryo under normalized loading levels $G_{\text{II}}/G_{\text{II}cd}$ of 0.75 and 0.50 are illustrated in Fig. 42 and Fig. 43, respectively. The dependence of the activation energy on the crack front driving force from a series of such solutions is plotted in Fig. 44.

To obtain the dependence of the activation energy on mode I loading for dislocation nucleation on the inclined slip plane, we assume that the nucleation process is essentially equivalent to the mode II crack case under a loading equal to the effective stress intensity factor on the inclined plane. The effective stress intensity factors, which are defined as those at the tip of a small crack emanating from the crack tip in the direction of the slip plane, are given by Cotterell and Rice [33] as

$$K_I^{\text{eff}} = K_I \cos^3(\theta/2), \quad (59a)$$

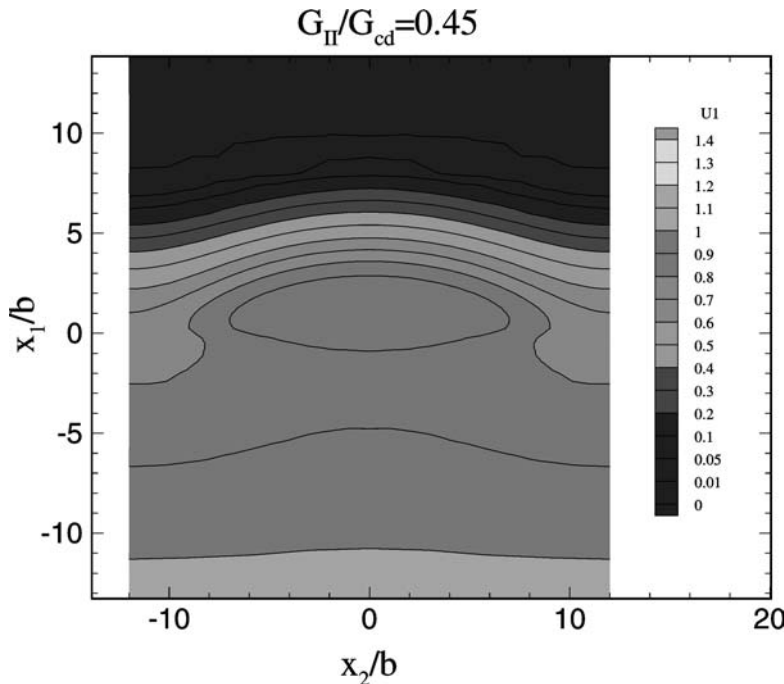


Fig. 31. The saddle point configuration at $G_{II}/G_{cd} = 0.45$ under mode II loading, $\beta = 2$. The contour variable U_1 represents the inelastic shear displacement in x_1 -axis.

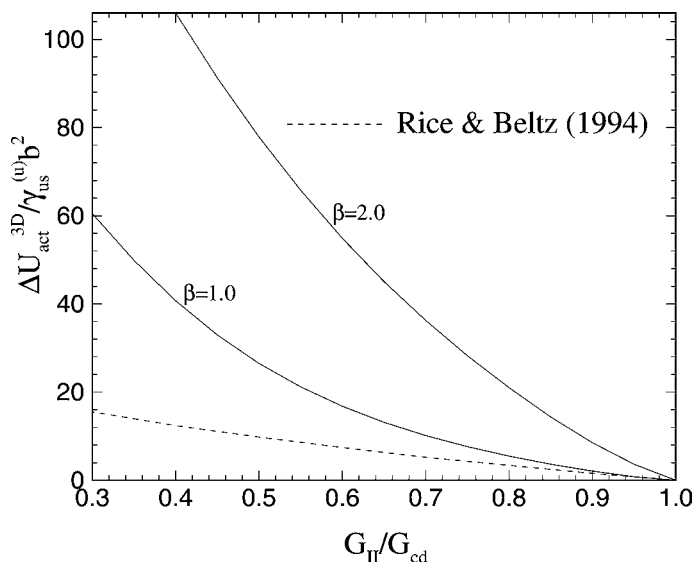


Fig. 32. The activation energy for three-dimensional dislocation emission under mode II loading scaled by the unstable stacking energy.

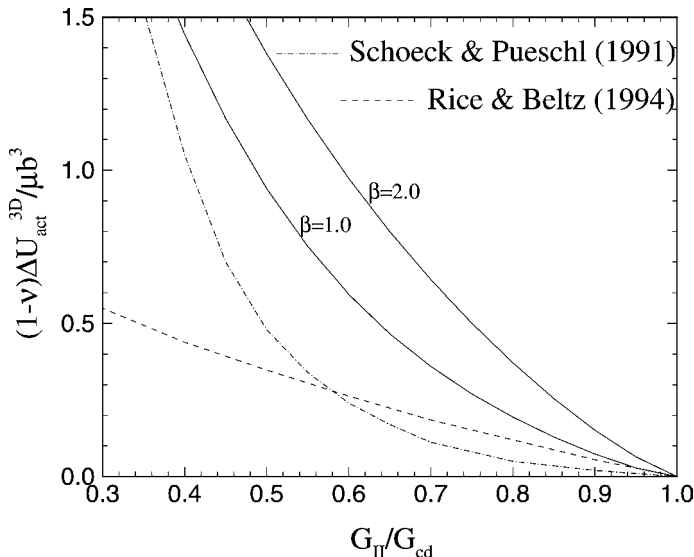


Fig. 33. The activation energy for three-dimensional dislocation emission under mode II loading scaled by the line tension.

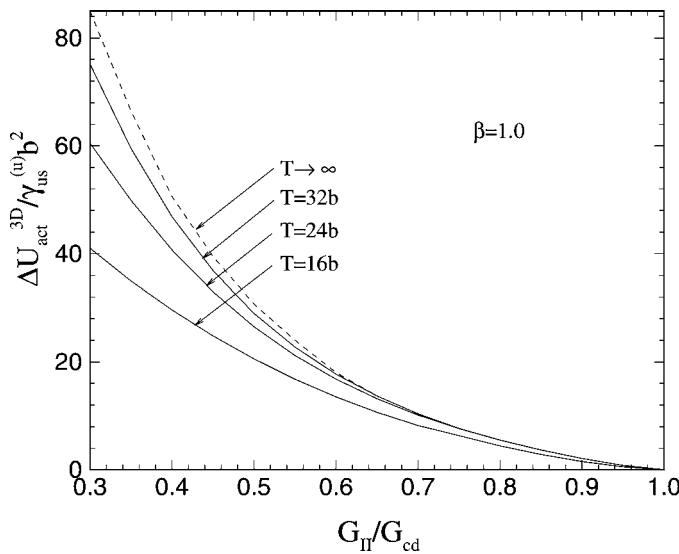


Fig. 34. The effect of the size of the periodic cell on the activation energy for three-dimensional dislocation emission under mode II loading. The curve for a cell of infinite dimensions is obtained by extrapolation.

$$K_{II}^{\text{eff}} = K_I \cos^2(\theta/2) \sin(\theta/2). \quad (59b)$$

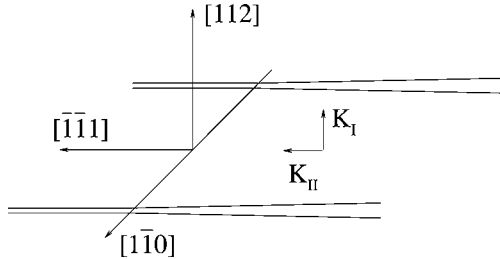


Fig. 35. The geometry of a crack under mixed mode loading.

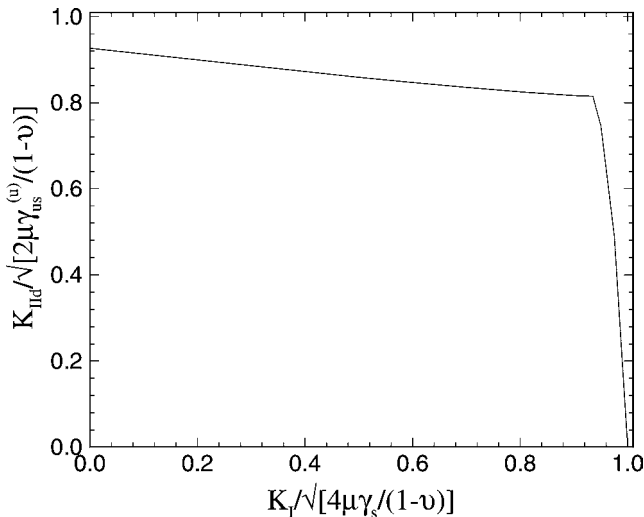


Fig. 36. The dependence of the critical K_{II} on K_I for nucleation of a dislocation in the $1/2[\bar{1}\bar{1}1](112)$ system of α -Fe.

The dependence of the activation energy on mode I loading for actual dislocation nucleation on the inclined slip plane can then be obtained in Fig. 45 by rescaling the curve in Fig. 44 through (59b). We note that this estimate, which considers neither tension softening nor surface production resistance, underestimates the activation energies for most transition metals and intermetallics based on the presented analysis of nucleation of the straight dislocation on the inclined slip plane.

6.5. Dislocation nucleation on the oblique plane

In this section, we provide a direct analysis for dislocation nucleation on the oblique slip plane in α -Fe. A comparison of resolved shear stresses on all potential active slip systems points to the configuration in Fig. 16(b) as the most favorable configuration for dislocation nucleation. We artificially constrain the cleavage plane from propagating to enable

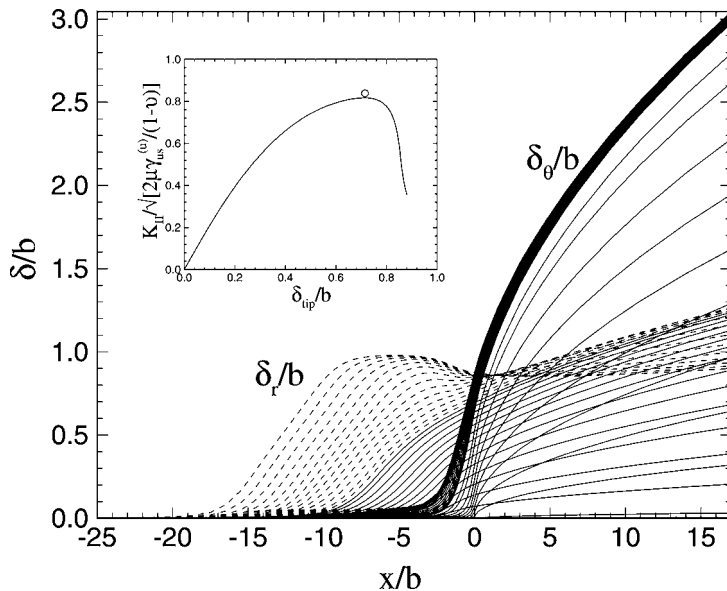


Fig. 37. The sequence of shear and opening displacements under mixed mode loading. K_I is increased from 0 to $0.9K_{IC}$ followed by displacement control in shear. The inset gives the variation of K_{II} with the crack tip inelastic shear displacement at $K_I = 0.9K_{IC}$.

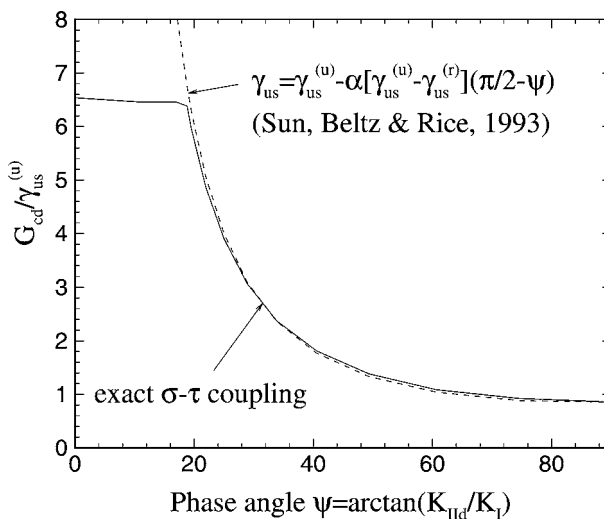


Fig. 38. The dependence of the critical driving force G_{cd} on the phase angle ψ for dislocation nucleation in the $1/2[111](112)$ system of α -Fe.

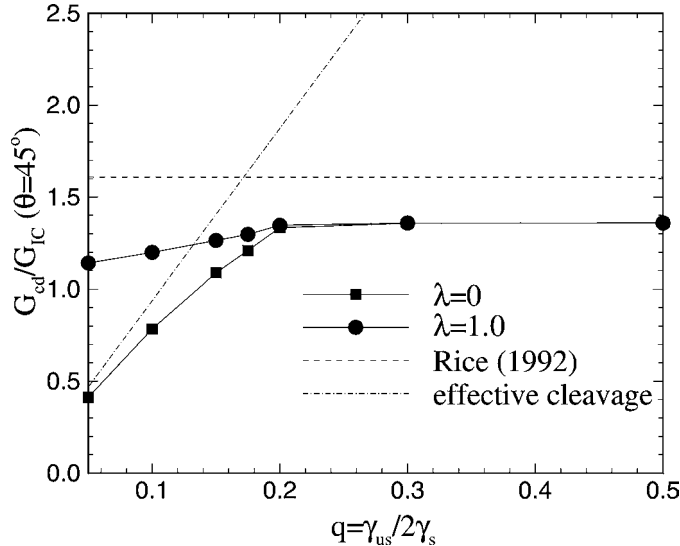


Fig. 39. Dependence of the critical driving force G_{cd}/G_{IC} on q for dislocation nucleation at 45° . λ is the parameter defined in equation (32).

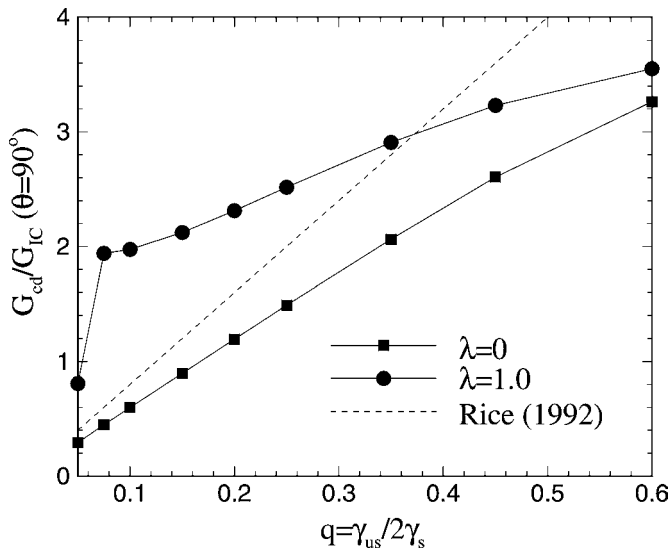


Fig. 40. Dependence of the critical driving force G_{cd}/G_{IC} on q for dislocation nucleation at 90° . λ is the parameter defined in equation (32).

the computation of the critical driving force for dislocation nucleation. The crystal may be viewed as intrinsically ductile if the resulting athermal critical driving force is less than G_{IC} for cleavage. Contrariwise, the crystal is cleavable or intrinsically brittle. For the

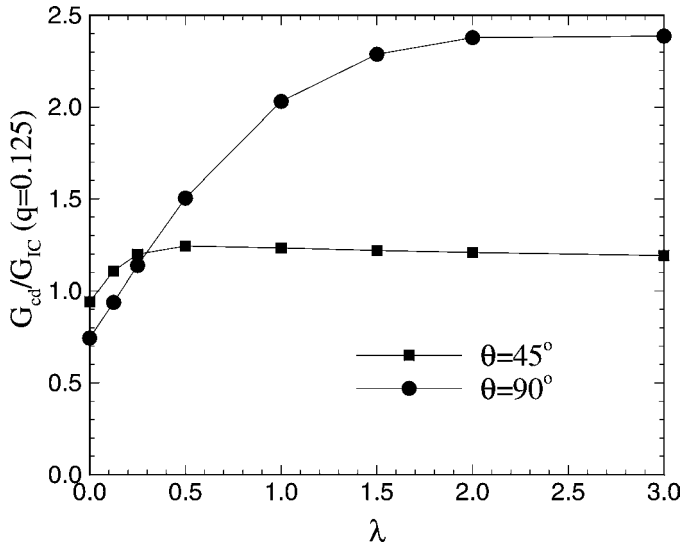


Fig. 41. Dependence of the critical loading on λ for dislocation nucleation on 45° and 90° inclined planes.

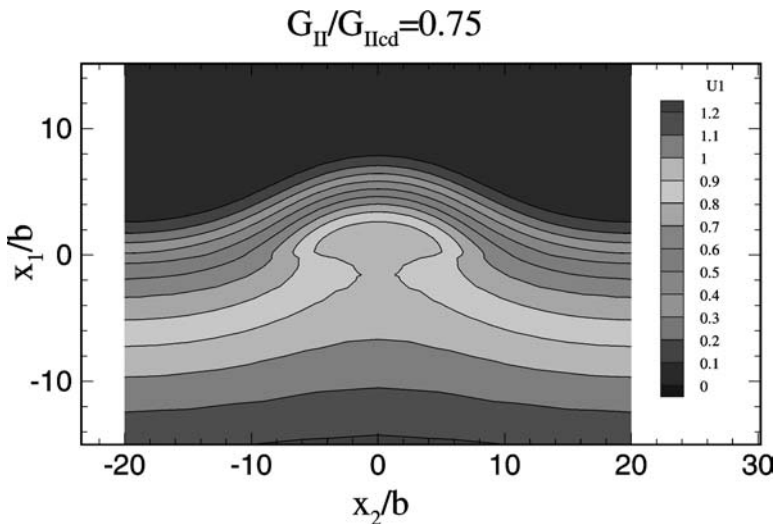


Fig. 42. The saddle point configuration at $G_{HII}/G_{HIcd} = 0.75$ under mode II loading.

later case, at the verge of crack propagation by cleavage, nucleation of dislocations may nevertheless still be possible through thermal activation. The calculation of the required activation energy for such thermally assisted dislocation nucleation is therefore of primary interest.

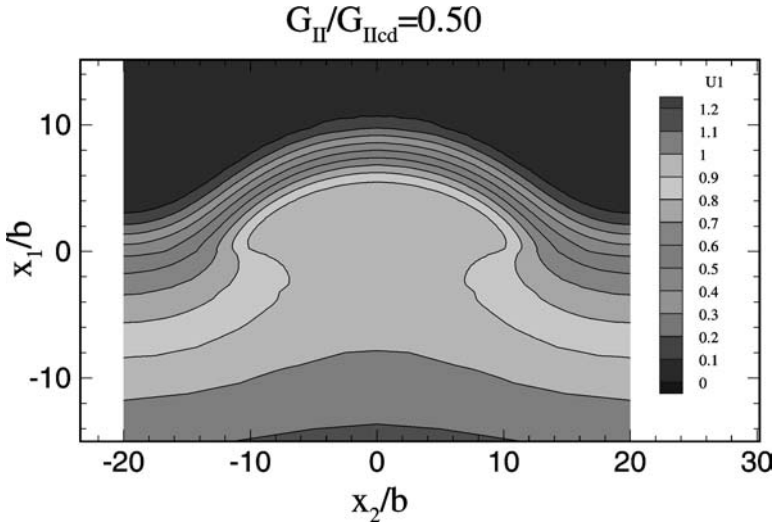


Fig. 43. The saddle point configuration at $G_{II}/G_{IICd} = 0.50$ under mode II loading.

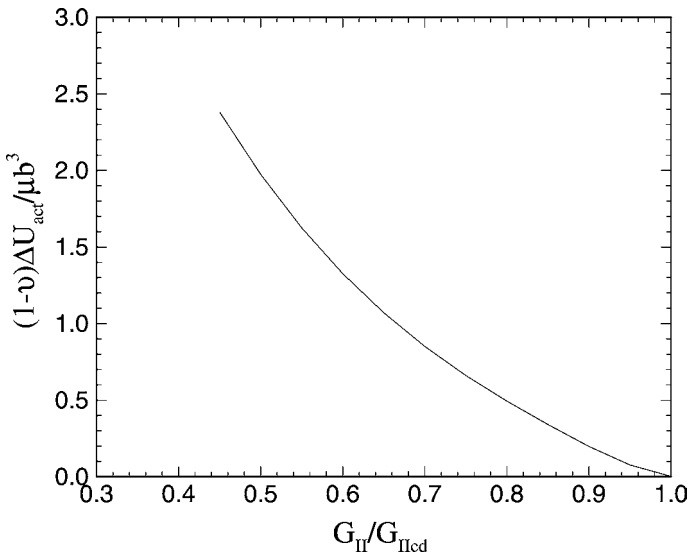


Fig. 44. Dependence of the activation energy on the driving force for dislocation nucleation under mode II loading.

Fig. 46 shows the typical mesh used in the analysis for the geometry of Fig. 16(b). A close-up view of a typical saddle point configuration of an embryonic dislocation emanating from the crack tip is shown in Fig. 47. The calculated dependence of the activation energy on the crack driving force is shown in Fig. 48. The critical driving force at the

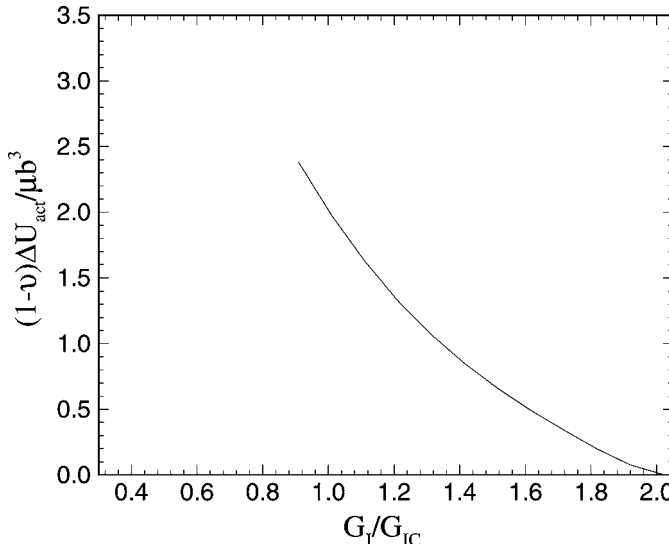


Fig. 45. Dependence of the activation energy on the crack driving force for dislocation nucleation on the inclined {112} slip plane in α -Fe under mode I loading.

athermal threshold and the attendant activation energies are so high that they render the nucleation mechanism highly improbable. The rather demanding computation was discontinued at $G_I/G_{IC} = 1.6$ when the improbability of the mechanism had become amply clear. $G_I/G_{IC} = 1.0$ can be obtained by extrapolation, which provides an adequate basis for reaching a firm negative conclusion on the likelihood of the nucleation mechanism. One factor that contributes to rendering the mechanism ineffective is the fact that the resolved shear stress field is angular dependent, making the area-averaged shear stress smaller than that on the inclined slip plane.

It should be noted that the inelastic displacements across the slip plane were treated as total displacements in the analysis for the convenience of the computation. This tends to underestimate the activation energy as will be demonstrated subsequently. Moreover, we only considered two-sided activation configurations. A one-sided configuration, in which the embryonic dislocation expands primarily on one side of the oblique plane, may conceivably require lower activation energy. However, in view of the results just presented, it seems unlikely that this reduction in the activation energy is sufficient to justify a detailed analysis of one-sided configurations.

The above analysis establishes convincingly that dislocation nucleation on the oblique plane in the interior of the cracked solid is quite unlikely. A very different conclusion may be reached, however, for this mechanism where the crack front reaches a free surface where no plane strain stress is present, and the resolved shear stress on the oblique plane becomes much higher. An estimate of this enhanced nucleation probability on the oblique plane near the surface may be obtained by rescaling the driving forces in Fig. 48 in proportion to the resolved shear stress on the oblique slip plane near the free surface against that in

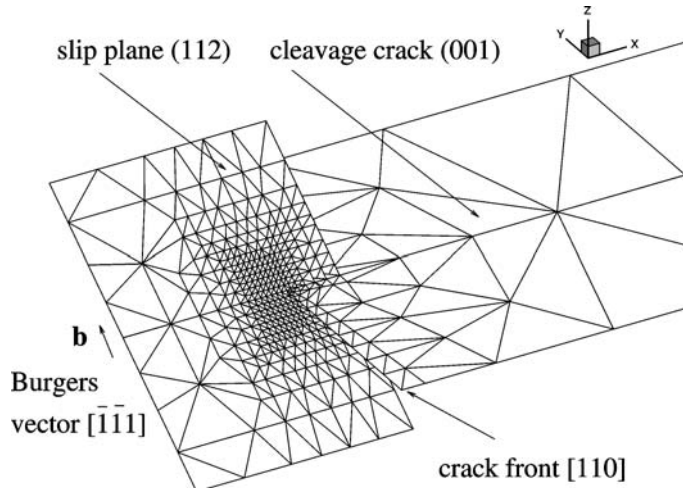


Fig. 46. Mesh used in the analysis of dislocation nucleation on the oblique slip plane in α -Fe for the geometry shown in Fig. 16(b).

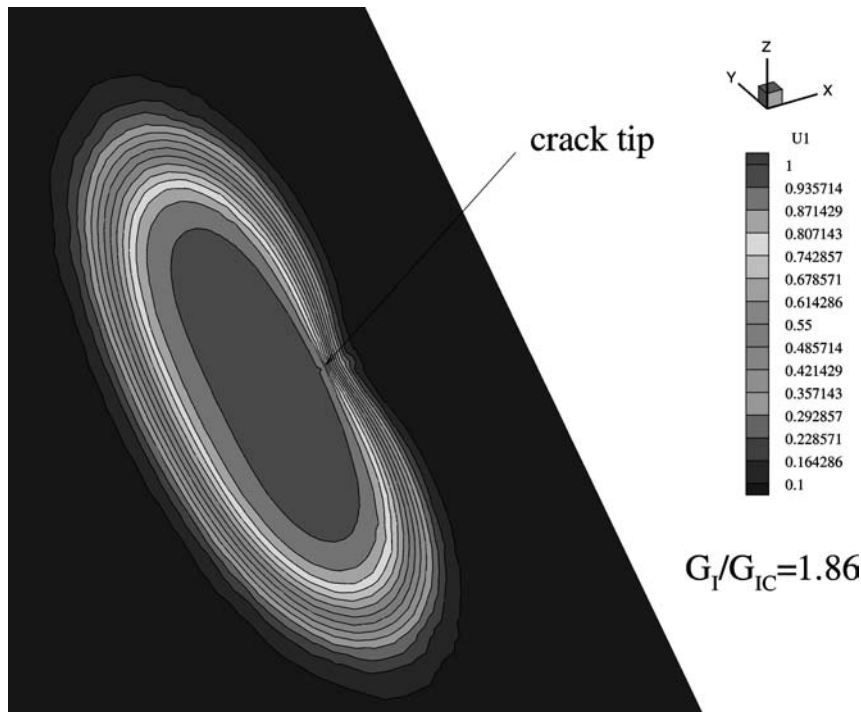


Fig. 47. The saddle point configuration of an embryonic dislocation emanating from the crack tip on the oblique slip plane.

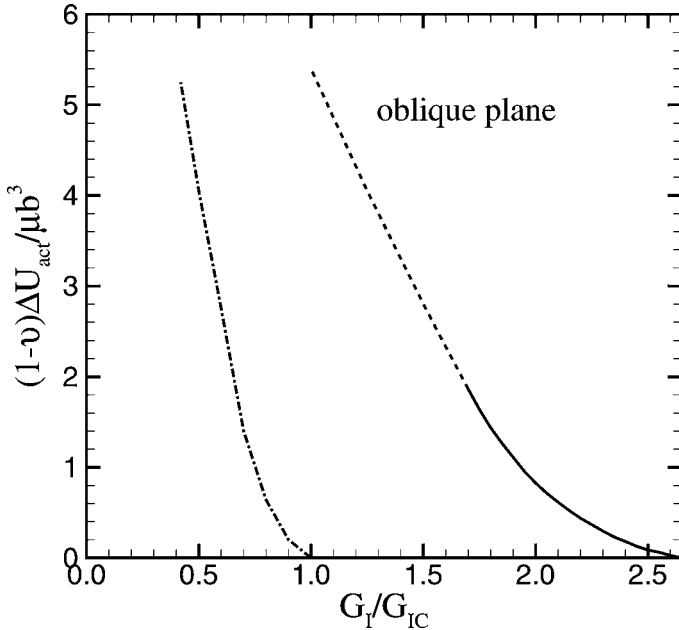


Fig. 48. Activation energy for dislocation nucleation on the oblique plane in the interior (solid line & dashed line) and near a free surface (dashdot line).

the interior. By adopting the asymptotic stress field at the crack tip and the linear elastic analysis, we find

$$\frac{G_{Is}}{G_{Ii}} = \left(\frac{3 - 4\nu}{3} \right)^2, \quad (60)$$

where G_{Is} and G_{Ii} are respective energy release rates required for initiation of a dislocation near the free surface and in the interior. The result for α -Fe with $\nu = 0.291$ is shown as the dashdot curve in Fig. 48, which now suggests almost spontaneous dislocation nucleation near the free surface. This, however, can be a complicated issue, since in this case at least a partial surface ledge must be produced, which makes dislocation nucleation more difficult, but presumably still easier than in the interior. Experimental observation indicated the existence of such nucleation events [18].

6.6. Dislocation nucleation on the cleavage ledge

Cleavage surfaces in most crystals invariably contain ledges parallel to the direction of crack propagation. These ledges are likely to form when the principal tension driving the crack deviates slightly at a local scale, requiring the crack to make small adjustments along its front. This microroughness of the cleavage surface depends also on the crystallographic

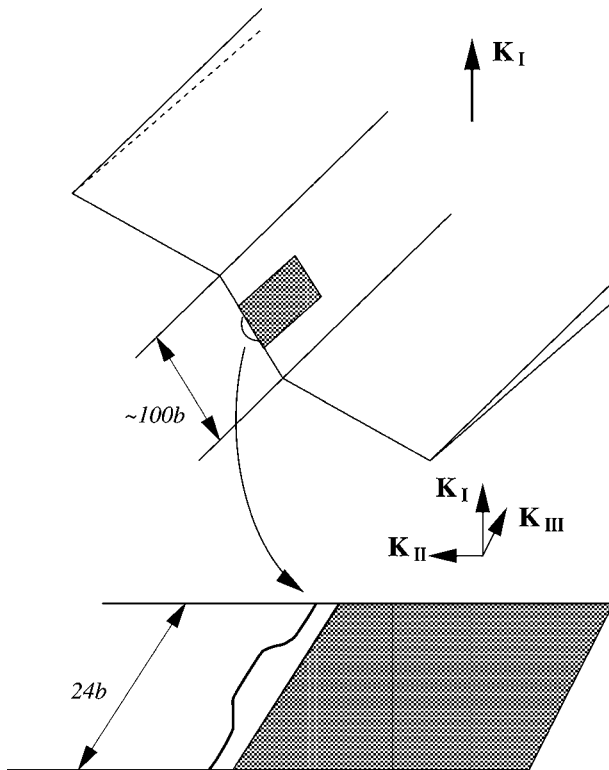


Fig. 49. Dislocation nucleation on a cleavage ledge.

cleavage planes and crack propagation direction as well as on temperature. The height of the observed ledges can range from several atomic spacings to micrometers. Experimental observations [18,51] have revealed that dislocation nucleation at the crack front is a relatively rare phenomenon associated with crack front heterogeneities. This strongly suggests that ledges are likely the sites for heterogeneous nucleation of dislocations. In what follows we analyze this mechanism as it is likely to operate in α -Fe.

Consider a cleavage crack propagating under mode I loading. The crack contains ledges of a width of roughly a hundred atomic spacings distributed along its front, as depicted in Fig. 49. The presence of a considerable local mode III stress intensity factor acting on the ledge is expected to promote dislocation nucleation. Moreover, since the direction of the Burgers vector of the dislocation embryo is parallel to the local crack front, nucleation requires no fresh surface production. In view of the mesh size requirements to resolve adequately the dislocation embryo, a direct simulation of the complete system does not appear to be practical. This difficulty, however, can be sidestepped by the approximate two-scale approach illustrated in Fig. 49. The distribution of the stress intensity factors along the crack front, including the ledge, is first calculated by recourse to the linear elastic analysis regardless of dislocation nucleation on the ledge. The small stretch of the ledge on which the dislocation embryo nucleates is then idealized as a semi-infinite crack subject

to the local stress intensity factors determined in the first analysis. Because of the large disparate scale of the ledge and activation configuration, the results obtained in the manner just outlined are presumably identical with those obtained from the direct simulation.

The distribution of the stress intensity factors along the crack front can be readily solved using the variational boundary integral method for arbitrary three-dimensional cracks developed by Xu and Ortiz [46]. Fig. 50 shows an example of the mesh used in the analysis. To facilitate the calculations, another complementary ledge is introduced to enforce a convenient periodic condition. For small width-to-separation ratios, the interaction between two ledges is expected to be negligible. The calculated stress intensity factors along one period of crack front are shown in Fig. 51. On the ledge, the two stress intensity components are: $K_I^{\text{ledge}} \sim 0.81K_I$ and $K_{\text{III}}^{\text{ledge}} \sim 0.35K_I$. On the verge of brittle fracture, it therefore follows $K_{\text{III}}^{\text{ledge}} \sim 0.35K_{\text{IC}}$. For a simple mode III loading, Rice [14] has determined the athermal critical condition for nucleation of a screw dislocation to be

$$G_{\text{IIIcd}} = \gamma_s = \frac{1}{2\mu} K_{\text{IIIcd}}^2. \quad (61)$$

Using the relation

$$G_{\text{IC}} = 2\gamma_s = \frac{1-\nu}{2\mu} K_{\text{IC}}^2, \quad (62)$$

we obtain

$$K_{\text{IIIcd}} = \sqrt{\frac{(1-\nu)\gamma_s}{2\gamma_s}} K_{\text{IC}} = 0.357 K_{\text{IC}} > 0.35 K_{\text{IC}}. \quad (63)$$

This calculation suggests that screw dislocations can not be nucleated spontaneously below the critical condition for cleavage, which is consistent with the expectation that the single crystal α -Fe be intrinsically brittle. However, the small difference between the numerical factors is most likely to be below the accuracy of the calculation to validate the argument to a considerable extent. Indeed, consideration of tension softening, the effect of anisotropy, and uncertainties in the material parameters can all change (63) to some degree. Nevertheless, the calculation does provide a first indication that nucleation of screw dislocations on cleavage ledges may indeed be much favorable than nucleation on inclined and oblique slip planes.

Next we consider a semi-infinite crack under mode III loading. Tension softening has been shown to be of little consequence up to values of K_I of the order of $0.9K_{\text{IC}}$ in Section 6.3 and can therefore be safely neglected here to reduce the degrees of freedom in computation. Figs 52 and 53 show two saddle point configurations of the embryonic screw dislocation for the normalized loading levels, $G_{\text{III}}/G_{\text{IIIcd}} = 0.75$ and 0.50 . Interestingly, these saddle point configurations are flatter than those of edge dislocations, as shown in Figs 42 and 43. This is consistent with the fact that the screw dislocation tends to adopt a less sharp curvature because it has the lower line energy and consequently high line tension. As the screw dislocation bows out, it tends to form double kinks with shorter edge

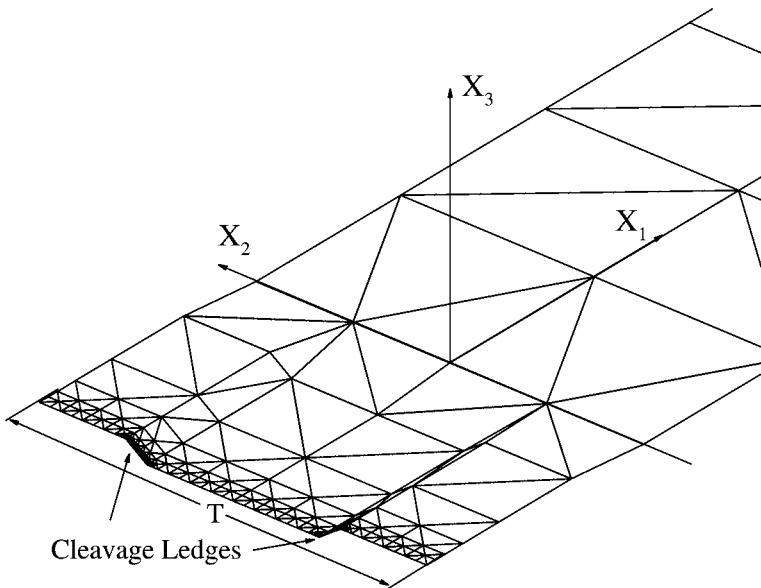


Fig. 50. Mesh used in the computation of the distribution of the stress intensity factors along the crack front containing cleavage ledges.

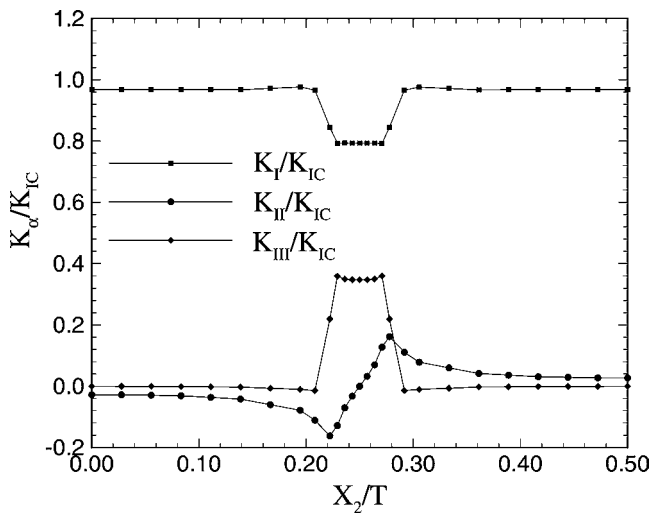


Fig. 51. Distribution of the stress intensity factors on the cleavage ledge.

components. By contrast, the screw double kinks of the edge dislocation embryo tend to be longer and the edge segment shorter. Computationally, this requires a larger periodic domain in the case of the screw embryo indicated in Figs 52 and 53. The dependence of the

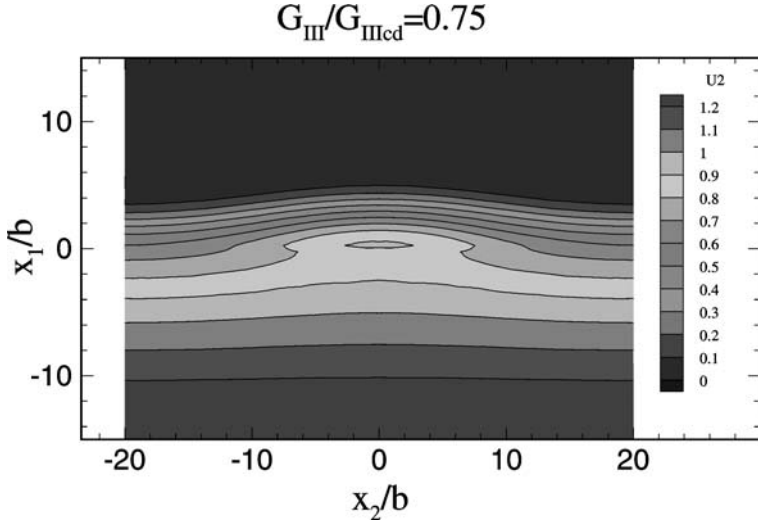


Fig. 52. The saddle point configuration of a screw dislocation, $G_{\text{III}}/G_{\text{IIIcd}} = 0.75$. The contour variable U_2 represents the inelastic shear displacement in x_2 -axis.

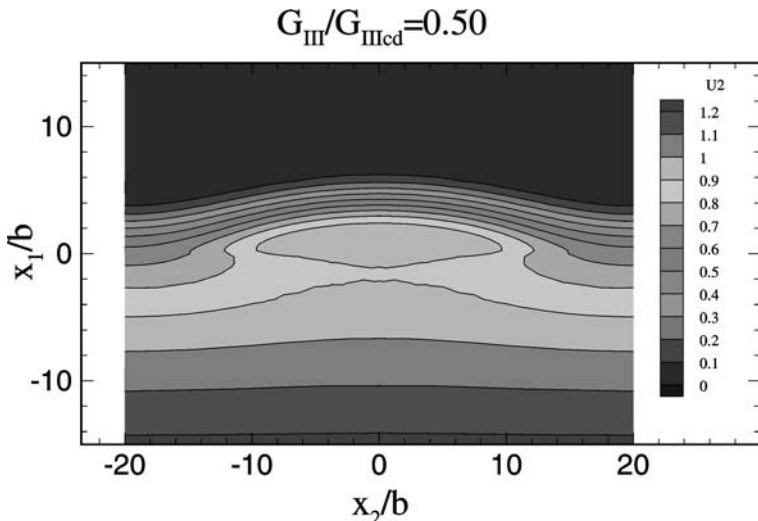


Fig. 53. The saddle point configuration of a screw dislocation, $G_{\text{III}}/G_{\text{IIIcd}} = 0.50$. The contour variable U_2 represents the inelastic shear displacement in x_2 -axis.

activation energy on the local crack driving force is shown in Fig. 54. The lower value of the activation energy relative to those computed for nucleation on the inclined and oblique planes is particularly noteworthy.

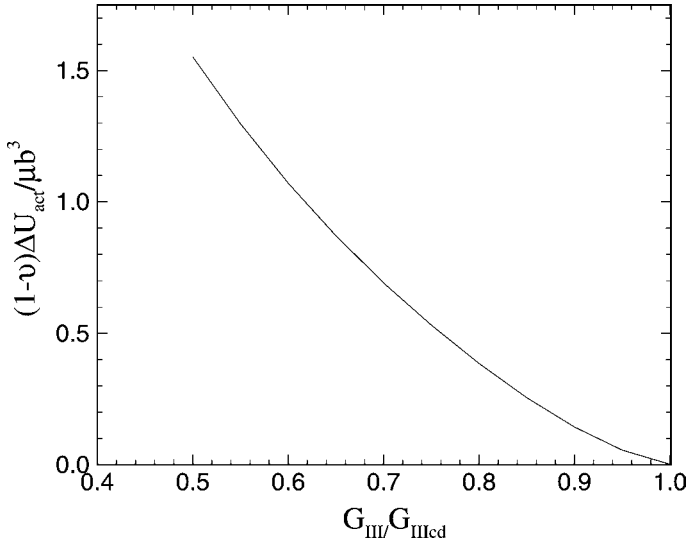


Fig. 54. The activation energy for dislocation nucleation under mode III loading.

Finally, we endeavor to ascertain the magnitude of the errors incurred as the result of the various simplifications adopted in the calculations. To estimate the effect of tension softening, we consider the simple two-dimensional problem of a semi-infinite crack subject to mixed mode I and III loading. We take the ratio K_{III}/K_1 to be $0.35/0.81 = 0.43$, which is the case of interest in the ledge problem. We also wish to estimate the effect of identifying the interlayer inelastic displacements with the total displacements, that is of setting $\Delta = \delta$, a simplification adopted in computation of dislocation nucleation on the oblique plane. Physically, this corresponds to the assumption originally adopted in the Peierls–Nabarro dislocation model. We also want to know the effect of setting parameter $p = 0$, in the cases where p can not be definitely determined. Fig. 55 shows the effect of variations in these parameters on the activation energy. As is evident from the figure, the $\Delta = \delta$ approximation accounts for the modest errors of the order of 15% at most, over much of the range of G_1/G_{IC} . The effect of tension softening in the range of small ratio G_1/G_{IC} is indeed negligible. The lowest curve for the activation energy has been calculated for $p = 0.217$ as a reasonable estimate under mixed loading. It shows that non-zero values of p can reduce the activation energy significantly, which indicates the need for more reliable estimates of this parameter. However, this is very difficult because of ambiguity of the physical meaning of this parameter at the crack tip instead of between two block crystals described in Section 2. This issue probably can only be resolved through the atomic simulation.

7. Estimates of the brittle to ductile transition temperature

Following the viewpoint that the brittle to ductile transition in bcc transition metals, and particularly in α -Fe, is most likely controlled by the process of dislocation nucleation at

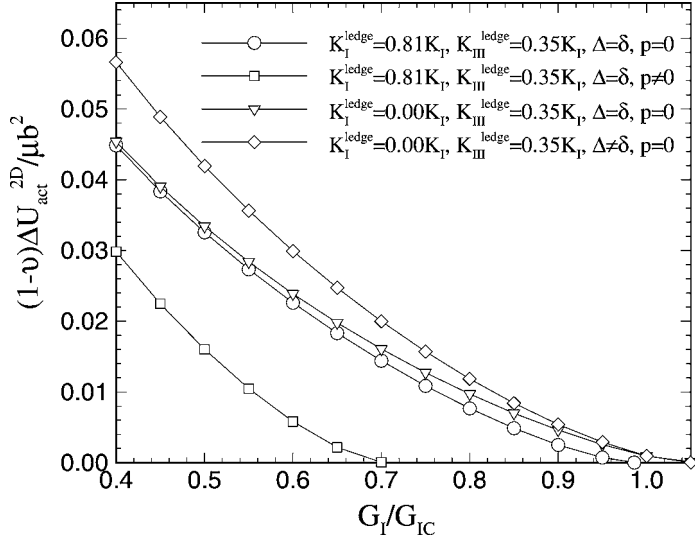


Fig. 55. Parametric sensitivity of the activation energy for dislocation nucleation.

crack tips, the preceding results can then be used to estimate the brittle to ductile transition temperatures attendant to the three nucleation modes considered. No precise experimental data on the transition temperature of single crystal α -Fe are available. The transition temperature for polycrystal low carbon steel is about 250 K, as determined from Charpy impact experiments [57]. In the absence of more direct measurements, we postulate the transition temperature for pure α -Fe to be in the range of 250–300 K. A number of different scenarios may be constructed to describe a brittle to ductile transition. We consider here a relatively precise process described by Argon [7], in which a brittle cleavage crack in α -Fe propagates up a temperature gradient with a given constant velocity v_c . According to the Arrhenius-type relation, the mean reciprocal activation time or activation rate of nucleation of a critical dislocation embryo from the crack tip is

$$\frac{1}{t_a} = v_G \exp\left(-\frac{\Delta U_{act}}{k T_{BD}}\right), \quad (64)$$

where T_{BD} is the brittle to ductile transition temperature, $k = 1.38 \times 10^{-23}$ J/K is Boltzmann constant, and v_G is the normal mode frequency of an atom cluster of the size R_d encompassing the saddle point configuration of the dislocation embryo at the crack tip, for which a good estimate should be

$$v_G \sim v_D \frac{b}{R_d}, \quad (65)$$

where v_D is the fundamental atomic frequency (Debye frequency). When the residence time t_r of the traveling singular crack tip field advancing with a velocity v_c over a distance

of order R_d is equal to the mean activation time t_a there is high probability of the formation of a dislocation embryo of critical shape. Thus, when

$$t_r = \frac{R_d}{v_c} = t_a = \frac{1}{v_G} \exp\left(\frac{\Delta U_{act}}{kT_{BD}}\right), \quad (66)$$

the temperature along the crack path where this condition is met should be the brittle to ductile transition temperature if the formation of the critical embryo also triggers the processes of the wholesale dislocation multiplication. Then the condition for the brittle to ductile transition becomes

$$\frac{v_G R_d}{v_c} = \exp\left(\frac{\Delta U_{act}}{kT_{BD}}\right). \quad (67)$$

Recognizing

$$v_D = v_s/b, \quad (68)$$

and defining the normalized activation energy

$$\gamma = (1 - \nu) \Delta U_{act} / \mu b^3, \quad (69)$$

we can recast the condition for the brittle to ductile transition as

$$T_{BD} = \frac{\mu b^3}{k(1 - \nu)} \frac{\gamma}{\ln(v_s/v_c)}. \quad (70)$$

Here v_s is the velocity of a sound wave. If the temperature dependence of shear modulus is further taken into account to the first order approximation through

$$\mu = \mu_0 \left(1 - \eta \frac{T}{T_m}\right), \quad (71)$$

where μ_0 is the shear modulus at 0 K and η is typically of the order 0.5 for most metals, we find that

$$T_{BD} = T_0 \left[\frac{\ln(v_s/v_c)}{\gamma} + \eta \frac{T_0}{T_m} \right]^{-1}, \quad (72)$$

where $T_0 = \mu_0 b^3 / k(1 - \nu) = 1.2 \times 10^5$ K, the melting point $T_m = 1809$ K for α -Fe. The selection of the typical value $v_c \sim 1$ cm/s results in $\ln(v_s/v_c) \sim 10$.

The dependence of the activation energy for dislocation nucleation on the crack driving force is plotted in Fig. 56 for each of the three modes of nucleation considered. The normalized activation energy γ at the critical driving force for cleavage, i.e. at $G_I/G_{IC} = 1$, determines the transition temperatures through (72). This relation is plotted in Fig. 57, together with the estimates of transition temperatures associated with the three modes of nucleation.

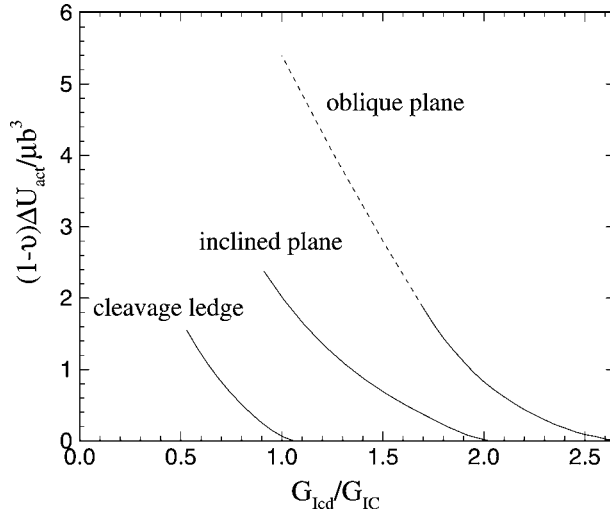


Fig. 56. The activation energies for dislocation nucleation at a crack tip in α -Fe for three different modes of nucleation.

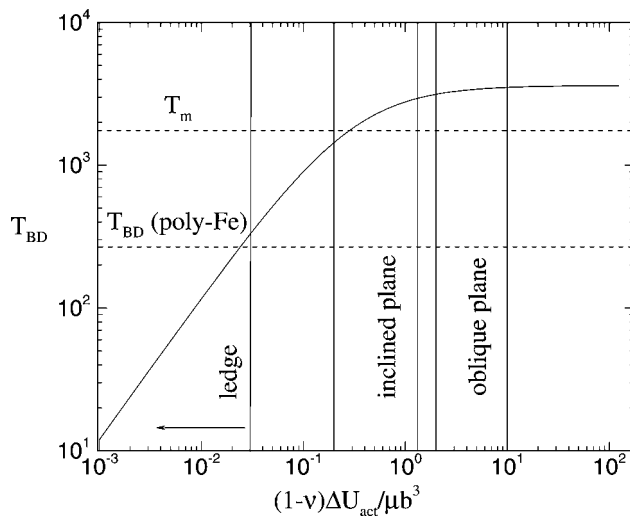


Fig. 57. The estimated brittle to ductile transition temperatures in α -Fe.

Also shown in the figure is the value of the transition temperature for polycrystalline Fe. It is evident from this comparison that only nucleation on the cleavage ledge furnishes the transition temperature that is in the range of the expected value of α -Fe. The other two mechanisms grossly overestimate the transition temperature. These results strongly suggest that dislocation nucleation from the crack tip is an inhomogeneous process. The dis-

location loops, which eventually shield the crack, are most likely emitted from the ledges distributed along the crack front.

8. Summary and discussions

We have presented the recent studies of dislocation nucleation from crack tips and its implications on brittle to ductile transitions in cleavage fracture. The analysis builds on the viewpoint that for certain intrinsic brittle crystals, typically bcc transition metals for which dislocation mobility is high, the brittle to ductile transition is arbitrated by thermally assisted dislocation nucleation at the crack tip. In this regard, various modes of dislocation nucleation from crack tips are studied based on a modified Peierls–Nabarro dislocation model in which the coupled tension and shear potential between the adjacent atomic layers is incorporated into the variational boundary integral method. This approach eliminates the ambiguity of the core cut-off parameter introduced in the previous analysis [3,7], and establishes the linkage between the newly defined solid state parameter of unstable stacking energy and energetics of dislocation nucleation from crack tips. The identification of the critical saddle point configurations of the embryonic dislocations allows for the determination of the energy barriers required for dislocation nucleation. The previous existing gap between experimental and theoretical studies as indicated by Argon [7] has been substantially closed through the study of energetics of dislocation nucleation in α -Fe for the three possible modes, namely, nucleation on the inclined slip plane, the oblique slip plane, and the cleavage ledge. The main finding that the key event is the process of heterogeneous dislocation nucleation is well in keeping with most other nucleation-controlled phenomena in nature (see [58] for a discussion).

The model described in this paper represents the best minimum-commitment approach to an atomic analysis. Consequently, we view our results as less than a final answer quantitatively. One refinement is the consideration of the anisotropic effect, which can be treated straightforwardly in the present framework. The corresponding elastic energy of a three dimensional crack in the general anisotropic solid is given by Xu [59]. The study in α -Fe indicate that anisotropy may alter the results by about 30% for nucleation of straight dislocations [60]. Therefore such an effect probably can not reverse our conclusion that dislocation nucleation is the rare event at the crack tip. Further refinements of the model can be derived from the direct atomic simulation of the crack tip processes. This, however, has proven unwieldy in the past, especially for the computation of the saddle point configurations. The combined atomic and continuum approach may now be readily attempted, in which the present method of the analysis furnishes initial coordinates for the atoms making up the saddle point configurations.

By contrast to the model that the fracture transition in bcc transition metals is controlled by dislocation nucleation from the crack tip, the transition in semi-conductors and compounds is believed to be controlled by the mobility of dislocations away from the crack tip [9]. The distinguishing characteristics between these two models is the mobility of kinks on dislocations, which is high in bcc transition metals, and very low in silicon and other compounds for which good information on dislocation mobility exists [61]. The mobility controlled fracture can also be addressed within the present framework. A perceptive

model of Brede [62] should be amenable to a more rigorous analysis by the variational boundary integral method. In particular, the rate effect can be accounted within the present theory by introducing a rate and temperature-dependent resistance law for dislocation motion.

An additional mechanism that can influence fracture behavior is crack tip shielding by general background plasticity. A particularly elegant and compelling analysis of this mechanism was advanced by Freund and Hutchinson [63], who have demonstrated that brittle-like fracture should take place at high crack propagation velocities with progressively diminishing inelastic response. However, this transition is smooth and spread out, and far from being abrupt. The importance of background plasticity effects has been demonstrated experimentally by Hirsch et al. [64], who have shown that the sharp brittle to ductile transition in dislocation-free Si becomes diffuse, and moves to somewhat lower temperatures when the crystals are initially dislocated by a pre-deformation step. The effect of background plasticity can therefore be regarded to modulate the brittle to ductile transition, with the ultimate controlling mechanism still residing in crack tip initiated processes.

We note that the explanation of the fracture behavior in polycrystalline steel is a complex issue because of effects of many microstructural complexities such as grain boundaries, carbides, and other related internal heterogeneities. Roberts et al. [65] conducted an interesting investigation of cleavage fracture of ferritic steels at cracked grain boundary carbides using a 2D discrete dislocation simulation of the plastic zones associated with a microcrack under triaxial loading. For microcracks in the size range $0.1\text{--}10 \mu\text{m}$, they found that the applied stress at fracture is independent of the yield stress in a wide range 200–1600 MPa and therefore of temperature. This result appears to be in agreement with the viewpoint that the brittle to ductile transition in iron is arbitrated by the thermal process of dislocation nucleation but rather dislocation mobility in the crack tip region. Their analysis also indicates that the dependence of fracture stress on the crack size deviates from the Griffith type relation as a consequence of dislocation induced plastic shielding. Apart from a somewhat heuristic treatment of dislocation nucleation criterion, this rather precise analysis elucidates the exclusive shielding effect of those dislocations emitted from the crack tip, which is neglected in our analysis of dislocation nucleation since friction resistance to dislocation motion is implicitly assumed to be zero. It would be of interest to understand the shielding effect on dislocation nucleation, though this effect does not seem to be likely to affect the conclusion that the brittle to ductile transition in iron is controlled by the process of dislocation nucleation at geometrical heterogeneities along the crack front.

Finally, we also note that brittle to ductile transition has been studied in an alternative approach by Khanta et al. [66,67], who have advocated a cooperative dislocation nucleation mechanism akin to statistical mechanical theories of defect-mediated melting. However, the preponderance of the observational evidence appears to support the crack tip initiated nucleation mechanism. The detailed and meticulous direct X-ray imaging experiments of George and Michot [18] of the stages of evolution of the crack tip plastic response, starting from nucleation at crack tip heterogeneities and followed by the very rapid spread and multiplication of dislocation length from such sources, is a very convincing direct demonstration of the vast number of degrees of freedom available to dislocations in populating the highly stressed crack tip zone. Furthermore, this theory also seems to contradict with the observation that dislocation nucleation in the crack tip region occurs not on the most

highly stresses slip plane but rather on the one that is most energetically preferred for dislocation nucleation from the crack tip. As a final note, the study of energetics of homogenous nucleation of dislocation loops under stress in perfect crystals also further reaffirms that, under the usual stress levels, the energy barriers are far too high to suggest that thermal motion could play a role in homogeneous nucleation of dislocation loops [23].

Acknowledgements

I am indebted to Professor Ali S. Argon of Massachusetts Institute of Technology and Professor M. Ortiz of California Institute of Technology for their advice and collaboration in accomplishing this work, to Professors J.R. Rice and E. Kaxiras of Harvard University, and Dr. R. Thomson of the National Institute of Standards and Technology for a number of fruitful discussions, and to Professor Nabarro for his numerous comments and suggestions which have significantly improved this manuscript. Finally, Professor J.R. Rice's kind permission for adopting the contents in his papers is gratefully acknowledged.

References

- [1] R.W. Armstrong, Mater. Sci. Engng. 1 (1966) 251.
- [2] A. Kelly, W.R. Tyson and A.H. Cottrell, Phil. Mag. 15 (1967) 567.
- [3] J.R. Rice and R. Thomson, Phil. Mag. 29 (1974) 73.
- [4] S.J. Burns and W.W. Webb, J. Appl. Phys. 41 (1970) 2078.
- [5] S.J. Burns and W.W. Webb, J. Appl. Phys. 41 (1970) 2086.
- [6] J.J. Gilman, C. Knudsen and W.P. Walsh, J. Appl. Phys. 29 (1958) 600.
- [7] A.S. Argon, Acta Metall. 35 (1987) 185.
- [8] K.S. Cheung, A.S. Argon and S. Yip, J. Appl. Phys. 69 (1991) 2088.
- [9] C. St John, Phil. Mag. 32 (1975) 1193.
- [10] M. Brede and P. Haasen, Acta metall. 36 (1988) 2003.
- [11] P.B. Hirsch and S.G. Roberts, Phil. Mag. A 64 (1991) 55.
- [12] P.B. Hirsch and S.G. Roberts, Acta Mater. 44 (1996) 2361.
- [13] G. Schoeck and W. Pueschl, Phil. Mag. A 64 (1991) 931–649.
- [14] J.R. Rice, J. Mech. Phys. Solids 40 (1992) 235.
- [15] G. Xu, A.S. Argon and M. Ortiz, Phil. Mag. A 72 (1995) 415.
- [16] G. Xu, A.S. Argon and M. Ortiz, Phil. Mag. A 75 (1997) 341.
- [17] S.J. Zhou and R. Thomson, J. Mater. Res. 6 (1991) 639.
- [18] A. George and G. Michot, Mater. Sci. Eng. A 164 (1993) 118.
- [19] R.E. Peierls, Proc. Phys. Soc. A 52 (1940) 34.
- [20] F.R.N. Nabarro, Proc. Phys. Soc. A 59 (1947) 256.
- [21] J.D. Eshelby, Phil. Mag. 40 (1949) 903.
- [22] J.P. Hirth and J. Lothe, Theory of Dislocations (Wiley, New York, 1982).
- [23] G. Xu and A.S. Argon, Phil. Mag. Lett. 80 (2000) 605.
- [24] G. Xu, unpublished research.
- [25] V. Vitek, Phil. Mag. 18 (1968) 773.
- [26] M. Yamaguchi, V. Vitek and D. Pope, Phil. Mag. 43 (1981) 1027.
- [27] Y. Sun, G.E. Beltz and J.R. Rice, Mater. Sci. and Eng. A 170 (1993) 67.
- [28] E. Kaxiras and M.S. Duesbery, Phys. Rev. Lett. 70 (1993) 3752.
- [29] A.T. Paxton, P. Gumbsch and M. Methfessel, Phil. Mag. Lett. 63 (1991) 267.

- [30] J.R. Rice, G.E. Beltz and Y. Sun, in: Topics in Fracture and Fatigue, ed. A.S. Argon (Springer, Berlin, 1992).
- [31] G. Schoeck, Phil. Mag. A 81 (2001) 1161.
- [32] J.R. Rice and G.E. Beltz, J. Mech. Phys. Solids 42 (1994) 333.
- [33] B. Cotterell and J.R. Rice, Int. J. Fract. 16 (1980) 155.
- [34] J.H. Rose, J. Ferrante and J.R. Smith, Phys. Rev. Lett. 47 (1981) 675.
- [35] G.E. Beltz and J.R. Rice, in: Modeling the Deformation of Crystalline Solids: Physical Theory, Application and Experimental Comparisons, eds T.C. Lowe, A.D. Rollett, P.S. Follansbee and G.S. Daehn (TMS, Warrendale, PA, 1991) p. 457.
- [36] G. Simmons and H. Wang, Single Crystal Elastic Constants and Calculated Aggregate Properties (The M.I.T. Press, Cambridge, 1971).
- [37] L.R. Curnich, PhD thesis, University of Minnesota, 1972.
- [38] A.J. Foreman, M.A. Jaswon and J.K. Wood, Proc. Phys. Soc. A 64 (1951) 156.
- [39] W.L. Bragg and W.M. Lomer, Proc. Roy. Soc. A 196 (1949) 171.
- [40] W.M. Lomer, Proc. Roy. Soc. A 196 (1949) 182.
- [41] L.T. Shi and A.S. Argon, Phil. Mag. A 46 (1982) 255.
- [42] J.R. Rice, private communication.
- [43] S.J. Zhou, A.E. Carlsson and R. Thomson, Phys. Rev. Lett. 72 (1994) 852.
- [44] Y. Juan and E. Kaxiras, Phil. Mag. A 74 (1996) 1367.
- [45] R.D. Mindlin, Int. J. Solids Structures 1 (1965) 417.
- [46] G. Xu and M. Ortiz, Int. J. Num. Methods Eng. 36 (1993) 3675.
- [47] M. Ortiz and J. Blume, Int. J. of Fracture 42 (1990) 117.
- [48] Y.H. Chiao and D.R. Clarke, Acta Metall. 47 (1989) 203.
- [49] J. Samuels and S.G. Roberts, Proc. Roy. Soc. A 421 (1989) 1.
- [50] P.B. Hirsch, J. Samuels and S.G. Roberts, Proc. Roy. Soc. A 421 (1989) 25.
- [51] B.J. Gally and A.S. Argon, Phil. Mag. A 81 (2001) 699.
- [52] J.W. Hutchinson and W.T. Koiter, Appl. Mech. Rev. 23 (1970) 1353.
- [53] B. Budiansky, Adv. Appl. Mech. ed. C.-S. Yih (Academic Press, 1974).
- [54] A.F. Bower and M. Ortiz, J. Mech. Phys. Solids 38 (1990) 443.
- [55] G.H. Vineyard, J. Phys. Chem. Solids 3 (1957) 121.
- [56] R.W. Clough and J. Pluzilu, Dynamics of Structures (McGraw-Hill, New York, 1975).
- [57] F.A. McClintock and A.S. Argon, Mechanical Behavior of Materials (Addison Wesley, Reading, MA, 1966) Chapter 17.
- [58] J.W. Martin and R.D. Doherty, Stability of Microstructure in Metallic Systems (Cambridge University Press, Cambridge, England, 1976).
- [59] G. Xu, J. App. Mech. 67 (2000) 403.
- [60] Y. Sun and G.E. Beltz, J. Mech. Phys. Solids 42 (1994) 1095.
- [61] V.V. Bulatov, S. Yip and A.S. Argon, Phil. Mag. A 72 (1995) 452.
- [62] M. Brede, Acta Metall. et Mater. 41 (1993) 211.
- [63] L.B. Freund and J.W. Hutchinson, J. Mech. Phys. Solids 33 (1985) 169.
- [64] P.B. Hirsch, S.G. Roberts, J. Samuels and P.D. Warner, in: Advances in Fracture Research, vol. 1, eds K. Salama, K. Ravi-Chandar, D.M.R. Taplin and P. Rama Rao (Pergamon, Oxford, 1989) p. 139.
- [65] S.G. Roberts, S.J. Noronha, A.J. Wilkinson and P.B. Hirsch, Acta Mater. 50 (2002) 1229.
- [66] M. Khanta, D.P. Pope and V. Vitek, Phys. Rev. Lett. 73 (1994) 684.
- [67] M. Khanta, D.P. Pope and V. Vitek, Scripta Metall. Mater. 31 (1994) 1349.

This page intentionally left blank

Dislocations and Disclinations in Mesomorphic Phases

MAURICE KLEMAN

*Laboratoire de Minéralogie-Cristallographie de Paris (CNRS UMR 7590), Université Pierre-et-Marie-Curie,
case 115, 4 place Jussieu, 75252 Paris cédex 05, France*

OLEG D. LAVRENTOVICH

*Chemical Physics Interdisciplinary Program and Liquid Crystal Institute, Kent State University, Kent, Ohio
44242, USA*

and

YURIY A. NASTISHIN

Institute for Physical Optics, 23 Dragomanov Street, Lviv, 79005, Ukraine

Contents

1. Introduction	150
2. Topological classification of defects	157
2.1. Why a topological classification	157
2.2. The order parameter space	158
2.3. The first homotopy group (the fundamental group) of the OP space	159
2.4. Some important fundamental groups of OP spaces	159
2.5. Homotopy groups for defects of different dimensionalities	162
2.6. Relations between the Volterra process and the topological approach	163
3. Defects in nematic phases	164
3.1. Experimental observations	165
3.2. Elastic theory of defects	170
3.3. Defects in phase transitions	172
3.4. Some rheological properties	175
4. Defects with isometric properties in smectic phases	178
4.1. The isolated focal conic domain	178
4.2. Energy of an isolated FCD-I	180
4.3. How do FCD's pack in space: oily streaks	183
4.4. How do FCD-I's pack in space: laws of association	186
4.5. Surface anchoring energy: an illustration of its role	187
5. Dislocations vs disclinations. Grain boundaries in smectics	190
5.1. Tilt grain boundaries	190
5.2. Screw dislocations and twist grain boundaries	195
6. Defects with isometric properties in columnar phases	200
6.1. General considerations	200
6.2. Simple developable domains	202
7. Role of defects in weak shear deformations	203
7.1. General considerations	203
7.2. Obstacles to the flow	204
7.3. Concepts used to describe dislocation movement	206
7.4. Movement of an isolated dislocation in a SmA phase	207
7.5. Collective behaviour of dislocations: climb of edge lines	209
7.6. Collective behaviour of dislocations: motion of screw lines	210
8. Defects in liquid lamellar phases	212
8.1. Structures, order parameters	212
8.2. Defects in a SmC phase	215
8.3. Defects in a SmC* phase	219
8.4. Defects in a SmC _A * phase	225
9. Defects in cholesteric liquid crystals (N*)	226
9.1. Elastic description	226
9.2. Disclinations λ , τ , and χ	227
9.3. Linear and non-linear elastic models of edge dislocations in a 1D periodic structure	229
9.4. Core structure and splitting	233
9.5. Glide and kinksindexkinks	235
9.6. Textures in N*'s, oily streaks	237
9.7. Robinson spherulites	241
10. Competitive interactions in liquid crystals. Spontaneous defects, frustration	242

10.1. Definitions and classification	242
10.2. Double twist configurations. Blue phases	245
10.3. Grain boundaries in smectics	250
10.4. Chiral columnar phases	260
Acknowledgments	264
Appendix: Fluorescent confocal polarizing microscopy	264
References	265

1. Introduction

More than twenty years ago [1,2] were published in the very same series three articles on the general theory of disclinations in liquid crystals (LC) [1], essentially nematics, in magnetic systems [2], and on disclinations and sets of disclinations (textures), essentially in smectics and cholesterics [3]. The science of defects in mesomorphic phases (liquid crystals, colloidal crystals, most generally organized soft matter,) was at that time rather young—it started with Frank’s renowned paper [4]—and, by necessity, its first results bore the marks of its origins taken in the theory of defects in solids, as it was founded by Volterra, Somigliana, Burgers, etc. [5,7,15].

Let us recall the main results obtained at that time—the reader is urged to go back to refs [1,3] and [6] for a more detailed account. Starting from the Volterra process (VP), the definition and experimental recognition of the invariants (rotation vectors, that are the analogs of the Burgers vectors) attached to a line were established, as well as a distinction between *wedge* and *twist disclinations* (as we have screw and edge dislocations); the line tensions were calculated. These results were obtained for *nematics* (N) (N), i.e., the simplest liquid crystalline phase in the sense that it is a 3D liquid, and that its LC character is restricted to its simplest, but most characteristic, feature, namely the existence of a director—symbolized by a field of unit vectors $\mathbf{n}(\mathbf{r}) \equiv -\mathbf{n}(\mathbf{r})$. In the N ground state the director is a constant, $\mathbf{n}(\mathbf{r}) = \text{const}$. In the nematic phase disclinations break the finite rotational symmetries (any axis perpendicular to the optical axis,—the director,—, is a two-fold axis), Fig. 1, at the expense of a small energy of curvature, $\sim k_B T$ per molecular length of line defect [e.g., $\pi K_1 a/4 = 3.66 k_B T$ for 5CB (p-pentyl-p'-cyanobiphenyl; $K_1 = 0.64 \times 10^{-10}$ N, $a \approx 3$ nm), $T = 298$ K], in full analogy with the case of dislocations in solids [e.g., $\mu b^3/4\pi = 5.19 k_B T$ for Al ($\mu = 2.70 \times 10^{10}$ N/m², $b = 0.286$ nm, $T = 700$ K)], T being of the order of the melting point.

On the other hand the continuous translation and rotation symmetries yield disclination densities and dislocation densities. Thanks to a remark of Jacques Friedel, according to which a disclination in a nematic should carry, for obvious reasons of stability (see [1,6]), its rotation vector attached to each of its points—which implies that the rotation vector is a constant in modulus and direction, but not in position—it appears that dislocation densities should be considered in a full description of defects in nematics, Fig. 2.

Friedel’s model of interplay between dislocation densities and disclinations is particularly attractive to describe fluid relaxation. Because some mesomorphic phases possess at the same time finite disclinations and finite dislocations, the same type of interplay fully explains some observations of which Fig. 3 is a remarkable illustration.

Coming back to nematics, these complications with respect to the usual theory of defects were soon attended by two remarks of paramount importance.

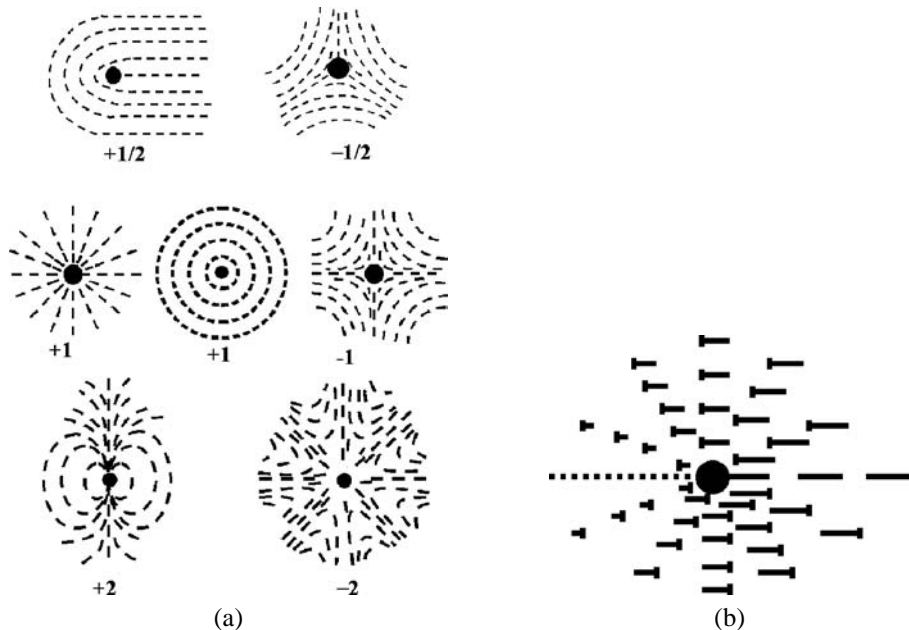


Fig. 1. (a) Wedge lines of strength $k = 1/2, -1/2, 1, -1, 2, -2$ and (b) a twist line of strength $|k| = 1/2$ in a uniaxial nematic phase. The wedge lines are obtained by employing the Volterra process about a twofold axis (see ref. [6]) and the twist line by a somewhat more complex process which involves the relaxation of dislocation densities, as in Fig. 2 (see refs [1,6]).

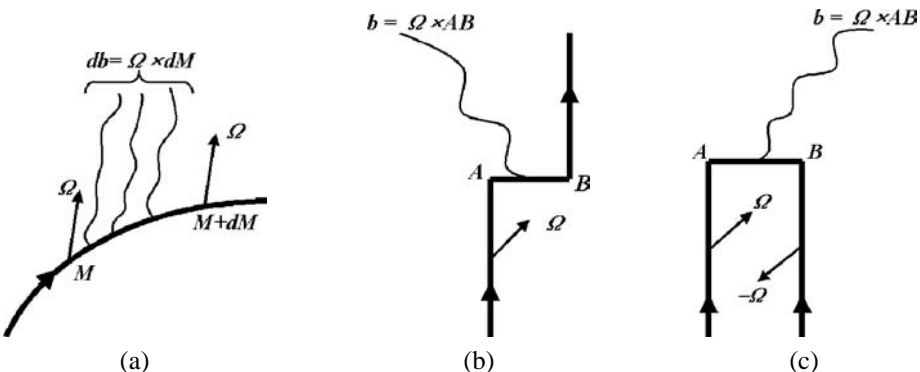


Fig. 2. Dislocation densities in a nematic. (a) Sketch of a curved disclination line whose rotation vector Ω is attached to each point of the line. The disclination must carry a density of dislocations $db = \Omega \times dM$, between two points M and $M + dM$. The disclination is of wedge character where Ω is colinear to the line, of twist character if Ω is perpendicular to the line. (b) Sketch of a kink (twist character) on a disclination of strength Ω , of length AB , where b ($b = \Omega \times AB$) is the total dislocation Burgers vector carried by AB . This situation can exist in a medium with finite Burgers vectors. (c) Same as (b) with another orientation of part of the line, exhibiting the equivalence of a dislocation and two disclinations of opposite signs at a distance AB [7].

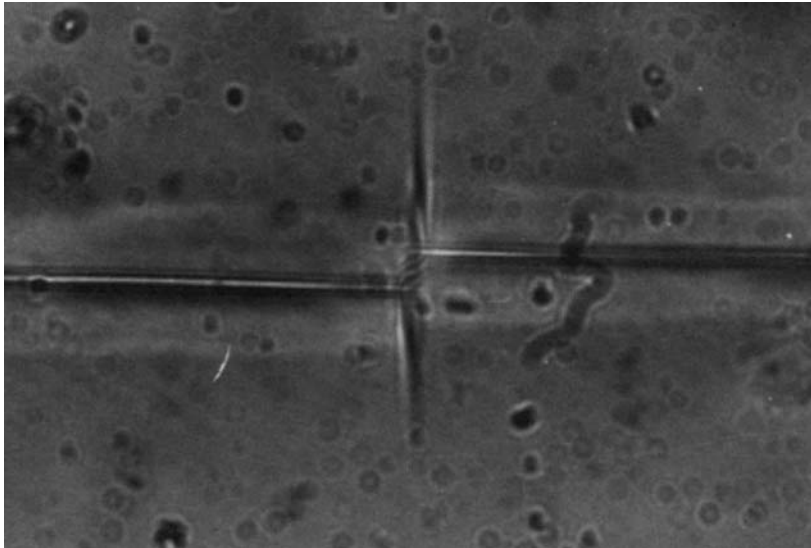


Fig. 3. A wall of dislocations attached to a kink in a columnar (D) phase (courtesy Oswald).

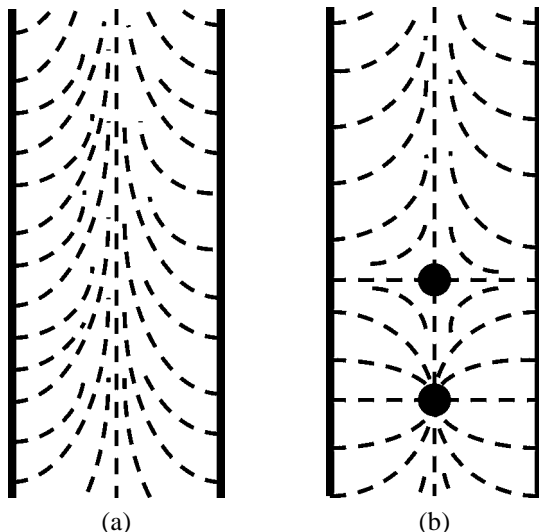


Fig. 4. (a) Escape in the 3rd dimension and (b) singular points on a disclination line of strength $k = 1$. Cut in a meridian plane.

- (a) The core of disclinations of 2π rotation vector can ‘escape in the third dimension’,—an expression coined by R.B. Meyer [8], meaning that the core singularity can vanish away [9] according to the model of Fig. 4. The same is true for disclinations of any $2\pi k$ rotation vector, $k \in \mathbb{Z}$.

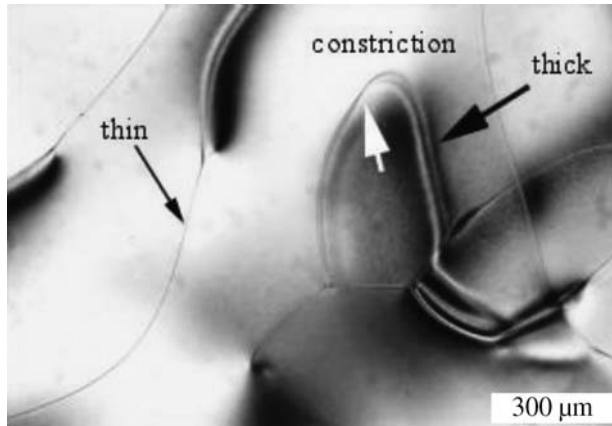


Fig. 5. Thicks, thins, constriction in a nematic.

- (b) Point singularities: just because the escape can take place either ‘upwards’ or ‘downwards’, Fig. 4(b), one expects that point singularities (called point disclinations, or disclination points) can appear. This is very often observed; these disclination points can be present as *constrictions* on the thick lines (*thicks*) visible in the optical polarizing microscope, representative of integer k lines, while thin lines (*thins*) come about because their singular cores (for k being a half-integer) strongly scatter light, Fig. 5.

The detailed investigations made on defects in nematics, alluded to and illustrated above, have yielded a rather clear if not complete understanding of the static properties of disclination lines and points, and opened the path to the study of other LC defects, where the notion of disclination is essential. At the same time, advances were made in cholesterics (N^*) and in smectics with liquid layers (SmA mainly). We shall not review these already ancient results in detail, but rather start from the corpus of concepts they have provided. We present now, with comments, how our review is constructed.

In order to set on a sound theoretical basis the peculiar characters reported above, the investigations on liquid crystals have developed into a general theory of defects, valid for all ordered media and for defects of any dimensionality. The rudiments of this approach were given in the appendix of [1]. Section 2 of this survey is therefore devoted to a more developed, although still incomplete, account of the *topological classification of defects*, and its application to some interesting case in LC’s, namely: uniaxial nematics (N , the standard case already discussed in [1]); biaxial nematics (N_B); cholesterics (N^*); smectics A (SmA); smectics C (SmC). Each of these examples illustrates different aspects of the way the topological theory deals with defects. An important result obtained in the frame of the topological theory is that it allows the classification of not only *line defects*, but also *point defects* (of the type of Fig. 4(b)), and 3D knotted configurations (i.e., 3D geometries that are nowhere singular, but cannot be continuously unknotted to a perfect ground state of the ordered medium).

Uniaxial nematics continue to be much studied, from various points of view:

- (i) On the theoretical side.
 - (a) Because their elasticity, which is devoid of terms of positional order, provides typical features of 3D curvature elasticity, they have attracted the attention of mathematicians [10], in particular for line and point defects.
 - (b) The question of the core has been, and still is, much studied using analytical and numerical methods, in its static as well as its dynamic states.
- (ii) On the experimental side, much has been done in the domain of their rheological properties: usual (thermotropic) small molecule chemicals (SMLC); liquid crystal polymers (LCP) either thermotropic (polyesters, Vectra[®], etc. which are high temperature systems), or lyotropic (biological polymers), such as hydroxypropylcellulose—HPC—, xanthan, polybenzyl L-glutamate—PBL-G—, etc.); solutions of more or less rigid viruses, that form nematics or cholesteric phases below a certain degree of dilutions, due to steric hindrances; etc. Most of these systems are not nematic in their ground state at rest (they are N* or N_B, but behave as N as soon as they are sheared).
- (iii) Also, a deep motivation for a continuous interest in their properties is display applications [11].

It would have been impossible to bring credit to all the aspects of research in nematic compounds. We have thus limited ourselves in Section 3 to some generalities, and to another aspect, namely the suspected analogy between the isotropic–nematic first order phase transition (and other phase transitions)—because of the appearance of defects—and the phase transitions during the evolution of the early Universe. This analogy has been a strong motivation for many interesting experiments. Also, a short presentation of the rheology of nematic phases when it relates to defects is presented, see subsection 3.4.

We present in Section 4 defects in SmAs (smectics A), which are representative of layered phases, 1D solids with 2D *liquid* layers; the directors are along the normal to the layers. Focal Conic Domains (FCD), described in [3]—are, together with disclinations in N, the earliest type of defects ever investigated [12], long before dislocations in solids. They have still been actively studied in the last 20 years, due to the discovery of a manifold of lamellar phases: either thermotropic (single component media) or lyotropic (made of amphiphilic molecules in a solvent specific of a part of the molecule). Their elastic properties are now well understood, even if the core properties of their conjugate disclinations (an ellipse, a hyperbola) are still far from being unraveled. FCDs are an example of a type of defects whose geometry is subordinated to a competition between two types of elastic contributions—*strain* elasticity, here the compressibility of the layers; *curvature* elasticity, here the curvature of the layers—whose ranges of action are different [13]. Let R be the typical size of a domain submitted to some compression or tension; the strain energy is of the order of BR^3 , and the curvature energy, of the order of KR . Here K and B are elastic moduli, and the free energy density can be written:

$$f = 1/2K(\Delta_{\perp}u)^2 + 1/2B(\partial u/\partial n)^2 = f_{\text{curvature}} + f_{\text{strain}}, \quad \lambda^2 = K/B, \quad (1)$$

where $u(x, y, z)$ is the elastic displacement of a layer at level z before deformation, λ a microscopic length comparable to the layer thickness d_0 , $\Delta_\perp = \partial^2/\partial x^2 + \partial^2/\partial y^2$ and $\partial/\partial n$ the derivative along the layer local normal. The ratio of the two energies

$$f_{\text{strain}}/f_{\text{curvature}} \approx (R/\lambda)^2 \quad (2)$$

is larger than 1 as soon as $R > \lambda$. Therefore one expects that the only distortion that would affect a layered medium (Sm) on a macroscopic length R is a curvature distortion, i.e., the layers curve while keeping a constant interdistance not significantly different from d_0 and conserving parallelism (what we call *isometric distortions*). Of course such a constraint imposes drastic conditions on the shape of the singularities that are, as stated above, an ellipse and a hyperbola which are conjugate. Section 4 is devoted to a review of these special, but rather common, distortions.

Columnar systems (D, from *discotic*; molecules building such phases are disk-like), which are 2D solids, 1D liquids, display an elastic competition of the same type: the typical deformations are developable domains (DD), which are briefly described in Section 6.

FCDs and DDs singularities are disclinations. However, dislocations in smectics and in columnar phases do not lack interest, for at least three reasons: (a) their particular elasticity (the case of edge dislocations in SmA's is treated in [1]); (b) their interplay with FCDs and DDs—we shall discuss an interesting example of tilt boundary that can be constructed either with dislocations or with FCD's with dislocations attached; twist grain boundaries will also be discussed; (c) the role dislocations play in the rheological behavior of these mesomorphic phases; little is yet known of this role, but what is known is promising. These questions are reviewed in Sections 5 (for grain boundaries in SmAs) and 7 (role of defects in SmA weak shear deformations).

There are other types of layered media, characterized by various types of 2D order (SmB, etc.), but we shall not expatiate on them. Contrariwise, we shall discuss at some length, in Section 8, 2D *liquid* phases other than SmA, namely, SmC, SmC* (the chiral version of the SmC phase), and SmC_A*. The symmetry point group of the SmC* and SmC_A* chiral phases, namely C2, implies a non vanishing macroscopic polarization, arranged either in a ferroelectric or antiferroelectric fashion.

The description of defects in cholesterics [3] (Section 9) comprehends observations at two length scales: below a pitch length, where N* defects are most similar to nematic ones—the helicity is hardly visible—, and beyond a pitch length. At such larger scales, one observes defects that are analogous to some extent to FCDs in SmAs, due to the layered structure of the N* phase; but also, because the order parameter (OP) of the N* phase is not of the same type as the OP of SmAs, a rich zoology of disclinations. The classifications of disclinations in N*'s and N_Bs are the same, because in both cases the geometry of the OP is one of a trihedron of directors; there are three director fields in N_B and N*, whereas there is only one director field in a SmA (the field of the normal to the layers). As we shall explain, what could be thought of as an antinomy, namely the existence of FCD's in N* but not in N_B, is explained by the fact that, of course, there is a 1D periodic structure in a N* phase, but also because two director fields are *immaterial* in N*'s. In relation with this remark is the classification of some non-singular defects in N* (called *distortions with double topological character*), by topological methods that overtake the classification discussed in the next section, see [14]. Notice finally that, because the cholesteric

pitch is often so large (in the μm range and above), the dislocations of the layered structure (whose repeat distance is the half pitch) in N^* 's are easily observed and studied, in particular edge dislocations, for their kinks, jogs, mobility, etc. This is developed in Section 9.

Chirality has been, and still is, a source of novel problems of the highest interest. Chirality, which is in its most strict sense a lack of mirror symmetry, lies at the heart of nature. It plays a crucial role in the existence of life, in the stability and phenomena of macro- and micro-world; it is responsible for the structures and properties of condensed matter at very different levels of structural organization from crystals to biological objects. In liquid crystals one can distinguish two types of chiral mesophases: those that are constituted with achiral molecules but are chiral because of their low orientational ordering (point symmetry C_2 and lower) and those that are chiral due to the chirality of molecular conformations. Often molecular chirality leads to a *helical* orientational ordering of the mesophases in one or more space directions, left or right. Sometimes structural chirality without molecular chirality is also attended by helical orientational ordering, left and right in equal proportions. Although helicity is a type of orientational ordering, it requires a coordinate description and is characterized by a translation-rotation space group. It turns out that because of the topological constraints the uniform helical orientational order can be realized in not more than one space direction, in N^* , SmC^* , SmC_A^* . In Sm^* 's, the helical axis has to be parallel to the layer normal to avoid the appearance of defects. Sm^* phases are discussed in Section 8, as already mentioned. In all other cases the space field of the order parameter contains defects giving rise to so called *frustrated* mesophases. The interest in frustrated mesophases is enhanced by a deep analogy with frustration in other condensed matter systems, like the amorphous Phases. The first example of a frustrated mesophase in Section 10 is the Cholesteric Blue Phase, in which the director field is twisted along helices whose axes are perpendicular to the director—the full space double twist (DT) configuration can be modeled by DT cylinders packing the space. The double twist configuration can be realized in whole space only at the expense of introducing line disclinations. The self-organization of these defects results in three types of Cholesteric Blue Phases (BPI, BPII, BPIII). Interference of helicity with positional ordering gives rise to other frustrated mesophases: Smectic Blue Phases (three phases similar to the Cholesteric Blue Phases), TGB Phases (TGBA, TGBC, TGBC * , TGBC $_A$, U-TGBC *), chiral columnar phases (TGB-like columnar phase, Moiré phase). We review ordering and defects in these mesophases in Section 10.

Most of the compounds considered hereunder as illustrations of the defects are *thermotropic*, i.e., made of one chemical species. The same symmetries, and consequently the same defect classification, are found in *lyotropic* materials, i.e., made of amphiphilic molecules in a solvent with affinity for one part of the molecule, no affinity for the other part. It happens that the lyotropic phase and the thermotropic phase with the same symmetry are designated by different acronyms, e.g., L_α is the acronym of a lyotropic phase with the symmetries of a SmA.

2. Topological classification of defects

2.1. Why a topological classification

Some characteristic features of defects in LC's with no equivalent in usual solid crystals have been recalled in the introduction; these are: disclinations whose core singularity vanishes away, point singularities and 3D knotted non-singular configurations. The fundamental entity at the heart of the usual classification of defects is the Volterra process (VP), which puts in correspondence *line* defects and elements of the group of symmetry of the crystal: *dislocations* are classified by the symmetries of translation, *disclinations* (also called dislocations of rotation) are classified by the symmetries of rotation, see [7, 15]. liquid crystals that have finite translational symmetries, and provides the classification of their dislocations (in smectics, cholesterics, hexagonal phases, blue phases, etc.), but fails to work efficiently for disclinations. For example, in a N phase, (a) the VP correctly describes straight wedge disclinations of strength $|k| = 1/2$ (i.e., rotational symmetries of angle $\omega = \pm\pi$), but cannot be extended to $|k| > 1/2$, i.e., angles $\omega = (2n \pm 1)\pi$, $n \neq 0$, $n \in \mathbb{Z}$, except at the price of very artificial procedures; (b) twist dislocations cannot be constructed, except locally (for an illustration, see [16]); (c) the ‘escape in the 3rd dimension’ obviously does not come out of the VP.

The question therefore arises of whether disclinations are still classified by the rotational elements of symmetry, in the Volterra spirit, although the VP does not work properly, and if they are, how should the VP be modified. A few remarks are in order:

- (a) The existence of *curved* wedge lines in N, N*, and NB phases is satisfactorily described by the introduction of continuous densities of dislocations. This has been already illustrated in Fig. 2. Observe that this works all the more because there are no finite quantized translational symmetries in these media. Furthermore, continuous densities of dislocations provide a physical approach to the question of the mobility of wedge lines, as a result of the viscous relaxation of such densities [6]. The topological classification does not bring such a conceptual possibility.
- (b) In the case of finite quantized translational symmetries, as in Sm or D phases, it follows from the indications in the introduction that there is a large difference in the order of magnitude of energies carried by dislocations (which strain the medium) and by disclinations (which curve the medium). As a consequence, in most circumstances dislocations (and their associated strain energy) are restricted to small length scales, and disclinations take very special shapes, in order to avoid the appearance of strain. The final geometry of the samples is thus most often divided into *domains* (FCDs in Sm phases, DDs in D phases) whose boundaries can be described in terms of disclinations. When this happens, the VP definition of disclinations is of little use, and the most efficient way of analyzing the domains is in terms of 1D (smectic) or 2D (columnar) *isometric* distortions (no strain) of the perfect state.
- (c) But in most cases, one has to revisit the VP, which we do in the present section. We shall keep to a shortened version of the theory of the topological classification of defects, which has been fully reviewed in a number of places ([6], chapt. 10, [17–19]).

A detailed reading of the rest of this section requires the acquiring of some familiarity with the methods of algebraic topology, but is not necessary for a full understanding of the rest of this paper.

2.2. The order parameter space

The topological classification of defects relies on the application to ordered media of the methods and concepts of algebraic topology; many excellent handbooks treat this subject [21–23]. The analysis starts from a special manifold, the manifold V of internal states, also called the *vacuum* or the *order parameter space* (OP space). This is the space of all the possible different positions and orientations of the perfect crystal in (flat) Euclidean space. Let H be the group of symmetry of the crystal, $G = E(3) = R^3 \square O(3)$ the group of Euclidean isometries of E^3 . The symbol \square is for the semi-direct product of groups. R^3 is the 3D group of continuous translations, $O(3) = SO(3) \times Z_2$ the full group of rotations, with centre of symmetry included. The symbol \times is for the direct product of groups. H is a subgroup of G , V is the quotient space G/H . Notice that V is not a group, generically, except if H is a normal subgroup of G .

Each orientation and position in space of the perfect crystal can be put into correspondence with a left coset of H , as follows. Let $g(\mathbf{r}_0, \mathbf{r}, \boldsymbol{\omega}) \in G$ an element, which brings some perfect realization in \mathbf{r}_0 of the perfect crystal, to a position \mathbf{r} , with a rotation $\boldsymbol{\omega}$. If $g(\mathbf{r}_0, \mathbf{r}, \boldsymbol{\omega}) \in H(\mathbf{r}_0)$, the group of symmetry at \mathbf{r}_0 , then the realizations of the perfect crystal at \mathbf{r}_0 and \mathbf{r} coincide; if $g(\mathbf{r}_0, \mathbf{r}, \boldsymbol{\omega}) \notin H(\mathbf{r}_0)$, all the elements of the left coset:

$$l_c(\mathbf{r}_0, \mathbf{r}, \boldsymbol{\omega}) = \sum_h g(\mathbf{r}_0, \mathbf{r}, \boldsymbol{\omega})h(\mathbf{r}_0), \quad (3)$$

also do not belong to $H(\mathbf{r}_0)$; here $h(\mathbf{r}_0) \in H(\mathbf{r}_0)$. All the elements of the left coset $l_c(\mathbf{r}_0, \mathbf{r}, \boldsymbol{\omega})$ bring the perfect crystal from a realization at \mathbf{r}_0 to a realization at \mathbf{r} , with rotation $\boldsymbol{\omega}$, and only those elements do so. G is a sum of such left cosets, which bring the realization in \mathbf{r}_0 to any other possible realization $\{\mathbf{r}, \boldsymbol{\omega}\}$.

$$G = \sum_{\mathbf{r}, \boldsymbol{\omega}} l_c(\mathbf{r}_0, \mathbf{r}, \boldsymbol{\omega}). \quad (4)$$

G/H is the set of all the cosets, each of them reduced to a point by identification of all its elements. It is easy to show that the group of symmetry of the realization in \mathbf{r} (the ‘little group’ in \mathbf{r}) is

$$H(\mathbf{r}) = g(\mathbf{r}_0, \mathbf{r}, \boldsymbol{\omega})H(\mathbf{r}_0)g^{-1}(\mathbf{r}_0, \mathbf{r}, \boldsymbol{\omega}). \quad (5)$$

Examples of OP spaces are given in [6]; we recall that the OP space of a uniaxial nematic $V(N) = P^2$, the projective plane; the OP space of a 3D crystal Xal, regarding only the translations, is $V(Xal) = T^3$, the 3D torus.

2.3. The first homotopy group (the fundamental group) of the OP space

Let us now consider how the OP space V enters into the issue of the topological classification of defects. Start from a distorted ordered medium, in which the order parameter is broken along a line L . In order to test the topological nature of the breaking, surround L by a closed loop γ entirely located in the *good* portion of crystal, good in the sense of the usual theory of dislocations in solids. It is possible to attach to each point r belonging to γ a ‘tangent’ perfect crystal, which maps in a unique way onto some point $R \in V$. When r traverses the closed loop γ , R traverses a closed loop Γ on V . Call ϕ this well-defined continuous mapping

$$\phi : \gamma \rightarrow \Gamma. \quad (6)$$

The function ϕ can be extended continuously to the whole continuous domain D of the ordered medium in which the OP is well defined, since the OP is expected to vary continuously in D . Therefore any continuous motion of γ in D maps on a continuous motion of Γ . There is in consequence a relation of equivalence between the different images Γ ’s; it is this equivalence that is described by the notion of homotopy, see [21]. All the Γ ’s belonging to the same class of equivalence are represented by an element $[\Gamma]$ of a group, the so-called fundamental group (or first homotopy group) $\Pi_1(V)$. More precisely, $\Pi_1(V)$ is the group of classes of oriented loops belonging to V , equivalent under homotopy, and all having the same base point. This latter technicality has no incidence on the classification of defects. More important is the remark that, in most cases, the fundamental group is *not* commutative, a property that is related to the fact that the *topological charge* of a defect—the corresponding element in $\Pi_1(V)$ —is modified when defect $[\Gamma]$ has circumnavigated about a defect $[\Gamma']$; it is changed to $[\Gamma'][\Gamma][\Gamma']^{-1}$, an element of the same conjugacy class. It is therefore usual to consider that all the elements of a given class of conjugacy represent the same defect. We give hereunder an example of the physical nature of the non-commutativity of $\Pi_1(V)$.

2.4. Some important fundamental groups of OP spaces

The classes of conjugacy of $\Pi_1(V)$, therefore, provide a classification of the types of *line* defects of the ordered medium. The similarities and differences between the homotopy classification for line defects and the VP classification have been discussed [24,25]. Let us just remind the reader of some results already presented in [1,2] and [13].

- (1) Nematic phase N. $\Pi_1(N) \sim Z_2$ is a commutative group with two elements, the identity I and the non-trivial element σ ; $\sigma^2 = I$. The identity element represents the defects whose core can ‘escape in the 3rd dimension’, namely those whose rotation vector is a multiple of 2π ; because the core is non singular, there is no doubt that it is possible to transform smoothly a $|k| = n$ defect into a $|k| = n'$ defect, $n, n' \in Z$. The non-trivial element σ represents the defects $|k| = n \pm 1/2$, which all belong to the same class of defects; it is indeed possible to show that there is a continuous path to transform a $k = 1/2$ wedge (σ , say) into a $k = -1/2$ wedge (σ^{-1} say); see [26],

[27] for a pictorial illustration). Therefore these two lines, which are different in the Volterra sense, correspond to the same topological defect. Extension to all defects with $n \neq 0$ is straightforward, because $|k| = n$ represents a null defect (with rotation vector multiple of 2π). This is the topological explanation of the ‘escape in the 3rd dimension’.

- (2) Biaxial nematic N_B and disclinations in a cholesteric phase: $\Pi_1(N_B) = \Pi_1(N^*) = Q$, the group of quaternions, 8 elements, non-commutative. Call $I, J, \sigma_i, \sigma_i^{-1}$, $i = 1, 2, 3$ these elements; I is the identity element. They obey the relations $J^2 = I$, $\sigma_i \sigma_j = J \sigma_j \sigma_i = \sigma_k$, $i, j, k =$ any circular permutation of $\{1, 2, 3\}$, $\sigma_i^2 = \sigma_1 \sigma_2 \sigma_3 = J$, $J \sigma_i = \sigma_i J = \sigma_i^{-1}$. The symmetry point group can be represented by three orthogonal directors, labeled 1, 2, 3. Each of them is therefore a twofold axis of symmetry, $\pm\pi$. Each set $\{\sigma_i, \sigma_i^{-1}\}$ depicts a defect of rotation angle $\pm\pi$ about one of the directors. It is easy to show that, e.g., $\sigma_1 \sigma_2 \sigma_1^{-1} = \sigma_2^{-1}$. Therefore σ_i and σ_i^{-1} belong to the same class of conjugacy; the group counts five classes, the identity class $\{I\}$, the class $\{J\}$, and the three classes $\{\sigma_i, \sigma_i^{-1}\}$. Because the three last ones represent the three types of defects that break $\pm\pi$ rotations, the class $\{J\}$ represent the $\pm 2\pi$ disclinations, and the class $\{I\}$ the $\pm 4\pi$ disclinations. The $\{I\}$ defects can escape in the 3rd dimension, since they belong to the identity class, but not the defects of the $\{J\}$ class. The essential differences with the defects in a uniaxial nematic are therefore twofold: (1) each set of disclination i ($i = 1, 2, 3$) contains singularities for $\pi(\sigma_i$ and $\sigma_i^{-1})$ and $2\pi(J = \sigma_i^2)$ rotations, and no singularity for a 4π rotation ($I = \sigma_i^4$); (2) elements of these sets for the π rotations do not commute. We give below, in the next subsection, an example of what has to be understood by this property of non-commutativity. We have indicated above that the classification of disclinations in N_B is the same as in N^* , because of the similarity of the OP for rotations. We summarize the N^* classification at the end of Section 9.2, Table 1. It suffices to associate the directions λ , χ , and τ to the three directors in N_B to read this table (except of course the identification of the χ -disclinations with dislocations) as the table of the disclination lines in N_B .
- (3) $\Pi_1(\text{SmA}) \sim Z \square Z_2$. The order parameter of a SmA phase contains two parts, a nematic OP, since the director \mathbf{n} is oriented as in a nematic phase, and a 1D density modulation with the period of the layers repeat distance d_0 . The first part of the OP yields the Z_2 subgroup, $\{I, \sigma\}$, of Π_1 , i.e., the *disclinations*; the second part of the OP yields the Z subgroup, i.e., the *dislocations* (which we note additively, $0, \pm 1, \pm 2$, etc.). $\Pi_1(\text{SmA})$ is the semi direct product of Z_2 and Z . Let (p, α) , $p \in Z$, $\alpha \in Z_2$ be an element of $\Pi_1(\text{SmA})$; we have the composition law $(p, \alpha)(q, \beta) = (p + \alpha(q), \alpha\beta)$, where: $\alpha(q) = q$, if $\alpha = I$; $\alpha(q) = -q$, if $\alpha = \sigma$. The change of sign indicates that the rotations $\pm\pi$ (involved in a σ defect) reverse the translations. As alluded to above, the disclinations take special shapes in order to obey the constraint of isometry; it is well known that they gather by pairs of conjugate conics: an ellipse and an hyperbola [3,6]. Notice that this is not a topological constraint so that it can be possibly broken, at some energy expense. The *dislocations* are the usual Volterra screw, edge, or mixed dislocations, whose Burgers vector is of the form nd_0 ; their energetic properties are totally different from those of dislocations in classical crystals.

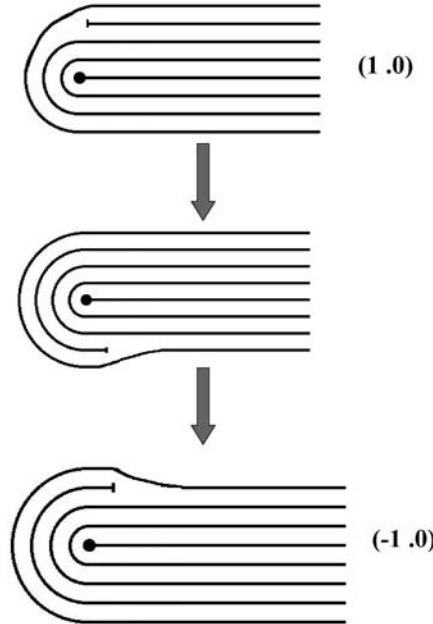


Fig. 6. An illustration of non-commutativity: circumnavigation of a dislocation $b = d_0$ about a disclination $k = 1/2$ in a layered phase. The dislocation has changed sign.

Notice that $(0, \sigma)(p, I)(0, \sigma) = (-p, I)$, and that $(0, \sigma)$ is equal to its inverse $(0, \sigma)^{-1}$. This non-commutativity is represented in Fig. 6, where is pictured a dislocation $p = 1$ which circumnavigates about a σ -disclination; it is visible that the dislocation has changed sign after a complete turn about the disclination.

- (4) $\Pi_1(\text{SmC}) \sim Z \square Z_4$. The derivation of this expression is given in ref. [28] for a full discussion of the topological classification, and in [29] for the VP classification, compared to the topological one. One sees that there are two types of defects, *dislocations*, classified by Z , and *disclinations*, classified by Z_4 (which we do note $I, \sigma, \sigma^2, \sigma^3, \sigma^4 = I$). Let (p, α) , $p \in Z$, $\alpha \in Z_4$ be an element of $\Pi_1(\text{SmC})$; the composition law is $(p, \alpha)(q, \beta) = (p + \alpha(q), \alpha\beta)$, where: $\alpha(q) = q$, if $\alpha = I, \sigma^2$; $\alpha(q) = -q$, if $\alpha = \sigma, \sigma^3$. The change of sign indicates that the rotations $\pm\pi$ (involved in the σ, σ^3 defects) reverse the translations.

There is a continuous way (a 2nd-order phase transition) to change a SmC phase into a SmA phase, just by tilting the director axis towards the normal to the layer. This is reflected in some geometrical relations between the OP spaces $V(\text{SmA})$ and $V(\text{SmC})$, and how they reproduce the relations between the defects of both phases. All the possible orientations of the director axis of the SmC phase about the normal define a circle S^1 . Therefore the OP space $V(\text{SmC})$ is obtained by attaching a circle to each point of $V(\text{SmA})$: in mathematical terms S^1 is the *fiber* of a *fiber bundle* with *base* $V(\text{SmA})$ and *bundle* $V(\text{SmC})$ [21–23]: all the orientations of the

SmC phase are indeed reached once and only once when one builds $V(\text{SmC})$ as indicated.

Consider now the set of all loops on $V(\text{SmC})$ whose homotopy class is the class of 2π disclinations about the normal to the layers, namely loops of the $(0, \sigma^2)$ homotopy class. It is clear that the fibers S^1 defined above belong to this class of homotopy. The corresponding disclinations disappear in the $\text{SmC} \rightarrow \text{SmA}$ transformation. Therefore $V(\text{SmA})$ is obtained from $V(\text{SmC})$ by identifying on $V(\text{SmC})$ all the points of each loop of a family of loops fibering $V(\text{SmC})$. How is this operation reflected on $\Pi_1(\text{SmC})$? All the elements in $\Pi_1(\text{SmC})$ which are in the conjugacy class of $(0, \sigma^2)$ or which pertain to the smallest subgroup containing this conjugacy class must disappear when $V(\text{SmC}) \rightarrow V(\text{SmA})$. This subgroup contains the elements $(0, I)$ and $(0, \sigma^2)$. Hence: $\Pi_1(\text{SmA}) \sim \Pi_1(\text{SmC})/Z_2 \sim Z \square Z_2$.

Notice that $(0, \sigma^2)$ is equal to its own inverse. Geometrically, this means that an oriented loop belonging to this class on $V(\text{SmC})$ can change orientation when each of its points has performed a closed path on $V(\text{SmC})$. Thus $V(\text{SmC})$ cannot be obtained as a direct product of $V(\text{SmA})$ by S^1 : $V(\text{SmC}) \neq V(\text{SmA}) \times S^1$ [28]. This situation is analogous to that one in which, by fiberizing a circle S^1 (the base) by a line segment L^1 (the fiber), one gets a Moebius ribbon, not a usual ribbon with two sides.

2.5. Homotopy groups for defects of different dimensionalities

Homotopy considerations can be extended to:

- (1) 0D defects (point defects)—surround the defect by a 2 sphere S^2 , or a S^2 -homotopic manifold, δ ; its image Δ in V is the representation of an element of the group $\Pi_2(V)$, the second homotopy group, which is always Abelian

$$\phi : \delta \rightarrow \Delta; \quad (7)$$

- (2) 3D defects (called *configurations* in [17]) for which

$$\phi : \psi \rightarrow \Psi \quad (8)$$

maps the full sample onto V , such that all the points at the boundary of the sample are equivalent (the OP value is constant on the boundary). Such a mapping requires therefore that the sample be first mapped continuously on a 3 sphere S^3 , or a S^3 -homotopic manifold, ψ , and does not display any singularity of the order parameter. Ψ is an element of the group $\Pi_3(V)$, the third homotopy group, always Abelian. Solitons are examples of configurations, ref. [6].

- (3) Surface defects; they are of two types, either these specific of the boundary—classified by the homotopy groups of the restriction of the OP to the boundary—or those representative of the intersection of a bulk defect with the boundary. Surface defects were first introduced in [30]. The concept of surface defects has been used

to classify defects in quasicrystals, which can be considered as 3D boundaries of 6D hypercubic crystals [31].

The calculation of the groups $\Pi_2(V)$ and $\Pi_3(V)$ are to be found in textbooks. The full results for ordered phases are in refs [17] and [32]. The calculation of $\Pi_1(V)$ is worth some comments, given hereunder, because it sheds some light on the relationship between the Volterra and the topological classifications, see [24,25].

Defects that correspond to non-trivial elements of the homotopy groups are qualified as *topologically stable* (ts). The reason of this qualification is that certain defects corresponding to trivial elements may be singular, notwithstanding their ‘topological instability’; e.g., k integer lines in nematics, due to special values of the material constants or special conditions of preparation. Conversely, certain configurations, i.e, defects showing no singular part, while ‘topologically stable’ from the point of view of the homotopy classification, might never appear, in solids, columnar and smectic phases, as emphasised by Trebin in [20]: because of integrability conditions, homotopy arguments are not adequate for these systems. By methods of differential topology it is proved that in 3D topological defects of this type are not feasible, but that there are non-singular fields in higher dimensions that cannot decay to a uniform ground state. It means, in practice, that such topologically non-feasible configurations are necessarily attended by a density of singular defects, e.g., dislocations.

2.6. Relations between the Volterra process and the topological approach

The standard method to compute the first homotopy group sheds some light on the relation between the topological and the Volterra classifications. We define, as above, $V = G/H$; H is a group of isometries of G considered as a space, and the quotient space G/H is the fundamental domain which tiles G . H is a group of (generalized) translations which bring one fundamental domain onto another, isometrically in G . In other words, G and H define together a crystal in some (usually curved) space G , whose unit cell is V . As an example, take $G = \mathbb{R}^2$, that is the Euclidean group restricted to the translations; a suitable subgroup H of \mathbb{R}^2 is the group of quantized translations $\mathbb{Z} \times \mathbb{Z}$ (also noted \mathbb{Z}^2) in a 2D crystal. The quotient $V = \mathbb{R}^2/\mathbb{Z}^2$ is the 2-torus T^2 , which can be represented as a quadrilateral with opposite faces identified, i.e., as the unit cell of a 2D crystal \mathbb{R}^2 , in which we do not consider rotations. Using the identity of opposite faces, any non trivial (i.e., non homotopic to the trivial loop) closed loop Γ in T^2 can be extended in \mathbb{R}^2 as an open path which links two equivalent points in two distant cells. This second representation is akin to the Burgers circuit representation of the Burgers vector. Observe that the classification of defects is just $H = \mathbb{Z}^2$, which is the group of the classes of paths on \mathbb{Z}^2 .

Coming back to the generic case, we see that the fundamental group $\Pi_1(V)$ of the order parameter space $V = G/H$ is H itself, as soon as any closed loop in V , except the trivial loop, can be lifted to an open path in G tiled with V . But there is no guarantee that any closed loop in V , extended to a path in G , is an open path. For this to happen, it is necessary (and sufficient) that G be simply connected, namely that its fundamental

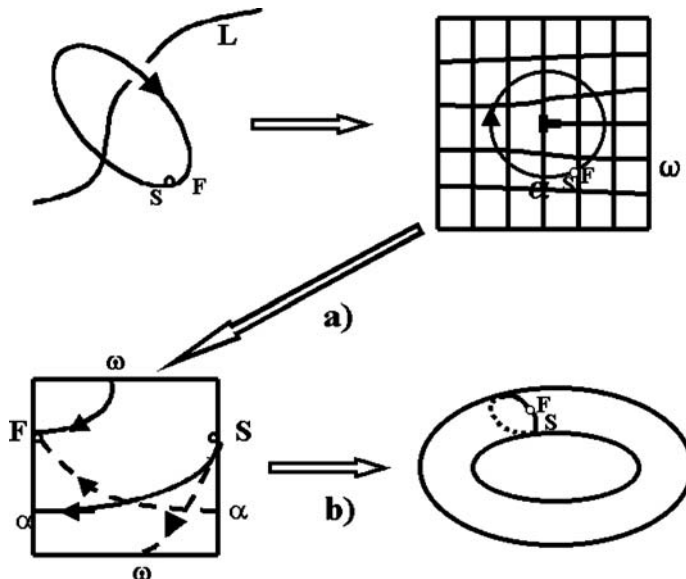


Fig. 7. Volterra and topology (see text).

group be trivial $\Pi_1(G) \sim I$. If this is not the case, it suffices to replace G by its *universal cover* \tilde{G} , which is a connected, simply connected manifold, by definition, and H by its lift \tilde{H} in \tilde{G} . Then, $\Pi_1(V) \sim \tilde{H}$. The following simple example can help intuition: take for G a circular cylinder G_C , obviously a group, and tile G_C by the same quadrilaterals as above, in a commensurate manner (p quadrilaterals close a loop about the cylinder, say). G_C is not simply connected, obviously, and H_C is the Abelian group $Z^p \times Z$. But the universal cover of G_C is $\tilde{G}_C = R^2$, because any point of G_C can be lifted to a (countable) infinity of periodic points on R^2 , in an obvious way, just by rolling the cylinder on the plane. Therefore $\Pi_1(G_C/H_C) \sim \Pi_1(\tilde{G}_C/\tilde{H}_C) \sim \tilde{H}_C \sim Z^2$. This arbitrariness on the choice of G and H can be employed to distinguish, in the classification of line singularities, defects of different nature (see [31], for a review of the present point of view and an application to quasicrystals).

3. Defects in nematic phases

Leaving solitons (and configurations) aside, there are two types of defects in the uniaxial nematic phase: line defects (disclinations) and point defects (hedgehogs and boojums). Wall defects are unstable, but might become stable in the presence of external fields. The reader is referred to textbooks on liquid crystals: of general interest: [33,34], on defects: [13], and on textures: [35]. More specialized texts are in [6,17–20,26,27,36–38].

3.1. Experimental observations

3.1.1. Flat nematic slabs; polarizing microscopy and fluorescence confocal polarizing microscopy

When a thick nematic sample is viewed under the microscope, the disclinations are seen as thin and thick threads, Fig. 5. Thin threads strongly scatter light and show up as sharp lines. These are true disclinations, along which the nematic symmetry of rotation is broken. The disclinations are topologically stable in the sense that no continuous deformation can transform them into a state with a uniform director field, $\mathbf{n}(\mathbf{r}) = \text{const}$. Thin disclinations are singular in that sense that the director, that is the ‘degeneracy parameter’ or ‘phase’ of the order parameter of the nematic phase, is not defined along the line. Thick threads are line defects only in appearance; they are not singular disclinations. The director is smoothly curved and well defined everywhere; it can be, at least in principle, transformed into a uniform state $\mathbf{n}(\mathbf{r}) = \text{const}$; obstacles might be imposed by the conditions at the walls of the sample or by other defects.

In thin nematic samples ($1\text{--}50\ \mu\text{m}$) in which the bounding plates favor \mathbf{n} to be parallel to the plates (the so-called tangential or planar alignment), the threads are perpendicular to the bounding plates. Under a polarizing microscope, the threads show up as centres with emanating dark brushes, giving rise to the so-called *Schlieren texture*, Fig. 8. The dark brushes display the areas where \mathbf{n} is either in the plane of polarization of light or in the perpendicular plane. A simple exercise in crystal optics (see, e.g., [6]) of a flat nematic slab viewed between two crossed polarizers, leads to the following dependence of the intensity of transmitted light on the angle β that the director (or its projection onto the slab’s plane if the director is tilted in the vertical plane) makes with the direction of light polarization:

$$I = I_0 \sin^2 2\beta \sin^2[(\pi h/\lambda)(n_{\text{e,eff}} - n_0)], \quad (9)$$

where I_0 is the intensity of incident light, β is the angle between the polarization direction of light at the entry point and the optical axis (which is \mathbf{n}), projected onto the plane of the slab, λ is the wavelength of light in vacuum, $n_{\text{e,eff}}$ is the effective refractive index that depends on the ordinary index n_0 , the extraordinary index n_{e} , and the director orientation in the vertical plane. Eq. (9) allows one to relate the number $|k|$ of director rotations by $\pm 2\pi$ around the defect core, to the number B of brushes. According to eq. (9), any two in-plane director orientations that differ by $\pm\pi/2$ result in the same intensity of transmitted light; therefore,

$$|k| = B/4. \quad (10)$$

Eq. (10) is valid only when the rate of the director rotation does not change sign. In some textures, especially when the centres show more than four brushes, this restriction is not satisfied and there is no simple relationship between $|k|$ and B , see [39].

The number $|k|$ is an important characteristic of a line defect. Taken with a sign that specifies the direction of rotation, k is called the *disclination strength*, and is related to the more general concept of topological charge, but does not coincide with it, as non-trivial

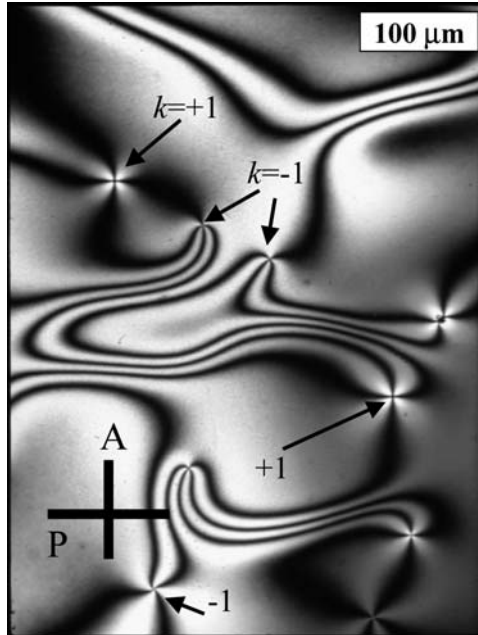


Fig. 8. Schlieren texture of a thin slab of 5CB exhibiting centres with four brushes. The director is in the plane of the sample. Crossed polarizers.

integer values of k correspond to a trivial topological charge and topologically unstable lines (escape in the 3rd dimension).

There are usually two types of centres in the Schlieren textures, Fig. 9: with two and four dark brushes. They correspond to the thin and thick threads of Fig. 5, respectively. The centres with two dark bands have a sharp (singular) core, insofar as can be seen, of sub-micrometer dimensions and correspond to the ends of singular stable disclinations. The director rotates by an angle $\pm\pi$ when one goes around such a centre. Presence of centres with two brushes signals that \mathbf{n} is parallel to the bounding plates: the in-plane $\pm\pi$ rotation brings the director into its equivalent state.

The centres with four brushes correspond to isolated point defects. The director undergoes a $\pm 2\pi$ rotation around the centre. One can observe the difference between the two-brushes and four brushes centres by gently shifting one of the bounding plates, Fig. 9. Upon separation in the plane of observation, the centres with two brushes leave a clear singular trace—a disclination—, while the centres with four brushes leave a non-singular fuzzy trace in the nematic bulk. Nevertheless, the defects at the surface represent truly topologically stable point defects, called *boojums* [18]. The main difference between the regular point-hedgehog defects and boojums is that boojums can exist only at the surface while the hedgehog cores can be located either in the bulk or at a surface [40]. In addition to the integer. Boojums can be characterized by a ‘two-dimensional’ topological charge k of the unit vector field \mathbf{t} projected by the director onto the boundary and by a three-dimensional charge N that reflects their point nature.

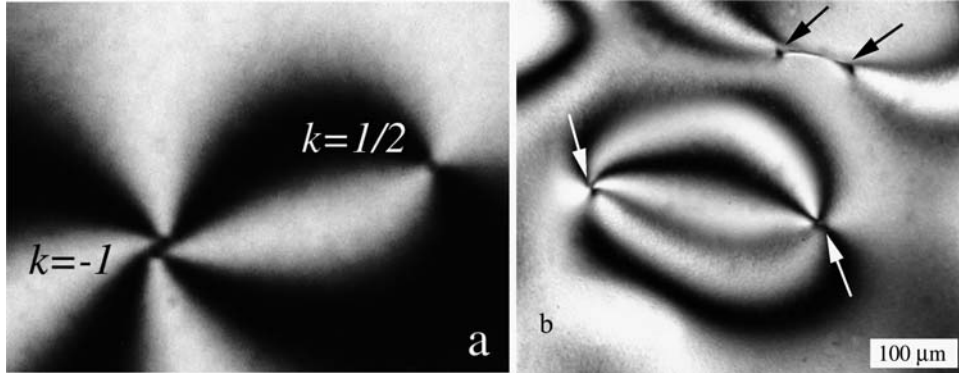


Fig. 9. A polarizing-microscope texture of a nematic slab (a) reveals two types of apparently point-like defects at the bounding plates, with two and four brushes. Shifting of the two glass plates with respect to each other (b) shows that the two are in fact very different: defects with two brushes represent the ends (black arrows) of the line defects-disclinations connecting the two glass plates and the four-brushes centres represent the surface point defects—boojums (white arrows).

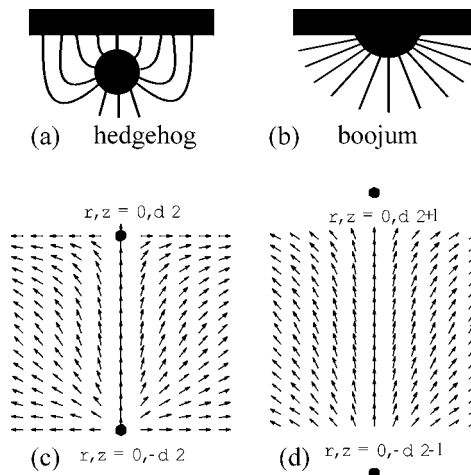


Fig. 10. Point defects—hedgehog (a) and boojums (b, c, d) at the surface of a uniaxial nematic. Parts (c, d) show a vertical cross-section of a flat nematic slab with strong (c) and weak (d) surface anchoring.

The energetical stability of boojums at plates with different strengths of surface alignment is discussed in [41]. Fig. 10 demonstrates the director configurations for hedgehogs in the bulk (Fig. 10(a)) and boojums at the tangentially anchored surface of a semi-infinite sample (Fig. 10(b)). Depending on the strength of surface anchoring, the core of the boojum is located either “exactly” at the boundary, Fig. 10(c), or at some distance from it, Fig. 10(d), outside the LC, as first described in [38]. This distance is roughly equal to the *anchoring extrapolation length*, defined as $l = K / W_a$, where K is the representative Frank elastic constant and W_a is the anchoring coefficient, measuring the work (per unit

area) needed to deviate the director from the orientation imposed by the anisotropy of the molecular interactions at the interface.

As follows from the discussion above, polarizing microscopy is a somewhat limited instrument as it provides only a 2D image of a 3D sample. The recently developed Fluorescence Confocal Polarizing Microscopy (FCPM) allows one to visualize the whole 3D director structure, see [42,43] and Appendix on FCPM.

3.1.2. Nematic droplets

When left intact, textures with defects in flat samples relax into a more or less uniform state. Disclinations with positive and negative k find each other and annihilate. There are, however, situations when the equilibrium state *requires* topological defects. Nematic droplets, Fig. 11, suspended in an isotropic matrix such as glycerin, water, polymer, etc. [44–46], and inverted systems, such as water droplets in a nematic matrix [47] are the most evident examples.

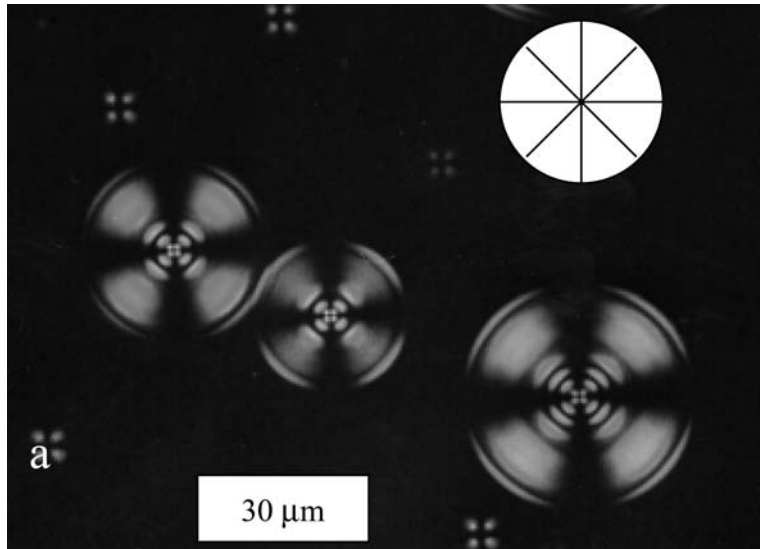
Consider a spherical nematic droplet of a radius R and the balance of the surface anchoring energy $\sim W_a R^2$, and the elastic energy $\sim KR$; K is some averaged Frank constant. Small droplets with $R \ll K/W_a$ avoid spatial variations of \mathbf{n} at the expense of violated boundary conditions. In contrast, large droplets, $R \gg K/W_a$, satisfy boundary conditions by aligning \mathbf{n} along the preferred direction(s) at the surface. Since the surface is a sphere, the result is a distorted director field in the bulk, for example, a radial hedgehog when the surface orientation is normal, Fig. 11(a), or a pair of boojums at the poles, when the surface orientation is tangential, Fig. 11(b). The characteristic radius R is macroscopic (microns), since $K \sim 10^{-11} \text{ N}$ and $W_a \sim 10^{-5}\text{--}10^{-6} \text{ J/m}^2$.

Note that topological defects such as hedgehogs and boojums in large systems with $R \gg K/W_a$, must satisfy restrictions on their total topological charge. These restrictions have their roots in the Poincaré and Gauss theorems of differential geometry and write as:

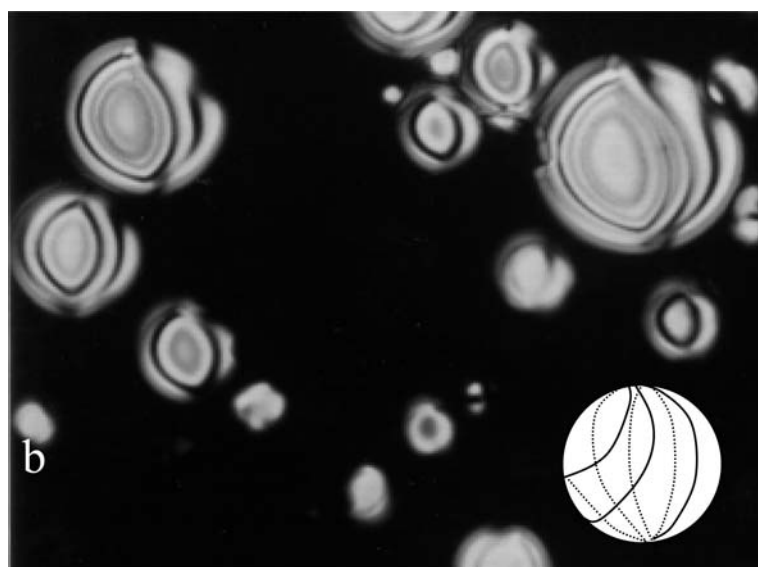
$$\sum_j k_j = E \quad \text{and} \quad \sum_j N_j = E/2. \quad (11)$$

Here E is the Euler characteristic of the boundary. For a sphere $E = 2$ and for a torus $E = 0$. N is the degree of mapping of the surface surrounding the core of the point defect in real space on the OP [6]. Fig. 11(a) illustrates an example with $N = 2/2 = 1$ while Fig. 11(b) is with $k_1 = k_2 = 1$.

The conservation laws given by eq. (11) may influence the late stages of the first-order isotropic-to-nematic phase transition that occurs through nucleation of nematic droplets. The droplets grow by adding molecules from the surrounding isotropic matrix and by coalescence. At early stages, the droplets are small and thus practically uniform; they might form defects upon coalescence according to the Zurek–Kibble mechanism (see Section 3.3). However, as soon as the droplets grow beyond the size $\sim K/W_a$, a more powerful source of defects comes into play, namely, surface anchoring and the topological constraints considered above. In experiments, the growing nematic droplets are clearly seen containing stable topological defects caused by the surface anchoring.



(a)



(b)

Fig. 11. Because of the difference in surface anchoring conditions, nematic droplets freely suspended in glycerin doped with a surfactant lecithin (a) and in pure glycerin (b) exhibit different director structures, either a point defect—hedgehog in the centre of the droplet (a) or a pair of surface point defects—boojums at the poles (b). The director is normal to the interface in (a) and tangential to the interface in (b). Note that the droplets with tangential anchoring (b) have a twisted director structure and are thus optically active despite the fact that the nematic is not chiral; the effect is caused by the smallness of the twist elastic constant as compared to the bend and splay elastic constants.

3.2. Elastic theory of defects

The relative stability of stable disclinations depends on the Frank elastic constants of splay (K_{11}), twist (K_{22}), bend (K_{33}) and saddle-splay (K_{24}) in the Frank–Oseen elastic free energy density functional;

$$f = 1/2K_{11}(\operatorname{div} \mathbf{n})^2 + 1/2K_{22}(\mathbf{n} \cdot \operatorname{curl} \mathbf{n})^2 + 1/2K_{33}(\mathbf{n} \times \operatorname{curl} \mathbf{n})^2 - K_{24}\operatorname{div}(\mathbf{n} \operatorname{div} \mathbf{n} + \mathbf{n} \times \operatorname{curl} \mathbf{n}). \quad (12)$$

The K_{24} term, being a divergence, integrates to a boundary term, and is most often lumped into the anchoring energy.

Frank [4] considered ‘planar’ disclinations with \mathbf{n} perpendicular to the line. In this case, the K_{24} term in the line’s energy vanishes. In the approximation $K_{11} = K_{22} = K_{33} = K$, the equilibrium director configuration around the line writes as

$$\mathbf{n} = \{\cos[k\varphi + c], \sin[k\varphi + c], 0\}, \quad (13)$$

where $\varphi = \arctan(y/x)$, x and y are Cartesian coordinates normal to the line, c is a constant; the other constant k is the familiar integer or semi-integer number, the *strength* of the disclination, that shows the number of rotations of the director around the line.

The energy per unit length (line tension) of a planar disclination is

$$F_{1l} = \pi K k^2 \ln(L/r_C) + F_C, \quad (14)$$

where L is the characteristic size of the system, r_C and F_C are respectively the radius and the energy of the disclination core, a region in which the distortions are too strong to be described by a phenomenological theory. Non-planar lines have been considered in [48]. We leave aside a discussion of the core structures. We refer the reader to refs [49,50] for theoretical investigations of the OP variation in the $k = 1/2$ disclination core in small molecule Ns, to [51] for observations of the $k = -1/2$ and $k = +1/2$ wedge line cores in polymeric Ns—the cores of the $k = -1/2$ and $k = +1/2$ lines are considerably different, yielding different mobilities—and to [52] for Monte-Carlo simulations of $k = -1/2$ wedge lines. The theoretical approaches emphasize the existence of a biaxial component of the OP in the core.

The Frank theory does not distinguish lines of integer and semi-integer strength, which are both singular in this theory, except for the fact that the lines with $|k| = 1$ tend to split into pairs of lines $|k| = 1/2$, which reduces the energy, according to eq. (14). The lines of integer $|k|$, as already discussed, are fundamentally unstable. Imagine a circular cylinder with normal orientation of \mathbf{n} at the boundaries, Fig. 4. The planar disclination would have a radial-like director field normal to the axis of the cylinder, $k = 1$. However, the director can be reoriented along the axis, Fig. 4(a). This ‘escape in the third dimension’, is energetically favorable, since the energy of the escaped configuration is only $3\pi K$ [8,9]. When opposite directions of the ‘escape’ meet, a point defect-hedgehog is formed, Fig. 4(b).

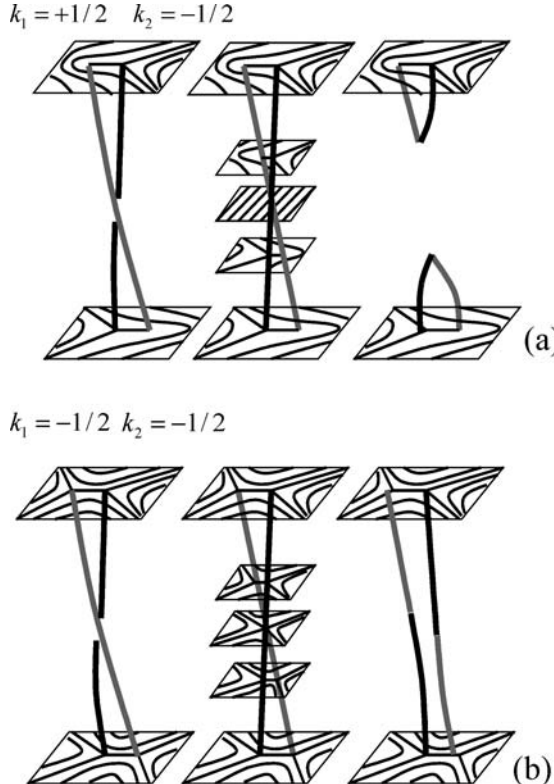


Fig. 12. (a) Two disclinations of the opposite sign with ends fixed at two surfaces recombine and disconnect in the horizontal plane, shortening the total length of the defects pair. (b) Two disclinations of the same sign with ends fixed at two surfaces recombine and disconnect in the vertical plane, leaving the total length practically the same.

In a uniaxial nematic, any two disclinations can cross each other. They can exchange ends (reconnection), or not, depending on the original geometry, as documented experimentally [53], see also Fig. 12. In N_B , some pairs of disclinations produce a third line when passing through each other, as already discussed in Section 2.

Unlike point defects such as vacancies in solids, topological point defects in nematics cause disturbances over the whole volume. The curvature energy of the point defect is proportional to the size R of the system. For instance,

$$F_{\text{rh}} = 8\pi R(K_{11} - K_{24}) + F_{\text{cr}} \quad \text{and} \quad F_{\text{hh}} = 8\pi R(K_{11}/5 + 2K_{33}/15 + K_{24}/3) + F_{\text{ch}},$$

for the radial hedgehog with $\mathbf{n} = (x, y, z)/(x^2 + y^2 + z^2)^{1/2}$, and the hyperbolic hedgehog with $\mathbf{n} = (-x, -y, z)/(x^2 + y^2 + z^2)^{1/2}$, respectively. The point defects might spread into topologically equivalent defects—disclination loops—, when favored by the combination of elastic constants [54,55].

3.3. Defects in phase transitions

Topological defects might form during the symmetry-breaking phase transitions such as the isotropic-to-nematic phase transition. Topological stability of defects might leave a long-lasting impact on the dynamics of structural relaxation during the phase transition. Originally, defect network density and its dynamics have been considered by Kibble [56] for phase transitions during the evolution of the Early Universe; it was assumed that the cosmological analogs of disclinations—strings—might have served as seed inhomogeneities in the Universe mass density that gave rise to galaxies. Although the data on the cosmic microwave background anisotropy do not support the original hypothesis that the strings alone are responsible for the observed significant density variations, the strings are still considered to be an important part of Universe evolution and of such effects as generation of magnetic fields, high-energy cosmic rays, or baryogenesis, see [57]. As the direct experiments on earlier Universes are impossible, the activity in the field quickly shifted towards the condensed matter analogs, especially after the Zurek articles [58,59] on defects during phase transitions in superfluids. The first ‘cosmology in the laboratory’ experiments were conducted for nematic liquid crystals [60–62].

Defects might appear during a first- or a second-order phase transition. It is easier to explain the mechanism by using the first-order transition as an example. The transition occurs by nucleation of droplets (bubbles) of a less symmetric phase, located at random positions in the bulk. Suppose for simplicity that the low-symmetry phase has a scalar OP with the degeneracy parameter (phase) $0 \leq \varphi < 2\pi$ and that consequently the OP space is a circle S^1 . A relevant liquid crystal model would be a transition from a SmA to SmC, or an electric-field-induced quench of a nematic liquid crystal, if in both cases the molecular orientation is quenched from vertical to ‘tilted’. To the best of our knowledge, neither of these two possibilities has been studied. In the first-order transition, each droplet is surrounded by a ‘melted’ material with a zero value of the order parameter and thus chooses the particular value of phase φ independently of other droplets. The droplets grow and eventually merge. When two droplets with φ^1 and φ^2 coalesce, the phase would change in space smoothly between the two values, presumably along the shortest path connecting the two values φ^1 and φ^2 . For example, if $\varphi^1 = 0$ and $\varphi^2 = \pi/2$, the phase would change in the range $0 \leq \varphi \leq \pi/2$ rather than in the range $\pi/2 \leq \varphi \leq 2\pi$. This *geodesic rule* is justified by the idea that the system will tend to minimize the gradient elastic energy (such as the Frank energy in the nematic case). When three droplets meet, there is a chance that the values of φ^1 , φ^2 , and φ^3 , are such that the junction traps a defect for which the total phase change is $\pm 2\pi$. The domain structure in the system of merging droplets sketched very roughly in Fig. 13(a)) illustrates the appearance of a $+2\pi$ defect (circular core) and -2π (square core). The probability of the defect creation at the junction of three droplets can be easily shown to be $1/4$ (provided the geodesic rule is valid and the three phases are independent). If ξ is the distance between the nuclei, in a 3D unit volume the total length of the line defects is about $L \sim 1/\xi^2$.

The Zurek–Kibble mechanism: how do the defects generate during a second-order phase transition? In contrast to a first-order transition with nucleating ‘bubbles’, the standard thermodynamic view is that the new phase appears simultaneously in the whole volume. It is clear that to keep the state uniform everywhere, the system must be capable of com-

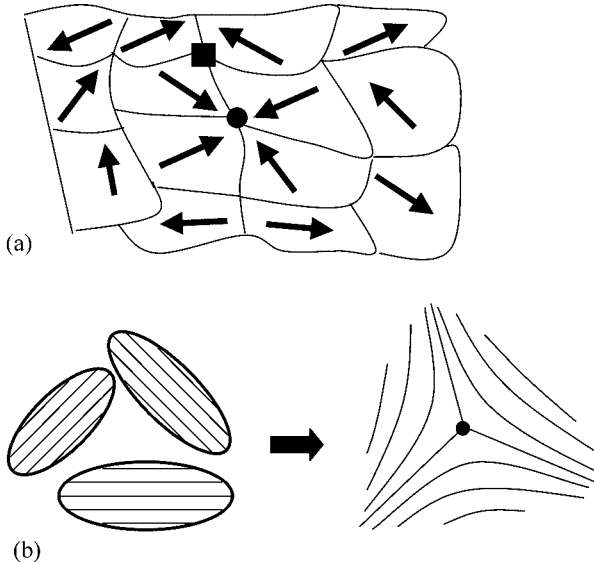


Fig. 13. Kibble mechanism for the system with the order parameter space S^1 (a) and for the formation of defects in a nematic liquid crystal (b).

municating the information about its state between all its points. However, the speed with which the relevant information can travel (it might be the speed of light in quantum field theory or the speed of second sound in condensed matter) is always finite. A pair of sufficiently separated regions might not have time to adjust to each other if the phase transition occurs over a finite period of time, which is the case of all laboratory or natural systems. This causal argument is a fundamental mechanism of defect appearance during the phase transition, as was first observed by Kibble [56].

Zurek [59] has applied the causal principle to the second-order phase transitions in condensed matter physics, by observing that the time-dependent correlation length $\xi(t)$ would evolve differently at the beginning of the quench and at some time after the quench started. Let us assume that the temperature changes linearly with time, i.e., that the temperature and time are related through $dT/dt = -T_c/\tau_Q$, where τ_Q is the ‘quenching time’ (imposed by the experimentalist or external factors) and T_c is the critical temperature. For an infinitely-slow transition, one can introduce an ‘equilibrium’ correlation length $\xi_{\text{eq}}(t)$ of the order parameter field that diverges at $T = T_c$ (i.e., at $t = 0$), as

$$\xi_{\text{eq}}(t) = \xi_{\text{eq}}[T(t)] = \xi_0 |t/\tau_Q|^{-\nu}, \quad (15)$$

where ξ_0 is some material constant and $\nu = 1/2$ if we use the Ginzburg–Landau model. If $c(t) = \xi_{\text{eq}}(t)/\tau(t)$ is the maximum speed with which the order parameter can change, then the relaxation time of the order parameter depends on the time of the experiment as

$$\tau(t) = \tau_0 |t/\tau_Q|^{-1}, \quad (16)$$

where τ_0 is another material constant. The *true non-equilibrium* correlation length $\xi(t)$ might have not enough time to adjust to the new temperature during the quench if the quench time is finite and smaller than the time $\tau(t)$ required to maintain the equilibrium value $\xi_{\text{eq}}(t)$. The quench is ‘instantaneous’ for the evolving order parameter near the critical temperature. The non-equilibrium correlation length then becomes approximately constant (frozen); this freeze-out length ξ_{fr} defines the typical size of the domains that have different ‘frozen’ values of the order parameter phase, as in the example with nucleating bubbles above. If we denote this causality-constrained freeze-out time t_{fr} , then the condition $\tau(t_{\text{fr}}) = t_{\text{fr}}$ together with eq. (15) in which $v = 1/2$ and eq. (16) leads to the conclusion that $t_{\text{fr}} = (\tau_0 \tau_Q)^{1/2}$ and $\xi_{\text{fr}} = \xi_0 (\tau_Q / \tau_0)^{1/4}$. Assuming that the length of defects per unit volume is $\sim 1/\xi_{\text{fr}}^2$, one expects that the number of defects increases as the quench time τ_Q decreases: $n \sim 1/\xi_0^2 (\tau_0 / \tau_Q)^{1/2}$. Currently, many experimental groups are testing the scenario using different condensed-matter systems, see refs [57,62] for the latest updates.

The causal generation of defects during phase transitions is often called the Zurek–Kibble mechanism. However, one should bear in mind that the Zurek scenario is applied only to second order transitions; for more insights into the relevant nomenclature and the physics of dynamics of phase transitions, see [57,63].

Similar arguments apply to the formation of disclinations in the first-order isotropic–nematic transition. In fact, the first experimental verification of the Kibble mechanism has been performed for this transition, when it is caused by a quick quench (by rapid pressure jumps) [61]. It was observed that the predominant role in the coarsening dynamics of the system after the quench belongs to singular disclinations. After the quench, the density of disclinations was determined to decrease with time as $\sim 1/t$. Such a behavior was indeed expected [64,65] and can be qualitatively explained by the fact that the characteristic size of the tangle of defects grows with time as $\xi(t) \sim t^{1/2}$; therefore, $L \sim 1/\xi^2 \sim 1/t$. Note that in 3D nematics, one might expect that the Kibble mechanism might be applied not only to the line defects but to the point defects—hedgehogs. However, no point defects (hedgehogs) were observed in [65] until some significant time (a few seconds) after the quench, when the network of line defects coarsens appreciably; besides, the hedgehogs disappear again faster than a naïve estimate would predict. This apparent contradiction has been explained [66] on the basis of the observation that one needs an arrangement of twelve (rather than three as in the case of line defects) uncorrelated adjacent droplets to produce a point defect in a 3D nematic. The density of hedgehogs was calculated to be approximately $n \sim 10^{-8}/\xi^3$, i.e. much smaller than the naïve expectation $n \sim 1/\xi^3$.

The cited work on nematics clearly demonstrated that defects did appear during the phase transition and relax with time; however, they did not answer the question how the defects formed. This issue was addressed in an experiment in which the liquid crystal was formed by cooling down a drop of an isotropic melt [60]. The formation of nematic “bubble” droplets that grow in size and coalesce, forming yet larger droplets, was clearly observed. The experimentally observed individual droplets have a diameter increasing from approximately $1 \mu\text{m}$ (which is roughly the limit of polarizing-microscopy resolution) to at least about $50 \mu\text{m}$ before a continuous nematic layer is formed. By then measuring the total length of disclinations formed in the continuous slab and dividing it by the number of nematic droplets, it was found that there is about 0.6 disclination per nematic droplet.

This number is in agreement with calculations based on the Kibble mechanism of defect formation.

However, the analysis does not exclude an alternative explanation of the experiment, in which the reason for defect appearance is of a completely different nature, related to surface anchoring at the bubble surface. Recall that the nematic droplets have been grown to the macroscopic size of tens of microns before the continuous nematic film formed. For the isotropic-nematic interface, the surface anchoring coefficient is of the order of $W_a \sim 10^{-6}$ J/m² [67]. Therefore, for the droplets of size $R_C = K/W_a \sim 1 \mu\text{m}$ and larger, the director will be distorted to satisfy the boundary conditions at the expense of director distortions in the bulk, as in the case already illustrated in Fig. 11. As the angle at the nematic–isotropic interface for the materials studied is about 64 degree [67], the boundary conditions might lead to a number of different defect configurations, with hedgehogs, boojums and, importantly, disclination loops, as described in [44] and as illustrated by Fig. 13.19 in [6]. When the disclination loops are present, the number of disclinations per droplet should be close to 1, as measured in [60], as each droplet bears one loop.

It is of interest to compare the critical anchoring size $R_C = K/W_a \cong 1 \mu\text{m}$ to the critical size of the nematic nuclei. According to a well-known nucleation mechanism, a viable growing nucleus must be larger than some critical size r_C defined by the balance of the (positive) interfacial energy and the (negative) bulk energy associated with its formation: $\Delta F \sim 4\pi r^2 \sigma + (4\pi/3)r^3 f$, where σ is the interfacial energy coefficient, and $f \sim \Delta H \Delta T / T_{NI} < 0$ is the gain in the free energy density when the temperature drops across the phase transition line by $\Delta T < 0$, ΔH is the latent heat of the phase transition, and T_{NI} is the temperature of the transition. Minimization yields $r_C = -2\sigma/f$; with typical experimental data, namely, $\sigma \sim 10^{-5}$ J/m² for the 5CB nematic–isotropic interface [67], $\Delta H \sim 10^{-5}$ J/m³ [68] and $\Delta T/T_{NI} \cong 1/300$, one finds that $r_C \cong 0.1 \mu\text{m}$, only one order of magnitude smaller than $R_C = K/W \cong 1 \mu\text{m}$. Therefore, although at the beginning of nucleation the nematic droplets might remain defect-free, their growth above R_C might produce defects because of both the Kibble and the anchoring mechanisms. Detailed experimental studies of these processes are not performed yet.

3.4. Some rheological properties

3.4.1. Isolated disclination at a low shear rate

Off-core: the low shear rate regime is characterized by the condition $De \ll 1$, where $De = \gamma \tau_r$ is the Deborah number; γ is the shear rate, τ_r the molecular relaxation time. In this range of values the OP amplitude—see ([6], Chapt. 3) for definition—is not perturbed by the flow, the phase transitions are not modified, and the hydrodynamical behavior can be discussed in the frame of the linear Leslie–Ericksen equations, or in the frame of the Harvard model [69,70]. Typically, $\tau_r \cong 10^{-8}$ s for any Small Molecule LC (SMLC) N phase so that these linear theories are well adapted for usual shear rates. A further simplification comes from the fact that the characteristic time for the propagation of linear momentum on a distance d , $\tau_{lin} = \rho d^2/\eta$ (η a viscosity, ρ the mass density) is largely inferior to the characteristic time for the propagation of angular momentum on the same distance, $\tau_{ang} = \eta d^2/K$ (K a Frank constant). Hence it is the director orientation that rules

the dynamical process, and backflow is often negligible. These simplifying assumptions are debatable for the disclination core regions.

The analysis of the mobility of an isolated disclination has been first carried out by Imura et al. [71], and refined in ref. [72]. The relevant equation, backflow ignored and outside the core, for a planar twist disclination of strength k , located along the z -direction, moving with velocity v in the x -direction is:

$$K(\partial^2\phi/\partial x^2 + \partial^2\phi/\partial y^2) - \gamma_1 \partial\phi/\partial t = 2\pi k\delta(x - vt)\delta(y). \quad (17)$$

γ_1 is the twist viscosity coefficient, ϕ is an angle with a fixed direction in the xy -plane. The dissipated power, calculated outside a core region of size $r_1 = K/\gamma_1 v$, is, per unit length of line, $\Sigma_1 = f_{\text{drag}}v$, with f_{drag} , the force of friction exerted on the line,

$$f_{\text{drag}} = \pi\gamma_1 k^2 v \ln(3.6/Er). \quad (18)$$

$Er = \eta vd/K$, the so-called *Ericksen number*, is the natural substitute to the Reynolds number $Rer = \rho vd/\eta$, when backflow is negligible.

Two parallel wedge disclinations of opposite strengths, at a distance L , attract under a force of interaction:

$$f_{\text{int}} = -2\pi Kk^2/L. \quad (19)$$

Balancing f_{drag} and f_{int} yields:

$$L^2 = \text{const.} K/\gamma_1(t_{\text{end}} - t). \quad (20)$$

This expression has been reasonably well verified in MBBA [N -(*p*-methoxybenzilidene)-*p'*-butylaniline], see [73].

Observe that f_{int} , eq. (19), appears as the analogue of a Peach and Koehler force. Es-helby [74] has noticed that f_{int} is a real force, not a fictional one as in solids. It has therefore to be balanced in a N phase, inasmuch as the disclinations see no other friction force than the drag force above, which is vanishing at rest.

We refer the reader to refs [75,76] for the mobility of *point* disclinations in N; see also the discussion of Section 3.3 and [77].

Core: as already stated in the introduction, the distortion carried by a twist disclination, and more generally a curved disclination, can be represented by a density of dislocations. Conjointly, the motion of a disclination is accompanied by a process of emission (or absorption) of dislocations. In a N phase, the viscous dispersion of the dislocation densities relaxes the elastic curvature energy and provides precisely the mechanism by which the rotation vector Ω follows the line to a new position, Fig. 14. Thus, the movement of a disclination is generically accompanied by backflow, which is important in the core region, creating a wake of approximate size $r_2 = 2\gamma_2/\rho v$, γ_2 being the viscosity for fluid motion [78]. Also, the core might show a longitudinal instability [79]. One gets for the in-core dissipation power $\Sigma_2 \approx \gamma_2 k^2 v^2$, i.e., the same order of magnitude as Σ_1 , the off-core contribution. Notice that $r_2/r_1 > 1$: the dislocation core mechanism affects quite a

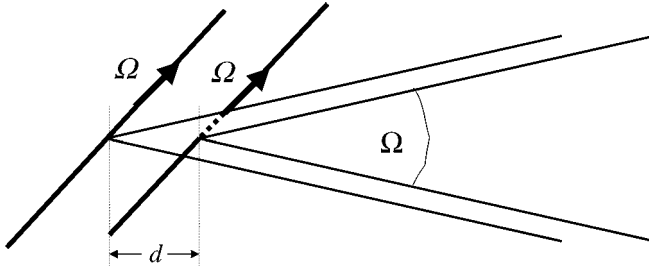


Fig. 14. Displacement of a wedge disclination parallel to itself by a distance d , equivalent to the introduction of a dislocation of Burgers vector $b = 2 \sin(\Omega/2)(1/\Omega)\Omega \times d$, if Ω follows the line.

large region. Furthermore, one expects that the core is much distorted, and in fact enlarged, with respect to its configuration at rest; this has been experimentally observed [80], and theoretically confirmed [81] for disclinations in N^* .

3.4.2. Instabilities and defect textures

The nature of instabilities and disclination sets (defect textures) in N^* 's depends on the sign of some combination of viscosity coefficients [6,34], which leads to the partition of N^* 's into *flow aligning* N^* s and *tumbling* N^* s. Most SMLC nematics are flow aligning, but with a few exceptions [82], whereas practically all LC polymer (LCP) nematics are tumbling.

Instabilities: nematic phases display a number of remarkable electrohydrodynamical instabilities, resulting in regular patterns and transitions between different patterns. These patterns are often attended by the appearance of defects. There is a vast literature on the subject: see for instance refs [83,84].

Flow aligning: at sufficiently large Er , SMLC N^* s align along the flow, which proceeds at constant orientation. Below this regime, at a rather low shear rate ($\gamma \cong 1 \text{ s}^{-1}$, say), loops of thins and thicks nucleate close to the boundaries (where the usual no-slip condition is obeyed, hence a local larger distortion) and elongate in the flow, where they tumble at some higher shear rate ($\gamma \cong 10 \text{ s}^{-1}$, say). They soon cover the entire field, but relax quickly to point disclinations and a few defects possibly attached to the boundaries, after ceasing of the shear. This regime is described in [85,86].

Tumbling: roll-cell instabilities are well documented in most LCPs, at small Er [87]. At higher Er numerous disclinations appear between the roll-cells; they multiply with increasing Er , leading eventually to *director turbulence* [88,89].

3.4.3. Large Deborah numbers

The molecular relaxation time τ_r is considerably longer in LCP nematics than in SMLCs. For instance $\tau_r \cong 0.1 \text{ s}$ in a 13 wt% solution of PBDG [poly-(benzyl (right) glutamate] in water, molecular weight 298 000. In these conditions, even at a very small shear rate De is large, and the Leslie–Ericksen approach invalid. One has to use Doi's equations [90], which take into account the OP change under shear.

The Doi regime corresponds approximately to $De > 0.1$. It is characterized by a sequence of transitions independent of the sample thickness, most similar for thermotropic

copolyesters and biopolymers in solution. The observed defect textures observed by different authors [91–95], as the shear rate increases, seem to correlate well with the sequence of viscoelastic regimes (defined experimentally by the bulk viscosity and the first normal stress difference). One first observes a *worm texture* (a polydomain texture at a μm scale with a multiplication of defects), then an *ordered texture*, which is birefringent and becomes uniform for the highest shear rates. For details see [93,94].

4. Defects with isometric properties in smectic phases

4.1. The isolated focal conic domain

G. Friedel's investigations [12] of liquid crystals are a milestone in the history of the physics of defects. He was conscious from the start of the full attributes of the modern concept of defect, namely its geometrical and topological relationship with the symmetry of the medium. A striking result of his approach is the discovery of: (a) the molecular structure of nematics, which he inferred from the light microscopy observation of thread-like defects (disclinations, to-day), (b) the lamellar structure of SmA's, which he inferred from the light microscopy observation of large-scale defects in the shape of conjugate pairs of conics. He was not aware of the existence of dislocations. This section and the next one are devoted to the advances in smectic defects (FCD's, dislocations) in the last 20 years.

A *focal conic domain* (FCD) is the region in space that is relating to a given pair of conjugate conics present as singularities in the sample. As already indicated, the SmAs large-scale defect geometry is dominated by the fact that the preferred elastic distortions are such that curved layers keep parallel at a distance equal to the equilibrium repeat distance d_0 . Instead of the material layers, let us consider their mid-surfaces L_i . The L_i 's being parallel, their normals are straight lines [96,97]. An elementary result is that parallel surfaces have the same centres of curvature C_1 and C_2 at all their intersections μ with the same normal: the principal radii of curvature are the signed lengths μC_1 and μC_2 ; $\sigma_1 = 1/\mu C_1$, $\sigma_2 = 1/\mu C_2$ are the principal curvatures at μ . The centres of curvature C_1 and C_2 describe two surfaces that are the envelopes of the normals, the focal surfaces F_1 and F_2 of the set of parallel surfaces L_i . At the contact of a layer L_i with the focal surfaces, one of the radii of curvature vanishes (the curvature is infinite); henceforth the focal surfaces are the sets of singular points of the geometry of parallel layers, Fig. 15. This situation is reminiscent of the propagation of light rays in an isotropic medium of constant index of refraction, in the approximation of geometrical optics: the light rays are the analogs of the normals to the layers, the surfaces of equal phase the analogs of the layers, and the caustics—where the light intensity diverges—the analogs of the focal surfaces—where the free energy density diverges. Details can be found in [6].

In order to minimize the total energy, the focal surfaces, which are generically 2D defects, degenerate into focal lines (1D). It can be shown [96,97] that these lines are *necessarily* a pair of *conjugate conics*, i.e., an ellipse E and one of the branches of an hyperbola H , located in two mutually orthogonal planes, such that the foci of the ellipse (resp. the hyperbola) are at the apices of the hyperbola (resp. the ellipse). The layers take the shape

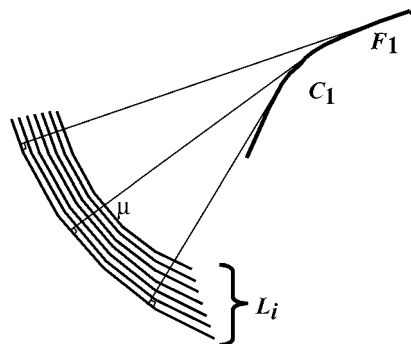


Fig. 15. Geometrical characteristics of a set of parallel surfaces. A 1D section of only one of the focal surfaces is represented (see text).

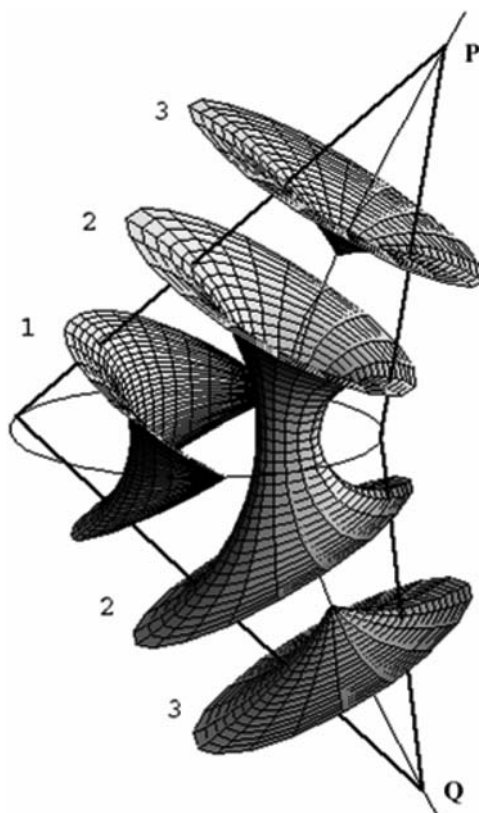


Fig. 16. A complete focal conic domain is the region bounded by the two conic surfaces of apices P and Q and merging on the ellipse. A few Dupin cyclides are represented. The locations of P and Q are arbitrary. The largest possible complete domain, for a given ellipse, is when $P, Q \rightarrow \infty$. The FCD then consists of two circular cylinders both limited by the ellipse.

of surfaces called *Dupin cyclides*. In the simple case when the ellipse is degenerate to a circle—the hyperbola is then a straight line orthogonal to the circle and passing through its centre—the Dupin cyclides are parallel nested tori. A complete torus displays two kinds of regions, one of negative Gaussian curvature $\sigma_1\sigma_2 < 0$ (this is the inner part of the torus; the tangent plane at any point in such a region intersects the torus), one of positive Gaussian curvature $\sigma_1\sigma_2 > 0$ (this is the outer part of the torus; a tangent plane, at any point in such a region, is entirely on one side of the torus). These two regions merge on the circles that define the upper and the lower tangent planes. The same division into *two* regions of opposite Gaussian curvatures is true for generic types of parallel Dupin cyclides. This distinction is physically relevant—it is observed that in a given material, one type of region is predominant over the other. In fact, all thermotropic smectics, as far as we know, exhibit FCD's with *negative Gaussian curvature* only, called *of the first kind*, FCD-I. Lyotropic smectics (L_α phases) often show *spherolites*, i.e., nested spherical sets of layers, that are special cases of the geometry with *positive Gaussian curvature*, FCD's of the second kind, FCD-II [98]. We shall restrict ourselves to FCD-I's. Fig. 16 represents a *complete* FCD-I, i.e., the largest possible set of layers L_i of negative Gaussian curvature ascribed to a generic pair of conjugate conics.

4.2. Energy of an isolated FCD-I

The curvature energy of the FCD-I is defined as the integral over the volume of the energy density f associated with the mean and Gaussian layer curvatures:

$$f = 1/2K(\sigma_1 + \sigma_2)^2 + \bar{K}\sigma_1\sigma_2; \quad (21)$$

K and \bar{K} are respectively the splay and the saddle-splay elastic constants. The strain energy (B term) is not included. K governs the mean curvature $\sigma_1 + \sigma_2$ and is a usual positive elastic constant, which measures the energy fluctuation from the ground state $\sigma_1 = \sigma_2 = 0$. On the other hand, \bar{K} can be negative, because the Gaussian curvature is a very special kind of deformation. Let \mathbf{n} be the normal to the layers; it can be shown [99] that

$$\sigma_1\sigma_2 = 1/2 \operatorname{div}(\mathbf{n} \operatorname{div} \mathbf{n} + \mathbf{n} \times \operatorname{curl} \mathbf{n}). \quad (22)$$

This is a divergence term, so that $\bar{K} \iiint \sigma_1\sigma_2$ can be integrated to a surface term by using Gauss theorem. Observe the similarity with eq. (12), with $\bar{K} = -2K_{24}$; but notice that the interpretation in terms of Gaussian curvature requires the existence of surfaces orthogonal to the director field, which is true if and only if $\mathbf{n} \times \operatorname{curl} \mathbf{n} = 0$. In general, terms of that kind are not taken into account, because they play no role in the derivation of the Euler-Lagrange equations of the problem, but it would be most erroneous to do so in the case of lamellar phases, because the defects of a lamellar phase can take various *topologies* that change the nature of the boundary conditions. Let us be more explicit.

It is most natural to split the integration of $\iiint \sigma_1\sigma_2$ into a 2D integral on the layers, and a 1D integral along their normals, by choosing suitable local coordinates. The consideration of the 2D integral is rewarding. The integral $\iint \sigma_1\sigma_2$ over a *closed* manifold is a constant

($\iint \sigma_1 \sigma_2 = 2\pi E$); E is the Euler characteristic of the manifold, e.g., $E = 2$ for a sphere S^2 , $E = 0$ for a torus T^2 [96]. The extension to *open* manifolds is the Gauss–Bonnet theorem:

$$\iint \sigma_1 \sigma_2 + \int 1/\rho_g = 2\pi E, \quad (23)$$

the first integral is taken over an element of area and the second integral is taken along the boundary of this area, ρ_g being the geodesic curvature along the boundary. Important consequences can be drawn from this analysis, (a) the integral on a closed manifold does not depend on the precise shape of the manifold, but on its topology; therefore it does not depend on the fluctuations and distortions of S^2 or T^2 , or of an infinite planar layer; (b) the integral over a half-torus, either $\sigma_1 \sigma_2 > 0$ or < 0 , is a constant ($E = +2$ or $E = -2$). It is then apparent that the energy of a deformed Sm phase depends critically on the sign of the saddle-splay modulus \bar{K} .

The *topological* contributions and the *curvature elastic* contributions separate when rewriting the free energy as follows:

$$f = 1/2K(\sigma_1 - \sigma_2)^2 + \Lambda \sigma_1 \sigma_2. \quad (24)$$

In this expression $\Lambda = \bar{K} + 2K$. In fact, both terms K and \bar{K} contribute to the topology, since they appear in $f' = \Lambda \sigma_1 \sigma_2$. There is no topology (i.e., no contribution that reduces to a surface term) in the $f = 1/2K(\sigma_1 - \sigma_2)^2$ term.

The summation of the f' -term over the volume, $W' = \iiint f'$, most conveniently done by summing over the layers and adding all the layers contributions, contains a non-singular term

$$W'_{\text{non-sing}} = 4\pi K a (1 - e^2) \mathbf{K}(e^2) \ln(2\sqrt{1 - e^2}) \quad (25)$$

and an integral that diverges on the conics, which fact can be taken into account by introducing as usual a core radius r_C , $W'_{\text{sing}} = 4\pi K a (1 - e^2) \mathbf{K}(e^2) \ln(a/r_C)$ — a is the major semiaxis of the ellipse. Altogether, one gets for the non-topological contribution, which is necessarily positive:

$$W' = 4\pi K a (1 - e^2) \mathbf{K}(e^2) \ln(2a\sqrt{1 - e^2}/r_C) + W_C, \quad (26)$$

where r_C is typically of the order of the repeat distance of the layers. The core energy, W_C , has been discussed in [100,101], where the variation of r_C along the conics and associated strain energy (B -term) is taken into account. $\mathbf{K}(e^2)$ is the complete elliptic integral of the first kind.

The $W'' = \iiint f''$ term, integrated in the same way, gives the topological contribution, whose sign depends on the sign of Λ :

$$W'' = -4\pi \Lambda a (1 - e^2) \mathbf{K}(e^2). \quad (27)$$

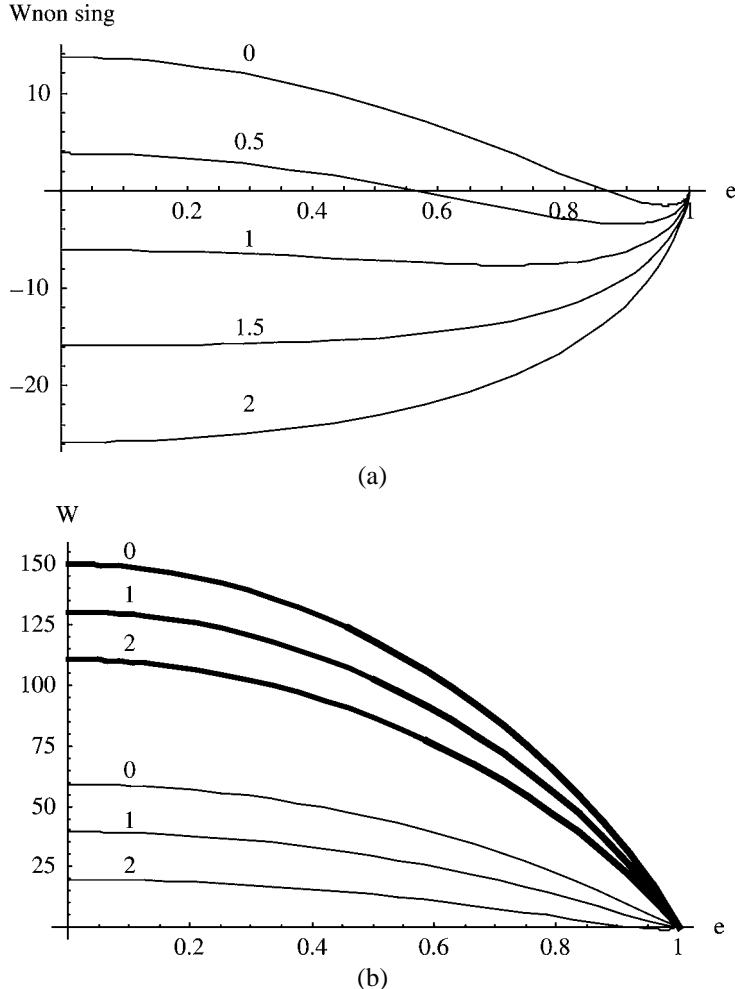


Fig. 17. Energies of FCD-I's vs eccentricity e for different values of Λ/\bar{K} renormalized units with $K = 1$ and $a = 1$. (a) Non-singular terms vs e . Note that Λ (equivalently, \bar{K}) shifts the position of the energy minimum towards a smaller e . (b) Total energy W vs e for FCD-I's of a rather small size ($a/r_C = 10$) and for different Λ 's; larger domains, $a/r_C \gg 10$, have an energy minimum at $e \rightarrow 1$.

The final expression for the total curvature energy W , valid for an arbitrary eccentricity $0 \leq e < 1$, adopts a very compact form [102]:

$$W_e = 4\pi a(1 - e^2)\mathbf{K}(e^2)[K \ln(2a\sqrt{(1 - e^2)/r_C}) - \Lambda] + W_C. \quad (28)$$

This is the place to report some results related to the stability of a phase whose free energy can be written in the form of eq. (21), with no B term included. It can be shown that:

- (1) For $\bar{K} < 0$, $\Lambda > 0$, the ground state satisfies the relation $\sigma_1\sigma_2 = 0$, the layered phase is stable.
- (2) For $\bar{K} < 0$, $\Lambda < 0$, the ground state satisfies the relation $\sigma_1\sigma_2 > 0$, the micellar phase is stable.
- (3) For $\bar{K} > 0$, $\Lambda > 0$, the ground state satisfies the relation $\sigma_1\sigma_2 < 0$, $\sigma_1 + \sigma_2 = 0$, the layers take the shape of minimal surfaces.

The first case is the case we are investigating. Clearly, one expects that the sign of Λ favors FCD-I's in lamellar phases. This is true in thermotropics. Now the present analysis of the stability strictly applies to a membrane or an isolated layer, not to a stack of layers, since there is no compressibility term in eq. (21) and eq. (24). Hence, strictly speaking, case (2) applies to a dilute phase of micelles, case (3) to a dilute ‘sponge’ phase L₃, which we shall not discuss any longer—see [103,104] for details. The domain of existence of the lamellar phase is extended if the compressibility is taken into account, and this is why one expects to meet FCD-II, in layered phases belonging to case (2), and FCD-I in layered phases belonging to case (1).

We assume in the sequel that we are in case (1). \bar{K} must be within the range $-2K < \bar{K} < 0$ or $0 < \Lambda < 2K$ (K is always positive).

Eq. (28) is the curvature energy of a FCD-I with an arbitrary eccentricity. It allows one to trace the role of different parameters, e.g., \bar{K} and e , Fig. 17.

The dependence of the curvature energy eq. (28) on the saddle-splay elastic constant is obvious: the larger \bar{K} , the smaller the energy, because of the negative sign of the Gaussian curvature of the Dupin cyclides. Notice also that the minimum of the sum of the non-singular terms $W'_{\text{non-sing}} + W''$ in W is shifted from $e \rightarrow 1$ to $e \rightarrow 0$, when Λ increases. The tendency of this term to reach a minimum at small eccentricity $e \rightarrow 0$ is, of course, in competition with the increase of the singular term. One sees that the minimum of curvature energy can be achieved at e substantially different from 1 only when the domains are extremely small $a/r_C \sim 10$ (and when the saddle-splay constant is close to its upper limit $\bar{K} = 0$). But, for a/r_C very small, the effects of compressibility become important, and the present analysis is no longer valid. Generally, for a reasonably large domain, $a/r_C > 10$, the curvature energy becomes minimum only at $e \rightarrow 1$. However, it would be a mistake to conclude that a FCD-I tends to increase its eccentricity as much as possible on the ground of eq. (28), for several reasons. Some of them are of minor importance.

First, the direct comparison of energies on the plots of Fig. 21 are misleading, because they correspond to a fixed major semiaxis, $a = \text{const}$, and not a fixed volume. Secondly, because a FCD is a large object at the scale of a sample, its total energy generally involves surface anchoring energies, that are rather large in smectic phases [105,106]. But the reason that limits e is more universal: it is relating to the fact that any FCD-I with a non-zero eccentricity must emit dislocations. This is the object of the next subsection.

4.3. How do FCD's pack in space: oily streaks

It is visible from Fig. 16 that, when an isolated FCD-I is embedded into a system of flat layers, the tilt of smectic layers *inside* the FCD-I (with respect to the horizontal plane)

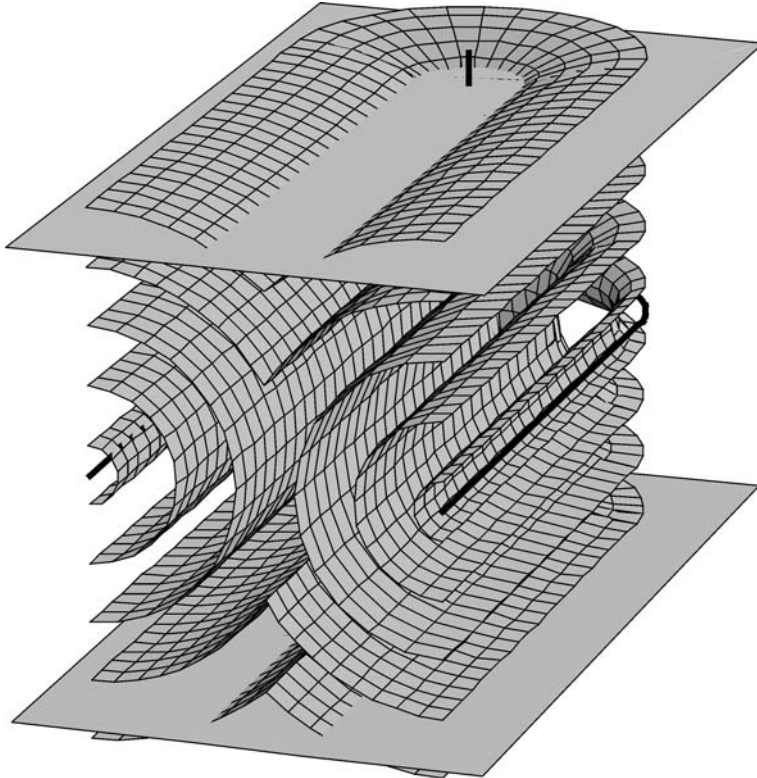


Fig. 18. The simplest model of the cholesteric oily streaks; $b_{\text{tot}} = 0$. In this case the oily streak can terminate as shown.

requires a set of matching dislocations attached to the FCD-I outside. Observe that such a requirement, whose geometric necessity is here apparent, satisfies the analysis reported above of the relationship between a curved disclination (the FCD ellipses are disclinations of strength $k = 1/2$, as one can convince oneself by noticing that the layers inside the FCD fold about the ellipse in a $k = 1/2$ manner) and the attached dislocations. The total Burgers vector b_{tot} attached to an ellipse is directly related to its eccentricity and its size [107]: $b_{\text{tot}} = 2ae$.

As a matter of fact, FCD's often gather along line-like objects, in such a way that the ellipses all belong to the same plane, that their major axes are all parallel, and all transverse to the line direction. Such linear clusters, called *oily streaks* by G. Friedel, are in fact made of a pair of parallel edge dislocations of huge Burgers vectors of opposite signs, $|n'|d_0$, $|n''|d_0$, $b_{\text{tot}} = nd_0 = \pm(|n'| - |n''|)d_0$. Oily streaks are a common feature of many lamellar liquid crystals (smectics but also cholesterics, see Section 9.6). In a flat cell with layers parallel to the bounding plates, oily streaks appear as long bands that divide ideal domains of flat layers. The splitting of the total dislocation b_{tot} into a FCD chain is a frequent occurrence [107], but there are other splitting modes of instabilities, like layer undulations. The inner structure depends in fact on many parameters, most notably on elastic constants

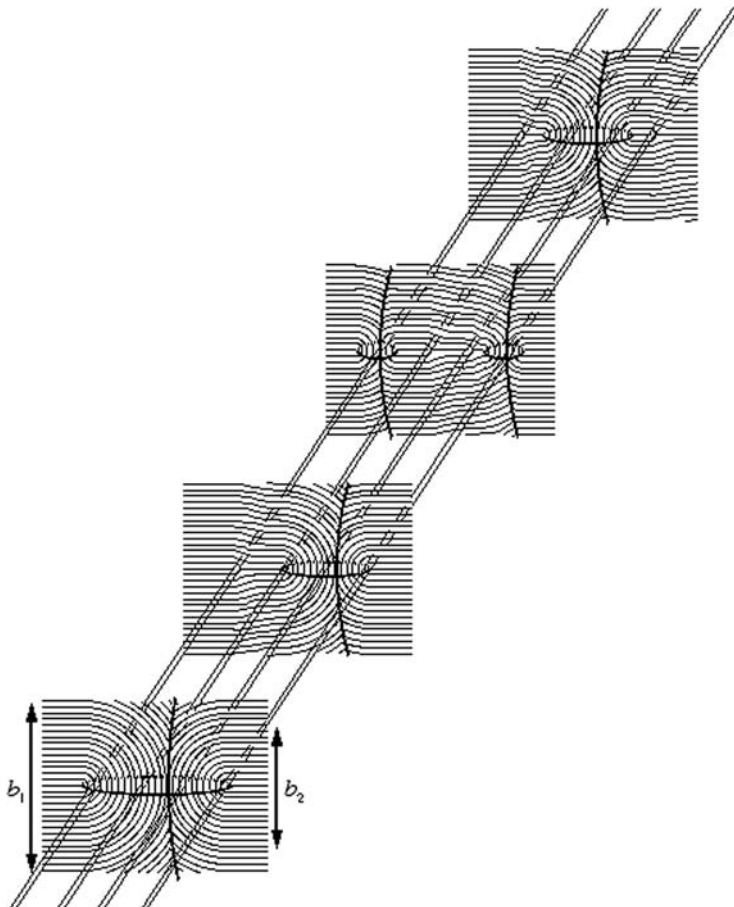


Fig. 19. Sketch of an oily streak (adapted from [107]).

(including the saddle-splay elastic constant) and the surface anchoring. The simplest type of oily streak is shown Fig. 18. We restrict to the FCD mode of splitting in the rest of this subsection.

Of course, b_{tot} keeps constant all along the streak. In a SmA, the dislocation Burgers vectors are quantized. Between the FCD's which constitute the oily streak, the total dislocation b_{tot} is generally split into microscopic Burgers vectors of a few d_0 s, see Fig. 19.

An edge dislocation in a smectic system carries an elastic energy that is proportional to the Burgers vector [6], $\simeq (BK)^{1/2}b_{\text{tot}} = B\lambda b_{\text{tot}}$ (per unit length), if the Burgers vector is small enough. Thus, although the trend $e \rightarrow 1$ is favored by the curvature of layers *inside* the FCD-I, an opposite trend $e \rightarrow 0$ is favored by the line tension $\simeq (BK)^{1/2}ae$ of the dislocations *outside* the FCD-I. Note also that the compressibility energy density results in additional e -dependent energy terms for the inside configurations, since near the cores of confocal pairs the layer equidistance is not perfect, as already alluded to, see ref. [100,101].

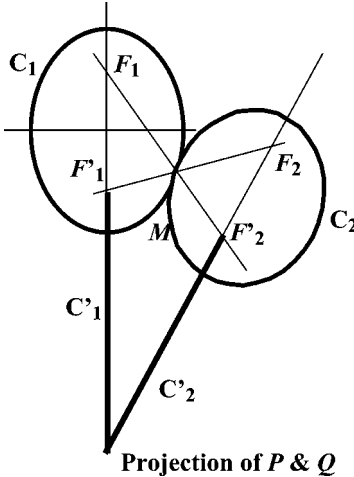


Fig. 20. Law of corresponding cones (2D view in the plane of the ellipses).

4.4. How do FCD-I's pack in space: laws of association

Finally, in some instances, the value of e is not a parameter of energy minimization at all. This question arises when several FCD's gather into 2D or 3D clusters where they are in contact. Because of nontrivial shapes, FCD's *do not tile space*, and their contacts obey special rules, independent of e . The special and most frequent cases, which occurs when all the clustering FCD's have the same eccentricity, are studied in Section 5: the toric FCD-I Apollonian packing ($e = 0$; Section 5.1.1), the generalized Apollonian packing ($e \neq 0, 1$; Section 5.1.2).

The non-tiling generic case responds to laws of association first experimentally established by G. Friedel [12]. These laws correspond physically to the tendency to fill space by insuring the *continuity of the layers* from one domain to the other, at the places where they are in contact, and by maintaining a *constant thickness* of the layers. Numerous discrepancies are observed, but it is precisely the analysis of these discrepancies with respect to the laws of association that can be rewarding.

The most frequent experimental situation met in thermotropic systems is that two FCD's are tangent to each other along *two* generatrices, and that the conics carried by these domains touch each other in pairs, i.e., pairs of conics either interrupt each other or are tangent to each other. Alternatively, if two FCD's are tangent along only one generatrix, it means that the conics they carry do not touch each other in pairs. These geometries obey the following laws.

- (i) Law of impenetrability: two FCD's cannot penetrate each other; if they are in tangential contact at a point M , they are tangent to each other along at least one generatrix common to two of the bounding cones. As a consequence we infer that the interactions between FCD's are of a steric nature.
- (ii) Law of corresponding cones (lcc): when two conics C_1 and C_2 belonging to two different FCD's are in contact at a point M , the two cones with a common vertex M ,

which rest on the two other conics C'_1 and C'_2 of the two FCD's, coincide. Therefore C'_1 and C'_2 have two points of intersection P and Q on the common cone, and the straight lines PM and QM are two generatrices along which the two FCD's are in contact.

The law of corresponding cones has:

- (i) A geometrical content. The demonstration employs a theorem according to which any cone whose apex M is on one of the conics of a FCD and which rests on one of the conics is a cone of revolution; the axis of revolution is the tangent to the conic in M . The result is represented Fig. 20 (for details, see [108]): if two conics are *coplanar*, the triples F_1, M, F'_2 , and F'_1, M, F_2 , are aligned; F_1, F_2, F'_1, F'_2 , are the foci of C_1 and C_2 . Point A is the common projection of the two intersections P and Q of C'_1 and C'_2 . Fig. 1 of ref. [109] illustrates the law of corresponding cones in the coplanar case for a photograph of FCD's in contact (due to C. Williams). Fig. 21 restitutes in 3D the continuity of the cyclides along the generatrices of contact in the case of two incomplete FCD's obeying the law of corresponding cones.
- (ii) A physical content [108]: the points of contact P and Q are the centres of curvature of the Dupin cyclides passing through all the points μ on the segment PQ , whether they are considered to belong to one FCD or to the other. Therefore, $\sigma_{\mu,P} = \sigma_{1,P} = \sigma_{2,P}$, $\sigma_{\mu,Q} = \sigma_{1,Q} = \sigma_{2,Q}$, where σ_P and σ_Q are the principal curvatures at μ ; μP and μQ are signed lengths. The same property applies of course to all the points ν on the segment PQ . As we know, eq. (24), the free energy density of a SmA depends on the two invariants $\sigma_{\mu,P} + \sigma_{\mu,Q}$ and $\sigma_{\mu,P}\sigma_{\mu,Q}$, and no other term if the layers are parallel and equidistant. Therefore the free energy densities of the two FCD's are equal at the points of contact, since the curvatures are the same; consequently there is no special line energy attached to the line of contact, and there are no forces exerted from one FCD towards the other. The geometry of contact is metastable. This is probably the best physical justification of law of corresponding cones.

4.5. Surface anchoring energy: an illustration of its role

Overall, the problem of finding an equilibrium e requires the consideration of the presence of additional dislocations, of compressibility, and of anchoring terms, in addition to the curvature energy. This should be kept in mind when analysing different results on FCD energies. For example, it has been possible to carry out the estimation [107] of the saddle-splay elastic constant \bar{K} from the features of FCD-I's in oily streak only for $B = 0$. As explained in [107], the assumption of $B = 0$ leads to a large positive \bar{K} which is thus only an indicator that the system favors deformations with a negative Gaussian curvature rather than with a positive Gaussian curvature. Lifting the restriction $B = 0$ contributes to the decrease of e and thus decreases the effective \bar{K} due to the dislocations and compressibility effects; the exact analytical analysis of the oily streaks for $B \neq 0$ is still lacking.

Fig. 22 illustrates the important role of surface anchoring in establishing the FCD configurations. Anisotropic molecular interactions at the bounding plates set a particular director orientation at the boundaries. In the lamellar phases, the most frequently met are

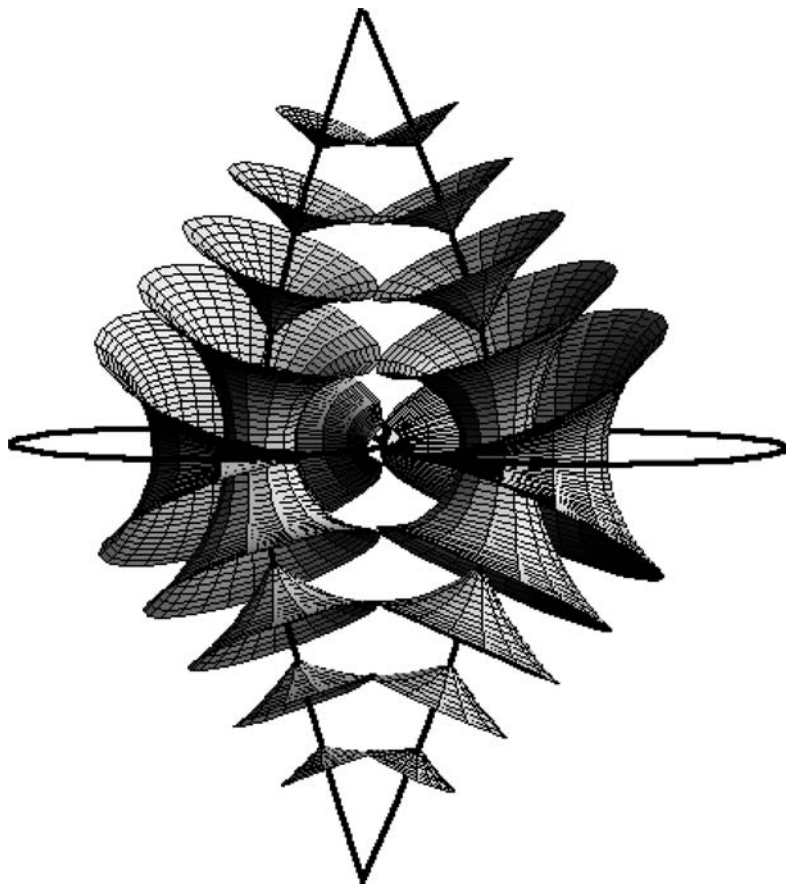


Fig. 21. Law of corresponding cones (3D view).

homeotropic (the director is perpendicular to the substrate) and tangential (the director is parallel to the substrate) equilibrium configurations.

In the cells with homeotropic boundary conditions filled with a smectic of a negative dielectric anisotropy, an electric field applied across the cell can nucleate FCD's with $e \rightarrow 0$ [106]. The elliptic bases of these FCD's are located in the bulk of the sample, as evidenced by the fluorescence confocal polarizing microscopy (FCPM), see Appendix, Fig. 22(a, b) [42,43]. Placing the elliptic base too closely to the boundary would dramatically increase the angle between the smectic layers and the substrate, which implies a large surface anchoring energy. Interestingly, as the radius of FCD and thus the surface tilt increase with the applied field, the surface anchoring causes a dramatic pattern change: above some critical radius, the circular FCD transform into oily streaks of zero Burgers vector that grow by one-dimensional elongation preserving a constant width controlled by the surface anchoring energy [106].

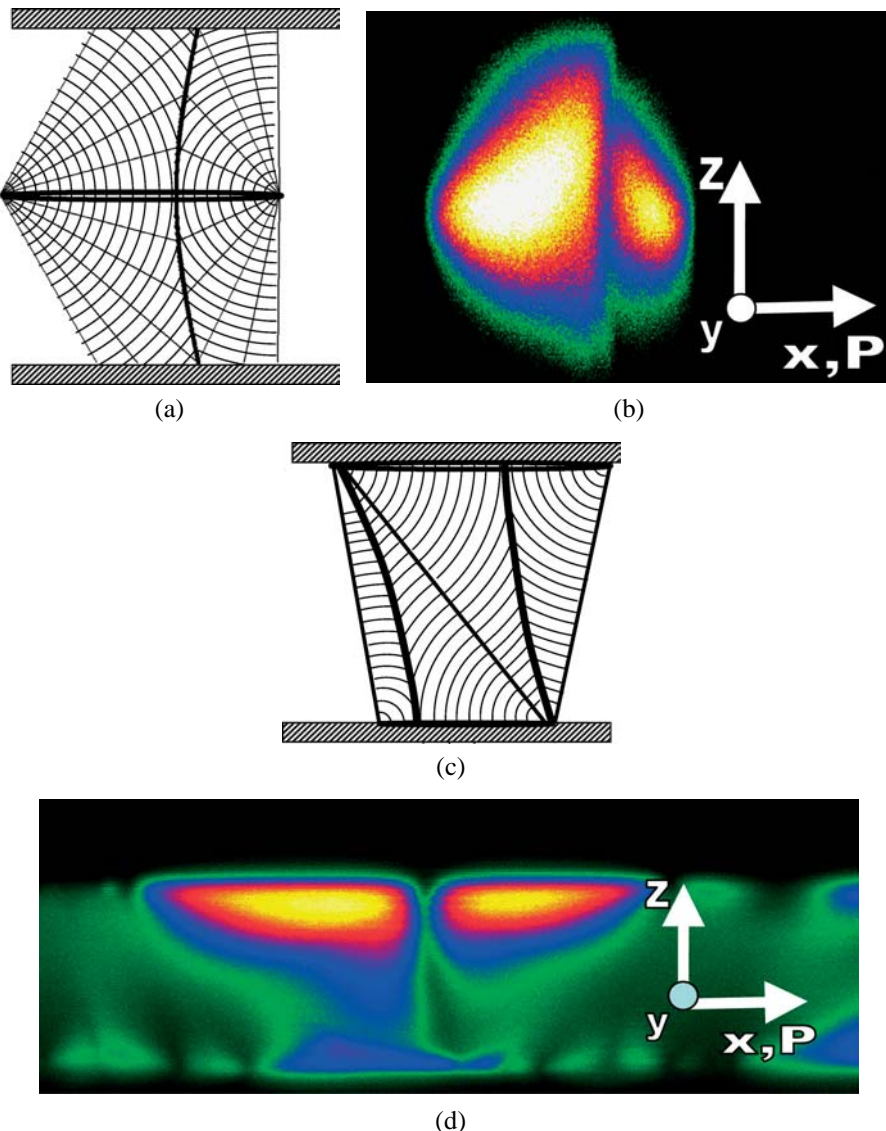


Fig. 22. FCD-I's with the elliptical bases located either in the bulk (a, b) or at the bounding surfaces (c, d) of a flat lamellar sample with predominantly homeotropic (a, b) and planar (c, d) boundary conditions for the director field. Parts (a) and (c) show the configuration of bent layers in the vertical cross section of the cell; the straight lines are the director lines. Parts (b) and (d) are the corresponding fluorescence polarizing microscopy textures (courtesy I. Smalyukh), taken for smectic 4'-trans-butyl-4-cyano-4-trans-heptyl-1,1'-bicyclohexane (CCN-47), doped with a fluorescent dye n,n'-bis(2,5-di-tert-butylphenyl)-3,4,9,10-perylenedicarboximide (BTBP); see text.

In contrast, in tangential cells, the elliptic bases are located at the sample's boundaries, as such an arrangement guarantees that the director is parallel to the plate, Fig. 22(c, d). FCD's

with their elliptical bases at the smectic surface have originally been observed by G. Friedel in the so-called *bâtonnets*, which are elongated smectic nuclei emerging from the isotropic melt. Within each FCD base, the molecules are nearly parallel to the smectic–isotropic interface; this orientation corresponds to the minimum of the interfacial energy. Outside the base, the molecules are perpendicular to the interface. The size b^* of the smallest FCD base is determined by the surface energy anisotropy W_a and the bend elastic constant K , $b^* \simeq K / W_a$, see refs [100,110].

5. Dislocations vs disclinations. Grain boundaries in smectics

5.1. Tilt grain boundaries

In smectics, tilt grain boundaries (T_i GB) with a disorientation angle ω can be achieved according to three different geometries: curvature walls, [13], (Fig. 23(a)), dislocation walls (Fig. 23(b))—a small angle dislocation wall can be prepared in a wedge of angle ω with homeotropic boundary conditions, this is a *Grandjean wedge*; FCD walls (Fig. 23(c)). We consider here the often met case of tilt walls split into FCD's; a question is then how the residual gaps between the FCD's are filled.

Let ω be the angle of misorientation between two adjacent monodomains. The FCD hyperbolae must be perpendicular to the layers at a distance from the wall, i.e., their asymptotes must be parallel one to the other. The angle between the asymptotes measures the disorientation between the two grains. This implies that all the FCD ellipses, which all belong to the tilt wall, have the same eccentricity $e(\omega) = \sin(\omega/2)$, and have parallel major (resp. minor) axes. Their size distribution results from a minimization of the total energy, viz., the FCD energies, eq. (24), and the energy of the *residual* zones between the FCD's, depending on the nature of these zones.

Observe that all the FCD's are complete, and that any pair of domains in contact at any point M on two ellipses carry the same pair of vertices P and Q at infinity, Fig. 24, so that the law of corresponding cones is obeyed. Because the energy of a domain is small (curvature energy), one expects that the tilt wall will be composed of FCD's in contact, with smaller ellipses located between larger ones, in contact with them, forming an *iterative filling* of space.

How are the ellipses distributed in size, and how are the residual areas between them filled? We discuss these questions first for a rather special case, the $\omega = 0$ tilt boundary (no misorientation, but a wall of toric domains), then for the generic case.

5.1.1. The $\omega = 0$ Apollonian packing

This iterative filling has been introduced in ref. [111]. The hyperbolae are degenerate to straight lines, the ellipses are degenerate to circles, the FCD's are toric. Toric FCD's built on coplanar tangent circles trivially obey Friedel's laws. As a matter of fact, such a packing of tori appears as a pure representation of the mind, with little chance of physical reality, since its energy is positive, while the vanishing limit $\omega = 0$ should have vanishing energy. However the interest is manifold: (a) the iterative geometry with $\omega = 0$ becomes physically relevant when applied to an *interface* between a lamellar and an isotropic phase rather than

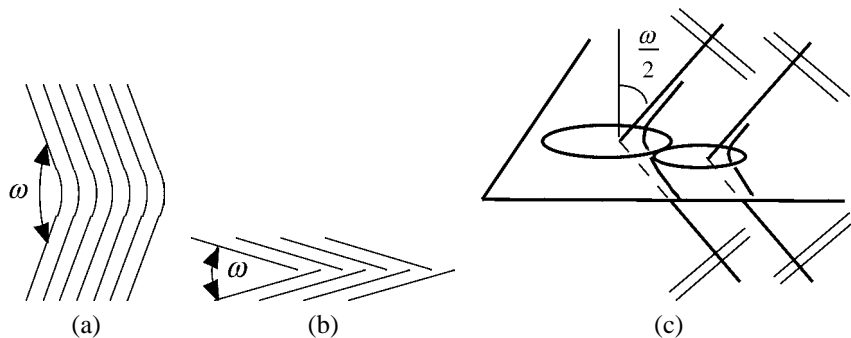
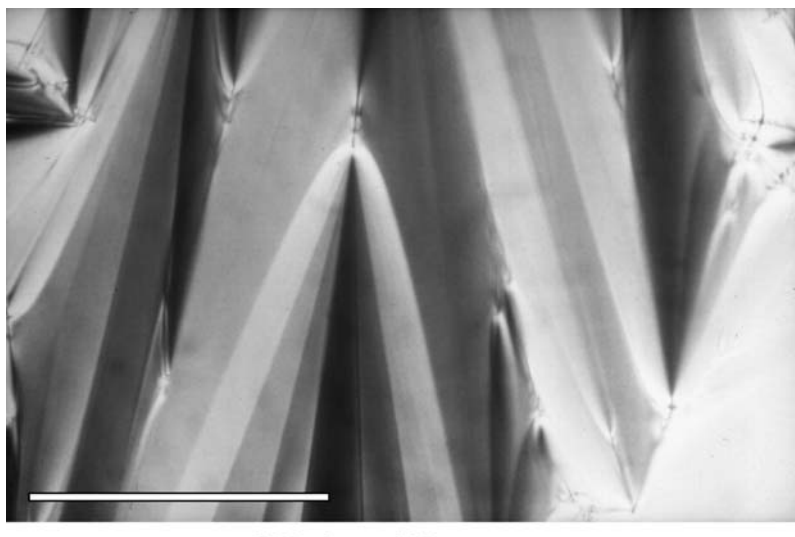


Fig. 23. Tilt grain boundary: (a) curvature wall; (b) dislocation wall; c) FCD wall.



8CB, bar ~100μm.

Fig. 24. Tilt grain boundaries split into FCD's (courtesy C. Meyer). Note that the hyperbolae do not strictly meet at infinity. Therefore ω slightly varies along the GB. This is the most common case. 8CB is 4-n-octyl-4'-cyanobiphenyl.

to a grain boundary in the bulk. At the interface, the bases of the TFCD's and the residual areas differ in surface director orientation and thus bring different surface energies to the total energy balance; e.g., in a thermotropic SmA [110] and in a lyotropic L_α [112] (L_α is a periodic succession of layers of surfactant and of solvent); (b) even if it does not apply to the bulk, the Apollonian packing (i) puts into evidence the relationship between the *geometric parameters* of the packing and their *scaling* physical properties—these properties extend nicely from the $\omega = 0$ packing to a grain boundary of non-vanishing disorientation, (ii) does *raise* the question of the role of the residual areas—these regions outside the FCD's—in the energy balance.

The *geometric* part of the $\omega = 0$ packing problem contains the two following steps: iteration of a compact packing of circles in a plane (known in mathematics as Apollonius' problem; at each step of the iteration the radius of the newly introduced circles, tangent to the circles which are already present, decreases), calculation of the size of the remaining gaps such that the global energy is minimized. The unknowns are: (1) the number of circles of radius $R > b$, when the iteration reaches circles of radius b : let $g(b)$ be this number; (2) the total perimeter of these circles, $P(b)$; (3) the residual uncovered surface area, $\Sigma(b)$. Let L be the size of the largest circles; one expects that all the relevant quantities scale algebraically with the dimensionless quantity L/b . We can write:

$$g(b) = \text{const}(L/b)^t; \quad P(b) = \text{const } b(L/b)^t; \quad \Sigma(b) = \text{const } b^2(L/b)^t. \quad (29)$$

Numerical calculations [113] indicate that the exponent t is approximately 1.306.

The *energy* part of the $\omega = 0$ packing problem of the grain boundary is discussed in [111] as follows:

The energy of a FCD of radius b scales as $K_1 b$, hence the contribution to the total energy of the circles of radius $R > b$ scales as $W_{\text{line}} \sim K_1 P(b) = \text{const } K_1 b(L/b)^t$. The residual regions are *assumed* to be elastically deformed over a distance from the plane of the boundary of order $\lambda = \sqrt{(K_1/B)}$, the penetration length; hence $W_{\text{resid}} \sim B\lambda \Sigma(b) = \text{const } Bb^2\lambda(L/b)^t$. After minimization of $W_{\text{line}} + W_{\text{resid}}$ with respect to b , the value of b at the final iteration is $b^* \sim \sqrt{(K_1/b)} = \lambda$, i.e., b^* is a microscopic length in this model. The total energy per unit area of the grain boundary is $W \sim (L/b^*)^t Bb^*\lambda^2$.

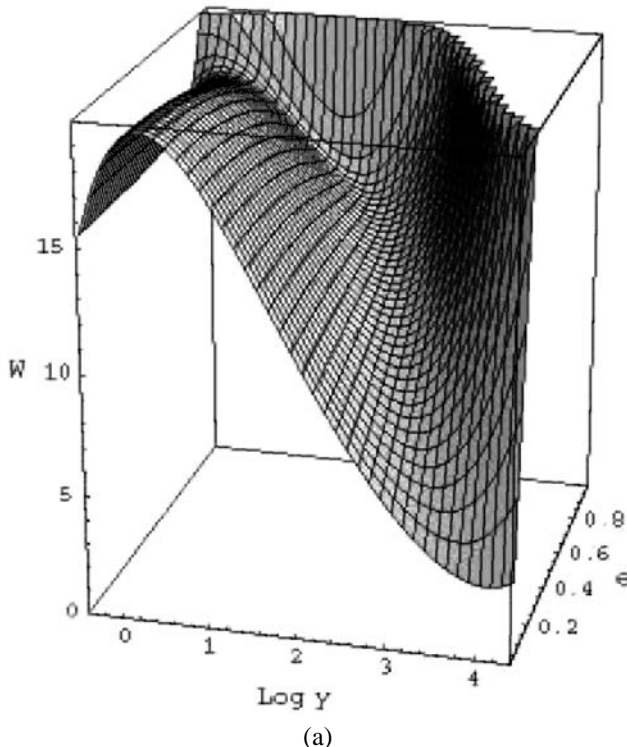
5.1.2. The $\omega \neq 0$ Apollonian packing

The generalization to a realistic T_i GB $\omega \neq 0$ is as follows [108]. There is a complete mapping between the Apollonian packing and the $\omega \neq 0$ packing, such that each circle of the Apollonian packing is replaced by an ellipse of eccentricity $e = \sin \omega/2$. The ellipses have parallel major and minor axes, and all the asymptotic directions of the related hyperbolae are parallel. Each FCD of the ω - T_i GB is complete and is in contact with a neighboring complete FCD along two generatrices, Fig. 23, and is in one-to-one relationship with a complete toric domain belonging to the Apollonius tiling.

We shall not dwell longer on this geometry, and we refer the reader to ref. [108] for a complete discussion of the generic T_i GB. We shall here restrict ourselves to a few comments relating to the residual zones.

5.1.3. The residual regions

The residual regions are pieces of grain boundaries and henceforth must adopt either a model of curvature wall or of a dislocation wall (also called the Grandjean model). The calculation of the energy of the T_i GB shows that the Grandjean model is favored for small disorientations, the curvature model for large ones. In Fig. 25(a), (Grandjean wall case) we have plotted the total energy per unit area W as a function of the eccentricity e and the dimensionless variable $y = b_{\min}/\lambda$, where b_{\min} is a typical size for a residual area embedded between FCD's in contact. It appears that for each value of e , i.e., of the disorientation ω , there are two solutions in b_{\min}/λ that make the derivative vanish. The solution with the smaller, microscopic b_{\min}/λ is a maximum, while the other one is a minimum. This is the



(a)

Fig. 25. Elastic energy W (arb. units) vs e and $\log_{10} y$ for the FCD-split boundary. The residual areas are relaxed either by dislocations (a) or by curvature walls (b). In both cases, $L = 50 \mu\text{m}$, and $\lambda = 2 \text{ nm}$. Adapted from [108].

valid solution; it varies rather quickly with e (or ω). The residual area is large for small disorientations ω , and the energy is small; at $\omega = 0$, the ‘residual’ area invades the whole boundary. It is only for very large disorientations that the residual area becomes microscopic. Fig. 25(b) refers to the curvature wall case; the residual areas are of macroscopic size. Comparing Figs 25(a) and 25(b), it appears that the dislocation and curvature models of the residual areas in the FCD-split grain boundary are complementary, the first being favorable at smaller e and the second at larger e .

The residual regions embedded in the T_i GB obey either topological (dislocation wall) or geometrical (curvature wall) relationships.

- (i) The Grandjean model; topological considerations. Again, the dislocations that are attached to the ellipse of an isolated FCD, characterized by the quantities a and e , have a total Burgers vector $b_{\text{tot}} = 2ae$. This conservation law applies to the FCD’s of a T_i GB. In a toric FCD, the circle is of zero eccentricity, $b_{\text{tot}} = 2ae = 0$; there are no dislocations attached to it. A toric FCD can be smoothly embedded into a system of flat and parallel layers with $\omega \equiv 0$.

Experimental realizations of ellipses and their attached dislocations have been observed in light microscopy, in both thermotropic [114] and lyotropic [112] SmA’s.

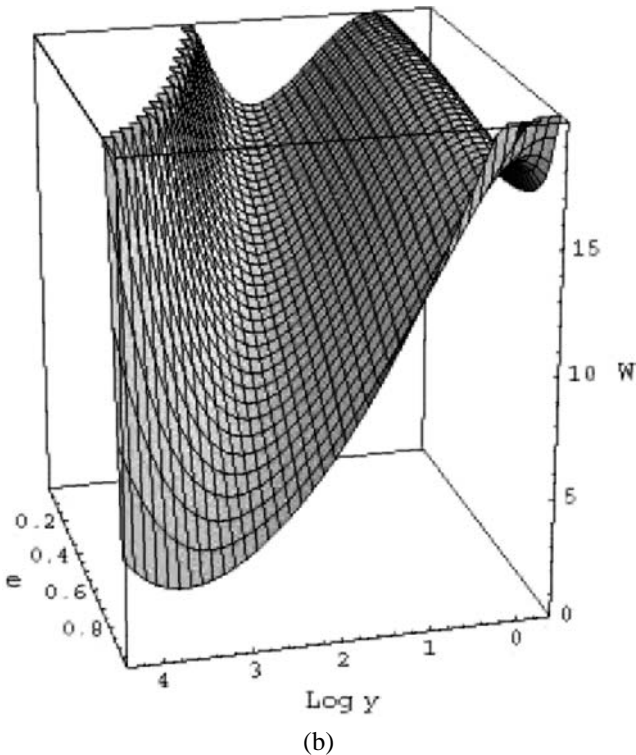


Fig. 25. (Continued).

It is directly visible that the dislocations have large, giant Burgers vectors, whose magnitude scales with the size of the ellipses, and that they are located in the plane of the ellipses. The dislocation lines have an edge character. This is in contrast with the result obtained for $\omega = 0$ (above), which predicts residual regions of microscopic size.

- (ii) The curvature model. At large disorientations, the residual areas are relaxed by curvature walls. Each layer of the curved region is tangent to a Dupin cyclide all along a circle of contact, and we expect that the physical realization of this particular geometry is not too costly [111]. In fact, the energy cost has two origins: the curvature walls in the residual regions (but the layers do not abut abruptly on the grain boundary), and a mismatch in curvatures of the Dupin cyclides and the layers outside the FCD-I's. The curvature wall energy (per unit area) can be written [112]:

$$F_{\text{curv}} = 2B\lambda(\tan \theta/2 - \theta/2) \cos \theta/2, \quad (30)$$

where $\theta = \pi - \omega$.

Two remarks:

- (i) An implicit assumption of the model is the existence of an Apollonian tiling, i.e., a compact packing with tiles of different sizes, not fixed in advance, and with no entropy of mixing, since an iterative filling obeys quasi deterministic rules (see ref. [115] for a comparison between scaled and entropic tilings). The smaller conics are certainly those that would contribute more to the entropy, but such objects are not present, because the residual areas are macroscopic. This remark might be a strong indication of the physical reality of the Apollonian tiling.
- (ii) The model above has been discussed for a SmA. However, its basic features are expected to remain valid for other lamellar phases, e.g., SmC liquid crystals, in which *chevron* walls are often split into FCD's [116,117]. The chevron formation is ruled by surface anchoring at the plates bounding the liquid crystal slab; depending on the actual geometry. Therefore, chevron analysis requires additional consideration of the surface anchoring energies. In the SmC phase the tilt of molecules within the smectic layers causes another complication, both topological (disclination lines in the vector field of molecular projections onto the layers [29,118]) and energetical (a finite energy of tilt), see Section 8.3.1(2).

5.1.4. The $\omega = \pi$ packing

Tilt grain boundaries for $e = 0$ (Apollonian packing) and $e \neq 0, 1$ (generalized Apollonian packing) appear thus as special cases of the law of corresponding cones. The case of parabolic FCD's ($e = 1$; both conics are degenerate to parabolae) is apart; it has been considered experimentally and theoretically [119,120]. There is a practically (but not strictly) smooth matching between two PFCD's as soon as their axes are parallel. But PFCD's are not obtained as an analytical limit of the FCD's when the eccentricity of the ellipse tends towards $e = 1$. We shall not expatiate on this subject.

5.2. Screw dislocations and twist grain boundaries

5.2.1. Isolated screw dislocation

A remarkable feature of an isolated screw dislocation in a SmA phase is that the layers affect the shape of a *minimal surface*. This geometry [121] minimizes the non-linear free energy $\int\int\int f$

$$f = 1/2K(\operatorname{div} \mathbf{n})^2 + 1/2B(1 - d/d_0)^2, \quad (31)$$

and can be considered as exact for dislocations of small Burgers vectors: $\operatorname{div} \mathbf{n} \equiv \sigma_1 + \sigma_2 = 0$; the energy reduces to a (small) strain energy per unit length of line

$$W = (Bb^4/128\pi^3)(r_C^{-2} - R^{-2}) + W_C. \quad (32)$$

R is the size of the sample, r_C the size of the core, $b = nd_0$ the Burgers vector. The strain energy density diverges for $r \rightarrow 0$. For $|n| = 1$, the layer is folded along a half ruled helicoid, i.e., a surface generated by a half infinite straight line whose extremity meets the axis

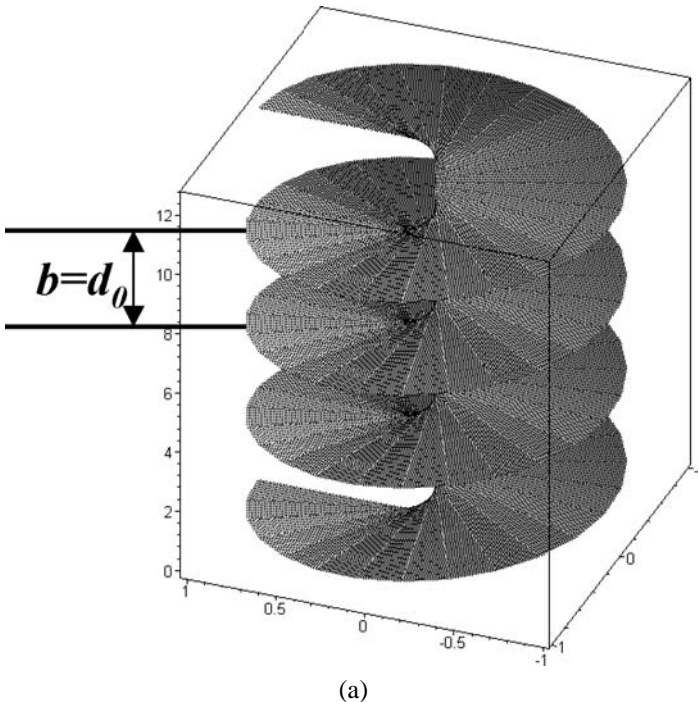


Fig. 26. Models for screw dislocations. (a) Half-helicoid, Burgers vector $b = d_0$, eq. (33a); (b) full helicoid, Burgers vector $b = 2d_0$, eq. (33b). The interlayer distance is the same in (a) and (b). Screw dislocation of a giant Burgers vector: (c) schematical representation of a cut along a meridian plane (adapted from [13]); (d) 3D perspective view: stacking of helicoidal layers on each side of the central ruled helicoid, the two helical disclinations $k = 1/2$ about which they are folded. Only the central region inside the cylinder limited by the disclinations is drawn.

of the dislocation at a right angle, and which rotates helically about this axis with a pitch equal to the Burgers vector. The equation of the ruled half helicoid is:

$$\xi = z - (\pm d_0/2\pi)\theta = \text{const}, \quad \xi > 0, \quad (33a)$$

ξ being the abscissa along the mobile half infinite line; ξ is the position of the material point before deformation, and is defined but to a constant; see Fig. 26(a). The geometry of the core is singular. But if $|n| = 2$, the layer is folded along a *full* ruled helicoid ($-\infty < \xi < +\infty$), and there is no geometrical singularity of the core, although the energy diverges, see Fig. 26(b).

$$\xi = z - (\pm 2d_0/2\pi)\theta = \text{const}, \quad \xi \in R. \quad (33b)$$

If $n > 2$, all the layers, whether they are full or half helicoids, occupy the position $r = 0$, and the configuration is singular on the core. In any case, it is to be expected that solutions of the type (33) are not obeyed in a region of size $r_C \simeq b/2\pi$ (assuming that the core

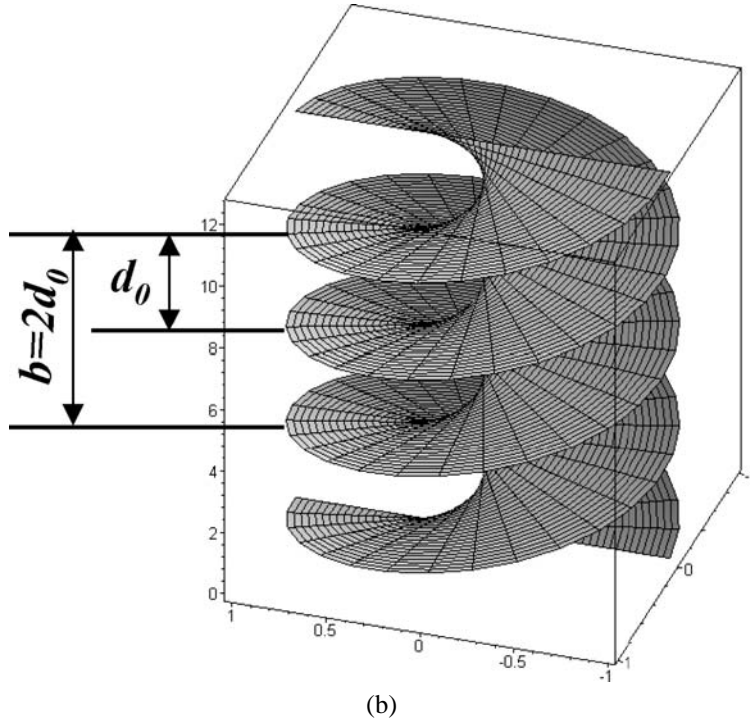


Fig. 26. (Continued).

energy scales as r_C^2), where the smectic OP is certainly perturbed [122]. The core might be very different in thermotropic LC's, which is the case discussed in [122], and in lyotropic LC's, where one can expect that the solvent occupies the core region. We do not discuss this question.

Whatever the case may be, eq. (32) tells that the favored screw dislocations have a small Burgers vector, certainly $n = 1$, and that their energy is extremely small, in fact much smaller than their line tension (see [6]), which is, very classically:

$$\tau \simeq Bb^2/4\pi \ln R/r_C. \quad (34)$$

One therefore expects that screw dislocations are very numerous (see [123]), and rectilinear.

On the other hand, the energy of eq. (32) becomes rapidly prohibitive for large n , and a screw dislocation $n > 1$ should be unstable against splitting into $n = 1$ dislocations. But, one observes giant Burgers vector screw dislocations [124]! This question is addressed now.

5.2.2. Screw dislocation with a giant Burgers vector [13, 125]

In the model above, the core scales as the Burgers vector and becomes huge if the Burgers vector is huge. Again, inside the core, the smectic OP is perturbed. But we know from the discussion in Section 1 that a Sm phase distorted on a scale larger than the penetration

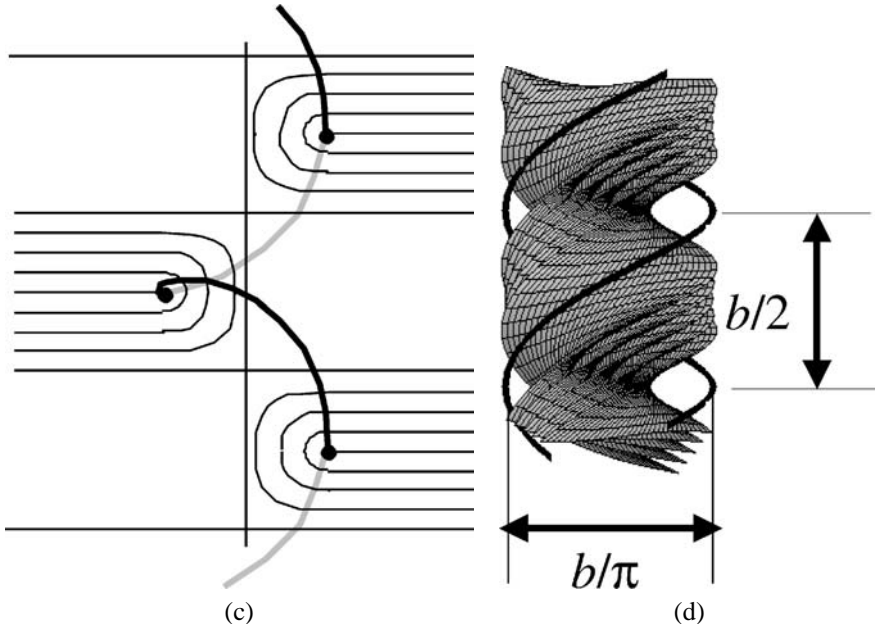


Fig. 26. (Continued).

length $\lambda = \sqrt{K_1/B}$ adopts a geometry of parallel layers, certainly more favored. Therefore, a mere extension of the model of Section 5.2.1 to huge Burgers vectors is not allowed. Let us instead consider the following geometry, Fig. 26(c, d). The central layer, which contains the axis of the screw dislocation, is a ruled helicoid (a minimal surface) of pitch $p = b$; call it $H(0)$. The other layers $H(i)$ are stacked upon $H(0)$ at distances id_0 , $i = 0, 1, 2, \dots, n - 1$; all the $H(i)$'s being parallel to $H(0)$ and parallel between themselves have common straight normals. Notice that all the $H(i)$'s are helicoids (they can be generated by helices of pitch p rotating about the axis $r = 0$), but are not ruled helicoids. Therefore there is some curvature energy (governed by the term K_1), but the unpleasant divergence of the strain energy has disappeared. In fact the strain energy is now vanishing, and the curvature energy keeps small, because the $H(i)$'s are not very different from a ruled helicoid, at least for those helicoids which are closer to $H(0)$. Furthermore, there is no core singularity.

However, a singularity still exists, but it is rejected along the *focal surfaces* of the parallel $H(i)$'s. These focal surfaces are two equal helicoids, with the same pitch as the dislocation; each of them has a helical cuspidal edge, located at a distance $b/2\pi$ of the axis. As shown in ([13], Fig. 5.35), the region immediately beyond the focal surface is covered twice by the layers. A choice has to be made, which in our case consists in the layer pattern sketched in Fig. 26(a) outside the cylindrical region defined by the helical cuspidal edges. The cuspidal edges then appear as *two disclinations* of strength $k = 1/2$ about which the helicoids are folded. The energy is approximately:

$$W \sim 1.8K_1 + 10^{-3}Bb^2 + W_C. \quad (35)$$

A numerical calculation indicates that the splitting of the dislocation into two helical disclinations is favored for $n > 20$, approximately.

5.2.3. Twist grain boundaries

A twist grain boundary (T_w GB) is a set of parallel screw dislocations lying in a plane, with a repeat distance l_d . In the linear approximation, the deformation induced by this set is the linear sum of the deformations induced by each dislocation, represented by the phase function $\zeta = z - (b/2\pi)\theta$. For the total set, one gets:

$$\zeta = z - \sum_m (b/2\pi)\theta_m, \quad (36)$$

θ_m being an angle with vertex in $x = 0$, $y_m = m l_d$. The T_w GB occupies the plane $x = 0$. The director is $\mathbf{n} = \text{grad } \zeta / |\text{grad } \zeta|$. Summing over m , and applying the Poisson formula [126], one gets:

$$\begin{aligned} \partial \zeta / \partial x &= (b/2l_d) \sin \beta / D_-, & \partial \zeta / \partial y &= -(b/2l_d) \sinh \alpha / D_-, \\ |\text{grad } \zeta|^2 &= 1 + (b/2l_d)^2 D_+ / D_-, \end{aligned} \quad (37)$$

$\alpha = (2\pi/l_d)x$, $\beta = (2\pi/l_d)y$, $D_+ = \cosh \alpha + \cos \beta$, $D_- = \cosh \alpha - \cos \beta$. The half-angle $\omega(x, y)/2$ between two directors that are symmetric with respect to the T_w GB is given by $\cos[\omega(x, y)/2] = |\text{grad } \zeta|^{-1} \simeq 1 - 1/2(b/2l_d)^2(D_+/D_-)$, i.e., far from the T_w GB, $2\sin \omega/2 = b/l_d$, or $\omega \approx b/l_d$ for a subgrain boundary, as expected. But the similarity with a T_w GB in a solid does not go further: the energy density diverges at a distance, because there is only one set of screw dislocations, not two orthogonal sets as in a solid. The energy of a (sub)-grain boundary, with density $f = (1/2)K(\text{div } \mathbf{n})^2 + (1/2)B\varepsilon^2$, $\varepsilon = 1 - |\text{grad } \zeta|$, can indeed be written (per unit length along the z -axis):

$$\begin{aligned} \iiint f \, dx \, dy &= 1/512\pi^2 B b^2 \omega^2 \iiint (D_+/D_-)^2 \, d\alpha \, d\beta + O(1/4096\pi^2 B b^2 \omega^5) \\ &\quad + O(1/128 K \omega^6). \end{aligned} \quad (38)$$

This expression diverges. Isolated T_w GB's are thus not expected, except at the prize of a extra smooth distortion that relaxes the stresses at infinity [127]. And indeed, the classic case where T_w GB's are invoked is the now well investigated *twist grain boundary* phase — usually noted TGB —, to be discussed in Section 10, which is a thermodynamically stable phase, made of a set of parallel, equidistant, T_w GB's.

We have noticed above that the layers of an isolated screw dislocation affect the shape of minimal surfaces. But the linear sum of eq. (36) is not a minimal surface, although it does not differ much, as we see below. On the other hand, minimal surfaces that act as large-angle twist grain boundaries are quite often evocated in the description of a number of lamellar systems, like diblock copolymers [128], cubic phases [129], or the SmQ phase [130]. There is a full set of periodic minimal surfaces with various groups of symmetry, as discussed in Nitsche's book [131]. We are here alluding to one of them, Scherk's first

surface, which is the geometry common to the three cited examples. It is shown in [127] that Scherk's first surface is a linear T_w GB dilated along the twist axis by a factor $\cos \omega/2$, i.e., $\cong 1 - 1/2(\omega/2)^2$ for a small-angle T_w GB. The Scherk's surface can be thought of as a set of parallel periodic helicoids, smoothly matching along helices surrounding the periodic screw dislocations in the z -direction of this special twist grain boundary. In the immediate vicinity of each dislocation line, one can figure out the shape of the dislocation as generated by a straight segment of line whose midpoint is on the dislocation axis. Therefore, the pitch of the helicoid is twice the distance between two points of the helicoidal layer, measured parallel to the z -direction; the Burgers vector is thus $2d_0$ (see discussion in Section 5.2.1).

6. Defects with isometric properties in columnar phases

6.1. General considerations

By definition, in a isometrically distorted state, the columns are parallel. Consider then any surface Σ containing such entire columns. Σ can be safely defined in the continuous limit, because the distance a between columns is small compared to their length. On any Σ the orthogonal trajectories of a column are *geodesic lines*, because these trajectories cut orthogonally a set of *parallel* columns (this result refers to the property of frontality of geodesic lines; for a simple and illustrative review of this geometrical concept, see [96]).

Two different surfaces Σ_i and Σ_j intersect along a column, and make a constant angle equal to the angle in the undistorted state along this intersection, as required by the condition of isometry. The analysis which follows is reproduced from [132]. Joachimstahl's theorem states that if two surfaces cut at a constant angle along their intersection, then the intersection is either a line of curvature on both surfaces, or is on none. In the present case, the intersection is necessarily a line of curvature, for if it were not, it would not be possible to avoid a certain quantity of twist $q = -\mathbf{t} \cdot \text{curl } \mathbf{t}$, attended in turn by elastic distortions, as shown in [132]; \mathbf{t} is a unit vector along the column. Each column being a line of curvature on any Σ implies that the orthogonal trajectories of the columns are at the same time geodesic lines and lines of curvature. Therefore the orthogonal trajectories of the columns are *planar* curves, because being lines of curvature means that their geodesic torsion must vanish, and being geodesic lines means that their geodesic torsion is equal to their natural torsion [96,97].

Hence, in a situation of isometric distortion, the columns are *orthogonal* to a family of *planes* P , which also means that each surface Σ is generated by a planar curve invariable in shape (the geodesic line) moving in such a way that the velocities of all its points are normal to the planes P which contains this planar curve. Σ surfaces are Monge's surfaces, by the name of the famous geometer who studied them in detail for the first time [133].

Fig. 27 represents two infinitesimally close P planes; their line of intersection Δ envelops a curve L when the plane P moves. The infinitesimal motion of P can be divided in a motion of pure rotation about Δ , viz. $d\phi$, and a motion about a normal to P passing through the point of contact of Δ with L , viz. $d\psi$.

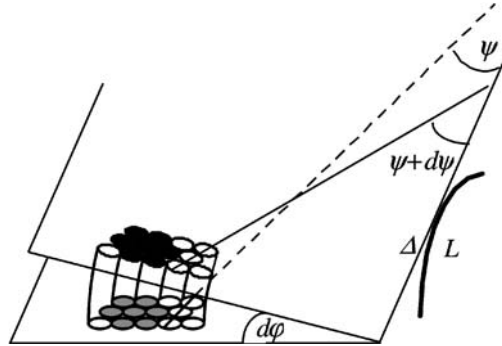


Fig. 27. Disposition of columns between two infinitesimally close P planes; on each plane there is a perfect 2D lattice. See text for details.

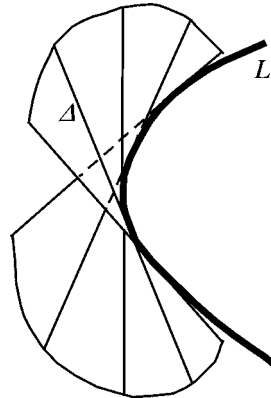


Fig. 28. Sketch of a developable surface generated by the tangents Δ to a space curve L , the so-called cuspidal edge of the developable.

Consider now any column (for a detailed analytical treatment, see [132]): its centre of curvature is on D , and its osculating plane perpendicular to D . Its curvature is

$$1/R = |\mathbf{t} \times \text{curl } \mathbf{t}| = |d\phi/ds|, \quad (39)$$

s is the curvilinear abscissa along the column. In what concerns $d\psi$, it is related to the curvature of L at its point M of contact with Δ , i.e., $1/\rho = |\psi'/ds'|$, where σ is the curvilinear abscissa along L . The osculating plane of L in M is P . Properties of reciprocity exist between L and any column:

$$\rho/\tau = -T/R, \quad (40)$$

T and τ are respectively the torsions of the column and of L , oriented by the motion of the P planes. The curvature $1/R$ of a column becomes infinite on Δ , whose locus is

consequently the curvature defect of the system. This locus is a developable surface that is the boundary of the domain of existence of columns, Fig. 28. We call it a *developable domain* (DD). For a complete classification of DDs, and a possible relation between a DD and densities of dislocations and disclinations, see [132]. For an alternative introduction to DDs, see [134]. We give now two simple examples of DDs.

6.2. Simple developable domains

When the developable is a circular cylinder of radius a ; the curve L reduces to a point at infinity in the direction of the generatrices of the cylinder, and the planes P cut a straight

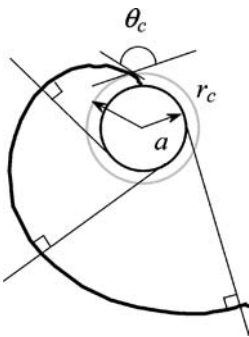


Fig. 29. Cross section of a developable domain equivalent to a disclination of strength unity; a is the radius of the developable, r_c is the radius of the core. The columns are evolutes of the circle.

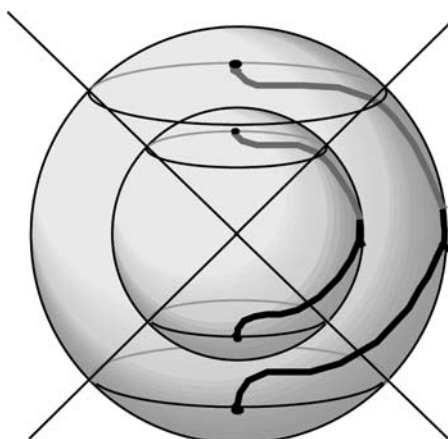


Fig. 30. A singular point as a developable domain. Columns are along spherical curves joining one point on a circle of intersection of the sphere with a fixed cone to another point on the other circle of intersection. Other columns on the same sphere obtained by axisymmetry. The spheres carrying the columns are of course all centered on the singular point.

section of this cylinder along the tangents to the circle of radius a ; the columns are evolutes of this circle, see Fig. 29. Such a configuration is a disclination line of strength $k = +1$, of core radius r_c necessarily larger than a so that we expect an empty core, or a core in which the columns take an orientation entirely different from the orientation outside, for example parallel to the axis of the cylinder. These objects are frequently observed in very thin samples of discotic phases where columns orient parallel to the surface; for an illustration see [6]. The $k = 1$ lines are most often split into two $k = +1/2$ lines; for a more detailed analysis, see [135].

Another simple developable domain is when the cuspidal edge L is a point at finite distance and the developable is a cone of revolution. It can be shown that the columns are spherical curves (the spheres centered on L are Monge's surfaces of the problem) that are orthogonal trajectories of a set of great circles (which are here the geodesic lines of the problem) drawn on the sphere and bitangent to the intersection of the cone with the sphere, Fig. 30. The columns are obtained by equispacing and symmetry about the axis of the core. The solution can be either right-handed (as in Fig. 30) or left-handed, which means that it is possible to define a chirality for a set of columns without twist (since $t \cdot \text{curl } t = 0$)!

7. Role of defects in weak shear deformations

7.1. General considerations

Experiments on the rheological bulk properties of lamellar systems [136–139] have shown the important role played by the texture (defects, instabilities) in the rheological response of these materials, whether this texture is made, e.g., of PFCD [140], of oily streaks [141], or of multilamellar vesicles (also called onions) in swollen surfactants [142]—a much more recent studied texture, not yet alluded to in this review. To each type of those textures corresponds a different type of *steady state* rheological response $\gamma = A(T)\sigma^m$ [143], each of them characterized by a different type of exponent m (in this expression, γ is the shear rate, σ is the stress). In principle, the Newtonian case ($m = 1$, $\eta = \text{const}$; η is a viscosity) is exhibited by perfect samples (not so easy to prepare), when the layers are strictly parallel to the shear velocity. However, it also obtains with well-ordered textures of parabolic focal domains [119,120].

Just a few words about the onion texture. The flat lamellar phase can become, in some shearing conditions, a texture of tightly packed spherulites. Notice that onions are akin to FCD-II. This texture was observed in the optical microscope, in light scattering experiments, and by freeze-fracture, for the first time in a lamellar system made of SDS [sodium dodecyl sulfate]/pentanol/dodecane/water [142,144]. There is no clear explanation of the strong increase of curvature of the layers, but several theoretical models stress the importance of an undulation instability [145,146] or of an hydrodynamic effect [147] in the formation of this texture. The onion texture, which has been documented in a manifold of swollen surfactants, independently of the chemical nature of the surfactant, yields $m \cong 5$.

Incidentally, all these results point towards a universal behavior of lamellar phases, irrespective of their chemical nature. Such a universal behavior has been documented for, e.g., their rheological responses G' , G'' under oscillatory shear [148].

The foregoing examples refer to macroscopic textures, fully observable under the optical microscope, i.e., mostly FCD's, which are macroscopic objects. FCD's are of the disclination type; the movement of an isolated FCD, as indicated in Section 3.4, is attended by the emission or absorption of dislocations, of finite or infinitesimal Burgers vector, according to the case. The question is probably still more involved for clusters of FCD's. These are difficult problems, which have not yet received a full attention. In the case of low shear rates, for which the macroscopic defects play the role of *obstacles* to the flow, rather than taking part in it, a few observations have been made, reported below, Section 7.2.

But the largest part of this section is devoted to small Burgers vector dislocations in smectics (mesoscopic objects), assuming no interactions with FCD's. Therefore, to be valid, one should carry this analysis at not too large stresses and apply it to well-oriented samples. At high stresses, or high shear rates, instabilities do often appear. For instance, linear undulations of the layers under a tensile stress grow easily into edge dislocations, whose motion by climb relaxes the applied stresses [149]. At larger stresses focal conic domains appear, sometimes forming either regular patterns, or more frequently irregular arrangements [120]. A few experiments, detailed below, have put into evidence climb of edge dislocations in SmA (Section 7.5) and motion of screw dislocations (Section 7.6), playing a role in the flow of the sample under a small shear rate, giving reality to the concept of *plastic shear rate*. The ensuing rheological phenomena are akin to some extent to those relating to the plasticity of solids at high temperature, but also present features characteristic of partially ordered liquid materials. On the other hand, layered phases with order in the layers (SmB's, not discussed in this survey) are fully 3D ordered solids, characterized by a weak coupling between layers and henceforth by a strong anisotropy of the viscoelastic constants. Their plasticity properties can be, to a large extent, discussed in terms of purely metallurgical concepts, at least in what concerns simple geometries [150,151]. They will not be touched upon in the sequel.

7.2. Obstacles to the flow

The rheological properties of shear-induced textures of parabolic FCD have been investigated in [140]. These textures subsist after their nucleation, Fig. 31. In the best cases, i.e., when the layers are strongly anchored to the glass plates (homeotropic anchoring), one obtains a nice square pattern of PFCD's whose parabolic axes are perpendicular to the sample boundaries [119,120,152]. The mid region of the sample is distorted by the PFCD's, whereas the region near the boundaries is made of more or less perfectly aligned layers. The apparent viscosity of the smectic material measured in this geometry is found to in-

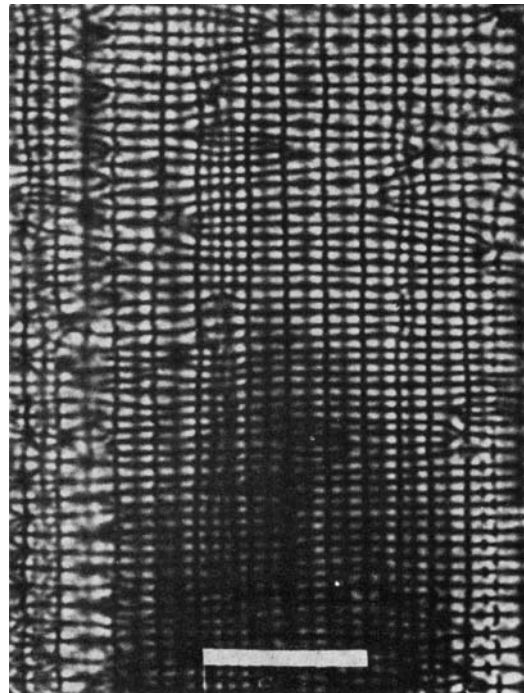


Fig. 31. Optical micrograph of a square texture of PFCD's obtained under shear; the direction of shear is vertical.
Bar 100 μm . (Courtesy R.G. Horn [140].)

crease with the fraction of the sample which contains the PFCD texture, i.e., the disordered material. One gets a Bingham type law:

$$\sigma = \bar{\omega} + \eta^* \gamma, \quad (41)$$

$\bar{\omega}$ is a yield stress which increases with the density of PFCD's, as the shear proceeds. It practically vanishes when there are no PFCD's. Here η^* is a viscosity-like term, which tends to the viscosity η of the layers gliding past one another, when $\bar{\omega} \rightarrow 0$. It increases with $\bar{\omega}$ increasing.

A finite yield stress implies that objects that impede the flow are immobilized; flow can start only after overcoming the immobilizing forces. One can imagine that the forces to overcome are those arising from the laws of association. Because these forces are mostly curvature forces, one can write a dimensional relation

$$\bar{\omega} \sim K/l^2, \quad (42)$$

l being a characteristic repeat distance of the square network. It appears that the order of magnitude thus obtained, for 8CB (4-n-octyl-4'-cyanobiphenyl), gives reasonably well the value measured for $\bar{\omega}$, when the sample is fully packed with PFCD's.

Other examples of a flow impeded by an obstacle can be found in [153,154].

7.3. Concepts used to describe dislocation movement

The ingredients necessary to describe the movement of a dislocation, apart the usual material parameters B and the splay constant K_1 for the static behavior are the following: (i) dynamic material constants such as the intralayers self-diffusion D_{\perp} and the permeation coefficient λ_p (analogous to the interlayer self-diffusion D_{\parallel} : $\lambda_p = D_{\parallel} \omega_m / kT$; ω_m is a molecular volume); (ii) actual parameters such as the applied stresses, the stresses due to the other dislocations (internal stresses), or the shear rates. The second set of parameters results in a Peach and Koehler (PK) force

$$\mathbf{f} = (\boldsymbol{\sigma} \cdot \mathbf{b}) \times \mathbf{t} \quad (f_i = \varepsilon_{ijk} b_l \sigma_{lj} t_k) \quad (43)$$

(\mathbf{f} is a force per unit length of dislocation line, \mathbf{t} is a unit vector along the dislocation line, \mathbf{b} the Burgers vector). Care must be taken in the order of the indices of the stress components; the stress tensor is usually asymmetric in a liquid crystal, due to the presence of torques [6]). The PK force is exerted on the dislocation *configuration*. Finally, the shear rate γ due to a mobile dislocation density ρ , in movement with a uniform velocity v , obeys the *Orowan relation*:

$$\gamma = \rho b v. \quad (44)$$

This relation is purely geometrical; it yields the constitutive law of the medium by expressing the velocity as a function of the stresses.

As in solids, we distinguish two types of movement of a dislocation: glide, and climb. The PK force due to an applied shear stress $\sigma_{23} = \sigma_{32}$ induces a pure glide motion for a $\mathbf{t} = (1, 0, 0)$ edge dislocation, and vanishes for a $\mathbf{t} = (0, 1, 0)$ edge dislocation. In a Grandjean wedge, a geometry where the layers are anchored to the boundaries and the midplane is occupied by a tilt boundary of small disorientation (this wall is then made of edge dislocations), Fig. 23(b), a compressive stress $\sigma_{32} < 0$ creates a PK force in the tilt plane. This force displaces the dislocations by climb in the direction of the greater thicknesses.

Eq. (44) needs another comment: v is the *configurational velocity* of the dislocation, i.e. its velocity in a frame of reference where matter is at rest at infinity. The movement of the dislocation configuration in *glide* requires a *topological shift* (TS) of the layers in the core region, half a layer changing partner with another half layer, involving their breaking in the case of edge dislocations in smectics, i.e. incidentally requiring a large activation energy. Climb is generally easier than glide in smectics [155]. Eq. (44) also applies to screw lines and to edge lines in *climb*, see ref. [156]. In all cases the movement requires a core TS, more or less costly according to the case. For instance, the movement of screws in smectics is opposed by a small flow friction [157], which involves a low activation energy [158,159], comparable to a diffusion barrier. To conclude, the shear rate described above is much akin to its homonym in solids; it deserves to be called a *plastic* shear rate.

The Orowan relation for a set of parallel edge dislocations moving in their glide plane is

$$\gamma_{pl} = \rho_e b v_z, \quad (45)$$

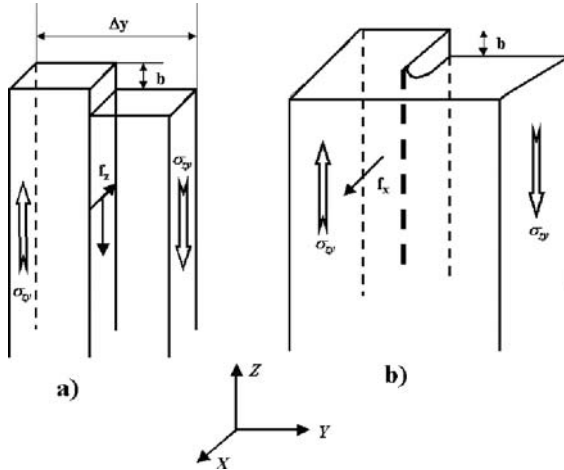


Fig. 32. Orowan relation: equivalence of the glide of an edge dislocation along the x -direction and the glide of a screw dislocation located along the z -direction (adapted from ref. [77]).

ρ_e is the density of mobile *edge* dislocations of both signs, piercing the yz -plane, b their Burgers vector, and v_z their configurational velocity (according to the PK formula). The same type of shear rate obtains by the movement of *screw* dislocations parallel to the z -direction, moving in the x -direction. The equation for edge lines is substituted by:

$$\gamma_{pl} = \rho_s b v_x. \quad (46)$$

ρ_s is the density of mobile screw lines, and v_x the configurational velocity of the dislocations. See Fig. 32 for a pictorial representation of the comparison between eqs (45) and (46).

7.4. Movement of an isolated dislocation in a SmA phase

The movement of a screw dislocation always occurs by glide. In solids, edge dislocation glide is easier than climb, but this is not so in smectics, as alluded to above.

- (1) *Mobility of an edge dislocation in climb; role of permeation.* The model of ref. [160] figures out that the edge dislocation behaves in the flow as a semiinfinite rigid plate of zero thickness, limited by the line, located along the smectic plane in the region down the flow. A boundary layer forms along the plate, on both sides. The layers are supposed to be fixed in the frame of the plate, and the molecules *permeate* through them. The total friction experienced by the plate on each side is balanced by the PK force $b\sigma_{33}$, and one finds that the resulting mobility $M = v/\sigma_{33} = \kappa^{-1}/2\eta$ ($\kappa^{-2} = \lambda_p \eta$) can be written:

$$M \sim \lambda_p \kappa \sim (\lambda_p \eta^{-1})^{-1/2} \sim D_{||} \omega_m / k T d_0. \quad (47)$$

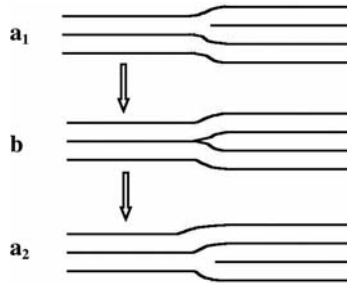


Fig. 33. Glide of an edge dislocation between two (assumed) positions of minimal energy (a_1) and (a_2), through a position of higher energy (b).

This expression of the mobility has been used to measure the coefficient of permeation [153,154,161]. A typical value is $\lambda_p \cong 10^{-13} \text{ cm}^2/\text{poise}$ in a thermotropic SmA where $\eta \cong 1 \text{ poise}$; this value is in agreement with the value of D_{\parallel} measured from NMR or neutron quasielastic scattering [162]. See also [163].

The above expression of the mobility results from a *hydrodynamical* model, where most of the effects originate in diffusion *far from* the core. A similar expression results from a *metallurgical* model where the largest effect comes from the diffusion of molecules *near* the core. Let v_m be the velocity of the molecules diffusing from one layer to the next. According to Einstein's relation, v_m can be written:

$$v_m = D_{\parallel} f_m / kT, \quad (48)$$

f_m being the force exerted on the molecules due to the acting stress σ_{33} . We have $f_m \simeq \sigma_{33} a^2$, where a^2 is the molecule cross-section in a smectic layer. Because the velocity v of the dislocation is related to v_m by the relation of conservation $vb = v_m a$, one gets:

$$M = v/\sigma_{33} \simeq (a/b) D_{\parallel} a^2 / kT = (a/b) D_{\parallel} \omega_m / kT d_0. \quad (49)$$

This expression is akin to eq. (47), except for the presence of the factor a/b , which takes into account the Burgers vector. The difference is unphysical for small Burgers vectors, but the effect of the core could be quite considerable for large b 's.

- (2) *Edge dislocation under glide.* Elementary edge dislocations involve a change in the nature of the core, from e.g., the configuration of Fig. 33(a) to that of Fig. 33(b), one of them being energetically more favorable. Glide needs breaking of layers, while climb requires diffusion or/and permeation, these latter two processes being easier in a liquid. As already stated, glide is more difficult than climb.

The foregoing considerations assume that the line is moving parallel to itself. But the glide of dislocations of small Burgers vector can also proceed by activated jumps between equivalent configurations of lower energy, along finite segments of the dislocation line (kinks of screw character). Edge dislocations with large Burgers vectors, whose core is split into two disclinations (see [1,2]), are not mobile, except

under relatively high stresses: their motion indeed involves the motion of disclinations which cannot proceed without the creation and annihilation of elementary edge dislocations, i.e., in the present case, with the exchange of such edge dislocations between the two disclinations. Finally, in lyotropics, glide could be the result of complex interactions between membranes, involving the formation of passages under stress.

- (3) *Glide of a screw dislocation; flow in the layers.* The velocity field and the layer structure of a screw dislocation moving with constant velocity perpendicular to the screw axis have been calculated by solving the hydrodynamic equations [157]: according to these results, such a motion does not involve diffusion of molecules, as long as the dislocation does not oscillate. Furthermore permeation is negligible: the molecules flow inside the layers, taking a small z -component velocity due to the screw geometry. The motion is opposed by (a) a drag force $f_{x,\text{dr}}$ of frictional origin, similar to the force exerted on a solid cylinder of radius r_c (the core radius) in a simple fluid, given by Oseen formula below, and (b) a friction force $f_{x,\text{sc}}$ specific of the screw layer structure:

$$f_{x,\text{dr}} = 4\pi\eta_\perp v(1/2 - Eu - \ln Re/4), \quad (50)$$

$$f_{x,\text{sc}} = \eta v(b/r_c)^2/4\pi, \quad (51)$$

$Eu = 0.577\dots$ is the Euler constant, $Re = \rho r_c v / \eta_\perp$ is the Reynolds number of the flow, η_\perp is the viscosity for symmetrized velocity gradient tensor components $A_{12} = 1/2(\gamma_{12} + \gamma_{21})$, A_{11}, A_{22} , $\gamma_{ij} = \partial v_i / \partial x_j$, and η is the viscosity for components A_{13}, A_{23} . The Oseen formula (and the whole theory of the motion of a screw dislocation) is valid for small Reynolds number, i.e. for rather small velocities $v < \eta_\perp r_h / \rho$. The hydrodynamic core value r_h is believed to be larger than the core radius at rest r_c .

A screw dislocation in a shear flow $\sigma_{32} = \eta\gamma$, with the shear rate $\gamma = \gamma_{23}$, experiences a PK force $f_{\text{PK}} = (b\sigma_{32}, 0, 0) = (b\eta\gamma, 0, 0)$ which is perpendicular to the shear plane $0yz$. It therefore acquires in the x -direction a velocity v obtained by balancing $F_{x,\text{PK}}$ and $f_x = f_{x,\text{dr}} + f_{x,\text{sc}}$. This velocity is rather small compared to any velocity $v_y \simeq \gamma d$ related to shear, where d is a characteristic size of the sample. In effect, the dislocation is also dragged along by the shear, while keeping anchored by its extremities to the boundaries of the sample. However, as we shall see below, this small effect can yield an important contribution to the flow.

7.5. Collective behaviour of dislocations: climb of edge lines

Consider a Grandjean wedge of angle ω . This is the kind of sample one obtains by enclosing the geometry depicted in Fig. 23(b) between two glass plates forming a wedge of the same angle. The anchoring on the plates is homotropic. A tilt boundary sits in the mid plane of the wedge, with edge dislocations separated by a distance $l = b/\alpha$. We assume that the dislocations are elementary ($b = d_0$) and that the wedge is perfect in the sense

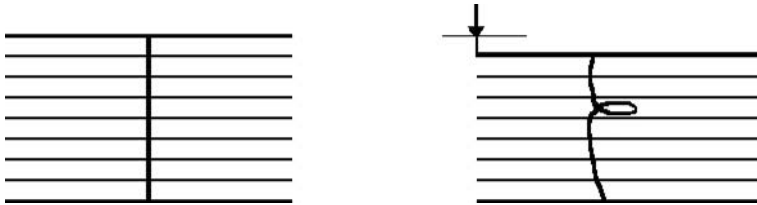


Fig. 34. Helical instability under a compressive stress.

that no other defects are present. Under the action of a compressive stress $\sigma_0 = |\sigma_{33}|$, the dislocations climb cooperatively to relax the stress, to the right of the figure. Let x be the displacement of a dislocation. This displacement relaxes the compressive stress:

$$\sigma = \sigma_0 - (B/L)\omega x. \quad (52)$$

Here L is the thickness of the sample. Because ω is so small (typically 10^{-3} rad), one can neglect the variation in thickness of the sample. Let $v = M\sigma$ be the velocity of the dislocation: $v = dx/dt$. Hence, [164]:

$$\sigma(t) = \sigma_0 \exp(-t/\tau), \quad \tau = L/MB\omega. \quad (53)$$

These equations are valid as long as the stresses are small enough and the dislocations move parallel one to another. The experiments yield measurements of σ_0 , i.e. of B ($= \sigma_0 L/d_0$) and of M , i.e., of either the coefficient of self-diffusivity or the coefficient of permeation. The temperature dependence of $M \sim \exp(-U/kT)$ yields the activation energy for the self-diffusivity [162].

At higher stresses, above some yield stress σ_c typically of the order of $10^{-5}B$, i.e., rather small, the sample shows an exponentially increasing deformation rate [165] $\gamma = \gamma_0 \exp(+t/\tau^*)$, where τ^* is no longer equal to τ , but shows a quite complex behaviour. The simplest interpretation of the exponential increase of γ with time is that the dislocation density, initially $\rho_0 = \omega/b$, increases with time.

Experimentally, in the regime below σ_c , the relaxation time τ varies by successive jumps when the applied stress is increased [166,167]. This has been explained by the onset of an *helical* instability of the screw dislocation lines, under the action of the compressive (or dilative) stress, Fig. 34. The helical shape corresponds to the removal (in compression) or addition (in dilation) of an extra layer in the area πr^2 bounded by the cylinder on which the helical line is inscribed. The larger the modulus of the strain, the smaller the pitch and the more numerous the helix turns. The chirality of the helix depends on the signs of the strain and of the Burgers vector b of the initial screw dislocation. Eventually each helix turn separates from the screw line and transforms to an edge loop, which contributes to the multiplication of the edge lines alluded to above, for $\sigma > \sigma_c$.

7.6. Collective behaviour of dislocations: motion of screw lines

A new type of steady-state behavior under shear, arising in some definite range of weak shear stresses and temperature, characterized by a power-law behaviour $\gamma = A(T)\sigma^m$ and

an exponent $m \simeq 1.67$, has been reported for lamellar phases differing widely one from the other by their molecular microstructures and their material constants. This behavior has been observed in two thermotropic LC's and two concentrated lyotropic LC's, one of surfactants, the other of block copolymers. This new behavior is attributed to the glide of screw dislocations [168].

A theoretical model, based on the theory of high-temperature creep in solids, reproduces correctly the experimental exponent of 1.67. More precisely, this model advocates that the glide of a density of screw dislocations counterbalances plastically the macroscopic vorticity due to the applied strain rate (or stress). This assumption is formally equivalent (it yields the same equation as the Orowan relation) to the usual assumption made in solids, according to which the internal stress is equal to the applied stress, at steady-state, but makes more sense in a liquid.

We consider a sample submitted to a shear stress σ_{23} . As in other places in this section, the layer normal is along the z -axis; σ_{23} is thus a force per unit area acting on the xy -plane in the y -direction. The sample is sheared in the y -direction, the yz -plane is the shear plane. Such an experiment is conveniently achieved in a cone-and-plate device: the sample is homeotropically oriented, the local y -direction is normal to the radial direction, the local x -direction is along the radial direction, the z -direction is the same all over the sample, see ref. [168]. The macroscopic shear stress σ_{23} induces in the liquid a macroscopic shear stress $\sigma_{32} = \sigma_{23}$ which in turn induces a PK force acting on the $t = (0, 0, 1)$ screw lines along the x -direction, and on the edge lines whose direction has a component $t_1 \neq 0$. The $t = (0, 1, 0)$ lines do not see the applied shear, which explains why the oily streaks, which are clusters of such edge dislocations, all align along the $(0, 1, 0)$ direction in the steady state, Fig. 35. The glide force which acts on the $t = (1, 0, 0)$ edge lines is largely ineffective (the stresses small) because glide is so difficult. In the steady state σ_{32} acts mostly upon the screws.

Assume therefore, in the spirit of high-temperature steady creep, that the applied, viscous, stresses are relaxed by the elastic stresses carried by the mobile screw dislocations. This condition can be expressed in terms of shear *rates*. The macroscopic viscous shear rate $\gamma (= \gamma_{23} = dv_2/dz)$ imposed by the applied shear stress $\sigma (= \sigma_{23})$ is ‘balanced’ by a *plastic shear rate* $\gamma_{pl} = \gamma_{32}$, due to the movement of the screw dislocations, in such a way that the total vorticity $2\omega_1 = \gamma_{32} - \gamma_{23}$ vanishes: $\omega_1 = 0$ (this is the condition of relaxation above). Thus, the total torque acting on the layers vanishes, a very beneficial result in a layered liquid, that in this way can resist layer instabilities, and stays aligned. A relationship between σ and γ_{pl} can be obtained in two steps: first one uses eq. (45) then one turns this relation into a *constitutive equation*.

The expression of the stresses for an isolated dislocation [169] is:

$$\sigma_{23} = -B(1 - \mathbf{n} \cdot \nabla \zeta)(\mathbf{n} \cdot \nabla \zeta)n_2 n_3, \quad (54)$$

where \mathbf{n} is the director (the normal to the layers) and $\zeta = z - b\theta/2\pi$ is the equation of the layers about the screw dislocation; B is the modulus of compressibility of the layers; $\mathbf{n} = \nabla \zeta / |\nabla \zeta|$.

Let x be the mean separation distance between screws. We get for instance from eq. (54):

$$\sigma_{32,int} = -(B/16\pi^3)b^3x^{-3}(1 - 1/2b^2x^2 + \dots). \quad (55)$$

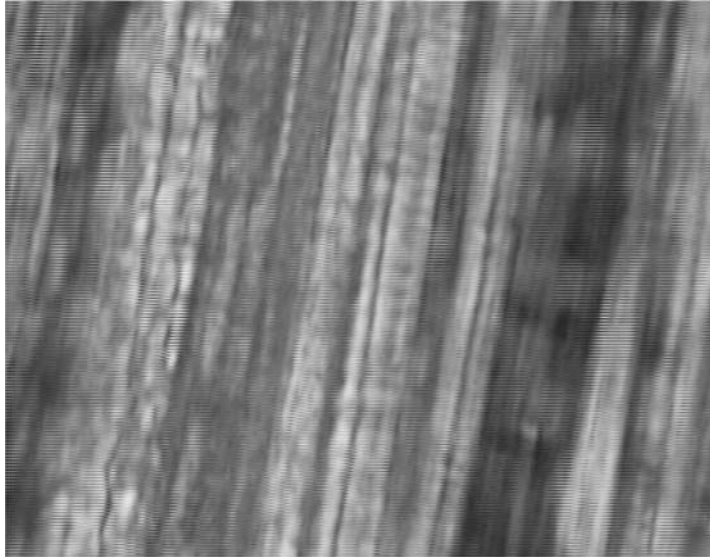


Fig. 35. Oily streaks in the direction of the shear velocity (courtesy C. Meyer).

With $\xi \simeq x$, and taking notice that b must be much smaller than x , so as that the interaction between dislocations is negligible, one sees that the stresses vary as:

$$\sigma_{32,\text{int}} = -(B/16\pi^3)b^3\xi^{-3}. \quad (56)$$

Thus, the density of dislocations reads $\xi^{-2} = 4\pi^2 B^{-2/3} b^{-2} \sigma^{2/3}$ according to eq. (56). Assuming that all the screws glide and that the $\sigma_{32,\text{int}}$ stresses comes uniquely from them, one obtains, using eq. (45):

$$\gamma \approx MB^{-2/3}b^{-1}\sigma^{5/3}. \quad (57)$$

The experimental value (1.67), obtained with different compounds, comes remarkably close to the theoretical one (5/3) of the exponent m for all the studied lamellar phases. Also, the coefficient $MB^{-2/3}b^{-1}$ is well retrieved experimentally.

8. Defects in liquid lamellar phases

8.1. Structures, order parameters

This section is devoted to lamellar phases other than SmA, namely SmC, SmC*, and SmC_A*. This list does not exhaust the *liquid*—or supposed so—lamellar phases (to which we restrict), but these are the only such materials for which there is a reasonable knowledge of their line defects. SmC* and SmC_A* have attracted a deep interest, because of

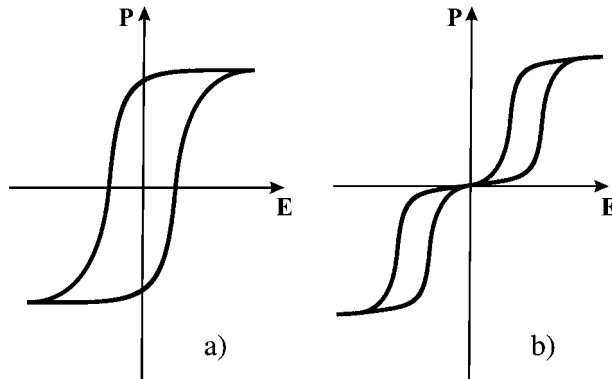


Fig. 36. Hysteresis loops for: (a) a ferroelectric LC; (b) an antiferroelectric LC.

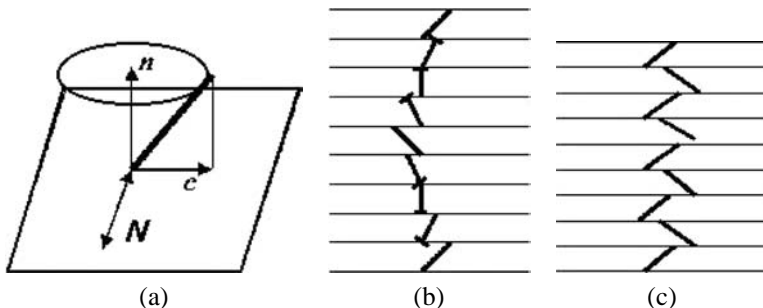
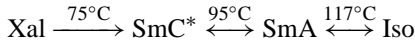


Fig. 37. (a) The c , n , N trihedron. Schematic representations of: (b) SmC^* , helicity not represented; (c) SmC_A^* , helicity not represented.

their ferroelectric (SmC^*) and antiferroelectric (SmC_A^*) properties, which prove important for switching devices [170]. SmC^* and SmC_A^* are helical phases; non-helical, non-antiferro versions of the SmC_A^* phase are indicated below. Ferro vs antiferro properties are easily discriminated with the help of a P (polarization)- E (electric field) hysteresis loop. The ferroelectric loop is much akin to the hysteresis loop of a ferromagnetic compound; the antiferroelectric loop shows two regions symmetric with respect to $E = 0$, Fig. 36.

- (1) *SmC phase*: optically biaxial. The long axis of the molecule is tilted with respect to the layer normal n . The plane containing the molecular direction v and n is a plane of symmetry. Hence, the projection c of v onto the layer is well defined; c is not a director, but a vector, c and $-c$ corresponding to opposite tilts of the molecular direction. The SmC local orientation (the OP) can be represented by the orthonormal trihedron c , n , $N = c \times n$; c and n are 2π axes of rotation, but N is a two-fold axis, Fig. 37(a).
- (2) *SmC* phase* (chiral SmC phase): this phase is *ferroelectric*; there is, on symmetry grounds, a spontaneous polarization normal to the long axis of the molecules

and parallel to the layers [171], Fig. 37(b). The first discovered compound of this type, DOBAMBC (p-decyloxybenzylidene-p'-amino-2-methylbutylcinnamate), has a small number of phase modifications:



(there is a monotropic transition which brings back the SmC* phase to the Xal phase through a SmI* phase; SmI* has short range hexagonal order). In the ground state, the spontaneous polarization averages out to zero. A rather small dc electric field ($E \cong 4 \text{ V/cm}$), applied in the plane of a free standing film of DOBAMBC, suffices to orient it, yielding a small polarization density at saturation $P_S \cong 36 \text{ esu/cm}^2$ ($\cong 12 \times 10^{-5} \text{ C/m}^2$).

The OP of a SmC* phase is described, locally, by the same orthonormal trihedron as above c , n , $N = c \times n$, where N is along the local polarization. The symmetry of the set of N vectors and of the layers is that one of a helix carrying periodically arranged marks (at a distance d_0 measured along the helix axis). There is a twofold axis passing through each mark and resting on the axis of the helix, and a twofold axis halfway between a pair of neighboring marks, whatever the incommensurability of the pitch p vs the layer thickness d_0 may be. Finally, the (commutative) product of a translation d_0 and a rotation θ_0 , noted $\{d_0, \theta_0\}$, is an element of symmetry ($2\pi/\theta_0$ is the number of layers per pitch, generally not an integer).

- (3) SmC_A^{*}: this phase is *antiferroelectric*, meaning that the spontaneous polarization alternates in sign layer-by-layer. If the molecules are tilted with respect to the layer normal, they also alternate in the sign of tilt (*anticlinicity*), Fig. 37(c). The prototype of anticlinic, antiferroelectric, molecules is MHPOBC (4-(1-methylheptyloxy-carbonyl) phenyl-4'-octyloxybiphenyl-4-carboxylate) [172] which has a rather rich sequence of layered phases:



Not all of the structures of these phases are fully understood yet, not to mention their textures and defects. Resonant X-ray scattering has shown the existence, according to the phase or the material, of 2, 3, or 4 layer superlattices [173]. Compounds of this class, whatever the phase under consideration may be, are called antiferroelectric liquid crystals (AFLC).

It is believed [170] that the polar properties play an important role in the stability of AFLC's. Most of them have a quite high value of the polarization density at saturation ($\cong 10^{-3} \text{ C/m}^2$), and a small value of the pitch, compared to FLC's (ferroelectric LC's). The OP of a SmC_A^{*} phase is the same as the OP of a SmC* phase; the twofold axes are along the polarization vectors perpendicular to the molecules, in the middle of the layers.

- (4) *Non-chiral molecules*. It is worth mentioning here two other kinds of compounds, in relation with the above compounds, either because they have similar OPs, without being chiral and/or without displaying ferroelectric properties, or because they

show ferro/antiferro properties and helical *conformations*, whereas the molecules themselves are not chiral. In the first category, we mention the SmC_A phase, made for example of a racemic mixture of AFLC's [174], the SmO phase [175,176], the SmC₂ phase [177], a dimeric LC molecule whose two moieties are linked by a flexible spacer. In the second category, we place the now most-studied bent-core shaped molecules (*banana* molecules), which have planar conformations and ferro/antiferro properties [178]. Structurally, these banana compounds are layered phases; some compounds display helical features, probably metastable. They show spectacular textures, whose investigation is still in infancy [179].

SmC and SmC* are liquid layers, and as such they rather easily form FCD's of the first type (see below). The presence of FCD's has not been investigated in SmC_A*'s, to the best of our knowledge. We shall not discuss in this review phases with 2D positional correlations in the layers (SmB, SmI, etc.). More generally, our knowledge of defects and textures in most lamellar phases has not progressed at the same pace as in SmA's. A useful monograph on textures in LC's, illustrated with many examples taken in lamellar thermotropic phases, is the book of Demus and Richter [35]. A more recent collection of photographs and comments, devoted uniquely to smectics, is ref. [180]; see also [181].

8.2. Defects in a SmC phase

8.2.1. Line defects

They can be tackled by methods inspired by the VP [29], leading to the following classification:

- (1) *Dislocations* with Burgers vector nd_0 , called d lines. There are few results in the literature; see [182] for edge dislocations (optical observations) and [183] for screw dislocations (theory). Meyer et al. [184] have made a direct observation of edge dislocations at the SmA \rightarrow SmC transition by taking advantage of the phase transition induced in the core of the defects by the internal stresses, at a slightly greater temperature than the transition temperature.
- (2) *Disclinations* corresponding to the rotational symmetries of the c, n, N trihedron, namely disclinations multiple of 2π about any direction of the trihedron, called $t(\pm 2\pi)$ lines, and disclinations multiple of π about the direction N , called $l(\pm \pi)$ lines. Disclinations multiple of 4π , noted $t(\pm 4\pi)$, can escape in the 3rd dimension.

Special $t(\pm 2\pi)$ lines are those about the n axis, called $m(\pm 2\pi)$; they affect the c field (and the N field, rendering it singular but with no physical consequence, because the N field is not materialized) but leave invariant the layers; they are very numerous in homeotropic samples, under their *wedge* avatar, forming *Schlieren* textures similar to those observed in nematics under the polarizing microscope, but with this exception that defects that carry two black brushes only are not observed between crossed polarizers, because this would be the signature of forbidden $m(\pm \pi)$ wedge lines. It is easy to figure out the *e*configuration of a $m(\pm 2\pi)$ wedge at constant n field; it is akin to the director configuration of a $k = \pm 1$ wedge

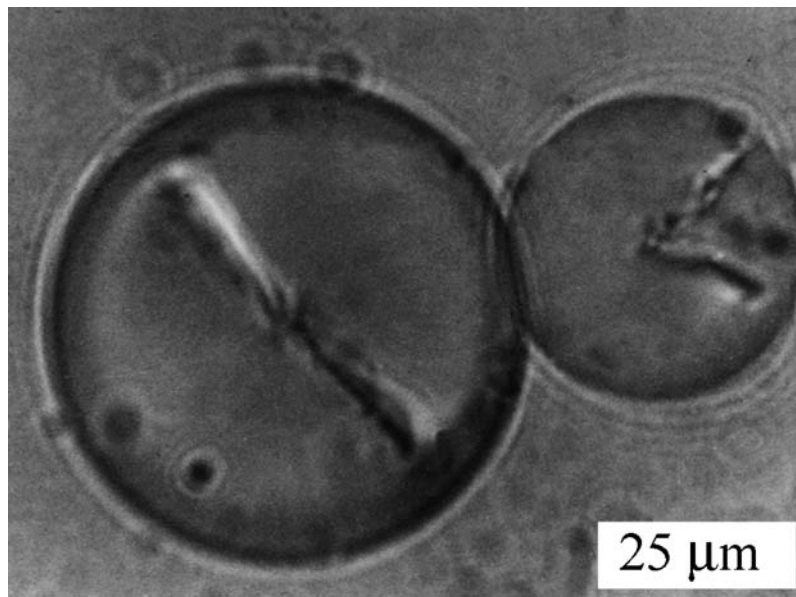
disclination in the Frank model of a nematic, and has a comparable small energy $\sim K \ln R/r_C$.

The relaxation of $t(\pm 4\pi)$ to null lines (by escape in the 3rd dimension) is akin to that mentioned in Section 2.4 for N_B 's and N^* 's and also to the dipole-locked phase of A^3He [185]. In this latter case the OP is a trihedron with all three axes of order 1 (symmetry rotations multiple of 2π). The OP space is the projective 3-plane $P^3 = SO(3)$, $\Pi_1(A^3He) \sim Z_2$; the $\pm\pi$ disclinations being not topologically stable, the non-trivial element of this group represents the $\pm 2\pi$ disclinations [186]. The SmC OP is much similar, except for the presence of the N director, which allows $\pm\pi$ disclinations; the topological classification of disclinations is then different: $\Pi_1(\text{SmC}) \sim Z_4$. The N_B or N^* OP trihedron is made of three directors, $\Pi_1(N_B) \sim Q$, the group of quaternions; $\pm 2\pi$ but also $\pm\pi$ disclinations are topologically stable, and $\pm 4\pi$ disclinations can escape in the 3rd dimension, as in the SmC phase. It is intriguing to notice how the topological classifications can be so much different—except the $\pm 4\pi$ escape, which is common to SmC, N_B (N^*), and A^3He —for phases whose OPs are so much similar. See ([13], Fig. 6.4) for an illustration of the escape of a trihedron.

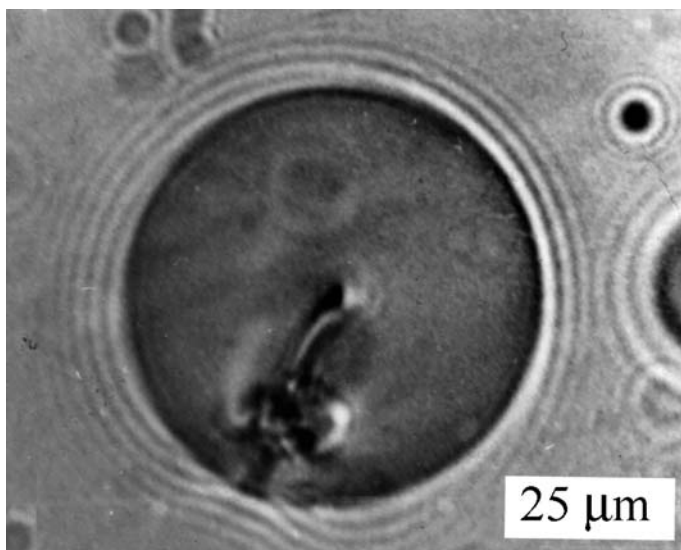
Disclinations $m(+2\pi)$ and $m(+4\pi)$ in SmC are conveniently observed in the so-called monopole structures often formed in SmC droplets suspended in an isotropic fluid. Consider first a SmA droplet-spherulite made of concentric layers. It is the energetically stable state of a SmA droplet when the surface anchoring favors normal director orientation (which happens when the fluid matrix is for example, glycerin with a small addition of lecithin). The centre is a singular disclination point, namely a radial hedgehog for the field of layer normals. If the material undergoes a $\text{SmA} \rightarrow \text{SmC}$ transition, the molecules, formerly along the normals, tilt. The field of c unit vectors tangent to the surface of any of the concentric spheres cannot be continuous; it necessarily displays, on each sphere, point singularities whose total strength is equal to the Euler characteristic of the sphere, namely $\sum_i k_i = E = 2$. This topological property—first recognized for N droplets with tangential anchoring by Harris [187] and Nabarro [188]—tells that disclination lines are necessarily attached to the centre and go through the spherulite, Fig. 38(a, b) [189]. The analogy with a Dirac monopole is often evoked, the disclinations emerging from the centre being akin to a Dirac string when they gather into a $k = 2$ line, as in Fig. 38(b).

Disclinations of the $l(\pm 2\pi)$ type affect the n field (i.e., the lamellar structure), and the c field, rendering them singular. As in SmA's (where the only affected field is the n field; there is no materialized c field); the singular ellipse lines of FCD's are defects of this type.

- (3) *FCD's.* Because the layers are liquid, one expects FCD's much similar to those in SmA's; but because the c field is a physical field (materialized), one expects some differences. The most striking one is the *broken* character of the SmC layers, corresponding to different orientation domains of the c field in a well-formed Dupin cyclide. Illustrations of broken FCD's can be found in [35, 119, 120, 180, 181]. Hence the presence of *walls* of the c field, uncoupled to the n field (the layers), of various types [190]. Furthermore, *disclination* lines appear in FCD's at the $\text{SmA} \rightarrow \text{SmC}$ transition; their role is to relax topologically the elements of symmetry that disap-



(a)

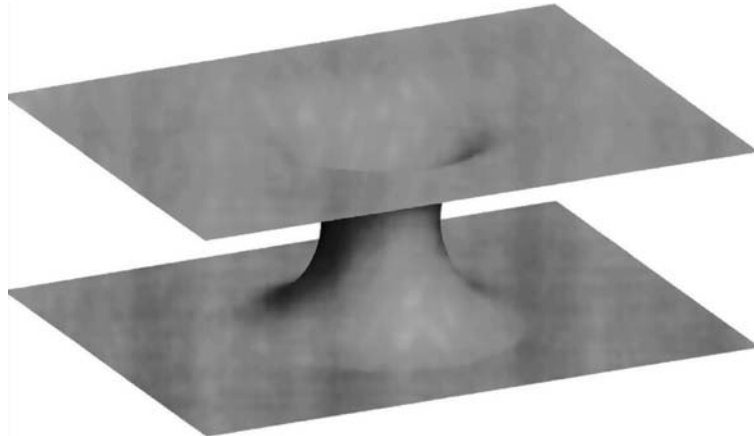


(b)

Fig. 38. Monopole structures in the SmC droplets freely suspended in glycerin-lecithin matrix with (a) two $k = 1$ disclinations and (b) one $k = 2$ disclination; modified from ref. [189]; (c) A line defect in a SmC FCD (courtesy Claire Meyer); (d) sketch of a passage between two layers.



(c)



(d)

Fig. 38. (Continued).

pear in the transition. In particular one observes a $m(-2\pi)$ line, Fig. 38(c), which links two points on the ellipse through the vertex of the hyperbola, at the focus of the ellipse (where the physical hyperbola meets the plane of the ellipse); see [118, 191] for details. These lines can be explained by a topological argument akin to the one used for the monopole structures in Fig. 38(a, b), with some modifications. The FCD Sm layers located between the ellipse and the hyperbola have the topology of parallel layers with a passage, thus have the Euler characteristic $E = -2$. Therefore any vector field drawn on such a surface contains a singular point $k = -2$ or two singular points $k = -1$.

8.2.2. Disclination points, thin films

Disclination points are not topologically allowed in a SmC, as we just discussed using the example of a spherulite undergoing a SmA–SmC phase transition, Fig. 38(a, b).

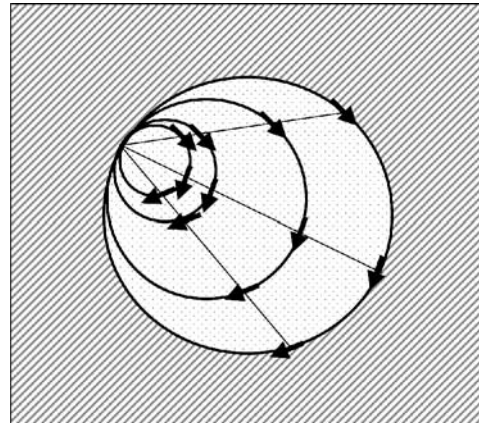


Fig. 39. Sketch of a boojum on the side of a droplet of a tilted phase in an isotropic matrix, infinite anchoring energy.

On the other hand, Sm LC's can form freely suspended films as thin as two molecular layers [12,192]. Such thin films are experimental realizations of 2D XY systems, and as such have attracted much attention. The χ -field can carry different types of defects: $k = \pm 1$ disclination points, walls, ‘swirl patterns’ [193–195], which can be observed from rather simple light microscopy experiments. The dynamics of disclination points in SmC and SmC* films has been theoretically studied [196,197]; leading to the prediction of the Brownian nature of their motion. The experiments of [195] yield values of the disclination point diffusion constant in fair agreement with Pleiner’s predictions [194].

When the XY phase nucleates in an isotropic matrix, a 2D boojum pattern might appear, in which the in-plane molecular orientation turns continuously and molecules with the same orientation are located on straight lines, crossing at a defect point expelled from the drop. This remarkable texture, sketched Fig. 39, has been observed at the coexistence between drops of the tilted condensed phase L₂ (a surfactant analog of SmC) and the gaseous phase of palmitic acid in a Langmuir monolayer at the air–water interface [198]. The boojum is most generally virtual, being expelled from the droplet. Its distance to the boundary and the eventual shape of the droplet result of course from a competition between the anchoring strength, which favors alignment of the c director parallel to the boundary, and the inner elastic energy of deformation. The smaller the anchoring strength, the larger is the distance of the expulsion point (in Fig. 39, this distance is vanishingly small). The ingredients of a full calculation, which classifies the droplets shapes and inner structures in function of the material constants, can be found in [199].

8.3. Defects in a SmC* phase

8.3.1. Line defects

- (1) *Disclinations.* The local SmC* trihedron has the same OP properties as the SmC trihedron; we thus expect the same types of topologically stable disclinations as in a

SmC. However, \mathbf{N} being along the local polarization, \mathbf{P} is materialized physically, so that its singularities do import; also, space charges due to the spontaneous polarization $\rho = -\text{div } \mathbf{P}$ have to be taken into account. Situations where these charges are, on average, zero, are favored.

- (2) *Surface stabilized ferroelectric liquid crystals (SSFLC).* If the specimen is introduced between two glass plates with a strong planar anchoring, a non-twisted region forms near the boundaries, which in sufficiently thick samples is separated from the helicoidally twisted bulk by a lattice of pairs of line defects (often called dechiralization lines) that affects the molecular distribution but not the layer distribution. The layers keep perpendicular to the boundaries (*bookshelf* texture). Two such geometries have been investigated, with parallel planar anchoring on the two boundaries—the Brunet–Williams (BW) geometry [200,201], and with antiparallel planar anchoring—the Glogarova–Pavel (GP) geometry [202], see Fig. 40. See [203,204] for another type of disclination (inversion line), which appears when the layers are tilted with respect to the boundary (*chevron* layer texture).

In the BW and GP geometries, the defects can be thought of as $m(\pm 2\pi)$ *twist* disclinations. A great attention has been given to these types of samples, because under an electric field they can be unwound completely with a high-speed response time [205]. In that process the disclinations move and eventually disappear at the boundaries, if the anchoring is not too strong.

The free energy density contains \mathbf{c} -curvature and dipolar contributions, to which one has to add a surface anchoring energy; there is no strain contribution. Consider first the terms of curvature; they read, assuming isotropic elasticity in the layer planes ($B_1 = B_2$):

$$f = 1/2B_1(\partial\phi/\partial x + \partial\phi/\partial y)^2 + 1/2B_3(\partial\phi/\partial z - q)^2. \quad (58)$$

ϕ is the angle of \mathbf{c} with a fixed direction in the x – y plane, $q = 2\pi/p$ the inverse pitch in the ground state, B_1 and B_3 are curvature moduli. The general solution of eq. (58) is given in [206].

We consider first the simple case of an infinite straight line defect in the middle plane of the sample, assuming infinite anchoring [207], Fig. 41. Such a geometry occurs for SSFLC's cells which are thin enough (h , the sample thickness, comparable to the pitch). It can then be shown that the line energy W_{curv} is the smallest when the line is along the layers, if $B_1 > B_3$ (this is the condition that one meets in practice [190]).

$$W_{\text{curv}} = -\pi[B_1B_3]^{1/2}\ln|\sin(\pi r_C/h)| \simeq \pi[B_1B_3]^{1/2}\ln(R/r_C), \quad (59)$$

if $h \gg r_C$, the core size; $R \sim h$ is a typical distance between disclinations.

Pushing the disclination towards the boundary with an appropriate electric field, one observes that the core of a disclination segment attached to a boundary is split into two partial disclinations $\pm\pi$ separated by a well defined ribbon whose width depend on the material constants, among them, necessarily,

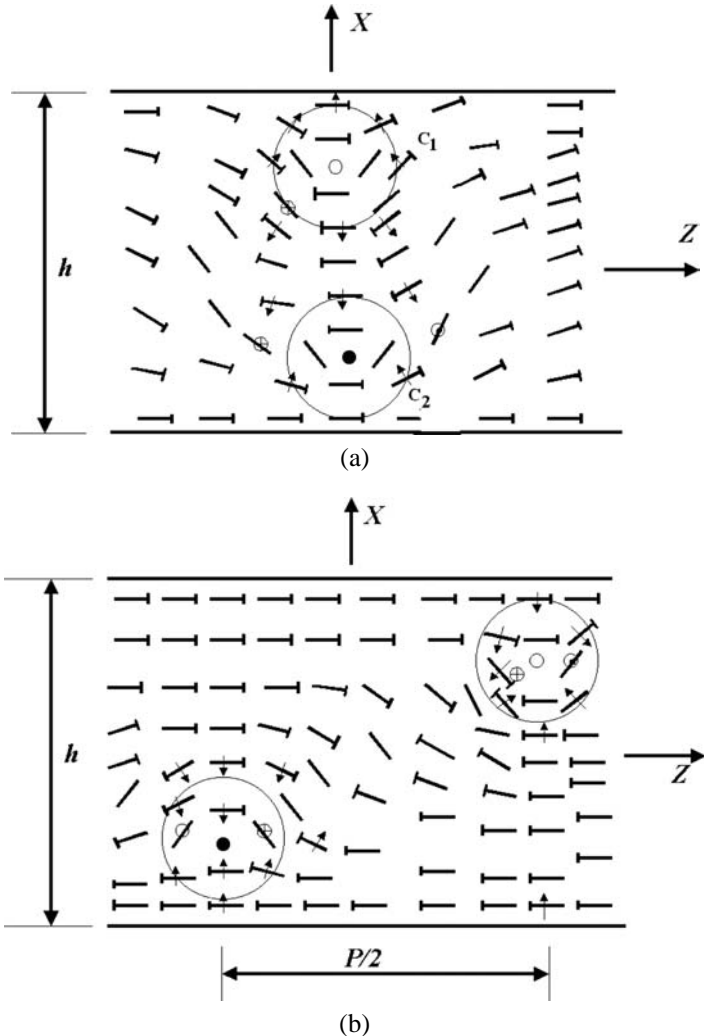


Fig. 40. Models for SSFLC's; (a) the BW geometry; (b) the GP geometry.

an (actually finite) anchoring energy $w_S(\phi_S)$; ϕ_S is the angular position of c at the boundary. This type of splitting is reminiscent of the Shockley bimodal splitting ([15], p. 211), further analysed into infinitesimal dislocations as in the Peierls–Nabarro model of a dislocation in a solid [15]. Observe that the PN model has been employed in the study of the core width of nematic disclinations attached to a boundary [208]; the same approach yields here the equation:

$$-\frac{dw_S(z)}{d\phi_S} = [(B_1 B_3)^{1/2}/\pi] \int d\phi_S(z')/(z - z'), \quad (60)$$

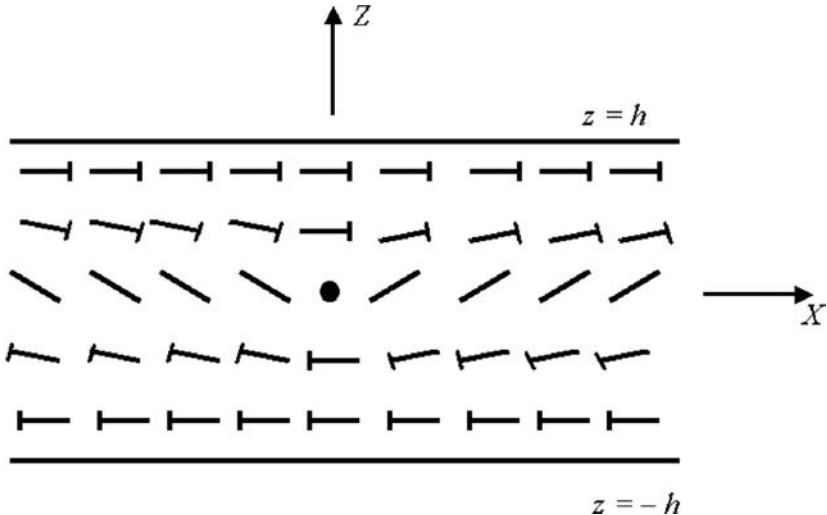


Fig. 41. Twist disclination line in the middle of a SSFLC; GP antiparallel boundary orientations, infinite anchoring.

which expresses the balance of the torque due to the molecular twist deformation acting on the interface vs the torque due to the anchoring. A well known result of the PN model is that the energy of the split core does not depend on the explicit form of $w_S(\phi_S)$; here we get:

$$W_S = 2\pi(B_1 B_3)^{1/2}. \quad (61)$$

The surface energy functional $w_S(\phi_S)$ can be estimated by taking a $\phi_S(z)$ susceptible to describe a realistic splitting of the core, with $\pm\pi$ disclinations at $+z_0$ and $-z_0$ for example

$$\phi_S(z) = \arctan[(z - z_0)/\xi_\pi] + \arctan[(z + z_0)/\xi_\pi]. \quad (62)$$

The quantities $2z_0$ and ξ_π (the π disclination core) can in principle be measured (at least estimated) on the photographs. The theory relates them to the relative minimum w_S^m of w_S , which is reached in the ribbon between the partials, and the maximum w_S^M of w_S , which is reached at the core of the partials, Fig. 42. One gets $2w_S^m \simeq \pi(B_1 B_3)^{1/2}/z_0$, $2w_S^M \simeq (B_1 B_3)^{1/2}/\xi_\pi$.

When the polarization at saturation P_S is large, typically > 100 nC/m², as in AFLC's, the electrostatic effects dominate over the curvature elasticity [74]. In this case the only possibility to eliminate $\operatorname{div} P_S \neq 0$ can be the elimination of *twist* disclinations, if the space charges are not screened by free

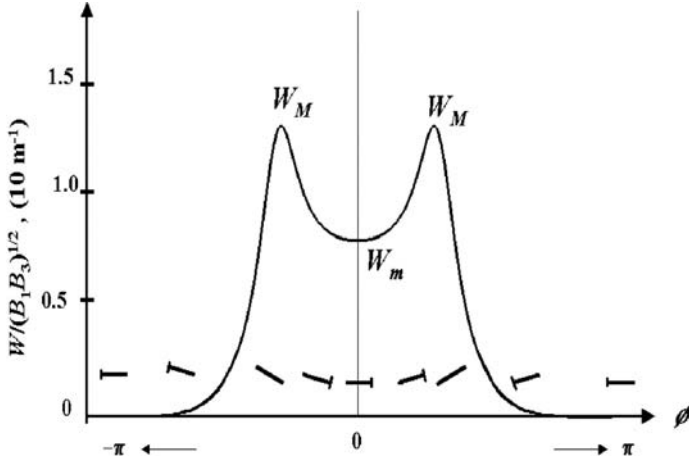


Fig. 42. Schematic profile of the anchoring energy $w_S(\phi_S)$ in the extended core of a $m(2\pi)$. Adapted from [207].

charges. The charge Q per unit length of a twist disclination of length Λ reads [210]:

$$Q = -4g\Delta_{\text{pol}}P_S R, \quad (63)$$

g is some function of B_3/B_1 only. Assuming that all the charges are concentrated on the line, the electrostatic self-energy is:

$$W_{\text{elec}} = 1/2(Q^2/4\pi\varepsilon_0)\ln[\Lambda/r_0]. \quad (64)$$

In these formulae Δ_{pol} , the *depolarization factor*, is an ad hoc coefficient which vanishes if the space charges are completely screened, and is equal to unity if they are not at all screened. Δ_{pol} is not known accurately but is estimated to be a few hundredths in most samples. Such small values are however sufficient to make W_{elec} and W_{curv} comparable for sizes as small as $R \cong 1 \mu\text{m}$, in a specimen with $P_S \cong 10^{-3} \text{ C/m}^2$, $B_1 \cong 10^{-11} \text{ N}$, $(B_3/B_1)^2 \cong 0.1$. Therefore, W_{elec} and W_{curv} are, in usual samples, at least comparable. The interaction energies $W_{\text{int,elec}}$ and $W_{\text{int,curv}}$ are then also comparable.

Ref. [211] discusses BW and GP arrays of $m(\pm 2\pi)$ twist disclinations. In the BW configuration, disclinations of opposite topological charge also have opposite space charge; there is therefore a critical thickness h_C ($\cong p/(4B_3/B_1)^{1/2}$) above which the array of dechiralization lines is stable, but below, where they just assemble in the middle of the sample; h_C is predicted to be appreciably larger than the pitch, which is verified. In the GP configuration, disclinations of opposite topological charge have the same space charge; when the electrostatic term overcomes the curvature term, the disclinations are pushed towards the boundary, and the anchoring contribution becomes important.

(3) *Dislocations and dispirations.* The $\{d_0, \theta_0\}$ invariance yields mixed translation-rotation line defects, called *dispirations*, first introduced by Harris [212]. A dispiration in a SmC* is either a wedge-screw line or a twist-edge line, whichever is appropriate. More complex geometries are topologically possible, but less probable. Therefore, there are no dislocations of translation *sensu strictu*, in a SmC*, except if the pitch and the lamellar thickness are commensurate. However, θ_0 is so small (p is large, typically a few μm ; $\theta_0 = d_0/p$) that one can neglect in a first approximation the θ_0 component in the analysis of the defects. Reciprocally the dislocations which have often been observed in SSFLC's, and which are a nuisance for high-speed display panels, are in fact dispirations. Forgetting for a while the θ_0 component, in the line of [213], one can see that there is a strong interaction between a 2π ($k = \pm 1$) m wedge line and a screw dislocation—in the case of a wedge-screw dispiration; between a $2\pi m$ twist line and an edge dislocation—in the case of a twist-edge dispiration. Ref. [213] illustrates the wedge-screw case, assuming that the \mathbf{P} field rotates about the core of the screw along a helical path, by an angle $\pm 2\pi$ (in fact $\pm 2\pi \pm \theta_0$) for each turn of the dislocation; a possible choice is the *double-twisted* configuration:

$$\mathbf{P} = P_S \{-y, x, b/2\pi\}/N, \quad (65)$$

$N = (x^2 + y^2 + (p/2\pi)^2)^{1/2}$ being a normalisation factor. This configuration has three advantages: (i) its integral lines are helices which can be scribed on a set of helicoidal layers about the dispiration line, and whose pitch is equal to the Burgers vector, (ii) the \mathbf{P} field is non-singular, (iii) the space charges $\text{div } \mathbf{P}$ vanish. Because the optical contrast of non-singular $k = \pm 1$ disclination in polarizing microscopy is the same as a thick in a nematic, the dislocations (dispirations) are made visible. As shown in [193–195], the disclination configuration attached to the screw dislocation is modified under the action of an electric field, whereas the dislocation does not move. More observations are certainly needed, and a complete theory that would take the θ_0 term into account is still wanting.

8.3.2. Other types of defects

For the same reason as in SmC's, there are no topologically stable points in SmC*. Again, free suspended thin films have attracted attention. The boojum texture alluded to in Section 8.2.2 for SmC's was in fact first observed in a chiral compound, HOBACPC [$R(-)$ -hexyloxybenzylidene p' -amino-2-chloropropyl cinnamate], with a phase transition between a SmC* and a SmI* phase; SmI* droplets nucleate in the SmC* film under cooling. Another texture appearing in the same conditions, when the droplets merge, is made of parallel stripes. We refer the reader to refs [214,215] for a full discussion of these textures. Polar Sm films obtained by wetting the SmC* film with a liquid also exhibit interesting defects of boojum and spiraling types [216].

8.4. Defects in a SmC_A^{*} phase

Disclinations in a SmC_A^{*} phase are not different from those in the SmC^{*} phase, the trihedron OP being the same; in particular, one expects $m(\pm 2\pi)$ lines. The surface stabilized antiferroelectric liquid crystal (SSAFLC) bookshelf geometries have been much studied from that point of view. According to [217], they differ from the previous SSFLC geometries by the nature of the anchoring energy, which can be written, \mathbf{v} being the normal to the boundary

$$F_S = -\gamma_1(\mathbf{v} \cdot \mathbf{P})^2 - \gamma_2(\mathbf{v} \cdot \mathbf{P}) - \gamma_3(\mathbf{v} \cdot \mathbf{A})^2, \quad (66)$$

\mathbf{A} is a vector describing the anti ferroelectric character. The presence of an important γ_3 term favors the splitting of the core on the boundaries. We refer the reader to ref. [217] for details.

An interesting novelty comes from the existence in SmC_A^{*} (or SmC_A) structures of simultaneous symmetry operations of the type $\{d_0, \mathbf{P} \rightarrow -\mathbf{P}\}$, where d_0 is the layer thickness, which is half the repeat distance of the \mathbf{P} modulation. The SmC_A^{*} phase is also left invariant by the simultaneous operations $\{2d_0, \theta_0\}$, $\theta_0 = 2d_0/p$, which are akin to the $\{d_0, \theta_0\}$ symmetry operations of the SmC^{*} phase, the essential difference being that the repeat distance of the modulation is now $2d_0$. There are therefore *two* types of dispirations in a SmC_A^{*} phase, and only one in a SmC_A, but much different from that one met in the SmC^{*} phase. We do not discuss the $\{2d_0, \theta_0\}$ dispiration, because nothing new is expected if compared to the $\{d_0, \theta_0\}$ dispiration.

The $\{d_0, \mathbf{P} \rightarrow -\mathbf{P}\}$ dispiration is a remarkable object which binds together m ($\pm\pi$) partial disclinations and $\pm d_0$ partial dislocations. As stressed by Takanishi et al. [218] the topological possibility of dispirations with a large rotation component provides a simple method to characterize the AFLC structure. These authors have observed that the Schlieren textures of the racemic AFLC compound TFMHPDOPB, and of the BB9 compound (a dimeric molecule ordering into a SmC₂ phase; see also [219]) exhibit, apart the expected $k = \pm 1$ defects, many $k = \pm 1/2$ defects. They disappear at the AF SmC_A \rightarrow SmC phase transition (BB9 has no SmC phase).

In a Schlieren texture, the dispirations are wedge-screw dispirations, but wedge-screw dispirations of opposite signs can be linked by twist-edge dispirations, which are quite visible as horizontal lines under the optical microscope [220]. Finally, [221], a number of situations display closely located π and 2π wedge disclinations of the same sign (hence 3π altogether, six brushes under the polarizing microscope), the whole set being inevitably associated with a screw dislocation set, probably a d_0 attached to the π wedge.

We know of only one investigation, ref. [222], of dislocations in a chiral SmC_A^{*} phase, the C8-tolane. These are edge dislocations of Burgers vector d_0 in a Grandjean wedge, visualized over the entire temperature range by employing the phenomenon of selective reflection of circularly polarized light. The authors have in fact used the same technique to observe defects for all the helical phases shown by this compound and some others.

The energy stability of dispirations in AFLC's has been much investigated by the Prague group [223–225]. Let us indicate the essential results of this theory. Observe first that, on topological grounds, wedge disclinations of opposite signs ($+\pi, -\pi$) couple equally well

with the same d_0 ; conversely, screw dislocations of opposite helicities couple topologically equally well with the same partial disclination. This does not mean that such pair of objects are physically equivalent. For example, it is claimed in ref. [223] that the $\{\pm\pi, b\}$ and $\{\pm\pi, -b\}$ wedge-screw dispirations in chiral materials do not have the same energy, due to the presence of elastic moduli of opposite signs relating to chirality. On the other hand, in the SmO phase [224], which is not chiral, there is an intriguing term of interaction between the two elements of the dispiration which favors $\{-\pi, b\}$ wedge-screw dispirations—i.e., the $k = -1/2$ configuration—against $\{+\pi, b\}$, whatever the sign of b may be. Of course, this term is also present in chiral phases. The interaction of a $\{\pm\pi, b\}$ with a 2π disclination, alluded to above, depends on the sign of the Burgers vector $|b| = d_0$. For a given sign of some elastic modulus, the dispiration $\{\pm\pi, b\}$ and the disclination $\pm 2\pi$ attract each other, as observed in [221], while the dispiration $\{\pm\pi, -b\}$ and the disclination $\pm 2\pi$ repel each other. The opposite would happen for the opposite sign. On the other hand, pairs of the type $\{[\pm\pi, b]; \mp 2\pi\}$ would always attract, yielding a $\{\mp\pi, b\}$ dispiration. Twist-edge dispirations are considered in [225]. All together, it appears that the question of dispirations in materials of the SmC_A type, chiral and non-chiral, is a rich and open question, which certainly deserves more experiments and theoretical work.

9. Defects in cholesteric liquid crystals (N^*)

In the ground state of a N^* phase made of chiral molecules the local director \mathbf{n} is twisted into a helix. The spatial scale of background deformations, e.g., the pitch p of the helix, is normally much larger than intermolecular distances ($p > 0.1 \mu\text{m}$) since the interactions that break the inversion symmetry are weak. Properties of defects and deformations that occur at scales smaller than p and larger than p are quite different. As a result, two complementary approaches are used to describe distortions in weakly twisted cholesterics ($L/p \ll 1$) and in strongly twisted ($L/p \gg 1$) cholesterics. In the second limit, one uses the coarse-grained model that describes the cholesteric liquid crystal as a lamellar phase. Experimentally, it is often much easier to study deformations in cholesterics rather than in regular lamellar phases such as SmA, as p is often of the orders of a few microns and each cholesteric “lamella” can be visualized by optical means.

9.1. Elastic description

9.1.1. Weakly twisted cholesterics

In the absence of external fields or bounding surfaces, the director of the uniaxial cholesteric phase is helically twisted to minimize the elastic free energy density

$$f = 1/2K_{11}(\operatorname{div} \mathbf{n})^2 + 1/2K_{22}(\mathbf{n} \times \operatorname{curl} \mathbf{n} + q_0)^2 + 1/2K_{33}(\mathbf{n} \times \operatorname{curl} \mathbf{n})^2 - K_{24}\operatorname{div}(\mathbf{n} \operatorname{div} \mathbf{n} + \mathbf{n} \times \operatorname{curl} \mathbf{n}), \quad (67)$$

where $q_0 = 2\pi/p$.

When $L/p \ll 1$, the cholesteric does not differ much from the nematic phase. No wonder therefore that optical observations for weakly twisted cholesterics reveals ‘thick’ (non-singular) and ‘thin’ (singular) line defects—disclinations similar to those of the nematic phase. Moreover, in droplets of the so-called ‘compensated’ cholesteric mixtures with extremely small L/p , one can observe point defects [226] that, from the topological point of view, are allowed only in a uniaxial nematic phase.

The behavior of weakly twisted structures depends on the relative values of the elastic constants in eq. (67). As the twist-constant K_{22} is significantly smaller (a factor of 2 or so) than K_{11} and K_{33} for many materials, splay and bend distortions are often relaxed by twist. Importantly, twist distortions (and hence helicity and its related optical activity) might occur as an equilibrium state of the liquid crystalline system even if the molecules are non-chiral (or the system contains an even amount of left-handed and right-handed isomers). For example, a spherical nematic droplet in which the director is forced to be parallel to the boundary by the so-called surface anchoring, readily adopts a twisted structure despite the fact that neither the liquid crystal nor the matrix in which the droplet is suspended are chiral [44]. A similar director twist appears in sessile nematic droplets [227].

9.1.2. Strongly twisted cholesterics

At $L/p \gg 1$, N^* elastic properties are close to those of the lamellar phases. Here again, two different situations are possible. When the layer deviations from the flat geometry are substantial, the deformations are characterized by the principal curvatures of the N^* layers and the elastic free energy can be cast in the form of eq. (21) already discussed for SmA.

However, the cholesteric layers might be only slightly bent and preserve the topology of flat surfaces. These small deformations can be described by a single scalar variable, the component of the displacement u of the layers along the normal of the nonperturbed layers, taken as the z -axis. The free energy density in terms of the layer dilatation and small tilts writes

$$f = 1/2K(\partial^2 u / \partial x^2)^2 + 1/2B[\partial u / \partial z - 1/2(\partial u / \partial x)^2]^2, \quad (68)$$

the elastic constants B and K (the later describes the splay of the cholesteric axis) are related to the Frank elastic constants of twist and bend: $B = K_{22}q_0^2$ and $K = 3K_{33}/8$, according to the coarse-grain model of de Gennes and Lubensky [34].

9.2. Disclinations λ , τ , and χ

According to the orientation of the line defect with respect to the direction of the broken rotation, one distinguishes wedge disclinations, which are parallel to the broken rotation, twist disclinations, which are perpendicular to it, and mixed disclinations. A defect which makes singular the two sets of directors, τ and χ , but leaves continuous the λ field, is called a ‘ λ disclination’. Such a situation is pictured in Fig. 43(a) for a wedge disclination of strength $k = -1/2$, featuring a breaking of symmetry of angle $2\pi|k| = \pi$ for the χ and τ vector fields (both rotate by an angle of π when traversing a loop surrounding the disclination). Consequently there is some place inside the loop where χ and τ directors

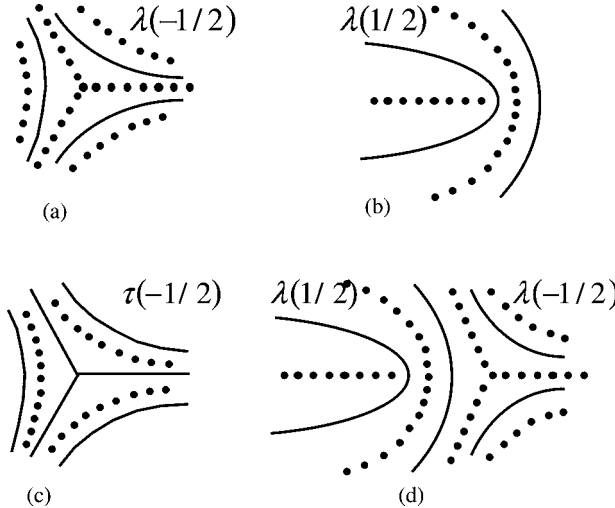


Fig. 43. Disclinations in a cholesteric liquid crystal: (a) λ^- ; (b) λ^+ ; (c) τ^- ; (d) $\lambda^- \lambda^+$ pair.

are not defined and where the defect line is located. This disclination is noted λ^- . The λ^+ line, of opposite strength $k = +1/2$, is shown in Fig. 43(b). Fig. 43(c) pictures a τ^- , i.e. a wedge line of strength $k = -1/2$, singular for the χ and λ fields and continuous for the τ field. A λ^- can be annihilated by a collapse with a λ^+ . One can also feature χ lines, i.e. disclination lines that preserve the continuity of the χ -field; in fact, χ lines are directly related to dislocations and will be discussed separately.

Is it possible to extend the concept of *escape in the third dimension*, which is well understood in nematics, to these results, which are reminiscent of lines in nematics? The answer is negative for a λ^{2+} ($k = 1$), Fig. 43(d), which cannot be made continuous for the two fields τ and χ simultaneously. The same result holds for a τ^{2+} or a χ^{2+} . On the other hand λ^{4+} , τ^{4+} and χ^{4+} ($k = 2$) defects can be made entirely continuous. More generally, any line χ , λ , or τ with a strength $k = 2m$, where m is an integer, can be made non-singular by escape in the third dimension. This result can be fully justified in the frame of the topological theory of defects, see Section 2.4.

Fig. 44(a) pictures a χ^+ wedge disclination (the χ field is continuous, while λ and τ both rotate by π about the defect). The same object can as well be considered as a *screw dislocation*, since a π -rotation along the χ axis and a $p/2$ -translation along the same axis add up to the same operation of symmetry. In the final configuration each cholesteric plane yields a 2D $k = 1/2$, Fig. 44(a), whose configuration rotates helically along the χ line with a pitch p , the resulting Burgers vector is $b = -p/2$. Fig. 44(b) extends to *edge dislocations vs twist χ disclinations* the equivalence just demonstrated between screw dislocations and χ disclinations. Dislocations and χ -disclinations are equivalent, whatever the shape of the line. In the general case, one gets:

$$b = -kp. \quad (69)$$

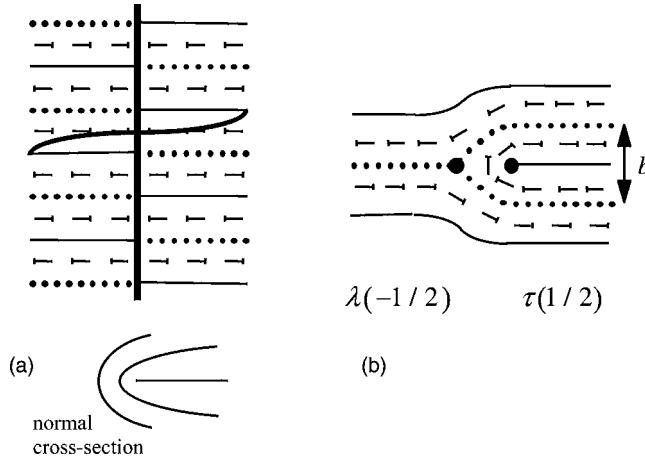


Fig. 44. Disclinations of the χ type: (a) wedge disclination (or screw dislocation); (b) twist disclination (or edge dislocation).

Table 1

Correspondence between the Volterra (λ , τ , and χ) classification and the topological classification of defect lines in cholesteric liquid crystals (m is an integer).

C_1	\bar{C}_J	$C_\lambda (= C_X)$	$C_\tau (= C_Y)$	$C_\chi (= C_Z)$
$\lambda(2m)$	$\lambda(2m+1)$	$\lambda(m+1/2)$		
$\tau(2m)$	$\tau(2m+1)$		$\tau(m+1/2)$	
$\chi(2m) \equiv$ $\{b = -2mp\}$	$\chi(2m+1) \equiv$ $\{b = -(2m+1)p\}$			$\chi(m+1/2) \equiv$ $\{b = -(m+1/2)p\}$

As already repeatedly stressed, distorted cholesteric liquid crystals at large scales can be described as any other 1D periodic lamellar system, eq. (21). On the other hand, the macroscopic period of cholesterics (microns) make it possible to directly analyze the structural features of the defects. Therefore, cholesterics offer a unique opportunity for experimental testing of 1D periodic media elastic models. One example is the layer configurations around an elementary edge dislocation (far away from the core region) that we consider in detail below.

Table 1 summarizes the various types of defects in N^* , classified by the classes of conjugacy of the group of quaternions.

9.3. Linear and non-linear elastic models of edge dislocations in a 1D periodic structure

The first solution for the edge dislocation in a 1D periodic system has been suggested by de Gennes [228] within the framework of a linear theory, in which the compressibility term is just $1/2B(\partial u/\partial z)^2$, and the corresponding Euler–Lagrange equation is $\lambda^2\partial^4 u/\partial x^4 - \partial^2 u/\partial z^2 = 0$; here λ is the elastic penetration length (not to be confused with the notation

for the local director and a non-singular disclination). Let the edge dislocation be centered at $(x, z) = (0, 0)$. The solution that satisfies the boundary conditions $u(x < 0, z = +0) = 0$ and $u(x > 0, z = +0) = b/2$ —we consider the upper half-plane $z > 0$ only, thanks to the symmetry $u(z) = -u(-z)$, is

$$u(x, z) = \frac{b}{4} \left[1 + \operatorname{erf}\left(\frac{x}{2\sqrt{\lambda z}}\right) \right], \quad (70)$$

where $\operatorname{erf}(\dots)$ is the error function. The tilt of the layers around the dislocation,

$$\theta(x, z) = \frac{\partial u}{\partial x} = \frac{b}{4\sqrt{\pi\lambda z}} \exp\left(-\frac{x^2}{4\lambda z}\right), \quad (71)$$

is significantly different from zero only inside the parabola $x^2 = 4\lambda z$. Within this parabola, the tilt decreases slowly with z and rapidly with x . The inflection points of the curved layers are located exactly at the z -axis.

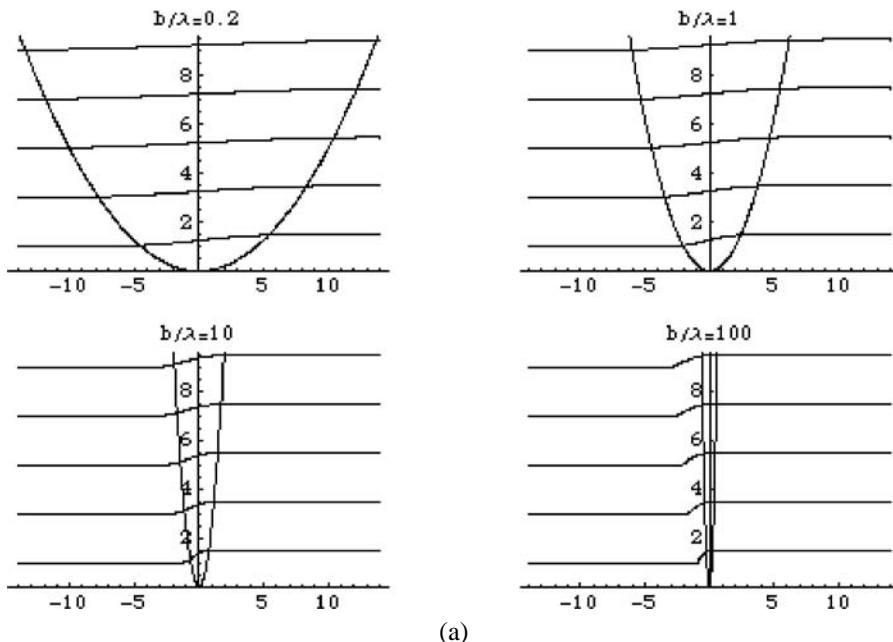
The results (70, 71) of the linear theory are valid only if the non-linear contribution is negligible, i.e., $(\partial u / \partial z)^2 \ll |\partial u / \partial z|$. Within the parabola $x^2 = 4\lambda z$, one estimates $(\partial u / \partial z)^2 / |\partial u / \partial z| \sim b/\lambda$. Therefore, the linear theory is justified only for the materials with $b \ll \lambda$, which means that in the best case only defects with a small Burgers vectors can be satisfactorily modeled. Fortunately, as shown recently by Brener and Marchenko [229], the non-linear model of the edge dislocation is tractable, and the general expression for an edge dislocation in a lamellar phase is of the form

$$u(x, z) = 2\lambda \ln \left\{ 1 + \frac{\exp(b/4\lambda) - 1}{2} \left[1 + \operatorname{erf}\left(\frac{x}{2\sqrt{\lambda z}}\right) \right] \right\}, \quad (72)$$

eq. (72) reduces to the result of the linear model when $b \ll \lambda$. Fig. 45 shows how the last solution depends on the ratio b/λ .

As seen in Fig. 45, the main difference between the linear and nonlinear models is the asymmetry of the dislocation profile. In the linear theory, the displacement field is symmetric with the points of inflection at $x = 0$. The non-linear theory predicts that the inflection points are located at $x < 0$ and that the displacement changes mainly in the region of negative x . If b/λ becomes very large, the dislocation profile transforms dramatically, see the plots labeled $b/\lambda = 100$ in Fig. 45. The structure of the dislocation becomes more and more similar to the special model of a dislocation proposed in ([13], Fig. 5.25), for the case $b \ll \lambda$. The model allows the layers to bend but not to change their thickness; the only exception is a parabolic singular wall ending at the dislocation core, which can be considered as the limiting case of the set of inflection points in Brener–Marchenko solution.

Experimental quantitative verifications of edge dislocation profiles in 1D periodic media are scarce. Maaloum et al. [230] used atomic force scanning microscopy to study the free surface profile of a smectic copolymer domain deposited onto a silicon wafer surface. However, the pattern of layers is strongly influenced by the free surface tension [231], which is itself a subject of investigation [232]. The first experimental veri-

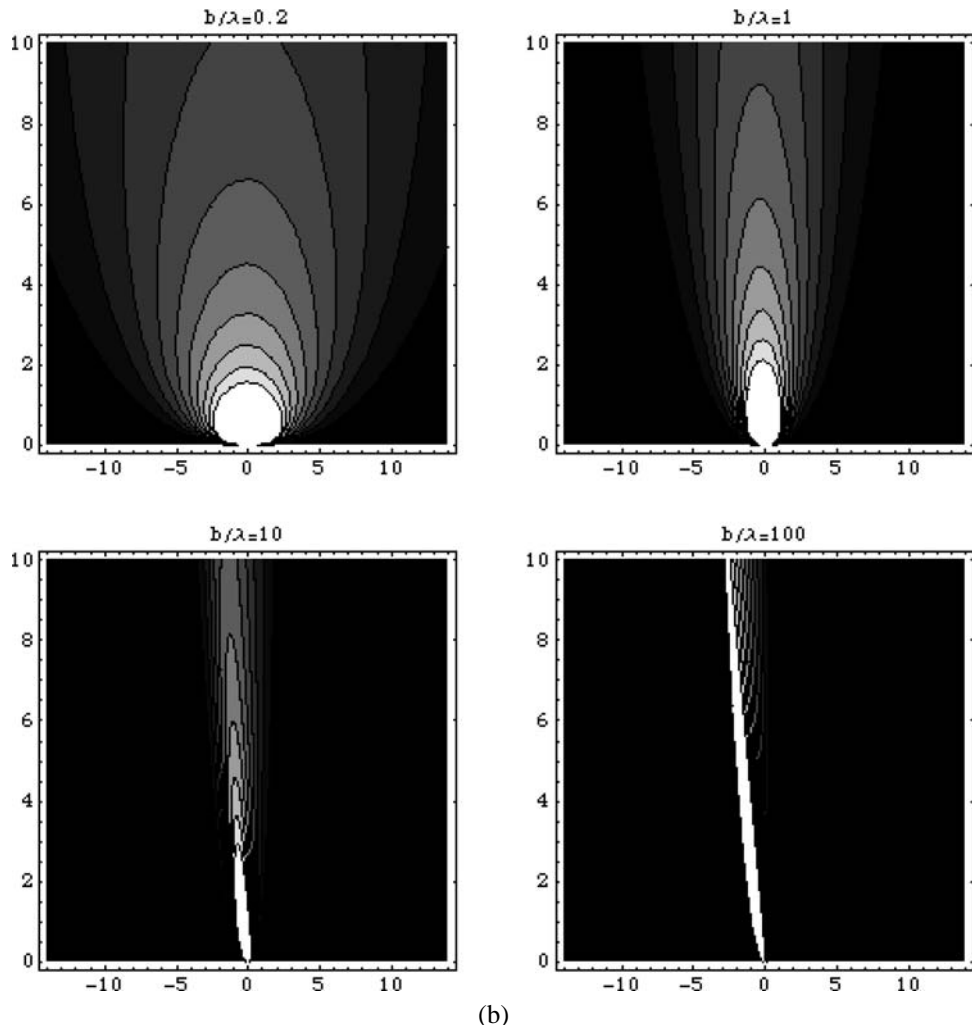


(a)

Fig. 45. Properties of the edge dislocation according to the non-linear Brener–Marchenko model eq. (72), as a function of the ratio b/λ : (a) layers profile; (b) contour plots of layers tilt; (c) dilations/compressions of the layers $\partial u/\partial z - 1/2(\partial u/\partial x)^2$, or, equivalently, the curvature-related quantity $\lambda\partial^2 u/\partial x^2$.

fication of the dislocation profile in the bulk was performed for large ‘fingerprint’ samples of cholesteric liquid crystals, specially prepared to eliminate the influence of surface anchoring on the layers profile around the dislocation [233], Fig. 46. In the experiment, the cell plates were treated with a homeotropic alignment layer, which sets perpendicular director orientation, so that the cholesteric axis is in the plane of the sample. The preferred layer orientation around the dislocations is achieved by a uniform magnetic field; however, the measurements of the dislocation profile are performed when the field is removed.

The results [233] clearly demonstrate that the dislocation profile is well described by the non-linear theory, eq. (72). It comes as a little surprise, as the coarse-grained cholesteric model predicts that the elastic length λ is smaller than the cholesteric pitch p . Really, as $\lambda/p = (K/B)^{1/2}/p = 1/2\pi(3K_{33}/8K_{22})^{1/2}$, the values $\lambda/p \sim 0.1–0.3$ should be considered typical. In fact, the ratio λ/p can be determined experimentally by fitting the experimental profile of an edge dislocation; $\lambda/p \sim 0.18$ has been reported in ref. [233]. Note here that in the geometry of the fingerprint texture with homeotropic alignment, in which the core of the edge dislocation extends from one plate to another, the true cholesteric period is p rather than $p/2$ [234,235]. The reason is that the surface anchoring breaks the bulk symmetry of the cholesteric, see ref. [86] for more details. Therefore, the smallest Burgers vector allowed in a typical fingerprint texture is often $b = p$.



(b)

Fig. 45. (Continued).

Edge dislocations in cholesterics have been shown to be effective producers of optical vortices in a laser beam propagating normally through the cholesteric cell [236]. Optical vortices correspond to wave fronts of a helical form with the singularity at the axis, where the amplitude of the field is zero and the phase is not determined. Away from the core region, the phase of the wave changes by a multiple of 2π when one circumnavigates about the axis once, in direct analogy to dislocations in condensed matter. The wave dislocations are, in fact, a rapidly growing field in optics, initiated by the Nye and Berry article [237]. The interested reader is referred to two recent books [238,239].

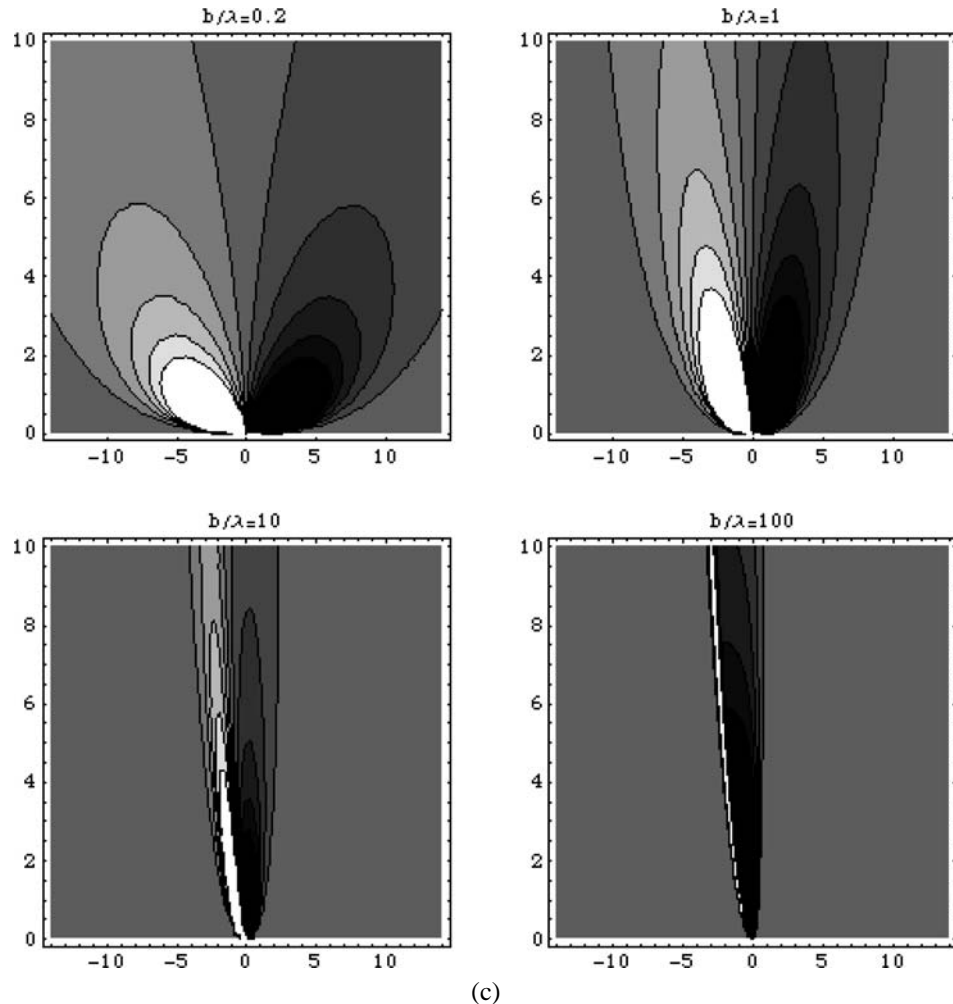


Fig. 45. (Continued).

9.4. Core structure and splitting

Fig. 45 demonstrates one of the most important features of dislocations in 1D layered media, namely, the tendency of their cores to split into pairs of disclinations, such as λ and/or τ disclinations of opposite signs, at a distance multiple of $p/4$. The splitting of a dislocation (equivalently: of a χ disclination) into two disclinations λ or τ of strength $|k| = 1/2$, i.e. of rotation $\pm\pi$, relates to the fact that the product of two opposite π -rotations along two parallel axes is a translation [240]. Split edge dislocations have been observed and studied in *Grandjean–Cano* wedge samples. The recently developed FCPM technique has proven itself to be especially useful in studying the core structure of defects in these samples,

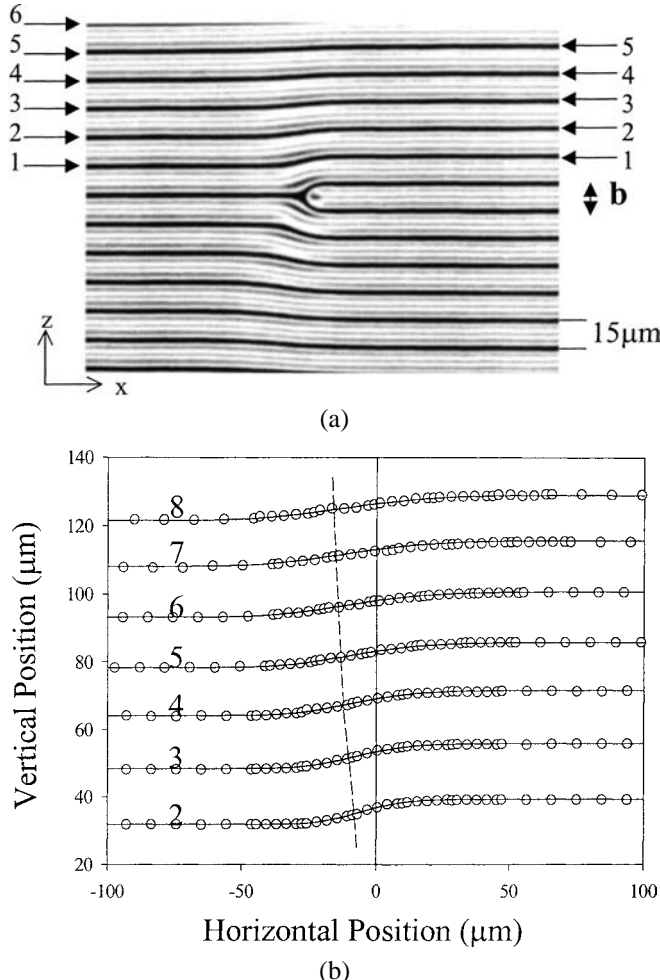


Fig. 46. An elementary edge dislocation in a cholesteric sample (a) and the fit of layers distortions with the non-linear theory [229]; fitting allows one to obtain the value of the elastic material length $\lambda = (K/B)^{1/2}$.

by imaging director configuration in the vertical cross-section of the samples [241], see Appendix.

Imagine that a lamellar phase is confined between two flat planes that are tilted with respect to each other by a small angle $0 < \omega \ll 1$, Fig. 47. If the layers are rigidly clamped by an appropriate substrate treatment to be parallel to the plates, the result is a ω tilt grain boundary with a edge dislocation lattice running parallel to the dihedron edge, as first observed by Grandjean [242]. Fig. 47 depicts different parts of the sample imaged by the FCPM technique. The dislocation Burgers vectors in the thin part are always $b = p/2$, while they are always $b = p$ in the thick part. The dislocations are split into pairs of discli-

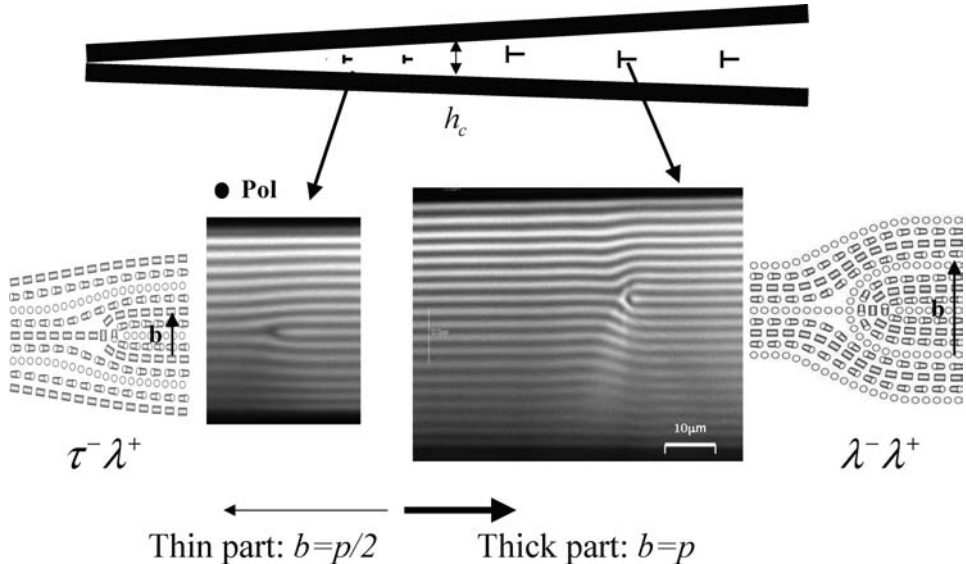


Fig. 47. Dislocations $b = p/2$ and $b = p$ with the corresponding director structures as seen in the vertical cross-section of a cholesteric wedge sample by FCPM; see ref. [241].

nations, Fig. 47. A $b = p/2$ dislocation splits into λ^+ and τ^- disclinations at a distance $p/4$ from each other. A $b = p$ dislocation splits into a λ^+ and λ^- pair of disclinations.

9.5. Glide and kinksindexkinks

In the flat or wedge samples bounded by rigid plates with strong anchoring, the dislocations are repelled from the substrates. Assuming an infinitely strong anchoring, the layer displacement satisfies the boundary condition $\partial u / \partial z|_{z=\pm h/2} = 0$, which yields a Peach–Kohler stress driving the dislocation toward the bisector plane. The PK stress can be estimated by placing image dislocations of the same Burgers vector b on the two sides of the bounded sample (see [243]) and analyzing their interaction with the dislocation in question. For a small displacement δ_z off the bisector plane, one finds [241]

$$\sigma_{zx}^E(\delta_z) \approx K b \delta_z / \lambda^{3/2} h^{5/2}, \quad (73)$$

where h is the local thickness of the slab.

Recall now that the cholesteric has a periodic structure and that the dislocation core is split into a pair of disclinations. Moving a dislocation core along the helix axis z would change the core structure of the disclination pair, which is energetically costly, especially when a non-singular λ -disclination has to be replaced by a singular τ -disclination. Dislocations in cholesteric phase thus experience a Peierls–Nabarro friction that hinders glide (but not climb). The PN stress caused by the increase in the core energy E_{core} of dislocations can be estimated as $\sigma_{\text{PNcore}} \approx 2\pi E_{\text{core}} / pb$. Therefore [241], if a non-singular core

of radius p in the $\lambda^-\lambda^+$ disclination pair needs to be replaced by a singular core of a (molecular) radius $r_c \ll p$, the Peierls–Nabarro stress would be huge,

$$\sigma_{\text{PNcore}}^{\lambda\lambda} \approx \frac{2\pi K}{pb} \ln \frac{p}{r_c}. \quad (74)$$

In contrast, as the $\tau^-\lambda^+$ pair already contains a singular core; changing this core from a $\tau^-\lambda^+$ to a $\lambda^-\tau^+$ configuration implies a modest increase of the total elastic energy; the associated Peierls–Nabarro stress is then estimated as

$$\sigma_{\text{PNcore}}^{\tau\lambda} \approx \frac{2\pi cK}{pb}, \quad (75)$$

where the numerical constant c is of the order of only 0.01, as we shall see later in this section.

In the experimental cholesteric wedge cells with a strong surface anchoring that keeps the director parallel to the bounding plates, FCPM reveals that the dislocations tend to accumulate close to the bisector plane and never approach the bounding plates closely. The tendency is especially clear for $b = p/2$ dislocations that find themselves exactly in the bisector plane or not farther than $p/2$ from it [241]. Initial filling of the cell might form dislocations in other locations, but they eventually move to the bisector plane. The lines do not glide as a whole, but via kinks, usually of height $p/4$ and $p/2$ in the case of $b = p/2$ dislocations, Fig. 48, and of height p in the case of $b = p$ dislocations, Fig. 49. The kinks make it possible for the dislocation to glide, by moving along the dislocation line and changing its vertical coordinate.

FCPM shows that the kinks along the $b = p/2$ and $b = p$ dislocations are very different. The kinks along the $b = p/2$ dislocations make a very small angle ψ with the dislocation itself, Fig. 50; they are relatively long, about $5p$ – $10p$, and confined to the glide plane of the parent $b = p/2$ dislocation. The core structure of the kink along $b = p/2$ dislocations is changing from a $\tau^-\lambda^+$ to a $\lambda^-\tau^+$ pair. For small ψ , one can directly apply the kink model developed for solid crystals [7], in which $\psi = \sqrt{2E_{\text{PN}}^{p/2}/E_{p/2}}$ is determined by the line tension of an edge dislocation (assumed constant), which is practically that of the dislocation core, $E_{p/2} \approx E_{c,\tau\lambda} \approx \pi/2K \ln(p/4r_c)$ and by the PN energy $E_{\text{PN}}^{p/2} \approx cK$. Since for a kink of height $p/4$ the tilt angle is determined by the kink width (length) w as $\psi \approx p/4w$, one can express the kink length as a function of the pitch and the constant c in the PN energy, as $w \approx \frac{p}{4} \sqrt{\frac{\pi}{4c} \ln \frac{p}{4r_c}}$. With the experimental data $w \approx (5 - 10)p$, $p \approx 5 \mu\text{m}$, and $r_c \approx 5 \mu\text{m}$, one arrives at a very small estimate, $c \sim 0.01$. This result means that the core energy variation associated with the $\tau^-\lambda^+ \leftrightarrow \lambda^-\tau^+$ transformation is small, only a fraction of K per unit length.

The situation with a $b = p$ dislocation is very different, as the kinks are relatively short, Fig. 49. The dislocation core retains the character of the non-singular $\lambda^-\lambda^+$ disclination pair. The fit is achieved by a helicoidal twist of the $\lambda^-\lambda^+$ pair around the cholesteric axis. In this way, the local director remains always parallel to the core of both disclination lines. The geometry requires both disclinations to deviate from the glide plane and to form a

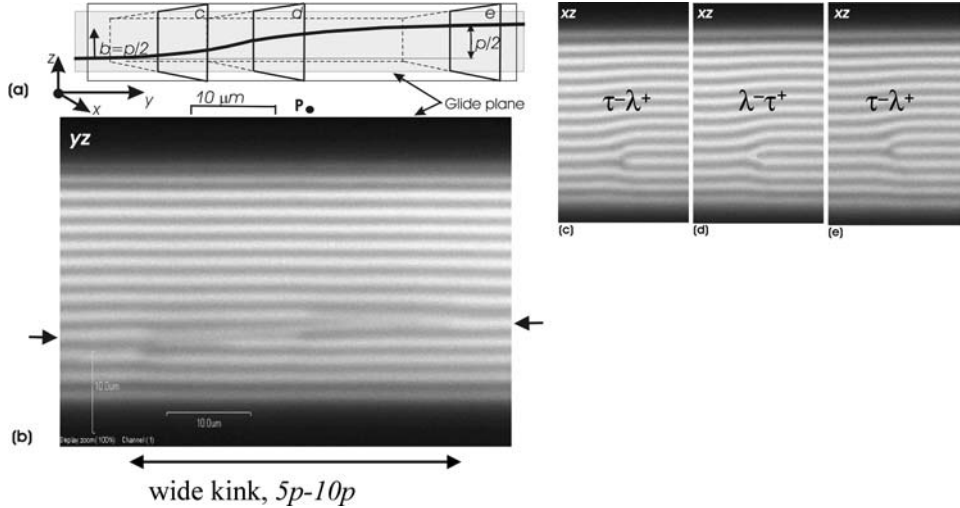


Fig. 48. Dislocation $b = p/2$ with a kink: (a) scheme of the vertical cross-section along the glide plane; the kink is almost parallel to the dislocation line; (b) FCPM texture of the glide plane; (c–e) FCPM textures of vertical cross-sections demonstrating a changing character of the disclination pair along the kink. See ref. [241] for more details.

cusp, Fig. 49. The energy density per unit length of kink is of the order of K and is thus not very different from the line tension of the dislocation itself (which implies that the kinks should be short, as in experiments).

It is important to stress that the sole reason for the dislocation lattice to exist in the Grandjean–Cano wedge is the surface anchoring that forces the molecules and thus the N^* layers to be parallel to the bounding plates. Obviously, the surface anchoring strength cannot be infinitely large and one can imagine that a dislocation will be able to escape the sample through the surface if the anchoring is sufficiently weak. This is exactly what was recently observed in Grandjean–Cano wedges with a weak surface anchoring [244], Fig. 50. This also offers a model of coarse-grained cholesteric anchoring that predict either repulsion or attraction between an edge dislocation and the flat bounding plate, depending on the anchoring strength.

9.6. Textures in N^* s, oily streaks

Most frequently, at large scales $L \gg p$, cholesterics present domains analogous to the *focal domains* of smectics, as one might expect from the existence of a 1D periodicity. These objects have been discussed in detail in Section 4. Note here only that in N^* s, the layers can suffer large thickness distortions (contrarily to SmA's), since it is possible to let the pitch vary in a large range at the moderate expense of some twist energy K_2 . As a rule, the N^* layers are saddle-shaped in focal conic domains.

For a review of the various large scale textures characteristic of N^* phases, see ref. [3, 13]. Below we concentrate on *oily streaks*, Figs 18, 51, which are complex aggregates

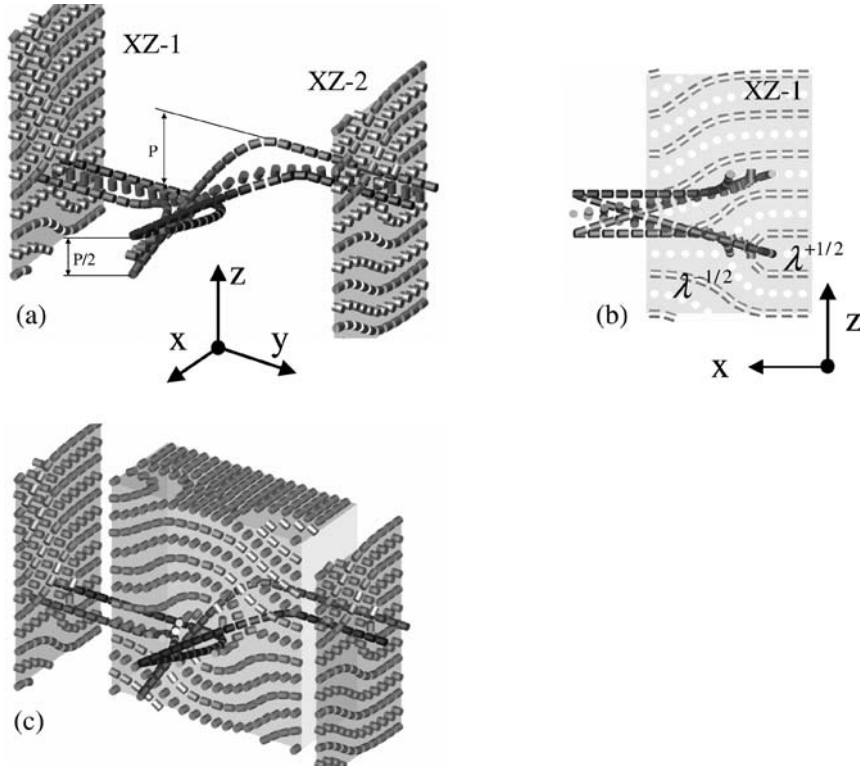


Fig. 49. Model of a kink along the dislocation $b = p$. The dislocation is split into two nonsingular disclinations of λ^- and λ^+ type; the director at the core is parallel to the local direction of the core. To preserve the nonsingular core, the disclinations twist forming a cusp. (a) The director configuration in two vertical cross-sections XZ perpendicular to the dislocation and far away from the kink; the central region shows the director fields at the core of the disclinations and between the cores. (b) The same, with the director configuration within the XZ-1 cross-section and the projection of the disclinations cores onto the XZ-1 plane. Note that the kink changes the vertical position of the disclinations by p ; far away from the kink the two disclination core are located at one horizontal line, while at the cusp they are located on top of each other. At the cusp, the disclinations λ^- transforms into λ^+ and λ^+ transforms into λ^- . (c) The same, supplemented with the director field configuration in the vertical plane YZ. See ref. [241] for more details.

of edge dislocations of large and opposite Burgers vectors, as mentioned in Section 4.3, present in samples where the cholesteric layers are mostly parallel to the bounding plates. Oily streaks in SmA's and N*'s are of the same topological nature. See Fig. 18 for the simplest type possible. Oily streaks and liquid crystals were discovered simultaneously. In 1888, F. Reinitzer studied cholesterylbenzoate and noticed elongated 'fluid' inclusions in a N* sample [245]; these were the oily streaks in question.

Because the line tension (the free energy per unit length) of the oily streaks is normally positive, their networks coarsen with time. It has been suggested [141] that one could stabilize the oily streak networks by adding micron-size colloidal particles to the N* phase. The particles gather at the nodes of the network. The stabilized network of connected oily

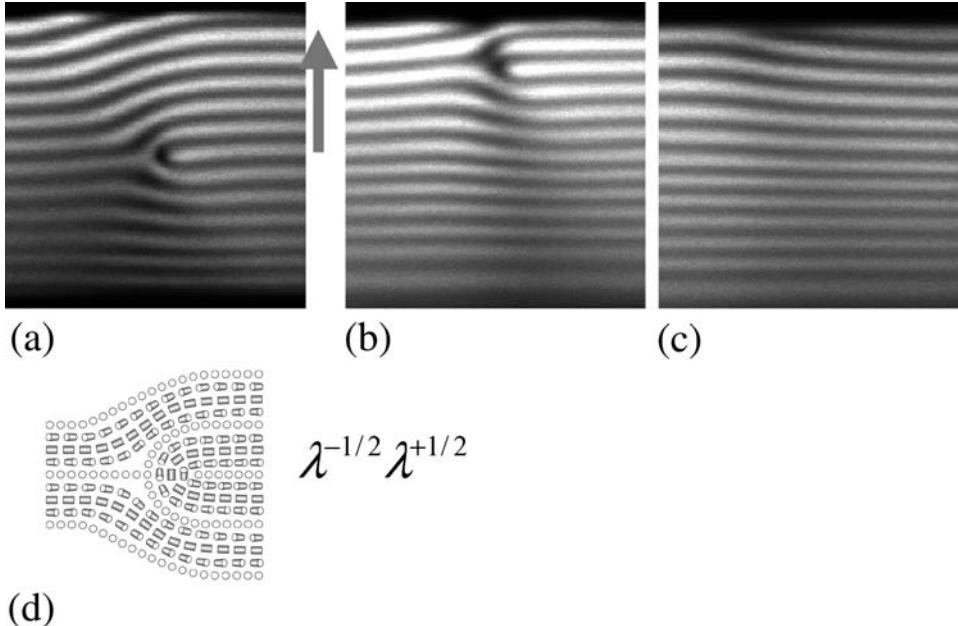


Fig. 50. FCPM textures of the vertical cross-section of a cholesteric wedge sample bounded by plates with a weak anchoring strength. The edge dislocation with $b = p$, initially in the bulk of the sample (a), glides towards the upper plate (direction of glide is shown by the arrow) (b), ending up at the upper surface of the sample (c). Parts (a, b, c) correspond to the same vertical cross-section of the sample taken within a time interval of few hours. Part (d) shows the director configuration near the core which is split into the nonsingular $\lambda^- \lambda^+$ pair of disclinations. Local thickness of the sample: approx. 30 μm .

streaks greatly modifies the rheological properties of the system, making it gel-like. In contrast to a defect-free N^* fluid that exhibits liquid-like rheology, stabilized oily streaks exhibit macroscopic rubber-like elasticity [141].

Usually, the layers within the FCD's and the oily streaks, and the layers outside these defects have different orientation at the sample boundaries; thus, the problems of surface anchoring and of layer curvature in these defects are strongly connected. This relationship is well illustrated by an experiment in which the oily streak line tension is controlled by an applied electric field [246]. The electric field changes the line tension and can even drive it negative, in which case the oily streaks buckle and proliferate rather than coarsen.

Fig. 51(a) shows a network of connected oily streaks in a N^* sample, when the electric field is absent. The bounding plates of the sample are treated to align the molecules parallel to the plates, so that the χ field is normal to the bounding plates. The edges that separate the uniform domains are oily streaks, provoked by inhomogeneities such as plastic spacers that keep the bounding glass plates apart. The width $2a$ of the oily streak is defined by the number of layers that undergo a π -turn.

The sign of the dielectric anisotropy is such that the layers tend to orient along the electric field E . Thus, applying E perpendicular to the plates has the effect of expanding

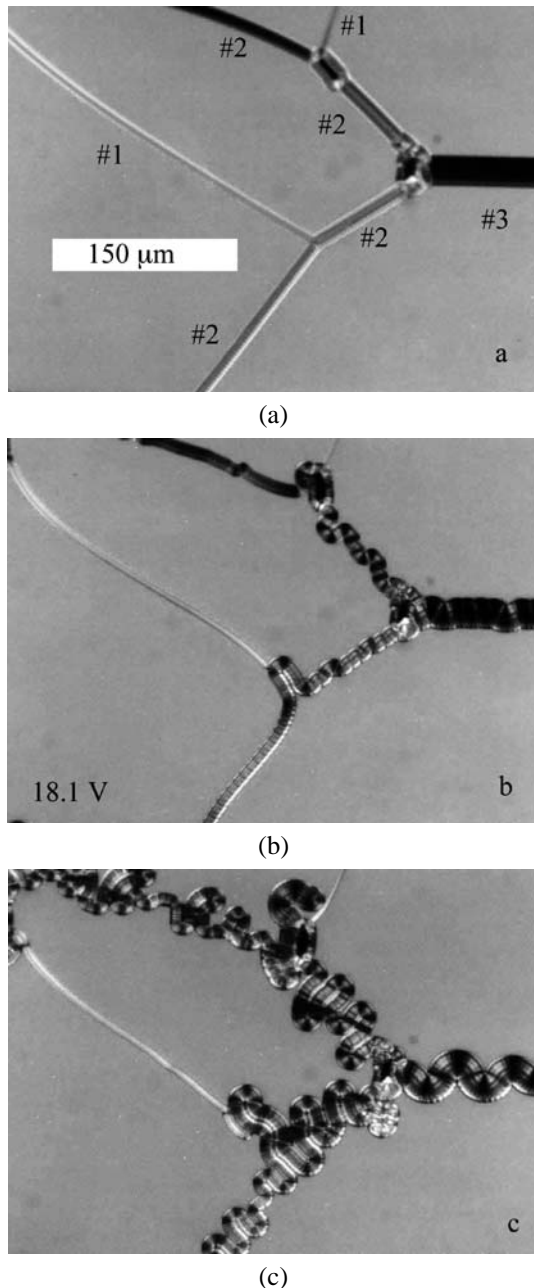


Fig. 51. Network of oily streaks in a cholesteric planar texture. Cell thickness $15 \mu\text{m}$, cholesteric pitch $0.48 \mu\text{m}$. The oily streaks are straight at zero voltage (a) but buckle when the voltage exceeds some threshold value (b, c). The narrow streaks (#1) and the widest streaks (#3) do not buckle while the streaks of an intermediate width (#2) start to buckle at voltages higher than some threshold voltage (b); as the voltage increases, the widest streaks buckle too (c).

the length of the oily streaks at constant Burgers vectors (because the field has no incidence on the topology), making them buckle, Fig. 51(b, c). Interestingly, as the voltage increases, only the oily streaks of an intermediate width (#2 in Fig. 51(b, c)) buckle; the thinnest (#1) and widest (#3) streaks remain straight. Although the phenomenon is similar in appearance to the buckling of dislocations in Grandjean wedges [247,248], it cannot be understood solely as a dielectric response [247] of the cholesteric, because oily streaks are sufficiently large to be influenced by the surface anchoring at the bounding plates. The anchoring term is caused by the tilt of the cholesteric layers at the boundaries. The tilt angle increases from 0 outside the streak to $\theta_{\max} = \arctan \xi$ at the vertical middle plane of the streak; here $\xi = 2a/h$ is the width of the streak renormalized by the cell thickness h . The anchoring penalty increases when $2a$ increases (since θ_{\max} increases); this increase can be avoided if the oily streak simply elongates, preserving $\theta_{\max} = \text{const}$.

A quantitative analysis [247] with the model of the oily streak depicted in Fig. 18, shows that the elastic, dielectric and anchoring contributions to the line tension F of the oily streak depend differently on the width of the streak. Let ξ be the dimensionless width of the oily streak, defined as the actual width divided by the sample thickness. The elastic term is practically linear with ξ . The dielectric and anchoring energies per unit length scale as ξ^2 when $\xi \ll 1$, but switch to a linear scaling $\sim \xi$ when $\xi \gg 1$. Thus narrow oily streaks (#1) are always dominated by the elastic energy and $F > 0$ for any applied voltage. Anchoring takes over at $\xi \gg 1$, so that the line tension of the wide streaks (#3) is also positive. For intermediate $\xi \sim 1$, when the field is higher than some threshold value, the (negative) dielectric contribution outbalances both the elastic and anchoring terms and drives the line tension negative. The oily streak (such as streaks #2 in Fig. 51(b, c)) elongates preserving the width that corresponds to the minimum of the line tension per unit length, $F(\xi)$. Interestingly, a good quantitative agreement between the model and the experiment can be obtained only when there is an ‘intrinsic’ contribution $W_a \sim K/p$ to the anchoring coefficient. It comes from the layered structure of the cholesteric and has no analog in the nematic phase (but has a counterpart in smectics). The estimate $W_a \sim K/p$ is natural since the number of cholesteric layers crossing the boundary is of the order of θ/p and each layer has to be distorted (continuously or through dislocations) to accommodate for the anchoring direction at the boundary. The energy of these distortions is $\sim K$ per layer. Hence $W_a \sim K/p$.

9.7. Robinson spherulites

Semiflexible cholesteric biopolymers (but also some thermotropic cholesterics, Fig. 52), have other types of layer textures, the *Robinson spherulites*, observed by Robinson and explained by Frank and Pryce [249,250]. The layers are approximately along concentric spheres. The molecular orientation is singular, since it is impossible to outline a continuous field of directors on a sphere. The total strength of these singularities is $k = 2$. Observations tell us indeed that either a $k = 1$ singularity goes through the whole spherulite along a diameter, or a $k = 2$ line defect extends from the surface to some point inside (generally the centre of the spherulite). The $k = 2$ line is believed to relax to a non-singular configuration, by escape [251]. It has been possible to observe in a thermotropic material the



Fig. 52. Concentric packing of a cholesteric layers in a spherical droplets, called either Robinson spherulite, or Frank and Pryce texture, or magnetic monopole texture.

transformation of defects in a droplet with a Frank and Pryce texture into nematic defects, in a droplet formed by a mixture of left-handed and right-handed cholesterics. Changing the temperature, one changes the sense of chirality; when the pitch becomes much larger than the droplet size, the $k = 2$ line with the end at the centre of the droplet transforms into point defects, either a pair of boojums at the surface or a hedgehog, depending on the surface anchoring conditions [226].

10. Competitive interactions in liquid crystals. Spontaneous defects, frustration

10.1. Definitions and classification

It is convenient, for the purpose of this section, to divide the singularities of the OP of a condensed phase into two categories: *induced* defects and *spontaneous* defects.

By induced defect, we mean a *metastable*, topologically stable—in the sense of the classification of defects in Section 2—defect configuration; the stability of the defect is reduced to its topological stability. All the defects we have studied up to now are induced defects.

By spontaneous defect, we mean an energetically *stable* (i.e., thermodynamically stable) defect configuration. For instance, the usual point defects met in solids (vacancies, intersti-

tials)¹ obey this definition; their stability is insured by an entropic contribution. Still in this second category, and more interesting from the point of view of topology, are the defects that are invoked in melting theories. For instance: (i) in 2D systems, a number of smectic phases (SmI, SmF, hexatic phases, etc.) are known to display dislocations and disclinations, whose density, cooperative behavior, etc., depend on temperature, and which play a role at the phase transitions between such smectic phases; for a review, see [252]. (ii) In 3D solids, it has been argued that first-order phase transitions are ruled by the appearance of a large density of dislocation loops in the vicinity of the transition; for a review see [253]. All the foregoing examples are taken in condensed matter systems whose symmetries are defined as subgroups of the Euclidean group $E(3) = R^3 \square SO(3)$ for 3D systems, or of $E(2) = R^2 \square SO(2)$ for 2D systems (the correlation between layers being quite frequently lost in layered phases); the OP extends to infinity in the whole 3D (or 2D) space, but is broken at the locations of the thermodynamic defects, whose topology is in accord with the symmetry group.

There are in liquid crystals numerous examples of simultaneously topologically and energetically stable defect textures induced by external fields—such as walls appearing under the action of a magnetic or electric field—or by the presence of incompatible anchoring orientations. These are *induced frustrated* geometries. They are reviewed in [254]; we do not consider them here.

Finally, there are condensed systems, in which the interactions that compete on short distances yield local molecular configurations that cannot extend geometrically on large scales. As a result, the medium divides into low-energy domains where these competitive tendencies are more or less simultaneously satisfied. Spontaneous defects appear as regions of high strain between domains, in the form of walls or arrays of defect lines. These systems, which are thermodynamically stable systems, are often called *frustrated phases* (the word *frustration* has been popularized by G. Toulouse for spin-glass lattices). In contrast to induced defects, these spontaneous defects are structural elements of the phase, and removing or displacing them increases the energy of the system. It is not so much their entropy (as in the last paragraph but one) as their mutual interactions that are responsible for their stability.

Frustrated phases are many. First, outside the realm of LC's, a classical example is the Frank and Kasper (FK) crystalline phases of intermetallic alloys [255], and the amorphous states [256]; in both cases the local atomic order is *icosahedral*, as it is in metallic isotropic liquids [257]. The symmetry of an icosahedron does not belong to any of the seven crystal systems, hence, icosahedra do not tile our usual (flat) space. Another example, often put in the category of frustrated phases [254], is the superconducting Abrikosov phases. There are many examples in LC's: we list several local director fields that generate frustration (in parenthesis is the corresponding mesophase where such fields are achieved): (i) double twist (DT) domains; (N and Sm Blue Phases—BP). (ii) Director twist in the presence of Sm layers, about an axis non-colinear to the Sm layer normal (TGB phases). (iii) Director twist in the presence of columns: (a) twist of the director about an axis perpendicular to the columns (Columnar TGB phase); (b) double twist of the columns (Moiré phase). We now expatiate on these phases.

¹Point defects have not yet been much investigated in Sm LC's endowed with positional ordering inside the layers (e.g., SmB phases).

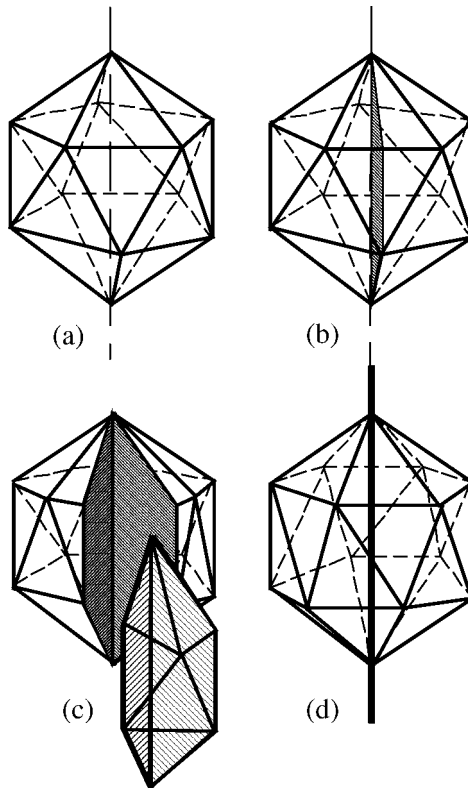


Fig. 53. Introducing a disclination line into an icosahedron $Z = 12$. The final polyhedron (still a deltahedron) is $Z = 14$.

The classification of induced defects and distortions in frustrated mesophases is still an open field, except for defects of the TGBA phase. The theory of induced defects and distortions in the TGBA phase is reviewed in Section 10.3.2.

One of the key concepts to describe frustration is the concept of *curvature* [256,258]. It applies beautifully to FK and BP's. We illustrate it in the FK case. Icosahedral symmetry frustration can be relieved in a curved space of constant curvature, the 3D sphere S^3 , where it is possible to build a 3D ‘crystal’ of finite extent (a regular polytope—for this geometrical concept, see [259]), made of 600 regular tetrahedra, 5 meeting about each edge, 20 about each vertex, where they form an icosahedron; the coordination is $Z = 12$. In Schläfli notations, the 3D polytope is denoted $\{3, 3, 5\}$ —the facets are 3-gons (triangles); 3 facets meet at a vertex; 5 tetrahedra meet along an edge. This polytope is nothing else than the 3D analog of a 2D polyhedron, the $\{5, 3\}$ dodecahedron on S^2 . The relationship between the $\{3, 3, 5\}$ polytope and the FK phases is as follows. Disclinations of strength multiple of $2\pi/5$ (in order to respect the 5-fold symmetry along the edges of $\{3, 3, 5\}$) are introduced along some edge lines, with the purpose of decurving S^3 by the introduction of extramatter, up to flattening S^3 into a piece of E^3 , Fig. 53.

In this process, some edge lines transform into edge lines with vertices $Z = 14, 15, 16$, etc. coordinated. Because of the quantized nature of the disclinations, the process has no chance to exactly fit the Euclidean space; therefore, one has to complete the decurving in the disclination mode by the introduction of deformations (and internal stresses). The distance between disclination lines (which are regularly disposed in a FK phase) depends on a complex balance between the elastic energy of the bulk and the energy of the defect lines, and is expected to scale with the radius of the sphere, which maps on one *flat* unit cell (a domain). Note that there are many ways to flatten S^3 into a domain, so that the same process, but with lines at random, gives a model of an amorphous medium with local icosahedral symmetry.

10.2. Double twist configurations. Blue phases

In Blue phases (BP), the director field is *twisted* in all the directions perpendicular to the director. The distribution is as in Fig. 54, i.e., a cylindrical set of directors aligned along helices arranged like strands in a string. Observe that the neighborhood of the director varies with the distance to the central axis. The helix pitch increases with the distance to the central axis; when one proceeds to an infinite distance from the axis, the geometry is locally the same as in a N* phase: the director is single twisted (about a radial direction), as in a N* phase. The cylindrical double twist configuration cannot extend through all space. There are two main types of double twist structures, whether translational ordering is superimposed on the double twist (Sm BP) or not (BP *stricto sensu* or N BP).

10.2.1. Blue phases

The stability of the double twist configuration is favored by a *divergence term* in the now familiar free energy:

$$\begin{aligned} f_{N^*} = & 1/2K_1(\operatorname{div} \mathbf{n})^2 + 1/2K_2(\mathbf{n} \cdot \operatorname{curl} \mathbf{n} + q)^2 + 1/2K_3(\mathbf{n} \times \operatorname{curl} \mathbf{n})^2 \\ & - K_{24} \operatorname{div}(\mathbf{n} \operatorname{div} \mathbf{n} + \mathbf{n} \times \operatorname{curl} \mathbf{n}). \end{aligned} \quad (76)$$

K_{24} is the *saddle-splay* coefficient.² One has $\iiint f_{24} dV = -K_{24} \iint \mathbf{p} \cdot (\mathbf{n} \operatorname{div} \mathbf{n} + \mathbf{n} \times \operatorname{curl} \mathbf{n}) dS$; \mathbf{p} is the outward normal of the domain whose energy is calculated. Consider a cylindrical domain limited to the radius r_0 for which $n_3 = \sin \psi$, ($\psi_0 = 0$ for $r = 0$). The integral lines of the director are along helices of chirality opposite to the chirality of the director about the radii. With $n_r = 0$, $n_\theta = -\sin \psi(r)$, $n_z = \cos \psi(r)$, in cylindrical coordinates, one gets $\iiint f_{ss} dV = -2\pi K_{24} \sin^2 \psi_0$ per unit length of cylinder. This term is negative for any value of $\psi_0 \neq 2\pi n$, when $K_{24} > 0$ [260]. Therefore, assuming $K_{24} > 0$, the nucleation of a cylindrical double twist geometry is favored. Cylinders cannot fill space totally, and it is believed that in the BP, the cylinders are in contact two by two along perpendicular directions, forming locally orthogonal sets of three cylinders. The gap between these three cylinders is either a nonsingular $k = 1$ disclination, Fig. 55(a), or

²Some authors use the inverse sign ($-K_{24}$ instead of K_{24}).



Fig. 54. The double twist cylinder.

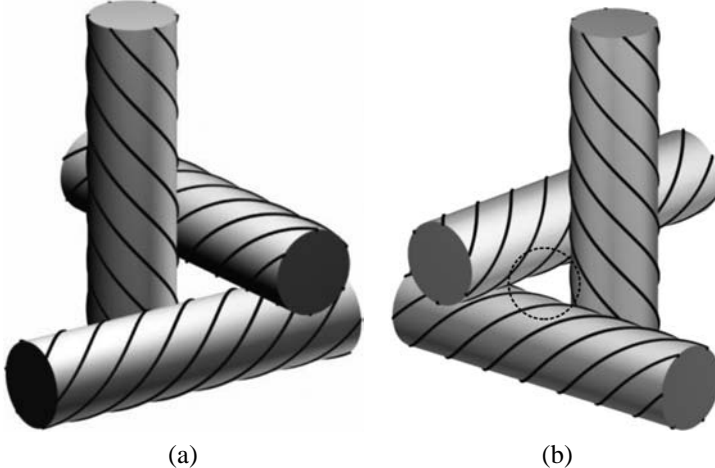


Fig. 55. The contact point of two cylinders is not singular if the director comes to the cylinder surface at the angle $\pi/4$ with respect to the orientation on its axis. A choice is possible in the relative stacking of three cylinders: (a) nonsingular distribution of the director in the gap; (b) singular distribution of the director in the gap; three cylinders form a singular gap, which extends as a disclination line of strength $k = -1/2$. The core of the disclination is indicated by the circle.

accommodates a disclination line of strength $k = -1/2$, Fig. 55(b), according to the relative stacking of the three cylinders [261,262]. The point of contact of two perpendicular cylinders is not singular if the director at the surface of each cylinder is at a $\pi/4$ angle with respect to the orientation of its axis. Therefore, the radius of a cylinder is approx. $p/4$. Coming back to the disclinations, observe that the same type of integration as above, done on the core of a $k = -1/2$ line, yields a term $-\pi K_{24}$ which is also negative for $K_{24} > 0$, and is independent of the core size. To summarize, the condition $K_{24} > 0$ favors the sta-

bility of a BP with spontaneous defects. The final balance includes positive terms like the bend term, ruled by K_3 , and the energy of the inner core, probably in a liquid isotropic state, i.e, proportional to the temperature difference $|\Delta T|$ to the transition to the isotropic phase.

The change in orientation of a molecule on the cylinder axis (where the DT condition is best achieved), when one moves along any radial direction, is perpendicular to the radius. This condition can be written $n_i n_{j,i} = 0$. We also have $n_j n_{j,i} = 0$, because $n_j n_j = 1$. Hence, expressing that the rotation along any radius has pitch $p = 2\pi/q$, one gets [261]:

$$n_{j,i} = -q \varepsilon_{ijk} n_k. \quad (77)$$

Sethna [261] has shown, considering parallel transport around an infinitesimal closed loop, that this set of three equations cannot be satisfied in any finite volume. The DT is frustrated. In this transport

$$D_i n_j = n_{j,i} + q \varepsilon_{ijk} n_k \quad (78)$$

is to be understood as the covariant derivative of \mathbf{n} on a space with curvature; this derivative vanishes for the parallel transport of N BP.

Notice that eq. (76) can be written

$$f_{DT} = 1/2K(D_i n_j)^2 + 1/2Kq^2 \quad (79)$$

so that the DT equations $D_i n_j = 0$ clearly appear as the conditions to get an absolute minimum (the ground state) in the elastic one-constant approximation defined by $K = K_1 = K_2 = K_3 = 2K_{24}$, provided the term ruled by K_{24} is taken into account. Again, the surface term appears as the leading factor to explain frustration at a phenomenological level.

It is shown in [261,263] that the frustration is completely relieved if the director lives in a S^3 sphere. The DT configuration is uniform everywhere on the sphere S^3 while in R^3 the ideal double twist exists only, strictly speaking, on the axis of the DT cylinder; it smoothly becomes a 1D cholesteric twist on large distances. We develop now this curved representation for a N BP.

Start with the analytic expression for a 3D sphere:

$$x_0^2 + x_1^2 + x_2^2 + x_3^2 = R^2, \quad (80)$$

and consider the field of 3D unit vectors

$$\mathbf{n}(\mathbf{r}) = 1/R(-x_1, x_0, x_3, -x_2). \quad (81)$$

This field satisfies the DT condition and is homogeneous through all S^3 space; hence, no frustration. Any field obtained by rotating all $\mathbf{n}(\mathbf{r})$ of eq. (81) is another homogeneous DT field, with the same pitch $p = 2\pi R$. A different choice, like

$$\mathbf{n}(\mathbf{r}) = 1/R(-x_1, x_0, -x_3, x_2) \quad (82)$$

cannot be obtained by a rotation of the above field, but also obeys DT; it has the opposite pitch $p = -2\pi R$.

The integral lines of both types of fields are equidistant great circles of S^3 , also called Clifford parallels (right parallels for $p > 0$, left parallels for $p < 0$), that are in mutual skew positions. In each set, they are therefore at the same time double-twisted and parallel; see ref. [260] and [264] for a detailed discussion and application of the Clifford geometry to N* instabilities and molten polymers.

Topological considerations predict the existence of frustration but do not provide a specific information on the space organization of the resulting frustrated structure. Akin to the FK case discussed above, there is a large number of ways to organize space when frustration is allowed. Three different phases labeled BPI (lowest temperature), BPII, BPIII (highest temperature), have been reported [265]. They all correspond to different DT cylinder packings. BPI and BPII grow as well faceted specimens, which indicates crystalline structures. This crystalline character is caused by an ordered 3D organization of the director field associated with the DT cylinders. This periodic order does not imply any periodic order in the distribution of molecular centres of mass, as the molecules in BPs are free to move around.

Director configurations in BPI and BPII form body centered and simple BPI and BPII cubic (bcc and sc respectively) lattices of $k = -1/2$ disclination lines. It is believed that BPIII is an amorphous phase of cylinders, also called a *blue fog*.

A conclusion on the structure of a given frustrated system can be drawn only via a comparison of the energies of the possible structures and fitting the models to experimental data. For BP's, such an estimation is done in [265]. Their results and comparison with experiments allow one to state that BPI and BP2 both have cubic symmetry with space groups $O^8(I4_132)$ and $O^2(P4_232)$, which correspond to bcc and sc lattices shown in Fig. 56. The disclinations in the O^8 structure do not intersect, whereas in the O^2 structure they go along half of the cube diagonals and hence intersect, Fig. 57. See [266] for a classification of the space organizations, i.e., of the classes of textures which satisfy DT with frustration.

The $-1/2$ disclinations are arranged as in Fig. 57.

10.2.2. Smectic blue phases

The interest for the blue phase state has grown again when a strong smectic order has been observed in some BP's [267–272]. Three such different Sm BP's have been found, labeled BPSm1, BPSm2, and BPSm3. For all of them, there is evidence of smectic ordering with a repeat distance equal to the length of the molecule; the correlation length along the chiral axis of about 15 smectic layers, for both BPSm1 and BPSm2. The phase BPSm3 is an amorphous (isotropic) state [269]. BPSm1 is cubic [270] when on the temperature phase diagram there is a TGBA phase just below the transition; it is then labeled BPSm(A)1. On the other hand BPSm1 is hexagonal [271] for a TGBC-BPSm phase sequence and is then called BPSm(C)1. According to [272], BPSm2 is orthorhombic for a material exhibiting a TGBA phase.

The simplest but naive way to describe Sm BP's is to superimpose smectic layers perpendicular to the BP director. Besides the frustration resulting from the problem of close packing for cylinders in the R^3 space, additional defects would exist within each dou-

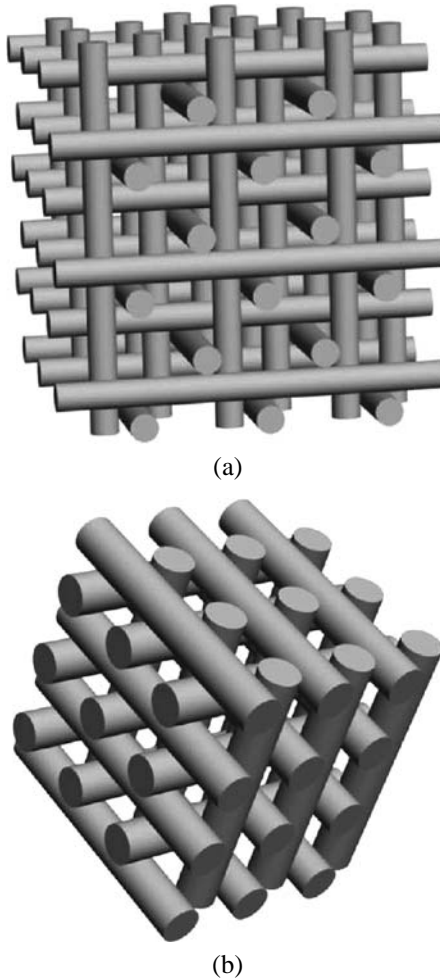


Fig. 56. Unit cells of the (a) O^8 and (b) O^2 structures.

ble twist cylinder. These are parallel *twist grain boundaries* composed by equidistant *screw dislocations*, appearing as the result of the twist deformation of the Sm layers, and *edge dislocation densities* induced by the cylindrical geometry of the twist grain boundaries.

Attempts to combine smectic order with 3D double twisted orientation ordering have been done in [273]—a cubic lattice of smectic double twist cylinders stacked as in N BP's, yielding O^5 symmetry, and in [274]—a combination of minimal surface patches of Sm layers (Schwartz P surface or Schoen's $I\text{-}WP$ surface) with cylindrical tubes. See Figs 1 and 3 in [274].

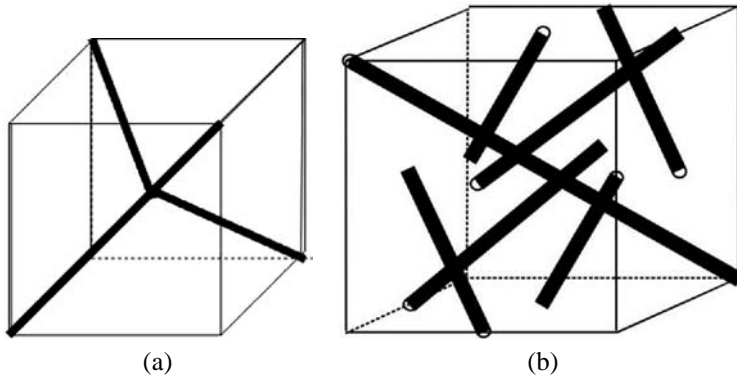


Fig. 57. Array of disclination lines corresponding to (a) BPI and (b) BPII.

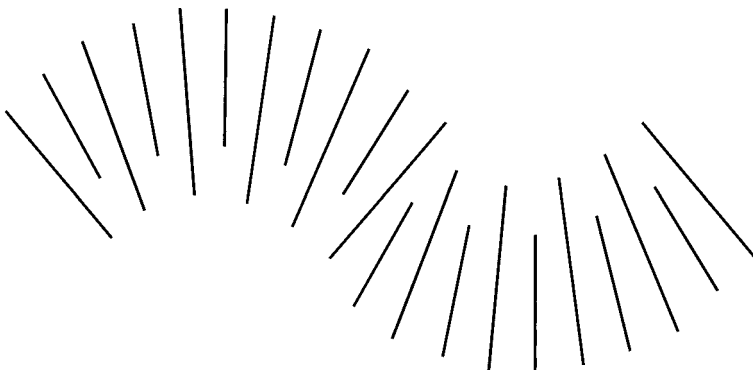


Fig. 58. Edge dislocations induced by the bend deformations of the director field. Bending of the director is equivalent to splay of the layers.

10.3. Grain boundaries in smectics

Disclinations in Sm phases yield strain deformation, except in the case of $k = 1/2$ (see Fig. 6) and circular $k = 1$ wedge lines and in the special, but common, case of FCDs, where a wedge $k = 1$ and a mixed character $k = 1/2$ disclinations are coupled. The strain accompanying a *wedge* disclination can be relaxed by edge dislocation densities, see Fig. 58. If the relaxation is total, the energy of the lines is essentially reduced to their core energy, and the most important energy contribution left is the *bend* of the layer normals, represented by the vector $\mathbf{B} = \mathbf{n} \times \text{curl } \mathbf{n} \neq 0$, ruled by the K_3 curvature modulus. Similarly, the strain accompanying a *twist* disclination can be relaxed by screw dislocation densities. This latter situation is illustrated by the twist grain boundary discussed in Section 5.2.3. The line bounding a twist grain boundary of limited extent is indeed a disclination loop of strength ω ,—with $2 \sin(\omega/2) = d_0/l_d$, d_0 is the Burgers vector, l_d the separation between screw lines. If the relaxation is total, the energy of the lines is essentially reduced to their core energy, and the most important energy contribution left is the *twist* of the layer normals,

represented by the pseudoscalar $T = -\mathbf{n} \times \operatorname{curl} \mathbf{n} \neq 0$, ruled by the K_2 curvature modulus. In spite of the analogy, *mutatis mutandis*, between the edge and the screw cases, there is a conceptual difference. The condition $\mathbf{B} \neq 0$ yields a layer thickness variation that does not break the OP, in the sense that the layers still exist. On the other hand, the condition $T \neq 0$ implies a true breaking of the OP: the necessary (and sufficient) condition for the existence of a layering (i.e., of a set of surfaces orthogonal to the field of normals), is $T \equiv 0$.

If the OP of a Sm phase displays a spontaneously bent director field or a spontaneous twist director field, as it is assumed in [275], the energy of deformation of the Sm phase is restricted to the energy of the lines (which can be small or possibly negative, remember the case of the $k = -1/2$ lines in BP's). Thus, there can be a phase transition between the usual SmA (or SmC) phase and a layered phase with spontaneous bend or twist. This situation shows a deep analogy with the normal metal–superconductor transition [276]. Consider the spontaneous twist case. The Sm phase is the analog of the superconducting state, the N* phase is the analog of the normal state, and the screw dislocations, along which the twist penetrates, are the analogs of the vortex lines, along which the magnetic flux penetrates. A phase containing an array of spontaneous edge or twist dislocations would be an analog of the Abrikosov phase in superconductors. To the best of our knowledge, only frustrated smectic phases with spontaneous twist are documented. These phases are called TGB (twist grain boundary) phases.

10.3.1. TGB structures

In the TGB phases, the director field is of the cholesteric type but molecules are packed in smectic 2D fluid layers. As already dislocations. Thus a smectic phase, in which the director spontaneously twists around a perpendicular axis, should carry a density of screw dislocations ordered into a network. This network is a set of regularly spaced (repeat distance l_b) twist grain boundaries made of equidistant screw dislocations (Fig. 59), playing the role of the lattice of the Abrikosov vortices, separating SmA blocks rotated one with respect to the next by an angle w , such that $2 \sin(w/2) = d_0/l_d$ [277].

The superconducting analogy approach to the TGB phases is discussed in many textbooks and we shall not expand on it. The energy of the TGBA phase dislocation geometry has been studied [278], including nonlinear elastic effects [279].

Two additional TGB phases: TGBC and TGBC* have been predicted [280,281] for which the smectic slabs are of the SmC and SmC* type respectively. Defining \mathbf{m} , χ and \mathbf{n} as the smectic slab normal, the helical axis and the director, respectively, one has $\mathbf{m} \times \chi = \mathbf{n} \times \chi = 0$, $\mathbf{m} \times \mathbf{n} \neq 0$. Another model, in which $\mathbf{n} \times \chi = 0$, $\mathbf{m} \times \chi \neq 0$, $\mathbf{m} \times \mathbf{n} \neq 0$, illustrated in Fig. 60, has been inferred from experiment [282]. A transition between these two structures has been recently predicted [283].

The TGBA [284–286], TGBC [287], TGBC* [288] phases are now documented in several materials. Pramod et al. [289,290] reported observations of an undulated TGBC* phase (U-TGBC*), characterized by the appearance of a square grid pattern due to the undulation in the plane perpendicular to the helical axes. These undulations have been characterized by polarizing microscopy and fluorescence polarizing confocal microscopy in free standing films [291].

An antiferroelectric twist grain boundary phase, denoted TGBCa, with an anticlinic organization of the adjacent layers, has recently been discovered [292,293]. The structure

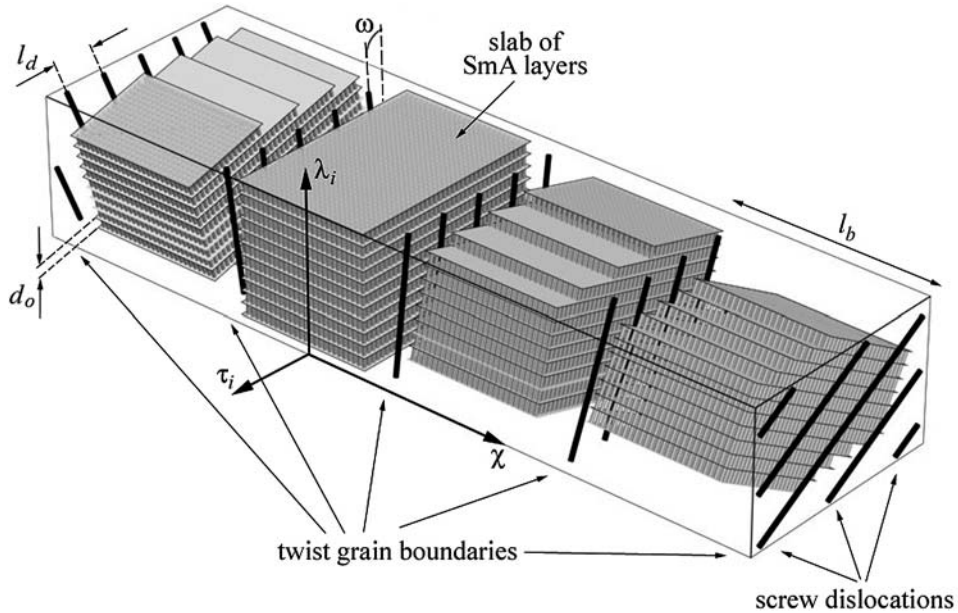


Fig. 59. TGBA phase, schematic.

of the TGBCa phase differs from that of the TGBA and TGBC phases. Instead of grain boundaries composed by screw dislocations, there are grain boundaries of parallel dispirations. In each grain boundary neighbor dispirations are of opposite sign, as it is shown in Fig. 61.

10.3.2. Induced defects in a TGBA phase

Because of their close structural relationship, namely the existence of a unique helical axis, denoted χ , the TGBA phase, in a sense, is akin to a N^* phase clad with Sm layers parallel to the χ axis. TGBA defects are thus much similar to N^* defects, and the observation of Grandjean wedges yields much similar textures [294], except for the presence of *dispirations*, hardly visible but anyway observed [295]. We shall see that other geometries are more favorable for discriminating between the two phases.

10.3.2.1. Topological classification of defects [296] At a scale where the inner smectic structure of a block is not taken into account, the symmetry group H_{TGBA} of the TGBA phase is

$$H \approx (R^2 \times Z) \square D_2. \quad (83)$$

D_2 stands for the dihedral symmetry group of the three directors \mathbf{c} , \mathbf{l}_i (along the normal to the smectic layers inside the blocks) and $\mathbf{t}_i = \mathbf{l}_i \times \mathbf{c}$, R^2 for the 2D continuous translations in the plane P parallel to twist grain boundaries, and Z for the quantized translations-rotations $\{nl_b, nw\}$, $n \in Z$, along the \mathbf{c} -axis (perpendicular to the P plane). Compare to the

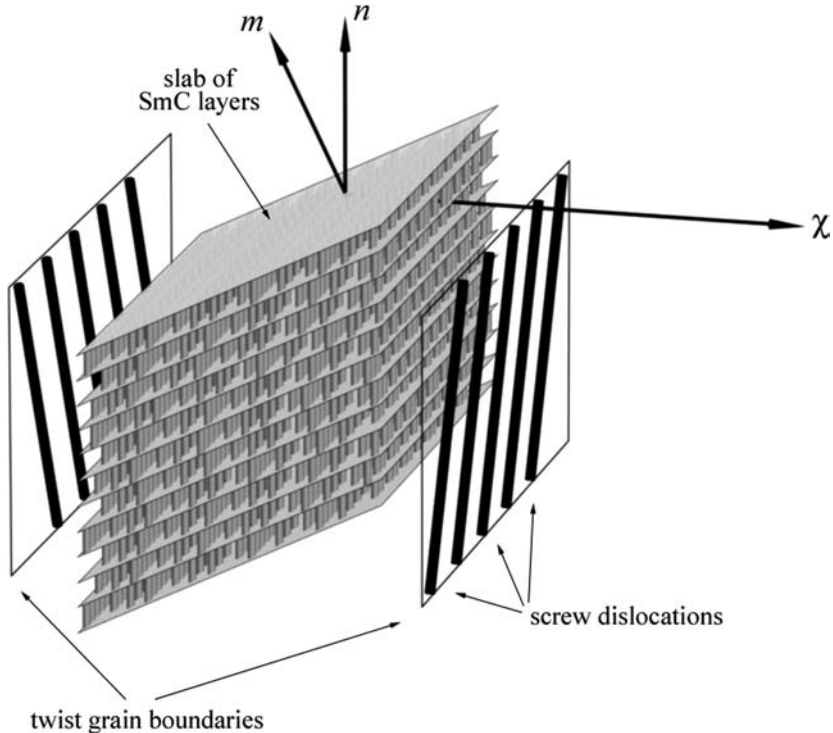


Fig. 60. A possible model for the TGBc phase, displaying helielectric properties. The smectic layers are tilted with respect to the helical axis (adapted from [282]).

N^* symmetry group, $H_{N^*} = (R^2 \times He) \square D_2$, where He is a continuous translation-rotation (helical) group.

The topological classification of defects is given by the first homotopy group of the quotient manifold $E(3)/H$ (see Section 2). Applying standard calculation rules [28] one gets:

$$\Pi_1(\text{TGBA}) = Z \square Q, \quad (84)$$

$$\Pi_2(\text{TGBA}) = 0, \quad (85)$$

$Q = SO(3)/D_2$ is the group of quaternions.

According to eq. (84), there are two fundamental types of line defects: (a) *dispirations* classified by Z and corresponding to translation-rotation symmetries; (b) *disclinations* classified by Q , as in the N^* phase. The symmetry of the so-called NL^* phase, which is a TGBA phase but with disordered screw lines, predicted in [297] and documented in [298], does not differ from the symmetry of a N^* phase; thus, $\Pi_1(NL^*) = Q$; there are no dispirations.

Similarly to N^* , there are no topological point defects in the TGBA phase.

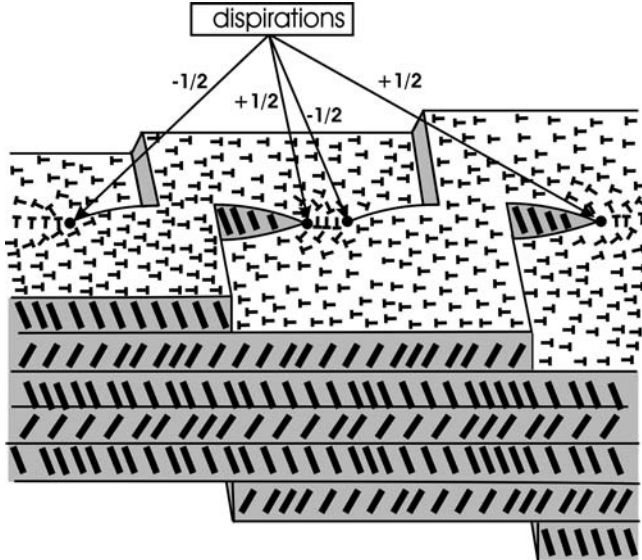


Fig. 61. TGBCa, schematically (after [293]).

10.3.2.2. Survey of line defect observations

- (i) *Dispirations.* As it follows from eq. (84), dispirations are distinctive induced defects of the TGB phases. Their appearance on cooling from the N^* phase could be used for the identification of the phase transition point to a TGBA phase. The simplest geometry for the observation of dispirations in TGBA is a Grandjean–Cano wedge [295]. With parallel anchoring, the texture of a cholesteric sample is made of equidistant defect lines parallel to the dihedral edge of the wedge (see Section 9). The pitch value can be directly calculated knowing the wedge angle and the distance between these lines. When the sample transforms to the TGBA phase a new set of regularly spaced parallel lines of much weaker contrast appears, called slab-dislocations in [295]. Fig. 62 illustrates their origin: each such a line separates regions with a different number of smectic slabs.

Because the number of smectic slabs is geometrically coupled to the rotation parameter ω , the positional discontinuity in the core of a slab dislocation in a TGB phase is always accompanied by a λ -director orientational mismatch between two regions separated by the slab dislocation. This is the very property of a dispiration. Therefore, the slab dislocations that are observed in the TGB Grandjean–Cano wedge are twist-edge dispirations classified by Z in eq. (84).

The number of slab-dislocations visualized as new lines appearing between Grandjean–Cano lines is less than it can be expected from a purely geometrical consideration. The authors [295] address this difference to an escape of a certain portion $\delta\rho/\rho = \delta l_d/l_d$ of density $\rho = 1/l_d$ of screw dislocations from one layer to the next, through an edge dislocation segment. Another possibility would be that the dislocations change direction cooperatively, while staying in the same layer, by

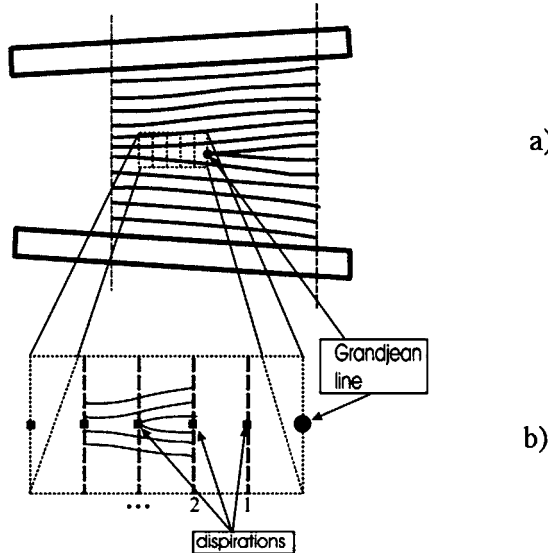


Fig. 62. TGB phase in a Grandjean–Cano wedge: (a) origin of Grandjean–Cano lines, (b) origin of dispirations.

an angle $\delta\theta$, yielding, $\delta\rho/\rho = (\delta\theta)^2/2$, with a negligible cost in energy. Another conclusion is that the dispirations should not appear beyond some critical thickness, as was observed in the experiment. The critical thickness is a function of the wedge angle and elastic constants; it is much larger in the TGBC phase than in TGBA.

- (ii) *Disclinations in Grandjean wedges.* As it follows from eq. (84), the TGBA disclination lines are topologically akin to the N^* disclination lines (same OP, geometrically presented by a set of three directors λ , τ and χ). However the observations of ref. [299] show that there are differences between N^* and TGBA disclinations. These differences are physical, not topological. Line defects of N^* are discussed in Section 9. As indicated in [297], Grandjean–Cano lines clearly take the place of the Grandjean–Cano lines in N^* at the $N^* \rightarrow$ TGBA transition. Therefore they should have the same topology as the defects in N^* , i.e. be elements of the C_λ or J classes, and not dispirations. They are obviously equivalent to edge dislocations with Burgers vectors multiple of $p/2$ (i.e., χ -lines).
- (iii) *Disclinations in spherulites.* Another type of realization of disclinations in TGBA takes place in spherical Robinson droplets [249,250]: a Robinson *disclination radius* (DR) of the N^* phase, whose topological type is I (i.e., it is a $k = 2$ disclination), transforms into a I of the TGBA phase, also along a radius of the spherulite [299]. But, in the transformation, the extremity of the DR opens up into a $k = |1/2|$ loop, Fig. 63, and the DR splits into two helical J-lines that rotate one about the other. This is an important characteristic of the TGBA phase. Its origin is related to three physical characteristics of disclinations in TGBA. They are considered below.

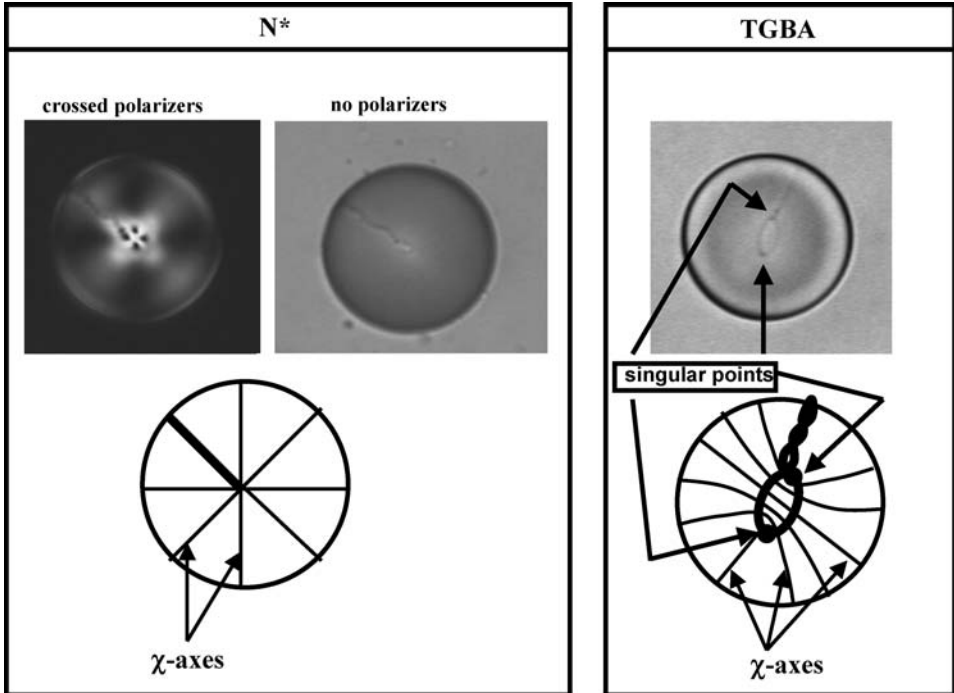


Fig. 63. Textures and the χ -director field in (a) cholesteric and (b) TGBA droplets.

10.3.2.3. Characteristics of disclinations in TGBA vs N^*

- (i) *Materialization of the χ -director.* In the N^* phase the χ -director field has a geometry, which at first sight looks similar to the hedgehog point defect. This defect is expected at the bulk termination of the DR and hence is not a *point defect sensu stricto*. On the other hand due to escaping into third dimension the DR core is not singular and as a result the χ -director field in the vicinity of the bulk termination of the DR strongly deviates from the hedgehog geometry. Indeed, there are no topologically stable singular points in cholesterics. The escaping into the third dimension becomes possible physically because the χ -director field is not materialized in cholesterics. If the χ -director materialized the distortions of the χ -director field would cost additional energy; the core of the DR could be locked from escaping by the structure of χ -director field similarly as in the monopole structures in SmC [189], SmC* and SmC_A* droplets, where the DR remains singular, because its core is locked by the smectic structure, or splits into a *disclination diameter* (see Section 8.2, and Fig. 38(b)). Note that even in these cases the central point is not a singular point, but a termination of the DR. In TGBA the smectic slabs are attached to the χ -director field. Thus, the singularities in the χ -director field would appear as mismatches of smectic slabs. One then expects that the core singularity would have an extent of the order of the slab thickness l_b , and an energy $\approx k_B(T_c - T)\rho_M(l_b)^3 N_A/M$ (ρ_M , mass density, $\approx 1 \text{ g/cm}^3$; N_A , Avogadro number;

M (molecular weight) = 527 for CN; $l_b \approx 10$ nm), namely $1.6 \times 10^{-13} (T_c - T)$ erg, which is prohibitive, even very close to the transition, when compared to a typical core energy Kd ($\approx 10^{-20}$ erg). We believe that this is the main reason of the opening of the termination of the DR into a loop observed at the phase transition from N* to TGBA. The transformation of the χ -director field at this transition is shown in Fig. 63.

- (ii) *Parallelism of smectic layers.* In N* the DR is a line defect, belonging to the homotopy class $I \in Q$; thus it is nonsingular. The transformation of the N* $k = 2$ line into a $k = 2$ TGBA line is limited by the necessity of keeping the slab smectic layers as parallel as possible. It is proposed in [296] that in TGBA escaping of DR into the 3rd dimension is achieved by its splitting into two helically wound disclinations each of charge $k = 1$, staying at a distance not much larger than the pitch. These two $k = 1$ lines are most probably λ -lines (see next paragraph).
- (iii) *Predominance of λ -lines.* The singular point of the χ field, at the centre of the spherulite opens up into two L ($|k| = 1/2$), both joining the two terminations of the two branches of the DR. The global geometry of the distorted χ field opposes the presence of a C_χ . The λ -director is uniformly oriented inside the loop (perpendicular to the smectic layers, Fig. 63), which is slightly elongated in the direction of this director, in order to facilitate a λ non-singular geometry in the core, i.e. favoring a wedge C_λ line vs a twist C_λ line. The extremities of the loop are therefore locations of stronger singularities, and are preferred locations for the short segment. These singularities are often observed and are shown in Fig. 63 by arrows.

10.3.2.4. Density of edge dislocations Edge dislocation densities of the smectic layers, of the type represented Fig. 58, parallel to the slabs, are certainly present in TGBA's. They contribute, in a continuously deformed TGBA, to the curvature relaxation of the TGBA slabs. This will be discussed in more detail below.

10.3.2.5. Generic textures in the TGBA phase

- (i) *The condition of least energy curvature.* Consider a TGBA distorted sample. By the condition of *curvature of least energy*, we mean in the following that any two neighboring twist grain boundaries (TGB) of the sample, T_i and T_{i+1} , are parallel surfaces and that the vortex lines form on T_i and T_{i+1} two sets s_i, s_{i+1} of curves at a constant distance l_d . We require also that the two sets be at a fixed angle w , that is the angle of the local projection of one set onto the other, along the (common) normal to the surfaces, as in the ground state, Fig. 59. In other words, the curved TGB's reproduce locally the geometry of TGB's in the ground state of the TGBA phase. The curvature energy is then limited to the energy of distortion of the SmA layers inside each slab; this distortion can be easily accommodated by edge dislocation densities as alluded to above. There is no variation in the density of vortex lines, and no additional edge lines. The details of the model can be found in [296]. Here we add only that in order to satisfy the condition of least curvature energy, each of the individual TGBs has to be a *developable surface* (DS). But at the same time, continuously distorted TGBs have to be parallel. This latter condition leaves little

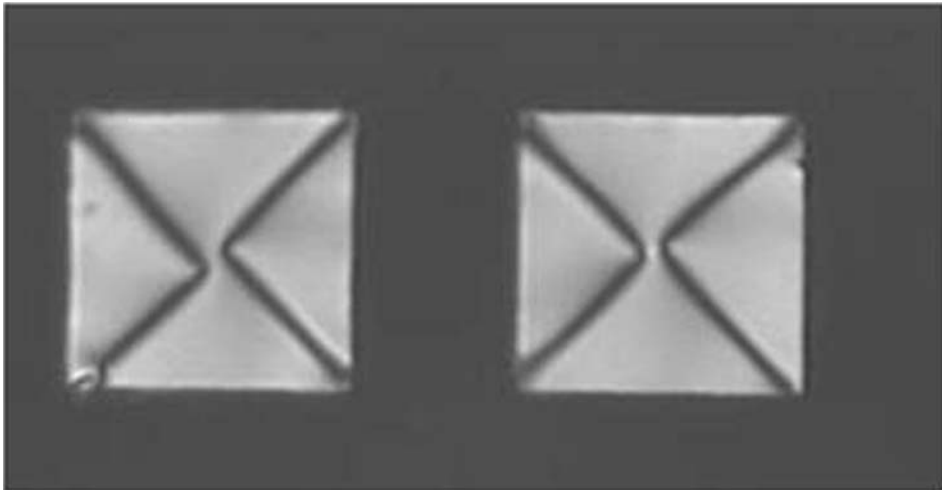


Fig. 64. Free standing films in TGBA; the crossed polarizers are oriented along the diagonals. Edge of a square hole $\sim 42 \mu\text{m}$.

choice on the possible TGB's that fulfil both conditions. A simple solution is when the TGB's are parallel cylindrical surfaces; the vortex lines are along geodesics of the cylinders.

It is important to notice that this type of structural organization does not have the same degree of generality for the TGBA as FCD have for Sm's, and DD for columnar phases. There are indeed in TGBA structural possibilities of comparable energy that can be obtained by continuous modifications of the least curvature energy domains. Such modifications would require change of density of vortex lines in the TGB's, correlated introduction of dispirations and dislocation densities, etc. However, one can expect that numerous textures are not far from obeying the least-energy condition.

- (ii) *DD vs FCD.* It is known that at a scale larger than p , most N*’s distortions are much akin to FCD’s, implying that the cholesteric layers keep a fairly constant thickness. But in TGBA FCD’s are disfavored for two reasons. An obvious one is that the conjugate focal lines (an ellipse, a branch of hyperbola) are singularities of the χ field, which is materialized in the TGBA phase. The core of such a singularity extends over a region that scales as the slab thickness l_b and the related energy cost would be prohibitive (see above). A second reason is because TGB’s, do not tolerate Dupin cyclide geometries, which are very far from obeying the condition of least curvature alluded to above. On the other hand, simple DD’s made of parallel cylinders have been observed [299]. The TGB’s play the role of the spiraling surfaces that carry the bent columns, the χ -axes stay rectilinear in this kind of deformation; Fig. 64 can be easily interpreted in this way. The similarity between TGBA and the columnar phase goes further: one also observes, as in ref. [135], a splitting of the $k = 1$ central disclination into two $k = 1/2$. Theoretical considerations can be found in [296].

10.3.2.6. Elastic energy of the TGBA phase The TGBA energy density has been discussed in [300], for ω irrational, in the harmonic elastic approximation. In principle, one expects three contributions to the elasticity:

$$f = f_\chi + f_{\text{int}} + f_b, \quad (86)$$

where

$$f_\chi = \frac{1}{2} \tilde{K}(\sigma_1 + \sigma_2)^2 + \frac{1}{2} B_p \left(\frac{\Delta p}{p} \right)^2 + \frac{1}{2} B_b \left(\frac{\Delta l_b}{l_b} \right)^2, \quad (87a)$$

$$f_{\text{int}} = \sum_i E(w_i - w_{i+1})^2, \quad (87b)$$

$$f_b = \sum_i \frac{1}{2} \tilde{K}_d (\sigma_{i,1} + \sigma_{i,2})^2 + \frac{1}{2} B_d \left(\frac{\Delta d}{d} \right)^2, \quad (87c)$$

all the summations being on the set of slabs i .

The first contribution f_χ relates to the effects of compression along the χ -axis and of curvature σ_1, σ_2 , of the slabs, including two independent compression terms [296]. Apart the B_b term, it is reminiscent of the N^* character of the TGBA phase (p is the pitch; $\tilde{K} = (3/8)K_3$ and $B_p = K_2 q^2 = 4\pi^2 K_2 / p^2$ in the de Gennes–Lubensky coarse-grained model of a N^* [34]). The relative weight of these terms depends on temperature: at higher temperatures, close to N^* , one might expect that B_p is dominant. Experiment shows that the TGBA material prefers to deform at constant pitch, i.e. at constant vortex lines density, i.e. $\Delta p = \Delta l_b = 0$. The term $1/2K(\sigma_1 + \sigma_2)^2$ accounts for the curved slab energy. In the model of least curvature [296] this term plays no role.

The second contribution, f_{int} is related to the interaction between slabs. This contribution also vanishes in the model of least curvature.

The last one, f_b , concerns the deformation inside the slab [296]. In order to analyze this term, we use again the language of dislocation densities. Consider a slab submitted to a very simple type of curvature, with only one non-vanishing component (such a geometry realizes in a DD), $(\sigma_i = 0, \sigma_j \neq 0, i, j = 1, 2)$, such that the axis of rotation is either perpendicular ($\sigma_1 = 0, \sigma_2 \neq 0$) or parallel ($\sigma_1 \neq 0, \sigma_2 = 0$) to the layers of the slab under consideration, i.e., parallel or perpendicular to the direction that bisects the angle w between the vortex lines on both sides of the TGB. In the first case, the curvature is relaxed by molecular diffusion along the layers, whose effect is to maintain a constant mass density. In the language of dislocations, one would say that the curvature is relaxed by a density of infinitesimal edge dislocations [6] (a concept first introduced in [301] for metals), whose line directions and Burgers vectors both stand parallel to the layers. This effect, which is present in a cholesteric, is already represented in eq. (87a) by the K -term. The second case specializes to a true TGBA, but not to a NL^* phase. The ($|\sigma_1| = 0, |\sigma_2| \neq 0$) curvature of the slab is relaxed by a surface density $|\sigma_2|/d$ of edge dislocation lines perpendicular to the vortex lines, carrying an energy density of the order of $B_d d^2 |\sigma_2|/d = B_d d |\sigma_2|$, see Fig. 65. B_d is a typical smectic elastic compression modulus, larger than B_p or B_b in the cases

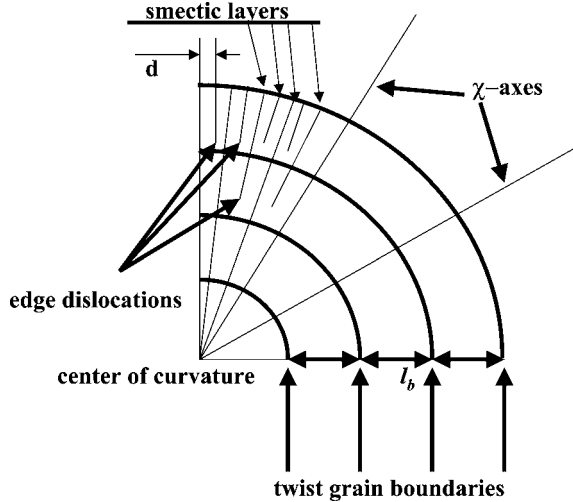


Fig. 65. Edge dislocation densities in a TGBA phase with curved slabs.

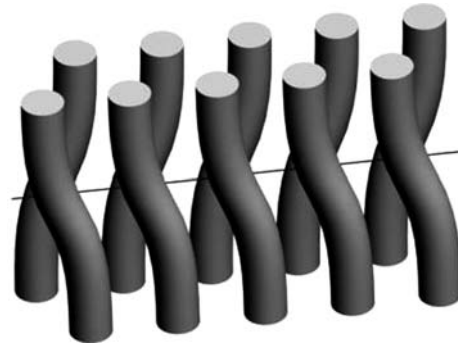


Fig. 66. Twist of the columnar director generates a screw dislocation. Observe that there is no column discontinuity.

of interest. Therefore one expects that this term which conveys the anisotropic properties of the slabs does not play a role if $B_{dd}|\sigma_2| \ll B_b, B_p$, i.e. if the condition $|\sigma_2| \ll qk_2^2$ is satisfied (we have used the relations $ql_b l_d = d$):

$$|\sigma| \ll qk_2^2, \quad (88)$$

where k_2 is a LC material constant, analogous to the superconductor Ginzburg–Landau constant (see [277] and [296]).

10.4. Chiral columnar phases

Twist of the columnar director always generates screw dislocations (Fig. 66). There is no discontinuity of the columns in the vicinity of the columnar screw dislocation. Columnar

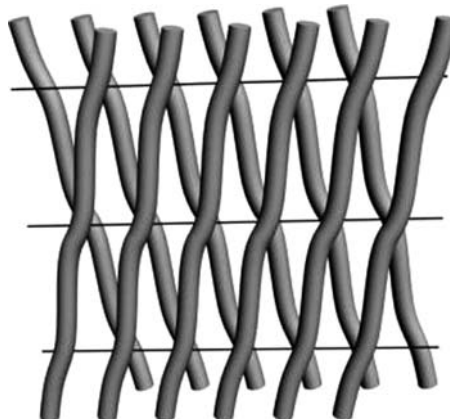


Fig. 67. “Tilt grain” boundary. The solid lines represent screw dislocations.

screw dislocations have been discussed in refs [134] and [302]. There are two principal possibilities to introduce twist into a columnar system. These two possibilities are basic geometries for the frustrated chiral columnar structures discussed below.

10.4.1. *Tilt grain boundary phase*

This phase [303,304] is an analog of the Renn–Lubensky TGB phase [277]; it consists in a set of parallel twist grain boundaries which introduce a finite rotation of the columnar direction, Fig. 67. A word of caution: in order to differentiate it from the Twist-grain boundary (TGB) built on a lamellar structure, the authors of [303,304] have called it a *tilt grain boundaries* phase, but it is a true twist grain boundary phase, built on a columnar structure. The director rotates in a cholesteric fashion around an axis that is perpendicular to the average polymer direction as well as to the grain boundaries.

As for the smectic TGB phases there is a superconducting analogy according to which for the type II material the screw dislocations proliferate if their energy cost is smaller than the energy gain from introducing twist. When the term representing this energy gain is small, screw dislocations are excluded and a perfect crystalline phase persists in the same way that the Meissner phase expels an external magnetic field below the lower critical field H_{c1} . The analogy with superconductors and smectic TGB phases is strict with a small difference that in the columnar TGB phase the parameter δ which is the analog of the Ginzburg–Landau parameter switches the type of the behavior at $\delta = 1$, namely for $\delta < 1$ the material is of type I and for $\delta > 1$ it is of type II. The estimations with the experimental values measured for DNA gives $\delta \approx 5$. Hence long chiral biological polymers forming columnar phases are expected to be analogs of the type II superconductors and the TGB phase is greatly favored.

10.4.2. *Moiré phase*

The second possibility concerns polymers with very long molecules. It consists in rotation of the local bond-orientational order and results in a braiding of the polymer molecules along an average direction. The phase with twisted bond order proposed in [303,304] is also

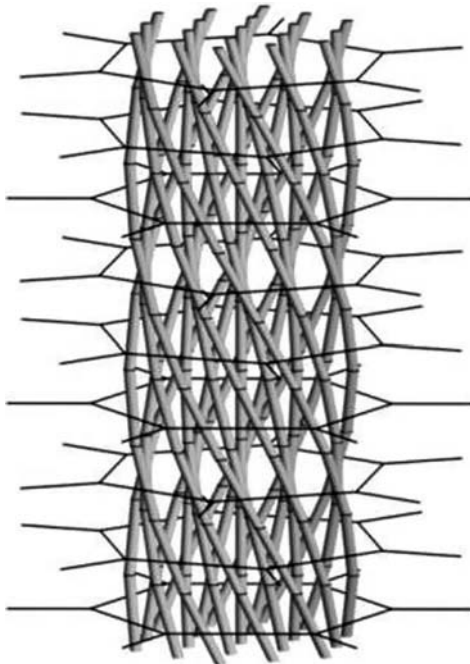


Fig. 68. The Moiré phase. The columnar director is double twisted as the nematic director is in BP. Dark lines represent a stacking of honeycomb arrays of screw dislocations.

an analog of the TGB phase [279] and is called a *Moiré* phase. The Moiré state consists of elementary configurations at which a single polymer at the centre of a bundle is surrounded by hexagonally placed polymers twisting around it. The columnar director field is double twisted like in a double twist cylinder of a cholesteric blue phase. The hexagonal order of the columns competes with the twist and a set of parallel walls perpendicular to the polymer chains, consisting of a honeycomb array of screw dislocations is expected (Fig. 68).

The Moiré state is favored by two terms: one is of the cholesteric type and another is a chiral term in the order of the field θ_6 related to the hexagonal packing of polymer chains. To the best of our knowledge this phase has not yet been discovered experimentally.

10.4.3. Coexistence of helical and 2D positional ordering in biological objects

It is observed that in solutions biological molecules may form finite-size objects which clearly display helicity when observed under the microscope (optical or electron) and exhibit a tendency to local hexagonal ordering. These conditions are incompatible on large scales. It has been proposed in [125] that the finite size of such objects results from their frustrated ordering. Two cylindrical frustrated geometries (below labeled “a” and “b”) for the coexistence of helical arrangement of long biological polymers locally satisfying 2D positional ordering were developed [125]. In both of them molecules are parallel to two families of helicoidal surfaces, i.e. preserving 2D ordering, and simultaneously adopting the double twist orientational order.

These helical structures appear as modifications of the Frank and Kleman [13] model for the splitting of screw dislocations of large Burgers vector in SmA (see Section 5.2). But in the present case the helicoids are substrates for the long polymeric molecules. The “b” model corresponds to a double twisted director field configuration realized in the Blue Phase, but with 2D positional order superimposed on it (see also ref. [264] for details).

A simplified “a” model, which stresses the relationship with a giant screw dislocation, is the following. A set of layers $H(\lambda)$ composed by columns are parallel to a parent surface $H(0)$ which is a ruled helicoid—the surface generated by a straight line $\alpha\beta$ perpendicular to an axis, staying on this axis and rotating helically about this axis with a pitch p (see Fig. 26(d)). λ is the distance from $H(\lambda)$ to $H(0)$ measured along the oriented normal ν . The full set of layers is a SmA screw dislocation whose singularity is not along its axis (that belongs to the ruled helicoid), but takes the shape of *two* helical disclinations of strength $k = 1/2$, rejected at a distance $\bar{w} = b/2\pi$ from the axis, along the cuspidal edges of the focal surfaces of the set of helicoids, such that Burgers vector b is equal to the pitch p of the helicoids ($b > 0$ when the helicoids are right-handed, < 0 otherwise). The parallel columns are located in the layers described as a family of parallel surfaces:

$$H(\lambda) \equiv \{x = r \cos \theta + (\lambda \bar{w}/N) \sin \theta, y = r \sin \theta - (\lambda \bar{w}/N) \cos \theta, z = \bar{w}\theta + \lambda r/N\}, \quad (89)$$

$N^2 = r^2 + \bar{w}^2$; θ and r are polar coordinates. To get a surface obtained by the rotation of a full straight line but not a half-line, r has to change from $-r$ to $+r$. In this model, the geometry is physically limited to a diameter $D = p/\pi$, which is the distance between the two $k = 1/2$ singular helices.

The configurations considered are therefore frustrated. Energy considerations show that the “a” solution is favored when the elastic constants satisfy the condition $K_3 > K_1$. The term ruled by the K_{24} coefficient is small ($\sim (D/p)^4$), and hence does not stabilize the geometry “a” for $K_{24} > 0$ or even $K_{24} < 0$. The nucleation of the “a” configuration is facilitated by the 2D positional ordering tendency.

Case “b” seems favored when $K_1 > K_3$ and is facilitated by a positive, large saddle-splay coefficient K_{24} (see Section 10.2).

The columnar arrangement “a” fits the observations of the chromosome of dinoflagellate [305]. According to Livolant and Bouligand [305] the chromosome has a shape of a rod with double-helical grooves. Two situations that differ by the pitch-over-diameter ratio (p/D) are documented in [305]:

- (1) intact chromosome: $p/D \ll \pi$;
- (2) extended chromosome: $p/D \approx \pi$.

These two situations can be met under different experimental conditions (see [305] for details). Case 2 definitely agrees with the model “a”. Case 1 is more complicated and needs a modification of the model “a”. A possibility to overcome the prohibition on the lateral growth set by the condition $p/D \approx \pi$, hence to achieve situation 1, is discussed in [125].

Both “a” and “b” are frustrated geometries and their topological properties can be discussed via mappings in curved space. Case “b”, which exhibits the topology of a DT cylinder, has already been discussed in Section 10.2. Case “a” is also a DT configuration and can equally be mapped on a sphere S^3 .

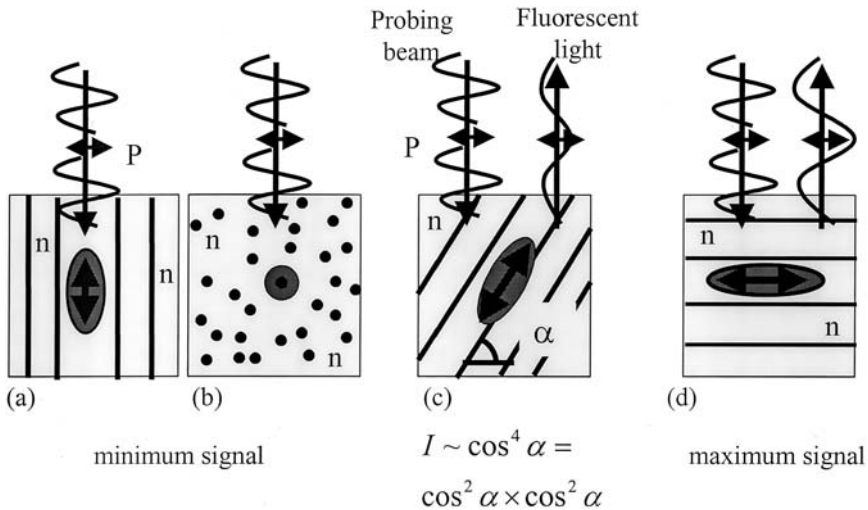


Fig. 69. Principle of visualizing the director configuration in FCPM. The fluorescent molecules (ellipsoids) are aligned by the director. Polarized probing beam excites the dye molecules and causes fluorescence. The efficiency of excitation depends on the angle between the transition dipole of dye molecule (double-headed arrows) and the polarization of the probing beam. The efficiency is minimum in cases (a) and (b), intermediate in case (c) and maximum in case (d). The contrast can be enhanced if the fluorescent light is also routed through a polarizer before reaching a detector. The detected signal will be maximum when the polarization of the fluorescent light is parallel to the direction of polarizer.

Acknowledgments

MK and ODL thank the NSF U.S.–France Cooperative Scientific Program, Grant No INT-9726802 for partial support of their collaboration. ODL acknowledges the NSF for the partial support through the grant DMR-0315523. MK and YuN thank the Université Denis-Diderot (Paris-7) for the support of their collaboration through a position of Invited Professor for YuN. YuN is grateful to Bohdan Senyuk for his help in the preparation of figures.

Appendix: Fluorescent confocal polarizing microscopy

As follows from the discussion in the text, the polarizing microscopy of liquid crystal textures is a somewhat limited instrument as it provides only a 2D image of a 3D sample. The recently developed Fluorescence Confocal Polarizing Microscopy (FCPM) allows one to visualize the whole 3D director structure, see refs [42,43] and Fig. 69.

FCPM is a particular mode of confocal microscopy (CM). In CM, the sample region inspected at a time is a small (submicron) voxel (= 3D pixel) [306]. Signals from nearby voxels are suppressed by a special (confocal) optical design with a pinhole in the image space. The point source of light, the inspected voxel and the pinhole are confocal. Light coming from the neighborhood of the inspected voxel is blocked from reaching the detector. To obtain a 3D image of the whole sample, the tightly focused laser beam scans

the specimen voxel by voxel. Using a computer, the data, that describe an essentially 3D pattern, can be presented as horizontal or vertical cross-sections of the sample.

FCPM adds two distinctive features to CM: (1) the medium under examination is doped with an anisometric fluorescent probe that is aligned by the LC host; (2) the observation is performed in (usually linearly) polarized light. A simple view of how the FCPM visualizes a 3D director field in a nematic sample is as follows.

Imagine a uniaxial nematic composed of elongated molecules and doped with anisometric fluorescent dye molecules. The transition dipoles of both excitation and fluorescence align along \mathbf{n} . The linearly polarized incident light causes fluorescence of the dye. The efficiency of light absorption is determined by the angle between the polarization of incident light and the direction of the absorption transition dipole of the dye molecule, i.e., \mathbf{n} . The excited dye fluoresces. The light intensity detected through another polarizer (or the same, in case of the reflective mode) depends on the angle α between the polarizer and the emission transition dipole of the dye, usually as $\sim \cos^4 \alpha$. Note that in the polarizing microscopy, two complementary director fields that differ everywhere by an angle $\pm\pi/2$ are not resolved (a quartz plate or a similar optical element is needed in the optical pathway of the microscope to resolve this degeneracy). Such a problem does not exist in FCPM; however, one has to be aware that the angle α defines a cone of directions. The degeneracy can be lifted by making observations with different polarization directions.

Apparently, the best resolution of the reflective mode FCPM, close to $0.5 \mu\text{m}$, can be obtained in the vicinity of the entry plane. As the penetration inside the birefringent volume increases, the resolution worsens because of the spatial defocusing of the ordinary and extraordinary modes. However, for a typical optical birefringence of a liquid crystal, ~ 0.1 , and the typical depth of scanning, $10 \mu\text{m}$, the defocusing is only about $1 \mu\text{m}$, therefore the resolution of the microscope remains good.

References

- [1] M. Kleman, in: *Dislocations in Solids*, ed. F.R.N. Nabarro 5 (1980) 243.
- [2] M. Kleman, in: *Dislocations in Solids*, ed. F.R.N. Nabarro 5 (1980) 349.
- [3] Y. Bouligand, in: *Dislocations in Solids*, ed. F.R.N. Nabarro 5 (1980) 299.
- [4] F.C. Frank, *Disc. Farad. Soc.* 25 (1958) 1.
- [5] A.E.H. Love, *A Treatise on the Mathematical Theory of Elasticity* (Dover, New York, 1944).
- [6] M. Kleman and O.D. Lavrentovich, *Soft Matter Physics, an Introduction* (Springer, New York, 2003).
- [7] J. Friedel, *Dislocations* (Pergamon Press, London, 1964).
- [8] R.B. Meyer, *Philos. Mag.* 27 (1973) 405.
- [9] P.E. Cladis and M. Kleman, *J. Physique* 33 (1972) 591.
- [10] See for instance E. Virga, *Variational Theories for Liquid Crystals* (Chapman and Hall, London, 1991).
- [11] For a ref. on display devices, display theory, etc., see for instance ed. L. Vicari, *Optical Applications of Liquid Crystals* (Institute of Physics Publishing, Bristol and Philadelphia, 2003).
- [12] G. Friedel, *Ann. Physique* (Paris) 18 (1922) 273.
- [13] M. Kleman, *Points, Lines and Walls* (Wiley, Chichester, 1982).
- [14] Y. Bouligand, B. Derrida, V. Poénaru, Y. Pomeau and G. Toulouse, *J. Physique* 39 (1978) 863.
- [15] F.R.N. Nabarro, *Theory of Crystal Dislocations* (Clarendon, Oxford, 1967).
- [16] W.F. Harris, *Scientific American* 237 (1977) 130.
- [17] L. Michel, *Rev. Mod. Phys.* 52 (1980) 617.
- [18] N.D. Mermin, *Rev. Mod. Phys.* 51 (1979) 591.

- [19] H.-R. Trebin, *Adv. Phys.* 31 (1982) 194.
- [20] H.R. Trebin, *Phys. Rev. Lett.* 50 (1983) 1381.
- [21] N. Steenrod, *The Topology of Fiber Bundles* (Princeton U.P., Princeton, 1957).
- [22] W.S. Massey, *Algebraic Topology: an Introduction* (Harcourt, Brace and World Inc., New York, 1967).
- [23] T. Frankel, *The Geometry of Physics, An Introduction* (Cambridge University Press, Cambridge, 1997).
- [24] V. Poénaru and G. Toulouse, *J. de Physique* 38 (1977) 887.
- [25] M. Kleman, *J. Physique Lett.* 38 (1977) L199.
- [26] Y. Bouligand, in: *Physics of Defects* (Les Houches, 1980).
- [27] R. Balian, M. Kleman and J.-P. Poirier, eds (North-Holland, Amsterdam, 1981) p. 665.
- [28] M. Kleman and L. Michel, *J. Physique Lett.* 39 (1978) L29.
- [29] Y. Bouligand and M. Kleman, *J. de Physique* 40 (1979) 79.
- [30] V.P. Mineyev and G.E. Volovik, *Phys. Rev. B* 18 (1978) 3197.
- [31] M. Kleman, *J. Physique I France* 2 (1992) 69.
- [32] M. Kleman and L. Michel, *Phys. Rev. Lett.* 40 (1978) 1387.
- [33] S. Chandrasekhar, *Liquid Crystals* (Cambridge University Press, Cambridge, 1992).
- [34] P.G. de Gennes and J. Prost, *The Physics of Liquid Crystals* (Oxford Science Publ., Oxford, 1993).
- [35] D. Demus and L. Richter, *Textures of Liquid Crystals* (VEB Deutscher Verlag für Grundstoffindustrie, Leipzig, 1980).
- [36] S. Chandrasekhar and G.S. Ranganath, *Advances in Physics* 35 (1986) 507.
- [37] M.V. Kurik and O.D. Lavrentovich, *Sov. Phys. Uspekhi* 31 (1988) 196.
- [38] M. Kleman, *Rep. Prog. Phys.* 52 (1989) 555.
- [39] O.D. Lavrentovich and Yu.A. Nastishin, *Europhys. Lett.* 12 (1990) 135.
- [40] G.E. Volovik, *Sov. Phys. JETP Lett.* 28 (1978) 59.
- [41] C. Chiccoli, I. Feruli, O.D. Lavrentovich, P. Pasini, S.V. Shiyanovskii and C. Zannoni, *Phys. Rev. E* 66 (2002) 030701 (R).
- [42] I.I. Smalyukh, S.V. Shiyanovskii and O.D. Lavrentovich, *Chem. Phys. Lett.* 336 (2001) 88.
- [43] S.V. Shiyanovskii, I.I. Smalyukh and O.D. Lavrentovich, in: *Defects in Liquid Crystals: Computer Simulations, Theory and Experiment*, eds O.D. Lavrentovich, P. Pasini, C. Zannoni and S. Zumer (Kluwer Academic Publishers, the Netherlands, 2001) p. 229.
- [44] G.E. Volovik and O.D. Lavrentovich, *Sov. Phys. JETP (USA)* 58 (1984) 1159.
- [45] P.S. Drzaic, *Liquid Crystal Dispersions* (World Scientific, Singapore, 1995).
- [46] O.D. Lavrentovich, *Liquid Crystals* 24 (1998) 117.
- [47] P. Poulin, H. Stark, T.C. Lubensky and D.A. Weitz, *Science* 275 (1997) 1770.
- [48] S.I. Anisimov and I. Dzyaloshinskii, *Sov. Phys. JETP* 36 (1972) 774.
- [49] I.F. Lyuksyutov, *Sov. Phys. JETP* 48 (1978) 178.
- [50] N. Schopol and T.J. Sluckin, *J. Physique (France)* 49 (1988) 1097.
- [51] G. Mazelet and M. Kleman, *Polymer* 27 (1986) 714.
- [52] S.D. Hudson and R.G. Larson, *Phys. Rev. Lett.* 70 (1993) 2916.
- [53] T. Ishikawa and O.D. Lavrentovich, *Europhys. Lett.* 41 (1998) 171.
- [54] H. Mori and H. Nakanishi, *J. Phys. Soc. Japan* 57 (1988) 1281.
- [55] O.D. Lavrentovich, T. Ishikawa and E.M. Terentjev, *Mol. Cryst. Liq. Cryst.* 299 (1997) 301.
- [56] T.W.B. Kibble, *J. Phys. A* 9 (1976) 1387.
- [57] M. Sakellariadou, in: *Patterns of Symmetry Breaking*, eds H. Arodz, J. Dziarmaga and W.H. Zurek (Kluwer Academic Publishers, the Netherlands, 2003), p. 83.
- [58] W.H. Zurek, *Nature* 317 (1985) 505.
- [59] W.H. Zurek, *Phys. Rep.* 276 (1996) 17.
- [60] M.J. Bowick, L. Chandar, E.A. Schiff and A.M. Srivastava, *Science* 263 (1994) 943.
- [61] I. Chuang, R. Durrer, N. Turok and B. Yurke, *Science* 251 (1991) 1336.
- [62] S. Digal, R. Ray and A.M. Srivastava, *Phys. Rev. Lett.* 83 (1999) 5030.
- [63] A.J. Gill, *Contemporary Physics* 39 (1998) 13.
- [64] G.F. Mazenko and M. Zannetti, *Phys. Rev. B* 32 (1985) 4565.
- [65] H. Toyoki and K. Honda, *Prog. Theor. Phys.* 78 (1987) 237.
- [66] M. Hindmarsh, *Phys. Rev. Lett.* 75 (1995) 2502.

- [67] S. Faetti and V. Palleschi, Phys. Rev. A30 (1984) 3241.
- [68] H.J. Yokoyama, Chem. Soc. Faraday Trans. 2-84 (1988) 1023.
- [69] F.M. Leslie, Adv. Liq. Cryst. 4 (1979) 1.
- [70] P.C. Martin, O. Parodi and P.S. Pershan, Phys. Rev. A6 (1972) 2401. See ([6], Chapt. 6) for a comparison between both approaches.
- [71] H. Imura and K. Okano, Phys. Lett. 42A (1973) 403.
- [72] G. Ryskin and H. Kremenetsky, Phys. Rev. Lett. 67 (1991) 1574.
- [73] H. Orihara, T. Nagaya and Y. Ishibashi, in: Formation, Dynamics and Statistics of Patterns, eds K. Kawasaki and M. Suzuki (World Scientific, Singapore, 1993) p. 157.
- [74] J. Eshelby, Philos. Magaz. A42 (1980) 359.
- [75] P.E. Cladis and W.F. Brinkman, Physics Today 35 (1982) 48.
- [76] A. Pargellis, N. Turok and B. Yurke, Science 251 (1991) 1336.
- [77] M. Kleman and C. Meyer, in: Defects in Liquid Crystals: Computer Simulations, Theory and Experiment, eds O.D. Lavrentovich, P. Pasini, C. Zannoni and S. Zumer (Kluwer Academic Publishers, the Netherlands, 2001) p. 301.
- [78] M. Kleman, in: Dislocations, eds P. Vayssi  re et al. (Editions du CNRS, Paris, 1984) p. 1.
- [79] J. Friedel, J. Physique Colloq. 40 (1979) C3-45.
- [80] J.A. Geurst, A.M. Spruijt and G.J. Gerritsma, J. Physique 36 (1975) 653.
- [81] O. Parodi, G. Durand, G. Malet and J.J. Marignan, J. Physique Lett. 43 (1982) L727.
- [82] P.T. Mathey, D.S. Pearson and R.G. Larson, Liq. Cryst. 20 (1996) 539.
- [83] Spatio-Temporal Patterns in Non-Equilibrium Complex Systems, eds P.E. Cladis and P. Palfy-Muhoray, Santa-Fe Institute XXI (Addison-Wesley Pub Cy, Reading MA, 1995).
- [84] Pattern Formation in Liquid Crystals, eds A. Buka and L. Kramer (Springer Press, New York, 1995).
- [85] D.J. Graziano and M.R. Mackley, Mol. Cryst. Liq. Cryst. 106 (1984) 103.
- [86] P.T. Mathey, D.S. Pearson and R.G. Larson, Liq. Cryst. 20 (1996) 527.
- [87] R.G. Larson and D.W. Mead, Liq. Cryst. 15 (1993) 151.
- [88] P. Maneville and E. Dubois-Violette, J. Physique 37 (1976) 285.
- [89] P.E. Cladis and W. van Sarloos, in: Solitons in Liquid Crystals, eds L. Lam and J. Prost (Springer Press, New York, 1992) p. 11.
- [90] M. Doi and S.F. Edwards, The Theory of Polymer Dynamics (Clarendon Press, Oxford, 1986).
- [91] G. Marrucci and P.L. Mafettone, Macromolecules 22 (1989) 4076.
- [92] R.G. Larson, Macromolecules 23 (1990) 3983.
- [93] T. De'N  e  , M. Kleman and P. Navard, C.R. Acad. Sci. Paris s  rie II 316 (1993) 1037.
- [94] T. De'N  e  , P. Navard and M. Kleman, J. Rheol. 37 (1993) 515.
- [95] G. Marrucci and F. Greco, Adv. Chem. Phys. 86 (1989) 331.
- [96] D. Hilbert and S. Cohn-Vossen, Geometry and the Imagination (Chelsea Pub Cy, New York, 1952).
- [97] G. Darboux, Th  orie G  n  rale des Surfaces (Chelsea Pub Cy, New York, 1954).
- [98] P. Boltenhagen, M. Kleman and O.D. Lavrentovich, C.R. Acad. Sci. Paris 315 s  rie II (1992) 931.
- [99] C.E. Weatherburn, Differential Geometry I (Cambridge University Press, Cambridge, 1961).
- [100] J.-B. Fournier and G. Durand, J. Physique II, France 1 (1991) 845.
- [101] J.-B. Fournier, Phys. Rev. Lett. 70 (1993) 1445.
- [102] M. Kleman and O.D. Lavrentovich, Phys. Rev. E61 (2000) 1574.
- [103] M.E. Cates, D. Roux, D. Andelman, S.T. Milner and S.A. Safran, Europhys. Lett. 5 (1988) 733.
- [104] O.D. Lavrentovich, C. Quilliet and M. Kleman, J. Chem. Phys. B101 (1997) 420.
- [105] G. Durand, Liq. Cryst. 14 (1993) 159.
- [106] Z. Li and O.D. Lavrentovich, Phys. Rev. Lett. 73 (1994) 280.
- [107] P. Boltenhagen, O.D. Lavrentovich and M. Kleman, J. Phys. II, France 1 (1991) 1233.
- [108] M. Kleman and O.D. Lavrentovich, Eur. Phys. J. E2 (2000) 47.
- [109] J.P. Sethna and M. Kleman, Phys. Rev. A26 (1982) 3037.
- [110] O.D. Lavrentovich, Sov. Phys. JETP 64 (1987) 984.
- [111] R. Bidaux, N. Boccara, G. Sarma, L. de S  ze, P.G. de Gennes and O. Parodi, J. Physique 34 (1973) 661.
- [112] C. Blanc and M. Kleman, Eur. Phys. J. B10 (1999) 53.
- [113] P.B. Thomas and D. Dhar, J. Phys. A: Math. Gen. 2257 (1994) 27.

- [114] C. Williams and M. Kleman, *J. de Physique* 36 (1975) C1-315.
- [115] P. Boltenhagen, M. Kleman and O.D. Lavrentovich, *J. Physique II, France* 4 (1994) 1439.
- [116] A. Fukuda, Y. Ouchi, H. Arai, H. Takano, K. Ishikawa and H. Takezoe, *Liquid Crystals* 5 (1989) 1057.
- [117] M. Brunet, private communication.
- [118] L. Bourdon, J. Sommeria and M. Kleman, *J. Physique* 43 (1982) 77.
- [119] C. Rosenblatt, R. Pindak, N.A. Clark and R.B. Meyer, *J. Physique* 38 (1977) 1105.
- [120] P. Oswald, J. Béhar and M. Kleman, *Philos. Mag. A* 46 (1982) 899.
- [121] M. Kleman, *Philos. Mag.* 34 (1976) 79.
- [122] H. Pleiner, *Liq. Cryst.* 1 (1986) 197; 3 (1998) 249.
- [123] M. Allain, *J. Physique* 46 (1985) 225.
- [124] C.E. Williams, *Philos. Mag.* 313 (1975) 79.
- [125] M. Kleman, *J. Physique* 46 (1985) 1193.
- [126] J.P. Hirth and J. Lothe, *Theory of Dislocations* (McGraw Hill Book Cy, New York, 1968).
- [127] R.D. Kamien and T.C. Lubensky, *Phys. Rev. Lett.* 82 (1999) 2892.
- [128] S.P. Gido et al., *Macromolecules* 26 (1993) 4506.
- [129] D.W. Bruce et al., *J. Physique France II* 5 (1995) 289.
- [130] A.M. Levelut et al., *J. Physique France II* 7 (1997) 981.
- [131] J.C.C. Nitsche, *Lectures on Minimal Surfaces* (Cambridge University Press, Cambridge, 1989).
- [132] M. Kleman, *J. Physique* 41 (1980) 737.
- [133] G. Monge, *Applications de l'analyse à la géométrie* (chez Courcier, Imprimeur-Libraire pour les mathématiques, Paris, 1807).
- [134] Y. Bouligand, *J. Physique* 41 (1980) 1297.
- [135] P. Oswald and M. Kleman, *J. Physique* 42 (1981) 1461.
- [136] For instance: P. Sierro and D. Roux, *Phys. Rev. Lett.* 78 (1997) 1496.
- [137] G. Basapa, V. Kumaran, P.R. Nott, S. Ramaswamy, V.M. Naik and D. Rout, *Eur. Phys. J. B* 12 (1999) 269.
- [138] S. Muller, C. Börschig, W. Gronski, C. Schmidt and D. Rout, *Langmuir* 15 (1999) 7558.
- [139] A. Léon, D. Bonn, J. Meunier, A. Al-Kahwaji, O. Greffier and H. Kellay, *Phys. Rev. Lett.* 84 (2000) 6. and ref. below.
- [140] R.G. Horn and M. Kleman, *Ann. Physique* 3 (1978) 229.
- [141] M. Zapotocky, L. Ramos, P. Poulin, T.C. Lubensky and D.A. Weitz, *Science* (1999) 209.
- [142] O. Diaf and D. Roux, *J. Physique II France* 3 (1993) 1427.
- [143] Or equivalently $\eta \equiv \frac{\sigma}{\dot{\gamma}} = B(T)\gamma^{-\alpha}$, where η is the viscosity and $\alpha = 1 - m^{-1}$. Most authors express the viscosity in function of the shear rate. We adopt the metallurgical usage.
- [144] T. Gulik-Krzywicki, J.-C. Dedieu, D. Roux, C. Dergert and R. Laversanne, *Langmuir* 12 (1996) 4668.
- [145] P. Oswald and S.I. Ben-Abraham, *J. Physique* 43 (1982) 1193.
- [146] G. Zilman and R. Granek, *Eur. Phys. J. B* 11 (1999) 593.
- [147] A.-S. Wunnenberger-Krepper and A. Colin, *Eur. Phys. J. E* 2 (2000) 277.
- [148] R.G. Larson et al., *Rheol. Acta* 32 (1993) 245.
- [149] R. Bartolino and G. Durand, *Phys. Rev. Lett.* 39 (1977) 1346.
- [150] P. Oswald, *J. Physique* 45 (1984) L-1037.
- [151] P. Oswald, *J. Physique* 46 (1985) 1255.
- [152] N.A. Clark and A.J. Hurd, *J. Physique* 43 (1982) 1159.
- [153] P. Oswald, *J. Physique* 43 (1982) 1193.
- [154] N.A. Clark, *Phys. Rev. Lett.* 40 (1978) 1663.
- [155] M. Kleman and C.E. Williams, *J. Physique Lett.* 35 (1974) L49.
- [156] J.-P. Poirier, *Creep of Crystals* (Cambridge University Press, Cambridge, 1985).
- [157] H. Pleiner, *Philos. Mag.* 54 (1986) 421.
- [158] C. Meyer, S. Asnacios, C. Bourgault and M. Kleman, *Mol. Cryst. Liq. Cryst.* 332 (1999) 531.
- [159] C. Meyer, S. Asnacios, C. Bourgault and M. Kleman, *Rheol. Acta* 39 (2000) 223.
- [160] Orsay Liquid Crystal Group, *J. Physique* 36 (1975) C1-305.
- [161] W.K. Chan and W.W. Webb, *J. Physique* 42 (1981) 1007.
- [162] G.T. Krüger, *Phys. Rep.* 82 (1982) 231.
- [163] P. Oswald and M. Allain, *J. Physique* 46 (1985) 831.

- [164] P. Oswald and M. Kleman, *J. Physique Lett.* 43 (1982) L411.
- [165] R. Bartolino and G. Durand, *Mol. Cryst. Liq. Cryst.* 40 (1977) 117.
- [166] P. Oswald and M. Kleman, *J. Physique Lett.* 45 (1984) L319.
- [167] L. Bourdon, M. Kleman, L. Lejeck and D. Taupin, *J. Physique* 42 (1981) 261.
- [168] C. Meyer, S. Asnacios and M. Kleman, *Eur. Phys. J. E6* (2001) 245.
- [169] M. Kleman and O. Parodi, *J. Physique* 36 (1975) 671.
- [170] S.T. Lagerwall, *Ferroelectric and Antiferroelectric Liquid Crystals* (Wiley-VCH, Weinheim, 1999).
- [171] R.B. Meyer, L. Liébert, L. Strzelecki and P. Keller, *J. Physique Lett. France* 36 (1975) L69.
- [172] A.D.L. Chandani, E. Gorecka, Y. Ouchi, H. Takezoe and A. Fukuda, *Jpn. J. Appl. Phys.* 28 (1989) L1265.
- [173] P. Mach, R. Pindak, A.-M. Levelut, P. Barois, C.C. Huang and L. Furenlid, *Phys. Rev. Lett.* 81 (1998) 1015.
- [174] A. Ikeda, Y. Takanishi, H. Takezoe, A. Fukuda, S. Inui, S. Kawano, M. Saito and H. Iwane, *Jpn. J. Appl. Phys.* 30 (1991) L1032.
- [175] Y. Galerne and L. Liébert, *Phys. Rev. Lett.* 64 (1990) 906.
- [176] Y. Galerne and L. Liébert, *Phys. Rev. Lett.* 66 (1991) 2891.
- [177] J. Watanabe and M. Hayashi, *Macromolecules* 22 (1989) 4083.
- [178] T. Niori, T. Sekine, J. Watanabe, T. Furukawa and H. Takezoe, *J. Mater. Chem.* 6 (1996) 1231.
- [179] Yu.A. Nastishin, M.-F. Achard, H.T. Nguyen and M. Kleman, *Eur. Phys. J. E12* (2003) 581.
- [180] G.W. Gray and J.W.G. Goodby, *Smectic Liquid Crystals* (L. Hill, Glasgow, 1984).
- [181] I. Dierking, *Textures of Liquid Crystals* (Wiley-VCH, Weinheim, 2003).
- [182] R. Bartolino and G. Durand, *Ann. Physique* 3 (1978) 257.
- [183] M. Kleman and L. Lejeck, *Philos. Mag.* 42 (1980) 671.
- [184] R.B. Meyer, B. Stebler and S.T. Lagerwall, *Phys. Rev. Lett.* 41 (1978) 1393.
- [185] P.-G. de Gennes, in: *Collective Properties of Physical Systems*, Nobel 24 (1973) 113.
- [186] P.W. Anderson and G. Toulouse, *Phys. Rev. Lett.* 30 (1977) 508.
- [187] W.F. Harris, *Fundamental Aspects of Dislocation Theory*, N. B. S. Spec. Publ. 317-1 (1970) 579.
- [188] F.R.N. Nabarro, *Fundamental Aspects of Dislocation Theory*, N. B. S. Spec. Publ. 317-1 (1970) 593.
- [189] M.V. Kurik and O.D. Lavrentovich, *Sov. Phys. JETP* 58 (1983) 299.
- [190] C. Allet, P. Vidal and M. Kleman, *J. Physique* 39 (1978) 181.
- [191] A. Perez, M. Brunet and O. Parodi, *J. Physique Lett.* 39 (1978) L353.
- [192] C.Y. Young, R. Pindak, N.A. Clark and R.B. Meyer, *Phys. Rev. Lett.* 40 (1978) 773.
- [193] R. Pindak, C.Y. Young, R.B. Meyer and N.A. Clark, *Phys. Rev. Lett.* 45 (1980) 1193.
- [194] D.H. van Winkle and N.A. Clark, *Phys. Rev. A38* (1988) 1573.
- [195] C.D. Muzny and N.A. Clark, *Phys. Rev. Lett.* 68 (1992) 804.
- [196] R. Loft and T.A. DeGrand, *Phys. Rev. B35* (1987) 8528.
- [197] H. Pleiner, *Phys. Rev. A37* (1988) 3986.
- [198] S. Rivière and J. Meunier, *Phys. Rev. Lett.* 74 (1995) 2495.
- [199] K.-K. Loh and J. Rudnick, *Phys. Rev. Lett.* 81 (1998) 4935.
- [200] M. Brunet and C.E. Williams, *Ann. Physique* 3 (1978) 237.
- [201] M. Brunet and P. Martinot-Lagarde, *J. Phys. II France* 6 (1996) 1687.
- [202] M. Glogarova and J. Pavel, *J. Physique* 45 (1984) 143.
- [203] M.A. Handschy and N.A. Clark, *Ferroelectrics* 59 (1984) 69.
- [204] M. Brunet and L. Lejeck, *Liquid Crystals* 19 (1995) 1.
- [205] N.A. Clark and S.T. Lagerwall, *Appl. Phys. Lett.* 36 (1980) 899.
- [206] L. Lejeck and F. Kroupa, *Czech. J. Phys. B38* (1988) 302.
- [207] L. Lejeck, M. Glogarova and J. Pavel, *Phys. Stat. Sol.* 82 (1984) 47.
- [208] V. Vitek and M. Kleman, *J. Physique*, 36 (1975) 59.
- [209] N.A. Clark, D. Coleman and J.E. MacLennan, *Liquid Crystals* 27 (2000) 985.
- [210] L. Lejeck, *Czech. J. Phys.* 51 (2001) 581.
- [211] L. Lejeck, *Ferroelectrics* 278 (2002) 21.
- [212] W.F. Harris, *Philos. Mag.* 22 (1970) 949.
- [213] K. Ishikawa, T. Uemara, H. Takezoe and A. Fukuda, *Jpn. J. Appl. Phys.* 23 (1984) L666.
- [214] S.A. Langer and J.P. Sethna, *Phys. Rev. A34* (1986) 5035.

- [215] J.M. Carlson, S.A. Langer and J.P. Sethna, *Europhys. Lett.* 5 (1988) 327.
- [216] I. Kraus and R.B. Meyer, *Phys. Rev. Lett.* 82 (1999) 3815.
- [217] J. Pavel, P. Gisse, H.T. Nguyen and P. Martinot-Lagarde, *J. Physique II. France* 5 (1995) 355.
- [218] Y. Takanishi, H. Takezoe, A. Fukuda, H. Komura and J. Watanabe, *J. Mater. Chem.* 2 (1992) 71.
- [219] H.R. Brand, P.E. Cladis and H. Pleiner, *Macromolecules* 25 (1992) 7223.
- [220] Y. Takanishi, H. Takezoe, A. Fukuda and J. Watanabe, *Phys. Rev. B* 45 (1992) 7684.
- [221] Y. Takanishi, H. Takezoe and A. Fukuda, *Ferroelectrics* 149 (1993) 133.
- [222] W. Kuczinski, J. Pavel and H.T. Nguyen, *Phase Transitions* 68 (1999) 643.
- [223] L. Lejcek and V. Dvorak, *Czech. J. Phys.* 44 (1994) 703.
- [224] L. Lejcek, *Czech. J. Phys.* 45 (1995) 503.
- [225] L. Lejcek, *Czech. J. Phys.* 52 (2002) 865.
- [226] M.V. Kurik and O.D. Lavrentovich, *JETP Lett.* 35 (1982) 444.
- [227] O.D. Lavrentovich, *Phys. Rev. A* 46 (1992) R722.
- [228] P.-G. de Gennes, C.R. Hebd. Séances Acad. Sci. 275B (1972) 549.
- [229] E.A. Brener and V.I. Marchenko, *Phys. Rev. E* 59 (1999) R4752.
- [230] M. Maaloum, D. Ausserré, D. Chatenay, G. Coulon and Y. Gallot, *Phys. Rev. Lett.* 68 (1992) 1575.
- [231] M.S. Turner, M. Maaloum, D. Ausserré, J.-F. Joanny and M. Kunz, *J. Physique France II* 4 (1994) 689.
- [232] R. Holyst and P. Oswald, *Int. J. Mod. Phys. B* 9 (1995) 1515.
- [233] T. Ishikawa and O.D. Lavrentovich, *Phys. Rev. E* 60 (1999) R5037.
- [234] D. Subacius, P.J. Bos and O.D. Lavrentovich, *Appl. Phys. Lett.* 71 (1997) 1359.
- [235] D. Subacius, P.J. Bos and O.D. Lavrentovich, *Appl. Phys. Lett.* 71 (1997) 3323.
- [236] D. Voloschenko and O.D. Lavrentovich, *Optics Letters* 25 (2000) 317.
- [237] J.F. Nye and M.V. Berry, *Proc. Roy. Soc. Lond.* A336 (1974) 165.
- [238] J.F. Nye, *Natural Focusing and Fine Structure of Light: Caustics and Wave Dislocations* (Institute of Physics Publishing, Bristol, 1999).
- [239] Optical Vortices, eds M. Vasnetsov and K. Staliunas (Nova Science Publishers, Inc. Commach, NY, 1999).
- [240] J. Friedel and M. Kleman, in: *Fundamental Aspects of Dislocation Theory*, eds J.A. Simmons, R. de Wit and R. Bullough, Special Publication No. 317 (Washington D.C.: National Bureau of Standards) 1 (1970) 715.
- [241] I.I. Smalyukh and O.D. Lavrentovich, *Phys. Rev. E* 66 (2002) 051703.
- [242] F. Grandjean, C.R. Hebd. Séances Acad. Sci. 172 (1921) 71.
- [243] P.S. Pershan, *J. Appl. Phys.* 45 (1974) 1590.
- [244] I.I. Smalyukh and O.D. Lavrentovich, *Phys. Rev. Lett.* 90 (2003) 085503.
- [245] F. Reinitzer, *Monatsh. Chem.* 9 (1888) 421.
- [246] O.D. Lavrentovich and D.-K. Yang, *Phys. Rev. E* 57 (1998) R6269.
- [247] Orsay Liquid Crystal Group, *Phys. Lett.* A28 (1969) 687.
- [248] M. Kleman and J. Friedel, *J. Physique* 30 (1969) C4-43.
- [249] C. Robinson, *Trans. Faraday Soc.* 52 (1956) 571.
- [250] C. Robinson, J.C. Ward and R.B. Beavers, *Discuss. Faraday Soc.* 25 (1958) 29.
- [251] Y. Bouligand and F. Livolant, *J. Physique* 45 (1984) 1899.
- [252] B.I. Halperin, Les Houches, session XXXV 1980, *Physics of Defects*, eds R. Balian, M. Kleman and J.-P. Poirier (North Holland Publishing Company, 1981) p. 813.
- [253] J.-P. Poirier, *Geophys. J. R. Astr. Soc.* 85 (1986) 315.
- [254] R.D. Kamien and J.V. Selinger, *J. Phys. Condens. Mat.* 13 (2001) R1.
- [255] F.C. Frank and J.S. Kasper, *Acta Cryst.* 11 (1958) 184; 12 (1959) 483.
- [256] M. Kleman and J.-F. Sadoc, *J. Physique Lett.* 40 (1979) L-569.
- [257] F.C. Frank, *Proc. Roy. Soc. A* 215 (1952) 43.
- [258] M. Kleman, *Adv. Phys.* 38 (1989) 605.
- [259] H.S.M. Coxeter, *Regular Polytopes* (Dover Pub., New York, 1973).
- [260] M. Kleman, *Physica Scripta* T19 (1987) 565.
- [261] J.P. Sethna, *Phys. Rev. B* 31 (1985) 6278.
- [262] E. Dubois-Violette and B. Pansu, *Mol. Cryst. Liq. Cryst.* 165 (1988) 151.
- [263] J.P. Sethna, D.C. Wright and N.D. Mermin, *Phys. Rev. Lett.* 51 (1983) 467.

- [264] M. Kleman, J. Physique Lett. 46 (1985) L723.
- [265] S. Meiboom, M. Sammon and W.F. Brinkman, Phys. Rev. A27 (1983) 438.
- [266] E. Dubois-Violette and B. Pansu, J. Physique 48 (1987) 1861.
- [267] B. Pansu, M.H. Li and H.T. Nguyen, J. Physique France II 7 (1997) 751.
- [268] B. Pansu, E. Grelet, M.H. Li and H.T. Nguyen, Phys. Rev. E62 (2000) 658.
- [269] P. Jamee, G. Pitsi, M.H. Li, H.-T. Nguyen, G. Sigaud and J. Thoen, Phys. Rev. E62 (2000) 3687.
- [270] E. Grelet, B. Pansu, M.H. Li and H. T. Nguyen, Phys. Rev. Lett. 86 (2001) 3791.
- [271] E. Grelet, B. Pansu, M.H. Li and H.T. Nguyen, Phys. Rev. E64 (2001) 010703(R).
- [272] E. Grelet, B. Pansu, M.H. Li and H.T. Nguyen, Phys. Rev. E65 (2002) 050701(R).
- [273] R. Kamien, J. Physique France II 7 (1997) 743.
- [274] B.A. DiDonna and R.D. Kamien, Phys. Rev. Lett. 89 (2002) 215504.
- [275] P.G. de Gennes, Solid State Commun. 10 (1972) 753.
- [276] V.V. Schmidt, The Physics of Superconductors. Introduction to Fundamentals and Applications (Springer-Verlag, Berlin, Heidelberg, 1997).
- [277] S.R. Renn and T.C. Lubensky, Phys. Rev. A38 (1988) 2132.
- [278] I. Bluestein, R.D. Kamien and T.C. Lubensky, Phys. Rev. E 63 (2001) 061702.
- [279] I. Bluestein and R.D. Kamien, ArXiv:cond-mat/0201035, v1, 3 Jan 2002.
- [280] S.R. Renn and T.C. Lubensky, Mol. Cryst. Liq. Cryst. 209 (1991) 349.
- [281] S.R. Renn, Phys. Rev. A45 (1992) 953.
- [282] L. Navailles, R. Pindak, P. Barois and H.-T. Nguyen, Phys. Rev. Lett. 74 (1995) 5224.
- [283] A. Kundagrami and T.C. Lubensky, arXiv:cond-mat/0303365, v1, 18 Mar 2003.
- [284] J.W. Goodby, M.A. Waugh, S.M. Stein, E. Chin, R. Pindak and J.S. Patel, Nature 337 (1988) 449.
- [285] O.D. Lavrentovich, Yu.A. Nastishin, V.L. Kulishov, Yu.S. Narkevich, A.S. Tolochko and S.V. Shiyanovskii, Europhys. Lett. 13 (1990) 313.
- [286] K.J. Ihn, A.N. Zasadzinski, R. Pindak, A.J. Slaney and J.W. Goodby, Science 258 (1992) 275.
- [287] H.-T. Nguyen, A. Bouchta, L. Navailles, P. Barois, N. Isaert, R.J. Twieg, A. Maaroufi and C. Destrade, J. Physique II France 2 (1992) 1889.
- [288] M. Brunet, L. Navailles and N.A. Clark, Eur. Phys. J. E7 (2002) 5.
- [289] P.A. Pramod, R. Pratibha and N. Madhusudana, Curr. Sci. 73 (1997) 761.
- [290] P.A. Pramod, N.V. Yashodhan Hatvalne and N.V. Madhusudana, Liq. Cryst. 28 (2001) 525.
- [291] I.I. Smalyukh, R. Pratibha, O.D. Lavrentovich and N.V. Madhusudana, Liq. Cryst. 30 (2003) 877.
- [292] A.S. Petrenko, M. Hird, R.A. Lewis, J.G. Meier, J.C. Jones and J.W. Goodby, J. Phys.: Cond.Matter. 40 (2000) 8577.
- [293] P. Rudquist, J.P.F. Lagerwall, J.G. Meier, K. D'havé and S.T. Lagerwall, Phys. Rev. E66 (2002) 061708.
- [294] I. Dierking and S.T. Lagerwall, Liq. Cryst. 26 (1999) 83.
- [295] N. Isaert, L. Navailles, P. Barois and H.T. Nguyen, J. Physique II France 4 (1994) 1501.
- [296] M. Kleman, Yu.A. Nastishin and J. Malthête, Eur. Phys. J. E8 (2002) 67.
- [297] R.D. Kamien and T.C. Lubensky, J. Physique II France 3 (1993) 2131.
- [298] L. Navailles et al., J. Physique II France 6 (1996) 1243.
- [299] Yu.A. Nastishin, M. Kleman, J. Malthête and H.T. Nguyen, Eur. Phys. J. E5 (2001) 353.
- [300] J. Toner, Phys. Rev. B43 (1991) 8289; B46 (1992) 5715.
- [301] J.F. Nye, Acta Metall. 1 (1953) 153.
- [302] M. Kleman and P. Oswald, J. Physique 43 (1982) 655.
- [303] R.D. Kamien and D.R. Nelson, Phys. Rev. E53 (1996) 650.
- [304] R.D. Kamien and D.R. Nelson, Phys. Rev. Lett. 74 (1995) 2499.
- [305] F. Livolant and Y. Bouligand, Chromosoma 80 (1980) 97.
- [306] R.H. Webb, Rep. Prog. Phys. 59 (1996) 427.

This page intentionally left blank

Scanning Probe Microscopy and Dislocations

C. COUPEAU

LMP UMR 6630 CNRS, Bd P.&M. Curie, University of Poitiers, France

J.-C. GIRARD

CNRS-LPN, Site d'Alcatel, Marcoussis, France

and

J. RABIER

LMP UMR 6630 CNRS, Bd P.&M. Curie, University of Poitiers, France

Contents

1. Introduction	275
2. Scanning probe microscopy	275
2.1. Work principle	275
2.2. SPM: a tool for material science studies	279
2.3. Dislocations and surface: what is expected	280
2.4. Some examples of surface topography	284
3. Plasticity	290
3.1. Slip-line patterns	294
3.2. In situ plastic deformation AFM studies: cases of LiF and γ phase single crystals	313
3.3. Localized plasticity around indentations	327
3.4. Dislocation locking effects at the film/substrate interface	331
4. Conclusion	335
Acknowledgements	336
References	336

1. Introduction

The aim of this chapter is to develop the contribution of Scanning Probe Microscopy to the study of dislocations. The work principle of this recent technique is briefly discussed in the first part and its potential is compared to classical dislocation imaging techniques. Some relevant studies by scanning probe microscopies are then presented to illustrate the surface topography that can be found in the vicinity of dislocations. It is here worth noting that this chapter is restricted to Scanning Tunneling Microscopy and Atomic Force Microscopy but there are other related scanning probe microscopies that can be used to study dislocations. As an example, the scattering of hot electrons by individual misfit dislocations leads to significant contrast in the Ballistic Electron Emission Microscopy images [1,2]. The second part is more particularly devoted to the motion of dislocations under stress and the resulting effects generated at the free surface. The potential of this technique is evidenced to analyze the fine structure of slip lines and to give interesting information about plastic mechanisms taking place in the bulk crystal.

2. Scanning probe microscopy

2.1. Work principle

Scanning Probe Microscopy (SPM) has developed into an invaluable and powerful technique and provides a new insight for surface analysis. Due to its wide applicability, SPM has been adopted by many scientific discipline including solid-state physics, materials research and chemistry. SPM has emerged in the last ten years as a novel surface analysis tool with the unprecedented feature to obtain three-dimensional images with lateral and vertical resolution of a tenth of an angstrom, allowing investigation of real-space surface structures down to the atomic level. Since its invention in 1981 by Binnig and Rohrer [3–6], Scanning Tunneling Microscopy (STM) technique has grown rapidly followed by the development in 1986 of the Atomic Force Microscopy (AFM) invented by Binnig, Quate and Gerber [7, 8]. Afterwards, more than twenty related SPM techniques have been reported [9]. They all represent imaging techniques which have in common a tip-shaped probe that senses some specific interaction very close to the surface of the sample and may vary locally while scanning the tip over the surface.

The operating principles of the most developed technique, STM and AFM, are presented in this chapter.

2.1.1. Scanning tunneling microscopy

STM imaging relies on electron tunneling through the energy barrier between two conductors, a sharp metal tip and the surface of a conductive or semiconductive material to be

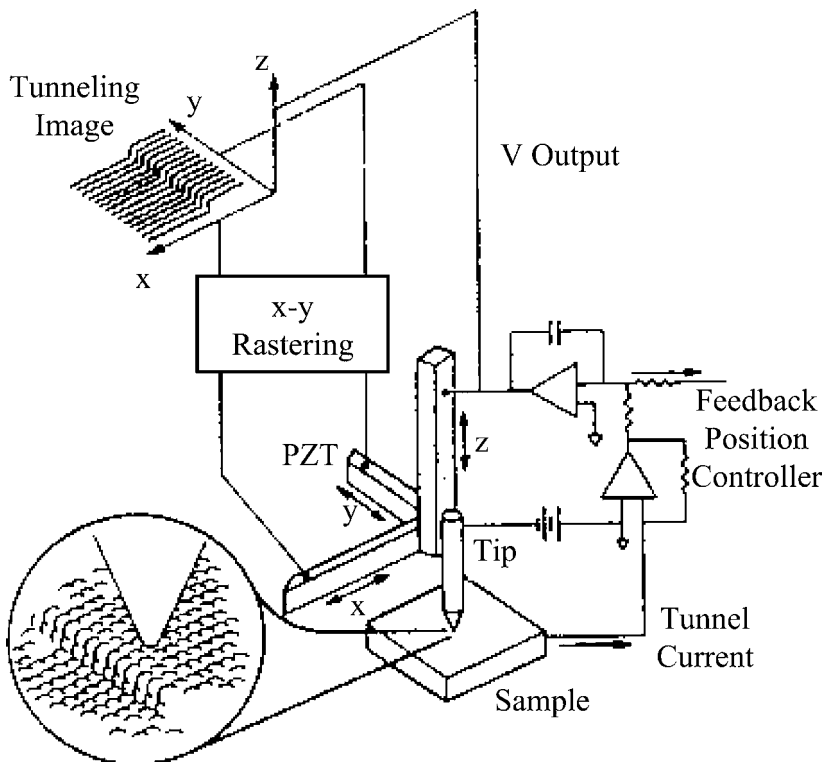


Fig. 1. Schematic set up of a scanning tunnelling microscope. The inset shows the apex of the tip and the sample at the atomic level. The movement of the tip is controlled by three piezo ceramics. The tunneling current is measured through a feedback loop and controls the z distance between the tip and the sample.

investigated (Fig. 1). Under a bias voltage, a minute tunnel current in the range of pA to nA flows between the two electrodes separated by only a few Angstroms distance. The tunneling probability decreases exponentially as the tip-surface separation is increased. When the tunneling gap is small and the voltage low, the expression of the tunneling current can be simplified to:

$$I \propto V \exp(-A\phi^{1/2}d),$$

where $A = 1.025 (\text{eV})^{-1/2} \text{\AA}^{-1}$, ϕ is the average barrier height between the sample and the tip, V is the bias voltage between the sample and the tip and d is the separation distance. Based on this exponential dependence of the current with the separation distance, STM can achieve vertical resolution on the order of 10 pm reproducing the variations of the sample topography.

As a result of the WKB approximation for planar tunneling, the tunneling current can be written as [10–12]:

$$I\alpha \int_0^{eV} \rho_s(E)\rho_t(\mathbf{r}, E - eV)T(E, V, r)dE,$$

where $\rho_s(E)$ and $\rho_t(E)$ are the surface local density of states of the sample and the tip respectively at location \mathbf{r} and the energy E , measured with respect to their individual Fermi levels and $T(E, V, \mathbf{r})$ is the tunneling transmission coefficient of the barrier at the voltage V . This makes the STM a spectroscopic technique; the image contrast can be interpreted as originating from a local modulation of electron density of states of the surface. An STM image is a complex combination of topographical and electronical informations about a surface [13,14].

2.1.2. Atomic force microscopy

AFM does not require electron conductive materials and therefore is capable of resolving surface structures of both conductors and insulators (dielectrics) on the atomic scale. The sample is placed on an xyz translator and is scanned below a sharp probe integrated on a cantilever. While scanning, surface features cause the cantilever to bend. However AFM does not measure force; it measures the deflection of the cantilever as small as 0.001 nm whose spring constant (ranged to 0.01–10 N/m) is weak. The deflection of the cantilever is measured by detecting the angular deflection of a laser beam reflected off the back of the cantilever (Fig. 2). The reflection from the back of the cantilever is monitored with a position-sensitive photodetector with four segments. The difference in intensity ($V_A - V_B$) is used as a vertical deflection signal and ($V_C - V_D$) as the lateral deflection signal. The vertical signal feeds a feedback loop that controls the z motion of the xyz translator in such a way that the cantilever deflection stays constant and hence the force applied by the tip to the sample is kept constant. An image is thus obtained by plotting the vertical motion of the xyz translator as a function of position over the surface. The variation in voltage applied to the z segment constructs the height images which shows the topography of the sample with the color scale corresponding to the height of the sample (Fig. 3(a)). Another way to make an image is to collect the error signal by monitoring the deflection signals with the gains set as high as possible without the feedback loop oscillating to emphasize fine features of the sample surfaces. This produces an effect similar to a high pass filter (or to the first derivative of a height mode image) in which quantitative information is lost. The images are thus not calibrated in the z -axis but present a great visual interest because of the enhancement of fine details (see the dendrite-like structures around buckling pattern α , in Fig. 3(b)).

AFM can be performed in three different modes: contact, noncontact and intermittent contact mode.

- Contact mode makes use of repulsive forces that come into play when the tip touches the sample, causing the tip and the sample to repel each other. In air the force is typically 10^{-7} – 10^{-9} N due to additional meniscus forces due to water condensation in a thin film on the surface.

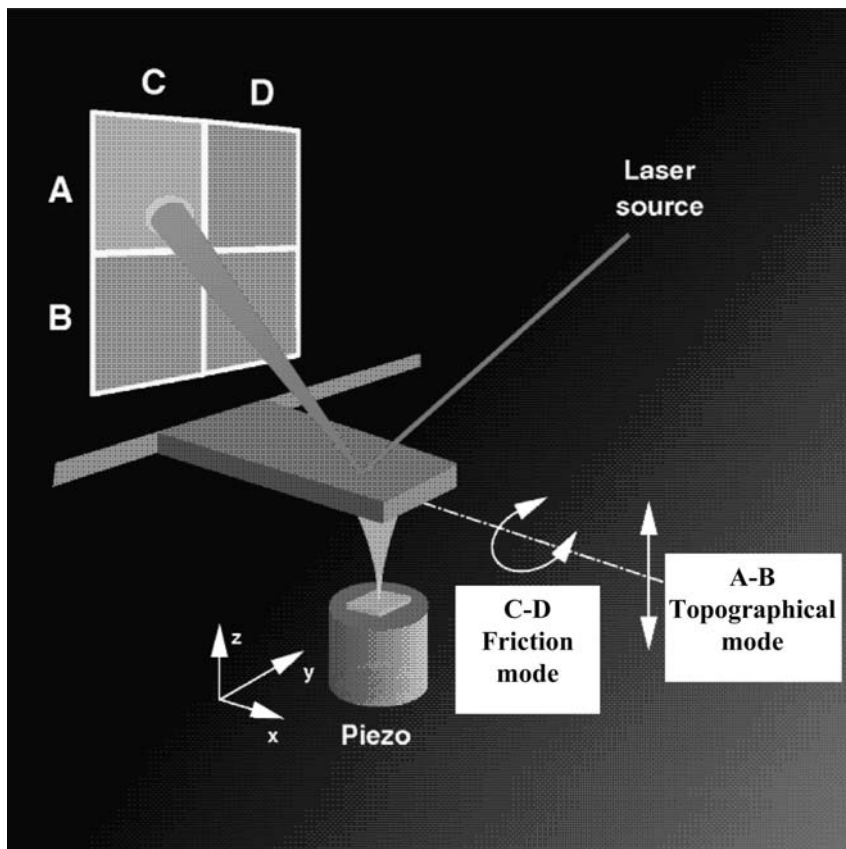


Fig. 2. Schematic diagram of an atomic force microscope based on optical detection of the cantilever deflection.

- In the non-contact mode of operation, the tip is made to scan over the sample surface with a constant spacing of 5–20 nm. Here the cantilever is made to vibrate slightly off its resonant frequency. The long-range force gradient between the tip and the sample causes the tip vibration amplitude to fluctuate according to the surface topography or specific properties. A feedback loop is applied to keep the vibration amplitude constant during scanning. The advantage of this mode is that friction forces inherent in the contact mode are eliminated limiting the damage on soft samples, but the lateral resolution is 10 to 20 nm typically much lower than in the contact mode due to the integration on the tip apex of the long-range tip–sample interaction.
- The intermittent contact imaging mode called tapping mode is a hybrid of the former modes. The tip oscillates with an amplitude of 100 nm and near its resonant frequency of 300 kHz. Rather than maintaining continuous contact with the surface the tip momentarily taps the sample at the end of each vibration (slightly damping the oscillation amplitude). The amplitude is kept constant while scanning over the surface by adjusting the sample height using the feedback loop. Less force is exerted on the sample, thus

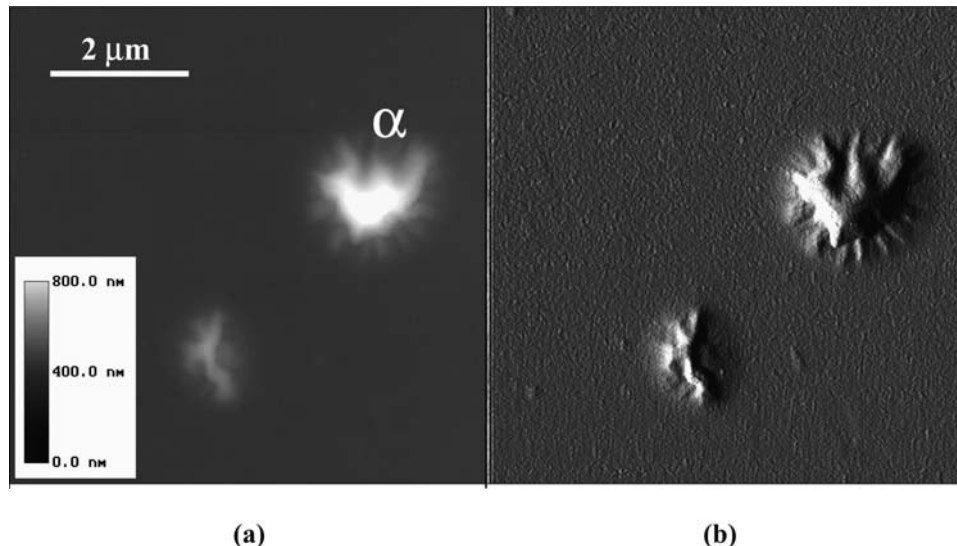


Fig. 3. Buckling pattern on 240 nm thick nickel film on polycarbonate substrate (a) topographical mode AFM image (b) simultaneous signal error mode AFM image. The left image is calibrated in the z -axis whereas the right one is not.

minimizing damaging lateral and eliminating the meniscus force, but the resolution is comparable to that obtained in the contact mode.

2.2. SPM: a tool for material science studies

Numerous techniques are widely used for the imaging and characterization of dislocations [15]. SPM imaging techniques provide useful complementarity with conventional electron microscopes and analytical techniques such as X-ray Photoelectron Spectroscopy (XPS) and Low Energy Electron Diffraction (LEED). Their resolutions are comparable to or even exceeding those achieved by electron microscopes. Transmission Electron Microscopy (TEM) which achieves, under specific conditions, atomic resolution is incomparably adapted to the study of the crystallographic defects in the volume of materials but nearly insensitive to their surface, with the exception of a specific application such as topographical imaging. Moreover, no quantitative measurements can be drawn from the observed topographical contrast. Scanning probe microscopy has great advantages over other high-resolution techniques like TEM in that no extensive and time-consuming specimen preparation such as thinning to insure electron transparency is required. This has to be compared to the cleaning procedure performed by low energy ionic sputtering and annealing of almost any materials under ultra-high vacuum (UHV) on which atomic resolution can be resolved by SPM or the (easy sample preparation by) simplicity of cleavage to obtain clean surfaces. This could be crucial for examination of dislocations, since thin film effects and surface annealing of dislocation could affect the initial dislocation structure.

Even without any further sample preparation at all, epitaxial layers can be grown in UHV and investigated in the same vacuum system by STM and AFM. Due to its high resolution the core of a dislocation threading to the surface can be studied at the atomic level. STM and AFM offer thus the possibility of resolving surface topography as well to study respectively electronic and mechanical properties at the atomic scale.

Furthermore, conventional diffraction techniques such as LEED fail in the study of the surface of bulk insulators due to repulsion or deviation of the electronic probe by surface charges which on the other hand could be used by AFM to get additional images correlated to the standard topographic contrast images. The ability to characterize non-periodic surface structures can be regarded as the main advantages of SPM compared with other surface analysis techniques.

In decoration methods or in etching techniques, the deviations in physical properties in the vicinity of the dislocation from those in the undisturbed bulk are used to bring the defects into the reach of visibility by optical instruments. Overlaps of the etch pits are numerous. This chemical etching enhancement could be greatly reduced by the use of the high resolution of SPM and hence higher dislocation densities could be detected.

A unique feature of SPM, as compared to conventional surface analytical techniques, is their non-dependence on environmental conditions. They can be operated in almost any environment: in air, in inert gas atmospheres, in ultra high vacuum (UHV), in liquids and from low temperature up to several hundred degrees centigrade. Many materials under these conditions are not accessible by any other technique in the size range from < 1 nm to 50 nm.

2.3. Dislocations and surface: what is expected

Fig. 4 illustrates the way a dislocation interacts with surfaces: imaging the surface with SPM techniques will give information about dislocations being located close to the surface, intersecting the surface or that have intersected the surface. As far as topographical contrasts due to a dislocation located close to the surface are concerned, what is available at the surface is a strain field due to the defect. This strain field is not relative only to the characteristics of the dislocation but is the superposition of the strain fields of the dislocation and its image. Indeed, strain fields of dislocations are modified by surface effects and image forces may cause glissile dislocations to be lost to the foil surface or straight dislocation inclined to the surface to rotate toward the screw orientation as the surface is approached.

In order to discuss information that can be obtained by SPM on dislocations, two simple cases are considered in what follows: dislocation lines parallel to the surface and dislocation lines perpendicular to the surface.

2.3.1. Dislocation parallel to the surface

When a rectilinear dislocation is located close to a free surface in a crystal with shear modulus μ , and Poisson ratio ν , it is attracted by the vacuum with a force per unit length $F = \mu b^2 / 4\pi K a$, where $K = 1$ or $1 - \nu$ following the screw or edge character of the dislocation, \mathbf{b} is the Burgers vector, and a the distance between the dislocation and the free

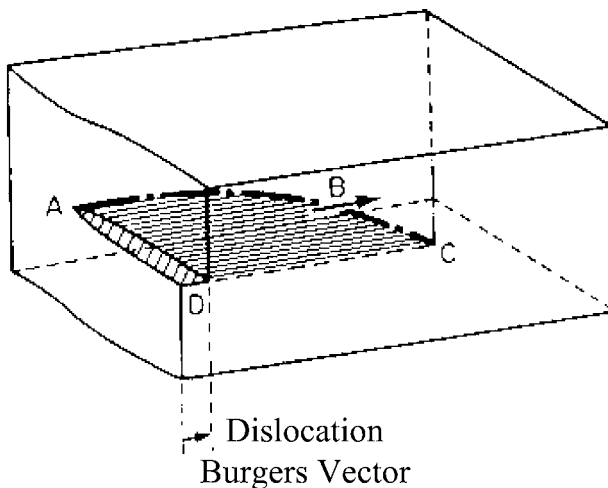


Fig. 4. Schematic of a mixed dislocation. The curved dislocation ABC emerges as a pure edge at C and pure screw at A (Introduction to Dislocations; D. Hull; Materials Science and Technology, Volume 16, editor D.W. Hopkins).

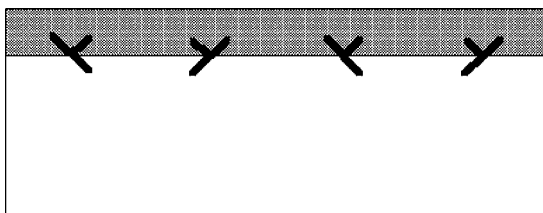


Fig. 5. Misfit dislocations located close to a free surface and having a Burgers vector component perpendicular to the surface.

surface. Under the action of the image force which becomes infinite when a goes to 0, the dislocation tends to escape from the surface yielding a step, the height of which is equal to the component, perpendicular to the surface, of the Burgers vector. For the dislocation to stay in the crystal, forces which oppose the dislocation displacement are required to stabilize the position of the dislocation close to the surface; alternately dislocation could be sessile with respect to the geometry of the material or the thermodynamical conditions. This could be the case when a large Peierls–Nabarro force is felt by the dislocation or when the dislocation to move out of the crystal needs a climb component whereas no supersaturation of point defects is available. Dislocations can also be locked when they are geometrically required in some place, such as misfit dislocations that are located in an interface close and parallel to the surface (Fig. 5). Note also that it has been shown that dislocations can be located at surfaces just because the structure of the surface layer can be different from that of the bulk material [16].

For a dislocation located near the surface having a component perpendicular to the surface, deformation contrast is similar to that of a relaxed surface step [17]. The displacement

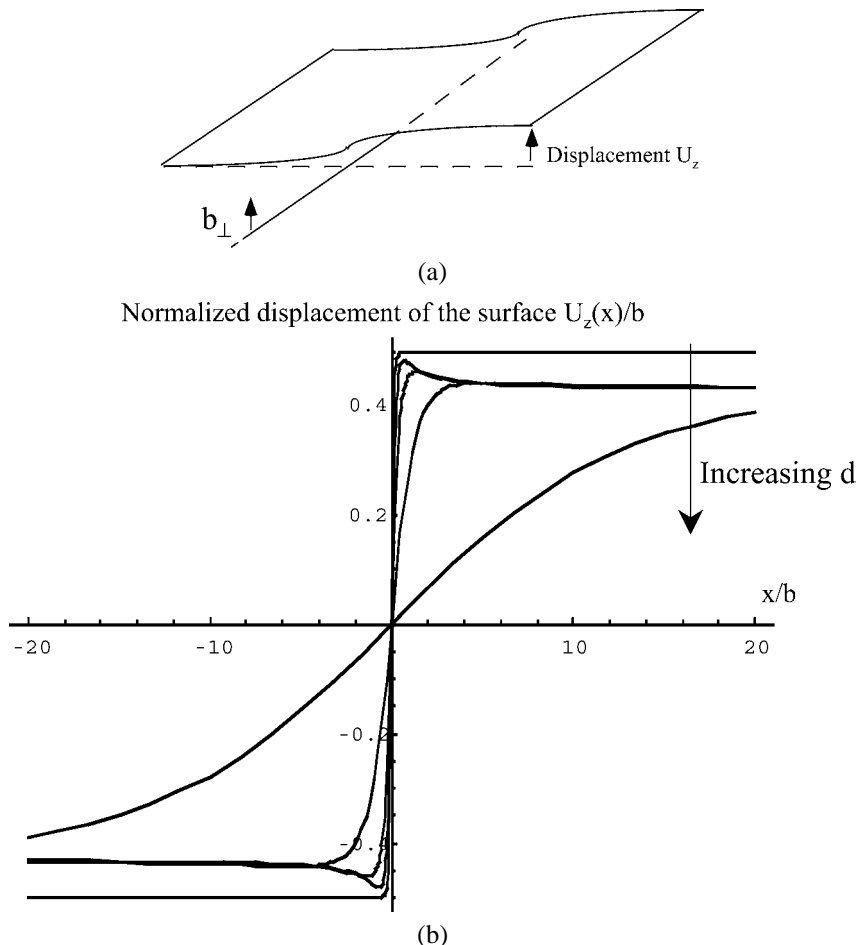


Fig. 6. Dislocation lying parallel to the surface. (a) Relaxed surface step due to a dislocation lying parallel to the surface; b_{\perp} is the Burgers vector component perpendicular to the surface. (b) Surface profile for various distances d of the dislocation from the surface calculated from linear elasticity (courtesy of J. Colin).

field can be deduced from atomistic calculations for a dislocation position close to the surface but elasticity theory is a useful tool to derive the main features as a function of the dislocation location [18]. Indeed this deformation contrast depends on the position of the dislocation with respect to the surface (Fig. 6). The deeper the dislocation, the larger the deformation around the step is spread out on the surface. The length on which the deformation extends on the surface is of the same order as the distance between the surface and the dislocation. This shows that the discrimination between two dislocations at a distance d from the surface can be achieved providing that their distance is larger than d .

A dislocation that emerges at the surface leaves a step whose height is equal to the component of the Burgers vector of the dislocation perpendicular to the surface. This gives post mortem informations about dislocations that have emerged out of the crystal. Note

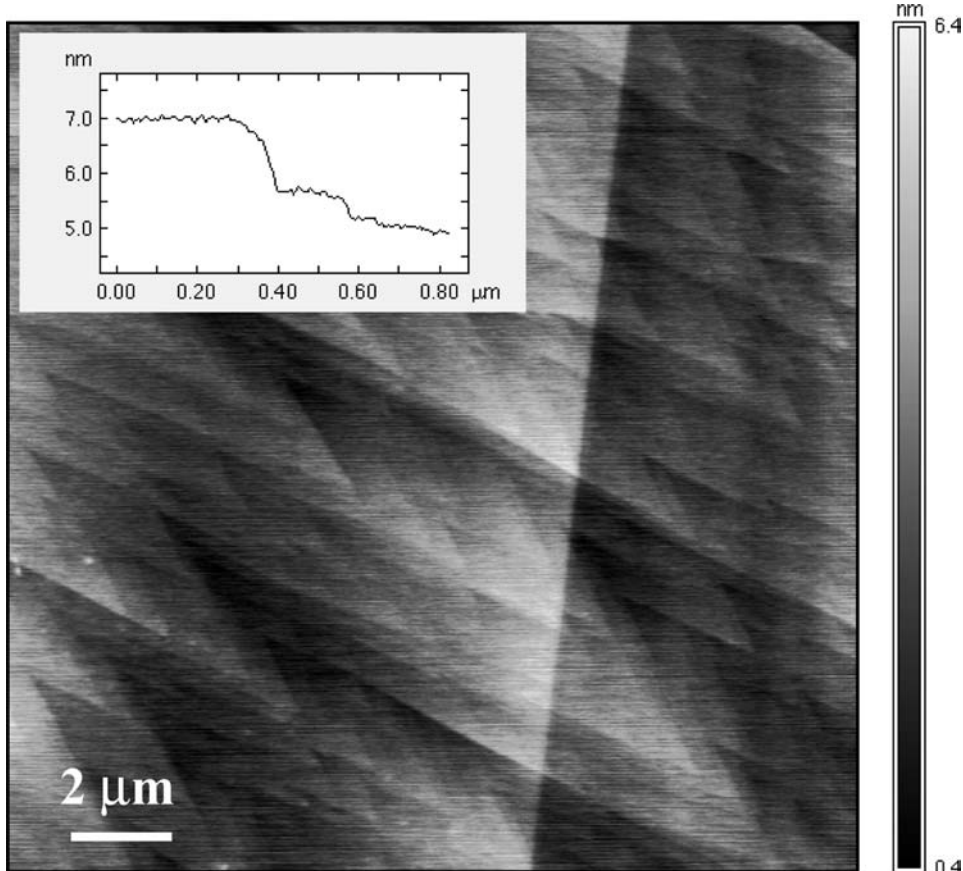


Fig. 7. Appearance of slip line in the first stage of plasticity of LiF single crystals. The cross section is enclosed in the top left of the image and shows that the slip line lying along the [010] direction is composed of two individual steps resulting from the emergence of six and two dislocations respectively.

that those steps can be related to the emergence of several dislocations so that steps can have heights of several times the Burgers vector component (Fig. 7). The orientation of the steps, as well as their heights, can be used to determine the glide plane and the number of dislocations emitted providing the active Burgers vector has been characterized by other methods (cf. Section 3.1).

2.3.2. Dislocation perpendicular to the surface

In this geometry the dislocation core is seen edge on. This geometry is very similar to that used in High Resolution Electron Microscopy (HREM), although in this latter case the contrast arises from the whole atomic column perpendicular to the surface of the thin foil (Fig. 8(a)). However HREM is only sensitive to displacements which are perpendicular to the electron beam, which precludes any observation of screw components for the dislocations characterized.

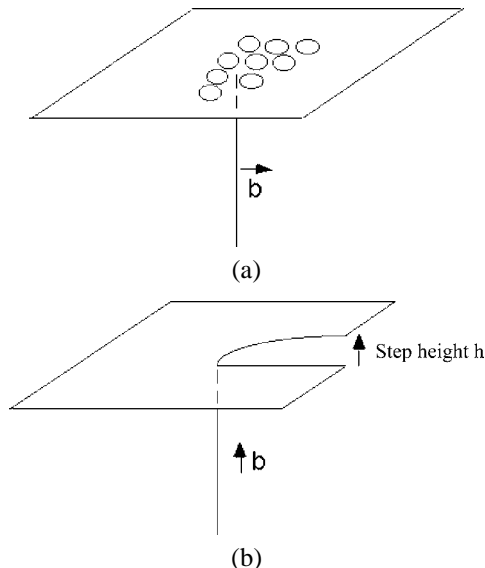


Fig. 8. Dislocation perpendicular to the surface. (a) Edge dislocation: atomic resolution is needed. (b) Screw dislocation with its related surface step.

Such displacements along the dislocation line can be measured using SPM techniques. Determination of the screw component of the Burgers vector is easier since this corresponds to a discontinuity, i.e. a step, on the surface (Fig. 8(b)). Associated to an atomic resolution the measured z displacements can in principle allow resolving the core structure of a screw dislocation.

To allow for the determination of Burgers vector edge component, i.e. the displacements within the surface plane, atomic resolution is needed around the point where the dislocation reaches the surface in order to be able to draw a Burgers circuit around the dislocation core. This is exemplified in Fig. 9 [19]. This method is that used to determine Burgers vector from HREM images.

2.4. Some examples of surface topography

2.4.1. Cleavage steps

Many surfaces obtained by cleavage of brittle materials were investigated by the scanning probe microscopy (Fig. 10) [20–22]. The topography showed river mark and/or fan pattern, ditches and cleavage steps similar to those observed by the scanning electron microscope, but once more the height and the width of these features can accurately measured at the atomic scale from the STM and AFM images.

2.4.2. Interfacial dislocations and dislocation networks

STM and AFM interactions are essentially confined to the very first surface layers, but some studies showed that this statement does not really apply in the case of dislocations,

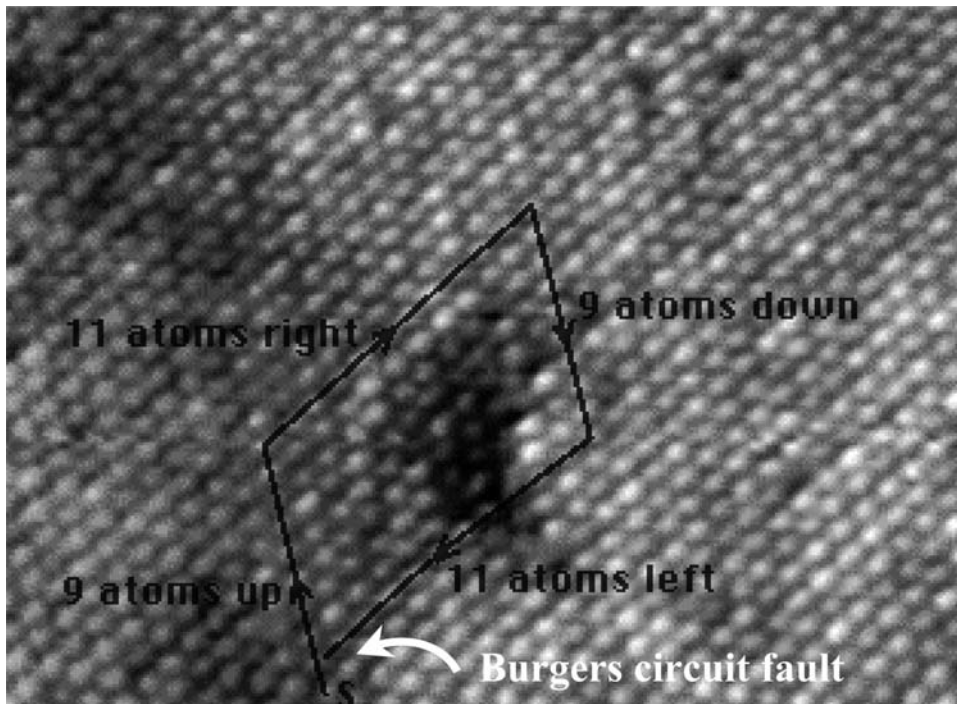


Fig. 9. Burgers circuit drawn around the emergence of a dislocation line at the surface of a sputtered platinum–nickel alloy (courtesy of M. Schmid).

as their effects remain visible by conventional constant-current mode STM even if dislocations are buried up to more than 10 nm below the surface. A surface contrast of a regular honeycomb network of protruding lines associated to vertical atomic displacement which is due to the misfit dislocations present at the CoSi₂ interface in the case of overcritical relaxed layers has been detected by STM topographs. It was concluded that in addition to the lattice displacement explained by simple elastic theory, a quantitative understanding of the surface contrast must take into account an important role of electronic effects linked to variation of the local density of states due to the strain field of the lattice distortion [23].

Some of the defects commonly observed by STM on the (0001) cleavage plane of pyrolytic graphite can be interpreted as dislocation networks associated with different kinds of grain boundaries which may be encountered on the basal plane or in its vicinity [24].

2.4.3. Growth dislocations and micropipes

The factor that has prevented widespread study of silicon carbide by AFM is the relatively high defect density in available wafers and particularly the presence of a type of defects characteristic of hexagonal semiconductors, called micropipes [25–27].

Micropipes are empty hollow tubes penetrating the crystal with diameters in the 1–10 μm range that can propagate along the *c*-axis of the hexagonal crystallographic structure. The density of micropipes is in the range 50–1000 cm^{-2} , usually higher in crystals

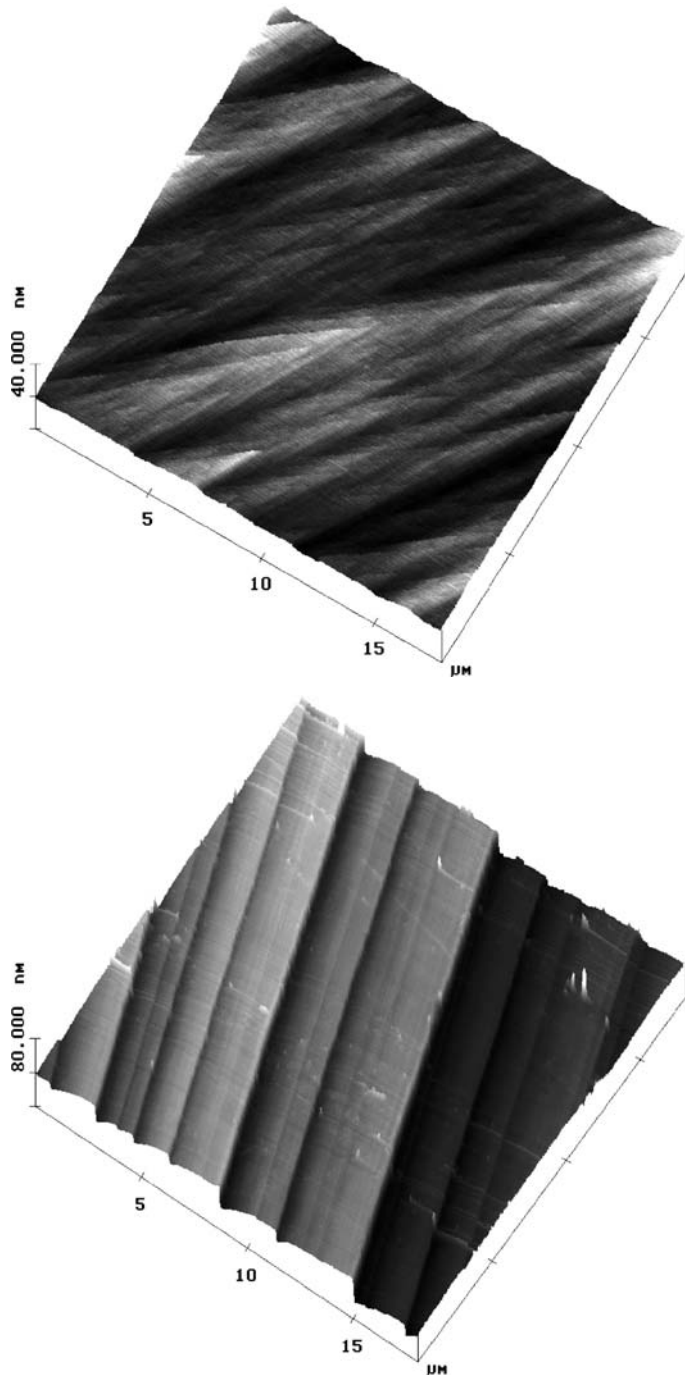


Fig. 10. Three-dimensional AFM images of main surface features of CaF_2 river cleavage patterns.

with larger dimensions. One plausible explanation for the stability of such a narrow cylindrical void was proposed by Frank [28]. If a dislocation with a sufficiently large Burgers vector threads the length of a crystal, it can be energetically favorable to replace the most highly strained part of the crystal in the vicinity of the dislocation line with an empty cylinder. A local equilibrium can be achieved by balancing the elastic energy of the dislocation against the surface energy of facets bounding a narrow cylinder. One of the fundamental prediction of Frank's theory is that the pipe radius r_F should be proportional to the square of the Burgers vector \mathbf{b} and is given as follows:

$$r_F = \frac{Gb^2}{8\pi^2\gamma K},$$

where γ is the surface energy, G the shear modulus and K is a constant determining the character of the dislocation.

Several pieces of experimental evidence are available to support Frank's theory, mainly by optical microscopy. Taking advantage of its high spatial resolution, the AFM is particularly suited to make measurements and has provided interesting information about growth mechanisms which can be speculated from the surface structure and the real nature of micropipes, their origin and formation.

The following conclusions can be emphasized from AFM studies of the 6H-SiC (0001) growth surface:

- All of the micropipes are origins of spiral steps as shown in Fig. 11, indicating that dislocations intersect the surface at these points [29]. Micropipes appear in AFM as black spots (ϕ in Fig. 11) since the probe extends to its lower limit at these voids.
- All observed micropipes are associated with dislocations that have Burgers vector of $N\mathbf{b}_0$, where $N \geq 4$ and \mathbf{b}_0 is the Burgers vector of a unit screw dislocation aligned along the c -axis. Growth spirals formed by dislocations with small Burgers vectors where $N = 1$ or 2 terminate abruptly without forming a micropipe or depression.
- The dimensions and shape of the void have been determined and have confirmed the parabolic relationship between the dislocation Burgers vector and the core radius [30].
- The configurations of the step structures around micropipes are dependent on the polarity (Si- or C-face) and the polytype of the SiC growing surface [31]. A single large step with a step height of $8\mathbf{b}_0$ and 18 steps with a height $\mathbf{b}_0/2$ have been typically observed to propagate from micropipes at the center of each spiral on Si- and C-face respectively, as shown in Fig. 12.
- Heterogeneous objects with micron-scale lateral resolution are often found in the vicinity of the surface/micropipe intersection. Base on these observations, J. Giocondi et al. [29] proposed a model for the formation of super-dislocation/micropipe complexes that involves the coalescence of unit screw dislocations that are forced towards one another as large steps grow around heterogeneous material on the surface.
- The locations and motions of dislocations have been investigated by AFM through a successive chemical etching. Three types of etch pits have been revealed on (0001)Si-face corresponding to micropipes, screw and edge dislocations. It is shown that screw dislocations shifted 10–40 μm outwards from the centre of the spiral during the vertical

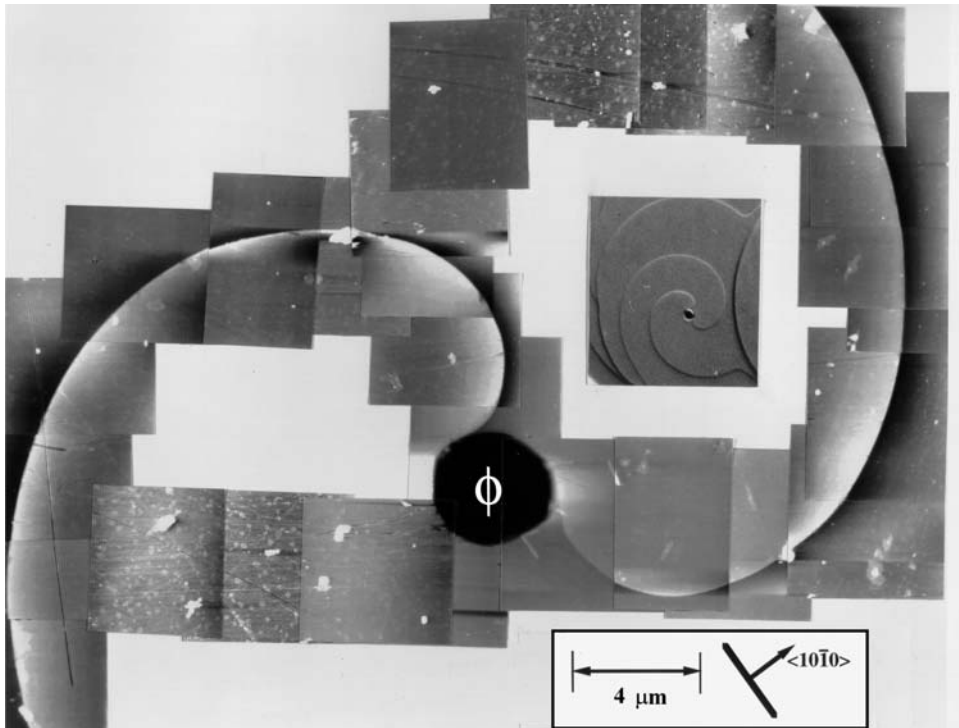


Fig. 11. AFM images showing double spiral on the 6H-SiC(0001) grown surface. The intersection of the micropipe with the surface is labelled ϕ . The inset is a Nomarski optical micrograph of the same feature showing the extended step structure of this defect (courtesy of G. Rohrer).

growth (modified Lely method) of the crystal. On the other hand, the edge dislocations glided in any direction [31].

Dislocation hollow cores have also been observed on the surfaces of a variety of crystal grown from vapours [32,33] and solutions [34,35]. AFM study has been recently carried out on L-arginine phosphate monohydrate single crystals (LAP) [22]. The interest of this material results from its easy cleavage along the {100} planes and its extensive use as substrates for the growth of epitaxial layers for a variety of applications. It has been shown that the origins of monolayer cleavage steps have often hollow cores on LAP, as seen on Fig. 13. Moreover a change of curvature of the steps in the vicinity of their origins is often associated with the presence of micropipes. In contrast with AFM observations on semiconductors, micropipes on LAP cleaved surfaces are of low dimensions roughly cylindrical in geometry, with a maximum observed depth of about 2 nm and a void radius of only few tens of nanometers.

Considering both the elastic and core energies associated with dislocations, van der Hoek et al. derived thermodynamic conditions for the formation of hollow cores at their emergence points [36] and found that a hollow core of radius r_{hc} is always produced during growth when the ratio of Frank's radius r_F to the radius r_c of a critically-sized two-

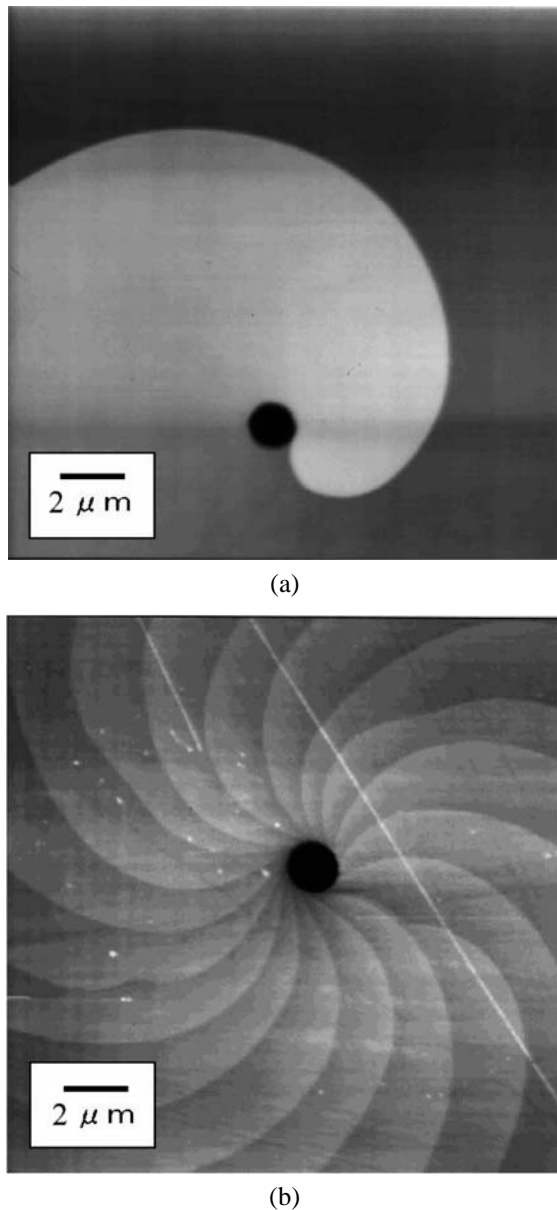


Fig. 12. Topographical AFM images of step structures around a micropipe on the growing surface of 6H-SiC grown on (a) Si-face, (b) C-face (courtesy of N. Sugiyama).

dimensional nucleus lies in a particular range. The condition for the formation is thus given by:

$$r_F = r_{hc} + \frac{r_{hc}^2}{r_c} \quad \text{and} \quad -0.255 < r_F/r_c < 1.78.$$

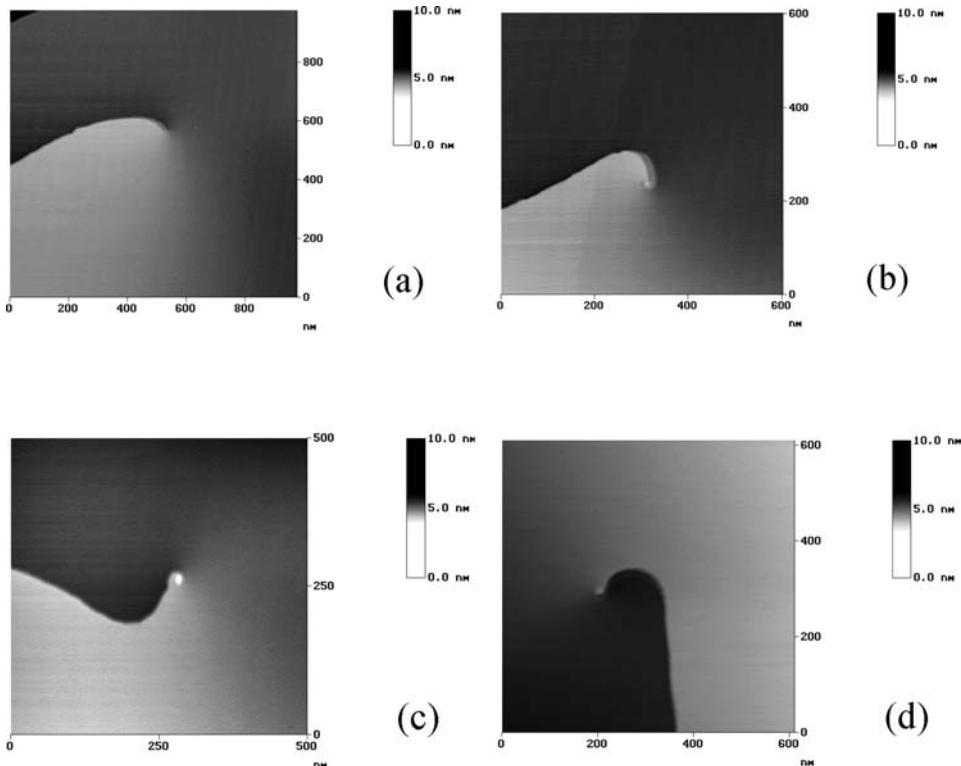


Fig. 13. Typical examples of AFM images showing (a) absence and (b-d) presence of hollow cores at the points of origin of elementary cleavage steps on the (100) cleavage face of L-arginine phosphate monohydrate single crystals. Note that close to the hollow cores the curvatures of steps in (c) and (d) change from positive to negative (courtesy of K. Sangwal).

The experimental results obtained by AFM agree well with the r_F/r_c interval predicted by the theory of Van der Hoek.

3. Plasticity

Observation of the surfaces of materials after or during deformation has always been an important and straightforward way to study plasticity. The analysis of slip lines on deformed single crystals in the thirties [37] is thus at the origin of plastic theories based on slip systems and the dislocation concept [38–40]. Transmission electron microscopy (TEM) is now used extensively to determine both dislocation Burgers vectors and slip planes. Nevertheless surface observation is always carried out since it remains the simplest method to determine the active slip planes in a given material.

Among the recent techniques to analyze the fine slip line structure one can note the kinetic observation method by optical microscopy proposed by H. Neuhäuser [41–43] and

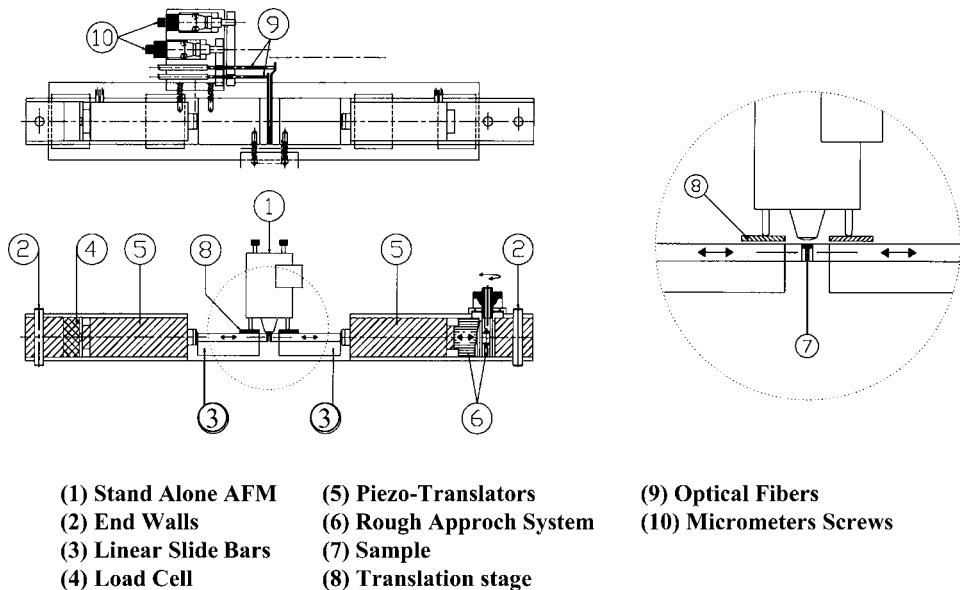


Fig. 14. Experimental apparatus cross sections.

more recently the development of tensile testing inside a scanning electron microscope (SEM) [44–46]. However these techniques do not have a sufficient resolution to follow the emergence of single dislocations characterized by the formation of low-height steps at the surface. This kind of experiment may be successfully carried out taking advantage of the high spatial resolution provided by AFM.

The main difficulty of the method is the necessity to produce a sample surface of low roughness. Indeed, in addition to being chemically inert, the sample must be ‘atomically’ flat over a large area; otherwise steps resulting from the emergence of individual dislocations would be difficult to detect and to analyze. Another requirement in using AFM for the plasticity study arises from the Burgers vector of the dislocations considered which must have a component perpendicular to the surface studied to generate a detectable step.

During the past twenty years, *in situ* deformation on thin foils in TEM has been developed and permits the study of deformation dynamics and the direct observation of the moving dislocations. In a similar way, an experimental apparatus allowing *in situ* surface analysis by AFM during deformation has been recently developed [47,48] and consists of a compression machine interfaced with a Stand Alone AFM. The system shown in Fig. 14 operates in air at room temperature. The specimen is deformed by two piezo-electric translators (PZT) in a symmetrical configuration (number 5), which introduces minimal mechanical vibrations into the system and limits the sample shift with respect to the scanning tip. Each translator is able to extend up to 60 μm in length by minimum increments of 6 nm and can support 30 kN in force. Two linear slide-bars (number 11) have been installed to insure a perfect alignment of the applied stress. Assuming there is no friction between the parts, the applied stress is determined by a load cell (number 4) included behind one of

the two PZT at the end of the system. Two groups of optical fibres bundled together allow the measurement of the movement of the sample edges at the contact surfaces with each piezo translator and thus the determination of the sample strain. All the parts of the device are held rigidly in an Invar tube (near zero thermal expansion coefficient). This apparatus is supported by a pneumatic isolation system to reduce as well as possible the transmission of external vibrations.

The SAAFM works in contact mode so that atoms located on tip and sample repel one another. Contrary to a classical AFM, the SAAFM relies on an optical interference method to detect the deflection of the cantilever. The interference system is mounted directly at the end of the piezo-tube so that adaptation of the deformation machine to the lower part of the microscope is possible. The standard motorized stage used to bring the sample into contact with the scanning tip has been replaced in the SAAFM by a manual adjustment system made up of three finely-threaded screws whose rounded ends rest on the work surface (table or specimen). The maximum observation scan size of this microscope is $18 \mu\text{m} \times 18 \mu\text{m}$ with a vertical displacement of $4.3 \mu\text{m}$. The SAAFM is held on a x - y micrometer stage allowing the translation of the microscope above the sample surface (number 7 and 8).

During a compression test, the scanning tip is always in contact with the surface and the sample is scanned continuously, in spite of additional noise created by the movement of the sample under the microscope. Such an image, on which one scan line corresponds to one strain value assuming the deformation and scan rates are synchronous, has a great interest. However to study plasticity and analyze the fine structure of slip lines the compression machine is stopped just prior to scanning the surface. Thus an entire image corresponds to one specific strain value so that cinephotography can be undertaken. As an example, Fig. 15 shows both the experimental stress-strain curve and three-dimensional AFM views of an LiF surface during deformation. The irregularities observed on the curve are accounted for by both the slight drift of the piezotranslators and the specimen stress relaxation. The grey arrows are used to locate the slip line structures of each image from each to the other. This apparatus is thus particularly suited to follow *in situ* the course of plastic flow from the emergence of the first dislocations from the bulk through the stages of work hardening and the activation of secondary slip systems.

A few relevant examples are presented in the first part of what follows to show the potential of atomic force microscopy to analyze the fine slip line patterns and to give relevant information about plastic mechanisms taking place in the bulk crystal. The second part is devoted to the study of LiF and Ni-based superalloy γ phase single crystals and the contribution of *in situ* observations. A statistical analysis of slip line structures is presented to compare plastic mechanisms in these materials and quantitatively study the surface effects of plastic deformation. These two materials were chosen since they exemplified very different step patterns: LiF has been extensively studied by the past and is characterized by an homogeneous plastic deformation, whereas plasticity in the γ phase is highly heterogeneous on a micrometer scale due to the propagation of planar dislocation pile-ups.

Localized plasticity around indentations and locking effects of dislocations at film/substrate interface are also briefly discussed in the last parts.

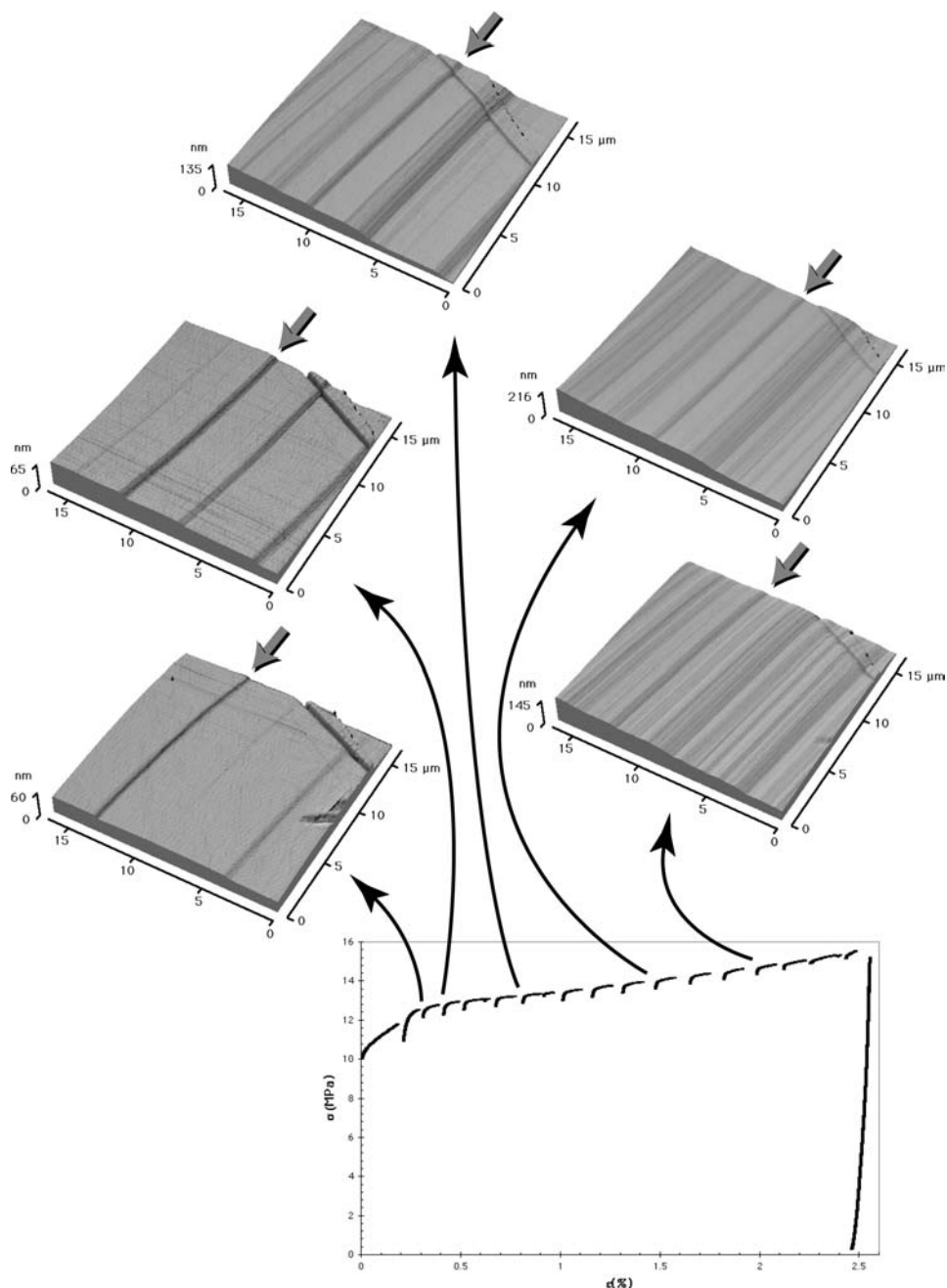


Fig. 15. LiF stress-strain curve with the associated three-dimensional AFM images. The arrows relate the images to the stress-strain curves.

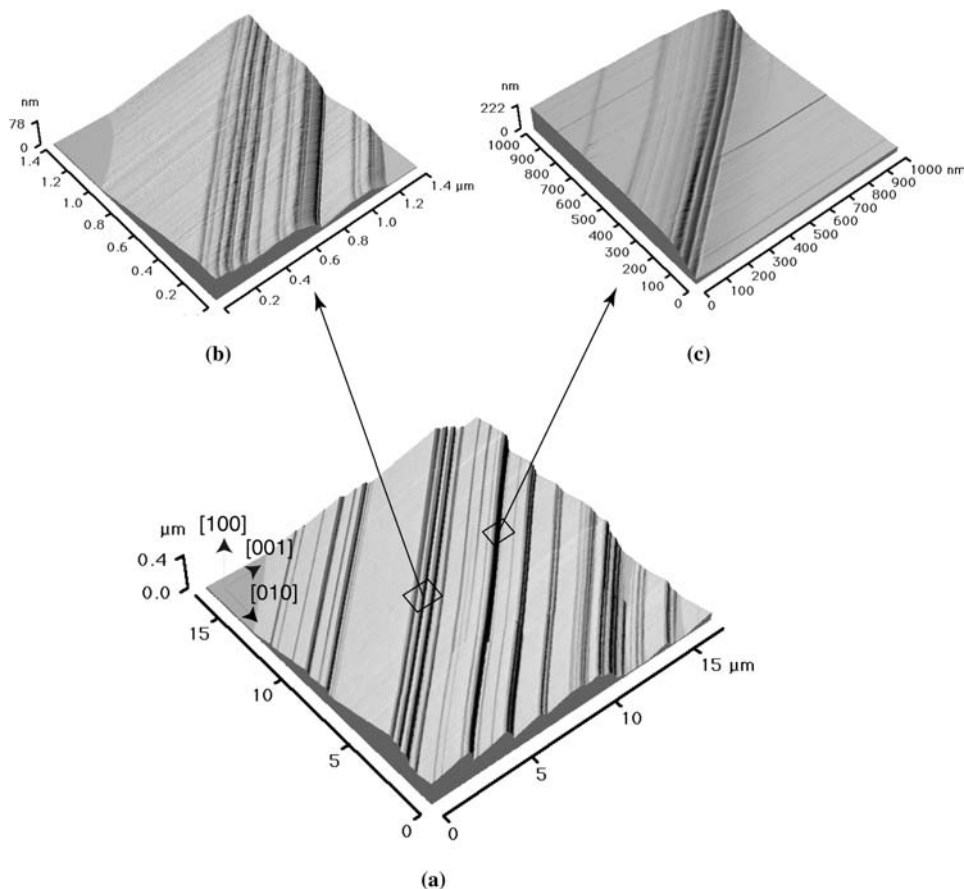


Fig. 16. Three-dimensional AFM view of a deformed single crystal. (a) The surface exhibits slip lines lying in preferential crystallographic direction. (b, c) A closer look at the fine structure of the slip lines seen in (a). The periodic distance between step feature is about 20 nm.

3.1. Slip-line patterns

3.1.1. Fine structure of slip lines

A typical three-dimensional AFM image of a deformed γ phase single crystal is shown in Fig. 16(a). The scan size is about $16 \mu\text{m} \times 16 \mu\text{m}$ with a grey bar of around 400 nm. The surface exhibits slip lines, and the step structure obtained by averaging a few consecutive sections perpendicular to slip lines is presented in Fig. 17. It is clearly seen that slip lines which appear to be individual on a micrometer scale are in most cases composed of many steps of lower height, as observed in Fig. 16(b, c).

AFM observations at a lower scan size, i.e. with a higher lateral resolution, can thus be performed to investigate the fine structure of slip lines. In Fig. 18(a and b), are reported cross-sections perpendicular to slip lines of Fig. 16(b and c) respectively and Fourier trans-

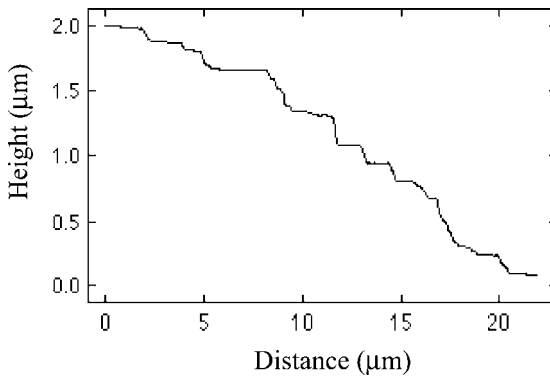


Fig. 17. Step structure obtained by averaging a few cross-sections perpendicular to the slip lines.

forms of these profiles. In this case, an experimental critical distance of 18–20 nm is determined and corresponds to the smallest distance between pile-ups. It must be noticed that the lateral resolution for AFM images presented here is about 2–3 nm, so that this critical value is not an artefact of the experimental apparatus. Moreover, the periodicity of this slip line distance inside a step cluster is clearly resolved by the observation of specific peaks on the Fourier transform. Such a distance between two neighboring glide planes can be also determined by TEM observations (Fig. 19) [49]. These two techniques (TEM and AFM) appear to be complementary as far as plasticity mechanisms are concerned, since the first one investigates dislocations located (post mortem study) or moving (*in situ* TEM) in the bulk crystal, whereas AFM reports on the effects of dislocations which have moved in this bulk crystal and emerged at the sample surface.

3.1.2. Cross-slip effects

In the standard analysis of glide lines, cross slip is usually evidenced by optical microscopy through the occurrence of wavy glide lines. These wavy glide lines can result from double cross-slip process (significant cross-slip effects are seen in A and B in Fig. 20) but can also be due to the mutual annihilation of screw dislocations that are gliding in different primary planes. The mechanism is then driven by the mutual interaction between the screw components of dislocations of opposite sign. In these conditions it may usually be difficult to determine the actual cross-slip plane.

Moreover not all of dislocations are required to take part in such a mechanism: part of them can thus cross slip in another glide plane whereas the others remain in the initial one. Taking advantage of the high vertical resolution of AFM, the number of dislocations splitting into two specific crystallographic planes can therefore be determined unambiguously.

As an example, Fig. 21 represents a residual indent obtained with a 0.5 N load at room temperature in polycrystalline silicon nitride. In the grain G₂ (Fig. 21(a)), numerous slip bands are observed and some of them are enlarged in Fig. 21(b). It appears clearly that some slip bands are split into ones; for example, band A is split into B and C. The Burgers vector of dislocations involved in the formation of those slip bands is likely to be $\mathbf{b} = [0001]$ perpendicular to the surface. Measurements show that the height of the A band equals the

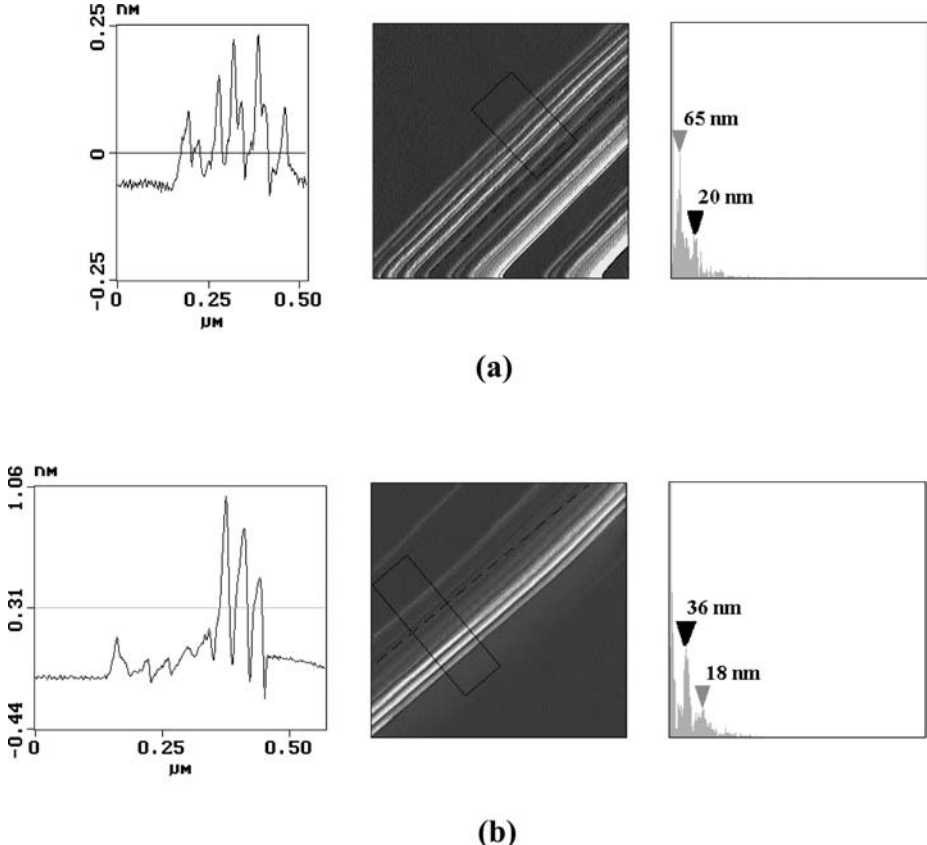


Fig. 18. Cross-sections of slip line pattern (signal error mode) and Fourier transform of these profiles of AFM images presented in Fig. 16(b and c), respectively.

sum of the heights of B and C bands (Fig. 21(c)). This is consistent with dislocation cross slip, the number of dislocations responsible for the creation of the band A being spread out into bands B and C. Moreover the crystallographic plane of A and C is the same whereas planes A and B are at an angle of about 120° , which bears witness to cross-slip events between $\{10\bar{1}0\}$ planes [50].

3.1.3. Chronological activation order of slip systems

The chronological activation order of various slip systems can be determined by local observations of slip line patterns on post mortem samples. As stated previously, the emergence of a single dislocation creates a surface step with a height equal to the Burgers vector component perpendicular to the surface. The emergence of a second dislocation moving on another crystallographic slip plane induces a similar feature at the surface, but a shearing of the first slip line, labeled d in Fig. 22, is observed and characterizes the chronological order



Fig. 19. Bright-field image ($\mathbf{g} = [1\bar{1}\bar{1}]$) showing characteristic dislocation pattern of plastic deformation. In this case, dislocations are principally gliding on (111) crystallographic planes with the $\mathbf{b} = (a/2)[1\bar{1}0]$ Burgers vector (courtesy of M. Jouiad and A. Coujou).

of the dislocation emergence process. In this case, the shift d corresponds to the Burgers vector parallel to the slip traces of the second dislocation.

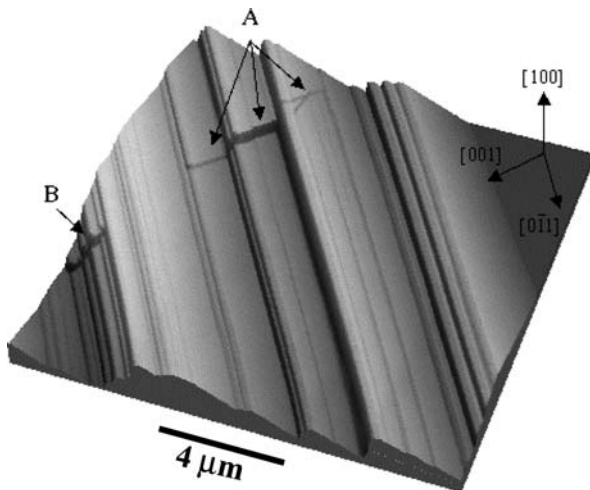


Fig. 20. 3D view AFM image showing cross slip effects (A and B) on deformed γ phase single crystals.

In Fig. 23 is presented a signal error mode AFM image of a deformed γ phase single crystal. The formation of the step structure presented here is thus deduced from the analysis of the slip line fine structure. The image in the lower right corner corresponds to a zoom at a higher lateral resolution of the slip line pattern labeled Z. A shift of the black line is noticed and is accounted for by the subsequent crossing of several white slip lines which have sheared the black one. From this observation, the following conclusions can be emphasized with the surface emergence of pile-ups A, B, C and D in chronological order. It is worth noting that a slip line (S) distinguishes itself from the others through the propagation of pile-up heads in both right and left directions, which is characteristic of a neighboring Frank–Read source just beneath the observed surface.

3.1.4. Quantitative analysis of slip system activation

Considering two symmetrical system, for instance $(011)[0\bar{1}\bar{1}]$ and $(0\bar{1}\bar{1})[011]$ in a cubic sample (Fig. 24): when associated to a compressive stress along the [010] direction two step structures, increasing or decreasing, are produced at the surface but lie along the same [100] crystallographic direction. These two symmetrical slip planes which consequently produced identical slip traces can thus not be differentiated by classical observations. Taking advantage of the topographic resolution offered by AFM, the analysis of slip line patterns is an interesting way to determine unambiguously the active slip planes depending on both direction and shape of step structure.

On Fig. 25 is presented signal error mode AFM images of step structures of a γ phase single crystal compressed along the [001] crystallographic direction. The primary slip system is the $\{111\}\langle 110 \rangle$. The black and white lines correspond respectively to increasing and decreasing steps from left to right and the associated active slip planes are indicated. The plastic deformation is highly heterogeneous with large areas with no slip lines. An evident asymmetry of active planes is also noticed; slip lines at the surface come principally from the activation of the $(\bar{1}11)[101]$ slip system. In Table 1, the degree of slip plane activation

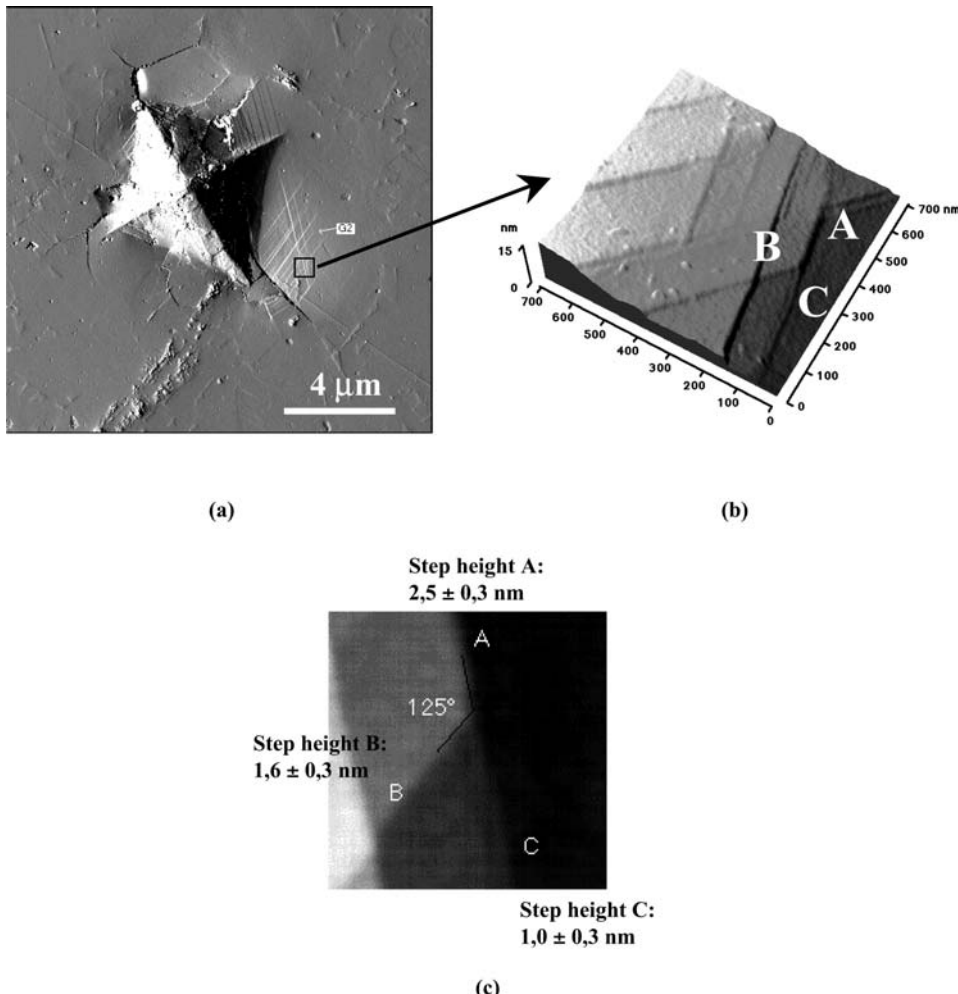


Fig. 21. Slip line structure around an indentation in Si_3N_4 . (a) Signal error mode AFM image of a 0.5 N load indentation. (b) 3D AFM of slip line structure in grain labelled G2. (c) Step structure resulting from a twinning mechanism (courtesy of X. Milhet).

is reported in percentage of slip lines in the observed scan size of about 70 μm . No apparent effects have been noticed due to the system $(111)[\bar{1}01]$. The activation of $(111)[0\bar{1}\bar{1}]$, $(\bar{1}\bar{1}1)[0\bar{1}1]$, $(1\bar{1}\bar{1})[011]$ and $(11\bar{1})[011]$ slip systems does not induce step structure at the surface but could be deduced from slip line shearing, which requires studies at a shorter scan size.

3.1.5. Fractal analysis of slip line structure

Fractal analysis has been first introduced by Mandelbrot [51] in order to describe irregular patterns. In the 1980's, several authors applied this kind of approach to slip line struc-

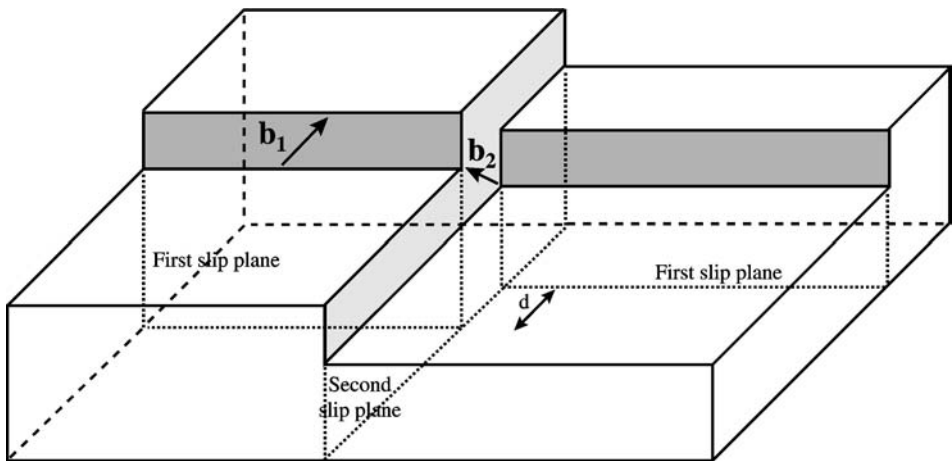


Fig. 22. Theoretical step structure induced by the emergence of two dislocations gliding on different crystallographic planes.

Table 1
Degree of slip system activation in percentage of slip lines.

(111)[$\bar{1}01$]	0%	($\bar{1}11$)[101]	83%	(1 $\bar{1}\bar{1}$)[$\bar{1}01$]	14%	(11 $\bar{1}$)[101]	3%
(111)[011]	shear	(111)[011]	shear	(111)[011]	shear	(111)[011]	shear

tures in single crystals [52–54,54]. The slip lines on cadmium single crystals plastically deformed in uniaxial tension, viewed by scanning electron microscopy (SEM) at different magnification, reveal self-similarity in their lateral structure. The slip pattern exhibits thus a fractal behavior depending on the homogeneity and degree of deformation, in magnifications ranging from 1000 to 20 000 [55]. The high resolution provided by AFM allows to analyze a larger interval of magnifications ranging from 1100 to 1 110 000 and consequently to extend the method down to a nanometer scale.

As an example, in Fig. 26 is presented three-dimensional AFM pictures for various magnifications M of the slip line pattern on the surface of a GaAs/GaAlAs heterostructure on GaAs substrate deformed in tension at room temperature by three-point bending [56].

Deformed thin films on substrate systems have been recently extensively studied by AFM to demonstrate the feasibility and efficiency of a new method proposed by Peyrade et al. [57–59], where plasticity is used to generate quantum wires through the occurrence of controllable steps on a surface. So, if the slip can be controlled by choosing relevant parameters, such as crystal orientations, stress conditions, density of Frank–Read sources and temperature, there is a possibility to produce steps at the free surface perfectly defined in height and lateral size. Dislocations are thus used as an atomic saw to cut existing two-dimensional structures (thin films) in order to obtain one dimensional wires. This process is strongly dependent on the capability of dislocations to create regular steps with specific height and high degree of reproducibility. Statistical analysis of the slip line structure can be carried out to determine the efficiency of the method and also evaluate the influence of

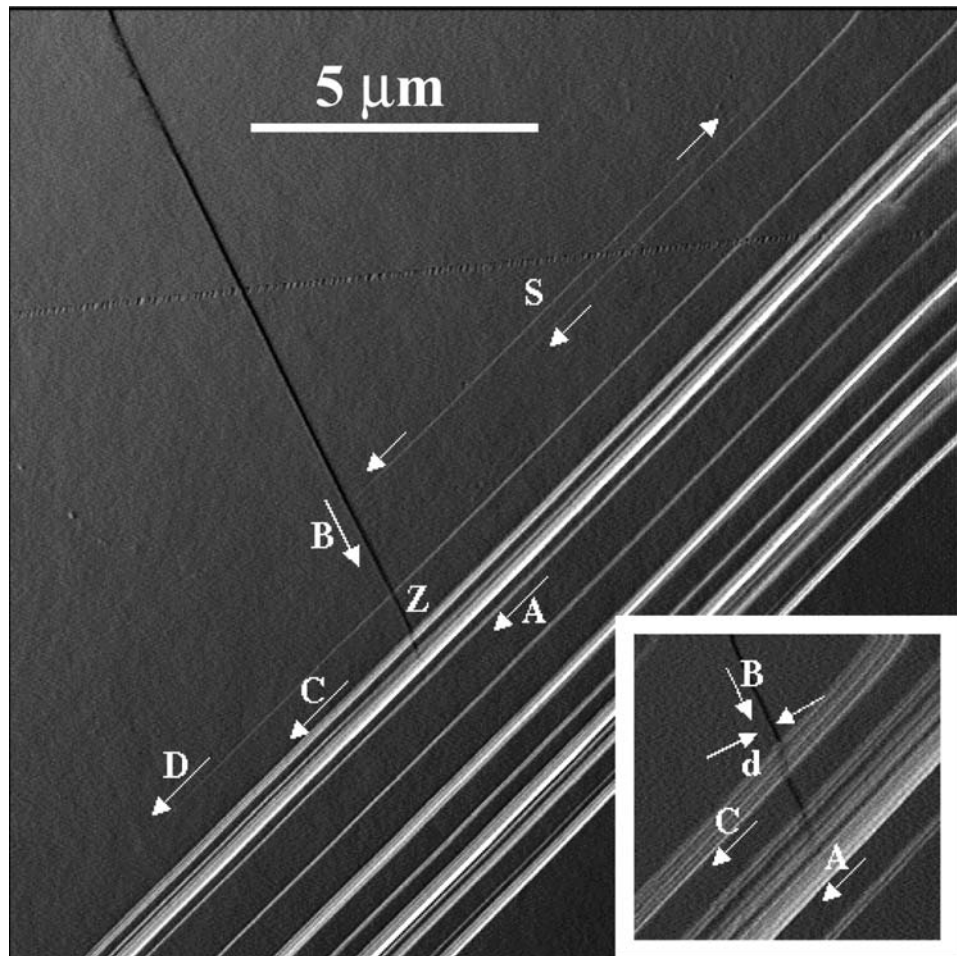


Fig. 23. Formation of slip line pattern with the emergence of pile-ups A, B, C and D in chronological order. Step structure Z is examined closely in the lower right part of the image. (S) symbolises the presence of a Frank–Read source just beneath the surface.

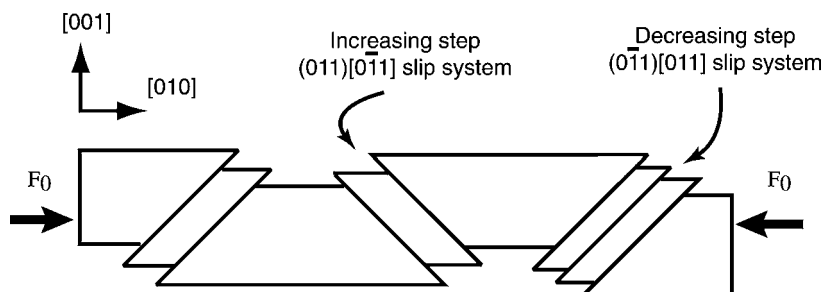


Fig. 24. Compression of a single crystal in a cubic configuration giving rise to increasing and/or decreasing steps.

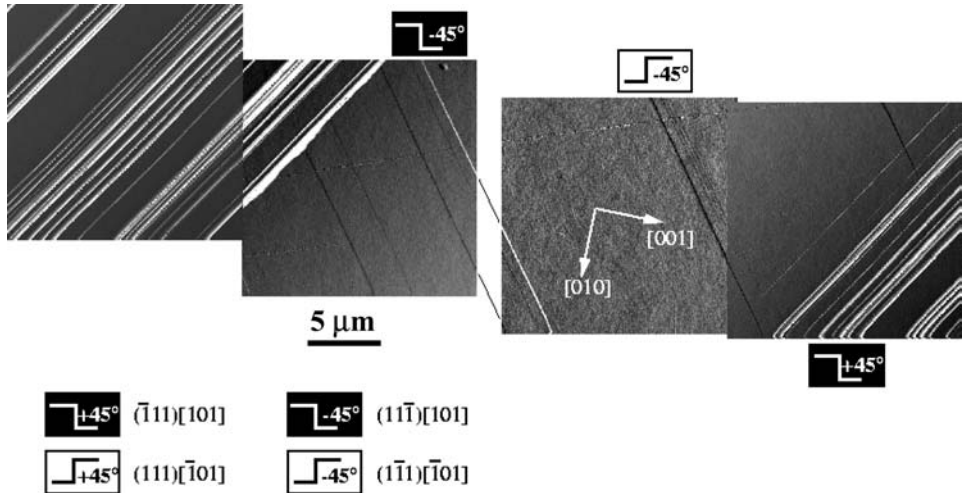


Fig. 25. Heterogeneity of plastic deformation of γ phase single crystals. The compression axis is the [001] direction. Black and white slip lines correspond respectively to increasing and decreasing steps from left to right. Active slip systems are indicated by specific symbols.

Table 2

Region i	A ($\varepsilon = 11\%$)			B ($\varepsilon = 6\%$)		
	$J = 1$	$J = 2$	$J = 3$	$J = 1$	$J = 2$	$J = 3$
D_j^i	0	0.5	0.84	0	0.7	0.84
L_j^i (Å)	...	31	455	0	447	900

plastic strain. This statistical analysis is not presented here since it is extensively described in Section 3.2.3.

In addition, it must be pointed out that this method can also be used in a similar manner to create quantum boxes by choosing suitable orientations of the crystal in order to activate different slip planes. As an example, Fig. 27 presents a three-dimensional AFM picture of a 2 nm thick Fe film after a plastic strain of 4% along the [110] direction of the MgO substrate. It clearly reveals perpendicular slip lines along the [110] and [110] crystallographic directions which cut the initially continuous Fe film into boxes.

The method to determine the fractal dimension consists in intersecting the slip line pattern by straight perpendicular line and is based on the following equation:

$$\ln N_s = C - D \ln M,$$

where N_s is the number of slip lines (cutting an arbitrary constant straight line of length L), M is the magnification of the image studied and C and D are constants. The slip line pattern is then supposed fractal only if $0 < D < 1$. The $\ln N_s$ vs $\ln M$ curve is presented in Fig. 28. The two regions studied A and B correspond to a deformation ε at the surface of 11% and 6% respectively and L has been fixed to 110 mm in this study [56]. In Table 2 is reported

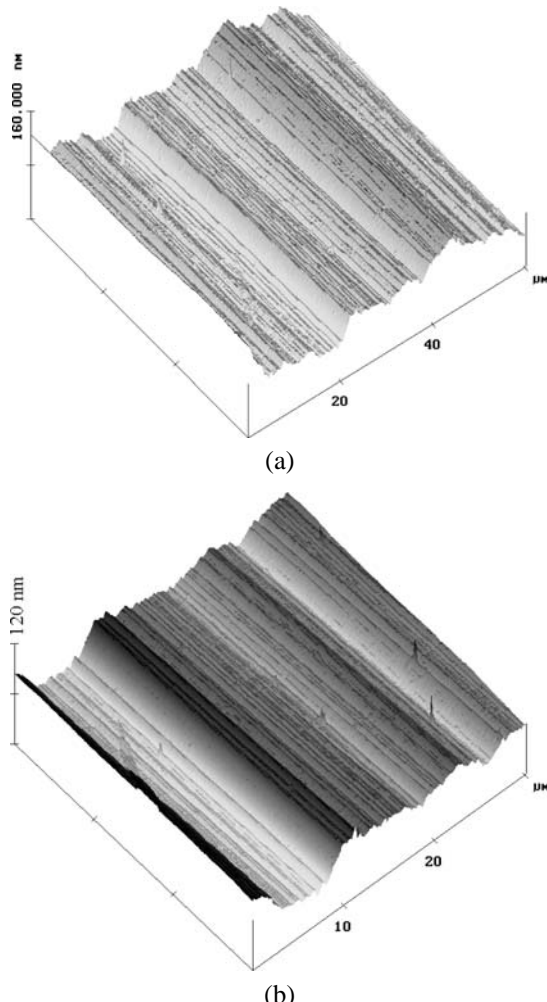


Fig. 26. Three-dimensional AFM images with various magnifications M and their related squared scan sizes S . (a) $M = 44000/S = 60 \mu\text{m}$, (b) $M = 66000/S = 30 \mu\text{m}$, (c) $M = 11000/S = 10 \mu\text{m}$, (d) $M = 22000/S = 5 \mu\text{m}$, (e) $M = 110000/S = 1 \mu\text{m}$, (f) $M = 147000/S = 0.8 \mu\text{m}$, (g) $M = 220000/S = 0.5 \mu\text{m}$, (h) $M = 1110000/S = 0.1 \mu\text{m}$ (courtesy of L. Ressier).

the slope D_j^i giving the different similarity dimension of the slip line pattern in part of curve j in the region i of the specimen, and the theoretical mean distances $L_j^i = L/M_j^i$ between neighboring slip lines of D_j^i fractal dimension, resulting from the intersections M_j^i of least-square lines with the axis $N_s = 1$.

Three linear parts are clearly noticed in both regions A and B of the deformed GaAs/GaAlAs sample:

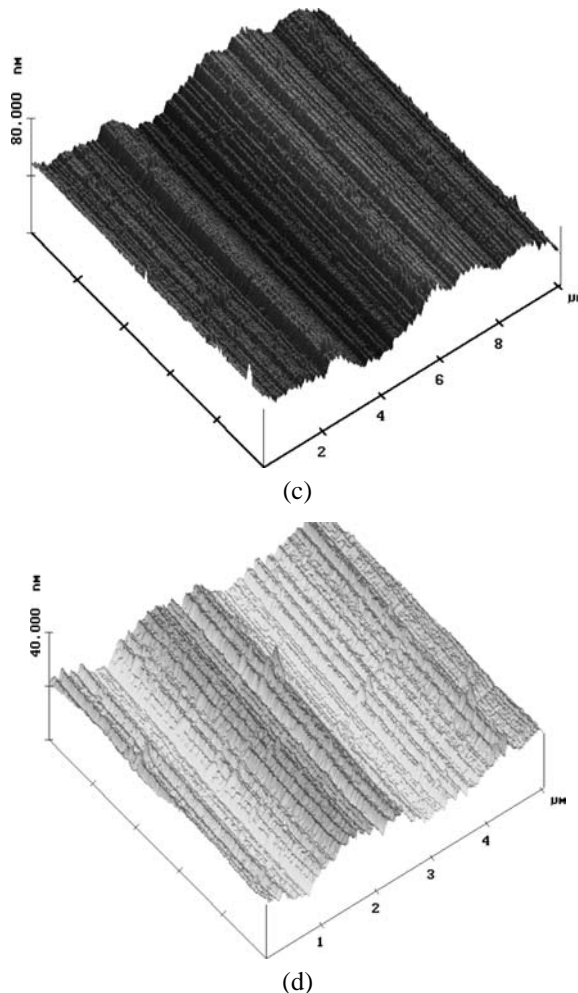


Fig. 26. (Continued).

- In part 1, $D_1 = 0$ for AFM pictures with scan sizes ranging from 100 to 15 μm . This nonfractal behavior is unambiguously due to the AFM picture resolution.
- In part 2, $0.4 < D_2 < 0.80$ for scan sizes ranging from 15 μm to 2.5 μm . This part corresponds to the observation of slip bands and is characterized by a similarity dimension of 0.50 and 0.70 for regions A and B respectively. The fractal character is all the more pronounced as the strain is higher. In early stages of strain, dislocation motion is individual with a weak fractal behavior, whereas for higher deformation a more collective behavior of dislocation appears with the emergence of slip bands and results in a more fractal pattern ($D = 0.5$).
- Part three (for AFM scan sizes ranging from 2.5 μm to 100 nm) corresponds to the observation of slip lamellae with a slope of 0.84 for both regions A and B. The inter-

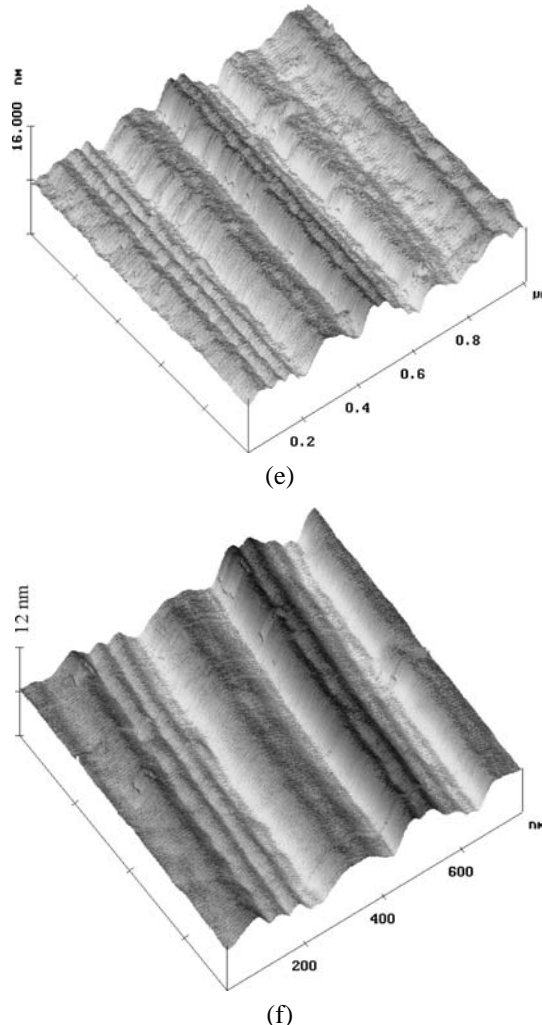


Fig. 26. (Continued).

polation with the axis $N_s = 1$ gives a mean distance between neighboring slip lines, i.e. mean width of lamellae, of about 455 Å and 900 Å in regions A and B respectively. The fractal dimension comes closer to 1, which corresponds to equidistant slip lines, i.e. nonfractal structure.

3.1.6. Twinning mechanisms

Twin related parts of single crystals are such as that one is the mirror image of the other; this geometry can be described by a homogeneous shear of the lattice parallel to the mirror plane. This can be readily observed by optical microscopy since the twinned surface is tilted so that light is reflected in a different direction.

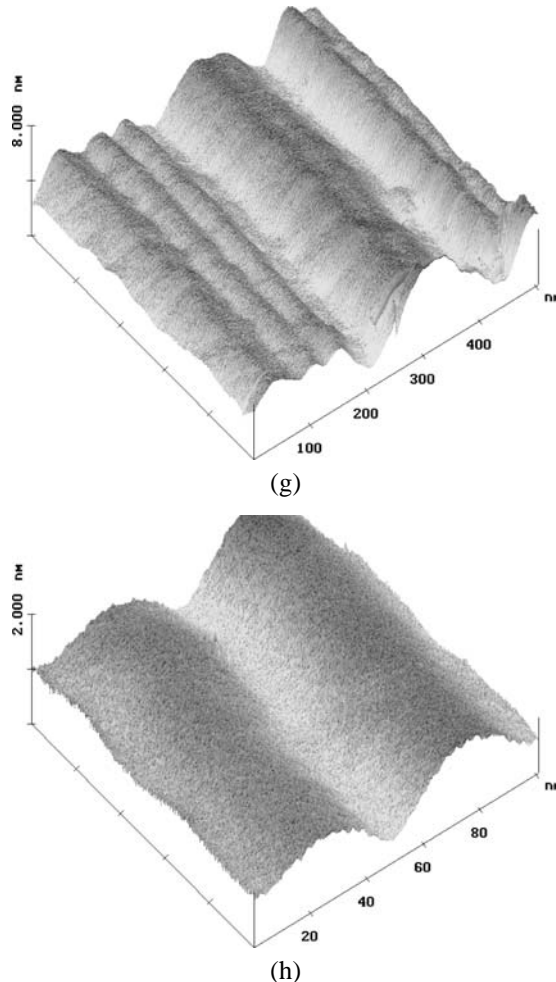


Fig. 26. (Continued).

Twins are a common feature in fcc metals with a low stacking-fault energy γ and can be induced by plastic deformation under suitable conditions. The low value of γ induces widely dissociated dislocations, so that under large applied stress the movement of individual partial dislocations can be decorrelated. This leads to the generation of large stacking faults whose character can be either extrinsic or intrinsic [60–62]. As a consequence a mechanical twin, which is formed by the shearing of partial dislocations within successive planes, can consist of a succession of intrinsic or extrinsic stacking faults. Inside such configuration, it is impossible to determine by TEM the nature of the constitutive stacking fault of the twin.

One of the method to discriminate between twin being built with intrinsic or extrinsic stacking faults is the AFM analysis of the surface steps induced by twins. Indeed, the

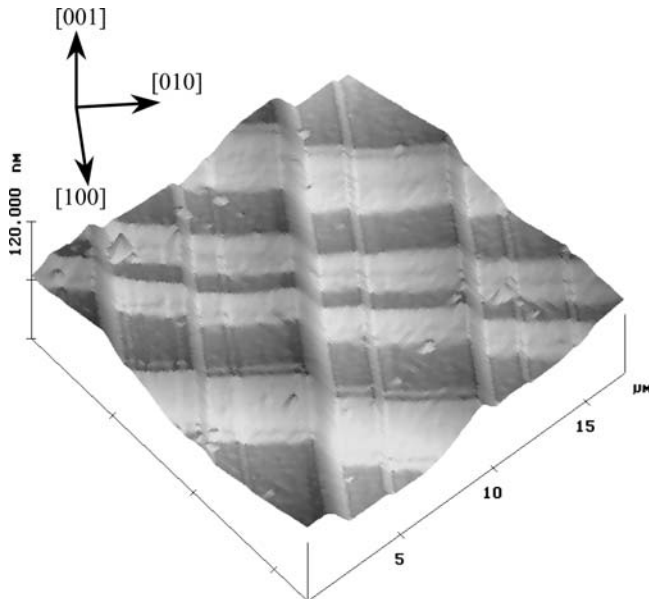


Fig. 27. Three-dimensional AFM picture of Fe boxes obtained for a plastic strain of 4% (courtesy of L. Ressier).

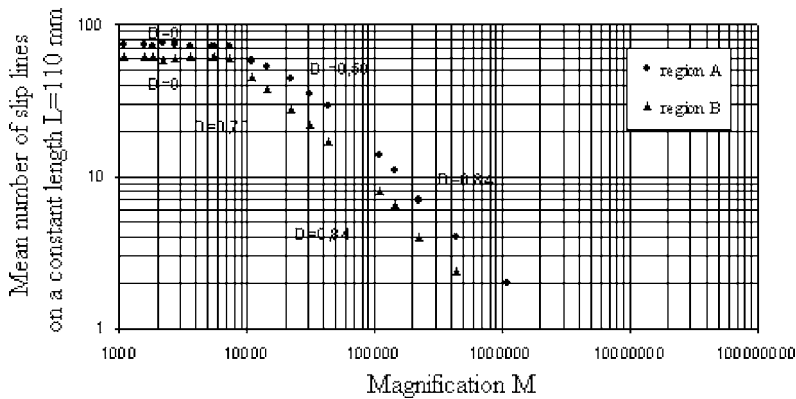


Fig. 28. Bilogarithmic dependence of the mean number of slip lines N_s (on a constant length $L = 110$ mm) on magnification M (courtesy of L. Ressier).

AFM atomic-scale resolution allows to determine the θ value corresponding to the angle between the twinned and initial surfaces and thus to differentiate between the two possible twin mechanisms.

In this context is presented in Fig. 29 a three-dimensional AFM image of a stacking fault of low energy ($\gamma = 10 \text{ mJ/m}^2$) in a Cu–12.7 at.% Al single crystal deformed up to 0.47% in compression along the $\langle 111 \rangle$ direction. The scan size is about $16 \mu\text{m} \times 16 \mu\text{m}$ with a height extension of 300 nm. The $(11\bar{2})$ surface has a roughness R_q of 15.1 nm, almost

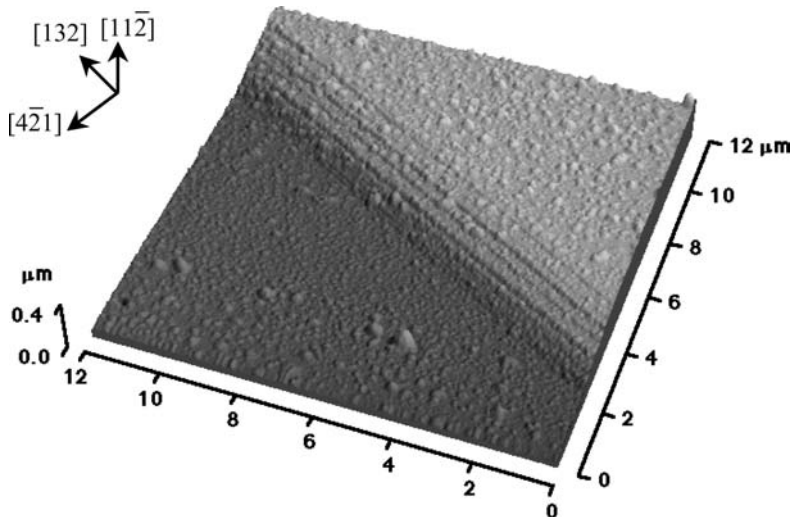


Fig. 29. Three-dimensional AFM picture of CuAl single crystal twinned band.

certainly due to preferential chemical etching. Nevertheless, the emergence of the first few dislocations is clearly distinguishable with the appearance of slip lines at 22.5° from the compression axis, which corresponds to the [132] direction. The cluster of surface steps, called a twin micro-band, results from the twinning mechanism and is composed of several individual twins, as seen in the topographical image in Fig. 30. The experimental θ value, obtained by averaging a few consecutive sections perpendicularly to one individual twin, ranges from 7 to 20° with an average value θ_a of 12.7°.

The theoretical angle θ for extrinsic and intrinsic stacking faults can be derived as follows:

The observed slip lines lie along the [132] direction which corresponds to the (1̄1̄) (110) system activation in this material. The $\frac{1}{2}(110)$ Burgers vectors may be dissociated following the reaction:

$$DC = D\alpha + \alpha C \quad \text{or} \quad DB = D\alpha + \alpha B,$$

$$\frac{1}{2}[110] = \frac{1}{6}[121] + \frac{1}{6}[21\bar{1}], \quad \frac{1}{2}[011] = \frac{1}{6}[121] + \frac{1}{6}[\bar{1}12],$$

where $\mathbf{b}^{\text{ex}} = D\alpha$ corresponds to the leading partial dislocation in the case of extrinsic stacking fault, and $\mathbf{b}^{\text{in}} = \alpha C$ (or αB) for the intrinsic case.

Projecting Shockley vectors on vectors \mathbf{n}_1 perpendicular to the surface, \mathbf{n}_2 parallel to the slip lines and \mathbf{n}_3 perpendicular to \mathbf{n}_1 and \mathbf{n}_2 leads to:

$$b_1^{\text{ex}} = \mathbf{b}^{\text{ex}} \cdot \mathbf{n}_1 = \frac{1}{6}b_S, \quad b_1^{\text{in}} = \mathbf{b}^{\text{in}} \cdot \mathbf{n}_1 = \frac{5}{6}b_S \left(\text{or } b_1^{\text{in}} = \frac{2}{3}b_S \right),$$

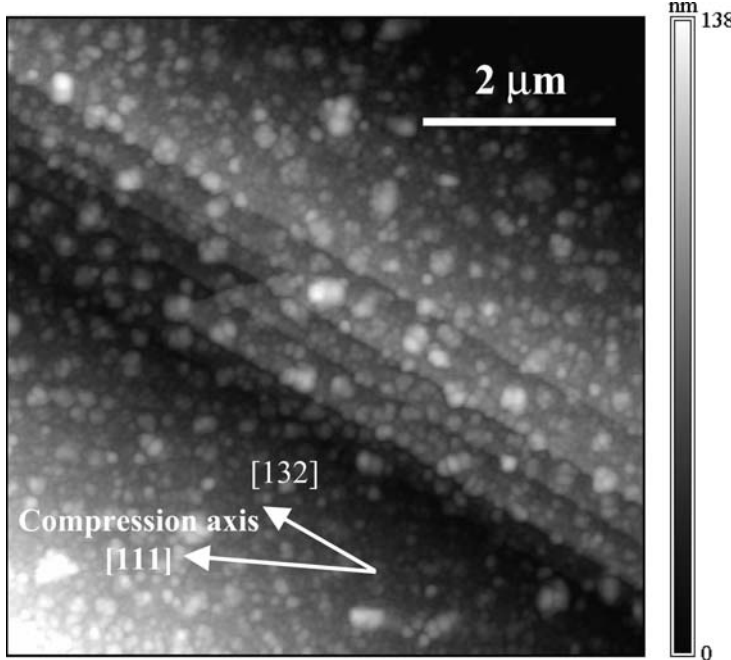


Fig. 30. Twinned band fine structure. The scan size is about $6 \times 6 \mu\text{m}^2$ with a height extension of 138 nm.

$$b_2^{\text{ex}} = \mathbf{b}^{\text{ex}} \cdot \mathbf{n}_2 = \frac{1}{3\sqrt{14}} b_S \quad \text{and} \quad b_2^{\text{in}} = \mathbf{b}^{\text{in}} \cdot \mathbf{n}_2 = \frac{5}{3\sqrt{14}} b_S \quad \left(\text{or } b_2^{\text{in}} = \frac{4}{3\sqrt{14}} b_S \right),$$

$$b_3^{\text{ex}} = \mathbf{b}^{\text{ex}} \cdot \mathbf{n}_3 = \frac{9}{2\sqrt{21}} b_S, \quad b_3^{\text{in}} = \mathbf{b}^{\text{in}} \cdot \mathbf{n}_3 = \frac{3}{2\sqrt{21}} b_S \quad \left(\text{or } b_3^{\text{in}} = \frac{3}{\sqrt{21}} b_S \right),$$

where $\mathbf{n}_1 = \frac{1}{\sqrt{6}}[11\bar{2}]$, $\mathbf{n}_2 = \frac{1}{\sqrt{21}}[4\bar{2}1]$, $\mathbf{n}_3 = \frac{1}{\sqrt{14}}[132]$, $b_S = \frac{a}{\sqrt{6}}$ and a is the lattice parameter.

In the case of an extrinsic stacking fault, the twin mechanism involves the propagation of only one partial dislocation along two crystallographic planes (Fig. 31). Hence the θ_{ex} angle is given by the following equations:

$$\tan \theta_{\text{ex}} = \frac{b_1^{\text{ex}}}{2d_{\text{ex}} - b_2^{\text{ex}}},$$

$$d_{\text{ex}} = \frac{\sqrt{2}}{\sin \varphi_{\text{ex}}} b_S,$$

$$\tan \varphi_{\text{ex}} = \frac{b_1^{\text{ex}}}{b_2^{\text{ex}}}.$$

One obtains $\theta_{\text{ex}} = 2.06^\circ$.

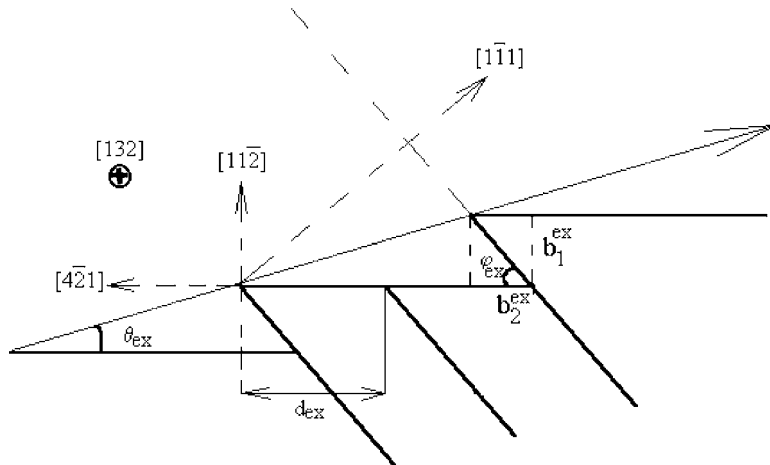


Fig. 31. Extrinsic stacking fault twin mechanism (not drawn).

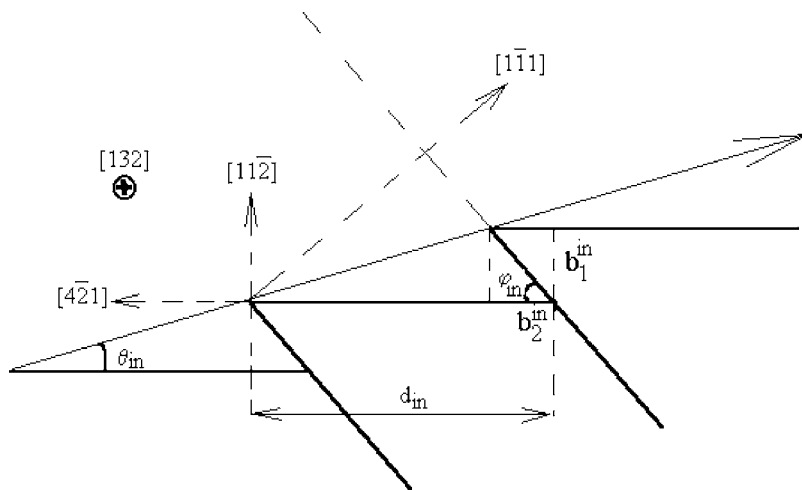


Fig. 32. Intrinsic stacking fault twin mechanism (not drawn).

The twin mechanism may also be accounted for by the propagation of only one Shockley partial dislocation along each crystallographic plane yielding to an intrinsic stacking fault (Fig. 32). θ_{in} is defined as follows:

$$\tan \theta_{\text{in}} = \frac{b_1^{\text{in}}}{d_{\text{in}} - b_2^{\text{in}}},$$

$$d_{\text{in}} = \frac{\sqrt{2}}{\sin \varphi_{\text{in}}} b_S,$$

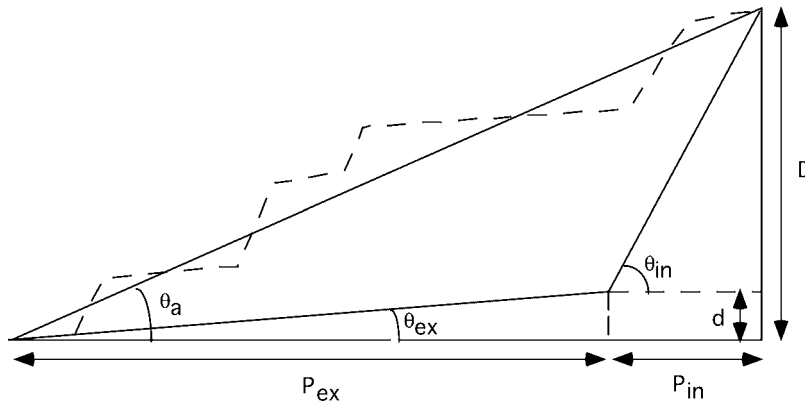


Fig. 33. Schematic representation of the respective contributions P_{in} and P_{ex} of each mechanism in twinning.

$$\tan \varphi_{in} = \frac{b_1^{in}}{b_2^{in}}.$$

This leads to $\theta_{in} = 35.8^\circ$ (or 31.9°) depending on the Burgers vector.

In this case, the crystallographic orientations of the applied stress and the observation surface are such that the angles between the inclined faces of the twinned bands and the initial surface plane have very different theoretical values, depending on the nature of the stacking fault, intrinsic (in) or extrinsic (ex). It should be noted that the same angular range is found for the two cases of intrinsic stacking fault, compared to the case of extrinsic for which this parameter is considerably lower.

Twining by the formation of only an extrinsic stacking fault is not possible, because θ would be about 3° or smaller. It is here worth noting that the resolution of the images used for the analysis, i.e. the distance between two experimental points, is of the order of 10 nm. As the thickness of the twins studied is around the same order of magnitude than those observed by transmission electron microscopy [63], the possibility of unresolved fine structure composed of nanotwins separated by undeformed regions has to be rejected. It is thus concluded that individual twins are not also created by the intrinsic mechanism alone; both extrinsic and intrinsic stacking faults have to be taken into account. The respective contributions P_{ex} and P_{in} of each mechanism (ex or in) occurring during twinning can be deduced from the average θ_a value obtained on one *individual* twin, as shown in Fig. 33. One therefore obtains:

$$P_{in} = \frac{\operatorname{tg} \theta_a - \operatorname{tg} \theta_{ex}}{\operatorname{tg} \theta_{in} - \operatorname{tg} \theta_{ex}},$$

$$P_{ex} = 1 - P_{in}.$$

A value $\theta_{in} = 32.8^\circ$ (average of the two possible intrinsic mechanisms) is used for the calculation which leads to $P_{in} = 25.8\%$ and $P_{ex} = 74.2\%$. Thus about 75% of the twinning occurs via extrinsic mechanism in these CuAl alloys [64].

3.1.7. Dislocation mean free path: application to stress anomaly in Ni₃Al intermetallics

In the framework of dislocation theory, the macroscopic plastic deformation ε is related to microscopic quantities according to the relation:

$$\varepsilon = \sum_i \rho_i^m b_i L_i,$$

where ρ_i^m is the mobile dislocation density of dislocation family i , b_i the elementary plastic deformation associated with a dislocation of family i and L_i the mean distance travelled by dislocations i between their sources and sinks. In practice, this relation cannot be used for estimating ε since it would require the knowledge of ρ_i^m 's, which are not accessible to experiment. In the contrary, the distances L_i can be estimated from the length of the slip markings on the surfaces of deformed crystalline materials and can yield very useful information for the understanding of plastic behavior. Such measurements have been performed on the Ni₃Al intermetallic, which exhibits a positive temperature dependence of its flow stress [65–68]. Single crystalline specimens have been deformed in compression at three deformation temperatures in the flow stress anomaly domain, 293 K, 500 K and 720 K, and have been examined *post mortem* at room temperature by using an AFM.

A general observation is that, whatever the deformation temperature, the slip traces appear to be rather straight, without exhibiting any appreciable deviations from the primary (111) octahedral glide planes. AFM imaging indicates that the intimate structure of the slip lines consists of several finer lines on parallel planes, but in the limit of the resolution of the apparatus these slip lines are not connected by cross-slip events [69]. Another striking feature concerns the shortening of the slip line length with increasing temperature, which is easily discernible on the AFM images by the numerous slip traces that end in the scan areas (Fig. 34) [70]. Slip line lengths (L_m) have been therefore estimated from these observations and are reported in Fig. 35 as a function of temperature. These results clearly indicate that, in the anomaly domain of Ni₃Al, the distance travelled by the mobile dislocations becomes shorter and shorter with increasing temperature.

Two interpretations can be proposed for explaining this feature that are a large decrease either of the dislocation velocity, v or of the dislocation mean free path, Λ (or a combination of both effects). A decrease of v may to some extent contribute to the shortening of the slip lines, however from dislocation velocity measurements a drastic change in $v = v(\sigma, T)$ is not expected [71]. Thus, the observed decrease in the slip line length with increasing deformation temperature must be essentially ascribed to the decrease of Λ . Since L_m is a measure of the dislocation mean free path before they become ultimately locked, its decrease with increasing temperature suggests an exhaustion mechanism of mobile dislocations that becomes more and more efficient when the temperature is raised. This result supports the idea that a thermally activated exhaustion mechanism leading to a complete locking of mobile dislocations is responsible for the positive temperature dependence of the flow stress of Ni₃Al.

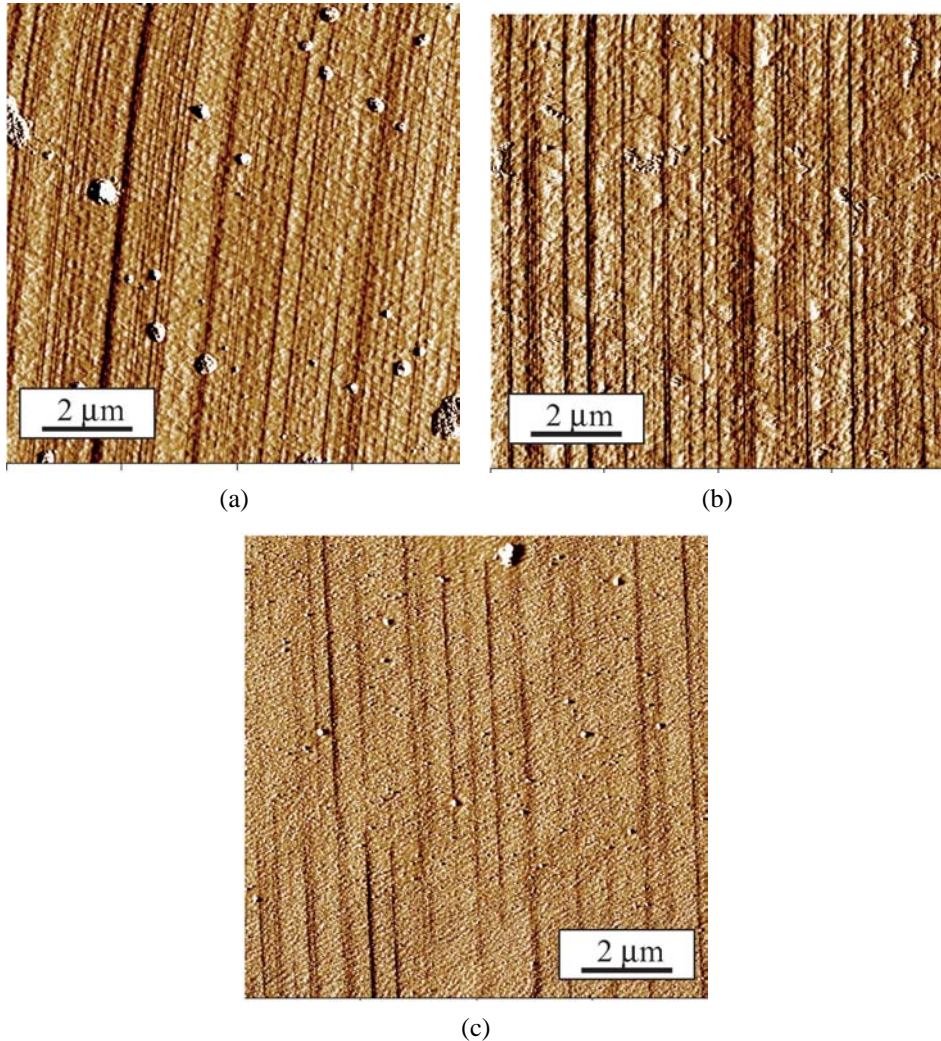


Fig. 34. Typical slip line structures of $\text{Ni}_{75}\text{Al}_{24}\text{Ta}$ intermetallic alloys observed by AFM after 1% plastic strain and for various temperature. (a) 293 K, (b) 500 K, (c) 720 K.

3.2. In situ plastic deformation AFM studies: cases of LiF and γ phase single crystals

3.2.1. Evolution of LiF single crystals during deformation

Fig. 36 shows the evolution of an LiF single crystal surface during deformation. The specimen strain value is indicated below each image and the scan size of the signal error mode AFM images is about $10 \times 10 \mu\text{m}^2$. The geometry of the LiF deformed single crystals is shown in Fig. 37: the compression axis is [001] and the observation face is parallel to

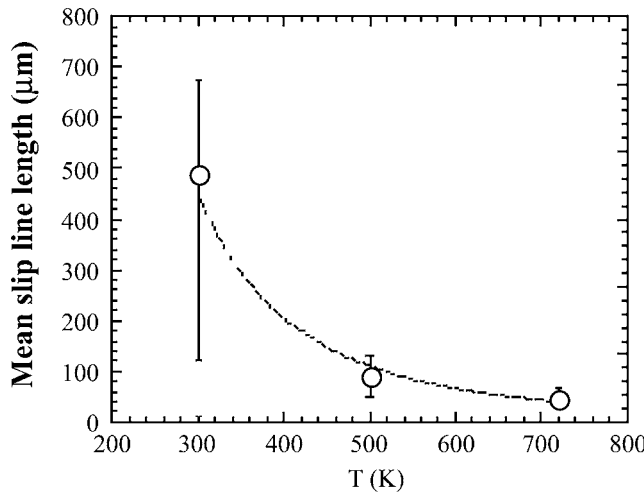


Fig. 35. Mean slip line length L_m as a function of temperature (the error bars indicate the distribution of parameter about its mean value).

the (100) plane. The primary slip system in LiF is the $\{110\}\langle110\rangle$, with a Burgers vector of $a/2[110]$, where a represents the lattice parameter. From the Schmid factors, slip lines are expected to lie respectively in the [010] direction perpendicularly to the compression axis. The unit step height corresponding to the emergence of one dislocation is equal to the Burgers vector component perpendicular to surface: $h_e = b_{\perp} = b \cos \frac{\pi}{4} = \frac{a}{2}$; so a step $h_e = 0.201$ nm corresponds to one perfect dislocation getting out of the crystal. Slip lines running along the [010] preferred crystallographic direction are observed on the (100) plane when the sample is submitted to the compressive stress, consist with the activation of the glide systems.

Surface plastic deformation in LiF single crystals occurs in three consecutive stages; this is exemplified in Fig. 36. In the first stage, at a very small stress, the first slip lines appear as the result of the first dislocations emerging at the surface. It can be noticed that the slip line structure created at surface is composed principally of low-height steps due to the propagation of only few dislocations in the bulk crystal (A, B, C and D). The cleavage structure (α , β and γ) which is the result of the crack boundary intersection with the initial dislocation density is always clearly visible with a river-pattern running from the upper left to the lower right corner. These cleavage features may be still distinguished at the final strain of 2.54%. Because of the activation of two symmetrical slip planes, a structure of increasing and decreasing steps is expected (Section 3.1.4). A cross-section perpendicular to the slip lines shows that only one slip system is activated. Increasing the strain induces a widening step-by-step of the slip lines and therefore creation of slip bands which may become wide, as seen in E, F, G and H. Large terraces are still distinguishable up to 1.5% strain. Then a shearing of the remaining terraces is observed (I, J and K), so that the surface becomes homogeneously deformed on a micrometer scale and no terraces can be reasonably identified. This homogeneous slip line structure was confirmed by further scans at various areas on the sample surface. In spite of the increase of slip line density,

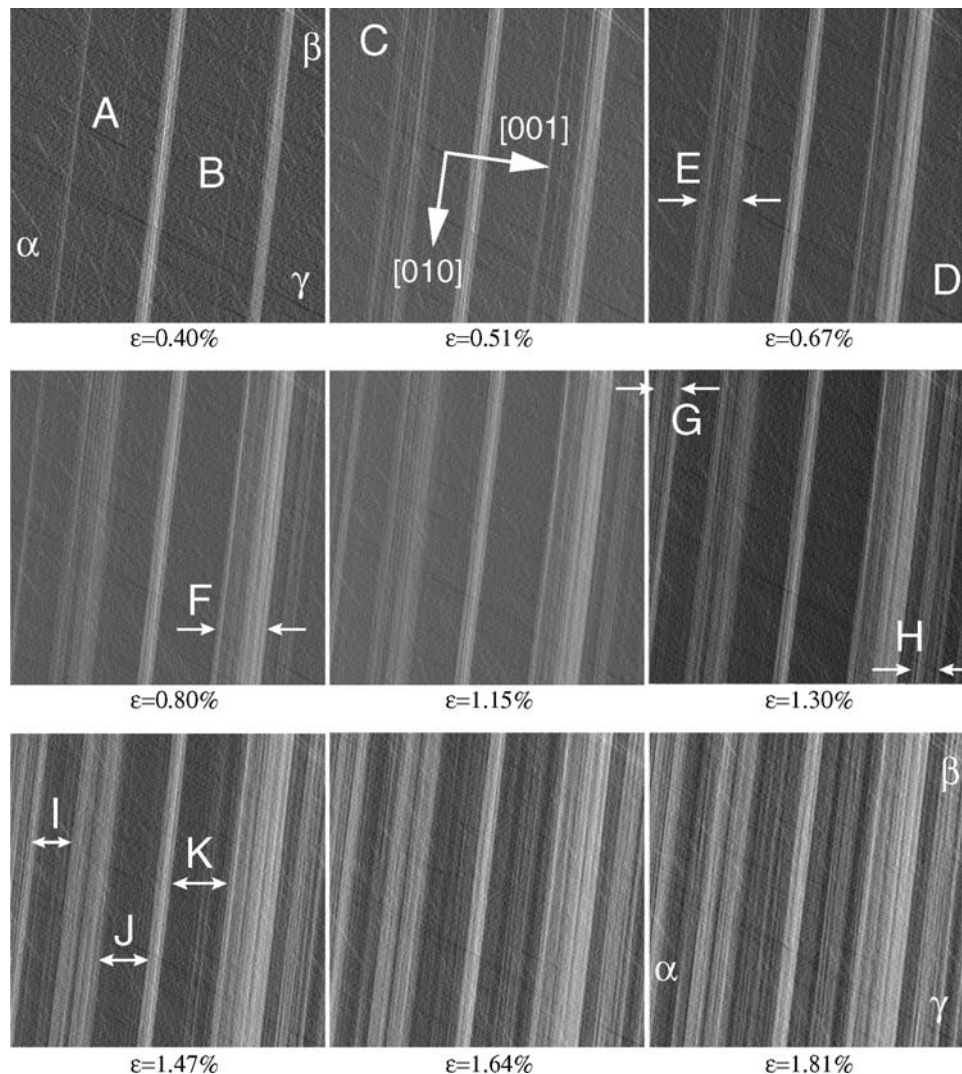


Fig. 36. Evolution of LiF single crystal surface during deformation. AFM images have been taken in signal error mode. The scan size is about $10 \times 10 \mu\text{m}^2$ and the sample strain value is indicated below each image. The compression axis is at 7° to the horizontal base line.

the step height remains very low. Hence plastic deformation occurs in this material by propagation of dislocations moving individually and independently from each other and is not the result of the collective behavior of dislocations. The multiplication of slip lines, their distribution and their widening can be interpreted by a rapid locking of Frank–Read sources, activation of secondary Frank–Read sources and the modification of loop glide planes when crossing the pre-existing Frank network dislocations. It is worth noting that

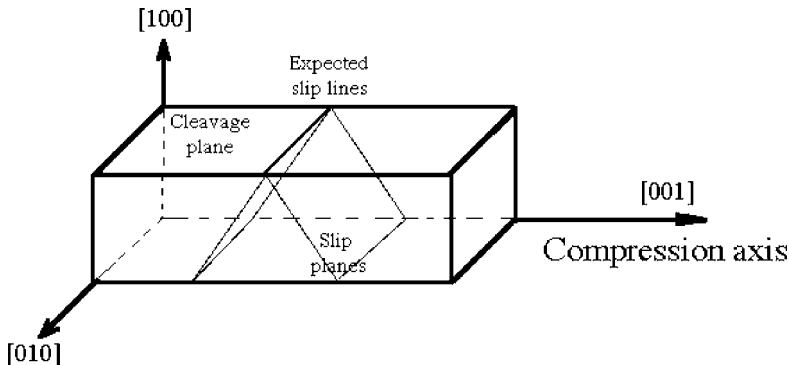


Fig. 37. Sample configuration and expected slip lines for LiF single crystals.

no cross-slip effects on the slip line structure have been observed. The same holds true for closer scan sizes of higher lateral resolution.

3.2.2. Evolution of γ phase single crystals during deformation

The evolution of the γ phase of a MC2 nickel based superalloy is shown in Fig. 38, and the configuration in Fig. 39. The primary slip system in γ phase is the $\{111\}\langle110\rangle$, with a Burgers vector of $a/2[110]$. Slip lines are expected to lie in the $\langle011\rangle$ direction at $\pm 45^\circ$ to the compression axis, with $h_e = 0.176$ nm.

As expected, the surface exhibits slip lines running along [010] preferred crystallographic directions. Surface plastic deformation in the γ phase occurs in only few areas and is therefore highly heterogeneous with dense step-clusters separated by wide terraces which are still clearly distinguishable at the final strain of 1.86%. A few dislocation pile-ups (A and B) are seen in equilibrium in the bulk. They are composed respectively of approximately 25 and 10 dislocations moving from left to right.

This uncommon behavior can be explained by the high friction stress applied on the first few dislocation pairs at the pile-up head which comes from the short and/or long range ordering existing in this material [72, 73]. The propagation of the first dislocation in this structure creates a “diffuse antiphase boundary” [74]. The second dislocation, by gliding on the same plane, restores partially the initial order while subsequent dislocations do not modify it. Thus the presence of a dislocation pair at the head of the pile-up is associated with a large gain of energy.

Two pile-ups moving on parallel crystallographic planes in opposite direction are also observed (C and D).

During deformation, the active plastic zone shifts from the lower right to the upper left corner, with the successive appearance of the structures α , β , γ and δ . The step structure labeled α created from the very first stage of plastic deformation has barely evolved whereas large terraces are systematically sheared with increasing strains. Plastic deformation occurs by a step-by-step activation of Frank–Read sources which leave behind a plastic zone of low activity. The evolution of slip line structure profiles is presented in Fig. 40 and

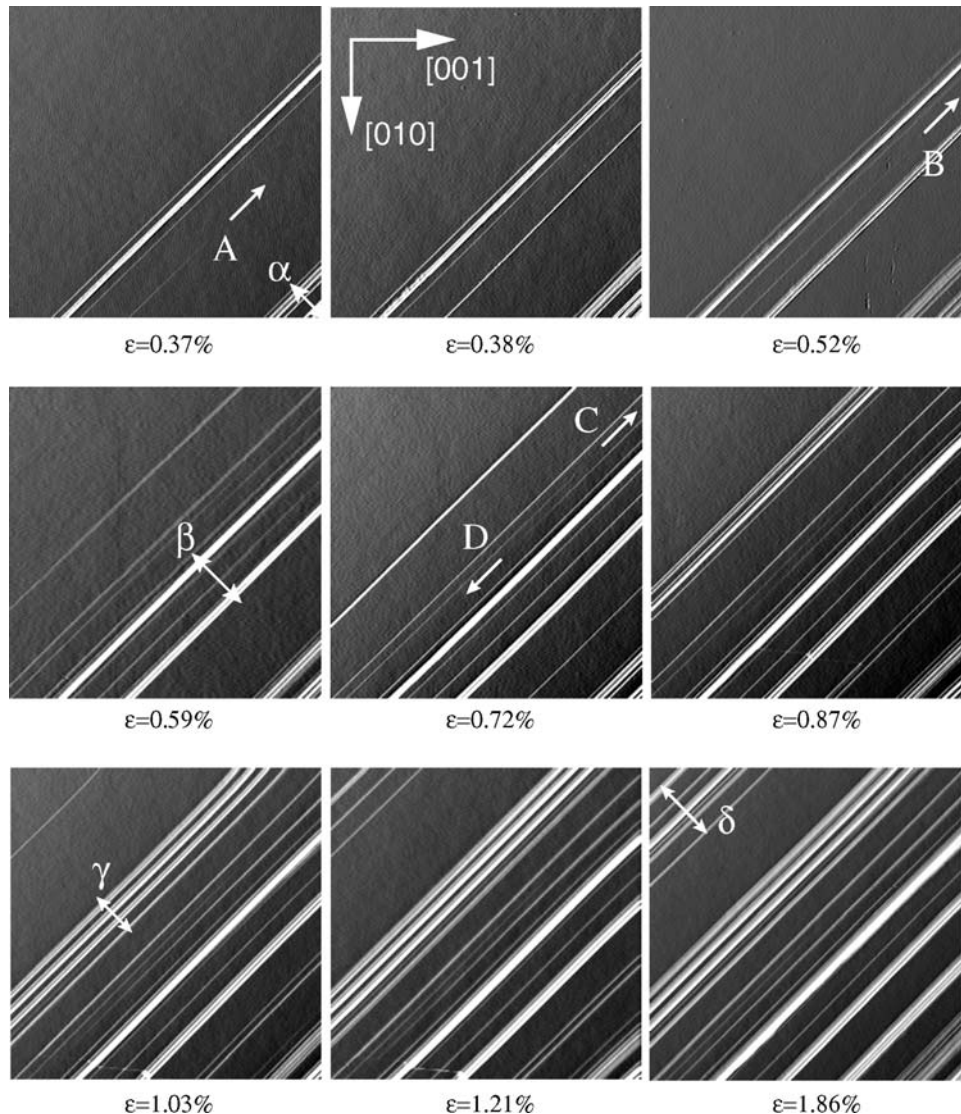


Fig. 38. Evolution of the γ phase single crystal surface during deformation. AFM images have been taken in signal error mode. The scan size is about $10 \times 10 \mu\text{m}^2$ and the sample strain value is indicated below each image.

The compression axis is parallel to the horizontal base line.

shows clearly this shift of the active plastic zone. Moreover, unlike the LiF observations, the step height is often very high and is accounted for by the fact that plasticity occurs principally by dislocation pile-up propagation, since the friction stress is high enough to prevent dislocations from moving individually through the bulk crystal [75,76].

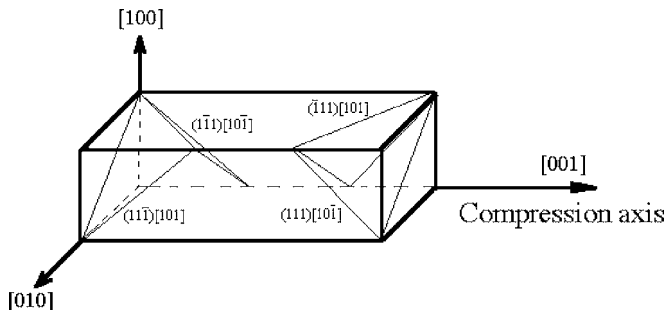


Fig. 39. Sample configuration for γ phase single crystals.

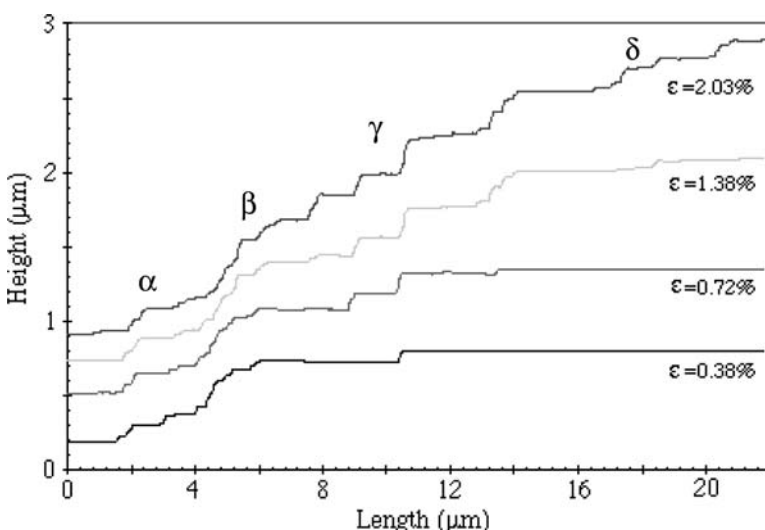


Fig. 40. Evolution of the γ phase slip line structure profile plot obtained by averaging a few consecutive sections perpendicular to slip lines.

3.2.3. Statistical analysis of slip line structures

A statistical analysis of LiF and γ phase slip line patterns is presented in the following to compare plastic mechanisms taking place in the bulk crystals and quantitatively study the surface effects of plastic deformation. Several relevant parameters can be determined in order to characterize the evolution of slip line structure during plastic deformation:

- the total number $N_{\text{e.d.}}$ of dislocations emerging at the sample surface,
- the slip line density N_L and consequently the average number of dislocations per slip line $N_{\text{D/L}}$.

$N_{\text{e.d.}}$ is determined per unit length l_0 , that is, scan size of the images ($16.6 \mu\text{m}$), as $N_{\text{exp.}}$, $N_{\text{b.d.}}$ and N_L described in the following.

A limitation of this statistical analysis arises however in materials such γ phase, in which plasticity is highly heterogeneous, so that the AFM image studied does not characterize the surface evolution of the whole specimen. In this case, the evolution of one slip band during plastic deformation may be only studied in function of time, and can not be correlated to the sample strain.

3.2.3.1. Emerged dislocation density in LiF The total number $N_{\text{e.d.}}$ of dislocations emerging is deduced from a topographical mode AFM profile:

$$N_{\text{e.d.}} = \frac{H}{h_e} = \frac{2H}{a},$$

where H is the total height of the step structure.

Due to the homogeneous plastic deformation in LiF single crystals, the local strain ε_l , i.e. the strain associated with the AFM image, is considered to be equal to the macroscopic strain value ε_m of the sample. In Fig. 41 is presented the evolution of $N_{\text{e.d.}}$ with plastic deformation $\varepsilon_m = \varepsilon_l$. A linear behavior is observed during the first stage of plasticity, ranging from 0 to 2.2% and leads to an emerged dislocation number per strain % of 580 (dashed line).

This value is compared to the specific dislocation number expected to emerge at the sample surface $N_{\text{exp.}}$ and deduced from ε_m . From geometrical considerations, the propagation of an individual dislocation through the whole crystal leads to a compression of $\Delta l_{\text{LiF}} = a/2 = 0.201 \text{ nm}$. Thus one obtains:

$$\varepsilon_m \equiv \varepsilon_l = \frac{N_{\text{exp.}} \cdot \Delta l_{\text{LiF}}}{l_0} = \frac{N_{\text{exp.}} \cdot a}{2l_0}.$$

This behavior, referred to as *expected* in the following, is reported in the continuous straight line in Fig. 41.

$$\frac{N_{\text{exp.}}}{\varepsilon_l} = \frac{2l_0}{a} = 830 \text{ dislocations}/\% \text{ strain.}$$

A dislocation deficit $\Delta N = N_{\text{exp.}} - N_{\text{e.d.}}$ of approximately 250 (per % strain and unit length l_0) is thus determined. The macroscopic plastic strain value is in fact the result of both the emergence process of dislocations leading to slip line structure at the sample surface, and the propagation of dislocations which are still found in the bulk crystal and contribute to the macroscopic deformation of the specimen.

$$\varepsilon_m \equiv \varepsilon_l \equiv \varepsilon_{\text{emerged.dislocations}} + \varepsilon_{\text{bulk.dislocations}},$$

$$\Delta\varepsilon = \varepsilon_{\text{b.d.}} = \varepsilon_l - \varepsilon_{\text{e.d.}} = \frac{\Delta N \cdot a}{2l_0}.$$

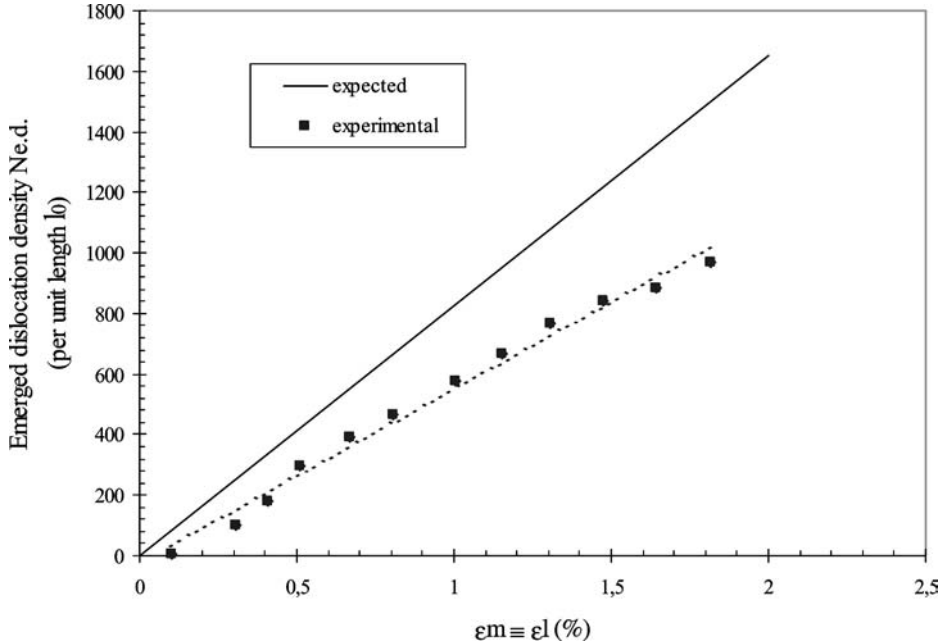


Fig. 41. Emerged dislocation density $N_{e.d.}$ (per unit length l_0) versus sample strain curve, for LiF single crystal.

$\varepsilon_{b.d.}$ depends on the dislocation number still present in the bulk crystal, but also on the average surface S_m swept up by these dislocations during the deformation process.

$$\varepsilon_{b.d.} = \sum_{\text{dislocs}} \left(\eta_i \frac{\Delta l_i}{l_0} \right) = \eta \frac{a}{2l_0} N_{b.d.} .$$

One obtains therefore:

$$N_{b.d.} = \frac{\Delta N}{\eta} ,$$

where η is the ratio between the average surface S_a sheared by dislocations and the whole section S_0 along the active slip plane. η is ranging from 0 to 1:

$$0 \leq \eta = \frac{S_a}{S_0} \leq 1 .$$

To estimate this parameter η , the activation of one Frank–Read source and the propagation of the nucleated dislocations in a crystallographic slip plane have been roughly determined, as schematically shown in Fig. 42. In what follows, two shapes of dislocation loops are considered to provide a validity range of η .

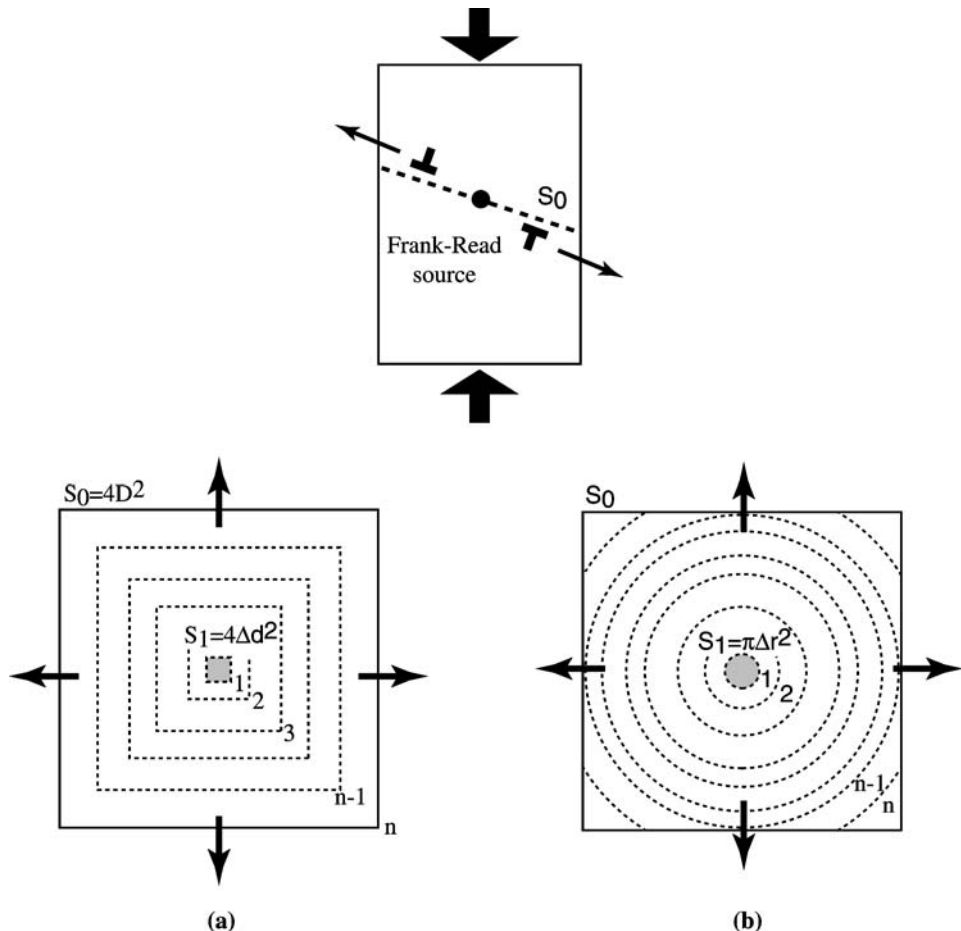


Fig. 42. Activation of Frank-Read source and subsequent propagation of dislocation pile-up in a crystallographic plane (section S_0) in the case of (a) square and (b) circular dislocation loops.

In the case of square dislocation loops (Fig. 42(a)), the surface scanned by the pile-up composed of n dislocations is given by:

$$S_n = \sum_{i=1}^n S_i = 4\Delta d^2 \sum_i (1 + \dots + n^2) = 2\Delta d^2 \frac{n(n+1)(2n+1)}{3},$$

where Δd is the distance between two successive dislocations. $S_0 = 4D^2 = 4n^2\Delta d^2$ represents the surface sheared by the first dislocation which emerged at the free surface, i.e. the section of the sample along the glide plane, as defined previously.

The average surface scanned by one dislocation is:

$$S_a = \lim_{n \rightarrow \infty} \left(\frac{S_n}{n} \right) = \frac{1}{3} S_0.$$

By similar considerations, the propagation of circular dislocation loops (Fig. 42(b)) leads to:

$$S_a = \lim_{n \rightarrow \infty} \left(\frac{S_n}{n} \right) = \frac{\pi}{12} S_0.$$

The nucleation and propagation of dislocations from a Frank–Read source lead therefore to $\eta = \pi/12$ and $\eta = 1/3$ in the case of square and circular geometric loops respectively. However it is well known that dislocations in a real pile-up are not regularly distributed on the crystallographic glide plane and have a strong tendency to accumulate at the pile-up head. The sheared surface is consequently underestimated. The η parameter may thus be to a good approximation between 25 and 50%, depending on the material.

An estimated value $N_{b.d.}$ of 500–1000 dislocations (per % strain and per unit length) have thus still not emerged at the sample surface, which represents 45–65% of the total dislocation number nucleated by the Frank–Read sources in the first stage of plasticity.

The dislocation density stored in the bulk crystal is given by $\rho^2 = A\varepsilon + \rho_0^2$, where ρ_0 is the initial dislocation density. At low strain values, one obtains:

$$\rho \cong \rho_0(1 + a\varepsilon).$$

During the first stage of plasticity, the dislocation density ρ stored in the bulk crystal depends linearly on ε (dashed straight line in Fig. 43) and is a significant contribution of the macroscopic deformation of the sample, as observed experimentally in Fig. 41. At higher strains, the contribution due to the dislocation density in the bulk becomes negligible since it follows a square root function and the deformation is then mainly due to dislocations which have emerged at the free surface $\varepsilon_{e.d.}$, as schematically shown in Fig. 43.

3.2.3.2. Dislocation average number of dislocations per slip line In Fig. 44, slip line density versus strain is represented. A number of slip lines N_L (per percent strain) of 35 is determined for LiF. The simultaneous evolution of $N_{e.d.}$ and N_L allows the determination of the average number of dislocations per slip line $N_{D/L}$. This relevant parameter characterizes the main plastic mechanism taking place in the bulk crystal. Indeed, a high $N_{D/L}$ value characterizes a plastic behaviour by propagation of planar dislocation pile-ups or by a large number of dislocations resulting from the activation of a few Frank–Read sources on consecutive crystallographic slip planes. On the contrary, the lowest value of $N_{D/L} = 1$ is the result of the activation of specific non-planar Frank–Read sources, such as movable, helicoidal and spiral ones [77]. Such a value may also bear witness a twin mechanism resulting from Shockley dislocation propagation [78,79]. It is however worth noting that the slip line structure at the specimen surface is accounted for by both the nature of the Frank–Read sources and the forest interactions in the bulk.

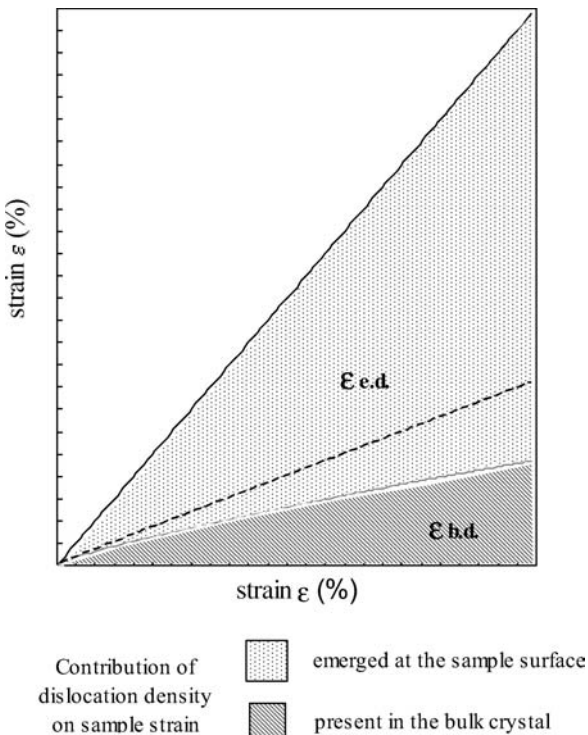


Fig. 43. Schematic representation of the contribution on the macroscopic sample strain of dislocations both stored in the bulk crystal and emerged at the sample surface.

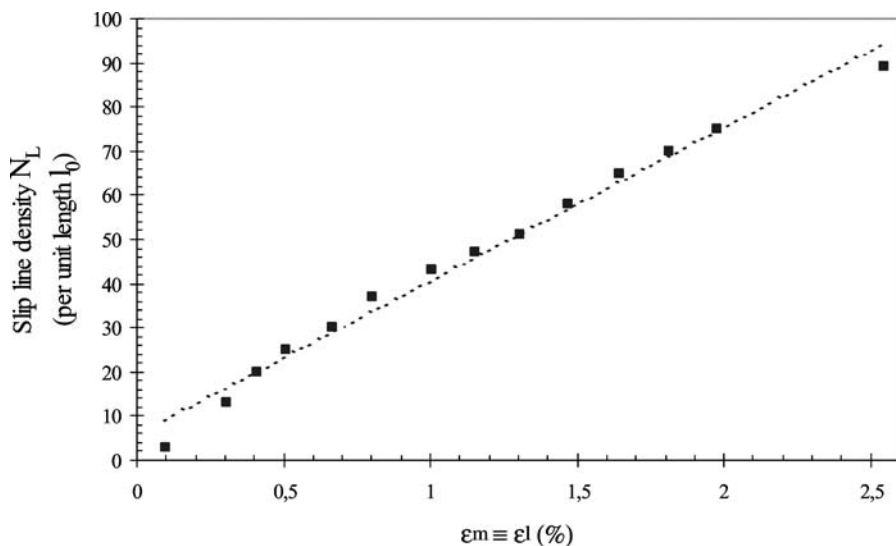


Fig. 44. Slip line density N_L (per unit length l_0) versus sample strain curve for LiF.

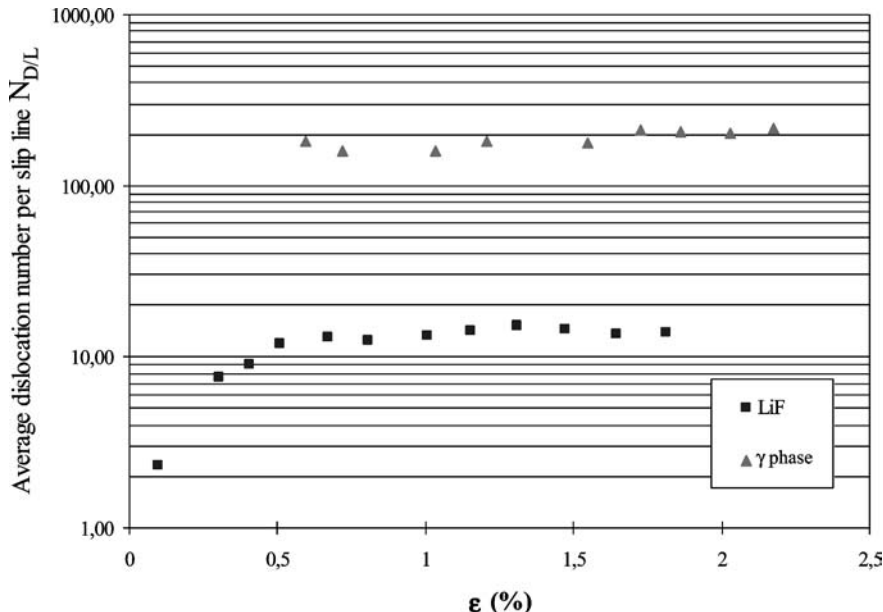


Fig. 45. Strain dependence of the average dislocation number per slip line $N_{D/L}$ of both LiF and γ phase single crystals.

As seen in Fig. 45, a $N_{D/L}$ value of 14 ± 1 dislocations/slip line is obtained for LiF, which corresponds to an average step height h_m of about 28 ± 2 Å. This corresponds to an upper limit due to the scan size of AFM images, i.e. lateral resolution, which may prevent a few slip lines from being detected. The $N_{D/L}$ value suggests that the Frank–Read sources are rapidly locked in the bulk crystal and the multiplication of slip lines at the surface is the result of both secondary source activation and interactions of the moving dislocations with the Frank network. A continuous activation of planar Frank–Read sources can not be the main mechanism of plastic deformation.

In the case of γ phase, $N_{D/L}$ ranges from 160 to 220 dislocations per slip line inside the slip band. This result is consistent with the fact that plasticity in this material is the result of the propagation of dislocation pile-ups.

In both materials the slip line height saturates rapidly to a fixed total value during the first stage of plastic deformation.

3.2.4. Motion of dislocation pile-ups

Two pile-ups gliding in opposite directions have been observed *in situ* during deformation of a γ phase single crystal. The equilibrium positions of these two pile-up heads, (A) and (B) respectively in Fig. 46, can be calculated taking into account the high friction stress τ_f due to the local order existing in this material [72–76] and internal stresses resulting from dislocation interactions. These pile-ups have difficulty in moving away once they crossed over, as observed in the sequence of micrographs (Fig. 46(a–d)). The critical resolved shear stress is indicated below each image. Increasing the applied stress induces an increase of

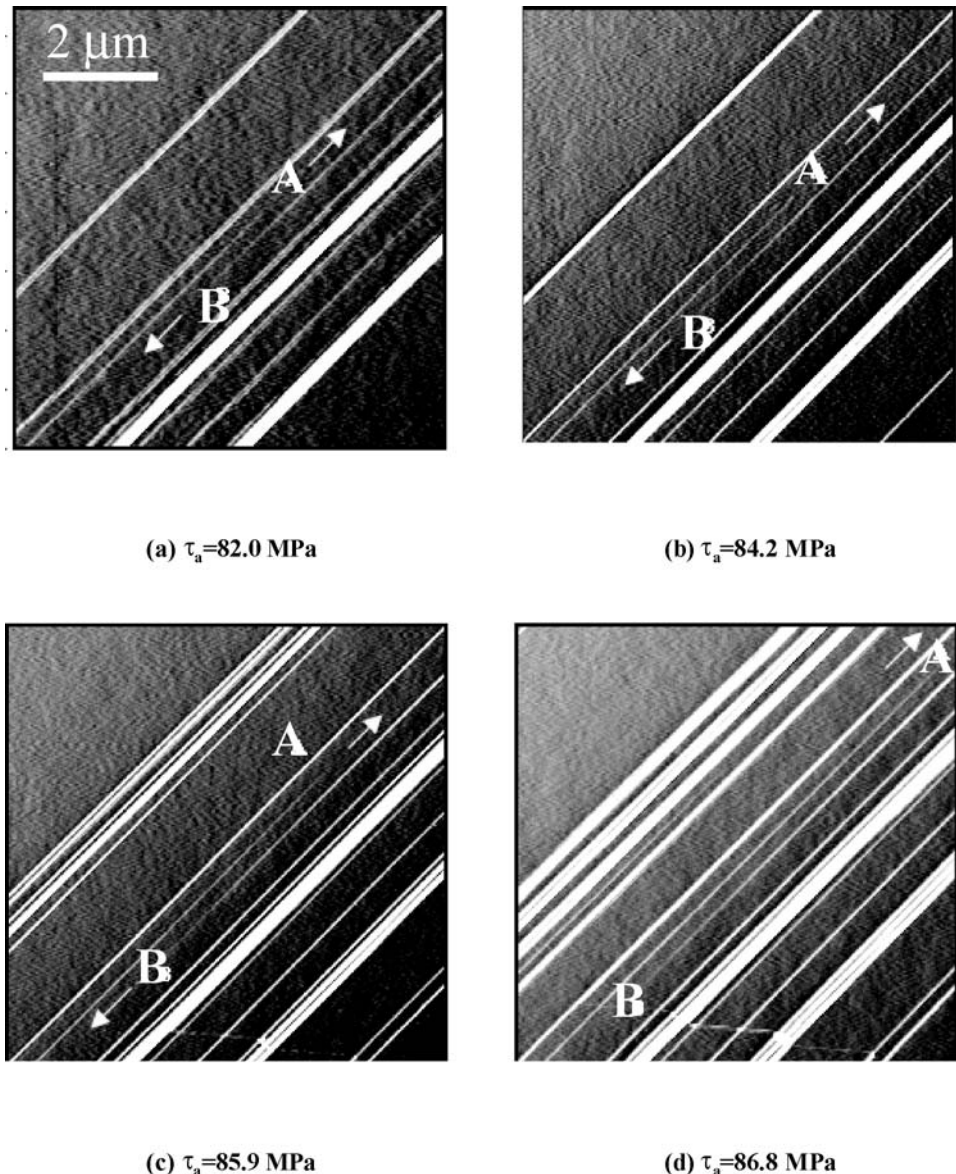


Fig. 46. Error signal mode AFM in situ observations of two pile-ups moving in opposite directions. Each pile-up is composed of ten dislocations and moves on two crystallographic planes 260 nm apart.

the distance A-B. Finally in Fig. 46(d), pile-up (A) is still moving away, while pile-up (B) is locked on another slip line resulting from a cross-slip effect. Each pile-up is composed of 10 dislocations and they move on two crystallographic planes 260 nm apart.

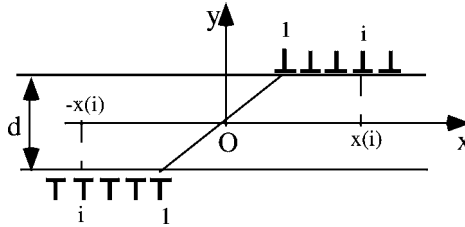


Fig. 47. Configuration and notation for the simulation.

To estimate the high friction stress τ_f acting on the first few dislocation pairs at the pile-up head, two dislocation pile-ups moving in opposite directions have been simulated.

The applied τ_a and friction τ_f stresses have been taken into account, as well as the internal stresses τ_i and τ_{ld} due to interactions between dislocations belonging to the same and to an antagonist pile-up respectively. Each pile-up is composed of n dislocations and is gliding on a plane separated from the other by distance d (Fig. 47). The origin O is the symmetric configuration point. The dislocations are considered to be perpendicular to the (xOy) plane and both screw and edge Burgers vector components are considered. The dislocations are numbered from 1 to n (1 is the nearest dislocation from the origin in each pile-up) and $x(i)$ is the position of the i th dislocation of one pile-up. Due to symmetry, the position of the j th dislocation in the second pile-up is $-x(j)$ where $x(j)$ is the position of the j th dislocation in the first pile-up. The force acting on dislocation i is the sum of forces due to applied τ_a and friction τ_f stresses, and interactions with the other dislocations. The interactions between two dislocations i and j are given by [80]:

$$F_x^{se} = \frac{\mu b_e^2}{2\pi(1-\nu)} \frac{1}{x(i) - x(j)}, \quad \text{for two edge dislocations of the same pile-up;}$$

$$F_x^{de} = -\frac{\mu b_e^2}{2\pi(1-\nu)} r \frac{r^2 - d^2}{(r^2 + d^2)^2}, \quad \text{for two edge dislocations of different pile-ups;}$$

$$F_x^{ss} = \frac{\mu b_s^2}{2\pi} \frac{1}{x(i) - x(j)}, \quad \text{for two screw dislocations of the same pile-up;}$$

$$F_x^{ds} = -\frac{\mu b_e^2}{2\pi} \frac{r}{r^2 + d^2}, \quad \text{for two screw dislocations of different pile-ups,}$$

where $r = x(i) + x(j)$ and b_e and b_s are the edge and screw component of Burgers vector respectively.

In Fig. 48 is reported the τ_f vs. τ_a curve. A τ_a value of around 33 MPa is obtained for zero friction stress and is accounted for by the additional lattice friction stress of 30 MPa applied in these calculations on all dislocations except the first. For a resolved applied stress of approximately 85 MPa corresponding to the previous observations, a friction stress τ_f of about 300 MPa is determined. Together with in situ TEM observations [81], in situ AFM studies can thus be carried out to estimate the friction stress using the dislocation pile-ups as a microscopic probe to scan the bulk crystal.

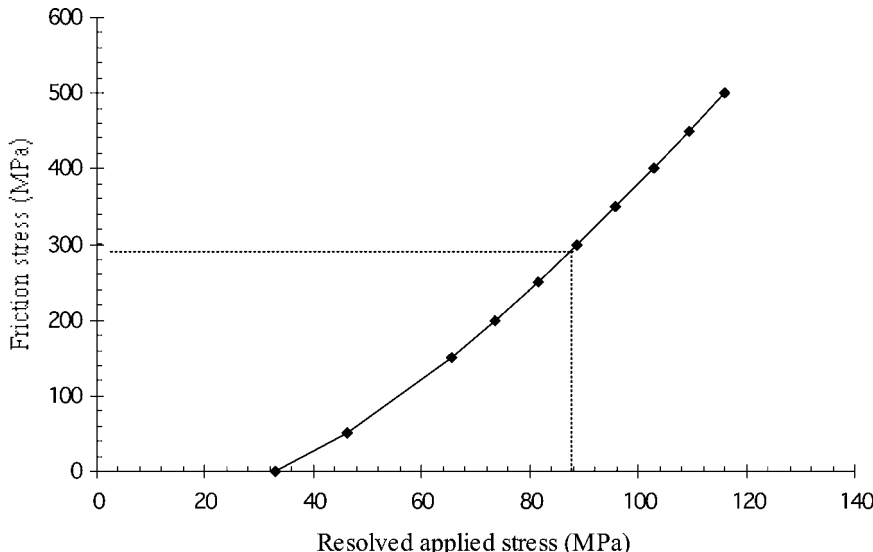


Fig. 48. Frictional stress τ_f as a function of applied stress τ_a . The simulation has been performed with the distance d between slip planes equal to 260 nm and the number n of dislocations equal to ten for each pile-up (courtesy of S. Brochard).

The equilibrium positions of each dislocation and hence the necessary applied stress τ_a to cross over the two pile-ups for various values of d have been also determined considering that τ_f acts only on the first head dislocation at room temperature [82].

Fig. 49 shows the evolution of τ_a as a function of d , for various values of n . As dislocations of the same and different pile-ups repel and attract each other respectively, a competition between these mechanisms occurs. As observed on the graph, increasing the number of dislocations in each pile-up induces a decrease of the necessary applied stress τ_a , which implies that the pile-up effect, i.e. more and more dislocations, is the easiest method to move the pile-up head forward. Moreover, a significant increase of τ_a is observed for small values of d . This demonstrates unambiguously the impossibility for two pile-ups to cross over at a distance smaller than a few tens of nanometers and is consistent with the characteristic distance determined by AFM observations (Section 3.1.1).

3.3. Localized plasticity around indentations

The previous paragraphs have shown the potential of atomic force microscopy to investigate the formation and growth of slip bands. Localized plasticity can be also studied; this is the case of the first stage of dislocation nucleation around nanoindentations [83–85]. AFM is thus particularly suited to analyze the fine structure of slip lines or rosette arms in the vicinity of these indented areas and to characterize the dislocation structure just beneath the free surface. Nanohardness measurements associated to AFM observations on γ phase single crystals show the strong dependence of local mechanical properties on the

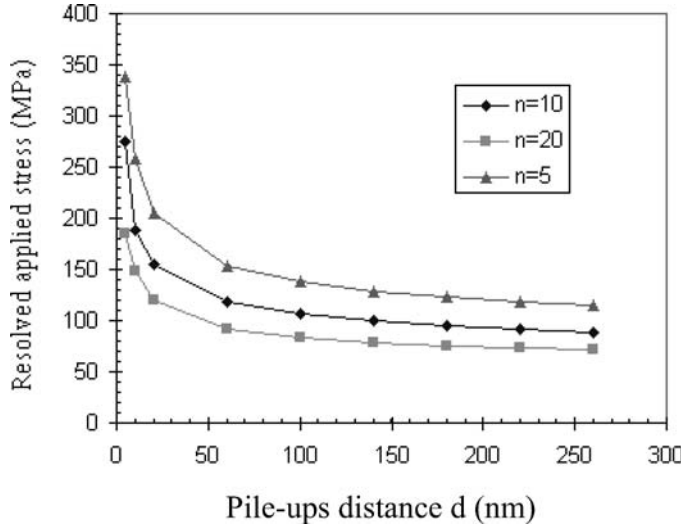


Fig. 49. Curve of applied stress τ_a against distance d between slip planes. The frictional stress τ_f is set at 300 MPa and the simulation has been carried out for several various values of n .

dislocation structures just beneath the surface [86]. In this paragraph, we focus only on the contribution of AFM observations to the study of the pop-in phenomenon observed in specific materials such as GaAs [87], Fe-Si [88], W [89] and Au [90], and characterized by an abrupt increase in penetration depth at a critical load F_{Pi} .

In Fig. 50(a) is presented a typical nanoindentation curve in (001) cleaved MgO single crystals. Loading starts with an elastic deformation (A), followed by a pop-in (B), i.e. a fast increase in penetration occurring for a critical load. Then loading goes on with an elasto-plastic behavior (C). Finally tests end with quasi-elastic unloading (D).

AFM studies have shown that no residual deformation, i.e. no imprint, is observed below the critical load. The deformation is characterized in this case by an elastic behavior and the loading and unloading parts of the curve are perfectly superimposed.

A three-dimensional AFM image of a residual imprint resulting from indentation stopped just after the pop-in is presented in Fig. 51. The scan size of the image is about 800 nm × 800 nm with a height at full extent of 12 nm. Although cleavage steps are clearly distinguishable running along the preferred [010] crystallographic direction, the surface exhibits only an indenter shaped imprint which corresponds exactly to the extent of the pop-in and no slip lines are observed [91].

At higher load, the plastic deformation extends outside the contact area, through the development of a four rosette arm pattern (Fig. 50(b)) [92]. The deformation associated with the pop-in event is thus localized within the contact area between the indenter and the specimen. The steps forming the rosette arms which appear as straight lines in the signal error mode AFM image (Fig. 50(c)) are clearly resolved, extending inside the indent and showing that two opposite arms develop simultaneously. As shown on cross section in Fig. 50(d), the U shaped arms are depressed troughs extending along ⟨100⟩ directions and gently sloping up to the surface. It can also be seen that the center of the indent presents

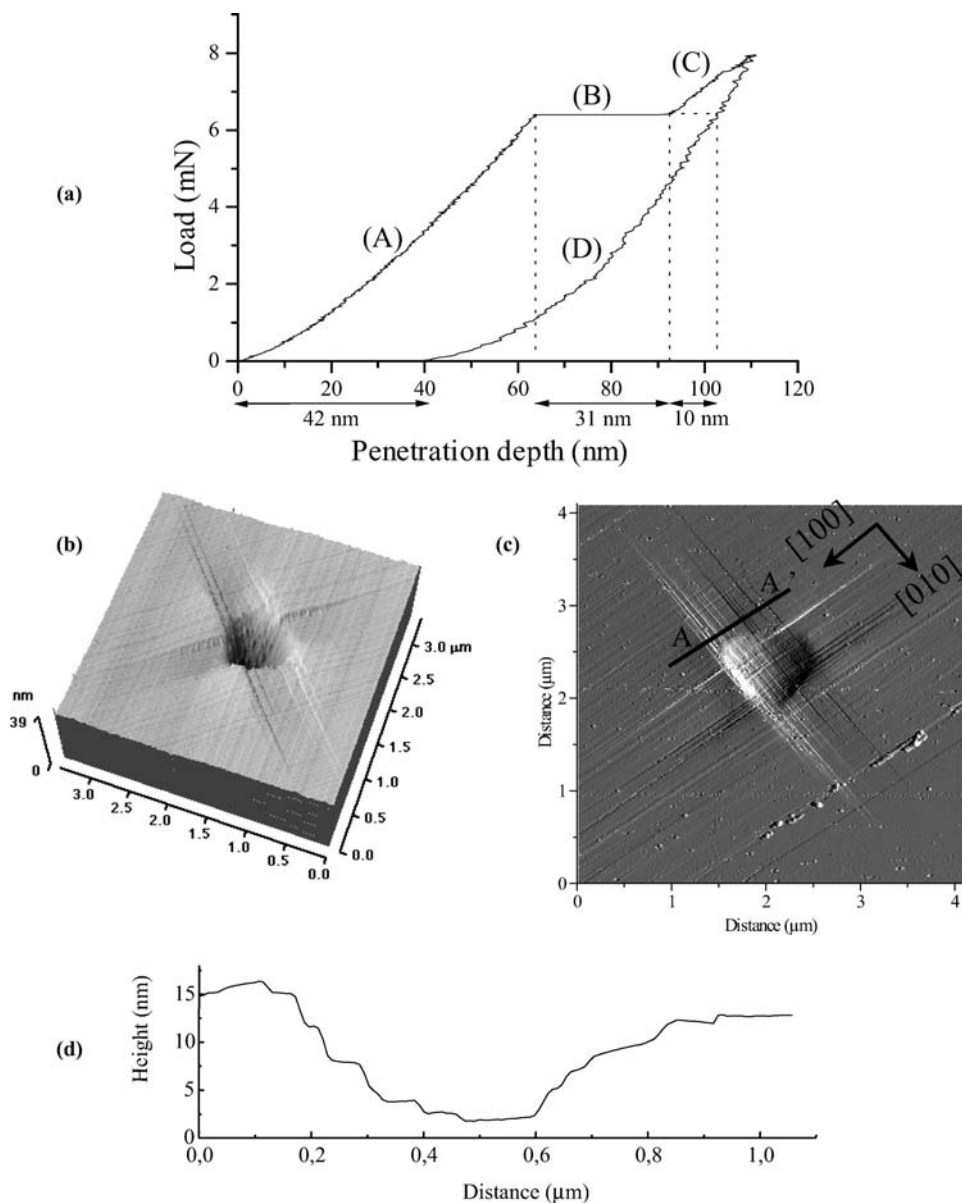


Fig. 50. Characteristics of a nanoindentation with an applied load higher than the pop-in critical load. (a) Load-penetration curve in force controlled mode. (b) Three-dimensional tapping mode AFM image. (c) Signal error mode AFM image enhancing the rosette arm slip lines. (d) Cross section AA' (courtesy of C. Tromas).

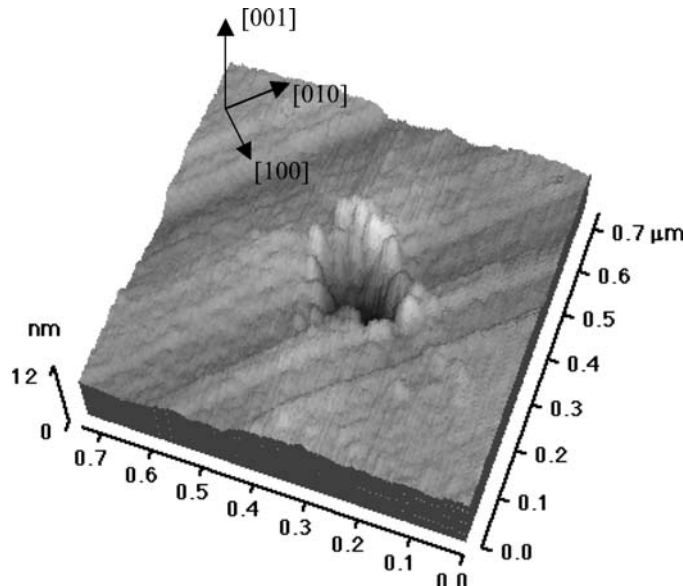


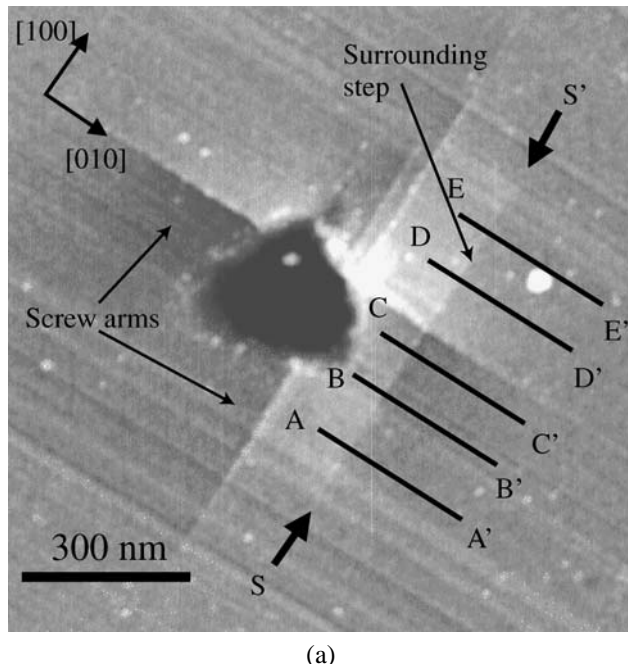
Fig. 51. Three-dimensional AFM image of a nanoindentation stopped just after the pop-in phenomenon (courtesy of C. Tromas).

an unsheared $140 \times 140 \text{ nm}^2$ square shaped bottom, corresponding to the crossing of the rosette arms, flat bottoms.

Each stage of the associated nanoindentation curve can be thus correlated with the surface topography observed by AFM. The total remaining depth penetration, 42 nm, deduced from the curve in Fig. 50 agrees with the 41 nm indent depth measured by AFM. Moreover, the curve shows a 10 nm residual penetration after the pop-in, which can be linked to the rosette arm depth measured by AFM just around the indent, that is, outside the other two orthogonal rosette arms. The correspondence between these two measurements indicates that the second regime of indentation, just after the pop-in, corresponds to the rosette arm formation. The 31 nm amplitude of the pop-in added to the 10 nm rosette arms depth is exactly the depth of the indent, either measured on the indentation curve or by AFM.

The pop-in corresponding to a sudden and strictly plastic bunching appears as the first stage of the plastic deformation during nanoindentation on this material. From AFM investigations, this phenomenon is accounted for by the nucleation of interstitial dislocation loops just below the indenter and is followed by an elasto-plastic process responsible for the rosette arm formation and resulting from the dissociation of dislocation loops [91].

In the case of microindentations performed at much higher loads, square shaped slip lines are commonly observed [93,94]. The early stage of formation of this pattern may be investigated since the fine structure of these surrounding steps can be clearly resolved by AFM. On Fig. 52(a) is shown an AFM image of an indentation performed in an MgO single crystal. Rosette arms described previously are clearly distinguishable and are limited in this case to less than ten dislocations, and only one surrounding step is observed. As shown in various cross sections in Fig. 52(b), this step has a variable height of 0.2, 0.4 and



(a)

Fig. 52. Indentation performed on an MgO single crystal at a $530 \mu\text{N}$ load. (a) Tapping mode AFM observation, (b) perpendicular cross sections (courtesy of C. Tromas).

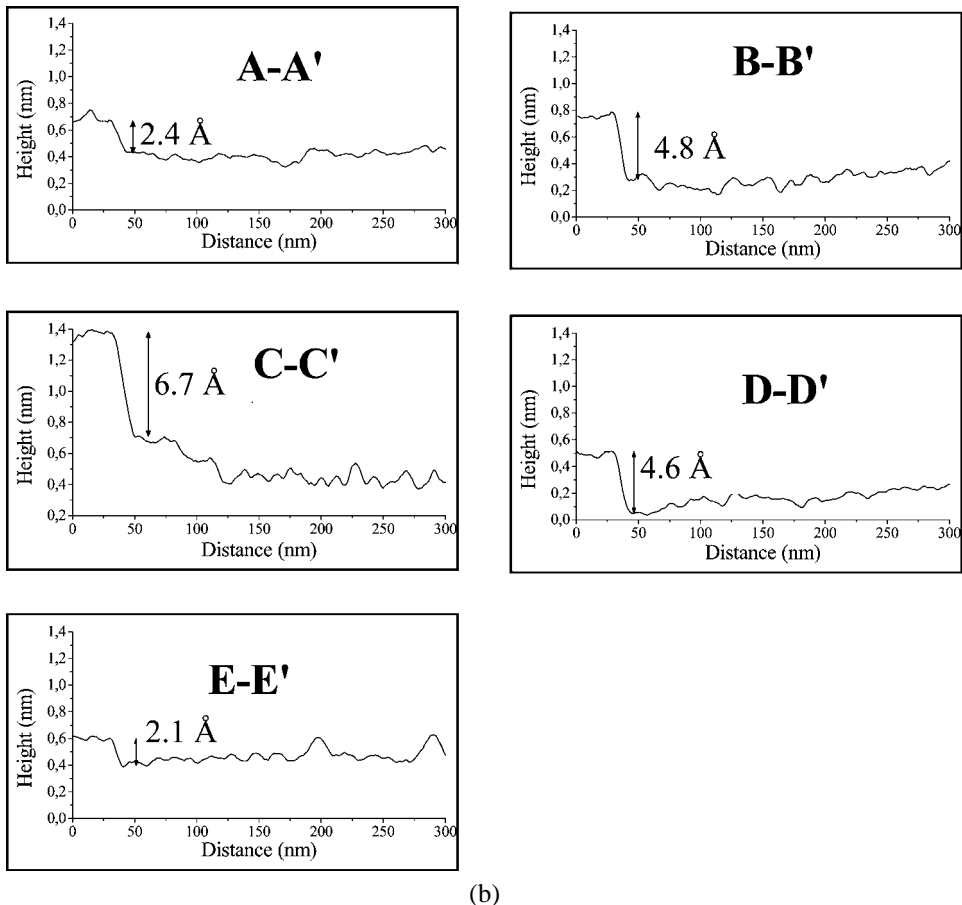
0.6 nm corresponding to the emergence of one, two and three dislocations respectively, which characterizes the activation of a spiral Frank–Read source just beneath the surface (Fig. 53) [95].

In conclusion, AFM is proved to be a valuable complementary tool for elucidating elementary deformation mechanisms taking place during the first stage of an indentation test.

3.4. Dislocation locking effects at the film/substrate interface

The mechanical behavior of thin films under stress has been extensively studied in the recent years, in particular with their wide use in microelectronics for production of integrated circuits and semi-conductor devices. The quality of coated parts in practical use is influenced by the stability of the thin films and coatings. In particular, buckling phenomenon [96–100] is supposed not to appear.

The interface between the film and the substrate is an essential region since dislocations moving in the substrate can be locked and/or pass through it. On the one hand, dislocations can be used as an atomic saw to cut the thin film and the efficiency of this process which is strongly dependent on the capability of dislocations to create regular steps can be estimated by AFM, as discussed in Section 3.1.5. On the other hand, the shearing of films may be



(b)

Fig. 52. (Continued).

an undesirable effect, in particular in the case of wear-protective coatings. It has thus been shown that a 0.2–1 μm thick Al alloy film considerably improves the lifetime in fatigue of a 316L stainless steel single crystal [101,102].

Taking advantage to the high resolution of AFM, the locking effect of dislocations at the interface of film/substrate systems can be quantitatively analyzed. As an example is presented in Fig. 54, the evolution of a gold film 150 nm thick on LiF single crystal substrate under compressive stress [103]. A specific landmark labeled α is used to point the relative position of the images. The scan size of each image is about $16.6 \times 16.6 \mu\text{m}^2$ leading to a lateral resolution of around 30 nm and the values of ε are indicated. The initial aspect of the specimen is presented in Fig. 54(a) where the river pattern of the cleavage steps and the columnar thin film structure are still distinguishable.

The first topographical change consists in the emergence of the first set of dislocations, estimated to about 40 (emerged dislocation number), when the strain reaches a critical value of $\varepsilon^* = 0.94\%$ (Fig. 54(b)).

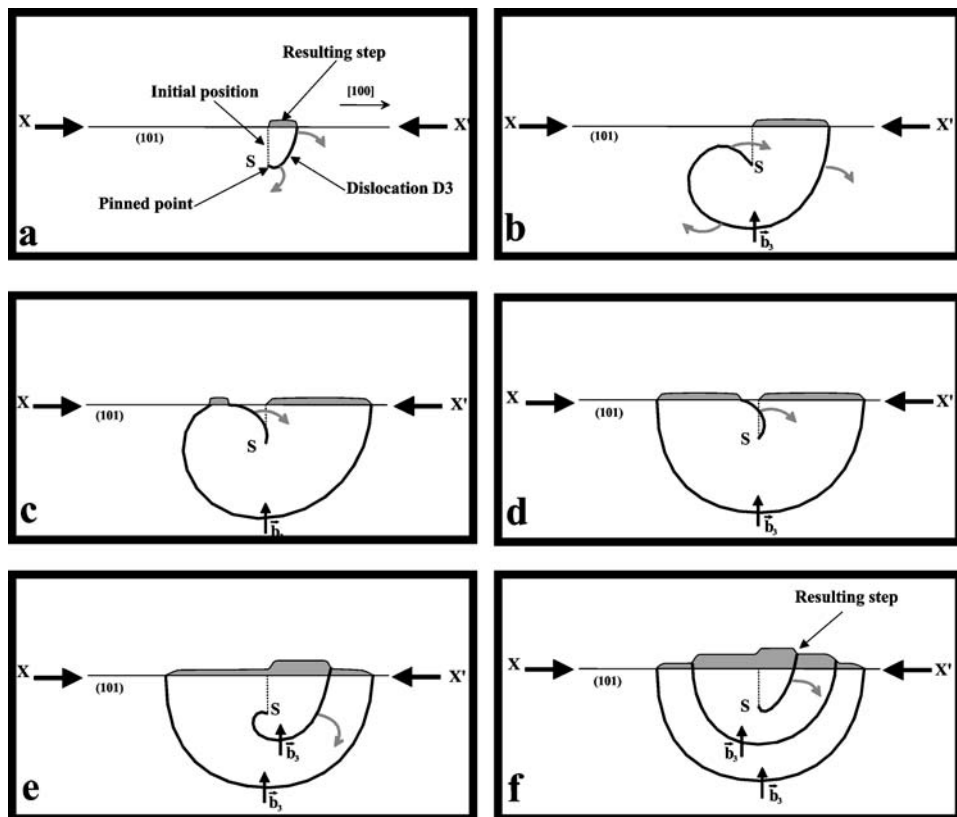
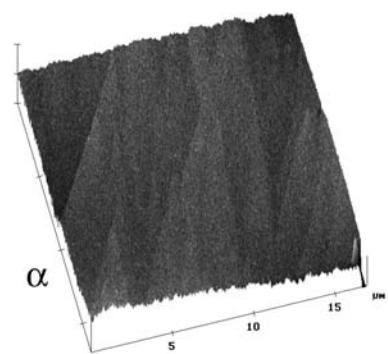


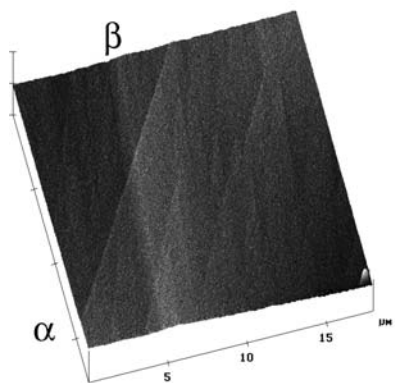
Fig. 53. Schematic of the surface spiral source (courtesy of C. Tromas).

Whereas LiF single crystals are characterized by homogeneous plastic deformation (Section 3.2.1), the dislocation emergence process in this coated sample is heterogeneous since only a few steps are observed (Fig. 54(b, c)). For instance, under similar deformation conditions, an average height and slip line spacing of 2.8 nm (14 dislocations) and around 180 nm are determined respectively for pure LiF.

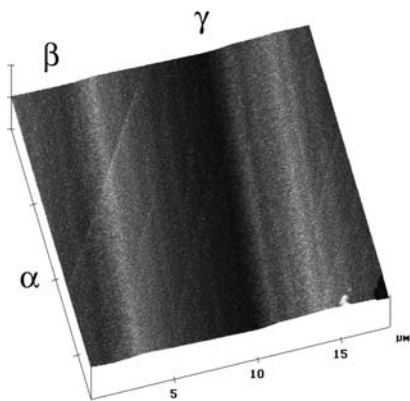
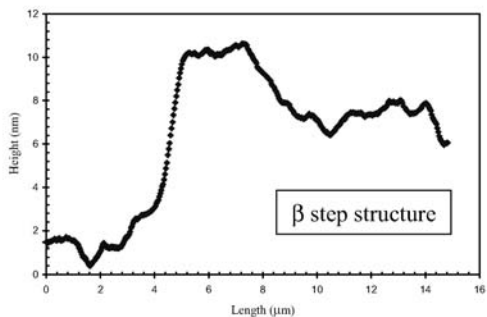
The emerged dislocation density (Section 3.2.3.1) versus strain ε has been determined (Fig. 55). The experimental emerged dislocation density for pure LiF single crystals and for associated coated samples are compared. An emerged dislocation rate (number of dislocations per % strain and unit length l_0) of about 580 is determined for LiF single crystals (dotted line). A locking phenomenon taking place in the coated samples is evident since no dislocation appears at the specimen surface (Part I); dislocations are locked at the film/substrate interface up to the critical value ε^* . Then the dislocations shear the thin film and this mechanism occurs in only a few areas. At a given strain, the emerged dislocation density is obviously lower than these for uncoated LiF single crystals but the emergence process rate is enhanced, estimated to be about 900 (straight line in Part II). Dislocations moving in the substrate are thus piled up at the interface as long as the stress is insufficient



(a)



(b)



(c)

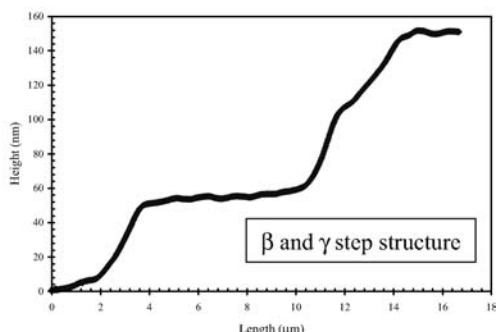


Fig. 54. Three-dimensional AFM images of a gold thin film on LiF single substrate under compressive stress (a) $\varepsilon = 0\%$, (b) $\varepsilon = 0.94\%$, (c) $\varepsilon = 1.60\%$. α characterises the river cleavage pattern, β and γ the step structures.

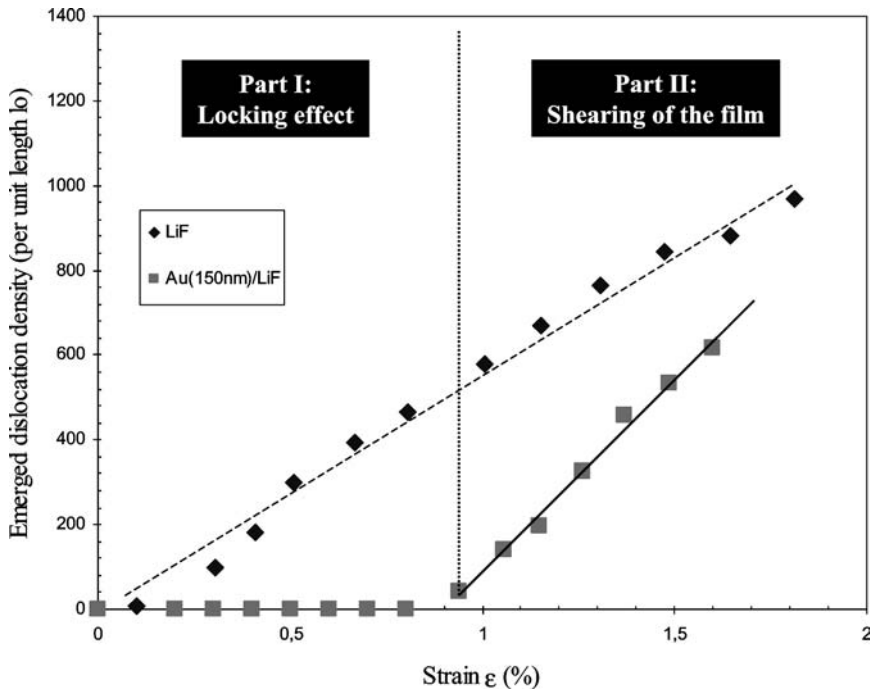


Fig. 55. Emerged dislocation density (per unit length l_0) versus plastic strain, of LiF single crystals and 150 nm thick gold films on LiF substrates.

to shear the thin film. A critical stress for the shearing of the film may then be reached resulting in the emergence of all dislocations of the pile-up considered. This explains that only a small number of slip lines appear for this coated sample and the high rate of dislocation emergence process determined for these slip lines.

4. Conclusion

This paper has been mainly devoted to the study of dislocations by SPM techniques by using the topographic contrast induced by the apparent strain field of dislocations which is generated at the surface. SPM appears to be valuable tools for studying dislocation interactions with the surfaces taking in mind that the dislocation characteristics are modified by surface effects. These techniques appear quite easy to handle but very good surface quality is needed to extract valuable data. Cleavage seems to be one of the easiest way to get proper surfaces for studying bulk materials.

Owing to the characteristics of the dislocation and the technique, it appears more straightforward to deduce informations from off surface displacements. This has been widely used to study growth dislocations that are screw and perpendicular to the surface of the material. In the same way the fine analysis slip lines available with these techniques has proved to be very efficient in deducing bulk behaviour of dislocations and geometrical

features of deformation (twinning mechanism, cross slip mechanisms, dislocation sources operation...). Dynamical effects can also be quantified using *in situ* measurements.

In-plane observation of dislocation characteristics is more difficult to achieve since it requires obtaining atomic resolution. Such resolution associated to the measurement of off-surface displacements could be of great interest in getting insights into screw dislocation core configurations, which are not available by HREM techniques. Associated to an *in situ* deformation machine this would provide information at the atomic scale on cross slip mechanisms.

In addition to the topographic contrast of dislocations related to their apparent strain field at the surface, local changes in physical properties (electronic, thermal, magnetic effects) induced by dislocation cores can also be probed using specific equipments associated to SPM techniques. Local spectroscopic methods can also provide information on the nature and the concentration of impurity atoms located within the dislocation cores. Such techniques associated to topographic data measurements are likely to improve drastically the knowledge of the physics of dislocations in the near future.

Acknowledgements

The authors wish to thank Prs J. Grilhé and J. Bonneville and Drs S. Brochard, F. Cleymand, J. Colin, X. Milhet and C. Tromas for fruitful discussions and useful suggestions.

References

- [1] H. Von Känel, T. Meyer and H. Sirringhaus, Journal of Crystal Growth 175 (1997) 340.
- [2] H. Sirringhaus, T. Meyer, E.Y. Lee and H. Von Känel, Phys. Rev. B 53 (1996) 944.
- [3] G. Binnig, H. Rohrer, Ch. Gerber and E. Wiebel, Appl. Phys. Lett. 40 (1982) 178.
- [4] G. Binnig, H. Rohrer, Ch. Gerber and E. Wiebel, Phys. Rev. Lett. 49 (1982) 57.
- [5] G. Binnig and H. Rohrer, Helv. Phys. Acta 55 (1982) 726.
- [6] G. Binnig and H. Rohrer, Physica B 127 (1984) 37.
- [7] G. Binnig, C.F. Quate and Ch. Gerber, Phys. Rev. Lett. 56 (1986) 930.
- [8] G. Binnig, Ultramicroscopy 42 (1992) 7.
- [9] H.K. Wickramasinghe, Scanned Probe Microscopy, AIP Conference Proceedings (1992) 241.
- [10] J. Tersoff and D.R. Hamann, Phys. Rev. Lett. 50 (1983) 1998; Phys. Rev. B 31 (1985) 805.
- [11] N.D. Lang, Phys. Rev. B 34 (1986) 5947.
- [12] S. Gauthier and C. Joachim, Scanning Probe Microscopy: Beyond the Images (Editions de physique, France, 1992).
- [13] R.M. Feenstra, J. Stroscio, J. Tersoff and A. Fein, Phys. Rev. Lett. 58 (1987) 1192.
- [14] M.F. Crommie, C.P. Lutz and D.M. Eigler, Science 262 (1993) 218.
- [15] C.J. Humphreys, Dislocations in Solids, Vol. 5, ed. F.R.N. Nabarro (North Holland, Amsterdam, 1980) pp. 1–56.
- [16] K. Takayanagi, Surf. Sci. 205 (1988) 637.
- [17] N. Junqua and J. Grilhé, Phil. Mag. Lett. 75 (1997) 125.
- [18] M. Dynna, J.L. Vassent, A. Marty and B. Gilles, J. Appl. Phys. 80 (1996) 2650.
- [19] M. Schmid, A. Biedermann, H. Stadler and P. Varga, Phys. Rev. Lett. 69 (1992) 925.
- [20] Y. Mera, T. Hashizume, K. Maeda and T. Sakurai, Ultramicroscopy 42 (1992) 915.
- [21] R.M. Overney, H. Haefke, E. Meyer and H.J. Güntherodt, Surface Science 277 (1992) 22.

- [22] K. Sangwal, J. Torrent-Burgues, F. Sanz and J. Servat, *Surface Science* 374 (1997) 387.
- [23] R. Stadler, H. Sirringhaus, N. Onda and H. van Känel, *Ultramicroscopy* 42 (1992) 781.
- [24] J. Garbarz, E. Lacaze, G. Faivre, S. Gauthier and M. Schott, *Phil. Mag. A* 65 (1992) 853.
- [25] D.L. Barett, J.P. McHugh, H.M. Hobgood, R.H. Hopkins, P.G. McMullin, R.C. Clarke and W.J. Choyke, *Journal of Crystal Growth* 128 (1993) 358.
- [26] R.C. Glass, L.O. Kjellberg, V.F. Tsvetkov, J.E. Sundgren and E. Janzen, *Journal of Crystal Growth* 132 (1993) 504.
- [27] H.M. Hobgood, D.L. Barett, J.P. McHugh, R.C. Clarke, S. Sriram, A.A. Burk, J. Greggi, C.D. Brandt, R.H. Hopkins and W.J. Choyke, *Journal of Crystal Growth* 137 (1994) 181.
- [28] F.C. Frank, *Acta Crystall.* 4 (1951) 497.
- [29] J. Giocondi, G.S. Rohrer, M. Skowronski, V. Balakrishna, G. Augustine, H.M. Hobgood and R.H. Hopkins, *Journal of Crystal Growth* 181 (1997) 351.
- [30] J. Giocondi, G.S. Rohrer, M. Skowronski, V. Balakrishna, G. Augustine, H.M. Hobgood and R.H. Hopkins, III-Nitride SiC and Diamond Materials for Electronic Devices, *Mat. Res. Soc. Proc.*, Pittsburgh, PA 423 (1996) 539.
- [31] N. Sugiyama, A. Okamoto, K. Okumura, T. Tani and N. Kamiya, *Journal of Crystal Growth* 191 (1998) 84.
- [32] K. Sangwal and R. Rodriguez-Clemente, *Surface Morphology of Crystalline Solids* (Trans. Tech., Zurich, 1991).
- [33] B. Van der Hoek, J.P. Van der Eerden and P. Bennema, *Journal of Crystal Growth* 56 (1982) 621.
- [34] K. Sato and M. Okada, *Journal of Crystal Growth* 63 (1983) 177.
- [35] J.J. De Yoreo, T.A. Land and B. Dair, *Phys. Rev. Lett.* 73 (1994) 838.
- [36] B. Van der Hoek, J.P. Van der Eerden, P. Bennema and I. Sunagawa, *Journal of Crystal Growth* 58 (1982) 365.
- [37] E. Schmid and W. Boas, *Kristallplastizität* (Springer, Berlin, 1936).
- [38] J. Friedel, *Dislocations* (Pergamon Press, 1964).
- [39] J.P. Hirth and J. Lothe, *Theory of Dislocations* (McGraw-Hill, 1968).
- [40] D. Hull, *Introduction to Dislocations* (Pergamon Press, 1975).
- [41] H. Neühauser, R. Rodloff, H. Flor and Ch. Schwink, *Proc. 4th Int. Conf. Strength of Metals and Alloys* (Nancy, 1976).
- [42] Ch. Schwink and H. Neühauser, *Phys. Stat. Sol.* 6 (1964) 679.
- [43] H. Neühauser and R. Rodloff, *Acta Met. Mat.* 22 (1974) 375; *Phys. State Solid.* 49 (1978) 445.
- [44] M. Ignat, M. Ducarroit, M. Lelogeais and J. Garden, *Thin Sol. Films* 220 (1992) 271.
- [45] M. Ignat, P. Scafidi, E. Duloisy and J. Dijon, *Mat. Res. Soc. Symp. Proc.* 338 (1994).
- [46] M. Ignat and P. Scafidi, *Strength of Materials—The Japan Institute of Metals* (1994) 849.
- [47] C. Coupeau, J.-C. Girard and J. Grilhé, *Journal of Vacuum Science Technology B* 16 (4) (1998) 1964.
- [48] C. Coupeau, J.-C. Girard and J. Grilhé, *MRS Proceeding, Fundamentals of Nanoindentation and Nanotribology*, 107, San Francisco Spring Meeting 98.
- [49] C. Coupeau, S. Brochard, M. Jouiad, A. Coujou and J. Grilhé, *Phil. Mag. A* 79 (3) (1999) 627.
- [50] X. Milhet, J.-C. Girard, J.-L. Demenet and J. Rabier, *Phil. Mag. Lett.* 81 (9) (2001) 623.
- [51] B.B. Mandelbrot, *The Fractal Geometry of Nature* (Freeman, New York, 1983).
- [52] B. Sprusil and F. Hnilica, *Czech. J. Phys. B* 38 (1988) 188.
- [53] T. Kleiser and M. Bocek, *Z. Mettkd.* 77 (1986) 582.
- [54] I.R. Gobel, *Z. Mettkd.* 82 (1991) 858.
- [55] B. Sprusil and F. Hnilica, *Czech. J. Phys. B* 35 (1985) 897.
- [56] L. Ressier, F. Voillot, M. Goiran and J.P. Peyrade, *Appl. Phys. Letters* 79 (11) (1996) 8298.
- [57] J.P. Peyrade, F. Voillot, M. Goiran, H. Atmani, A. Rocher and E. Bedel, *Appl. Phys. Letters* 60 (20) (1992) 2481.
- [58] L. Ressier, J.P. Peyrade, J. Barrau and F. Voillot, *Superlattices and Microstructures* 22 (1997) 35.
- [59] L. Ressier, J. Diaz and J.P. Peyrade, *Appl. Phys. Letters* 70 (16) (1997) 2195.
- [60] F. Tranchant, J. Vergnol and J. Grilhé, *Scripta Met. Mat.* 17 (1983) 175.
- [61] J. Vergnol and J. Grilhé, *J. Phys.* 45 (1984) 1479.
- [62] F. Tranchant, J. Vergnol, M.F. Denanot and J. Grilhé, *Scripta Met.* 21 (1987) 269.

- [63] J. Vergnol, Thesis of University of Poitiers (France, 1980).
- [64] C. Coupeau, F. Tranchant, J. Vergnol and J. Grilhé, Eur. Phys. J. Appl. Phys. 6 (1999) 1.
- [65] D. Caillard and A. Couret, Dislocations in Solids, eds F.R.N. Nabarro and M.S. Duesbery (Elsevier Science, Amsterdam) (1996) p. 69.
- [66] P. Veyssiére and G. Saada, Dislocations in Solids, eds F.R.N. Nabarro and M.S. Duesbery (Elsevier Science, Amsterdam) (1996) p. 253.
- [67] P.H. Thornton, R.G. Davies and J.L. Johnston, Metall. Trans. 1 (1970) 207.
- [68] N. Baluc, J. Bonneville and J.-L. Martin, Physica Scripta T49 (1993) 393.
- [69] C. Coupeau, J. Bonneville, B. Matterstock, J. Grilhé and J.-L. Martin, Scripta Met. Mat. 41 (9) (1999) 945.
- [70] C. Coupeau, T. Kruml and J. Bonneville, in: High Temperature Ordered Intermetallic Alloys IX, Vol. 646, eds J. Schneibel, R. Noebe, S. Hanada, K. Hemker and G. Sauthoff (Materials Research Society, Pittsburgh, 2001) N5.14.1.
- [71] C.B. Jiang, S. Patu, Q.Z. Lei and C.X. Shi, Phil. Mag. Lett. 78 (1998) 1.
- [72] N. Clément, L'ordre et le désordre dans les matériaux, eds F. Reynaud, N. Clément and J.J. Couderc (Les Editions de Physique, les Ulis, France, 1984) pp. 167–182.
- [73] P. Schwander, B. Schönfeld and G. Kostorz, Phys. Sta. Sol. B 172 (1992) 73.
- [74] L. Reinhardt, B. Schönfeld, G. Kostorz and W. Buhrer, Verh. DPG 22 (1987) M13.
- [75] J. Olfe and H. Neuhäuser, Phys. Sta. Sol. A 109 (1988) 149.
- [76] Ch. Schwink, Rev. Phys. Appl. 23 (1988) 395.
- [77] C. Coupeau and J. Grilhé, European Physical J. Applied Physics 5 (1999) 231.
- [78] P. Pirouz, Scrip. Met. Mat. 23 (1989) 401.
- [79] P. Pirouz and P.M. Hazzledine, Scrip. Met. Mat. 25 (1991) 1167.
- [80] D. Hull, Introduction to Dislocations 2nd edn (Pergamon Press, 1975) pp. 98–99.
- [81] F. Pettinari, Thesis n° 3338 of University Paul Sabatier, Toulouse II, France (1999).
- [82] M. Jouiad, Thesis n° 2484 of University Paul Sabatier, Toulouse II, France (1996).
- [83] J. Woigard and J.C. Dargent, Meas. Sci. Tech. 6 (1995) 16.
- [84] J. Woigard and J.C. Dargent, J. Mater. Res. 12 (1997) 2455.
- [85] C. Tromas, J. Colin, C. Coupeau, J.-C. Girard, J. Woigard and J. Grilhé, Eur. Phys. J. Appl. Phys. 8 (1999) 123.
- [86] C. Coupeau, J. Grilhé, F. Oulevey, A. Kulik and W. Benoit, Jour. Mat. Sci. Lett. 19 (2000) 259.
- [87] A.B. Mann and J.B. Pethica, Mat. Res. Symp. 436 (1997) 153.
- [88] W.W. Gerberich, S.K. Venkataraman, H. Huang, S.E. Harvey and D.L. Kohlstedt, Acta Metall. Mater. 43 (4) (1995) 1569.
- [89] S.A. Syed Asif and J.B. Pethica, Phil. Mag. A 76 (1997) 1105.
- [90] J.E. Houston and T.A. Milchaskie, Mat. Res. Soc. Symp. Proc. 436 (1997) 3.
- [91] C. Tromas, J.C. Girard, V. Audurier and J. Woigard, J. Mater. Sci. 34 (1999) 5337.
- [92] R.W. Armstrong and C.M. Wu, J. Am. Ceram. Soc. 61 (1978) 102.
- [93] M.M. Chaudhri, Phil. Mag. A 53 (1986) 55.
- [94] A.S. Keh, J.C.M. Li and Y.T. Chou, Acta Met. 7 (1959) 694.
- [95] C. Tromas, J.-C. Girard and J. Woigard, Phil. Mag. A 80 (10) (2000) 2325.
- [96] C. Coupeau, J.F. Naud, F. Cleymand, P. Goudeau and J. Grilhé, Thin Solid Film 353 (1999) 194.
- [97] V. Branger, C. Coupeau, P. Goudeau and J. Grilhé, Journal of Materials Science Letters 19 (2000) 353.
- [98] F. Cleymand, C. Coupeau, J. Colin and J. Grilhé, European Phys. J. of Appl. Phys. 10 (2000) 3.
- [99] J. Colin, F. Cleymand, C. Coupeau and J. Grilhé, Phil. Mag. A. 80 (11) (2000) 2559.
- [100] F. Cleymand, C. Coupeau and J. Grilhé, Scripta Mat. 44 (2001) 2623.
- [101] P. Villechaise, J. Mendez and J. Delafond, The Minerals, Metals and Materials Society (1991) 335.
- [102] S. Peraud, P. Villechaise and J. Mendez, Materials Science and Engineering A 225 (1997) 162.
- [103] C. Coupeau, F. Cleymand and J. Grilhé, Scripta Mat. 43 (2000) 187.

Dislocations and Mechanical Properties of Ceramics

T.E. MITCHELL

Structure-Property Relations Group, MST-8, Los Alamos National Laboratory, Los Alamos, NM 87545, USA
and

A.H. HEUER

*Department of Materials Science and Engineering, Case Western Reserve University, Cleveland, OH 44106,
USA*

Contents

1. Introduction	341
2. The critical resolved shear stress	342
2.1. Experimental observations	342
2.2. Kink mechanism for deformation	343
2.3. Modification of the model for kink pair nucleation on point defects	346
2.4. Modification of the model for kink nucleation on partial dislocations	349
2.5. Comparison between theory and experiment	350
3. Crystallography of slip	353
3.1. Crystal structures	353
3.2. Slip systems	355
3.3. Dislocation dissociations	356
4. Dislocations in particular oxides	357
4.1. MgO and other oxides with the rock-salt structure	357
4.2. BeO and other oxides with the wurtzite structure	360
4.3. ZrO ₂ and other oxides with the fluorite structure	363
4.4. TiO ₂ and other oxides with the rutile structure	367
4.5. SiO ₂ (quartz)	368
4.6. Al ₂ O ₃ (sapphire)	370
4.7. SrTiO ₃ and other oxides with the perovskite structure	375
4.8. MgO-Al ₂ O ₃ and other spinels	378
4.9. Mg ₂ SiO ₄ (forsterite)	382
4.10. Other oxides	384
4.11. SiC, Si ₃ N ₄ and other non-oxide ceramics	386
4.12. Climb versus glide dissociation	387
5. Work hardening	388
5.1. Work hardening in MgO	388
5.2. Work hardening and work softening in spinel	389
5.3. Work hardening in sapphire	391
6. Solution hardening	393
6.1. Isovalent cations	393
6.2. Aliovalent cations	395
7. Closing remarks	396
Acknowledgments	397
References	397

1. Introduction

When the concept of the dislocation was first introduced in 1934, its immediate success was in explaining why pure metals are soft and easy to deform plastically. Ceramics by comparison were seen as hard and often impossible to deform plastically. In fact a great deal of early work had been done by 1934 on the deformation of ceramic-like materials, involving single crystals of natural minerals. In their classic book, Schmid and Boas [1] devote a chapter to the plasticity and strength of ionic crystals. They present a table listing the glide and twin elements of 30 different minerals, which is essentially a condensation of a much longer listing from the 1927 Landolt–Börnstein tables [2]. Much of the work was done by Otto Mügge, whose pioneering work included the determination of not only the glide elements of copper, silver and gold [3], but also the glide and twinning elements of literally dozens of different minerals.

Mügge and others found that the only minerals that could easily be deformed under ambient conditions were the alkali halides and a few sulphides and carbonates. An exception to this was periclase (MgO), which deformed by $\{1\bar{1}0\}\langle110\rangle$ dodecahedral glide in the same way as halite (NaCl). A recently discovered exception is SrTiO_3 with the cubic perovskite structure, which can be deformed plastically at ambient and high temperatures but is brittle at intermediate temperatures, as described in Section 4.7. Other oxides and silicate minerals either cleaved or twinned when attempts were made to deform them at normal temperatures and pressures [1].

The application of dislocation theory to ceramics developed slowly over the years, with the exception of the alkali halides [4,5]. The main reason for this was the difficulty of inducing plastic flow in many ceramics, as well as the sparsity of available crystals. This experimental barrier was overcome by Wachtman and Maxwell [6], who developed high temperature mechanical testing techniques and were able to deform single crystals of sapphire ($\alpha\text{-Al}_2\text{O}_3$) at temperatures above 900°C , periclase (MgO) at temperatures above 1100°C and rutile (TiO_2) at temperatures above 600°C . This opened up the field of dislocations and plastic deformation of ceramics, and was followed by the seminal papers by Kronberg [7] on dislocations in sapphire and by Hornstra [8] on dislocations in spinel (MgAl_2O_4). The seventies and eighties saw much activity in this field, especially in the application of electron microscopy to the study of dislocations in ceramics, and there was the usual mixture of predicted and unpredicted observations, stimulating the need for more research. “Ductile” ceramics have remained elusive and perhaps that is the reason for the present quiescent stage of research. “Toughened” ceramics based on zirconia and silicon nitride emerged as a reality [9] but discussion of this topic is beyond the scope of the present article.

The present review will concentrate on oxide ceramics. Related reviews are available on ionic crystals by Haasen [5] and by Sprackling [4], on covalent crystals by Hirsch [10] and by Alexander [11] and on silicate minerals by Paterson [12]. Previous reviews on oxides

by Wachtman [13], Terwillinger and Radford [14], Bretheau et al. [15], and Mitchell [16] are also available.

2. The critical resolved shear stress

2.1. Experimental observations

Most ceramics are brittle at low and medium temperatures and can be deformed plastically above the brittle-to-ductile transition temperature. The critical resolved shear stress (CRSS) then decreases rapidly with increasing temperature. In many cases there is a linear relationship between $\log(\text{CRSS})$ and temperature, as first shown by Castaing for semiconductor crystals [17]. Examples are shown in Figs 1–4. For MgO in Fig. 1 [5], the relationship is well obeyed for both easy slip on the {110} plane and hard slip on the {001} plane; the CRSS is ~ 40 times higher for the latter compared to the former at 800 K. MgO can be deformed at very low temperatures on the {110} slip plane. For spinel in Figs 2 and 3 [18], the behavior is more complicated. The $\log(\text{CRSS})-T$ relationship is obeyed at very high temperatures for both {111}{110} and {110}{110} slip. The CRSS values are about the same for the two systems for stoichiometric spinel but lower on the {110} plane for non-stoichiometric compositions. Note that the CRSS is almost two orders of magnitude lower for $n = 3.5$ crystals than for $n = 1.1$ crystals. The data at low temperatures were obtained either under a high confining pressure [19,20] or under a hardness indent [21]. The interpolated lines between the high and low temperature data show a sharp change in slope for {111}{110} slip (Fig. 2) and a yield stress anomaly with a maximum at $\sim 1200^\circ\text{C}$

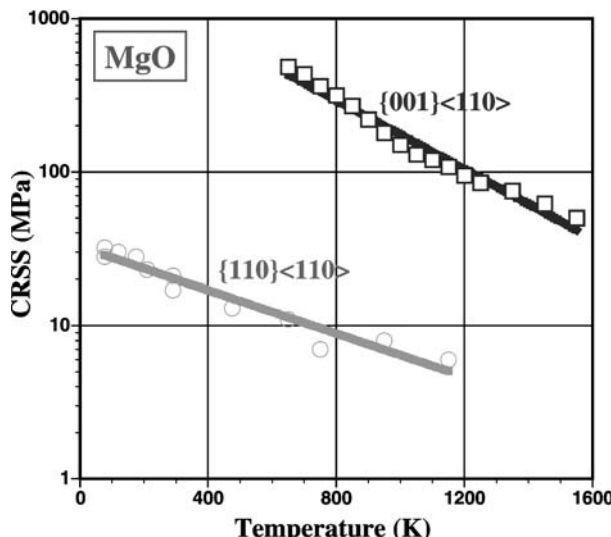


Fig. 1. $\log(\text{CRSS})$ vs. temperature for the {110}{110} and {001}{110} slip systems in MgO (data from Haasen [5]).

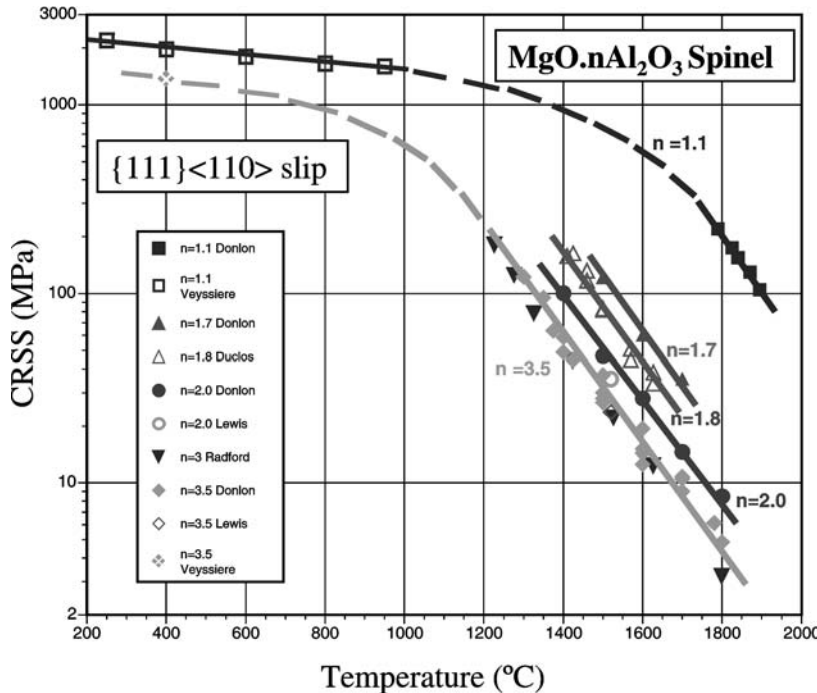


Fig. 2. Log(CRSS) vs. temperature for $\{111\}\langle 110 \rangle$ slip in spinel of various stoichiometries. The low temperature data represent either high pressure confinement experiments or hardness tests [18].

for $\{110\}\langle 110 \rangle$ slip. Dissociated screw dislocations cross-slip from $\{110\}$ to $\{001\}$ planes at low temperatures [19], thereby becoming immobilized, and we think that this is the reason for the yield stress anomaly [18]. The softening of non-stoichiometric crystals has been ascribed to cation vacancies assisting kink diffusion at high temperatures, as described in Section 2.5. The behaviour of sapphire in Fig. 4 is different. The $\log(\text{CRSS})-T$ law is obeyed approximately for both basal and prism plane slip. However, the slopes are different so that the curves cross at ~ 900 K, with prism plane slip becoming easier at low temperatures. The curves in Fig. 4 are not straight lines but were fitted from eq. (5), as described in the Section 2.5. The behavior of other ceramics are described in Section 4.

2.2. Kink mechanism for deformation

In the standard treatment of Hirth and Lothe [22], their eq. (15-27) gives the kink pair nucleation rate as

$$J = \frac{\sigma b h}{a^2 k T} D_k \exp\left(-\frac{F^*}{k T}\right), \quad (1)$$

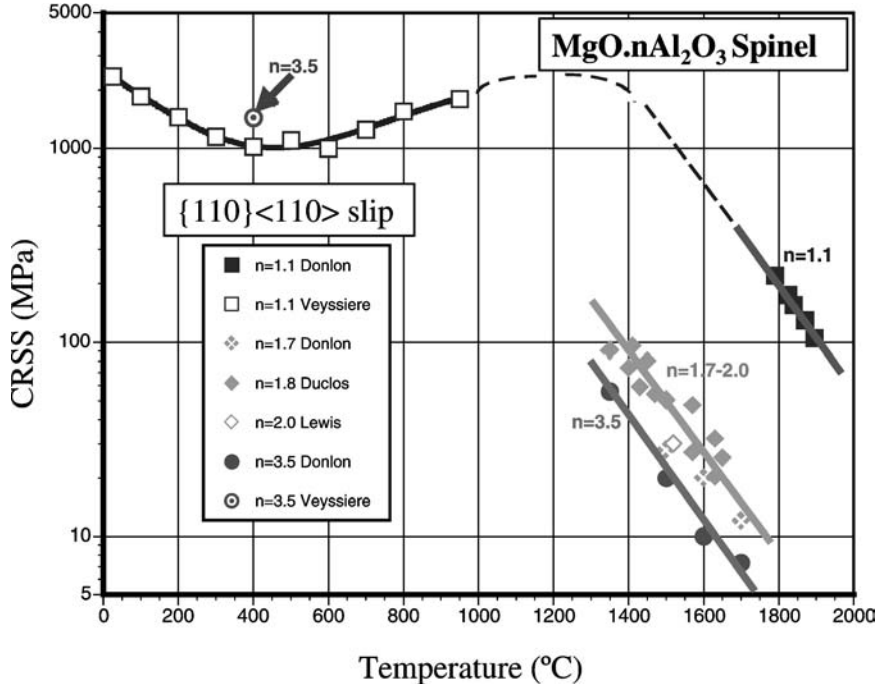


Fig. 3. Log(CRSS) vs. temperature for {110}<110> slip in spinel of various stoichiometries. The low temperature data represent either high pressure confinement experiments or hardness tests. Note the yield stress anomaly for $n = 1.1$ crystals [18].

where σ is the stress acting on the dislocation, b is the Burgers vector of the dislocation (which may be partial or perfect), h is the periodicity of the Peierls barriers in the glide plane, a is the periodicity for the kinks along the dislocation line, D_k is the kink diffusion rate and F^* is the activation energy for kink pair nucleation. F^* in turn is given by

$$F^* = 2F_k - \left(\frac{\mu\sigma b^3 h^3}{2\pi} \right)^{1/2}, \quad (2)$$

where F_k is the free energy of formation of a single kink. The second term in eq. (2) is commonly ignored but is retained here. The kink diffusion rate is given by

$$D_k = a^2 v e^{-Q_D/kT}, \quad (3)$$

where Q_D is the activation energy for a kink to overcome its own Peierls barrier (again sometimes ignored), and the strain rate is

$$\dot{\varepsilon} = \rho b v = \rho b J L h, \quad (4)$$

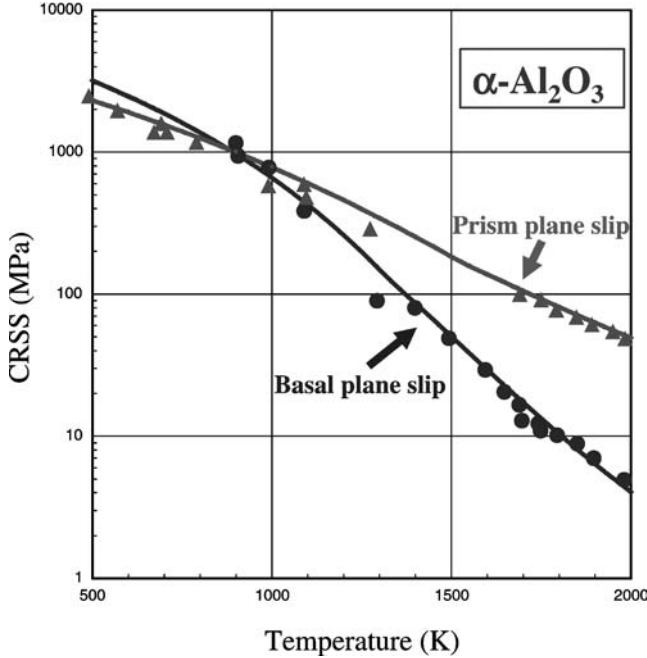


Fig. 4. Plots of $\log(\text{CRSS})$ versus temperature for basal and prism plane slip in sapphire showing both experimental data and curves fitted from eq. (5) [24].

where ρ is the mobile dislocation density, b is the Burgers vector of a perfect dislocation, v is the average dislocation velocity and L is the length of a dislocation segment (the distance to which the kink pairs will expand). Combining eqs (1) to (4), we obtain

$$\dot{\varepsilon} = \dot{\varepsilon}_0 \frac{\sigma/\mu}{kT/\mu b^3} \exp\left(-\frac{Q_D + 2F_k}{kT}\right) \exp\left(\frac{\mu(bh)^{3/2}}{kT\sqrt{2\pi}}\left(\frac{\sigma}{\mu}\right)\right), \quad \dot{\varepsilon}_0 = \rho h^2 L v / b. \quad (5)$$

In the next two sections we will show how eq. (5) can be modified to include the influence of point defects on kink pair nucleation and also the influence of the stacking fault energy for the case of kink pair nucleation on partial dislocations.

For the model to be self consistent, eq. (15-32) of Hirth and Lothe [22] must give a critical kink pair separation distance $(\mu b h / 8\pi\sigma)^{1/2}$ greater than a core-sized dimension of about $5b$. This condition holds for all data considered here, becoming marginal only for the lowest temperature datum for sapphire in Fig. 4. Secondly, the factor $(\sigma \mu b^3 h^3 / 8\pi k^2 T^2)$ in eq. (15-36) of Hirth and Lothe [22] must be less than unity. This condition is valid in the present case only at high temperatures (greater than $\sim 1000^\circ\text{C}$). Hence, the relatively simple kink pair model described by eq. (5) is only applicable at such high temperatures.

In general, the pre-exponential term in eq. (5) should be divided by a factor α which is unity at high temperatures and is given by

$$\alpha = \left(\frac{\sigma \mu b^3 h^3}{8\pi k^2 T^2} \right)^{1/4} \quad (6)$$

when the combination of high stress and low temperature is such as to make α greater than unity.

Because stress and temperature occur in several places inside and outside the exponents of eq. (5), it has to be solved numerically. The activation energy, $Q = 2F_k + Q_D$, can be determined approximately from the slope of an Arrhenius plot or the slope of a plot of $\log \sigma$ against T . However, the apparent activation energy determined in this way is up to $\sim 20\%$ lower than the actual activation energy [23]. In general, both the activation energy and the pre-exponential factor, $\dot{\varepsilon}_0 = \rho b L v$, must be determined numerically from experimental curves of CRSS against temperature [24]. Also the stress exponent (determined by assuming that the strain rate is proportional to some power of stress) varies continuously from 10 or more at high stresses and low temperatures to unity at low stresses and high temperatures [23].

The relative contributions of the kink formation energy ($2F_k$) and the kink diffusion energy (Q_D) are unknown. However, F_k should be of the form $\alpha' \mu b_k^2 h$ where α' is a constant of the order of unity for an abrupt kink (a kink with a width of atomic dimensions) and an order of magnitude smaller for a relaxed kink (a kink with a width much greater than atomic dimensions) [22], so that

$$Q = 2\alpha' \mu b_k^2 h + Q_D, \quad (7)$$

where b_k is the Burgers vector associated with the kink. Kinks should be abrupt in high Peierls stress materials, such as ceramics and intermetallics, and relaxed for low Peierls stress materials, such as fcc metals. In Section 4, we will examine how this applies to particular oxides.

2.3. Modification of the model for kink pair nucleation on point defects

In $MgO \cdot nAl_2O_3$ ($n > 1$), the CRSS decreases dramatically with increasing deviation from stoichiometry, i.e., increasing n . In fact, the CRSS is proportional [25] to $[V_c]^{-2}$, where $[V_c]$ is the concentration of charge-compensating cation vacancies which is related to n by

$$[V_c] = \frac{n - 1}{3(3n + 1)}. \quad (8)$$

The dependence on T and n is illustrated in Fig. 5 where $[V_c]\sigma^{1/2}$ is plotted logarithmically against linear temperature for slip on both $\{111\}$ and $\{110\}$ planes. The data fall on two separate straight lines, with a fair amount of scatter but clearly showing that

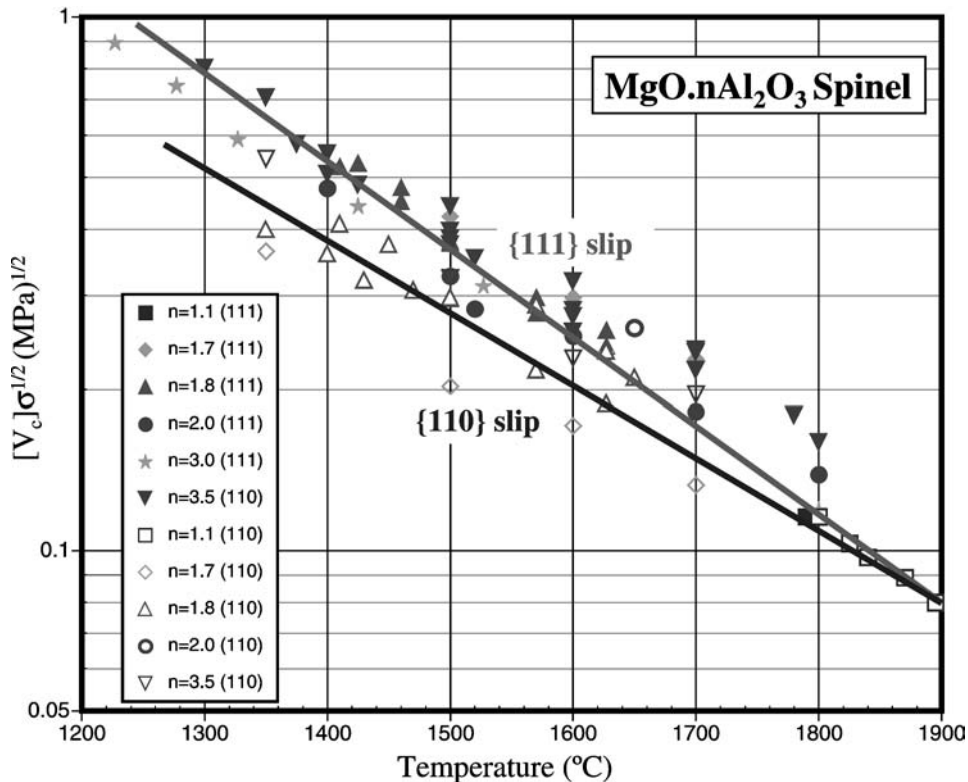


Fig. 5. $[V_c]\sigma^{1/2}$ plotted logarithmically against linear temperature for slip on both {111} and {110} planes in $\text{MgO}\cdot n\text{Al}_2\text{O}_3$ spinel for a range of values of n . $[V_c]$ is the concentration of cation vacancies and σ is the CRSS.

Only the high temperature data of Figs 2 and 3 have been used [18].

{110} slip has a lower CRSS (σ) over the entire temperature range and has a smaller slope. The proportionality between σ and $[V_c]^{-2}$ suggests strongly that cation vacancies are catalysts for kink nucleation and possibly kink diffusion as well. We now examine how point defects can influence the equations developed in the previous section.

In the absence of point defects, the equilibrium concentration of kinks on a dislocation line is given by eq. (14-12) of Hirth and Lothe [22]:

$$c_k^+ c_k^- = \frac{1}{a^2} \exp\left(-\frac{2F_k}{kT}\right), \quad (9)$$

where c_k^{+-} refers to positive and negative kinks. Neighboring positive and negative kinks make up a kink pair. If a kink has an attractive interaction with a point defect, such as a

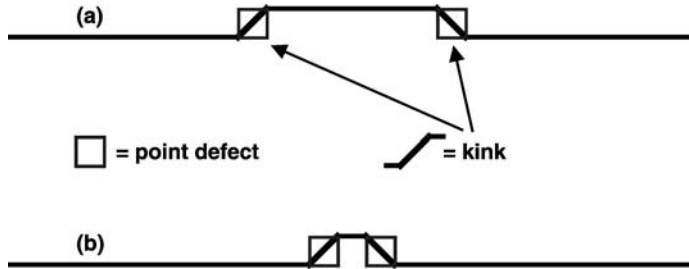


Fig. 6. Diagrams showing kink pair nucleation (a) at two separate vacancies and (b) at a divacancy [24].

cation vacancy in spinel, then there is an equilibrium constant, K_e , relating the concentration of kink pairs decorated with vacancies to those without vacancies

$$K_e = \frac{c'_{2k}}{c_{2k}[V_c]^2} = \exp\left(\frac{2\Delta F'}{kT}\right) \quad (10)$$

so that

$$c'_{2k} = c_{2k}[V_c]^2 \exp\left(\frac{2\Delta F'}{kT}\right). \quad (11)$$

Here c_{2k} is the concentration of double kinks in the absence of point defects, given by eq. (9), c'_{2k} is the new concentration of double kinks and $\Delta F'$ is the positive interaction energy between a kink and vacancy on the dislocation line. If there is a binding energy F_B between cation vacancies and the dislocation core, the core concentration of vacancies will be linearly proportional to $[V_c]$, whereupon eq. (5) still holds but $\Delta F'$ then also includes F_B . Eq. (5) will be true whether kinks nucleate separately at two independent vacancies or at a single divacancy [24], as illustrated in Fig. 6. The form of eq. (11) means that eq. (5) must be modified as follows, both in the pre-exponential factor

$$\dot{\varepsilon}_0 = \beta \rho b L v [V_c]^2, \quad (12)$$

where β is a constant of the order of unity, and in the activation energy, Q , which is replaced by

$$Q' = 2F_k + Q'_D - 2\Delta F', \quad (13)$$

where Q'_D is the new activation energy for kink migration in the presence of a point defect. In principle, Q'_D could be smaller than, larger than, or the same as Q_D . In spinel, it is likely that, at the high temperatures of deformation, the cation vacancies can move rapidly with the kinks by pipe diffusion along the dislocation lines, effectively reducing the activation energy.

2.4. Modification of the model for kink nucleation on partial dislocations

Kink nucleation on partial dislocations has recently been considered [26] because of the experimental observation that the critical resolved shear stress for $\{110\}\langle 111 \rangle$ slip in molybdenum disilicide decreases when substitutional alloying elements are added that decrease the stacking fault energy, and increases when substitutional elements are added that increase the stacking fault energy [27]. This modification may apply, not only to other intermetallics but also to ceramics such as spinel, where increasing deviation from non-stoichiometry both increases the concentration of cation vacancies and decreases the stacking fault energy.

The modification to the kink nucleation model for the case of extended dislocations is illustrated in Fig. 7. Kink pair nucleation can occur on either the leading or trailing partial (Figs 7(a) and 7(b)) and it turns out that these are equally likely, if the partials are initially at their equilibrium separation. Kink pair nucleation will occur simultaneously on both partials (Fig. 7(c)), if the stacking fault energy is high, so that the ribbon width is a few Burgers vectors or less; in this case there is no modification to the theory given in Section 2.2. If the stacking fault energy is low enough that kink pair nucleation occurs

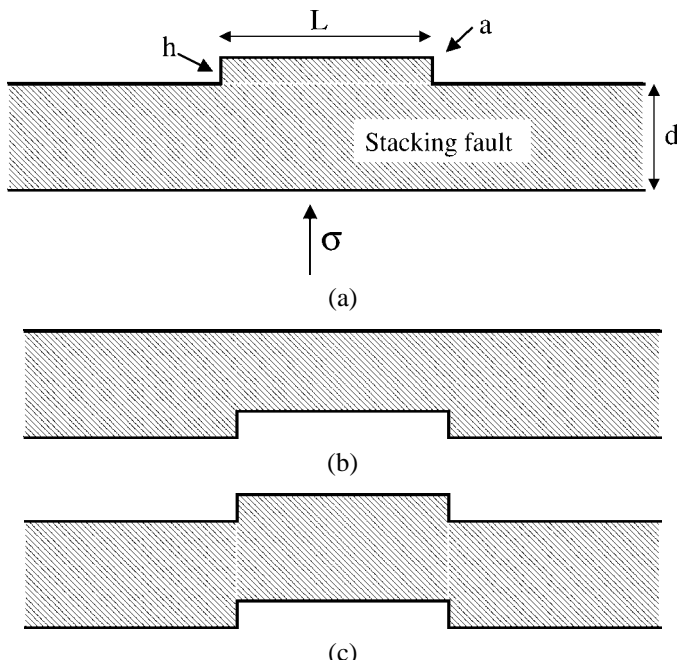


Fig. 7. (a) Kink pair nucleation on the leading partial of a dissociated dislocation; (b) kink pair nucleation on the trailing partial; (c) simultaneous nucleation on both partials [24,26].

independently on the partials, Mitchell et al. [26] show that the activation energy for kink pair nucleation in eq. (2) is now given by

$$F^* = 2F'_k - \frac{\sigma' b_1^{3/2} h^{3/2}}{\sqrt{2\pi}}, \quad (14)$$

where the effective stress, σ' , is given by

$$\sigma' = \sigma - \frac{\pi \gamma^2 h}{\mu b_1^3}. \quad (15)$$

F'_k in eq. (14) is the energy of a single kink on a partial and b_1 is the burgers vector of a partial. The strain rate in eq. (5) is then modified to be

$$\dot{\varepsilon}_1(\sigma, T, \gamma(c), L) = \rho_m b Lv \frac{\sigma' b_1 h^2}{\alpha k T} \exp\left(-\frac{Q'_D + 2F'_k}{kT}\right) \exp\left(\frac{(\sigma' b_1 h^2 \cdot \mu b_1^2 h)^{1/2}}{\sqrt{2\pi} k T}\right). \quad (16)$$

The authors also consider the effect of the segment length, as to whether kinks move apart to a node or whether they annihilate at other kinks. They also consider the possibility of kinks nucleating near a solute atom where the local stacking fault energy is different from the average stacking fault energy. They find the best agreement with experiment for the latter case. However, in all cases, eq. (16) and modified versions of it can be inverted to give a solution of the form

$$\frac{\sigma(\dot{\varepsilon}, T, \gamma(c))}{\mu} = \frac{\pi \gamma^2 h}{\mu^2 b_1^3} + g(\dot{\varepsilon}, T, \text{structure}), \quad (17)$$

where g is a function of strain-rate, temperature and structure from the solution of eq. (16). Note that eq. (17) predicts that the stress should change as the square of the stacking fault energy, as observed experimentally [26]. For the local stacking fault energy modification, there is an additional dependence on concentration through the spacing between solute atoms, but the essence of eq. (17) is maintained.

2.5. Comparison between theory and experiment

2.5.1. Sapphire and stoichiometric spinel

In this section we will confine ourselves to discussing sapphire and spinel, as in the original analysis of the application of kink nucleation theory to ceramics [24]. Applicability to other ceramics will be considered in Section 4. Experimental and fitted curves (by numerical solution of eq. (5)) of CRSS plotted logarithmically against linear temperature are shown in Fig. 4 for basal and prismatic slip in sapphire. Parameters and curve-fitting results for

Table 1
Parameters for eq. (5) describing slip in sapphire and stoichiometric spinel [24].

	Sapphire	Sapphire	Spinel (n = 1)	Spinel (n = 1)
	Basal slip	Prism slip	{111} slip	{110} slip
Perfect b (nm)	0.476	0.824	0.571	0.571
Partial b_1 (nm)	0.275	0.275	0.286	0.286
Shear modulus μ (GPa)	156.8	156.8	98.7	98.7
μb_1^3 (eV)	20.36	20.36	14.41	14.41
Q (eV)	1.9	1.5	4.7	4.7
$\dot{\varepsilon}_0$ (s^{-1})	1.8×10^3	6.7	3.4×10^7	3.4×10^7

sapphire and stoichiometric spinel are shown in Table 1. The Burgers vectors of the partial dislocations have been used in the calculations since the activation energy Q scales with b^2 (eq. (7)); using the Burgers vectors of the perfect dislocations gives unreasonably large values of Q . For example, the values of Q deduced from using the partial Burgers vectors would be multiplied by a factor of 4 for spinel, 3 for basal slip in sapphire, and 9 (!) for prism plane slip if the Burgers vector of a perfect dislocation were used instead.

The fitted curves for stoichiometric spinel (not shown) are as good as those for sapphire, at least in the high temperature regime, and the parameters are given in Table 1. A number of points can be made from Fig. 4 and Table 1:

- The value of Q is higher for basal slip (1.9 eV) than prism plane slip (1.5 eV) in sapphire, as expected from the stronger temperature dependence of the CRSS for the former.
- The value of Q is much higher for stoichiometric spinel (4.7 eV) which has an even stronger temperature dependence. Q is given the same value for {111} and {110} slip because the CRSS is reported to be the same for stoichiometric spinel [25]. However, in non-stoichiometric spinel (Fig. 5), the CRSS values are lower for {110} slip and have a lower temperature dependence (lower Q).
- Since $Q = 2F_k + Q_D$, it is uncertain how much the kink formation energy and activation energy contribute to Q . F_k can be expressed as $\alpha' \mu b_1^2 h$, where α' is a constant with a value as high as 0.1 for an abrupt kink and an order of magnitude smaller for a relaxed kink. For sapphire, if we select a value of $\alpha' = 0.04$, then $2F_k = 1.6$ eV and Q_D would be near zero for prism plane slip and small but finite for basal slip. The kink pair geometry implies that $2F_k > Q_D$ but a value of $\alpha' = 0.04$ does not satisfy this condition. However, taking $\alpha' = 0.1$ for spinel gives $2F_k = 2.9$ eV, so that $Q_D = 1.8$ eV. Other values of α' would give different answers but the point is that the behavior of sapphire and spinel on their various slip systems can be explained by ascribing different contributions from the kink formation and diffusion energies.
- The estimated value of $\dot{\varepsilon}_0 = \rho b L v$ is smaller for prism plane slip (6.7) than basal slip (1.8×10^3) in sapphire but much larger in spinel (3.4×10^7). A simple estimate with $\rho = 10^8 \text{ m}^{-2}$, $L = \rho^{-1/2}$ and $v = 10^{13} \text{ s}^{-1}$ gives $\dot{\varepsilon}_0 \sim 3 \times 10^7$, so that the spinel value is reasonable. The lower values for sapphire can only be explained by lower values of ρ , the mobile dislocation density, and/or L , the mean distance of movement of a kink along a dislocation line. A possible reason for this is that dislocations in sapphire are trapped to form dipoles which quickly break up by self-climb into strings of loops (see Figs 15

and 16 in Section 4.6), thereby reducing the pool of mobile dislocations and limiting the slip distance.

2.5.2. Non-stoichiometric spinel

For the case of non-stoichiometric spinel, we will first consider the applicability of the modification described in Section 2.3 for kink nucleation on point defects. Curve-fitting was performed on the CRSS values in Fig. 5 for non-stoichiometric spinel; the results are shown in Table 2 [24]. For $\{111\}\langle 110 \rangle$ slip, since the curves for $n > 1$ are all approximately parallel, they were all assigned the same optimal value of Q' but different values of $\dot{\varepsilon}_0$. Evidently, $\dot{\varepsilon}_0$ increases with the cation vacancy concentration, $[V_c]$, given by eq. (8), but the scatter is too great to affirm that the dependence is in accord with eq. (12). Q' is less than Q for stoichiometric spinel and, from eq. (13), $Q - Q' = Q_D - Q'_D + 2\Delta F' = 1.9$ eV. The lower activation energy could thus be due either to a lower kink diffusion energy or to the interaction energy between kink and vacancy. The data for $\{110\}\langle 110 \rangle$ slip in non-stoichiometric spinel are comparatively limited, especially for $n = 1.8$ which showed a poor correlation factor. Q' varied from 1.9 to 2.4 eV (Table 2) which is significantly lower than for $\{111\}\langle 110 \rangle$ slip (2.8 eV); this is likely to be due to a lower activation energy for kink migration on $\{110\}$ planes.

Comparison between Tables 1 and 2 shows that $\dot{\varepsilon}_0$ is higher for stoichiometric spinel than any of the non-stoichiometric spinels. Firstly, we should point out that the lower strength of all the non-stoichiometric spinels relative to stoichiometric spinel is mostly due to the reduction of the activation energy from $Q = 4.7$ eV to $Q' = 2.8$ eV. As stated above, this reduction could be due either to a lower kink diffusion energy or to the interaction energy between kink and vacancy. We prefer the lower kink diffusion energy argument because, at ambient temperature where vacancies would be immobile, non-stoichiometric crystals are *harder* [18]. The continued softening with increasing n at high temperatures must then be due to the increasing $[V_c]$, i.e., increasing $\dot{\varepsilon}_0$ from eq. (20). It is not immediately clear why $\dot{\varepsilon}_0$ should be so much higher for stoichiometric spinel. One possible reason is that it has a much higher stacking fault energy and a narrower ribbon width [18]. Non-stoichiometric spinels dissociate by climb with large ribbon widths reducing their glide mobility and decreasing the mobile dislocation density.

It is also possible that the softening observed in non-stoichiometric spinel is due to a reduction in the stacking fault energy, using the modification described in the previous section. Table 3 shows the experimental and calculated softening due to the reduction of stacking fault energy with increasing values of n in non-stoichiometric $MgO \cdot nAl_2O_3$

Table 2
Parameters for eq. (5) describing slip in non-stoichiometric spinel [24].

n	$[V_c]$	$\{111\}\langle 110 \rangle$ slip		$\{110\}\langle 110 \rangle$ slip	
		Q' (eV)	$\dot{\varepsilon}_0$ (s^{-1})	Q' (eV)	$\dot{\varepsilon}_0$ (s^{-1})
1.7	0.057	2.8	2.2×10^4	2.4	6.9×10^3
1.8	0.061	2.8	3.6×10^4	(1.9)	(1.7×10^2)
2.0	0.067	2.8	6.8×10^4	—	—
3.0–3.5	0.083–0.088	2.8	1.7×10^5	2.3	1.2×10^4

Table 3

Experimental and theoretical changes in the yield stress of $\text{MgO} \cdot n\text{Al}_2\text{O}_3$ spinel due to a change in stacking fault energy. The sixth column gives the contribution of the stacking fault energy term to the yield stress in eq. (17) for the average SFE model. The last column gives the predicted yield stress for the local SFE model (taken from [26]).

Deformation temperature (°C)	n	c_v	γ (mJ/m ²)	σ (expt.) (MPa)	$\pi\gamma^2h/\mu^2b_1^3$ (MPa)	Δe (eV)	σ (eq. (30)) (MPa)
1400	1	0	180	1000	13	—	1000
	2	0.048	50	100	1	-1.17	97
	3	0.067	20	60	0.2	-1.04	84
1800	1	0	180	200	13	—	200
	2	0.048	50	7	1	-1.17	23
	3	0.067	20	3	0.2	-1.04	21

spinel [26]. Data are given for $n = 1, 2$ and 3 crystals at 1400°C and at 1800°C [18,25]. The important defects are thought to be the charge-compensating cation vacancies (and associated excess trivalent Al cations). Hence, the fractional concentration of cation vacancies, c_v , given in the third column of Table 3, was used in the calculations. The sixth column gives the contribution of the stacking fault energy term to the yield stress in eq. (17) for the average SFE model; the effect is seen to be much too small to explain the observed data. The last column gives the predicted yield stress for the local SFE model. The parameters were adjusted so that the yield stress for stoichiometric spinel ($n = 1$) is the same as the experimental value. The predicted softening is in remarkable agreement with experiment, especially at 1400°C. Unfortunately there is no way of deciding whether softening is due to kink nucleation on point defects or kink nucleation on partials, although we find the latter is perhaps the more satisfying. At least we now have two possible (and plausible) explanations for solution softening in non-stoichiometric spinel whereas for many years there was none!

3. Crystallography of slip

In this section we will examine the crystal structures of ceramics (confined to oxides for simplicity) and the implications of crystal geometry to dislocation behavior.

3.1. Crystal structures

A number of oxides can be described in terms of fcc or hcp packing of the oxygen anions, with the cations occupying octahedral or tetrahedral interstitial sites. These are listed in Table 4, along with some other oxides that cannot be described in this way. Care must be taken in describing the structures as close-packed—the analogy with metals can be misleading, as the following examples will show: (a) the anions in spinel are not in perfect fcc packing (see Fig. 8); (b) the anion basal planes in sapphire are flat but irregular hexagons, while the cations are in puckered layers in between the anion layers (see Fig. 9); (c) rutile is tetragonal but the anions can be thought of being in a distorted hcp array which is

Table 4
Crystal structures of some oxides.

Oxide	Space group	Anion packing	Cation occupancy		Other oxides
			Octahedral	Tetrahedral	
MgO	<i>Fm</i> 3 <i>m</i>	fcc	1	0	NiO, CoO, etc.
BeO	<i>P</i> 6 ₃ <i>mc</i>	hcp	0	1/2	ZnO
UO ₂	<i>Fm</i> 3 <i>m</i>	simple cubic	—	—	ThO ₂ , c-ZrO ₂
TiO ₂	<i>P</i> 4 ₂ / <i>mnm</i>	~ hcp	1/2	0	—
SiO ₂	<i>P</i> 3 ₁ 21	—	—	—	(quartz form)
Al ₂ O ₃	<i>R</i> 3 <i>c</i>	hcp	2/3	0	Cr ₂ O ₃ , Fe ₂ O ₃
Y ₂ O ₃	<i>Ia</i> 3̄	—	—	—	Rare earth oxides
SrTiO ₃	<i>Pm</i> 3̄ <i>m</i>	—	—	—	Many perovskites
MgAl ₂ O ₄	<i>Fm</i> 3̄ <i>m</i>	fcc	1/2	1/8	Many spinels
Mg ₂ SiO ₄	<i>Pbnm</i>	~ hcp	1/2	1/8	Fe ₂ SiO ₄ , etc.
Y ₃ Al ₅ O ₁₂	<i>Ia</i> 3̄ <i>d</i>	—	—	—	Many garnets
MgAl ₂ O ₄	<i>Fm</i> 3̄ <i>m</i>	fcc	1/2	1/8	Many spinels

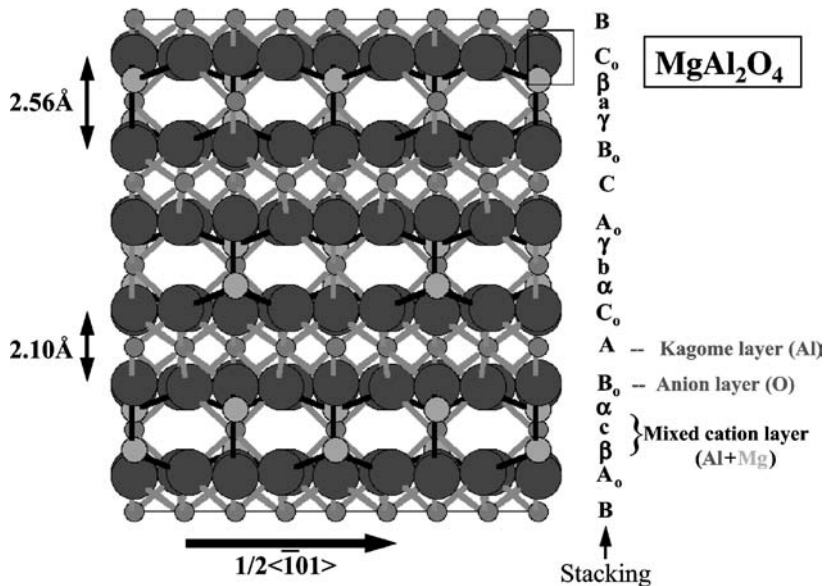


Fig. 8. Stacking of {111} planes in spinel viewed along (211). A₀B₀C₀ refers to oxygen stacking, ABC to Al stacking in the Kagomé layers, abc to Al stacking in the mixed cation layers, and $\alpha\beta\gamma$ to stacking of Mg cations. Note that the oxygen fcc packing is imperfect and that the {111} anion layers are alternately separated by 0.210 nm and 0.256 nm [18].

useful for describing the “crystallographic shear” structures in reduced rutile; (d) forsterite (Mg₂SiO₄) is orthorhombic but the anion packing is close to hcp, giving a structure which is the hexagonal analogue of cubic spinel; (e) the cations in fluorite-structured crystals (e.g., urania) are in fcc array but the anions are in simple cubic packing. The other oxides listed in Table 4 are included because their mechanical properties have received some at-

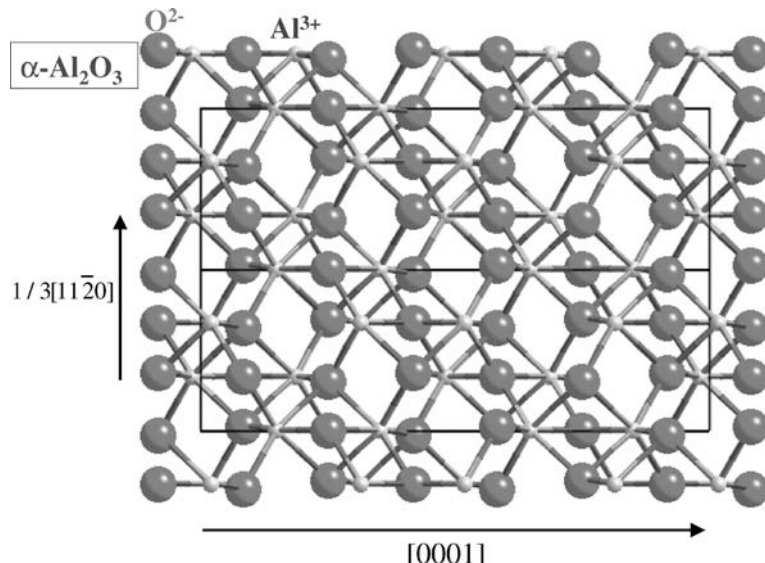


Fig. 9. Structure of sapphire viewed along $(1\bar{1}00)$. The oxygen anion planes are flat but consist of linked larger and smaller triangles. The aluminum cation planes are puckered. The unit cell is outlined.

tention (especially quartz). Quartz is by no means close-packed because of the stability of the $[\text{SiO}_4]$ tetrahedron. Yttria and the rare-earth sesquioxides and the mixed oxide garnet structures are compact, in spite of their complexity, but cannot be described as close-packed in the traditional sense; in fact, the C-type M_2O_3 structure of yttria can be thought of as having the fluorite structure of urania with one-quarter of the anion sites vacant.

3.2. Slip systems

Crystals generally slip on close-packed planes in close-packed directions, such that the Burgers vector is equal to the shortest lattice vector. This is true in metals and is expected from Peierls stress arguments. It is also true in ceramics but there are exceptions to the rule. Observed slip systems are summarized in Table 5. In general, the Burgers vectors are well behaved: in crystals with fcc lattices, $\mathbf{b} = 1/2\langle 110 \rangle$; in crystals indexed on a hexagonal unit cell, $\mathbf{b} = 1/3\langle 11\bar{2}0 \rangle$; in both cases \mathbf{b} is the shortest lattice vector. However, the magnitude of the Burgers vector varies widely according to the size of the unit cell. In terms of the distance, d_O , between oxygen anions, \mathbf{b} is equal to d_O for MgO and BeO , and is equal to $2d_O$ for MgAl_2O_4 , TiO_2 and Mg_2SiO_4 . For prism plane slip in $\alpha\text{-Al}_2\text{O}_3$, \mathbf{b} is $\langle 1010 \rangle$, which has a magnitude of $3d_O$ ($= 0.822$ nm). Even larger Burgers vectors are encountered in the garnets and cubic rare-earth sesquioxides (see Table 5).

Slip plane behavior is less consistent. In MgO , the separate anion and cation closest-packed planes are $\{111\}$ but the combined anion and cation closest-packed planes are $\{100\}$; the observed $\{110\}$ slip plane is explained in terms of the lower repulsion between like ions during slip on this plane compared with $\{100\}$ [28]. In more complex

Table 5
Slip systems in oxides.

Oxide	Slip system	Burgers vector (nm)	Other slip systems
MgO	{110}\{110}	1/2\{110} = 0.298	\{001}\{110}
BeO	(0001)\{11\bar{2}0}	1/3\{11\bar{2}0} = 0.270	\{1\bar{1}00}\{11\bar{2}0}, (0001)\{10\bar{1}0}
UO ₂	\{001}\{110}	1/2\{110} = 0.387	\{1\bar{1}1}\{110}
TiO ₂	\{100}\{011}	\{011} = 0.546	\{110]\{001]
SiO ₂	(0001)\{11\bar{2}0}	1/3\{11\bar{2}0} = 0.491	\{11\bar{2}0]\{0001}, \{10\bar{1}0]\{0001}, Section 4.5
Al ₂ O ₃	(0001)\{11\bar{2}0}	1/3\{11\bar{2}0} = 0.476	\{1\bar{2}10}\{10\bar{1}0}, \{01\bar{1}2}\{01\bar{1}11}
Y ₂ O ₃	\{110}\{1\bar{1}1}	1/2\{111} = 0.918	See Section 4.10
SrTiO ₃	\{110}\{110}	\{110} = 0.552	See Section 4.7
MgAl ₂ O ₄	\{1\bar{1}1}\{110}	1/2\{110} = 0.594	\{1\bar{1}0}\{110}
Mg ₂ SiO ₄	(100)[001], \{110][001]	[001] = 0.599	(100)[010], [0k\bar{l}]\{100}
Y ₃ Al ₅ O ₁₂	\{110}\{1\bar{1}1}	1/2\{111} = 1.040	\{112}\{111}, \{132}\{1\bar{1}1}

structures, it becomes difficult to decide which is the closest-packed plane and the simple-minded approach loses its value. In MgAl₂O₄, for example, stoichiometric crystals prefer the close-packed {111} anion planes (see Fig. 1), whereas non-stoichiometric crystals (MgO · *n*Al₂O₃, *n* > 1) slip on {110} planes as in rock salt. On the other hand, garnets and rare-earth sesquioxides, in spite of the complexity of their structures, follow the dictates of the underlying bcc lattice and slip on the {110}\{111} system, as in bcc metals.

3.3. Dislocation dissociations

As pointed out in Section 1, Kronberg [7] and Hornstra [8] wrote seminal papers on the dissociation of dislocations in ceramics, particularly sapphire and spinel. Kronberg suggested that basal dislocations in sapphire should dissociate according to



creating a fault in the cation sublattice but leaving the anion sub-lattice unfaulted. He suggested a further dissociation into Shockley-like quarter partials with the creation of a fault in the anion sublattice as well. Kronberg pointed out that the motion of the quarter partials requires the anions and cations to move along different paths in a process known as synchroshear. However, he based his analysis on the idealized structure of sapphire, rather than the puckered structure shown in Fig. 9. In fact, as pointed out by Bilde-Sørensen et al. [29], dislocations should be able to move more easily through the puckered layers in Fig. 9 on an electrically neutral plane. Such slip via motion of 1/3\langle 10\bar{1}0 \rangle partials only involves half the cations in a given puckered layer; synchroshear is then unnecessary.

For spinel, Hornstra suggested that 1/2\langle 110 \rangle dislocations should dissociate into collinear half-partial



again with the formation of a cation fault only. The further dissociation into the equivalent of Shockley partials in the fcc anion sublattice (shown later in Fig. 19) creates an anion fault

Table 6
Dissociation of dislocations in oxides.

	Dissociation reaction	Reference
MgO	None reported	[15,16]
BeO	$1/3\langle 11\bar{2}0 \rangle \rightarrow 1/3\langle 10\bar{1}0 \rangle + 1/3\langle 01\bar{1}0 \rangle$	[43]
UO ₂	None reported	[15,16]
TiO ₂	$\langle 101 \rangle \rightarrow 1/2\langle 101 \rangle + 1/2\langle 101 \rangle$ (see Section 4.4)	[77]
SiO ₂	$1/3\langle 11\bar{2}0 \rangle \rightarrow 1/6\langle 11\bar{2}0 \rangle + 1/6\langle 11\bar{2}0 \rangle$ (see Section 4.5)	[90,91]
Al ₂ O ₃	$1/3\langle 11\bar{2}0 \rangle \rightarrow 1/3\langle 1010 \rangle + 1/3\langle 0110 \rangle$ $\langle 10\bar{1}0 \rangle \rightarrow 1/3\langle 10\bar{1}0 \rangle + 1/3\langle 10\bar{1}0 \rangle + 1/3\langle 10\bar{1}0 \rangle$	[15,16]
Y ₂ O ₃	$\langle 100 \rangle \rightarrow 1/2\langle 100 \rangle + 1/2\langle 100 \rangle$	[174]
Er ₂ O ₃	$1/2\langle 111 \rangle \rightarrow 1/4\langle 110 \rangle + 1/4\langle 112 \rangle$	[175]
SrTiO ₃	$\langle 110 \rangle \rightarrow 1/2\langle 110 \rangle + 1/2\langle 110 \rangle$	[114,119]
MgAl ₂ O ₄	$1/2\langle 110 \rangle \rightarrow 1/4\langle 110 \rangle + 1/4\langle 110 \rangle$	[15,16]
Mg ₂ SiO ₄	$[001] \rightarrow 1/2[001] + 1/2[001]$ [010] undissociated [100] undissociated	[12,86]
Y ₃ Al ₅ O ₁₂	$1/2\langle 111 \rangle \rightarrow 1/4\langle 111 \rangle + 1/4\langle 111 \rangle$	[182]

in addition to the cation fault. Again the second dissociation has never been observed. As in sapphire, anion fault energies in spinel must be very large. However, both dissociations (18) and (19) are commonly observed, albeit often by climb, as described below. Dissociations which have been observed in these and other oxides are summarized in Table 6. Particular oxides are discussed in the next section.

4. Dislocations in particular oxides

We begin with monoxides (Sections 4.1 and 4.2), followed by dioxides (Sections 4.3 to 4.5), then sesquioxides (Section 4.6), mixed oxides (Sections 4.7 to 4.9), other oxides (Section 4.10) and non-oxides (Section 4.11).

4.1. MgO and other oxides with the rock-salt structure

The rock-salt structure is frequently found amongst the oxides of the alkaline earth metals (MgO, CaO, etc.) and the transition metals (MnO, FeO, CoO, NiO). In the latter case, the oxides are non-stoichiometric and should be written $M_{1-x}O$, due to the existence of trivalent ions and their charge-compensating cation vacancies. In all cases the easy slip system is $\{110\}\langle 110 \rangle$, as described in Sections 2.1 and 3.2. Slip on the $\{001\}$ plane is much more difficult and slip on $\{111\}$ has never been reported. This is discussed below for MgO, followed by discussion of the effect of non-stoichiometry in the transition metal oxides.

4.1.1. Magnesium oxide

Slip on the $\{110\}\langle 110 \rangle$ system occurs at low stresses and plastic deformation is possible at low temperatures [5,30]. In fact the CRSS extrapolated to 0 K is only 30 MPa, as shown in Fig. 1. The CRSS for $\{001\}\langle 110 \rangle$ slip is more than an order of magnitude higher, as is also

shown in Fig. 1. The activation energy for $\{110\}\langle 110 \rangle$ slip can be estimated from eq. (5) to be ~ 0.1 eV. Since the activation energy is the sum of the elastic energy of the kink pair and the migration energy (eq. (7)), both must be very small for the easy slip system. In fact, since dislocations in MgO are undissociated, the appropriate value of b in eq. (7) is 0.298 nm (Table 5) and so $\mu b_k^2 h$ is calculated to be about 20 eV. This means that either the kinks are diffuse (α' is small) and the secondary Peierls barrier is very low, or the Peierls stress is so low that the kink mechanism does not apply. The activation energy for $\{001\}\langle 110 \rangle$ slip can be estimated from the slope of the CRSS curve in Fig. 1 to be ~ 1 eV. This is lower than for sapphire or spinel (Table 1) but again the perfect Burgers vector should be used in eq. (7) and so α' would have to be in the order of 0.01, i.e., a diffuse kink with a low secondary Peierls barrier.

Why slip on the $\{001\}$ plane in MgO is so much more difficult than on the $\{110\}$ plane is an interesting question. Gilman [28] pointed out that, in the former case, each ion is required to move past a pair of ions of like sign at the half-slipped position; in the $\{110\}$ case, a pair of ions of like sign is again present at the half-slipped position but a single ion of *opposite* sign is present at a slightly closer distance. This is believed to alleviate the charge problem, even though the $\{110\}$ planes are less close-packed than the $\{001\}$ planes. Atomistic calculations of $1/2\langle 110 \rangle$ dislocations in MgO have been performed by Woo and Puls [31] and, more recently, by Watson et al. [32]; unfortunately, they did not tackle the problem of the slip plane. However, Woo and Puls calculated the Peierls stress for slip on the $\{110\}$ plane and found it to be quite low, ~ 70 MPa. This is about a factor of 2 higher than the CRSS extrapolated to 0 K but should be considered to be in satisfactory agreement in terms of the computing techniques of the time.

4.1.2. Transition metal oxides and the effect of stoichiometry

Plastic deformation of single crystals of the transition metal oxides $M_{1-x}O$ with the rock-salt structure has been studied for $M = Mn$ [33], Fe [34], Co [35–38] and Ni [39,40]. The maximum value of x varies from 0.001 for Ni and 0.013 for Co to 0.15 for Fe and Mn. $Fe_{1-x}O$ is unstable below $\sim 570^\circ C$ and cannot therefore be deformed plastically at low temperatures. There are no reports of low temperature deformation of $Mn_{1-x}O$ but there is no reason to believe that this should not be possible. On the other hand, plastic deformation on the $\{110\}\langle 110 \rangle$ slip system occurs readily in $Co_{1-x}O$ and $Ni_{1-x}O$ at low temperatures [36,38–40]; in fact $Co_{1-x}O$ has even been deformed at 4.2 K [38]. Care must be taken in the case of $Co_{1-x}O$ to cool crystals in a low p_{O_2} atmosphere so as to avoid the precipitation of Co_3O_4 , which causes hardening [38]. The resulting crystals have a CRSS of ~ 100 MPa at 4.2 K, comparable with that of MgO on the same system (Fig. 1). The range of stoichiometry at low temperatures is small and so there is no effect on the CRSS except through the possibility of precipitation.

It is a different story at high temperatures, where there have been a number of studies of the influence of stoichiometry on the creep rate [33–35,37,39] or the flow stress [33,37] (only the more recent studies are cited). Typically, for a given applied stress, the creep rate increases with increasing p_{O_2} , i.e., as the crystals become more stoichiometric (i.e., as x decreases). However, the behavior is not so straightforward in $Mn_{1-x}O$; at temperatures between 1000 and 1400°C, the flow stress first increases with increasing p_{O_2} and then decreases with further increase in p_{O_2} —by a factor of about 2 in each case.

Table 7

Values of m (the p_{O_2} exponent in the creep rate eq. (20)) for various oxygen defects in the transition metal oxides with the rock-salt structure [34].

Defect	Symbol	m
Neutral oxygen vacancy	V_O^x	-0.56
Singly-charged oxygen vacancy	V_O^\bullet	-0.33
Doubly-charged oxygen vacancy	$V_O^{\bullet\bullet}$	-0.11
Neutral oxygen interstitial	O_i^x	+0.42
Singly-charged oxygen interstitial	O_i'	+0.20
Doubly-charged oxygen interstitial	O_i''	+0.03

The creep behavior is often analyzed in terms of the phenomenological equation

$$\dot{\varepsilon} = A \sigma^n p_{O_2}^m \exp\left(-\frac{Q}{kT}\right), \quad (20)$$

where n and m are exponents and Q is an activation energy. Eq. (20) is interpreted in terms of climb-controlled glide. Thus Q is the activation energy for diffusion of the rate-controlling species; the value of m is used to identify the diffusing species (see Table 7) and the value of n is used to identify the climb mechanism. For example, Jolles and Monty [34] studied wüstite ($Fe_{1-x}O$) at temperatures between 850 and 1150°C and determined that $Q \sim 3$ eV, independent of temperature; they interpreted this as the activation energy for oxygen self-diffusion (the slowest moving species). The value of m (0.03–0.11) indicated that the rate-controlling species was doubly-charged oxygen interstitials, O_i'' , with a contribution from singly-charged interstitials, O_i' , at the highest temperature. The value of n was unusually high (~ 9) but they still suggested that the mechanism was a recovery-controlled process involving dislocation climb. The dominant charge-compensating defects are cation vacancies, V_{Fe}'' , but these are thought to be highly mobile and so do not affect dislocation motion. Oxygen interstitials are presumably minority charge-compensating defects and so they are the defects which control diffusive processes.

The behavior of $Co_{1-x}O$ makes an interesting contrast. Dominguez-Rodriguez et al. [35] also analyzed creep data at temperatures from 1000 to 1450°C using eq. (20) and found that Q increases from 2.5 eV at low temperatures and high p_{O_2} to 5 eV at high temperatures and high p_{O_2} . Their m values increase from 0.5 to 0.1 with increasing temperature, independent of temperature, while the n values decrease from 8.5 to 6.5 with increasing temperature. They also interpret their results in terms of recovery controlled by oxygen diffusion, with the rate-controlling species being *neutral* oxygen interstitials at low T and high p_{O_2} and oxygen vacancies at high T and high p_{O_2} . The interstitials have a lower activation energy for diffusion than the vacancies.

The constant strain-rate compression tests performed by Routbort [37] on $Co_{1-x}O$ and Goretta and Routbort [33] on $Mn_{1-x}O$ single crystals give different insight into the deformation mechanisms. In both cases, yield points are observed followed by steady-state flow. For $Mn_{1-x}O$, the steady state flow stresses were analyzed in terms of eq. (20) over a temperature range from 900 to 1400°C and a p_{O_2} range from 10^{-11} to 10^2 Pa; the m values were positive (~ 0.6 to 0.25) at low p_{O_2} and negative (~ -0.2 to -0.5) at high p_{O_2} . The

primary rate-controlling species are then singly-charged oxygen vacancies at low p_{O_2} and neutral oxygen interstitials at high p_{O_2} . For $Co_{1-x}O$ compressed over a similar range of T and p_{O_2} , constant strain-rate tests give similar results to the creep tests described above; for small x , oxygen vacancies are rate-controlling and for larger x , oxygen interstitials control the deformation rate. However, there are complications; serrated yielding is observed at 1000°C for small x , suggesting that impurities are causing dynamic strain-aging (the Portevin–Le Chatelier effect). In addition, there is a prominent yield-point and the upper yield stress has a different dependence on x than the steady-state flow stress. In both cases the yield stress first increases with increasing x (increasing p_{O_2}) and then decreases with further increase in x . Since it is unlikely that climb can control yielding (as happens during steady-state flow), the initial increase may represent solution hardening due to the cation vacancies, while the subsequent decrease in yield stress may represent solution softening from the same cation vacancies.

We believe that caution should be exercised in using eq. (20) to determine the exact rate-controlling mechanism. For high Peierls stress materials, serious errors occur in the use of such empirical expressions to determine activation energies and stress exponents [23]. For low Peierls stress materials, such as in the present case, a well-grounded theoretical equation needs to be developed for the particular diffusion-controlled model which is thought to be extant. Only then can the empirical values of m , n , and Q be used to imply mechanisms with confidence. Another point is that the high values of n reported above sometimes implies that σ in eq. (20) should be replaced by $(\sigma - \sigma_0)$, σ_0 being an internal stress or friction stress; the value of n is then reduced.

4.2. BeO and other oxides with the wurtzite structure

BeO and ZnO are technologically the most important tetrahedrally coordinated oxides that crystallize in the hexagonal wurtzite structure, space group $P6_3/mmc$. This structure involves hcp packing of the oxygen sublattice, with the cations occupying half of the tetrahedral interstices, as illustrated in Fig. 10. Curiously, in marked contrast to sulfides, no oxide examples are known that crystallize with the zinc blende or sphalerite structure, in which oxygen anions are in fcc stacking with cations in half the tetrahedral interstices. In neither case is there an extensive literature on single crystal deformation.

4.2.1. Beryllium oxide

Early work on BeO single crystals by Bentle and Miller [41] identified four slip systems; basal slip, $\{0001\}\langle 1\bar{1}\bar{2}0 \rangle$; prismatic slip, $\{1\bar{1}00\}\langle 1\bar{1}\bar{2}0 \rangle$ and $\{1\bar{1}00\}\langle 0001 \rangle$; and pyramidal slip $\{\bar{1}\bar{1}22\}\langle 1\bar{1}\bar{2}3 \rangle$. Not surprisingly, significant plastic anisotropy was found. At 1000°C, the yield stresses for these systems were as follows: 35 MPa for basal slip; 49 and 110 MPa for prismatic slip along $\langle 1\bar{1}\bar{2}0 \rangle$ and $\langle 0001 \rangle$, respectively; and > 250 MPa for pyramidal slip.

More recent work on creep deformation in BeO single crystals by Corman [42] confirmed the anisotropic plastic deformation behavior; this work also revealed that basal slip in BeO could be activated at surprisingly low temperatures. For example, at 50 MPa and using crystals with a high Schmid factor for basal slip (compression direction along $\langle \bar{1}101 \rangle$),

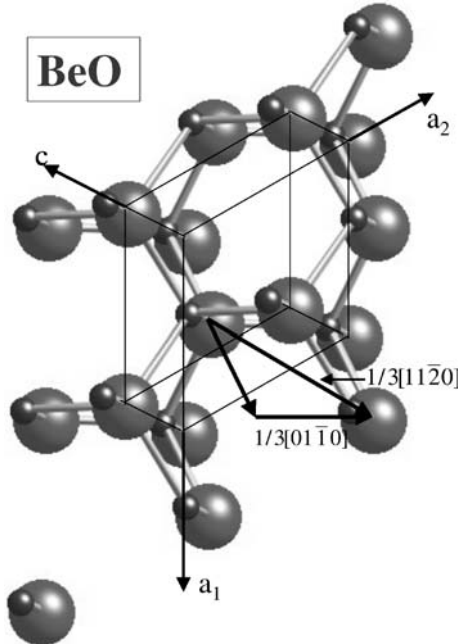


Fig. 10. The wurtzite structure of BeO, showing the small cations and large anions in tetrahedral co-ordination. A hexagonal unit cell is outlined. The $1/3[11\bar{2}0]$ Burgers vector is shown with its dissociation into two $1/3<10\bar{1}0>$ partials.

a creep rate of $1.3 \times 10^{-7}/\text{s}$ was found at 650°C , which increased to $7.3 \times 10^{-7}/\text{s}$ for a stress of 70 MPa.

By way of contrast, temperatures of 1650 to 1850°C had to be used for samples compressed along $[1\bar{1}00]$ and $[0001]$. Most of the $[1\bar{1}00]$ samples buckled but it was possible to determine a creep rate of $7.2 \times 10^{-9}/\text{s}$ for one sample at a stress of 50 MPa at 1650°C , increasing to $1.6 \times 10^{-7}/\text{s}$ for a stress of 100 MPa. For a $[0001]$ oriented sample, an upper bound for the creep rate of $1.7 \times 10^{-8}/\text{s}$ at 1750°C and 100 MPa could be determined.

4.2.2. Dislocation dissociation in BeO and other crystals with the wurtzite structure

Suzuki et al. [43] studied dislocations in a number of crystals with the wurtzite structure—ZnO, BeO, AlN, GaN and InN. The dislocations were introduced at ambient temperature by pulverization during specimen preparation. Most of the dislocations were screw in character, with a $1/3<11\bar{2}0>$ Burgers vector. They used weak-beam and high resolution TEM to show that they were dissociated into a pair of $1/3<10\bar{1}0>$ Shockley-type partials (shown schematically in Fig. 10). The stacking fault energies determined from the ribbon width are shown in Table 8. Also included in Table 8 are values for CdS, CdSe and SiC; in the last case it is assumed that the SFE for 2H-SiC (with the wurtzite structure) is between that for 4H- and 6H-SiC [44]. Suzuki et al. found that there was a good correlation between the normalized stacking fault energy (the energy per bond across the stacking fault between anions and cations in the basal plane) and the c/a ratio. This is shown in Table 7

Table 8
Stacking fault energy and c/a ratio for a number of crystals with the wurtzite structure.

Crystal	SFE (mJ/m ²)	Reduced SFE (meV/bond)	c/a ratio	Reference
CdSe	10	10	1.635	[43]
SiC	3–15	3–15	1.633	[44]
CdS	10	9	1.632	[43]
BeO	41	16	1.623	[43]
InN	41	27	1.611	[43]
ZnO	100	57	1.603	[43]
AlN	220	115	1.600	[43]

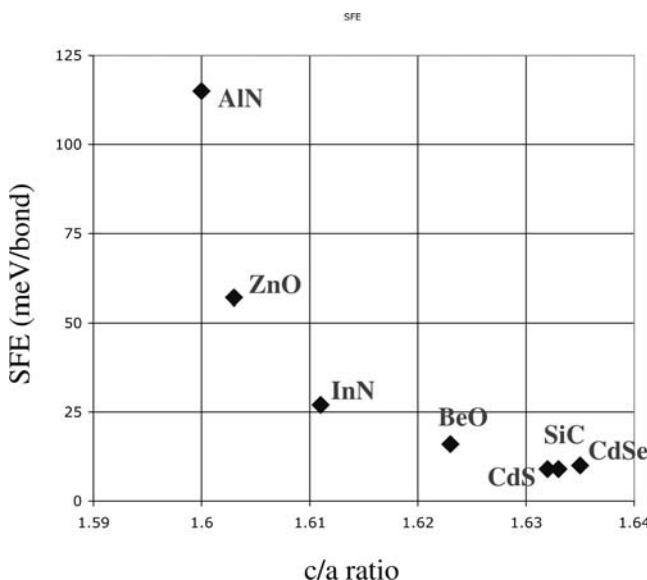


Fig. 11. Normalized stacking fault energy (energy per bond across the basal fault plane) versus c/a ratio for various crystals with the wurtzite structure (adapted from Suzuki et al. [43]).

and plotted in Fig. 11. They interpreted this correlation in terms of the second-nearest-neighbor π -electron interaction, which is an attractive Coulombic force between unlike ions. The stronger this interaction, the shorter will be the c-axis; hence the inverse correlation between normalized SFE and c/a ratio in Fig. 11. They also point out that the wurtzite structure is more stable than the zinc blende structure in crystals with a high ionicity and that a stacking fault in wurtzite represents a small region of zinc blende. It is certainly true in Fig. 11 that CdS and CdSe have a low SFE and occur in both the wurtzite and zinc blende structures.

4.2.3. Zinc oxide

Information of dislocations and plasticity in ZnO is surprising sparse, especially given that sizable ZnO single crystals are now available. Detailed studies on ZnO would be most welcome.

4.3. ZrO_2 and other oxides with the fluorite structure

Simple oxides with large cations— Zr^{4+} , Th^{4+} , U^{4+} , etc.—crystallize with the fluorite structure (the mineral fluorite itself is CaF_2). ZrO_2 and UO_2 have been most studied and we will emphasize these in this review. Neither story is simple.

4.3.1. Zirconia

The cubic form of pure ZrO_2 is only stable from its melting point ($\sim 2750^\circ\text{C}$) to $\sim 2400^\circ\text{C}$, where it undergoes a distortion to tetragonal symmetry. A further transformation to monoclinic symmetry occurs below $\sim 1200^\circ\text{C}$, which is martensitic in character. Solid solution additions of various “stabilizers” such as CaO , Y_2O_3 , and CeO_2 reduce the temperature of these transformations. While the tetragonal \rightarrow monoclinic transformation forms the basis of the technologically important phenomenon of “transformation toughening” [45,46], which has led to a commercially very useful class of advanced ZrO_2 -containing structural ceramics, the issue of transformation dislocations is beyond the scope of this review.

Single crystals of cubic Y_2O_3 -stabilized ZrO_2 are readily available [47], as the 9.4 m/o (nominal) composition is widely sold as imitation diamonds (the refractive index and dispersion of Y_2O_3 -stabilized cubic ZrO_2 are very similar to diamond; in fact, jewelers must resort to measurement of thermal properties to distinguish between natural or synthetic diamonds on the one hand, and the ZrO_2 -based imitation diamonds on the other). Thus, there has been much work studying cubic Y_2O_3 -stabilized ZrO_2 with solute contents between 9.4 and 20 mol% Y_2O_3 . In addition to the intrinsic scientific interest, very high flow stresses (300–400 MPa) are found for higher solute content crystals at elevated temperatures (1400°C) [48,49], suggesting the possibility of some technological exploitation of this material.

4.3.2. Ferroelasticity in zirconia

Lower Y_2O_3 content crystals are also of interest. Lower solute content crystals can, depending on solute content and thermal history, undergo one of two types of phase transformations on cooling from elevated temperatures: (i) a displacive but non-martensitic cubic-to-tetragonal transformation, leading to the so-called t' structure [50,51] and (ii) a diffusion-controlled precipitation reaction, the cubic phase decomposing to a low- Y_2O_3 content tetragonal precipitate phase in a high- Y_2O_3 content cubic matrix. Deformation of t' ZrO_2 can occur ferroelastically (see Messerschmidt et al. [52] and Baither et al. [53] for review). In crystals of suitable composition, the ferroelastic deformation can be followed by conventional dislocation plasticity [53] and impressively high flow stresses at 1400°C of ~ 700 MPa are then possible.

Ferroelastic deformation occurs as follows: the t' structure is composed of three tetragonal domains, essentially $\{110\}$ twin variants (any of the three cube axes of cubic ZrO_2

can become the c axis of the product tetragonal phase during the displacive cubic \rightarrow tetragonal transformation). Under load, the glissile {110} twin boundaries migrate at a critical coercive stress; during such ferroelastic deformation, favorably oriented domains grow at the expense of their unfavorably oriented neighbors. The ferroelastic transformation strain is of order 0.4%; the coercive stress varies from ~ 700 MPa at 500°C to ~ 400 MPa at 1400°C [53]. After this ferroelastic deformation, the resulting sample can be a tetragonal single crystal, or possibly a simply twinned tetragonal crystal, depending on the orientation of the applied stress relative to the original domain microstructure.

4.3.3. Plastic deformation of zirconia

The two-phase “single crystals”—the high-solute content cubic matrix containing low solute content tetragonal precipitates—show potent high temperature precipitation hardening, and flow stresses of 500 MPa at 1400°C have been reported (in the “soft” direction—see below) [54]. The nature of the precipitate hardening is reasonably well understood [52, 55], but this topic is again beyond the scope of this review.

The “early” work on plastic deformation of cubic Y_2O_3 -stabilized ZrO_2 was performed by Heuer, Dominguez-Rodriguez and their collaborators [56–58] and was done mostly at elevated temperatures, 1400°C and higher. They identified {001}{110} as the easy slip system, but also noted slip on {111}. On the other hand, if cube slip is suppressed, for example by deforming along {100} [58], {110} slip can also occur [59]. Messerschmidt and his collaborators [60] later showed that, by careful alignment, deformation of cubic ZrO_2 was possible along the soft {112} direction at temperatures down to 400°C. Under hydrostatic confirming pressures, deformation down to 250°C is possible [61], as shown in the plot of yield stress against temperature in Fig. 12.

The wide temperature range employed by the Messerschmidt group (400–1400°C, see Fig. 12 [49]) has revealed that cubic ZrO_2 displays essentially textbook behavior of dislocation plasticity. At all temperatures, part of the flow stress is of an athermal nature, due to long range dislocation–dislocation interactions, and to the back stress of dislocation segments bowing out between large jogs. This type of athermal deformation dominates crystals containing 10 m/o Y_2O_3 deforming by easy slip between ~ 1000 and $\sim 1250^\circ\text{C}$; the flow stresses decrease at higher temperatures and increase at lower temperatures. At these lower temperatures, the Peierls mechanism causes a large increase in the flow stress, to 1 GPa or more at 400°C [59].

At the highest temperatures, say 1400°C and above, deformation is controlled by recovery [60,62,63]. One consequence is a reduction in the plastic anisotropy, as shown in Fig. 12. A marked apparent solution hardening at these elevated temperatures is most likely explained by the strong effect of Y^{3+} concentration on bulk diffusion kinetics; the diffusivity of the rate controlling (slower) species decreases by an order of magnitude in going from 9.6 to 20 mol% Y_2O_3 [64,65]. At lower temperatures, say below 1000°C, the size misfit between Zr^{4+} and Y^{3+} can cause a more “classical” solid solution hardening.

Although Y^{3+} ions present only weak obstacles to dislocation motion [49], they are present in high concentrations and theoretically could yield a large contribution to the flow stress. However the crystals presently available apparently contain very small precipitates of ZrN [66] which provide stronger obstacles to slip than do unassociated Y^{3+} ions [49,67,68]. However, these unassociated Y^{3+} ions do cause plastic instabilities—dynamic strain

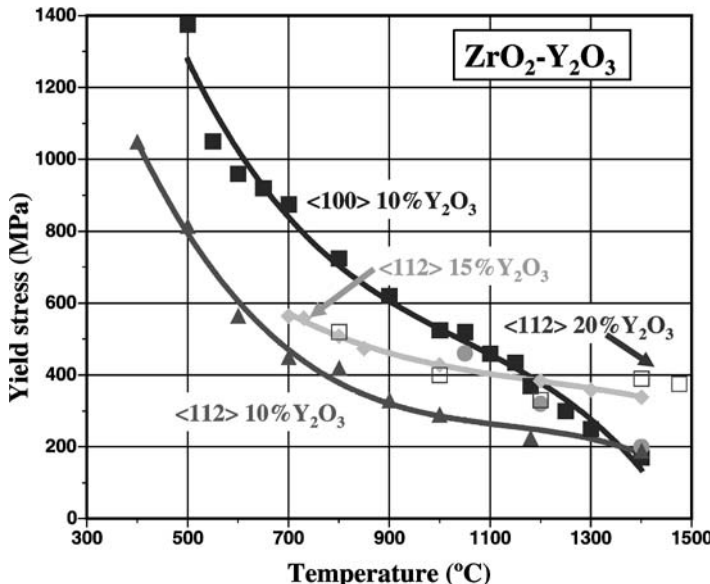


Fig. 12. Yield stresses of $\text{ZrO}_2\text{-Y}_2\text{O}_3$ single crystals versus temperature. $\langle 100 \rangle$ and $\langle 112 \rangle$ in the legend refer to the compression axis; the percentages are the mole % of Y_2O_3 . Strain rates are variable (see Tikhonovsky et al. [49]).

aging or the Portevin–LeChâtelier effect in high solute content crystals deformed over a broad range of temperatures between 800 and 1400°C [67,68].

4.3.4. Uranium oxide

The other fluorite-structured material that has been well studied is UO_{2+x} ; in this case, the non-stoichiometry is an issue, as the value of x can extend from zero (stoichiometric UO_2) to 10^{-2} or larger. The most comprehensive recent study is by Keller et al. [69], to which the reader is referred for reference to the earlier literature. Following these authors, we will consider deformation at low and high temperatures separately.

4.3.5. Deformation of UO_2 at lower temperatures

Firstly, UO_2 has a surprisingly low brittle-ductile transformation. The preferred slip system at low temperatures (in fact the only slip system observed at low temperatures) is $\{111\}\langle 110 \rangle$ and does not depend on stoichiometry. Sources of mobile dislocation are an issue, however, and to achieve deformation at temperatures below 600°C, crystals must be pre-deformed at 600°C. With such pre-deformed crystals, deformation to plastic strains $> 1\%$ is possible with modest yield stresses, 80 MPa at 450°C, 110 MPa at 400°C, and 120 MPa at 250°C. Attempts to deform these crystals at room temperature were not successful; possibly, more careful alignment of the load train might have allowed plastic deformation at temperatures lower than 250°C. Microindentation at room temperature is always possible, however, and the Knoop hardness anisotropy at room temperature is also consistent with $\{111\}$ slip [69].

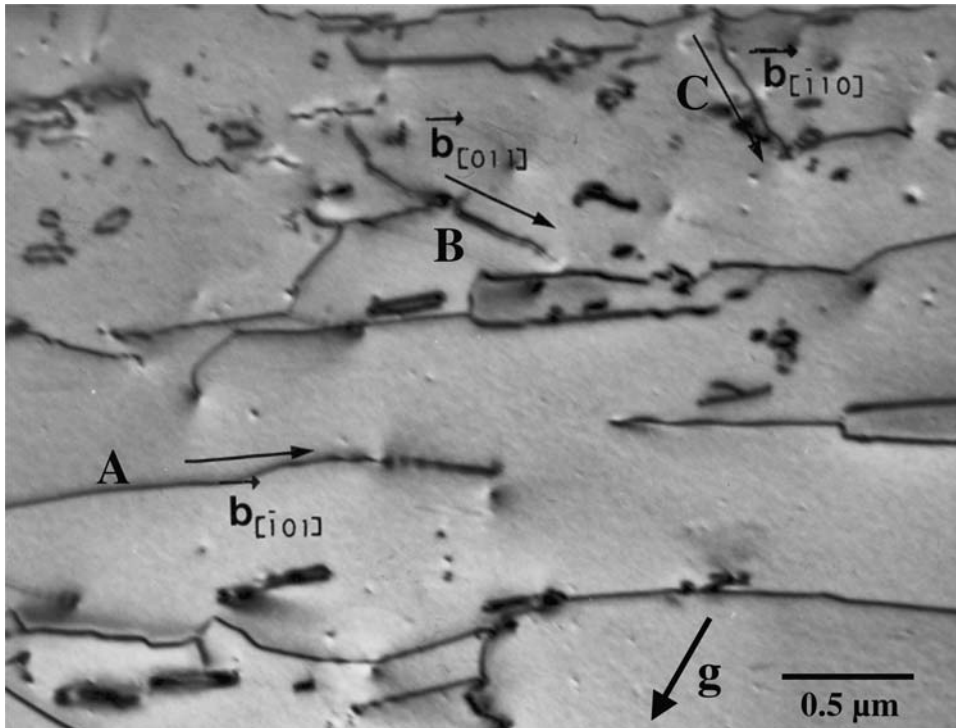


Fig. 13. Dislocation structure in UO_{2+x} ($x = 0.0001$) deformed at 600°C . Primary screw dislocations are marked A and secondary dislocations are marked B and C. Debris in the form of loops and dipoles are also seen. Foil cut parallel to the (111) slip plane (from Keller et al. [69]).

The yield stress at 600°C was variable but surprisingly was not a function of the O/U ratio; plastic deformation appeared to be controlled by the interaction of mobile screw dislocations with unknown but extrinsic impurity defects. Screw dislocation debris dominated the dislocation substructures (as shown in Fig. 13), indicating that screw dislocations were less mobile than edge dislocations at these low temperatures. The Knoop hardness did increase with increasing nonstoichiometry at room temperature but this may be due to precipitation of U_4O_{9-y} on cooling from elevated temperatures—samples with $x = 0.01$ or greater are in the two phase $(\text{UO}_{2+x} + \text{U}_4\text{O}_{9-y})$ phase field at room temperature.

4.3.6. Deformation of UO_2 at higher temperatures

The situation at higher temperatures (800 – 1400°C) is more complex. The primary glide plane depends on orientation, temperature and O/U ratio. $\{001\}\langle 110 \rangle$ slip is most common at low O/U ratios and higher temperatures, while $\{111\}\langle 1\bar{1}0 \rangle$ slip dominates at high O/U ratios and lower temperatures. The CRSS for $\{001\}$ slip is nearly independent of O/U ratio, while that for $\{111\}$ glide decreases with increasing x .

At low values of x , the flow stress for slip is controlled by extrinsic impurity defects as at low temperatures, whereas at high O/U ratios, it appears that oxygen interstitial defects

(“Willis defects” [70]), necessarily present in crystals with high O/U ratios, actually reduce the hardening effect of these extrinsic impurities. Keller et al. [69] suggest, somewhat speculatively, that the core structure of the glide dislocations is changed by the presence of Willis defects in such a way that dislocations on {111} can overcome the hardening effect of impurity defects, whereas those on {100} cannot. Experiments with purer crystals than those available to Keller et al. [69] would be most desirable to understand the plasticity of UO_{2+x} crystals, particularly issues related to the non-stoichiometry.

4.3.7. Dislocation dissociation in oxides with the fluorite structure

Dislocation dissociation has never been reported in any of the oxides with the fluorite structure. This is not surprising since the $1/2\langle 110 \rangle$ Burgers vector joins neighboring anions and neighboring cations. Dissociation into, say, Shockley-type partials would create a high energy fault.

4.4. TiO_2 and other oxides with the rutile structure

Although binary oxides with a relatively large quadrivalent cation in octahedral coordination can occur in a variety of crystal structures (the anatase form of TiO_2 , the ramsdellite form of MnO_2 , etc.), the rutile structure is generally the stable form and is found in a number of 3d transition metal oxides (TiO_2 , VO_2 , CrO_2 , MnO_2 , etc.). Of these, only rutile itself— TiO_2 —has received much attention with regard to dislocation activity and we will concentrate on its behavior.

In the seminal paper of Wachtman and Maxwell [6,71] that began the modern era of studies of dislocation plasticity in oxides, the brittle → ductile transition of TiO_2 was reported to be 600°C , lower than that they found for Al_2O_3 (900°C) or MgO (1100°C). The first systematic studies of crystal plasticity was carried out by Ashbee and Smallman [71], who identified the active slip systems as $\{101\}\langle\bar{1}01\rangle$ and $\{110\}[001]$. Blanchin and Faissart [72] and Blanchin et al. [73] confirmed $\{101\}\langle\bar{1}01\rangle$ as the easy slip system, and deformed [001] oriented crystals at temperatures as low as 600°C ; at this temperature, yielding occurred at a resolved flow stress of ~ 45 MPa. Neither extended faults on {101} nor dissociation of {101} dislocations were observed [74], in agreement with elastic energy calculations [75] but not with some early experiments [71,76]. However, Bursill and Blanchin [74], using HREM, found dissociation near the surface of foils. More recently Suzuki et al. [77] found a 1 nm dissociation into half-partials of the {101} dislocation and Blanchin et al. [78] observed a much larger dissociation in Cr_2O_3 -doped rutile.

The secondary $\{110\}[001]$ system could be activated above 900°C but the total plastic strain achieved prior to fracture was limited [78]. Reduced rutile and Cr- and Al-doped TiO_2 have also been studied [78]; significant solution hardening occurs, involving glissile dislocations interacting with both point defects and extended defects. In some cases, this gives rise to dynamic strain aging (DSA) [73].

4.5. SiO_2 (quartz)

α -quartz is the polymorph of SiO_2 that is stable at ambient temperature and pressure and is one of the most important of the rock-forming minerals. Plastic deformation of quartz-rich rocks occurs whenever there is tectonic activity, and many studies of quartz deformation have appeared in the earth science literature. α -quartz is trigonal, space group $P3_121$, and transforms displacively to β -quartz, space group $P6_222$, at 573°C . The finite dilatation associated with the $\alpha \rightarrow \beta$ transformation often involves cracking and has hampered study of plastic deformation of quartz at elevated temperature. It has accordingly not proven possible to deform quartz in the laboratory under ambient pressure. Furthermore, if the quartz is “dry,” i.e., has little if any dissolved H_2O or other water-related species, such as H^+ , OH^- , etc., present, deformation is difficult even under hydrostatic confining pressures. For example, under a confining pressure of 1.5 GPa, Griggs and Blacic [79,80] found the CRSS for basal slip of dry quartz to be ~ 2.2 GPa at 300°C and ~ 1.6 GPa at 700°C , about 5% of the shear modulus of 40 GPa. This intrinsic resistance to plastic deformation of quartz remains high to at least 1300°C , $\sim 0.8T_m$, where the CRSS is still in excess of 0.5 GPa [12,81]. Where deformation has been induced under hydrostatic confining pressures, various slip planes— (0001) , $\{10\bar{1}0\}$, $\{11\bar{2}0\}$, $\{10\bar{1}1\}$, $\{011\bar{1}\}$ —and dislocations with various Burgers vectors— $1/3\langle 11\bar{2}0 \rangle$, $[0001]$, and $1/3\langle 11\bar{2}3 \rangle$, have often been found. These Burgers vectors correspond to the three shortest lattice translations in quartz, 0.491, 0.541, and 0.730 nm, respectively.

4.5.1. Hydrolytic weakening in quartz

In the presence of even small quantities of water, plastic deformation in the laboratory becomes much easier, albeit still necessitating hydrostatic confining pressures; pressure, moreover, expands the stability field of α -quartz to higher temperatures (to $\sim 1300^\circ\text{C}$ at 3.4 GPa confining pressure, for example [82]). This “hydrolytic weakening” was discovered by Griggs and Blacic [79,80] and has resulted in a very large literature devoted to understanding the softening effect of water (such weakening also occurs in olivine, as described in Section 4.9). The dramatic effect of water content is illustrated in Fig. 14 which shows the stress-strain curves obtained by Ord and Hobbs [83] under various buffered assemblies at 800°C under a confining pressure. The buffering issue is beyond the scope of the present review; we will focus only on the “dry” and “ H_2O only” curves of Fig. 14. The following still-tentative summary on the effect of water on the deformation of quartz is taken from Paterson [81].

As distinct from some of the other oxides discussed here (MgO , Section 4.1, UO_2 , Section 4.3), it is primarily dislocation mobility and not dislocation density limitations that determine the ability to deform quartz to large strains. There is evidence, however, that water can influence nucleation of potentially mobile dislocations in both synthetic and natural quartz [84,85] (see also McLaren [86]). Water apparently influences dislocation mobility by (i) facilitating the nucleation and diffusion of kinks and (ii) in facilitating dislocation climb [87]. Atomistically, the water appears to accelerate the self-diffusion of oxygen and/or silicon by mechanisms that are still obscure. This suggests that three regimes of deformation in quartz can be recognized [87]: the *intrinsic* regime at relatively low tem-

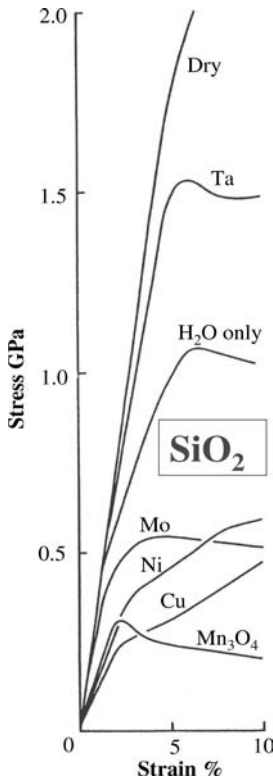


Fig. 14. Stress–strain curves of quartz deformed in compression under a confining pressure of 1.6 GPa in various buffered assemblies at 800°C and a strain rate of 10^{-5} s^{-1} . The effective water content increases from the top to the bottom curve (from Ord and Hobbs [83]).

peratures and controlled by the Peierls stress; a *hydrolytic glide control* regime involving kink nucleation and/or diffusion; and a *recovery controled* regime at high temperatures.

In the hydrolytic glide regime, dislocation activity and the mechanism of water weakening depend on the water content of the quartz. High quality synthetic quartz can be relatively dry, ~ 100 at. ppm $[\text{H}]/[\text{Si}]$, and in these samples, the water is accommodated in the quartz lattice by point defects, specifically a $(4\text{H})_{\text{Si}}$ species (i.e., one Si is formally replaced by 4H [88]). “Wetter” crystals containing say 1000 at. ppm $[\text{H}]/[\text{Si}]$ contain aggregated molecular water—bubbles. These can be fluid inclusions which have no long range strain fields associated with them, or water clusters under a high internal pressure and showing strain contrast [89]; on heating, these clusters evolve into strain-free bubbles and associated prismatic dislocation loops with $b = 1/3(11\bar{2}0)$.

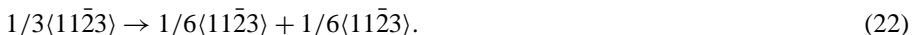
4.5.2. Dislocation dissociation in quartz

Dislocation dissociation in quartz was first observed by McLaren et al. [90] in a natural dry quartz deformed at 500°C and has been studied most recently by Cordier and Doukhan [91] in a synthetic crystal containing ~ 100 at. ppm $[\text{H}]/[\text{Si}]$. Using a crystal oriented to

have high Schmid factors for basal slip $(0001)1/3\langle 11\bar{2}0 \rangle$, prism plane slip $\{11\bar{2}0\}[0001]$, and pyramidal slip $\{10\bar{1}0\}1/3\langle 1\bar{2}\bar{1}3 \rangle$, and deformed under a hydrostatic pressure of 1.0–1.1 GPa, they found a flow stress at 500°C of nearly 3 GPa, which decreased to ~ 2 GPa at 900°C. (At the higher temperatures, the sample had transformed to β quartz.) These high flow stresses correspond to a significant fraction of the shear modulus and reflect the fact that the quartz is relatively dry. Slip at 500°C was heterogeneous (in slip bands) but conformed to the basal slip system. Some of the basal dislocations were widely dissociated (0.5 to 5 μm (!)) into collinear partials by the reaction



while others appeared undissociated; however, dissociation widths < 10 nm would not have been detected using the weak beam TEM technique they employed. At 700°C and a flow stress of ~ 2.5 GPa, similar evidence for basal slip was found, although pyramidal slip had also occurred. The pyramidal dislocations were also widely dissociated into collinear partials via the reaction



At 900°C, in the β quartz phase field, pyramidal glide dominates, the dislocations again being widely dissociated. In a few regions, which the authors suggested had a higher water content than the average, dislocation microstructures typical of recovery was observed. Thus, these authors provide direct evidence of dissolved water enhancing both glide and climb of dislocations.

No attempt was made to derive stacking fault energies for quartz, as the variable but very widely spaced stacking faults clearly indicate non-equilibrium structures, undoubtedly due to the very high flow stresses at which the dislocations were gliding. The atomic structure of stacking faults in quartz has been considered by Doukhan and Trepied [87]; low energy faults on (0001) and on $\{10\bar{1}0\}$, as observed experimentally by Cordier and Doukhan [91], have all the Si and O atoms in the planes adjacent to the fault, forming $[\text{SiO}_4]$ tetrahedra which are bonded to neighboring tetrahedra at all four corners; furthermore, no dangling bonds, or stretched or distorted Si–O–Si bonds are present.

4.6. Al_2O_3 (sapphire)

Sapphire ($\alpha\text{-Al}_2\text{O}_3$) was the first synthetic gemstone to be grown in the laboratory by Verneuil over a century ago [92] and Verneuil crystals were widely used as the raw material for the “jewels” in fine Swiss watches in the first half of the 20th century. The ready availability of undoped and Cr-doped Al_2O_3 (ruby) single crystals led to the first demonstration of laser action in synthetic ruby by Maiman in 1960 [93], and sapphire wafers (up to 8" in diameter (!)) have been substituted for Si wafers in certain demanding electronic integrated circuit applications.

The availability of sizable single crystals has led to a significant literature on the deformation of sapphire of various orientations and at various temperatures. As we already

noted, the first such study was by Wachtman and Maxwell in 1954 [6], who activated basal slip, $(0001)1/3\langle 11\bar{2}0 \rangle$, at 900°C via creep deformation. Since that time, it has become clear that basal slip is the preferred slip system at high temperatures, but that prism plane slip, $\{11\bar{2}0\}\langle 1\bar{1}00 \rangle$, can also be activated and becomes the preferred slip system at temperatures below $\sim 600^\circ\text{C}$. Additional slip systems, say on the pyramidal plane $\{\bar{1}012\}1/3\langle 10\bar{1}1 \rangle$, have very high CRSS's and are thus difficult to activate. Both basal and rhombohedral deformation twinning are also important in Al_2O_3 and will be discussed further below.

The yield stress for both basal and prism plane slip as a function of temperature have been determined over a wide temperature range (Fig. 4). The “Castaing Law”— $\ln(\text{CRSS})$ decreasing linearly with temperature—has been explained by Mitchell et al. [24] in terms of conventional kink pair nucleation and kink diffusion, as discussed in Section 2.

4.6.1. Dislocation dissociation in sapphire

Dislocation dissociation has been an important issue in studies of basal deformation in sapphire since the seminal work of Kronberg [7]. He suggested that basal dislocations would dissociate into half partials via the reaction



with each half partial further dissociating into quarter partials via the reaction



Reaction (23) involves faulting only in the cation sublattice, as $1/3\langle 10\bar{1}0 \rangle$ is a translation vector of the anion sublattice. Reaction (24) involves faulting of both sublattices, and must lead to a very high stacking fault energy, as no reliable evidence for quarter partial dislocations has ever been put forward.¹ Kronberg utilized an idealized version of the corundum structure of Al_2O_3 —a perfect hcp oxygen sublattice and flat as opposed to puckered cation layers—in considering reactions (23) and (24) and imagined that the *motion* plane for the dislocations was between cation and anion layers.

4.6.2. Basal slip in sapphire

Bilde-Sørensen et al. [29] presented a new model for basal slip, in which the motion plane is within the puckered cation layer. Each $1/3\langle 10\bar{1}0 \rangle$ partial transports only half of the cations as it moves to the half-slipped position; motion of the trailing partial restores perfect lattice without any charge transport. Because of the rhombohedral symmetry of $\alpha\text{-Al}_2\text{O}_3$, $\langle 10\bar{1}0 \rangle$ and $\langle 0110 \rangle$ directions are not crystallographically equivalent. Based on these considerations, the new model of basal slip led to a unique basal stacking fault (one of four possible basal stacking faults that can be imagined in Al_2O_3). *Ab initio* calculations by Marinopolous and Elsässer [95] showed that this fault has the lowest basal SFE in Al_2O_3 , 1.49 J/m^2 ; it is also the basis for a new model of basal twinning (see below).

¹Kronberg's *synchroshear* model of basal dislocation motion required these quarter partials; they were also involved in his model of basal twinning. As first emphasized by Bilde-Sørensen et al. [29] and as further discussed by Heuer et al. [94], this requires that dislocation motion involves charge transport, a significant impediment to slip in a material with such strongly ionic bonding as Al_2O_3 .

Table 9
Experimental and theoretical fault energies for sapphire on various planes.

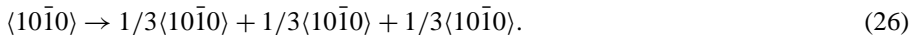
Fault vector	Fault plane	Fault energy (J/m ²)	Method
1/3<10̄10>	{10̄10}	0.4	TEM study of faulted 1/3<1̄210> dipole [97]
1/3<10̄10>	{1010}	0.23, 0.16	TEM study of elongated <10̄10> loop [206]
1/3<10̄10>	{1010}	0.64	TEM study of faulted loop produced by radiation [207]
1/3[0001]	{1010}	0.5, 0.5	Atomistic calculation [208]
1/3<10̄10>	{1120}	0.15	TEM study of faulted 1/3<1̄210> dipole [206]
1/3<10̄10>	{1̄210}	0.3	TEM study of <10̄10> glide dissociation [209]
1/3<10̄10>	{2110}	0.4	TEM study of <10̄10> climb dissociation [210]
1/3<10̄10>	{1̄210}	~0.1	TEM study of elongated <10̄10> loop [206]
1/3[0001]	{1120}	0.5	Atomistic calculation [208]
1/3<10̄10>	{101̄2}	0.25	TEM study of <10̄10> climb dissociation [206]
1/3[0001]	(0001)	0.27	TEM study of faulted loop produced by radiation [207]
1/3<10̄10>	(0001)	1.2, 2.3	Atomistic calculation [208]

4.6.3. Prism-plane slip in sapphire

Prism-plane slip occurs by the motion of <10̄10> dislocations on the {1̄210} plane, rather than 1/3<1̄210> dislocations in the {10̄10} plane, in spite of the unusually large magnitude of the Burgers vector of <10̄10> dislocations. Such dislocations might be expected to be unstable and *decompose* according to the reaction



This reaction can occur by glide in the basal plane only for screw dislocations, and is thought to be the mechanism for the formation of a dislocation network in crystals undergoing deformation by prism plane slip [96]. Alternatively, the dislocation can lower its energy by dissociating into three collinear partials according to the reaction (Table 9):



This dissociation has been observed to occur by climb for high temperature deformation but can also occur by glide.

4.6.4. Dipoles and climb dissociation in sapphire

Dislocation substructures formed after basal glide are similar to those found in hcp metals, in that a high density of dislocation dipoles is seen, as shown in Fig. 15. However, because of the high temperatures required for deformation (> 1200°C), dislocation climb is relatively easy and the dipoles tend to break up into strings of loops. This climb process occurs by redistribution of point defects by pipe diffusion along the dislocation, i.e., the climb occurs conservatively (self-climb). Narrow dipoles form faulted dipoles by a process of climb dissociation of the individual dislocations and annihilation of the inner partials, as

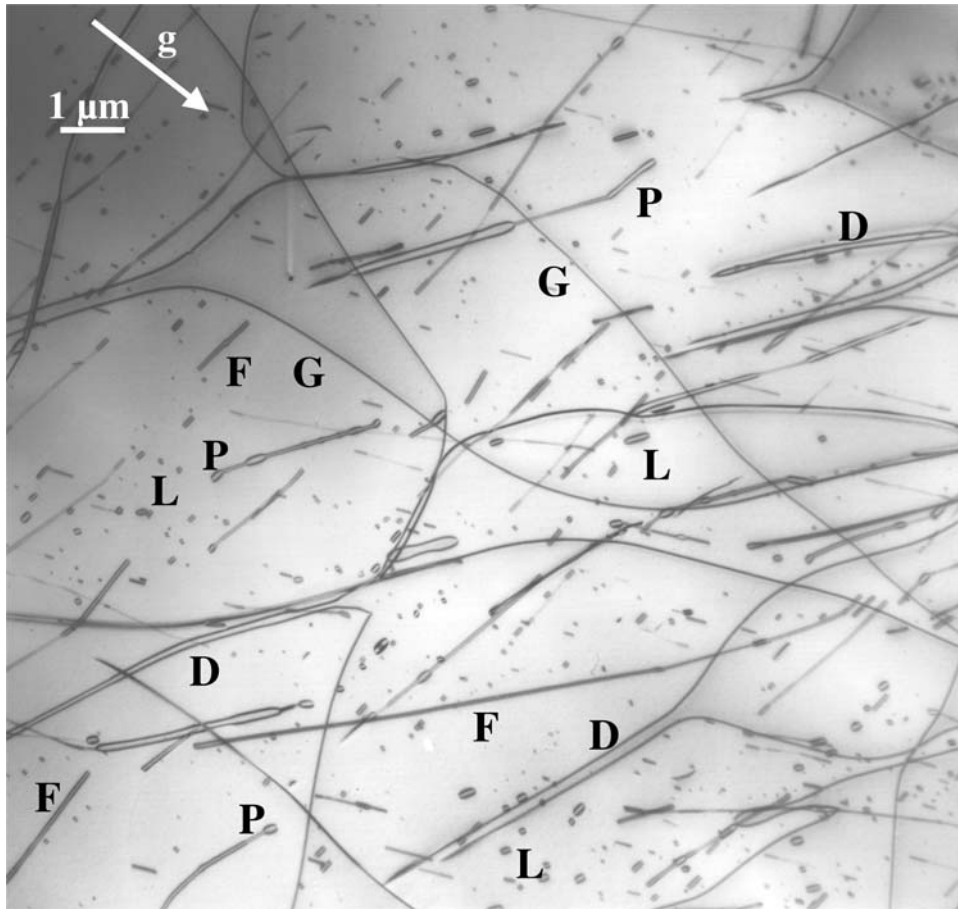


Fig. 15. Dislocations in sapphire deformed on the basal plane to 3.6% shear strain at 1400°C. Examples of glide dislocations (G), regular dipoles (D), faulted dipoles (F), isolated loops (L) and loops in the process of pinching off (P) are indicated. Foil parallel to (0001), bright field image, $g = 03\bar{3}0$.

illustrated in Fig. 16. Again, this can occur by conservative climb. The faulted dipole can break up into a string of faulted loops, just as a perfect dipole can break up into a string of perfect loops.

Climb dissociation initially occurs on $\{11\bar{2}0\}$ planes, as expected for the edge dipoles. Subsequently, the $1/3\langle 10\bar{1}0 \rangle$ faulted dipoles rotate into the $\{10\bar{1}0\}$ plane so as to bring them into the edge orientation. The whole process of dipole break-up has been explained in terms of elasticity theory [97,98]. The faulted dipoles form via the Kronberg dissociation, eq. (23), although as already mentioned, Kronberg envisioned the dissociation occurring by glide rather than climb.

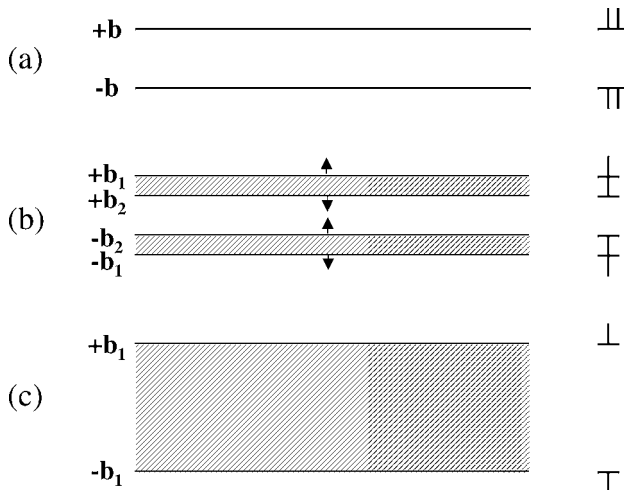


Fig. 16. Formation of a faulted dipole in sapphire: (a) original perfect dislocation dipole; (b) dipole with each partial undergoing conservative climb dissociation; (c) faulted dipole formed by the annihilation of the inner partials.

4.6.5. Stacking fault energy of sapphire

These various glide and climb configurations have been used to estimate stacking fault energies in sapphire. These are summarized in Table 9 and compared with atomistic calculations. In general the SFE on the prismatic planes is lower than that on the basal plane, both for experimental and calculated values. The exception is the value on the basal plane measured from the diameter of faulted loops (produced by radiation) at which the loops unfault. We think that this is probably a non-equilibrium situation and a value of about 1.5 J/m^2 for the SFE in the basal plane is most likely. Such a value would give only a core dissociation for glide dislocations in the basal plane, in agreement with the fact that dislocations dissociated in the basal plane have never been observed.

4.6.6. Deformation twinning in sapphire

Of the oxides mentioned in this review, deformation twinning is most important in the case of sapphire. Two twinning systems are known, on the rhombohedral and basal planes, and dislocation models for each have been suggested and confirmed by TEM.

Rhombohedral twinning is the deformation mode with the smallest CRSS in sapphire [99] and can occur at temperatures as low as -196°C [100]. The twin law is as follows: $K_1 = \{01\bar{1}2\}$; $\eta_1 = \langle 01\bar{1}1 \rangle$; $K_2 = \{0\bar{1}14\}$; $\eta_2 = \langle 02\bar{2}1 \rangle$; and $s = 0.202$ [100]. The dislocation model suggested for rhombohedral twinning [101] is based on the double cross slip mechanism proposed by Pirouz [102] for silicon (see also Lagerlöf et al. [103]). Briefly, twin nucleation involves a pinned zonal dislocation undergoing the following dissociation

$$1/3\langle 01\bar{1}1 \rangle \rightarrow 1/21.9\langle 0\bar{1}11 \rangle + [1/3\langle 01\bar{1}1 \rangle - 1/21.9\langle 0\bar{1}11 \rangle]. \quad (27)$$

The leading dislocation, with $b_t = 1/21.9(0\bar{1}11)$, bows out, in the same manner as a Frank–Read source, to form a loop of faulted crystal. Because b_t is a partial dislocation, it cannot bow out again on the same plane but can, if in screw orientation, cross slip onto an adjacent plane and bow out again. Continued growth of the faulted loop on each plane and cross slip onto neighboring planes allow for twin growth. The unusual magnitude of b_t arises from the notion that twinning involves shear of every neighboring $(01\bar{1}2)$ plane, by a partial dislocation with $b_t = 0.07$ nm. The $(01\bar{1}2)$ interplanar spacing is 0.348 nm; a shear of $1/21.9(0\bar{1}11)$ causes the observed twinning shear of 0.202 ($0.0703/0.348 = 0.202$) [101]. This model predicts that the rhombohedral twin is a screw twin— η_1 being a two-fold screw axis—rather than a type I or type II twin. The proposed structure of the twin interface has been confirmed by HREM, most recently by Nufer et al. [104]; finally, *ab initio* calculations by Marinopoulos and Elsässer [105] show that the energy of the twin interface predicted by this model, 0.63 J/m^2 , is much lower than that of two other possible structural models of a rhombohedral twin boundary, 1.35 and 3.34 J/m^2 .

Basal twinning can also occur in sapphire [106] and involves the following twin law: $K_1 = (0001)$; $\eta_1 = \langle 10\bar{1}0 \rangle$; $K_2 = \{10\bar{1}1\}$; $\eta_2 = \langle \bar{1}012 \rangle$; and $s = 0.635$. A cross slip model has also been employed for this case [94,107,108] and involves a $1/3\langle 10\bar{1}0 \rangle$ twinning dislocations produced via either reaction (22) or (25). The model predicts that the twin is type II (η_1 is a two-fold rotation axis) and theoretical calculations [109] indicate a twin boundary energy of 0.73 J/m^2 , much lower than other possible basal twin boundaries with either mirror or glide symmetry, which have energies of 1.99 and 2.63 J/m^2 , respectively. Persuasive TEM evidence supporting this model, and involving a nucleating dislocation produced by reaction (26), has recently been published [108]. In particular, twin boundaries containing three $1/3\langle 10\bar{1}0 \rangle$ partials have been imaged, as well as the presence of a threading dislocation within the twin; the latter is the “fingerprint” of the double cross slip twinning model.

4.7. SrTiO₃ and other oxides with the perovskite structure

The oxide perovskites comprise a technologically important family of ceramics, as all practical inorganic ferroelectrics and piezoelectrics crystallize in this structure. Furthermore, the structure of the so-called high- T_c superconductors is closely related, and perovskite single crystals such as SrTiO₃ are widely used as substrates for thin film deposition of the high- T_c materials and other useful “functional” oxides. Lastly, it is widely believed that olivines, $(\text{Mg}, \text{Fe})_2\text{SiO}_4$, the principal constituent of the Earth’s upper mantle, transform to magnesio-wüstite $(\text{Mg}, \text{Fe})\text{O}$ and a $(\text{Mg}, \text{Fe})\text{SiO}_3$ perovskite in the lower mantle. Thus, understanding the high temperature rheology of perovskites is of crucial importance for understanding mantle convection. Unfortunately, it is not possible to make such silicate perovskites in the laboratory, and it has been necessary to study such non-silicate surrogates as BaTiO₃, CaTiO₃, and SrTiO₃ for understanding tectonic processes in the earth. The structure of cubic perovskite is shown in Fig. 17.

4.7.1. Inverse BDT in SrTiO₃

Until recently, most studies focused on high temperature creep deformation and identified $\{110\}\langle 1\bar{1}0 \rangle$ as the dominant slip system for both BaTiO₃ and SrTiO₃ [110,111]. Evidence

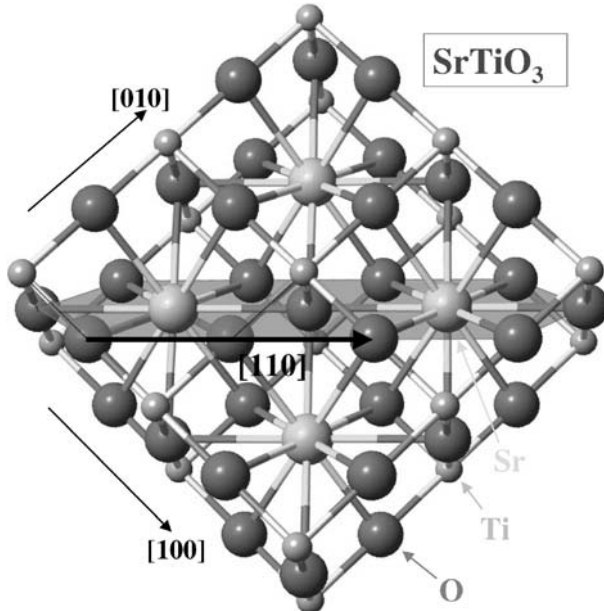


Fig. 17. The crystal structure of cubic SrTiO_3 (4 unit cells), viewed in perspective approximately along the [001] direction. The [110] Burgers vector is shown. Splitting into two collinear $1/2[110]$ partials obviously maintains the oxygen anion packing but puts Sr cations in juxtaposition across the {110} fault plane (shown shaded).

also exists for $\langle 100 \rangle$ Burgers vectors [112,113] and $\{100\}$ slip planes [112,114]. Most recently, Brunner et al. [115] and Gumbsch et al. [116] found unexpected low temperature plasticity and an “inverse” brittle-to-ductile transition (DBT) (a brittle \rightarrow ductile transition on *decreasing* temperature) in SrTiO_3 deformed along $\langle 100 \rangle$ or $\langle 110 \rangle$, and involving $\{110\}/\{\bar{1}\bar{1}0\}$ slip, as shown in the yield stress versus temperature curves in Fig. 18. Such behavior is similar to the yield stress anomaly found in some ceramics such as $\text{MgO}-\text{Al}_2\text{O}_3$ spinels [18] and in many intermetallics such as MoSi_2 (see Mitchell et al. [117]) and a number of Li_2 and B2 compounds (see Caillard [118]). The difference is that, for the yield stress anomalies, the materials remain plastic in the intermediate temperature range where the yield stress increases with increasing temperature, whereas strontium titanate is brittle in the intermediate temperature range and its fracture stress increases with increasing temperature. As shown in Fig. 18, at temperatures below about 900 K, the critical resolved shear stress for $\{110\}/\{\bar{1}\bar{1}0\}$ slip is low, about 50 MPa, and only weakly dependent on temperature; below 300 K, it begins to rise, but at 100 K, it is still only ~ 300 MPa.

4.7.2. Dislocation dissociation and SFE in strontium titanate

The $\langle 110 \rangle$ Burgers vector for SrTiO_3 is quite long, 0.552 nm and its dominance over the shorter $\langle 100 \rangle$ Burgers vector (0.391 nm) is at first sight surprising. However evidence for dissociation of $\langle 110 \rangle$ dislocations has been obtained in samples deformed at room temperature, which implies a low stacking fault energy (SFE) on the $\{110\}$ plane of SrTiO_3 .

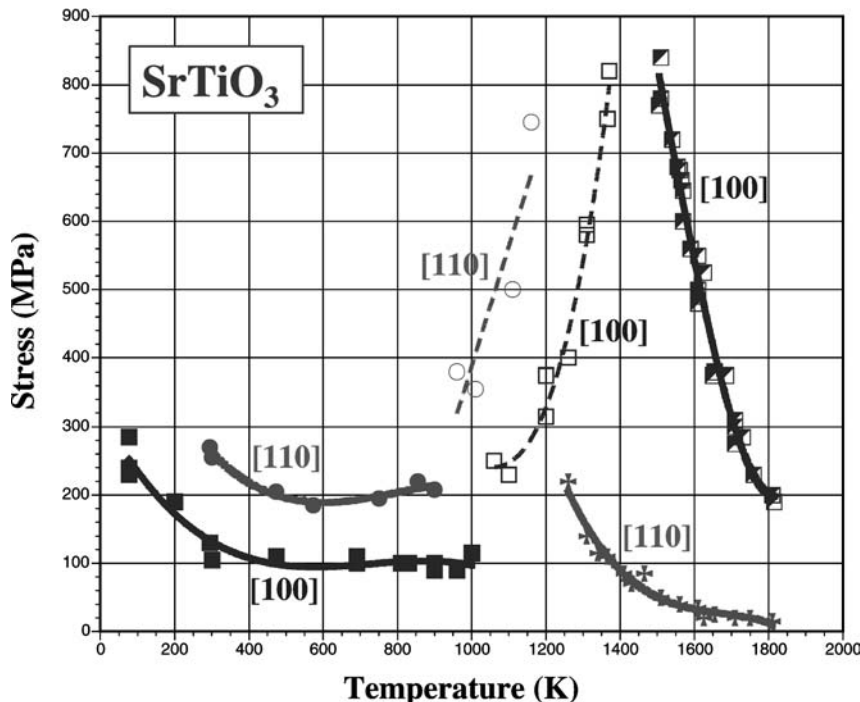


Fig. 18. Yield stress versus temperature for SrTiO_3 crystals compressed along $\langle 100 \rangle$ and $\langle 110 \rangle$. No measurable plastic flow occurs in the intermediate temperature range and the fracture stress is indicated by open symbols (from Brunner et al. [115] and Gumbsch et al. [116]).

Mao and Knowles [114] studied dissociation of lattice dislocations in sintered SrTiO_3 and found that the reaction



occurred for mixed $\langle 110 \rangle$ dislocations lying along the $\langle 100 \rangle$ direction. The dissociation is illustrated in Fig. 17 and shows that the fault juxtaposes the large Sr cations across the fault plane but maintains the anion sublattice. Mao and Knowles calculated a SFE of 145 mJ/m^2 for glide dissociation on (001) and 245 mJ/m^2 for climb dissociation on (010) . Surprisingly, different SFEs are found for the glide and climb cases, since the fault planes, (001) and (010) , respectively, are crystallographically equivalent. On the other hand, Matsunaga and Saka [119] found that $\langle 110 \rangle$ dislocations introduced by Vickers indentation at room temperature were dissociated by glide into two $1/2\langle 110 \rangle$ partials on $\{1\bar{1}0\}$ planes and, from the ribbon width, deduced a SFE of 136 mJ/m^2 .

The inverse BDT for SrTiO_3 deformed along $\langle 100 \rangle$ or $\langle 110 \rangle$ is believed to be due to transformation of the dislocation core structure [116]; Gumbsch et al. [116] suggest a possible climb dissociation (more properly a *decomposition*) via the reaction



However, the $\langle 100 \rangle$ product dislocations in reaction (29) are both perfect dislocations and are perpendicular to one another. Frank's rule indicates that, to first order, such a reaction would not lead to reduction in the dislocation line energy, whether it occurs by glide or climb. Of course, if we take into account the screw/edge character of the $\langle 110 \rangle$ dislocation, then more precise calculation shows that reaction (29) is favorable for an edge dislocation and unfavorable for a screw dislocation.

On the other hand, as discussed later in Section 4.12, and barring a pathological anisotropy of the SFE, the climb configuration for reaction (29) should always have a lower energy than a glide configuration. We believe that the structural transformation at the heart of the inverse BDT in SrTiO_3 is the climb of dissociated $\langle 110 \rangle$ dislocations into a sessile configuration, and that the onset temperature of the inverse BDT, $\sim 750^\circ\text{C}$, can be correlated with the temperature at which pipe diffusion kinetics permit climb along the dislocation cores to effect the core transformation. In fact, climb-dissociated $\langle 110 \rangle$ dislocations have been found by Zhang et al. [120] in a hot-pressed SrTiO_3 bicrystal containing a 5° $\langle 110 \rangle[001]$ tilt boundary [121]; however, the SFE indicated by the separation of the partials was high, 720 mJ/m^2 , compared with the values obtained from glide dissociation described above. Although the dissociation is by climb rather than by glide, the stacking fault plane is also $\{110\}$. Perhaps the partials had not achieved their equilibrium separation by climb.

4.8. $\text{MgO-Al}_2\text{O}_3$ and other spinels

The mechanical properties of $\text{MgO-Al}_2\text{O}_3$ spinel single crystals have been studied extensively by both creep and constant strain-rate compression tests at high temperature [18–20, 25, 122–143], as well as by indentation testing [21, 133, 144]. Work has also been done on other oxides with the spinel structure, such as magnetite (Fe_3O_4) [145], manganese zinc ferrite ($\text{Mn}_{0.7}\text{Zn}_{0.2}\text{Fe}_{2.1}\text{O}_4$) [146, 147], manganese aluminum spinel ($\text{Mn}_{1.8}\text{Al}_{1.2}\text{O}_4$) [148], nickel ferrite ($\text{Ni}_{0.7}\text{Fe}_{2.3}\text{O}_4$) [149–151], and chromite (FeCr_2O_4) [152]. Perhaps the most unusual mechanical behavior exhibited by $\text{MgO} \cdot n\text{Al}_2\text{O}_3$ spinel is the compositional softening (discussed earlier in Section 2.5) whereby the critical resolved yield stress decreases by almost two orders of magnitude when the stoichiometry is changed from $n = 1$ (stoichiometric) to $n = 3.5$ [20, 25, 123, 125, 134, 139, 143]. Stoichiometric crystals can be deformed plastically only at temperatures above $\sim 1700^\circ\text{C}$, while non-stoichiometric crystals can be deformed at temperatures down to about 1200°C . (Actually, this refers to ambient pressure conditions; under a high confining pressure, spinel can be deformed plastically down to ambient temperatures [20, 134].) The temperature dependence of the CRSS has already been discussed in Section 2.5 in terms of kink pair nucleation and migration on dislocations. Compositional softening is due either to kink pair nucleation on cation vacancies or kink pair nucleation on partial dislocations and the decrease in SFE with increasing deviation from stoichiometry.

4.8.1. Slip planes in spinels

The slip direction in spinel is always parallel to the $\langle 110 \rangle$ close-packed direction of the fcc lattice, i.e., $1/2\langle 110 \rangle$ is the shortest perfect Burgers vector. In terms of the approximate

Table 10
Slip planes in oxides with the spinel structure.

Spinel oxide	Slip planes	Reference
$\text{MgO} \cdot n\text{Al}_2\text{O}_3$	{111}, {110}, {100}	[20,25,122–125,127–130,135,136]
Fe_3O_4	{111}, {100}	[145]
$\text{Mn}_{0.7}\text{Zn}_{0.2}\text{Fe}_{2.1}\text{O}_4$	{111}, {110}	[146,147]
$\text{Mn}_{1.8}\text{Al}_{1.2}\text{O}_4$	{110}	[148]
$\text{Ni}_{0.7}\text{Fe}_{2.3}\text{O}_4$	{111}, {110}, {100}	[150,151]
FeCr_2O_4	{111}, {110}, {100}	[152]

fcc packing of the oxygen anion sublattice (Fig. 8), $1/2\langle 110 \rangle$ represents two interatomic distances. On the other hand, the observed slip plane is variable, as shown in Table 10 for Mg-Al spinel and a few other oxide spinels that have been tested. The most commonly observed slip planes are {111} and {110}, although {100} has been reported in magnetite, nickel ferrite and chromite. Slip on {100} planes has also been observed in Mg-Al spinel but this was at temperatures below 1000°C under confining pressure for crystals compressed along the $\langle 111 \rangle$ axis [20]. The Schmid factor for all the {110}{110} slip systems is zero for the $\langle 111 \rangle$ compression axis, while that for {111}{110} slip is small (0.27) and that for {100}{110} slip is relatively large (0.47).

Slip in spinel can be rationalized by examining the crystal structure. As shown in Fig. 8, the stacking of the {111} planes can be written in the following 18-layer sequence:

$$\dots A_O \beta c \alpha B_O A C O \alpha \beta \gamma A_O C B_O \gamma \alpha \beta C_O B \dots, \quad (30)$$

where $A_O B_O C_O$ refers to the approximate fcc stacking of the oxygen anions, $A B C$ refers to octahedral Al cations in the two-thirds occupied Kagomé layers (shown in Fig. 19), $\alpha \beta \gamma$ refers to the octahedral Al cations in the one-third occupied mixed layers and $\alpha \beta \gamma$ refers to the tetrahedral Mg cations in the one-quarter occupied mixed layers. Several interesting features emerge from Fig. 8:

- The anion planes on either side of the mixed $\beta c \alpha$ layer have a spacing of 0.256 nm whereas those surrounding the Kagomé layer have a significantly smaller spacing of 0.210 nm; the difference is due to the fact that the tetrahedral sites have to expand in order to accommodate the larger Mg^{2+} cations.
- The individual layers are all charged but the Kagomé layers, along with half the anions on either side, have a neutral composition of Al_2O_3 . The mixed layers have a neutral composition of $\text{Mg}_3\text{Al}_2\text{O}_6$.
- The $1/2\langle 110 \rangle$ slip vector corresponds to two inter-anion distances but the anions are not evenly spaced, because of the non-ideality of the fcc packing (see Fig. 19).

{110} planes can be analyzed in a similar way [18]. The stacking sequence is given as ...ABCD... although it would be ...ABAB... but for the non-ideality of the fcc anion packing. The compositions of the A and B planes are MgAlO_2 and Al_2O_4 respectively, and so edge dislocations on the {110} planes would be charged, although not so much as dislocations on the {111} plane. The spacing between the {110} planes is 0.143 nm compared with 0.105 nm for the spacing between the {111} anion and cation planes in the Kagomé layer. This may explain why {110} slip is easier. The spacing of the {100} planes

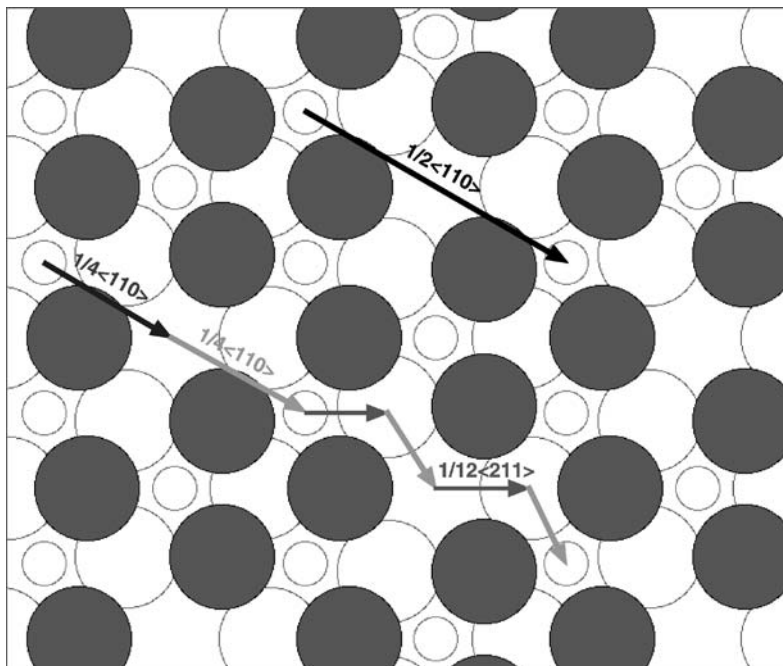


Fig. 19. The {111} Kagomé layer in spinel. The large open circles are the lower anion layer, the large filled-in circles are the upper anion layer and the small open circles are the middle cation layer. The perfect $1/2\langle 110 \rangle$ Burgers vector is shown, as well as possible dissociation schemes. Note the larger anion octahedra surrounding the empty cation sites and the imperfect fcc stacking.

(0.101 nm) is even smaller than the {111} planes, so that slip on {100} planes should only be observed under favorable circumstances, as described above.

4.8.2. Dislocation dissociations and the SFE in magnesium aluminate spinel

The Hornstra dissociation into collinear half-partials (eq. (19)) is commonly observed, most often by climb. However, evidence has been found for combinations of glide and climb dissociation on both rational and irrational planes. The {100} fault plane predominates, regardless of stoichiometry, followed by {110}, {112}, {113} and {111} [25]. Occasionally, pure glide dissociation is observed, for example, of screw dislocations on the {110} plane of stoichiometric crystals [25]. Although faults in spinel exhibit a clear preference for the {100} plane and other low index planes, they are also observed to be wavy and lie on irrational planes (see Fig. 20). Apparently, the fault energy is relatively isotropic, in much the same way as anti-phase domain boundaries in ordered alloys. Estimates of the fault energy have been made from ribbon widths. Values of γ from the literature [18, 25, 124, 126, 128, 132] are plotted against n in Fig. 21. The stacking fault energy is seen to decrease by about a factor of ten with increasing non-stoichiometry as n goes from 1 to 3.5. There is fair agreement between different investigations. The most serious discrepancy is for stoichiometric spinel, where Welsch et al. [126] determined $\gamma = 180 \text{ mJ m}^{-2}$

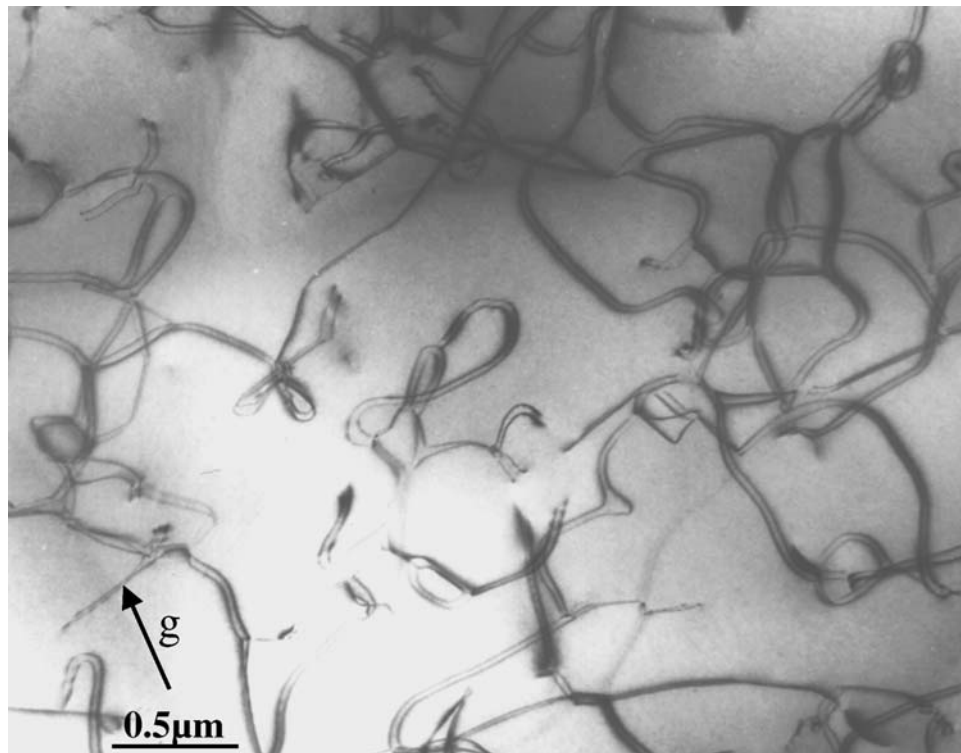


Fig. 20. Typical three-dimensional climb structure in a $n = 3.5$ spinel deformed 5% along the $\langle 111 \rangle$ axis at 1500°C. Note the widely extended, and appropriately named, ribbons. TEM bright-field image, $g = 440$.

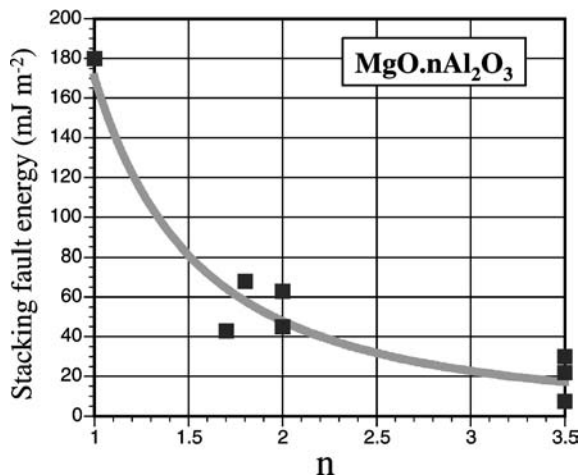


Fig. 21. SFE of $\text{MgO} \cdot n\text{Al}_2\text{O}_3$ versus n [18].

for edge dislocations on the {111} plane produced by deformation at 1800°C; in contrast Veyssiére and Carter [19] determined $\gamma = 530 \text{ mJ m}^{-2}$ for screw dislocations on the {001} plane produced by deformation at 400°C under a confining pressure. The latter value is not shown on Fig. 21. It is not known if the difference is due to the different dissociation planes or the different deformation temperatures. Various fault planes are represented in Fig. 21 and there is no consistency about the variation of γ from one plane to another. It is also possible that segregation of vacancies or impurities to stacking faults could occur at high temperatures, giving a lower fault energy than would otherwise be the case.

4.9. Mg_2SiO_4 (forsterite)

Olivine, the mineral name given to the solid solution series between forsterite (Mg_2SiO_4) and fayalite (Fe_2SiO_4), is thought to be the dominant component in the Earth's upper mantle. Thus, its deformation behavior has aroused considerable geophysical interest. The structure of forsterite is illustrated in Fig. 22; it can be considered the hcp equivalent of spinel, i.e., oxygens are in almost perfect hcp packing, with the larger divalent ions occupying half of the octahedral interstices, and the smaller Si ions occupying one quarter of the tetrahedral interstices. A small distortion of the hcp oxygen sublattice (similar to the small departure from perfect fcc packing in the oxygen sublattice in spinel) leads to orthorhombic symmetry, space group $Pbnm$,² with lattice parameters (for pure forsterite) of $a = 0.476 \text{ nm}$, $b = 1.023 \text{ nm}$ and $c = 0.599 \text{ nm}$. There are two types of octahedra, one more distorted than the other, and the $[\text{SiO}_4]$ tetrahedra point alternately up and down along the a axis. Dislocations with the shorter [100] and [001] Burgers vectors dominate the deformation, as expected [153–155]. ([100] and [001] actually correspond to the [0001] and $(1\bar{1}\bar{2}0)$ directions in the pseudohexagonal oxygen sublattice of olivine [156].) Furthermore, slip in these directions can occur without disruption of the SiO_4 tetrahedra, since the core structure of the dislocations need not involve breaking of covalent Si–O bonds but only rearrangement of the more ionic Mg(Fe)–O bonding, as discussed by Paterson [12,81].

High temperature creep deformation of synthetic forsterite crystals, studied by Darot and Gueguen [157], occurred by (010)[100] slip, which is apparently the preferred slip system. This same slip system was detected around Vickers indents produced at temperatures of 600°C and above by Gaboriaud et al. [158,159], who used natural olivine single crystals from San Carlos, AZ; (110)[001] slip was also activated. There have been many other extensive deformation studies of the olivine minerals (see, for example, Kohlstedt and Ricoult [160] and Poumellec and Jaoul [161]).

4.9.1. Water-weakening and dislocation dissociation in olivine

As noted in Section 4.8, “water weakening” can occur in olivine, as in quartz [162–165]. It has been suggested by Mackwell et al. [165] that water enhances climb mobility, but more detailed explanations are still lacking. Another possibility is that the point defects associated with the addition of water cause enhanced kink nucleation and/or kink diffusion, as described in Section 2.3.

²The “official” space group in the International Tables of X-ray Crystallography is $Pnma$ (no. 62) but the historical axes given above mean that the space group permutes to $Pbnm$.

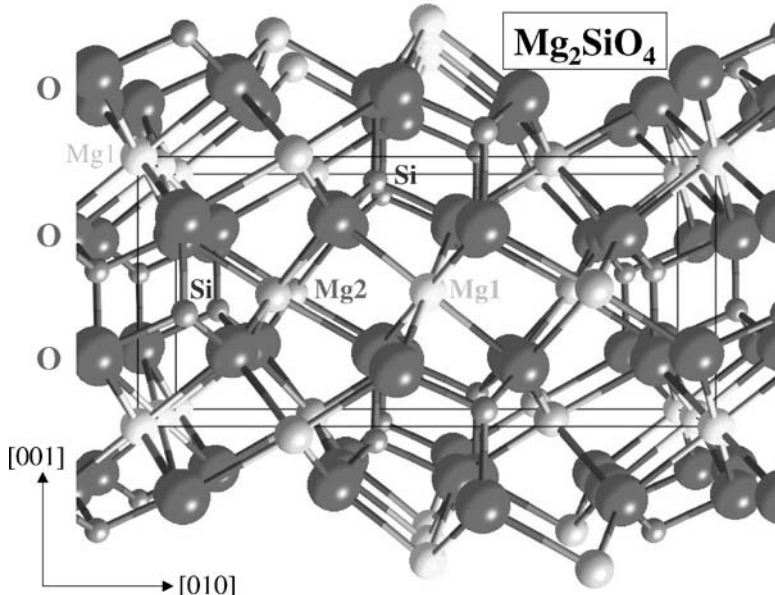


Fig. 22. The crystal structure of forsterite, Mg_2SiO_4 , viewed in perspective along the [100] direction. The isolated SiO_4 tetrahedra alternately point up and down in rows along the \mathbf{a} axis. The $\text{Mg}1$ octahedra are at the corners of the indicated unit cell and half way along the \mathbf{a} axis in rows. The $\text{Mg}2$ octahedra are more distorted. The irregular close-packed anion planes are seen edge-on, parallel to (001).

Dislocation dissociation has also been an issue in olivine since the early work by Poirier et al. [156,166]. TEM evidence for such dissociation was first reported by Vander Sande and Kohlstedt [167], and more recently by Smith et al. [168] and Drury [169]. The dissociation (eqs (31) and (32)) suggested by Poirier assumes that the oxygen ions can be considered as hard spheres

$$[100] \rightarrow \left[\frac{1}{6} \frac{\bar{1}}{36} \frac{\bar{1}}{4} \right] + \left[\frac{2}{3} 00 \right] + \left[\frac{1}{6} \frac{1}{36} \frac{1}{4} \right] \quad (31)$$

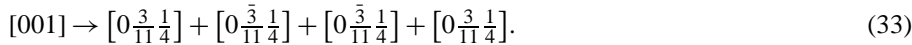
for dislocations on (010) and

$$[100] \rightarrow \left[\frac{1}{6} \frac{\bar{1}}{9} \frac{1}{6} \right] + \left[\frac{2}{3} 00 \right] + \left[\frac{1}{6} \frac{1}{9} \frac{\bar{1}}{6} \right] \quad (32)$$

for dislocations on (001). TEM evidence for reactions (31) and (32) was reported by Vander Sande and Kohlstedt [167], as well as for dissociation of a [001] dislocation lying on (100). In all these cases, the extent of the dislocation dissociation was small, less than three Burgers vectors in glide and less than ten Burgers vectors in climb [169].

Hydration-induced climb dissociation of dislocations in naturally deformed mantle olivine has been reported by Drury [169]. Here the dissociation is pronounced and involves

climb of [001] dislocations (rather than [100] dislocations) on (001) and {021} planes via the reaction



The partial Burgers vectors of this dissociation reaction are close (2.6°) to but not exactly parallel to $\langle 011 \rangle$. Two of the planar defects produced by reaction (33) are cation-deficient and probably stabilized by H^+ to produce layers with composition $(Mg, Fe)(OH)_2$, isostructural with the OH-rich layer of the humite group of minerals. (The humite group of minerals consists of $(Mg, Fe)(OH)$ layers separated by n olivine (002) layers, where n ranges from 1 to 4, as described by White and Hyde [170].) The central planar defect is formed by removing (conceptually) a stoichiometric layer of olivine and hence does not involve any local chemical change. Drury suggests that the climb-dissociated dislocations may be involved in the olivine \rightarrow humite transformation, which occurs in mafic rocks.

The lack of significant glide dissociation in dry olivine suggests that glide is controlled by kink pair nucleation on perfect dislocations. For the case of hydrated olivine, it is not known whether the wider dissociation applies to glide as well as climb dissociation. If it does, then it could well be that kink nucleation is occurring on partials for hydrated olivine and on perfect dislocations for dry olivine, hence explaining water weakening. As described in Section 4.12, the climb-dissociated configuration has a lower energy than the glide-dissociated configuration (provided that the stacking fault energy is fairly isotropic), so that the observation of the former does not necessarily mean that climb is rate-controlling. In materials with a high Peierls stress, kink pair nucleation and propagation should always be rate-controlling, even when extensive climb occurs.

4.10. Other oxides

Slip systems in other oxides are summarized in Table 5 and observed dislocation dissociation in Table 6. None of the other oxides appear to exhibit the diversity of behaviour of sapphire and spinel with regard to dislocation substructures and dissociations; this may be because they have not received the same attention. Given that the stacking fault energy is likely to be high, particularly if anion faults are involved, it is not surprising that dissociation has not been observed in the rock salt oxides, as described in Section 4.1. Similarly, no dissociation has been reported in the fluorite-structured oxides ZrO_2 - Y_2O_3 and UO_2 [69], or in the anti-fluorite oxide, Cu_2O [171]. In all cases, a high energy cation plus anion fault would be created. An exception is BeO , as described in Section 4.2.2, where the fault represents a unit slice of the sphalerite structure.

Two other oxide structures are listed in Tables 4 to 6 that deserve further discussion—the rare-earth sesquioxides (M_2O_3) and oxides with the garnet structure. Both are compact oxides, but not close-packed in the traditional sense, with a large unit cell based on a body-centered cubic I lattice. The shortest lattice vector, $1/2\langle 111 \rangle$, is very large in both cases (0.92 and 1.04 nm respectively) and plastic deformation is only possible at very high temperatures.

4.10.1. Oxides with the cubic rare-earth sesquioxide structure

Plastic deformation has been studied in single crystals of Y_2O_3 [172–174] and Er_2O_3 [175, 176]. For Y_2O_3 , Gaboriaud et al. [173] report the presence of $1/2\langle 111 \rangle$, $\langle 100 \rangle$ and $\langle 110 \rangle$ dislocations after creep deformation at temperatures from 1550 to 1800°C and stresses from 20 to 140 MPa. It is not clear whether the $\langle 110 \rangle$ dislocations (with a 1.5 nm Burgers vector!) result from glide on $\{001\}$ planes or from reactions between $1/2\langle 111 \rangle$ dislocations. The $\langle 100 \rangle$ dislocations are important in the high temperature range and are dissociated by climb into $1/2\langle 100 \rangle$ collinear partials. The $1/2\langle 111 \rangle$ dislocations are dissociated by glide in the $\{110\}$ plane according to



The $\langle 110 \rangle$ dislocations are dissociated into four $1/4\langle 110 \rangle$ collinear partials. The SFE of the middle fault is surprisingly low, $\sim 80 \text{ mJ/m}^2$, and it is suggested that this is because only the fourth plane–plane interactions are changed by the fault [174]. For Er_2O_3 single crystals [175,176], temperatures in excess of 1600°C and stresses of $\sim 100 \text{ MPa}$ were required for plastic deformation at a strain rate of $\sim 10^{-4} \text{ s}^{-1}$. Only $\langle 111 \rangle\{110\}$ slip was observed. The $1/2\langle 111 \rangle$ dislocations were found to be dissociated according to eq. (34) and the authors point out that the partial Burgers vectors connect cation positions in the structure.

4.10.2. YAG and other oxides with the garnet structure

Synthetic garnets such as YAG (yttrium aluminum garnet, $\text{Y}_3\text{Al}_5\text{O}_{12}$), YIG (yttrium iron garnet) and GGG (gadolinium gallium garnet) are of interest for use as substrates for bubble memory and other electronic devices, while natural silicate garnets are of interest because they are the dominant minerals in the transition zone of the earth's mantle and hence may control its rheology [177]. For the synthetic garnets, YIG single crystals can be deformed plastically at temperatures as low as 1200°C [178,179], GGG can be deformed at temperatures above $\sim 1450^\circ\text{C}$ [180–182], while YAG requires temperatures as high as 1600°C [183,184]. As pointed out by Karato et al. [177], the stress–temperature behavior of the various garnets (including natural minerals) scales as the elastic modulus and melting temperature. In all cases, the slip direction is $\langle 111 \rangle$, as expected for the bcc lattice; the most commonly observed slip plane is $\{110\}$ but $\{112\}$ and $\{123\}$ slip planes are also frequently seen. Such behavior is reminiscent of simple bcc metals. Indeed, Rabier and Garem [182] find that GGG slips on $\{011\}$ planes when compressed along $[001]$ and $\{112\}$ slip planes (in the twinning sense) when compressed along $[110]$; such behavior is similar to the slip asymmetry observed in bcc metals. They suggest that the core structure of screw dislocations in garnets is also asymmetrical. All of the synthetic garnets exhibit dissociation of $1/2\langle 111 \rangle$ dislocations into two collinear partials [178,179,182,183]:



The ribbon width is variable and involves both glide and climb, so that it may be non-equilibrium. The $1/4\langle 111 \rangle$ fault vector causes initially empty sites in the perfect structure

to be filled by tetrahedral and dodecahedral cations, so that the SFE should be high. Reaction (35) could not be detected in dislocations introduced into silicate garnets by compression under a high confining pressure at temperatures of 1000°C and above [185], indeed suggesting that the SFE in all the garnets is high.

4.11. SiC, Si_3N_4 and other non-oxide ceramics

In the present review, we have concentrated on oxide-ceramics. However, there is a considerable literature on non-oxide ceramics—principally borides, carbides and nitrides—that would be worthy of another review. In this section, we will confine ourselves to a few remarks about two important structural ceramics, silicon carbide and silicon nitride. However, it is worth mentioning the so-called refractory hard metals, typified by the carbides and nitrides of the group IVA and VA transition metals. These have the rock-salt structure but, unlike the alkali halides, single crystals are not ductile and require temperatures greater than about 900°C for plastic deformation, in spite of the fact that the $1/2\langle 110 \rangle$ dislocations are dissociated, as in fcc metals, into Shockley partials on the {111} plane [186]. Most of these refractory compounds have a wide range of stoichiometry. In TiC_{1-x} , for example, Tsurekawa et al. [187] observed that the CRSS decreased by $\sim 50\%$ as x increased from 0.05 to 0.14, i.e., compositional softening occurred. It then increased again when x increased to 0.25, a phenomenon that the authors attributed to ordering. Also, solution softening occurred when Mo was substituted for Ti. We believe that these results need to be re-evaluated in terms of the kink model presented in Section 2, including the possible role of SFE and point defects.

4.11.1. Silicon carbide

As mentioned in Section 4.2, SiC has a relatively low SFE. This is reflected in the fact that SiC occurs in numerous polytypes with different stacking of the Si–C tetrahedra. The β -phase consists of a single 3C cubic polytype with the sphalerite structure while the α -phase consists of a mixture of hexagonal or rhombohedral polytypes. Only the hexagonal 6H polytype is available in large enough single crystal form for plastic deformation studies. Pirouz [188] has summarized the results of such studies. 6H-SiC is highly anisotropic and deforms at high temperature on the basal plane. If crystals are compressed parallel to the basal plane, kinking occurs but only at stresses of ~ 6 GPa and temperatures above 1000°C [189]. For crystals oriented for basal slip, plastic deformation occurs at much lower stresses (down to ~ 20 MPa) in the temperature range of 800–1400°C [188]. In the higher temperature range the $1/3\langle 11\bar{2}0 \rangle$ dislocations are dissociated into Shockley partials with a separation corresponding to a SFE $\sim 2 \text{ mJ m}^{-2}$. In the lower temperature range only Shockley partials are observed; in heavily deformed regions the motion of the partials is such as to induce the $\alpha \rightarrow \beta$ transformation. Pirouz points out that the core structure of the two types of partials are quite different, one with C–C bonds and the other with Si–Si bonds, so that the activation energies for kink pair formation and/or kink migration are also quite different. This possibility was not allowed for in the analysis of kink behavior on partial dislocations in Section 2.4 but certainly could be.

4.11.2. Silicon nitride

There are two phases of silicon nitride, $\alpha\text{-Si}_3\text{N}_4$ and $\beta\text{-Si}_3\text{N}_4$. The β form is hexagonal ($P6_3/m$) with $a = 0.761$ nm and $c = 0.291$ nm while the α form is trigonal ($P31c$) with roughly the same dimensions for the a axis and approximately double the dimensions for the c axis. Synthesized powder consists generally of $\alpha\text{-Si}_3\text{N}_4$ and subsequent sintering converts the structure to the β form. Most interest in silicon nitride has been in using sintering additives to control the grain shape and the grain boundary phase to produce a polycrystalline material with high toughness and high temperature creep resistance. Plastic deformation at high temperatures is due to grain boundary sliding with little contribution from dislocation motion [190]. Single crystals of $\alpha\text{-Si}_3\text{N}_4$ suitable for plastic deformation studies have been grown by chemical vapor deposition. These could be deformed plastically at a yield stress of ~ 250 MPa at 1760°C and ~ 50 MPa at 1820°C . Such a steep drop in yield stress indicates a high activation energy, as would be expected for kink pair nucleation with a large Burgers vector [191]. In fact TEM observations revealed $1/3\langle 11\bar{2}0 \rangle$ dislocations (0.78 nm Burgers vector) with no discernible dissociation [191]. The slip plane was $\{1\bar{1}01\}$. Knoop hardness anisotropy indicated the same slip system at room temperature [192]. There have been no comparable studies of $\beta\text{-Si}_3\text{N}_4$; however, dislocations with Burgers vectors $1/3\langle 11\bar{2}0 \rangle$, $[0001]$ and $1/3\langle 11\bar{2}3 \rangle$ occur in sintered material [190]. The same Burgers vectors are found in as-grown $\alpha\text{-Si}_3\text{N}_4$ single crystals [193]. Note that the $[0001]$ Burgers vector in $\beta\text{-Si}_3\text{N}_4$ is relatively short (0.291 nm) and we would expect this to be the most active dislocation in plastically deformed single crystals.

4.12. Climb versus glide dissociation

One phenomenon of interest that became apparent during the early application of electron microscopy to the study of dislocations in ceramics was the predominance of climb dissociation in many oxides during high temperature deformation. This was first discovered in sapphire and spinel but has, since then, become a commonplace observation in other ceramics such as perovskite and forsterite, and also in many intermetallics deformed at high temperatures. Climb dissociation involves redistribution of matter between the half planes of the partials by short circuit diffusion along the fault plane (see Fig. 16). It is easily shown that the climb configuration has the lowest energy barring some pathological anisotropy in the fault energy. This is shown by writing down the sum of the interaction energy and the fault energy per unit length

$$\frac{W_{12}}{L} + \frac{W_{SF}}{L} = \frac{\mu b_1 b_2}{2\pi(1-\nu)} \left[-\ln \frac{r}{\rho} - \sin^2 \theta \right] + \gamma(\theta)r, \quad (36)$$

where b_1 and b_2 are the Burgers vectors of the two partials (assumed here for simplicity to be collinear), ρ is the core radius, $\gamma(\theta)$ is the fault energy, r is the spacing of the partials and θ is the angle between the fault plane and slip plane. Differentiation of eq. (5) gives the equilibrium separation

$$r_{eq} = \frac{\mu b_1 b_2}{2\pi(1-\nu)\gamma(\theta)}, \quad (37)$$

which is independent of θ except through γ . The difference in energy between the glide ($\theta = 0^\circ$) and climb ($\theta = 90^\circ$) configurations is

$$\frac{\Delta W}{L} = \frac{\mu b_1 b_2}{2\pi(1-\nu)} \left[\ln \frac{\gamma(90)}{\gamma(0)} - 1 \right], \quad (38)$$

which is positive provided $\gamma(90) > 2.72\gamma(0)$, i.e., the climb configuration should have the lowest energy unless the fault energy in the glide plane is very small. Table 9 shows that the fault energy in sapphire is not very anisotropic and so that climb configuration should always dominate.

Glide dissociation should always make glide easier by reducing the Peierls barrier, while climb dissociation would make glide more difficult. However, at elevated temperatures, where short circuit diffusion between the partials is rapid, it is possible for a dislocation to change quickly from a climb-dissociated to a glide-dissociated configuration as the dislocation starts to move under stress, and to adopt the climb-dissociated configuration when stationary. This can be accomplished by simultaneous glide of one partial and climb of the other partial onto the glide plane. A number of mechanisms were at one time proposed to explain how climb dissociation controls the flow stress [16]; however, we now think that the stress is controlled by a kink mechanism, as described in the Section 2. Nevertheless, climb dissociation has been a fascinating side-show.

5. Work hardening

Oxide crystals exhibit a variety of work hardening behavior. We will discuss only three systems in this section—MgO, spinel and sapphire.

5.1. Work hardening in MgO

MgO crystals are generally found to show two-stage hardening, a region of low hardening rate after yielding, followed by a linear region with a work hardening rate $\sim \mu/300$ [30]. The latter value is the standard rate observed in stage II of fcc crystals. MgO crystals can only be deformed in compression out to a strain $\sim 10\%$ and so it is possible that a third stage is never reached. The dominant features of the deformation microstructure of MgO in stage I are dipoles and elongated loops [194], much as in stage I of fcc metals. The hardening mechanisms are likely the same, namely that the dipoles are formed by the trapping of dislocations of opposite signs on parallel slip planes and this controls the hardening [195]. At higher temperatures the dipoles tend to break up into rows of loops, as in sapphire (Fig. 15). We recall that, in the rock-salt structure, the $\{110\}\langle 1\bar{1}0 \rangle$ and $\{1\bar{1}0\}\langle 110 \rangle$ slip systems have the same Schmid factor and are both activated. Apparently, these two systems do not intersect in stage I but are forced to do so in stage II. At high temperatures, where climb can occur, a cell structure is formed but climb also contributes to recovery and the work hardening rate decreases. The hardening rate in stage II of $\sim \mu/300$ occurs in the temperature range of 200–500 K [30] where no cell structure forms and the most

significant microstructural features are the elongated loops and dipoles. In the absence of a cell structure, the mechanism for the stage II work hardening rate in MgO must be quite different from that in fcc metals (see, for example Hirsch and Mitchell [196]). The likely mechanism for MgO is that slip on one system has to cut through the debris (dipoles, elongated loops) formed on the other system. In the alkali halides, a small amount of slip is observed on the oblique $\{110\}\langle 110 \rangle$ systems and this may also contribute to work hardening [4]. The alkali halides in addition exhibit a stage III with a decreasing hardening rate which is ascribed to recovery by cross-slip on the $\{001\}$ plane [4].

5.2. Work hardening and work softening in spinel

$\text{MgO} \cdot n\text{Al}_2\text{O}_3$ spinel reveals a variety of stress-strain behaviors, depending on stoichiometry, orientation and temperature. Examples are shown in Fig. 23 [25,137]. Some general observations are as follows:

- There is sometimes a yield-point but the yield-point is never as sharp as has been reported in, for example, sapphire [197,198].
- Sometimes the yield-point is followed by an extensive region of work-softening, especially in stoichiometric spinel.
- Sometimes the yield-point is followed by a region of easy glide (low work-hardening rate) but it is never as extensive or obvious as in sapphire [199] or MgO [30].
- By 10% shear strain or before, the flow stress has reached a steady state value or, in other words, the specimen is creeping at the imposed strain rate under the resulting flow stress, i.e., the work hardening and recovery rates are equal.
- Stress-strain curves for $\{111\}\langle 110 \rangle$ and $\{110\}\langle 110 \rangle$ slip show similar features although work softening appears to be more dramatic for $\{110\}\langle 110 \rangle$ slip in stoichiometric spinel (see Fig. 23d).

The work hardening rate in the first percent or so of strain is very high, with values given by

$$\theta = \frac{d\tau}{d\gamma} \approx 2000 \text{ to } 3000 \text{ MPa} \approx \frac{\mu}{40} \text{ to } \frac{\mu}{60}, \quad (39)$$

where τ and γ are the shear stress and shear strain respectively. This should be compared with the value of $\theta \sim \mu/300$ for stage II hardening in fcc metals. The high initial hardening rate in spinel has been ascribed to the rapid build-up in the dislocation density to a value of about 10^{13} m^{-2} at a strain of less than 1% [137]. The rapid build-up is due to the small slip distance which in turn is due to the formation of a three-dimensional dislocation network by climb. Apparently the very first dislocation sources emit dislocations which travel far enough to give the observed slip lines on the surface. Dislocations which remain in the crystal are able to climb into low energy dislocation networks which then form effective barriers to further dislocation glide, reducing the slip distance and increasing the dislocation density. Donlon et al. [137] estimate the slip distance at the maximum in the shear stress to be $\sim 2 \mu\text{m}$ in stoichiometric spinel.

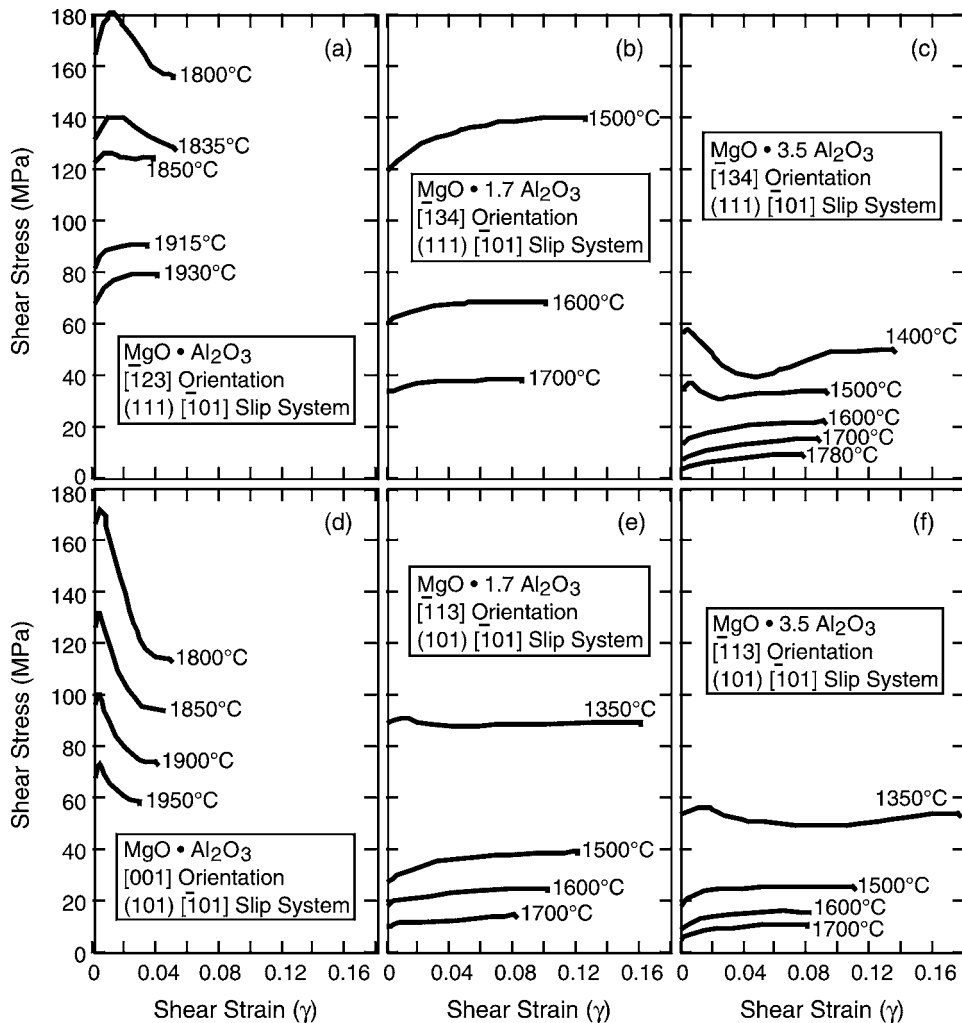


Fig. 23. Stress-strain curves of spinel single crystals of stoichiometry $n = 1$ (left), $n = 1.7$ (middle) and $n = 3.5$ (right) for slip on $\{111\}$ planes (top) and $\{110\}$ planes (right) [18].

The work softening phenomenon is then due to a *reduction* in dislocation density with increasing strain. This was shown clearly by Donlon et al. [137] who measured the dislocation density, ρ , by transmission electron microscopy. They measured the dislocation density as a function of stress for stoichiometric spinel deformed at various stresses and temperatures and found

$$\tau = \tau'_0 + \alpha \mu b \rho^{1/2}, \quad (40)$$

where $\tau'_0 \sim 30$ MPa is a constant frictional stress and α is a constant estimated to be ~ 0.7 from the data. This value of α is at the upper end of the range from 0.1 to 1.0 typically found in other materials. However, it should be appreciated that most of the data were obtained in the work softening regime, whereas eq. (40) is usually used to describe work hardening! For example, for the 1800°C data, they found that the dislocation density decreased as the strain increased from 1.5% to 30%. Normally, yield-points are ascribed to dislocation multiplication and the concomitant increase in mobile dislocation density and decrease in average dislocation velocity. In spinel, the initial dislocation multiplication leads to work hardening and subsequent dislocation annihilation by climb leads to work softening. The role of the mobile dislocation density is not at all clear. Possibly, climb effectively immobilizes the majority of the dislocations so that the available mobile dislocation density (for glide) remains approximately constant. Of course, both glide and climb of dislocations contribute to the strain rate; however, Donlon et al. [137] estimate that glide is roughly twice as important as climb in controlling the strain rate.

5.3. Work hardening in sapphire

Stress-strain curves in sapphire exhibit three-stage hardening both for basal and prism plane slip [96,199]. The mechanisms for each are quite different from each other and from those described above.

5.3.1. Basal plane slip

Typical basal slip stress-strain curves are shown in Fig. 24 [199]. A yield point is followed by a short region of easy glide, then a region of high work hardening (called stage A), after which the work hardening rate decreases (stage B) until a plateau is reached (stage C).

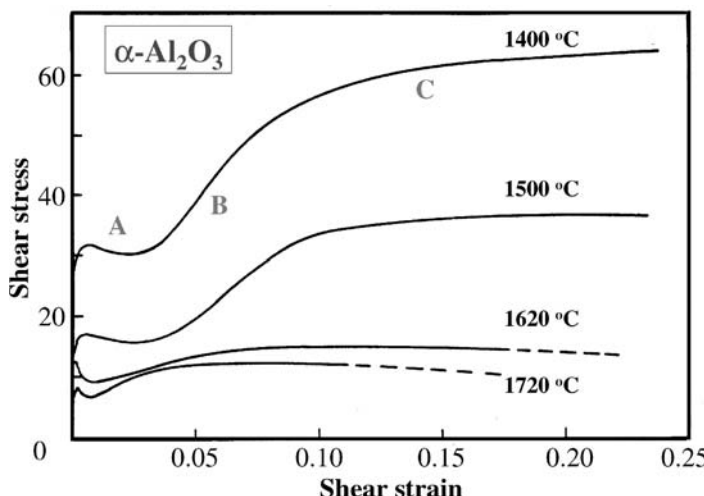


Fig. 24. Stress-strain curves of sapphire deformed in basal glide at various temperatures [199].

Dislocation density measurements gave results consistent with eq. (40). The region after the yield point is characterized by the accumulation of dipoles and elongated loops, as in fcc metals, although, even at this early stage, the dipoles have started to break up into small loops, both faulted and unfaulted (see Fig. 15). Stage A work hardening is thought to be due to the interaction of glide dislocations with loops, which have accumulated to the point that they can block a glide dislocation all around its perimeter [199]. Recovery in stage B is due to the annihilation of loops by climb; in stage C, the rate of accumulation of loops by dipole break-up is balanced by their rate of annihilation by climb. That work hardening occurs at all is because dipole break-up is controlled by pipe diffusion while annihilation is controlled by self-diffusion (of oxygen ions). The interaction cross-section is related to the product of the length of a loop, l , and its height, h ; the latter is inversely proportional to the stress. The rate of accumulation of loops is calculated from the number of dipoles formed and the wavelength, λ , for the break-up of the dipoles. Pletka et al. [199] show that the stage A work hardening rate is

$$\theta_A = \frac{\mu l}{48\pi(1-\nu)\lambda} = \frac{\mu}{96\pi(1-\nu)}, \quad (41)$$

assuming that $l/\lambda \approx 1/2$. Eq. (41) yields a work hardening rate of about $\mu/225$, in good agreement with the experimental value of $\mu/300$ in stage A. Stages B and C are easily modeled by taking into account standard expressions for the shrinkage rate of the loops [199], giving for the work hardening rate in region B

$$\theta = \frac{\mu}{96\pi(1-\nu)} \left[1 - \frac{\mu b^4 D}{0.3kT\dot{\varepsilon}h^3} \right], \quad (42)$$

where D is the oxygen diffusion coefficient, $\dot{\varepsilon}$ is the strain-rate, and h is the average height of a newly formed dipole given by

$$h = \frac{\mu b}{16\pi(1-\nu)(\tau - \tau_0)}. \quad (43)$$

Good agreement is obtained with experiment for stage B from eq. (42). The plateau stress τ_p is easily obtained by equating (42) to zero, giving

$$\tau_p - \tau_0 = \frac{\mu b}{75(1-\nu)} \left(\frac{kT\dot{\varepsilon}}{\mu b^4 D} \right)^{1/3}. \quad (44)$$

Diffusion rates calculated from this are again in good agreement with experiment [199]. Overall, the model for work hardening and recovery, based on loop accumulation by dipole break-up and loop annihilation by climb, is very satisfactory.

5.3.2. Prism plane slip

Stress-strain curves similar to those in Fig. 24 are observed for prism plane slip, except that the hardening rate in region A is much higher, $\sim \mu/40$ [96]. Although many loops are

observed in deformed crystals, the most important feature of the dislocation substructure is thought to be the 3-dimensional network that forms. The network is mostly made up from $1/3\langle 11\bar{2}0 \rangle$ dislocations and it is suggested that these arise from the decomposition of the $\langle 10\bar{1}0 \rangle$ prism plane dislocations that have cross-slipped onto the basal plane via the decomposition reaction [96]:



The network acts as a “forest” threading the prism slip plane and impeding slip on this plane. A forest theory of hardening is inapplicable to metals because the model is too homogeneous; it does not take into account the observed cell structure and gives a hardening rate that is too high [195]. By contrast, the forest theory is well suited for explaining the high work hardening rate in sapphire deforming by prism plane slip, because the observed network is relatively homogeneous and the slip distance is just a few times the network spacing. However, Cadoz et al. [96] had difficulty explaining quantitatively the level of the plateau stress. They developed an expression similar to eq. (44) by equating the rate of accumulation of dislocations in the network by glide and the rate of the annihilation of dislocations in the network by climb. However, the calculated diffusion rates were too fast for bulk diffusion and could only be explained by pipe diffusion.

6. Solution hardening

Solution hardening in oxides can occur by the substitution of either isovalent or aliovalent cations (substitutional anions have not been studied). Aliovalent cations give much greater hardening rates. Solution hardening theory basically follows along the lines developed for metals. Solution hardening due to isovalent cations is due to a combination of size and elastic modulus misfit. Solution hardening due to aliovalent cations is due to the asymmetric distortion around defect complexes formed with charge-compensating defects. Solution hardening is more rapid at low temperatures and there is usually a plateau in the temperature dependence at high temperatures. At low temperatures and low concentrations where the solutes act as point obstacles, Friedel–Fleischer statistics are followed and the yield stress increases as $c^{1/2}$. In the plateau region and at higher concentrations, where the solutes act as diffuse obstacles, Mott–Labusch statistics are followed and the yield stress increases as $c^{2/3}$. However, even in metals, where there are much more data, these simple rules are not always obeyed very well. We will discuss solution hardening due to isovalent substitutionals first.

6.1. Isovalent cations

There has been little systematic study of solution hardening by isovalent solutes in oxides compared, say, with substitutional solutes in fcc metals. For sapphire, Pletka et al. [200] have compared the effects of Cr^{3+} and Ti^{3+} on the yield strength at high temperatures.

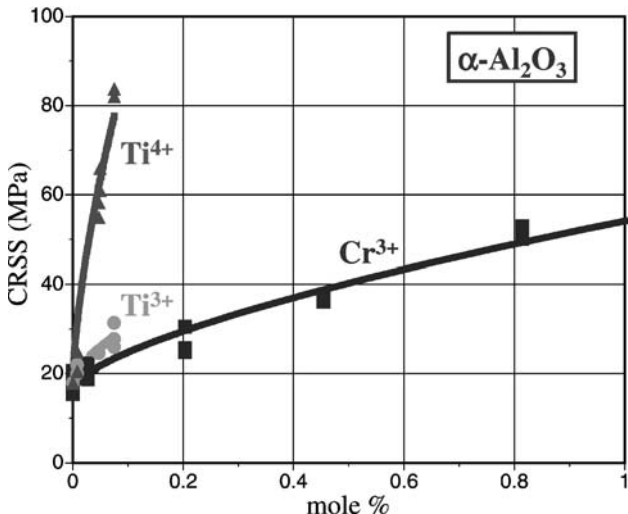


Fig. 25. Critical resolved shear stress versus mole % of oxide solute (for cations in the form of Cr³⁺, Ti³⁺ and Ti⁴⁺) in sapphire deformed at 1500°C. The curves through the data correspond to a $c^{2/3}$ dependence (data from Pletka et al. [200]).

Their results are shown in Fig. 25; the curves through the data correspond to a $c^{2/3}$ dependence which is a slightly better fit than the $c^{1/2}$ dependence for the Cr³⁺ data while the Ti³⁺ data is too sparse to distinguish between them. The hardening rate due to Ti³⁺ is about a factor of two higher than that due to Cr³⁺. Yield stress curves at other temperatures were found to be parallel to those in Fig. 25, suggesting that the stress due to solution hardening is additive with the yield stress of pure sapphire, and that the data are in the plateau regime of solution hardening behavior.

The only data for MgO appear to be for isovalent Ni²⁺ additions [201]. The hardening rate at ambient temperature is somewhat higher than that for Ti³⁺ in sapphire and the data best fits a $c^{1/2}$ law. The plateau regime begins at about 400°C for MgO (at least for Fe³⁺ additions [202]) and so the yield stress behavior is in the low temperature region where the solution hardening rate is temperature dependent.

Pletka et al. [200] analyzed the solution hardening rate in sapphire using the Labusch model [203] where the increment in yield stress due to solution hardening in the plateau regime is given by

$$\Delta\tau = z_L \mu c^{2/3} \varepsilon_L^{4/3}, \quad (46)$$

where z_L is a constant equal to 1/750 and ε_L is given by

$$\varepsilon_L = (\eta'^2 + \alpha^2 \delta^2)^{1/2}, \quad (47)$$

where α is equal to 3 for screw dislocations and 16 for edge dislocations and the modulus and size misfit parameters are given respectively by

$$\eta' = \frac{\eta}{1 + |\eta|/2}, \quad \eta = \frac{1}{\mu} \frac{d\mu}{dc}, \quad (48)$$

$$\delta = \frac{1}{a} \frac{da}{dc}. \quad (49)$$

Mostly edge dislocations are observed at high temperatures in sapphire, so that α is taken as 16. This means that the size misfit term δ in eq. (49) dominates. Pletka et al. [200] show that δ for Ti^{3+} additions is about 1.6 times larger than for Cr^{3+} additions and this explains quantitatively the difference in the hardening rates in Fig. 25.

6.2. Aliovalent cations

The most extensively studied systems are Ti^{4+} in sapphire (Fig. 25) and Fe^{3+} in MgO (Fig. 26). Fig. 25 shows that the hardening rate due to Ti^{4+} is about a factor of 6 times that due to Ti^{3+} [200]. There is no equivalent data for Fe^{2+} compared with Fe^{3+} in MgO but the hardening rate due to Fe^{3+} is also about a factor of six times that due to Ni^{2+} in MgO [201]. As stated above, this is due to the formation of charge-compensating defect complexes—three Ti^{4+} substitutionals with one Al cation vacancy (or a titanium–oxygen interstitial defect [204]) in the sapphire case and two Fe^{3+} substitutionals with one Mg cation vacancy

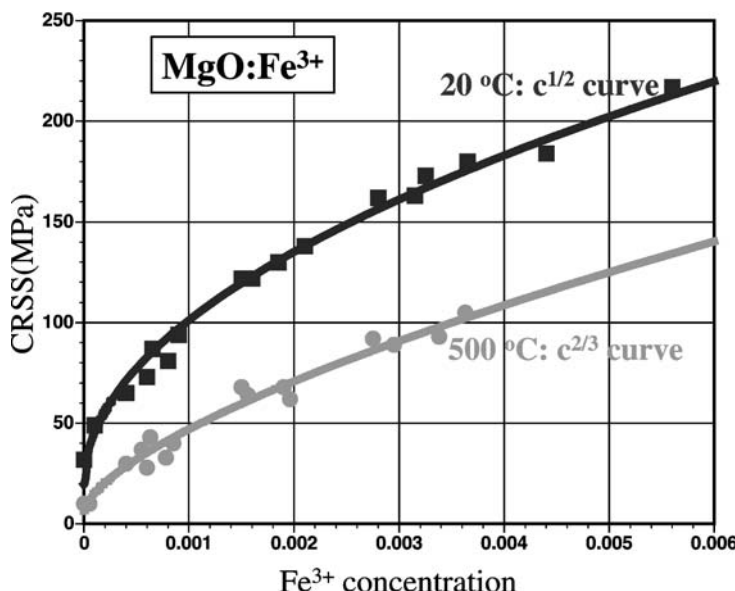


Fig. 26. Yield stress versus concentration of Fe^{3+} dopant in MgO (data from Reppich [202]).

in the MgO case. The elastic strains around such complexes are asymmetrical (the so-called “tetragonal” distortion) and they interact more strongly with dislocations than do isostructural cations. Fig. 26 shows that the hardening due to Fe³⁺ in MgO follows a $c^{1/2}$ dependence at low temperatures and a $c^{2/3}$ dependence in the plateau regime at high temperatures [202]. The data for Ti⁴⁺ in Al₂O₃ are too sparse to distinguish between the two laws.

The $c^{1/2}$ law at low temperatures implies Friedel–Fleischer statistics for the increment of yield stress due to solution hardening:

$$\Delta\sigma_y = f_m^{3/2} c_p^{1/2} / (2\Gamma)^{1/2} b, \quad (50)$$

where f_m is maximum force between defect and dislocation and c_p is the planar concentration of defects (i.e., the number of defects per unit area in the glide plane of the dislocation). c_p is related to the concentration of defects per unit volume, c_v , and the fractional concentration, c , by $c_p = \beta c_v n_d d = \beta(c/n_d \Omega) n_d d = \beta c d / \Omega$, where d is the diameter of the defect (or the separation of the aliovalent cation and its charge compensating defect), n_d is the number of cation impurities per defect cluster, and β is the fraction of defects oriented to interact with the dislocation. The line tension can be written as $\Gamma = \alpha \mu b^2$ and so eq. (50) becomes

$$\Delta\sigma_y = \left(\frac{\beta f_m^3 d}{2\alpha \mu b^4 \Omega} \right)^{1/2} c^{1/2} \quad (51)$$

with f_m given by

$$f_m = \frac{\mu \Delta \varepsilon \Omega^{\text{def}} \sqrt{2}}{\pi b} \approx \frac{1}{3} \mu \Delta \varepsilon b^2, \quad (52)$$

where $\Delta \varepsilon$ is the tetragonality (the difference in strain along two orthogonal directions) and Ω^{def} is the volume of the defect. Eq. (52) therefore predicts that the yield stress should increase as the square root of the concentration, as is generally observed at low temperatures. This analysis can be made more sophisticated by using anisotropic elasticity [205]. The solution hardening rates from eqs (51) and (52) strictly apply only at 0 K. Reppich [202] found that the MgO/Fe³⁺ system followed a $\sigma^{1/2} - T^{1/2}$ law and so the yield stress data can be extrapolated to 0 K. From this the tetragonality can be calculated to be 0.12 [205]. No such extrapolation is possible for the Al₂O₃/Ti⁴⁺ system but use of the high temperature data in Fig. 25 gives ~ 0.05 . Of course, the defect clusters are in no sense tetragonal and so the value of $\Delta \varepsilon$ represents the strength of the cluster.

7. Closing remarks

We have shown that the commonly held belief that the words “ceramic” and “brittle” are synonymous is not exactly tenable. Oxide single crystals with the rock-salt structure can be deformed plastically at liquid helium temperatures. Strontium titanate shows an inverse ductile-to-brittle transition and can be deformed plastically at ambient temperatures and

below. Oxides with the fluorite structure can be deformed plastically at temperatures of a few hundred degrees, especially if great care is taken to use crystals that are free of defects and well-aligned. There is also the issue of crystal purity. We believe that lessons could be learned from experience with bcc metals which were thought to be brittle in the early days before techniques were developed to reduce interstitial contents to the level of a few ppm. Who knows how crystals such as BeO and ZnO would behave if such levels of purity could be achieved. Of course, it is unlikely that oxides with large unit cells such as garnets, spinels and rare-earth sesquioxides would lower their brittle-to-ductile transition temperatures significantly. However, with the surprising behavior of the perovskite strontium titanate, we submit that a renewed effort would be worthwhile.

For those ceramics with a high Peierls stress, we have shown that the CRSS can be understood consistently in terms of a model of kink pair nucleation and motion on dislocations. The steep temperature dependence is governed by an activation energy that is the sum of the elastic energy for kink pair formation and the energy for the kinks to overcome their secondary Peierls barriers.

The kink model has been modified to take into account kink nucleation on point defects and kink nucleation on partial dislocations. Kink nucleation on partial dislocations is easier because the elastic energy is so much less. We suggest that this is the reason for plasticity at low temperatures in SrTiO₃ and possibly for the remarkable softening observed in non-stoichiometric MgO-Al₂O₃ spinel as the SFE is reduced. Most ceramic oxides have a high SFE and so kink nucleation is forced to occur on perfect dislocations at much higher stresses. We predict that, if the SFE of a given oxide could be reduced by alloying, the BDT temperature would also be reduced. So far as kink nucleation on point defects is concerned, it is a viable mechanism for explaining the water weakening phenomenon that is well known in quartz but also occurs in olivine and alumina. It is also a possible mechanism for softening in spinel, in competition with the SFE effect.

Acknowledgments

Over the years, our research on plastic deformation of ceramics at CWRU was supported by the National Science Foundation, the Air Force Office of Scientific Research, the Army Research Office and the Department of Energy, Office of Basic Energy Sciences. The latter supported this research at Los Alamos, along with the Laboratory-Directed Research and Development program. We have also enjoyed collaborations with many students and colleagues, such as the late J. Cadoz, J. Castaing, D.S. Cheong, A. Dominguez-Rodriguez, W.T. Donlon, J.P. Hirth, R.J. Keller, K.P.D. Lagerlöf, K.J. McClellan, the late D.S. Phillips, P. Pirouz and B.J. Pletka, to name but a few.

References

- [1] E. Schmid and W. Boas, *Kristallplastizität* (Springer, Berlin, 1935).
- [2] H. Landolt and R. Bornstein, *Physikalische-chemische Tabellen* (Springer, Berlin, 1927).
- [3] O. Mügge, *Götting. Nachr.* (1899) 56.

- [4] M.T. Sprackling, *The Plastic Deformation of Simple Ionic Crystals* (Academic Press, London, 1976).
- [5] P. Haasen, in: *Dislocations and Properties of Real Materials*, ed. M.H. Loretto (The Institute of Metals, London, 1985) p. ???.
- [6] J.B. Wachtman and L.H. Maxwell, *J. Amer. Ceram. Soc.* 37 (1954) 291.
- [7] M.L. Kronberg, *Acta Metall.* 37 (1957) 291.
- [8] J. Hornstra, *J. Phys. Chem. Solids* 15 (1960) 311.
- [9] A.G. Evans and A.H. Heuer, *J. Amer. Ceram. Soc.* 63 (1980) 241.
- [10] P.B. Hirsch, in: *Dislocations and Properties of Real Materials*, ed. M.H. Loretto (Institute of Metals, London, 1985) p. 333.
- [11] H. Alexander, in: *Dislocations in Solids*, ed. F.R.N. Nabarro (North Holland, Amsterdam, 1986) p. 113.
- [12] M.S. Paterson, in: *Dislocations and Properties of Real Materials*, ed. M.H. Loretto (Institute of Metals, London, 1985) p. 359.
- [13] J.B. Wachtman, *Amer. Ceram. Soc. Bull.* 46 (1967) 756.
- [14] G.R. Terwilliger and K.C. Radford, *Amer. Ceram. Soc. Bull.* 53 (1974) 172.
- [15] T. Bretheau, J. Castaing, J. Rabier and P. Veyssiére, *Adv. Phys.* 28 (1979) 835.
- [16] T.E. Mitchell, K.P.D. Lagerlöf and A.H. Heuer, *Mater. Sci. Tech.* 1 (1985) 944.
- [17] J. Castaing, P. Veyssiére, L.P. Kubin and J. Rabier, *Philos. Mag. A* 44 (1981) 1407.
- [18] T.E. Mitchell, *J. Amer. Ceram. Soc.* 82 (1999) 3305.
- [19] P. Veyssiére and C.B. Carter, *Philos. Mag. Lett.* 57 (1988) 211.
- [20] P. Veyssiére, S.H. Kirby and J. Rabier, *J. Phys. (Paris)* 41 (1980) 175.
- [21] J.H. Westbrook, *Rev. Hautes Tempér. et Réfract.* 3 (1966) 47.
- [22] J.P. Hirth and J. Lothe, *Theory of Dislocations* (Krieger, Melbourne, FL, 1992).
- [23] T.E. Mitchell, J.P. Hirth and A. Misra, *Acta Mater.* 50 (2002) 1087.
- [24] T.E. Mitchell, P. Peralta and J.P. Hirth, *Acta Mater.* 47 (1999) 3687.
- [25] W.T. Donlon, A.H. Heuer and T.E. Mitchell, *Philos. Mag. A* 78 (1998) 615.
- [26] T.E. Mitchell, P.M. Anderson, M.I. Baskes, S.P. Chen, R.G. Hoagland and A. Misra, *Philos. Mag. A* 83 (2003) 1329.
- [27] H. Inui, K. Ishikawa and M. Yamaguchi, *Intermetallics* 8 (2000) 1131.
- [28] J.J. Gilman, *Acta Metall.* 7 (1959) 608.
- [29] J.B. Bilde-Sørensen, B.F. Lawlor, T. Geipel, P. Pirouz, A.H. Heuer and K.P.D. Lagerlöf, *Acta Mater.* 44 (1996) 2145.
- [30] M. Srinivasan and T.G. Stoebe, *J. Mater. Sci.* 9 (1974) 121.
- [31] C.H. Woo and M.P. Puls, *Philos. Mag.* 35 (1977) 1641.
- [32] G.W. Watson, E.T. Kelsey and S.C. Parker, *Philos. Mag. A* 79 (1999) 527.
- [33] K.C. Gorecka and J.L. Routbort, *Acta Metall.* 35 (1987) 1047.
- [34] E. Jolles and C. Monty, *Philos. Mag. A* 64 (1991) 765.
- [35] A. Dominguez-Rodriguez, M. Sanchez, R. Marquez, J. Castaing, C. Monty and J. Philibert, *Philos. Mag. A* 46 (1982) 411.
- [36] J. Castaing, M. Spendel, J. Philibert, A.D. Rodriguez and R. Marquez, *Revue Phys. Appl.* 15 (1980) 277.
- [37] J.L. Routbort, *Acta Metall.* 30 (1982) 663.
- [38] A. Dominguez-Rodriguez, J. Castaing, H. Koizumi and T. Suzuki, *Revue Phys. Appl.* 23 (1988) 1361.
- [39] J. Cabrero-Cano, A. Dominguez-Rodriguez, R. Marquez, J. Castaing and J. Philibert, *Philos. Mag. A* 46 (1982) 397.
- [40] A. Dominguez-Rodriguez, J. Castaing and J. Philibert, *Mater. Sci. Eng.* 27 (1977) 217.
- [41] G.G. Bentle and K.T. Miller, *J. Appl. Phys.* 38 (1965) 4247.
- [42] G.S. Corman, *J. Amer. Ceram. Soc.* 75 (1992) 71.
- [43] K. Suzuki, M. Ichihara and S. Takeuchi, *Jpn. J. Appl. Phys.* 33 (1994) 1114.
- [44] M.H. Hong, A.V. Samant and P. Pirouz, *Philos. Mag. A* 80 (2000) 919.
- [45] A.H. Heuer, *J. Amer. Ceram. Soc.* 70 (1987) 689.
- [46] D.J. Green, R.H.J. Hannink and M.W. Swain, *Transformation Toughening of Ceramics* (CRC Press, Boca Raton, 1989).
- [47] J.F. Wenckus, *J. Crystal Growth* 128 (1993) 13.
- [48] A. Dominguez-Rodriguez, K.P.D. Lagerlöf and A.H. Heuer, *J. Amer. Ceram. Soc.* 69 (1986) 281.

- [49] A. Tikhonovsky, M. Bartsch and U. Messerschmidt, *Phys. Stat. Sol.* (2004).
- [50] V. Lanteri, A.H. Heuer and T.E. Mitchell, *Adv. Ceram.* 12 (1984) 118.
- [51] A.H. Heuer, R. Chaim and V. Lanteri, in: *Science and Technology of Zirconia*, ed. H. Hanaiga (American Ceramic Society, Westerfield, 1988) p. 3.
- [52] U. Messerschmidt, D. Baither, B. Baufeld and M. Bartsch, *Mater. Sci. Eng. A* 23 (1997) 61.
- [53] D. Baither, M. Bartsch, B. Baufeld, A. Tikhonovsky, M. Rühle and U. Messerschmidt, *J. Amer. Ceram. Soc.* 319 (2001) 342.
- [54] A.H. Heuer, V. Lanteri and A. Dominguez-Rodriguez, *Acta Metall.* 37 (1989) 559.
- [55] J. Martinez-Fernandez, M. Jimenez-Melendo, A. Dominguez-Rodriguez, P. Cordier, K.P.D. Lagerlöf and A.H. Heuer, *Acta Metall. Mater.* 43 (1995) 1917.
- [56] D.S. Cheong, A. Dominguez-Rodriguez and A.H. Heuer, *Philos. Mag. A* 60 (1989) 107.
- [57] D.S. Cheong, A. Dominguez-Rodriguez and A.H. Heuer, *Philos. Mag. A* 63 (1991) 377.
- [58] A. Dominguez-Rodriguez, D.S. Cheong and A.H. Heuer, *Philos. Mag. A* 64 (1991) 923.
- [59] B. Baufeld, B.V. Betukhov, M. Bartsch and U. Messerschmidt, *Acta Mater.* 46 (1998) 3077.
- [60] B. Baufeld, D. Baither, M. Barsch and U. Messerschmidt, *Phys. Stat. Sol. A* 166 (1998) 127.
- [61] P. Teracher, H. Garem and J. Rabier, in: *Strength of Metals and Alloys*, eds D.G. Brandon, R. Chaim and A. Rosen (Freund Publishers, London, 1991) p. 217.
- [62] D. Gomez-Garcia, J. Martinez-Fernandez, A. Dominguez-Rodriguez, P. Eveno and J. Castaing, *Acta Mater.* 44 (1996) 991.
- [63] U. Messerschmidt, B. Baufeld, K.J. McClellan and A.H. Heuer, *Acta Metall. Mater.* 43 (1995) 1917.
- [64] M. Kilo, G. Borchadt, S. Weber, S. Scherrer and K. Tinschert, *Ber. Bunsen-Ges. Phys. Chem.* 101 (1997) 1361.
- [65] F.R. Chien and A.H. Heuer, *Phil. Mag. A* 73 (1996) 681.
- [66] D. Gomez-Garcia, J. Martinez-Fernandez, A. Dominguez-Rodriguez and K.H. Westmacott, *J. Amer. Ceram. Soc.* 79 (1996) 487.
- [67] M. Bartsch, A. Tikhonovsky and U. Messerschmidt, *Phys. Stat. Sol.* (2004).
- [68] K.J. McClellan, A.H. Heuer and L.P. Kubin, *Acta Mater.* 44 (1996) 2651.
- [69] R.J. Keller, T.E. Mitchell and A.H. Heuer, *Acta Metall.* 36 (1988) 1061.
- [70] B.T.M. Willis, *Acta Cryst. A* 34 (1978) 88.
- [71] K.H.G. Ashbee and R.E. Smallman, *Proc. Roy. Soc. Lond. A* 274 (1963) 195.
- [72] M.G. Blanchin and P. Faisant, *Rev. Phys. Appl.* 14 (1979) 619.
- [73] M.G. Blanchin, G. Fontaine and L.P. Kubin, *Philos. Mag. A* 41 (1980) 261.
- [74] L.A. Bursill and M.G. Blanchin, *Philos. Mag. A* 49 (1984) 365.
- [75] Y. Motohashi, M.G. Blanchin, E. Vicario, G. Fontaine and S. Otake, *Phys. Stat. Sol. A* 54 (1979) 355.
- [76] K.H.G. Ashbee, R.E. Smallman and G.K. Williamson, *Proc. Roy. Soc. Lond. A* 216 (1964) 54.
- [77] K. Suzuki, M. Ichihara and S. Takeuchi, *Philos. Mag. A* 63 (1991) 657.
- [78] M.G. Blanchin, L.A. Bursill and C. Lafage, *Proc. Roy. Soc. A* 429 (1990) 175.
- [79] D.T. Griggs and J.D. Blacic, *Science* 147 (1964) 292.
- [80] D.T. Griggs and J.D. Blacic, *Trans. Amer. Geophys. Union* 45 (1964) 102.
- [81] M.S. Paterson, in: *Rheology of Solids and of the Earth*, eds S. Karato and M. Toriumi (Oxford University Press, London, 1989) p. 107.
- [82] C. Frondel, *The System of Mineralogy* of J. D. and E. S. Dana (Wiley, New York, 1962).
- [83] A. Ord and B.E. Hobbs, in: *Mineral and Rock Deformation: Laboratory Studies*, eds B.E. Hobbs and H.C. Heard (American Geophysical Union, Washington, D.C., 1986) p. 51.
- [84] A.C. McLaren, J.D. Fitzgerald and J. Gerretson, *Phys. Chem. Minerals* 16 (1989) 465.
- [85] J.D. Fitzgerald, J.N. Boland, A.C. McLaren, A. Ord and B.E. Hobbs, *J. Geophys. Res.* 96 (1991) 2139.
- [86] A.C. McLaren, *Transmission Electron Microscopy of Minerals and Rocks* (Cambridge University Press, Cambridge, 1991).
- [87] J.C. Doukhan and L. Trepied, *Bull. Mineral.* 108 (1985) 97.
- [88] P. Cordier, J.A. Weil, D.F. Howarth and J.C. Doukhan, *Eur. J. Mineral.* 6 (1994) 17.
- [89] A.C. McLaren, R.F. Cook, S.T. Hyde and R.C. Tobin, *Phys. Chem. Minerals* 9 (1983) 79.
- [90] A.C. McLaren, J.A. Retchford, D.T. Griggs and J.M. Christie, *Phys. Stat. Sol.* 19 (1967) 631.
- [91] P. Cordier and J.C. Doukhan, *Philos. Mag. A* 72 (1995) 497.

- [92] A. Verneuil, Compt. Rend. Paris 104 (1887) 501.
- [93] T.H. Maiman, Nature 187 (1960) 493.
- [94] A.H. Heuer, K.P.D. Lagerlöf and J. Castaing, Philos. Mag. A 78 (1998) 747.
- [95] A.G. Marinopoulos and C. Elsässer, Philos. Mag. Lett. 81 (2001) 329.
- [96] J. Cadoz, J. Castaing, D.S. Phillips, A.H. Heuer and T.E. Mitchell, Acta Metall. 30 (1982) 2205.
- [97] T.E. Mitchell, B.J. Pletka, D.S. Phillips and A.H. Heuer, Philos. Mag. 34 (1976) 441.
- [98] D.S. Phillips, B.J. Pletka, T.E. Mitchell and A.H. Heuer, Acta Metall. 30 (1982) 491.
- [99] W.D. Scott and K.K. Orr, J. Amer. Ceram. Soc. 66 (1983) 27.
- [100] A.H. Heuer, Phil. Mag. 13 (1966) 379.
- [101] T. Geipel, K.P.D. Lagerlöf, P. Pirouz and A.H. Heuer, Acta Metall. Mater. 42 (1994) 1367.
- [102] P. Pirouz, Scripta Metall. Mater. 21 (1987) 1463.
- [103] K.P.D. Lagerlöf, J. Castaing and A.H. Heuer, Philos. Mag. A 82 (2002) 2841.
- [104] S. Nufer, A.G. Marinopoulos, T. Gemming, C. Elsässer, W. Kurtz, S. Köstmeier and M. Rühle, Phys. Rev. Lett. 86 (2001) 5066.
- [105] A.G. Marinopoulos and C. Elsässer, Acta Mater. 48 (2000) 4375.
- [106] K. Veit, Neues Jahrb. Mineralogie 45 (1921) 121.
- [107] P. Pirouz, Acta Metall. Mater. 44 (1996) 2153.
- [108] A. He, K.P.D. Lagerlöf, J. Castaing and A.H. Heuer, Philos. Mag. A 82 (2002) 2855.
- [109] A.G. Marinopoulos, S. Nufer and C. Elsässer, Phys. Rev. B 63 (2001) 165112.
- [110] J. Nishigaki, K. Kuroda and H. Saka, Phys. Stat. Sol. A 128 (1991) 319.
- [111] N. Doukhan and J.C. Doukhan, Phys. Chem. Min. 13 (1986) 403.
- [112] S. Takeuchi, K. Suzuki, M. Ichihara and T. Suzuki, in: Lattice Defects in Ceramics, eds T. Suzuki and S. Takeuchi (Japanese Journal of Applied Physics, Tokyo, 1989) p. 17.
- [113] J.P. Poirier, J. Peyronneau, J.Y. Gesland and G. Brebec, Phys. Earth Planet. Interior 33 (1983) 273.
- [114] Z. Mao and K.M. Knowles, Philos. Mag. A 73 (1996) 699.
- [115] D. Brunner, S. Taeri-Baghbadrani, W. Cigle and M. Rühle, J. Amer. Ceram. Soc. 84 (2001) 1161.
- [116] P. Gumbusch, S. Taeri-Baghbadra, D. Brunner, W. Sigle and M. Rühle, Phys. Rev. Lett. 87 (2001) 85505.
- [117] T.E. Mitchell, M.I. Baskes, S.P. Chen, J.P. Hirth and R.G. Hoagland, Philos. Mag. A 81 (2001) 1079.
- [118] D. Caillard and A. Couret, in: Dislocations in Solids, eds F.R.N. Nabarro and M.S. Duesbery (Elsevier, 1996) p. 69.
- [119] T. Matsunaga and H. Saka, Phil. Mag. Lett. 80 (2000) 597.
- [120] Z. Zhang, W. Sigle, W. Kurtz and M. Rühle, Phys. Rev. B 66 (2003) 214112.
- [121] Z. Zhang, W. Sigle and M. Rühle, Phys. Rev. B 66 (2002) 94108.
- [122] K.C. Radford and C.W.A. Newey, Proc. Brit. Ceram. Soc. 9 (1967) 131.
- [123] C.W.A. Newey and K.C. Radford, in: Anisotropy in Single Crystal Refractory Compounds, eds F.W. Vahldiek and S.A. Mersol (Plenum Press, New York, 1968) p. 321.
- [124] M.H. Lewis, Philos. Mag. 17 (1968) 481.
- [125] N. Doukhan, R. Duclos and B. Escaig, J. Phys. (Paris) 37 (1976) 566.
- [126] G. Welsch, L. Hwang, A.H. Heuer and T.E. Mitchell, Philos. Mag. 29 (1974) 1374.
- [127] L. Hwang, A.H. Heuer and T.E. Mitchell, in: Deformation of Ceramic Materials, eds R.C. Bradt and R.E. Tressler (Plenum Press, New York, 1975) p. 257.
- [128] T.E. Mitchell, L. Hwang and A.H. Heuer, J. Mater. Sci. 11 (1976) 264.
- [129] N. Doukhan, R. Duclos and B. Escaig, J. Phys. (Paris) 34 (1973) 397.
- [130] R. Duclos, N. Doukhan and B. Escaig, J. Mater. Sci. 13 (1978) 1740.
- [131] P. Veyssiére, J. Rabier and H. Garem, Philos. Mag. A 39 (1979) 815.
- [132] W.T. Donlon, T.E. Mitchell and A.H. Heuer, Philos. Mag. A 40 (1979) 351.
- [133] N. Doukhan, J. Phys. Lett. 40 (1979) L603.
- [134] S.H. Kirby and P. Veyssiére, Philos. Mag. A 41 (1980) 129.
- [135] R. Duclos, N. Doukhan and B. Escaig, Philos. Mag. 43 (1981) 1595.
- [136] R. Duclos, J. Phys. (Paris), 42 (1981) 49.
- [137] W.T. Donlon, T.E. Mitchell and A.H. Heuer, Philos. Mag. A 45 (1982) 1013.
- [138] N. Doukhan, R. Duclos and B. Escaig, J. Phys. (Paris) 43 (1982) 1149.
- [139] R. Duclos, N. Doukhan and B. Escaig, Acta Metall. 30 (1982) 1381.

- [140] H. Suematsu, T. Suzuki, T. Iseki and T. Mori, *J. Am. Ceram. Soc.* 72 (1989) 306.
- [141] G.S. Corman, *Ceram. Eng. Sci. Proc.* 12 (1991) 1745.
- [142] G.S. Corman, *J. Mater. Sci. Lett.* 11 (1992) 1657.
- [143] T.E. Mitchell, W.T. Donlon and A.H. Heuer, *Scripta Mater.* 39 (1998) 537.
- [144] T. Yano, M. Ikari, T. Iseki, E.H. Farnum, F.W. Clinard and T.E. Mitchell, *J. Amer. Ceram. Soc.* 78 (1995) 1469.
- [145] P. Charpentier, P. Rabbe and J. Manenc, *Mater. Res. Bull.* 3 (1968) 69.
- [146] T. Ito, *J. Amer. Ceram. Soc.* 54 (1971) 24.
- [147] S.L. Callahan, R.E. Tressler, D.W. Johnson and M.J. Reece, in: *Deformation of Ceramic Materials II*, eds R.E. Tressler and R.C. Bradt (Plenum Press, New York, 1984) p. 177.
- [148] E.H.L. Dekker and G.D. Rieck, *J. Mater. Sci.* 9 (1974) 1839.
- [149] P. Veyssiére, J. Rabier, H. Garem and J. Grihlé, *Philos. Mag. A* 38 (1978) 61.
- [150] P. Veyssiére, J. Rabier, H. Garem and J. Grihlé, *Philos. Mag. B* 33 (1976) 143.
- [151] P. Veyssiére, J. Rabier and H. Garem, *Philos. Mag.* 39 (1979) 815.
- [152] N. Doukhan, J.-C. Doukhan, A. Nicholas and D. Secher, *Bull. Minéral.* 107 (1984).
- [153] N.L. Carter and H.G. AveLallement, *Geol. Soc. Amer. Bull.* 81 (1970) 2181.
- [154] P.P. Phakey, G. Dollinger and J.M. Christie, in: *Geophys. Monogr.*, eds H.C. Heard, I.Y. Borg, N.L. Carter and C.B. Raleigh (Amer. Geophys. Union, Washington, 1972) p. 117.
- [155] C.B. Raleigh, *Science* 150 (1968) 739.
- [156] J.P. Poirier, *J. Geophys. Res.* 80 (1975) 4059.
- [157] M. Darot and Y. Gueguen, *Bull. Mineral.* 104 (1981) 261.
- [158] R.J. Gaboriaud, *Bull. Mineral.* 109 (1986) 185.
- [159] R.J. Gaboriaud, M. Darot, Y. Gueguen and J. Woirgard, *J. Microsc. Spectrosc. Electron.* 12 (1981).
- [160] D.L. Kohlstedt and D.L. Ricoult, in: *Deformation of Ceramic Materials II*, eds R.E. Tressler and R.C. Bradt (Plenum Press, New York, 1984) p. 251.
- [161] B. Poumellec and O. Jaoul, in: *Deformation of Ceramic Materials II*, eds R.E. Tressler and R.C. Bradt (Plenum Press, New York, 1984) p. 281.
- [162] S. Karato, in: *Rheology of Solids and of the Earth*, eds S. Karato and M. Toriumi (Oxford University Press, Oxford, 1989) p. 176.
- [163] S. Karato, M.S. Paterson and J.D. Fitzgerald, *J. Geophys. Res.* 91 (1986) 8151.
- [164] J.D. Blacic, in: *Geophys. Monogr. Ser.*, eds H.C. Heard, I.Y. Borg, N.L. Carter and C.B. Raleigh (Amer. Geophys. Union, Washington, 1972) p. 109.
- [165] S.J. Mackwell, D.L. Kohlstedt and M.S. Paterson, *J. Geophys. Res.* 88 (1985) 3122.
- [166] J.P. Poirier and B. Vergrobbi, *Phys. Earth Plan. Int.* 16 (1978) 370.
- [167] J.B. VanderSande and D.L. Kohlstedt, *Philos. Mag.* 34 (1976) 653.
- [168] B.K. Smith, F.M. Allen and P.R. Buseck, *EOS Trans. Amer. Geophys. Union* 68 (1987) 426.
- [169] M.R. Drury, *Phys. Chem. Minerals* 18 (1991) 106.
- [170] T.J. White and B.G. Hyde, *Phys. Chem. Min.* 8 (1982) 55.
- [171] A. Audouard, J. Castaing, J.P. Rivière and B. Sieber, *Acta Metall.* 29 (1981) 1385.
- [172] R.J. Gaboriaud, *Philos. Mag. A* 44 (1981) 561.
- [173] R.J. Gaboriaud, M.F. Denatot, M. Boisson and J. Grihlé, *Phys. Stat. Sol. (a)* 46 (1978) 387.
- [174] M. Boisson and R.J. Gaboriaud, *J. Mater. Sci.* 16 (1981) 3452.
- [175] A.A. Sharif, A. Misra, J.J. Petrovic and T.E. Mitchell, *Mater. Sci. Eng. A* 290 (2000) 164.
- [176] A.A. Sharif, A. Misra, J.J. Petrovic and T.E. Mitchell, *Key Eng. Mater.* 171–174 (2000) 801.
- [177] S. Karato, Z. Wang, B. Liu and K. Fujino, *Earth Planet. Sci. Lett.* 130 (1995) 13.
- [178] J. Rabier, P. Veyssiére and H. Garem, *Philos. Mag. A* 44 (1981) 1363.
- [179] J. Rabier, P. Veyssiére, H. Garem and J. Grihlé, *Philos. Mag. A* 39 (1979) 693.
- [180] Z. Wang, S. Karato and K. Fujino, *Phys. Chem. Minerals* 23 (1996) 73.
- [181] H. Garem, J. Rabier and P. Veyssiére, *J. Mater. Sci.* 17 (1982) 878.
- [182] J. Rabier and H. Garem, in: *Deformation of Ceramic Materials II*, eds R.E. Tressler and R.C. Bradt (Plenum, New York, 1984) p. 187.
- [183] S. Karato, Z. Wang and K. Fujino, *J. Mater. Sci.* 29 (1994) 6458.
- [184] W.R. Blumenthal and D.S. Phillips, *J. Amer. Ceram. Soc.* 79 (1996) 1047.

- [185] V. Voegele, J.I. Ando, P. Cordier and R.C. Liebermann, *Phys. Earth Planet. Interiors* 108 (1998) 305.
- [186] G.E. Hollox, *Mater. Sci. Eng.* 3 (1968/69) 121.
- [187] S. Tsurekawa, H. Kurishita and H. Yoshinaga, in: *Lattice Defects in Ceramics*, eds T. Suzuki and S. Takeuchi (*Japanese Journal of Applied Physics*, Tokyo, 1989) p. 47.
- [188] P. Pirouz, in: *Understanding Materials*, ed. C.J. Humphreys (*Institute of Materials*, London, 2002) p. 225.
- [189] H. Suematsu, T. Suzuki, T. Iseki and T. Mori, *J. Amer. Ceram. Soc.* 74 (1991) 173.
- [190] C.M. Wang, X. Pan, M. Rühle, F.L. Riley and M. Mitomo, *J. Mater. Sci.* 31 (1996) 5281.
- [191] H. Suematsu, J.J. Petrovic and T.E. Mitchell, *Mat. Res. Soc. Symp. Proc.* 287 (1993) 449.
- [192] H. Suematsu, J.J. Petrovic and T.E. Mitchell, *J. Ceram. Soc. Japan* 105 (1997) 842.
- [193] D.S. Zhou and T.E. Mitchell, *J. Amer. Ceram. Soc.* 78 (1995) 3133.
- [194] G.W. Groves and A. Kelly, *Proc. Roy. Soc. Lond.* A275 (1963) 233.
- [195] P.B. Hirsch and T.E. Mitchell, in: *Work Hardening*, eds J.P. Hirth and J. Weertman (*Gordon and Breach*, New York, 1968) p. 365.
- [196] P.B. Hirsch and T.E. Mitchell, *Canad. J. Phys.* 45 (1967) 663.
- [197] H. Conrad, *J. Amer. Ceram. Soc.* 48 (1965) 195.
- [198] M.L. Kronberg, *J. Amer. Ceram. Soc.* 45 (1962) 274.
- [199] B.J. Pletka, A.H. Heuer and T.E. Mitchell, *Acta Metall.* 25 (1977) 25.
- [200] B.J. Pletka, T.E. Mitchell and A.H. Heuer, *Phys. Stat. Sol. (a)* 39 (1977) 301.
- [201] M. Srinivasan and T.G. Stoebe, *J. Appl. Phys.* 41 (1970) 3726.
- [202] B. Reppich, *Mater. Sci. Eng.* 22 (1976) 71.
- [203] R. Labusch, *Phys. Stat. Sol.* 41 (1970) 659.
- [204] D.S. Phillips, T.E. Mitchell and A.H. Heuer, *Philos. Mag. A* 42 (1980) 417.
- [205] T.E. Mitchell and A.H. Heuer, *Mater. Sci. Eng.* 28 (1977) 81.
- [206] K.P.D. Lagerlöf, T.E. Mitchell, A.H. Heuer, J.P. Rivière, J. Cadoz, J. Castaing and D.S. Phillips, *Acta Metall.* 32 (1984) 97.
- [207] D.G. Howitt and T.E. Mitchell, *Philos. Mag.* 44 (1981) 229.
- [208] P.R. Kenway, *Philos. Mag. B* 68 (1993) 171.
- [209] J.B. Bilde-Sørensen, A.R. Tholen, D.J. Gooch and G.W. Groves, *Philos. Mag.* 33 (1976) 877.
- [210] D.S. Phillips and J.L. Cadoz, *Philos. Mag. A* 46 (1982) 583.

Dislocations in Energetic Crystals

R.W. ARMSTRONG

*Emeritus Professor, Department of Mechanical Engineering, University of Maryland, College Park,
MD 20742, USA*

Senior Scientist, Air Force Research Laboratory, Munitions Directorate, Eglin AFB, FL 32542, USA

and

W.L. ELBAN

Professor, Department of Engineering Science, Loyola College, Baltimore, MD 21210, USA

Contents

1. Introduction	405
2. Crystal dislocation characteristics	405
2.1. Large Burgers vectors	406
2.2. Chemical effects	407
2.3. Self-energies	409
3. Crystal morphologies and perfections	409
4. Mechanical properties	413
4.1. Early mechanical testing of anthracene/naphthalene	413
4.2. Micro-indentation hardness testing	415
4.3. Drop-weight impact testing for crystal sensitivity	419
4.4. Shock loading	424
4.5. Laser damage experiments	426
5. Chemical reactivity	428
5.1. Cleavage-induced chemical reaction	428
5.2. Polymerization related to sucrose decomposition	429
5.3. AP decomposition	430
5.4. Spectroscopy	432
5.5. X-radiation induced decomposition	432
5.6. Shock reactivity	433
6. Molecular modeling	433
6.1. Crystal densities	433
6.2. The P-N stress for anthracene	435
6.3. Model dislocation displacements	436
6.4. Hot spots in MD simulations	438
6.5. Shock mechanochemistry and atomic force microscopy	439
7. Summary	440
Acknowledgements	441
Note added in proof	441
References	442

1. Introduction

Dislocations in molecularly bonded energetic crystal lattices are associated with an interesting contrast in mechanical properties: the crystals are elastically soft, plastically hard, and brittle. The combination of properties is shown here to relate to the important consideration of mechanically enhanced chemical decomposition possibly leading to explosive detonation. A variety of dislocation Burgers vectors and line vectors occur in individual crystals because of the characteristically weak intermolecular bonding among oddly-shaped molecules that are packed into otherwise low-symmetry crystal structures. Large Burgers vector dimensions occur as a result of the weak molecular bonding and outweigh the low magnitude of elastic stiffnesses to give relatively large dislocation self-energies, consonant with low dislocation densities being observed in such crystals.

Despite the weak bonding, dislocation movement is reasoned to be intrinsically hindered in the lattice structures because of cross-blockages among the intertwined, oddly-shaped molecules. An important consequence is that the crystals exhibit limited operation of restricted slip or twinning systems. Models of the molecular displacements occurring for identified slip systems show molecular interactions in agreement with detected chemical decompositions. Alternatively, energetic crystals have relatively low (anisotropic) values of surface energies that lead to low values of theoretical cleavage stresses. Thus, energetic crystals are elastically compliant, relatively hard, and brittle.

The relatively high crystal yield stresses and low cleavage stresses provide only a narrow range in stress level for dynamic dislocation behavior. In this range, localized hot spot heating from the dislocation work, though involving only small numbers of dislocations in pile-up avalanches, is significantly enhanced because of characteristically low material thermal conductivities. In shock wave studies, hindrance to dislocation movement at, and behind, the shock wave front is an important consideration, as is the generation of nanoscale dislocation clusters at large shock pressures and the role of anharmonic lattice strains at the dislocation cores in allowing either “*in situ*” hot spot heating or direct electronic excitations.

2. Crystal dislocation characteristics

The combination of large Burgers vectors and low elastic stiffnesses for energetic crystal lattices leads to large dislocation self-energies and consequently low dislocation densities in crystals that are mostly grown from solution. The low symmetry of the crystal lattice structures leads also to a variety of dislocation Burgers vectors and line vectors; however, the intertwined packing of oddly-shaped molecules produces strong intrinsic resistance to dislocation movement that allows only few slip or twinning systems to operate. The crystal surface energies are low and, with restricted plastic flow, cleavage is relatively easy.

2.1. Large Burgers vectors

The large Burgers vector dimensions in molecularly bonded lattice structures, and in related crystal structures characterized by large interatomic or intermolecular lattice parameters, provided an opportunity in the early days of dislocation studies of optically detecting dislocation end points at intermolecular-scale ledge heights on otherwise flat crystal surfaces exposed during growth from the vapour [1]. Very fine striated ledge structures had been observed with the optical microscope on the surfaces of vapour-grown crystals subjected to supersaturations less than the theoretical value required for growth on a perfectly flat surface. Cabrera and Burton showed that such ledges had to be a non-equilibrium phenomenon [2]. Frank [3] gave a model explanation for the generation of such ledges spiraling outward from emergence sites of screw dislocations and thus explained the growth of crystals at low vapour supersaturations through the continuous availability of such ledges for attachment of atoms or molecules.

Griffin [4] first reported from the Royal Holloway College (RHC) a screw dislocation-type spiral marking on the surface of a beryl crystal. Verma [1] followed shortly thereafter, also while at the RHC, with optical phase contrast microscopy observations of spiral ledges terminating at presumed dislocation positions threading otherwise molecularly flat surfaces of silicon carbide crystals brought from India. With supervision from S. Tolansky, the optical microscope technique was pushed to provide quantitative measurement using multiple beam interferometry of a 1.5 nm step height along the [0001] growth surface normal, equivalent to a *c*-axis unit cell length for a dislocation Burgers vector in a 6H (hexagonal) crystal [5]. Fig. 1 shows an example.

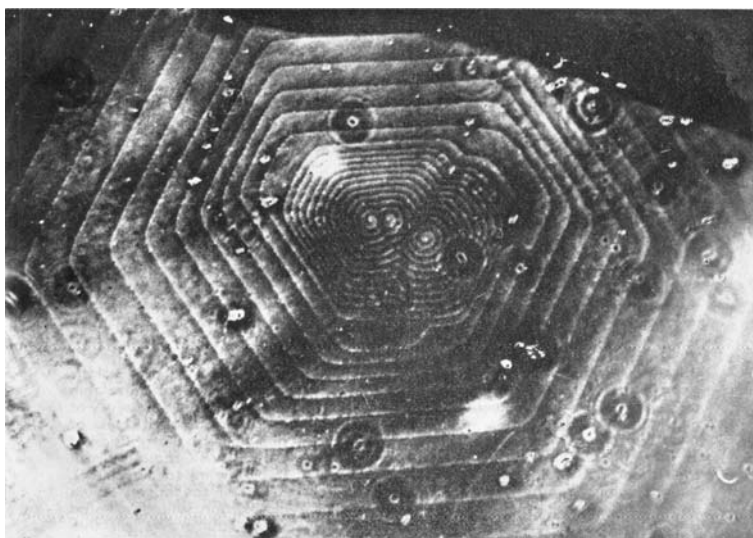


Fig. 1. A phase contrast micrograph of the (0001) face on a 6H SiC crystal showing the growth pattern due to three dislocations of like sign close together and giving rise to three cooperating growth spirals. The central or the last part of the growth is circular while the rest is hexagonal. ($\times 500$). After Verma [1].

It is interesting to note the important consequence of there being relatively few dislocations with such [0001] Burgers vectors in these silicon carbide or related hexagonal crystals because the optical microscope observations and measurements were facilitated by the low areal density of dislocations. Such growth spirals were observed on silicon carbide crystals also by Amelinckx [6], and on the (0001) surfaces of n-paraffin crystals by Dawson and Vand [7], and on the surface of an n-nonatriacontane crystal by Anderson and Dawson [8]. Not long after report of these optical microscope observations, Menter [9] obtained electron microscope pictures of dislocations in copper and platinum phthalocyanine crystals by imaging the Burgers vector displacements along 1.2 nm separations of (201) lattice planes.

The preceding observations were made before dislocations were directly observed in the transmission electron microscope (TEM) via strain field imaging of the defects in thin metal foils [10,11]. The TEM technique allowed high magnification observations of dislocations to be made through strain-induced changes in the local diffracted intensity, say, over regions extending radially tens of nms from the dislocation cores, even with the much smaller Burgers vectors of dislocations in metals and alloys. Whereas a low dislocation density is generally required to make successful dislocation step height measurements on crystal growth surfaces with an optical microscope, much higher dislocation densities are conveniently studied with the higher magnifications employed in the TEM. Unfortunately, electron beam damage often interferes with molecular crystal defect observations in the TEM.

The same low dislocation density requirement of optical step height measurements applies for the observation of dislocations by the two techniques of chemical etch pitting or X-ray diffraction topography. X-ray topography involves optical microscope enlargement of strain-induced contrast in the diffracted X-ray intensity, thus occurring at dislocations for the same reason as in the TEM technique, but here in Laue or Bragg diffraction images recorded on fine grained nuclear emulsions. Ref. [12] gives a description of dislocation observations by optical, X-ray, electron and field ion microscopy. The chemical etch pitting and X-ray topography techniques have been applied very successfully to observing dislocations in energetic crystals. Connick and May [13] first reported etch pitting observations of dislocations in cyclotrimethylenetrinitramine (RDX) crystals, and Lang [14] first reported that dislocations had been observed in RDX crystals by transmission X-ray topography. RDX has an orthorhombic crystal structure with space group *Pbca* [15].

2.2. Chemical effects

Nabarro [16] points out that Faraday [17] reported the observation of efflorescence occurring at mechanical scratches put into, for example, surfaces of otherwise perfectly stable crystal surfaces of sodium sulphate decahydrate. Reference to the original article shows that the same observation was made on other related decahydrate crystals. Faraday described the effects "as a curious illustration of the influence of mechanical forces over chemical affinity". Nabarro suggested, because efflorescence involves only a change in part of the molecular unit cell structure, that imperfect dislocations might be involved in the scratching deformation as compared with perfect dislocations participating in the crystal growth process, and thereby being relatively inert. He also pointed out that etch pits and dehydration points were reported to be uncorrelated in gypsum.

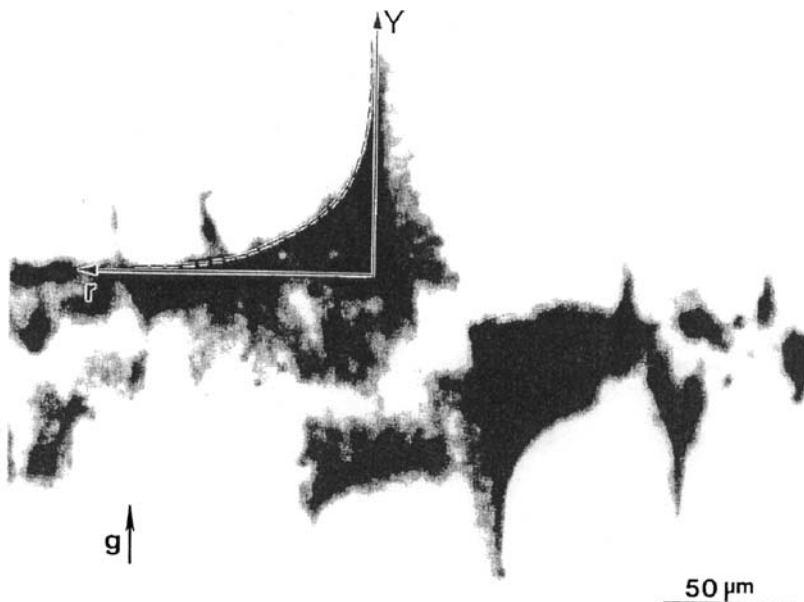


Fig. 2. An (0006) section X-ray transmission topograph showing an image of a screw dislocation micropipe, M; after Dudley, Si, Wang, Carter, Glass and Tsvetkov [20].

The segregation of solute atoms or molecules at the cores of dislocations in crystals of any type is a natural consideration because of the severe state of strain at the dislocation centers, and occurs frequently enough to have led to coining of the term "dislocation decoration". This influence is well known in atomic diffusion studies and, also, in deformation studies of discontinuous yielding and follow-on plastic flow. For the case of large Burgers vector dislocations, however, the strain state is relatively so severe as to allow dislocation cores in vapour-grown crystals to be hollow. The condition for this occurring was theoretically predicted by Frank [18]. Also, for crystals grown from solution, as is the main method of production of energetic crystals, the dislocation cores may contain a residual amount of solvent. Thomas [19], while commenting also on Faraday's observations with decahydrate crystals, pointed out that sufficient water occurred in the channels of dislocation cores in sucrose crystals to appreciably affect their electrical conductivities.

Fig. 2 shows a modern X-ray section topograph that reveals the strain field of a screw dislocation in a 6H silicon carbide crystal plate [20]. The dislocation core is demarcated by a hollow "micropipe". Scanning electron microscope (SEM) images were obtained of the emergent holes at the micropipe intersections with the crystal surface. Different micropipe diameter measurements were shown to be proportional to the square of the X-ray derived dislocation Burgers vectors, as predicted by Frank [18]. In fact, the micropipes were only observed at double Burgers vector or larger dislocation centers; and, the largest micropipes took on an hexagonal cross-section. Hirth [21] has recently extended the Frank model consideration to include the case of a micropipe being represented by an elliptical hole.

Table 1

Comparison of dislocation strain energies and Peierls–Nabarro Stresses for RDX, LiF, and MgO, after Armstrong and Elban [22].

Material	Dislocation strain energy coefficient ($E_{\perp/p}$) (J)	$(\frac{E_{\perp/p}}{\Delta H_{f/m}})$	Peierls– Nabarro stress (τ_p) (N/mm ²)	$(\frac{\tau_p}{G})$
RDX	6.3×10^{-19}	12	580	0.077
LiF	0.9×10^{-19}	2.1	3100	0.050
MgO	2.4×10^{-19}	1.9	8000	0.054

$$E_{\perp/p} = (Gb^2 \Delta \varepsilon / 4\pi \bar{a}).$$

$$\tau_p (= \tau_{P-N}) = [2G/(1-\nu)] \exp[-2\pi d/(1-\nu)b].$$

2.3. Self-energies

Beyond the dislocation core structure and its associated energy, there is the important far-reaching linear elastic strain energy component of the total self-energy. The well-known formula for the elastic strain energy per unit length of the dislocation line is expressed in terms of the product of a strain energy coefficient, involving the material shear modulus and square of the Burgers vector, and the logarithmic ratio of outer and inner cut-off radii. The inner cut-off radius is determined by the dislocation core property; however, the logarithmic term is generally thought to be a minor variable in determining the dislocation energy.

Table 1, from Armstrong and Elban [22], gives in column 2 computed values of the strain energy coefficient, multiplied by unit intermolecular length along the dislocation line, for a [100](040) edge dislocation in RDX compared to 110 edge dislocations in LiF and MgO. The elastic strain energy is seen to be greater for RDX. In column 3, the elastic strain energy coefficient is divided by the heat of formation per molecule for each of the materials to show that the dislocation strain energy is greater for RDX. Thus, the lower shear modulus of RDX is more than compensated by the larger Burgers vector influence and, also, the larger reference length along the dislocation line. Also in Table 1, computed values are given for the conventional Peierls–Nabarro (P-N) stress that depends linearly on the shear modulus and exponentially on the ratio of interplanar spacing and Burgers vector [23]. Although RDX has a lower computed P-N stress, it is shown to be a larger fraction of the shear modulus. Of course, such estimate is vitiated by the consideration of cross-blockage between adjacent molecules and so, an even higher dislocation movement stress should be expected.

3. Crystal morphologies and perfections

Energetic crystals form a subgroup of the broader class of molecular organic crystals that are mostly grown in solution from supersaturated liquids. Gem-like crystals with flat,

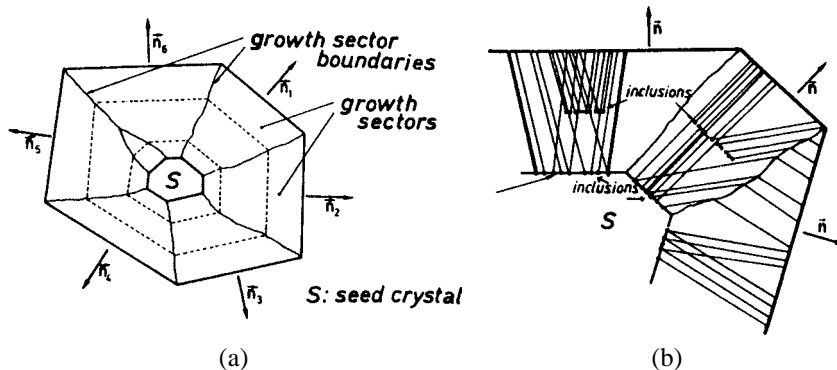


Fig. 3. Schematic illustration of (a) division of a crystal into growth sectors according to different growth directions including indication of (dashed) contours at different stages of growth; and (b) typical geometry of grown-in dislocation lines initiated at inclusion particles. After Klapper [26].

nearly specular, external habit planes are produced in the growth process. Dislocation bundles, as occur even in the natural production of diamonds, pierce the individual planar facets and facilitate growth by producing molecular scale step heights in accordance with the Frank [3] model of crystal growth. Internally, the crystals are built up of striated growth bands, parallel to the planar facets, that meet at impurity-associated growth sector boundaries.

Connick and May [13], in a study of RDX crystal growth, provided an example of the variety of external crystal morphologies that can be produced from different supersaturated solvents. Thus, tabular crystals with dominant (001) habit planes were produced by growth from cyclohexanone solution while prismatic crystals with prominent (001) axes were grown from solution in acetone or dimethyl formamide. Elban and Armstrong [24] reported crystals having both the morphology described by Connick and May and a new crystal morphology with prominently exposed $\{210\}$ surfaces when grown by slow evaporation of reagent-grade acetone with Holston RDX Class D (specifying 1–2 mm size crystals) put into solution. The relatively large crystals were several mm in size. Klapper [25] has produced beautiful color pictures of the natural appearances of such inorganic and organic crystals as cesium-alum, benzil, salol and benzophenone.

Fig. 3 shows, from Klapper [26], a schematic vapour- or solution-growth representation of the relation between external growth planes and an internal microstructure, first, of growth sectors with growth banding parallel to the external crystal facets, secondly, of growth sector boundaries defining the intersection of growth sectors and, lastly, separate “sprays” of straight dislocation bundles spreading through individual crystal growth sectors. As indicated, the dislocation bundles are oriented roughly perpendicular to the external crystal facets. Fig. 4 shows a sectioned (001) surface of an RDX crystal that has been etched to reveal its internal growth sector pattern [27]. The planar (Miller-index type) surfaces of the growth bands are identified in the figure from the trace intersections based on a stereographic projection method of analysis [28]. Such internal growth structures are particularly well documented by X-ray topography studies of both solution-grown and vapour-grown crystals [26,29], including silicon carbide and sapphire crystals.

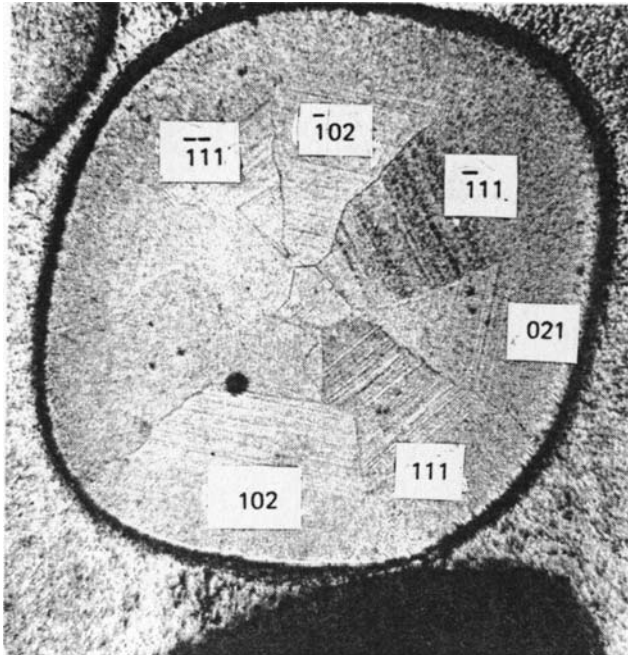


Fig. 4. Growth sector structure within a sectioned RDX crystal, after van der Steen and Duvalois [27], with growth band (planar) trace identifications, after Armstrong [28].

The straight line dislocation bundles, that are very often impurity decorated, are those generally associated with the type of ledge structure described by Frank [3] to participate fundamentally in the crystal growth process. These dislocations have been shown either to propagate from a crystal seed, to nucleate at the seed interface, particularly at inclusion particles or to arise from perturbations in the crystal growth conditions. In the latter case, the observation of incorporated liquid inclusions has been attributed to local variations of supersaturation and solvent flow at the liquid-crystal interface [26]. Gross [30] reported the observation of solvent inclusions in RDX crystals. Klapper accounts for the straight line character of the dislocation bundles on a minimum energy basis, thus favoring the identification of screw dislocation growth, as described by Frank [3]. However, bundled dislocations with edge and mixed screw plus edge characters have been identified also to participate in the crystal growth process.

Both the dislocation core energy and the anisotropic character of elastic constants that determine the coefficient for the elastic self-energy [31], as mentioned for Table 1, enter into the determination of the dislocation growth line orientations. The striated growth bands themselves are caused by local variations in the impurity content grown into the crystals through the ledge structures. The growth sector boundaries appear to mark small localized impurity-dependent mismatches in lattice parameter or slight planar misorientations. Van Enckevort and Klapper [32] report a modern example of matching X-ray topography measurements with highly sensitive differential interference contrast optical microscopy

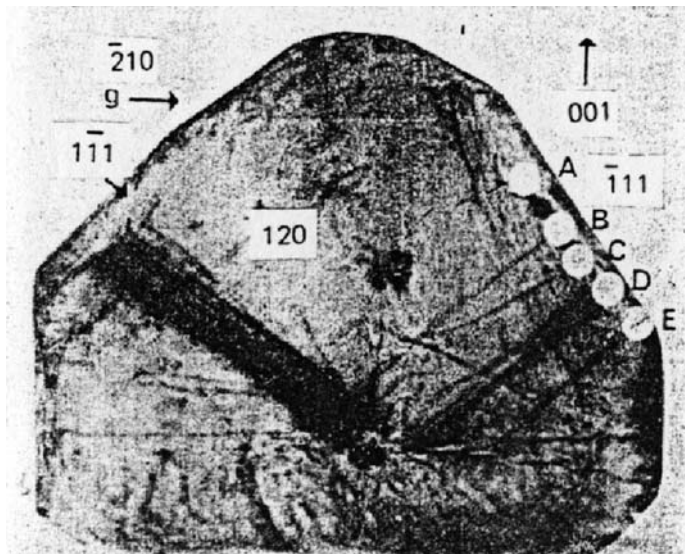


Fig. 5. A {210} X-ray transmission topograph of an RDX crystal showing dislocation bundles spreading from a central seed position to the external crystal growth surfaces; after McDermott and Phakey [33].

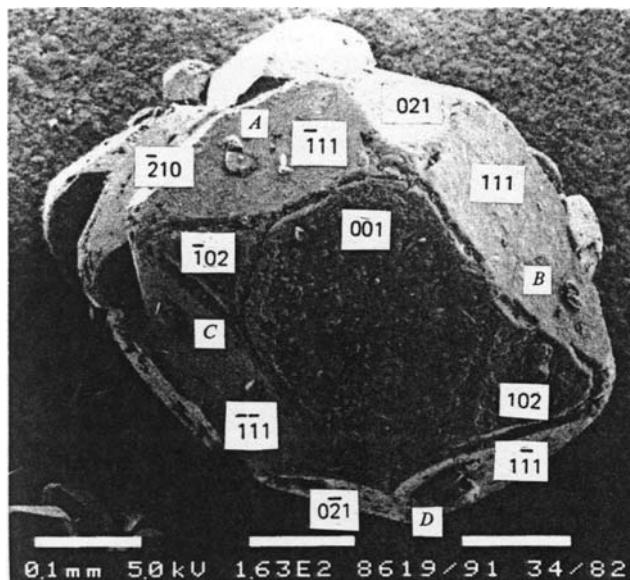


Fig. 6. A scanning electron micrograph of an RDX crystal, after van der Steen and Duvalois [27], with crystallographically-identified planar growth surfaces, also with A to D locations marked for growth protuberances at positions of dislocation bundle emergence, after Armstrong [28].

showing 1.8 and 0.9 nm (unit cell and half-unit cell, respectively) steps on the growth faces of nickel sulphate hexahydrate crystals, relating to the observations mentioned above from Faraday [17] and Verma [1]. In this case, pure screw dislocation outcrops were responsible for the growth features.

McDermott and Phakey [33] showed by X-ray topography and etch pitting a one-to-one match of a small dislocation bundle with etch pits of the individual dislocations on the crystal growth surface of an RDX crystal, as shown in Fig. 5. An opposite case of outcropping pill boxes at dislocation line end points was identified also on the surfaces of the same batch of RDX crystals studied in cross-section by van der Steen and Duvalois, as shown with identified plane indices in Fig. 6 [27,28]. Rather detailed X-ray topography results were reported for dislocation Burgers vectors and line vectors in laboratory-grown RDX crystals by Halfpenny et al. [34]. A large variation in both dislocation Burgers vectors and line vectors was determined. The variety of dislocation line shapes in carefully grown crystals of cm scale dimensions, including the observation of dislocation helices, was interpreted to indicate that significant post-growth dislocation movement had occurred. A combination of X-ray topography and etch pitting results were reported also to lead to expectation of a variety of dislocation types in energetic pentaerythritol tetranitrate (PETN) crystals [35].

4. Mechanical properties

Despite the large variety of dislocation Burgers vectors and line vectors in energetic crystals, the crystals are hard and easily cracked. The behavior has been traced to the difficulty of mechanically-forced dislocation movement. Such movement, whose dynamic characteristics are narrowly limited between relatively high yield and low cleavage stresses, is capable of conveying outcropping appendages of adjacent molecules into critical reaction coordinate distances. Chemical reaction is enhanced by the localized “hot spot” heating produced by the dislocation work.

4.1. Early mechanical testing of anthracene/naphthalene

Kochendörfer [36] did early work on the deformation of naphthalene as an example of determining slip systems for a molecular crystal, in this case, having a monoclinic crystal structure and nm scale lattice parameters ($a = 0.86$ nm, $b = 0.60$ nm and $c = 1.12$ nm). Robinson and Scott [37] followed later with tensile stress-strain measurements of the critical shear stress for structurally similar anthracene crystals as a function of temperature and strain rate. Although the ends of the melt-grown crystal rods were cleaved along (001) surfaces to provide shorter tensile specimens, the crystals thus tested were quite ductile with single slip occurring on the (001)[010] system or, with greater strain hardening, the (001)[110] system. Robinson and Scott pointed out that the same slip systems were known then to occur in pure naphthalene crystals.

Despite lack of knowledge of the thirteen elastic constants for the anthracene crystal structure, the P-N stress was reasoned by Robinson and Scott to be an important factor

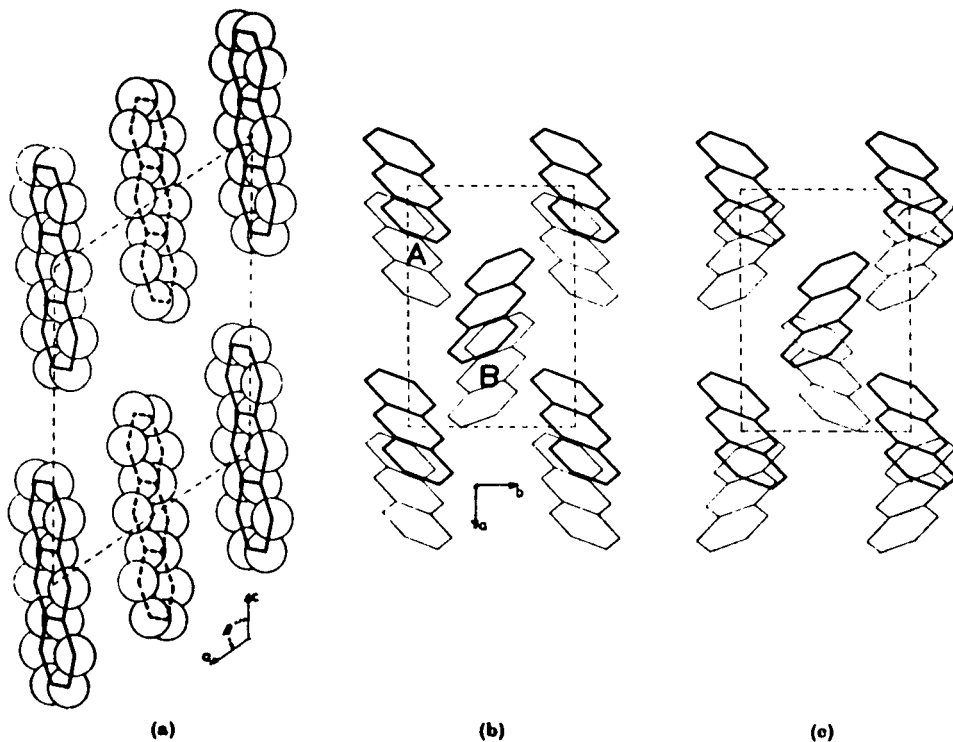


Fig. 7. Schematic plane sections of the crystal structure of anthracene: (a) (010) projection of the unit cell, with a and c axes identified, and showing carbon atoms and carbon–carbon bonds; (b) (001) projection, with a and b axes marked, and showing carbon–carbon bonds, with the light lines applying for molecules at height c above the dark line molecules; (c) a faulted (001) structure relating to (b). After Robinson and Scott [37].

in determining the crystal strength properties. Of greater importance in this study was the schematic demonstration on a lattice model basis, as indicated by identified plane projections and directions in Fig. 7(a, b), that slip should occur relatively easily across (001) along [010] but should occur with greater difficulty along [110]. Although arranged in a layered herring-bone lined-up array of uniaxial molecules, the crystal model nevertheless shows reasonably unobstructed pathways for the proposed [010] shear displacements between the rows of molecules.

Perhaps more closely related to results to be described for an energetic crystal, di Persio and Escaig [38] reported “in-situ” X-ray topographic observations made during mechanical testing of a reasonably simple body-centered cubic structure obtained for hexamethylene tetramine crystals. Deformation in constant strain rate compression tests and in tensile creep tests was monitored. The crystals were free of growth bands and contained very low dislocation densities. Cracking occurred often in the compression tests, even at the lowest machine testing speed. From the compression tests and tensile creep observations, it was concluded that the dislocations must have a large P-N stress, also reasoned to occur because of molecular misfit difficulties associated with displacements in the dislocation cores. Dif-

ficulties proposed for adjacent intermolecular nitrogen–hydrogen interactions during dislocation movement in a $\langle 111 \rangle$ slip direction were briefly discussed.

4.2. Micro-indentation hardness testing

The brittleness of most energetic crystals and, also, interest in testing small material samples for personal safety led to micro-indentation hardness testing providing an excellent means of obtaining information on crystal plasticity and cracking mechanisms in these materials. Elban and Armstrong [24] first reported etch pitting evidence of highly localized plastic flow surrounding Knoop micro-indentation hardness impressions in RDX crystals. Fig. 8 provides an example of etch pits surrounding various Knoop and diamond pyramid indentations put into the (210) surface of an RDX crystal [24,39,40]. The areas covered by the hardness-produced dislocation pits in RDX were approximately eleven times greater than the residual impression sizes, as compared with an area about ninety times larger for the X-ray determined plastic strain field of an indentation in LiF. Previous measurements on MgO crystals showed etch pit and X-ray contrast zones were roughly comparable [41]. Halfpenny et al. [35] also reported etch pitting evidence of restricted plastic flow at indentations in RDX crystals and, in PETN crystals, somewhat larger areas of very directionally distributed dislocation pits were observed at indentations. In a subsequent study, Gallagher et al. [42] investigated the orientation dependence of Knoop microhardness measurements in both RDX and PETN crystals and correlated the results with a model of the hardness anisotropy being determined by the orientation dependence associated with achieving the critical resolved shear stress for dislocation slip.

Well-defined crystallographic cracking was observed at the micro-indentation sites in each of the preceding studies [24,35,40]. Earlier, Hagan and Chaudhri [43] measured the crack size dependence of diametral cracking at diamond pyramid micro-indentations in RDX and PETN crystals and, in line with a model of the predicted crack size dependence on load [44], determined fracture surface energies for such cracking. These experiments led Elban [45] to make a comparison of the mechanically determined surface energies and those determined separately from contact angle measurements in wettability studies. The fracture surface energies were found to be larger by less than a factor of two for RDX and less than a factor of three for PETN. Possible explanations for the differences in the energies were given of plastic work being associated with the cracking process or significant anisotropy in energy being associated with different surfaces. Hagan and Chaudhri commented that substantial plastic flow had occurred in association with the cracking in PETN. Also, they found a higher fracture surface energy in RDX for (100) cracking than (001) cracking, in agreement with the qualitative observation by Connick and May [13] that (001) cracking was easiest.

There are two dislocation flow considerations that bear on affecting mechanically-induced fracture surface energy measurements: cracks are formed or small cracks made larger because of dislocation flow; and, dislocation generation and movement can occur at crack tips to blunt or otherwise restrict crack growth. The role of dislocation flow in forming a crack is well illustrated by the case of $\{110\}\langle 110 \rangle$ slip on adjacent slip planes in MgO crystals combining to form cleavage cracks on the relatively unfavorable $\{110\}$

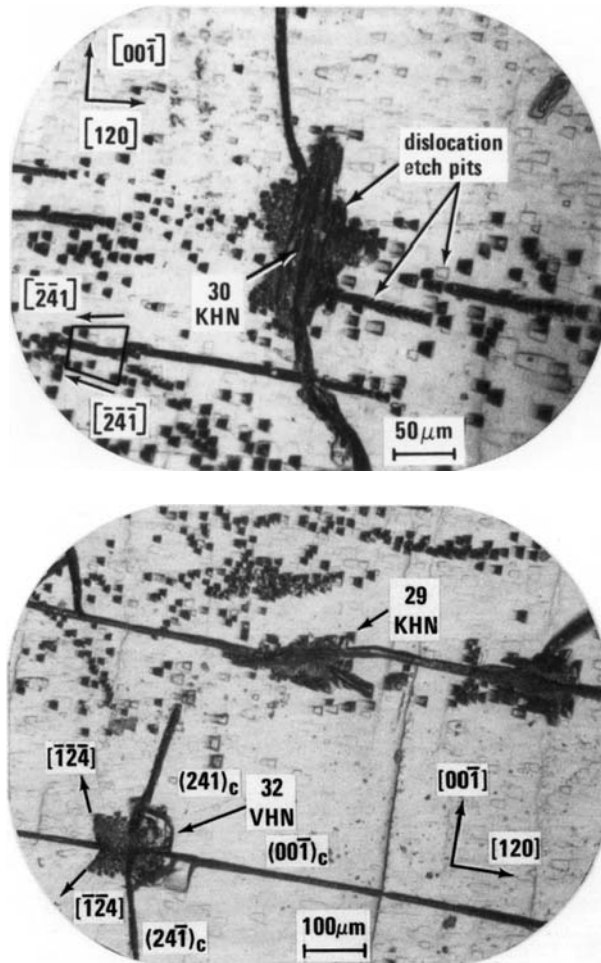


Fig. 8. Dislocation etch pits centered on microindentations in the (210) plane growth surface of RDX: (top) Knoop indentation with long axis parallel to [001]; and (bottom) identified Vickers diamond pyramid indentation with one equiaxed diagonal length parallel to [001]. The long black lines in the figures are cracks. After Elban and Armstrong [24].

cleavage planes [46]. Fig. 9 shows a comparison of residual diamond pyramid diagonal lengths and tip-to-tip diagonal crack extensions measured for indentations on (001) MgO and (210) RDX crystal surfaces [22,40,47,48]. The cm-size RDX crystal on which the major (triangular point) measurements had been made was supplied by H.H. Cady, Los Alamos National Laboratory. Note the reasonable agreement with Hagan and Chaudhri's reported crack size measurements [43] on RDX, although the lowest load datum measured by them is shown in the figure to deviate from the theoretical indentation exponential (3/2) dependence predicted on an indentation fracture mechanics basis [44]. This low indenta-

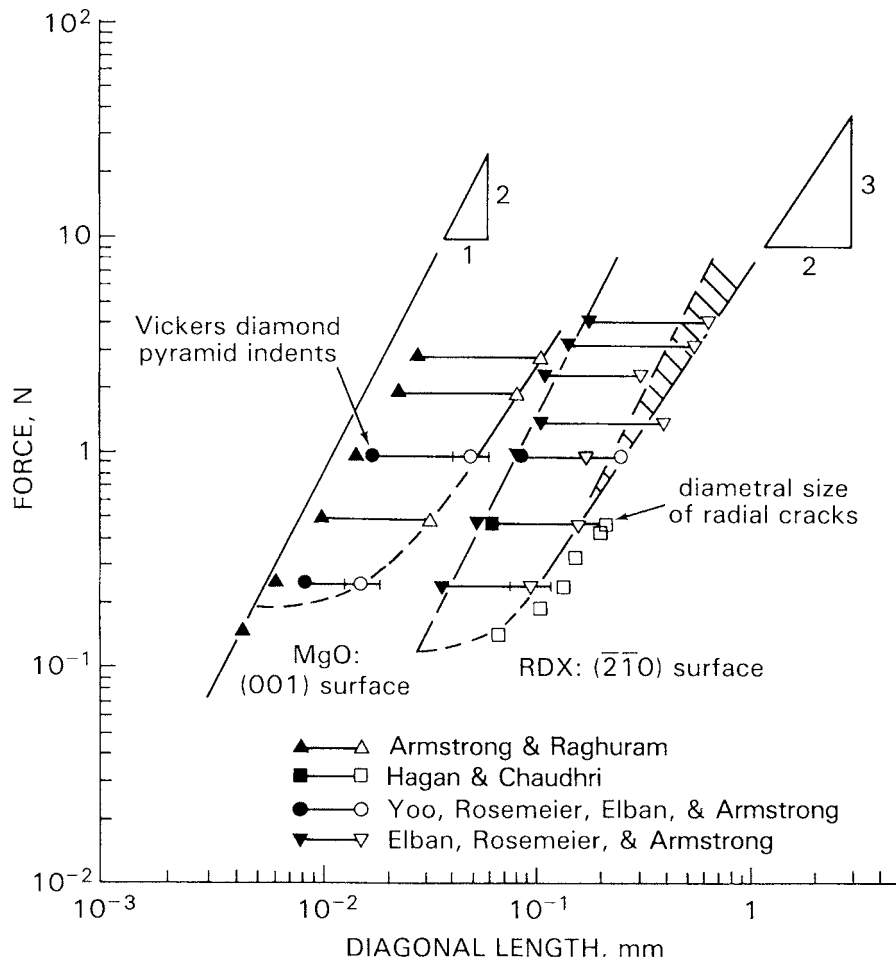


Fig. 9. Logarithmic dependence, according to constant hardness or constant indentation fracture stress intensity, of applied indenter force on diagonal indentation and crack lengths for RDX and MgO crystals; after Armstrong and Elban [22].

tion load datum plus the low load measurements shown for MgO are in the regime where visible cracking first occurs.

In Fig. 9, the force dependencies of the indentation diagonal lengths and diagonal tip-to-tip crack sizes of {110} cracks in MgO and (001) cracks in RDX present an interesting comparison. The (left-side) line of slope 2 in the figure applies for a constant hardness. For MgO, the dependence of the indentation force on indentation size follows the same indentation-fracture-mechanics-based (3/2) dependence as shown for the crack size measurements. The cracking-controlled decrease in hardness at larger indentation sizes was attributed to the positive influence of cracking on dissipating the pent-up dislocation pile-up strain energies. X-ray topography evidence was obtained on MgO showing reduced

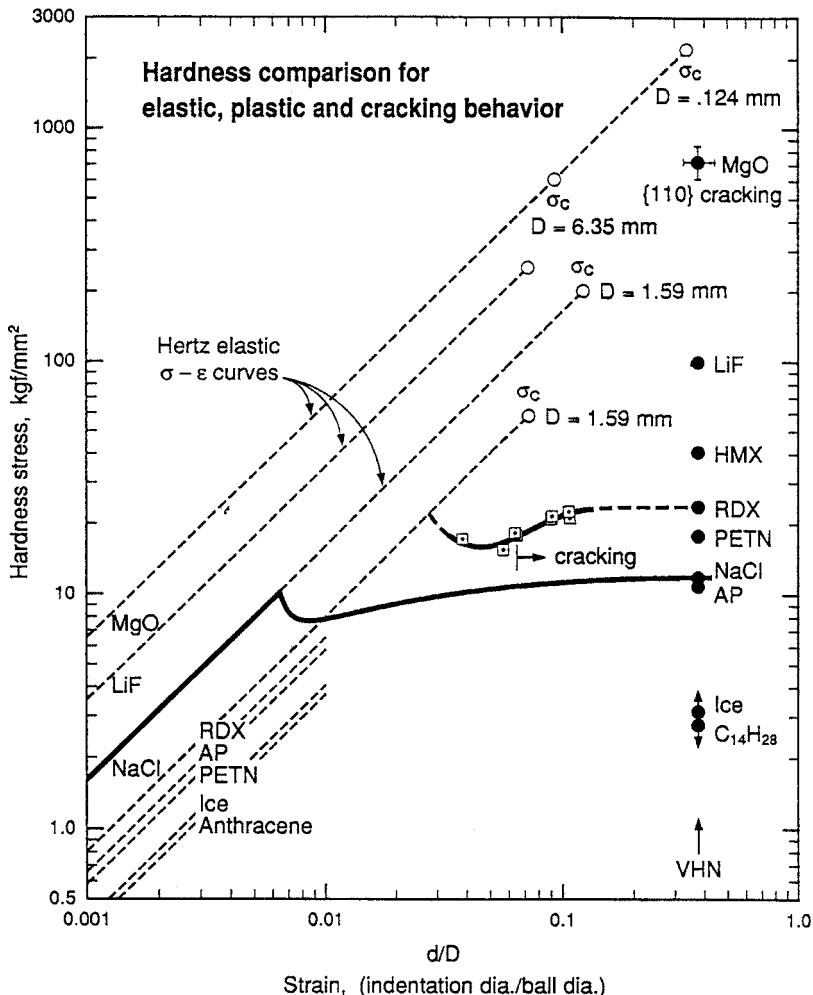


Fig. 10. Hardness stress-strain basis for comparing the elastic, plastic and cracking behaviors of crystal materials, including calculation of the terminal elastic cracking stresses for different ball sizes; after Hammond and Armstrong [49].

strain fields associated with such cracking in larger ball indentation tests [47]. By contrast, RDX shows in Fig. 9 an apparently negligible influence of cracking on the material hardness, that is seen to be essentially constant at all crack sizes. The combined indentation and crack size measurements for RDX are controlled by the dislocation flow, consistent with the proposed intermolecular-mechanism-based difficulty of dislocation movement.

Another hardness-based method for comparison of plastic flow or cracking behavior that is informative of the position of RDX and related energetic materials among a wider range of materials is shown in Fig. 10, as developed by Hammond and Armstrong [49]. Here, a hardness stress, defined as the mean pressure on a ball indentor of diameter, D , is plotted

versus a measure of the hardness strain, defined by the ratio of the circular contact diameter, d , divided by D . For elastic loading behavior, a linear hardness stress dependence on (d/D) can be computed from the elastic constants of the ball and test material in accordance with the theory of Hertz [50]. In Fig. 10, all of the linear dependencies are computed for a steel ball indenting the various materials that are identified: AP is ammonium perchlorate; and anthracene, as discussed above, is shown on the left side of the figure to have the lowest elastic loading curve, that is to be compared, on the right-side figure location, with indication of a low value for the conventional diamond pyramid, or Vickers hardness number, VHN. The elastic loading lines are raised in order of increasing material elastic stiffnesses. Also, at the end points of the elastic loading lines for a number of materials are the theoretical hardness stresses for cracking, σ_c , as computed on an indentation fracture mechanics basis for different ball sizes [51,52]. The Hertzian cracking stress is seen to be lower at larger ball sizes.

Experimental ball indentation test results are shown in Fig. 10 (as open square points) for an RDX (210) crystal surface indented with a steel ball of 1.59 mm D value and d values determined from optical measurements of the residual indentation sizes. As noted, several smaller indents were free of cracking. The hardness values with associated cracks are lower than the theoretical Hertzian stress for cracking, shown at the terminus of the elastic loading line, because of the role of dislocations on promoting cracking. However, the plastically-cracked material measurements are not very far below the theoretical elastic cracking stress, and so Fig. 10 gives indication of only a relatively limited range in stress level for dynamic dislocation behavior preceding cracking in RDX, say, compared to the much larger range shown for NaCl.

Diamond pyramid, or Vickers, hardness test results are supposed to give a plastic hardness stress equivalent to that obtained in a ball indentation test with $(d/D) = 0.375$ [53], and so, on the right side of Fig. 10, representative diamond pyramid hardness, or VHN, values are shown for a variety of materials. Consider the comparative hardness curves shown for MgO, RDX and NaCl crystals, in the latter case, where a continuous hardness stress-strain determination produced excellent agreement with the measured value of the conventional hardness [49,50]. MgO is at the top of the vertically distributed conventional hardness values with an indicated hardness of approximately 7 GPa (1 GPa = 98.1 kgf/mm²), falling below a theoretical Hertzian stress value, for the same hardness-determined ball size, in excess of 20 GPa. The lower hardness is obtained because of the dislocation promoted cracking that has been described. NaCl has a lower elastic stiffness than MgO, of course, but greater elastic stiffness than RDX. However, RDX has a greater plastic hardness than NaCl and lower theoretical cracking stress. The comparison establishes a quantitative basis for concluding that RDX is elastically compliant, plastically hard, and relatively brittle.

4.3. Drop-weight impact testing for crystal sensitivity

Early work on the initiation of explosives by mechanical loading, particularly, by drop-weight impact testing, led to an explanation of localized hot spot heating being responsible for the effect [54,55]. Field et al. [56] set out the main mechanisms for the generation of hot

Table 2

The types of pressure-time curves shown by various materials subjected to impact, after Heavens and Field [58].

No pressure disturbance	Slight pressure disturbance	Series of pressure fluctuations	Sharp drop in pressure	Sharp drop, pressure falling to zero
Charcoal	NaCl	Tetryl [†]	NH ₄ ClO ₄ *	PETN*
Graphite	KBr	Picric acid	NaN ₃	RDX*
Glass	Borax	Composition B	BaNO ₃	HMX*
CaCO ₃	HgI	Oxalic acid	Sulphur	TNT
Na ₂ CO ₃	Polyvinyl alcohol	Ammonium oxalate	Phenolphthalein	NH ₄ NO ₃
LiF		Ammonium acetate		KNO ₃
Cellulose (sawdust)		Numerous organic solids		KN ₃
NG [†]				NH ₄ Cl
NC [†]				Tartaric acid
Blasting gelatine [†]				Sucrose
				Gunpowder
				Polystyrene

*These materials ignited at the instant of the pressure drop.

†These materials ignited but not at the instant of a pressure drop.

spots as: (1) adiabatic compression of gas pores; (2) viscous heating of extruded material between grains or at external surfaces; (3) frictional heating between contacting surfaces; and, (4) localized adiabatic shear during mechanical failure. Modern demonstration of such hot spots was produced by Coffey and Jacobs in drop-weight impact tests of explosive particles placed onto heat sensitive film [57].

Important evidence for discontinuous load drop behavior, analogous to yield point behavior, being associated with the hot spot heating and chemical decomposition was provided by Heavens and Field [58] who monitored the transmitted pressure wave in impact tests on thin layers of powder particles. The results are summarized in Table 2 in columns under schematically-drawn impact stress-time responses shown for an assortment of energetic and inert materials that were tested. Explosive initiations were obtained for the "sharp drop" type curves characteristic of the energetic materials shown in the right hand column of Table 2, and for ammonium perchlorate (NH₄ClO₄, AP) in the second-from-right-hand column. Other evidence for the need of the deformation to be concentrated in narrow shear bands associated with the sharp load drop behavior and, also, with adiabatic heating, was obtained in a companion study by Winter and Field [59], who investigated the reverse situation of small particles impacting onto larger explosive crystal surfaces. Such adiabatic shear bands are associated with discontinuous load drops.

Armstrong et al. [60] pointed out that achievement of appreciable hot spot temperatures at the slip band level required the non-uniformly distributed dislocations to be blocked by strong obstacles and, also, that the pile-up energy had to be dissipated by an avalanche-type of collapse of the obstacles. Theoretical description of the dynamic release of a pile-up

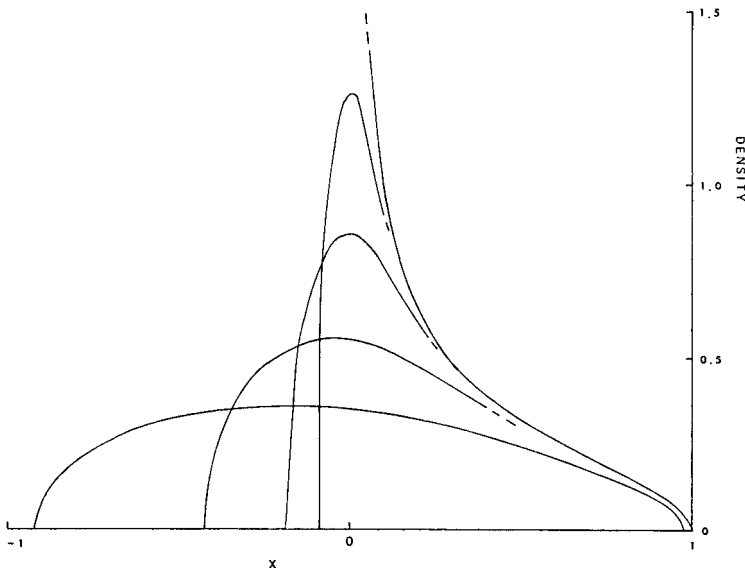


Fig. 11. Release of a dislocation pile-up from its blocking obstacle, showing the shape of the dislocation distribution as it moves from right to left, at sequential (dimensionless) time steps, $t = 0, 0.01, 0.03, 0.10$ and 0.30 , after Head [61].

had been provided on a dislocation group basis by Head for the case where there is a linear dislocation velocity dependence on the shear stress [61]. Fig. 11 gives an example of sequential steps of spreading (to the left) of an initial pile-up, viewed on a continuous distribution of infinitesimal dislocations basis, after the pile-up block was removed suddenly. The local dislocation density, compared to the average value in the normalized initial slip length, is shown to spread rapidly on initial release of the pile-up. At one hundredth of the time it would take for a single dislocation to travel the length of the pile-up when driven by the external stress, and with a linear stress-velocity law, about one-fifth of the released dislocations have raced ahead to a distance of about one tenth of the unit pile-up length. Thus, the consideration obtains that an initial build-up of strain energy might proceed isothermally until, at critical microstructural stress intensity, breakthrough occurs and the stored energy is released adiabatically [60]. Other related model descriptions of dynamic dislocation pile-up properties have been given by Gerstle and Dvorak [62] and Ockendon and Ockendon [63]. Such pile-ups are now known to be an integral part of slip band propagation against planar boundary obstacles in all materials including, for example, ice polycrystals [64].

An important feature of significant dislocation pile-up activity coming into play in determining the mechanical properties of a material is that crystal size or, within a polycrystal, the grain size influence becomes very recognizable [65]. For polycrystalline metals, the onset of yield point behavior for plastic yielding [66,67] and subsequent plastic flow stress [68] both follow a Hall-Petch dependence on the reciprocal square root of the polycrystal grain diameter. An increased slope for the grain size dependence, now termed the microstructural stress intensity after fracture mechanics connection, is associated with greater

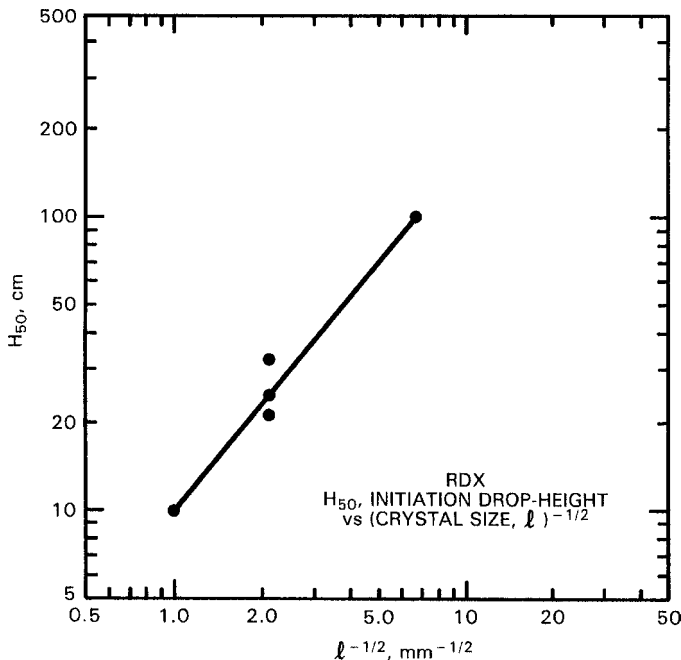


Fig. 12. Drop-weight impact height for 50% probability of initiation as it depends on crystal size, including, for 0.25 mm size crystals, an indication of influence of variation of crystal quality in different batches, after Armstrong, Coffey, DeVost and Elban [70].

pile-up activity [65]. Somewhat analogous pile-up formation, and sudden release, at slip band intersections is directly observable via birefringent transmitted light experiments during tensile deformation of MgO crystals. Also, the subject of crystal size influence on initiation and explosion of energetic crystals has been of scientific interest since early impact deformation results were reported by Bowden and Singh [69].

Application of the pile-up model to drop-weight impact test results obtained on RDX crystals led to prediction of greater drop-weight heights being required to initiate smaller size crystals on a logarithmic basis of drop-weight height versus reciprocal square root of crystal size [70]. Fig. 12 shows experimental measurements demonstrating the effect for RDX crystals. A strongest obstacle of cleavage cracking was assumed to release the pile-up avalanche for hot spot generation. Bowden et al. [71] had proposed that the speed of cracking itself, with an associated plastic zone at its tip, could be responsible for chemical decomposition. Fox and Soria-Ruiz [72] produced evidence for the consideration from experiments on several carbonate and azide crystals. In the latter study, an interesting association of crystal hardness and estimated crack tip temperature was described.

Connection of the pile-up avalanche model for deformation-induced crystal initiation was made, also, with theoretical work of Boddington [73] who derived a relationship between the hot spot size and temperature required for direct initiation of thermal explosion. Reasonable estimations were determined from the pile-up model of deformation-induced temperature rises [74] and of hot spot sizes and lifetimes [70]. Comparison of calculated

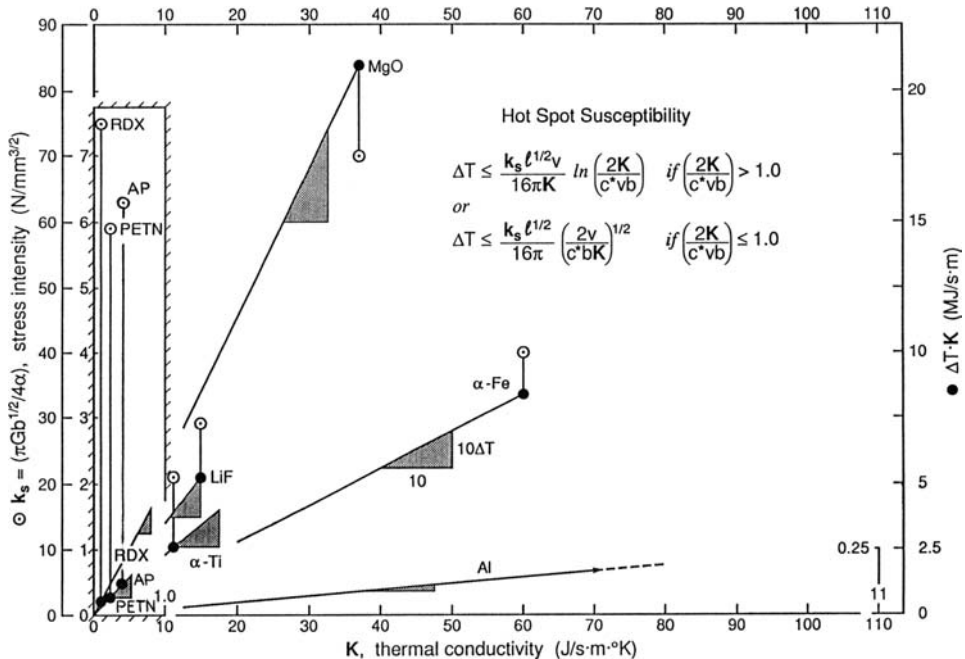


Fig. 13. Graphical basis for illustrating hot spot susceptibility of materials on a dislocation pile-up avalanche model description, including different hot spot temperature expressions for metallic and ionic materials as compared with energetic RDX and PETN, after Armstrong, Coffey and Elban [60].

RDX and PETN crystal deformation-induced hot spot temperatures, relative to their thermal explosion temperatures, led to the conclusion of PETN being more sensitive because of the lesser stability of its molecular structure. For more ductile metallic materials, the dislocation pile-up avalanche model has been suggested to provide the fundamental mechanism for adiabatic shear banding at small plastic strains [75]. Based on the model, Fig. 13 shows a derived graphical basis for comparison of the shear banding susceptibilities of a number of metallic, ionic and energetic materials [76]. In the figure, a greater slope to the material point is indicative of greater shear band susceptibility.

The two dependencies shown in Fig. 13 for the theoretical avalanche-induced temperature rise apply for different material property combinations, among which the microstructural stress intensity, k_s , and thermal conductivity, K , show the greatest material variations [60]. For metals and ionic solids, then, lines of greater slope to the different (open circle) material points in the figure establish a greater shear band susceptibility, that reasonably agree with the (closed circle) upper limiting temperature rise predictions shown using the right-hand ordinate scale of the figure. In the figure, RDX, PETN and AP follow the second inequality and are seen, at the necessarily reduced scale dimensions, to be relatively shear band prone even compared, for example, to α -iron whose low-temperature shear banding behavior is very well known.

4.4. Shock loading

Shock wave phenomena, modeled hydrodynamically to involve discontinuities in pressure, temperature and density, across an idealized shock “front”, are associated with explosive decompositions of energetic materials and their formulations [76]. A one-dimensional state of strain obtains in the shock propagation direction. For the real case, the shock front is taken to be a narrow zone of nanometric-scale dimensions experiencing shear stresses comparable to the theoretical strength.

Dislocation model aspects of shock wave loading began with a pioneering description by Smith of the creation of dislocations at the shock wave front in metals [77]. Meyers [78] has extended the model in a modern account. Fig. 14 shows another model description of distributed nanometer-scale dislocation loops proposed to produce a residual state of one-dimensional strain in the shock propagation direction across a presumed non-planar shock front [79]. An analysis has been given of the dislocation structure [80]. The shear stress state across the compressional front is shown in the top left corner of the figure near to the indicated sectioned crystal edge. Assumed nanometer-scale dislocation shear loops are distributed so as to give, at the curved arrow positions, reacted dislocations with Burgers vectors parallel to the shock propagation direction, hence, the residual, essentially one-dimensional, strain state.

The presence of such a nanometer-scale structure should promote shear banding, also, for subsequent plastic flow from the originally resident dislocation structure whose thermally-activated movement lags behind the shock front that travels at a velocity elastically-determined for one-dimensional strain [81]. The situation is proposed to be analogous to dislocation channeling that occurs in post-deformation of neutron-irradiated metals, where follow-on dislocation movement is made easier through slip band channels cleared by first dislocation movements sweeping out the neutron-induced dislocation loops.

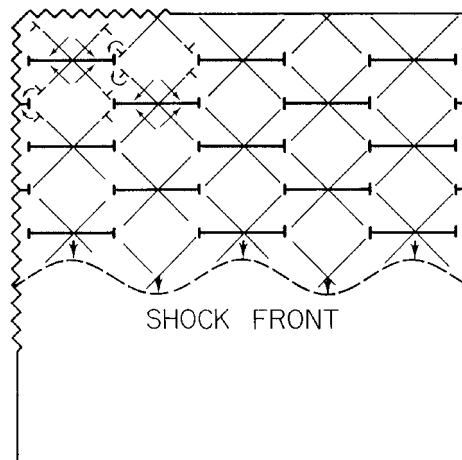


Fig. 14. Shock model for nanometer-scale dislocation loops that produce a residual deformation state of one-dimensional compression, after Armstrong, Miller and Sandusky [79], as elaborated by Bandak, Armstrong and Douglas [80].

Otherwise, considerable research has been performed by Gupta and colleagues [82,83] on the shock wave deformation of LiF crystals, for example, as described in a later paper on investigating details of stress relaxation at shocked crystal surface layers previously hardened by solute diffusion [84].

Special challenges occur for dislocation mechanics in the regime of shock wave loading both because of the nanometric size of events at the shock front and its speed of passage that requires dislocation-connected reaction times from picoseconds to nanoseconds [85]. Results in the low shock regime are presumed to connect with normal high strain rate deformation results, for example, as achieved in split Hopkinson pressure bar tests and Taylor cylinder impact tests [81]. At these strain rates, deformation twinning is favored over dislocation slip for a number of metals and alloy systems [86]. Follow-on thermally-activated slip trails behind the shock front. For larger amplitude shocks, creation of a dislocation nanostructure occurs at the shock front and then interaction of the trailing viscoplastic flow with the newly created nanoscale dislocation clusters is an important consideration. At the highest shock amplitudes, “*in situ*” initiation is envisioned to occur within the strain fields of dislocation cores [81,85]. At the most fundamental level, the mechanism of vibrational energy (up pumping) enhancement should be favored at dislocation cores because of the importance of anharmonic coupling to the process [87–89].

An early experiment on the shock initiation of individual cm-size RDX crystals, measured on a microsecond time scale, was reported by Adams and colleagues [90]. The crystals were found to be less sensitive to shock initiation than powdered material; however, once shocked the crystals were significantly more sensitive to a second shock. The result was explained on the basis that the first shock produced internal damage that provided sources of hot spots. Sandusky et al. [91] obtained sub-microsecond optical observations of luminous slip and cracking systems trailing behind the shock front of AP crystals supplied by T.L. Boggs, Naval Air Warfare Center, China Lake, CA. Significant light generation occurred from the shock interaction with microhardness impressions put into the crystal surface before shocking. X-ray photoelectron spectroscopy (XPS) measurements made on the shocked AP crystals demonstrated that perchlorate decomposition occurred at the shocked indentation sites [92]. Higher shock pressures applied to nitramine crystals were also shown to produce deformation-associated luminosity in RDX and cyclotetramethylenetrinitramine (HMX) crystals [93].

The importance of crystal orientation on the shock initiation sensitivity of cm-size body-centered tetragonal PETN crystals was established in a series of papers by Dick and colleagues [94–96]. The experiments built onto very complete information being known about the linear and volume compression of shocked PETN crystals [97], their elastic-plastic properties [98] and elastic constants [99]. The times and shock propagation distances from the impacted crystal surface for “run-to-detonation” were very different for different crystal orientations. Match with the dislocation Burgers vectors and slip systems led to correlation of this measure of crystal sensitivity for {110} directed shocks with difficult shearing across {100} planes of interleaved molecules, where it was reasoned significant “steric hindrance” should oppose molecular displacements.

For {100} directed shocks that should produce shearing across the primary {110} slip planes, having essentially no interleaved molecules, relatively easy slip occurred and the crystals did not detonate. Intermolecular distances between outcropping arms of adjacent

molecules were computed for different shear displacements across the crystal planes to demonstrate the occurrence of steric hindrance. In [96], the PETN results were connected with a similar dislocation model analysis for RDX of intermolecular interactions proposed to explain the formation of nitroso compounds [100]. In a follow-on analysis, Dick suggests that, because of the low stiffness coefficients of PETN compared to metallic, ionic and covalent crystals, the theoretical perfect crystal strength might have been reached in his crystals so as to produce homogeneous slip and thus explain equally well the experimental results [101]. The model of steric hindrance was also applied by Dick [102] to explain the explosive behavior reported for nitromethane crystals when rapidly loaded in a diamond anvil, high pressure cell [103].

4.5. Laser damage experiments

The use of a laser beam to probe damage processes within individual energetic crystals or powder compacts is also of interest to the energetic materials community [104]. For dislocation-based interest in the present report, brief descriptions are given here of very low power ignition of melt spots on an RDX crystal surface, in order to investigate thermal stress influences on the combustion process [105], and, at the opposite extreme, high energy input for initiation of detonation [106,107]. Fig. 15 shows, from the thermomechanically-

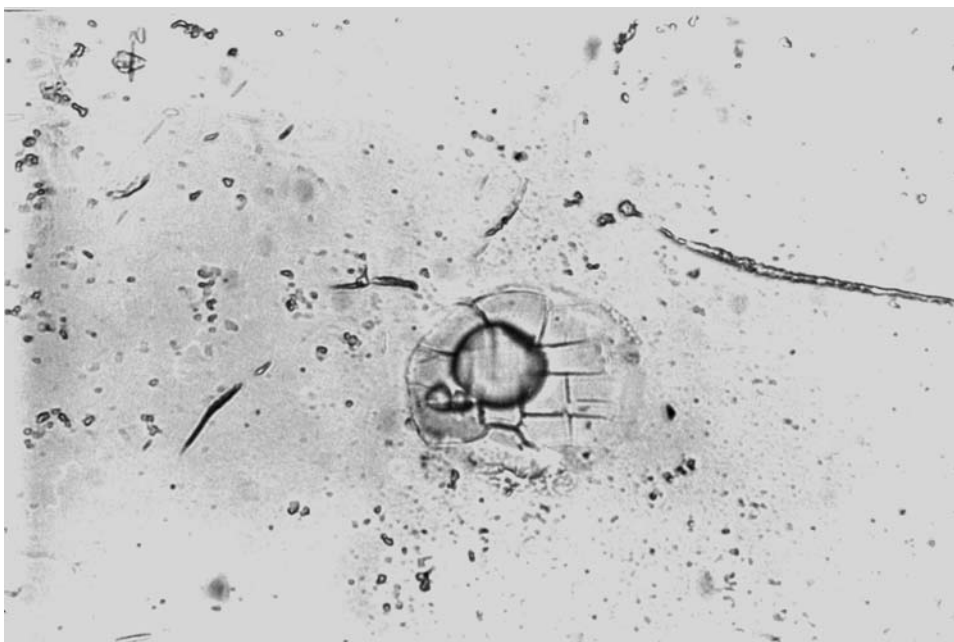


Fig. 15. Combustion residue and microcracking at an RDX (210) crystal surface burn spot after laser irradiation; the vertical separation of parallel microcracks is ~ 5 micrometers. After Armstrong, Ramaswamy and Field [105], as further analyzed by Elban, Armstrong and Russell [108].

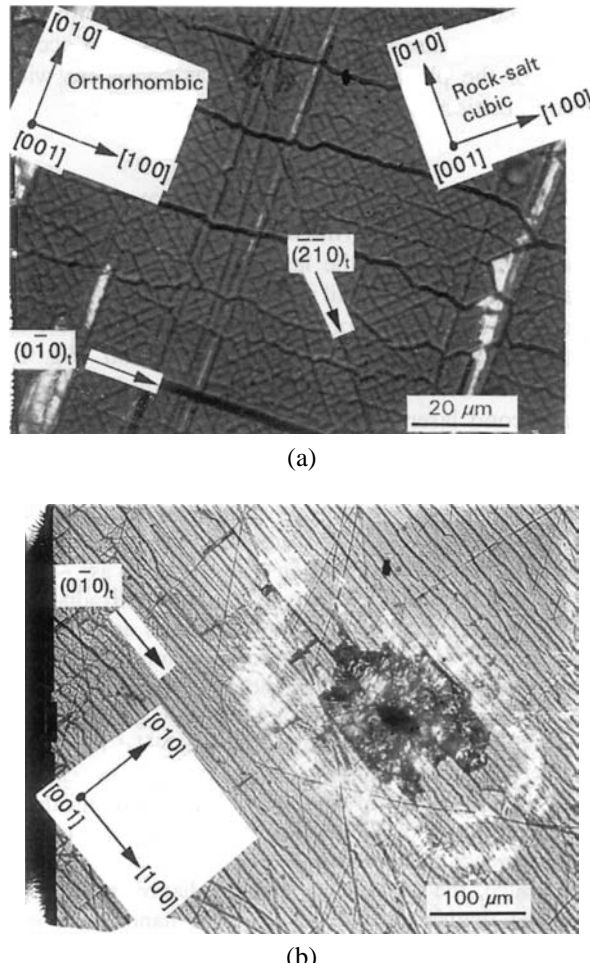


Fig. 16. Laser-impacted (001)AP crystal surface (a) at high magnification to show the sequential macroscopic (210) cracking in the low temperature orthorhombic phase and higher temperature, finer scale, (010) cracking retained from the rocksalt-type cubic phase; and (b) lower magnification view of the central drilled hole exhibiting a whitish halo of sub-surface (001) cracking. After Ramaswamy, Shin, Armstrong, Lee and Sharma [109].

based combustion study, a re-solidified melt spot produced with an impinging laser beam directed onto an RDX crystal surface at a grazing angle of about ten degrees. A micrometer-scale network of cracking is observed underneath the circumferentially-enclosed melt spot-crystal interface. Cracking was reasoned to occur more easily inside the melt spot because only the liquid–solid interfacial energy had to be supplied [108].

A very different appreciably laser-damaged situation is shown in Fig. 16(a, b), where heavy damage is shown at a hole (Fig. 16(b)) drilled into an AP crystal surface from a straight-on focused, nanosecond pulsed, laser beam [109]. In this case, the crystal was

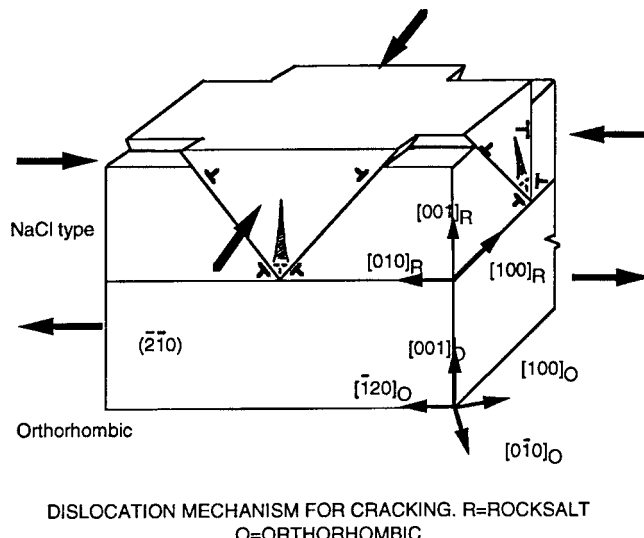


Fig. 17. Schematic dislocation model for explanation of the {010} cracking shown in Fig. 16(a) for the higher temperature rocksalt-type cubic structure of AP; after Ramaswamy et al. [109].

laser-heated through the low-temperature orthorhombic-to-rocksalt cubic phase transformation and cracking occurred sequentially in both crystal phases. The initial macro-scale cracking on the ambient temperature (010) cleavage plane of the orthorhombic structure is observed in Fig. 16(a), for a magnified region of Fig. 16(b), while residual microscopic cracking is observed in Fig. 16(a) on the previous {010} planes of the laser-heating-induced transformed cubic (rocksalt) structure. Fig. 17 gives a dislocation reaction description of the compressive stress state leading to the {010} cubic cracking, based on the complementary crystal axes shown in both figures. The hydrostatic tensile stress state of the reacted <100> dislocations was reasoned to contribute to sub-surface hollow decomposition sites observed with the scanning electron microscope. X-ray photoelectron spectroscopy (XPS) measurements gave evidence of decomposition to ammonium chloride and atomic force microscopy images gave indication of transformation product [109].

5. Chemical reactivity

5.1. Cleavage-induced chemical reaction

As mentioned earlier, the concept of chemical decomposition of thermally unstable solids resulting from elastic strain energy released during crack propagation breaking intramolecular bonds was introduced by Bowden et al. [71]. The amount of decomposition gas generated during fracture within a closed chamber was measured for β -lead azide, sodium azide, PETN and several inert solids, as given in Table 3. The results and their interpretation were

Table 3

Fracture-induced cleavage surface chemical decompositions, after Bowden, Fox and Soria-Ruiz [71] and Fox and Soria-Ruiz [72].

Material	No. of expts.	Amount of decomposition (molecules cm ⁻²)	Average No. of monolayers decomposed
Magnesium oxide	9	< 12 ¹²	< 0.001
Calcium carbonate (calcite)	14	2 × 10 ¹³	0.09
Magnesium carbonate (magnesite)	14	1 × 10 ¹⁴	0.37
Lead carbonate (cerussite)	8	~ 7 × 10 ¹⁴	~ 2
Sodium azide	5	1 × 10 ¹³	0.02
β -Lead azide	10	~ 3 × 10 ¹⁵	~ 10
PETN	7	2 × 10 ¹⁵ (for mass 28)	~ 2

presented subsequently in more detail [72]. Particularly noteworthy was the obtainment of estimates of the effective temperature at the various crack tips, calculated assuming that the mechanism occurring is the same as for conventional thermal decomposition.

In a separate study, Fox and Soria-Ruiz [110,111] associated differences in decomposition kinetics of calcite as a function of temperature with the movement (rather than mere presence) of dislocations on several different slip planes. Easy decomposition occurred on those planes in which the carbonate (CO_3^{2-}) ion was favorably oriented, being essentially perpendicular to the plane. As such, this provided an early indication that solid-state chemical reactivity involved particular crystallographic arrangements of ions (or molecular species, more generally), rather than being just a bulk phenomenon.

More recent fracture-induced decomposition results for PETN were obtained by Hauser et al. [112]. Using mass spectroscopy, distinctly different decomposition products were obtained depending on the rate of crack propagation. Slow, low energy cracks, achieved by a machine-driven chisel, caused the cleavage of the outer molecule CH₂O-to-NO₂ bonds, such as occurs in conventional thermal decomposition. Rapid, high energy cracks, resulting from an explosively-driven chisel, caused the breaking of the inner and stronger C–C bonds at the centre of the molecule. Thus, it was concluded that the reaction pathway for decomposition was influenced by the amount of energy transmitted to the crack tip.

5.2. Polymerization related to sucrose decomposition

Enhanced reactivity at dislocations in inert (non-energetic) solids has been extensively reviewed by Thomas [113,114]. The emphasis has been primarily on inorganic materials, but photomicrographs were presented [19] that indicate common aspects [115] exist between the initial stages of solid-state polymerization and the beginning stages of decomposition of molecular crystal sucrose, also associated with the presence of dislocations.

5.3. AP decomposition

The most extensive work on an energetic (oxidizer) solid to connect chemical decomposition with the presence of dislocations has been reported for single crystal ammonium perchlorate, AP. Pioneering results were obtained by Galwey and Jacobs [116], showing that decomposition of as-grown orthorhombic (stable room temperature phase) AP crystals is initiated by defects and occurs primarily at mosaic crystal boundaries. Decomposition then proceeds in a three-dimensional manner, consuming the boundary regions. Subsequently, Herley and Levy [117] investigated the effect of exposing similar crystals to γ -ray irradiation before thermal decomposition occurred. Assuming the same decomposition mechanism, the authors concluded that irradiation shortened the induction period for initial decomposition while the reaction rate constant was found to be enhanced for the acceleratory period of decomposition. The change in rate constant was attributed to an increase in the number of decomposition nuclei (presumably associated with dislocations) that were produced by the irradiation.

Much more detailed thermal decomposition results were reported by Herley and Levy [118,119] for millimeter size and powdered AP crystals unirradiated and exposed to X- or γ -ray irradiation. Previous observations concerning the effect that irradiation has on induction period and acceleratory period decomposition rate were confirmed. Separate microscopic examination of partially decomposed crystals revealed that the number of decomposition nuclei increased in the irradiated crystals. Irradiation also increased the rate at which potential decomposition sites became active. The combined kinetic and microstructural results show that the same decomposition processes take place in both unirradiated and irradiated AP, but that irradiation increases the rate constants.

The most direct evidence relating thermal decomposition sites in laboratory-grown single crystals of AP to dislocations was obtained by Herley et al. [120]. Initial nucleation processes involved in establishing thermal decomposition sites were investigated using both light and (transmission and scanning) electron microscopies. Both unstrained and plastically deformed (i.e., from pre-compression) crystals were heated at relatively mild elevated temperatures (170–210°C) in order to study the initial stages of decomposition by surface nucleation. On the (001) surface of unstrained crystals, isolated, circular nucleation sites appear to occur at random. This was also observed for some sites on the (210) surface, but other sites were aligned crystallographically.

For the strained crystals, the nucleation sites were well aligned in both surfaces and were mostly in the same crystallographic directions as pits that formed in chemical etch pitting studies on separate crystals. The close correspondence in the two sets of observations led to the conclusion that the decomposition nuclei form preferentially at dislocations that intersect the surfaces. The initial decomposition nuclei stop growing when a critical size is reached, and new nuclei (originating a little below the surface) form and grow until the top surface layer has completely reacted. Nucleation of deeper interior decomposition sites is also reasoned to be associated with dislocations based on observations that relate to the activity of known slip systems.

The effects that X- and γ -ray irradiation have directly on the chemical decomposition of AP was also investigated by Herley and Levy [121]. As with thermal decomposition, circular decomposition nuclei (resembling etch pits) formed having approximately the same

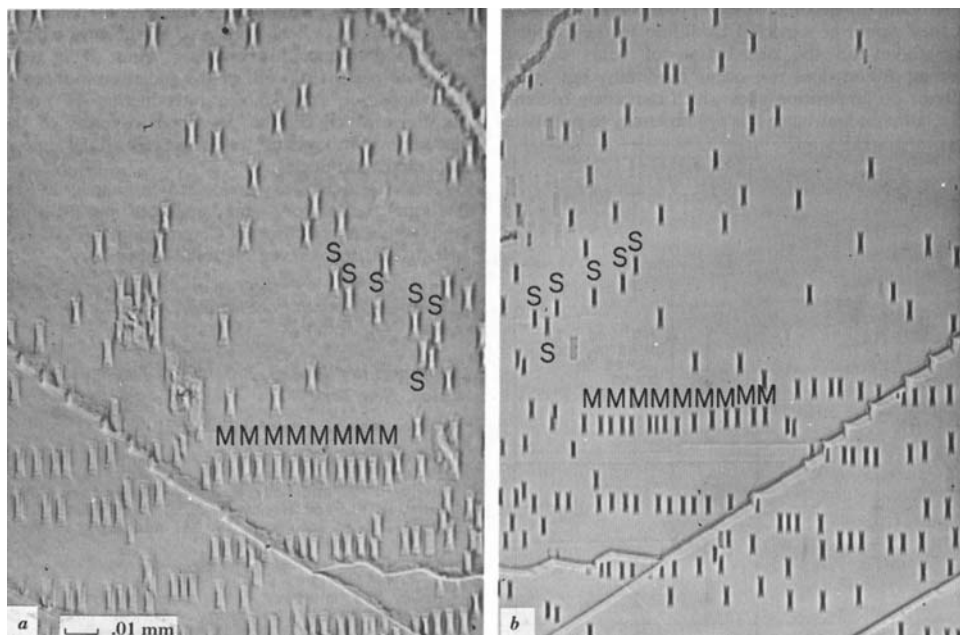


Fig. 18. Photomicrographs of matching AP (210) cleavage surfaces showing radiation-induced dislocation movement. Side a was not irradiated but side b received a dose of 10^4 rad gamma-ray exposure. A set of dislocations which have moved during irradiation is labeled M while set S has remained stationary. After Herley and Levy [122,123].

size and surface density ($2\text{--}40 \times 10^6/\text{cm}^2$). Many of the nuclei formed by irradiation were aligned in the same crystallographic directions observed in the thermal decomposition studies of pre-irradiated and pre-stressed crystals. Thus, it was concluded that dislocations are also involved in this type of decomposition. Irradiation-induced decomposition sites form initially throughout the exposed volume, in a roughly uniform distribution, while thermal decomposition sites appear on the surface initially and grow inward subsequently.

Having established the direct involvement that dislocations have in the radiation-induced decomposition of AP, Herley and Levy [122,123] reported measurements of dislocation density as a function of radiation level. Fig. 18 shows etch pit observations on matching crystal surfaces indicating dislocation movement caused by the irradiation. The threshold for dislocation generation was found to be about 10^5 rad. Between 10^5 and 10^6 rad, the dislocation density increased linearly with irradiation, and above 10^6 rad, the density was too high to measure reliably. It was concluded that the observed accelerated decomposition rates occurred because additional decomposition nuclei formed at dislocations generated during irradiation. Further, it was proposed that interior gaseous decomposition products created stress levels in the lattice high enough for Frank-Read sources to operate, thus providing an explanation for radiation-induced dislocation generation. The interesting results are, no doubt, very particular to the stability of the AP molecule, its lattice energy and the gaseous decomposition products.

5.4. Spectroscopy

Tang et al. [124] have reported mass spectrographic results for the decomposition of RDX, PETN, silver azide and lead azide crystal surfaces impacted with a focused laser beam. The work followed on from interest at the University of Cambridge Cavendish Laboratory [125] in detecting molecular fragments via time-of-flight mass spectroscopy after fracturing crystals of PETN and lead azotetrazole. The work relates as well to the results reported by Fox and Soria-Ruiz [110]. Although significant damage sites were shown by scanning electron microscope observations of cratering and cracking on the various crystal surfaces, no dislocation connection via slip traces or other crystallographic markings were reported. Rather, the results were interpreted in terms of the reaction pathways taken by the different molecules in the decomposition process. In this regard, such measurements relate as well to the important consideration of the decomposition of energetic crystals in combustion studies of propellant formulations. Brill [126] has given a description of surface chemistry considerations employing Fourier infrared (FTIR) spectrometry to identify the chemical reaction steps for decomposition of AP, RDX, HMX and other energetic compounds for different burn rate conditions. Behrens and Bulusu [127] have detected early nitroso compound formation via mass spectroscopy observations made during thermal decomposition and pointed out that the measurements were consistent with decomposition in the solid phase as reported also from mechanical test results [128].

5.5. X-radiation induced decomposition

Synchrotron X-ray topography was used by Bhat et al. [129] to investigate beam-induced low-level decomposition (about 1%) in large AP single crystals. Significant structural damage was observed in the outer layers of the crystal causing bending to occur by slip on previously reported systems. An enhancement in the decomposition rate was reported with dislocations serving as the decomposition nuclei. The precipitation of decomposition products at the nuclei causes crystals (initially transparent) to become opaque in a process that resembles the formation of a colloidal suspension. Importantly, the synchrotron white beam is able to image the resultant defect structure at higher levels of decomposition than was possible in conventional laboratory experiments using monochromatic radiation.

The use of X-ray topography to examine sub-structural changes occurring during chemical reactions in several crystalline solids, including single crystal AP, was reported by Sheen and Sherwood [130]. The suitability of using laboratory and synchrotron sources to study solid-state decomposition was characterized in more detail. Using white beam synchrotron, transmission Laue diffraction topographs of AP were obtained as a function of absorbed doses. Graded absorption of the available wavelengths across the crystal thickness caused the crystal to bend initially with the development of a large amount of dislocation structure. Eventually, the strain equalized and flexure of the crystal was eliminated, followed by detection of chemical decomposition based on image broadening and subsequent formation of product powder rings.

5.6. Shock reactivity

The roles that deformation, fracture and material microstructure have on the shock reactivity of single crystal AP were investigated by Sandusky et al. [91]. Experiments were conducted in a mineral-oil bath with the shock being provided by a small explosive donor. This arrangement allowed samples to be recovered for subsequent chemical analysis and microstructural characterization. Particularly noteworthy experiments involved shocking crystals possessing a large surface strain center created by a Vickers indenter. High-speed photographic coverage revealed distinct diagonal lines immediately behind the shock front corresponding to (010)[001] slip, a moving luminous band believed associated with a propagating crack and light near to the hardness impression that was conjectured to be due to chemical reaction.

A subsequent experiment was conducted [131] on an AP crystal containing several Vickers impressions and shocked at the reaction threshold. High-speed photographs again showed luminosity near impressions. The recovered crystal was cleaved through two of the impressions, allowing spatial chemical analysis to be performed in the crystal interior by using the XPS technique to scan areas 1.0×1.0 mm. The line widths of XPS spectra were correlated [92] with dislocation densities that were measured directly using a chemical etch pit technique and related to somewhat analogous irradiation results obtained by Herley and Levy [121–123] that were discussed earlier. The linewidth of the Cl(2p_{3/2}) spectra ranged from 1.70 eV for the region of greatest visible damage to 1.22 eV for the region with no visible damage or for an as-grown (control) crystal.

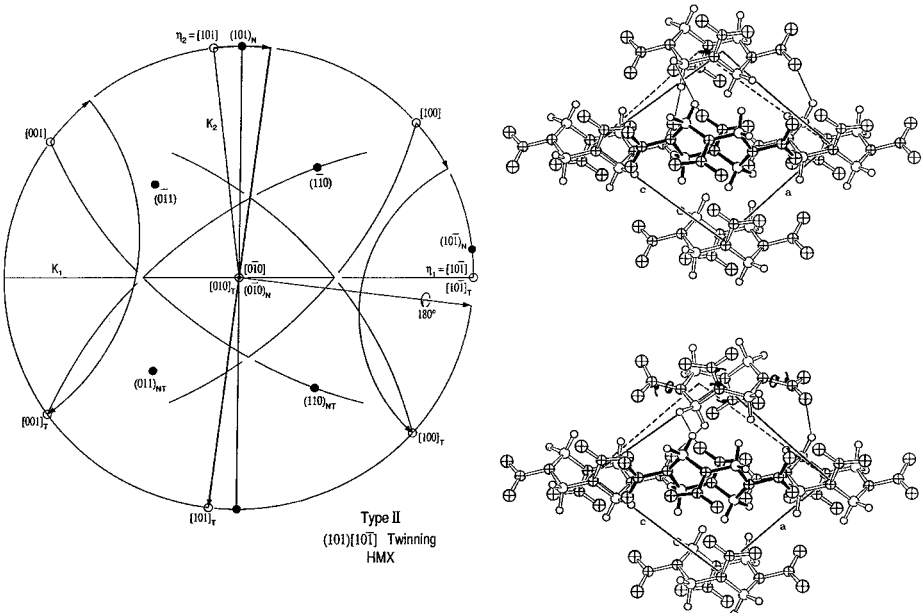
The broadening of the photoelectron lines was attributed to the lattice distortion present in the immediate vicinity of the dislocations. On the same freshly cleaved surfaces, the largest amounts of chemical decomposition were associated with the hardness impressions. However, the highest levels were not detected in the areas immediately adjacent to the impressions where dislocation densities were found (based on line-width measurements) to be highest. Rather, the highest decomposition levels were found in areas where the dislocation densities had intermediate values and appeared to be associated with a prominent (001) crack or irregular cleavage steps emanating from an impression. It was concluded that the observed luminosity resulted from chemical reaction occurring either at the tip of the (001) crack or in its plastic zone.

6. Molecular modeling

The various methods of molecular modeling have been applied mainly to prediction of crystal structures and densities, determination of the P-N stress, dislocation displacements relating to intermolecular interactions and shock wave properties, including electronic or vibrational excitations and shear wave characteristics.

6.1. Crystal densities

Prediction of energetic crystal densities is important because, in addition to interest in greatest energy density for explosiveness, both the detonation pressure and the velocity



Position Å	$(T1PE^*)_{tr}$ Kcal/mol	Position Å	$(T2PE^{**})_{tr}$ Kcal/mol
0.000	-41.97	0.000	-29.95
0.265	-40.91	0.265	-32.43
0.530	-36.79	0.530	-35.91
0.790	-36.40	0.790	-37.58
1.060	-34.19	1.060	-38.06 [#]

* Type 1 Potential Energy

** Type 2 Potential Energy

Type 2 Potential Energy + 21° rotation of N-N bond

Fig. 19. Crystallography of Type II $\{101\}\langle 101 \rangle$ twinning in HMX; on a stereographic projection basis at top left, and $\{010\}$ plane projection of pre-and post-twin positions at top right, with tabulated sequential potential energy evaluations for the indicated lattice point displacements, also involving required N-N bond rotation. After Armstrong, Ammon, Du, Elban and Zhang [135].

increase with density [132]. The topic relates to X-ray and neutron diffraction methods employed in crystal structure determinations. Computer-assisted modeling and graphics programs are employed with energy minimization techniques. Stine [133] has summarized empirical methods for predicting densities and heats of formation of proposed high explosives. Gilardi [134] has given a crystal structure-based description of interest in polycyclic energetic compounds for enhancing performance and/or safety. An interesting connection with such modeling efforts is provided by the description given by Armstrong et al. [135]

for deformation twinning in the monoclinic beta-HMX crystal structure where the crystal structure-derived potential energy was followed in identifying a type II $\{101\}\langle 101 \rangle$ twinning mechanism; see Fig. 19. Twinning was concluded to be favorable over slip in the beta-HMX structure because of the flexibility of the HMX molecule. Density considerations have been investigated on a molecular fragmentation basis also, so as to understand proposed explosive versus non-explosive behaviors of related molecular structures [136].

6.2. The P-N stress for anthracene

The computer simulation of an $[010](001)$ edge dislocation in anthracene has been reported [137]. The structure relates to that described by Robinson and Scott [37] for Fig. 7. Fig. 20 shows equipotential contours in the (001) plane. A dislocation width of 6.2 times the Burgers vector was obtained, indicative of a relatively low P-N stress for the material. The hardness stress-strain result indicated for anthracene in Fig. 10 is consistent with a low shear strength being observed for the material, presumably because of only minor intermolecular blockages occurring in the slip process. An interesting consideration in regard

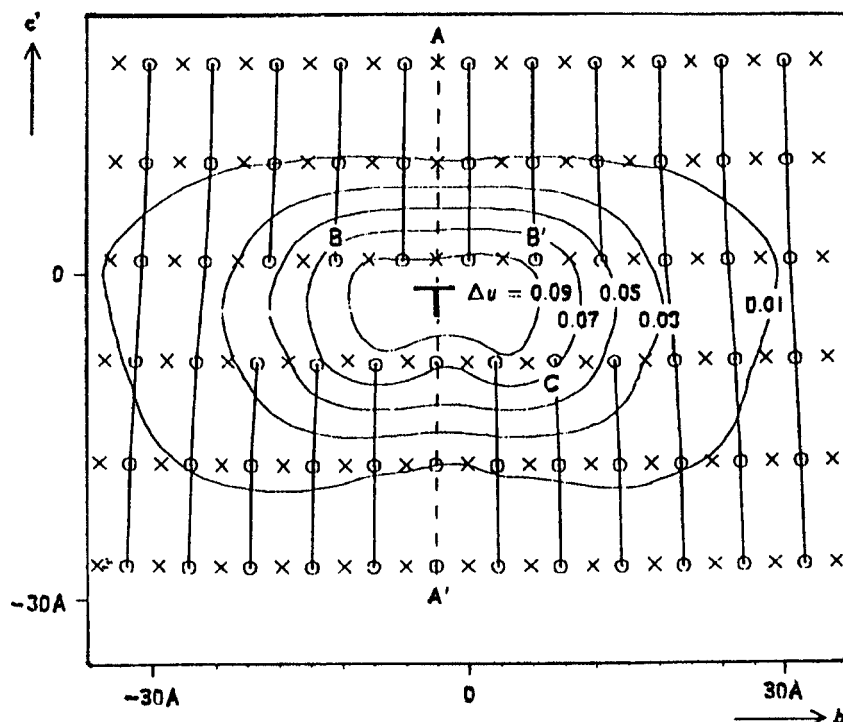


Fig. 20. A projection in the (100) plane of molecular centres at an edge dislocation core in anthracene after relaxation of the lattice positions and with equipotential curves (in units of eV). The crosses denote corner molecules and circles, centre molecules. After Ide, Okada and Kojima [137].

to the intermolecular blockage of adjacent molecules is the suggestion of Nabarro that taking account of the displacement normal to the slip plane in evaluating the P-N stress should give a more accurate value. Lee and Dundurs [138] found in evaluating the suggestion on a conventional basis that the stress was lowered.

6.3. Model dislocation displacements

A schematic picture is shown in Fig. 21 for a [100] Burgers vector dislocation with line direction along [001] one half-cell deep in an RDX crystal. The dislocation has been reasoned to slip on (040) because of the minimized intermolecular interferences for shear displacements during movement [100]. The indicated molecular positions at the dislocation core are clearly far out of order relative to normal nearest neighbor associations. Based on the consideration that dislocation cores in such molecular crystals might be hollow, as predicted by Frank [18], see Section 2.2, the hollow core radius computed for RDX is greater than 7 nm, that is about 6 unit cell distances, thus relating as well to the relatively large values of the dislocation self-energies.

The issue of molecular interferences associated with dislocation movement is demonstrated as well for the RDX lattice structure by examination of slip across the (021) slip

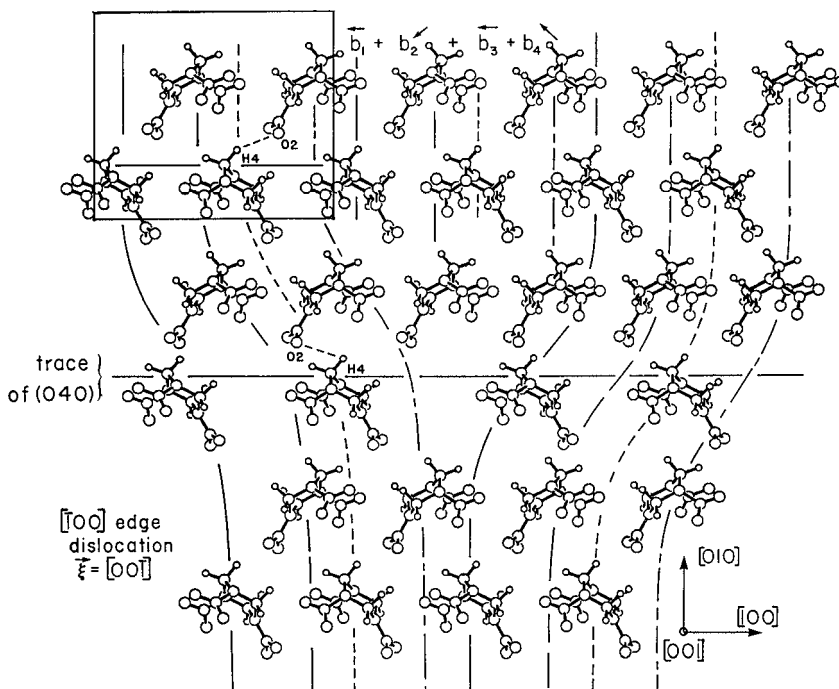


Fig. 21. Schematic view of RDX molecule positions for an [001] edge dislocation on the (040) plane, after Armstrong [28].

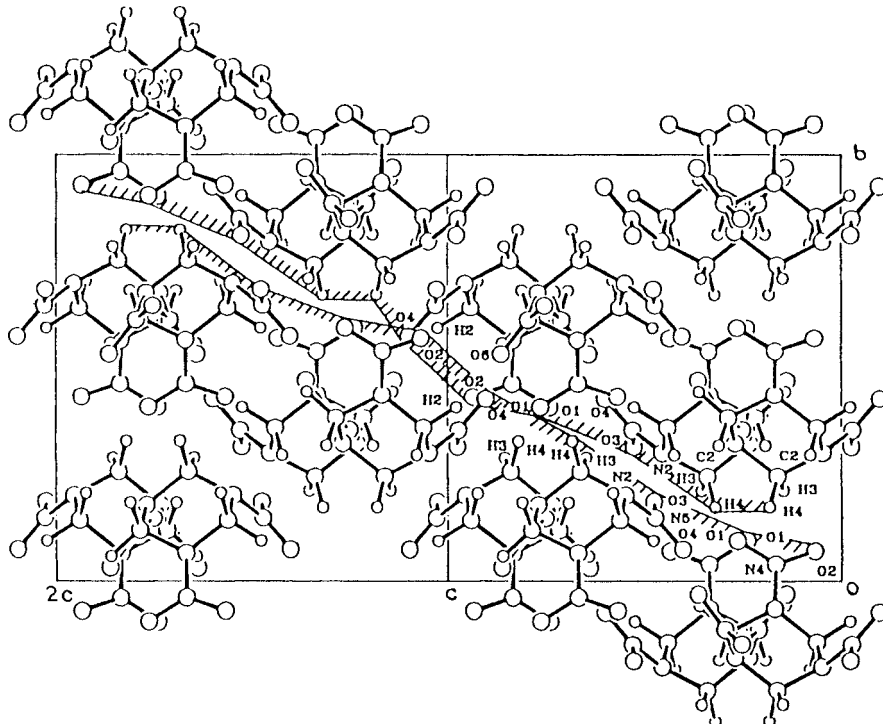


Fig. 22. For RDX, dinitroso-related interactions from [100](021) slip, in and out of the surface-projected (100); after Armstrong [28] and relating to experimental results both from Hoff Sommer, Glover and Elban [128] and Behrens and Bulusu [127].

plane that was identified at hardness micro-indentation sites by Elban et al. [139]. Fig. 22 gives a (100) view of the molecular blockages occurring for shearing across the (021) slip plane, in and out of the projected plane of observation, along [100]. The nitrogen-oxygen interactions indicated by the cross-hatched areas of overlapping molecules when displaced along [100] are just those favoring the creation of nitroso compounds detected in “go/no-go” drop-weight impact tests [128] and in thermal decomposition experiments [127].

Dick and Ritchie [140] followed up also on the earlier work by Dick and colleagues [94–96], and in extension of individual reports of their own [141,142], to evaluate the importance of molecular interferences, or steric hindrances, in causing shorter run-to-detonation distances in PETN crystals shocked along different directions, that is, the distance along a crystal rod traversed by a shock wave before detonation is initiated. Also, elastic precursor stress levels specifying different shock strengths were measured along the different directions using a light gas gun facility. Unhindered [100] and [101] directions were tested along with hindered [110] and [001] tests. The elastic precursor strength increased in that same order. The results are in agreement with the reasoning for dislocation passage being blocked by interferingly-close intermolecular distances. Intermolecular interactions were evaluated with a molecular mechanics program, AMBER, developed for biochemical sys-

tems. Snapshots of the differently sheared lattice were presented. The computations were stated to support the elastic precursor measurements; and, intramolecular bond rotations and angular strains were found to be relatively important as compared with little changes occurring in bond lengths.

6.4. Hot spots in MD simulations

Molecular dynamics (MD) methods lend themselves to shock wave modeling considerations because of the nm-scale sharpness of the shock front and presumed femtosecond-to-picosecond time scale of fundamental events. Karo and colleagues performed pioneering computations relating to energy partitioning and transfer processes, thermal versus athermal characteristics, bond rupturing and defect influences [143]. Tsai [144,145] has described the influence of a cluster of vacancies on enhancing hot spot development through structural relaxation at the clustered defect site. During such relaxation, apparent slip bands

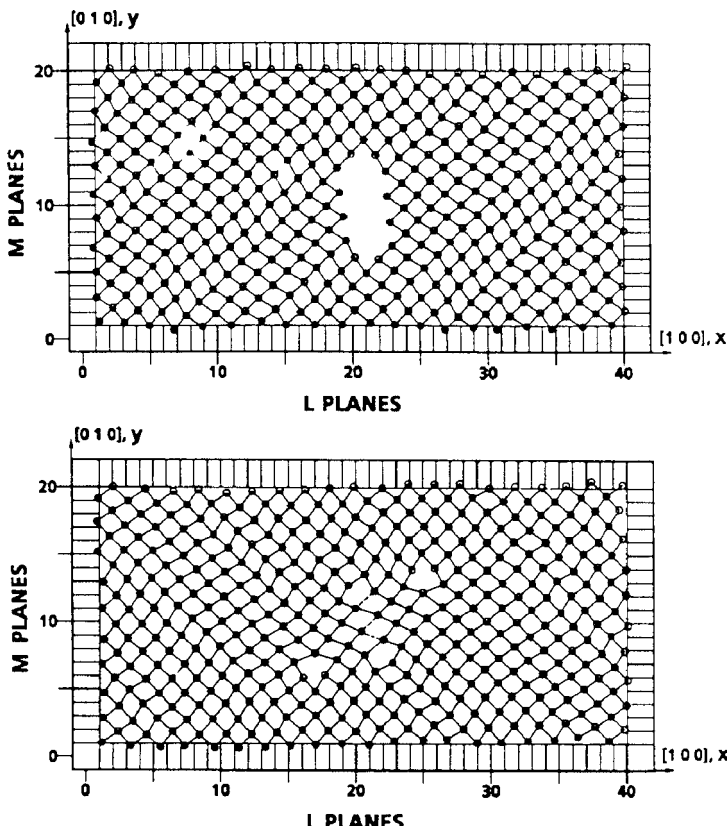


Fig. 23. Molecular dynamics modeling of the collapse of a vacancy cluster into a pair of edge dislocation dipoles, after Bandak, Tsai, Armstrong and Douglas [146].

developed at the cluster site and spread across the specimen. Bandak et al. [146] elaborated on the model. Fig. 23 shows an (001) body-centered cubic lattice cell of Morse-potential-type atoms, also containing a ten-vacancy cluster that relaxed under the MD process of rapid compression to form a pair of dislocation dipoles. The stress-strain behavior of the system was followed to show apparent yielding during relaxation of the vacancy cluster. In a follow-up study of a simple molecular lattice containing vacant molecules, Tsai and Armstrong emphasized that such permanent relaxation was associated with conversion of the higher potential energy of molecules adjacent to the defect structure to thermal hot spot energy [147]. The important point is that significant hot spot heating is always associated with mechanical relaxation, and so a hot spot influence is always present at such sites. The same conclusion was obtained for adaptation of the MD method to a lattice of eight-membered molecular units [148].

The issue of an MD description being appropriate for the comprehensive description of the generation and propagation of shock waves, covering the gamut from match with the continuum theory of planar detonation to connection with local defect properties, as described above, was taken up by C.T. White and colleagues [149]. The associated hot spot mechanism of void collapse was confirmed for a model diatomic lattice [150]. Other MD aspects have been reported for shock compressions and hot spot properties, as follows: model assessment of the multi-phonon up-pumping time scale [151], vibrational heating of naphthalene molecules [152] and picosecond MD resolution of events behind a modeled shock front in polymethylmethacrylate to compare with dye-monitored experimental measurements [153].

6.5. Shock mechanochemistry and atomic force microscopy

Gilman [154] has pointed to historical evidence, stemming from Bridgman's experiments, for the importance of shear deformations in promoting chemical reactions. Based on an analysis of detonation front velocity, Gilman argues that the front propagation is too fast for thermally-activated chemical reactions to occur [155], and homogeneous shear-induced electronic excitations akin to metallization then provide the mechanism for chemical decomposition. The issue relates to earlier discussion [76,85] of the various stages: dislocation movement behind a shock front contributing to initiation of decomposition for weak shocks; that dislocation structure moving behind the shock front, for stronger shocks, and interacting with nanoscale dislocation clusters formed at the front; and, to "in-situ" dislocation core enhancement of decomposition for even stronger shocks. In principle, the importance of anharmonic coupling to the mechanism of vibrational up pumping so as to provide chemistry in the shock front is enhanced within the strain field of the dislocation cores [89]. The Frank hollow core consideration [18] that appears to apply at the nm-scale for energetic crystals should be involved.

Recent results on energetic crystal surfaces obtained with atomic force microscopy (AFM) by Sharma, and analyzed with colleagues, may help to further quantify deformation and thermal influences on energetic material decompositions, for example, relating to recent description of post-shock examination of RDX crystals having undergone an allotrophic phase transformation [156]. Sub-molecular-sized shear crack displacements were

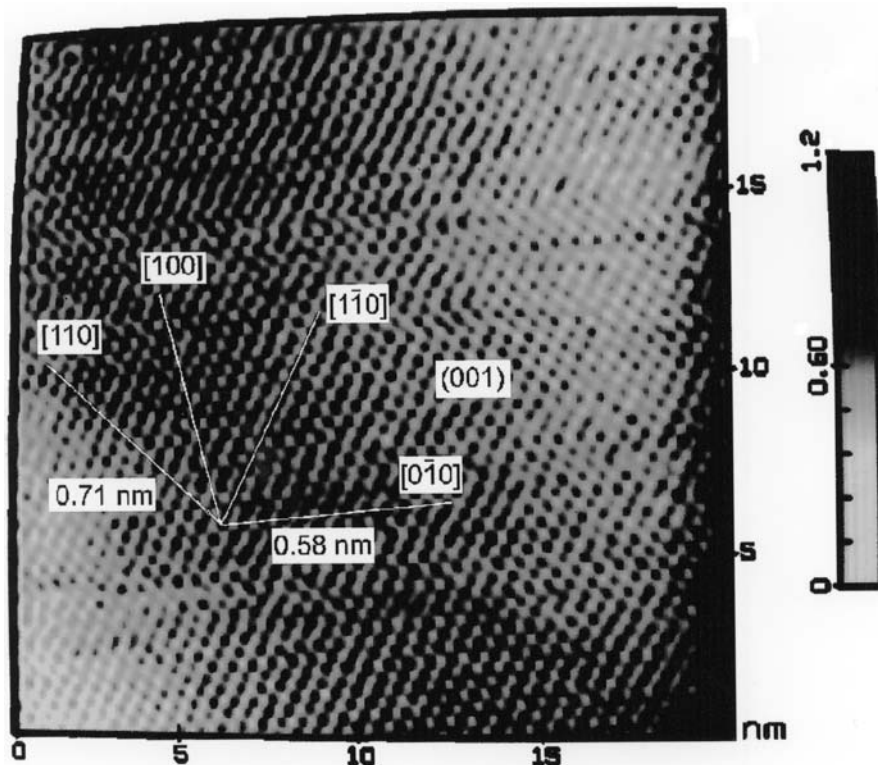


Fig. 24. Atomic force microscope image of molecule positions on an identified RDX (001) cleavage surface, after Sharma, unpublished; see J. Sharma et al. [159].

detected within nanometric-sized crystals formed by multiple fracturing of the initial bulk crystal specimen [157]. Recent measurements have included examination of nanoindentations made within the AFM [158]. Fig. 24 shows an AFM picture of the RDX crystal lattice at nm-scale resolution of individual molecule “spots” [159]. Other AFM examinations of laboratory-grown RDX crystals, in an as-cleaved condition and after various deformations and/or heat treatments, have shown differently oriented surface step structures and clustered zones of disordered molecules.

7. Summary

The enhanced visibility of steps associated with the large Burgers vectors of dislocations in energetic/molecular crystals is aided indirectly by the occurrence of low dislocation densities also associated with the large Burgers vectors that lead to relatively high self-energies. A significant variation in dislocation Burgers and line vectors occurs during crystal growth because of the low symmetry of the molecular crystal structures, conformational require-

ments of positioning oddly-shaped, relatively large, molecules and their relatively weak intermolecular bonding.

Dislocation movement, whether in static indentation tests, under drop-weight impact, or in shock wave loading, is relatively hindered by intermolecular cross-blockages of adjacent juxtaposed molecules, thus giving plastic flow stress values near to the theoretical limit for cleavage cracking. The high self-energies of the dislocations make dislocation nucleation prohibitive while, once present, their strain fields can assist chemical decomposition under suitable thermal and environmental circumstances.

Local concentration of strain energy within the relatively more stable energetic crystals is required to induce intramolecular decomposition, relating to (intermolecular-type) hydrogen and (intramolecular) nitrogen/oxygen bond breakages, for example, as indicated in Figs 19, 21 and 22. Dislocation pile-ups provide an explanation of crystal size effects in energetic crystal decompositions. Such molecular crystals give relative enhancement of local heating from plastic work because of their insulating character.

An interesting recent connection is with the thermomechanical aspect of energetic crystal combustion when serving as an ingredient of a propellant motor. Such combustion occurs over a melt layer formed on the individual crystal surfaces. Micro-cracking, as indicated in Fig. 15, is enhanced at the liquid-solid interface because of need to supply only the lower liquid-solid interfacial energy of cracks, as compared with the far larger solid-vapour value [108]. Recent model fracture mechanics estimates of the pressures required to propagate such micro-crack networks, relating to the indentation fracture mechanics measurements in Fig. 9, give indication of possible crystal shattering instabilities for combustion under high pressure conditions [160].

The role of dislocations in shock wave initiation of detonations is not resolved. Possible mechanisms begin with dislocation activity following behind the shock front for low shocks, shock front generation of dislocations for greater shocks also connecting with follow-on movement of the previously-resident dislocation structure, and, finally, “in-situ” initiation at dislocation cores for high shocks.

Acknowledgements

The authors express appreciation to the many colleagues who have contributed valuable help with our research activities on this topic. Research support has been received with appreciation from the Office of Naval Research, the Naval Surface Warfare Center, both White Oak Laboratory and Indian Head Division, and, most recently, the Air Force Office of Scientific Research. Byron Allmon is thanked for help with compiling the article tables and figures. And, lastly, appreciation is expressed to Michael Duesbery for suggesting that the article be written, and, especially, to Frank Nabarro for many helpful and guiding comments received during his review.

Note added in proof

An updated reference for direct evidence of chemical reactions induced by shear strains is J.J. Gilman, in: *Synthesis, Characterization and Properties of Energetic/Reactive Nanoma-*

terials, eds R.W. Armstrong, N.N. Thadhani, W.H. Wilson, J.J. Gilman and R.L. Simpson (Mater. Res. Soc., Warrendale, PA, 2004) Vol. 800, p. 287.

References

- [1] A.R. Verma, in: International School on Synthesis, Crystal Growth and Characterization of Materials for Energy Conversion and Storage (National Physical Laboratory, New Delhi, 1981) p. 1.
- [2] N. Cabrera and W.K. Burton, Discuss. Faraday Soc., No. 5 (Gurney and Jackson, London, 1949) p. 40.
- [3] F.C. Frank, Discuss. Faraday Soc., No. 5 (Gurney and Jackson, London, 1949) p. 48, General Discussion, *Ibid.*, p. 67; Philos. Mag. 41 (1950) 200.
- [4] L.J. Griffin, Philos. Mag. 41 (1950) 196.
- [5] A.R. Verma, Nature 167 (1951) 939.
- [6] S. Amelinckx, Nature 167 (1951) 939.
- [7] I.M. Dawson and V. Vand, Proc. Roy. Soc. London A206 (1951) 555.
- [8] N.G. Anderson and I.M. Dawson, Proc. Roy. Soc. London A218 (1953) 255; see J.P. Hirth and J. Lothe, Theory of Dislocations (McGraw-Hill Book Co., N.Y., 1968) p. 10.
- [9] J.W. Menter, Proc. Roy. Soc. London A236 (1956) 119.
- [10] P.B. Hirsch, R.W. Horne and M.J. Whelan, Philos. Mag. 1 (1956) 677.
- [11] W. Bollmann, Phys. Rev. 103 (1956) 1588.
- [12] J.B. Newkirk and J.H. Wernick (eds), Direct Observations of Imperfections in Crystals (Interscience Publishers, N.Y., 1961).
- [13] W. Connick and F.G.J. May, J. Cryst. Growth 5 (1969) 65.
- [14] A.R. Lang, quoted in "Diffraction and Imaging Techniques in Materials Science", eds S. Amelinckx, R. Gevers and J. Van Landuyt, Vol. II (North-Holland Publishers, Amsterdam, 1978) p. 678.
- [15] C.S. Choi and E. Prince, Acta Cryst. B28 (1972) 2857.
- [16] F.R.N. Nabarro, Theory of Crystal Dislocations (Dover Publications, N.Y., 1967) p. 302.
- [17] M. Faraday, Philos. Trans. Roy. Soc. London (1834) 55.
- [18] F.C. Frank, Acta Cryst. 4 (1951) 497.
- [19] J.M. Thomas, Endeavor 29 (1970) 149.
- [20] M. Dudley, W. Si, S. Wang, C. Carter, Jr., R. Glass and V. Tsvetkov, Il Nuovo Cimento 19D (1997) 153.
- [21] J.P. Hirth, Acta Mater. 47 (1999) 1.
- [22] R.W. Armstrong and W.L. Elban, Mater. Sci. Eng. A111 (1989) 35.
- [23] J.P. Hirth and J. Lothe, Theory of Dislocations (McGraw-Hill Book Company, N.Y., 1968) p. 216.
- [24] W.L. Elban and R.W. Armstrong, Seventh Symposium (International) on Detonation (Naval Surface Weapons Center, Silver Spring, MD, 1982), NSWC MP 82-334, p. 771.
- [25] H. Klapper, Die waage 33 [1] (1994) 28.
- [26] H. Klapper, in: Characterization of Crystal Growth Defects by X-ray Methods, eds B.K. Tanner and D.K. Bowen (Plenum Press, N.Y., 1980) p. 133; R.W. Armstrong, Characterization of Materials by X-ray Diffraction Topography, in: Crystal Properties and Preparation (Trans Tech Publications, Switzerland, 1988) 16, p. 1; also, Advanced Techniques for Microstructural Evaluation, eds R. Krishnan, T.R. Anantharaman, C.S. Pande and O.P. Arora Proceedings of Indo-U.S. Workshop, DST/ONR, 1988, p. 1.
- [27] A.C. van der Steen and W. Duvalois, in: ONR/TNO Workshop on Desensitization of Explosives and Propellants, ed. A.C. van der Steen (TNO Prins Maurits Laboratory, Rijswijk, The Netherlands, 1991) 3, p. 1.
- [28] R.W. Armstrong, J. de Phys. IV — Coll. 5 (1995) C4-89.
- [29] H. Klapper, in: Crystals 13 (Springer-Verlag, Berlin, 1991) p. 109.
- [30] K.A. Gross, J. Crystal Growth 6 (1970) 210.
- [31] J.D. Eshelby, W.T. Read and W. Shockley, Acta Metall. 1 (1953) 251.
- [32] W.J.P. van Enckevort and H. Klapper, J. Cryst. Growth 80 (1987) 91.
- [33] I.T. McDermott and P.P. Phakey, J. Appl. Cryst. 4 (1971) 479; Phys. Stat. Sol. (a) 8 (1971) 505.
- [34] P.J. Halfpenny, K.J. Roberts and J.N. Sherwood, Philos. Mag. 53 (1986) 531.

- [35] P.J. Halfpenny, K.J. Roberts and J.N. Sherwood, *J. Mater. Sci.* 19 (1984) 1629.
- [36] A. Kochendörfer, *Zeits. Kristallogr.* 97 (1937) 263.
- [37] P.M. Robinson and H.G. Scott, *Acta Metall.* 15 (1967) 1581.
- [38] J. di Persio and B. Escaig, *Phys. Stat. Sol. (a)* 40 (1977) 393.
- [39] R.W. Armstrong and W.L. Elban, in: *Microindentation Techniques in Materials Science and Engineering*, eds P.J. Blau and B.R. Lawn (Amer. Soc. Test. Mater., Phila., PA, 1986) p. 109.
- [40] W.L. Elban, R.W. Armstrong, K.-C. Yoo, R.G. Rosemeier and R.Y. Yee, *J. Mater. Sci.* 24 (1989) 1273.
- [41] R.W. Armstrong and A.C. Raghuram, in: *The Science of Hardness Testing and Its Research Applications*, eds J.H. Westbrook and H. Conrad (Amer. Soc. Metals, Metals Park, OH, 1973) p. 174.
- [42] H.G. Gallagher, P.J. Halfpenny, J.C. Miller and J.N. Sherwood, *Philos. Trans. Roy. Soc. Lond.* A339 (1992) 293.
- [43] J.T. Hagan and M.M. Chaudhri, *J. Mater. Sci.* 12 (1977) 1055.
- [44] B.R. Lawn and E.R. Fuller, *J. Mater. Sci.* 10 (1975) 2016.
- [45] W.L. Elban, *J. Mater. Sci.* 14 (1979) 1008.
- [46] R.W. Armstrong and C.Cm. Wu, *J. Amer. Ceram. Soc.* 61 (1978) 102; M.M. Chaudhri, *Phil. Mag. Letters* 53 (1986) L55.
- [47] K.-C. Yoo, R.G. Rosemeier, W.L. Elban and R.W. Armstrong, *J. Mater. Sci. Lett.* 3 (1984) 560.
- [48] W.L. Elban, J.C. Hoffsommer, D.J. Glover, C.S. Coffey and R.W. Armstrong, *Summary Report: Microstructural Origins of Hot Spots in RDX Explosive and Several Reference Inert Materials* (Naval Surface Weapons Center, White Oak, MD, 1984) NSWC MP 84-358.
- [49] B.L. Hammond and R.W. Armstrong, *Philos. Mag. Lett.* 57 (1988) 41.
- [50] R.W. Armstrong and W.H. Robinson, *New Zealand J. Sci.* 17 (1974) 429.
- [51] F.C. Frank and B.R. Lawn, *Proc. Roy. Soc. London* A299 (1967) 291.
- [52] B.R. Lawn, *J. Appl. Phys.* 39 (1968) 4828.
- [53] D. Tabor, *The Hardness of Metals* (Oxford, Clarendon Press, 1951).
- [54] F.P. Bowden and A.D. Yoffe, *Initiation and Growth of Explosion in Liquids and Solids* (Cambridge University Press, London, 1952); *Fast Reactions in Solids* (Buttersworths Scientific Publications, London, 1958).
- [55] G.T. Afanas'ev and V.K. Bobolev, *Initiation of Solid Explosives by Impact* (Israel Program for Sci. Transl., Jerusalem, 1971).
- [56] J.E. Field, G.M. Swallowe and S.N. Heavens, *Proc. Roy. Soc. A382* (1982) 231.
- [57] C.S. Coffey and S.J. Jacobs, *J. Appl. Phys.* 52 (1981) 6991.
- [58] S.N. Heavens and J.E. Field, *Proc. Roy. Soc. London* A338 (1974) 77; G.M. Swallowe and J.E. Field, *Ibid. A379* (1982) 389.
- [59] R.E. Winter and J.E. Field, *Proc. Roy. Soc. A343* (1975) 399.
- [60] R.W. Armstrong, C.S. Coffey and W.L. Elban, *Acta Metall.* 30 (1982) 2111.
- [61] A.K. Head, *Philos. Mag.* 27 (1973) 531.
- [62] F.P. Gerstle and G.J. Dvorak, *Philos. Mag.* 29 (1974) 1337; *Ibid.* (1974) 1347.
- [63] H. Ockendon and J.R. Ockendon, *Philos. Mag. A47* (1983) 707.
- [64] F. Liu, I. Baker and M. Dudley, *Philos. Mag.* 71 (1995) 15.
- [65] R.W. Armstrong, in: *Yield, Flow and Fracture of Polycrystals*, ed. T.N. Baker (Applied Science Publ., Barking, U.K., 1983) p. 1.
- [66] E.O. Hall, *Proc. Phys. Soc. London* B64 (1951) 747.
- [67] N.J. Petch, *J. Iron Steel Inst.* 174 (1953) 25.
- [68] R.W. Armstrong, I. Codd, R.M. Douthwaite and N.J. Petch, *Philos. Mag.* 7 (1962) 45.
- [69] F.P. Bowden and K. Singh, *Nature* 172 (1953) 378.
- [70] R.W. Armstrong, C.S. Coffey, V.F. DeVost and W.L. Elban, *J. Appl. Phys.* 68 (1990) 979.
- [71] F.P. Bowden, P.G. Fox and J. Soria-Ruiz, *Nature* 220 (1968) 778.
- [72] P.G. Fox and J. Soria-Ruiz, *Proc. Roy. Soc. A317* (1970) 79.
- [73] T. Boddington, *The Growth and Decay of Hot Spots and the Relation between Structure and Stability*, Ninth Symposium (International) on Combustion, The Combustion Inst. (Academic Press, N.Y., 1963) p. 287.
- [74] R.W. Armstrong and W.L. Elban, *Mater. Sci. Eng. A122* (1989) L1.

- [75] R.W. Armstrong and F.J. Zerilli, *Mech. Mater.* 17 (1994) 319.
- [76] R.W. Armstrong, *J. de Phys. IV — Coll.* 5 (1995) C4-89.
- [77] C.S. Smith, *Trans. Metall. Soc., Amer. Inst. Min. Metall. Eng.* 212 (1958) 574.
- [78] M.A. Meyers, *Scripta Metall.* 12 (1978) 21.
- [79] R.W. Armstrong, R.S. Miller and H.W. Sandusky, in: *Indentation Hardness Testing, Defect Structure and Shock Model for RDX Explosive Crystals*, ONR Workshop on Dynamic Deformation, Fracture and Transient Combustion (Chemical Propulsion Information Agency, 1987) CPIA Publication 474, p. 77.
- [80] F.A. Bandak, R.W. Armstrong and A.S. Douglas, *Phys. Rev.* 46 (1992) 3228.
- [81] R.W. Armstrong and F.J. Zerilli, in: *EXPLOMET 2000, Fundamental Issues and Applications of Shock-Wave and High-Strain-Rate Phenomena*, eds K.P. Staudhammer, L.E. Murr and M.A. Meyers (Elsevier Science Ltd, N.Y., 2001) Chapter 15, p. 115.
- [82] Y.M. Gupta and G.R. Fowles, in: *Metallurgical Effects at High Strain Rates*, eds R.W. Rohde, B.M. Butcher, J.R. Holland and C.H. Karnes (Plenum Press, N.Y., 1973) p. 367.
- [83] Y.M. Gupta, G.E. Duvall and G.R. Fowles, *J. Appl. Phys.* 46 (1975) 532.
- [84] K.S. Tunison and Y.M. Gupta, in: *Shock Waves in Condensed Matter 1987*, eds S.C. Schmidt and N.C. Holmes (Elsevier Science Publ. B.V., N.Y., 1988) p. 277.
- [85] R.W. Armstrong, *Roles Possibles des Dislocations dans les Detonations par Choc dans les Cristaux Energétiques*, Traduction: J. Boileau, *Revue Scientifique et Technique de la Defense* 16 [2] (1992) 161.
- [86] W.C. Leslie, in: *Metallurgical Effects at High Strain Rates*, eds R.W. Rohde, B.M. Butcher, J.R. Holland and C.H. Karnes (Plenum press, N.Y., 1973) p. 571.
- [87] D.D. Dlott, *Ann. Rev. Phys. Chem.* 37 (1986) 157.
- [88] D.D. Dlott and M.D. Fayer, *J. Chem. Phys.* 92 (1990) 3798.
- [89] A. Tokmakoff, M.D. Fayer and D.D. Dlott, *J. Phys. Chem.* 97 (1993) 1901.
- [90] G.K. Adams, J. Holden and E.G. Whitbread, *The Explosive Initiation of a Single Crystal of Cyclotrimethylenetrinitramine*, Extrait du Compte-rendu du XXXIe Congrès International de Chimie Industrielle (Imprimerie Mercurius—Anvers, Fr., 1958) p. 1.
- [91] H.W. Sandusky, B.C. Glancy, D.W. Carlson, W.L. Elban and R.W. Armstrong, *J. Propulsion and Power* 7 (1991) 518.
- [92] B.C. Beard, H.W. Sandusky, B.C. Glancy and W.L. Elban, *J. Mater. Res.* 7 (1992) 3266.
- [93] J.W. Forbes, D.G. Tasker, R.H. Granholm and P.K. Gustavson, in: *Shock Compression of Condensed Matter — 1989*, eds S.C. Schmidt, J.N. Johnson and L.W. Davison (Elsevier Publ. B.V., N.Y., 1990) p. 709.
- [94] J.J. Dick, *Appl. Phys. Lett.* 44 (1984) 859.
- [95] J.J. Dick, E. Garcia and D.C. Shaw, in: *Shock Compression of Condensed Matter — 1991*, eds S.C. Schmidt, R.D. Dick, J.W. Forbes and D.G. Tasker (North Holland Publ., Amsterdam, 1992) p. 349.
- [96] J.J. Dick, R.N. Mulford, W.J. Spencer, D.R. Pettit, E. Garcia and D.C. Shaw, *J. Appl. Phys.* 70 (1991) 3572.
- [97] B. Olinger, P.M. Halleck and H.H. Cady, *J. Chem. Phys.* 62 (1975) 4480.
- [98] P.M. Halleck and J. Wackerle, *J. Appl. Phys.* 47 (1976) 976.
- [99] C.E. Morris, in: *Proc. Sixth Symposium (International) on Detonation* (Office of Naval Research, Arlington, VA, 1976) ACR-221, p. 396.
- [100] R.W. Armstrong and W.L. Elban, in: *ONR Workshop on Energetic Material Initiation Fundamentals* (Chemical Propulsion Information Agency, 1987) CPIA Publ. 475, p. 171.
- [101] J.J. Dick, *Appl. Phys. Lett.* 60 (1992) 2494.
- [102] J.J. Dick, *J. Phys. Chem.* 97 (1993) 6193.
- [103] G.J. Piermarini, S. Block, R. Damavarapu and S. Iyer, *Propellants, Explosives and Pyrotechnics* 16 (1991) 188.
- [104] A.L. Ramaswamy, *Laser Ignition of Secondary Explosives*, Ph.D. thesis (Cambridge University, 1993).
- [105] R.W. Armstrong, A.L. Ramaswamy and J.E. Field, in: *ONR/SNPE/ONERA Workshop on Combustion Mechanisms*, ed. R.W. Armstrong (ONR London, U.K. 1991) p. 168.
- [106] A.L. Ramaswamy and J.E. Field, *J. Appl. Phys.* 79 (1996) 3842.
- [107] A.L. Ramaswamy, J.E. Field and R.W. Armstrong, in: *Pyrotechnics: Basic Principles, Technology and Applications* (Fraunhofer Institut Chemische Technologie, Karlsruhe, 1995) p. 18-1.
- [108] W.L. Elban, R.W. Armstrong and T.P. Russell, *Philos. Mag.* A78 (1998) 907.

- [109] A.L. Ramaswamy, H. Shin, R.W. Armstrong, C.H. Lee and J. Sharma, *J. Mater. Sci.* 31 (1996) 6035.
- [110] P.G. Fox and J. Soria-Ruiz, *Proc. Roy. Soc. London* A314 (1970) 79.
- [111] P.G. Fox, in: *Physics of Materials*, eds D.W. Borland, L.M. Clarebrough and A.J.W. Moore (Commonwealth Scientific and Industrial Research Organization, Australia, and University of Melbourne, 1979) p. 73.
- [112] H.M. Hauser, J.E. Field and V.K. Mohan, *Chem. Phys. Lett.* 99 (1983) 66.
- [113] J.M. Thomas, in: *Advances in Catalysis and Related Subjects*, Vol. 19, eds D.D. Eley, H. Pines and P.W. Weisz (Academic Press, N.Y., 1969) p. 293.
- [114] J.M. Thomas, *Philos. Trans. Roy. Soc. London* A277 (1974) 31.
- [115] C.H. Bamford and G.C. Eastmond, *Rev. Chem. Soc.* 23 (1969) 271.
- [116] A.K. Galwey and P.W.M. Jacobs, *Proc. Roy. Soc. London* A254 (1960) 455.
- [117] P.J. Herley and P.W. Levy, *Nature* 211 (1966) 1287.
- [118] P.J. Herley and P.W. Levy, *J. Chem. Phys.* 49 (1968) 1493.
- [119] P.J. Herley and P.W. Levy, *J. Chem. Phys.* 49 (1968) 1500.
- [120] P.J. Herley, P.W.M. Jacobs and P.W. Levy, *Proc. Roy. Soc. London* A318 (1970) 197; *J. Chem. Soc. (A)* (1971) 434; see also J.O. Williams, J.M. Thomas, Y.P. Savintsev and V.V. Boldyrev, *J. Chem. Soc. (A)* (1971) 1757.
- [121] P.J. Herley and P.W. Levy, in: *Proc. Amer. Nucl. Soc., AIAA Conference on Natural and Man-made Radiation in Space* (NASA Technical Memorandum X-2440, 1972) p. 584.
- [122] P.J. Herley and P.W. Levy, *Nature Physical Science* 232 (1971) 66.
- [123] P.J. Herley and P.W. Levy, in: *Reactivity of Solids: Proceedings of the Seventh International Symposium on the Reactivity of Solids* (Chapman and Hall, London, 1972) p. 387; in: *Reactivity of Solids* (Plenum Press, London, 1977) p. 355.
- [124] T.B. Tang, M.M. Chaudhri, C.S. Rees and S.J. Mullock, *J. Mater. Sci.* 22 (1987) 1037.
- [125] R.W. Armstrong, in: *European Scientific Notes* (ONR London, 1983) ESN 37-7, p. 290.
- [126] T.B. Brill, in: *Structure and Properties of Energetic Materials*, eds D.H. Liebenberg, R.W. Armstrong and J.J. Gilman (Materials Research Society, Pittsburgh, PA, 1993) Vol. 296, p. 269.
- [127] R. Behrens, Jr. and S. Bulusu, *J. Phys. Chem.* 96 (1992) 8877.
- [128] J.C. Hoffsommer, D.J. Glover and W.L. Elban, *J. Energetic Mater.* 3 (1985) 149.
- [129] H.L. Bhat, P.J. Herley, D.B. Sheen and J.N. Sherwood, in: *Applications of X-Ray Topographic Methods to Materials Science*, eds S. Weissmann, F. Balibar and J.-F. Petroff (Plenum Press, N.Y., 1984) p. 401.
- [130] D.B. Sheen and J.N. Sherwood, in: *Reactivity of Solids: Proceedings of the Tenth International Symposium on the Reactivity of Solids*, eds P. Barret and L.-C. Dufour (Elsevier Publ. B.V., N.Y., 1985) p. 93.
- [131] W.L. Elban, H.W. Sandusky, B.C. Beard and B.C. Glancy, *J. Propulsion and Power* 11 (1995) 24.
- [132] D.T. Cromer, H.L. Ammon and J.R. Holden, *A Procedure for Estimating the Crystal Densities of Organic Explosives*, Los Alamos National Laboratory Report LA-11142-MS, UC-45 (1987).
- [133] J.R. Stine, in: *Structure and Properties of Energetic Materials*, eds D.H. Liebenberg, R.W. Armstrong and J.J. Gilman (Mater. Res. Soc., Pittsburgh, PA, 1993), Vol. 296, p. 3.
- [134] R. Gilardi, in: *Structure and Properties of Energetic Materials*, eds D.H. Liebenberg, R.W. Armstrong and J.J. Gilman (Mater. Res. Soc., Pittsburgh, PA, 1993), Vol. 296, p. 233.
- [135] R.W. Armstrong, H.L. Ammon, Z.Y. Du, W.L. Elban and X.J. Zhang, in: *Structure and Properties of Energetic Materials*, eds D.H. Liebenberg, R.W. Armstrong and J.J. Gilman (Mater. Res. Soc., Pittsburgh, PA, 1993) Vol. 296, p. 227.
- [136] P. Rudel, S. Odiot, J.C. Mutin and M. Peyard, *J. Chim. Phys.* 87 (1990) 1307.
- [137] N. Ide, I. Okada and K. Kojima, *J. Phys.: Condens. Matter* 2 (1990) 5489.
- [138] M.-S. Lee and J. Dundurs, *Philos. Mag.* 26 (1972) 929.
- [139] W.L. Elban, J.C. Hoffsommer and R.W. Armstrong, *J. Mater. Sci.* 19 (1984) 552.
- [140] J.J. Dick and J.P. Ritchie, *J. Appl. Phys.* 76 (1994) 2726.
- [141] J.J. Dick, in: *The Structure and Properties of Energetic Materials*, eds D.H. Liebenberg, R.W. Armstrong and J.J. Gilman (Mater. Res. Soc., Pittsburgh, PA, 1993), Vol. 296, p. 75.
- [142] J.P. Ritchie, in: *Structure and Properties of Energetic Materials*, eds D.H. Liebenberg, R.W. Armstrong and J.J. Gilman (Mater. Res. Soc., Pittsburgh, PA, 1993), Vol. 296, p. 99.
- [143] J.R. Hardy, A.M. Karo and F.E. Walker, in: *Progress in Aeronautics and Astronautics*, eds J.R. Bowen et al. (AIAA, 1981) Vol. 75, p. 209.

- [144] D.H. Tsai, *J. Chem. Phys.* 95 (1991) 7497.
- [145] D.H. Tsai, in: *Structure and Properties of Energetic Materials*, eds D.H. Liebenberg, R.W. Armstrong and J.J. Gilman (Mater. Res. Soc., Pittsburgh, PA, 1993) Vol. 296, p. 113.
- [146] F.A. Bandak, D.H. Tsai, R.W. Armstrong and A.S. Douglas, *Phys. Rev. B* 47 (1993) 11681.
- [147] D.H. Tsai and R.W. Armstrong, *J. Phys. Chem.* 98 (1994) 10997.
- [148] R.W. Armstrong, H.L. Ammon, W.L. Elban and D.H. Tsai, *Thermochimica Acta* 384 (2003) 303.
- [149] C.T. White, D.H. Robertson, M.L. Elert, J.W. Mintmire and D.W. Brenner, in: *Structure and Properties of Energetic Materials*, eds D.H. Liebenberg, R.W. Armstrong and J.J. Gilman (Mater. Res. Soc., Pittsburgh, PA, 1993) Vol. 296, p. 123.
- [150] J.W. Mintmire, D.H. Robertson and C.T. White, *Phys. Rev. B* 49 (1994) 14859.
- [151] J. Belak, in: *High-Pressure Science and Technology — 1993*, eds S.C. Schmidt, J.W. Shaner, G.A. Samara and M. Ross (Amer. Inst. Phys., N.Y., 1994) AIP Conf. Proc. 309, Part 2, p. 1063.
- [152] H. Kim and Y. Won, *J. Phys. Chem.* 100 (1996) 9495.
- [153] I.-Y.S. Lee, J.R. Hill, H. Suzuki, D.D. Dlott, B.J. Baer and E.L. Chronister, *J. Chem. Phys.* 103 (1995) 8313.
- [154] J.J. Gilman, *Science* 274 (1996) 65.
- [155] J.J. Gilman, *Philos. Mag. B* 67 (1993) 207; *Philos. Mag.* 71 (1995) 1057.
- [156] J. Sharma, S.M. Hoover, C.S. Coffey, A.S. Tompa, H.W. Sandusky, R.W. Armstrong and W.L. Elban, in: *Shock Compression of Condensed Matter — 1997*, eds S.C. Schmidt, D.D. Dandekar and J.W. Forbes (Amer. Inst. Phys., N.Y., 1998) Vol. CP429, p. 563.
- [157] J. Sharma, R.W. Armstrong, W.L. Elban, C.S. Coffey and H.W. Sandusky, *Appl. Phys. Letters* 78 (22 Jan 2001) 457.
- [158] J. Sharma, C.S. Coffey, R.W. Armstrong, W.L. Elban and S.M. Hoover, in: *Shock Compression of Condensed Matter — 2001*, eds M.D. Furnish, N.N. Thadhani and Y. Horie (Amer. Inst. Phys., N.Y., 2002) Vol. CP620, Part 1, p. 657.
- [159] J. Sharma, R.W. Armstrong, W.L. Elban and C.S. Coffey, in: *Proceedings of the Eleventh Symposium (International) on Detonation* (Omnipress, Omnipress-CD, 2000) p. 443.
- [160] R.W. Armstrong, C.F. Clark and W.L. Elban, in: *Combustion of Energetic Materials*, eds K.K. Kuo and L. DeLuca (Begell House, Inc., N.Y., 2002) p. 354.

Dislocations and Indentations

M. MUNAWAR CHAUDHRI

Cavendish Laboratory, Madingley Road, Cambridge CB3 0HE, UK

Contents

Symbols and definitions (units in brackets)	449
1. Introduction	451
2. Indentation stress fields	452
2.1. Pointed indenters	452
2.2. Spherical indenters	457
3. Dislocation rosettes	463
3.1. Ionic crystals	465
3.2. Semiconductors	474
3.3. Metals	487
4. Cracking around indentations due to dislocation interactions	490
4.1. Quasi-static observations	490
4.2. Dynamic observations	505
5. Dislocations within the indentation itself	511
5.1. Elemental semiconductors Si and Ge	513
5.2. Ceramic crystals	519
5.3. Metals	526
5.4. Diamond, silicon carbide, and silicon nitride	526
6. Indentation-enhanced cathodoluminescence and photoluminescence	529
6.1. Ionic oxides	530
6.2. Non-oxide materials	539
7. Nano indentation and dislocations	540
8. Concluding remarks	544
Acknowledgements	546
Note added in the proof	546
References	547

Symbols and definitions (units in brackets)

<i>a</i>	radius of circle of contact between an axisymmetric indenter and a half space or test solid; one half side of square indentation (m)
α	semi included angle of conical indenter (rad/degree)
<i>B</i>	strength of ‘blister’ field caused by the indentation process (N m)
B'	viscous drag coefficient for fast moving dislocations ($N m^{-2} s$)
<i>b</i>	Burgers vector of dislocations (m)
β	universal constant relating the critical resolved shear stress of a crystal to its indentation hardness
<i>E</i>	Young’s modulus of half space or test solid ($N m^{-2}$)
E_1, E_2	Young’s moduli of test solid and indenter, respectively ($N m^{-2}$)
F, F^+, F^{++}	colour centres in ionic crystals
<i>f</i>	degree of compaction/densification of indented solid within immediate vicinity of indenter
<i>G</i>	shear modulus of test solid ($N m^{-2}$)
<i>g</i>	acceleration due to gravity ($m s^{-2}$)
<i>gf</i>	gramme-force (9.806×10^{-3} N)
<i>H</i>	indentation hardness of test solid, defined as the indentation load divided by the projected area of indentation ($N m^{-2}; kgf mm^{-2}$)
H_v	Vickers hardness of test solid, defined as the indenter load divided by the surface area of indentation ($N m^{-2}; kgf mm^{-2}$)
<i>h</i>	indenter tip depth below the original specimen surface (m)
h_c	contact depth of the indenter, measured as the distance along the symmetry axis from the indenter tip to the circle/edge of contact between the indenter and the test solid (m)
K'	a constant dependent upon E_1, E_2, v_1, v_2 ($N^{-1} m^2$)
<i>k</i>	shear yield stress of the test solid ($N m^{-2}$)
<i>L</i>	distance along a slip direction on the indented surface of the leading dislocation from the initial point of contact between the indenter and the test solid (m)
<i>v</i>	Poisson’s ratio of half space or test solid
v_1, v_2	Poisson’s ratios of test solid and indenter, respectively
P, P_1, P_2	indenter loads (N)
P_d	dynamic load (N)
P_{\max}	maximum indenter load (N)
p_d	dynamic mean pressure or dynamic hardness ($N m^{-2}; kgf mm^{-2}$)
p_h	component of hydrostatic pressure within the deformed zone around the indenter ($N m^{-2}$)

p_m	mean pressure/stress over the circle of contact (N m^{-2} ; kgf mm^{-2})
p_0	normal pressure at $\rho = 0$ (N m^{-2} ; kgf mm^{-2})
$(p_m)_{\max}$	maximum mean normal pressure over the circle of contact (N m^{-2})
$p(\rho)$	normal pressure distribution over the circle of contact in cylindrical co-ordinates (N m^{-2})
q	uniform resistive 2-dimensional pressure acting on the deformation zone in a direction normal to the indenter axis (N m^{-2})
R	radius of spherical indenter (m)
ρ	density (kg m^{-3})
r, r_1, r_2	radial distances from the initial point of contact between the indenter and the test solid (m)
ρ, θ, z	cylindrical coordinates (m, rad, m)
r, θ, ϕ	spherical polar coordinates (m, rad, rad)
$\sigma_\rho, \sigma_\theta, \sigma_\phi$	normal stresses in spherical polar coordinates (N m^{-2})
τ_c	critical resolved shear stress of test crystal; critical shear stress for dislocation glide (N m^2)
τ_{\max}	maximum shear stress
$(\tau_{xy})_{\text{Bouss}}$	shear stress due to Boussinesq point loading field in rectangular coordinates (N m^{-2})
$(\tau_{xy})_{\text{blister}}$	shear stress due to blister field in rectangular coordinates (N m^{-2})
$\Delta\tau$	shear stress on the leading dislocation by all the dislocations following it in a row of parallel dislocations of the same sign (N m^{-2})
t	time (s)
$\tau_{r\theta}, \tau_{r\phi}, \tau_{\theta\phi}$	shear stresses in spherical polar coordinates (N m^{-2})
\mathbf{u}, \mathbf{v}	Burgers vectors of dislocations (m)
u_e, v_e	edge components of the Burgers vectors \mathbf{u} and \mathbf{v} , respectively (m)
u_s, v_s	screw components of the Burgers vectors \mathbf{u} and \mathbf{v} , respectively (m)
V	volume of indentation (m^3)
v	impact velocity (m s^{-1})
v_d	dislocation velocity (m s^{-1})
v_0	incident impact velocity of projectile (m s^{-1})
W	strain energy density (J m^{-3})
Y	uniaxial yield stress of test solid (N m^{-2})
x, y, z	Cartesian/rectangular coordinates (m)
χ	a constant dependent upon the elastic constants E and ν of test solid and the degree of compaction/densification, f
z_0	maximum penetration of the projectile below the original specimen surface located at $z = 0$ (m)

Lateral cracks	cracks approximately parallel to the indented surface, which usually form during indenter unloading
Berkovich indenter	an equilateral triangle-based pyramid having an angle of 77.05° between the symmetry axis and any one of the three edges of the pyramid
Knoop indenter	A rhombus-based pyramid having angles of 172.5° and 130° between its opposite edges
Vickers indenter	a square-based pyramid having an angle of 136° between its two opposite faces

Note that the units of stress used here are N m^{-2} and kgf mm^{-2} , and the units of force used are N and gf.

1. Introduction

Indentation hardness investigations of solids are usually carried out with indenters made of very hard materials, such as diamond, cubic boron nitride, sapphire and tungsten carbide. The indenter shapes may be broadly classified into two categories. These are (i) pointed indenters including cones and pyramids, and (ii) blunt indenters, such as spheres, paraboloids and ellipsoids.

When a very hard pointed indenter, made of diamond, is loaded on to a flat solid surface, the shear stresses at the indenter tip are so high that even the hardest material, such as diamond, has been found to deform plastically, involving generation and mobility of dislocations. The indentation test thus provides a very simple, convenient and quite unique method for studying plasticity and its effects in any material. These effects can be indentation-induced phase transitions, dislocation mobility within the hinterland around the indentation, enhanced photoluminescence and cathodoluminescence, dislocation interactions giving rise to cracking and electrical charging, and others. Examples of some of these effects are presented in the various sections given below.

In the case of the loading of a flat solid surface with a hard blunt indenter, such as a sphere, the elastic stresses are dependent upon the applied load, the radius of the sphere, and the elastic constants of the indenter and the surface. Plasticity will occur only when the applied indenter load is high enough. In the elastic regime, the maximum shear stress for a given indenter load occurs not at the indenter/sample interface, but along the load axis at about $0.5a$ below the surface, where a is the radius of contact between the indenter and the flat [1,2]. If the applied indenter load is sufficiently high, giving rise to a high enough maximum shear stress below the contact, plasticity will initiate at this subsurface region. In crystalline materials this will result in the creation, movement and multiplication of dislocations, which can be monitored by chemical etching, transmission electron microscopy and X-ray topography. Therefore, the indentation test also provides a relatively simple means for determining the yield stress of a crystal.

2. Indentation stress fields

Before giving examples of the various effects mentioned in the above, we first summarize the stress distributions around pointed and blunt indenters.

2.1. Pointed indenters

We consider here a rigid conical indenter of a semi apical angle α and having an infinitely sharp tip (i.e. a perfect point). The indenter is loaded at $z = 0$ on to a solid half space $z \geq 0$ under a load P (Fig. 1). In cylindrical coordinates (ρ, θ, z) the normal pressure distribution $p(\rho)$ over the surface of contact of radius a is given by [3]:

$$p(\rho) = \frac{1}{2} \frac{E}{(1 - \nu^2)} \cot(\alpha) \cosh^{-1}\left(\frac{a}{\rho}\right), \quad (1)$$

where E and ν are Young's modulus and Poisson's ratio of the solid, respectively. It will be seen from eq. (1) that at the apex the normal pressure p_0 is infinite. The magnitude of the mean normal pressure p_m over the contact area is, however, finite and is given by [3,4]:

$$p_m = \frac{\text{load}}{\pi a^2} = \frac{P}{\pi a^2} = \frac{1}{2} \frac{E}{(1 - \nu^2)} \cot \alpha. \quad (2)$$

Note that in eq. (2), p_m is independent of the applied indenter load P .

In the case of compressible solids (i.e. $\nu \neq 0.5$), the shear stress at the apex of the conical indenter is also infinite and, therefore, plastic yielding will occur at the apex for indenters of all cone angles even at very small indenter loads. Once plastic yielding has occurred, the stress field is modified and the pressure distribution and the mean pressure are no longer given by the above eqs (1) and (2). The situation now comprises both elastic and plastic deformation and although there are several approximate models [5,6], which give the stress field around an elastic/plastic indentation, the one given by Yoffe [7] for an isotropic solid appears to be the most realistic physically. This model is also convenient to use for understanding the various physical phenomena accompanying indentation. The details of

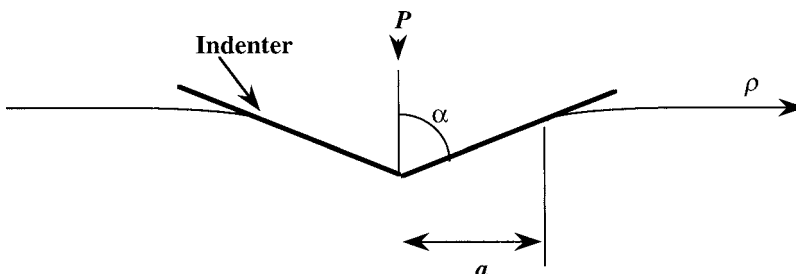


Fig. 1. The elastic loading of a conical indenter of semi-apical angle α on a half space. The indenter load is P and the radius of contact is a .

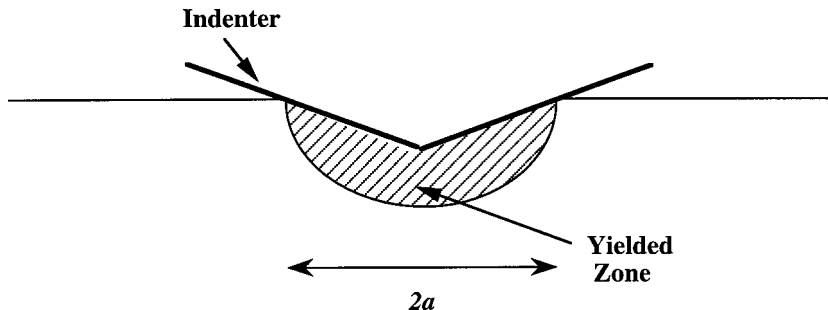


Fig. 2. The yielded zone (shaded) under an indenter. Note that this yielded zone is confined within the contact zone.

the model can be found in the original article [7], but we give here only a brief account of some aspects of the model which are particularly relevant to the situation discussed below.

In the case of the deformation of a solid by a rigid conical indenter, the Yoffe model [7] assumes that the zone of deformation/plastic yielding is limited by the boundary of contact between the solid and the indenter, as shown in Fig. 2. This assumption is supported by the experimental work of Peter [8] who showed that when a flat surface of a soda-lime glass specimen was indented with a diamond sphere of $20\ \mu\text{m}$ radius, the shear flow lines, as observed *in situ* under load, were confined to the contact zone. The projected area of contact is taken as that of a circle of radius a . (At this stage pyramidal indenters, such as Vickers, Knoop and Berkovich types, are avoided because of the complications which would be caused by their edges, but the overall conclusions will be approximately the same.) The process of local yielding may be by compaction (*i.e.* densification) or by shear deformation, or both, depending upon the properties of the solid.

In a situation like this, the volume within the deformed zone may not be conserved. However, the material within this deformed zone is under stress, both before yielding and on yielding. It is further suggested in ref. [7] that on yielding and reaching an equilibrium, the yielded material should be in a state of minimum strain energy density. Since the strain energy density is proportional to the square of the stress components, it is reasonable to assume that on reaching equilibrium the pressure distribution over the circle of contact will be uniform and that the magnitude of this uniform pressure will be equal to the mean pressure p_m such that $\pi a^2 p_m = P$, where P is the applied indenter load. At present there are apparently no experimental measurements of the stress distribution over a plastically deformed contact, but some numerical calculations have been carried out by Hardy, Baronet and Tordion [9] for the case of an elastoplastic indentation of a half space by a rigid sphere. Their results predict that the normal pressure distribution is quite uniform. During the yielding process, the elastically deformed material surrounding the yielded zone will resist the expansion of the latter with a uniform side (*i.e.* two-dimensional) pressure q , normal to p_m (see Fig. 3). Then, contrary to the belief of several investigators, the stress state within the deformed zone will not be purely hydrostatic. This picture is supported by the fact that the material within the yielded zone is on the verge of further yielding.

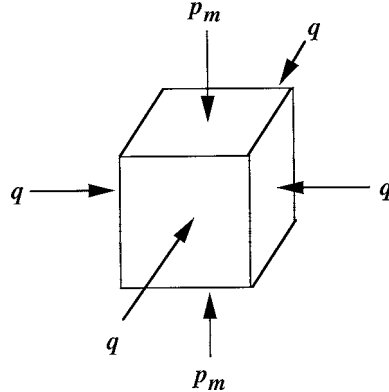


Fig. 3. Schematic diagram of the confining pressure within the yielded zone. p_m is the normal pressure, assumed uniform, over the contact region between the indenter and the specimen. The side two-dimensional pressure opposing the expansion of the yielded zone is q , and the two pressures are related by eq. (3). From Yoffe [7].

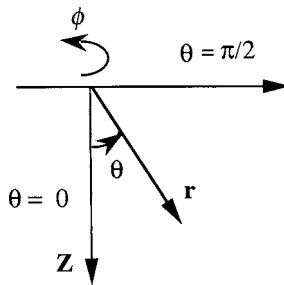


Fig. 4. Spherical polar coordinate system (r, θ, ϕ). The z -axis is along $\theta = 0$.

Now, for a fixed p_m the strain energy density W in the yielded zone will vary with q ; W will be a minimum when $\partial W / \partial q = 0$. Applying this condition we have [7],

$$q = \frac{\nu p_m}{(1 - \nu)}, \quad (3)$$

where ν is Poisson's ratio of the solid. In spherical polar coordinates (Fig. 4), the various stress components within the yielded zone are given by [7]:

$$\begin{aligned} \sigma_r &= -p_m \cos^2 \theta - q \sin^2 \theta, \\ \sigma_\theta &= -p_m \sin^2 \theta - q \cos^2 \theta, \\ \sigma_\phi &= -q, \\ \tau_{r\theta} &= (p_m - q) \sin \theta \cos \theta. \end{aligned} \quad (4)$$

The component of hydrostatic pressure p_h within the deformed zone may be obtained from eq. (4). Thus

$$p_h = \frac{1}{3}(\sigma_r + \sigma_\theta + \sigma_\phi),$$

or

$$p_h = -\frac{1}{3}\left(p_m + \frac{2\nu p_m}{(1-\nu)}\right),$$

or, for $\nu = 0.25$, we have

$$p_h \approx -0.56p_m. \quad (5)$$

It is clear from eq. (5) that the hydrostatic component of the stress within the deformed zone is only about a half of the mean normal pressure p_m or the indentation hardness. Also, the negative sign indicates that the pressure is compressive during indenter loading.

Outside the plastically deformed zone the elastic stress field may be represented as a combination of two fields [7], one due to a point force on the elastic half space (i.e. the Boussinesq field) and the other due to the localized plastic deformation/compaction of the solid at the contact. Because of its relative localized nature, Yoffe [7] has called the second field as the ‘blister’ field. The name blister is probably given, as the deformed volume is like a blister on a smooth surface causing lasting discomfort and stress. The Boussinesq field varies as $1/r^2$, whereas the blister field varies as $1/r^3$, where r is the distance from the initial point of contact between the indenter and the half space. The combined elastic stress fields in spherical polar coordinates (Fig. 4) for $\nu = 0.25$ and for an indenter load of P are given by eqs (6) below.

$$\begin{aligned} \sigma_r &= \frac{P}{4\pi r^2}(1 - 7\cos\theta) + \frac{B}{r^3}(19\cos^2\theta - 7), \\ \sigma_\theta &= \frac{P}{4\pi r^2}\left(\frac{\cos^2\theta}{1 + \cos\theta}\right) - \frac{B}{r^3}\cos^2\theta, \\ \sigma_\phi &= \frac{P}{4\pi r^2}\left(\cos\theta - \frac{1}{1 + \cos\theta}\right) + \frac{B}{r^3}(2 - 3\cos^2\theta), \\ \tau_{r\theta} &= \frac{P}{4\pi r^2}\frac{\sin\theta\cos\theta}{1 + \cos\theta} + \frac{5B}{r^3}\sin\theta\cos\theta, \\ \tau_{r\phi} &= \tau_{\theta\phi} = 0, \end{aligned} \quad (6)$$

where B is the strength of the blister field, yet to be determined. In eqs (6) the first terms on the right side correspond to the Boussinesq field, and the second terms to the blister field.

To find the value of B in the above equations for a given situation, we note that in the model [7] the material displaced by the indenter flows out radially; but note that the flow is non-uniform (see eq. (5) of [7]). However, the total volume of material flowing out

through any hemisphere centred at the initial point of contact between the indenter and the solid is the same. This volume, for $v = 0.25$, is given by $(5/6)(B/E)\pi$ and is equal to the volume Vf in which V is the volume of the indentation and f is a numerical factor with limiting values of 0 and 1, corresponding to 100% and 0% compaction/densification, respectively. In the case of single crystals, f is likely to be ~ 1 ; for solids having an open structure, such as fused silica, f will be much smaller than 1. (It may be noted here that scanning tunnelling microscopy of Vickers indentations of diagonal lengths of $\sim 5 \mu\text{m}$ in single crystals of p-doped Si(111) and W have been carried out by Walls et al. [10] and by Stelmashenko et al. [11]. Both these groups were able to determine from unloaded indentations the volume of an indentation lying below the original specimen surface and the volume of material appearing above the original surface. Their findings from the Si studies were that in some cases the volume of material appearing above the original specimen surface was about 80% of the indentation volume below it. In the case of the indentations in W single crystals, only 27 to 60% of the indentation volume appeared above the original surface. The difference between the volume displaced by the indenter and that appearing above the original surface is elastically stored in the bulk of the specimen, probably partly in the immediate vicinity of the indenter and the remainder in the rest of the bulk. It is not known yet whether all the elastically stored material will reappear above the original specimen surface if the indented surface is well annealed.)

Thus we have,

$$Vf = \frac{5\pi B}{6E}. \quad (7)$$

Now, for a plastic conical indentation of semi-apical angle α and contact depth

$$\begin{aligned} h_c &= a \cot \alpha, \\ V &= \left(\frac{1}{3} \pi a^3 \cot \alpha \right). \end{aligned} \quad (8)$$

Therefore,

$$\frac{5\pi B}{6E} = \left(\frac{1}{3} \pi a^3 \cot \alpha \right) f. \quad (9)$$

If we assume that the indentation hardness $H = p_m$ is independent of the applied indenter load P , then

$$a = \left(\frac{P}{\pi H} \right)^{\frac{1}{2}}. \quad (10)$$

Using eqs (9) and (10) and $\alpha = 68^\circ$, we get

$$B = (0.029) f E \left(\frac{P}{H} \right)^{3/2}. \quad (11)$$

It should be noted that B is dependent upon the maximum applied indenter load P_{\max} . Therefore, eq. (11) becomes

$$B = (0.029) f E \left(\frac{P_{\max}}{H} \right)^{3/2}. \quad (12)$$

The reason for choosing the case of $\alpha = 68^\circ$ is that such a cone has approximately the same relationship between volume and depth as a Vickers or Berkovich indenter.

As the indenter load is then gradually decreased from P_{\max} , the first terms on the right hand side of eq. (6) decrease correspondingly, but the second terms will remain unaltered. On complete unloading of the indenter, that is, $P = 0$, eqs (6) become

$$\begin{aligned} \sigma_r &= +\frac{B}{r^3}(19 \cos^2 \theta - 7), \\ \sigma_\theta &= -\frac{B}{r^3} \cos^2 \theta, \\ \sigma_\phi &= +\frac{B}{r^3}(2 - 3 \cos^2 \theta), \\ \tau_{r\theta} &= +\frac{5B}{r^3} \sin \theta \cos \theta, \\ \tau_{r\phi} &= \tau_{\theta\phi} = 0. \end{aligned} \quad (13)$$

In eqs (13) the value of B to be used is that given by eq. (12). Eqs (6) and (13) have been successfully used in explaining various cracking patterns observed around indentations in ceramics and glasses [7]. It should be noted that the stress equations given in this section are for an isotropic solid. Also, a point force has been used to represent the loading with a cone over a contact circle of radius a . In addition, most crystals are anisotropic and have specific slip systems. Therefore, the applicability of these equations to situations involving single crystals is only approximate. The equations given in this section will be used in Section 3.

2.2. Spherical indenters

In the case of the elastic loading of a half space by a hard spherical indenter of radius R , the contact stresses are given by the Hertz equations [12]. The mean normal contact pressure p_m is given by

$$p_m = \frac{P^{1/3}}{\pi \left(\frac{4K'R}{3} \right)^{2/3}}, \quad (14)$$

where $K' = \frac{9}{16} \left[\frac{(1-v_1^2)}{E_1} + \frac{(1-v_2^2)}{E_2} \right]$ in which E_1 and v_1 and E_2 and v_2 are Young's moduli and Poisson's ratios of the half space and indenter, respectively.

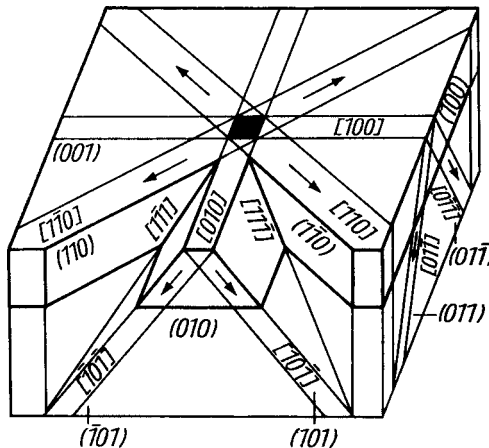


Fig. 5. Schematic representation of material flow around an indentation on a (001) plane of a single crystal of LiF. The arrows show the direction of material displacement. Note that the centre of the dark square (i.e. indentation) is at $[\frac{1}{2}, \frac{1}{2}, 1]$. From [14].

The mean normal pressure p_m increases with increasing indenter load and when $p_m \sim 1.1Y$, plastic yielding is initiated on the load axis at $z \sim 0.5a$, where a is the radius of contact between the sphere and the flat [2]. It is this property of spherical indentations which makes it particularly useful for determining the uniaxial yield stress Y of materials. Indeed Davies [2] used this method reasonably successfully for determining the uniaxial yield stress of a number of metals and alloys, such as mild steel, armour plate and nickel chrome steel. In the case of the mild steel, the yield stress determined by the ball indentation method was 1.6 times higher than that found by uniaxial compression tests. On the other hand, for the armour plate, the ratio of the yield stress determined by the ball indentation method to the yield stress determined by the compression method was in the range of 1.01 to 1.23.

Gilman and Johnston [13] extended this technique to ionic crystals. As said in the above, the onset of plastic yielding in crystals is associated with the nucleation and movement of dislocations. Therefore, if the newly created dislocations can be monitored experimentally, then the stress conditions can be identified under which plastic yielding occurs. Gilman and Johnston [13] pioneered a chemical etching technique for making direct observations of dislocations in ionic crystals. When a crystal surface containing freshly created dislocations is etched with a suitable etchant, characteristic pits are produced. Gilman and Johnston [13] have shown, from their extensive studies, the one-to-one correspondence between etch pits and freshly created dislocations. They have used the etch pit method for detecting the onset of plastic yielding in single crystals of LiF which has the NaCl f.c.c. structure. The slip system in this type of crystals is $\{110\}\langle 1\bar{1}0\rangle$. When, for example, plastic flow in a single crystal of LiF is caused by loading a pyramidal indenter on a (001) surface, the various slip planes and material flow directions involved are as shown schematically in Fig. 5. Here there are two sets of slip planes. In one set the slip planes are inclined to the (001) surface at an angle of 45° ; these planes are referred to as the $\{110\}_{45}$ planes. In the second

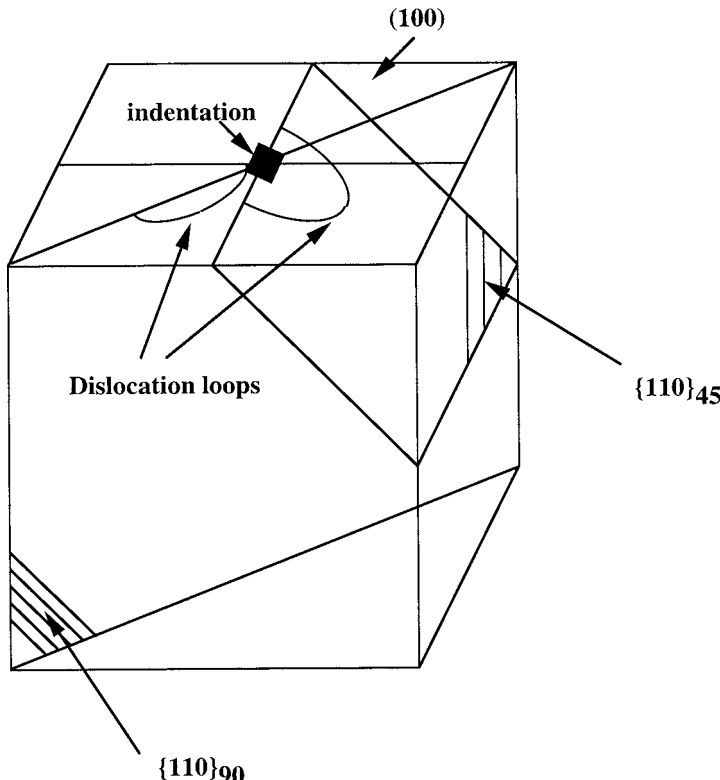


Fig. 6. Schematic representation of dislocation loops on the $\{110\}_{45}$ and the $\{110\}_{90}$ planes around an indentation made on a (001) face of a LiF single crystal.

set, the slip planes are inclined to the (001) surface at 90° ; these planes are referred to as the $\{110\}_{90}$ planes. A schematic representation of the dislocation loops around a plastic indentation is shown in Fig. 6. Note that in the $\{110\}_{45}$ slip planes the dislocation loops surround the indentation, whereas in the $\{110\}_{90}$ planes the entire individual loops are on one side or another side of the indentation.

If a dislocation-free region of a LiF crystal surface is loaded with a hard sphere and the load is gradually increased from zero, then beyond a certain applied load dislocations will start appearing within the circle of contact between the sphere and the loaded crystal surface. Loading can also be caused by the impact of a hard sphere on to the test surface. Gilman and Johnston [13] used this impact method for the determination of the stress conditions in single crystals of LiF for generating dislocations. A schematic diagram of the experimental arrangement used by them is shown in Fig. 7. A 12.7 mm diameter sphere of single crystal LiF, with a well-polished surface, was suspended from a rigid surface using a 1.83 m long piece of nylon string. Both the sphere and the test crystal were first cooled down to 77 K. The sphere was then allowed to impact the test crystal surface in such a way that at the instant of impact, the LiF sphere was travelling normal to the test crystal surface

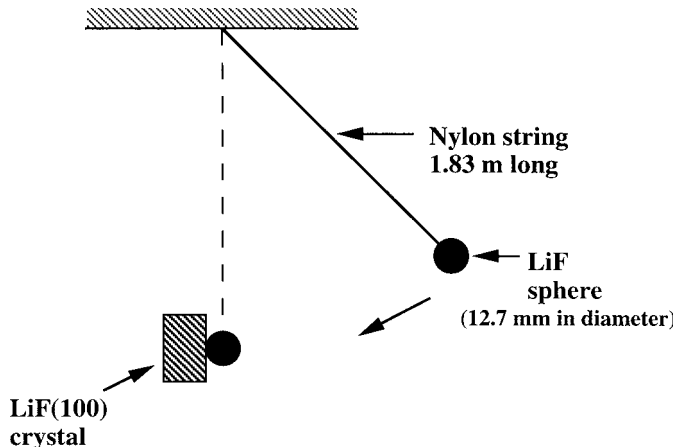


Fig. 7. Schematic diagram of the apparatus used for detecting the onset of plastic yielding in LiF single crystals using a ball impact technique. After Gilman and Johnston [13].

(Fig. 7). The impact velocities were in the range of 20 to 30 mm s⁻¹ and only single impacts were allowed. (It was not stated in [13] whether for every impact test a fresh surface area of the impacting sphere was chosen, but it is assumed that it is likely to have been the case.) In this manner several impact sites were made on the crystal surface, which was then etched to reveal any dislocation activity. It was found that when the impact velocity was 29 mm s⁻¹ etch pits due to the freshly created dislocations were formed within the contact circle. If the impact velocity was less than 20 mm s⁻¹, no fresh dislocation etch pits were formed. From such experiments Gilman and Johnston [13] concluded that the impact stresses generated at an impact velocity of 29 mm s⁻¹ had reached the critical value for the generation and movement of fresh dislocations.

For impact velocities up to the critical value, the stresses can be calculated using the Hertz [12] equations. Therefore, for a LiF sphere of radius R and Young's modulus E impacting a thick flat crystal of LiF at a velocity v , the maximum mean normal pressure $(p_m)_{\max}$ created over the circle of contact between the sphere and the crystal flat is given by (see, e.g. ref. [13])

$$(p_m)_{\max} = \frac{1}{\pi} \left(\frac{5}{3} \pi \rho \right)^{\frac{1}{5}} \left(\frac{4}{3} K' \right)^{-\frac{4}{5}} v^{2/5}, \quad (15)$$

where ρ is the density of LiF, and K' has been defined in the above with $E_1 = E_2 = E$. Using $v = 29$ mm s⁻¹, $E = 9.45 \times 10^{10}$ Pa, $\nu = 0.27$, $\rho = 2.6 \times 10^3$ kg m⁻³, and $R = 6.35 \times 10^{-3}$ m, the maximum mean normal pressure $(p_m)_{\max}$ generated over the circle of contact as calculated from eq. (15) is 2.4×10^8 Pa; the maximum shear stress τ_{\max} which will occur at $\sim 0.5a$ below the surface is

$$\tau_{\max} \sim 0.47(p_m)_{\max} = 0.47 \times 2.4 \times 10^8 = 1.13 \times 10^8 \text{ Pa.}$$

We may call this value of 1.13×10^8 Pa the critical shear stress of the LiF crystal. This shear stress may be compared with the critical shear stress of magnitude 5×10^7 Pa found from the three-point bend tests carried out by Gilman and Johnston [13] on the LiF(100) crystals cooled down to 77 K. It may be noted that the latter shear yield stress is about a half of the critical shear stress as determined from the sphere impact test. A possible reason for this discrepancy may be that in the ball impact test, the dislocation sources are subsurface, whereas in the bending tests the plastic yielding initiates on the surface where the dislocation sources may be larger. Another reason may be that in the impact test the strain rate is considerably higher, thus possibly giving rise to a higher shear yield stress.

Using the Hertz [12] equations, the estimated maximum impact force and the corresponding radius of contact a between the LiF sphere and the LiF crystal surface are ~ 3.74 N and $70.4\text{ }\mu\text{m}$, respectively. And since the maximum shear stress occurs at a depth of $\sim 0.5a$ along the load axis, we expect the dislocation sources to be at a distance of $\sim 35\text{ }\mu\text{m}$ below the loaded surface. Also, since the maximum shear stress directions lie in the $\{110\}_{45}$ planes, we expect the nucleation and glide of dislocations to occur initially on the $\{110\}_{45}$ planes. When the dislocation loops on these planes come up to the impacted (001) surface, on etching they will give rise to etch pits lying along the $\langle 100 \rangle$ directions within the contact circle. This is confirmed by the cross formed by the two mutually perpendicular rows of etch pits shown in Fig. 8. A diagrammatic representation of the dislocation loops on a $\{110\}_{45}$ slip plane which would produce a row of etch pits within the contact circle is shown in Fig. 9. Note that according to this picture, during the very initial stages of the dislocation nucleation and glide the very central region of the contact will be devoid of any dislocation activity, as was indeed observed by Gilman and Johnston [13]. As the load on the indenter is increased further, more and more $\{110\}_{45}$ slip planes will become operative and the number density of the etch pits within the circle of contact will also increase.

Spherical quasistatic indentation experiments on single crystals of LiF (100), similar to those of Gilman and Johnston [13] have been carried out by others [15], who have confirmed the findings of Gilman and Johnston [13].

An interesting point which emerges from the experiments of Gilman and Johnston [13] is that at the moment of dislocation nucleation, the ratio a/R is ~ 0.01 . This has significant implications for modelling the very initial stages of development and growth of the plastically deformed region under a spherical indenter.

In the experiments of Gilman and Johnston [13], the critical shear stress value for the nucleation and glide of dislocations was determined to be $\sim 1/300$ th of the shear modulus of LiF. If homogeneous nucleation of dislocations were to occur, the critical shear stress ought to be as high as 1/10th to 1/30th of the shear modulus [16]. These authors carried out further experiments on heavily etched surfaces of LiF crystals [17]. They dropped 75 to $100\text{ }\mu\text{m}$ diameter aluminium oxide spheres on to the heavily etched surfaces from a height of 10 mm and then the crystals were given a light etch. It was found that at the particle impact sites dislocation rosettes of freshly nucleated dislocations had formed. Simple calculations showed that in this case the maximum shear stress generated was as high as $G/80$, where G is the shear modulus of LiF. This calculated value of $G/80$ is close to the theoretical shear strength of the crystals [16]. It is possible that if still smaller diameter spheres are used, critical shear stress values for the nucleation of dislocations may come to



Fig. 8. Dislocation etch pits on a cleaved (100) face of a LiF single crystal. After cleaving, the crystal was etched heavily and then a 12.7 mm diameter LiF single crystal sphere was allowed to impact the crystal at a velocity of 29 mm s^{-1} . The crystal was then etched lightly, which resulted in two mutually normal rows of etch pits (see at centre of the micrograph and note that the centre of the micrograph may not be the centre of the contact), indicating the nucleation and growth of dislocations by the impact. The estimated radius of contact between the sphere and the crystal flat is $70 \mu\text{m}$, which means that the entire field of view is from within the contact circle.

From Gilman and Johnston [13].

be in agreement with the theory. Such experiments have indeed been carried out recently [18] using nanoindentation machines which are capable of applying indenter loads down to μN . Furthermore, during a nanoindentation test both the load and the indenter displace-

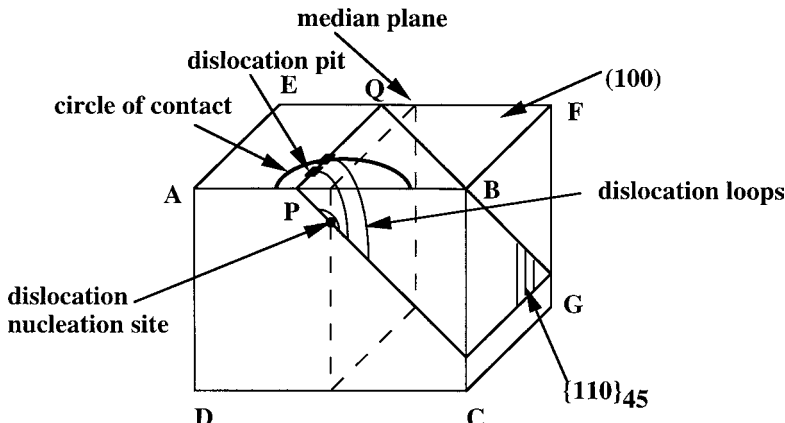


Fig. 9. Schematic diagram showing a median plane, ABCD, cross-sectional view of the subsurface site of dislocation nucleation, and some enlarged dislocation loops on a $\{110\}_{45}$ plane when a sphere is loaded on to the (100) surface just beyond the critical load required for the nucleation of dislocations. As the loops enlarge on this plane, they intersect the loaded surface ABFE at individual points which lie along the straight line PQ, as indicated in the diagram with two small, solid rectangles. With increasing load, the loops will grow in size and numbers, and in addition, similar dislocation activity will occur on the other $\{110\}_{45}$ planes. When the indented surface is etched, dislocation pits lying along mutually perpendicular straight lines will appear on the indented surface, as shown in Fig. 8. Note also that at the very initial plasticity stages, dislocations will emerge on the loaded surface at a distance of $\sim 0.5a$ from the load axis, where a is the radius of contact between the sphere and the crystal flat.

ment, which can be as low as a few nm, are recorded simultaneously. Tungsten indenters of tip diameters of 350 nm were loaded on to single crystals of gold and it was found that as the load on the indenter was gradually increased from zero, sudden load drops occurred in the load-displacement curve when the indenter load reached some critical values. These sudden load drops have been interpreted as clear indications of homogeneous nucleation of dislocations, and the critical shear stress at the moment of the nucleation of dislocation was estimated to be ~ 1.8 GPa, which was estimated to be about $G/15$ [18]. This high critical shear stress value was thought by the authors to be equal to the theoretical shear stress of gold. It should be noted that although nanoindentation experiments provide a powerful method for determining the critical shear stress of solids for homogeneous nucleation of dislocations, much further work is required on a wide variety of materials before the nanoindentation method is generally accepted as a routine technique. Experimentally, the challenging parts remain the accurate measurements of the applied load, the indenter displacement and the diameter (or the projected contact area) of the indentation. (Further brief details of nanoindentation studies are given in Section 7.)

3. Dislocation rosettes

After the nucleation of dislocations under an indenter, as the indenter load is increased further, more dislocations form and they move out further and further around the indent-

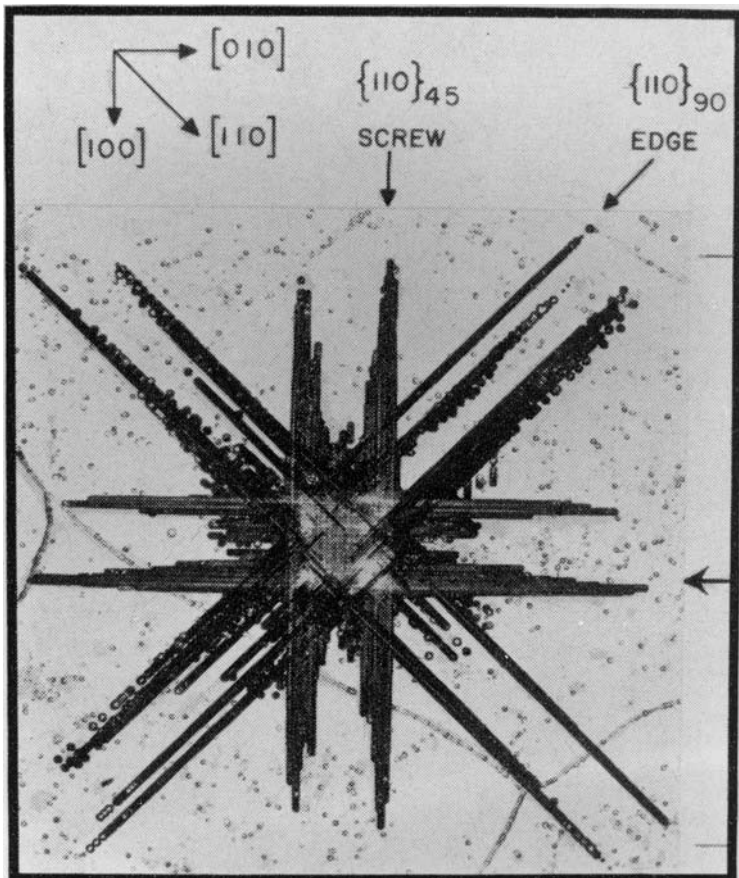


Fig. 10. A typical dislocation rosette around an indentation made with a 2 mm diameter ball under a load of 10 kgf on a {100} surface of an annealed single crystal of MgO. The points of emergence of the dislocations were revealed by chemical etching. In the diagram it is indicated that the edge dislocations lie on the {110}₉₀ planes, whereas the screw dislocations are on the {110}₄₅ planes. The etchant used was: 5 parts saturated ammonium chloride, 1 part sulphuric acid, and 1 part distilled water. The total width of the frame, including the border lines, is 1.24 mm. From Keh [20].

tion centre. It should be said that 'old' dislocations existing before the indentation is made are not moved by the indentation stress field; only the 'fresh' dislocations created by the process of indentation will move under its stress field [19]. These well spread out arrays of dislocations around the indentation form a rosette, but the formation of a rosette requires that dislocations are nucleated at the point of loading by the indenter. An example of an indentation rosette in a single crystal of MgO is shown in Fig. 10. Indentation rosettes have been observed in single crystals of ionic crystals, semiconductors and metals and the size of rosette arms has been used by several investigators for examining the effects of nuclear particle irradiation in MgO crystals, critical resolved shear stress, dislocation pinning and

doping effects in semiconductors, and the polarity effects in semiconducting compounds. We shall review the behaviour of indentation rosettes in different materials separately.

3.1. Ionic crystals

Simple ionic crystals, such as NaCl, LiF, KCl, and MgO have a f.c.c. structure and as noted earlier the primary slip system in all of them is $\{110\}\langle\bar{1}\bar{1}0\rangle$. Also, the $\{110\}$ planes are thought to be the closest packed [21] (this is debatable, however) and the shortest lattice translation distance is along the $\langle110\rangle$ directions. In some alkali halide crystals, secondary slip systems have also been reported [22]. These are $\{001\}\langle\bar{1}\bar{1}0\rangle$ and $\{111\}\langle\bar{1}\bar{1}0\rangle$ for NaCl

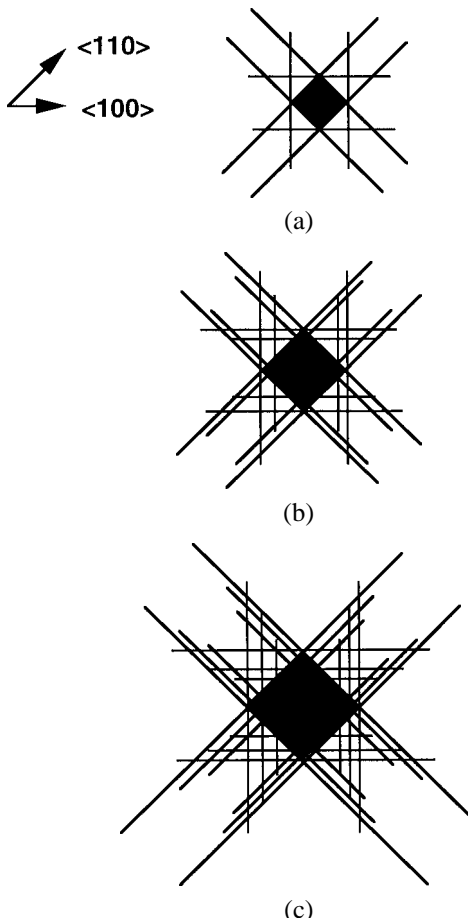


Fig. 11. Schematic representation showing the growth of the indentation rosettes around a Vickers diamond indentation on a (100) face of a single crystal of LiF with increasing indenter load. The lines of dislocation pits are shown by solid lines. The load increases from (a) to (c) and note that at any load the outermost lines of the dislocation pits are the longest.

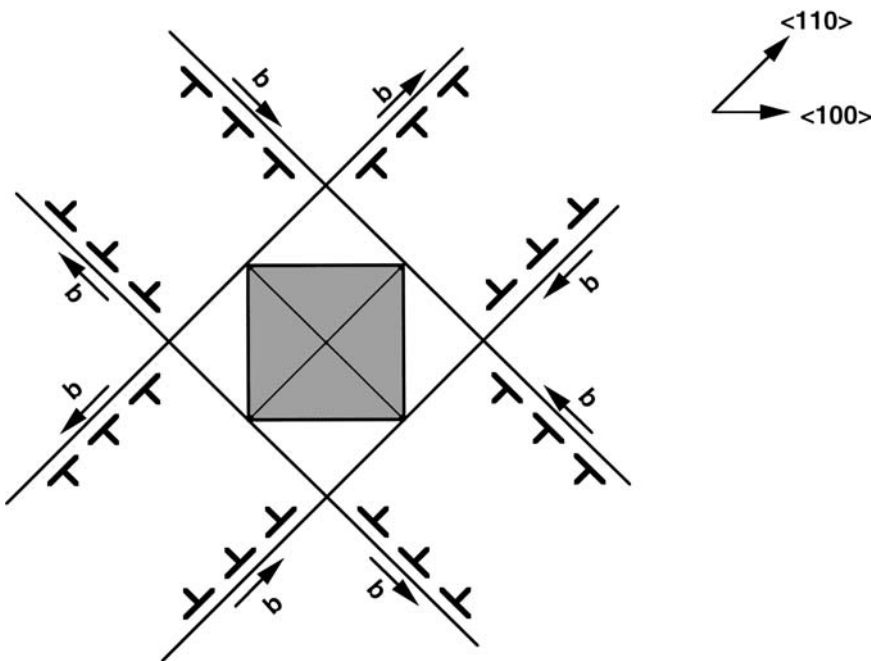


Fig. 12. Schematic representation of dislocations in the 'edge' arms of a dislocation rosette around a Vickers indentation (central grey square) on a (100) face of a LiF single crystal. The Burgers vectors b of the dislocations are also shown. Note that the 'screw' arms of the rosette have not been shown here.

and $\{001\}/\bar{1}\bar{1}0$ for LiF and AgCl. The distribution of dislocation etch pits in indentation rosettes in single crystals of NaCl and LiF is very similar to that in the rosette shown in Fig. 10. The etch pits lie along straight lines which are parallel to the $\langle 100 \rangle$ and $\langle 110 \rangle$ directions. With increasing indenter load, the lengths of the lines of etch pits develop as shown schematically in Fig. 11. It is interesting to note that the outermost etch pit lines are the longest [23]. A simple explanation of this observation is that the largest shear stress at any loading stage will be on the slip planes lying at the current contact edge between the indenter and the crystal.

The various slip planes and the dislocation loops which give rise to the rosette structure have already been shown in Figs 5 and 6, respectively. There are two $\{110\}_{90}$ and four $\{110\}_{45}$ planes. The half loops on the $\{110\}_{90}$ planes are so situated that one end of a half loop remains adjacent to the indentation, whereas the other end spreads out further and further from the indentation with increasing indenter load; note that these half loops do not enclose the indentation. On the other hand, the half loops on the $\{110\}_{45}$ planes enclose the indentation and the ends of the loops do not remain fixed to the indentation. The Burgers vectors of the edge dislocations in the rosette wings have been established by applying uniaxial compression or tension along the $\langle 100 \rangle$ directions to crystals containing indentation rosettes and then re-etching them to see how the dislocations moved [19,20]. The Burgers vectors of the edge dislocations around an indentation on a $\{100\}$ surface are shown schematically in Fig. 12.



Fig. 13. Optical interferogram (a) and surface displacement (b) around an indentation with a 0.4 mm diameter sapphire sphere on a {100} face of a KCl single crystal made under a load of 0.3 kgf. The surface has sunk in considerably below the original level along the <100> directions, but it has piled up to a smaller extent along the <110> directions. From Chaudhri [24].

The material displaced by the indenter is pushed into the bulk along the {110}₄₅ planes, whereas the tangential material displacement occurs along the {110}₉₀ planes [19]. Therefore, the projected shape of a residual indentation is dependent upon the indenter shape and its orientation with respect to the crystallographic directions. For example, when a hard spherical indenter is loaded on to a (100) surface of a KCl crystal, the projected boundary of contact of the residual indentation is not circular, but it is almost rectangular, with circular corners. Using optical interference microscopy it can be shown that although the projected shape of a spherical indentation looks approximately rectangular, the entire surface of the indentation is actually spherical. An example is shown in Fig. 13(a). This is confirmed by the perfectly circular fringes within the indentation. The reason for the projected shape of a spherical indentation to appear rectangular is that there is material pile up along the <110> directions, which in turn is probably due to the pile up of edge dislocations

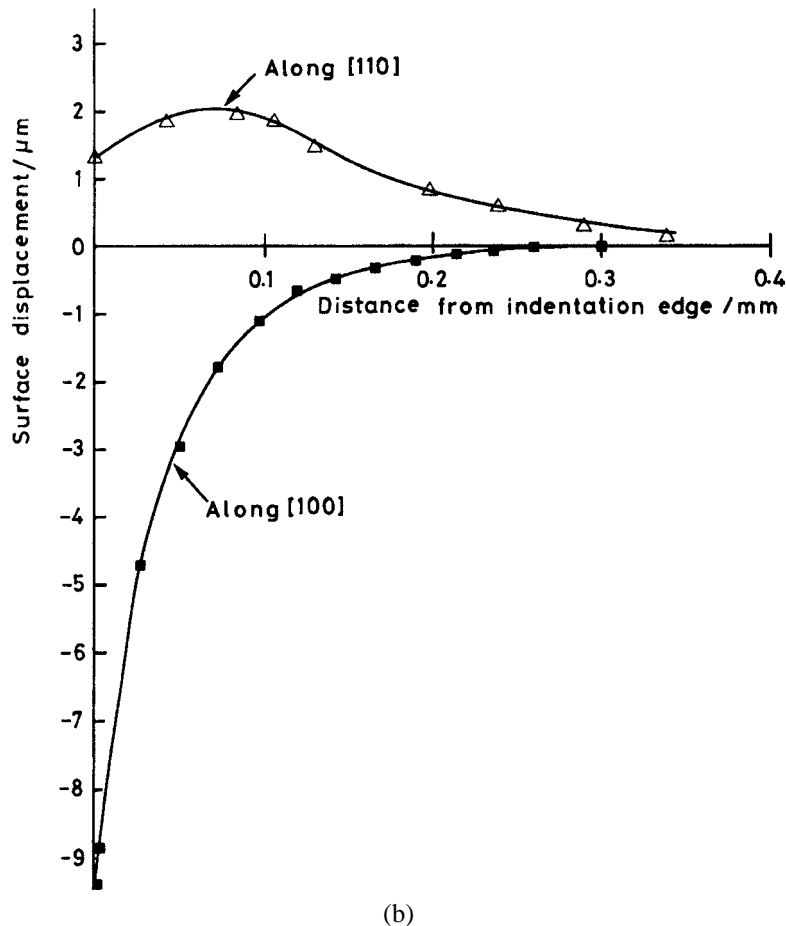


Fig. 13. (Continued).

in these directions. In addition, there is sinking in along the $\langle 100 \rangle$ directions due to the screw dislocations displacing the material into the bulk. Both the piling up along the $\langle 110 \rangle$ directions and the sinking in along the $\langle 100 \rangle$ directions occur during indenter loading. The magnitudes of the pile up and sinking around the indentation shown in Fig. 13(a) along the $\langle 110 \rangle$ and $\langle 100 \rangle$ directions are given in Fig. 13(b). Another example of piling up and sinking in around an indentation in a much harder crystal, such as MgO, is shown in Fig. 14. The complete circular fringe marks the indentation contact edge. Slip bands lying parallel to the $\langle 100 \rangle$ directions and passing through the indentation are caused by the formation and growth of dislocation loops on the $\{110\}_{45}$ planes. These slip bands can be clearly seen in the figure.

To get some understanding of the indentation-induced shear stresses which drive the dislocations lying close to the indented surface, we consider Fig. 15. Here it is assumed, for the sake of simplicity, that the indentation is made with a Vickers pyramid under a load

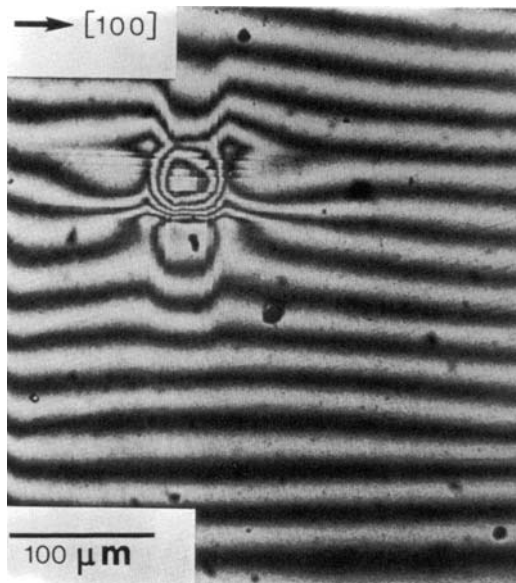


Fig. 14. Optical interferogram showing the surface profile around an indentation with a 0.4 mm diameter tungsten carbide sphere under a load of 1.01 kgf on a {100} surface of a cleaved single crystal of MgO. Note that around the indentation the surface has subsided along the ⟨100⟩ directions, but it has piled up along ⟨110⟩ directions. Several slip bands lying along the ⟨100⟩ directions and passing through the centre of the indentation can be clearly seen. From Chaudhri [24].

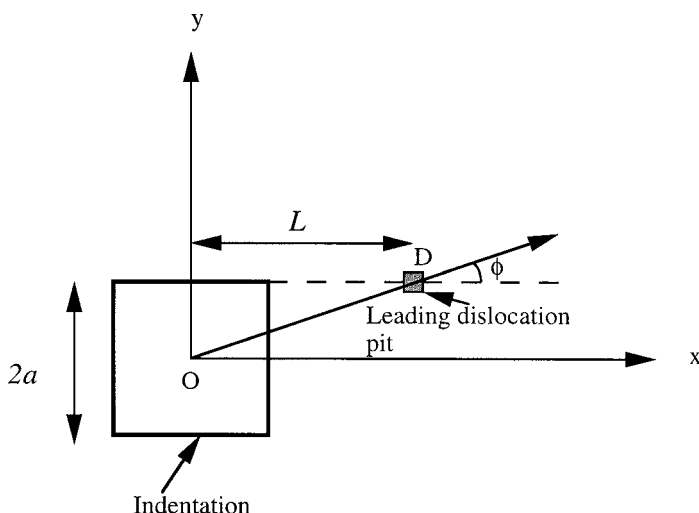


Fig. 15. Schematic diagram used for deriving an expression for the shear stress at the leading dislocation, located at D, in a dislocation rosette 'edge' arm around an indentation. The x-axis is along a ⟨110⟩ slip direction.

P_{\max} , which produces a square indentation of side $2a$; the slip direction is along the x -axis, which is also a $\langle 1\bar{1}0 \rangle$ direction. The leading dislocation is at a point D with coordinates $x = L$, $y = a$, $z = 0$, as shown. We need to know the magnitude of the shear stress τ_{xy} at D due to indenter loading. The centre of indentation is at O and the line OD makes an angle ϕ to the x -axis, as shown, and $OD = r$. As described earlier, τ_{xy} may be equated to the sum of the Boussinesq and the blister shear stress fields during indenter loading. On the removal of the indenter load, the shear stress driving the dislocations will be due to the blister field alone. During loading, the shear stress $(\tau_{xy})_{\text{Bouss}}$ due to the Boussinesq field (assuming that the elastic field due to loading on a square is similar to that generated by point loading at O) is given by

$$(\tau_{xy})_{\text{Bouss}} = \left(\frac{(1-2\nu)}{2\pi r^2} P_{\max} \sin 2\phi \right), \quad (16)$$

where $r^2 = L^2 + a^2$.

For $L \gg a$, $r \sim L$, and eq. (16) becomes

$$(\tau_{xy})_{\text{Bouss}} = \left(\frac{(1-2\nu)}{2\pi L^2} P_{\max} \sin 2\phi \right). \quad (17)$$

Note that in eq. (17) the shear stress is positive, and it will tend to drive the dislocations towards the indentation rather than driving them farther out. On the other hand, the shear stress $(\tau_{xy})_{\text{blister}}$ at D due to the blister field is given by

$$(\tau_{xy})_{\text{blister}} = -\frac{6B(1-\nu)}{r^3} \sin 2\phi, \quad (18)$$

where, as before, $r \sim L$. Therefore,

$$(\tau_{xy})_{\text{blister}} = -\frac{6B(1-\nu)}{L^3} \sin 2\phi. \quad (19)$$

The negative sign on the right hand side of eq. (19) indicates that the shear stress due to the blister field will tend to move the dislocations away from the centre of indentation. So, during indenter loading the two components of the shear stress work against each other, as far as the dislocations on the indented surface are concerned. *Therefore, for a given indenter load the dislocations will come to rest at a set of positions corresponding to a stable equilibrium. These positions will depend upon the Boussinesq and the blister fields and the interaction field of the dislocations themselves.* On complete removal of the indenter load, the shear stress due to the Boussinesq field will become zero, but that due to the blister field, corresponding to the maximum applied load P_{\max} , remains. Therefore, on the removal of load, the magnitude of the shear stress tending to drive the dislocation at D away from the indentation centre is higher. This also means that the dislocations in the rosette will tend to move out further when the indenter load is removed. This has been observed from recent *in situ* indentation experiments (see Section 4.1).

Since in most studies of indentation rosettes, the lengths of the rosette arms are measured after the removal of the indenter load, the relevant shear stress is that due to the blister field given by eq. (19).

In addition to the indentation-induced shear stresses, there will also be the shear stress $\Delta\tau$ on the leading dislocation (i.e. the one at D in Fig. 15) due to all the dislocations following it. This component of shear stress $\Delta\tau$ will tend to drive the leading dislocation away from the indentation centre, and is given by [25]:

$$\Delta\tau = \frac{Gb}{2\pi(1-\nu)} \sum_{i=2}^n \frac{1}{(L-x_i)}, \quad (20)$$

where G is the shear modulus of the crystal, ν its Poissons ratio, x_i is the x -coordinate of the i th dislocation, n is the total number of dislocations in the rosette arm, and b is the Burgers vector of the dislocations.

Assuming that at the location of the leading dislocation, that is at D (Fig. 15), the sum of $(\tau_{xy})_{\text{blister}}$ and $\Delta\tau$ is equal to the critical shear stress τ_c of the crystal, we have

$$\left(\frac{6B(1-\nu)}{L^3}\right) \sin 2\phi + \Delta\tau = \tau_c. \quad (21)$$

Since $\sin \phi \cos \phi \approx \frac{a}{L}$, and for hardness $H = \frac{P_{\max}}{4a^2}$, assumed independent of load, eq. (21) becomes

$$\left(\frac{12B(1-\nu)}{L^4}\right) \frac{1}{2} \frac{P_{\max}^{\frac{1}{2}}}{H^{\frac{1}{2}}} = \tau_c - \Delta\tau. \quad (22)$$

Substituting the value of B from eq. (12) into eq. (22), we have

$$6(0.029fE) \frac{P_{\max}^{\frac{3}{2}}}{H^{\frac{3}{2}}} \frac{P_{\max}^{\frac{1}{2}}}{H^{\frac{1}{2}}} \frac{(1-\nu)}{L^4} = \tau_c - \Delta\tau, \quad (23)$$

$$\text{or } 6(0.029fE(1-\nu)) \frac{1}{H^2} \frac{P_{\max}^2}{L^4} = \tau_c - \Delta\tau,$$

$$\text{or } \frac{\chi}{H^2} \frac{P_{\max}^2}{L^4} = \tau_c - \Delta\tau, \quad (24)$$

in which $\chi = 6\{0.029fE(1-\nu)\}$ (for a Vickers indentation, $\chi = 6\{0.026fE(1-\nu)\}$).

Rearranging eq. (24), and assuming that $H = \beta\tau_c$, where β is a universal constant, and that $\Delta\tau$ is much smaller than τ_c , we finally get

$$\frac{P_{\max}}{L^2} = \frac{\beta}{\chi^{\frac{1}{2}}} \tau_c^{\frac{3}{2}}. \quad (25)$$

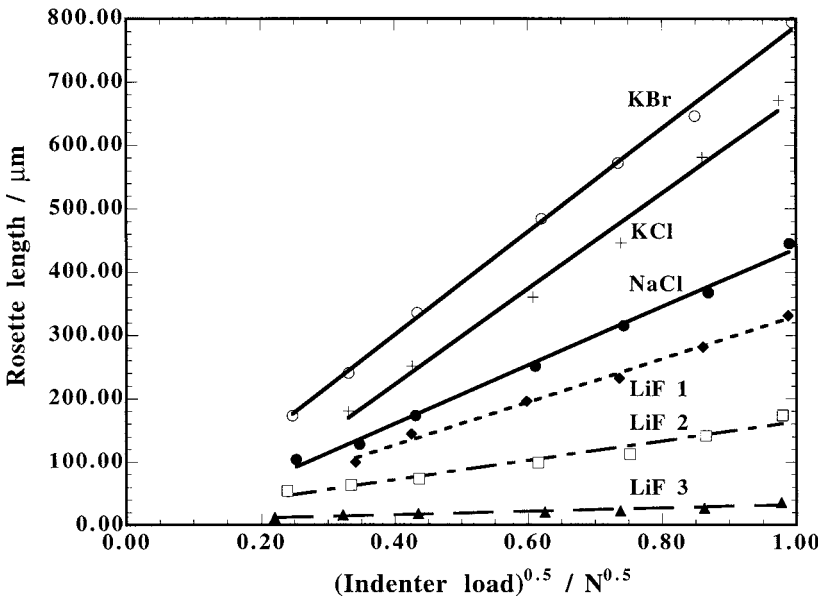


Fig. 16. Variation of the length of arms of dislocation rosettes with the square root of the indenter load for a number of alkali halide single crystals. Also included in the figure are the data from three LiF single crystals having yield stress values of 10^6 , 7×10^6 , and 7.7×10^7 Pa for LiF1, LiF2, and LiF3, respectively. Note that with increasing yield strength, the slope of the lines decreases systematically. Data from Gridneva et al. [26].

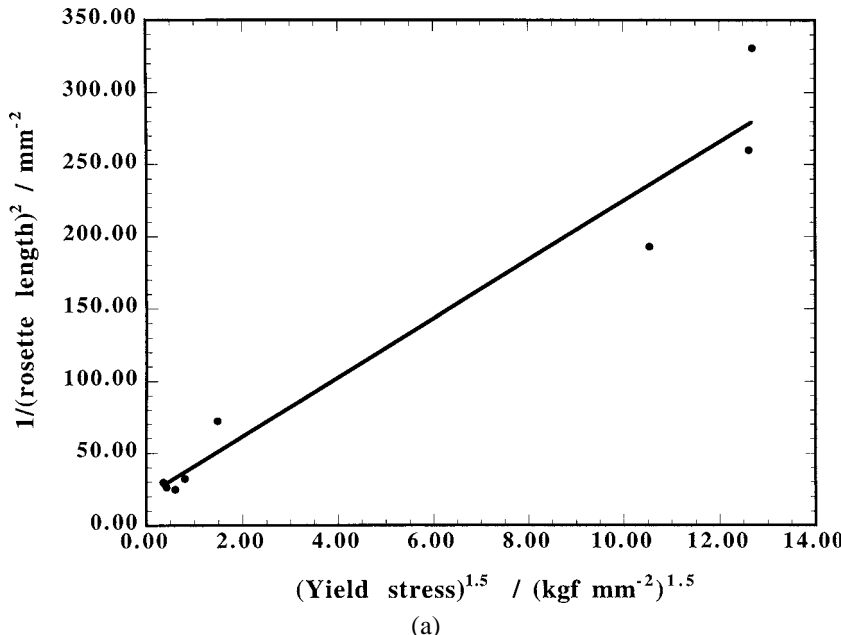
In eq. (25) the right hand side is constant for a given crystal. Therefore, the length L of a rosette arm of a crystal should vary as $(P_{\max})^{1/2}$. Thus eq. (25) may be used for studying (i) the variation of the length L of the rosette arms with the applied maximum indenter load, and (ii) for a constant maximum indenter load, the variation of the length of the rosette arm with the critical shear stress τ_c of the test crystal. If the τ_c of a crystal is reduced by raising its temperature to above that at which it was indented, then according to eq. (25) the length L of the rosette arm would also increase.

Fig. 16 shows plots of L versus $(P_{\max})^{1/2}$ for several ionic crystals [26] and it will be seen that all the plots are good straight lines, and except for the KCl crystal, all the other straight lines pass very close to the origin, as would be expected from eq. (25). Also, according to eq. (25), the slopes of the straight line plots would decrease with increasing τ_c . This is also borne out by the plots of the three LiF crystals shown in Fig. 16.

If the τ_c of an ionic crystal is varied by changing its impurity content or by irradiation with X-rays or nuclear particles, then for a maximum indenter load P_{\max} the length L of an indentation rosette arm will vary as

$$\frac{1}{L^2} = \beta \left(\frac{1}{\chi} \right)^{\frac{1}{2}} \frac{1}{P_{\max}} \tau_c^{\frac{3}{2}}. \quad (26)$$

Shaskol'skaya and Dobrzhanskii [27] have studied the lengths of the rosette arms around 50 gf Vickers indentations in single crystals of LiF (100) containing different amounts of



(a)

Fig. 17. (a) Variation of the length of dislocation rosette arms around 50 gf Vickers indentations in single crystals of LiF containing different amounts of impurities which altered their yield stress. With increasing yield stress, the length of the rosette arms decreases systematically and follows the relation given by eq. (26). Data from Shaskol'skaya and Dobrzhanskii [27]. (b) Variation of the length of dislocation rosette arms around 30 gf Vickers indentations made on a (100) face of a single crystal of MgO whose critical resolved shear stress had been altered by different heat treatments. The critical resolved shear stress of each crystal was measured using a 3-point bend test. As in Fig. 17(a), in MgO crystals also the length of the dislocation rosette arms decreases with increasing critical resolved shear stress of the crystals and the data follow eq. (26) quite closely. Data from Davidge [28].

impurities, but the nature of the impurities was not given. They also measured the yield stress of these crystals in compression tests and found that with increasing yield stress of a crystal, the length of the rosette arms decreased systematically (see Fig. 17(a)), in accordance with eq. (26). It may be added here that these authors believed that the length of the rosette arms indicated the bulk strength of the crystals rather than that of the surface.

Similar indentation rosette investigations have been conducted by Davidge [28] for estimating the critical resolved shear stress of MgO(100) single crystals containing various levels of impurities. The data of Davidge [28], shown in Fig. 17(b), are very well fitted by eq. (26).

Using the indentation rosette technique, the influence of neutron irradiation on the mechanical strength of MgO(100) crystals has been investigated by Stablein [29]. To maintain the reproducibility of the results, he studied crystal pieces which were cleaved from the same parent crystal. Some of the crystals were irradiated with reactor neutrons (energies up to 2 MeV), then indented with a Vickers pyramid, which was followed by etching to reveal the distribution of dislocations around the indentations. He found that the size of the indentation dislocation rosettes in the neutron-irradiated crystals (dose: 10^{19} cm^{-2})

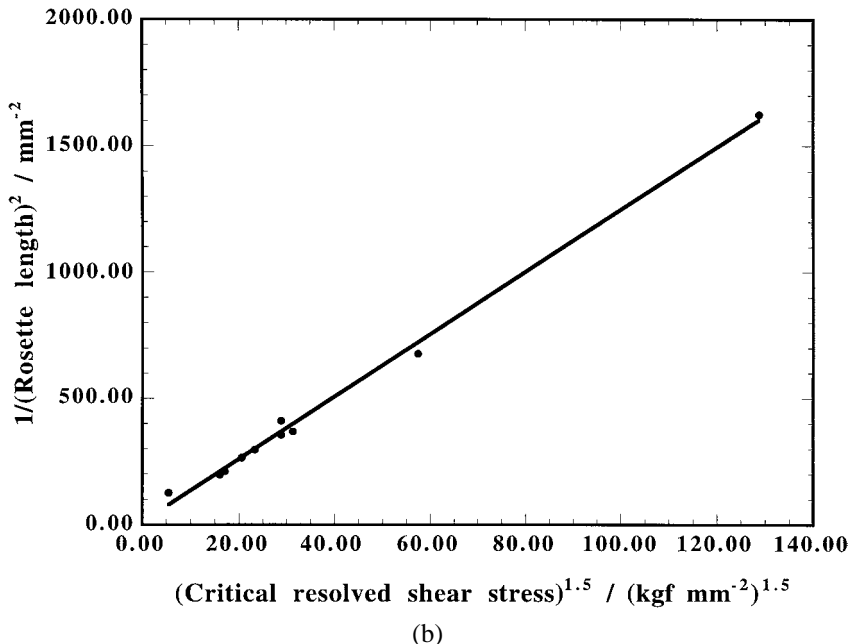
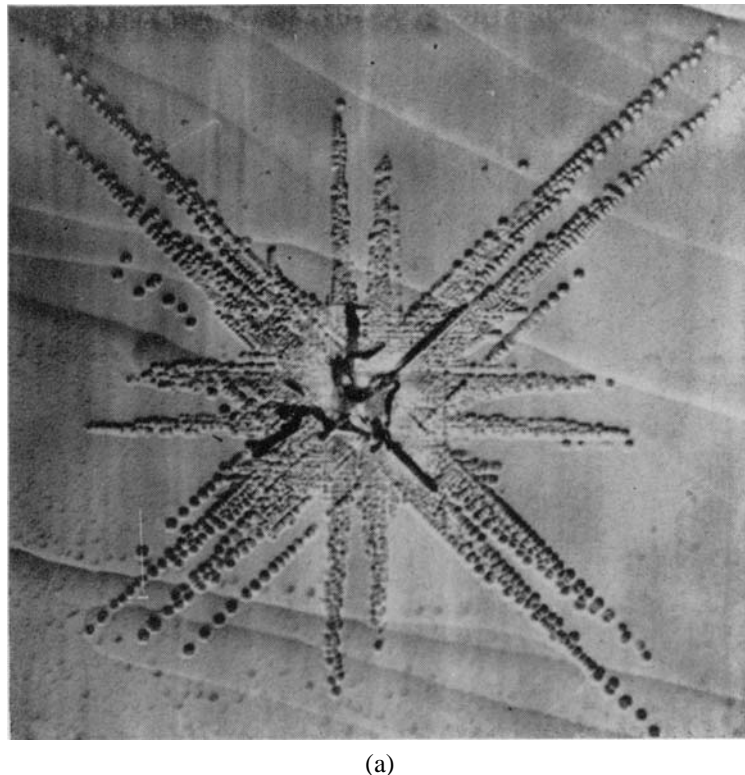


Fig. 17. (Continued).

was considerably smaller than in an unirradiated crystal (see Fig. 18(a, b)). This suggests that the shear stress required to move dislocations increased due to the irradiation with the reactor neutrons. Using a three-point bend test, Stablein [29] showed that the yield stress in bending increased by a factor of four to a value of 28 kgf mm^{-2} for crystals irradiated with $2 \times 10^{17} \text{ reactor neutrons cm}^{-2}$. Irradiation with thermal neutrons did not show any hardening of the crystals. A possible cause of the increased yield stress and the indentation hardness of the reactor neutron-irradiated crystals was given as the formation of vacancies, interstitials and Frenkel pairs, which would hinder the movement of dislocations. When these defects were removed by annealing the crystals at 1200°C for 21.5 h, the size of the indentation rosette became identical to that in an unirradiated crystal. Furthermore, the thermal neutrons are unlikely to produce the above types of defects and that is why no influence was found on the lengths of the rosette arms.

3.2. Semiconductors

Indentation dislocation rosettes in some of the important semiconductors, such as Si, Ge, and GaAs have been investigated by several workers [26,30–39]. Here we shall give examples of indentation dislocation rosettes in single crystals of these materials.

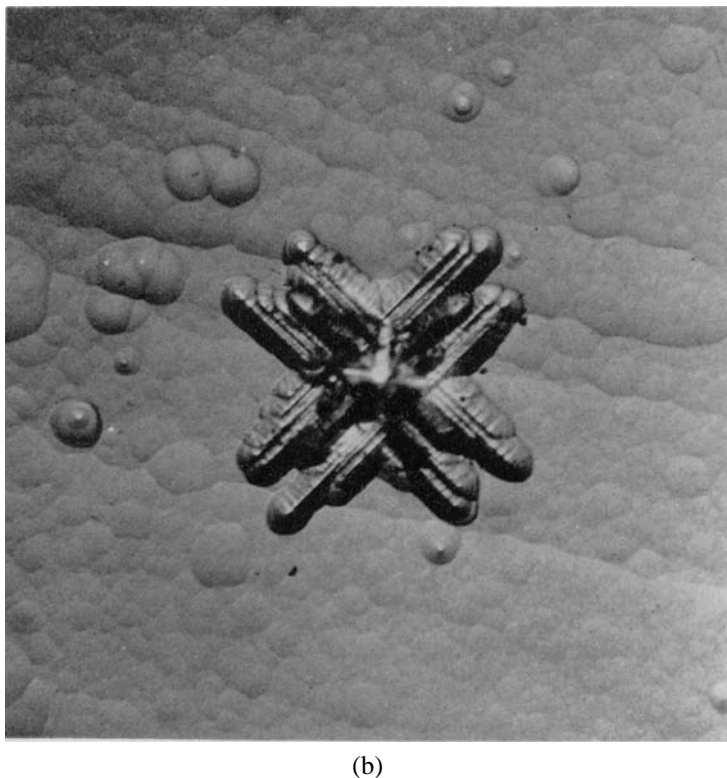


(a)

Fig. 18. This figure illustrates the hardening effect of irradiation of MgO single crystals with fast reactor neutrons. In (a) is shown a dislocation rosette around a 100 gf Vickers indentation on a (100) face of a non-irradiated MgO crystal, and in (b) is shown a dislocation rosette around a 200 gf Vickers indentation on a (100) face of an MgO crystal which had been irradiated with 10^{19} reactor neutrons cm^{-2} . Note that the irradiation has caused so much hardening that even for an indenter load of 200 gf, the rosette arm length is only $\sim 1/3$ rd of the rosette arm length in the non-irradiated crystal, but for half the indenter load. In both (a) and (b) the longer arms of the rosettes are along the (110) directions. The width of each frame is 0.144 mm. The etchant used was the same as that given in the caption of Fig. 10. Data from Stablein [29].

3.2.1. Silicon

Silicon has a cubic structure and the slip system in it is $\{111\}\langle\bar{1}\bar{1}0\rangle$ [36]. It is thought by some workers [40] that when an indentation is made in a single crystal of Si at room temperature, the displaced material is accommodated not by the generation and movement of dislocations, but by volume reduction accompanying a crystallographic phase change. However, several other workers hold a different view [41–43] and they have shown by transmission electron microscopy (TEM) that dislocations are indeed involved in room-temperature indentations. This point is discussed in more detail in Section 5.1. These dislocations appear to be confined to a region very close to the indentation. In order to form a well-developed rosette, indentations are made at temperatures higher than 400°C, which is regarded as the brittle/ductile transition temperature of Si [35]. The dislocation positions around the indentation are then revealed by chemical etching. Sometimes, after making an



(b)

Fig. 18. (Continued).

indentation at 600°C (say), the Si specimen was annealed at a higher temperature of 970°C so that when the annealed specimen was etched, the dislocation etch pits were better resolved under an optical microscope. However, the annealing most probably also causes an increase in the size of the dislocation rosettes, as has already been said in the previous section.

A typical dislocation rosette in a single crystal of Si(100) around a 25 gf Vickers diamond indentation made at a temperature of 600°C is shown in Fig. 19. It would appear from the shapes and clarity of the etch pits that the indented crystal was annealed at a higher temperature of 970°C before the emergence of the dislocation loops on the indented surface was revealed by chemical etching. It also appears that when the process of indentation of Si is carried out at a lower temperature of 400°C and then the chemical etching is carried out at room temperature, the rosette sizes are much smaller and the dislocation loops are too close to one another to be well resolved [38].

One of the early studies of indentation rosettes in Si(111) and Ge(111) is that by Tramposch and Rinder [31]. The indentations were made at room temperature with a Vickers diamond pyramid, then annealed at 500°C , followed by etching. Based on observations from these studies, Tramposch and Rinder [31] suggested that the rosettes consisted of shallow prismatic loops. The existence of these prismatic loops was then clearly shown

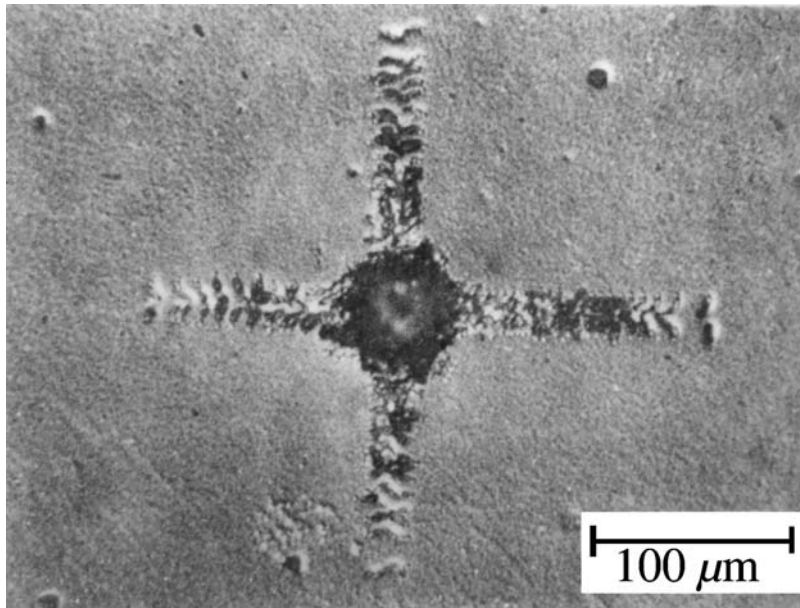


Fig. 19. A dislocation rosette around a 25 gf Vickers indentation on a (001) face of a p-type single crystal of Si grown by the Czochralski method. Its resistivity was 10 ohm cm. The indentation was made at 600°C and then the crystal was annealed at 970°C for 30 minutes before being etched in a Sirtl solution for 20 s. The arms of the rosette are along the $\langle 110 \rangle$ directions. The exact composition of the Sirtl solution used was not given by the author, but the usual composition is one part of 50 g Cr_2O_3 in 100 ml of distilled water and 1–1.5 parts of HF [39]. From Hu [35].

in a transmission electron microscopy study by Eremenko and Nikitenko [37]. Following these investigations, Hu [36] further confirmed that the indentation dislocation loops move on glide prisms, with each glide prism consisting of two intersecting $\{111\}$ planes and the indented (100) surface of the Si single crystal. A schematic diagram of the glide prisms and the dislocation loops is shown in Fig. 20. Further support for this picture was provided by studying the distribution of the etch pits in a Si(100) single crystal, which was deliberately oriented a few degrees from the {100} orientation [36]. It may be noted here that the prismatic punching of dislocation loops around indentations in Si and Ge single crystals is quite different from the loops observed around indentations in the NaCl structure crystals shown schematically in Fig. 6.

Using indenter loads in the range of 2 to 50 gf, Hu [36] has shown that the $(\text{length})^2$ of a rosette arm increases as the indenter load (Fig. 21); this behaviour is similar to that already described for the simple ionic crystals (see Section 3.1). Hu [36] also gave an approximate theoretical expression relating the rosette arm length in Si to its critical resolved shear stress τ_c by likening the indentation stress field to that of a surface cavity under a hydrostatic pressure equal to the indentation hardness of the Si. He ignored the interaction field of the dislocations and showed that L varied as $\tau_c^{-1/4}$. However, it appears that for rosettes around 25 gf Vickers indentations made in Si specimens, possessing different room-temperature

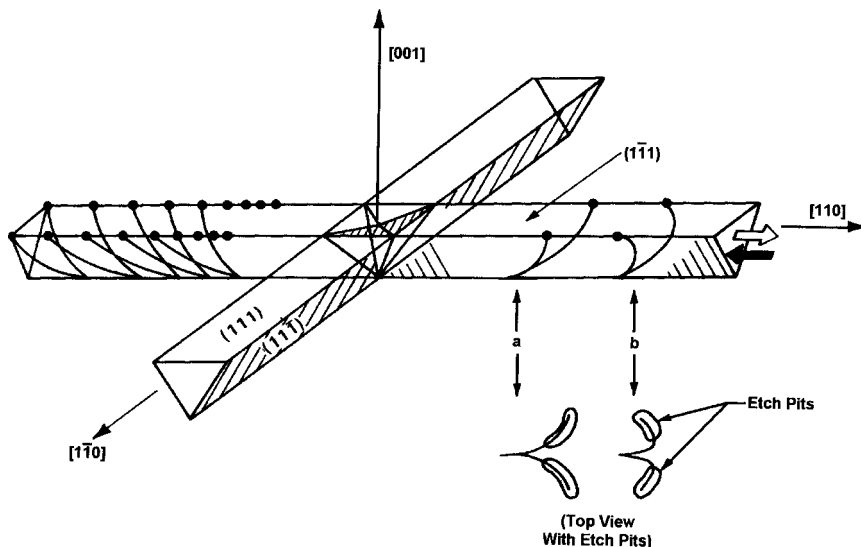


Fig. 20. Schematic representation of a dislocation rosette around a Vickers indentation on a {100} face of a Si single crystal. Dislocation loops, which give rise to the type of dislocation rosettes shown in Fig. 19, are confined to move on the surface of the prisms bounded by the {111} planes and the indented plane. Solid circles represent the points of emergence of the dislocations on the indented surface. Detail of the shapes of the etch pits are shown at the bottom right hand corner. Loops of the type a are due to those dislocations which move without any external hindrance, such as a surface film. However, if there is a surface film which drags the dislocation loops, etch pits of the type b form. From Hu [36].

τ_c values in the range of 0.2×10^7 to 4×10^7 Pa and heated to 600°C , the rosette arm length varied as $\tau_c^{-1/2}$ (see Fig. 6 of ref. [36]). A curious point about this result is that Hu [36] did not say how the specimens of Si were obtained whose τ_c values could be varied as regularly as those shown in Fig. 6 of ref. [36]. An explanation of the discrepancy was not proposed.

Several workers have investigated the dependence of the length of rosette arms on doping in single crystals of semiconductors [32,38]. Indentation rosette measurements, similar to those carried out by Hu [36], have been made by Roberts et al. [38] on single crystals of Si(100) containing various dopants in different concentrations, ranging from 10^{12} to 2×10^{18} atoms cm^{-3} . The various samples, their identification codes, types of dopant and their concentrations are given in Table 1.

Vickers diamond indentations were made on the samples heated to 400°C using indenter loads in the range of 10 to 200 gf [38]. For all indentations one of the indenter diagonals was oriented along the $\langle 110 \rangle$ direction. After the removal of the indenter load, the samples were annealed at 400°C for 30 minutes. The reason for this annealing of the samples was that when the indentations were made the indenter itself was not heated with the result that when an indentation was made, the sample temperature dropped to $\sim 320^\circ\text{C}$ (S.G. Roberts, 1999, private communication). The indented and annealed samples were then etched at room temperature to reveal dislocation etch pits.

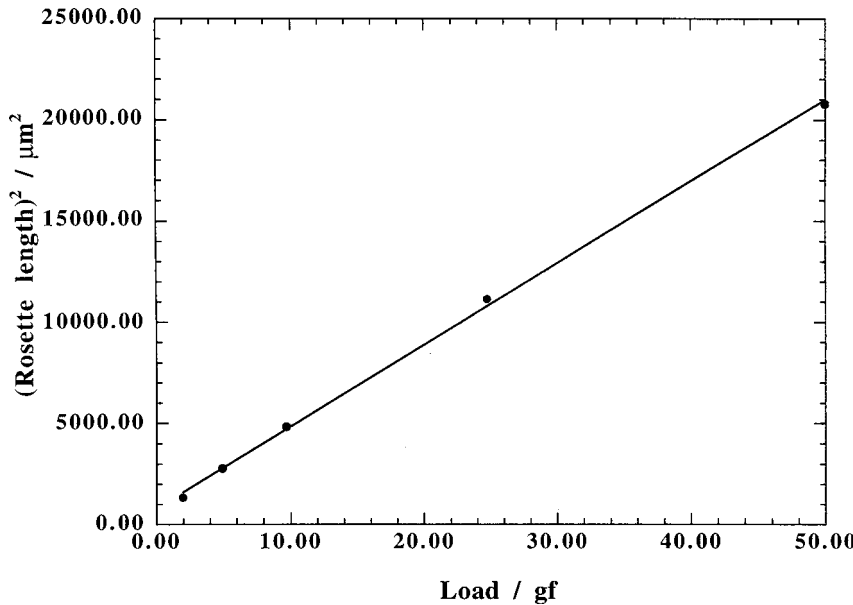


Fig. 21. Plot of the square of the rosette arm length as a function of the applied indenter load in single crystals of Si(100). Data from Hu [36].

Table 1

The identification codes of the various Si(100) single crystals, the methods of preparation, the types of dopant and their concentrations [38].

Code	Method of crystal growth	Type of dopant	Dopant concentration (atoms cm ⁻³)
IF	Float-zone	p	1×10^{12}
LP	Czochralski	p	7×10^{14}
LN	Czochralski	n	2×10^{15}
PC	Czochralski	p	2×10^{18}
NC	Czochralski	n	2×10^{18}
NF	Float-zone	n	2×10^{18}

Roberts et al. [38] reported that although the doping did not significantly alter the indentation hardness of the various silicon samples, there was a considerable variation in the lengths of the indentation rosette arms in them. It may be remarked here that the effect of doping on the indentation hardness of Si(100) is more apparent at sample temperatures below 300°C [32]. Using the data from Roberts et al. [38], we have plotted in Fig. 22 the (rosette length)² versus the indenter load. It is interesting to note that, as expected from eq. (25), all the plots are good straight lines and each line passes very close to the origin. However, the slopes of the various lines vary in a systematic manner. It will be seen from

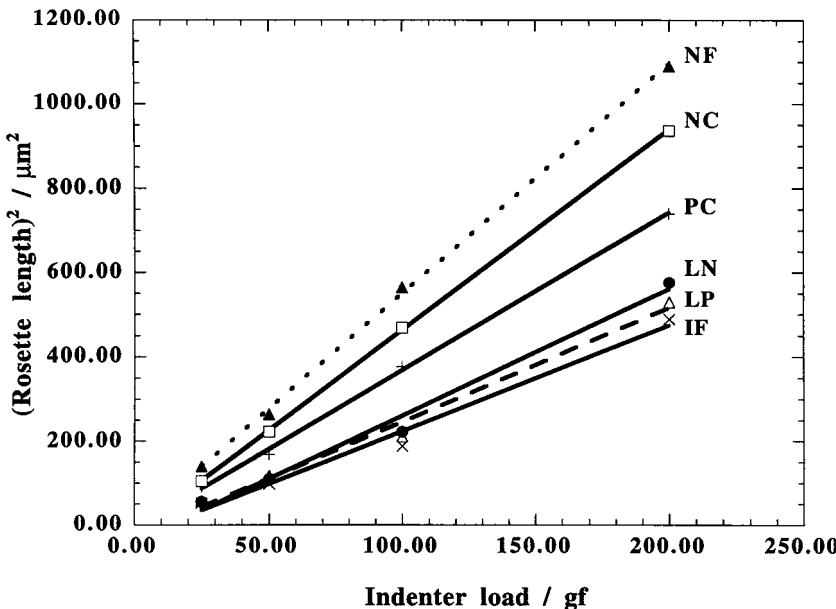


Fig. 22. The variation of the dislocation rosette arm length around Vickers indentations in Si(100) made at 400°C and under different indenter loads. See Table 1 for the codes of the various samples. Data from Roberts, Pirouz and Hirsch [38].

the figure that as the doping concentration increases the slope of the straight line also increases. There is also some tendency in the results which indicates that for a given doping level, the slope of the straight line is higher for the Si crystals containing the n-type dopants (see lines corresponding to codes NC and PC).

Roberts et al. [38] have not indicated whether the doping concentrations in their Si samples were uniform throughout the bulk or whether the doping was only in the surface of the samples. Nevertheless, the slopes of the various plots in Fig. 22 may be used to estimate approximately the critical shear stress of the various Si samples using eq. (25) and assuming that f remains constant at ~ 1 . Now, since the indentation hardness of a sample is related to its critical resolved shear stress and since the hardness was found to be independent of the doping levels, there appears to be a contradiction, which may be resolved only by assuming that for the indenter loads employed, the rosette arm lengths indicate a surface phenomenon which could not be monitored accurately by the microhardness measurements; in the measurements of Roberts et al. [38] the indentation depths were in the range of ~ 1 to $3 \mu\text{m}$. It is possible that if much shallower indentations had been made using a nanoindentation machine, the nanohardness might have been found to vary systematically with the doping levels. Another possible reason for the apparent independence of the microhardness on the doping level may be related to the phenomenon of phase transformation of Si under the indenter (see Section 5), which is likely to mask any differences in the microhardness of these silicon samples.

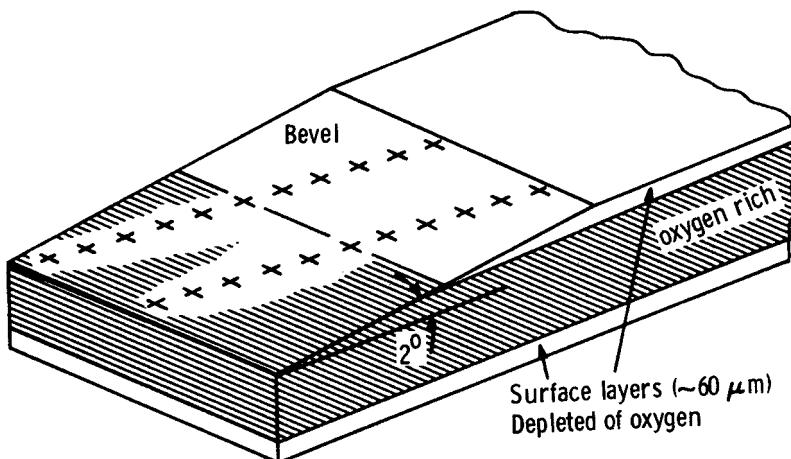
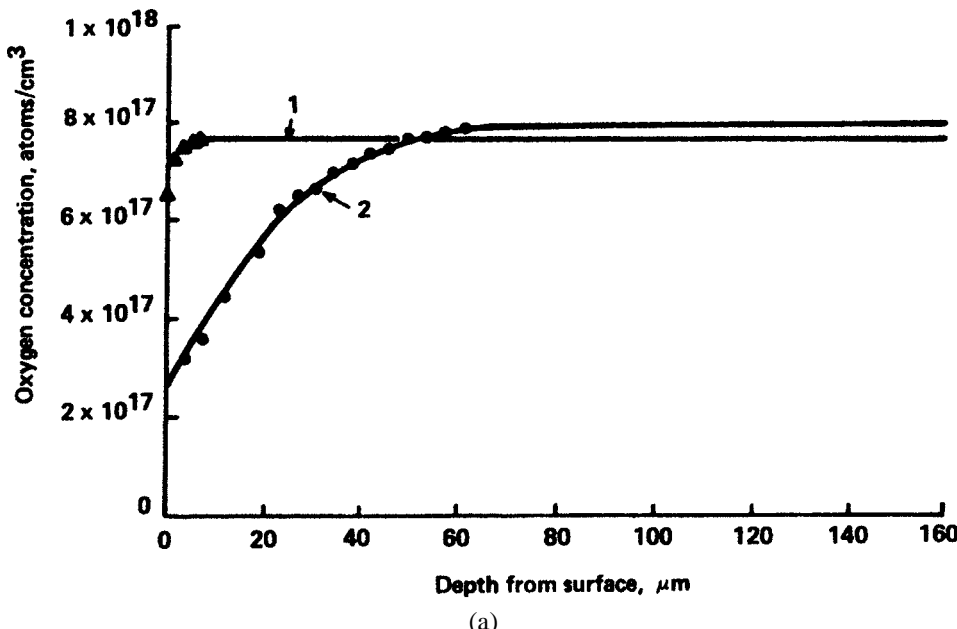


Fig. 23. Schematic diagram of a bevelled Si(100) specimen in which the surface layers of thickness of $\sim 60 \mu\text{m}$ have been depleted of the oxygen by heat treatment. Vickers indentations were then made on the inclined surface at positions indicated with an 'x'. From Hu [44].

A particularly important practical use of indentation rosettes has been made by Hu [44] for determining the relative mechanical strength of Si crystals grown by the Czochralski method. Crystals grown by this method contain oxygen in solution form. According to Hu [44], there are various possible effects of the oxygen in the Si. One harmful effect is that oxygen precipitates form (Hu [44] did not say whether the oxygen precipitates were purely oxygen or there were silicates as well), which can become dislocation sources in the Si when it is subjected to thermal stresses. Another effect is that oxygen may even increase the mechanical strength of the Si by the processes of dislocation pinning and increase of resistance to dislocation movement by the oxygen atoms. This effect would be beneficial, especially for very thin wafers in need of mechanical strength. To show the dislocation pinning effect of oxygen (it appears that Hu [44] has interpreted the pinning of dislocations to the increase in the value of the critical resolved shear stress), Hu [44] carried out indentation rosette length measurements on two samples $6 \text{ mm} \times 15 \text{ mm} \times 400 \mu\text{m}$ cut from the centre region of a 57-mm diameter single crystal Si wafer containing a suitably high concentration of oxygen. One sample served as a control, but in the 60 to $80 \mu\text{m}$ thick surface layer of the other the oxygen concentration had been deliberately varied continuously along the surface normal by the process of out-diffusion of oxygen by heat treatment at 1150°C for 8 h. In some Si samples precipitation (precipitates appear not to have been analysed) occurred, but for the indentation rosette experiments only those specimens were chosen which showed negligible precipitation. This heat treatment led to a gradual decrease over a surface thickness of $60 \mu\text{m}$ in the oxygen concentration from $\sim 8 \times 10^{17} \text{ atoms cm}^{-3}$ in the crystal bulk to $\sim 2 \times 10^{17} \text{ atoms cm}^{-3}$ at the specimen surface (see ref. [44] for details of the method). The specimens were rebevelled to 2° and the bevelled surfaces repolished to a mirror finish. Using an indenter load of 25 gf, Vickers indentations were made at different positions on the bevelled surfaces while the specimens were heated to a temperature of 600°C (Fig. 23). After making all the indentations and removing the



(a)

Fig. 24. (a) Curve 1 shows the oxygen concentration in an as-grown single crystal of Si(100) wafer, grown by the Czochralski method, at different distances from the surface. Curve 2 shows the oxygen concentration in a specimen which had been subjected to an oxygen out-diffusion heat treatment. The indentation dislocation rosette arm length measurements in both types of sample are shown in (b). Here curve 2 is for the treated Si wafer, whereas curve 1 is for the untreated Si wafer. Note that as the oxygen concentration decreases, the rosette arm length gets longer. This type of behaviour of the rosettes is a clear indication of the obstruction of the dislocations by the oxygen in the wafers. From Hu [44].

indenter, the specimens were heated at 900°C for 30 minutes to enlarge the span of the dislocation rosettes. These were then etched to reveal the positions of dislocations.

Fig. 24(a) shows the oxygen concentration before (curve 1) and after (curve 2) the heat treatment (i.e. out-diffusion of oxygen). It was found that with reducing oxygen concentration (i.e. towards the surface), the length of the rosette arms increased systematically (see Fig. 24(b)), thus showing reasonably conclusively that the dissolved oxygen has a strengthening effect. The results of Hu [44] suggest further that when the oxygen concentration dropped to below $\sim 2 \times 10^{17}$ atoms cm^{-3} , the effect on the rosette length became insignificant. As a mechanism, Hu [44] suggested that when the oxygen-containing wafers were heat-treated between 700 and 900°C, the oxygen atoms formed clusters, which were more effective in obstructing the movement of dislocations than were the individual atoms.

Similar indentation experiments have been carried out recently by Akatsuka et al. [45] on Si(100) wafers doped with boron to give a resistivity of > 5 ohm cm. These specimens were grown by the Czochralski and float-zone methods. The oxygen concentrations used were 3.7 to 15.5×10^{17} atoms cm^{-3} . Vickers indentations were made using an indentation load of 100 gf (the authors did say whether the indentations were made at room temperature). The wafers were then annealed at 900°C for 30 minutes in a nitrogen atmosphere and then

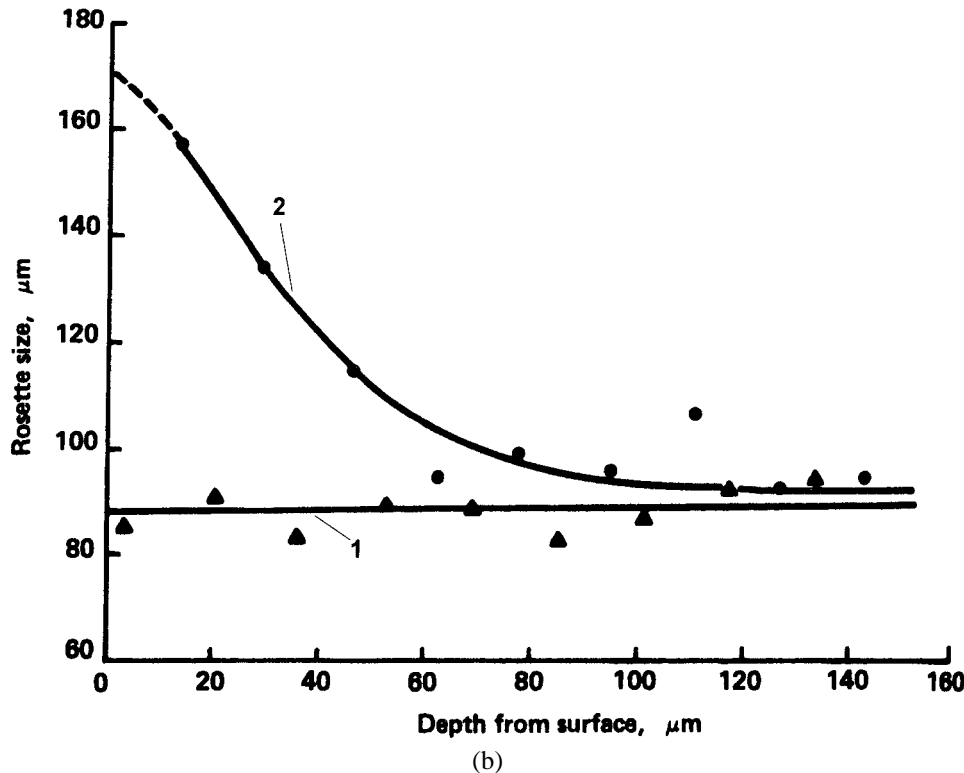


Fig. 24. (Continued).

the specimens were etched to reveal dislocations. Akatsuka et al. [45] reported that when the oxygen concentration in the Si specimens grown by the Czochralski method dropped to $\sim 2 \times 10^{17}$ atoms cm^{-3} , the length of the rosette arms was the same as that in the oxygen-free wafers grown by the float-zone method. These results are in agreement with those of Hu [44]. Akatsuka et al. [45] also found that the rosette arm length was related to the interstitial oxygen concentration by an empirical expression

$$L \propto (\text{oxygen concentration})^{-2/3}. \quad (27)$$

However, no explanation was given why this empirical expression should apply.

3.2.2. Germanium

An elegant study of indentation dislocation rosettes in single crystals of Ge(111) of resistivity 2 to 6 ohm cm, corresponding to an impurity content of 8×10^{14} to 1.5×10^{15} atoms cm^{-3} and a dislocation density of 10^3 to 10^4 cm^{-2} , has been carried out by Sumino and Hasegawa [34]. Using a Vickers diamond indenter and loads of 50, 100 and 300 gf, they indented the Ge(111) crystals at different temperatures in the range of 20 to 930°C. After having made the indentations, the crystals were etched at 75°C in the Billig

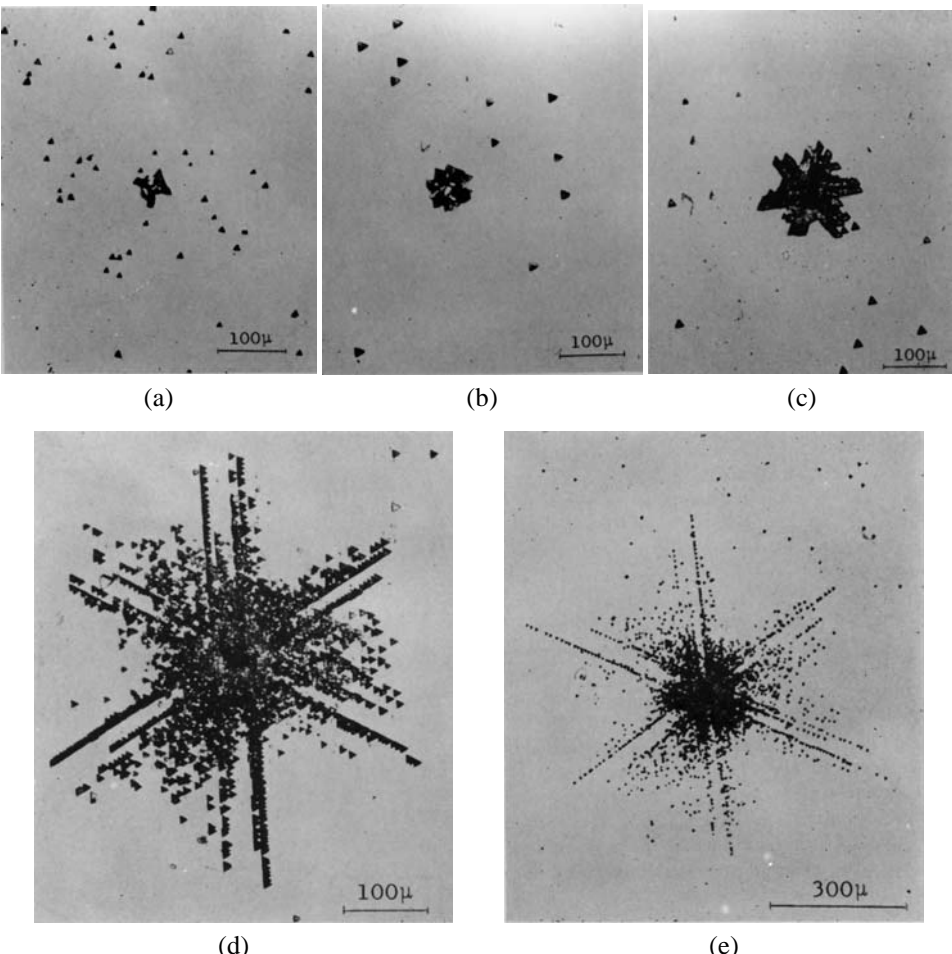


Fig. 25. Dislocation rosettes in single crystals of Ge(111) heated to different temperatures and then indented with a Vickers diamond pyramid under a load of 100 gf. The etching of the indented specimens was carried out with the Billig reagent heated to 75°C. The indentation temperatures corresponding to the various frames are (a) room temperature, (b) 300°C, (c) 400°C, (d) 490°C, (e) 550°C, (f) 600°C, and (g) 700°C. From Sumino and Hasegawa [34]. Etchant was 8 g of $K_3Fe(CN)_6$ + 12 g of KOH in 100 ml of warm distilled water [31].

reagent (see caption of Fig. 25 for chemicals). Sharp and discrete dislocation pits were formed lying along the $\langle 110 \rangle$ directions for crystals indented at temperatures in the range of 300 to 600°C (see Fig. 25). However, although an indentation was formed at room temperature and the Vickers hardness was evaluated as $\sim 875 \text{ kgf mm}^{-2}$, the authors suggested that no dislocation activity took place and possibly some unknown mechanism was involved in the formation of a permanent indentation. This suggestion seems unlikely to be correct and there is strong evidence that even for room temperature and 78 K indentations, dislocations are involved, but these dislocations remain very close to the indentation

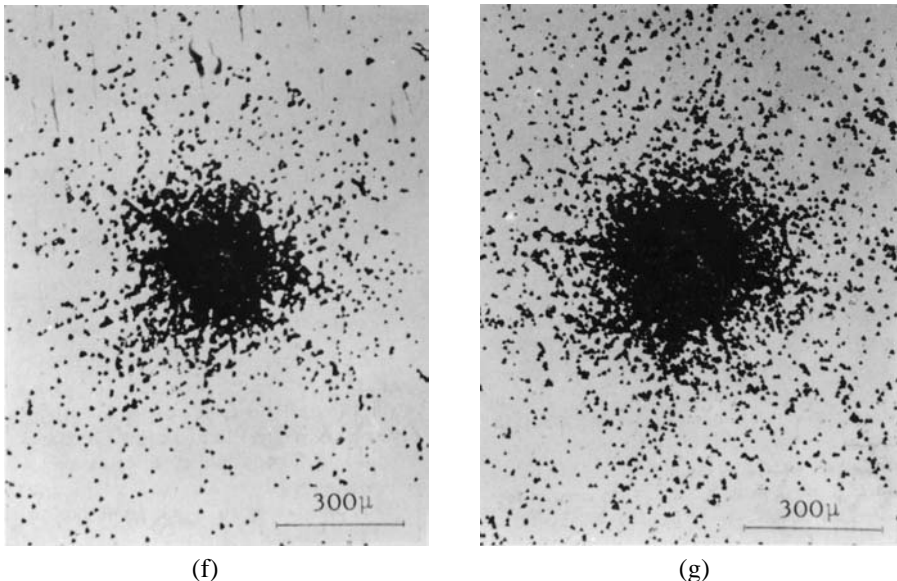


Fig. 25. (Continued).

site (see, for example, [30]), which can then be made to move out by annealing at $2/3T_m$, where T_m is the melting point of Ge [30].

It will be seen from Fig. 25 that when the indentations were made at temperatures in the range of 300 to 600°C, the lengths of the rosette arms extended systematically with increasing temperature. However, for higher indentation temperatures, the dislocation rosette pattern became less regular and at 700°C, the dislocation etch pits became concentrated around the indentation. *Away from the indentation, the etch pits were no longer aligned along crystallographic directions and they were randomly distributed.* Sumino and Hasegawa [34] interpreted the indentation rosette patterns in terms of the variation of Vickers hardness with temperature. The hardness was shown to have three temperature ranges. From room temperature to 200°C, there was only a slight decrease in the hardness with increasing temperature; in the temperature range of 300 to 600°C, the rate of decrease in the hardness with increasing temperature was much higher. At still higher temperatures, the hardness reduced to $\sim 1/10$ th of its room temperature value. These authors [34] believed that for temperatures higher than 600°C, other slip planes also became active, producing a metal-like response.

The influence of doping on the lengths of the rosette arms around Vickers indentations made in Ge(100) at temperatures in the range of 20 to 420°C has been investigated by Roberts, Pirouz and Hirsch [46]. The Ge crystals were grown by the Czochralski method, and three different types of doping were employed. These were (i) p-type (gallium) $3 \times 10^{15} \text{ cm}^{-3}$ (labelled as ‘intrinsic’), (ii) p-type (gallium) $2.3 \times 10^{19} \text{ cm}^{-3}$, and (iii) n-type (arsenic) $5.5 \times 10^{18} \text{ cm}^{-3}$. Around an indentation in the Ge(100) the dislocations in the rosettes are distributed along four arms lying along the $\langle 110 \rangle$ directions, as is the case for the dislocations in the indentation rosettes in Si(100) crystals (see Fig. 19).

Roberts et al. [46] reported that for all the indentation diagonal lengths normalised to a length of 20 μm , the lengths of the rosettes, made at any temperature, were the longest in the n-type Ge(100) and the shortest in the most heavily doped p-type Ge(100). These trends are in agreement with the Vickers hardness values of the three types of Ge(100) crystals. However, these differences in the lengths of the rosettes became much reduced at indentation temperatures of 500°C and higher. Roberts et al. [46] concluded that at 500°C the intrinsic carrier concentration became similar to that due to the doping. In other words, at these high temperatures the effect of the doping would become insignificant.

Although most of the experimental data obtained from the ionic crystals (see Section 3.1) have shown that for the room temperature indentations the length of the rosette arms increases as the square root of the indenter load, it has also been reported that the exponent of indenter load may be as low as 0.3 for indentations made in semiconductors, such as GaAs, Si, Ge, and InSb, at high temperatures in the range of 250 to 700°C [26]. A satisfactory explanation of this low value of the exponent is not yet available.

3.2.3. Semiconductor compounds

In the semiconductor compounds, such as GaAs, GaP, InSb which are the III–V type semiconductors, polarity effects have been observed in their hardness values [47,48]. The slip system in these materials is {111}\langle 1\bar{1}0 \rangle. It is a convention that if all the atoms of a crystal surface (111) are of the group III element, then it is represented as (111); on the other hand, if all the atoms of the surface are of a group V element, the surface is represented as (\bar{1}\bar{1}\bar{1}). Thus in GaAs, if all the atoms on a (111) surface are of Ga, the surface is represented as (111) or Ga(111), whereas if all the surface atoms are of As, it is represented as (\bar{1}\bar{1}\bar{1}) or As(\bar{1}\bar{1}\bar{1}). The same convention will apply to the {111} planes in GaP and InSb. Similarly, the edge components of dislocations are labelled differently depending upon the terminating atoms in their extra half planes. For example, in the case of GaAs, if the extra half plane of a dislocation terminates on Ga atoms, the dislocation is labelled as the α -type. On the other hand, if the extra half plane of a dislocation terminates on As atoms, it is labelled as the β -type. It has been shown that the velocity of the α -type dislocations in InSb is 10^2 to 10^3 times higher than that of the β -type dislocations [49]. It has been suggested by Warren, Pirouz and Roberts [50] that indentation rosette arm lengths may be able to show any differences between the dislocation velocities of the two types of dislocation. (In the opinion of the author, indentation rosette arm measurements are incapable of directly revealing dislocation velocities because the usual indentation dwell times are of the order of tens of seconds. This means that the indentations are effectively quasi-static and the dislocations would move away from the indentation centre only as far as allowed by eq. (25), which does not include dislocation velocities as one of the variables.)

In these semiconductor compound materials, when an indentation is made on a {001} surface, the prismatic dislocation loops in the indentation rosette arms lying in the [110] direction are the α -type, whereas the dislocation loops in the rosette arms lying along the [1\bar{1}0] direction are of the β -type. Warren et al. [50] reported that when an n-type single crystal of GaAs(100) was indented with a Vickers indenter at 350°C under a load of 100 gf and then etched to reveal the dislocations, the rosette arms corresponding to the α -type dislocations were longer than the rosette arms containing the β -type dislocations. However, in a recent transmission electron microscopy study of indentation rosettes in GaAs(001)

single crystals, no asymmetry was found in the rosette arm lengths corresponding to the α - and β -dislocations [51]. It appears that further work is needed to clarify this controversy.

Doping of GaAs crystals with n- and p-type dopants has been shown to have a significant effect on the rosette patterns around indentations. The authors of [32] indented undoped single crystals of GaAs(111) as well as crystals which were doped with n-type (Te) to concentrations of 2×10^{15} and $4 \times 10^{18} \text{ cm}^{-3}$ and p-type (Zn) to a concentration of $1.5 \times 10^{19} \text{ cm}^{-3}$. Indentations were made at 200°C and 350°C and then the crystals were etched to reveal dislocations. Mil'vidskii et al. [32] reported that up to an indentation temperature of 300°C , the doping only caused a change in the lengths of the rosette arms, without affecting the general features of the rosettes. However, when the indentations were made at 350°C , the characteristics of the rosettes changed considerably. For the undoped and the Zn-doped GaAs, the rosette arms became diffuse and broad, whereas for the Te-doped GaAs the rosettes had a sharp central region with sharp and narrow rosette arms. These authors [32] suggested that for the undoped and p-doped GaAs, transverse slip processes, activating new slip planes, came into operation and caused an increase in the width of the rosette arms. In the Te-doped GaAs, appreciable transverse slip was found to occur at temperatures higher than 400°C .

3.3. Metals

There are many more possible slip planes in ductile metals than in ionic crystals or semiconductor crystals. For example, in α -Fe crystals the different slip planes are {110}, {112}, and possibly {123} the dislocations are narrow and they can easily slip from one plane to another [52]. As a consequence, rather high-load indentations in ductile metals may generate irregular structures of dislocation etch pits. However, when relatively small indenter loads are used, distinct rosettes can be formed. One of the earlier studies on dislocation rosettes in metals was carried out by Kushnir, Mikhailova and Osip'yan [52], who used single crystals of α -Fe(100). Vickers indentations were made at temperatures of 20 and 196°C , using indenter loads of up to 50 gf. On etching, dislocation etch pits were found along the $\langle 110 \rangle$ directions corresponding to dislocation movement on the {110} and {112} slip planes. Then these authors carried out indentation experiments on the α -Fe crystals in which carbon had been added to an amount in the range of 0.007 to 0.02 weight %. It was found that some of the carbon-containing crystals produced rosette arms which extended along the $\langle 210 \rangle$ direction, corresponding to slip planes {211} and {123}. Kushnir et al. [52] suggested that these new slip planes necessarily excluded the {110} planes from the number of the possible active slip planes in these carbon-containing α -Fe crystals.

Among the f.c.c. metals (slip system, {111}\langle 10\bar{1} \rangle [21]), dislocations and rosettes around indentations in silver and copper single crystals have been studied by Chen and Hendrickson [53] and by Dyer [54], respectively. In the case of a Vickers indentation on a (111) face of a single crystal of silver of 99.999% purity and having grown-in dislocation densities of $\sim 10^4$ to $1 \times 10^7 \text{ cm}^{-2}$, good-quality dislocation rosettes consisting of 6 arms lying along the $\langle 110 \rangle$ directions were formed for indenter loads of up to 2 to 4 gf. At higher loads, the dislocation etch pits became more and more localised around the indentation, rather than spreading out further and further with increasing indenter load. At an indenter load of 10

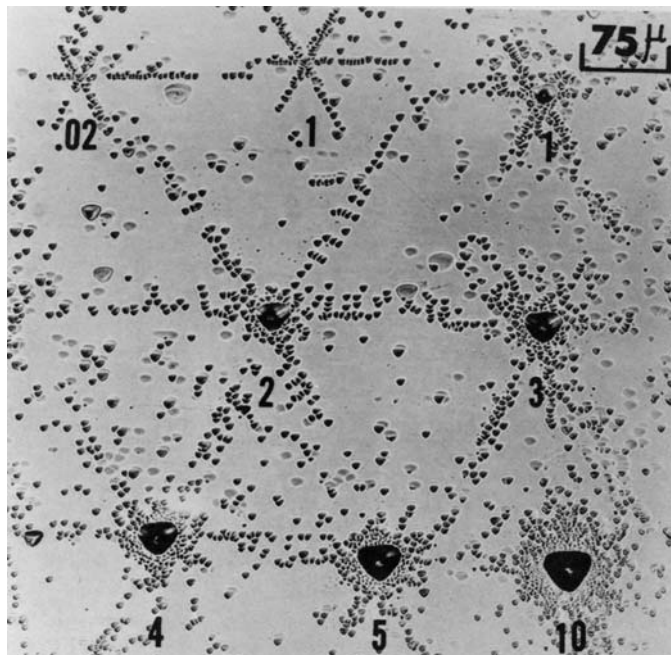


Fig. 26. Dislocation rosettes around room-temperature Vickers indentations in a (111) surface of a single crystal of Ag. Good-quality rosettes form for indenter loads as low as 0.02 gf and the rosette arm lengths grow for indenter loads of up to 4 gf. However, at higher loads the rosette structure becomes diffuse and for the 10 gf indentation the dislocation pits are uniformly and homogeneously distributed around the indentation and the rosette arms are no longer visible. From Chen and Hendrickson [53].

gf, the arms of the rosettes could not be distinguished from one another (see Fig. 26). Chen and Hendrickson [53] interpreted this observation as a manifestation of a change of the deformation mode.

When the etch pits in each of the six arms were examined closely, the pits were in the form of pairs, with each pair consisting of a large pit and a small pit (see Fig. 27). Following a suggestion by Livingston [55] about the different etching characteristics of parallel dislocations of opposite signs in copper, Chen and Hendrickson [56] explained these differences between the etch pit sizes by suggesting that each pair of pits is associated with a prismatic dislocation half loop gliding on two {111} planes, one of which makes an acute angle with the indented {111} plane, while the other plane is inclined to it at an obtuse angle; the smaller size etch pits were thought by them to be produced by the ends of the prismatic half loops gliding on the latter planes.

An interesting observation made by Chen and Hendrickson [56] was that for an indenter load of 0.02 gf, the volume of the displaced material amounted to $7 \times 10^{-13} \text{ cm}^3$. Each of the loops was $\sim 2 \mu\text{m}$ in length and $1.5 \mu\text{m}$ deep. Simple calculations indicated that if the displaced material were to be accounted for by the dislocation loops in the six arms of the rosettes, then a total of 800 dislocations ought to have formed. In fact, an etch pit count indicated that the actual dislocation number was only 165. This rather large discrepancy

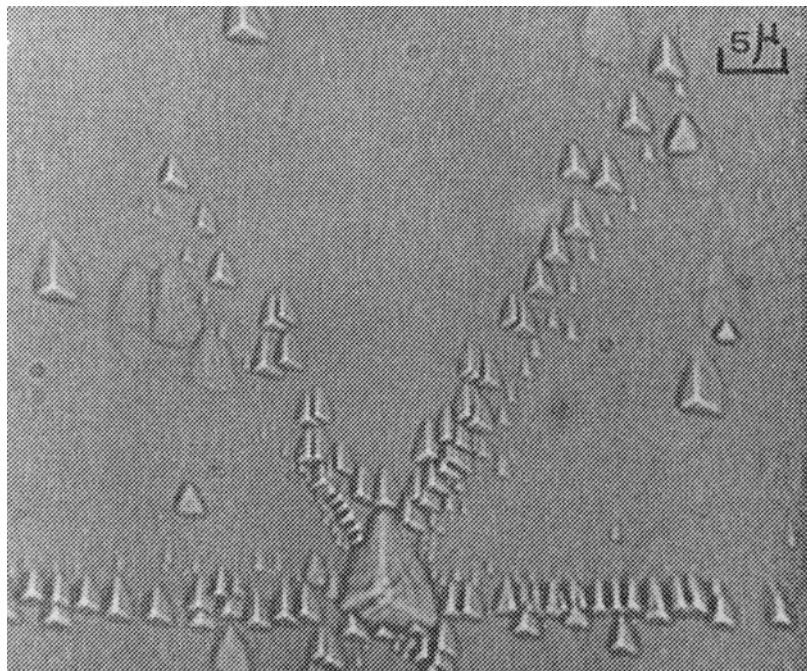


Fig. 27. Dislocation rosettes around a 0.02 gf Vickers indentation in a single crystal of Ag(111). This higher magnification micrograph shows detail in the etch pits. Each large pit has associated with it a smaller etch pit and this has been explained in the text. Interestingly, the indentation itself appears to be triangular rather than having a square shape, as would be expected for a Vickers pyramid. This is possibly due to the preferential etching of the silver. The etchant used was $50 \text{ cm}^3 \text{ NH}_4\text{OH}$, $20 \text{ cm}^3 30\% \text{ H}_2\text{O}_2$ and 1 cm^3 of solution made of $25 \text{ cm}^3 \text{ H}_2\text{O}$, $0.5 \text{ cm}^3 38\% \text{ HCl}$ and 5 g of CrO_3 . From Chen and Hendrickson [56].

suggests that a considerable amount of displaced material must have been pushed into the crystal bulk below the indenter in the form of dislocation loops. This statement is consistent with the experimental measurements which showed that on the removal of the indenter load not all the volume displaced by the indenter appeared above the original specimen surface [10,11].

Pharr and Oliver [57] also studied indentation rosettes in single crystals of Ag(111) of purity greater than 99.99%. They made nanoindentations using a Berkovich diamond indenter in an area of the crystal's face with a dislocation density of $3.3 \times 10^6 \text{ cm}^{-2}$. Most of their observations were similar to those of Chen and Hendrickson [53]. In addition, Pharr and Oliver [57] noted that at indentation loads below $\sim 0.017 \text{ gf}$ (i.e. 0.17 mN), no rosettes formed at all. This observation does not suggest that at such small indenter loads no dislocations formed, but it raises a possibility that in the very initial stages the dislocation loops are perhaps pushed into the bulk rather than being pushed out on to the indented surface. As said before, on the removal of the indenter load not all the material displaced by the indenter into the bulk appears to come back up on the surface, but some of it remains locked in elastically.

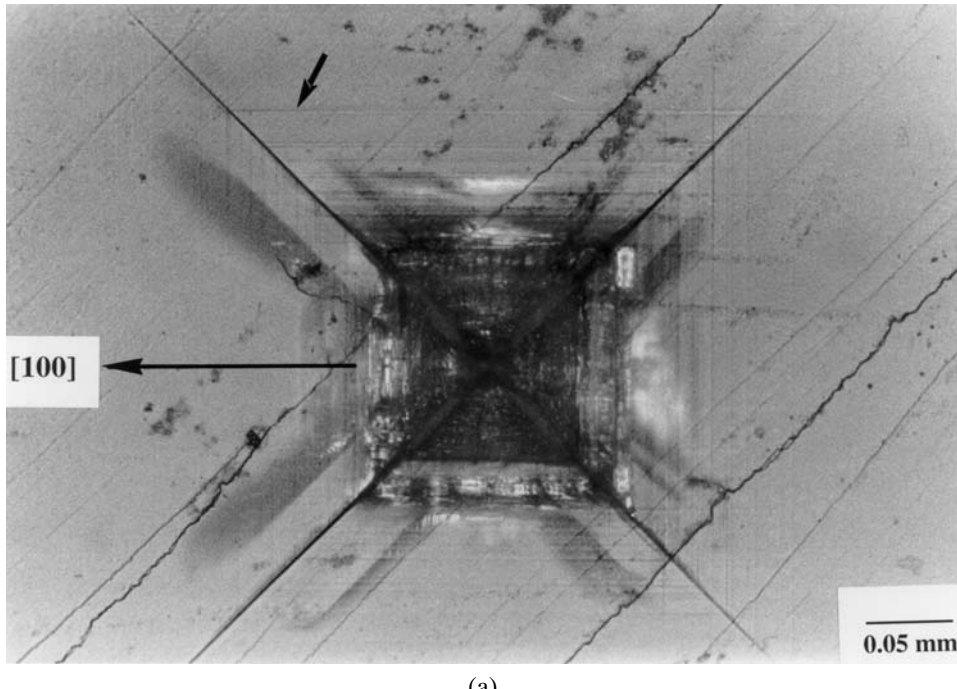
Dyer [54] has made an extensive study of the distribution of dislocations around room-temperature spherical indentations in single crystals of Cu(001) of 99.999% purity. By successively etching and removing layers of material parallel to the indented surface and by sectioning along the (111) planes lying at different distances from the indentation axis and etching the sections, he has been able to produce a three-dimensional picture of the distribution of dislocations around the indentation. Furthermore, as in the case of the spherical indentations in ionic crystals (see Figs 13 and 14), Dyer [54] also found that the residual indentations in the copper crystals, made with a spherical indenter, did not look circular when viewed along a direction normal to the indented surface. This was also explained by the formation of hills of displaced material along the <110> directions and depressions along the <100> directions. Dyer [54] further showed that the dislocation rosettes on the surface around an indentation also existed subsurface. Moreover, the maximum concentration of dislocations was at a subsurface region along the load axis. This would suggest that the maximum strain hardening would occur near to the bottom of the indentation and along the load axis and not at the edge of contact, as previously thought [58]. This observation of Dyer [54] has been confirmed recently by a study in which a 50 gf Vickers hardness mapping of a median plane section through a spherical indentation of $a/R = 0.52$ and $R = 1.5$ mm in polycrystalline copper of grain size 25–150 μm was made [59]. The maximum strain hardening was found along the load axis and close to the bottom of the spherical indentation.

4. Cracking around indentations due to dislocation interactions

4.1. Quasi-static observations

Simple ionic crystals, such as NaCl, LiF, KCl, and MgO are quite brittle and when an indentation is made in them under a sufficiently high load, certain types of crack may be generated around the indentation. These cracks are oriented specifically with respect to the crystallographic directions even in the case of indentations made with a Vickers pyramid with sharp edges. Examples of such cracks around indentations on a (100) face of an MgO crystal are shown in Fig. 28(a, b). Note that in Fig. 28(a), the indenter diagonals are along the <110> directions and the cracks are also in the same direction; if the indenter diagonals are rotated so that they are along the <100> directions, the cracks are still along the <110> directions (Fig. 28(b)). In fact, these cracks are on the {110}₉₀ planes. If instead of a Vickers indenter a spherical indenter is used, the cracks will still be along the <110> directions. These observations strongly suggest that this type of cracking is closely related to the slip system of the indented crystal. In the rest of this article, these cracks will be denoted as the {110}₉₀ cracks.

LiF, NaCl and KCl crystals are considerably softer than MgO and the indenter loads required for producing the {110}₉₀ cracks in them are higher than those for producing this type of cracking in MgO crystals. However, if these crystals are subjected to dynamic loading, causing plastic deformation at very high rates of strain, then even in these relatively soft crystals the {110}₉₀ cracking occurs rather readily even though the maximum dynamically generated load may be considerably smaller than the maximum quasi-static loads at



(a)

Fig. 28. Cracking in cleaved MgO(100) single crystals around Vickers indentations. In (a) the indenter diagonals are along the $\langle 110 \rangle$ directions and in (b) the indenter diagonals are along the $\langle 100 \rangle$ directions. However, in both cases the cracking is on the $\{110\}_{90}$ planes. The indenter loads in (a) and (b) are 0.5 and 0.3 kgf, respectively.

which these cracks do not form [60]. An example is shown in Fig. 29. Here a single crystal of LiF(100) was impacted normally with a $80 \mu\text{m}$ diameter tungsten sphere travelling at a velocity of 80 m s^{-1} , generating a maximum dynamic load of 1.5 kgf. The impact led to the formation of the $\{110\}_{90}$ cracks as well as the $\{100\}$ cleavage cracks. The latter cracks are most probably generated by the tensile hoop stresses around the impact site, whereas the former cracks are caused by the slip processes. On the other hand, when a LiF(100) crystal was loaded quasi-statically with a 0.4 mm diameter tungsten carbide sphere to a load of 10 kgf, no cracking occurred at all. It is believed that such differences in the cracking behaviour of these ionic crystals, when they are loaded quasi-statically or dynamically, are due to the enhanced brittleness with increasing rate of deformation [60].

It was proposed by Keh, Li and Chou [61] that the interactions of dislocations gliding on intersecting slip planes inclined to each other at an angle of 120° were the cause of formation of the $\{110\}_{90}$ cracks around an indentation. Their proposed scheme is shown schematically in Fig. 30. Here two intersecting planes (011) and (101) have dislocations gliding towards one another. The Burgers vector of the dislocations on the former plane is $\frac{a}{2}[0\bar{1}1]$ and the Burgers vector of the dislocations gliding on the (101) plane is $\frac{a}{2}[10\bar{1}]$. These dislocations react to give rise to a crack (shaded region in Fig. 30) on the $(\bar{1}\bar{1}0)$ plane, as shown. The dislocation reaction can be seen in more detail with the help

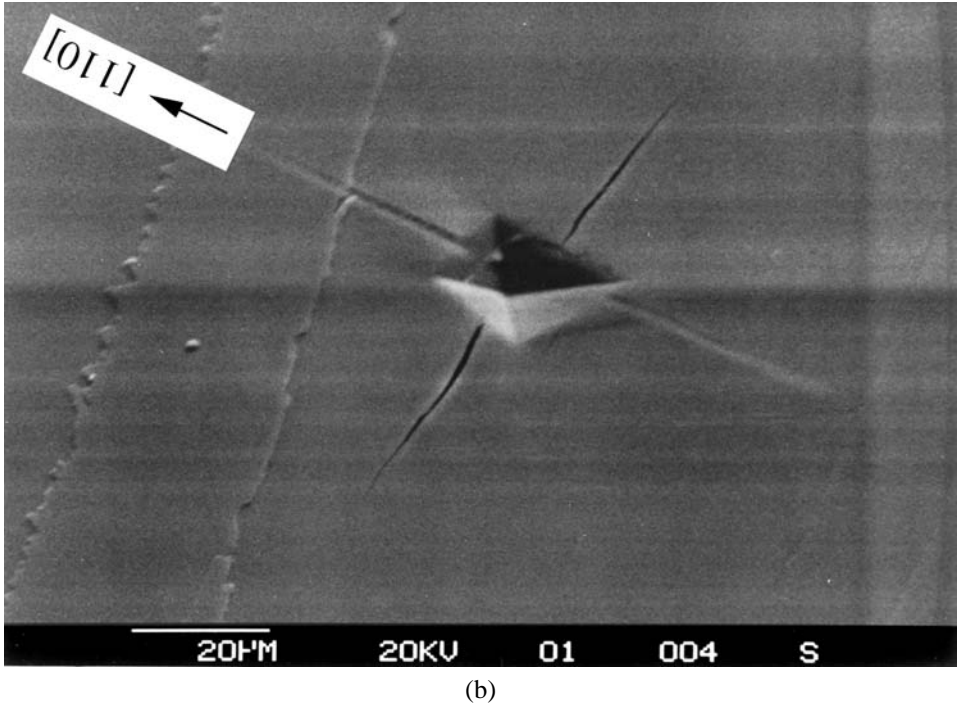


Fig. 28. (Continued).

of Fig. 31. Here two dislocation loops, with Burgers vectors \mathbf{u} and \mathbf{v} are gliding on two intersecting $\{110\}_{45}$ planes. The straight parts O_1P_1 and O_2P_2 of the loops interact to form a new dislocation line OP , with indices $[11\bar{1}]$. The screw components u_s and v_s of the two loops cancel each other, whereas the edge components u_e and v_e combine to give the Burgers vector of the new dislocation as $\frac{1}{2}a[1\bar{1}0]$. The overall dislocation reaction may be given as [61]

$$\frac{1}{2}a[0\bar{1}1] + \frac{1}{2}a[10\bar{1}] = \frac{1}{2}a[1\bar{1}0]. \quad (28)$$

This dislocation reaction leads to the lowering of the elastic strain energy and is thus favourable. However, the glide plane of the new dislocation line, containing the new dislocation line OP and its Burgers vector $\frac{1}{2}a[1\bar{1}0]$ has the indices (112) . This plane is not a normal slip plane in the NaCl structure crystals and therefore the new dislocation is immobile. With further dislocation interactions, dislocation pile up would occur leading to a crack on the $\{110\}_{90}$ plane. However, cracking will occur only when the minimum elastic strain energy conditions have also been satisfied.

A remarkable feature of the cracks, such as those shown in Fig. 28(a, b), is that the $\{110\}_{90}$ cracks around the indentations extend only to the corners of the outermost square of the slip bands around them. In addition to Keh et al. [61], several other workers have

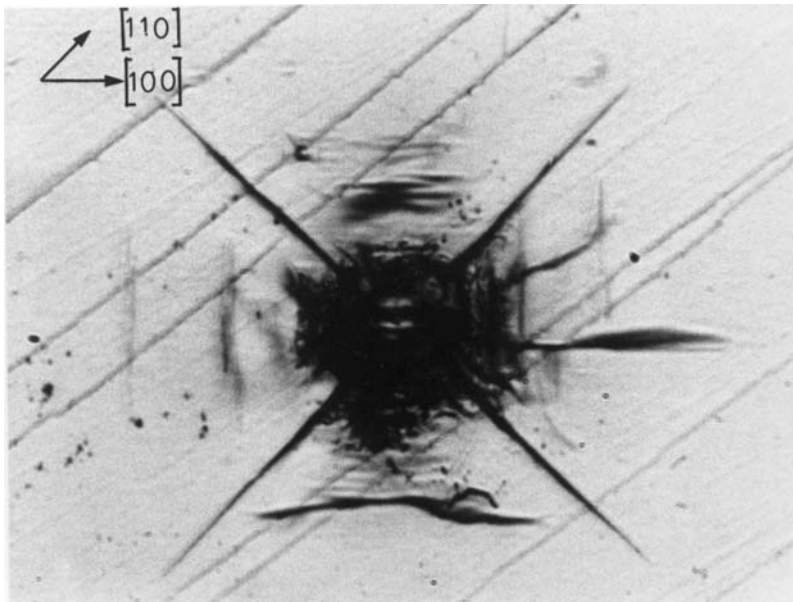


Fig. 29. The formation of the $\{110\}_{90}$ cracks in a single crystal of LiF when it was impacted at a normal incidence with a $80 \mu\text{m}$ diameter tungsten sphere travelling at 80 m s^{-1} . Here the $\{110\}_{90}$ cracking is certainly due to the high strain rates involved during the impact. The width of the frame is 0.34 mm . From Chaudhri, Wells and Stephens [60].

made similar observations from quasi-static indentations and from impacts with mm diameter and smaller size spherical projectiles on the $\{100\}$ faces of single crystals of MgO, LiF, NaCl and KCl [60,62–69]. It may be said that although Keh et al. [61] had correctly proposed the dislocation reaction as the origin of the $\{110\}_{90}$ cracking, these workers did not put forward an explanation for the formation of the ‘picture frame’ of the slip bands around the indentation and its relationship to the extent of the $\{110\}_{90}$ cracks. It was proposed by Chaudhri [24,64] that the formation of the $\{110\}_{90}$ cracks around an indentation on a $\{100\}$ face was closely related to the flow of material displaced by the indenter and the formation of the square-shaped picture frame of the slip bands around the indentation. According to this proposed scheme for the case of a spherical indentation (see Fig. 32), as the indenter load is gradually increased from zero, plasticity in the crystal is initiated when the mean indentation pressure p_m reaches a value of $\sim 1.1Y$, where Y is the uniaxial yield stress of the crystal (see Section 2.2). As shown earlier, at this stage only a few $\{110\}_{45}$ planes are operative in taking the displaced material into the bulk (see Fig. 32(a)). As the indentation load is increased, more $\{110\}_{45}$ planes become operative (Fig. 32(b)). Up to this stage the elastic compression within the crystal accommodates the displaced material. However, with further increase in the indenter load, the elastic compression can no longer accommodate any more material displaced by the indenter. Therefore, at this stage dislocations start moving up towards the indented surface along another set of the $\{110\}_{45}$ planes, as shown in Fig. 32(c). It is at this stage that the $\{110\}_{90}$ cracking tends to initiate.

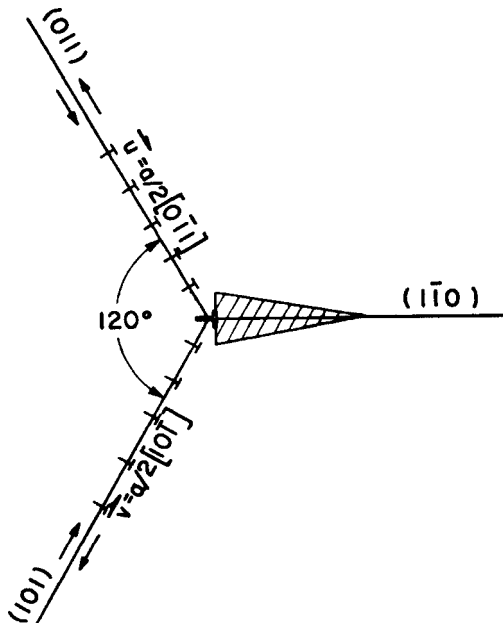


Fig. 30. Schematic diagram showing the formation of a crack on the $(1\bar{1}0)$ plane in an MgO crystal by the interaction of dislocations gliding on two intersecting planes (101) and (011) , inclined to each other at an angle of 120° . From Keh, Li and Chou [61].

The picture of the cracking is better represented in a three-dimensional schematic diagram (Fig. 33). For shallow indentations, the displaced material moves into the bulk along the $\{110\}_{45}$ slip planes OAB, OBC, OCD and ODA. For deeper indentations, the material starts moving up towards the indented surface via the $\{110\}_{45}$ slip planes, such as CBFG, DCGH, ADHE and BAEF. The picture frame of the square-shaped slip bands on the indented surface appears when dislocations gliding on these planes reach the surface; in this figure EFGH is one such square formed by the slip bands. The $\{110\}_{90}$ cracks are generated by the interactions among dislocations gliding on the intersecting $\{110\}_{45}$ planes. Looking at the process of cracking in a simple manner, the upwards (i.e. towards the indented surface) displacement of material along two intersecting planes inclined to each other at an angle of 120° will tend to cause the formation of the $\{110\}_{90}$ cracks OBF, OAE, ODH and OCG. Support for this model was provided by studying the different indentation stages at which the square-shaped picture frame of the slip bands formed and the $\{110\}_{90}$ cracking ensued [24]. It was shown that the latter developed only after the former had first formed.

Further support to the above model [24] has been provided more recently by Chaudhri and Enomoto [67]. These authors investigated *in situ* the entire process of the formation of the square-shaped picture frame of the slip bands and the generation of the $\{110\}_{90}$ cracks in a single crystal of MgO(100) when it was indented with a Vickers diamond pyramid. A schematic diagram of the apparatus used by the authors [67] is shown in Fig. 34. The Vickers indenter was cemented on to a steel stub and a calibrated load cell was placed, via a ball and spring assembly (not shown in Fig. 34), in between the stub and a steel loading

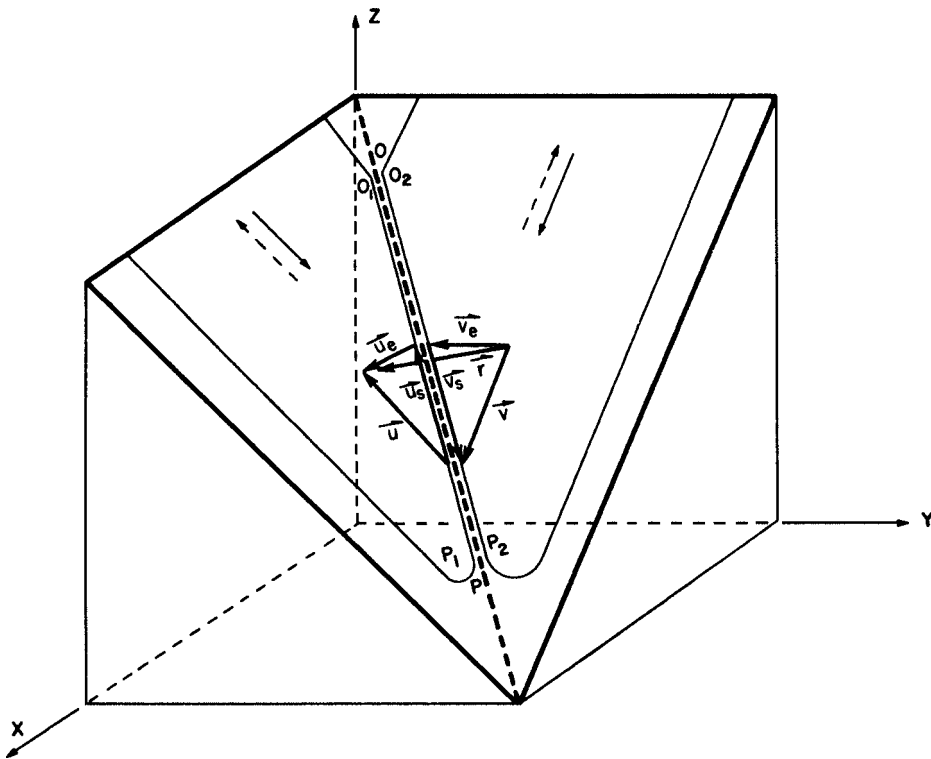


Fig. 31. A schematic representation of interaction of dislocation loops O_1P_1 and O_2P_2 with Burgers vectors \mathbf{u} and \mathbf{v} on two intersecting $\{110\}_{45}$ planes giving rise to the $\{110\}_{90}$ cracking. From Keh, Li and Chou [61].

shaft. The purpose of the ball and spring assembly was to stop completely the transmission of any torque to the specimen during indenter load increase or decrease. The MgO(100) crystals used for this work were 2–3 mm thick and were polished to a surface roughness of 1–2 nm and then annealed at 800°C in air.

A schematic diagram of the various slip bands and the crack systems which form around an indentation in a single crystal of MgO(100) is shown in Fig. 35. The various *in situ* observations will now be described with reference to this figure.

It was found that as the indenter load was gradually increased from zero, first the primary $\langle 100 \rangle$ slip bands formed, followed by the secondary $\langle 100 \rangle$ slip bands at higher indenter loads. Associated with the secondary $\langle 100 \rangle$ slip bands were the $\{110\}_{90}$ cracks. A typical example of the sequence of formation of the various slip bands and the $\{110\}_{90}$ cracks is given in Fig. 36(a–c). Fig. 36(a, b) shows the crystal behaviour during the loading cycle, whereas Fig. 36(c) gives its response during the unloading. In all the three sequences of photographs, the top right hand corner shows the indenter load in gf.

The first frame of Fig. 36(a) shows the contact zone between the indenter and the crystal at a load of 20 gf (see at arrow); the two sets of the primary $\langle 100 \rangle$ slip bands can be clearly seen, but there is no cracking as yet. As the indenter load is first increased to 55 gf and

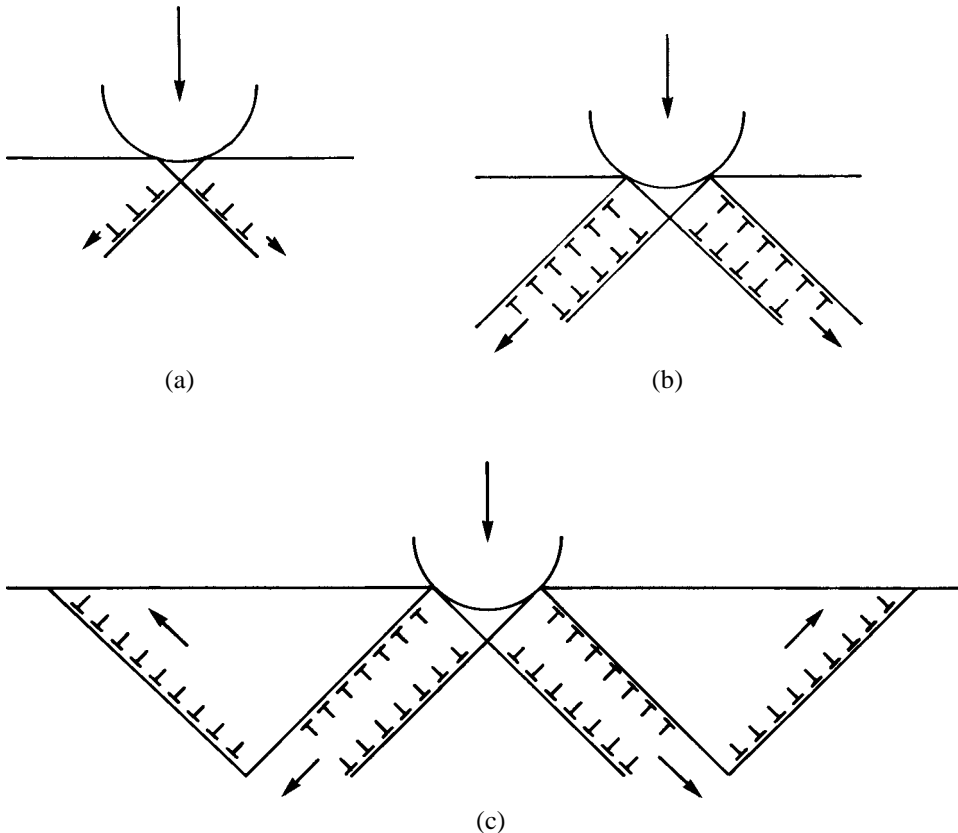


Fig. 32. Schematic diagram showing the displacement of material by dislocation glide on different $\{110\}_{45}$ planes as the load on the sphere indenting a (100) face of an MgO crystal increases from a low (a), through a moderate (b), to a high value (c). In (a) and (b) the material is pushed downwards into the bulk, whereas in (c) the dislocations move towards the indented surface as well. From Chaudhri [24].

then to 90 gf, the lengths of the primary $\langle 100 \rangle$ slip bands increase, but still there is no picture frame. However, when the load is increased to 160 gf, two primary $\{110\}_{90}$ cracks form, as indicated by the arrows. Note that at this stage some secondary $\langle 100 \rangle$ slip bands of a picture frame can also be seen. As the indenter load is increased to 370 gf, the size of the picture frame and that of the $\{110\}_{90}$ cracks increase. When the indenter load is further increased to 440 gf, along with an increase in the lengths of the existing $\{110\}_{90}$ cracks, a third $\{110\}_{90}$ crack also forms. The fourth $\{110\}_{90}$ crack forms when the load is increased to 510 gf (see Fig. 36(b)). At this stage the picture frame of the slip bands becomes quite clearly visible. Moreover, in this frame four light bands, approximately as wide as the indentation itself, lying along the $\langle 110 \rangle$ directions appear; one of them is indicated with an arrow in the frame corresponding to an indenter load of 635 gf (see at top left hand side in the frame). As the load is increased further to 820 gf, new slip bands form and the size of the picture frame increases and so does the size of the $\{110\}_{90}$

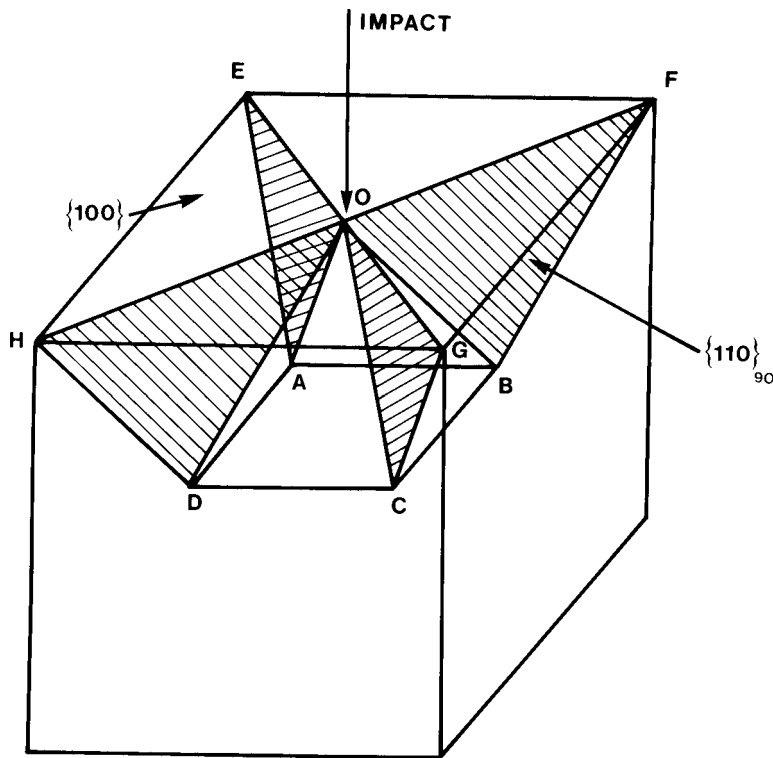


Fig. 33. Three-dimensional schematic diagram showing the formation of the square-shaped slip traces (for example, EFGH) and the $\{110\}_{90}$ cracks (shaded) such as OBF, OCG, ODH and OAE around an impact/indentation on an MgO(100) crystal. From Chaudhri [24].

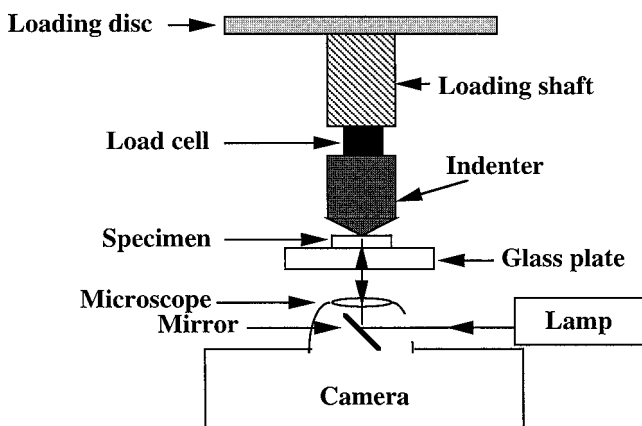


Fig. 34. Schematic diagram of the loading apparatus used for making in situ observations of the cracking around indentations in simple ionic crystals, such as MgO, LiF, NaCl and KCl. From Chaudhri and Enomoto [67].

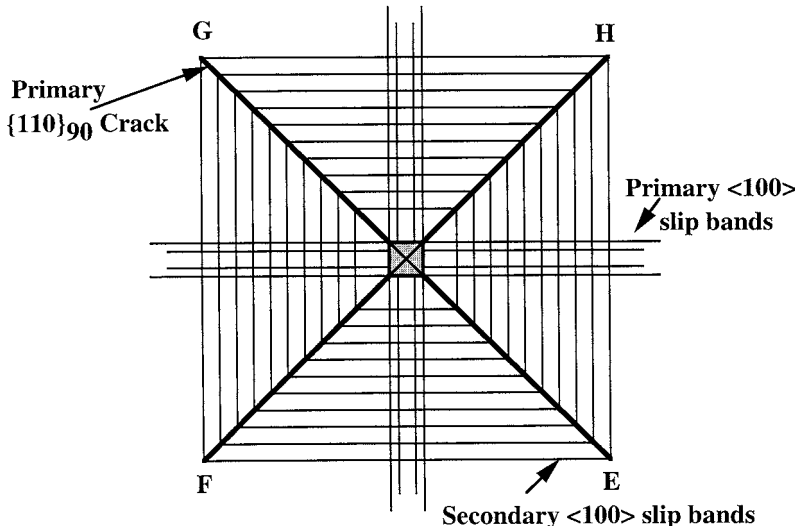
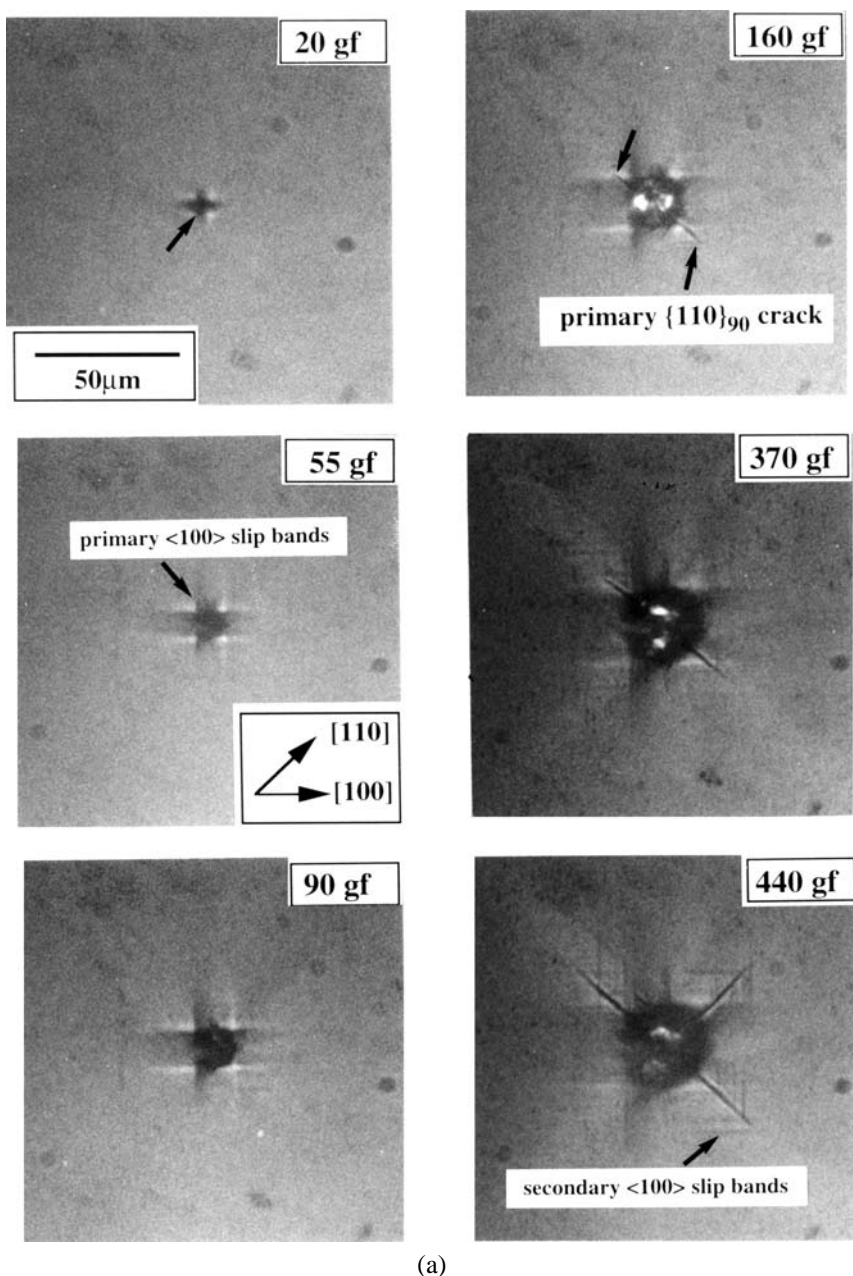


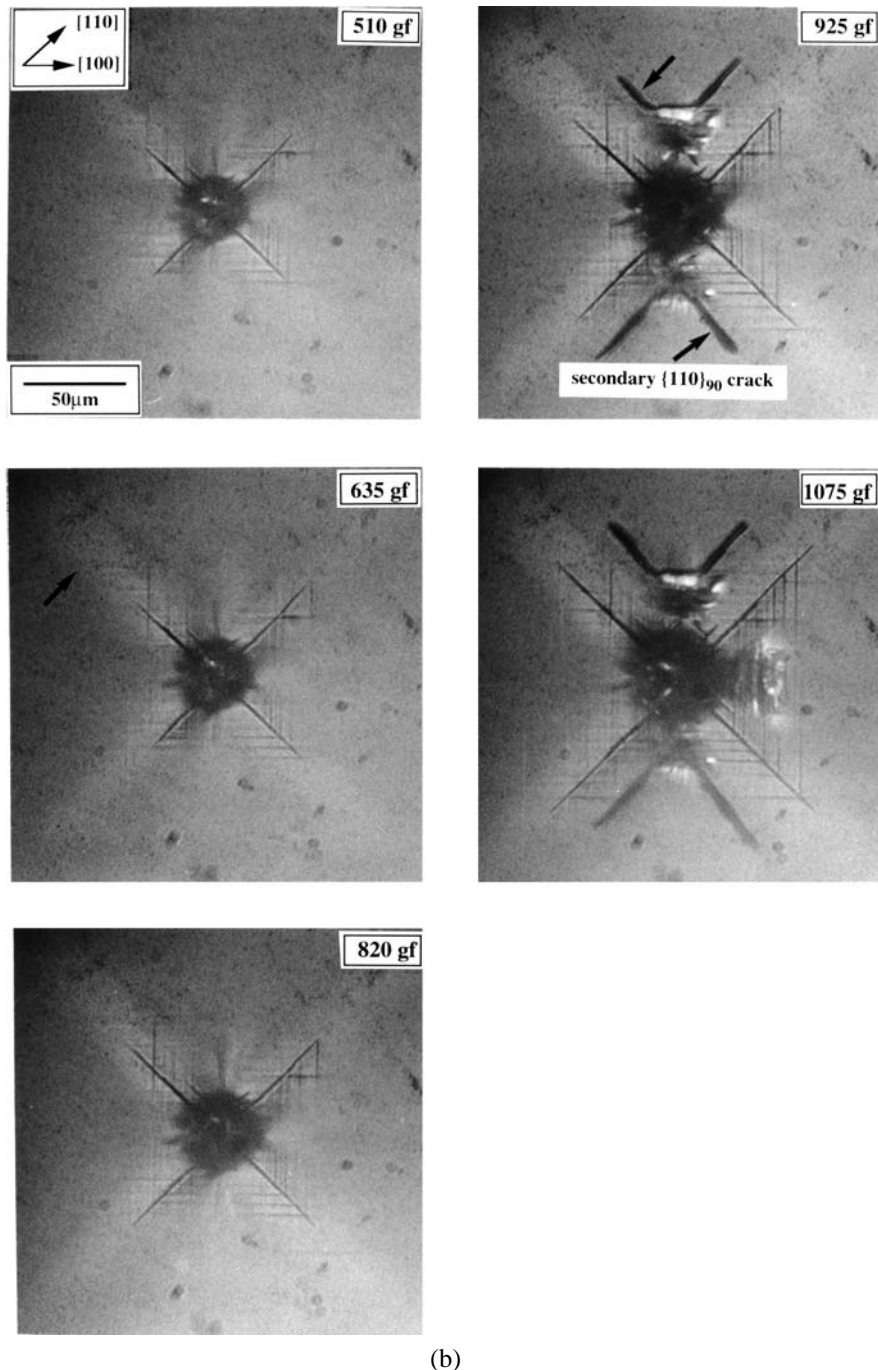
Fig. 35. Schematic diagram of the various slip bands and the traces of the $\{110\}_{90}$ cracks around an indentation on a (100) surface of an MgO(100) single crystal. From Chaudhri and Enomoto [67].

cracks. However, when the load is increased to 925 gf, two sets of secondary $\{110\}_{90}$ cracks appear (see at arrows). These secondary cracks are subsurface, as was revealed by further examination under an optical microscope working in the reflection or transmission mode. The sizes of both the primary $\{110\}_{90}$ and secondary $\{110\}_{90}$ cracks increased as the load was increased to its maximum value of 1075 gf. After holding the load at the maximum value for 60 seconds, gradual unloading was commenced. Photographs of the various cracks at different stages of unloading are shown in Fig. 36(c). It will be seen that as the indenter load was reduced, the size of the picture frame increased and so did the size of the $\{110\}_{90}$ cracks. To illustrate this, when the indenter load was reduced to 725 gf, a new secondary $\langle 100 \rangle$ slip band appeared on the indented surface. This new band is indicated in the corresponding frame with an arrow at the left hand bottom corner. This gradual appearance of the extra secondary $\langle 100 \rangle$ slip bands, in between the already existing bands and also beyond the outermost band, and the corresponding increase in the size of the primary $\{110\}_{90}$ cracks with decreasing load continued right down to complete unloading. In other words, dislocations moved during indenter unloading. However, it is interesting to mention that the secondary $\{110\}_{90}$ cracks did not appear to increase in size due to unloading. When the load was reduced to 190 gf, which is about 20% of the maximum applied load, subsurface lateral cracks on the $\{100\}$ planes appeared. These laterals are indicated by strong reflections in the frames corresponding to loads of 190, 95, 30 and 0 gf and their extent increased as the load was reduced to zero. The gradual increase in the size of the $\{110\}_{90}$ cracks during unloading is different from the picture suggested by Boyarskaya et al. [68], according to which the growth in the size of the $\{110\}_{90}$ cracks was abrupt due to the sudden burst of dislocations on complete unloading. Furthermore, the gradual increase in the $\{110\}_{90}$ crack length as the indenter load was decreased is a clear



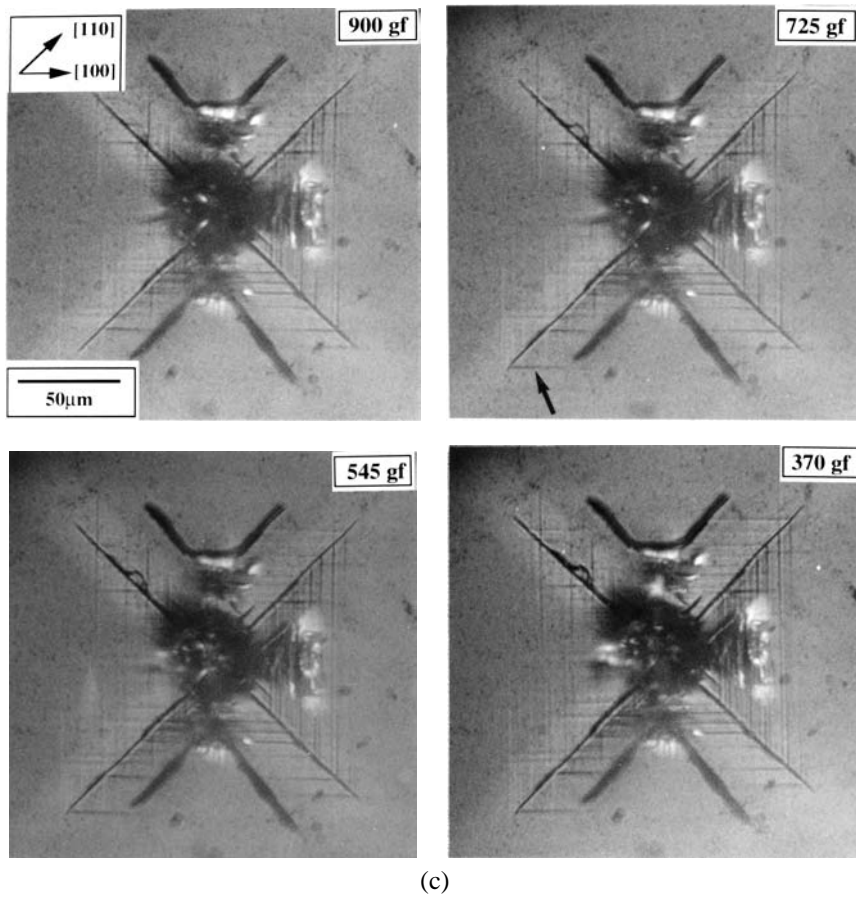
(a)

Fig. 36. (a) Loading sequence. The formation of the primary and secondary $\langle 100 \rangle$ slip bands in an MgO(100) single crystal and the initiation of the $\{110\}_{90}$ cracks as the indenter load is gradually increased. The loads are given in gf at the top right hand corner of each frame.



(b)

Fig. 36. (b) Continuation of loading process. Note that two sets of secondary $\{110\}_{90}$ cracks form suddenly as the load is increased to 925 gf (note that these cracks are subsurface). The picture frame of the secondary $\langle 100 \rangle$ slip bands is now quite prominent.



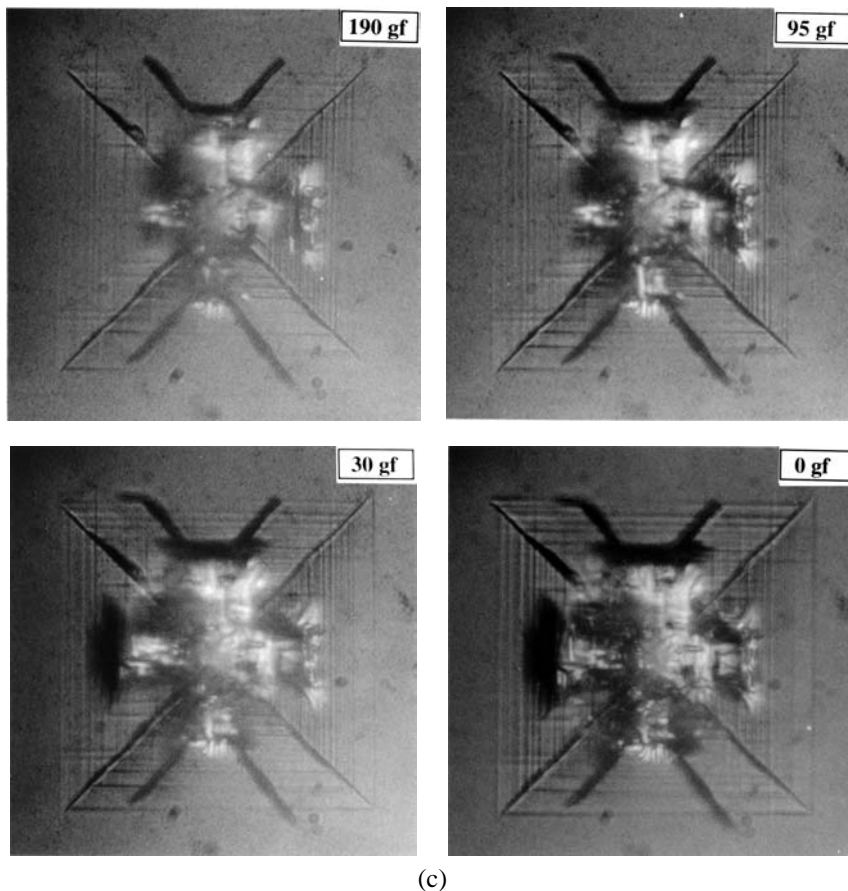
(c)

Fig. 36. (c) Unloading process. As the unloading commences, more secondary $\langle 100 \rangle$ slip bands form in between the already existing bands and also beyond the outermost slip band formed during the loading. One such new band is shown at the arrow in the frame corresponding to the load of 725 gf. Note also the increase in the size of $\{110\}_{90}$ cracks during unloading. Strong reflections in frames, corresponding to loads of 190, 95, 30 and 0 gf, represent the lateral cracks, which form on the subsurface $\{100\}$ planes. From Chaudhri and Enomoto [67].

manifestation of the existence of the blister field [7] (i.e. residual stress of the indentation); this stress becomes more and more dominant as the indenter load is gradually decreased to zero.

If the indented MgO surface is a (110) plane, then only two cracks form on the indented surface [69]; this observation is also consistent with our explanation based on dislocation interactions between dislocations gliding on intersecting $\{110\}_{45}$ slip planes.

Dislocation-generated cracks around 100 gf Vickers indentations in single crystals of InP(100) made at a temperature of 400°C , which is thought to be lower than the brittle–ductile transition temperature of InP, have also been observed recently [70]. These cracks



(c)

Fig. 36. (Continued).

were oriented along the $\langle 100 \rangle$ directions, irrespective of the orientation of the indenter diagonals.

The role of dislocation interactions in the indentation cracking of single crystals of TiC(100) has been examined by Serbena, Williams and Roberts [71] in the temperature range of 20° to 900°C. This is a very hard metal and has a Vickers hardness of $\sim 2600 \text{ kgf mm}^{-2}$ at room temperature [72]. Although at temperatures below 550°C the slip system in TiC is $\{110\}\langle 1\bar{1}0 \rangle$, which is the same as that in the NaCl structure crystals, cracking around an indentation occurs on the (100) cleavage planes. A possible explanation may be that the fracture surface energy of the {110} planes is higher than that of the (100) cleavage planes. The authors [71] have suggested that it is the tensile hoop stresses around the indentation that cause the {100} cleavage cracks.

Tungsten carbide (WC) is another very hard metal of considerable commercial importance. It is the major constituent in the WC–Co composites, which are extensively used for cutting tools and heavy-duty ball bearings. The plastic deformation and ensuing fracture

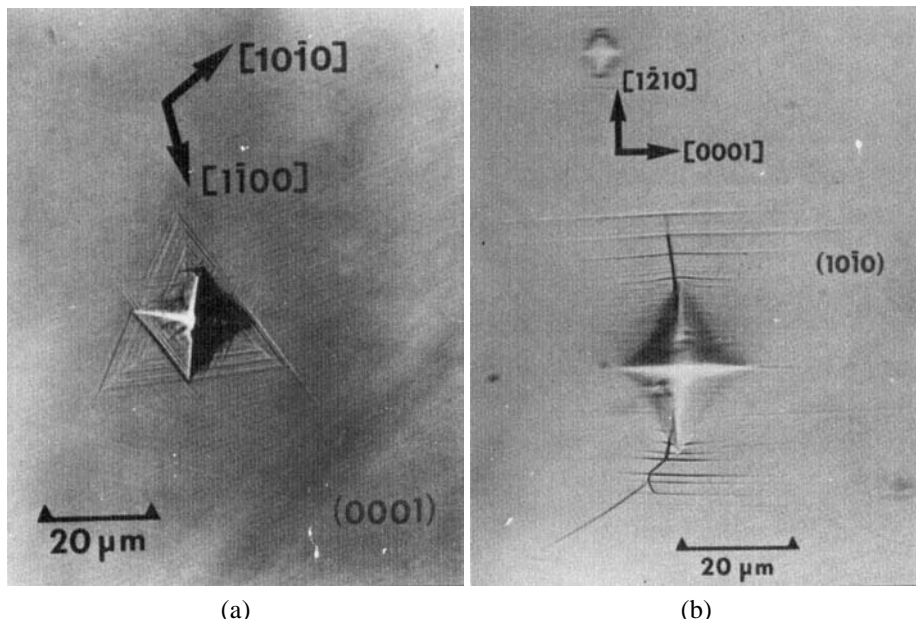


Fig. 37. Optical micrographs of Vickers diamond indentations on different planes of single crystals of tungsten carbide. (a) Indentation on a (0001) plane; (b) indentation on a (10̄10) plane. The authors did not specify the indenter loads. After Hibbs and Sinclair [76].

of WC is still not fully understood. During the last four decades several investigators have studied the deformation behaviour of single crystals of WC by indenting them with Vickers diamond pyramids [73–78].

WC has a simple hexagonal structure consisting of W atoms on the hexagonal lattice sites and the C atoms either all at 1/3, 2/3, 1/2 or all at 2/3, 1/3, 1/2 sites [73]. Each carbon atom has six tungsten neighbours located at the corners of a trigonal prism, with strong covalent bonding between the W and the C atoms. For an indenter load of 1 kgf, the Vickers hardness of the (0001), (1̄100) and (110̄1) planes have been measured to be 2100, 1080 and 1060 kgf mm⁻², respectively. These significant differences in the hardness values indicate anisotropic mechanical behaviour.

By studying the slip steps around 36 and 90 gf Vickers indentations on the (0001) and the {10̄10} faces of single crystals of WC and those produced due to the 3-point bend tests on single crystal specimens of WC, Luyckx [75] has determined that the slip occurs on the {1100} planes in the ⟨1123⟩ directions, forming the slip system {1100}⟨1123⟩.

When a Vickers indentation is made in a single crystal of WC under a sufficiently high load, cracks are generated within the deformation zone. However, unlike the {110}90 cracks seen around indentations in the NaCl structure crystals which are limited by the extent of the deformed zone (see Fig. 28), the cracks in WC crystals do seem to extend into the elastic region beyond the plastically deformed zone. An attempt has been made by Luyckx et al. [78] to explain the slip processes involved, including the piling up and sinking in of material, around Vickers indentations on the (0001) and {1100} faces of sin-

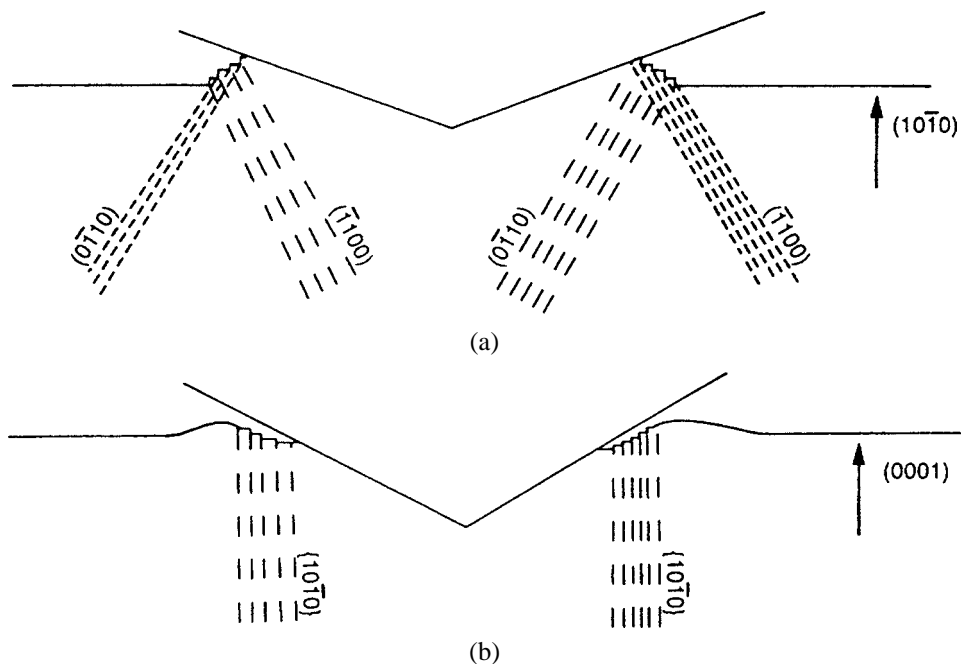
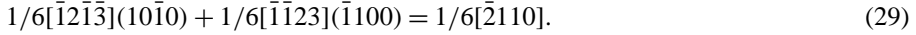


Fig. 38. Schematic diagrams of surface profiles around Vickers indentations in single crystals of tungsten carbide. When an indentation is made on a $(10\bar{1}0)$ plane, there is piling up of material at the contact edge (see (a)). On the other hand, when an indentation is made on a (0001) face there is sinking in of material at the contact edge (see (b)). However, in this case there is pile up at some distance from the contact edge. The dashed lines represent traces of the possible active slip planes. After Luyckx, Nabarro, Wai and James [78].

gle crystals of WC. Fig. 37(a, b) shows optical micrographs of typical indentations. It was reported by Luyckx et al. [78] that the material around an indentation of the type shown in Fig. 37(a) sinks in (these authors did not give the direction in the indented surface in which the sinking in was observed/measured), whereas for an indentation of the type shown in Fig. 37(b) the material around the indentation piles up (this pile up is presumably along the $[1\bar{2}10]$ direction). Schematic diagrams of line profiles across Vickers indentations on $(10\bar{1}0)$ and (0001) faces are given in Fig. 38(a, b). Also shown in this figure are the traces of the operative slip planes. It may be noted here that the pile up around an indentation is said to occur when the edge of contact between the indenter and the indented surface is above the original level of the indented surface; sinking in is said to occur when the edge of contact of an unloaded indentation is below the original level of the indented surface. Luyckx et al. [78] have suggested that different surface profiles around indentations on different crystallographic planes may be related to the work-hardening characteristics of the planes. They have applied the slip-line field theory, originally developed for an infinite width wedge indenting a rigid/perfectly plastic solid [79], to explain the observed plastic flow patterns in the WC crystals.

Hibbs et al. [77] and Luyckx et al. [78] have suggested that when the (0001) surface is indented, dislocations moving on the (10̄10) and the (11̄00) planes react to produce sessile dislocations according to the reaction [78]



These sessile dislocations will cause work hardening of the indented surface and will, therefore, produce sinking in around the indentation [78]. On the other hand, no sessile dislocations are generated when the (10̄10) surface is indented. In this case no work hardening would be expected and consequently there would be pile up around the indentation on this surface [78]. The underlying idea for drawing the above conclusions is that when a solid shows work hardening the material displaced by the indenter will be accommodated by the elastic hinterland and there will be no pile up next to the indenter and at the contact edge there will be sinking in. On the other hand, if the material does not work harden the material displaced by the indenter has to appear on the indented surface, thus producing a pile up.

Although the explanation proposed in ref. [78] seems quite plausible, a note of caution is necessary here. The slip-line field theory of indentation [79] is, strictly speaking, not valid for 3-dimensional indentations. Moreover, for a Vickers indentation in a sample of non-hardening mild steel (i.e. very heavily work-hardened mild steel), the deformation pattern has been found to be quite different from that predicted by the slip-line field theory [80], and the essential cutting mode predicted by the theory was completely absent.

Finally, as for the generation of cracks around indentations on the (0001) surface, it has been reported by Hibbs et al. [77] that for a sufficiently high indenter load cracks originate at the intersections of the slip planes. The traces of these cracks on the (0001) plane lie along the {11̄00} or the {11̄20} directions, with the corresponding crack planes being the {11̄20} or {11̄00} planes.

4.2. Dynamic observations

The formation of the {110}₉₀ cracks in ionic crystals of the NaCl structure due to localised dynamic loading offers a possibility of measuring the dislocation velocities in them, provided the furthest subsurface points of these cracks (such as, points A, B, C and D in Fig. 33) are directly related to the leading dislocations. Some evidence in support of this proviso comes from the fact that in dynamic loading experiments, as in quasi static experiments, the {110}₉₀ cracks extend only to the corners of the picture frame of the slip bands around the loading point [60]. Chaudhri [64] has used this approach to measure the dislocation velocities in the high velocity regime in single crystals of KCl(100).

A schematic diagram of the experimental set up used is shown in Fig. 39. Single crystals of KCl(100) of size $20 \times 10 \times 5 \text{ mm}^3$ were cleaved from larger pieces. They were not annealed and had a grown-in dislocation density of $\sim 10^5 \text{ cm}^{-2}$. The impurity content of the crystals was given by the supplier (BDH, UK) as 50 parts per million. To cause dynamic loading on a {100} face of the test crystal, a 0.7 mm diameter tungsten carbide sphere was projected normally on to it at velocities of up to $\sim 200 \text{ m s}^{-1}$ using an explosive gun [81].

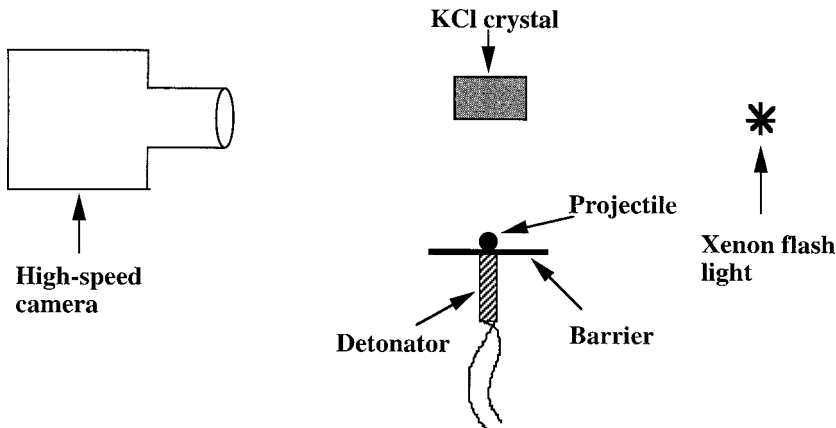


Fig. 39. Schematic diagram of the arrangement used for studying the formation and growth of the {110}₉₀ cracks by the impact of a small (about 1 mm diameter) sphere on a single crystal of simple ionic materials, using high-speed photography.

The impact led to the generation and propagation of the {110}₉₀ cracks, as well as the {100} cleavage cracks. As said before, only the former cracks form by the interaction of dislocations, whereas the cleavage cracks on the {100} planes are produced due to the tensile hoop stresses around the elastic/plastic dynamic indentation. The entire process of impact and the generation and propagation of the cracks was photographed with a high-speed framing camera at framing speeds of up to ~ 2 million frames per second. A typical sequence of photographs taken at an inter-frame time of $0.61\ \mu\text{s}$ and an exposure time per frame of $\sim 0.1\ \mu\text{s}$ is shown in Fig. 40. Here the tungsten carbide sphere just makes contact with the KCl crystal at a velocity of $145\ \text{m s}^{-1}$ in frame 3. In the next frame the {110}₉₀ and {100} cracks can be clearly seen. Both types of crack move at high velocities; the velocities of the {110}₉₀ and the {100} cracks are 600 and $1850\ \text{m s}^{-1}$, respectively. One of the {100} cleavage cracks is shown at C in frame 4 and one of the {110}₉₀ cracks is at D in frame 6. Both types of crack grow in size as the loading continues. In addition, some of the displaced material piles up around the impacting sphere, with the maximum velocity of the piling up material normal to the impacted surface being $90\ \text{m s}^{-1}$, which is 0.6 times the projectile impact velocity (see frame 5). The maximum penetration of the sphere into the crystal occurs in frame 9 (the penetration of the sphere below the original crystal surface is $0.29\ \text{mm}$ in this frame), after which the sphere begins to rebound. The entire loading time of the sphere is $3.7\ \mu\text{s}$, and the growth of the {110}₉₀ and {100} cracks appears to occur only during the loading period. (This observation is slightly different from that from the quasi-static loading experiments in which some definite growth of the {110}₉₀ cracks was observed during indenter unloading (see Fig. 36(c)). The reasons for this difference are not clear as yet.) During the rebound of the projectile (frames 10–12), subsurface lateral cracks (cracks parallel to the impacted/indented surface are called lateral cracks) on the {100} planes form and the piled up material begins to disintegrate.

It will be seen from Fig. 40 that the geometrical shape of the {110}₉₀ cracks is quite similar to that shown schematically in Fig. 33. It is assumed that the furthest subsurface

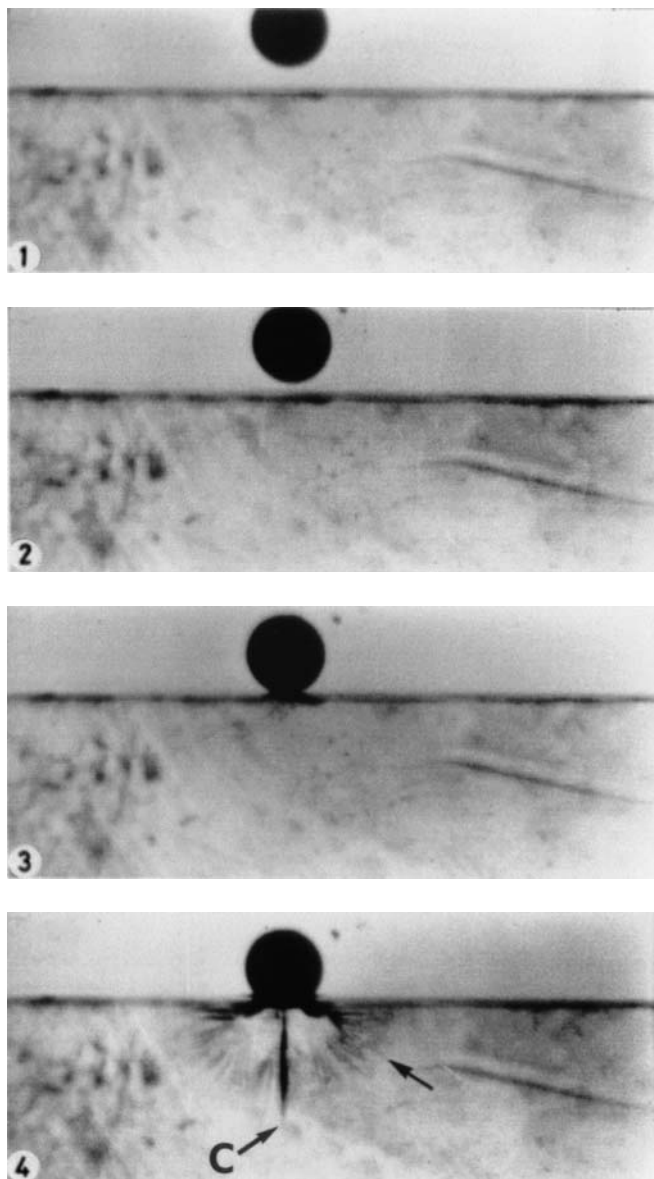


Fig. 40. A sequence of high-speed photographs showing the impact at normal incidence of a 0.7 mm diameter tungsten carbide sphere on a {100} face of a KCl single crystal at 145 m s^{-1} . {100} and $\{110\}_{90}$ cracks are clearly visible. One of the former types is shown at C in frame 4 and one of the latter types is shown at D in frame 6. The arrows in frames 4 to 8 mark the positions of the crack front of the second {100} crack which is normal to the optical axis of the camera. Inter-frame time is $0.61 \mu\text{s}$ and the exposure time for each frame is $0.1 \mu\text{s}$. From Chaudhri [64].

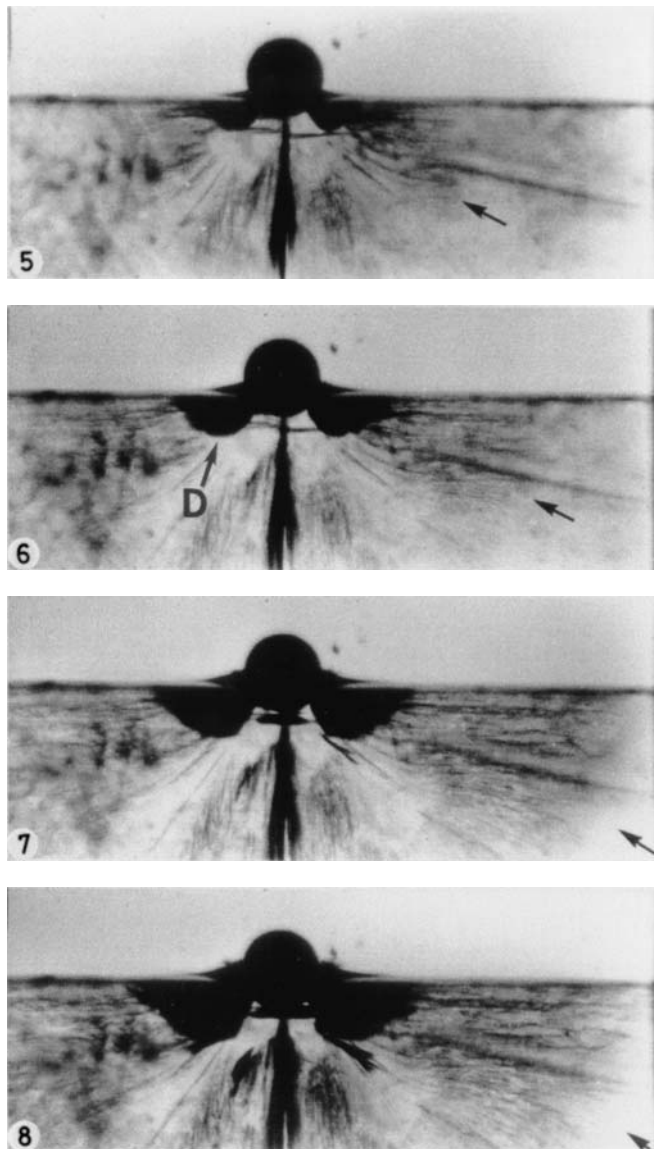


Fig. 40. (Continued).

point B for the OBF crack in Fig. 33 gives the position of the furthest dislocation on a $\{110\}_{45}$ slip plane in a $\langle 111 \rangle$ direction. Then by measuring the variation of the OB with time, we should be able to get the time variation of the dislocation velocity. Since the $\{110\}_{90}$ cracks are inclined to the optic axis of the camera at 45° , the length OB is obtained by multiplying the distance of the point B below the original crystal surface with a factor of 1.73 (as a cube diagonal is 1.73 times the cube edge). In this manner, it is found that the

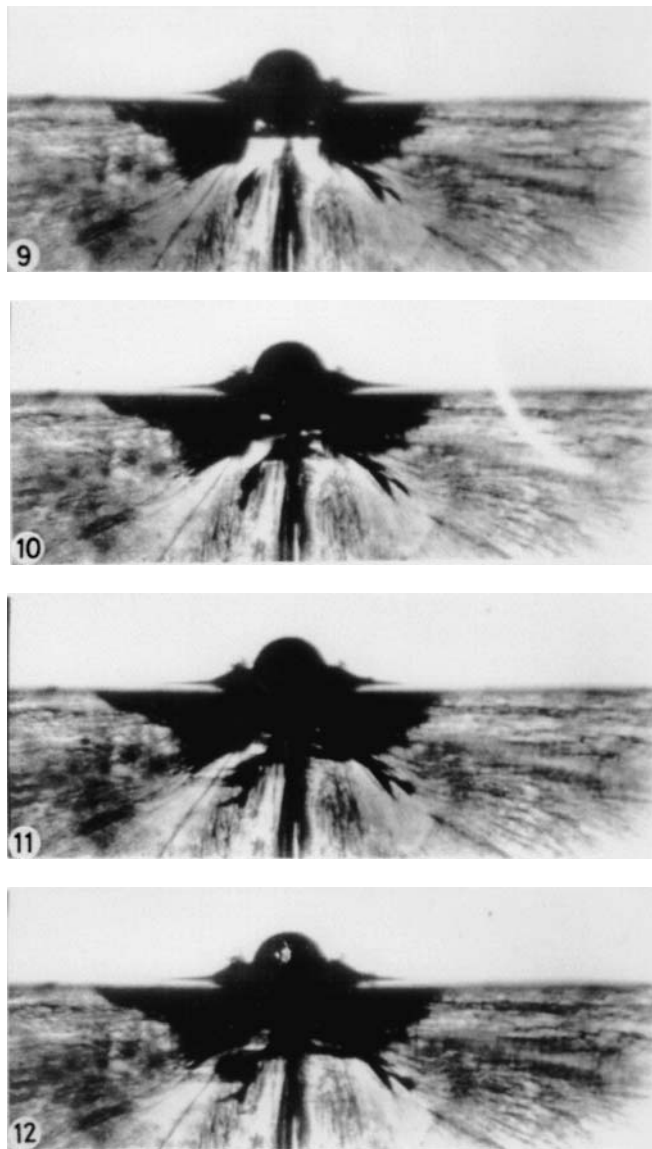


Fig. 40. (Continued).

velocity of the point B (see Fig. 33) between frames 3 and 4 is $\sim 600 \text{ m s}^{-1}$, whereas it is 370 m s^{-1} between frames 4 and 5. With further increase in time, the velocity of the crack corresponding to that of the point B drops further.

Now, to get a relationship between the dislocation velocity and the corresponding shear stress driving the dislocations from the high-speed photographic sequence, the impact load in each frame was required. This was estimated in the following way. If at any stage of

the impact the contact radius between the crystal and the impacting particle is a , then the dynamic load P_d at this stage is given by $\pi a^2 p_d$, where p_d is dynamic hardness of the KCl crystal at the strain rate imposed by the impact. Assuming that the total kinetic energy of the sphere is spent in penetrating the crystal to a measured depth of z_0 below the original specimen surface, the dynamic hardness p_d can be calculated using the incident velocity v_0 of the impacting sphere, its maximum penetration z_0 into the crystal and eq. (30) [64]

$$p_d = \frac{2R^3 v_0^2 \rho}{3(R - \frac{1}{3}z_0)z_0^2}, \quad (30)$$

where R and ρ are the radius and density of the projectile, respectively. (It is assumed in eq. (30) that the piled up material around the impacting sphere does not support the load, as it is considerably broken up.) In this manner, the dynamic hardness values of two KCl(100) crystals used for this work were found to be 3.8 and $4.2 \times 10^8 \text{ N m}^{-2}$; these hardness values are ~ 4 times the quasi-static hardness of a KCl crystal, measured using a spherical indenter for a dimensionless indentation size of $a/R = 0.4$. The Vickers hardness value of a single crystal of KCl(100) for an indenter load of 50 gf is $9.5 \times 10^7 \text{ N m}^{-2}$.

As the dynamic load and the crack length vary from one frame to the next, it is necessary to decide upon the value of the dynamic load and thus the dynamic shear stress that drives the dislocations, and hence the crack front. That is to say, if in a frame the dynamic load is P_1 and the length of the crack OB is r_1 , and in the next frame, taken after a time t , the two quantities are P_2 and r_2 , respectively, then the assumption is that the crack has been driven at a velocity of $(r_2 - r_1)/t$ by the shear stress corresponding to a point load of magnitude P_2 at the initial point of contact between the sphere and the test crystal. The shear stress at the point corresponding to r_2 along a $\{110\}_{45}$ plane and in the slip direction $\langle 110 \rangle$ is then calculated using the elastic stress field equations due to point loading. Though plasticity has occurred at the impact site, the use of the elastic stress equations is not inconsistent, as according to the picture the plastic/elastic boundary is at the leading edge of the cracks. Then, the magnitude of the shear stress τ in the slip plane at a distance r_2 from the loading point is

$$\tau = \frac{0.023 P_2}{r_2^2}. \quad (31)$$

Thus from the measurements made from the different frames in the photographic sequence shown in Fig. 40, the shear stress and the corresponding dislocation velocity were $0.023 P_2/r_2^2$ and $(r_2 - r_1)/t$, respectively. Using this approach, the variation of dislocation velocity with the dynamically applied shear stress obtained for two the KCl crystals is shown in Fig. 41. For both the crystals the dislocation velocities reach high values of ~ 600 to 700 m s^{-1} . Moreover, in each case the dislocation velocity varies approximately linearly with the applied dynamic shear stress. At the bottom of Fig. 41 a data point from the work of Lubenets and Startsev [82] is also shown; their dislocation velocity is 2 orders of magnitude smaller for the same applied shear stress. At present, there is no satisfactory explanation of the discrepancy between the values obtained by Chaudhri [64] and that given by Lubenets and Startsev [82].

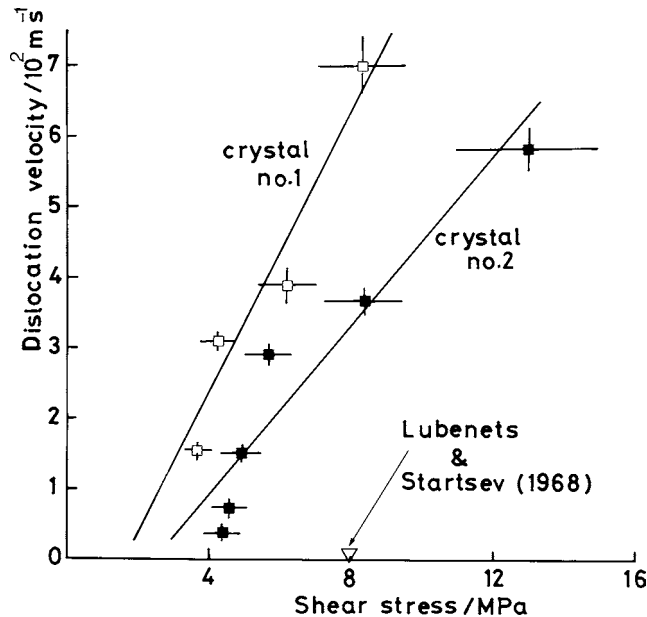


Fig. 41. Shear stress versus dislocation velocity on the {110}₄₅ planes of two KCl single crystals. From Chaudhri [64].

The linear dependence of the dislocation velocity v_d on the applied shear stress τ in this high velocity regime suggests that the resistance to dislocation mobility is likely to be by viscous drag; the drag coefficient B' is given by [83]

$$\tau b = B' v_d, \quad (32)$$

where b is the Burgers vector of the dislocations. The values of the viscous drag coefficient B' for the two KCl crystals 1 and 2 were determined to be 0.5×10^{-5} and $1.0 \times 10^{-5} \text{ N m}^{-2} \text{ s}$, respectively. It may be mentioned that in the case of annealed single crystals of LiF using the plate impact experiments, Clifton [84] also found that the dislocation velocity varied linearly with the applied shear stress. He determined the value of the drag coefficient as $2.9 \times 10^{-5} \text{ N m}^{-2} \text{ s}$, which is similar to the values of the B' determined for the KCl crystals [64].

5. Dislocations within the indentation itself

We have shown in Section 2 how dislocation rosettes are distributed on the indented surface outside the indentation in single crystals of a variety of materials. The question about the plastic deformation state of the material immediately beneath the indenter still needs to be answered. This question has intrigued investigators for many years. Some workers

have suggested that the material within the indentation recrystallizes leaving it dislocation-free [14]. Another suggestion put forward by Berger [85] and by L.M. Brown (see footnote on p. 156 of ref. [86]) is that within this zone there is a large stress gradient during indenter loading and this gradient drives out any dislocations from within it, again making this zone dislocation-free. (It may be added here that dislocations are driven by shear stress and not by stress gradient.)

To examine this region in the immediate vicinity of the indenter at a sufficiently high magnification, transmission electron microscopy (TEM) is an appropriate technique. However, specimen preparation for TEM studies is time consuming and difficult. Moreover, the processes of specimen preparation and handling may themselves introduce defects in the sample. Nevertheless, almost always the indented specimens are thinned down to a thickness of $\sim 1 \mu\text{m}$ or less. The thinning process may involve treatment with chemicals and bombardment with several keV ions of argon, gallium and others. Moreover, around an indentation there are significant residual stresses which can cause the existing dislocations to rearrange themselves during chemical thinning, thus causing stress relaxation [87,88] and complicating the conditions in the specimen. It appears that this stress relaxation problem does not occur when thinning is carried out by ion bombardment. There are, however, some other types of problem; these are radiation damage and the amorphisation of the specimen

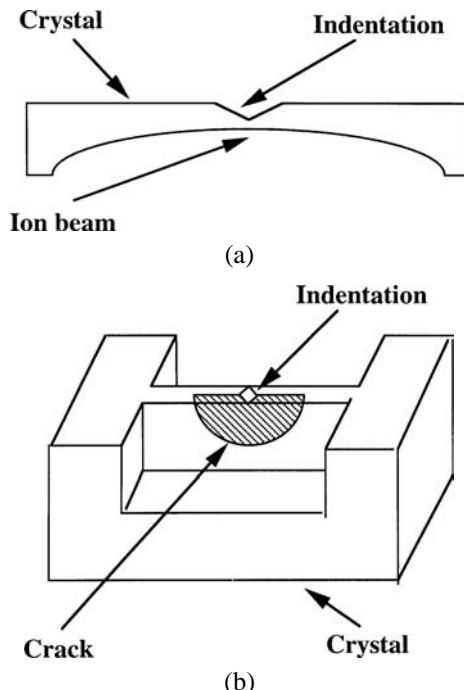


Fig. 42. Schematic diagrams of the thinned indented samples for (a) plan viewing and (b) cross-sectional viewing in a transmission electron microscope. In (b) a median crack associated with the indentation is also shown. Such a median crack is usually observed in brittle materials for indenter loads greater than some critical value, depending upon the test material and indenter shape.

[89,90]. Furthermore, if the chamber in which ion beam thinning is carried out is not thoroughly cleaned prior to thinning the specimen, there is the risk of the existing contaminants (e.g. from a previous thinning operation) in the chamber transferring on to the specimen to be thinned. Another useful precaution is to use a cooling stage in the specimen thinning chamber.

Two types of specimen geometry have been used in the TEM studies of indented specimens. One is suitable for the plan view of the sample (Fig. 42(a)); and the other is appropriate for a cross-sectional examination of the sample (Fig. 42(b)). Typical results from these studies are reviewed below separately.

5.1. Elemental semiconductors Si and Ge

Semiconductors such as Si and Ge are very brittle at room temperature and in compression and bending experiments at room temperature these materials fracture without any dislocation activity. For example, in the case of Ge crystals at room temperature Johnson and Gibbs [91] reached bending stresses of 388 kgf mm^{-2} at fracture, but no dislocations were found in the fracture zone. To cause a material to flow plastically, sufficiently high shear stresses are needed. However, during bending or uniaxial stressing of Si and Ge, fracture stresses are reached before the critical shear stress of the test material is attained. It was realised by Rinder and Tramposch [30] and by Nikitenko et al. [92] that sufficiently high shear stress values may be obtained in indentation experiments. This is because under an indenter there is a large component of hydrostatic stress (see eq. (5)), which discourages any cracking and at the same time high shear stresses are allowed to build up (here we are referring to pointed indenters and spherical indenters of radii less than $50 \mu\text{m}$). Thus, having considered the above points, Nikitenko et al. [92] indented at room temperature n-type single crystals of Si(111), having a resistivity of 200 ohm cm and a grown-in dislocation density of 10^2 to 10^3 cm^{-2} , with a Vickers diamond pyramid or a Knoop diamond indenter using indenter loads in the range of 0.5 to 4 gf. They found that permanent residual indentations were formed in the Si, which indicated that local plasticity had occurred. The indented crystals were then thinned according to the method shown in Fig. 42(a) and examined in a TEM operating at 150 keV. They reported that for the 4 gf Vickers indentations many dislocations lying along the $\langle 110 \rangle$ and $\langle 112 \rangle$ directions had formed, though the maximum distance to which they had spread from the edge of the indentation was only $\sim 1 \mu\text{m}$. However, for the 4 gf indentations some cracking had also occurred. Therefore doubts could be raised whether the observed dislocations were due to the cracking. When an indentation was made using an indenter load of 0.5 gf, no cracking was observed and the region adjacent to the indentation was so heavily strained that it was difficult to resolve any dislocations in it. When such a low-load indentation was annealed at 620°C for 150 minutes, many dislocations appeared around the indentation. It is quite reasonable to assume that at least some of the dislocations simply moved out farther from the indentation with increasing sample temperature due to the residual stress field.

Similar TEM investigations were carried out by Hill and Rowcliffe [41] for studying the region adjacent to an indentation. They also used n-type single crystals of Si(111) and Si(110) of resistivity 100 ohm cm . The crystals were dislocation-free and samples were

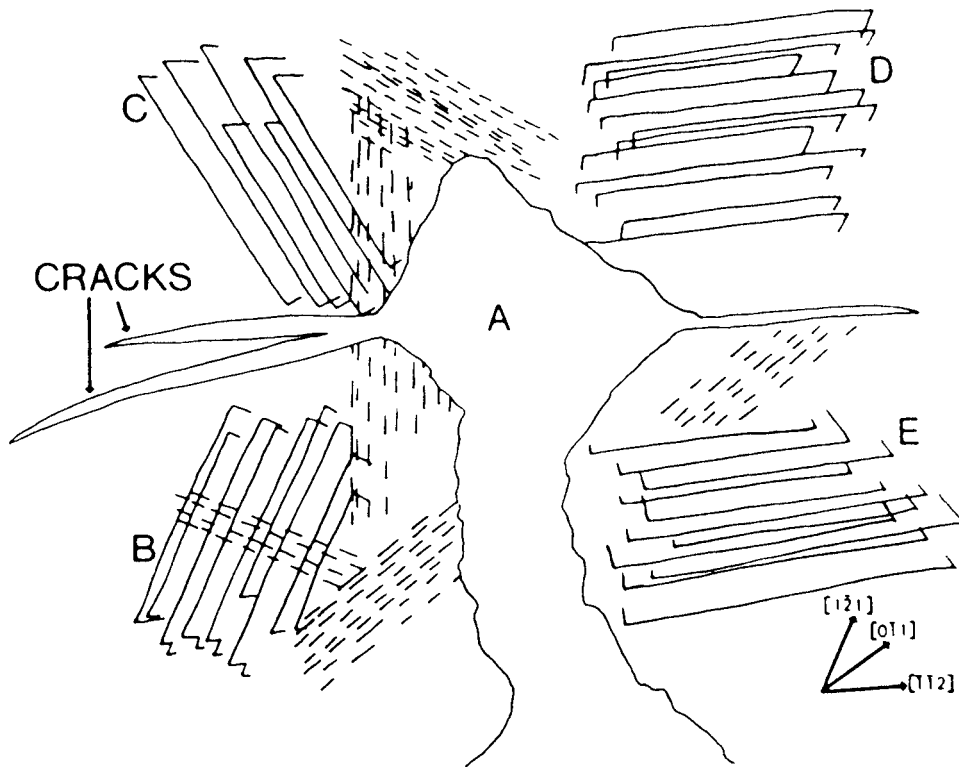


Fig. 43. Schematic drawing of the dislocation arrangement seen in a silicon foil in the transmission electron micrographs of the region around a room-temperature Vickers diamond indentation. Plane of the indented surface and the foil is (111). Broken lines indicate dislocation loops lying in the {111} planes inclined to the (111) plane.

The indentation is represented with the letter A. From Hill and Rowcliffe [41].

3 mm in diameter and 300 μm in thickness. Vickers diamond pyramid indentations were made at room temperature and at 300°C under a load of 100 gf. The indented samples were first thinned chemically to a thickness of 10 μm , and then by ion beam bombardment. Some of the indented samples were ion beam thinned from the indented side as well, so that the subsurface region close to the indented surface could also be examined. The thinned samples were examined in a transmission electron microscope operating at 100 keV. Some of the thinned samples were annealed *in situ* inside the electron microscope at temperatures of up to 1030°C. Hill and Rowcliffe [41] found that in the Si(111) crystals, the indentation had produced cracking which divided the crystal into four quadrants. Within each quadrant dislocation lobes had formed, which are represented schematically in Fig. 43. The slip occurred on all the four possible {111} slip planes. The dislocation lobes B, C, D and E in Fig. 43 consisted of dislocation loops in the (111) foil (i.e. thinned specimen) plane. One of the dislocation lobes, B, is shown in Fig. 44. Hill and Rowcliffe [41] found that the dislocation loops had moved out up to a distance of 8 μm from the edge of the indentation. This confirms the findings of Nikitenko et al. [92] that even at room tem-

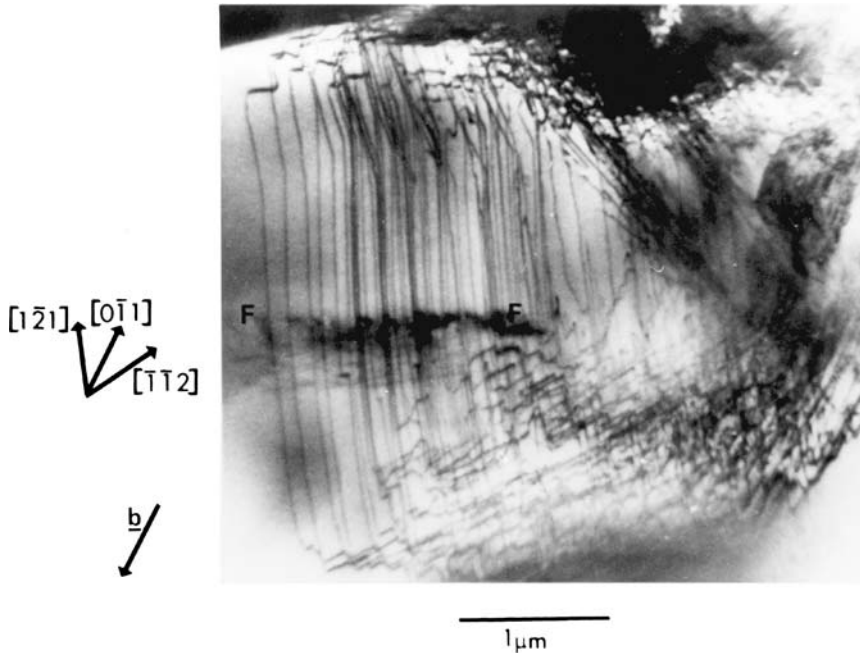


Fig. 44. Transmission electron micrograph showing the dislocation lobe B of Fig. 43. F, F indicate positions at which are dislocations lying on the three $\{111\}$ planes, which are inclined to the surface of the foil. These dislocations are less visible. From Hill and Rowcliffe [41].

perature dislocations can be generated in Si, which are capable of gliding to some distance from the indentation. Hill and Rowcliffe [41] also reported that similar dislocation loops formed around indentations in the Si(110).

When indentations were made at 300°C , dislocation loops similar to those formed around the room temperature indentations were observed [41]. However, in this case the loops had glided to a slightly larger distance of $10 \mu\text{m}$ from the centre of indentation. This observation is a clear piece of evidence that in Si dislocations can glide to longer distances at 300°C than they do at room temperature. Hill and Rowcliffe [41] also reported that the dislocation loops, all of which had the same geometry, consisted of a large straight section lying in a $\langle\bar{1}\bar{1}2\rangle$ direction, bounded at one end by a shorter segment lying in a second $\langle\bar{1}\bar{1}2\rangle$ direction, and at the other end by a second short segment lying in a $\langle1\bar{1}0\rangle$ direction. Also, note that the direction $\langle1\bar{1}0\rangle$ is normal to the long segment of the dislocation loops. The Burgers vector of the loops was determined to be $\langle01\bar{1}\rangle$, and the segments of the loops, with their line vectors along the $\langle\bar{1}\bar{1}2\rangle$ and the $\langle1\bar{1}0\rangle$ directions, were the 30° and the 60° dislocations, respectively (see Fig. 44).

Although the above investigations of Nikitenko et al. [92] and Hill and Rowcliffe [41] had clearly shown the existence of dislocations right at the edge of room-temperature indentations in Si, it was not clear whether within the indentation itself dislocations existed or not. This question was addressed by Clarke, Kroll, Kirchner, Cook and Hockey [93],

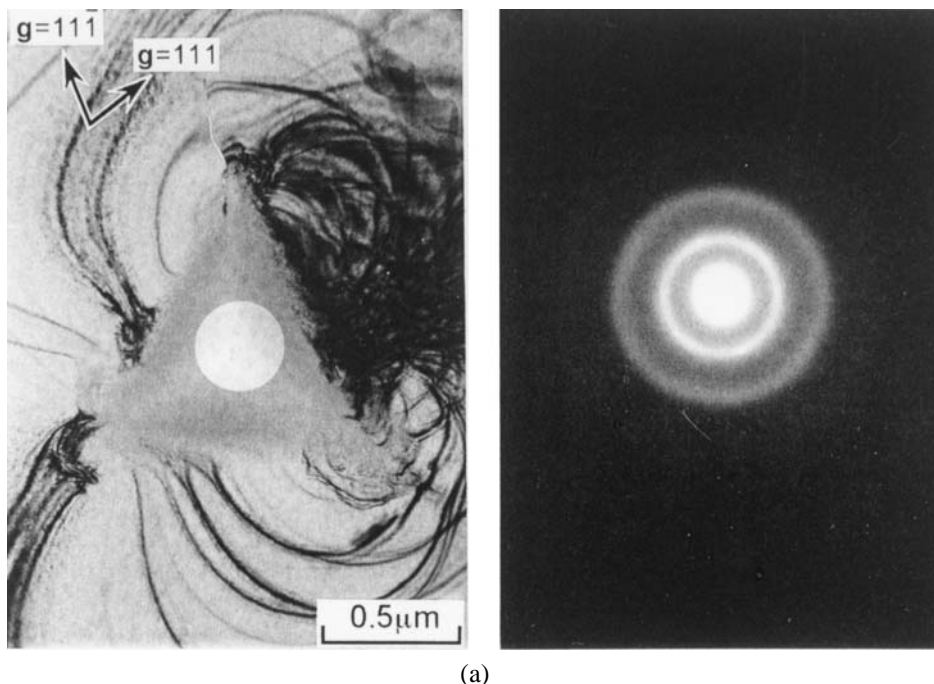
and later by Callhan and Morris [94], Suzuki and Ohmura [40], and by Shimatani, Nango, Suprijadi and Saka [43]. Clarke et al. [93] indented single crystals of Si of orientations (100), (110) and (111) at room temperature using Vickers and Knoop diamond indenters under loads of 10 to 50 gf. The TEM specimens were prepared for a plan-view examination (Fig. 42(a)). These workers found that within the indentation there was no structure at all, and from their electron diffraction patterns, which were haloes rather than discrete spots, Clarke et al. [93] interpreted that the material within the indentation was amorphous. It may be said here, however, that the haloes may not be a firm proof of the absence of nanocrystalline material and, therefore, further work is needed. In another series of experiments they measured the electrical resistance of the material layer immediately below the indenter tip in the Si when the indenter load was applied and when the indenter had been removed. To make these measurements, two thin metallic strips were deposited parallel to each other on the Si surface, with the distance between them being of the order of 1–2 μm . A dc voltage of a few volts was applied to the strips, with a sensitive ammeter connected in series. Then a Vickers diamond indenter was loaded on to the bare Si between the strips and the indenter load was made sufficiently high so that the indentation extended over both the metallic strips simultaneously. It was found that in the presence of the indenter load the electrical resistance of the material layer just below the indenter decreased markedly by about two orders of magnitude, but on the removal of the indenter load, the electrical resistance returned to the original higher value (i.e. before the indentation). Similar observations had been made several years earlier by Gridneva, Milman and Trifilov [95], who interpreted the decrease in the electrical resistance during indenter loading as being due to a structural phase transition from the cubic to a body centred tetragonal (β -Sn structure) type in the presence of a high hydrostatic component of stress. This suggestion seems a reasonable one as the β -Sn phase of Si has a much higher electrical conductivity than that of the cubic phase. Gridneva et al. [95] as well as Clarke et al. [93] suggested that the magnitude of the hydrostatic pressure within the indented material was the same as the room-temperature indentation hardness value, which has been measured to be in the range of 8 to 15 GPa [10, 94–96]. Now, according to Hu, Merkle, Menoni and Spain [97], the value of the hydrostatic pressure, as measured in a diamond anvil cell in the presence of a pressurising fluid, at which the phase transformation of the cubic phase of Si to the β -Sn phase occurred was in the range of 11.3 to 12.5 GPa. If there was no pressurising fluid in the diamond anvil cell, the onset of the transformation occurred at a lower pressure of 8.5 GPa because of the non hydrostatic stresses which gave rise to high shear stresses.

As shown earlier (see Section 2), although the component of hydrostatic stress under the indenter may not be as high as the indentation hardness value of the indented Si, the existence of large shear stresses and strains within the material in the immediate vicinity of the indenter may help the process of phase transformation of the Si from the cubic phase to the β -Sn phase [98]. It may be mentioned here that when 1–5 gf Vickers indentations were made in Si(111) (n-type; 200 ohm cm) heated to temperatures in the range of 450 to 700°C, a hexagonal phase of Si has also been identified after indenter removal, with the lattice parameters being $a = 0.386 \text{ nm}$, and $c = 0.631 \text{ nm}$ [37].

Returning to the TEM studies of Clarke et al. [93], although it seems quite plausible that during room-temperature indentations the cubic Si may transform to the body-centred tetragonal phase, it is still inexplicable why on the removal of the indenter the material

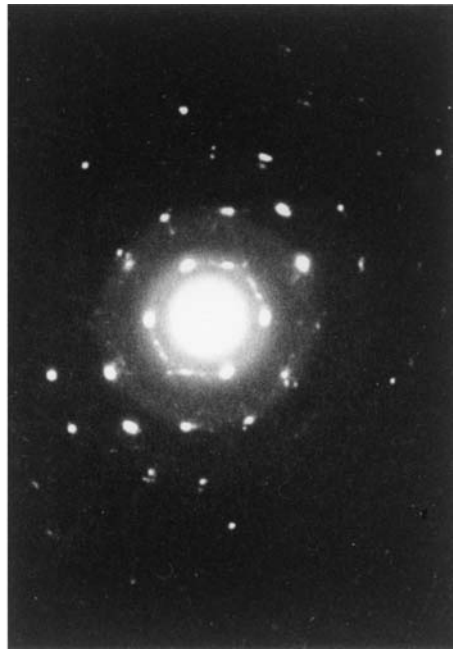
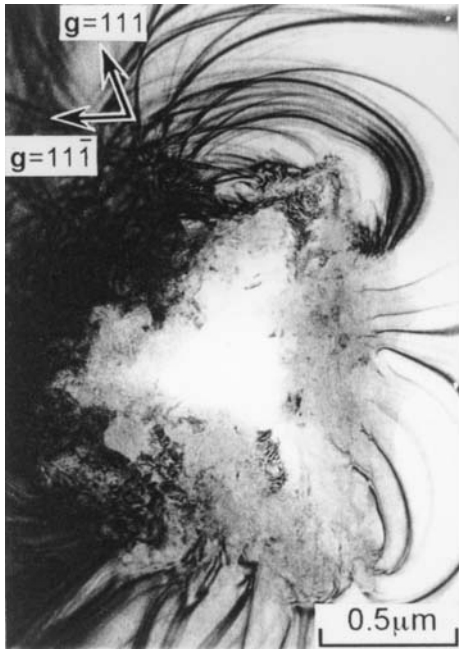
would not transform back to the cubic phase instead of becoming amorphous. Clarke et al. [93] also found that when the indented Si was annealed at 550°C or above, the amorphised material recrystallized into a fine-grain cubic Si.

The high-temperature studies were then extended by Suzuki and Ohmura [40]. They used Si(110) specimens, 3 mm in diameter and 1 mm thick, and indented them in vacuum at temperatures in the range of 20 to 750°C using a Berkovich diamond indenter under a load of 1 gf. The specimens were examined in the plan view (Fig. 42(a)) using a TEM. Electron micrographs and selected area diffraction patterns were obtained from the material within the indentations. Their typical results are shown in Fig. 45(a–c). It will be seen that in the case of the room-temperature indentation (Fig. 45(a)), there are no dislocations inside or even outside the indentation and the electron diffraction pattern consists of concentric haloes (it should be noted, however, that the absence of any dislocations in a region just outside the indentation is contrary to the observations of Nikitenko et al. [92] and Hill and Rowcliffe [41]). When an indentation was made at 250°C (Fig. 45(b)), dislocations were nucleated in the material within the indentation, but no dislocations existed just outside it, indicating their low mobility. The diffraction pattern consisted of spots of the cubic phase superimposed on the haloes, suggesting that the phase transition possibly occurred even at this temperature. This suggestion is consistent with the fact that at 250°C the indentation

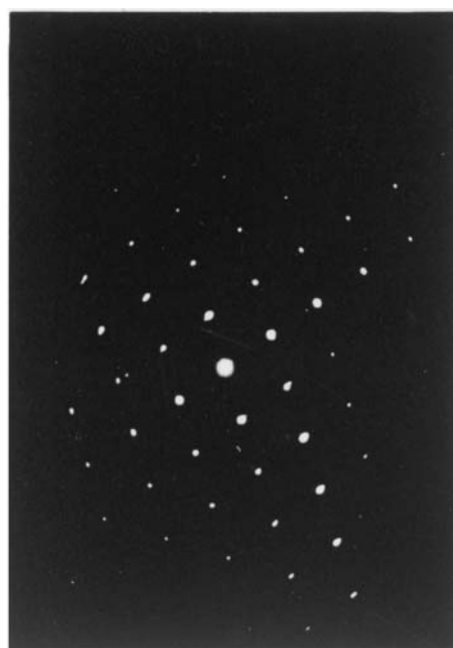


(a)

Fig. 45. Bright-field transmission electron micrographs and selected area electron diffraction patterns taken from inside the Berkovich diamond indentations (load 1 gf) in single crystals of Si(110). The indentations were made at different temperatures, with (a) 20°C, (b) 250°C, and (c) 750°C. In (c) the indentation centre is at the top right hand corner. From Suzuki and Ohmura [40].



(b)



(c)

Fig. 45. (Continued).

hardness and therefore the hydrostatic component of stress is almost the same as that at 20°C [96]. For an indentation made at 750°C, the electron diffraction pattern was in the form of sharp spots, consistent with the cubic Si structure, and there were dislocations just outside the indentation (Fig. 45(c)). Suzuki and Ohmura [40] did not indicate whether there were dislocations within the indentation itself, although it seems quite likely that there would probably be some in this region.

Following a suggestion by Callahan and Morris [94], Shimatani et al. [43] recently adopted a novel approach for the TEM studies of indented Si specimens. They indented dislocation-free Si(100) single crystals with a Vickers diamond indenter under loads of 10, 25, and 50 gf and used the thinning method shown schematically in Fig. 42(b) to prepare the (110) cross sections of the indented specimens. They then used a 1 MeV TEM for making electron micrographs and selected area diffraction patterns of the material within the indentations. An advantage of this approach was that the subsurface structure of the deformed zone could be examined in a much greater detail than is possible in a plan-view examination. A typical selection of electron micrographs and electron diffraction patterns from the subsurface region of a 25 gf Vickers indentation is shown in Fig. 46(a-f). Note that in Fig. 46(a) the material directly beneath the indentation has been divided into four distinct regions, with region 1 being next to the indenter and region 4 being furthest from it. Region 1 appears to be amorphous, and this observation is in agreement with those of the previous investigators [40,93,94], whereas region 2 is crystalline, as confirmed by the spot diffraction pattern (Fig. 46(b)). Region 3 is amorphous again, as confirmed by the electron diffraction pattern (Fig. 46(c)), and then the material in region 4 is crystalline (Fig. 46(d)), as would be expected for a region furthest away from the indenter tip. As to why the crystalline region 2 exists embedded within the amorphous material is not clear and the observation is rather surprising. Another puzzling observation reported by Shimatani et al. [43] is that in the case of a 50 gf Vickers indentation there was no amorphous zone at all. This observation was reproduced from all ten such 50 gf indentations. A further important observation from the crystalline region 2 (Fig. 46(b)) was that its orientation was the same as that of the original undeformed Si specimen.

5.2. Ceramic crystals

Only a few studies have been made of the material within indentations in single crystals of ceramics. Brown, Khan and Chaudhri [99] have investigated the indentation zone and the region just outside it for 25 gf room-temperature Vickers diamond indentations in single crystals of MgO(100), 3 mm in diameter and 300 µm in thickness. Some of the indented crystals were annealed in air at 900°C for one hour. The indented specimens were thinned according to the method shown in Fig. 42(a). Care was taken not to puncture the specimens during the ion beam thinning. The thinned specimens were examined with a TEM operating at 500 keV. Selected-area diffraction patterns of the material from within the indentation zone were also obtained. A many-beam bright field image of the material from within an unannealed Vickers indentation is shown in Fig. 47; the electron diffraction pattern from this zone is given at the top left hand corner of the figure. It will be seen that the centre of the indentation, which is just below the centre of the micrograph, is full of dislocations.

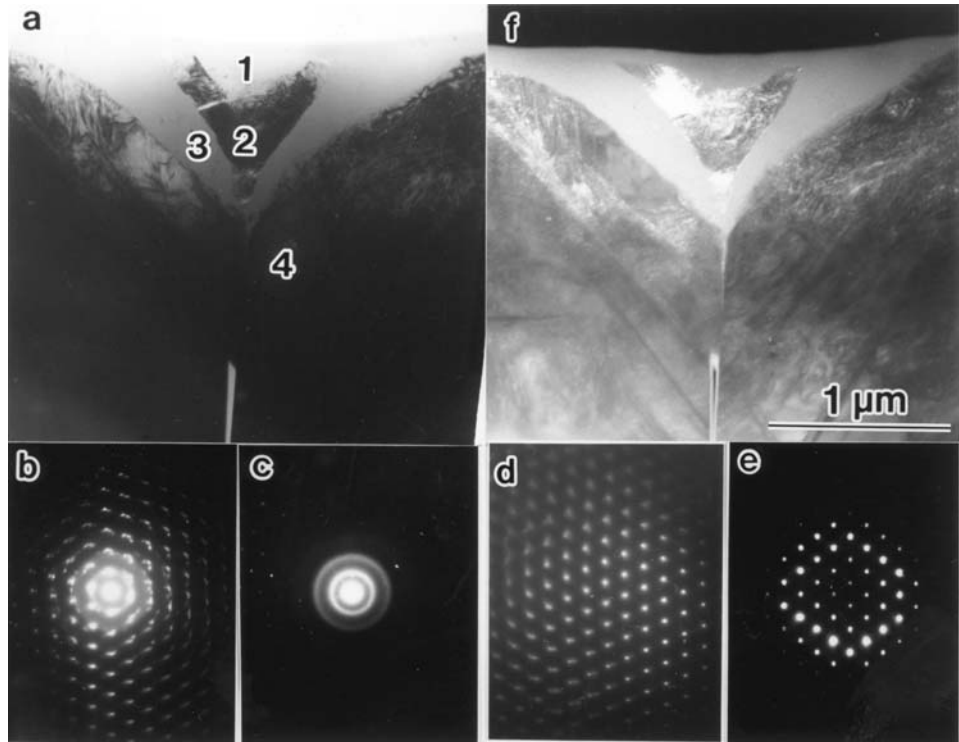


Fig. 46. High-magnification transmission electron micrographs of a 25 gf Vickers diamond room-temperature indentations in single crystals of Si(100) imaged in the bright-field mode. (a) Cross-sectional view of the subsurface regions around the indentation. (b), (c), (d), and (e) are the diffraction patterns taken from regions 2, 3, 4, and an undeformed region of the Si, respectively. (f) is a dark-field image taken with part of the haloes shown in (c). From Shimatani, Nango, Suprijadi and Saka [43].

This was confirmed by making TEM observations under different tilt conditions, which resulted in moving the contours (Fig. 48) [100]. Also, there are dislocations present in the region just outside the indentation (e.g. see the bottom right hand corner in Fig. 48). The diffraction pattern in Fig. 47 shows that the material within the indentation has the same orientation as that of the undeformed crystal. However, the diffraction spots show asterism, which is probably due to the existence of large plastic strains and residual stresses within the material. In the case of an annealed (1 h at 900°C) indentation in MgO(100) both the diffraction pattern and the contrast in the electron micrographs of the material from within the indentation zone become much sharper (see Fig. 49). However, the centre of the indentation still contains a large number of dislocation loops, and the dislocations in the region just outside the indentations move out further. Note that the annealing of the MgO crystal at 900°C has not been able to remove completely all the dislocations from within the indentation zone, though their number density may have decreased to some extent. Furthermore, the sharpening of the diffraction spots (i.e. decreased asterism) is consistent with the reduction of the residual stresses. A higher magnification image of the

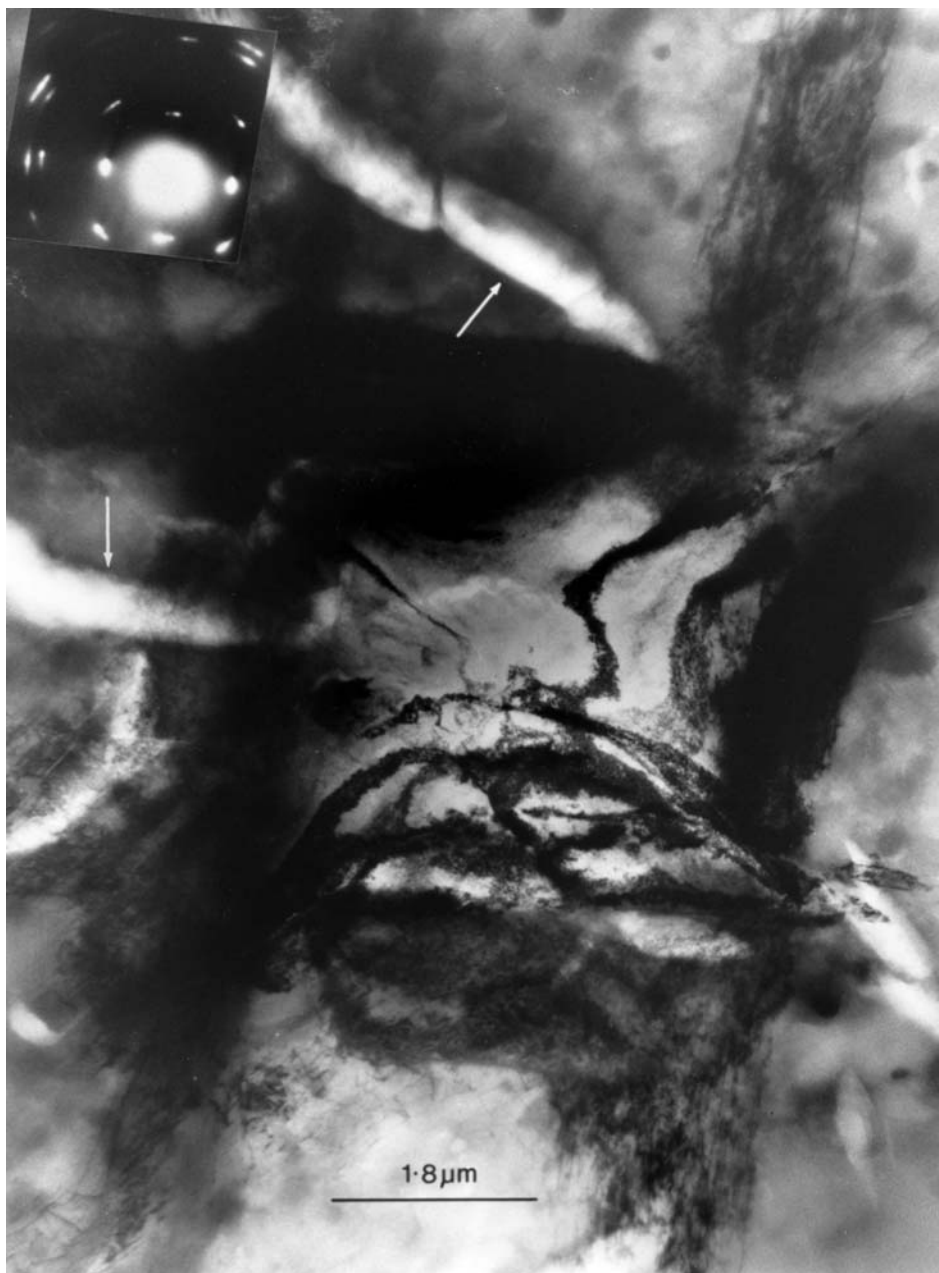


Fig. 47. Many-beam bright field image of a 25 gf room-temperature Vickers indent (unannealed) on a (100) face of a single crystal of MgO. Beam energy is 500 keV. The centre of the indentation is just below the centre of the micrograph. Arrows show surface artefacts. Selected-area diffraction pattern is shown at the top left hand corner.

From Brown, Khan and Chaudhri [99].

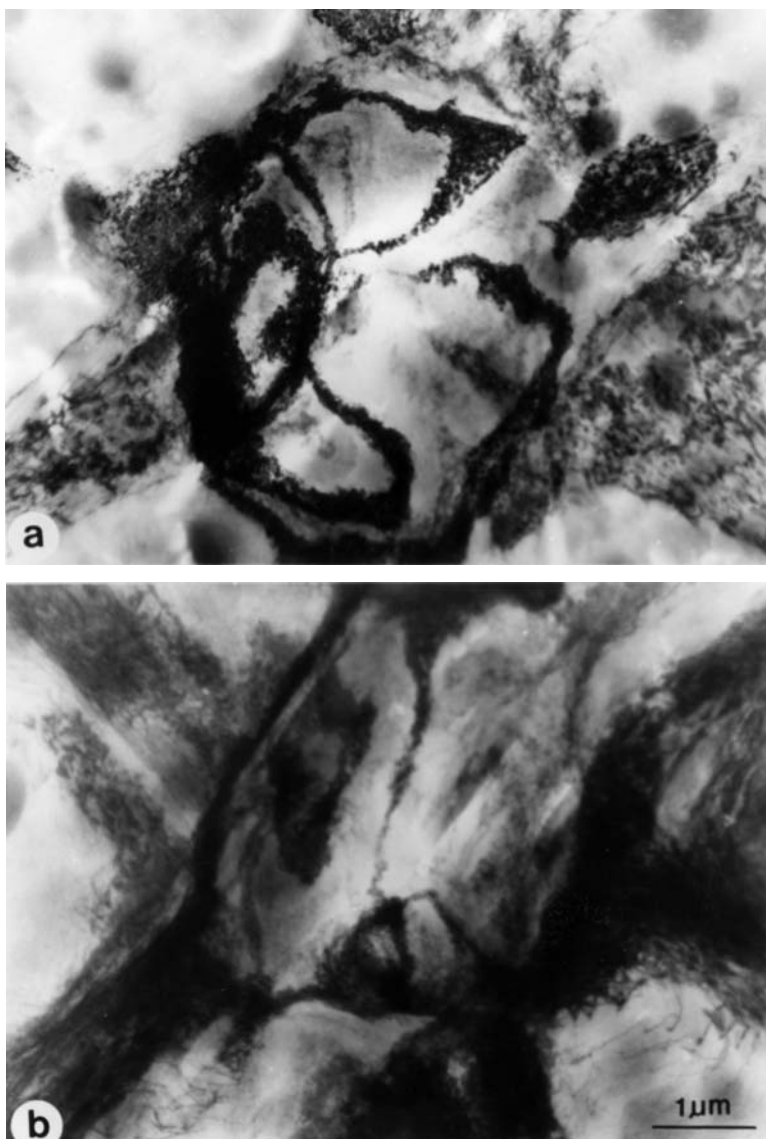


Fig. 48. Many-beam bright field images of a Vickers indentation (unannealed) made at room temperature under a load of 25 gf in a single crystal of MgO(100) taken under two different tilt conditions. In (a) the foil normal is along the [001] direction and the centre of indentation is at the centre of the micrograph. In (b) the specimen has been tilted through 26° with respect to its orientation in (a). The tilting results in moving the bend contours within the indentation and it will be seen that the entire centre of indentation is full of dislocations. From Khan [100].



Fig. 49. Many-beam bright-field image of a 25 gf room-temperature Vickers diamond indentation on a (100) face of an MgO single crystal. After making the indentation the crystal was annealed at 900°C in air for 1 h. Beam energy: 500 keV. Note that the diffraction pattern shown at the top left hand corner shows much less asterism than that shown in Fig. 47. Also, the dislocations within the indentation zone and those outside it are much clearer than the dislocations shown in Fig. 47. From Brown, Khan and Chaudhri [99].

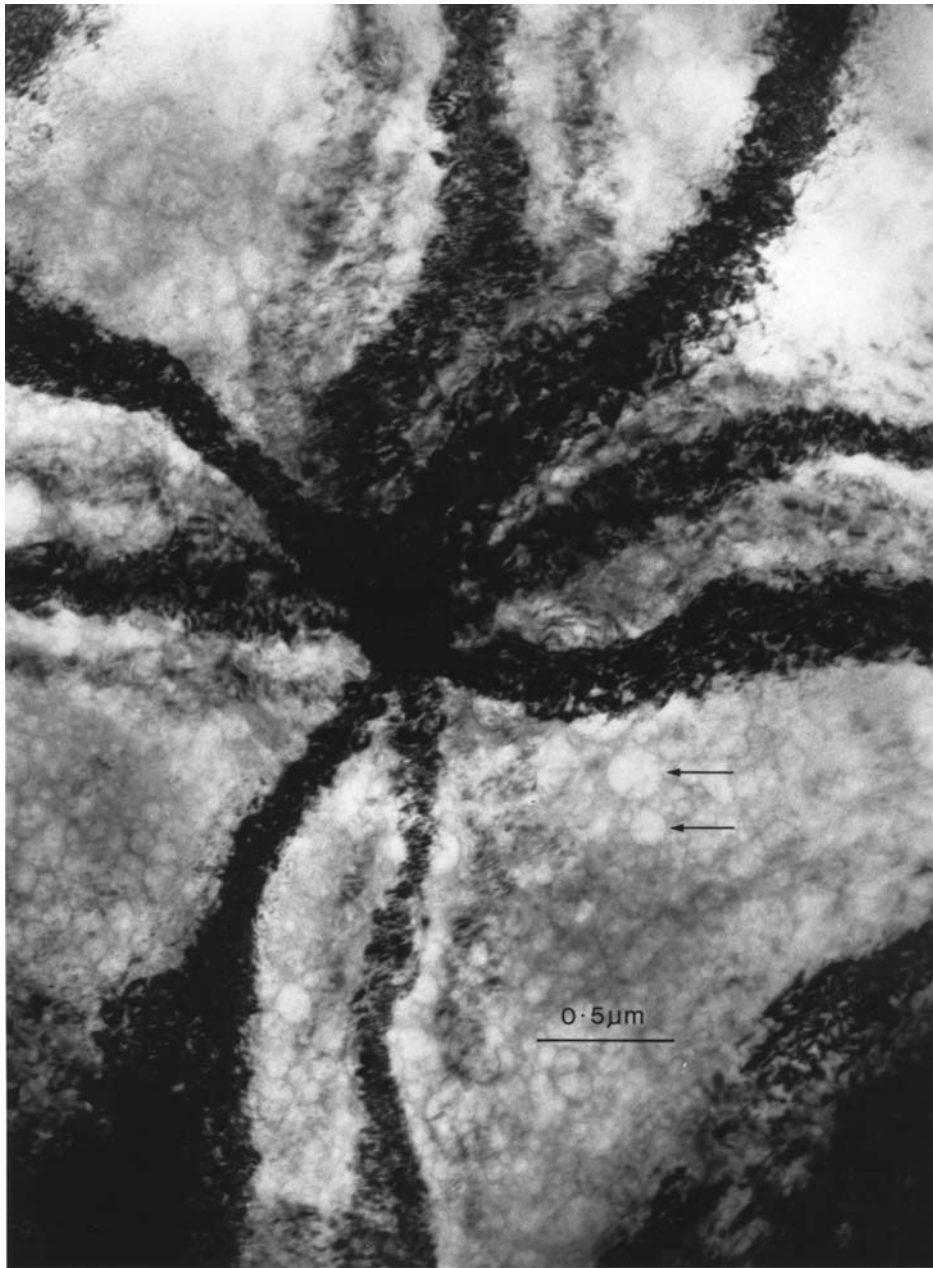


Fig. 50. High-magnification image of the indentation zone shown in Fig. 49. Beam energy: 500 keV. The indentation tip is at the centre of the micrograph. The faint circular markings, about 0.1 to 0.2 μm in diameter, shown at arrows, are thought to be artefacts produced either during specimen preparation or by radiation damage. The much finer structure seen near the dark bend contours is probably due to crystallographic defects created by the plastic deformation. From Brown, Khan and Chaudhri [99].

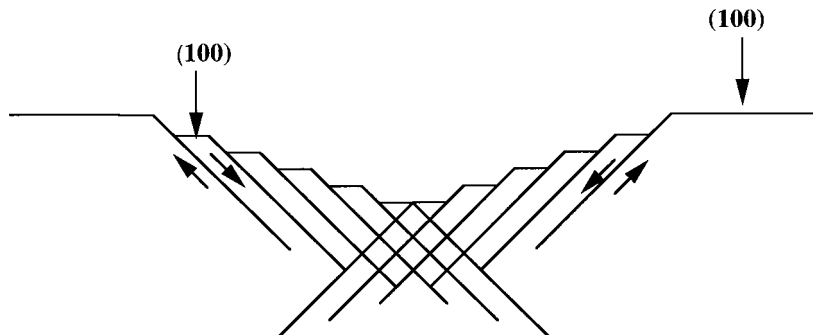


Fig. 51. Schematic diagram showing how when an indentation is made on a (100) face of an MgO single crystal, the material within the indentation maintains the same orientation as that of the original surface. This happens by the process of small size (100) steps combined with slip on the $\{110\}_{45}$ planes, as shown. By altering the size of the steps, indentations of any shape can be introduced without changing the orientation of the material within the indentation. The arrows indicate the slip directions. Here the $\{110\}_{45}$ slip planes taking some of the displaced material towards the indented surface outside the contact are not shown.

structure within the annealed indent of Fig. 49 is shown in Fig. 50. This micrograph clearly shows that the material is full of dislocation loops. However, their densities are too high to be measured at this magnification. For observations at still higher magnifications, thinner specimens are needed, but so far it has not been possible to make such thin specimens which are free from a considerable amount of radiation damage.

A schematic diagram of a suggested slip process, which allows the formation of a Vickers indentation in a single crystal of MgO(100) without changing the crystallographic orientation of the deformed material, is shown in Fig. 51. Here only the $\{110\}_{45}$ slip planes, along which the displaced material is pushed into the bulk, are shown.

Another important ceramic, which has exceptional physical and chemical properties, is alumina. Single crystals of this material are sapphire with Ti^{3+} impurities giving it a blue colour, and ruby with Cr^{3+} impurities, giving it a characteristic pink colour. However, often clear single crystals of alumina are also called sapphire. TEM studies of room-temperature indentations in sapphire crystals have been made by Rozhanskii et al. [101] and by Hockey [102,103]. Rozhanskii et al. [101] indented thin films of sapphire of thickness ~ 0.3 to $0.4 \mu m$, grown by oxidation of aluminium in the presence of humid hydrogen, with a Vickers diamond indenter under a load of 1 gf. They found clear evidence for the existence of dislocation loops within the indentations. These dislocations were reported to lie on the (0001) , $\{1\bar{2}11\}$, and the prismatic $\{1\bar{2}10\}$ planes. Similar studies have also been carried out by Hockey [102,103], who used both Vickers and Knoop diamond indenters on the various crystallographic planes, $(\bar{1}012)$, $(10\bar{1}0)$ and (0001) of relatively thick sapphire crystals using indenter loads in the range of 20 to 200 gf. He also found that in the room-temperature indentation process dislocations were involved. Also, twinning was identified on the (0001) and the $\{01\bar{1}2\}$ planes. Furthermore, close to the tip of a 50 gf Vickers indentation on a $\{10\bar{1}0\}$ surface of sapphire, numerous dislocations lying on the $\{01\bar{1}2\}$ and the (0001) planes were observed. Basal twins were often found in the regions surrounding indentations on non-basal surfaces. Hockey [103] concluded that the dislocations observed

in his TEM studies of room temperature indentations provided concrete evidence for the existence of partial dislocations in sapphire and thus supported the ‘synchro-shear’ displacement of quarter-partial dislocations on the basal planes [104,105].

A TEM study of the indentation zone of an AlN ceramic (polycrystalline with grain size $> 10 \mu\text{m}$) has been reported by Callahan [106]. His specimens were in the form of thin rectangular plates of dimensions $2 \text{ mm} \times 2 \text{ mm} \times 10 \mu\text{m}$. These were indented at room temperature with a Vickers diamond under a load of 1 gf producing indentation of depths $< 1 \mu\text{m}$. The indented specimens were ion-beam milled (4 kV Ar ions incident at 12°) (see Fig. 42(a)) for a TEM examination using an operating voltage of 200 kV. He reported that there were large densities of dislocations/defects, both inside and just outside the indentations.

5.3. Metals

TEM studies of the defect structure within indentations in metals have been made by several workers [107–109]. Zielinski et al. [108] indented Fe–3 wt% Si(100) single crystals, $\sim 35 \mu\text{m}$ thick, with a Vickers diamond indenter under a load which produced an indentation of $1 \mu\text{m}$ in depth. The indented specimens were then thinned in the manner shown in Fig. 42(a) and examined with a TEM operating at 300 keV. The indentation zone appeared to be full of defects, which could not be resolved very well (see Fig. 9 of ref. [108]). However, just outside the indentation zone individual dislocations were clearly visible and the primary slip system was identified to be $(112)\langle 111 \rangle$. A little distance below the indenter tip, dislocation activity on this slip system gave rise to a square pattern of dislocations. In the case of the room-temperature 1–12 gf Vickers indentations in Mo(001) single crystals (slip system, $\{211\}\langle 111 \rangle$), the 1 MeV TEM investigations of Leiko et al. [107] showed that the material in the immediate vicinity of the indenter was heavily dislocated.

In a different type of specimen preparation, Ma and Clarke [109] deposited a Ag/Au/Ag single crystal film sandwich with film thicknesses of $1.2 \mu\text{m}$, 50 nm and $50 \mu\text{m}$, respectively on single crystals of NaCl(100) in an ultra-high vacuum system. While still deposited on the substrate, the films’ sandwich was indented with a Berkovich indenter to depths in the range of 0.6 to $2 \mu\text{m}$. Afterwards, the silver films were dissolved away, and the remainder gold film was examined in an electron microscope operating at 200 keV. They found that within the indentations in the Au film there was a high density of defects. However, outside the indentation edges there were no dislocations. This absence of dislocations from the region just outside the indentation is rather unexpected, and it may be an artefact of the unusual geometry of the specimen.

5.4. Diamond, silicon carbide, and silicon nitride

At present diamond is still the hardest known material and it is not clearly established yet whether at room temperature plastic indentations can be made in it. Following room-temperature indentation experiments of Peters and Knoop [110] and Brookes [111] on

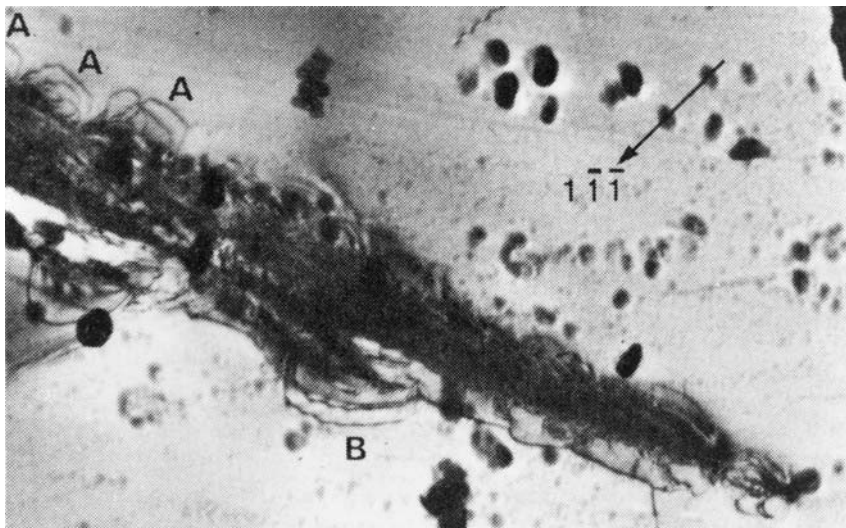


Fig. 52. Transmission electron micrograph of a room-temperature 150 gf Knoop diamond indentation on a (101) polished face of type II B diamond. The long axis of the indentation is close to the [010] direction. The long dark region, lying diagonally across the frame, is the heavily damaged indentation zone. However, at the edges of the indentation dislocation loops lying approximately on the $\langle 1\bar{1}\bar{1} \rangle$ plane can be seen at A, A, A and B. The diffraction vector is shown at the top right hand corner and the electron beam direction is close to [101]. The width of the frame is $\sim 4 \mu\text{m}$. From Humble and Hannink [112].

single crystals of diamond, Humble and Hannink [112] indented at room temperature polished {101} surfaces of type II B diamond with a Knoop diamond indenter under a load of 150 gf. The indented diamonds were thinned according to the method shown in Fig. 42(a). The thinned specimens were examined with a 200 keV electron microscope. Humble and Hannink [112] noted shear cracks within the indentations, but in addition, when the long diagonal of the indenter was along the [010] direction, some dislocations were seen just at the edges of the indentations. An example is shown in Fig. 52. In this figure dislocations are shown at A, A, A and B and their Burgers vectors were determined to be along the $\langle 110 \rangle$ directions. These authors found that the dislocation loops were close to being on the $\langle 1\bar{1}\bar{1} \rangle$ plane. This seems plausible, as it is known that at 1800°C the slip planes in diamond are $\{111\}$ [113]. It should be added here that the damage within the indentations themselves was so severe that it could not be examined with the TEM [112].

Silicon carbide (SiC) is another very hard and technologically useful material, though its hardness is considerably lower than that of diamond. Plastic deformation in this material has not been produced in compression at temperatures lower than $\sim 1100^\circ\text{C}$ [114]. However, permanent indentations have been made at room temperature [115]. Using a Knoop diamond indenter and a load of 500 gf, Maeda et al. [115] indented polished single crystals of 6H-SiC(0001) and 6H-SiC($1\bar{1}00$) in the temperature range of 20 to 1200°C . The indented specimens were ion-beam thinned according to the method shown in Fig. 42(a) and examined with a TEM. Although the indented region itself could not be examined, good-quality electron micrographs of dislocations lying just outside the indentations were

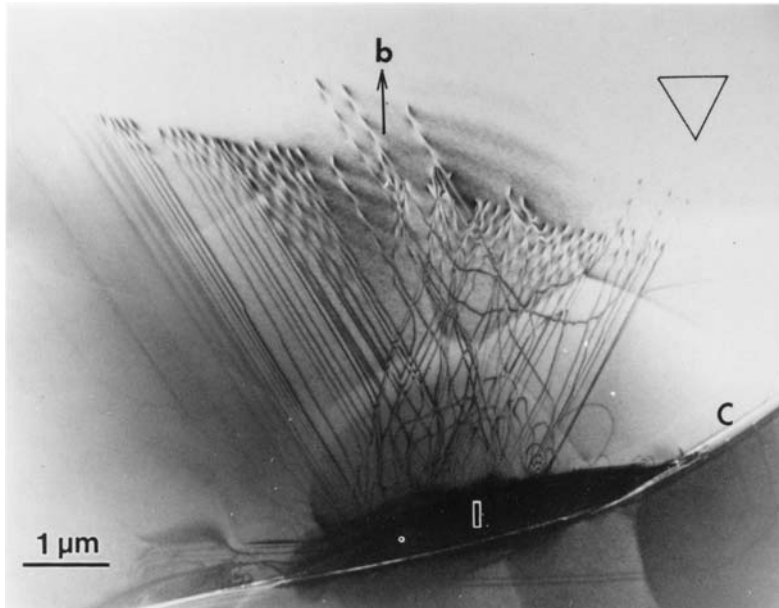


Fig. 53. Transmission electron micrograph showing a system of 30° partial dislocations introduced by a 500 gf room-temperature Knoop diamond indentation on a (0001) face of a single crystal of 6H-SiC. The $(1\bar{1}20)$ directions are indicated by the triangle at the top right hand corner. The indentation is shown at I at the bottom of the frame and an associated crack is shown at C. From Maeda, Suzuki, Fujita, Ichihara and Hyodo [115].

taken. In the case of the room temperature indentations on the (0001) plane, dislocations were found lying on the (0001) planes. However, they were dissociated into straight Shockley partials lying along the $(11\bar{2}0)$ directions and their Burgers vector was determined to be $\langle 1\bar{1}00 \rangle$ (see Fig. 53) [115]. On the other hand when the indentations were made on the $(1\bar{1}00)$ plane, the dislocations were in the form of irregular loops lying in the $(1\bar{1}00)$ plane and their Burgers vector was $[1\bar{2}10]$ (see Fig. 54) [115]. These dislocations were thought to be perfect types, belonging to the prismatic slip systems. When the indentations were made on the (0001) plane at temperatures higher than 400°C , the dissociated partials were no longer straight, but became irregular [115].

Similar TEM studies of indented single crystals of 6H-SiC(0001) have been made by Qin and Roberts [116]. They used a conical indenter (angle not specified) under a 50 gf load, and the specimens were heated to temperatures in the range of 500 to 1000°C when the indentations were made in them. As found by Maeda et al. [115], Qin and Roberts [116] also found that at 500°C the slip was by basal partials, but when the crystals were indented at 1000°C , the slip was by paired partials.

A TEM study of the indentation zone of 50 to 1500 gf room temperature indentations in the hexagonal phase $\beta'\text{-Si}_3\text{N}_4$ has been carried out by Lewis, Fung and Taplin [117]. Indentations were made in 0.5 mm thick specimens which were thinned according to the method shown in Fig. 42(a) and then examined in the TEM. They found that in the region in direct contact with the indenter the dislocation density was too high to permit imaging

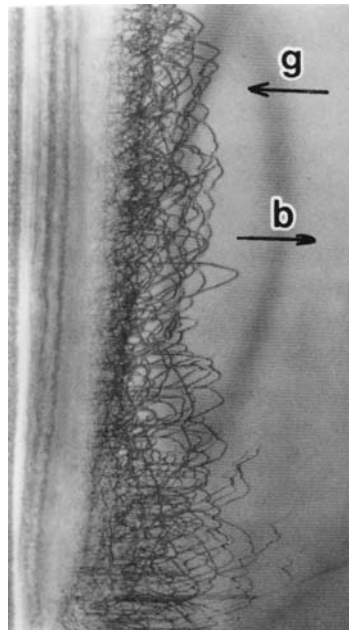


Fig. 54. Transmission electron micrograph showing prismatic perfect dislocation loops introduced by a 500 gf room-temperature Knoop indentation on a (1100) face of a 6H-SiC single crystal. The long axis of the indenter is along the length of the frame (i.e. vertical) and on the left hand side. The diffraction pattern vector is along 1210. Magnification not given by the authors, but it is guessed that the width of the frame is $\sim 3.4 \mu\text{m}$. From Maeda, Suzuki, Fujita, Ichihara and Hyodo [115].

of individual dislocations. However in the region near the edge of the heavily deformed zone dislocations could be resolved. The Burgers vector of the dislocations was identified to be $a[0001]$. They found that there was a strong tendency for dislocations on the prism planes $\{10\bar{1}0\}$ to have a screw orientation.

6. Indentation-enhanced cathodoluminescence and photoluminescence

Since plastic/elastic indentations usually involve large plastic strains and can produce a very high density of line and point defects, it is quite possible that these defects may give rise to enhancement or quenching of cathodoluminescence and photoluminescence. During the last 25 years or so several studies have been made to examine these effects and below we give separately results from such studies on some representative ionic oxides and semiconductor compounds.

6.1. Ionic oxides

Almost 50 years ago it was suggested by Seitz [118] that plastic flow in crystals could produce vacancies, and considerable experimental evidence has been provided in support of this suggestion [119]. In the case of MgO crystals, it has been shown using the technique of electron spin resonance that anion vacancies can be created by grinding [120], pulverisation by violent agitation [121], shock waves [122] and high strain rate deformation [123]. It has also been shown that either magnesium ion vacancies are not created by plastic flow, or if they are formed, they are not stable [124]. Therefore, it may be concluded that around an indentation involving dislocations in an ionic crystal, such as MgO, there will be a considerable increase in the number density of oxygen ion vacancies. These defects may then become different types of colour centre, namely F, F^+ , and F^{++} containing two, one and no captured electrons, respectively [125–128]. There is also the possibility of the formation of vacancy clusters. When F centres in MgO crystals are created by fast neutrons of energies greater than 1 MeV, the crystals are found to have new absorption bands with peaks at ~ 250 nm corresponding to F and F^+ centres. These absorption bands were found to have long tails extending to wavelengths greater than 325 nm [126].

In the photoluminescence studies of fast-neutron-irradiated MgO crystals strong emission bands were found at 517 nm [127], 520 nm [128] and 396–413 nm [125,128], which were identified as being due to F and F^+ centres, respectively. An interesting question arises: if neutron irradiated MgO crystals can give rise to enhanced photoluminescence, would plastically deformed crystals also show a similar response?

To answer this question, both photoluminescence and cathodoluminescence studies have been made of plastically deformed crystals of ionic materials. Thus Chen, Abraham, Turner and Nelson [129] showed that plastically deformed single crystals of MgO, CaO and SrO showed pronounced new photoluminescence bands at 2.9 (violet), 2.6 (blue) and 2.3 (green) eV, respectively. They also showed that the pronounced photoluminescence in the

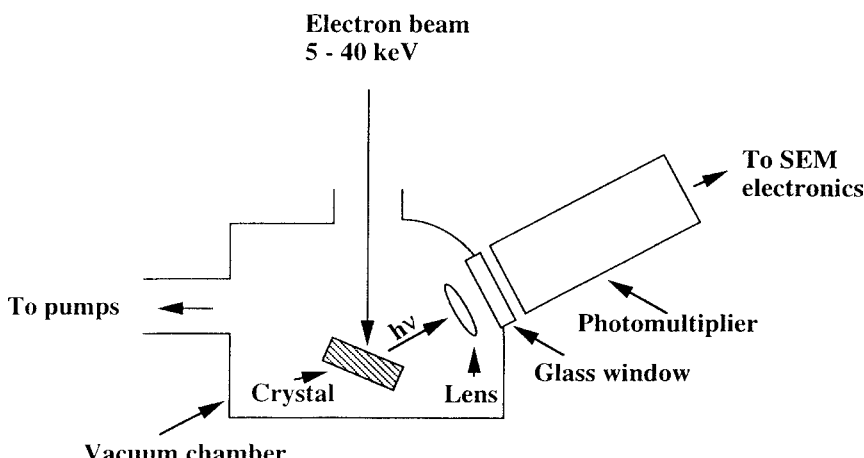


Fig. 55. A schematic diagram of the arrangement used for studying cathodoluminescence from indented MgO crystals using a scanning electron microscope (SEM).

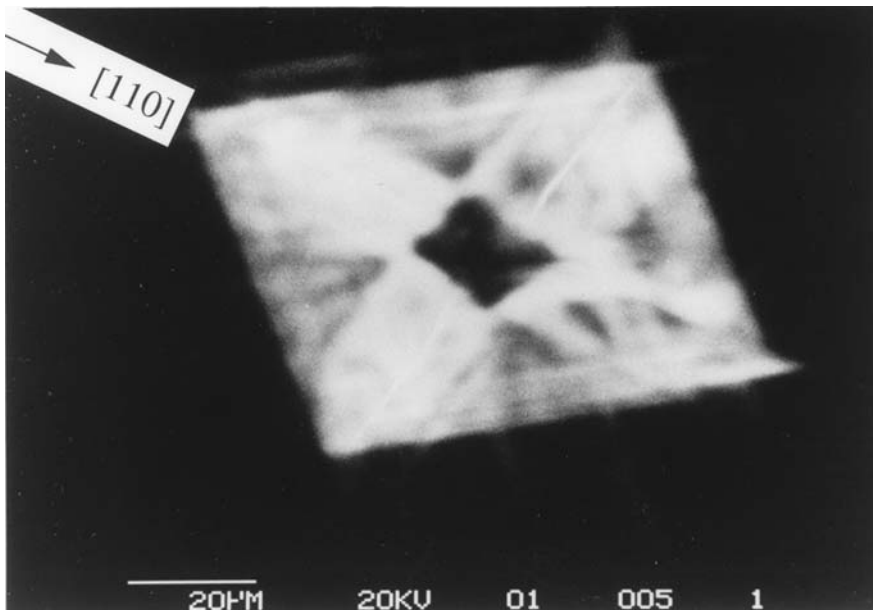


Fig. 56. A typical cathodoluminescence image of a 300 gf Vickers diamond indentation (unannealed) on a (100) face of a single crystal of MgO. Note that the indentation zone itself is non-luminescent, but the entire slip bands' region around it is markedly luminescent.

deformed crystals was concentrated at the slip bands. Similar photoluminescence observations from slip bands in uniaxially compressed MgO crystals have also been reported by Datta, Boswara and Holt [130]. The existence of dramatically luminescent slip bands was also shown by Velednitskaya et al. [14] in their cathodoluminescence studies of MgO(100) single crystals indented with a Vickers diamond pyramid. These observations have been confirmed by several other workers [131–134]. Generally, cathodoluminescence studies of indented crystals have been carried out using a scanning electron microscope working in the electron beam energy range of 5–40 keV. A schematic diagram of the arrangement used is shown in Fig. 55, and a typical cathodoluminescence image of an indented MgO(100) crystal is shown in Fig. 56. A most remarkable feature of this image is that although the slip bands around the indentations are markedly luminescent, the centre of the indent appears to be almost devoid of luminescence. Both the nature of the luminescence sources in the slip bands around the indentation and the apparent absence of luminescence from the indentation centre have puzzled many investigators and contradictory explanations have been put forward. Some have suggested that the luminescence from the slip bands is due to point defects [14,132,133,135–137], whereas some others have proposed that the dislocations in the slip bands give rise to their own energy levels within the band gap [131]. As for the apparent absence of cathodoluminescence from the centre of indentation, it has been suggested that the material in this zone does not contain any dislocations due to the process of recrystallization [14], or the dislocations are driven out of this zone because of a large stress gradient [85,86]. (As noted before, there appears to be a flaw in this argument.) As

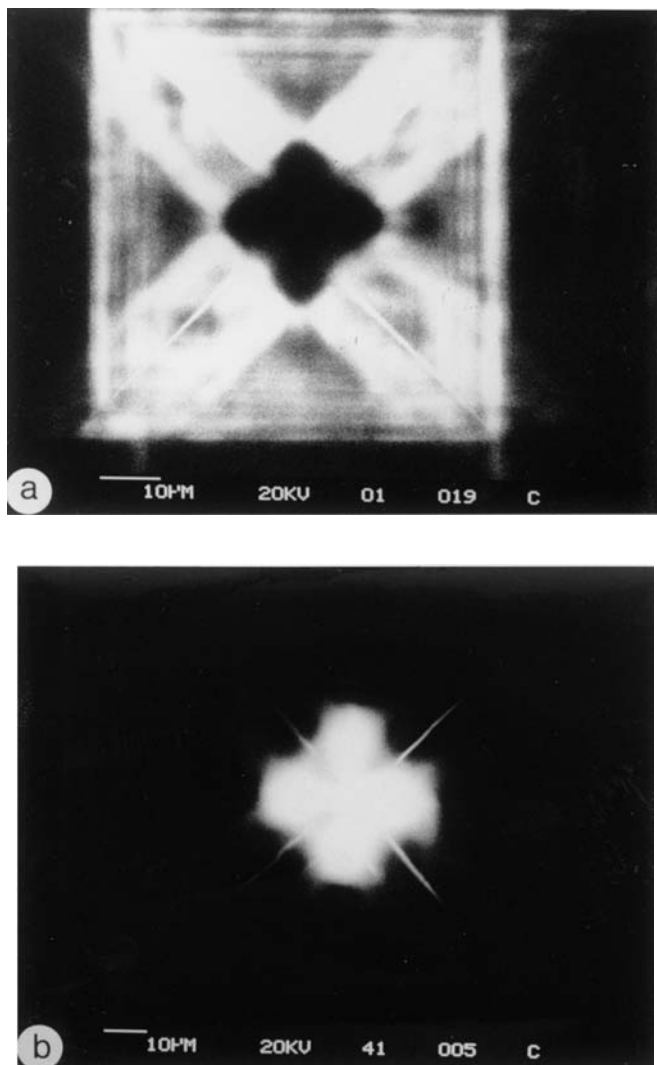
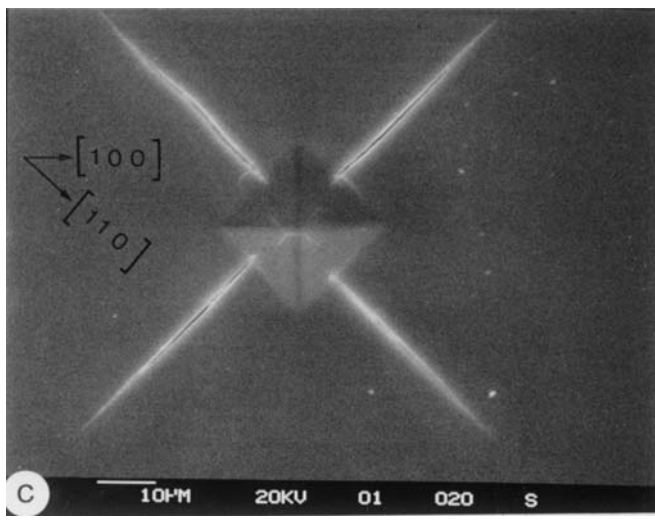
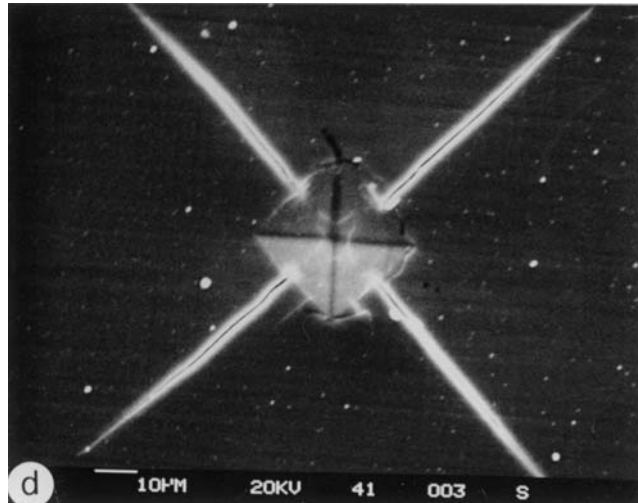


Fig. 57. The influence of annealing on the cathodoluminescence behaviour of indented MgO(100) single crystals. Frame (a) shows a cathodoluminescence image of a 300 gf Vickers diamond indentation. Frame (b) shows a cathodoluminescence image of a 500 gf room-temperature Vickers diamond indentation which had been annealed at 900°C for 1 h. Frames (c) and (d) are the secondary electron images of the indentations shown in frames (a) and (b), respectively. Note that whereas in the cathodoluminescence mode the centre of the unannealed indentation is dark and the slip bands' region around it is strikingly luminescent (see (a)), the annealing reverses the situation, with the indentation centre becoming luminescent and the slip bands' region losing practically all its luminescence (see (b)). From Khan [100].

shown in Section 5, the indentation zone in MgO(100) crystals is indeed full of crystalline line defects. Therefore, neither of the above two explanations seems correct.



(c)



(d)

Fig. 57. (Continued).

As far as the notion of dislocations in the slip bands being totally or partly responsible for the enhanced luminescence, it may be examined in the light of the transmission electron microscopy and the cathodoluminescence results from unannealed and annealed MgO crystals (see below). It has been shown by Velednitskaya et al. [14] that the spatial distribution of the cathodoluminescence changed dramatically when indented crystals were annealed in air at 800 to 900°C for a few minutes. The observation was that the lumines-

Table 2
Impurity content in the MgO crystals used for the photoluminescence work [139].

Impurity	Content (ppm)	
	99.9% purity MgO	99.99% purity MgO
Al	50	30–40
Ca	500	20–30
Cr	20	< 5
Fe	50	2–10
Mn	3	< 1
Ni	< 1	—
Ag	< 1	—
Na	2	1–3
V	20	—
B	—	0.2
Si	—	15–30
P	—	< 3
Ti	—	< 5
As	—	< 5
Zr	—	1–5
Ba	—	< 2
Pb	—	0.5
S	—	< 2
N	—	1–5
Zn	—	1–10

cence from the slip bands around the indentation decreased very considerably, whereas the centre of the indentation became very luminescent. An example of this effect is shown in Fig. 57 [100]. Now, as shown by Brown, Khan and Chaudhri [99], the process of annealing at 800 to 900°C does not remove the dislocations from the slip bands' region, though perhaps it may cause a decrease in their number densities. However, if dislocations were contributing to the cathodoluminescence, then it would be expected that the slip bands region would still be luminescent, though with somewhat reduced intensity. However, the almost total apparent absence of cathodoluminescence from the slip bands of an annealed MgO crystal clearly suggests that the dislocations themselves do not appear to contribute significantly to the total luminescence from the slip bands. It seems, therefore, that the luminescence may be due to the point defects created by the dislocation processes.

In the cathodoluminescence studies carried out using a scanning electron microscope, the energy of the electrons impacting on the test crystal is usually in the range of 5 to 40 keV. These relatively high energy electrons may change the valence states [138] of any colour centres present within the indentation and the deformed region around it.

To avoid the influence of any electron beam damage to the crystal and consequently to the luminescence sources, Chaudhri and Sands [139] carried out photoluminescence studies of indented unannealed and annealed MgO crystals using an ultraviolet/visible Raman microscope (Renishaw, UK), employing excitation radiation of wavelength 325 nm (i.e. ~ 3.82 eV) from a HeCd laser. The energy of this radiation is considerably smaller than the energy band gap of MgO, which has been experimentally determined to be 10.5 eV [140] and 7.77 eV [141] from reflectivity experiments.

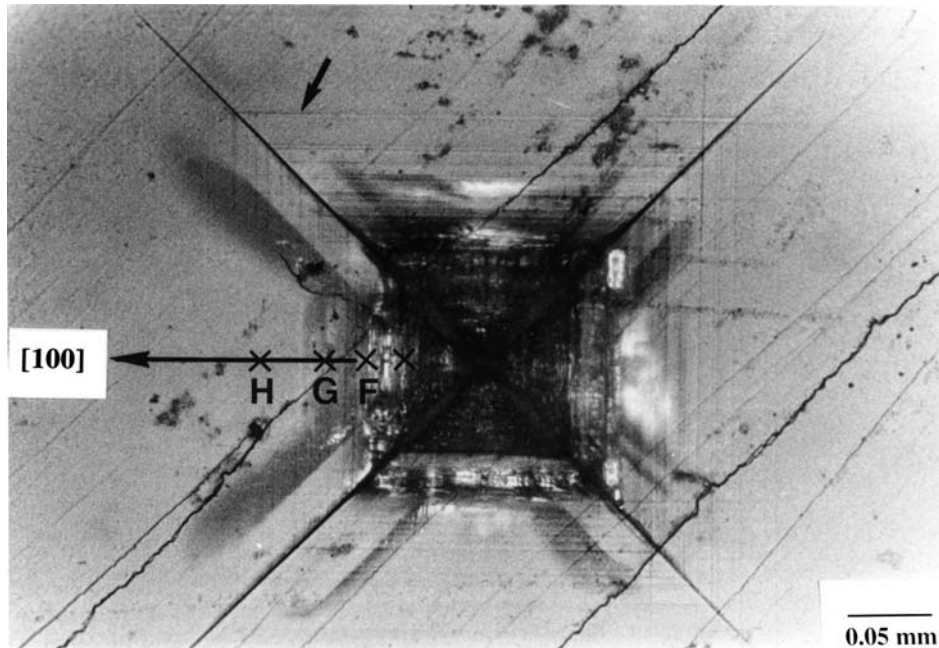
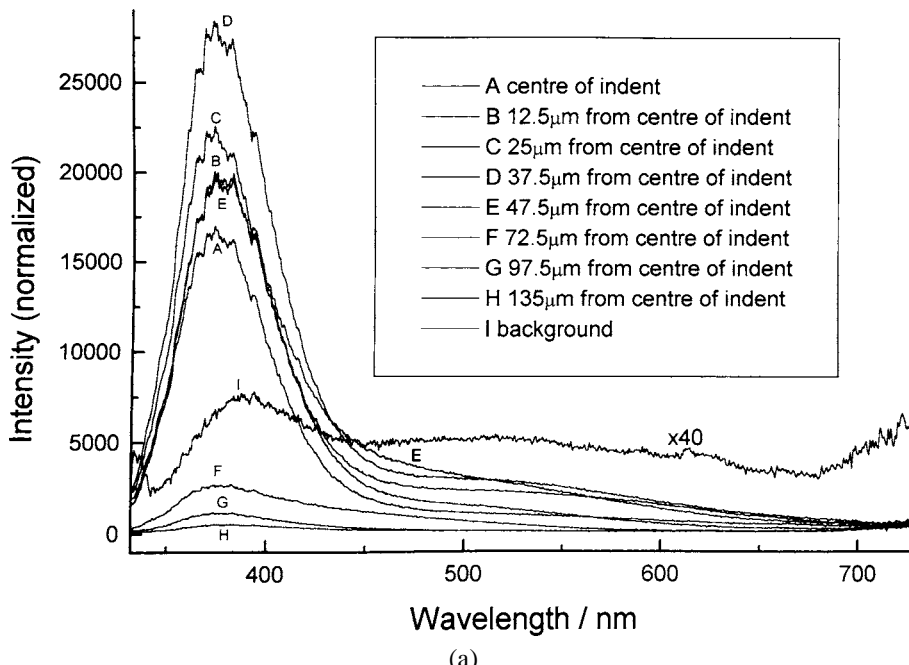


Fig. 58. Photomicrograph, taken with reflected light, of a 5 kgf Vickers diamond pyramid indentation in the 99.99% purity crystal, which was put in after the crystal was annealed. Four $\{110\}_{90}$ cracks emanating from the corners of the indentation and the slip bands around the indentation can be clearly seen. The cracks extend right to the boundary of the outermost slip bands; one of the prominent slip bands is shown at the arrow. Photoluminescence was studied from within the indentation and the slip bands' region outside it at several points lying along the arrowed [100] direction. Some of these points are shown with an 'x' and the lettering corresponds to the photoluminescence curves shown in Fig. 59(a). From Chaudhri and Sands [139].

Chaudhri and Sands [139] carried out experiments on two single crystals of MgO, both of (100) orientation, produced by cleaving. One crystal was of size $2 \times 10 \times 10 \text{ mm}^3$ and its purity was 99.9%. The second crystal was of size $3 \times 5 \times 5 \text{ mm}^3$, and its purity was 99.99%. Both crystals were very clear and their impurity content is shown in Table 2.

Each crystal was indented with a Vickers diamond under a load of 5 kgf; this resulted in the formation of the $\{110\}_{90}$ cracks as well as prominent $\langle 100 \rangle$ slip bands in both crystals. Each crystal was then placed in a fused silica tube, evacuated down to a pressure of 10^{-6} Torr, sealed, heated in a furnace to a temperature of 1000°C , kept at this temperature for 2 h and then allowed to cool down gradually to room temperature over a period of 12 h. The crystals were then removed from the silica tubes and in each crystal another 5 kgf Vickers diamond indentation was made at room temperature. The diagonals of all the four indentations were along the $\langle 110 \rangle$ directions.

The indentations which were made before the annealing of the crystals was carried out were called annealed indents, and the indents put in after the annealing had been carried out were designated as unannealed indents.



(a)

Fig. 59. (a) Photoluminescence spectra taken from different regions lying within the unannealed indentation (shown in Fig. 58) and the plastically deformed part outside the indentation in the 99.99% purity MgO crystal. The inset indicates the positions from where the spectra were obtained. Points A, B, C, D and E are within the indentation, whereas points F, G, and H are in the deformed zone outside the indentation. Curve I (shown at a higher magnification) was taken from an undeformed part of the crystal. (b) Photoluminescence spectra taken from different regions within the annealed indentation (indenter load = 5 kgf) and the plastically deformed part outside the indentation in the 99.99% purity MgO crystal. The inset indicates the positions from where the spectra were obtained. The points E, F, and G are in the plastically deformed region outside the indentation. The background from an undeformed part of the crystal is represented by the curve I. Note that the intensity of the curve I in (a) and the intensities of the curves F, G, and I in (b) have been magnified and the magnifications are indicated on the curves. From Chaudhri and Sands [139].

Photoluminescence from within the indentations, the deformed region around them and the undeformed parts of the crystals was studied at room temperature. The 325 nm radiation was allowed to strike the test crystal through a $\times 40$ fused silica objective lens of numerical aperture 0.5. The power of the excitation beam at the focal point, $\sim 2\text{--}3 \mu\text{m}$ in diameter, was 0.2 mW. The resulting photoluminescence spectrum was obtained with the grating spectrometer of the Raman microscope in the wavelength range of 325–726 nm. Each of the two indentations in the 99.99% purity crystal was examined for its photoluminescence at its centre, and at several other points lying along the arrowed straight line in a [100] direction (see Fig. 58) within the indentation and the surrounding plastically deformed region. Some of these points have been labelled with an 'x' and the lettering corresponds to the photoluminescence curves shown in Fig. 59(a, b). In the case of the two indentations in the 99.9% purity crystal, the photoluminescence spectra were obtained from the indentation

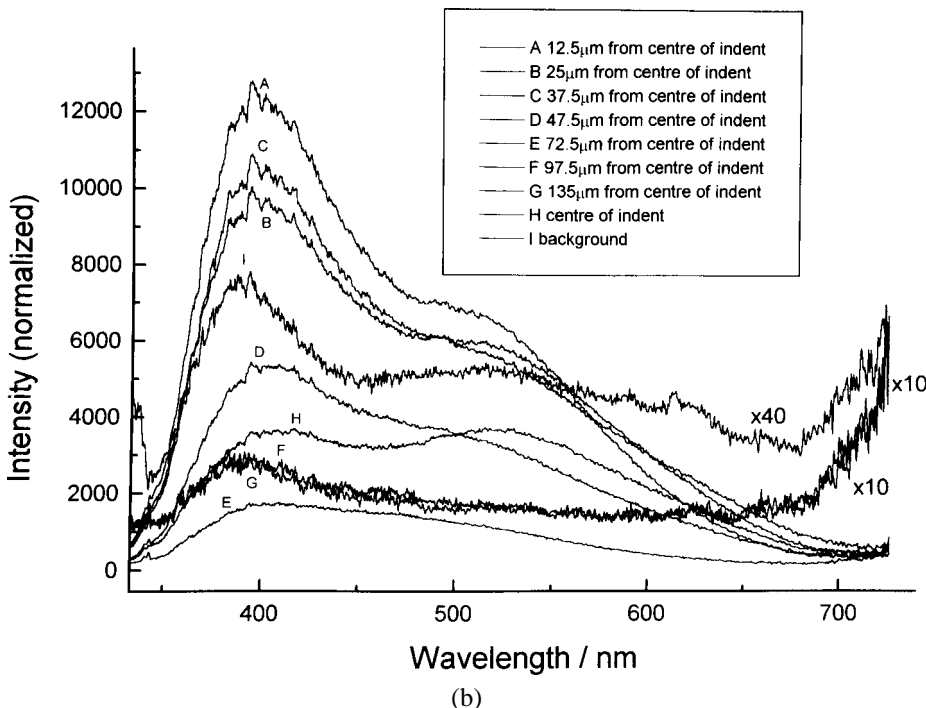


Fig. 59. (Continued).

centres (Fig. 60). Also, for both crystals the background spectra were obtained from the undeformed regions of the crystals.

Both the 99.99% and the 99.9% purity crystals showed quite dramatic effects of indentation and the annealing. It will be seen from Figs 59(a) and 60 that from within the indentations both crystals show a very pronounced band at ~ 375 nm. In other words, contrary to the cathodoluminescence results (Fig. 56), there is no lack of luminescence from within the centres of unannealed indentations. Moreover, the blue band (i.e. $\lambda = 375$ nm) is probably not due to any impurities in the crystals. In addition to the blue band, there is a broad band at ~ 526 nm (see curves B, C, and D in Figs 59(a, b)). On annealing, the character of the luminescence spectra changed in both crystals; the intensity of the 375 nm band decreased, whereas that of the red band (i.e. 526 nm) increased quite markedly. It is this change in the relative intensities of the blue and red bands due to the annealing which changes the colour composition of the cathodoluminescence of indented MgO crystals [14, 100, 133].

Chaudhri and Sands [139] have proposed that in an indented crystal of MgO both F and F^+ centres form due to dislocation interactions and that their number densities depend upon the amount of plastic strain. With increasing strain, the relative number density of F^+ centres also increases and beyond some critical plastic strain a large majority of the colour centres may then be of the F^+ type. Some of the conventional cathodoluminescence detection system may have soda-lime glass windows and therefore they may not be efficient

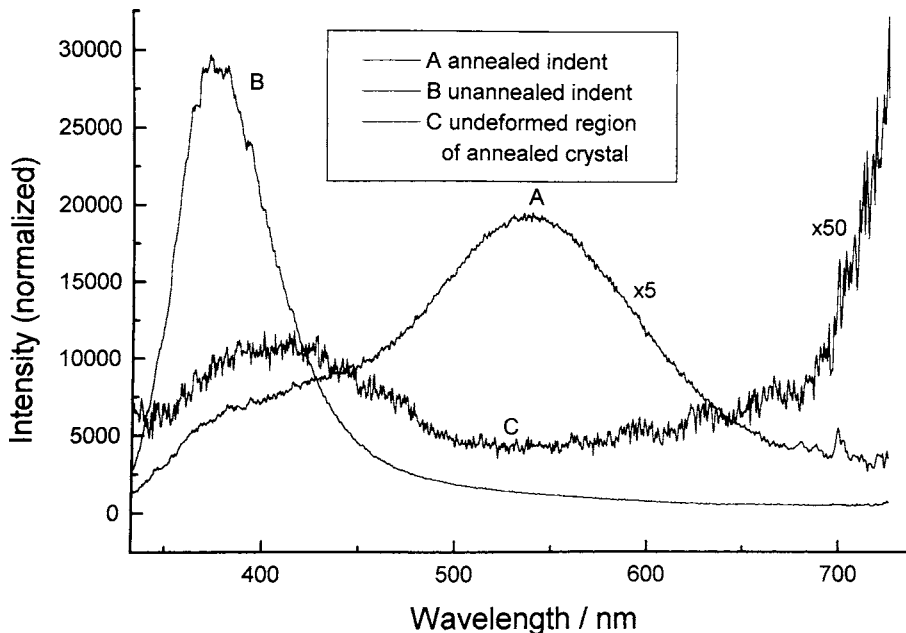


Fig. 60. Photoluminescence spectra taken from the centres of an unannealed 5 kgf Vickers diamond pyramid indent (curve B) and an annealed 5 kgf Vickers indent (curve A) in the 99.9% purity MgO crystal. The background (shown at a magnified intensity) from an undeformed part of the crystal is shown by the curve C. From Chaudhri and Sands [139].

in detecting the near ultraviolet band at 375 nm. This may be a reason why the centre of a Vickers unannealed indentation appears dark. On the other hand, when an indentation is annealed in the temperature range of 800 to 1000°C, some of the F and F⁺ centres are annihilated due to a decrease in the number density of oxygen ion vacancies [142] and some F⁺ centres are converted to F types [125,126]. As a result, in addition to a reduction in the overall intensity of the photoluminescence, the relative intensity of the band at 526 nm increases at the expense of the blue band at 375/395 nm (the annealing causes a shift of the blue band from 375 to 395 nm, but it is not known whether this is an effect of the removal of the residual stress). Figs 59(a) and 59(b) clearly indicate that in the case of the 99.99% purity crystal, the ratio of the peak heights of the 526 nm and the 375/395 nm bands increases from ~ 1/16th at the centre of the unannealed indentation to ~ 1 at the centre of the annealed indent. In the case of the 99.9% purity crystal (Fig. 60), the ratios of the intensities of the 525 and 325 bands are 1/20 to ~ 2.7 at the centres of the unannealed and annealed indentations, respectively. Thus from the overall experimental evidence, Chaudhri and Sands [139] concluded that the indentation enhanced photoluminescence and cathodoluminescence in MgO crystals is due to the creation of colour centres by the dislocation processes taking place during an indentation. It seems likely that the same conclusions will hold for crystals of SrO and CaO.

6.2. Non-oxide materials

It has been known that indentation-induced plasticity also affects the luminescence behaviour of materials other than the metal oxides we discussed in the above. Two such examples are given below.

6.2.1. $\alpha\text{-HgI}_2$

The red phase of mercuric iodide (i.e. α -mercuric iodide) has potential applications as a nuclear radiation detector at room temperature. Since during the handling and storage of this material there is a possibility of generating contact stresses which may lead to plasticity, it is of interest to understand the effect of plastic deformation on its luminescence behaviour. $\alpha\text{-HgI}_2$, has a tetragonal unit cell and its slip system has been determined to be $\{100\}\langle100\rangle$ [143]. Some studies of indentation-enhanced luminescence of single crystals of $\alpha\text{-HgI}_2(100)$ have been made by Petroff et al. [143]. Indentations were made at room temperature under a load of 10 gf and spectrally resolved images of the indentation region were made using a modified scanning transmission electron microscope operating at 150 keV, with the test crystal cooled down to 11 K. Petroff et al. [143] reported a new luminescence band at 2.263 eV (548 nm) from the freshly created dislocations arrays around the indentations. Interestingly, grown-in dislocations in the crystal did not show this band. Petroff et al. [143] attributed the new luminescence band at 2.263 eV to point defects gettered by the dislocations generated by the process of indentation-induced plasticity. However, the nature of the point defects was not discussed by the these workers.

6.2.2. CdTe

Cadmium telluride is an important substrate material on which epitaxial films of solid solution semiconducting devices are deposited. Such devices are operated at low temperatures and it is not known whether in the CdTe substrates plastic yielding could occur at liquid nitrogen temperature due to contact or thermal stresses. If it did, there could be an adverse effect on the performance of the semiconducting device supported on them. To model the effect of such stresses, Tarbaev, Shepel'skii and Schreiber [144] made 30 gf Vickers diamond indentations at 77 K on a single crystal of CdTe(111) and studied the cathodoluminescence behaviour of the indentation region in the temperature range of 4.2 to 77 K. They reported the emission of two new bands at 800 and 804.2 nm from the plastically deformed region. These new bands were attributed by these workers to metastable point defects generated by moving dislocations. These defects were thought to be metastable because if the indented crystal was allowed to warm up to the room temperature and then kept at this temperature for 1 h, these bands disappeared [144]. However, the nature of these point defects was not clarified either.

It is interesting that despite the new luminescence bands the integrated cathodoluminescence intensity was found to decrease by the process of dislocation quenching of the cathodoluminescence. Such quenching of the cathodoluminescence by mobile dislocations has been observed in other semiconductors as well (e.g. InP [70]).

7. Nano indentation and dislocations

Some reference to nano indentations has already been made in Section 2. Here brief details of the technique and relevant results obtained using it are given.

During the last 15–20 years several types of commercial indentation instrument have been developed which are capable of applying indenter loads as small as $1 \mu\text{N}$. Generally, in these machines Berkovich indenters are employed, especially, as said before, the radii of the tips of such indenters are much smaller than those of the tips of Vickers indenters. An important feature of such instruments is that during an indentation test, both the indenter load and the indenter displacement can be recorded continuously and simultaneously. However, since most of the machines are computer-operated, experimental data are usually logged at pre-selected time intervals. A typical time interval is about a third of a second. The indenter load P and indenter displacement h can be measured to accuracy of $< 0.05 \mu\text{N}$ and $< 0.2 \text{ nm}$, respectively. Indentations made using such machines are usually about a μm across or smaller and are often referred to as nano indentations.

A schematic diagram of a typical nano indentation machine is shown in Fig. 61. A sensitive load cell is rigidly fixed to a cross-beam, which is capable of moving up or down at a controlled speed along a load frame, as shown in the figure. A stiff indenter shaft, with an indenter fixed rigidly on one end, is mounted on the load cell. A rigid bracket is held firmly with screws on to the indenter shaft and at a small distance from it a displacement transducer, usually a non-contact type, is also fixed to the bracket with screws. The test specimen is placed on the sample base, which in turn is placed on the load frame, as shown.

The outputs of the load cell and the displacement transducer are fed into a computer or an X-Y chart recorder. Therefore, throughout indenter loading and unloading a complete record of the indenter load and the corresponding indenter displacement can be obtained.

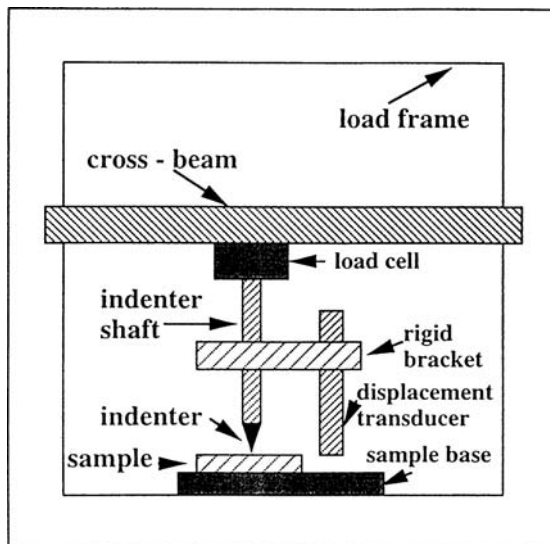


Fig. 61. Schematic diagram of a typical nano indentation apparatus.

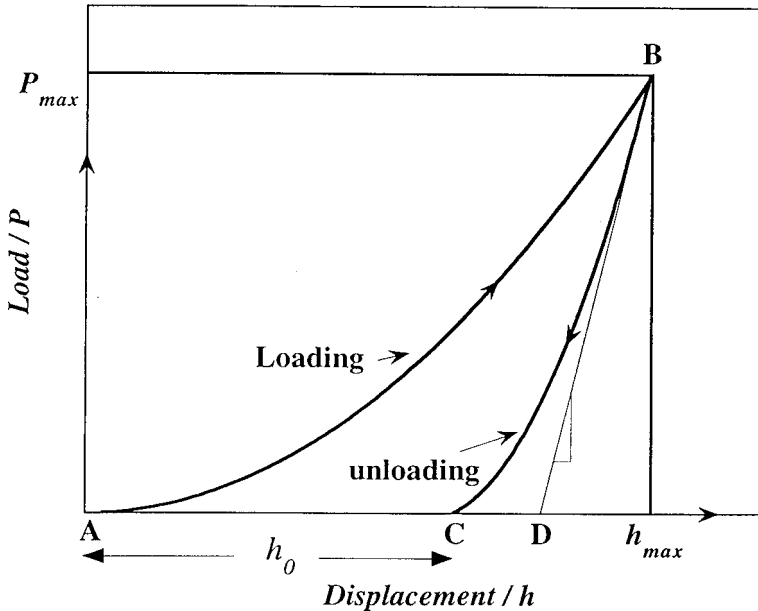


Fig. 62. Schematic representation of the elastic/plastic response of a solid flat surface as recorded with a monitoring instrument giving a continuous record of indenter load P versus indenter displacement h . AB and BC represent, respectively, the loading and unloading curves. The maximum indenter tip penetration h_{max} below the original flat surface occurs when the maximum load P_{max} is applied on the indenter. AD represents the contact depth h_c of the indentation.

A schematic diagram of a typical indenter loading–unloading curve for an elastic–plastic solid is shown in Fig. 62. The loading part of the curve is AB and the unloading part is BC, from which the indentation plastic contact depth h_c can be obtained (h_c is approximately equal to AD, depending on the shape of the indenter). AC represents the depth below the original indented surface of the residual indentation after the indenter load has been reduced to zero.

Since unloaded nano indentations are generally smaller than a μm across, it is difficult to measure accurately their sizes under an optical microscope. It is much more accurate to image them using a well calibrated atomic force microscope, a scanning tunnelling microscope, or a scanning/transmission electron microscope. The projected areas of indentations can then be obtained accurately from such images. However, during the last 10 to 15 years the unloading part of the load vs displacement curve has been extensively used for obtaining the projected areas of nano indentations [145,146]. But there are very serious problems with this approach, as the indentation contact areas determined from an analysis of the unloading part of the load–displacement curve has been shown to give errors of up to 50% [147,148].

When a nano indentation test is carried out on a crystalline solid with a low dislocation density so that the indenter tip loads on to a dislocation-free area, then, because the indenter tip is not a perfect point but is a small sphere of a radius of ~ 100 nm or even less, at very

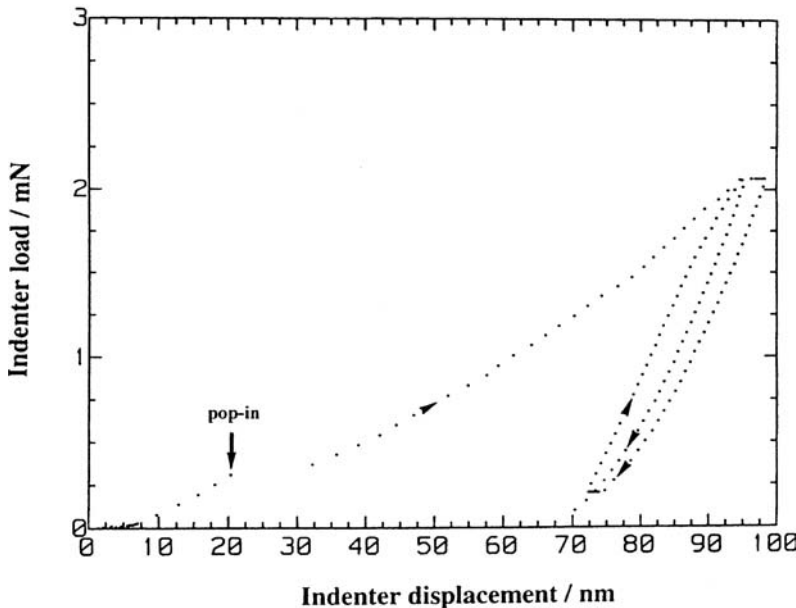


Fig. 63. Typical indenter load versus indenter displacement curve when a Berkovich diamond indenter is loaded on to a cleaved MgO(100) single crystal. When the load reaches a value of about 0.25 mN, a sudden jump of about 12 nm (i.e. from 20 to 32 nm) occurs in the indenter displacement; this sudden jump is thought to be related to the ‘pop-in’ of dislocations. From Chaudhri [149].

low indenter loads the deformation of the specimen surface is purely elastic. However, when the indenter load is increased to a sufficiently high value, homogeneous nucleation of dislocations occurs rather suddenly. At this stage the calculated mean contact pressure is $\sim 2.2k$, where, as before, k is the shear yield stress of the solid. On the load–displacement curve the abrupt nucleation of dislocations (also sometimes called ‘pop-in’ of dislocations) results in a step increase in indenter displacement or a sudden load drop, depending upon the type of the indentation machine being used. An example of such a pop-in of dislocations in a cleaved single crystal of MgO(100) is shown in Fig. 63 [149]. In this figure when the indenter load reaches just over 0.25 mN the displacement suddenly increases from 20 nm to 32 nm. Similar observations from nano indentations tests on cleaved MgO(100) crystals have been made by Woigard et al. [150]. These authors showed that associated with the step jumps in the indenter displacements were slip bands on the indented surface of the crystal around the indentations.

Transmission electron microscopy of single crystals of 6H-SiC(0001) which showed an abrupt jump in indenter displacement during a nano indentation test using a Berkovich indenter has also been carried out recently by Page, Riester and Hainsworth [151]. These workers found that for indenter loads of up to 1 mN, the behaviour of the 6H-SiC(0001) was perfectly elastic. However, when the load was increased to 1.5 mN, a single pop-in event occurred. The estimated maximum shear stress just below the contact corresponding to this load was $\sim G/20$, where G is the shear modulus of the silicon carbide. Such a high

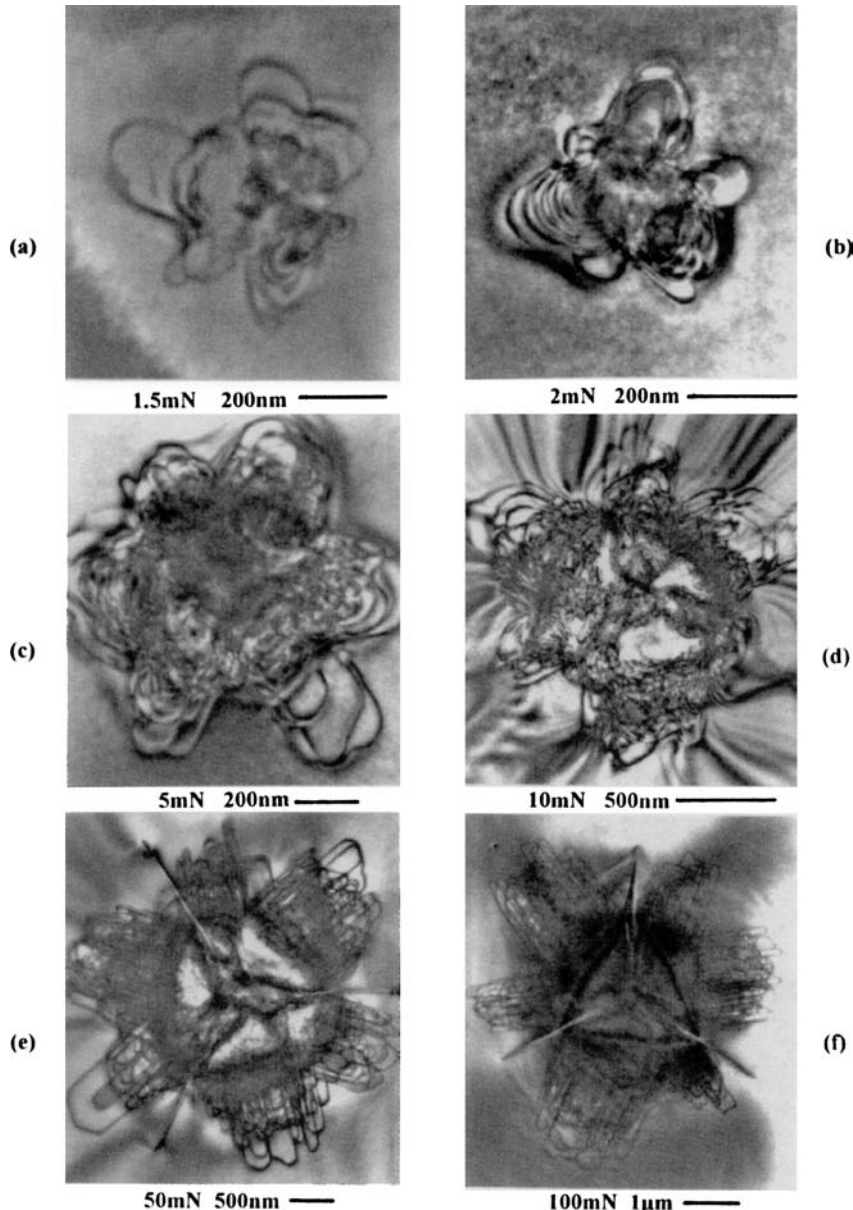


Fig. 64. Transmission electron microscope images of Berkovich nano indentations on the basal plane of single crystals of 6H-SiC for various indenter loads in the range of 1.5 to 100 mN. In (a) 3–4 dislocation loops can be seen around each of the three indentation sides; the corresponding load-displacement curve also showed a sudden jump in the indenter displacement as the indenter load was increased to 1.5 mN (not shown here). Frames (b) to (f) show that as the indenter load was increased, the dislocation density around the indentation also increased. All the micrographs are bright-field multi-beam images close to $(30\bar{3}0)$ 2-beam diffraction conditions. The load for each indentation is shown below the micrograph. After Page, Riester and Hainsworth [151].

value of the shear yield stress may be regarded as a reasonably good piece of evidence for homogeneous nucleation of dislocations. It was revealed in the TEM studies [151] that at this stage only 3–4 dislocation loops had formed around each of the three indentation sides. Moreover, the dislocation loop diameters were comparable to the indentation size (see Fig. 64(a)). Several specimens of the silicon carbide were examined in the TEM, each of which had a single indentation made under a different indenter load up to a maximum of 100 mN. The authors reported that with increasing indentation size the dislocation number density also increased (see Fig. 64(b–f)). This experimental result of the authors is particularly interesting, as it appears to contradict those theories of nano hardness, which predict an increase in dislocation density with decreasing nano indentation size (e.g. [11, 152]). It would be particularly useful to carry out similar TEM studies on other materials so that a general picture may be developed for the relation between indentation size and the corresponding dislocation density within the deformation zone.

8. Concluding remarks

Since the prediction of the existence of dislocations by Taylor [153], Orowan [154] and Polanyi [155] in the 1930s and the direct evidence of their existence in the 1950s by Hirsch, Horne and Whelan [156] using transmission electron microscopy and by Gilman and Johnston [13] using the etch pitting technique, very significant advances have been made in our understanding of the indentation processes in crystalline materials and we have progressed much further than was possible using the continuum mechanics slip-line field theory of Hill, Lee and Tupper [79]. Thus in this article it has been shown that when a hard pointed indenter is loaded on to a solid, the stress field is such that even the hardest material has been found to deform plastically around room-temperature indentations. Associated with the plasticity are the processes of nucleation and growth of dislocations. The former process has been shown to occur within the material in the immediate vicinity of the indenter, where the hydrostatic component of the stress has been estimated to be about a half of the indentation hardness of the indented material. It is this hydrostatic pressure which tends to inhibit the occurrence of cracking even in very brittle materials and encourages the development of the shear stress and the ensuing plasticity. There is, however, one material, namely Si, in which the material within a room-temperature indentation has been found to be without any dislocations, and, in fact, has been shown by several investigators to be amorphous. It has been suggested that the amorphisation follows a phase transition from the cubic Si to the tetragonal β -Sn phase during indenter loading, which on the removal of the load does not appear to transform back to the cubic phase, but becomes amorphous instead. However, some recent work of Saka and his coworkers [43] has indicated that this situation may not always occur, especially when the indenter load is relatively high, namely 50 gf. There is also the possibility that the material within an unloaded indentation in Si may be nanocrystalline, instead of being amorphous. Clearly, further work is required to resolve this problem.

It has also been shown that the heavily deformed material within an indentation in a crystalline solid has the same orientation as that of the original unindented surface. But,

because of the very large plastic strains which exist within the indented material, the electron diffraction spots show severe asterism. The latter, however, can be removed by careful annealing.

On a slightly larger scale, it has been shown how arrays of dislocations, distributed symmetrically, form around an indentation and create dislocation rosettes. The lengths of the rosette arms have been found to depend systematically on the indenter load and the strength properties of the indented surface. Using the elastic stress field of an indentation [7], analytical expressions have been developed which fit the experimental observation well.

In the case of spherical indenters, the process of nucleation and growth of dislocations within an indented specimen can be followed in a more controlled way and now with the availability of sensitive nanoindentation instruments and well-characterised indenter radii, it is becoming possible to investigate homogeneous nucleation of dislocations in a wide variety of materials.

It has also been shown in this article how the optical properties of heavily dislocated regions around indentations are altered in a striking manner. New luminescence bands around indentations in some materials have been observed, which have been thought to arise due to the point defects created by dislocation interactions. In addition to creating new luminescence bands, indentation-induced dislocations can also cause quenching, especially in semiconductor materials.

On a macroscopic scale, it has been shown how dislocation interactions around indentations can lead to cracking and how such cracks around dynamic indentations can be followed with high-speed photography to measure dislocation velocities in transparent ionic crystals in the high-velocity regime.

There are several other indentation-related phenomena, which have not been covered in this article. These are chemomechanical effects in non-metals, photoplastic effects in semiconductors, and charged dislocations in ionic crystals; these effects have been reviewed by Westwood, Ahearn and Mills [157], Koubaiti et al. [158] and Maeda and Takeuchi [159], and by Whitworth [160], respectively.

As for the future important directions for studies of dislocations and indentations, convincing evidence for the existence of dislocations within room-temperature indentations in very hard materials, such as diamond, still needs to be obtained. Since the processes of specimen thinning can give rise to artefacts, it would be appropriate to avoid the thinning process altogether. This can be achieved by starting with a thin enough specimen ($\sim 0.5 \mu\text{m}$ in thickness) which is transparent to the electron beam of a transmission electron microscope. Such a specimen can then be indented, using a suitable nanoindentation machine, at very low loads to produce crack-free indentations of depth of $0.1 \mu\text{m}$ or less. An examination of such an indented specimen in the electron microscope should be able to provide a more complete and uncontaminated picture of the dislocation processes within indentations.

Another important area is related to the understanding of the variation of nano hardness of materials of different strain-hardening characteristics with indenter load. Careful measurements have shown [148] that the nano hardness behaviour of f.c.c. metals, such as copper, depends upon the prior plastic strain within the test sample. It has, so far, not been possible to explain fully this behaviour using the existing models, but it is believed

that a good understanding of the creation and mobility of dislocation loops around the indentation may provide a satisfactory answer.

Acknowledgements

I should like to express my thanks to Dr E.H. Yoffe for many discussions, suggestions and critical comments on this piece of work. I should also like to thank Professors J.J. Gilman, K.E. Puttick and T. Suzuki for their comments on the indentation processes in Si. Furthermore, I am very grateful to Dr R. Hannink, Professors J.J. Gilman, K.E. Puttick, D. Rowcliffe, H. Saka and T. Suzuki for providing glossy prints of their published works. Finally, I should like to thank the Editor, Professor F.R.N. Nabarro for constructive and critical comments on the manuscript.

Note added in the proof

Since the submission of this article, a considerable amount of further work has been carried out on understanding indentation-induced phase transitions in single crystals of the cubic silicon (Si-I) and amorphous films of silicon. One of the relatively new and sensitive non-contact techniques being used at present for such studies is Raman spectroscopy. A particular advantage of Raman spectroscopy, especially when the power of the exciting laser beam is kept below about 5 mW, is that any artefacts are unlikely to be introduced into the test sample undergoing a Raman scattering examination. Thus in recent Raman microscopy investigations of Vickers diamond indentations made at 300 and 77 K in single crystals of Si(100) (i.e. Si-I) and 0.3 μm thick amorphous silicon ($a\text{-Si}$) deposited on a 0.4 mm thick plate of sapphire (1 $\bar{1}$ 02), some quite dramatic results have been reported by Khayyat, Banini, Hasko and Chaudhri [161]. In the case of 0.98 N residual Vickers indentations made at 300 K in a single crystal of silicon, several Raman peaks due to the Si-III phase and a peak due to the Si-I phase were found but there was little evidence of the existence of the amorphous phase of silicon. When the amorphous silicon film was indented at 300 K with a Vickers diamond under a load of 137 mN, the Raman spectrum of the material from within the residual indentation was found to show strong, sharp peaks corresponding to the Si-III phase. In addition, a weak peak due to the Si-I phase was also found, suggesting that possibly indentation-induced crystallization to the cubic Si-I had also occurred. However, some broad bands still existed, possibly corresponding to the amorphous silicon and to the Si-III phase.

On the other hand, when Vickers diamond indentations were made in the crystalline silicon (i.e. Si-I) and in the amorphous silicon film at 77 K, under loads of 9.8 and 7.85 N, respectively, the residual indentations which were examined after the indented samples had gradually warmed up to 300 K, revealed that neither in the crystalline silicon nor in the amorphous silicon any crystallization or phase transitions had occurred.

Based on these observations, Khayyat et al. [161] suggested that during Vickers indentations in single crystal silicon and in amorphous silicon at 300 K there is a significant temperature rise within the deformation zone, which helps the process of phase transition

to the Si-II phase during loading. The latter then converts to the Si-III phase on indenter removal. When indentations were made in the crystalline silicon and in the amorphous silicon at 77 K, indentation-induced temperature rise was kept to a minimum and as a result there was no transition to the Si-II phase during indenter loading and, therefore, when the indenter was removed, the Si-III phase did not form. Further experimental work on the influence of sample temperature on the phenomenon of indentation-induced phase transitions in important elemental semiconductors, such as silicon and germanium, will help clarify the processes involved.

References

- [1] H.R. Thomas and V.A. Hoersch, Bull. Univ. Ill. Engng Exp. Sta. no. 212 (1930). (This paper is for the case of a cylinder loading on to a flat surface, and it appears to be the first in which it was predicted and observed that the onset of plasticity occurs some distance below the loaded surface.)
- [2] R.M. Davies, Proc. Roy. Soc. (London) A197 (1949) 416.
- [3] I.N. Sneddon, Int. J. Engng. Sci. 3 (1965) 47.
- [4] A.E.H. Love, Quarterly J. Mathematics (Oxford Series) 10 (1939) 161.
- [5] R.F. Bishop, R. Hill and N.F. Mott, Proc. Phys. Soc. (London) 57 (1945) 147.
- [6] S.S. Chiang, D.B. Marshall and A.G. Evans, J. Appl. Phys. 53 (1982) 298.
- [7] E.H. Yoffe, Philos. Mag. A 46 (1982) 617.
- [8] K.W. Peter, J. Non-crystalline Solids 5 (1970) 103.
- [9] C. Hardy, C.N. Baronet and G.V. Tordion, J. Numer. Methods in Engng. Sci. 3 (1971) 451.
- [10] M.G. Walls, M.M. Chaudhri and T.B. Tang, J. Phys. D 25 (1992) 500.
- [11] N.A. Stelmashenko, M.G. Walls, L.M. Brown and Yu.V. Milman, Acta Metall. Mater. 41 (1993) 2855.
- [12] H. Hertz, in: *Miscellaneous Papers* (Macmillan, New York, 1896) Chapters 5 and 6.
- [13] J.J. Gilman and W.G. Johnston, in: *Dislocations and Mechanical Properties of Crystals*, eds J.C. Fisher, W.G. Johnston, R. Thomson and T. Vreeland (Wiley, New York, 1957) p. 116.
- [14] M.A. Velednitskaya, V.N. Rozhanskii, L.F. Comolova, G.V. Saparin, J. Schreiber and O. Brummer, Phys. Status Solidi A 32 (1975) 123.
- [15] M.V. Swain and B.R. Lawn, Phys. Status Solidi 35 (1969) 909.
- [16] A.H. Cottrell, *The Mechanical Properties of Matter* (Wiley, London, 1964) p. 271.
- [17] J.J. Gilman and W.G. Johnston, in: *Dislocations and Mechanical Properties of Crystals*, eds J.C. Fisher, W.G. Johnston, R. Thomson and T. Vreeland (Wiley, New York, 1957) p. 517.
- [18] J.D. Kiely and J.E. Houston, Phys. Rev. B 57 (1998) 12 588.
- [19] E.M. Nadgornyj and A.V. Stepanov, Sov. Phys. Solid State 5 (1963) 732.
- [20] A.S. Keh, J. Appl. Phys. 31 (1960) 1538.
- [21] J.J. Gilman, *Micromechanics of Flow in Solids* (McGraw-Hill, New York, 1969) p. 53.
- [22] M.T. Sprackling, *The Plastic Deformation of Simple Ionic Crystals* (Academic Press, London, 1976) p. 23.
- [23] A.A. Predvoditelev, V.N. Rozhanskii and V. M. Stepanova, Sov. Phys. Crystallography 7 (1962) 330.
- [24] M.M. Chaudhri, Phil. Mag. A 53 (1986) L55.
- [25] J.D. Eshelby, F.C. Frank and F.R.N. Nabarro, Philos. Mag. 42 (1951) 351.
- [26] I.V. Gridneva, Yu.V. Milman, V.I. Trefilov and S.I. Chugunova, Phys. Status Solidi A 54 (1979) 195.
- [27] M.P. Shaskol'skaya and G.F. Dobrzhanskii, Sov. Phys. Crystallography 7 (1962) 83.
- [28] R.W. Davidge, J. Mater. Sci. 2 (1967) 339.
- [29] P.F. Stublein, J. Appl. Phys. 34 (1963) 1867.
- [30] W. Rinder and R.F. Tramposch, J. Appl. Phys. 34 (1963) 758.
- [31] R.F. Tramposch and W. Rinder, Appl. Phys. Lett. 3 (1963) 42.
- [32] M.G. Mil'vidskii, V.B. Osvenskii and O.G. Stolyarov, Sov. Phys. Crystallography 12 (1968) 896.
- [33] V.B. Osvenskii, O.G. Stolyarov and M.G. Mil'vidskii, Sov. Phys. Solid State 10 (1969) 2540.
- [34] K. Sumino and H. Hasegawa, Trans. JIM 9 (supplement) (1968) 749.

- [35] S.M. Hu, *J. Appl. Phys.* 46 (1975) 1465.
- [36] S.M. Hu, *J. Appl. Phys.* 46 (1975) 1470.
- [37] V.G. Eremenko and V.I. Nikitenko, *Phys. Status Solidi* 14 (1972) 317.
- [38] S.G. Roberts, P. Pirouz and P.B. Hirsch, *J. de Phys.* 44 (1983) C4-75.
- [39] M. Yoshioka, *J. Appl. Phys.* 76 (1994) 7790.
- [40] T. Suzuki and T. Ohmura, *Philos. Mag.* A74 (1996) 1073.
- [41] M.J. Hill and D.J. Rowcliffe, *J. Mater. Sci.* 9 (1974) 1569.
- [42] K.E. Puttick, M.A. Shahid and M.M. Hosseini, *J. Phys. D* 12 (1979) 195.
- [43] A. Shimatani, T. Nango, Suprijadi and H. Saka, *Proc. Mat. Res. Soc. Symp.* 522 (1998) 71.
- [44] S.M. Hu, *Appl. Phys. Lett.* 31 (1977) 53.
- [45] M. Akatsuka, K. Sueoka, H. Katahama, N. Morimoto and N. Adachi, *Jpn. J. Appl. Phys.* 36 (1997) L 1422.
- [46] S.G. Roberts, P. Pirouz and P.B. Hirsch, *J. Mater. Sci.* 20 (1985) 1739.
- [47] K. Maeda, O. Ueda, Y. Murayama and K. Sakamoto, *J. Phys. Chem. Solids* 38 (1977) 1173.
- [48] P.B. Hirsch, P. Pirouz, S.G. Roberts and P.D. Warren, *Philos. Mag. B* 52 (1985) 759.
- [49] M. Mihara and T. Ninomiya, *Phys. Status Solidi A* 32 (1975) 43.
- [50] P.D. Warren, P. Pirouz and S.G. Roberts, *Philos. Mag. A* 50 (1984) L23.
- [51] C. Levade and G. Vanderschaeve, *Phys. Status Solidi A* 171 (1999) 83.
- [52] I.P. Kushnir, L.K. Mikhailova and Yu.A. Osip'yan, *Sov. Phys. Crystallography* 10 (1965) 68.
- [53] C.C. Chen and A.A. Hendrickson, in: *The Science of Hardness Testing and its Research Applications*, eds J.H. Westbrook and H. Conrad (American Society for Metals, Metals Park, Ohio, 1973) p. 274.
- [54] L.D. Dyer, *Trans. ASM* 58 (1965) 620.
- [55] J.D. Livingston, in: *Direct Observation of Imperfections in Crystals*, eds J.B. Newkirk and J.H. Wernick, (Interscience, New York, 1962) p. 115.
- [56] C.C. Chen and A.A. Hendrickson, *J. Appl. Phys.* 42 (1971) 2208.
- [57] G.M. Pharr and W.C. Oliver, *J. Mater. Res.* 4 (1989) 94.
- [58] D. Tabor, *Proc. Roy. Soc. A* 192 (1948) 247.
- [59] M.M. Chaudhri, *Philos. Mag. A* 74 (1996) 1213.
- [60] M.M. Chaudhri, J.K. Wells and A. Stephens, *Philos. Mag. A* 43 (1981) 643.
- [61] A.S. Keh, J.C.M. Li and Y.T. Chou, *Acta Met.* 7 (1959) 694.
- [62] R.W. Armstrong and C.C. Wu, *J. Amer. Ceram. Soc.* 61 (1978) 102.
- [63] J.T. Hagan, *J. Mater. Sci.* 14 (1979) 2975.
- [64] M.M. Chaudhri, *Proc. 16th Intl. Cong. on High-Speed Photography and Photonics*, Strasbourg, France 1984, SPIE 491 (1985) 595.
- [65] S.V. Hooker and W.F. Adler, in: *Fracture Mechanics of Ceramics*, Vol. 3, eds R.C. Bradt, D.P.H. Hasselman and F.F. Lange (Plenum, New York, 1978) p. 333.
- [66] N. Khasgiwale and H.M. Chan, *Acta Met.* 43 (1995) 207.
- [67] M.M. Chaudhri and Y. Enomoto, *Wear* 233–235 (1999) 717.
- [68] Yu.S. Boyarskaya, R.P. Zhitaru, D.Z. Grabko and V.A. Rahvalov, *J. Mater. Sci.* 33 (1998) 281.
- [69] M.Y. Khan, L.M. Brown and M.M. Chaudhri, *J. Phys. D* 25 (1992) A257.
- [70] E. Le Bourhis, J.P. Rivière and A. Zozime, *J. Mater. Sci.* 31 (1996) 6571.
- [71] F.C. Serbena, W.S. Williams and S.G. Roberts, *J. Hard-Mater.* 6 (1995) 17.
- [72] C.A. Brookes, *Wear* 9 (1966) 103.
- [73] T. Takahashi and E.J. Freise, *Philos. Mag.* 12 (1965) 1.
- [74] S. Bartolucci and H.H. Schlössin, *Acta Met.* 14 (1966) 337.
- [75] S.B. Luyckx, *Acta Met.* 18 (1970) 233.
- [76] M.K. Hibbs and R. Sinclair, *Acta Met.* 29 (1981) 1645.
- [77] M.K. Hibbs, R. Sinclair and D.J. Rowcliffe, *Acta Met.* 32 (1984) 941.
- [78] S.B. Luyckx, F.R.N. Nabarro, S.-W. Wai and M.N. James, *Acta Met.* 40 (1992) 1623.
- [79] R. Hill, E.H. Lee and S.J. Tupper, *Proc. Roy. Soc. A* 188 (1947) 273.
- [80] M.M. Chaudhri, *Phil. Mag. Lett.* 67 (1993) 107.
- [81] M.M. Chaudhri, C.G. Knight and M.V. Swain, *Proc. 12th Intl. Congress on High-Speed Photography*, Toronto 1976, SPIE 97 (1977) 371.
- [82] S.V. Lubenets and V.I. Startsev, *Sov. Phys.—Solid State* 10 (1968) 15.

- [83] J.J. Gilman, Micromechanics of Flow in Solids (McGraw-Hill, New York, 1969) p. 180.
- [84] R.J. Clifton, Inst. Phys. Conf. Ser. No. 47 (The Institute of Physics, London, 1979) p. 174.
- [85] S.D. Berger, Ph.D. dissertation (University of Cambridge, 1984).
- [86] D. Tabor, in: Microindentation Techniques in Materials Science and Engineering, ASTM STP 889, eds P.J. Blau and B.R. Lawn (American Society for Testing and Materials, Philadelphia, 1986) p. 129.
- [87] R.K. Ham, Philos. Mag. 7 (1962) 1177.
- [88] U. Valdré and P.B. Hirsch, Philos. Mag. 8 (1963) 237.
- [89] H.M. Naguib and R. Kelly, Radiation Effects 25 (1975) 1.
- [90] M.Y. Khan, L.M. Brown and M.M. Chaudhri, J. Electron Microscopy Technique 15 (1990) 377.
- [91] O.W. Johnson and P. Gibbs, in: Fracture of Solids, eds D.C. Drucker and J.J. Gilman (Interscience, New York, 1963) p. 315.
- [92] V.I. Nikitenko, M.M. Myshlyaev and V.G. Eremenko, Sov. Phys.—Solid State 9 (1968) 2047.
- [93] D.R. Clarke, M.C. Kroll, P.D. Kirchner, R.F. Cook and D.B. Hockey, Phys. Rev. Lett. 60 (1988) 2156.
- [94] D.L. Callahan and J.C. Morris, J. Mater. Res. 7 (1992) 1614.
- [95] I.V. Gridneva, Yu.V. Milman and V.I. Trefilov, Phys. Status Solidi A 14 (1972) 177.
- [96] V.I. Trefilov and Yu.V. Milman, Sov. Phys. Doklady 8 (1964) 1240.
- [97] J.Z. Hu, L.D. Merkle, C.S. Menoni and I.L. Spain, Phys. Rev. B 34 (1986) 4679.
- [98] J.J. Gilman, Czech. J. Phys. 45 (1995) 913.
- [99] L.M. Brown, M.Y. Khan and M.M. Chaudhri, Philos. Mag. A57 (1988) 187.
- [100] M.Y. Khan, Ph.D. dissertation (University of Cambridge, 1988).
- [101] V.N. Rozhanski, M.P. Nazarova, I.L. Svetlov and L.K. Kalashnikova, Phys. Status Solidi 41 (1970) 579.
- [102] B.J. Hockey, J. Amer. Ceram. Soc. 54 (1971) 223.
- [103] B.J. Hockey, in: The Science of Hardness Testing and its Research Applications, eds J.H. Westbrook and H. Conrad (American Society for Metals, Metals Park, Ohio, 1973) p. 21.
- [104] M.L. Kronberg, Acta Met. 5 (1957) 507.
- [105] S. Amelinckx, in: Dislocations in Solids, Vol. 2, ed. F.R.N. Nabarro (Elsevier, Amsterdam, 1979) p. 400.
- [106] D.L. Callahan, Ultramicroscopy 69 (1997) 13.
- [107] E.B. Leiko, A. Luft and E.M. Nadgornii, Phys. Status Solidi A 44 (1977) 285.
- [108] W. Zielinski, H. Huang, S. Venkatraman and W.W. Gerberich, Philos. Mag. A72 (1995) 1221.
- [109] Q. Ma and D.R. Clarke, J. Mater. Res. 10 (1995) 853.
- [110] C.G. Peters and F. Knoop, Metals and Alloys 13 (1940) 292.
- [111] C.A. Brookes, Nature 228 (1970) 660.
- [112] P. Humble and R.H.J. Hannink, Nature 273 (1978) 37.
- [113] T. Evans and R.K. Wild, Philos. Mag. A12 (1965) 479.
- [114] S. Fujita, K. Maeda and S. Hyodo, Philos. Mag. A 55 (1987) 203.
- [115] K. Maeda, K. Suzuki, S. Fujita, M. Ichihara and S. Hyodo, Philos. Mag. A57 (1988) 573.
- [116] C.-D. Qin and S.G. Roberts, Inst. Phys. Conf. Ser. No. 104 (Institute of Physics, Bristol, 1989) p. 409.
- [117] M.H. Lewis, R. Fung and D.M.R. Taplin, J. Mater. Sci. 16 (1981) 3437.
- [118] F. Seitz, Adv. Phys. 1 (1952) 43.
- [119] G.A. Andreev and B.I. Smirnov, in: Defects in Crystals, ed. E. Mizera (World Scientific, Singapore, 1987) p. 357.
- [120] J.H. Wertz, J.W. Orton and P. Auzins, Dicuss. Faraday Soc. 31 (1961) 140.
- [121] G.K. Walters and T.L. Estle, J. Appl. Phys. 32 (1961) 1854.
- [122] W.B. Gager, M.J. Klein and W.H. Jones, Appl. Phys. Lett. 5 (1964) 131.
- [123] M.J. Klein and W.B. Gager, J. Appl. Phys. 37 (1966) 4112.
- [124] Y. Chen, M.M. Abraham, L.C. Templeton and E. Sonder, Solid State Commun. 18 (1976) 61.
- [125] Y. Chen, J.L. Kolopus and W.A. Sibley, Phys. Rev. 186 (1969) 865.
- [126] L.A. Kappers, R.L. Kroes and E.B. Hensley, Phys. Rev. B1 (1970) 4151.
- [127] G.H. Rosenblatt, M.W. Rowe, G.P. Williams, R.T. Williams, Jr. and Y. Chen, Phys. Rev. B39 (1989) 10309.
- [128] P. Edel, B. Henderson, Y. Merle d'Aubinge, R. Romestain and L.A. Kappers, J. Phys. C 12 (1979) 5245.
- [129] Y. Chen, M.M. Abraham, T.J. Turner and C.M. Nelson, Philos. Mag. 32 (1975) 99.
- [130] S. Datta, I.M. Boswara and D.B. Holt, J. Phys. Chem. Solids 40 (1979) 567.
- [131] S.J. Pennycook and L.M. Brown, J. Lumin. 18/19 (1979) 905.

- [132] M.M. Chaudhri, J.T. Hagan and J.K. Wells, *J. Mater. Sci.* 15 (1980) 1189.
- [133] T.A. Nazarova, M.V. Nazarov, E.I. Rau and G.V. Saparin, *Scanning* 14 (1992) 91.
- [134] Yu.S. Boyarskaya, M.V. Nazarov, T.A. Nazarova, A.R. Gareeva and R.P. Zhitaru, *Phys. Status Solidi A* 142 (1994) 35.
- [135] Y. Enomoto and K. Yamanaka, *J. Mater. Sci.* 17 (1982) 3288.
- [136] J. Piqueras, J. Llopis and L. Delgado, *J. Appl. Phys.* 52 (1981) 4341.
- [137] J.T. Dickinson, L.C. Jensen, R.L. Webb and S.C. Langford, *J. Non-Cryst. Solids* 177 (1994) 1.
- [138] C. Ballesteros, J. Llopis and J. Piqueras, *J. Appl. Phys.* 53 (1982) 3201.
- [139] M.M. Chaudhri and H.S. Sands, *J. Appl. Phys.* 82 (1997) 785.
- [140] J.R. Nelson, *Phys. Rev.* 99 (1955) 1902.
- [141] D.M. Roessler and W.C. Walker, *Phys. Rev.* 159 (1967) 733.
- [142] W.A. Sibley, J.L. Kolopus and W.C. Mallard, *Phys. Status Solidi* 31 (1969) 223.
- [143] P.M. Petroff, Y.P. Hu and F. Milstein, *J. Appl. Phys.* 66 (1989) 2525.
- [144] N.I. Tarbaev, G.A. Shepel'skii and J. Schreiber, *Sov. Phys. Solid State* 31 (1989) 1348.
- [145] J.L. Loubet, J.M. Georges, O. Marchesini and G. Meille, *J. Tribology* 106 (1984) 43.
- [146] W.C. Oliver and G.M. Pharr, *J. Mater. Res.* 7 (1992) 1564.
- [147] Y.Y. Lim, M.M. Chaudhri and Y. Enomoto, *J. Mater. Res.* 14 (1999) 2314.
- [148] Y.Y. Lim and M.M. Chaudhri, *Philos. Mag. A* 79 (1999) 2979.
- [149] M.M. Chaudhri, *Philos. Mag. Lett.* 77 (1998) 7.
- [150] J. Woigard, C. Tromas, V. Audurier and J.C. Girard, *Mat. Res. Soc. Symp. Proc.* 522 (1998) 65.
- [151] T.F. Page, L. Riester and S.V. Hainsworth, *Mat. Res. Soc. Symp. Proc.* 522 (1998) 113.
- [152] W.J. Poole, M.F. Ashby and N.A. Fleck, *Scripta Mater.* 34 (1996) 559.
- [153] G.I. Taylor, *Proc. Roy. Soc. (London)* A145 (1934) 362.
- [154] E. Orowan, *Zeit. Phys.* 89 (1934) 605, 614, 634.
- [155] M. Polanyi, *Zeit. Phys.* 89 (1934) 660.
- [156] P.B. Hirsch, R.W. Horne and M.J. Whelan, *Philos. Mag.* 1 (1956) 677.
- [157] A.R.C. Westwood, J.S. Ahearn and J.J. Mills, *Colloids and Surfaces* 2 (1981) 1.
- [158] S. Koubaiti, J.J. Couderc, C. Levade and G. Vanderschaeve, *Acta Mater.* 44 (1996) 3279.
- [159] K. Maeda and S. Takeuchi, in: *Dislocations in Solids*, Vol. 10, eds F.R.N. Nabarro and M.S. Duesbery (Elsevier, Amsterdam, 1996) p. 445.
- [160] R.W. Whitworth, *Adv. Phys.* 24 (1975) 203.
- [161] M.M. Khayyat, G.K. Banini, D.G. Hasko and M.M. Chaudhri, *J. Phys. D* 36 (2003) 1300.

Author Index

Italic numbers refer to reference pages Numbers between brackets are the reference numbers. No distinction is made between first and co-author(s).

- Abraham, F.F. 77 [21]
Abraham, M.M. 549 [124]; 549 [129]
Abrosimov, N.V. 79 [120]
Achard, M.-F. 269 [174]
Ackland, G.J. 80 [185]; 80 [188]
Adachi, N. 548 [45]
Adams, G.K. 444 [90]
Adams, J.B. 77 [34]
Adler, W.F. 548 [65]
Afanas'ev, G.T. 443 [55]
Ahearn, J.S. 550 [157]
Akatsuka, M. 548 [45]
Al-Kahwaji, A. 268 [135]
Alex, V. 79 [120]
Alexander, H. 76 [1]; 77 [44]; 77 [47]; 77 [53];
78 [77]; 78 [84]; 398 [11]
Allain, M. 268 [119]; 268 [158]
Allen, F.M. 401 [168]
Allé, C. 269 [185]
Alshits, V.I. 76 [16]; 76 [17]
Amelinckx, S. 442 [6]; 549 [105]
Ammon, H.L. 445 [132]; 445 [135]; 446 [148]
Andelman, D. 267 [99]
Anderson, N.G. 442 [8]
Anderson, P.M. 398 [26]
Anderson, P.W. 269 [181]
Ando, J.I. 402 [185]
Andreev, G.A. 549 [119]
Anisimov, S.I. 266 [47]
Ansel, G. 79 [127]
Antonelli, A. 77 [64]
Arai, H. 268 [112]
Argon, A.S. 76 [7]; 77 [54]; 77 [62]; 77 [65];
78 [112]; 80 [189]; 144 [7]; 144 [8]; 144 [15];
144 [16]; 144 [23]; 145 [41]; 145 [51]; 145 [57];
145 [61]
Arias, T.A. 78 [68]; 78 [71]; 78 [82]; 79 [144]
Armstrong, R.W. 144 [1]; 338 [92]; 442 [22];
442 [24]; 442 [28]; 443 [39]; 443 [40]; 443 [41];
443 [46]; 443 [47]; 443 [48]; 443 [49]; 443 [50];
443 [60]; 443 [65]; 443 [68]; 443 [70]; 443 [74];
444 [75]; 444 [76]; 444 [79]; 444 [80]; 444 [81];
444 [85]; 444 [91]; 444 [100]; 444 [105];
444 [107]; 444 [108]; 445 [109]; 445 [125];
445 [135]; 445 [139]; 446 [146]; 446 [147];
446 [148]; 446 [156]; 446 [157]; 446 [158];
446 [159]; 446 [160]; 548 [62]
Ashbee, K.H.G. 399 [71]; 399 [76]
Ashby, M.F. 550 [152]
Ashkenazy, Y. 77 [20]
Asnacios, S. 268 [153]; 268 [154]; 269 [163]
Atmani, H. 337 [57]
Audouard, A. 401 [171]
Audurier, V. 338 [91]; 550 [150]
Augustine, G. 337 [29]; 337 [30]
Ausserré, D. 270 [225]; 270 [226]
Auzins, P. 549 [120]
AvéLallement, H.G. 401 [153]

Bacon, D.J. 80 [188]
Baer, B.J. 446 [153]
Bailat, C. 77 [39]
Baithor, D. 399 [52]; 399 [53]; 399 [60]
Baker, I. 443 [64]
Balakrishna, V. 337 [29]; 337 [30]
Balian, R. 266 [26]
Ballesteros, C. 550 [138]
Baluc, N. 77 [39]; 338 [68]
Baluffi, R.W. 79 [163]
Bamford, C.H. 445 [115]
Bandak, F.A. 444 [80]; 446 [146]
Banini, G.K. 550 [161]
Barett, D.L. 337 [25]; 337 [27]
Baroïs, P. 269 [168]; 271 [276]; 271 [281];
271 [289]
Baronet, C.N. 547 [9]
Barrau, J. 337 [58]
Barrett, C.S. 79 [127]
Barsch, M. 399 [60]
Bartolino, R. 268 [144]; 269 [160]; 269 [177]
Bartolucci, S. 548 [74]

- Bartsch, M. 399 [49]; 399 [52]; 399 [53]; 399 [59]; 399 [67]
 Basapa, G. 268 [133]
 Baskes, M.I. 77 [22]; 398 [26]; 400 [117]
 Baufeld, B. 399 [52]; 399 [59]; 399 [60]; 399 [63]
 Baufeld, B. 399 [53]
 Beard, B.C. 444 [92]; 445 [131]
 Beauchamp, P. 78 [74]
 Bedel, E. 337 [57]
 Beevers, R.B. 270 [244]
 Béhar, J. 268 [116]
 Behrens, R., Jr. 445 [127]
 Belak, J. 446 [151]
 Belak, J.F. 80 [197]
 Beltz, G.E. 144 [27]; 145 [30]; 145 [32]; 145 [35]; 145 [60]
 Ben-Abraham, S.I. 268 [140]
 Bennema, P. 337 [33]; 337 [36]
 Bennetto, J. 77 [55]; 77 [56]; 78 [67]; 78 [89]
 Benoit, W. 76 [14]; 338 [86]
 Bentle, G.G. 398 [41]
 Berger, S.D. 549 [85]
 Berry, M.V. 270 [232]
 Betukhov, B.V. 399 [59]
 Bhat, H.L. 445 [129]
 Bidaux, R. 267 [107]
 Biedermann, A. 336 [19]
 Bigger, J.R.K. 78 [70]
 Bilby, B.A. 79 [132]
 Bilde-Sørensen, J.B. 402 [209]
 Bilde-Sørenson, J.B. 398 [29]
 Binnig, G. 336 [3]; 336 [4]; 336 [5]; 336 [6]; 336 [7]; 336 [8]
 Bird, D.M. 78 [70]
 Bishop, R.F. 547 [5]
 Blacic, J.D. 399 [79]; 399 [80]; 401 [164]
 Blanc, C. 267 [108]
 Blanchin, M.G. 399 [72]; 399 [73]; 399 [74]; 399 [75]; 399 [78]
 Block, S. 444 [103]
 Bluestein, I. 271 [272]; 271 [273]
 Blume, J. 145 [47]
 Blumenthal, W.R. 401 [184]
 Boas, W. 79 [153]; 337 [37]; 397 [1]
 Bobolev, V.K. 443 [55]
 Boccaro, N. 267 [107]
 Bocek, M. 337 [53]
 Boddington, T. 443 [73]
 Boisson, M. 401 [173]; 401 [174]
 Boland, J.N. 399 [85]
 Bollmann, W. 442 [11]
 Boltenhagen, P. 267 [94]; 267 [103]; 268 [111]
 Bonn, D. 268 [135]
 Bonneville, J. 77 [29]; 338 [68]; 338 [69]; 338 [70]
 Borchadt, G. 399 [64]
 Bornstein, R. 397 [2]
 Börschig, C. 268 [134]
 Bos, P.J. 270 [229]; 270 [230]
 Boswara, I.M. 549 [130]
 Bouchta, A. 271 [281]
 Bouligand, Y. 265 [3]; 265 [13]; 266 [25]; 266 [28]; 268 [130]; 270 [245]; 271 [299]
 Bourdon, L. 268 [114]; 269 [162]
 Bourgaux, C. 268 [153]; 268 [154]
 Bowden, F.P. 443 [54]; 443 [69]; 443 [71]
 Bowen, D.K. 79 [140]; 79 [151]
 Bower, A.F. 145 [54]
 Bowick, M.J. 266 [58]
 Boyarskaya, Yu.S. 548 [68]; 550 [134]
 Bragg, W.L. 145 [39]
 Brand, H.R. 270 [214]
 Brandt, C.D. 337 [27]
 Branger, V. 338 [97]
 Brebec, G. 400 [113]
 Brede, M. 144 [10]; 145 [62]
 Brener, E.A. 270 [224]
 Brenner, D.W. 446 [149]
 Brenner, S.S. 76 [2]
 Bretheau, T. 398 [15]
 Brick, R.M. 79 [129]
 Brill, T.B. 445 [126]
 Brinkman, W.F. 267 [73]; 271 [259]
 Brion, H.G. 77 [48]
 Brochard, S. 337 [49]
 Brookes, C.A. 548 [72]; 549 [111]
 Brown, L.M. 547 [11]; 548 [69]; 549 [90]; 549 [99]; 549 [131]
 Bruce, D.W. 268 [125]
 Brummer, O. 547 [14]
 Brunet, M. 268 [113]; 269 [186]; 269 [195]; 269 [196]; 269 [199]; 271 [282]
 Brunner, D. 400 [115]; 400 [116]
 Buchholz, J. 79 [118]
 Budiansky, B. 145 [53]
 Buhrer, W. 338 [74]
 Bujard, M. 76 [14]
 Bulatov, V.V. 76 [6]; 77 [19]; 77 [21]; 77 [33]; 77 [38]; 77 [40]; 77 [41]; 77 [54]; 77 [58]; 77 [65]; 78 [75]; 78 [81]; 78 [87]; 78 [112]; 80 [164]; 80 [179]; 80 [189]; 145 [61]
 Bulusu, S. 445 [127]
 Burk, A.A. 337 [27]
 Burns, S.J. 144 [4]; 144 [5]
 Bursill, L.A. 399 [74]; 399 [78]
 Burton, W.K. 442 [2]
 Buseck, P.R. 401 [168]

- Cabrera, N. 442 [2]
 Cabrero-Cano, J. 398 [39]
 Cadoz, J. 400 [96]; 402 [206]
 Cadoz, J.L. 402 [210]
 Cady, H.H. 444 [97]
 Cagin, T. 80 [196]
 Cai, W. 77 [19]; 77 [33]; 77 [40]; 77 [54]; 78 [73];
 78 [75]; 78 [81]; 78 [87]; 78 [112]; 80 [164];
 80 [179]; 80 [186]; 80 [189]
 Caillard, D. 78 [85]; 338 [65]; 400 [118]
 Calder, A.F. 80 [188]
 Callahan, D.L. 549 [94]; 549 [106]
 Callahan, S.L. 401 [147]
 Canova, G.R. 79 [157]
 Carlson, D.W. 444 [91]
 Carlson, J.M. 270 [210]
 Carlsson, A.E. 145 [43]
 Carter, C., Jr. 442 [20]
 Carter, C.B. 398 [19]
 Carter, N.L. 401 [153]
 Castaing, J. 398 [15]; 398 [17]; 398 [35]; 398 [36];
 398 [38]; 398 [39]; 398 [40]; 399 [62]; 400 [94];
 400 [96]; 400 [103]; 400 [108]; 401 [171];
 402 [206]
 Cates, M.E. 267 [99]
 Celli, V. 79 [117]
 Chaim, R. 399 [51]
 Champier, G. 78 [95]; 78 [97]; 78 [98]
 Chan, H.M. 548 [66]
 Chan, W.K. 268 [156]
 Chandani, A.D.L. 269 [167]
 Chandar, L. 266 [58]
 Chandrasekhar, S. 266 [32]; 266 [35]
 Chang, G. 80 [196]
 Chang, J. 77 [19]; 77 [40]; 78 [75]; 80 [164]
 Charpentier, P. 401 [145]
 Chatenay, D. 270 [225]
 Chaudhri, M.M. 338 [93]; 443 [43]; 445 [124];
 547 [10]; 547 [24]; 548 [59]; 548 [60]; 548 [64];
 548 [67]; 548 [69]; 548 [80]; 548 [81]; 549 [90];
 549 [99]; 550 [132]; 550 [139]; 550 [147];
 550 [148]; 550 [149]; 550 [161]
 Chen, C.C. 548 [53]; 548 [56]
 Chen, S.P. 398 [26]; 400 [117]
 Chen, Y. 549 [124]; 549 [125]; 549 [127];
 549 [129]
 Cheong, D.S. 399 [56]; 399 [57]; 399 [58]
 Cheong, S.A. 76 [13]
 Cheung, K.S. 144 [8]
 Chiang, S.S. 547 [6]
 Chiao, Y.H. 145 [48]
 Chiccoli, C. 266 [40]
 Chien, F.R. 399 [65]
 Chin, E. 271 [278]
 Choi, B.W. 76 [3]
 Choi, C.S. 442 [15]
 Chou, Y.T. 338 [94]; 548 [61]
 Choyke, W.J. 337 [25]; 337 [27]
 Christie, J.M. 399 [90]; 401 [154]
 Chronister, E.L. 446 [153]
 Chuang, I. 266 [59]
 Chugunova, S.I. 547 [26]
 Cigle, W. 400 [115]
 Cladis, P.E. 265 [9]; 267 [73]; 267 [85]; 270 [214]
 Clark, C.F. 446 [160]
 Clark, N.A. 268 [115]; 268 [147]; 268 [149];
 269 [187]; 269 [188]; 269 [189]; 269 [190];
 269 [198]; 269 [200]; 269 [204]; 271 [282]
 Clarke, D.R. 145 [48]; 549 [93]; 549 [109]
 Clarke, L.J. 78 [70]
 Clarke, R.C. 337 [25]; 337 [27]
 Clément, N. 338 [72]
 Cleymand, F. 338 [96]; 338 [98]; 338 [99];
 338 [100]; 338 [103]
 Clifton, R.J. 549 [84]
 Clinard, F.W. 401 [144]
 Clough, R.W. 145 [56]
 Codd, I. 443 [68]
 Coffey, C.S. 443 [48]; 443 [57]; 443 [60]; 443 [70];
 446 [156]; 446 [157]; 446 [158]; 446 [159]
 Cohen, J.B. 79 [133]
 Cohn-Vossen, S. 267 [92]
 Coleman, D. 269 [204]
 Colin, A. 268 [142]
 Colin, J. 338 [85]; 338 [98]; 338 [99]
 Colombo, L. 77 [50]
 Comolova, L.F. 547 [14]
 Connick, W. 442 [13]
 Conrad, H. 79 [124]; 402 [197]
 Cook, R.F. 399 [89]; 549 [93]
 Cordier, P. 77 [45]; 399 [55]; 399 [88]; 399 [91];
 402 [185]
 Corman, G.S. 398 [42]; 401 [141]; 401 [142]
 Cotterell, B. 145 [33]
 Cottrell, A.H. 76 [11]; 79 [132]; 144 [2]; 547 [16]
 Couderc, J.J. 550 [158]
 Coujou, A. 337 [49]
 Coulon, G. 270 [225]
 Coupeau, C. 337 [47]; 337 [48]; 337 [49];
 338 [64]; 338 [69]; 338 [70]; 338 [77]; 338 [85];
 338 [86]; 338 [96]; 338 [97]; 338 [98]; 338 [99];
 338 [100]; 338 [103]
 Couret, A. 338 [65]; 400 [118]
 Coxeter, H.S.M. 270 [253]
 Cromer, D.T. 445 [132]
 Crommie, M.F. 336 [14]

- Csányi, G. 78 [82]
 Curnich, L.R. 145 [37]
- Dai, Y. 77 [39]; 77 [43]
 Dair, B. 337 [35]
 Damavarapu, R. 444 [103]
 Darboux, G. 267 [93]
 Dargenton, J.C. 338 [83]; 338 [84]
 Darot, M. 401 [157]; 401 [159]
 Datta, S. 549 [130]
 Davidge, R.W. 547 [28]
 Davies, R.G. 338 [67]
 Davies, R.M. 547 [2]
 Dawson, I.M. 442 [7]; 442 [8]
 de Gennes, P.-G. 269 [180]; 270 [223]
 de Gennes, P.G. 266 [33]; 267 [107]; 271 [269]
 de Koning, M. 77 [54]; 78 [81]
 de la Rubia, T.D. 77 [38]; 77 [41]; 77 [50]; 77 [54]
 de Sèze, L. 267 [107]
 De Yoreo, J.J. 337 [35]
 Deaven, D.M. 78 [69]
 Dedieu, J.-C. 268 [139]
 DeGrand, T.A. 269 [191]
 Dekker, E.H.L. 401 [148]
 Delafond, J. 338 [101]
 Delgado, L. 550 [136]
 Demenet, J.-L. 337 [50]
 Demenet, J.L. 77 [45]; 77 [49]
 Demus, D. 266 [34]
 Denanot, M.F. 337 [62]
 Denatot, M.F. 401 [173]
 De'Nève, T. 267 [89]; 267 [90]
 Dergert, C. 268 [139]
 Derrida, B. 265 [13]
 Destrade, C. 271 [281]
 Devincre, B. 77 [21]
 DeVost, V.F. 443 [70]
 Dhar, D. 267 [109]
 D'havé, K. 271 [287]
 di Persio, J. 443 [38]
 Diat, O. 268 [138]
 Diaz, J. 337 [59]
 Dick, J.J. 444 [94]; 444 [95]; 444 [96]; 444 [101];
 444 [102]; 445 [140]; 445 [141]
 Dickinson, J.T. 550 [137]
 DiDonna, B.A. 271 [268]
 Dierking, I. 269 [176]; 271 [288]
 Dietz, V. 78 [84]
 Digal, S. 266 [60]
 Dijon, J. 337 [45]
 Dimiduk, D.M. 77 [35]; 80 [192]
 Dlott, D.D. 444 [87]; 444 [88]; 444 [89]; 446 [153]
- Dobrzhanskii, G.F. 547 [27]
 Doherty, R.D. 145 [58]
 Doi, M. 267 [86]
 Dollinger, G. 401 [154]
 Dominguez-Rodriguez, A. 398 [35]; 398 [38];
 398 [39]; 398 [40]; 398 [48]; 399 [54]; 399 [55];
 399 [56]; 399 [57]; 399 [58]; 399 [62]; 399 [66]
 Donlon, W.T. 398 [25]; 400 [132]; 400 [137];
 401 [143]
 Dorn, J.E. 80 [167]
 Douglas, A.S. 444 [80]; 446 [146]
 Doukhan, J.-C. 401 [152]
 Doukhan, J.C. 399 [87]; 399 [88]; 399 [91];
 400 [111]
 Doukhan, N. 400 [111]; 400 [125]; 400 [129];
 400 [130]; 400 [133]; 400 [135]; 400 [138];
 400 [139]; 401 [152]
 Douthwaite, R.M. 443 [68]
 Drury, M.R. 401 [169]
 Drzaic, P.S. 266 [44]
 Du, Z.Y. 445 [135]
 Dubois-Violette, E. 267 [84]; 270 [256]; 271 [260]
 Ducarroit, M. 337 [44]
 Duclos, R. 400 [125]; 400 [129]; 400 [130];
 400 [135]; 400 [136]; 400 [138]; 400 [139]
 Dudley, M. 442 [20]; 443 [64]
 Duesbery, M.S. 77 [59]; 77 [60]; 79 [131];
 79 [138]; 79 [141]; 79 [151]; 79 [155]; 79 [156];
 79 [160]; 80 [168]; 144 [28]
 Duloisy, E. 337 [45]
 Dundurs, J. 445 [138]
 Durand, G. 267 [79]; 267 [96]; 267 [101];
 268 [144]; 269 [160]; 269 [177]
 Durrer, R. 266 [59]
 Duvall, G.E. 444 [83]
 Duvalois, W. 442 [27]
 Dvorak, G.J. 443 [62]
 Dvorak, V. 270 [218]
 Dyachenko-Dekov, D.V. 79 [120]
 Dyer, L.D. 548 [54]
 Dynna, M. 336 [18]
 Dzyaloshinskii, I. 266 [47]
- Eastmond, G.C. 445 [115]
 Edagawa, K. 80 [171]
 Edel, P. 549 [128]
 Edwards, S.F. 267 [86]
 Eigler, D.M. 336 [14]
 Elam, C.F. 79 [128]
 Elban, W.L. 442 [22]; 442 [24]; 443 [39]; 443 [40];
 443 [45]; 443 [47]; 443 [48]; 443 [60]; 443 [70];
 443 [74]; 444 [91]; 444 [92]; 444 [100];
 444 [108]; 445 [128]; 445 [131]; 445 [135];

- 445 [139]; 446 [148]; 446 [156]; 446 [157];
446 [158]; 446 [159]; 446 [160]
- Elert, M.L. 446 [149]
- Elkajbaji, M. 77 [27]
- Elsässer, C. 400 [95]; 400 [104]; 400 [105];
400 [109]
- Engeness, T.D. 78 [68]
- Enomoto, Y. 548 [67]; 550 [135]; 550 [147]
- Ercolossi, F. 77 [34]
- Eremenko, V.G. 548 [37]; 549 [92]
- Erofeev, V.N. 78 [109]
- Erofeeva, S.A. 79 [116]
- Escaig, B. 77 [29]; 400 [125]; 400 [129];
400 [130]; 400 [135]; 400 [138]; 400 [139];
443 [38]
- Escaravage, C. 78 [97]; 78 [98]
- Eshelby, J. 267 [72]
- Eshelby, J.D. 144 [21]; 442 [31]; 547 [25]
- Estle, T.L. 549 [121]
- Evans, A.G. 398 [9]; 547 [6]
- Evans, T. 549 [113]
- Eveno, P. 399 [62]
- Faetti, S. 267 [65]
- Faisant, P. 399 [72]
- Faivre, G. 337 [24]
- Faraday, M. 442 [17]
- Farber, B.Y. 78 [86]; 78 [103]; 78 [105]; 78 [106];
78 [107]
- Farnum, E.H. 401 [144]
- Fayer, M.D. 444 [88]; 444 [89]
- Fazzio, A. 77 [64]
- Feenstra, R.M. 336 [13]
- Fein, A. 336 [13]
- Ferrante, J. 145 [34]
- Feruli, I. 266 [40]
- Field, J.E. 443 [56]; 443 [58]; 443 [59]; 444 [105];
444 [106]; 444 [107]; 445 [112]
- Fitzgerald, J.D. 399 [84]; 399 [85]; 401 [163]
- Fleck, N.A. 550 [152]
- Flor, H. 337 [41]
- Fontaine, G. 399 [73]; 399 [75]
- Forbes, J.W. 444 [93]
- Foreman, A.J. 145 [38]
- Fournier, J.-B. 267 [96]; 267 [97]
- Fowles, G.R. 444 [82]; 444 [83]
- Fox, P.G. 443 [71]; 443 [72]; 445 [110]; 445 [111]
- Frank, F.C. 79 [134]; 265 [4]; 270 [249]; 270 [251];
337 [28]; 442 [3]; 442 [18]; 443 [51]; 547 [25]
- Frankel, T. 266 [22]
- Freise, E.J. 548 [73]
- Freund, L.B. 145 [63]
- Friedel, G. 265 [11]
- Friedel, J. 77 [25]; 265 [7]; 267 [77]; 270 [234];
270 [242]; 337 [38]
- Frondel, C. 399 [82]
- Fujino, K. 401 [177]; 401 [180]; 401 [183]
- Fujita, S. 549 [114]; 549 [115]
- Fujiwara, T. 78 [94]
- Fukuda, A. 268 [112]; 269 [167]; 269 [169];
269 [208]; 270 [213]; 270 [215]; 270 [216]
- Fuller, E.R. 443 [44]
- Fung, R. 549 [117]
- Furenlid, L. 269 [168]
- Furukawa, T. 269 [173]
- Gaboriaud, R.J. 401 [158]; 401 [159]; 401 [172];
401 [173]; 401 [174]
- Gager, W.B. 549 [122]; 549 [123]
- Gaigher, H.L. 79 [123]
- Galerne, Y. 269 [170]; 269 [171]
- Gallagher, H.G. 443 [42]
- Gallot, Y. 270 [225]
- Gally, B.J. 77 [62]; 145 [51]
- Galwey, A.K. 445 [116]
- Gao, F. 77 [42]
- Gao, H. 80 [194]
- Garbarz, J. 337 [24]
- Garcia, E. 444 [95]; 444 [96]
- Garden, J. 337 [44]
- Gareeva, A.R. 550 [134]
- Garem, H. 77 [45]; 399 [61]; 400 [131]; 401 [149];
401 [150]; 401 [151]; 401 [178]; 401 [179];
401 [181]; 401 [182]
- Garratt-Reed, A.J. 80 [178]
- Gauthier, S. 336 [12]; 337 [24]
- Geipel, T. 398 [29]; 400 [101]
- Gemmings, T. 400 [104]
- George, A. 77 [51]; 78 [95]; 78 [96]; 78 [97];
78 [98]; 78 [100]; 78 [102]; 78 [113]; 144 [18]
- Georges, J.M. 550 [145]
- Gerber, Ch. 336 [3]; 336 [4]; 336 [7]
- Gerberich, W.W. 338 [88]; 549 [108]
- Gerretson, J. 399 [84]
- Gerritsma, G.J. 267 [78]
- Gerstle, F.P. 443 [62]
- Gesland, J.Y. 400 [113]
- Geurst, J.A. 267 [78]
- Giannakopoulos, A.E. 76 [4]
- Gibbs, P. 549 [91]
- Gido, S.P. 268 [124]
- Gilardi, R. 445 [134]
- Gill, A.J. 266 [61]
- Gilles, B. 336 [18]

- Gilman, J.J. 80 [195]; 144 [6]; 398 [28]; 446 [154]; 446 [155]; 547 [13]; 547 [17]; 547 [21]; 549 [83]; 549 [98]
- Giocondi, J. 337 [29]; 337 [30]
- Girard, J.-C. 337 [47]; 337 [48]; 337 [50]; 338 [85]; 338 [95]
- Girard, J.C. 338 [91]; 550 [150]
- Gisse, P. 270 [212]
- Glancy, B.C. 444 [91]; 444 [92]; 445 [131]
- Glass, R. 442 [20]
- Glass, R.C. 337 [26]
- Glazov, M.V. 76 [6]
- Glogarova, M. 269 [197]; 269 [202]
- Glover, D.J. 443 [48]; 445 [128]
- Gobel, I.R. 337 [54]
- Goddard, W.A. 80 [196]
- Goiran, M. 337 [56]; 337 [57]
- Gomez-Garcia, D. 399 [62]; 399 [66]
- Gooch, D.J. 402 [209]
- Goodby, J.W. 271 [278]; 271 [280]; 271 [286]
- Goodby, J.W.G. 269 [175]
- Gorecka, E. 269 [167]
- Goretta, K.C. 398 [33]
- Gottschalk, H. 78 [84]
- Goudeau, P. 338 [96]; 338 [97]
- Gouldstone, A. 76 [4]
- Grabko, D.Z. 548 [68]
- Grandjean, F. 270 [236]
- Granek, R. 268 [141]
- Granholm, R.H. 444 [93]
- Gray, G.W. 269 [175]
- Graziano, D.J. 267 [81]
- Greco, F. 267 [91]
- Green, D.J. 398 [46]
- Greffier, O. 268 [135]
- Greggi, J. 337 [27]
- Grelet, E. 271 [262]; 271 [264]; 271 [265]; 271 [266]
- Gremaud, G. 76 [14]
- Gridneva, I.V. 547 [26]; 549 [95]
- Griffin, L.J. 442 [4]
- Griggs, D.T. 399 [79]; 399 [80]; 399 [90]
- Grihlé, J. 401 [149]; 401 [173]; 401 [179]
- Grilhé, J. 336 [17]; 337 [47]; 337 [48]; 337 [49]; 337 [60]; 337 [61]; 337 [62]; 338 [64]; 338 [69]; 338 [77]; 338 [85]; 338 [86]; 338 [96]; 338 [97]; 338 [98]; 338 [99]; 338 [100]; 338 [103]; 401 [150]
- Gronski, W. 268 [134]
- Gross, K.A. 442 [30]
- Groves, G.W. 402 [194]; 402 [209]
- Gueguen, Y. 401 [157]; 401 [159]
- Gulik-Krzywicki, T. 268 [139]
- Gumsch, P. 80 [194]; 144 [29]; 400 [116]
- Güntherodt, H.J. 336 [21]
- Gupta, Y.M. 444 [82]; 444 [83]; 444 [84]
- Gustavson, P.K. 444 [93]
- Haasen, P. 144 [10]; 398 [5]
- Haefke, H. 336 [21]
- Hagan, J.T. 443 [43]; 548 [63]; 550 [132]
- Hainsworth, S.V. 550 [151]
- Halfpenny, P.J. 442 [34]; 443 [35]; 443 [42]
- Hall, E.O. 443 [66]
- Halleck, P.M. 444 [97]; 444 [98]
- Halperin, B.I. 270 [246]
- Ham, R.K. 549 [87]
- Hamann, D.R. 336 [10]
- Hamilton, J.C. 80 [190]
- Hammond, B.L. 443 [49]
- Handschy, M.A. 269 [198]
- Hannink, R.H.J. 398 [46]; 549 [112]
- Hansen, L.B. 78 [69]
- Hardy, C. 547 [9]
- Hardy, J.R. 445 [143]
- Harris, W.F. 265 [15]; 269 [182]; 269 [207]
- Harry, T. 80 [188]
- Harvey, S.E. 338 [88]
- Hasegawa, H. 547 [34]
- Hashizume, T. 336 [20]
- Hasko, D.G. 550 [161]
- Hauser, H.M. 445 [112]
- Hayashi, M. 269 [172]
- Hazzledine, P.M. 80 [192]; 338 [79]
- He, A. 400 [108]
- Head, A.K. 443 [61]
- Heavens, S.N. 443 [56]; 443 [58]
- Heggie, M.I. 78 [66]; 78 [90]; 78 [91]
- Henderson, B. 549 [128]
- Hendrickson, A.A. 548 [53]; 548 [56]
- Henkelman, G. 80 [172]; 80 [173]
- Hensley, E.B. 549 [126]
- Herley, P.J. 445 [117]; 445 [118]; 445 [119]; 445 [120]; 445 [121]; 445 [122]; 445 [123]; 445 [129]
- Hertz, H. 547 [12]
- Heuer, A.H. 398 [9]; 398 [16]; 398 [25]; 398 [29]; 398 [45]; 398 [48]; 399 [50]; 399 [51]; 399 [54]; 399 [55]; 399 [56]; 399 [57]; 399 [58]; 399 [63]; 399 [65]; 399 [68]; 399 [69]; 400 [94]; 400 [96]; 400 [97]; 400 [98]; 400 [100]; 400 [101]; 400 [103]; 400 [108]; 400 [126]; 400 [127]; 400 [128]; 400 [132]; 400 [137]; 401 [143]; 402 [199]; 402 [200]; 402 [204]; 402 [205]; 402 [206]
- Hibbs, M.K. 548 [76]; 548 [77]

- Hilbert, D. 267 [92]
 Hill, J.R. 446 [153]
 Hill, M.J. 548 [41]
 Hill, R. 547 [5]; 548 [79]
 Hindmarsh, M. 266 [64]
 Hinton, R. 79 [133]
 Hird, M. 271 [286]
 Hirsch, P.B. 78 [93]; 79 [119]; 79 [135]; 144 [11];
 144 [12]; 145 [50]; 145 [64]; 145 [65]; 398 [10];
 402 [195]; 402 [196]; 442 [10]; 548 [38];
 548 [46]; 548 [48]; 549 [88]; 550 [156]
 Hirth, J.P. 76 [5]; 78 [108]; 144 [22]; 268 [122];
 337 [39]; 398 [22]; 398 [23]; 398 [24];
 400 [117]; 442 [21]; 442 [23]
 Hnilica, F. 337 [52]; 337 [55]
 Hoagland, R.G. 77 [22]; 398 [26]; 400 [117]
 Hobbs, B.E. 399 [83]; 399 [85]
 Hobgood, H.M. 337 [25]; 337 [27]; 337 [29];
 337 [30]
 Hockey, B.J. 549 [102]; 549 [103]
 Hockey, D.B. 549 [93]
 Hoersch, V.A. 547 [1]
 Hoffsommer, J.C. 443 [48]; 445 [128]; 445 [139]
 Holden, J. 444 [90]
 Holden, J.R. 445 [132]
 Hollox, G.E. 402 [186]
 Holt, D.B. 549 [130]
 Holyst, R. 270 [227]
 Honda, K. 266 [63]
 Hong, M.H. 398 [44]
 Hooker, S.V. 548 [65]
 Hoover, S.M. 446 [156]; 446 [158]
 Hopkins, R.H. 337 [25]; 337 [27]; 337 [29];
 337 [30]
 Horn, R.G. 268 [136]
 Horne, R.W. 442 [10]; 550 [156]
 Hornstra, J. 398 [8]
 Hosseini, M.M. 548 [42]
 Houston, J.E. 338 [90]; 547 [18]
 Howarth, D.F. 399 [88]
 Howitt, D.G. 402 [207]
 Hu, J.Z. 549 [97]
 Hu, S.M. 548 [35]; 548 [36]; 548 [44]
 Hu, Y.P. 550 [143]
 Huang, C.C. 269 [168]
 Huang, H. 338 [88]; 549 [108]
 Huang, J. 77 [36]
 Huang, Y.M. 78 [83]
 Hudson, S.D. 266 [51]
 Hull, D. 337 [40]; 338 [80]
 Hull, R. 77 [61]
 Humble, P. 549 [112]
 Humphreys, C.J. 336 [15]
 Huntington, H.B. 76 [8]
 Hurd, A.J. 268 [147]
 Hutchinson, J.W. 145 [52]; 145 [63]
 Hwang, L. 400 [126]; 400 [127]; 400 [128]
 Hyde, B.G. 401 [170]
 Hyde, S.T. 399 [89]
 Hyodo, S. 549 [114]; 549 [115]
 Ichihara, M. 398 [43]; 399 [77]; 400 [112];
 549 [115]
 Ide, N. 445 [137]
 Ignat, M. 337 [44]; 337 [45]; 337 [46]
 Ihn, K.J. 271 [280]
 Ikari, M. 401 [144]
 Ikeda, A. 269 [169]
 Imai, M. 78 [104]
 Imura, H. 267 [69]
 Imura, T. 79 [122]; 80 [177]
 Indenbom, V.L. 76 [16]; 76 [17]
 Inui, H. 398 [27]
 Inui, S. 269 [169]
 Isaert, N. 271 [281]; 271 [289]
 Iseki, T. 401 [140]; 401 [144]; 402 [189]
 Ishibashi, Y. 267 [71]
 Ishikawa, K. 268 [112]; 269 [208]; 398 [27]
 Ishikawa, T. 266 [52]; 266 [54]; 270 [228]
 Ismail-Beigi, S. 78 [82]; 79 [144]
 Ito, T. 401 [146]
 Iunin, Y.L. 78 [86]; 78 [107]; 79 [120]
 Iwane, H. 269 [169]
 Iyer, S. 444 [103]
 Jacobs, P.W.M. 445 [116]; 445 [120]
 Jacobs, S.J. 443 [57]
 Jacobsen, K.W. 76 [13]; 77 [30]; 77 [31]; 77 [32];
 78 [69]
 Jacques, A. 78 [113]
 Jamee, P. 271 [263]
 James, M.N. 548 [78]
 Janzen, E. 337 [26]
 Jaoul, O. 401 [161]
 Jaswon, M.A. 145 [38]
 Jensen, L.C. 550 [137]
 Jiang, C.B. 338 [71]
 Jimenez-Melendo, M. 399 [55]
 Joachim, C. 336 [12]
 Joannopoulos, J.D. 78 [71]
 Joanny, J.-F. 270 [226]
 Johnson, D.W. 401 [147]
 Johnson, O.W. 549 [91]
 Johnston, J.L. 338 [67]
 Johnston, W.G. 547 [13]; 547 [17]

- Jolles, E. 398 [34]
 Jones, J.C. 271 [286]
 Jones, R. 78 [66]; 78 [90]; 78 [91]; 78 [114]
 Jones, W.H. 549 [122]
 Jónsson, H. 77 [30]; 80 [172]; 80 [173]
 Joos, B. 77 [59]; 77 [60]
 Jouiad, M. 337 [49]; 338 [82]
 Juan, Y. 145 [44]
 Junqua, N. 336 [17]
 Justo, J.F. 77 [54]; 77 [58]; 77 [64]; 78 [81];
 78 [87]; 78 [112]
- Kabler, M. 79 [117]
 Kalashnikova, L.K. 549 [101]
 Kamien, R. 271 [267]
 Kamien, R.D. 268 [123]; 270 [248]; 271 [268];
 271 [272]; 271 [273]; 271 [291]; 271 [297];
 271 [298]
 Kamimura, Y. 77 [52]
 Kamiya, N. 337 [31]
 Kappers, L.A. 549 [126]; 549 [128]
 Karato, S. 401 [162]; 401 [163]; 401 [177];
 401 [180]; 401 [183]
 Kärnthalter, H.P. 77 [28]
 Karo, A.M. 445 [143]
 Kasper, J.S. 270 [249]
 Katahama, H. 548 [45]
 Kaufmann, H.-J. 79 [121]
 Kawano, S. 269 [169]
 Kaxiras, E. 144 [28]; 145 [44]
 Keh, A.S. 338 [94]; 547 [20]; 548 [61]
 Kelchner, C.L. 80 [190]
 Kellay, H. 268 [135]
 Keller, P. 269 [166]
 Keller, R.J. 399 [69]
 Kelly, A. 144 [2]; 402 [194]
 Kelly, R. 549 [89]
 Kelsey, E.T. 398 [32]
 Kelson, I. 77 [20]
 Kenway, P.R. 402 [208]
 Khan, M.Y. 548 [69]; 549 [90]; 549 [99]; 549 [100]
 Khanta, M. 145 [66]; 145 [67]
 Khasgiwale, N. 548 [66]
 Khayyat, M.M. 550 [161]
 Kibble, T.W.B. 266 [55]
 Kiely, J.D. 547 [18]
 Kilo, M. 399 [64]
 Kim, H. 446 [152]
 Kimerling, L.C. 78 [78]
 Kimura, H. 79 [122]; 80 [175]; 80 [177]
 King-Smith, R.D. 78 [70]
 Kirby, S.H. 398 [20]; 400 [134]
 Kirchner, H.O. 77 [27]
 Kirchner, P.D. 549 [93]
 Kiritani, M. 80 [183]
 Kisielowski-Kemmerich, C. 78 [79]
 Kjellberg, L.O. 337 [26]
 Klapper, H. 442 [25]; 442 [26]; 442 [29]; 442 [32]
 Klein, M.J. 549 [122]; 549 [123]
 Kleiser, T. 337 [53]
 Kleman, M. 265 [1]; 265 [2]; 265 [6]; 265 [9];
 265 [12]; 266 [24]; 266 [26]; 266 [27]; 266 [28];
 266 [30]; 266 [31]; 266 [37]; 266 [50]; 267 [75];
 267 [76]; 267 [89]; 267 [90]; 267 [94]; 267 [98];
 267 [100]; 267 [103]; 267 [104]; 267 [105];
 267 [108]; 268 [110]; 268 [111]; 268 [114];
 268 [116]; 268 [117]; 268 [121]; 268 [128];
 268 [131]; 268 [136]; 268 [150]; 268 [153];
 268 [154]; 269 [159]; 269 [161]; 269 [162];
 269 [163]; 269 [164]; 269 [174]; 269 [178];
 269 [185]; 269 [203]; 270 [234]; 270 [242];
 270 [250]; 270 [252]; 270 [254]; 271 [258];
 271 [290]; 271 [293]; 271 [296]
 Knight, C.G. 548 [81]
 Knoop, F. 549 [110]
 Knowles, K.M. 400 [114]
 Knudsen, C. 144 [6]
 Kochendörfer, A. 443 [36]
 Koh, H.-J. 76 [4]
 Kohlstedt, D.L. 338 [88]; 401 [160]; 401 [165];
 401 [167]
 Koisumi, H. 398 [38]
 Koiter, W.T. 145 [52]
 Koizumi, H. 77 [52]
 Kojima, K. 445 [137]
 Kolar, H.R. 76 [1]
 Kolopus, J.L. 549 [125]; 550 [142]
 Komatsu, M. 80 [183]
 Komura, H. 270 [213]
 Korner, A. 77 [26]; 77 [28]
 Köstmeier, S. 400 [104]
 Kostorz, G. 338 [73]; 338 [74]
 Koubaiti, S. 550 [158]
 Kraus, I. 270 [211]
 Kremenetsky, H. 267 [70]
 Kroes, R.L. 549 [126]
 Kroll, M.C. 549 [93]
 Kronberg, M.L. 398 [7]; 402 [198]; 549 [104]
 Kroupa, F. 79 [137]; 269 [201]
 Krüger, G.T. 268 [157]
 Kruml, T. 338 [70]
 Kubin, L. 77 [21]
 Kubin, L.P. 79 [157]; 398 [17]; 399 [68]; 399 [73]
 Kuczinski, W. 270 [217]
 Kukta, R.V. 77 [24]
 Kulik, A. 338 [86]

- Kulishov, V.L. 271 [279]
 Kumaran, V. 268 [133]
 Kundagrami, A. 271 [277]
 Kunz, M. 270 [226]
 Kurik, M.V. 266 [36]; 269 [184]; 270 [221]
 Kurishita, H. 402 [187]
 Kuroda, K. 400 [110]
 Kurtz, W. 400 [104]; 400 [120]
 Kushnir, I.P. 548 [52]
- Labusch, R. 402 [203]
 Lacaze, E. 337 [24]
 Lafage, C. 399 [78]
 Lagerlöf, K.P.D. 398 [16]; 398 [29]; 398 [48];
 399 [55]; 400 [94]; 400 [101]; 400 [103];
 400 [108]; 402 [206]
 Lagerwall, J.P.F. 271 [287]
 Lagerwall, S.T. 269 [165]; 269 [179]; 269 [200];
 271 [287]; 271 [288]
 Land, T.A. 337 [35]
 Landolt, H. 397 [2]
 Lang, A.R. 442 [14]
 Lang, N.D. 336 [11]
 Langer, S.A. 269 [209]; 270 [210]
 Langford, S.C. 550 [137]
 Lanteri, V. 399 [50]; 399 [51]; 399 [54]
 Larson, R.G. 266 [51]; 267 [80]; 267 [82];
 267 [83]; 267 [88]; 268 [143]
 Laversanne, R. 268 [139]
 Lavrentovich, O.D. 265 [6]; 266 [36]; 266 [38];
 266 [40]; 266 [41]; 266 [42]; 266 [43]; 266 [45];
 266 [52]; 266 [54]; 267 [94]; 267 [98];
 267 [100]; 267 [102]; 267 [103]; 267 [104];
 267 [106]; 268 [111]; 269 [184]; 270 [221];
 270 [222]; 270 [228]; 270 [229]; 270 [230];
 270 [231]; 270 [235]; 270 [238]; 270 [240];
 271 [279]; 271 [285]
 Lawley, A. 79 [123]; 79 [124]
 Lawlor, B.F. 398 [29]
 Lawn, B.R. 443 [44]; 443 [51]; 443 [52]; 547 [15]
 Lay, K. 79 [133]
 Le Bourhis, E. 548 [70]
 Lechatelier, F. 80 [187]
 Lee, C.H. 445 [109]
 Lee, E.H. 548 [79]
 Lee, E.Y. 336 [2]
 Lee, I.-Y.S. 446 [153]
 Lee, M.-S. 445 [138]
 Leffers, T. 77 [30]; 77 [31]; 77 [32]
 Lehto, N. 77 [57]
 Lei, Q.Z. 338 [71]
 Leiko, E.B. 79 [125]; 80 [180]; 80 [181]; 80 [182];
 549 [107]
 Ma, Q. 549 [109]
 Maaloum, M. 270 [225]; 270 [226]
- Lejcek, L. 269 [162]; 269 [178]; 269 [199];
 269 [201]; 269 [202]; 269 [205]; 269 [206];
 270 [218]; 270 [219]; 270 [220]
 Lelogeais, M. 337 [44]
 Lenosky, T. 77 [54]
 Léon, A. 268 [135]
 Leslie, F.M. 267 [67]
 Leslie, W.C. 444 [86]
 Levade, C. 78 [85]; 548 [51]; 550 [158]
 Levelut, A.-M. 269 [168]
 Levelut, A.M. 268 [126]
 Levy, P.W. 445 [117]; 445 [118]; 445 [119];
 445 [120]; 445 [121]; 445 [122]; 445 [123]
 Lewis, M.H. 400 [124]; 549 [117]
 Lewis, R.A. 271 [286]
 Li, J. 78 [75]; 80 [164]
 Li, J.C.M. 338 [94]; 548 [61]
 Li, M.H. 271 [261]; 271 [262]; 271 [263];
 271 [264]; 271 [265]; 271 [266]
 Li, Z. 267 [102]
 Libovicky, S. 79 [130]
 Liebermann, R.C. 402 [185]
 Liébert, L. 269 [166]; 269 [170]; 269 [171]
 Lim, Y.Y. 550 [147]; 550 [148]
 Liu, B. 401 [177]
 Liu, F. 443 [64]
 Livingston, J.D. 548 [55]
 Livolant, F. 270 [245]; 271 [299]
 Llopis, J. 550 [136]; 550 [138]
 Loft, R. 269 [191]
 Loh, K.-K. 269 [194]
 Lomer, W.M. 145 [39]; 145 [40]
 Lothe, J. 76 [5]; 144 [22]; 268 [122]; 337 [39];
 398 [22]; 442 [23]
 Lotsko, D.V. 80 [180]
 Loubet, J.L. 550 [145]
 Louchet, F. 77 [63]; 78 [101]; 78 [102]; 80 [191]
 Love, A.E.H. 265 [5]; 547 [4]
 Lubenets, S.V. 548 [82]
 Lubensky, T.C. 266 [46]; 268 [123]; 268 [137];
 271 [271]; 271 [272]; 271 [274]; 271 [277];
 271 [291]
 Luft, A. 79 [121]; 80 [181]; 80 [182]; 80 [184];
 549 [107]
 Lundqvist, B.I. 78 [69]
 Luppo, M.T. 77 [39]
 Lutz, C.P. 336 [14]
 Luyckx, S.B. 548 [75]; 548 [78]
 Lyuksyutov, I.F. 266 [48]

- Maaroufi, A. 271 [281]
 Mach, P. 269 [168]
 Mackley, M.R. 267 [81]
 Mackwell, S.J. 401 [165]
 Maclennan, J.E. 269 [204]
 Madhusudana, N.V. 271 [283]; 271 [284]; 271 [285]
 Maeda, K. 79 [115]; 79 [158]; 336 [20]; 548 [47]; 549 [114]; 549 [115]; 550 [159]
 Mafettone, P.L. 267 [87]
 Maiman, T.H. 400 [93]
 Makov, G. 77 [20]
 Malet, G. 267 [79]
 Mallard, W.C. 550 [142]
 Malthête, J. 271 [290]; 271 [293]
 Mandelbrot, B.B. 337 [51]
 Manenc, J. 401 [145]
 Maneville, P. 267 [84]
 Mann, A.B. 338 [87]
 Mao, Z. 400 [114]
 Marchenko, V.I. 270 [224]
 Marchesini, O. 550 [145]
 Marian, J. 77 [33]; 80 [198]
 Marignan, J.J. 267 [79]
 Marinopoulos, A.G. 400 [95]; 400 [104]; 400 [105]; 400 [109]
 Marklund, S. 78 [110]
 Marquez, R. 398 [35]; 398 [36]; 398 [39]
 Marrucci, G. 267 [87]; 267 [91]
 Marshall, D.B. 547 [6]
 Martin, G. 77 [18]; 77 [37]
 Martin, J.-L. 338 [68]; 338 [69]
 Martin, J.W. 145 [58]
 Martin, P.C. 267 [68]
 Martinez-Fernandez, J. 399 [55]; 399 [62]; 399 [66]
 Martinot-Lagarde, P. 269 [196]; 270 [212]
 Marty, A. 336 [18]
 Massey, W.S. 266 [21]
 Mathey, P.T. 267 [80]; 267 [82]
 Matsui, H. 79 [122]; 80 [175]; 80 [177]
 Matsuoka, Y. 80 [183]
 Matsunaga, T. 400 [119]
 Matterstock, B. 338 [69]
 Maxwell, L.H. 398 [6]
 May, F.G.J. 442 [13]
 Mazelet, G. 266 [50]
 Mazenko, G.F. 266 [62]
 McClellan, K.J. 399 [63]; 399 [68]
 McClintock, F.A. 145 [57]
 McDermott, I.T. 442 [33]
 McHugh, J.P. 337 [25]; 337 [27]
 McInnes, D.A. 78 [70]
- McLaren, A.C. 399 [84]; 399 [85]; 399 [86]; 399 [89]; 399 [90]
 McMullin, P.G. 337 [25]
 Mead, D.W. 267 [83]
 Mehl, R.F. 79 [127]
 Meiboom, S. 271 [259]
 Meier, J.G. 271 [286]; 271 [287]
 Meille, G. 550 [145]
 Mendez, J. 338 [101]; 338 [102]
 Menoni, C.S. 549 [97]
 Menter, J.W. 442 [9]
 Mera, Y. 336 [20]
 Merkle, L.D. 549 [97]
 Merle d'Aubinge, Y. 549 [128]
 Mermin, N.D. 265 [17]; 270 [257]
 Messerschmidt, U. 399 [49]; 399 [52]; 399 [53]; 399 [59]; 399 [60]; 399 [63]; 399 [67]
 Methfessel, M. 144 [29]
 Meunier, J. 268 [135]; 269 [193]
 Meyer, C. 267 [75]; 268 [153]; 268 [154]; 269 [163]
 Meyer, E. 336 [21]
 Meyer, M. 77 [36]
 Meyer, R.B. 265 [8]; 268 [115]; 269 [166]; 269 [179]; 269 [187]; 269 [188]; 270 [211]
 Meyer, T. 336 [1]; 336 [2]
 Meyers, M.A. 444 [78]
 Michel, D.J. 77 [60]
 Michel, L. 265 [16]; 266 [27]; 266 [31]
 Michot, G. 144 [18]
 Mihsara, M. 548 [49]
 Mikhailova, L.K. 548 [52]
 Milchaskie, T.A. 338 [90]
 Milhet, X. 337 [50]
 Miller, J.C. 443 [42]
 Miller, K.T. 398 [41]
 Miller, R.S. 444 [79]
 Mills, J.J. 550 [157]
 Milman, Yu.V. 547 [11]; 547 [26]; 549 [95]; 549 [96]
 Milner, S.T. 267 [99]
 Milstein, F. 550 [143]
 Mil'vidskii, M.G. 547 [32]; 547 [33]
 Minasyan, H.G. 78 [106]
 Mindlin, R.D. 145 [45]
 Mineyev, V.P. 266 [29]
 Mintmire, J.W. 446 [149]; 446 [150]
 Misra, A. 78 [108]; 398 [23]; 398 [26]; 401 [175]; 401 [176]
 Mitchell, T.E. 78 [108]; 398 [16]; 398 [18]; 398 [23]; 398 [24]; 398 [25]; 398 [26]; 399 [50]; 399 [69]; 400 [96]; 400 [97]; 400 [98]; 400 [117]; 400 [126]; 400 [127]; 400 [128]; 400 [132]; 400 [137]; 401 [143]; 401 [144];

- 401 [175]; 401 [176]; 402 [191]; 402 [192];
 402 [193]; 402 [195]; 402 [196]; 402 [199];
 402 [200]; 402 [204]; 402 [205]; 402 [206];
 402 [207]
- Mitomo, M. 402 [190]
 Miyata, M. 78 [94]
 Mohan, V.K. 445 [112]
 Möller, H.-J. 79 [118]
 Möller, H.J. 78 [111]
 Monge, G. 268 [129]
 Monty, C. 398 [34]; 398 [35]
 Mordehai, D. 77 [20]
 Mori, H. 266 [53]
 Mori, T. 401 [140]; 402 [189]
 Moriarty, J. 79 [142]; 79 [143]
 Moriarty, J.A. 79 [145]; 79 [146]; 80 [197]
 Morimoto, N. 548 [45]
 Morris, C.E. 444 [99]
 Morris, J.C. 549 [94]
 Motohashi, Y. 399 [75]
 Mott, N.F. 547 [5]
 Mügge, O. 397 [3]
 Mulford, R.N. 444 [96]
 Muller, S. 268 [134]
 Mullock, S.J. 445 [124]
 Murayama, Y. 548 [47]
 Mutin, J.C. 445 [136]
 Muzny, C.D. 269 [190]
 Myers, C.R. 76 [13]
 Myshlyaev, M.M. 549 [92]
- Nabarro, F.R.N. 76 [10]; 76 [12]; 144 [20];
 265 [14]; 269 [183]; 442 [16]; 547 [25]; 548 [78]
 Nadgornii, E.M. 549 [107]
 Nadgorny, E. 79 [126]
 Nadgorny, E.M. 79 [125]; 80 [180]; 80 [181];
 547 [19]
 Nagaya, T. 267 [71]
 Naguib, H.M. 549 [89]
 Naik, V.M. 268 [133]
 Nakanishi, H. 266 [53]
 Nango, T. 548 [43]
 Narkevich, Yu.S. 271 [279]
 Nastishin, Yu.A. 266 [38]; 269 [174]; 271 [279];
 271 [290]; 271 [293]
 Naud, J.F. 338 [96]
 Navailles, L. 271 [276]; 271 [281]; 271 [282];
 271 [289]; 271 [292]
 Navard, P. 267 [89]; 267 [90]
 Nazarov, M.V. 550 [133]; 550 [134]
 Nazarova, M.P. 549 [101]
 Nazarova, T.A. 550 [133]; 550 [134]
- Nelson, C.M. 549 [129]
 Nelson, D.R. 271 [297]; 271 [298]
 Nelson, J.R. 550 [140]
 Netühauser, H. 337 [41]; 337 [42]; 337 [43]
 Neuhäuser, H. 338 [75]
 Newey, C.W.A. 400 [122]; 400 [123]
 Newkirk, J.B. 442 [12]
 Ngan, A.H.A. 79 [159]
 Ngan, A.H.W. 80 [169]; 80 [170]; 80 [174]
 Nguyen, H.T. 269 [174]; 270 [212]; 270 [217];
 271 [261]; 271 [262]; 271 [263]; 271 [264];
 271 [265]; 271 [266]; 271 [276]; 271 [281];
 271 [289]; 271 [293]
 Nicholas, A. 401 [152]
 Nicholas, J.F. 79 [134]
 Nieh, T.-G. 76 [3]
 Nikitenko, V.I. 78 [86]; 78 [103]; 78 [105];
 78 [106]; 78 [107]; 78 [109]; 79 [120]; 548 [37];
 549 [92]
 Ninomiya, T. 79 [117]; 548 [49]
 Niori, T. 269 [173]
 Nishigaki, J. 400 [110]
 Nitsche, J.C.C. 268 [127]
 Noda, K. 79 [122]; 80 [177]
 Norlund, K. 77 [42]
 Noronha, S.J. 145 [65]
 Nott, P.R. 268 [133]
 Nufer, S. 400 [104]; 400 [109]
 Nunes, R.W. 77 [55]; 77 [56]; 78 [67]; 78 [89]
 Nye, J.F. 270 [232]; 270 [233]; 271 [295]
- Öberg, S. 77 [57]
 Oberg, S. 78 [91]
 Ockendon, H. 443 [63]
 Ockendon, J.R. 443 [63]
 Odiot, S. 445 [136]
 Ohmura, T. 548 [40]
 Okada, I. 445 [137]
 Okada, M. 337 [34]
 Okamoto, A. 337 [31]
 Okano, K. 267 [69]
 Okumura, K. 337 [31]
 Olfe, J. 338 [75]
 Olinger, B. 444 [97]
 Oliver, W.C. 548 [57]; 550 [146]
 Onda, N. 337 [23]
 Ord, A. 399 [83]; 399 [85]
 Orihara, H. 267 [71]
 Orlov, V.I. 78 [107]; 79 [120]
 Orowan, E. 550 [154]
 Orr, K.K. 400 [99]
 Orsay Liquid Crystal Group 268 [155]; 270 [241]

- Ortiz, M. 144 [15]; 144 [16]; 145 [46]; 145 [47]; 145 [54]
 Orton, J.W. 549 [120]
 Osip'yan, Yu.A. 548 [52]
 Osvenskii, V.B. 78 [109]; 547 [32]; 547 [33]
 Oswald, P. 268 [116]; 268 [131]; 268 [140]; 268 [145]; 268 [146]; 268 [148]; 268 [158]; 269 [159]; 269 [161]; 270 [227]; 271 [296]
 Otake, S. 399 [75]
 Ouchi, Y. 268 [112]; 269 [167]
 Oulevey, F. 338 [86]
 Ourmazd, A. 78 [93]
 Overney, R.M. 336 [21]
- Page, T.F. 550 [151]
 Palleschi, V. 267 [65]
 Pan, X. 402 [190]
 Pansu, B. 270 [256]; 271 [260]; 271 [261]; 271 [262]; 271 [264]; 271 [265]; 271 [266]
 Pargellis, A. 267 [74]
 Parker, S.C. 398 [32]
 Parodi, O. 267 [68]; 267 [79]; 267 [107]; 269 [164]; 269 [186]
 Parrinello, M. 80 [193]
 Pasini, P. 266 [40]
 Patel, J.R. 78 [78]
 Patel, J.S. 271 [278]
 Paterson, M.S. 398 [12]; 399 [81]; 401 [163]; 401 [165]
 Patu, S. 338 [71]
 Pavel, J. 269 [197]; 269 [202]; 270 [212]; 270 [217]
 Paxton, A.T. 144 [29]
 Payne, M.C. 78 [70]
 Pearson, D.S. 267 [80]; 267 [82]
 Pedersen, O.B. 77 [30]; 77 [31]; 77 [32]
 Peierls, R.E. 76 [9]; 144 [19]
 Pennycook, S.J. 549 [131]
 Peralta, P. 398 [24]
 Peraud, S. 338 [102]
 Perez, A. 269 [186]
 Perrin, R.C. 79 [140]
 Pershan, P.S. 267 [68]; 270 [237]
 Petch, N.J. 443 [67]; 443 [68]
 Peter, K.W. 547 [8]
 Peters, C.G. 549 [110]
 Pethica, J.B. 338 [87]; 338 [89]
 Petrenko, A.S. 271 [286]
 Petroff, P.M. 550 [143]
 Petrovic, J.J. 401 [175]; 401 [176]; 402 [191]; 402 [192]
 Pettinari, F. 338 [81]
 Pettit, D.R. 444 [96]
- Peyard, M. 445 [136]
 Peyrade, J.P. 337 [56]; 337 [57]; 337 [58]; 337 [59]
 Peyronneau, J. 400 [113]
 Phakey, P.P. 401 [154]; 442 [33]
 Pharr, G.M. 548 [57]; 550 [146]
 Philibert, J. 398 [35]; 398 [36]; 398 [39]; 398 [40]
 Phillips, D.S. 400 [96]; 400 [97]; 400 [98]; 401 [184]; 402 [204]; 402 [206]; 402 [210]
 Phillips, R. 77 [23]; 77 [24]
 Piermarini, G.J. 444 [103]
 Pindak, R. 268 [115]; 269 [168]; 269 [187]; 269 [188]; 271 [276]; 271 [278]; 271 [280]
 Piqueras, J. 550 [136]; 550 [138]
 Pirouz, P. 78 [93]; 338 [78]; 338 [79]; 398 [29]; 398 [44]; 400 [101]; 400 [102]; 400 [107]; 402 [188]; 548 [38]; 548 [46]; 548 [48]; 548 [50]
 Pitsi, G. 271 [263]
 Pizzagalli, L. 78 [74]
 Pleiner, H. 268 [118]; 268 [152]; 269 [192]; 270 [214]
 Pletka, B.J. 400 [97]; 400 [98]; 402 [199]; 402 [200]
 Plimpton, S.J. 80 [190]
 Pluzilu, J. 145 [56]
 Poénaru, V. 265 [13]; 266 [23]
 Poirier, J.P. 266 [26]; 268 [151]; 270 [247]; 400 [113]; 401 [156]; 401 [166]
 Polanyi, M. 550 [155]
 Pomeau, Y. 265 [13]
 Pontikis, V. 77 [36]
 Poole, W.J. 550 [152]
 Pope, D.P. 144 [26]; 145 [66]; 145 [67]
 Portevin, A. 80 [187]
 Poulin, P. 266 [46]; 268 [137]
 Poumellec, B. 401 [161]
 Pramod, P.A. 271 [283]; 271 [284]
 Pratibha, R. 271 [283]; 271 [285]
 Predvoditelev, A.A. 547 [23]
 Prekel, H.L. 79 [124]
 Prince, E. 442 [15]
 Prinz, F. 77 [26]
 Prost, J. 266 [33]
 Pueschl, W. 144 [13]
 Puls, M.P. 398 [31]
 Puttick, K.E. 548 [42]
- Qin, C.-D. 549 [116]
 Quate, C.F. 336 [7]
 Quilliet, C. 267 [100]
- Rabbe, P. 401 [145]

- Rabier, J. 77 [45]; 77 [49]; 77 [51]; 78 [74]; 78 [96]; 337 [50]; 398 [15]; 398 [17]; 398 [20]; 399 [61]; 400 [131]; 401 [149]; 401 [150]; 401 [151]; 401 [178]; 401 [179]; 401 [181]; 401 [182]
- Radford, K.C. 398 [14]; 400 [122]; 400 [123]
- Raghuram, A.C. 443 [41]
- Rahman, A. 80 [193]
- Rahvalov, V.A. 548 [68]
- Rajnak, S. 80 [167]
- Raleigh, C.B. 401 [155]
- Ralph, D.C. 76 [13]
- Ramaswamy, A.L. 444 [104]; 444 [105]; 444 [106]; 444 [107]; 445 [109]
- Ramaswamy, S. 268 [133]
- Ramos, L. 268 [137]
- Ranganath, G.S. 266 [35]
- Rao, S.I. 77 [35]; 79 [139]; 79 [147]
- Rasmussen, T. 77 [30]; 77 [31]; 77 [32]
- Rau, E.I. 550 [133]
- Ray, R. 266 [60]
- Read, W.T. 442 [31]
- Reece, M.J. 401 [147]
- Rees, C.S. 445 [124]
- Reinhardt, L. 338 [74]
- Reinitzer, F. 270 [239]
- Ren, Q. 77 [59]
- Renn, S.R. 271 [271]; 271 [274]; 271 [275]
- Reppich, B. 402 [202]
- Ressier, L. 337 [56]; 337 [58]; 337 [59]
- Retchford, J.A. 399 [90]
- Rice, J.R. 144 [3]; 144 [14]; 144 [27]; 145 [30]; 145 [32]; 145 [33]; 145 [35]; 145 [42]
- Richardson, G.Y. 79 [138]
- Richmond, D. 76 [6]
- Richter, L. 266 [34]
- Ricoult, D.L. 401 [160]
- Rieck, G.D. 401 [148]
- Riester, L. 550 [151]
- Riley, F.L. 402 [190]
- Rinder, W. 547 [30]; 547 [31]
- Ritchie, J.P. 445 [140]; 445 [142]
- Rivi  re, J.P. 401 [171]
- Rivi  re, J.P. 402 [206]
- Rivi  re, J.P. 548 [70]
- Rivi  re, S. 269 [193]
- Roberts, K.J. 442 [34]; 443 [35]
- Roberts, S.G. 144 [11]; 144 [12]; 145 [49]; 145 [50]; 145 [64]; 145 [65]; 548 [38]; 548 [46]; 548 [48]; 548 [50]; 548 [71]; 549 [116]
- Robertson, D.H. 446 [149]; 446 [150]
- Robinson, C. 270 [243]; 270 [244]
- Robinson, P.M. 443 [37]
- Robinson, W.H. 443 [50]
- Rocher, A. 337 [57]
- Rodloff, R. 337 [41]; 337 [43]
- Rodney, D. 77 [18]; 77 [23]; 77 [37]
- Rodriguez, A.D. 398 [36]
- Rodriguez-Clemente, R. 337 [32]
- Roessler, D.M. 550 [141]
- Rohrer, G.S. 337 [29]; 337 [30]
- Rohrer, H. 336 [3]; 336 [4]; 336 [5]; 336 [6]
- Romestain, R. 549 [128]
- Rose, J.H. 145 [34]
- Rosemeier, R.G. 443 [40]; 443 [47]
- Rosenblatt, C. 268 [115]
- Rosenblatt, G.H. 549 [127]
- Rossolenko, S.N. 79 [120]
- Rout, D. 268 [133]; 268 [134]
- Routbort, J.L. 398 [33]; 398 [37]
- Roux, D. 267 [99]; 268 [132]; 268 [138]; 268 [139]
- Rowcliffe, D.J. 548 [41]; 548 [77]
- Rowe, M.W. 549 [127]
- Rozhanskii, V.N. 547 [14]; 547 [23]; 549 [101]
- Rudd, R.E. 80 [197]
- Rudel, P. 445 [136]
- Rudnick, J. 269 [194]
- Rudquist, P. 271 [287]
- R  hle, M. 399 [53]; 400 [104]; 400 [115]; 400 [116]; 400 [120]; 400 [121]; 402 [190]
- Russell, T.P. 444 [108]
- Ryskin, G. 267 [70]
- Saada, G. 338 [66]
- Sadoc, J.-F. 270 [250]
- Safran, S.A. 267 [99]
- Saito, M. 269 [169]
- Saka, H. 79 [122]; 80 [177]; 400 [110]; 400 [119]; 548 [43]
- Sakamoto, K. 548 [47]
- Sakurai, T. 336 [20]
- Samant, A.V. 398 [44]
- Sammon, M. 271 [259]
- Samuels, J. 145 [49]; 145 [50]; 145 [64]
- Sanchez, M. 398 [35]
- Sands, H.S. 550 [139]
- Sandusky, H.W. 444 [79]; 444 [91]; 444 [92]; 445 [131]; 446 [156]; 446 [157]
- Sangwal, K. 337 [22]; 337 [32]
- Sankey, O.F. 78 [83]
- Sanz, F. 337 [22]
- Saparin, G.V. 547 [14]; 550 [133]
- Sarma, G. 267 [107]
- Sass, S. 79 [133]
- Sato, K. 337 [34]
- Scafidi, P. 337 [45]; 337 [46]

- Schaublin, R. 77 [39]
 Scherrer, S. 399 [64]
 Schiff, E.A. 266 [58]
 Schlössin, H.H. 548 [74]
 Schmid, E. 79 [153]; 79 [154]; 337 [37]; 397 [1]
 Schmid, H. 77 [26]
 Schmid, M. 336 [19]
 Schmidt, C. 268 [134]
 Schmidt, V.V. 271 [270]
 Schoeck, G. 76 [15]; 144 [13]; 145 [31]
 Schönfeld, B. 338 [73]; 338 [74]
 Schopol, N. 266 [49]
 Schott, M. 337 [24]
 Schreiber, J. 547 [14]; 550 [144]
 Schroeder, W. 79 [120]
 Schroter, W. 77 [48]
 Schröter, W. 78 [97]; 78 [98]
 Schulze, D. 79 [121]
 Schwander, P. 338 [73]
 Schwink, Ch. 337 [41]; 337 [42]; 338 [76]
 Scott, H.G. 443 [37]
 Scott, W.D. 400 [99]
 Secher, D. 401 [152]
 Seeger, A. 79 [149]
 Seitz, F. 549 [118]
 Sekine, T. 269 [173]
 Selinger, J.V. 270 [248]
 Serbena, F.C. 548 [71]
 Servat, J. 337 [22]
 Sestak, B. 79 [130]
 Sethna, J.P. 76 [13]; 267 [105]; 269 [209];
 270 [210]; 270 [255]; 270 [257]
 Shahid, M.A. 548 [42]
 Sharif, A.A. 401 [175]; 401 [176]
 Sharma, J. 445 [109]; 446 [156]; 446 [157];
 446 [158]; 446 [159]
 Shaskol'skaya, M.P. 547 [27]
 Shaw, D.C. 444 [95]; 444 [96]
 Sheen, D.B. 445 [129]; 445 [130]
 Shenoy, V.B. 77 [24]
 Shepel'skii, G.A. 550 [144]
 Sherwood, J.N. 442 [34]; 443 [35]; 443 [42];
 445 [129]; 445 [130]
 Shi, C.X. 338 [71]
 Shi, L.T. 145 [41]
 Shimatani, A. 548 [43]
 Shin, H. 445 [109]
 Shiyanova, S.V. 266 [40]; 266 [41]; 266 [42];
 271 [279]
 Shockley, W. 442 [31]
 Si, W. 442 [20]
 Sibley, W.A. 549 [125]; 550 [142]
 Sieber, B. 401 [171]
 Sierro, P. 268 [132]
 Siethoff, H. 77 [48]
 Sigaud, G. 271 [263]
 Sigle, W. 79 [148]; 400 [116]; 400 [120]; 400 [121]
 Simmons, G. 145 [36]
 Sinclair, R. 548 [76]; 548 [77]
 Singh, B.N. 77 [39]
 Singh, K. 443 [69]
 Sirringhaus, H. 336 [1]; 336 [2]; 337 [23]
 Sitch, P.K. 78 [91]
 Skowronski, M. 337 [29]; 337 [30]
 Slaney, A.J. 271 [280]
 Sluckin, T.J. 266 [49]
 Smallman, R.E. 399 [71]; 399 [76]
 Smalyukh, I.I. 266 [41]; 266 [42]; 270 [235];
 270 [238]; 271 [285]
 Smirnov, B.I. 549 [119]
 Smith, B.K. 401 [168]
 Smith, C.S. 444 [77]
 Smith, J.R. 145 [34]
 Sneddon, I.N. 547 [3]
 Soderlin, P. 79 [146]
 Soderlind, P. 79 [145]; 80 [197]
 Sommeria, J. 268 [114]
 Sonder, E. 549 [124]
 Soria-Ruiz, J. 443 [71]; 443 [72]; 445 [110]
 Spain, I.L. 549 [97]
 Spence, J.C.H. 76 [1]; 78 [83]
 Spencer, W.J. 444 [96]
 Spendel, M. 398 [36]
 Sprackling, M.T. 398 [4]; 547 [22]
 Spruijt, A.M. 267 [78]
 Sprusil, B. 337 [52]; 337 [55]
 Srinivasan, M. 398 [30]
 Srinivasan, M. 402 [201]
 Srinivasan, S.G. 77 [30]
 Sriram, S. 80 [192]; 337 [27]
 Srivastava, A.M. 266 [58]; 266 [60]
 St John, C. 144 [9]
 Stablein, P.F. 547 [29]
 Stadler, H. 336 [19]
 Stadler, R. 337 [23]
 Stark, H. 266 [46]
 Startsev, V.I. 548 [82]
 Stebler, B. 269 [179]
 Steenrod, N. 266 [20]
 Stein, S.M. 271 [278]
 Stelmashenko, N.A. 547 [11]
 Stepanov, A.V. 547 [19]
 Stepanova, V.M. 547 [23]
 Stephens, A. 548 [60]
 Stich, I. 78 [70]
 Stillinger, F.H. 78 [72]
 Stine, J.R. 445 [133]

- Stoebe, T.G. 398 [30]; 402 [201]
 Stokbro, K. 78 [69]
 Stolyarov, O.G. 547 [32]; 547 [33]
 Stracha, A. 80 [196]
 Streitz, F.H. 80 [197]
 Stroscio, J. 336 [13]
 Strzelecki, L. 269 [166]
 Subacius, D. 270 [229]; 270 [230]
 Suematsu, H. 401 [140]; 402 [189]; 402 [191]; 402 [192]
 Sueoka, K. 548 [45]
 Sugiyama, N. 337 [31]
 Sumino, K. 77 [46]; 78 [104]; 547 [34]
 Sun, Y. 144 [27]; 145 [30]; 145 [60]
 Sunagawa, I. 337 [36]
 Sundgren, J.E. 337 [26]
 Suprijadi 548 [43]
 Suresh, S. 76 [3]; 76 [4]
 Sutton, A.P. 78 [70]; 78 [92]; 79 [163]
 Suzuki, H. 446 [153]
 Suzuki, K. 398 [43]; 399 [77]; 400 [112]; 549 [115]
 Suzuki, T. 77 [52]; 78 [76]; 80 [171]; 398 [38]; 400 [112]; 401 [140]; 402 [189]; 548 [40]
 Svetlov, I.L. 549 [101]
 Swain, M.V. 547 [15]; 548 [81]
 Swain, M.W. 398 [46]
 Swallowe, G.M. 443 [56]
 Syed Asif, S.A. 338 [89]
- Tabor, D. 443 [53]; 548 [58]; 549 [86]
 Taeri-Baghbadrani, S. 400 [115]; 400 [116]
 Takahashi, T. 548 [73]
 Takanishi, Y. 269 [169]; 270 [213]; 270 [215]; 270 [216]
 Takano, H. 268 [112]
 Takayanagi, K. 336 [16]
 Takeuchi, S. 79 [158]; 80 [171]; 398 [43]; 399 [77]; 400 [112]; 550 [159]
 Takezoe, H. 268 [112]; 269 [167]; 269 [169]; 269 [173]; 269 [208]; 270 [213]; 270 [215]; 270 [216]
 Tang, M. 77 [50]; 79 [157]
 Tang, T.B. 445 [124]; 547 [10]
 Tani, T. 337 [31]
 Taplin, D.M.R. 549 [117]
 Tarbaev, N.I. 550 [144]
 Tasker, D.G. 444 [93]
 Taupin, D. 269 [162]
 Taylor, G.I. 79 [128]; 80 [178]; 550 [153]
 Teichler, H. 77 [53]
 Templeton, L.C. 549 [124]
 Teracher, P. 399 [61]
- Terentjev, E.M. 266 [54]
 Tersoff, J. 78 [88]; 336 [10]; 336 [13]
 Terwillinger, G.R. 398 [14]
 Thetford, R. 80 [185]
 Thibault-Desseaux, J. 77 [27]; 77 [63]
 Thoen, J. 271 [263]
 Tholen, A.R. 402 [209]
 Thomas, H.R. 547 [1]
 Thomas, J.M. 442 [19]; 445 [113]; 445 [114]
 Thomas, P.B. 267 [109]
 Thomson, R. 79 [117]; 144 [3]; 144 [17]; 145 [43]
 Thornton, P.H. 338 [67]
 Tikhonovsky, A. 399 [49]; 399 [53]; 399 [67]
 Tinschert, K. 399 [64]
 Tobin, R.C. 399 [89]
 Tokmakoff, A. 444 [89]
 Tokuoka, T. 78 [76]
 Tolochko, A.S. 271 [279]
 Tompa, A.S. 446 [156]
 Tondellier, T. 77 [45]
 Toner, J. 271 [294]
 Tordion, G.V. 547 [9]
 Torrent-Burgues, J. 337 [22]
 Toulouse, G. 265 [13]; 266 [23]; 269 [181]
 Toyoki, H. 266 [63]
 Tramposch, R.F. 547 [30]; 547 [31]
 Tranchant, F. 337 [60]; 337 [62]; 338 [64]
 Trebin, H.R. 266 [18]; 266 [19]
 Trefilov, V.I. 80 [180]; 547 [26]; 549 [95]; 549 [96]
 Trepied, L. 399 [87]
 Tressler, R.E. 401 [147]
 Tromas, C. 338 [85]; 338 [91]; 338 [95]; 550 [150]
 Tsai, D.H. 446 [144]; 446 [145]; 446 [146]; 446 [147]; 446 [148]
 Tsuji, T. 77 [22]
 Tsurekawa, S. 402 [187]
 Tsvetkov, V.F. 337 [26]; 442 [20]
 Tu, P. 78 [99]
 Tunison, K.S. 444 [84]
 Tupper, S.J. 548 [79]
 Turner, M.S. 270 [226]
 Turner, T.J. 549 [129]
 Turok, N. 266 [59]; 267 [74]
 Twieg, R.J. 271 [281]
 Tyson, W.R. 144 [2]
- Uberuaga, B.P. 80 [172]
 Ueda, O. 548 [47]
 Uemara, T. 269 [208]
 Umerski, A. 78 [90]
- Valdré, U. 549 [88]

- Valladares, A. 78 [92]
 Van der Eerden, J.P. 337 [33]; 337 [36]
 Van der Hoek, B. 337 [33]; 337 [36]
 van der Steen, A.C. 442 [27]
 van Enckevort, W.J.P. 442 [32]
 van Känel, H. 337 [23]
 van Sarloos, W. 267 [85]
 van Winkle, D.H. 269 [189]
 Vand, V. 442 [7]
 Vanderbilt, D. 77 [55]; 77 [56]; 78 [67]; 78 [89]
 VanderSande, J.B. 401 [167]
 Vanderschaeve, G. 78 [85]; 548 [51]; 550 [158]
 Varga, P. 336 [19]
 Vassent, J.L. 336 [18]
 Vasudevan, V.K. 80 [192]
 Vegge, T. 76 [13]; 77 [32]
 Veit, K. 400 [106]
 Velednitskaya, M.A. 547 [14]
 Venkataraman, S.K. 338 [88]
 Venkatraman, S. 549 [108]
 Vergnol, J. 337 [60]; 337 [61]; 337 [62]; 338 [63];
 338 [64]
 Vergrobbi, B. 401 [166]
 Verma, A.R. 442 [1]; 442 [5]
 Verneuil, A. 400 [92]
 Veyssiére, P. 338 [66]; 398 [15]; 398 [17]; 398 [19];
 398 [20]; 400 [131]; 400 [134]; 401 [149];
 401 [150]; 401 [151]; 401 [178]; 401 [179];
 401 [181]
 Vicario, E. 399 [75]
 Victoria, M. 77 [39]; 77 [43]
 Vidal, P. 269 [185]
 Viguier, B. 80 [191]
 Villechaise, P. 338 [101]; 338 [102]
 Vineyard, G.H. 145 [55]
 Virga, E. 265 [10]
 Vitek, V. 79 [131]; 79 [136]; 79 [137]; 79 [140];
 79 [151]; 79 [152]; 79 [161]; 79 [162]; 144 [25];
 144 [26]; 145 [66]; 145 [67]; 269 [203]
 Voegele, V. 402 [185]
 Vogel, J.F.L. 79 [129]
 Voillot, F. 337 [56]; 337 [57]; 337 [58]
 Voloschenko, D. 270 [231]
 Volovik, G.E. 266 [29]; 266 [39]; 266 [43]
 Von Känel, H. 336 [1]; 336 [2]

 Wachtman, J.B. 398 [6]; 398 [13]
 Wackerle, J. 444 [98]
 Wai, S.-W. 548 [78]
 Walker, F.E. 445 [143]
 Walker, W.C. 550 [141]
 Walls, M.G. 547 [10]; 547 [11]
 Walsh, W.P. 144 [6]
 Walters, G.K. 549 [121]
 Wang, C.M. 402 [190]
 Wang, G. 79 [150]
 Wang, H. 145 [36]
 Wang, S. 442 [20]
 Wang, Z. 401 [177]; 401 [180]; 401 [183]
 Ward, J.C. 270 [244]
 Warner, P.D. 145 [64]
 Warren, P.D. 548 [48]; 548 [50]
 Wasserbäch, W. 80 [176]
 Watanabe, J. 269 [172]; 269 [173]; 270 [213];
 270 [215]
 Watson, G.W. 398 [32]
 Waugh, M.A. 271 [278]
 Weatherburn, C.E. 267 [95]
 Webb, R.H. 271 [300]
 Webb, R.L. 550 [137]
 Webb, W.W. 144 [4]; 144 [5]; 268 [156]
 Weber, E. 78 [77]
 Weber, J. 78 [80]
 Weber, S. 399 [64]
 Weber, T.A. 78 [72]
 Weil, J.A. 399 [88]
 Weitz, D.A. 266 [46]; 268 [137]
 Wells, J.K. 548 [60]; 550 [132]
 Welsch, G. 400 [126]
 Wen, M. 79 [159]; 80 [174]
 Wenckus, J.F. 398 [47]
 Wernick, J.H. 442 [12]
 Wertz, J.H. 549 [120]
 Wessel, K. 77 [44]
 Westbrook, J.H. 398 [21]
 Westmacott, K.H. 399 [66]
 Westwood, A.R.C. 550 [157]
 Whelan, M.J. 442 [10]; 550 [156]
 Whitbread, E.G. 444 [90]
 White, C.T. 446 [149]; 446 [150]
 White, J.A. 78 [92]
 White, T.J. 401 [170]
 Whitworth, R.W. 550 [160]
 Wickramasinghe, H.K. 336 [9]
 Wiebel, E. 336 [3]; 336 [4]
 Wild, R.K. 549 [113]
 Wilkinson, A.J. 145 [65]
 Williams, C. 268 [110]
 Williams, C.E. 268 [120]; 268 [150]; 269 [195]
 Williams, G.P. 549 [127]
 Williams, R.T., Jr. 549 [127]
 Williams, W.S. 548 [71]
 Williamson, G.K. 399 [76]
 Willis, B.T.M. 399 [70]
 Winter, R.E. 443 [59]
 Wirth, B.D. 77 [38]; 77 [41]

- Woigard, J. 338 [83]; 338 [84]; 338 [85]; 338 [91]; 338 [95]; 401 [159]; 550 [150]
- Won, Y. 446 [152]
- Woo, C.H. 398 [31]
- Wood, J.K. 145 [38]
- Woodward, C. 77 [35]; 79 [139]; 79 [147]
- Wright, D.C. 270 [257]
- Wu, C.C. 548 [62]
- Wu, C.Cm. 443 [46]
- Wu, C.M. 338 [92]
- Wunenberger-Krepper, A.-S. 268 [142]
- Wuthrich, C. 79 [149]; 80 [165]; 80 [166]
- Yip, S. 77 [19]; 77 [21]; 77 [40]; 77 [54]; 77 [58]; 77 [65]; 78 [75]; 78 [87]; 78 [112]; 80 [164]; 80 [189]; 144 [8]; 145 [61]
- Yizhen, H. 78 [99]
- Yoffe, A.D. 443 [54]
- Yoffe, E.H. 547 [7]
- Yokoyama, H.J. 267 [66]
- Yonenaga, I. 77 [46]
- Yoo, K.-C. 443 [40]; 443 [47]
- Yoshinaga, H. 402 [187]
- Yoshioka, M. 548 [39]
- Young, C.Y. 269 [187]; 269 [188]
- Yurke, B. 266 [59]; 267 [74]
- Xu, G. 144 [15]; 144 [16]; 144 [23]; 144 [24]; 145 [46]; 145 [59]
- Xu, W. 79 [142]; 79 [143]; 79 [160]
- Yakimov, E.B. 78 [105]
- Yamaguchi, M. 79 [161]; 79 [162]; 144 [26]; 398 [27]
- Yamanaka, K. 550 [135]
- Yamashita, Y. 79 [115]
- Yang, D.-K. 270 [240]
- Yang, L.H. 79 [145]; 79 [146]; 80 [197]
- Yano, T. 401 [144]
- Yashodhaln Hatvalne, N.V. 271 [284]
- Yasunaga, K. 80 [183]
- Yasutomi, T. 78 [76]
- Yee, R.Y. 443 [40]
- Zannetti, M. 266 [62]
- Zannoni, C. 266 [40]
- Zapotocky, M. 268 [137]
- Zasadzinski, A.N. 271 [280]
- Zeng, K.-Y. 76 [4]
- Zerilli, F.J. 444 [75]; 444 [81]
- Zhang, X.J. 445 [135]
- Zhang, Z. 400 [120]; 400 [121]
- Zhitaru, R.P. 548 [68]; 550 [134]
- Zhou, D.S. 402 [193]
- Zhou, S.J. 144 [17]; 145 [43]
- Zhu, J. 77 [50]
- Zielinski, W. 549 [108]
- Zilman, G. 268 [141]
- Zozime, A. 548 [70]
- Zurek, W.H. 266 [56]; 266 [57]

This page intentionally left blank

Subject Index

- 2π disclinations, 162, 226
 J -integral, 90
 R^3 , 247, 248
 S^1 , 172
 S^2 , 162
 S^3 , 162, 244, 247
 $\Pi_1(V)$, 159
 α - and β -dislocations, 487
 α -Fe crystals, 487
 α -Fe(100), 487
 α -HgI₂, 539
 α -mercuric iodide, 539
 α -type, 486
 α -type dislocations, 486
 β -Sn phase, 516, 544
 β -Sn phase of Si, 516
 β -Sn structure, 516
 β -type, 486
 β -type dislocations, 486
 χ -disclinations, 160
 χ -field, 219
 c unit vectors, 216
 c -curvature, 220
 χ^+ wedge disclination, 228
 γ -surface, 86
(100) slip bands, 535
 $\omega = \pi$ packing, 195
 $\pm 2\pi$ disclinations, 160, 216
 $\pm 4\pi$ disclinations, 160
 $\pm \pi$ disclinations, 216
{110}{110}, 502
 $k = +1/2$ lines, 203
 $k = 1$ lines, 203
(thermotropic) small molecule chemicals (SMLC), 154
 $ab initio$ calculations, 84
{100}, 506
{100} cleavage cracks, 491, 502, 506
{100} cracks, 506, 507
{110}45, 459, 461, 463
{110}45 plane, 464, 466, 468
{110}45 planes, 458, 463, 493, 496, 511, 525
{110}45 slip plane, 461, 508
{110}45 slip planes, 459, 494, 525
{110}90, 466, 467, 490, 492, 506
{110}90 crack, 496, 498, 506, 507
{110}90 cracking, 490, 493–495
{110}90 cracks, 490, 491, 493–495, 497–499, 503, 505, 506, 508, 535
{110}90 cracks during unloading, 501
{110}90 plane, 464, 466
{110}90 planes, 459, 491
‘cosmology in the laboratory’, 172
‘degeneracy parameter’, 165
‘edge’ arms, 466
‘equilibrium’, 173
‘escape in the 3rd dimension’, 152, 157, 159, 160, 170
‘fresh’ dislocations, 464
‘old’ dislocations, 464
‘picture frame’, 493
‘planar’ disclinations, 170
‘pop-in’ of dislocations, 542
‘screw’ arms, 466
‘sponge’ phase L₃, 183
‘swirl patterns’, 219
‘synchro-shear’ displacement, 526
‘thick’, 227
‘thin’, 227
‘topological instability’, 163
non-equilibrium correlation length $\xi(t)$, 174
1 MeV TEM, 519
1D liquids, 155
2-beam diffraction conditions, 543
2-torus T^2 , 163
2D liquid layers, 154
2D defects, 178
2D liquid phases, 155
2D order, 155
2D ordering, 262
2D solids, 155
2nd-order phase transition, 161
3-dimensional indentations, 505
3-point bend test, 473, 503
3D crystal, 158
3D knotted, 157
3D topological defects, 163
6D hypercubic crystals, 163
6H-SiC single crystal, 529
6H-SiC(1100), 527

- 6H-SiC(0001), 527, 528, 542
 8CB (4-n-octyl-4'-cyanobiphenyl), 205
- a plastic shear rate, 206
 a screw dislocation, 209
 A^3He , 216
 Abelian, 162
 Abrikosov phase, 243, 251
 abrupt jump, 542
 absence of cathodoluminescence, 531, 534
 absence of dislocations, 517
 absorption bands, 530
 achiral molecules, 156
 activation energies, 84, 85, 112
 activation energy, 91, 114, 206, 210
 activation process, 84
 active slip planes, 487, 504
 activity, 463
 actual dislocation number, 488
 adiabatic heating, 420
 $AgCl$, 466
 aliovalent solute atoms, 393, 395, 396
 AlN ceramic, 526
 alumina, 525
 amorphisation, 512, 544
 amorphised material recrystallized, 517
 amorphous, 516, 517, 519, 544
 amorphous films of silicon, 546
 amorphous phase of silicon, 546
 amorphous silicon, 546
 amorphous silicon (α -Si), 546
 amorphous silicon at 77 K, 547
 amorphous silicon film, 546
 amorphous silicon film at 77 K, 546
 amorphous zone, 519
 amounts of impurities, 473
 anchoring coefficient, 241
 anchoring energy, 225
 anchoring extrapolation length, 167
 anchoring mechanisms, 175
 anchoring strength, 219, 237
 anchoring terms, 187
 anion vacancies, 530
 anisotropic, 457
 anisotropic mechanical behaviour, 503
 anisotropic solid, 142
 annealed, 476, 482, 520, 523
 annealed indent, 538
 annealed indentations, 538
 annealed indents, 535
 annealed MgO crystal, 534
 annealed single crystals of LiF, 511
 annealed specimen, 476
 annealing, 478, 520, 532
- anticlinic, 214, 251
 anticlinicity, 214
 antiferroelectric, 155, 213, 214, 225
 antiferroelectric twist grain boundary phase, 251
 apex, 452
 Apollonian packing, 186, 190–192, 195
 Apollonian tiling, 195
 Apollonius' problem, 192
 applied dynamic shear stress, 510
 applied indenter load, 451, 453, 456, 479
 applied load, 451, 463
 applied maximum indenter load, 472
 applied shear stress, 511
 applied stress, 211
 argon, 512
 armour plate, 458
 arrays, 539
 arrays of dislocations, 464, 545
 artefacts, 524, 526, 545, 546
 asterism, 523
 asymptotes, 190
 atomic decohesion, 83
 atomic force microscopy (AFM), 275, 277, 279, 280, 284–296, 298–300, 302–304, 306–308, 312, 313, 315, 317, 319, 324–332, 334, 541
 atomic potential, 84
 atomic simulation, 138
 atomistic simulation, 84
 axis of revolution, 187
 axisymmetric indenter, 449
- bâtonnets, 190
 backflow, 176
 background, 538
 background spectra, 537
 ball impact technique, 460
 ball impact test, 461
 ball indentation method, 458
 banana molecules, 215
 band gap, 531
 bands at 800 and 804.2 nm, 539
 basal partials, 528
 basal planes, 526, 543
 basal twins, 525
 base, 161
 base point, 159
 bend, 227, 250
 bend contours, 522, 524
 bend elastic constant K , 190
 bending, 513
 bent-core shaped molecules, 215
 Berkovich, 453, 457
 Berkovich diamond, 517

- Berkovich diamond indentations, 517
 Berkovich diamond indenter, 489
 Berkovich indenter, 451, 526, 540, 542
 Berkovich nano indentations, 543
 beryllium oxide, 360
 biaxial nematic Nb, 160
 biaxial nematics, 153
 Billig reagent, 484
 Bingham type law, 205
 blister, 455, 470
 blister field, 450, 455, 470, 471, 501
 blister shear stress fields, 470
 blockages, 441
 blue and red bands, 537
 blue band, 537, 538
 blue fog, 248
 Blue phases (BP), 245, 263
 blunt indenters, 452
 blunt indenters, such as spheres, paraboloids, ellipsoids, 451
 body-centred tetragonal phase, 516
 Boltzmann constant, 139
 bond-orientational order, 261
 boojums, 164, 166, 168, 175, 219, 224
 bookshelf texture, 220
 boron, 482
 Boussinesq, 470
 Boussinesq field, 455, 470
 Boussinesq point loading field, 450
 BP, 243
 BPI, 156, 248
 BPII, 156, 248
 BPIII, 156, 248
 Bragg bubble model, 95
 Brener–Marchenko model, 231
 bright-field, 543
 bright-field mode, 520
 bright-field transmission electron micrographs, 517
 brittle materials, 512
 brittle to ductile transition, 83, 85, 142
 brittle to ductile transition temperature, 85, 112, 139
 brittle–ductile transition temperature InP, 501
 brittle/ductile transition temperature of Si, 475
 buckling of dislocations, 241
 bulk defect, 162
 bulk strength of the crystals, 473
 Burgers circuit, 163
 Burgers vector, 86, 160, 163, 185, 188, 193, 195–197, 200, 204, 206–208, 210, 215, 226, 228, 234, 235, 263, 449, 466, 471, 491, 492, 511, 515, 528
 Burgers vectors, 238, 259, 450, 466, 492, 527
 Burgers vectors \mathbf{u} and \mathbf{v} , 450
 Burgers vectors \mathbf{u} and \mathbf{v} , 495
 C, 503
 cadmium telluride, 539
 camera, 507, 508
 CaO, 530
 carbon, 487
 carbon-containing α -Fe crystals, 487
 carbon-containing crystals, 487
 Cartesian/rectangular coordinates, 450
 cathodoluminescence, 451, 530–534, 537, 539
 cathodoluminescence behaviour, 539
 cathodoluminescence image, 531
 cathodoluminescence in MgO, 538
 cathodoluminescence results, 537
 cathodoluminescence studies, 531, 534
 caustics, 178
 cavity, 477
 CdTe, 539
 centre, 521
 centre of curvature, 201
 centre of indentation, 470
 centre of symmetry, 158
 centres of curvature, 178, 187
 ceramic, 276, 525
 ceramic crystals, 519
 ceramics, 341–343, 346, 349, 350, 353, 355, 356, 363, 375, 376, 386, 387, 397
 ceramics and glasses, 457
 changing the orientation, 525
 characteristic pits, 458
 charged dislocations, 545
 chemical decomposition, 405, 420, 422, 428, 430, 432, 433, 439, 441
 chemical etching, 451, 464, 475, 476
 chemical etching technique, 458
 chemical thinning, 512
 chemomechanical effects in non-metals, 545
 chevron layer texture, 220
 chevron walls, 195
 chiral, 156, 214, 224, 226, 227, 261
 chiral columnar phases, 156
 chiral molecules, 226
 chirality, 156, 203, 210, 226, 245
 cholesteric, 251, 254
 cholesteric biopolymers, 241
 cholesteric blue phase, 156, 262
 cholesteric liquid crystals at large scales, 229
 cholesteric phase, 160
 cholesteric planar texture, 240
 cholesterics, 184
 cholesterics (N^*), 153
 chromosome of dinoflagellate, 263

- circle S^1 , 161
 circle of contact, 450, 453, 459–461, 463
 circle of radius, 453
 circular fringes, 467
 class of conjugacy, 160, 229
 class of defects, 159
 classification of disclinations in Nb, 160
 cleavage, 405, 413, 415, 416, 422, 428, 429, 431, 433, 440, 441
 cleavage fracture, 83, 85, 92, 142
 cleavage ledge, 110, 111, 142
 Clifford parallels, 248
 climb, 204, 206, 207, 235
 closed loop, 163
 closed manifold, 180
 clusters, 482
 coarse-grain model, 227
 coarse-grained cholesteric, 231
 coarse-grained model, 226, 259
 coefficient of permeation, 208, 210
 colour centres, 449, 530, 534, 537, 538
 colour composition, 537
 columnar phases, 261
 columnar systems, 155
 columnar TGB phase, 243
 columns, 200, 203
 combined elastic stress fields, 455
 commutative group, 159
 compaction, 453
 compaction/densification, 456
 complete FCD-I, 180
 complete torus, 180
 component, 449, 455
 composition law, 160
 compressibility, 183, 187
 compressibility energy density, 185
 compressibility term, 183
 compressible solids, 452
 compression, 259, 513
 compression method, 458
 compressive stress, 210
 concentric haloes, 517
 condition of least curvature, 258
 cone-and-plate device, 211
 configurational velocity, 207
 configurations, 153, 162–164
 confining pressure, 454
 conical indenter, 449, 452, 528
 conics, 181, 187, 195
 conjugacy class, 159, 162
 conjugate conics, 160, 178, 180
 conjugate focal lines, 258
 constitutive equation, 211
 constrictions, 153
 contact area, 452
 contact circle, 457, 460–462
 contact depth, 456
 contact depth h_c of the indentation, 541
 contact depth of the indenter, 449
 contact edge, 504, 505
 contact of radius, 452
 contact or thermal stresses, 539
 contact radius, 510
 contact region, 454
 contact stresses, 457, 539
 contact zone, 453
 contaminants, 513
 continuous translation-rotation (helical) group, 253
 continuum mechanics slip-line field theory of Hill, Lee and Tupper, 544
 copper, 545
 copper crystals, 490
 copper single, 487
 core, 154, 159, 166, 167, 176, 195–197, 203, 206, 208, 220, 225, 231, 235, 246, 250, 256, 258
 core defects, 3, 4, 32, 36, 41, 59, 61
 core energy, 5, 26, 40, 60, 181
 core of disclinations, 152
 core radius, 181, 203
 core reconstruction, 22, 25, 27–30, 32, 36, 37, 40, 41, 56, 57, 61
 core singularity, 198
 core structure, 3–6, 8, 9, 12–15, 17, 22, 24–26, 28, 30–32, 35, 55, 57, 59–61, 63, 69
 core TS, 206
 correlation length, 173
 coupled tension and shear interlayer potential, 92
 coupled tension and shear potential, 142
 Cr^{3+} , 525
 crack, 491, 492, 494
 crack arrest, 83
 crack systems, 495
 crack-free indentations, 545
 cracking, 491, 492, 494, 495, 497, 502, 514
 cracking around indentations, 490
 cracking in MgO , 490
 cracking patterns, 457
 cracks, 490–492, 498, 503
 creation, 538
 creation and mobility of dislocation loops, 546
 creation of dislocations, 451
 creep, 211
 critical load required, 463
 critical plastic strain, 537
 critical resolved shear stress, 342, 349, 376, 394, 449, 450, 464, 473, 477, 480, 481
 critical shear stress, 461, 463, 471, 472, 480, 513

- critical shear stress for dislocation glide, 450
critical shear stress values, 461
critical values, 460, 463
cross-beam, 540
cross-kink, 70, 72, 73
cross-sectional examination, 513
cross-sectional viewing, 512
cross-slip, 16, 17, 21, 22, 30, 52, 55, 69, 70, 72, 75, 295, 296, 298, 312, 316, 325, 326
crystal, 451, 536
crystal of LiF, 460, 493
crystal plasticity, 3–5, 69, 75
crystalline, 519
crystalline line defects, 532
crystalline region 519
crystalline silicon, 546, 547
crystallization, 546
crystallographic defects, 524
crystallographic orientation, 525
crystallographic phase change, 475
crystals, 457, 538
cubic, 248, 516
cubic boron nitride, 451
cubic phase, 199, 517, 544
cubic Si, 516, 519, 544
cubic Si-I, 546
cubic silicon (Si-I), 546
curvature, 244
curvature defect, 202
curvature distortion, 155
curvature elasticity, 154
curvature energy, 154, 180, 183, 187, 190, 198
curvature models, 193, 194
curvature of least energy, 257
curvature of the layers, 203
curvature relaxation, 257
curvature wall energy, 194
curvature walls, 190, 193, 194
curved disclination, 176, 184
curved wedge lines, 157
cutting mode, 505
cutting tools, 502
cylindrical coordinates, 450, 452
Czochralski, 479, 481, 482, 485
Czochralski method, 477, 482, 483

dark-field image, 520
DD, 157, 258
Deborah number, De, 175, 177
Debye frequency, 139
dechiralization lines, 220, 223
decreased asterism, 520
decreasing nano indentation size, 544
defect core, 165

defect structure, 526
defect textures, 177
defect-hedgehog, 170
defects, 529, 530
defects in N*, 229
defects in SmAs (smectics A), 154
deform plastically, 451, 544
deformation pattern, 505
deformation zone, 450, 503, 544
deformation/plastic yielding, 453
deformed material, 525
deformed region, 534, 536
deformed volume, 455
deformed zone, 449, 453, 455, 503, 519, 536
degeneracy parameter, 172
degeneracy-removal, 65
degree of compaction/densification, 449, 450
densification, 453
density, 450, 460
density functional theory, 95
density modulation, 160
density of disclinations, 174
density of dislocations, 157, 176
density of edge dislocations, 257
density of screw dislocations, 211, 251
density of singular defects, 163
depolarization factor, 223
depth, 457
detonation, 405, 426, 433, 439
detonator, 506
developable domain (DD), 155, 202
developable surface, 202, 257
devoid of luminescence, 531
diagonal lengths, 456
diagonals, 535
diamond, 451, 526, 527, 545
diamond anvil, 516
diamond anvil cell, 516
diamond sphere, 453
diamond, silicon carbide, and silicon nitride, 526
diblock copolymers, 199
dielectric anisotropy, 188
diffraction pattern, 520, 523
diffraction pattern vector, 529
diffraction spots asterism, 520
diffusion, 206, 208, 209
dipole-locked phase of A-³He, 216
Dirac monopole, 216
direct observations of dislocations in ionic crystals, 458
direct product, 162
direct product of groups, 158
director, 150, 161, 199, 211, 231

- director n , 226
 director field, 155, 156, 165, 245
 directors, 160, 227
 directors in Nb, 160
 disclination, 160, 204
 disclination core, 170, 176
 disclination densities, 150
 disclination line of strength $k = +1$, 203
 disclination lines, 153, 245
 disclination lines in Nb, 160
 disclination loops, 171, 175
 disclination points, 153, 218
 disclination radius (DR), 255
 disclination strength, 165
 disclinations, 150, 157, 161, 164, 171, 202, 209, 215, 219, 223, 227, 243, 248, 253
 disclinations λ , τ , and χ , 227
 disclinations of strength $k = 1/2$, 184, 198
 discotic, 155
 discotic phases, 203
 discrete spots, 516
 dislocation nucleation site, 463
 dislocation, 156, 193, 206, 463, 470, 484, 486, 508
 dislocation activity, 460, 461, 513, 526
 dislocation arrangement, 514
 dislocation bundles, 410–413
 dislocation core, 3, 4, 9, 14, 17, 26, 31, 33–35, 41, 52, 53, 55–57, 60–62, 64, 69, 74, 75, 409, 411, 435, 439
 dislocation cores, 405, 407, 408, 414, 425, 436, 439, 441
 dislocation densities, 150, 259
 dislocation density, 206, 210, 483, 489, 528, 541, 543, 544
 dislocation dissociation, 356, 361, 367, 369, 371, 376, 380, 382, 383
 dislocation dynamics, 4, 13, 58, 76
 dislocation etch pits, 462, 476, 478, 485, 487
 dislocation glide, 496
 dislocation interactions, 490, 492, 501, 502, 537, 545
 dislocation interactions giving rise to cracking and electrical charging, 451
 dislocation is immobile, 492
 dislocation line, 492
 dislocation lobe B, 515
 dislocation lobes, 514
 dislocation loop diameters, 544
 dislocation loops, 459, 461, 463, 466, 468, 476–478, 486, 488, 489, 492, 514, 515, 520, 525, 527, 543, 544
 dislocation mobility, 3, 4, 8, 10, 11, 13, 18, 21, 24, 26, 28, 29, 32, 36, 41–47, 49–53, 66–68, 71, 74, 75, 84, 142, 451
 dislocation movement, 206
 dislocation multiplication, 140
 dislocation nucleation, 83, 85, 142, 461, 463
 dislocation nucleation, motion, and multiplication, 83
 dislocation number density, 544
 dislocation pile-up, 417, 423, 441, 492
 dislocation pinning, 464, 481
 dislocation pits, 463, 465, 484
 dislocation positions, 475
 dislocation processes, 534, 538, 545
 dislocation profile, 231
 dislocation quenching, 539
 dislocation reaction, 491–493
 dislocation rosette, 464, 466, 473, 475–478
 dislocation rosette ‘edge’ arm, 469
 dislocation rosette arm, 482
 dislocation rosette arm length, 480
 dislocation rosette arms, 473
 dislocation rosette around, 475
 dislocation rosette pattern, 485
 dislocation rosettes, 463, 473, 474, 476, 478, 483, 484, 487–490, 511, 545
 dislocation sources, 461, 481
 dislocation terminates, 486
 dislocation velocities, 486, 505, 510, 545
 dislocation velocity, 450, 508–511
 dislocation walls, 190
 dislocation-free, 459, 512, 513
 dislocation-free area, 541
 dislocation-free Si(100), 519
 dislocation-generated cracks, 501
 dislocations, 157, 160, 161, 163, 178, 184, 187, 193, 194, 202, 204, 209, 215, 224, 225, 243, 275, 279–285, 287, 288, 291, 292, 295–297, 300, 306, 308, 312, 314–328, 330–333, 335, 336, 341, 343, 345, 349, 351, 352, 356–358, 361, 363, 366–368, 370–379, 382, 383, 385–389, 391–393, 395–397, 447, 450, 459, 464, 466, 470, 471, 474, 475, 478, 482, 483, 486, 487, 491, 496, 515, 519, 520, 523, 527, 528, 531, 533, 534, 545
 dislocations gliding, 494, 501
 dislocations in columnar phases, 155
 dislocations in smectics, 155
 dislocations in the rosette, 470
 dislocations in the slip bands, 531
 dislocations of rotation, 157
 dislocations to rearrange themselves, 512
 dislocations within the indentation, 511, 519
 disorientation angle, 190
 disorientations, 192–194
 dispirations, 224, 225, 252, 253–255

- displaced material, 475, 488–490, 493, 494, 506, 525
 displacement, 210, 227, 494, 541
 displacement control, 108
 displacement of material, 496
 displacement transducer, 540
 dissociated partials, 528
 dissolved oxygen, 482
 distorted ordered medium, 159
 distortions with double topological character, 155
 distribution of dislocation etch pits, 466
 distribution of dislocations, 473, 490
 distribution of the etch pits, 477
 divergence term, 180, 245
 Doi regime, 177
 Doi's equations, 177
 dopant, 478, 479
 doping, 479, 487
 doping concentrations, 480
 doping effects, 465
 doping levels, 480
 double twist, 245
 double twist (DT) configuration, 156
 double twist (DT) domains, 243
 double twist (DT) cylinder, 156, 249, 262, 263
 double twist orientational order, 262
 double-twisted configuration, 224
 drag coefficient, 511
 drag force, 209
 drop-weight impact, 419, 420, 422, 441
 DT cylinder packings, 248
 ductile metals, 487
 Dugdale–Barenblatt crack, 108
 Dupin cyclide, 180, 183, 187, 194, 216, 258
 during indenter loading, 468
 dynamic hardness, 449, 510
 dynamic hardness P_d , 510
 dynamic indentations, 545
 dynamic load, 449, 510
 dynamic load P_d , 510
 dynamic loading, 490, 505
 dynamic mean pressure, 449
 dynamic observations, 505
 dynamic shear stress, 510
 dynamically, 491
 dynamically applied shear stress, 510
- Early Universe, 172
 eccentricity, 182, 183, 186, 190, 192, 193, 195
 edge, 160
 edge components, 450, 486
 edge components u_e and v_e , 492
 edge dislocation, 112, 185, 206–208, 230, 231
 edge dislocation densities, 249
 edge dislocations, 150, 156, 204, 206, 215, 228, 238, 255, 464, 466
 edge dislocations in SmA's, 155
 edge dislocations of huge Burgers vectors, 184
 edges of the indentations, 527
 Einstein's relation, 208
 elastic compression, 493
 elastic constants, 450, 451
 elastic deformation, 452
 elastic displacement, 155
 elastic energy, 185
 elastic field, 470
 elastic free energy density, 226
 elastic half space, 455
 elastic moduli, 154
 elastic one-constant approximation, 247
 elastic regime, 451
 elastic region, 503
 elastic strain energy, 105, 492
 elastic stress equations, 510
 elastic stress field, 455, 510, 545
 elastic stresses, 211, 451
 elasticity, 282
 elastic–plastic solid, 541
 elastic/plastic dynamic indentation, 506
 elastic/plastic indentation, 452
 elastic/plastic response, 541
 elastically stored, 456
 elastically stored material, 456
 elastoplastic indentation, 453
 electric field, 188, 213, 214, 220, 224, 239
 electrical conductivity, 516
 electrical resistance, 516
 electrohydrodynamical instabilities, 177
 electron beam damage, 534
 electron diffraction patterns, 516, 517, 519
 electron diffraction spots, 545
 electron micrographs, 519, 520
 electron micrographs and selected area diffraction patterns, 517
 electron microscope, 514, 545
 electron spin resonance, 530
 elemental, 513
 elemental semiconductors, 547
 ellipse, 154, 160, 178, 184, 190, 193, 216, 258
 embedded atom method, 95
 embryonic dislocations, 84, 85, 90, 91, 112, 142
 emission (or absorption) of dislocations, 176
 emission bands, 530
 empirical potentials, 84
 energetically stable, 242
 energy band gap of MgO, 534
 energy barrier, 83

- energy density, 180, 259
 energy levels, 531
 energy release rate, 89, 112
 enhanced brittleness, 491
 enhanced luminescence, 533
 enhanced photoluminescence, 451, 530
 enhancement or quenching of cathodoluminescence, 529
 ensuing plasticity, 544
 envelopes of the normals, 178
 equation of the ruled half helicoid, 196
 equilateral triangle-based pyramid, 451
 equilibrium, 453
 Ericksen number, Er , 176, 177
 Escaig stress, 45, 48–50
 escape in the 3rd dimension, 160, 166, 215, 228, 241, 256
 escape of a trihedron in the 3rd dimension, 216
 etch pit, 415, 431, 433
 etch pit count, 488
 etch pit method, 458
 etch pit sizes, 488
 etch pits, 407, 416, 458, 460, 461, 466, 476, 478, 487–489
 etch pitting, 407, 413, 415, 430
 etch pitting technique, 544
 etchant, 458, 464, 475, 484, 489
 etched, 463, 483, 486, 487
 etched surfaces, 461
 etching, 476, 487
 etching characteristics, 488
 Euclidean group, 163, 243
 Euclidean isometries, 158
 Euclidean space, 158, 245
 Euler characteristic, 168, 181, 216, 218
 Euler equation, 108
 Euler–Lagrange equations, 180
 evolutes of this circle, 203
 examination, 526
 exciting laser beam, 546
 existence of dislocations, 545
 explosive gun, 505
 exposure time, 507
 extended core, 8
 extraordinary index n_e , 165
- F and F^+ centres, 530, 537, 538
 F centres, 530
 F types, 538
 F^+ , 537
 F^+ centres, 537, 538
 F^+ , and F^{++} , 530
 f.c.c. metals, 487
 fast moving dislocations, 449
- fast neutrons, 530
 fast-neutron-irradiated MgO crystals, 530
 FCD, 155, 157, 178, 187, 188, 190, 204, 215, 239, 258
 FCD hyperbolae, 190
 FCD walls, 190
 FCD-I, 183, 186
 FCD-II, 183, 203
 ferroelectric, 155, 213, 214, 220, 225
 fiber, 161, 162
 fiber bundle, 161
 fibers S^1 , 162
 fine slip line structures, 290
 fine-grain cubic Si, 517
 fingerprint texture, 231
 first homotopy group, 159, 163, 253
 first kind, FCD-I, 180
 first order perturbation, 110, 114
 first order phase transition, 154, 243
 first- or a second-order phase transition, 172
 first-order isotropic–nematic transition, 168, 174
 first-order perturbation, 116
 first-order transition, 172
 FK, Frank and Kasper phases, 248
 float-zone, 479, 482, 483
 flow aligning, 177
 flow friction, 206
 flow of material, 493
 flow patterns, 504
 flow plastically, 513
 fluorescence confocal polarizing microscopy (FCPM), 165, 168, 188, 233, 236, 239
 focal conic domain (FCD), 154, 178, 204, 237
 focal lines, 178
 focal surfaces, 178, 198, 263
 foci, 187
 force of friction, 176
 fractal analysis, 299
 fracture, 513
 fracture stresses, 513
 fracture surface energy, 415, 502
 framing speeds, 506
 Frank and Kasper (FK) crystalline phases, 243
 Frank and Kleman model, 263
 Frank and Pryce texture, 242
 Frank constant, 175
 Frank elastic constants, 170, 227
 Frank energy, 172
 Frank theory, 170
 Frank–Oseen elastic free energy density, 170
 free energy, 181, 245
 free energy density, 154, 178, 187, 220, 227
 free standing film, 214, 251

- free suspended thin films, 224
freely suspended films, 219
Frenkel pairs, 474
fresh dislocation etch pits, 460
fresh dislocations, 460
fresh surface area, 460
freshly created dislocations, 458, 460, 539
freshly nucleated dislocations, 461
friction, 207
friction force, 209
Friedel's laws, 190
frustrated, 261, 262
frustrated mesophases, 156
frustrated phases, 243
frustration, 243, 244, 247, 248
full group of rotations, 158
full of dislocations, 522
full ruled helicoid, 196
fundamental group, 159, 163, 164
fused silica, 456
fused silica objective lens, 536
fused silica tube, 535
- GaAs, 474, 486, 487
GaAs(1̄1̄1), 487
GaAs(001), 486
GaAs(100), 486
gallium, 512
GaP, 486
garnet, 355, 356, 384–386, 397
Gauss theorem, 180
Gauss–Bonnet theorem, 181
Gaussian curvature, 180, 183
Gaussian layer curvatures, 180
Ge, 474, 486, 513
Ge(100), 485
Ge(111), 476, 483, 484
generalized stacking fault energy, 86
generation, 460
generatrices, 187
generatrices of the cylinder, 202
geodesic curvature, 181
geodesic lines, 200, 203
geodesic rule, 172
geodesic torsion, 200
germanium, 483, 547
giant Burgers vector screw dislocations, 197
giant Burgers vectors, 194
Ginzburg–Landau constant, 260
Ginzburg–Landau model, 173
Ginzburg–Landau parameter, 261
glide, 206–208, 211, 212, 235, 461, 515
glide plane, 236, 492
glide prisms, 477
- good-quality electron micrographs, 527
grain boundaries, 192, 195, 250
grain boundaries in SmAs, 155
grain boundary, 191, 192, 199
grains, 190
Grandjean model, 192, 193
Grandjean wall, 192
Grandjean wedge, 190, 252
Grandjean–Cano, 206
Grandjean–Cano wedge, 209, 225, 233, 237, 241, 254
grating spectrometer, 536
Griffith cleavage toughness K_{IC} , 119
grinding, 530
group of (generalized) translations, 163
group of continuous translations, 158
group of isometries, 163
group of quantized translations, 163
group of quaternions, 160, 216, 229, 253
group of symmetry of the crystal, 158
grown-in dislocation density, 487, 505
grown-in dislocation density of 10^2 to 10^3 cm^{-2} , 513
grown-in dislocations, 539
growth spirals, 406, 407
- half loops, 466
half ruled helicoid, 195
half space, 457
half-torus, 181
haloes, 516, 520
hard blunt indenter, 451
hard pointed indenter, 544
hard sphere, 459
hard spherical indenter, 457, 467
hardening effect of irradiation, 475
hardest known material, 526
hardness, 471, 480, 519
hardness stress, 418, 419, 435
Harvard model, 175
heavily deformed material, 544
heavily dislocated, 526
heavily dislocated regions, 545
heavy-duty ball bearings, 502
HeCd laser, 534
hedgehog point defect, 256
hedgehogs, 164, 166, 168, 175
helical, 215
helical conformations, 215
helical disclinations, 199, 263
helical instability of the screw dislocation, 210
helical orientational ordering, 156
helical phases, 213

- helicity, 155, 156, 227, 262
 helicoidal surfaces, 262
 helicoids, 198, 200, 263
 helix, 226
 Hertz equations, 457, 460, 461
 hexagonal lattice, 503
 hexagonal order, 262
 hexagonal phase β' -Si₃N₄, 528
 hexagonal phase of Si, 516
 hexagonal structure, 503
 high density of defects, 526
 high density of line and point defects, 529
 high energy electrons, 534
 high hydrostatic component of stress, 516
 high shear stresses, 513
 high strain rate deformation, 530
 high strain rates, 493
 high velocity regime, 511
 high-magnification image, 524
 high-speed camera, 506
 high-speed framing camera, 506
 high-speed photograph, 507
 high-speed photographic sequence, 509
 high-speed photography, 506, 545
 high-velocity regime, 545
 hinterland, 451
 homeotropic, 188, 215, 231
 homeotropic anchoring, 204
 homeotropic boundary conditions, 188
 homeotropically, 211
 homogeneous nucleation, 110, 545
 homogeneous nucleation of dislocations, 461, 463,
 542, 544
 homotopy, 159
 homotopy class, 162
 homotopy classification, 159, 163
 homotopy groups, 163
 hoop stresses, 506
 hot spot, 405, 413, 419, 420, 422, 423, 425, 438,
 439
 hydrodynamical model, 208
 hydrolytic weakening, 368
 hydrostatic component, 455, 519, 544
 hydrostatic pressure, 449, 455, 477, 516, 544
 hydrostatic stress, 513
 hyperbola, 154, 160, 178, 190, 218, 258
 hyperbolic hedgehog, 171
 icosahedron, 244
 identity class, 160
 identity class {I}, 160
 identity element, 160
 immaterial, 155
 impact, 459, 460, 506, 507, 510
 impact load, 509
 impact method, 459
 impact of a hard sphere, 459
 impact sites, 460
 impact stresses generated, 460
 impact test, 461
 impact velocity, 450, 460
 impact/indentation, 497
 impacted, 491, 493
 impacting particle, 510
 impacting sphere, 460
 imperfect dislocation, 84
 impurities, 525, 537
 impurity content, 472, 483, 505, 534, 535
 in situ observations, 497
 incident impact velocity, 450
 incident velocity v_0 , 510
 increasing rate, 491
 indentation, 458, 459, 464, 466, 467, 469, 470, 474,
 475, 484, 488, 493, 501, 505, 513, 520, 521,
 523, 532
 indentation centre, 471
 indentation cracking, 502
 indentation diagonal lengths, 486
 indentation dislocation loops, 477
 indentation dislocation rosettes, 474
 indentation fracture mechanics, 416, 419, 441
 indentation hardness, 449, 451, 455, 456, 477, 479,
 480, 544
 indentation hardness value, 516
 indentation process, 449
 indentation recrystallizes, 512
 indentation rosette, 464, 474, 481, 486
 indentation rosette arm, 472, 486
 indentation rosette arm lengths, 486
 indentation rosette measurements, 478
 indentation rosette patterns, 485
 indentation rosette technique, 473
 indentation rosettes, 464–466, 471, 481, 485, 489
 indentation rosettes in Si(111), 476
 indentation stress field, 452, 464, 477
 indentation temperatures, 485
 indentation volume, 456
 indentation zone, 519, 520, 524, 531
 indentation-enhanced cathodoluminescence and
 photoluminescence, 529
 indentation-enhanced luminescence of single crys-
 tals of α -HgI₂(100), 539
 indentation-fracture-mechanics, 417
 indentation-induced crystallization, 546
 indentation-induced dislocations, 545
 indentation-induced phase transitions, 451, 546
 indentation-induced plasticity, 539

- indentation-induced shear stresses, 468, 471
 indentation-induced temperature rise, 547
 indentations, 447, 456, 457, 473, 487, 520, 547
 indentations in Si and Ge, 477
 indented diamonds, 527
 indented Si, 517
 indenter, 451, 453, 457, 467, 526
 indenter axis, 450
 indenter diagonals, 490, 491
 indenter displacement, 463, 540, 542, 543
 indenter load, 449, 452, 457, 458, 463, 479, 540,
 541
 indenter loading, 455, 470
 indenter shaft, 540
 indenter shapes, 451
 indenter tip, 451
 indenter unloading, 498
 indenters, 452
 individual dislocations, 526
 individual loops, 459
 induced defect, 242, 254
 induced frustrated geometries, 243
 infinitesimal dislocations, 85
 influence of sample temperature, 547
 inhomogeneous nucleation, 122
 initial plasticity, 463
 initial stages of development, 461
 InP, 539
 InP(100), 501
 InSb, 486
 instabilities, 177, 204
 instant of impact, 459
 integer lines in nematics, 163
 integrated cathodoluminescence intensity, 539
 intensity, 538
 inter-frame time, 506, 507
 interaction, 494
 interaction field of the dislocations, 470
 interaction of dislocation loops, 495
 interaction of dislocations, 491, 506
 interface between a lamellar and an isotropic phase,
 190
 interlayer energy, 105
 interlayer potential, 85
 intermetallic compounds, 312, 313
 intermolecular, 441
 intermolecular blockage, 435, 436
 internal stress, 206, 211
 intersecting $\{110\}_{45}$ planes, 492, 494, 495
 intersecting $\{110\}_{45}$ slip planes, 501
 intersecting planes, 491, 494
 intersecting slip planes, 491
 intersections of the slip planes, 505
 interstitial oxygen concentration, 483
 interstitials, 474
 intralayers self-diffusion D_{\perp} , 206
 inversion line, 220
 inversion symmetry, 226
 ion beam bombardment, 512, 514
 ion beam thinning, 513, 519
 ion-beam thinned, 527
 ionic crystals, 449, 458, 465, 472, 486, 487, 490,
 491, 505, 530, 545
 ionic materials, 530
 ionic oxides, 529, 530
 irregular, 528
 irregular loops, 528
 isometric, 178
 isometric distortion, 155, 157, 200
 isometrically distorted state, 200
 isotropic solid, 452, 457
 isotropic–nematic, 154
 isotropic-to-nematic phase transition, 172
 isovalent solutes atoms, 393
 iterative filling, 190, 195
 Joachimstahl's theorem, 200
 jogs, 156
 junction, 11–15, 17, 21, 65, 66
 KCl, 465, 467, 472, 490, 493, 497
 KCl crystal, 467, 506, 510, 511
 KCl single crystal, 507, 511
 KCl(100), 510
 Kibble mechanism, 174, 175
 kink mechanism for deformation, 343
 kink migration, 10, 36, 39, 41, 45–47, 50, 62, 67,
 70
 kink-pair, 6, 35, 36, 38, 39, 41, 43, 45–48, 50, 62–
 66, 70, 71, 74
 kinks, 117, 156, 235–237
 Knoop, 453
 Knoop diamond, 513
 Knoop diamond indenter, 527
 Knoop indentation, 529
 Knoop indenter, 451
 L_{α} , 156
 L_{α} phases, 180
 Lagrange multipliers, 108
 lamellar liquid crystals, 184
 lamellar phase, 180, 226
 lamellar phases, 154, 183, 187, 195, 211, 212, 215,
 227
 lamellar systems, 199, 203, 229
 large densities of dislocations/defects, 526
 large plastic strain, 520

- large shear stresses and strains, 516
 largest shear stress, 466
 laser damage, 426
 laser-damaged, 427
 lateral cracks, 451, 498, 501
 lattice parameters, 516
 lattices, 248
 law of corresponding cones (lcc), 186, 187, 190, 195
 law of impenetrability, 186
 laws of association, 186, 205
 layer undulations, 184
 layered medium, 155
 layered phase, 183
 LC polymer (LCP) nematics, 177
 leading dislocation, 449, 450, 469–471
 leading edge, 510
 left coset, 158
 length of rosette arms on doping, 478
 lengths of the rosette arms, 471
 Leslie–Ericksen approach, 177
 Leslie–Ericksen equations, 175
 LiF, 458, 465, 466, 472, 490, 493, 497
 LiF crystal, 459, 461
 LiF single crystal, 459, 460, 462, 466
 LiF sphere, 459–461
 LiF(100), 491
 LiF(100) crystals, 461
 light bands, 496
 line, 154
 line defects, 153, 157, 164, 165, 174, 253
 line defects of the ordered medium, 159
 line singularities, 164
 line tension, 170, 197, 238, 241
 linear theory, 229
 lines of etch pits, 466
 liquid crystal polymers (LCP), 154
 load axis, 463
 load cell, 540
 load drop, 542
 load drops, 463
 load frame, 540
 load–displacement, 543
 load–displacement curve, 463, 541
 load/P , 541
 loaded quasi-statically, 491
 loaded surface, 461
 loading, 541
 loading apparatus, 497
 loading part, 541
 loading time, 506
 loading–unloading curve, 541
 local plasticity, 513
 local yielding, 453
 localised dynamic loading, 505
 localized plastic deformation/compaction, 455
 locus, 201
 Lomer–Cottrell (LC) lock, 12–15, 17, 21
 loops, 162, 463, 478, 492, 515
 low mobility, 517
 luminescence, 531, 532, 534, 537, 539
 luminescence band at 2.263 eV, 539
 luminescence behaviour, 539
 luminescence sources, 531, 534
 luminescence spectra, 537
 luminescent, 531, 532, 534
 luminescent slip bands, 531
 lyotropic, 154, 156, 193, 211
 lyotropic (biological polymers), 154
 lyotropic L_α , 191
 lyotropic LC's, 197
 lyotropic smectics, 180
 lyotropics, 209
 macroscopic polarization, 155
 magnesium ion vacancies, 530
 magnesium oxide, 357
 magnetic field, 231
 magnitude, 468
 manifold V of internal states, 158
 many-beam bright field image, 519, 521–523
 mapping, 162
 material displaced, 467
 material displaced by indenter, 455, 489, 493, 505
 material displacement, 458
 material flow, 458
 material pile up, 467
 materialization of the χ -director, 256
 materialized, 215, 220, 258
 materialized c field, 216
 maximum applied indenter load, 457
 maximum applied load, 470
 maximum dynamic load, 491
 maximum dynamically generated load, 490
 maximum impact force, 461
 maximum indenter, 449
 maximum indenter load, 472
 maximum indenter tip penetration h_{\max} , 541
 maximum mean normal pressure, 450, 460
 maximum penetration, 450, 506
 maximum penetration z_0 , 510
 maximum quasi-static loads, 490
 maximum shear stress, 450, 451, 460, 461, 542
 maximum strain hardening, 490
 Maxwell reciprocal relation, 94
 mean, 180
 mean contact pressure, 542

- mean curvature, 180
mean indentation pressure, 493
mean normal contact pressure, 457
mean normal pressure, 452, 455, 458
mean pressure, 452, 453
mean pressure/stress, 450
measurements, 453
mechanical properties, 354, 378
mechanical strength, 481
mechanical strength of MgO(100), 473
mechanical strength of Si crystals, 481
median crack, 512
median plane, 463
Meissner phase, 261
membrane, 183, 209
metal oxides, 539
metallurgical model, 208
metals, 487, 526
metals and the size of rosette arms, 464
metastable point defects, 539
method of crystal growth, 479
MgO, 464, 465, 468, 473, 490, 493, 494, 497, 501, 521, 530, 531, 534, 537
MgO crystal, 520, 536, 538
MgO crystals, 464, 530, 534, 537
MgO single crystal, 523, 525
MgO single crystals, 475
MgO(100), 491, 494, 519, 520, 522, 525, 531, 532
MgO(100) crystal, 497
MgO(100) crystals, 495, 542
MgO(100) single crystal, 498, 499
MgO(100) single crystals, 532
micellar phase, 183
micro-indentation hardness, 415
micrograph, 525
microhardness, 480
microhardness measurements, 480
micropipe, 285, 287–289
mild steel, 458, 505
minimal surface, 183, 195, 199
minimum elastic strain energy, 492
minimum strain energy density, 453
mixed dislocations, 160
Mo(001), 526
mobile dislocations, 539
mobility, 156, 157, 207
mobility of an isolated disclination, 176
mobility of dislocations, 451
mobility of point disclinations, 176
modelling, 3, 5, 18, 21, 32, 52, 75
modulus of compressibility, 211
Moebius ribbon, 162
Moiré phase, 156, 243, 262
molecular blockages, 437
molecular chirality, 156
molecular relaxation time, 175, 177
molecules, 441
molten polymers, 248
Monge's surfaces, 200, 203
monopole, 216
Monte-Carlo simulations, 170
movement, 460
movement of a disclination, 176
movement of dislocations, 451
moving dislocations, 539
multi-beam images, 543
multilamellar vesicles, 203
multiplication of dislocations, 451
mutually normal rows of etch pits, 462
- N*, 227
N*, cholesteric, 216
N*, cholesteric phase, 226, 237, 245, 248, 252
N*, cholesterics, 154
Nb_B, biaxial nematic, 154, 216
N, nematic, 154
N, nematic phase, 216, 243
n-type Ge(100), 486
n-type single crystal, 486
n-type single crystals of Si(111), 513
NaCl, 465, 466, 490, 493, 497
NaCl f.c.c. structure, 458
NaCl structure, 492
NaCl structure crystals, 503
NaCl(100), 526
nano hardness behaviour, 545
nano indentation, 540, 542
nano indentation and dislocations, 540
nano indentation apparatus, 540
nano indentation test, 541
nanocrystalline, 544
nanocrystalline material, 516
nanoindentation, 327–330, 463, 489
nanoindentation machine, 462, 480, 545
nanoindentation studies, 463
nanoindentation test, 462
natural torsion, 200
near ultraviolet band, 538
negative Gaussian curvature, 180, 187
nematic, 227
nematic droplet, 168
nematic OP, 160
nematic phase, 159, 241
nematics, 150
nested tori, 180
neutron irradiated MgO, 530
neutron irradiation, 473

- neutron-irradiated crystals, 473
 new luminescence bands, 539, 545
 newly created dislocations, 458
 Newton–Raphson iteration, 108
 Newtonian, 203
 Ni-based superalloy, 292
 nickel chrome steel, 458
 nitrogen atmosphere, 482
 non hydrostatic stresses, 516
 non-basal surfaces, 525
 non-chiral, 214, 227
 non-commutative group, 159, 160
 non-commutativity, 160, 161
 non-contact techniques, 546
 non-hardening, 505
 non-irradiated crystal, 475
 non-irradiated MgO, 475
 non-linear elastic models of edge dislocations in a 1D periodic structure, 229
 non-linear theory, 230, 231
 non-Schmid behaviour, 45, 58
 non-singular configurations, 157
 non-singular defects, 155
 non-trivial elements, 163
 normal pressure, 450, 452, 454
 normal pressure distribution, 450, 452, 453
 normal stresses, 450
 normal subgroup, 158
 nuclear particle irradiation, 464
 nuclear radiation detector, 539
 nucleation and glide of dislocations, 461
 nucleation and growth of dislocations, 545
 nucleation and growth of dislocations by the impact, 462
 nucleation and movement of dislocations, 458
 nucleation of dislocations, 461, 463
 number density, 461, 520, 530, 534, 537
 number density of oxygen ion vacancies, 538
 numerical calculations, 453
 N BP, cholesteric blue phase, 247
 occurrence of cracking, 544
 oddly-shaped, 441
 oddly-shaped molecules, 405
 oily streaks, 184, 185, 187, 188, 203, 237, 240
 olivine, 368, 375, 382, 383, 397
 one-to-one correspondence, 458
 onion texture, 203
 onions, 203
 onset, 460
 onset of plastic yielding, 458
 OP spaces, 161
 open manifolds, 181
 open structure, 456
 optical axis, 165, 507, 508
 optical interference microscopy, 467
 optical interferogram, 467, 469
 optical microscope, 204, 225
 optical vortices, 232
 order parameter, 159, 165
 order parameter space, 163
 order parameter (OP), 155, 160, 162, 172, 213, 214, 216, 219, 251, 255
 ordered media, 158
 ordered texture, 178
 ordinary index n_0 , 165
 orientation, 519
 oriented loop, 159, 162
 origin, 493
 Orowan relation, 206, 211
 orthonormal trihedron, 213
 Oseen formula, 209
 out-diffusion of oxygen, 481, 482
 outermost etch pit lines, 466
 oxides, 341, 346, 353, 354, 356, 358–360, 363, 367, 368, 374, 375, 378, 379, 384, 385, 387, 393, 397
 oxygen concentration, 481, 482
 oxygen ion, 530
 oxygen out-diffusion heat treatment, 482
 oxygen precipitates, 481
 oxygen-free, 483
 p-doped Si(111), 456
 p-type Ge(100), 486
 p-type single crystal of Si, 477
 packing of tori, 190
 pair of pits, 488
 paired partials, 528
 parabolic focal conic domain (PFCD), 195, 203–205
 parallel transport, 247
 partial dislocations in sapphire, 526
 partial kinks, 37–41
 particle impact sites dislocation rosettes, 461
 passage, 218
 Peach and Koehler (PK) force, 176, 206
 Peach–Koehler stress, 235
 Peierls barrier, 6, 9–11, 22, 46, 48, 55, 57, 62, 74
 Peierls potential, 11, 63
 Peierls stress, 5, 6, 9–11, 13, 28, 29, 31, 51, 57–67, 70, 71, 73, 74, 346, 355, 358, 360, 369, 384, 397
 Peierls–Nabarro (PN) model, 10
 Peierls–Nabarro dislocation model, 84–86, 110, 142
 Peierls–Nabarro friction, 235

- Peierls–Nabarro model, 62, 221
 penetration length, 198
 perfect types, 528
 perfectly elastic behaviour, 542
 permanent residual indentations, 513
 permeation, 207–209
 permeation coefficient λ_p , 206
 perovskite, 341, 375, 387, 397
 phase, 215
 phase transformation, 480
 phase transformation of the cubic phase of Si to the β -Sn, 516
 phase transition, 172, 517, 544, 546
 phonon drag, 11, 70–72, 74
 photographic sequence, 510
 photoluminescence, 529–531, 534–536, 538
 photoluminescence bands, 530
 photoluminescence spectra, 536, 538
 photoluminescence studies, 534
 photoplastic effects, 545
 picture frame, 494, 496, 500, 505
 picture frame increased, 498
 pile up, 420–422, 468, 504–506
 pile up of edge dislocations, 467
 piled up, 506
 piled up material, 510
 piling up, 468, 503, 504
 pitch, 155, 196, 198, 200, 210, 214, 223, 226, 231, 237, 247, 254, 259, 263
 PK force, 207, 209, 211
 plan view of the sample, 513
 plan viewing, 512
 plan-view examination, 519
 planar alignment, 165
 planar anchoring, 220
 planar twist disclination, 176
 plane, 492
 plastic conical indentation, 456
 plastic contact depth h_c , 541
 plastic deformation, 83, 452, 490, 502, 524, 527, 539
 plastic deformation state, 511
 plastic flow, 458, 530
 plastic indentation, 459, 526
 plastic mechanisms, 275, 292, 318, 322
 plastic shear, 211
 plastic shear rate, 204
 plastic strain, 529, 537
 plastic yielding, 452, 458, 460, 461, 539
 plastic/elastic boundary, 510
 plastic/elastic indentations, 529
 plastically deformed, 530, 536
 plastically deformed contact, 453
 plastically deformed crystals, 530
 plastically deformed part, 536
 plastically deformed region, 461, 536, 539
 plastically deformed zone, 455, 503
 plasticity, 451, 493, 539
 plate impact experiments, 511
 PN model, Pierls–Nabarro model, 222
 PN stress, 235
 point, 256
 point defects, 153, 154, 162, 164, 166, 227, 242, 531, 534, 539, 545
 point defects—hedgehogs, 174
 point inclinations, 153, 177
 point force, 455, 457
 point load, 510
 point loading, 470, 510
 point singularities, 153, 157, 216
 pointed indenter, 451, 452, 513
 pointed indenters including cones and pyramids, 451
 points, 153
 Poisson's ratio, 89, 449, 452, 454, 457, 471
 polarity effects, 465, 486
 polarization, 213, 220, 222
 polarizing microscope, 215
 polarizing microscopy, 165, 168, 224
 polycrystalline copper, 490
 polytope, 244
 pop-in of dislocations, 542
 positional ordering, 156
 positive Gaussian curvature, 180, 187
 prediction of the existence of dislocations, 544
 preferential etching of silver, 489
 pressure, 455
 pressure distribution, 452, 453
 pressurising fluid, 516
 primary {100} slip bands, 495, 496, 498
 primary {110}₉₀, 498
 primary {110}₉₀ crack, 496, 498
 primary and secondary {100} slip bands, 499
 primary slip system, 465, 526
 principal curvatures, 178, 187, 227
 principal radii of curvature, 178
 prior plastic strain, 545
 prismatic {1210} planes, 525
 prismatic dislocation half loop, 488
 prismatic dislocation loops, 486
 prismatic half loops, 488
 prismatic loops, 476
 prismatic perfect dislocation loops, 529
 prismatic punching of dislocation loops, 477
 prismatic slip systems, 528
 projected area, 453
 projected area of indentation, 449, 541

- projected areas of nano indentations, 541
 projected boundary of contact, 467
 projectile, 450, 506
 projectile impact velocity, 506
 projective 3-plane, 216
 projective plane, 158
 pronounced photoluminescence, 530
 pulverisation, 530
 purely elastic, 542
 purely hydrostatic, 453
 pyramid indentation, 535
 pyramidal indenter, 453, 458

 quantized translations-rotations, 252
 quarter-partial dislocations, 526
 quartz, 355, 368–370, 382, 397
 quasi-static, 486
 quasi-static hardness, 510
 quasi-static indentations, 493
 quasi-static loading experiments, 506
 quasi-static observations, 490
 quasicrystals, 163, 164
 quenching, 545
 quenching of the cathodoluminescence, 539
 quotient manifold, 253
 quotient space, 158, 163

 radial hedgehog, 168, 171, 216
 radially, 455
 radiation damage, 512, 524, 525
 radius of circle, 449
 radius of contact, 451, 452, 458, 461–463
 radius of spherical indenter, 450
 radius of the sphere, 451
 Raman microscope, 536
 Raman microscopy, 546
 Raman peaks, 546
 Raman scattering, 546
 Raman spectroscopy, 546
 Raman spectrum, 546
 reactor neutrons, 473–475
 rebound, 506
 rebound of projectile, 506
 reconstruction defect (RD), 15, 31–37, 39, 61–63
 recrystallization, 531
 rectangular coordinates, 450
 red band, 537
 red phase of mercuric iodide, 539
 reflectivity experiments, 534
 region 1, 519
 region 2, 519
 region 3, 519
 region 4, 519
 relative number density, 537

 relaxed unstable stacking energy, 94
 remains locked in elastically, 489
 residual area, 193
 residual indentation, 467, 490, 546
 residual regions, 192, 194
 residual stress, 501, 520, 538
 residual stress field, 513
 residual stresses, 512, 520
 residual Vickers indentations, 546
 residual zones, 190
 resistance to dislocation mobility, 511
 resistance to dislocation movement, 481
 resistivity, 477
 Reynolds number, 176, 209
 rheological behavior, 155
 rheology of nematic phases, 154
 rhombus-based pyramid, 451
 Rice–Thomson model, 83, 86
 rigid conical indenter, 452, 453
 rigid sphere, 453
 Robinson spherulites, 241
 room-temperature indentations, 516
 room-temperature indentations in Si, 515
 rosette, 464, 466, 477, 486
 rosette arm length, 475, 479, 482, 483, 487
 rosette arm length in Si, 477
 rosette arms, 471–474, 477, 479, 482, 483, 485–488, 545
 rosette length, 479, 482
 rosette patterns, 487
 rosette sizes, 476
 rosette structure, 466, 488
 rosettes, 475–477, 482, 486–488
 rosettes around indentations, 487
 rotation vector, 150, 159, 176
 rotations, 161
 roughening, 71, 74
 row of etch pits, 461
 ruby, 525
 ruled helicoid, 198, 263

 saddle point configuration, 84, 85, 90, 108, 112, 114, 142
 saddle-splay, 170
 saddle-splay coefficient, 245
 saddle-splay constant, 183
 saddle-splay elastic constant, 183, 185
 saddle-splay elastic constant \bar{K} , 187
 saddle-splay modulus \bar{K} , 181
 sapphire, 341, 343, 345, 350, 351, 353, 355–358, 370–375, 384, 387–389, 391, 393–395, 451, 525, 546
 sapphire crystals, 525

- sapphire sphere, 467
scanning electron microscope (SEM), 530, 531, 534
scanning probe microscopy (SPM), 275, 279, 280, 284, 335, 336
scanning transmission electron microscope, 539
scanning tunnelling microscope, or a scanning/transmission electron microscope, 541
scanning tunnelling microscopy, 456
Scherk's first surface, 200
Schläfli notations, 244
Schlieren textures, 165, 166, 215, 225
Schmid stress, 43, 45, 48–50
Schmid's law, 3, 43, 58, 59
Schoen's *I-WP* surface, 249
Schwartz *P* surface, 249
screw components, 450
screw components u_s and v_s , 492
screw dislocation, 135, 150, 195, 199, 224, 225, 228, 468
screw dislocations, 135, 197, 199, 204, 207, 211, 215, 226, 249, 251, 260, 464
second homotopy group, 162
second kind, FCD-II, 180
second-order phase transition, 172–174
secondary {100}, 498
secondary {100} slip bands, 495, 496, 500, 501
secondary {110}₉₀, 498
secondary {110}₉₀ cracks, 498, 500
secondary cracks, 498
secondary electron images, 532
secondary slip systems, 465
segments of the loops, 515
selected area diffraction patterns, 519, 521
selected area electron diffraction patterns, 517
self-diffusivity, 210
semi apical angle α , 452
semi direct product, 160
semi included angle, 449
semi-apical, 456
semi-apical angle, 452
semi-direct product of groups, 158
semi-infinite crack, 105, 106, 108
semiconducting compounds, 465
semiconducting device, 539
semiconductor compound materials, 486
semiconductor compounds, 486, 529
semiconductor crystals, 487
semiconductor materials, 545
semiconductors, 464, 465, 474, 478, 539, 545
semiconductors Si and Ge, 513
sensitive nanoindentation instruments, 545
sessile dislocations, 505
severe asterism, 545
shallow prismatic loops, 476
shapes, 478
sharpening of the diffraction spots, 520
shear cracks, 527
shear deformation, 453
shear flow lines, 453
shear modulus, 449, 461, 471
shear modulus of LiF, 461
shear rate, 175, 203, 206, 211
shear stress, 206, 211, 450, 451, 461, 469–471, 474, 509–513, 516, 544
shear stress τ , 510
shear stress at apex, 452
shear velocity, 203
shear yield stress, 449, 461, 544
shear yield stress of the solid, 542
shock wave, 405, 424, 425, 433, 438, 441, 530
Shockley partials, 15, 19, 25, 528
shuffle set, 22, 30
Si, 456, 474, 476–478, 480, 481, 486, 513, 516, 519, 520, 544
Si single crystal, 477, 478
Si(100), 476–482, 485, 546
Si(100) single, 479
Si(110), 513, 515, 517
Si(111), 514, 516
Si-I, 546
Si-I phase, 546
Si-II phase, 547
Si-III phase, 546, 547
side two-dimensional pressure, 453
silica tubes, 535
silicates, 481
silicon, 475, 480, 546, 547
silicon carbide (SiC), 386, 527, 544
silicon foil, 514
silicon nitride, 341, 386, 387
silver, 487
simple ionic crystals, 465, 477, 490, 497
simple ionic materials, 506
simply connected manifold, 164
simulation, 3–6, 9, 11, 13, 14, 17–21, 23, 24, 28, 31, 32, 37, 40, 41, 45–50, 55, 57–60, 64–69, 71, 72, 74–76
single crystal, 458, 465, 466, 477, 494, 525
single crystal of Ag, 488
single crystal of Ag(111), 489
single crystal of CdTe(111), 539
single crystal of KCl(100), 505
single crystal of LiF, 458, 459
single crystal of MgO, 464
single crystal of MgO(100), 495, 542
single crystal of Si, 475, 546

- single crystal specimens of WC, 503
 single crystals, 456, 457, 478, 501, 504, 525, 526,
 530
 single crystals of 6H-SiC, 543
 single crystals of Ag(111), 489
 single crystals of ceramics, 519
 single crystals of Cu(001), 490
 single crystals of diamond, 527
 single crystals of Ge(111), 483
 single crystals of gold, 463
 single crystals of ionic crystals, 464
 single crystals of KCl(100), 505
 single crystals of LiF, 458, 459, 461, 472, 473
 single crystals of MgO, 535
 single crystals of Si, 516
 single crystals of Si(100), 520
 single crystals of Si(110), 517
 single crystals of TiC(100), 502
 single crystals of WC, 503, 504
 single impacts, 460
 single pop-in event, 542
 singular, 166
 singular cores, 153
 singular disclination point, 216
 singular points, 178
 singularities, 160, 178
 singularity of the order parameter, 162
 sinking, 468
 sinking in, 503–505
 sinking in along the {100} direction, 468
 sinks in, 504
 Sirtl, 477
 Sirtl solution, 477
 size of the picture frame, 496
 slab-dislocations, 254
 slip, 528
 slip bands, 468, 469, 492–496, 498, 531–535, 542
 slip bands' region, 531, 532
 slip direction, 449, 469, 470, 510
 slip plane, 492, 510
 slip planes, 458, 459, 466, 485, 487, 504, 514
 slip planes in diamond, 527
 slip processes, 491, 503
 slip steps, 503
 slip system, 357, 358, 364, 365, 370, 371, 375, 382,
 387, 458, 486, 490, 502, 526
 slip system $\{1\bar{1}00\}\langle1\bar{1}\bar{2}3\rangle$, 503
 slip systems, 342, 355, 356, 360, 367, 379, 388,
 457
 slip-line field theory, 504, 505
 Sm Blue Phases, 243
 Sm BP, 245
 Sm phase, 181
 Sm* phases, 156
 SmA, 156, 172, 178, 187, 193, 195, 204, 212, 216,
 226, 227, 238, 257
 SmA phase, 160, 161
 SmA screw dislocation, 263
 small Burgers vector dislocations, 204
 small Burgers vectors, 195, 197, 208, 230
 Small Molecule LC (SMLC), 175, 177
 SmAs, 178
 SmC, 155, 172, 195, 212, 215
 SmC phase, 161
 SmC*, 155, 212, 215, 224
 SmC_A^{*}, 212, 225
 SmC_A, 225
 SmC, smectic C, 216
 Smectic Blue Phases, 156
 smectic elastic compression modulus, 259
 smectic layers, 183
 smectic OP, 197
 smectic phases, 183, 243
 smectic–isotropic interface, 190
 smectics, 153, 184, 204, 206, 215, 241
 smectic A (SmA), 153
 smectic C (SmC), 153
 SmI*, 224
 SmO phase, 215, 226
 SmQ phase, 199
 soda-lime glass, 453
 soda-lime glass windows, 537
 solitons, 162, 164
 solution hardening, 360, 364, 367, 393, 394, 396
 space charge, 223
 space field of the order parameter, 156
 space groups, 248
 spatial distribution, 533
 specimen, 512
 specimen preparation for TEM studies, 512
 specimen thinning, 545
 spectra, 536
 sphere, 451, 506
 sphere S^2 , 181
 sphere impact test, 461
 spherical indentation, 458, 490, 493
 spherical indenter, 457, 461, 490, 513, 545
 spherical polar coordinates, 450, 454, 455
 spherical projectiles, 493
 spherical quasistatic indentation experiments, 461
 spherulite, 180, 203, 216, 218, 255, 257
 spinel, 341–344, 347, 348, 350–352, 354, 356–358,
 376, 378, 380, 381, 384, 387–391, 397
 splay, 170, 227
 splay and the saddle-splay elastic constants, 180
 splitting of a dislocation, 233
 splitting of the dislocation, 199

- spontaneous defect, 242
spontaneous polarization, 213
spot diffraction pattern, 519
square indentation, 449, 470
square-based pyramid, 451
square-shaped picture, 493
square-shaped picture frame, 494
square-shaped slip bands, 494
square-shaped slip traces, 497
SrO, 530
SrO and CaO, 538
stable topological defects, 168
stacking fault, 7–11, 14–17, 22, 25–27, 37, 39, 45, 47–50, 55
stacking fault energy, 345, 349, 350, 352, 353, 361, 362, 371, 374, 376, 380, 384
stacking fault tetrahedra (SFT), 19–21, 68
stages, 463
steady-state, 210, 211
stiff indenter shaft, 540
strain elasticity, 154
strain energy, 154, 180, 198
strain energy density, 195, 450, 453, 454
strain rate, 461, 510
strain-hardening characteristics, 545
strength, 157
strength of ‘blister’ field, 449
strength of the disclination, 170
strength of surface anchoring, 167
strength of the blister field, 455
stress, 211, 455
stress anomaly, 312
stress components, 454
stress conditions, 459
stress distribution, 452, 453
stress equations, 457
stress field, 452, 464, 544
stress gradient, 512, 531
stress intensity factors, 89, 105, 112
stress relaxation, 512
stress state, 453
stresses, 206, 209, 210
strings, 172
strong covalent bonding, 503
strongly twisted ($L/p \gg 1$) cholesterics, 226, 227
structural chirality, 156
structural phase transition, 516
subgroup, 158, 162
subspace iteration procedure, 117
subsurface lateral crack, 506
subsurface structure, 519
successively etching, 490
sudden burst of dislocations, 498
sudden load drops, 463
suggested slip process, 525
surface, 230, 451
surface alignment, 167
surface anchoring, 168, 185, 187, 195, 216, 227, 231, 237, 239, 241, 242
surface anchoring energy, 168, 183, 188, 195, 220
surface area of indentation, 449
surface artefacts, 521
surface defects, 162
surface displacement, 467
surface energy, 94, 191, 222
surface energy anisotropy, 190
surface features, 277, 286
surface orientation, 168
surface production resistance, 92, 101
surface profile around an indentation, 469
switching devices, 213
symmetries of disclinations, 157
symmetries of rotation, 157
symmetries of translation, 157
symmetry axis, 451
symmetry breaking, 36
symmetry group, 243, 252
symmetry of rotation, 165
symmetry point group, 155, 160
symmetry-breaking, 32, 61
symmetry-breaking phase transitions, 172

T_wGB, 199, 200
tangential, 165, 168, 188
tangential material displacement, 467
Te-doped GaAs, 487
TEM, 513, 516, 517, 519, 525–528, 544
TEM investigations, 513, 526
TEM observations, 520
TEM specimens, 516
TEM studies, 512, 513, 519
temperature rise within the deformation zone, 546
tensile hoop stresses, 491, 502
tension softening, 84, 135
tension-softening effect, 118
test crystal, 459
TFCD, 192
TGB (twist grain boundary) phases, 251
TGB phase, 156, 243, 261
TGB-like columnar phase, 156
TGBA, 156, 251, 252
TGBA phase, 244, 248, 257
TGBC, 156, 248, 251
TGBC*, 156, 251
TGBC_A, 156
TGBCa, 251
theoretical shear strength, 83

- theoretical shear strength of crystals, 461
 theoretical shear stress of gold, 463
 theoretical tensile strength, 83
 theories of nano hardness, 544
 thermal decomposition, 429–432, 437
 thermal neutrons, 474
 thermal stresses, 481
 thermotropic, 154, 156, 186, 193, 211, 215
 thermotropic cholesterics, 241
 thermotropic LC's, 197
 thermotropic SmA, 191, 208
 thermotropics, 183
 thick, 153, 165, 166, 177
 thin, 153, 165, 166, 177
 thin films of sapphire, 525
 thinned chemically, 514
 thinning, 512
 thinning process, 512
 third homotopy group, 162
 Thompson tetrahedron, 8, 12
 three-dimensional picture the distribution of dislocations, 490
 three-point bend test, 461, 474
 Ti^{3+} , 525
 TiC, 502
 tilt boundary, 155, 206
 tilt conditions, 520, 522
 tilt grain boundaries, 190, 261
 tilt wall, 190
 topological charge, 166, 223
 topological charge of a defect, 159
 topological classification, 161, 163, 216
 topological classification of defects, 153
 topological defect, 160, 168, 172
 topological point defects, 253
 topological point defects in nematics, 171
 topological shift, 206
 topological stability, 172
 topological theory, 228
 topologically stable, 163, 165, 216, 219, 242, 256
 topology, 181
 toric FCD, 190, 193
 torsions of the column, 201
 torus T^2 , 181
 total curvature energy, 182
 total kinetic energy, 510
 total luminescence, 534
 total number of dislocations, 471
 total volume of material flowing out, 455
 translation-rotation space group, 156
 translation-rotation symmetries, 253
 translational symmetries, 157
 translations, 161
 transmission electron, 545
 transmission electron micrographs, 514, 520, 529
 transmission electron microscope, 512, 514
 transmission electron microscopy (TEM), 475, 512, 533, 544
 transmission electron microscopy of single crystals of 6H-SiC(0001), 542
 transmission electron microscopy study, 477, 486
 transmission electron microscopy X-ray topography, 451
 transparent ionic crystals, 545
 transverse slip processes, 487
 treated Si wafer, 482
 trigonal prism, 503
 trihedron, 219, 225
 trihedron of directors, 155
 trivial elements, 163
 trivial loop, 163
 tumbling, 177
 tungsten carbide, 451, 469, 502–504, 506
 tungsten carbide sphere, 491
 tungsten indenters, 463
 tungsten sphere, 493
 twinning, 299, 305, 308, 311, 336, 525
 twinning-antitwinning asymmetry, 69, 70
 twist, 170, 203, 227, 260
 twist χ disclinations, 228
 twist disclinations, 150, 176, 222, 250
 twist dislocations, 157
 twist grain boundaries (TGB), 155, 195, 199, 249, 251, 257, 261
 twist grain boundary phase, TGB, 199
 twist viscosity coefficient, 176
 twist-constant K_{22} , 227
 twist-edge dispiration, 224, 226, 254
 two-dimensional pressure, 454
 type of dopant, 479
 typical nano indentation machine, 540
 ultraviolet/visible Raman microscope, 534
 unannealed, 538
 unannealed indentation, 536, 537, 538
 unannealed indents, 535
 unannealed Vickers indentation, 519
 undeformed part, 536, 538
 undeformed part of the crystal, 536
 undeformed Si, 519
 undoped, 487
 undulated TGBC* phase (U-TGBC*), 156, 251
 undulation instability, 203
 undulations, 204
 uniaxial, 171
 uniaxial compression or tension, 466
 uniaxial compression tests, 458

- uniaxial nematic, 158
uniaxial nematic phase, 164
uniaxial nematics, 153
uniaxial stressing, 513
uniaxial yield stress, 458, 493
uniaxial yield stress of test solid, 450
uniaxially compressed MgO crystals, 531
uniform, 453
uniform pressure, 453
uniform resistive 2-dimensional pressure, 450
universal behavior of lamellar phases, 204
universal constant, 449, 471
universal cover, 164
unloaded nano indentations, 541
unloading, 541
unloading part, 541
unrelaxed unstable stacking energy parameter, 94
unstable stacking energy, 86, 142
unstable stacking energy γ_{us} , 86
untreated Si wafer, 482
upwards, 494
uranium oxide, 365
- vacancies, 474, 530
vacancies in solids, 171
vacancy clusters, 530
vacuum or the order parameter space (OP space), 158
valence states, 534
variation of nano hardness of materials, 545
variational boundary integral method, 85, 105, 135, 142
various slip bands, 495
various slip planes, 466
velocity, 208
velocity of the crack, 509
very heavily work-hardened, 505
very high rates of strain, 490
very large plastic strains, 545
Vickers, 453, 457
Vickers and Knoop diamond indenters, 516, 525
Vickers diamond, 503, 520, 523, 526, 532, 535, 546
Vickers diamond indentation, 465, 476, 478, 514, 531, 539, 546
Vickers diamond indenter, 483, 516, 519, 525
Vickers diamond pyramid, 476, 484, 494, 503, 513, 531, 538
Vickers hardness, 449, 484, 485, 502, 503, 510
Vickers indent, 521, 538
Vickers indentation, 466, 471, 475, 477, 478, 489, 503, 505, 522, 525, 546
Vickers indentations, 456, 472, 473, 477, 480–482, 485, 487, 488, 491, 501, 503, 504, 516, 526
Vickers indenter, 451, 486, 490, 494, 540
- Vickers pyramid, 468, 473, 489, 490
Vickers unannealed indentation, 538
Vineyard's theory, 117
violent agitation, 530
viscosity, 209
viscous drag, 511
viscous drag coefficient, 449, 511
viscous relaxation, 157
Volterra classifications, 163
Volterra dislocation, 85
Volterra process (VP), 157, 163
Volterra screw, 160
volume, 457
volume displaced by the indenter, 456, 489
volume of indentation, 450, 456
volume of material, 456
volume of the displaced material, 488
volume reduction, 475
volume within the deformed zone, 453
vortex lines, 259
vorticity, 211
VP, 157, 159
VP classification, 161
- W, 456, 503
wafer, 482
wall defects, 164
walls, 216, 219, 243
WC, 503
WC crystals, 504
WC under a sufficiently high load, 503
WC–Co composites, 502
weak shear deformations, 155, 203
weak surface anchoring, 237
weakly twisted cholesterics, 227
weakly twisted cholesterics ($L/p \ll 1$), 226
wedge disclination, 150, 157, 176, 225, 250
wedge indenting a rigid/perfectly plastic solid, 504
wedge line cores, 170
wedge lines, 157
wedge-screw dispiration, 224–226
well-developed rosette, 475
work hardening, 388, 389, 391–393, 505
work softening, 389–391
work-hardening characteristics, 504
worm texture, 178
- X-ray topography, 407, 410, 411, 413, 414, 417, 432
X-ray nuclear particles, 472
xenon flash light, 506
- yield stress, 205, 210, 451, 458, 473, 474

- yielded material, 453
yielded zone, 453, 454
yielding, 453
yielding process, 453
Young's modulus, 449, 452, 457, 460
- yttrium oxide, 385
zirconium oxide, 363
Zn-doped GaAs, 487
Zurek-Kibble mechanism, 168, 172, 174